Gear Geometry and Applied Theory

Second Edition

Faydor L. Litvin

Alfonso Fuentes

This page intentionally left blank

GEAR GEOMETRY AND APPLIED THEORY
Second Edition

Revised and expanded, *Gear Geometry and Applied Theory*, *2nd edition*, covers the theory, design, geometry, and manufacture of all types of gears and gear drives. *Gear Geometry and Applied Theory* is an invaluable reference for designers, theoreticians, students, and manufacturers. This new edition includes advances in gear theory, gear manufacturing, and computer simulation. Among the new topics are (1) new geometry for modified spur and helical gears, face-gear drives, and cycloidal pumps; (2) new design approaches for one-stage planetary gear trains and spiral bevel gear drives; (3) an enhanced approach for stress analysis of gear drives with FEM; (4) new methods of grinding face-gear drives, generating double-crowned pinions, and generating new types of helical gears; (5) broad application of simulation of meshing and TCA; and (6) new theories on the simulation of meshing for multi-body systems, detection of cases wherein the contact lines on generating surfaces may have their own envelope, and detection and avoidance of singularities of generated surfaces.

Faydor L. Litvin is Director of the Gear Research Center and Distinguished Professor Emeritus in the Department of Mechanical and Industrial Engineering, University of Illinois at Chicago. He holds patents for twenty-five inventions, and he was recognized as Inventor of the Year by the University of Illinois at Chicago in 2001.

Alfonso Fuentes is Associate Professor of Mechanical Engineering at the Polytechnic University of Cartagena.

Gear Geometry and Applied Theory

SECOND EDITION

Faydor L. Litvin
University of Illinois at Chicago

Alfonso Fuentes
Polytechnic University of Cartagena

CAMBRIDGE
UNIVERSITY PRESS

Contents

Foreword

The main topics of the book are the theory of gearing, computerized design, generation, simulation of meshing, and stress analysis of gear drives. The first edition of the book is already considered the leading reference in the field by the engineering community, but this edition complements the first with new chapters and thoughtful revision of the previous version, which will make it very useful for the design and manufacture of gear drives.

New ideas of gear design presented in the book include:

(1) Development of gear drives with improved bearing contact, reduced sensitivity to misalignment, and reduced transmission errors and vibration. These goals are achieved by (i) simultaneous application of local synthesis of gear drives and computerized simulation of meshing and contact and (ii) application of a predesigned parabolic function of transmission errors that is able to absorb linear functions of transmission errors caused by misalignments.
(2) Development of enhanced finite element analysis of stresses with the following features: (i) the contacting model of teeth is developed automatically, on the basis of analytical representation of equations of tooth surfaces; (ii) the formation of bearing contact is investigated for several pairs of teeth in order to detect and avoid areas of severe contact stresses.
(3) Improved conditions of load distribution in planetary gear trains by modification of the applied geometry and regulation of installment of planet gears on the carrier.

New approaches are presented for gear manufacture that enable (i) grinding of face-gear drives by application of a grinding worm of a special shape and (ii) design and manufacture of new types of helical gears with double-crowned pinions for obtaining localization of bearing contact and reduction of transmission errors.

The developed theory of gearing presented in the book will make the authors the experts in this area. The book includes the solution to the following important complex problems:

(i) development of new approaches for determination of an envelope to the family of surfaces including the formation of the envelope by two branches;
(ii) avoidance of singularities of tooth surfaces and undercutting in the process of generation; and

(iii) simplification of the contacting problem by a new approach for the determination of principal curvatures and directions of an envelope.

The developed ideas have been applied to the design of gear drives, including a new version of Wildhaber–Novikov helical gear drives, spiral bevel gears, and worm-gear drives. Computerized simulation of meshing and contact and testing of prototypes of gear drives have confirmed the effectiveness of the ideas presented in the book. Three patents for new manufacturing approaches have been obtained by Professor Faydor L. Litvin and representatives of gear companies.

The main ideas in the book have been developed by the authors and their associates at the Gear Research Center of the University of Illinois at Chicago. They have also been the subject of a great number of international publications of permanent interest. Thanks to the wonderful leadership of Professor Faydor L. Litvin, who is universally well known in the field of gears, this Center has involved representatives of various universities in the United States, Italy, Spain, and Japan in gear research. The publication of this book will certainly enhance the education and training of engineers in the area of gear theory and design of gear transmissions.

Prof. Eng. Graziano Curti
Politecnico di Torino, Italy

Preface

The contents of the second edition of the book have been thoroughly revised and substantially augmented in comparison with the first edition of 1994.

New topics in the second edition include the following new developments:

(1) A new geometry of modified spur gears, helical gears with parallel and crossed axes, a new version of Novikov–Wildhaber helical gears, a new geometry of face-gear drives, geometry of cycloidal pumps, a new approach for design of one-stage planetary gear trains with improved conditions of load distribution, and a new approach for design of spiral bevel gear drives with a reduced level of noise and vibration and improved bearing contact.

(2) Development of an enhanced approach for stress analysis of gear drives by application of the finite element method. The advantage of the developed approach is the analytical design of the contacting model based on the analytical representation of the gear tooth surfaces.

(3) Development of a new method of grinding of face-gear drives, new methods of generation of double-crowned pinions for localization of the bearing contact and reduction of transmission errors, and application of modified roll for reduction of transmission errors.

(4) Broad application of simulation of meshing and tooth contact analysis (TCA) for determination of the influence of errors of alignment on transmission errors and shift of the bearing contact. This approach has been applied for almost all types of gear drives discussed in the book.

(5) The authors have contributed to the development of the modern theory of gearing. In particular, they have developed in this new edition of the book (i) formation of an envelope by two branches, (ii) an extension of simulation of meshing for multi-body systems, (iii) detection of cases wherein the contact lines on the generating surface may have their own envelope, and (iv) detection and avoidance of singularities of generated surfaces (for avoidance of undercutting during the process of generation).

The authors are grateful to the companies and institutions that have supported their research and to the members of the Gear Research Center of the University of Illinois at Chicago who tested their ideas as co-authors of joint papers (see Acknowledgments).

Acknowledgments

The authors express their deep gratitude to the institutions and companies that have supported their research and to colleagues and co-authors of accomplished research projects. The following list of names only partially covers those to whom the authors are obliged for their valuable help and inspiration:

(1) Dr. John J. Coy, Assistant Director, NASA Airspace System Program, NASA Ames Research Center; formerly Manager, Mechanical Components Branch, NASA Glenn Research Center

(2) Dr. Robert Bill, Director; James Zakrajsak, Transmission Chief; Dr. Robert F. Handschuh, Senior Researcher; NASA John Glenn Research Center and Army Research Laboratory

(3) Dr. Gary L. Anderson, U.S. Army Research Office

(4) James S. Gleason, Chairman, The Gleason Corporation; Gary J. Kimmet, Vice-President, Worldwide Sales & Marketing, The Gleason Corporation; Ralph E. Harper, Secretary and Treasurer, The Gleason Corporation; John V. Thomas, Director of Gear Technology, The Gleason Works

(5) Ryuichi Yamashita, Vice-President; Kenichi Hayasaka, Manager, Gear Research and Development Group; Yamaha Motor Co., Japan

(6) Terrel W. Hansen, Manager; Robert J. King, former Manager; Gregory F. Heath, Project Engineer; The Boeing Company – McDonnell Douglas Helicopter Systems

(7) Dr. Robert B. Mullins, Director of Engineering; Ron Woods, Technical Resource Specialist; Bell Helicopter Textron

(8) Edward Karedes, Chief – Transmissions; Bruce Hansen, Manager, Research and Development; Sikorsky Aircraft Corporation

(9) Daniel V. Sagady P.E., Vice-President, Engineering & Product Development; Theresa M. Barrett, Executive Engineer; Dr. Mauro De Donno, Area Manager – Gears (Guanajuato Gear & Axle); Dr. Jui S. Chen, Senior Engineer Gear Design; American Axle & Manufacturing

(10) Tom M. Sep, Senior Technical Fellow; Visteon Corporation

1 **Coordinate Transformation**

1.1 HOMOGENEOUS COORDINATES

A position vector in a three-dimensional space (Fig. 1.1.1) may be represented (i) in vector form as

$$\mathbf{r}_m = \overline{O_m M} = x_m \mathbf{i}_m + y_m \mathbf{j}_m + z_m \mathbf{k}_m \qquad (1.1.1)$$

where $(\mathbf{i}_m, \mathbf{j}_m, \mathbf{k}_m)$ are the unit vectors of coordinate axes, and (ii) by the column matrix

$$\mathbf{r}_m = \begin{bmatrix} x_m \\ y_m \\ z_m \end{bmatrix}. \qquad (1.1.2)$$
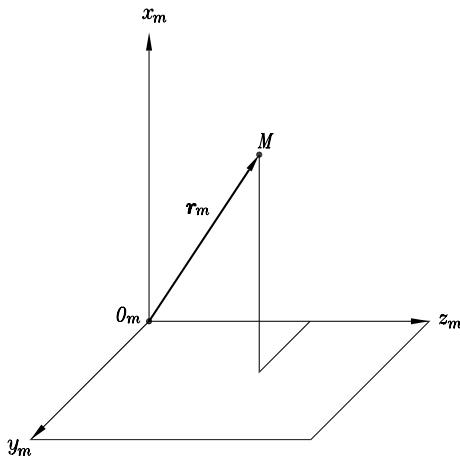
The subscript "m" indicates that the position vector is represented in coordinate system $S_m(x_m, y_m, z_m)$. To save space while designating a vector, we will also represent the position vector by the row matrix,

$$\mathbf{r}_m = [x_m \quad y_m \quad z_m]^{\mathrm{T}}. \qquad (1.1.3)$$

The superscript "T" means that $\mathbf{r}_m^{\mathrm{T}}$ is a transpose matrix with respect to $\mathbf{r}_m$.

A point – the end of the position vector – is determined in Cartesian coordinates with three numbers: x, y, z. Generally, coordinate transformation in matrix operations needs mixed matrix operations where both multiplication and addition of matrices must be used. However, only multiplication of matrices is needed if position vectors are represented with homogeneous coordinates. Application of such coordinates for coordinate transformation in theory of mechanisms has been proposed by Denavit & Hartenberg [1955] and by Litvin [1955]. Homogeneous coordinates of a point in a three-dimensional space are determined by four numbers (x^*, y^*, z^*, t^*) which are not equal to zero simultaneously and of which only three are independent. Assuming that $t^* \neq 0$, ordinary coordinates and homogeneous coordinates may be related as follows:

$$x = \frac{x^*}{t^*} \quad y = \frac{y^*}{t^*} \quad z = \frac{z^*}{t^*}. \qquad (1.1.4)$$

Figure 1.1.1: Position vector in Cartesian coordinate system.

With $t^* = 1$, a point may be specified by homogeneous coordinates such as $(x, y, z, 1)$, and a position vector may be represented by

$$\mathbf{r}_m = \begin{bmatrix} x_m \\ y_m \\ z_m \\ 1 \end{bmatrix} \text{ or}$$

$$\mathbf{r}_m = [x_m \quad y_m \quad z_m \quad 1]^\mathrm{T}.$$

1.2 COORDINATE TRANSFORMATION IN MATRIX REPRESENTATION

Consider two coordinate systems $S_m(x_m, y_m, z_m)$ and $S_n(x_n, y_n, z_n)$ (Fig. 1.2.1). Point M is represented in coordinate system S_m by the position vector
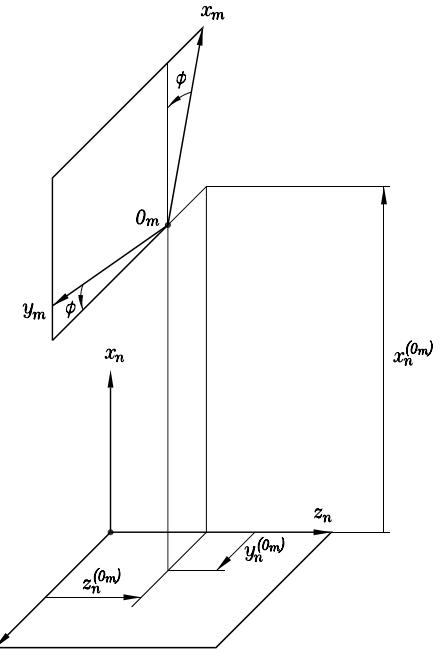
$$\mathbf{r}_m = [x_m \quad y_m \quad z_m \quad 1]^\mathrm{T}. \tag{1.2.1}$$

The same point M can be determined in coordinate system S_n by the position vector

$$\mathbf{r}_n = [x_n \quad y_n \quad z_n \quad 1]^\mathrm{T} \tag{1.2.2}$$

with the matrix equation

$$\mathbf{r}_n = \mathbf{M}_{nm}\mathbf{r}_m. \tag{1.2.3}$$

Figure 1.2.1: Derivation of coordinate transformation.

Matrix $\mathbf{M}_{nm}$ is represented by

$$\mathbf{M}_{nm} = \begin{bmatrix} a_{11} & a_{12} & a_{13} & a_{14} \\ a_{21} & a_{22} & a_{23} & a_{24} \\ a_{31} & a_{32} & a_{33} & a_{34} \\ 0 & 0 & 0 & 1 \end{bmatrix}$$

$$= \begin{bmatrix} (\mathbf{i}_n \cdot \mathbf{i}_m) & (\mathbf{i}_n \cdot \mathbf{j}_m) & (\mathbf{i}_n \cdot \mathbf{k}_m) & (\overline{O_nO_m} \cdot \mathbf{i}_n) \\ (\mathbf{j}_n \cdot \mathbf{i}_m) & (\mathbf{j}_n \cdot \mathbf{j}_m) & (\mathbf{j}_n \cdot \mathbf{k}_m) & (\overline{O_nO_m} \cdot \mathbf{j}_n) \\ (\mathbf{k}_n \cdot \mathbf{i}_m) & (\mathbf{k}_n \cdot \mathbf{j}_m) & (\mathbf{k}_n \cdot \mathbf{k}_m) & (\overline{O_nO_m} \cdot \mathbf{k}_n) \\ 0 & 0 & 0 & 1 \end{bmatrix}$$

$$= \begin{bmatrix} \cos(\widehat{x_n, x_m}) & \cos(\widehat{x_n, y_m}) & \cos(\widehat{x_n, z_m}) & x_n^{(O_m)} \\ \cos(\widehat{y_n, x_m}) & \cos(\widehat{y_n, y_m}) & \cos(\widehat{y_n, z_m}) & y_n^{(O_m)} \\ \cos(\widehat{z_n, x_m}) & \cos(\widehat{z_n, y_m}) & \cos(\widehat{z_n, z_m}) & z_n^{(O_m)} \\ 0 & 0 & 0 & 1 \end{bmatrix}. \qquad (1.2.4)$$

Here, $(\mathbf{i}_n, \mathbf{j}_n, \mathbf{k}_n)$ are the unit vectors of the axes of the "new" coordinate system; $(\mathbf{i}_m, \mathbf{j}_m, \mathbf{k}_m)$ are the unit vectors of the axes of the "old" coordinate system; O_n and O_m are the origins of the "new" and "old" coordinate systems; subscript "nm" in the designation $\mathbf{M}_{nm}$ indicates that the coordinate transformation is performed from S_m to

S_n. The determination of elements a_{lk} $(k = 1, 2, 3; l = 1, 2, 3)$ of matrix $\mathbf{M}_{nm}$ is based on the following rules:

(i)   Elements of the 3×3 submatrix

$$\mathbf{L}_{nm} = \begin{bmatrix} a_{11} & a_{12} & a_{13} \\ a_{21} & a_{22} & a_{23} \\ a_{31} & a_{32} & a_{33} \end{bmatrix} \tag{1.2.5}$$

represent the direction cosines of the "old" unit vectors $(\mathbf{i}_m, \mathbf{j}_m, \mathbf{k}_m)$ in the "new" coordinate systems S_n. For instance, $a_{21} = \cos(\widehat{y_n, x_m})$, $a_{32} = \cos(\widehat{z_n, y_m})$, and so on. The subscripts of elements a_{kl} in matrix (1.2.5) indicate the number l of the "old" coordinate axis and the number k of the "new" coordinate axis. Axes x, y, z are given numbers 1, 2, and 3, respectively.

(ii)   Elements a_{14}, a_{24}, and a_{34} represent the "new" coordinates $x_n^{(O_m)}$, $y_n^{(O_m)}$, $z_n^{(O_m)}$ of the "old" origin O_m.

Recall that nine elements of matrix $\mathbf{L}_{nm}$ are related by six equations that express the following:

(1)   Elements of each row (or column) are direction cosines of a unit vector. Thus,

$$a_{11}^2 + a_{12}^2 + a_{13}^2 = 1, \qquad a_{11}^2 + a_{21}^2 + a_{31}^2 = 1, \qquad \cdots . \tag{1.2.6}$$

(2)   Due to orthogonality of unit vectors of coordinate axes, we have

$$[a_{11}\ a_{12}\ a_{13}]\,[a_{21}\ a_{22}\ a_{23}]^{\mathrm{T}} = 0$$

$$[a_{11}\ a_{21}\ a_{31}]\,[a_{12}\ a_{22}\ a_{32}]^{\mathrm{T}} = 0. \tag{1.2.7}$$

An element of matrix $\mathbf{L}_{nm}$ can be represented by a respective determinant of the second order [Strang, 1988]. For instance,

$$a_{11} = \begin{vmatrix} a_{22} & a_{23} \\ a_{32} & a_{33} \end{vmatrix}, \qquad a_{23} = (-1)\begin{vmatrix} a_{11} & a_{12} \\ a_{31} & a_{32} \end{vmatrix}. \tag{1.2.8}$$

To determine the new coordinates $(x_n, y_n, z_n, 1)$ of point M, we have to use the rule of multiplication of a square matrix (4×4) and a column matrix (4×1). (*The number of rows in the column matrix is equal to the number of columns in matrix $\mathbf{M}_{nm}$.*) Equation (1.2.3) yields

$$\begin{aligned} x_n &= a_{11}x_m + a_{12}y_m + a_{13}z_m + a_{14} \\ y_n &= a_{21}x_m + a_{22}y_m + a_{23}z_m + a_{24} \\ z_n &= a_{31}x_m + a_{32}y_m + a_{33}z_m + a_{34}. \end{aligned} \tag{1.2.9}$$

The purpose of the *inverse* coordinate transformation is to determine the coordinates (x_m, y_m, z_m), taking as given coordinates (x_n, y_n, z_n). The inverse coordinate transformation is represented by

$$\mathbf{r}_m = \mathbf{M}_{mn}\mathbf{r}_n. \tag{1.2.10}$$

The inverse matrix $\mathbf{M}_{mn}$ indeed exists if the determinant of matrix $\mathbf{M}_{nm}$ differs from zero.

There is a simple rule that allows the elements of the inverse matrix to be determined in terms of elements of the direct matrix. Consider that matrix $\mathbf{M}_{nm}$ is given by

$$\mathbf{M}_{nm} = \begin{bmatrix} a_{11} & a_{12} & a_{13} & a_{14} \\ a_{21} & a_{22} & a_{23} & a_{24} \\ a_{31} & a_{32} & a_{33} & a_{34} \\ 0 & 0 & 0 & 1 \end{bmatrix}. \tag{1.2.11}$$

It is necessary to determine the elements of matrix $\mathbf{M}_{mn}$ represented by

$$\mathbf{M}_{mn} = \begin{bmatrix} b_{11} & b_{12} & b_{13} & b_{14} \\ b_{21} & b_{22} & b_{23} & b_{24} \\ b_{31} & b_{32} & b_{33} & b_{34} \\ 0 & 0 & 0 & 1 \end{bmatrix}. \tag{1.2.12}$$

Here,

$$\mathbf{M}_{mn} = \mathbf{M}_{nm}^{-1}, \quad \mathbf{M}_{mn}\mathbf{M}_{nm} = \mathbf{I}$$

where $\mathbf{I}$ is the identity matrix.

The submatrix $\mathbf{L}_{mn}$ of the order (3×3) is determined as follows:

$$\mathbf{L}_{mn} = \begin{bmatrix} b_{11} & b_{12} & b_{13} \\ b_{21} & b_{22} & b_{23} \\ b_{31} & b_{32} & b_{33} \end{bmatrix} = \begin{bmatrix} a_{11} & a_{21} & a_{31} \\ a_{12} & a_{22} & a_{32} \\ a_{13} & a_{23} & a_{33} \end{bmatrix} = \mathbf{L}_{nm}^{\mathrm{T}}. \tag{1.2.13}$$

The remaining elements (b_{14}, b_{24}, and b_{34}) are determined with the following equations:

$$b_{14} = -(a_{11}a_{14} + a_{21}a_{24} + a_{31}a_{34}) \Rightarrow - \begin{bmatrix} :a_{11}: & a_{12} & a_{13} & :a_{14}: \\ :a_{21}: & a_{22} & a_{23} & :a_{24}: \\ :a_{31}: & a_{32} & a_{33} & :a_{34}: \\ :0: & 0 & 0 & :1: \end{bmatrix}$$

$$b_{24} = -(a_{12}a_{14} + a_{22}a_{24} + a_{32}a_{34}) \Rightarrow - \begin{bmatrix} a_{11} & :a_{12}: & a_{13} & :a_{14}: \\ a_{21} & :a_{22}: & a_{23} & :a_{24}: \\ a_{31} & :a_{32}: & a_{33} & :a_{34}: \\ 0 & :0: & 0 & :1: \end{bmatrix}$$

$$b_{34} = -(a_{13}a_{14} + a_{23}a_{24} + a_{33}a_{34}) \Rightarrow - \begin{bmatrix} a_{11} & a_{12} & :a_{13}: & :a_{14}: \\ a_{21} & a_{22} & :a_{23}: & :a_{24}: \\ a_{31} & a_{32} & :a_{33}: & :a_{34}: \\ 0 & 0 & :0: & :1: \end{bmatrix}. \tag{1.2.14}$$

The columns to be multiplied are marked.

To perform successive coordinate transformation, we need only to follow the product rule of matrix algebra. For instance, the matrix equation

$$\mathbf{r}_p = \mathbf{M}_{p(p-1)}\mathbf{M}_{(p-1)(p-2)} \cdots \mathbf{M}_{32}\mathbf{M}_{21}\mathbf{r}_1 \tag{1.2.15}$$

represents successive coordinate transformation from S_1 to S_2, from S_2 to S_3, ..., from S_{p-1} to S_p.

To perform transformation of components of free vectors, we need only to apply 3×3 submatrices $\mathbf{L}$, which may be obtained by eliminating the last row and the last column of the corresponding matrix $\mathbf{M}$. This results from the fact that the free-vector components (projections on coordinate axes) do not depend on the location of the origin of the coordinate system.

The transformation of vector components of a free vector $\mathbf{A}$ from system S_m to S_n is represented by the matrix equation

$$\mathbf{A}_n = \mathbf{L}_{nm}\mathbf{A}_m \tag{1.2.16}$$

where

$$\mathbf{A}_n = \begin{bmatrix} A_{xn} \\ A_{yn} \\ A_{zn} \end{bmatrix}, \quad \mathbf{L}_{nm} = \begin{bmatrix} a_{11} & a_{12} & a_{13} \\ a_{21} & a_{22} & a_{23} \\ a_{31} & a_{32} & a_{33} \end{bmatrix}, \quad \mathbf{A}_m = \begin{bmatrix} A_{xm} \\ A_{ym} \\ A_{zm} \end{bmatrix}. \tag{1.2.17}$$

A normal to the gear tooth surface is a *sliding* vector because it may be translated along its line of action. However, we may transform the surface normal as a *free* vector if the surface point where the surface normal is considered will be transferred simultaneously.

1.3 ROTATION ABOUT AN AXIS

Two Main Problems

We consider a general case in which the rotation is performed about an axis that does not coincide with any axis of the employed coordinate system. We designate the unit vector of the axis of rotation by $\mathbf{c}$ (Fig. 1.3.1) and assume that the rotation about $\mathbf{c}$ may be performed either counterclockwise or clockwise.

Henceforth we consider two coordinate systems: (i) the fixed one, S_a; and (ii) the movable one, S_b. There are two typical problems related to rotation about $\mathbf{c}$. The first one can be formulated as follows.
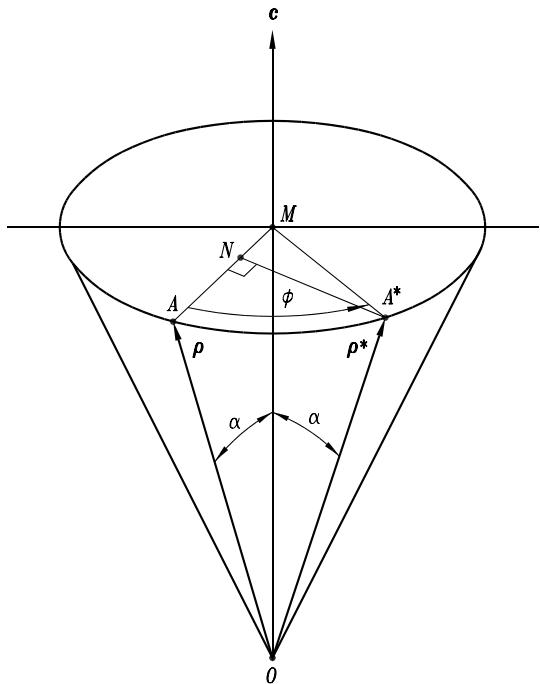
Consider that a position vector is rigidly connected to the movable body. The initial position of the position vector is designated by $\overline{OA} = \rho$ (Fig. 1.3.1). After rotation through an angle ϕ about $\mathbf{c}$, vector ρ will take a new position designated by $\overline{OA}^* = \rho^*$. Both vectors, ρ and ρ^* (Fig. 1.3.1), are considered to be in the *same* coordinate system, say S_a. Our goal is to develop an equation that relates components of vectors ρ_a and ρ_a^*. (The subscript "a" indicates that the two vectors are represented in the *same* coordinate system S_a.) Matrix equation

$$\rho_a^* = \mathbf{L}_a\rho_a \tag{1.3.1}$$

describes the relation between the components of vectors ρ and ρ^* that are represented in the same coordinate system S_a.

The other problem concerns representation of the *same* position vector in different coordinate systems. Our goal is to derive matrix $\mathbf{L}_{ba}$ in matrix equation

$$\rho_b = \mathbf{L}_{ba}\rho_a. \tag{1.3.2}$$

Figure 1.3.1: Rigid body rotation.

The designations ρ_a and ρ_b indicate that the *same* position vector ρ is represented in coordinate systems S_a and S_b, respectively. Although the *same* position vector is considered, the components of ρ in coordinate systems S_a and S_b are different and we designate them by

$$\rho_a = a_1 \mathbf{i}_a + a_2 \mathbf{j}_a + a_3 \mathbf{k}_a \tag{1.3.3}$$

and

$$\rho_b = b_1 \mathbf{i}_b + b_2 \mathbf{j}_b + b_3 \mathbf{k}_b. \tag{1.3.4}$$

Matrix $\mathbf{L}_{ba}$ is an operator that transforms the components $[a_1 \quad a_2 \quad a_3]^{\mathrm{T}}$ into $[b_1 \quad b_2 \quad b_3]^{\mathrm{T}}$. It will be shown below that operators $\mathbf{L}_a$ and $\mathbf{L}_{ba}$ are related.

Problem I. Relations between components of vectors ρ_a and ρ_a^*.

Recall that ρ_a and ρ_a^* are two position vectors that are represented in the *same* coordinate system S_a. Vector ρ represents the initial position of the position vector, *before* rotation, and ρ^* represents the position vector *after* rotation about $\mathbf{c}$. The following derivations are based on the assumption that rotation about $\mathbf{c}$ is performed counterclockwise. The procedure of derivations (see also Suh & Radcliffe, 1978, Shabana, 1989, and others) is as follows.

   Step 1: We represent ρ_a^* by the equation (Fig. 1.3.1)

$$\rho_a^* = \overline{OM} + \overline{MN} + \overline{NA^*} \tag{1.3.5}$$

where

$$\overline{OM} = (\mathbf{c}_a \cdot \boldsymbol{\rho}_a)\mathbf{c}_a = (\mathbf{c}_a \cdot \boldsymbol{\rho}_a^*)\mathbf{c}_a \tag{1.3.6}$$

and $\mathbf{c}_a$ is the unit vector of the axis of rotation that is represented in S_a.

Step 2: Vector $\boldsymbol{\rho}_a$ is represented by the equation

$$\boldsymbol{\rho}_a = \overline{OM} + \overline{MA} = (\mathbf{c}_a \cdot \boldsymbol{\rho}_a)\mathbf{c}_a + \overline{MA} \tag{1.3.7}$$

that yields

$$\overline{MA} = \boldsymbol{\rho}_a - (\mathbf{c}_a \cdot \boldsymbol{\rho}_a)\mathbf{c}_a. \tag{1.3.8}$$

We emphasize that a vector being rotated about $\mathbf{c}$ generates a cone with an apex angle α. Thus, both vectors, $\boldsymbol{\rho}$ and $\boldsymbol{\rho}^*$, are the generatrices of the same cone, as shown in Fig. 1.3.1.

Step 3: Vector $\overline{MN}$ has the same direction as $\overline{MA}$ and this yields

$$|\overline{MN}| = |\overline{MA^*}| \cos\phi = |\overline{MA}| \cos\phi = \rho \sin\alpha \cos\phi \tag{1.3.9}$$

where α is the apex angle of the generated cone, $|\overline{MA}| = \rho \sin\alpha$, and ρ is the magnitude of $\boldsymbol{\rho}$.

Equations (1.3.8) and (1.3.9) yield

$$\overline{MN} = |\overline{MN}| \frac{\overline{MA}}{|\overline{MA}|} = [\boldsymbol{\rho}_a - (\mathbf{c}_a \cdot \boldsymbol{\rho}_a)\mathbf{c}_a] \cos\phi. \tag{1.3.10}$$

Step 4: Vector $\overline{NA^*}$ has the same direction as $(\mathbf{c}_a \times \boldsymbol{\rho}_a)$ and may be represented by

$$\overline{NA^*} = \frac{\mathbf{c}_a \times \boldsymbol{\rho}_a}{|\mathbf{c}_a \times \boldsymbol{\rho}_a|} |\overline{NA^*}| = \sin\phi(\mathbf{c}_a \times \boldsymbol{\rho}_a). \tag{1.3.11}$$

Here,

$$|\overline{NA^*}| = |\overline{MA^*}| \sin\phi = \rho \sin\alpha \sin\phi, \quad |\mathbf{c}_a \times \boldsymbol{\rho}_a| = \rho \sin\alpha.$$

Step 5: Equations (1.3.5), (1.3.6), (1.3.10), and (1.3.11) yield

$$\boldsymbol{\rho}_a^* = \boldsymbol{\rho}_a \cos\phi + (1 - \cos\phi)(\mathbf{c}_a \cdot \boldsymbol{\rho}_a)\mathbf{c}_a + \sin\phi(\mathbf{c}_a \times \boldsymbol{\rho}_a). \tag{1.3.12}$$

Step 6: It is easy to prove that

$$(\mathbf{c}_a \cdot \boldsymbol{\rho}_a)\mathbf{c}_a = \mathbf{c}_a \times (\mathbf{c}_a \times \boldsymbol{\rho}_a) + \boldsymbol{\rho}_a \tag{1.3.13}$$

because

$$\mathbf{c}_a \times (\mathbf{c}_a \times \boldsymbol{\rho}_a) = (\mathbf{c}_a \cdot \boldsymbol{\rho}_a)\mathbf{c}_a - \boldsymbol{\rho}_a(\mathbf{c}_a \cdot \mathbf{c}_a).$$

Step 7: Equations (1.3.12) and (1.3.13) yield

$$\boldsymbol{\rho}_a^* = \boldsymbol{\rho}_a + (1 - \cos\phi)[\mathbf{c}_a \times (\mathbf{c}_a \times \boldsymbol{\rho}_a)] + \sin\phi(\mathbf{c}_a \times \boldsymbol{\rho}_a). \tag{1.3.14}$$

Equation (1.3.14) is known as the Rodrigues formula. According to the investigation by Cheng & Gupta [1989], this equation deserves to be called the Euler–Rodrigues, formula.

Step 8: Additional derivations are directed at representation of the Euler–Rodrigues formula in matrix form.

The cross product $(\mathbf{c}_a \times \boldsymbol{\rho}_a)$ may be represented in matrix form by

$$\mathbf{c}_a \times \boldsymbol{\rho}_a = \mathbf{C}^s \boldsymbol{\rho}_a \qquad (1.3.15)$$

where $\mathbf{C}^s$ is the skew-symmetric matrix represented by

$$\mathbf{C}^s = \begin{bmatrix} 0 & -c_3 & c_2 \\ c_3 & 0 & -c_1 \\ -c_2 & c_1 & 0 \end{bmatrix}. \qquad (1.3.16)$$

Vector $\mathbf{c}_a$ is represented by

$$\mathbf{c}_a = c_1 \mathbf{i}_a + c_2 \mathbf{j}_a + c_3 \mathbf{k}_a. \qquad (1.3.17)$$

Step 9: Equations (1.3.14), (1.3.15), and (1.3.16) yield the following matrix representation of the Euler–Rodrigues formula:

$$\boldsymbol{\rho}_a^* = \left[\mathbf{I} + (1 - \cos\phi)(\mathbf{C}^s)^2 + \sin\phi \mathbf{C}^s\right] \boldsymbol{\rho}_a = \mathbf{L}_a \boldsymbol{\rho}_a \qquad (1.3.18)$$

where $\mathbf{I}$ is the 3×3 identity matrix. While deriving Eqs. (1.3.14) and (1.3.18), we assumed that the rotation is performed counterclockwise. For the case of clockwise rotation, it is necessary to change the sign preceding $\sin\phi$ to its opposite. The expression for matrix $\mathbf{L}_a$ that will cover two directions of rotation is

$$\mathbf{L}_a = \mathbf{I} + (1 - \cos\phi)(\mathbf{C}^s)^2 \pm \sin\phi \mathbf{C}^s. \qquad (1.3.19)$$

The upper sign preceding $\sin\phi$ corresponds to counterclockwise rotation and the lower sign corresponds to rotation in a clockwise direction. In both cases the unit vector $\mathbf{c}$ must be expressed by the same Eq. (1.3.17) that determines the orientation of $\mathbf{c}$ but not the direction of rotation. The direction of rotation is identified with the proper sign preceding $\sin\phi$ in Eq. (1.3.19).

Problem 2. Recall that our goal is to derive the operator $\mathbf{L}_{ba}$ in matrix equation (1.3.2) that transforms components of the *same* vector (see Eqs. (1.3.3) and (1.3.4)). It will be shown below that the sought-for operator is represented as

$$\mathbf{L}_{ba} = \mathbf{L}_a^{\mathrm{T}} = \mathbf{I} + (1 - \cos\phi)(\mathbf{C}^s)^2 \mp \sin\phi \mathbf{C}^s. \qquad (1.3.20)$$

Operator $\mathbf{L}_{ba}$ can be obtained from operator $\mathbf{L}_a$ given by Eq. (1.3.19) by changing the sign of the angle of rotation, ϕ. The upper and lower signs preceding $\sin\phi$ in Eq. (1.3.20) correspond to the cases where S_a will coincide with S_b by rotation counterclockwise and clockwise, respectively. The proof is based on the determination of components of the same vector, say vector $\overline{OA}$ shown in Fig. 1.3.1, in coordinate systems S_a and S_b.

Step 1: We consider initially that vector $\overline{OA}$ is represented in S_a as

$$\boldsymbol{\rho}_a = [a_1 \ a_2 \ a_3]^{\mathrm{T}}. \qquad (1.3.21)$$

Step 2: To determine components of vector $\overline{OA}$ in S_b we consider first that coordinate system S_b and the previously mentioned position vector are rotated as one rigid body

about **c**. After rotation through angle ϕ, position vector $\overline{OA}$ will take the position $\overline{OA}^*$ and can be represented in S_b as

$$\overline{OA}^* = a_1\mathbf{i}_b + a_2\mathbf{j}_b + a_3\mathbf{k}_b. \tag{1.3.22}$$

It is obvious that vector $\overline{OA}^*$ has in S_b the same components as vector $\overline{OA}$ has in S_a.

Step 3: We consider now in S_b two vectors $\overline{OA}^*$ and $\overline{OA}$. Vector $\overline{OA}^*$ will coincide with $\overline{OA}$ after clockwise rotation about **c**. The components of vectors $\overline{OA}^*$ and $\overline{OA}$ in S_b are related by an equation that is similar to Eq. (1.3.19). The difference is that we now have to consider that the rotation from $\overline{OA}^*$ to $\overline{OA}$ is performed clockwise. Then we obtain

$$(\overline{OA})_b = \mathbf{L}_b(\overline{OA}^*)_b = \left[\mathbf{I} + (1 - \cos\phi)(\mathbf{C}^s)^2 - \sin\phi\mathbf{C}^s\right](\overline{OA}^*)_b. \tag{1.3.23}$$

Designating components of $(\overline{OA})_b$ by $[b_1 \ b_2 \ b_3]^\mathsf{T}$, we receive

$$[b_1 \ b_2 \ b_3]^\mathsf{T} = [\mathbf{I} + (1 - \cos\phi)(\mathbf{C}^s)^2 - \sin\phi\mathbf{C}^s][a_1 \ a_2 \ a_3]^\mathsf{T}. \tag{1.3.24}$$

Step 4: We have now obtained components of the same vector $\overline{OA}$ in coordinate systems S_a and S_b, respectively. The matrix equation that describes transformation of components of $\overline{OA}$ is

$$(\overline{OA})_b = \mathbf{L}_{ba}(\overline{OA})_a. \tag{1.3.25}$$

For the case in which rotation from S_a to S_b is performed counterclockwise we have obtained that

$$\mathbf{L}_{ba} = \mathbf{I} + (1 - \cos\phi)(\mathbf{C}^s)^2 - \sin\phi\mathbf{C}^s. \tag{1.3.26}$$

Similarly, for the case in which rotation from S_a to S_b is performed clockwise, we obtain

$$\mathbf{L}_{ba} = \mathbf{I} + (1 - \cos\phi)(\mathbf{C}^s)^2 + \sin\phi\mathbf{C}^s. \tag{1.3.27}$$

The general description of operator $\mathbf{L}_{ba}$ and the respective coordinate transformation are as follows:
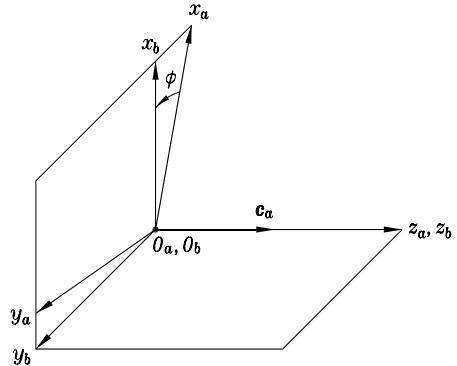
$$\boldsymbol{\rho}_b = \mathbf{L}_{ba}\boldsymbol{\rho}_a = \left[\mathbf{I} + (1 - \cos\phi)(\mathbf{C}^s)^2 \mp \sin\phi\mathbf{C}^s\right]\boldsymbol{\rho}_a. \tag{1.3.28}$$

The upper and lower signs preceding $\sin\phi$ correspond to the cases in which rotation from S_a to S_b is performed counterclockwise and clockwise, respectively.

In our identification of coordinate systems S_a and S_b we do not use the terms fixed and movable. We just consider that S_a is the previous coordinate system and S_b is the new one, and we take into account how the rotation from S_a to S_b is performed: counterclockwise or clockwise.

Matrix $\mathbf{L}_{ba}$

Using Eqs. (1.3.26) and (1.3.27), we may represent elements of matrix $\mathbf{L}_{ba}$ in terms of components of unit vector **c** of the axis of rotation and the angle of rotation ϕ. Thus,

Figure 1.3.2: Derivation of coordinate transformation by rotation.

we obtain

$$\mathbf{L}_{ba} = \begin{bmatrix} a_{11} & a_{12} & a_{13} \\ a_{21} & a_{22} & a_{23} \\ a_{31} & a_{32} & a_{33} \end{bmatrix}. \qquad (1.3.29)$$

Here,

$$\begin{aligned}
a_{11} &= \cos\phi \left(1 - c_1^2\right) + c_1^2 \\
a_{12} &= (1 - \cos\phi)c_1 c_2 \pm \sin\phi\, c_3 \\
a_{13} &= (1 - \cos\phi)c_1 c_3 \mp \sin\phi\, c_2 \\
a_{21} &= (1 - \cos\phi)c_1 c_2 \mp \sin\phi\, c_3 \\
a_{22} &= \cos\phi \left(1 - c_2^2\right) + c_2^2 \\
a_{23} &= (1 - \cos\phi)c_2 c_3 \pm \sin\phi\, c_1 \\
a_{31} &= (1 - \cos\phi)c_1 c_3 \pm \sin\phi\, c_2 \\
a_{32} &= (1 - \cos\phi)c_2 c_3 \mp \sin\phi\, c_1 \\
a_{33} &= \cos\phi \left(1 - c_3^2\right) + c_3^2.
\end{aligned} \qquad (1.3.30)$$

When the axis of rotation coincides with a coordinate axis of S_a, we have to make two components of unit vector $\mathbf{c}_a$ equal to zero in Eqs. (1.3.30). For instance, in the case in which rotation is performed about the z_a axis (Fig. 1.3.2), we have

$$\mathbf{c}_a = \mathbf{k}_a = [0 \ \ 0 \ \ 1]^\mathsf{T}. \qquad (1.3.31)$$

We emphasize again that in all cases of coordinate transformation only elements (1.3.30) of matrix $\mathbf{L}_{ba}$, and not the components of $\mathbf{c}_a$, depend on the direction of rotation. The unit vector $\mathbf{c}$ can be represented in either of the two coordinate systems, S_a and S_b, by the equations

$$\mathbf{c} = c_1 \mathbf{i}_a + c_2 \mathbf{j}_a + c_3 \mathbf{k}_a = c_1 \mathbf{i}_b + c_2 \mathbf{j}_b + c_3 \mathbf{k}_b. \qquad (1.3.32)$$

This means that the unit vector $\mathbf{c}$ of the axis of rotation has the *same* components in both coordinate systems, S_a and S_b. It is easily verified that

$$[c_1 \ \ c_2 \ \ c_3]^\mathsf{T} = \mathbf{L}_{ba}[c_1 \ \ c_2 \ \ c_3]^\mathsf{T}. \qquad (1.3.33)$$

Although the significance of this observation has not been recognized in the literature, it has been found to be advantageous in obtaining coordinate transformations in this book.

The proof of Eq. (1.3.32) is based on the following considerations. The unit vector $\mathbf{c}$ of the axis C of rotation is directed along the axis that is common to the two coordinate systems, S_a and S_b. Thus, the orientation of $\mathbf{c}$ is not changed when one of the two coordinate systems rotates with respect to the other about C. For instance, assume that a unit vector of S_a, say $\mathbf{i}_a$, is directed along $\overline{OA}$, and the unit vector $\mathbf{i}_b$ of S_b is directed along $\overline{OA^*}$ (see Fig. 1.3.1). Both unit vectors, $\mathbf{i}_a$ and $\mathbf{i}_b$, are the generatrices of the same cone and therefore

$$\mathbf{c} \cdot \mathbf{i}_a = \mathbf{c} \cdot \mathbf{i}_b = c_1.$$

Similarly, we may prove that

$$\mathbf{c} \cdot \mathbf{j}_a = \mathbf{c} \cdot \mathbf{j}_b = c_2, \quad \mathbf{c} \cdot \mathbf{k}_a = \mathbf{c} \cdot \mathbf{k}_b = c_3.$$

Thus, Eq. (1.3.32) is confirmed.

Employment of Additional Coordinate Systems

Generally, the axis of rotation does not coincide with any coordinate axis of S_a. The movable coordinate system S_b coincides with S_a in the beginning of rotation. Thus, there is no coordinate axis of S_b that coincides with the axis of rotation. Our goal is to employ two additional coordinate systems S_m and S_n that will enable us to make one of their coordinate axes coincide with the axis of rotation. The auxiliary coordinate system S_m is rigidly connected to S_a, and the auxiliary coordinate system S_n is rigidly connected to S_b.

The determination of the structure of matrix $\mathbf{L}_{ma}$ is based on the following considerations. Let us represent $\mathbf{L}_{ma}$ as

$$\mathbf{L}_{ma} = \begin{bmatrix} a_1 & a_2 & a_3 \\ b_1 & b_2 & b_3 \\ d_1 & d_2 & d_3 \end{bmatrix}. \tag{1.3.34}$$

A respective axis of S_m will coincide with $\mathbf{c}$ if one of three unit vectors ($\mathbf{a}$, $\mathbf{b}$, and $\mathbf{d}$) coincides with $\mathbf{c}$. We limit this discussion to the case in which the z_m axis coincides with $\mathbf{c}$. Two other cases can be discussed similarly. For the previously mentioned case we have

$$\mathbf{d} = [c_1 \ c_2 \ c_3]^{\mathrm{T}} \tag{1.3.35}$$

and

$$\mathbf{L}_{ma} = \begin{bmatrix} a_1 & a_2 & a_3 \\ b_1 & b_2 & b_3 \\ c_1 & c_2 & c_3 \end{bmatrix}. \tag{1.3.36}$$

Unit vectors $\mathbf{a}$ and $\mathbf{b}$ are represented as follows:

$$\mathbf{a} = [\mathbf{i}_m \cdot \mathbf{i}_a \ \ \mathbf{i}_m \cdot \mathbf{j}_a \ \ \mathbf{i}_m \cdot \mathbf{k}_a], \quad \mathbf{b} = [\mathbf{j}_m \cdot \mathbf{i}_a \ \ \mathbf{j}_m \cdot \mathbf{j}_a \ \ \mathbf{j}_m \cdot \mathbf{k}_a]. \tag{1.3.37}$$

It is obvious that

$$\mathbf{L}_{ma}\mathbf{c}_a = [0 \quad 0 \quad 1]^{\mathrm{T}} \tag{1.3.38}$$

because $\mathbf{a} \cdot \mathbf{c} = 0$, $\mathbf{b} \cdot \mathbf{c} = 0$, and $\mathbf{c} \cdot \mathbf{c} = 1$. While choosing one of the two unit vectors ($\mathbf{a}$ and $\mathbf{b}$), say $\mathbf{b}$, we have to take into account the following relations: (i)

$$b_1 c_1 + b_2 c_2 + b_3 c_3 = 0 \tag{1.3.39}$$

due to the orthogonality of $\mathbf{c}$ and $\mathbf{b}$, and (ii)

$$b_1^2 + b_2^2 + b_3^2 = 1 \tag{1.3.40}$$

because $\mathbf{b}$ is a unit vector. Equations (1.3.39) and (1.3.40) relate two of three components of $\mathbf{b}$, and only one of them can be chosen.

After determination of $\mathbf{c}$ and $\mathbf{b}$ we can define the unit vector $\mathbf{a}$ using the cross product

$$\mathbf{a} = \mathbf{b} \times \mathbf{c}. \tag{1.3.41}$$

The motion of movable coordinate system S_n with respect to S_m and S_a (S_m and S_a are rigidly connected) is rotation about the z_m axis through angle ϕ. Matrix L_{nm} can be determined in accordance with Eqs. (1.3.29) and (1.3.30). The coordinate transformation from S_a to S_n is based on the matrix equation

$$\rho_n = \mathbf{L}_{nm}\mathbf{L}_{ma}\rho_a. \tag{1.3.42}$$

We have discussed above the coordinate transformation from S_a to S_b that is represented by matrix equation (1.3.30).

At the start of motion, coordinate system S_b coincides with S_a, coordinate system S_n (which is rigidly connected to S_b) coincides with S_m (which is rigidly connected to S_a). With these considerations we can develop the following matrix equations:

$$\mathbf{L}_{nb} = \mathbf{L}_{ma} \tag{1.3.43}$$

$$\mathbf{L}_{nm}\mathbf{L}_{ma} = \mathbf{L}_{nb}\mathbf{L}_{ba} = \mathbf{L}_{ma}\mathbf{L}_{ba} \tag{1.3.44}$$

$$\mathbf{L}_{ma}^{-1}\mathbf{L}_{nm}\mathbf{L}_{ma} = \mathbf{L}_{ba}. \tag{1.3.45}$$

We may also prove the correctness of the matrix equations

$$\mathbf{L}_{ba}[c_1 \quad c_2 \quad c_3]^{\mathrm{T}} = \mathbf{L}_{ma}^{-1}\mathbf{L}_{nm}\mathbf{L}_{ma}[c_1 \quad c_2 \quad c_3]^{\mathrm{T}} = [c_1 \quad c_2 \quad c_3]^{\mathrm{T}} \tag{1.3.46}$$

and

$$\mathbf{L}_{nm}\mathbf{L}_{ma}[c_1 \quad c_2 \quad c_3]^{\mathrm{T}} = \mathbf{L}_{ma}\mathbf{L}_{ba}[c_1 \quad c_2 \quad c_3]^{\mathrm{T}} = \mathbf{m} = [m_1 \quad m_2 \quad m_3]^{\mathrm{T}}. \tag{1.3.47}$$

Here, $\mathbf{m}$ is the unit vector of the axis of S_m that is the axis of rotation (two components of $\mathbf{m}$ are equal to zero and the third is equal to one). Matrix equations (1.3.44) to (1.3.47) are illustrated in Problem 1.5.4.

1.4 ROTATIONAL AND TRANSLATIONAL 4 × 4 MATRICES

Generally, the origins of coordinate systems do not coincide and the orientations of the systems are different. In such a case the coordinate transformation may be based on the application of homogeneous coordinates and 4 × 4 matrices that describe separately rotation about a fixed axis and displacement of one coordinate system with respect to the other.
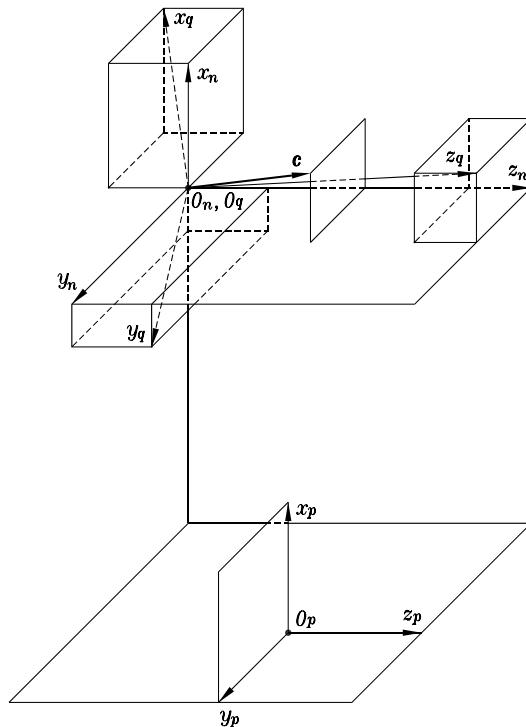
Consider that the same point must be represented in coordinate systems S_p and S_q (Fig. 1.4.1). The origins of S_p and S_q do not coincide and the orientations of coordinate axes in these systems is also different. It is useful in such a case to apply an auxiliary coordinate system, S_n, and a matrix, $\mathbf{M}_{np}$, that describes translation from S_p to S_n. Coordinate systems S_p and S_q have a common origin and the coordinate transformation from S_p to S_q is based on the Euler–Rodrigues equation.

The coordinate transformation from S_p to S_q is represented by the matrix equation

$$\mathbf{r}_q = \mathbf{M}_{qn}\mathbf{M}_{np}\mathbf{r}_p = \mathbf{M}_{qp}\mathbf{r}_p. \tag{1.4.1}$$

The 4×4 matrix $\mathbf{M}_{np}$ describes translation from S_p to S_n and is represented by

$$\mathbf{M}_{np} = \begin{bmatrix} 1 & 0 & 0 & a \\ 0 & 1 & 0 & b \\ 0 & 0 & 1 & c \\ 0 & 0 & 0 & 1 \end{bmatrix}. \tag{1.4.2}$$

Figure 1.4.1: Application of coordinate systems.

The 4×4 matrix $\mathbf{M}_{qn}$ describes rotation about a fixed axis with unit vector $\mathbf{c}$ and is represented as

$$\mathbf{M}_{qn} = \begin{bmatrix} a_{11} & a_{12} & a_{13} & 0 \\ a_{21} & a_{22} & a_{23} & 0 \\ a_{31} & a_{32} & a_{33} & 0 \\ 0 & 0 & 0 & 1 \end{bmatrix}. \tag{1.4.3}$$

The 3×3 submatrix of $\mathbf{M}_{qn}$ is determined with Eqs. (1.3.29) and (1.3.30). The inverse coordinate transformation is represented by the equations

$$\mathbf{r}_p = \mathbf{M}_{pq}\mathbf{r}_q = \mathbf{M}_{qp}^{-1}\mathbf{r}_q \tag{1.4.4}$$

$$\mathbf{M}_{qp}^{-1} = \mathbf{M}_{np}^{-1}\mathbf{M}_{qn}^{-1} = \mathbf{M}_{pn}\mathbf{M}_{nq}. \tag{1.4.5}$$

1.5 EXAMPLES OF COORDINATE TRANSFORMATION

The examples of coordinate transformation presented in this section are based on application of 4×4 rotational and translational matrices. The study of these problems will give the reader experience in coordinate transformation as it relates to the theory of gearing.

Problem 1.5.1

Coordinate systems S_1 and S_2 are rigidly connected to the gear and to the rack-cutter that perform rotational and translational motions with respect to the fixed coordinate system S_f (Fig. 1.5.1). A point M in coordinate system S_1 is represented by position vector $\overline{O_1M} = \mathbf{r}_1$.

(i) Determine the position vector $\mathbf{r}_2$ of the same point in coordinate system S_2.
(ii) Express the inverse matrix $\mathbf{M}_{12} = \mathbf{M}_{21}^{-1}$ in terms of elements of matrix $\mathbf{M}_{21}$ and then determine the position vector $\mathbf{r}_1$ considering that $\mathbf{r}_2$ is given.

Solution

(i) The coordinate transformation from S_1 to S_2 is based on the matrix equation
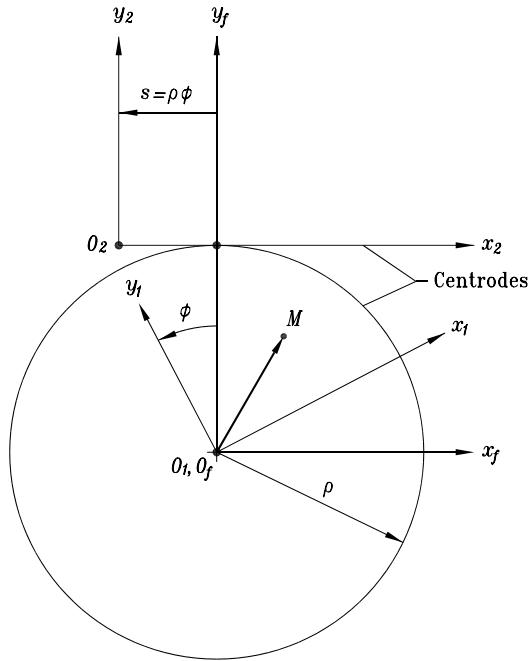
$$\mathbf{r}_2 = \mathbf{M}_{21}\mathbf{r}_1 = \mathbf{M}_{2f}\mathbf{M}_{f1}\mathbf{r}_1. \tag{1.5.1}$$

The rotational matrix $\mathbf{M}_{f1}$ describes rotation about the z_f axis with the unit vector,

$$\mathbf{c}_f = [0 \quad 0 \quad 1]^T. \tag{1.5.2}$$

The rotation from S_1 to S_2 is performed clockwise and the lower sign in Eq. (1.3.30) must be chosen. Taking into account that $c_1 = c_2 = 0$, $c_3 = 1$, we obtain the following expression for the rotational matrix $\mathbf{M}_{f1}$:

$$\mathbf{M}_{f1} = \begin{bmatrix} \cos\phi & -\sin\phi & 0 & 0 \\ \sin\phi & \cos\phi & 0 & 0 \\ 0 & 0 & 1 & 0 \\ 0 & 0 & 0 & 1 \end{bmatrix}. \tag{1.5.3}$$

Figure 1.5.1: Centrodes in translation–rotation motions.

The drawings of Fig. 1.5.1 yield that

$$(\overline{O_2 O_f})_f = [\rho\phi \quad -\rho \quad 0]^\mathrm{T},$$

and the translational matrix is

$$\mathbf{M}_{2f} = \begin{bmatrix} 1 & 0 & 0 & \rho\phi \\ 0 & 1 & 0 & -\rho \\ 0 & 0 & 1 & 0 \\ 0 & 0 & 0 & 1 \end{bmatrix}. \tag{1.5.4}$$

The position vectors $\mathbf{r}_2$ and $\mathbf{r}_1$ are

$$\mathbf{r}_2 = [x_2 \quad y_2 \quad z_2 \quad 1]^\mathrm{T}, \quad \mathbf{r}_1 = [x_1 \quad y_1 \quad z_1 \quad 1]^\mathrm{T}. \tag{1.5.5}$$

Equations (1.5.1) to (1.5.5) yield

$$\mathbf{M}_{21} = \begin{bmatrix} \cos\phi & -\sin\phi & 0 & \rho\phi \\ \sin\phi & \cos\phi & 0 & -\rho \\ 0 & 0 & 1 & 0 \\ 0 & 0 & 0 & 1 \end{bmatrix} \tag{1.5.6}$$

and

$$\begin{aligned} x_2 &= x_1 \cos\phi - y_1 \sin\phi + \rho\phi \\ y_2 &= x_1 \sin\phi + y_1 \cos\phi - \rho \\ z_2 &= z_1. \end{aligned} \tag{1.5.7}$$

(ii) Matrix $\mathbf{M}_{21}$ is not singular and the inverse coordinate transformation is possible. To determine the inverse matrix $\mathbf{M}_{12} = \mathbf{M}_{21}^{-1}$, we use equations (1.2.10) to (1.2.13), which yield

$$\mathbf{M}_{12} = \begin{bmatrix} \cos\phi & \sin\phi & 0 & \rho(\sin\phi - \phi\cos\phi) \\ -\sin\phi & \cos\phi & 0 & \rho(\cos\phi + \phi\sin\phi) \\ 0 & 0 & 1 & 0 \\ 0 & 0 & 0 & 1 \end{bmatrix}. \tag{1.5.8}$$

Then, using the matrix equation
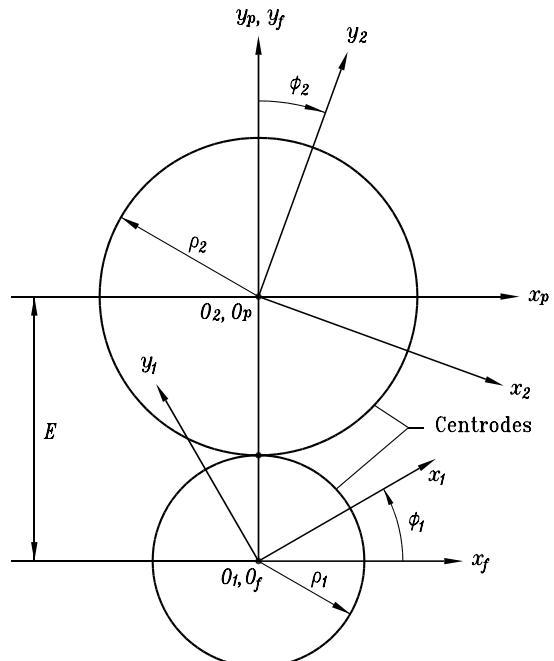
$$\mathbf{r}_1 = \mathbf{M}_{12}\mathbf{r}_2 \tag{1.5.9}$$

we obtain

$$\begin{aligned} x_1 &= x_2\cos\phi + y_2\sin\phi + \rho(\sin\phi - \phi\cos\phi) \\ y_1 &= -x_2\sin\phi + y_2\cos\phi + \rho(\cos\phi + \phi\sin\phi) \\ z_1 &= z_2. \end{aligned} \tag{1.5.10}$$

Problem 1.5.2

Coordinate systems S_1 (x_1, y_1, z_1) and S_2 (x_2, y_2, z_2) are rigidly connected to gears 1 and 2 that transform rotation between parallel axes (Fig. 1.5.2). Angles of gear rotation

Figure 1.5.2: Centrodes in rotational motions of opposite direction.

ϕ_1 and ϕ_2 are related with the equation

$$\frac{\phi_2}{\phi_1} = \frac{\rho_1}{\rho_2} \tag{1.5.11}$$

where ρ_1 and ρ_2 are the radii of gear centrodes (see Section 3.2). E is the shortest distance between the axes of rotation. The fixed coordinate system S_f is rigidly connected to the gear housing. S_p is an auxiliary coordinate system that is also rigidly connected to the gear housing.

(i) Derive equations for coordinate transformation from S_2 to S_1.
(ii) Derive equations for coordinate transformation from S_1 to S_2.

Solution

(i) The coordinate transformation in transition from S_2 to S_1 is based on the matrix equation

$$\mathbf{r}_1 = \mathbf{M}_{12}\mathbf{r}_2 = \mathbf{M}_{1f}\mathbf{M}_{fp}\mathbf{M}_{p2}\mathbf{r}_2 \tag{1.5.12}$$

where $\mathbf{M}_{1f}$ and $\mathbf{M}_{p2}$ are rotational matrices and $\mathbf{M}_{fp}$ is a translational matrix. Here,

$$\mathbf{r}_2 = \begin{bmatrix} x_2 \\ y_2 \\ z_2 \\ 1 \end{bmatrix}, \quad \mathbf{M}_{p2} = \begin{bmatrix} \cos\phi_2 & \sin\phi_2 & 0 & 0 \\ -\sin\phi_2 & \cos\phi_2 & 0 & 0 \\ 0 & 0 & 1 & 0 \\ 0 & 0 & 0 & 1 \end{bmatrix}$$

$$\mathbf{r}_1 = \begin{bmatrix} x_1 \\ y_1 \\ z_1 \\ 1 \end{bmatrix}, \quad \mathbf{M}_{1f} = \begin{bmatrix} \cos\phi_1 & \sin\phi_1 & 0 & 0 \\ -\sin\phi_1 & \cos\phi_1 & 0 & 0 \\ 0 & 0 & 1 & 0 \\ 0 & 0 & 0 & 1 \end{bmatrix}$$

$$\mathbf{M}_{fp} = \begin{bmatrix} 1 & 0 & 0 & 0 \\ 0 & 1 & 0 & E \\ 0 & 0 & 1 & 0 \\ 0 & 0 & 0 & 1 \end{bmatrix}. \tag{1.5.13}$$

Equations (1.5.13) yield

$$\mathbf{M}_{12} = \begin{bmatrix} \cos(\phi_1+\phi_2) & \sin(\phi_1+\phi_2) & 0 & E\sin\phi_1 \\ -\sin(\phi_1+\phi_2) & \cos(\phi_1+\phi_2) & 0 & E\cos\phi_1 \\ 0 & 0 & 1 & 0 \\ 0 & 0 & 0 & 1 \end{bmatrix}. \tag{1.5.14}$$

Using equations (1.5.12) and (1.5.14), we obtain

$$\begin{aligned} x_1 &= x_2\cos(\phi_1+\phi_2) + y_2\sin(\phi_1+\phi_2) + E\sin\phi_1 \\ y_1 &= -x_2\sin(\phi_1+\phi_2) + y_2\cos(\phi_1+\phi_2) + E\cos\phi_1 \\ z_1 &= z_2. \end{aligned} \tag{1.5.15}$$

(ii) The inverse matrix $M_{21} = M_{12}^{-1}$ can be expressed in terms of elements of M_{12} as follows [see Eqs. (1.2.10) to (1.2.14)]:

$$M_{21} = \begin{bmatrix} \cos(\phi_1 + \phi_2) & -\sin(\phi_1 + \phi_2) & 0 & E\sin\phi_2 \\ \sin(\phi_1 + \phi_2) & \cos(\phi_1 + \phi_2) & 0 & -E\cos\phi_2 \\ 0 & 0 & 1 & 0 \\ 0 & 0 & 0 & 1 \end{bmatrix}. \qquad (1.5.16)$$

The inverse coordinate transformation is based on the matrix equation
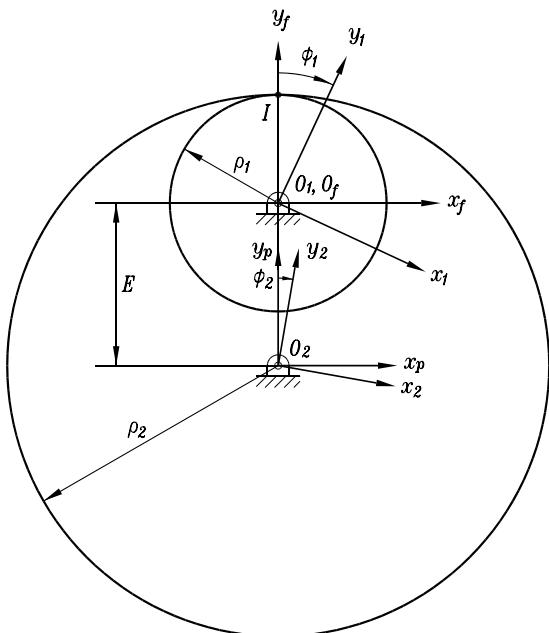
$$\mathbf{r}_2 = \mathbf{M}_{21}\mathbf{r}_1, \qquad (1.5.17)$$

which yields

$$\begin{aligned} x_2 &= x_1\cos(\phi_1 + \phi_2) - y_1\sin(\phi_1 + \phi_2) + E\sin\phi_2 \\ y_2 &= x_1\sin(\phi_1 + \phi_2) + y_1\cos(\phi_1 + \phi_2) - E\cos\phi_2 \\ z_2 &= z_1. \end{aligned} \qquad (1.5.18)$$

Problem 1.5.3

Consider that two gears transform rotation about parallel axes in the same direction (Fig. 1.5.3). Coordinate systems S_1 and S_2 are rigidly connected to gears 1 and 2; S_f and S_p are fixed coordinate systems; E is the shortest distance; ρ_1 and ρ_2 are the radii of gear centrodes (see Section 3.2). (i) Determine matrices M_{21} and $M_{12} = M_{21}^{-1}$ and (ii) perform the coordinate transformation in transition from S_1 to S_2 and from S_2 to S_1.

Figure 1.5.3: Centrodes in rotational motions of the same direction.

Solution

(i)

$$\mathbf{M}_{21} = \mathbf{M}_{2p}\mathbf{M}_{pf}\mathbf{M}_{f1}$$

$$= \begin{bmatrix} \cos(\phi_1 - \phi_2) & \sin(\phi_1 - \phi_2) & 0 & -E\sin\phi_2 \\ -\sin(\phi_1 - \phi_2) & \cos(\phi_1 - \phi_2) & 0 & E\cos\phi_2 \\ 0 & 0 & 1 & 0 \\ 0 & 0 & 0 & 1 \end{bmatrix} \qquad (1.5.19)$$

$$\mathbf{M}_{12} = \mathbf{M}_{21}^{-1}$$

$$= \begin{bmatrix} \cos(\phi_1 - \phi_2) & -\sin(\phi_1 - \phi_2) & 0 & E\sin\phi_1 \\ \sin(\phi_1 - \phi_2) & \cos(\phi_1 - \phi_2) & 0 & -E\cos\phi_1 \\ 0 & 0 & 1 & 0 \\ 0 & 0 & 0 & 1 \end{bmatrix}. \qquad (1.5.20)$$

(ii)

$$\begin{aligned} x_2 &= x_1\cos(\phi_1 - \phi_2) + y_1\sin(\phi_1 - \phi_2) - E\sin\phi_2 \\ y_2 &= -x_1\sin(\phi_1 - \phi_2) + y_1\cos(\phi_1 - \phi_2) + E\cos\phi_2 \\ z_2 &= z_1 \end{aligned} \qquad (1.5.21)$$

$$\begin{aligned} x_1 &= x_2\cos(\phi_1 - \phi_2) - y_2\sin(\phi_1 - \phi_2) + E\sin\phi_1 \\ y_1 &= x_2\sin(\phi_1 - \phi_2) + y_2\cos(\phi_1 - \phi_2) - E\cos\phi_1 \\ z_1 &= z_2. \end{aligned} \qquad (1.5.22)$$

Problem 1.5.4
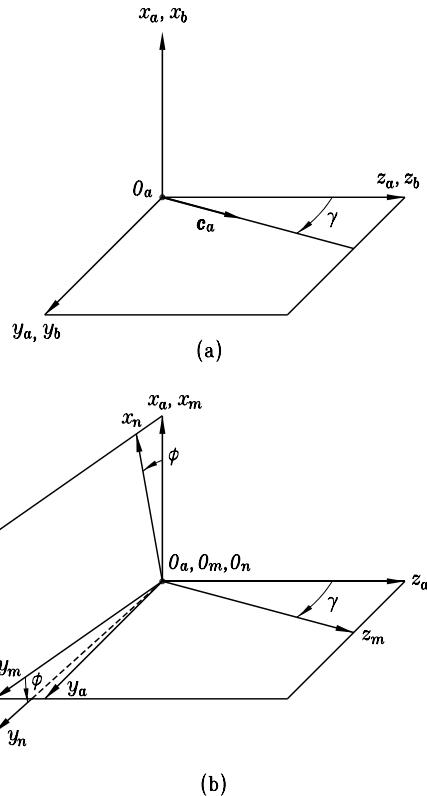
The purpose of this problem is to illustrate the verification of Eqs. (1.3.44) to (1.3.47). Figure 1.5.4(a) shows two coordinate systems S_a and S_b that coincide with each other initially. Coordinate system S_b is rotated counterclockwise about the axis with unit vector

$$\mathbf{c}_a = \begin{bmatrix} 0 & \sin\gamma & \cos\gamma \end{bmatrix}^{\mathrm{T}}. \qquad (1.5.23)$$

Matrix $\mathbf{L}_{ba}$ in accordance with Eqs. (1.3.30) is represented as follows:

$$\mathbf{L}_{ba} = \begin{bmatrix} \cos\phi & \sin\phi\cos\gamma & -\sin\phi\sin\gamma \\ -\sin\phi\cos\gamma & \cos\phi\cos^2\gamma + \sin^2\gamma & (1 - \cos\phi)\sin\gamma\cos\gamma \\ \sin\phi\sin\gamma & (1 - \cos\phi)\sin\gamma\cos\gamma & \cos\phi\sin^2\gamma + \cos^2\gamma \end{bmatrix}. \qquad (1.5.24)$$

Figure 1.5.4(b) shows an auxiliary coordinate system S_m that is rigidly connected to S_a. The coordinate axis z_m coincides with $\mathbf{c}_a$ whose components represent the elements of the third row in matrix $\mathbf{L}_{ma}$ represented by Eq. (1.3.36). Coordinate axis x_m coincides

Figure 1.5.4: Auxiliary coordinate systems: (a) illustration of coordinate systems S_a and S_b; (b) illustration of coordinate systems S_a, S_m, and S_n.

with x_a. According to Eq. (1.3.30), matrix $\mathbf{L}_{ma}$ is
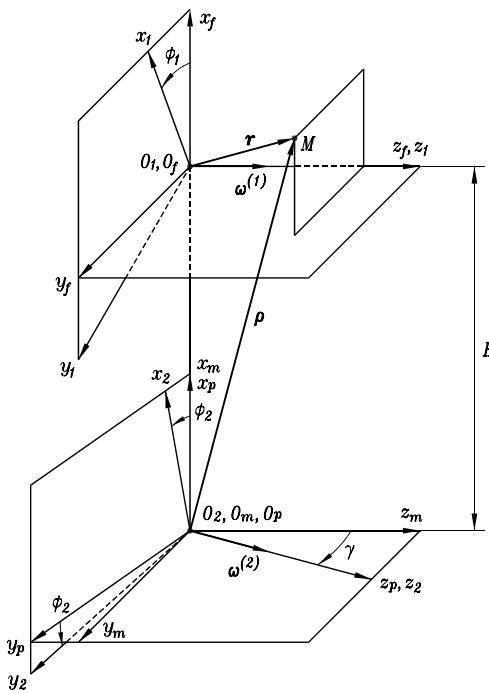
$$
\mathbf{L}_{ma} = \begin{bmatrix} 1 & 0 & 0 \\ 0 & \cos\gamma & -\sin\gamma \\ 0 & \sin\gamma & \cos\gamma \end{bmatrix}. \tag{1.5.25}
$$

Coordinate systems S_n and S_b which are rigidly connected to each other are rotated about $\mathbf{c}_m = \mathbf{k}_m$ through angle ϕ. Matrix $\mathbf{L}_{nm}$, in accordance with Eqs. (1.3.30), is represented by

$$
\mathbf{L}_{nm} = \begin{bmatrix} \cos\phi & \sin\phi & 0 \\ -\sin\phi & \cos\phi & 0 \\ 0 & 0 & 1 \end{bmatrix}. \tag{1.5.26}
$$

Matrix product $\mathbf{L}_{nm}\mathbf{L}_{ma} = \mathbf{L}_{na}$ is

$$
\mathbf{L}_{na} = \begin{bmatrix} \cos\phi & \sin\phi\cos\gamma & -\sin\phi\sin\gamma \\ -\sin\phi & \cos\phi\cos\gamma & -\cos\phi\sin\gamma \\ 0 & \sin\gamma & \cos\gamma \end{bmatrix}. \tag{1.5.27}
$$

Figure 1.5.5: General case of coordinate transformation.

Using Eqs. (1.5.24) to (1.5.27) we may be certain that matrix equations (1.3.43) and (1.3.45) are indeed observed. Equations (1.3.46) and (1.3.47) in the discussed case yield

$$\mathbf{L}_{ba}[0 \quad \sin\gamma \quad \cos\gamma]^{\mathrm{T}} = \mathbf{L}_{ma}^{-1}\mathbf{L}_{nm}\mathbf{L}_{ma}[0 \ \sin\gamma \ \cos\gamma]^{\mathrm{T}} \tag{1.5.28}$$
$$= [0 \quad \sin\gamma \quad \cos\gamma]^{\mathrm{T}}$$

$$\mathbf{L}_{nm}\mathbf{L}_{ma}[0 \quad \sin\gamma \quad \cos\gamma]^{\mathrm{T}} = \mathbf{L}_{ma}\mathbf{L}_{ba}[0 \quad \sin\gamma \quad \cos\gamma]^{\mathrm{T}} \tag{1.5.29}$$
$$= [0 \quad 0 \quad 1]^{\mathrm{T}}.$$

Problem 1.5.5

Gears 1 and 2 rotate about axes z_f and z_p that form the twist angle γ and the shortest distance E (Fig. 1.5.5). Coordinate systems S_1, S_2, and S_f are rigidly connected to gear 1, gear 2, and the frame, respectively. The auxiliary systems S_m and S_p are also rigidly connected to the frame. Derive equations for the coordinate transformation in transition from S_1 to S_2 and from S_2 to S_1.

DIRECTIONS. The coordinate transformation in transition from S_1 to S_2 is based on matrix equation

$$\mathbf{r}_2 = \mathbf{M}_{21}\mathbf{r}_1 = \mathbf{M}_{2p}\mathbf{M}_{pm}\mathbf{M}_{mf}\mathbf{M}_{f1}\mathbf{r}_1. \tag{1.5.30}$$

Here, matrix $\mathbf{M}_{mf}$ is a translational matrix; matrix $\mathbf{M}_{f1}$ describes rotation about the z_f axis; matrix $\mathbf{M}_{pm}$ describes the turn about the x_m axis to obtain the twist angle γ; matrix $\mathbf{M}_{2p}$ describes rotation about the z_p axis.

Solution
Matrix $\mathbf{M}_{21}$ is represented by

$$
\mathbf{M}_{21} =
\begin{bmatrix}
\cos\phi_1 \cos\phi_2 & -\sin\phi_1 \cos\phi_2 & -\sin\gamma \sin\phi_2 & E\cos\phi_2 \\
+\cos\gamma \sin\phi_1 \sin\phi_2 & +\cos\gamma \cos\phi_1 \sin\phi_2 & & \\
-\cos\phi_1 \sin\phi_2 & \sin\phi_1 \sin\phi_2 & -\sin\gamma \cos\phi_2 & -E\sin\phi_2 \\
+\cos\gamma \sin\phi_1 \cos\phi_2 & +\cos\gamma \cos\phi_1 \cos\phi_2 & & \\
\sin\gamma \sin\phi_1 & \sin\gamma \cos\phi_1 & \cos\gamma & 0 \\
0 & 0 & 0 & 1
\end{bmatrix}.
$$

$$(1.5.31)$$

The coordinate transformation in transition from S_1 to S_2 is represented by the equations

$$
\begin{aligned}
x_2 &= x_1(\cos\phi_1 \cos\phi_2 + \cos\gamma \sin\phi_1 \sin\phi_2) \\
&\quad + y_1(-\sin\phi_1 \cos\phi_2 + \cos\gamma \cos\phi_1 \sin\phi_2) \\
&\quad - z_1 \sin\gamma \sin\phi_2 + E\cos\phi_2 \\
y_2 &= x_1(-\cos\phi_1 \sin\phi_2 + \cos\gamma \sin\phi_1 \cos\phi_2) \qquad\qquad (1.5.32)\\
&\quad + y_1(\sin\phi_1 \sin\phi_2 + \cos\gamma \cos\phi_1 \cos\phi_2) \\
&\quad - z_1 \sin\gamma \cos\phi_2 - E\sin\phi_2 \\
z_2 &= x_1 \sin\gamma \sin\phi_1 + y_1 \sin\gamma \cos\phi_1 + z_1 \cos\gamma.
\end{aligned}
$$

The inverse matrix $\mathbf{M}_{12} = \mathbf{M}_{21}^{-1}$ is represented by

$$
\mathbf{M}_{12} =
\begin{bmatrix}
\cos\phi_1 \cos\phi_2 & -\cos\phi_1 \sin\phi_2 & \sin\gamma \sin\phi_1 & -E\cos\phi_1 \\
+\cos\gamma \sin\phi_1 \sin\phi_2 & +\cos\gamma \sin\phi_1 \cos\phi_2 & & \\
-\sin\phi_1 \cos\phi_2 & \sin\phi_1 \sin\phi_2 & \sin\gamma \cos\phi_1 & E\sin\phi_1 \\
+\cos\gamma \cos\phi_1 \sin\phi_2 & +\cos\gamma \cos\phi_1 \cos\phi_2 & & \\
-\sin\gamma \sin\phi_2 & -\sin\gamma \cos\phi_2 & \cos\gamma & 0 \\
0 & 0 & 0 & 1
\end{bmatrix}.
$$

$$(1.5.33)$$

The coordinate transformation in transition from S_2 to S_1 is represented by the equations

$$x_1 = x_2(\cos\phi_1\cos\phi_2 + \cos\gamma\sin\phi_1\sin\phi_2)$$
$$+ y_2(-\cos\phi_1\sin\phi_2 + \cos\gamma\sin\phi_1\cos\phi_2)$$
$$+ z_2\sin\gamma\sin\phi_1 - E\cos\phi_1$$

$$y_1 = x_2(-\sin\phi_1\cos\phi_2 + \cos\gamma\cos\phi_1\sin\phi_2) \qquad (1.5.34)$$
$$+ y_2(\sin\phi_1\sin\phi_2 + \cos\gamma\cos\phi_1\cos\phi_2)$$
$$+ z_2\sin\gamma\cos\phi_1 + E\sin\phi_1$$

$$z_1 = -x_2\sin\gamma\sin\phi_2 - y_2\sin\gamma\cos\phi_2 + z_2\cos\gamma.$$

1.6 APPLICATION TO DERIVATION OF CURVES

The technique of coordinate transformation can be successfully applied in the derivation of some curves and surfaces. It is assumed that the to-be-derived curve is generated by a point that performs a prescribed motion. Respectively, it is considered that the surface is generated by a curve that performs a prescribed motion as well (see Section 1.7).

Generation of Epicycloid

Consider two circles that are in external tangency [Fig. 1.6.1(a)]. The circles are centrodes and their relative motion is pure rolling. The radii of the circles are ρ_1 and ρ_2. Point M, which is rigidly connected to circle 2, traces out an *extended epicycloid* in the coordinate system that is rigidly connected to circle 1 [represented in coordinate system $S_1(x_1, y_1)$ as shown in Fig. 1.6.1(a)]. M_o and M are two positions of the tracing point.

Equations of the extended epicycloid may be derived by using the coordinate transformation in transition from S_2 to S_1. Coordinate systems S_1 and S_2 are shown in Fig. 1.6.1(b). The coordinate transformation from S_2 to S_1 has been represented in Problem 1.5.2 by Eqs. (1.5.15). The generating point M is represented in S_2 by [see Fig. 1.6.1(b)]

$$\left[x_2^{(M)} \quad y_2^{(M)} \quad z_2^{(M)} \quad 1\right]^{\mathrm{T}} = [0 \quad -a \quad 0 \quad 1]^{\mathrm{T}} \qquad (1.6.1)$$
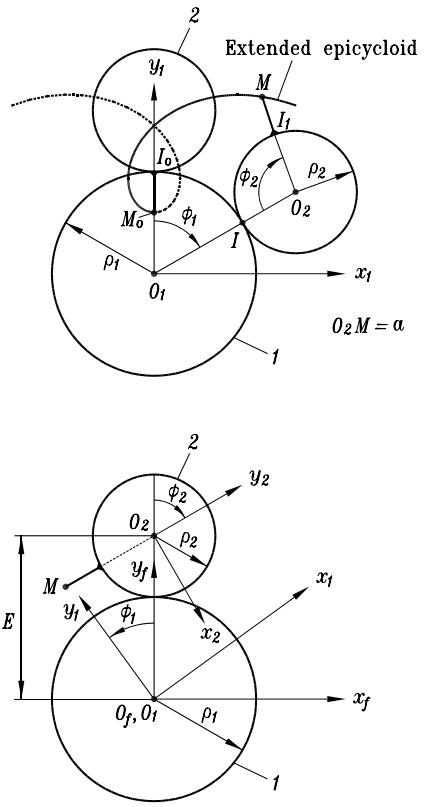
where $a = O_2 M > \rho_2$.

Equations (1.5.15) and (1.6.1) yield the following equations of the extended epicycloid:

$$x_1 = -a\sin(\phi_1 + \phi_2) + E\sin\phi_1$$
$$y_1 = -a\cos(\phi_1 + \phi_2) + E\cos\phi_1. \qquad (1.6.2)$$

Here,

$$E = \rho_1 + \rho_2, \quad \phi_2 = \phi_1\frac{\rho_1}{\rho_2}.$$

Figure 1.6.1: Generation of extended epicycloid: (a) illustration of generation of extended epicycloid; (b) illustration of coordinate transformation for derivation of extended epicycloid.

A shortened epicycloid is generated by point M with $a < \rho_2$. An ordinary epicycloid is generated with $a = \rho_2$.

Generation of Involute Curves
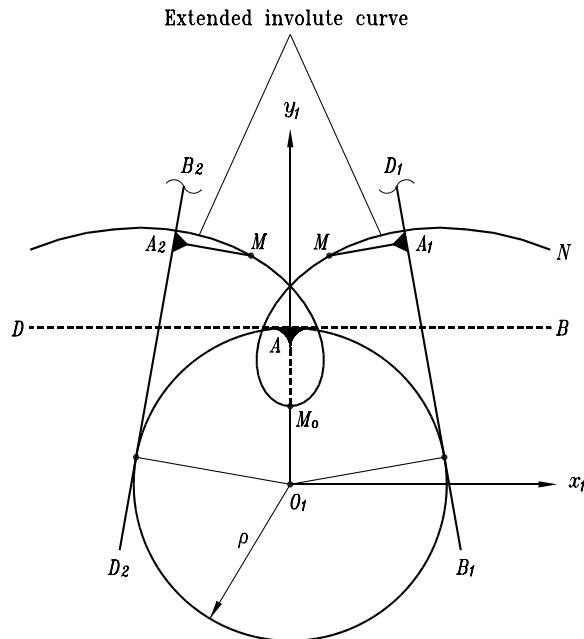
Henceforth we distinguish between an *ordinary* involute curve, an *extended* involute curve, and a *shortened* involute curve. Figure 1.6.2 shows that an extended involute curve is generated by a point M that is rigidly connected to the straight line $\overline{BD}$; this straight line rolls over the circle of radius ρ. The derivation of the extended involute is based on Eq. (1.5.10) which describes the coordinate transformation in transition from S_2 to S_1 (Figs. 1.5.1 and 1.6.3). The generating point is represented in S_2 (Fig. 1.6.3) by

$$\left[x_2^{(M)} \quad y_2^{(M)} \quad z_2^{(M)} \quad 1 \right]^{\mathrm{T}} = [0 \quad -a \quad 0 \quad 1]^{\mathrm{T}}. \tag{1.6.3}$$
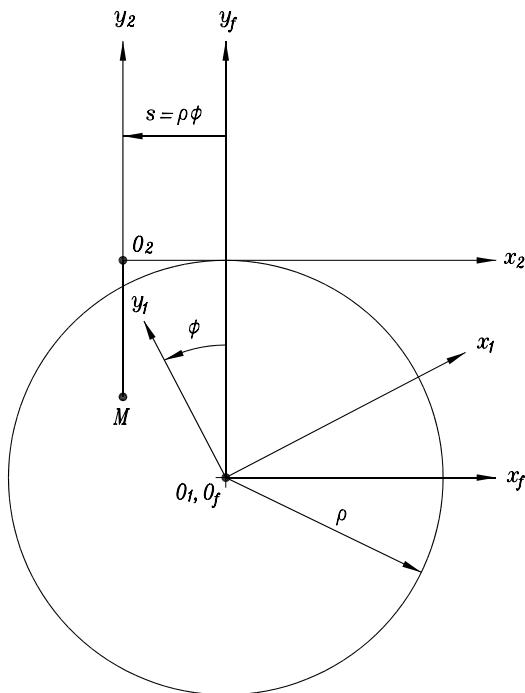
Equations (1.6.3) and (1.5.10) yield the following equations of the extended involute:

$$\begin{aligned} x_1 &= -a \sin\phi + \rho(\sin\phi - \phi\cos\phi) \\ y_1 &= -a \cos\phi + \rho(\cos\phi + \phi\sin\phi). \end{aligned} \tag{1.6.4}$$
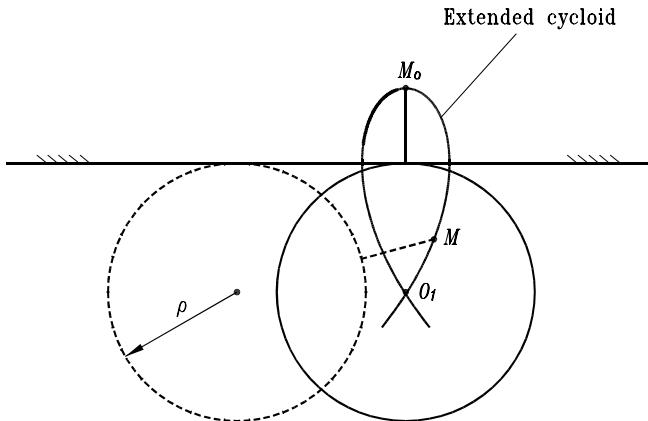
An ordinary involute curve will be generated if $a = 0$, and a shortened involute curve is generated if $y_2^{(M)} = a > 0$.

Figure 1.6.2: Illustration of generation of extended involute.

Figure 1.6.3: Generation of involute curve.

Figure 1.6.4: Generation of extended cycloid.

Problem 1.6.1
Derive the equations of the curve that is generated in S_1 by point M (Fig. 1.6.3) if point M is represented in S_2 by

$$\overline{O_2 M} = [0 \quad -\rho \quad 0 \quad 1] \tag{1.6.5}$$

Prove that the generated curve is the Archimedes spiral.

Solution
According to Eqs. (1.6.4) and (1.6.5), the generated curve is represented by

$$x_1 = -\rho\phi\cos\phi, \quad y_1 = \rho\phi\sin\phi. \tag{1.6.6}$$

The equation of this curve in polar coordinates (r, ϕ) is

$$r = \left(x_1^2 + y_1^2\right)^{1/2} = \rho\phi \tag{1.6.7}$$

where ϕ is the polar angle.

Generation of a Cycloid
An *extended* cycloid is generated by a point M that is rigidly connected to the circle while the circle of radius ρ rolls over a straight line (Fig. 1.6.4). Coordinate system S_1 is rigidly connected to the circle, and coordinate system S_2 is rigidly connected to the straight line (Fig. 1.5.1). The generating point is represented in S_1 by

$$\overline{O_1 M} = [0 \quad -a \quad 0 \quad 1]^{\mathrm{T}}. \tag{1.6.8}$$

The coordinate transformation in transition from S_1 to S_2 is represented by Eqs. (1.5.7). Equations (1.5.7) and (1.6.8) yield

$$x_2 = -a\sin\phi + \rho\phi, \quad y_2 = a\cos\phi - \rho. \tag{1.6.9}$$

A *shortened* cycloid is generated if $a < \rho$, and an *ordinary* cycloid is generated if $a = \rho$.

1.7 APPLICATION TO DERIVATION OF SURFACES

The technique of coordinate transformation can be also applied to the derivation of equations of a surface that is generated as a family of curves of the same shape. We illustrate this technique with the example of a helicoid that is generated by a planar curve performing a screw motion [Fig. 1.7.1(a)]. Figure 1.7.1(b) shows two coordinate systems: S_1, which is fixed, and a movable coordinate system S_a that performs a screw motion with respect to S_1. The angle of rotation and axial displacement in screw motion are designated by ψ and $p\psi$, respectively. Here, p is the parameter of screw motion – the **pitch** of the screw – and is given by

$$p = \frac{H}{2\pi} \tag{1.7.1}$$
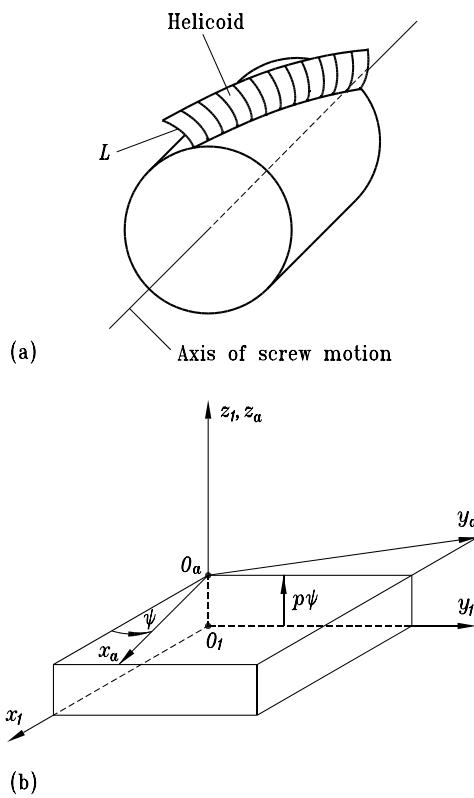
where H is the axial displacement corresponding to one complete revolution.

Assume that the planar curve L is represented in coordinate system $S_a(x_a, y_a, z_a)$ [Fig. 1.7.1(b)] by equations
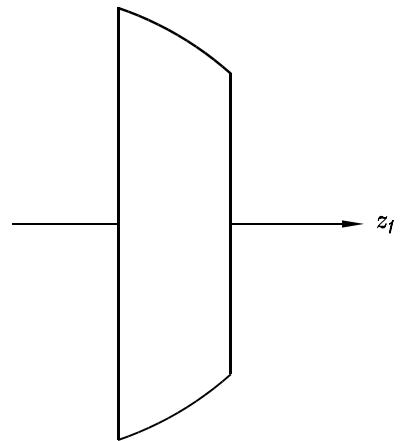
$$x_a = x_a(\theta), \quad y_a = y_a(\theta), \quad z_a = 0 \qquad \theta_1 \le \theta \le \theta_2 \tag{1.7.2}$$

where parameter θ is the independent variable. The generated surface is determined in coordinate system S_1 with the matrix equation

$$\mathbf{r}_1 = \mathbf{M}_{1a}\mathbf{r}_a \tag{1.7.3}$$

(a)

Figure 1.7.1: Generation of helicoid: (a) illustration of generation of a helicoid by screw motion of a planar curve; (b) illustration of coordinate systems S_a and S_1.

(b)

Figure 1.7.2: Surface of revolution.

where

$$\mathbf{r}_1 = \begin{bmatrix} x_1 \\ y_1 \\ z_1 \\ 1 \end{bmatrix}, \quad \mathbf{M}_{1a} = \begin{bmatrix} \cos\psi & -\sin\psi & 0 & 0 \\ \sin\psi & \cos\psi & 0 & 0 \\ 0 & 0 & 1 & p\psi \\ 0 & 0 & 0 & 1 \end{bmatrix}$$

$$(1.7.4)$$

$$\mathbf{r}_a = \begin{bmatrix} x_a(\theta) \\ y_a(\theta) \\ z_a(\theta) \\ 1 \end{bmatrix}.$$

Matrix equations (1.7.3) and (1.7.4) yield

$$\begin{aligned} x_1 &= x_a(\theta)\cos\psi - y_a(\theta)\sin\psi \\ y_1 &= x_a(\theta)\sin\psi + y_a(\theta)\cos\psi \\ z_1 &= p\psi \end{aligned}$$

$$(1.7.5)$$

where

$$\theta_1 \leq \theta \leq \theta_2, \quad \psi_1 \leq \psi \leq \psi_2.$$
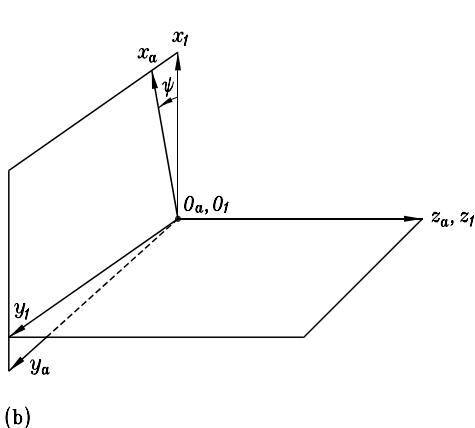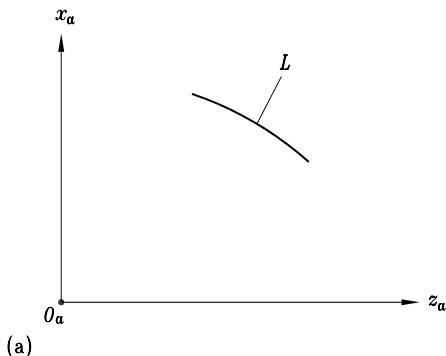
Equations (1.7.5) represent the generated helicoid with *surface coordinates* θ, ψ. By surface coordinates we mean that a point of the surface is uniquely specified by given values θ and ψ (see Chapter 5).

Problem 1.7.1

A surface of revolution is generated by rotation of a planar curve about the fixed axis z_1. Figure 1.7.2 shows the axial section of the surface. The generating curve [Fig. 1.7.3(a)] is represented in coordinate system S_a (x_a, y_a, z_a) by equations

$$x_a = x_a(\theta), \quad y_a = 0, \quad z_a = z_a(\theta). \tag{1.7.6}$$

The angle of rotation ψ [Fig. 1.7.3(b)] lies within the interval $0 \leq \psi \leq 2\pi$. Applying the matrix method of surface generation, derive the equations of the generated surface.

(a)

Figure 1.7.3: Generation of surface of revolution:
(a) representation of planar curve L in coordinate
system S_a; (b) illustration of coordinate systems S_a
and S_1.

(b)

Solution

$$x_1 = x_a(\theta) \cos \psi, \quad y_1 = x_a(\theta) \sin \psi$$
$$z_1 = z_a(\theta), \quad \theta_1 \le \theta \le \theta_2 \quad 0 \le \psi \le 2\pi. \tag{1.7.7}$$
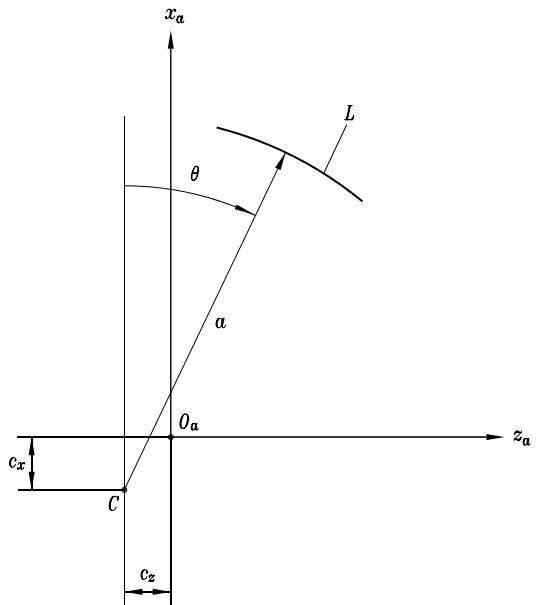
Problem 1.7.2
With the conditions of problem 1.7.1, determine the equations of the surface generated
by the segment of a circle centered at C (Fig. 1.7.4).

Solution

$$x_1 = (a \cos \theta + C_x) \cos \psi, \quad y_1 = (a \cos \theta + C_x) \sin \psi$$
$$z_1 = (a \sin \theta + C_x), \quad \theta_1 \le \theta \le \theta_2, \quad 0 \le \psi \le 2\pi \tag{1.7.8}$$
$$C_x < 0, \quad C_z < 0.$$

Problem 1.7.3
A spherical surface may be represented as a particular case of the surface represented
by Eqs. (1.7.7). Determine equations of a spherical surface that is centered at O_a
(Fig. 1.7.4).
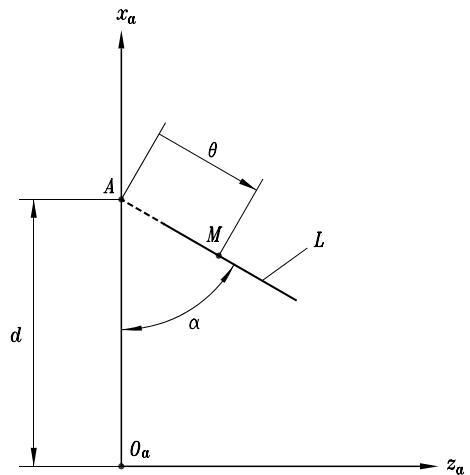
Figure 1.7.4: For generation of surface of revolution.

Solution
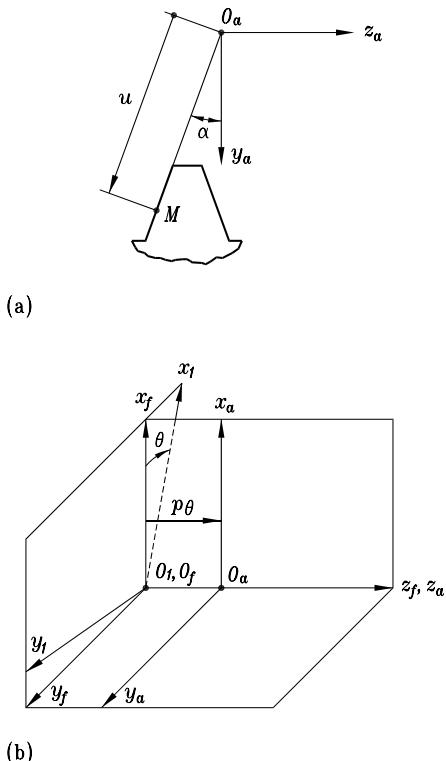
$$x_1 = a \cos\theta \cos\psi, \quad y_1 = a \cos\theta \sin\psi, \quad z_1 = a \sin\theta$$
$$\theta_1 \leq \theta \leq \theta_2, \quad 0 \leq \psi \leq 2\pi.$$

(1.7.9)

Problem 1.7.4

Straight line AL is represented in coordinate system S_a (Fig. 1.7.5). The location of a current point on AL is determined with parameter θ. Coordinate system S_a with the straight line performs rotation about the z_1 axis. Derive equations of the cone surface that is generated in S_1.

Figure 1.7.5: Cone generation.

(a)

Figure 1.7.6: Generation of screw surface: (a) illustration of generating blade; (b) illustration of coordinate systems S_1, S_a, and S_f.

(b)

Solution

$$x_1 = (d - \theta \cos \alpha) \cos \psi, \quad y_1 = (d - \theta \cos \alpha) \sin \psi$$
$$z_1 = \theta \sin \alpha. \tag{1.7.10}$$

Problem 1.7.5

A screw surface is generated by a straight-lined edge MO_a of a blade [Fig. 1.7.6(a)]. We consider three coordinate system S_a, S_1, and S_f that are rigidly connected to the blade, to the blank of the screw being generated, and to the frame of the cutting machine, respectively [Fig. 1.7.6(b)]. While the blank of the screw rotates through angle θ, the blade translates on the distance $p\theta$ where p is the screw parameter. The edge of the blade is represented in S_a by the equations [Fig. 1.7.6(a)]

$$x_a = 0, \quad y_a = u \cos \alpha, \quad z_a = -u \sin \alpha. \tag{1.7.11}$$

Here, u is the variable parameter that determines the location of a current point of the edge; α is the blade angle. Derive equations of the generated screw surface.

Solution

$$x_1 = -u \cos \alpha \sin \theta, \quad y_1 = u \cos \alpha \cos \theta, \quad z_a = -u \sin \alpha + p\theta$$

$$u_1 \leq u \leq u_2, \quad 0 \leq \theta \leq 2\pi. \tag{1.7.12}$$

2 Relative Velocity

2.1 VECTOR REPRESENTATION

The concept of relative velocity is used for the derivation of the equation of meshing (see Section 6.1) and for the derivation of centrodes and axodes (see Chapter 3). Consider that two bodies are rotated about crossed axes with angular velocities $\boldsymbol{\omega}^{(1)}$ and $\boldsymbol{\omega}^{(2)}$, respectively (Fig. 2.1.1). Vector $\boldsymbol{\omega}^{(1)}$ passes through the origin of fixed coordinate system S_f that is employed in the gear housing. The twist angle is γ and the shortest distance is E. Point M is common to both rotating bodies. The relative velocity of point $M^{(1)}$ of body 1 with respect to point $M^{(2)}$ of body 2 is represented by the equation

$$\mathbf{v}^{(12)} = \mathbf{v}^{(1)} - \mathbf{v}^{(2)} \tag{2.1.1}$$

where $\mathbf{v}^{(i)}$ is the velocity of point $M^{(i)}$ of body i ($i = 1, 2$).

The velocity $\mathbf{v}^{(1)}$ is represented by the equation

$$\mathbf{v}^{(1)} = \boldsymbol{\omega}^{(1)} \times \mathbf{r} \tag{2.1.2}$$

where $\mathbf{r}$ is the position vector that is drawn to point M from an arbitrary point on the line of action of $\boldsymbol{\omega}^{(1)}$, for instance, from point O_f. Similarly, we may represent the velocity $\mathbf{v}^{(2)}$ by

$$\mathbf{v}^{(2)} = \boldsymbol{\omega}^{(2)} \times \boldsymbol{\rho} \tag{2.1.3}$$

where $\boldsymbol{\rho}$ is drawn to point M from an arbitrary point on the line of action of $\boldsymbol{\omega}^{(2)}$, for instance, from point O_2. An alternative equation for $\mathbf{v}^{(2)}$ is based on the substitution of the sliding vector $\boldsymbol{\omega}^{(2)}$ with the line of action $O_2 - O_2'$ by an equal vector that passes through O_f and by the vector-moment,

$$\mathbf{m} = \mathbf{R} \times \boldsymbol{\omega}^{(2)}. \tag{2.1.4}$$

Here, $\mathbf{R}$ is a position vector that is drawn from O_f to an arbitrary point O_2' on the line of action of $\boldsymbol{\omega}^{(2)}$. For instance, we may choose that O_2' coincides with O_2 and $\mathbf{R} = \overline{O_f O_2} = \mathbf{E}$. Note that the moment $\mathbf{m}$ has the unit and physical meaning of linear velocity. By replacing $\boldsymbol{\omega}^{(2)}$ by an equal vector that passes through point O_f and moment $\mathbf{m}$, we may represent the velocity $\mathbf{v}^{(2)}$ as follows:

$$\mathbf{v}^{(2)} = (\boldsymbol{\omega}^{(2)} \times \mathbf{r}) + (\mathbf{R} \times \boldsymbol{\omega}^{(2)}). \tag{2.1.5}$$
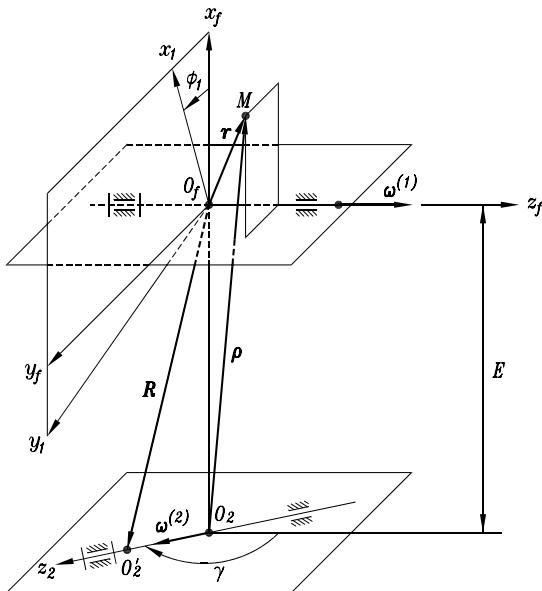
Figure 2.1.1: Rotation about crossed axes.

It is easy to prove that Eqs. (2.1.3) and (2.1.5) are equivalent by taking into account that $\mathbf{R} = \overline{O_f O_2} + \overline{O_2 O_2'}$ and $\mathbf{r} = \overline{O_f O_2} + \rho$. Then we obtain that

$$\mathbf{v}^{(2)} = \boldsymbol{\omega}^{(2)} \times (\mathbf{r} - \mathbf{R}) = \boldsymbol{\omega}^{(2)} \times \rho. \tag{2.1.6}$$

The final expression for the relative velocity may be represented as

$$\mathbf{v}^{(12)} = [(\boldsymbol{\omega}^{(1)} - \boldsymbol{\omega}^{(2)}) \times \mathbf{r}] - (\mathbf{E} \times \boldsymbol{\omega}^{(2)}) \tag{2.1.7}$$

where $\mathbf{E} = \overline{O_f O_2}$; $\mathbf{r} = \overline{O_f M}$. The relative velocity $\mathbf{v}^{(21)}$ of point M of body 2 with respect to point M of body 1 is

$$\mathbf{v}^{(21)} = -\mathbf{v}^{(12)} = [(\boldsymbol{\omega}^{(2)} - \boldsymbol{\omega}^{(1)}) \times \mathbf{r}] + (\mathbf{E} \times \boldsymbol{\omega}^{(2)}). \tag{2.1.8}$$

Consider now that points $M^{(1)}$ and $M^{(2)}$ are the points of gear tooth surfaces Σ_1 and Σ_2. If the coinciding points $M^{(1)}$ and $M^{(2)}$ form the point M of tangency of Σ_1 and Σ_2, the surfaces have a common normal at M, and $\mathbf{v}^{(12)}$ (as well as $\mathbf{v}^{(21)}$) lies in the plane that is tangent to Σ_1 and Σ_2 at M. Thus, we can say that the relative velocity of point $M^{(1)}$ with respect to $M^{(2)}$ is the *sliding* velocity of surface Σ_1 with respect to Σ_2 at the point of tangency M.

We have to emphasize that the velocity $\mathbf{v}^{(12)}$ can be seen by an observer located on the reference frame 2 (on gear tooth surface Σ_2) and watching the motion of body 1 (surface Σ_1) with respect to body 2 (surface Σ_2). Respectively, the observer must be located on reference frame 1 to watch $\mathbf{v}^{(21)}$.

The vector of sliding velocity, vector $\mathbf{v}^{(12)}$, can be represented in any of the three coordinate systems S_f, S_1, and S_2. To recognize the coordinate system in which, the

sliding velocity is represented, we use the following expression for $\mathbf{v}^{(12)}$:

$$\mathbf{v}_i^{(12)} = [(\boldsymbol{\omega}_i^{(1)} - \boldsymbol{\omega}_i^{(2)}) \times \mathbf{r}_i] - (\mathbf{E}_i \times \boldsymbol{\omega}_i^{(2)}) \qquad (i = 1, f, 2). \qquad (2.1.9)$$

The subscript "i" indicates that the vector is represented in coordinate system S_i.

Consider now that vector $\mathbf{v}^{(12)}$ is represented in a coordinate system, say S_f, and that it is necessary to represent $\mathbf{v}^{(12)}$ in coordinate systems S_1 and S_2. There are two solutions for this problem. The first one is based on Eq. (2.1.9) and representation of all vectors of this equation in the respective coordinate system.

The other solution is based on matrix equation

$$\mathbf{v}_m^{(12)} = \mathbf{L}_{mf} \mathbf{v}_f^{(12)} \qquad (m = 1, 2) \qquad (2.1.10)$$

for representation of $\mathbf{v}_m^{(12)}$ in coordinate system S_m. However, components of vector $\mathbf{v}_m^{(12)}$ are still represented in components of the position vector

$$\mathbf{r}_f = [x_f \ \ y_f \ \ z_f]^\mathrm{T}. \qquad (2.1.11)$$
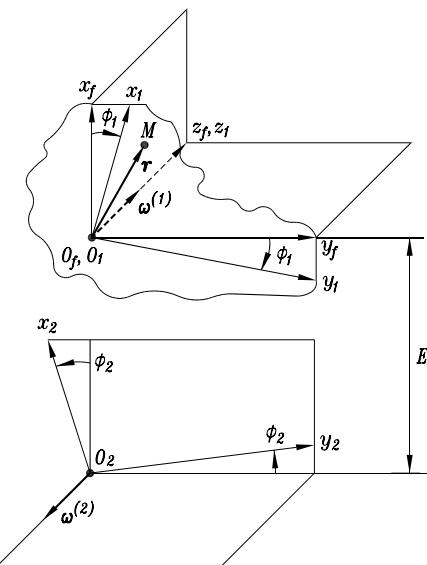
To represent $\mathbf{v}_m^{(12)}$ in components (x_m, y_m, z_m), we have to use the matrix equation

$$\mathbf{r}_f = \mathbf{M}_{fm} \mathbf{r}_m. \qquad (2.1.12)$$

The discussed approaches are illustrated with Problem 2.1.2.

Problem 2.1.1

Gears 1 and 2 transform rotation between two parallel axes with angular velocities $\boldsymbol{\omega}^{(1)}$ and $\boldsymbol{\omega}^{(2)}$ (Fig. 2.1.2). Derive and represent in coordinate system S_f the sliding velocity $\mathbf{v}^{(12)}$ for point M.

Figure 2.1.2: Rotation about parallel axes.

Solution
The solution is based on vector equation (2.1.9) whose vectors are represented in S_f as follows:

$$\boldsymbol{\omega}_f^{(1)} = [0 \quad 0 \quad \omega^{(1)}]^T, \quad \boldsymbol{\omega}_f^{(2)} = [0 \quad 0 \quad -\omega^{(2)}]^T$$

$$\mathbf{r}_f = [x_f \quad y_f \quad z_f]^T, \quad \mathbf{E}_f = [-E \quad 0 \quad 0]^T. \tag{2.1.13}$$

Equation (2.1.9) with expressions (2.1.13) yields

$$\mathbf{v}_f^{(12)} = [-y_f(\omega^{(1)} + \omega^{(2)})]\mathbf{i}_f + [x_f(\omega^{(1)} + \omega^{(2)}) + E\omega^{(2)}]\mathbf{j}_f \tag{2.1.14}$$

where $\mathbf{i}_f$, $\mathbf{j}_f$, and $\mathbf{k}_f$ are the unit vectors of the S_f coordinate system.

Problem 2.1.2
With the main conditions of problem 2.1.1, express the sliding velocity $\mathbf{v}_1^{(12)}$ in coordinate system S_1.

Solution
APPROACH 1. The solution is based on Eq. (2.1.9) whose vectors are represented in S_1 by the following expressions:

$$\boldsymbol{\omega}_1^{(1)} = [0 \quad 0 \quad \omega^{(1)}]^T, \quad \boldsymbol{\omega}_1^{(2)} = [0 \quad 0 \quad -\omega^{(2)}]^T$$

$$\mathbf{r}_1 = [x_1 \quad y_1 \quad z_1]^T, \quad \mathbf{E}_1 = \mathbf{L}_{1f}\mathbf{E}_f = [-E\cos\phi_1 \quad E\sin\phi_1 \quad 0]^T. \tag{2.1.15}$$

Here,

$$\mathbf{L}_{1f} = \begin{bmatrix} \cos\phi_1 & \sin\phi_1 & 0 \\ -\sin\phi_1 & \cos\phi_1 & 0 \\ 0 & 0 & 1 \end{bmatrix}. \tag{2.1.16}$$

Equations (2.1.9), (2.1.15), and (2.1.16) yield

$$\mathbf{v}_1^{(12)} = [-(\omega^{(1)} + \omega^{(2)})y_1 + \omega^{(2)}E\sin\phi_1]\,\mathbf{i}_1$$
$$+ [(\omega^{(1)} + \omega^{(2)})x_1 + \omega^{(2)}E\cos\phi_1]\,\mathbf{j}_1. \tag{2.1.17}$$

APPROACH 2. Consider that $\mathbf{v}_f^{(12)}$ is represented by Eq. (2.1.14). Determine $\mathbf{v}_1^{(12)}$ representing it in coordinate system S_1.

The solution is based on the following two steps.

Step 1: We use an equation that is similar to (2.1.10) and take into account that $\mathbf{L}_{1f}$ is represented by (2.1.16) and $\mathbf{v}_f^{(12)}$ is represented by (2.1.14). Then we obtain

$$\mathbf{v}_1^{(12)} = \mathbf{L}_{1f}\mathbf{v}_f^{(12)} = [-(\omega^{(1)} + \omega^{(2)})y_f\cos\phi_1 + (\omega^{(1)} + \omega^{(2)})x_f\sin\phi_1 + \omega^{(2)}E\sin\phi_1]\,\mathbf{i}_1$$
$$+ [(\omega^{(1)} + \omega^{(2)})y_f\sin\phi_1 + (\omega^{(1)} + \omega^{(2)})x_f\cos\phi_1 + \omega^{(2)}E\cos\phi_1]\,\mathbf{j}_1.$$

$$\tag{2.1.18}$$

Step 2: Equation (2.1.18) still contains coordinates (x_f, y_f). We may represent (x_f, y_f) in terms of (x_1, y_1, ϕ_1) using the matrix equation
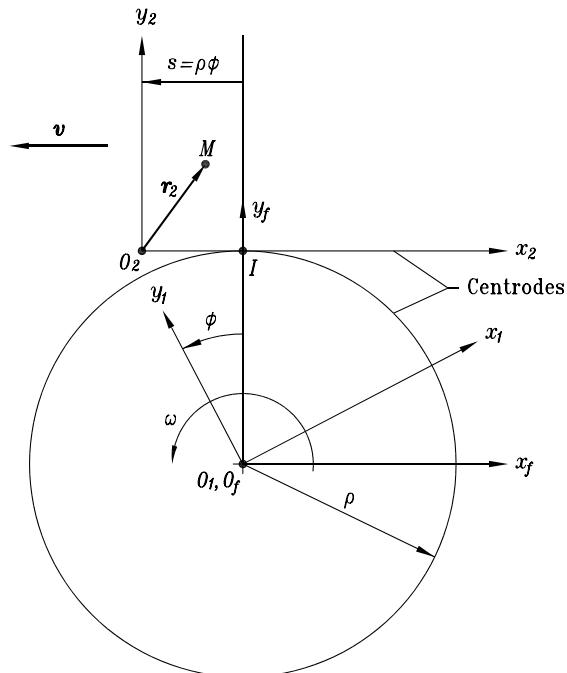
$$\mathbf{r}_f = \begin{bmatrix} \cos\phi_1 & -\sin\phi_1 & 0 & 0 \\ \sin\phi_1 & \cos\phi_1 & 0 & 0 \\ 0 & 0 & 1 & 0 \\ 0 & 0 & 0 & 1 \end{bmatrix} \mathbf{r}_1. \tag{2.1.19}$$

Matrix equation (2.1.19) allows us to represent x_f (and y_f) in terms of x_1 and ϕ_1 (and y_1, ϕ_1). Equations (2.1.18) and (2.1.19) yield equation (2.1.17) for representation of $\mathbf{v}_1^{(12)}$.

Problem 2.1.3

Consider three reference frames 1, 2, and f that are rigidly connected to a gear, a rack, and the housing of the train, respectively (Fig. 2.1.3). The rack translates with velocity $\mathbf{v}$ and the gear rotates with angular velocity ω. It is assumed that the ratio $|\mathbf{v}|/\omega$ is constant. The instantaneous center of rotation I is located on line $O_f I$ that is perpendicular to $\mathbf{v}$. The location of I satisfies the vector equation (see Section 3.1)

$$\mathbf{v} = \omega \times \overline{O_f I}. \tag{2.1.20}$$

Figure 2.1.3: Transformation of rotation into translation.

Point I is the point of tangency of centrodes of the rack and the gear. The gear centrode is a circle of radius

$$\rho = \frac{|\mathbf{v}|}{\omega}. \tag{2.1.21}$$

The relative motion of centrodes is pure rolling about I and the displacements of the rack and the angle of gear rotation ϕ are related by

$$s = \rho\phi. \tag{2.1.22}$$

The goal of the to-be-solved problem is to determine the sliding velocity $\mathbf{v}_2^{(21)}$ at point $M(x_2, y_2, z_2)$.

Solution

$$\mathbf{v}_2^{(21)} = \mathbf{v}_2^{(2)} - \mathbf{v}_2^{(1)}. \tag{2.1.23}$$

Here, $\mathbf{v}_2^{(2)} = \mathbf{v}_2$ is the velocity of the rack represented in S_2; $\mathbf{v}_2^{(1)}$ is the velocity of the gear at point M that is also represented in S_2.

The gear rotates about O_1 with angular velocity ω. Substituting sliding vector ω, which passes through O_1, with an equal vector that passes through O_2 and the respective vector-moment $\mathbf{m}$, we obtain

$$\mathbf{v}_2^{(1)} = (\boldsymbol{\omega}_2 \times \mathbf{r}_2) + (\mathbf{R}_2 \times \boldsymbol{\omega}_2) \tag{2.1.24}$$

where

$$\mathbf{R}_2 = \overline{O_2 O_1}. \tag{2.1.25}$$

The final expression for $\mathbf{v}_2^{(21)}$ is

$$\mathbf{v}_2^{(21)} = \mathbf{v}_2 - (\boldsymbol{\omega}_2 \times \mathbf{r}_2) - (\mathbf{R}_2 \times \boldsymbol{\omega}_2). \tag{2.1.26}$$

Vectors of Eq. (2.1.26) are represented in S_2 as follows:

$$\mathbf{v}_2^{(2)} = -v\mathbf{i}_2 = -\omega\rho\mathbf{i}_2, \quad \boldsymbol{\omega}_2 = \omega\mathbf{k}_2, \quad \mathbf{R}_2 = \overline{O_2 O_1} = \rho\phi\mathbf{i}_2 - \rho\mathbf{j}_2$$

$$\mathbf{r}_2 = x_2\mathbf{i}_2 + y_2\mathbf{j}_2. \tag{2.1.27}$$

Equations (2.1.26) and (2.1.27) yield

$$\mathbf{v}_2^{(21)} = \omega[y_2\mathbf{i}_2 + (\rho\phi - x_2)\mathbf{j}_2]. \tag{2.1.28}$$

Problem 2.1.4

Consider the reference frames S_1, S_2, and S_f that have been represented in Fig. 1.5.5. Gear 1 rotates with angular velocity $\omega^{(1)}$ about the z_f axis. Gear 2 rotates with angular velocity $\omega^{(2)}$ about axis $\overline{O_2 O_2'}$ (Fig. 2.1.1) that coincides with the z_2 axis (Figs. 1.5.5 and 2.1.1). Axes z_f and z_2 form the twist angle γ and the shortest distance between the axes is E. Derive the equation for the sliding velocity $\mathbf{v}^{(12)}$ and represent it in coordinate systems S_f and S_1.

Solution

$$\mathbf{v}_f^{(12)} = \begin{bmatrix} -y_f(\omega^{(1)} - \omega^{(2)}\cos\gamma) - z_f\omega^{(2)}\sin\gamma \\ \\ x_f(\omega^{(1)} - \omega^{(2)}\cos\gamma) - E\omega^{(2)}\cos\gamma \\ \\ (x_f + E)\omega^{(2)}\sin\gamma \end{bmatrix} \tag{2.1.29}$$

$$v_{1x}^{(12)} = -y_1(\omega^{(1)} - \omega^{(2)}\cos\gamma) - z_1\omega^{(2)}\sin\gamma\cos\phi_1$$
$$- E\omega^{(2)}\cos\gamma\sin\phi_1 \tag{2.1.30}$$

$$v_{1y}^{(12)} = x_1(\omega^{(1)} - \omega^{(2)}\cos\gamma) + z_1\omega^{(2)}\sin\gamma\sin\phi_1$$
$$- E\omega^{(2)}\cos\gamma\cos\phi_1 \tag{2.1.31}$$

$$v_{1z}^{(12)} = (x_1\cos\phi_1 - y_1\sin\phi_1 + E)\omega^{(2)}\sin\gamma. \tag{2.1.32}$$

2.2 MATRIX REPRESENTATION

Matrix representation of sliding velocity is an alternative solution to vector representation. The advantage of matrix representation is the possibility of formalizing and computerizing the design, especially when the meshing has to be simulated (see Section 6.1) and surface singularities (undercutting) have to be avoided (see Section 6.3).

The computational procedure is as follows.

Step 1: Consider the matrix equation

$$\mathbf{r}_2(x_2, y_2, z_2, 1) = \mathbf{M}_{21}(\phi)\mathbf{r}_1(x_1, y_1, z_1, 1) \tag{2.2.1}$$

that describes relations between homogeneous coordinates of position vectors $\mathbf{r}_1$ and $\mathbf{r}_2$ represented in coordinate systems S_1 and S_2, respectively. Parameter ϕ is the generalized parameter of motion. The goal is representation of relative velocity $\mathbf{v}^{(12)}$ in S_1 and S_2.

Step 2: Matrix equation (2.2.1) yields the relation

$$\boldsymbol{\rho}_2(x_2, y_2, z_2) = \mathbf{L}_{21}(\phi)\boldsymbol{\rho}_1(x_1, y_1, z_1) + [a_{14}(\phi) \quad a_{24}(\phi) \quad a_{34}(\phi)]^T. \tag{2.2.2}$$

Here, $\mathbf{L}_{21}(\phi)$ is the 3×3 submatrix of $\mathbf{M}_{21}$. Designations $a_{kl}(k = 1, 2, 3; l = 1, 2, 3, 4)$ indicate elements of matrices $\mathbf{M}_{21}$ and $\mathbf{L}_{21}$. Vectors $\boldsymbol{\rho}_i(i = 1, 2)$ are represented in terms of Cartesian coordinates.

Step 3: Differentiation of matrix equation (2.2.2) yields

$$\dot{\boldsymbol{\rho}}_2(x_2, y_2, z_2) = \{\dot{\mathbf{L}}_{21}(\phi)\boldsymbol{\rho}_1(x_1, y_1, z_1) + [\dot{a}_{14}(\phi) \quad \dot{a}_{24}(\phi) \quad \dot{a}_{34}(\phi)]^T\}\dot{\phi}. \tag{2.2.3}$$

We may interpret $\dot{\boldsymbol{\rho}}_2$ as follows:

(i) An observer located in coordinate system S_2 at point M_2 of S_2 will see that point M_1 of coordinate system S_1 is moving with respect to point M_2 of S_2 where the observer is located.

 (ii) M_1 is in motion because the parameter of motion ϕ is varied.
(iii) At the start of variation of ϕ, point M_1 coincides with M_2.

Based on the considerations above, we identify $\dot{\rho}_2$ as $v_2^{(12)}$. Thus, we can rewrite Eq. (2.2.3) as

$$v_2^{(12)} = \left\{ \dot{L}_{21}(\phi)\rho_1(x_1, y_1, z_1) + [\dot{a}_{14}(\phi) \quad \dot{a}_{24}(\phi) \quad \dot{a}_{34}(\phi)]^T \right\} \dot{\phi}. \qquad (2.2.4)$$

The designation "2" means that vector $v_2^{(12)}$ is represented in coordinate system S_2.
Step 4: The representation of $v^{(12)}$ in coordinate system S_1 is obtained by the following transformation:

$$v_1^{(12)} = L_{12}(\phi)v_2^{(12)}$$
$$= \left\{ L_{12}(\phi)\dot{L}_{21}(\phi)\rho_1(x_1, y_1, z_1) + L_{12}(\phi)[\dot{a}_{14}(\phi) \quad \dot{a}_{24}(\phi) \quad \dot{a}_{34}(\phi)]^T \right\} \dot{\phi}. \qquad (2.2.5)$$

Here, L_{12} is the inverse matrix of L_{21} and $L_{12}L_{21} = I$ where I_{12} is the unit matrix 3×3.

Note 1. The product $L_{12}\dot{L}_{21}$ is a skew-symmetric matrix (see Section 2.3).

Note 2. We may consider matrix equation

$$r_1(x_1, y_1, z_1, 1) = M_{12}(\phi)r_2(x_2, y_2, z_2, 1). \qquad (2.2.6)$$

Similar derivations enable us to obtain $v_1^{(21)} = \dot{\rho}_1$ and $v_2^{(21)} = L_{21}(\phi)v_1^{(21)}$, resulting in the following equations:

$$v_1^{(21)} = \left\{ \dot{L}_{12}(\phi)\rho_2(x_2, y_2, z_2) + [\dot{a}_{14}(\phi) \quad \dot{a}_{24}(\phi) \quad \dot{a}_{34}(\phi)]^T \right\} \dot{\phi} \qquad (2.2.7)$$

$$v_2^{(21)} = L_{21}(\phi)v_1^{(21)}$$
$$= \left\{ L_{21}(\phi)\dot{L}_{12}(\phi)\rho_2(x_2, y_2, z_2) + L_{21}(\phi)[\dot{a}_{14}(\phi) \quad \dot{a}_{24}(\phi) \quad \dot{a}_{34}(\phi)]^T \right\} \dot{\phi}. \qquad (2.2.8)$$

Elements $\dot{a}_{14}(\phi)$, $\dot{a}_{24}(\phi)$, and $\dot{a}_{34}(\phi)$ in Eqs. (2.2.4) and (2.2.5) do not coincide with corresponding elements $\dot{a}_{14}(\phi)$, $\dot{a}_{24}(\phi)$, and $\dot{a}_{34}(\phi)$ in Eqs. (2.2.7) and (2.2.8). These elements have to be obtained from matrices M_{21} and M_{12}, respectively.

Problem 2.2.1
Consider the coordinate transformation represented in Fig. 2.1.3. Derive and represent the sliding velocities $v_2^{(12)}$ and $v_1^{(12)}$.

Solution
Matrix M_{21} is represented as

$$M_{21}(\phi) = \begin{bmatrix} \cos\phi & -\sin\phi & 0 & \rho\phi \\ \sin\phi & \cos\phi & 0 & -\rho \\ 0 & 0 & 1 & 0 \\ 0 & 0 & 0 & 1 \end{bmatrix}. \qquad (2.2.9)$$

The performed derivations yield

$$
\mathbf{v}_2^{(12)} = \omega^{(1)} \begin{bmatrix} -x_1 \sin\phi - y_1 \cos\phi + \rho \\ x_1 \cos\phi - y_1 \sin\phi \\ 0 \end{bmatrix} \tag{2.2.10}
$$

$$
\mathbf{v}_1^{(12)} = \omega^{(1)} \begin{bmatrix} -y_1 + \rho \cos\phi \\ x_1 - \rho \sin\phi \\ 0 \end{bmatrix}. \tag{2.2.11}
$$

Considering matrix equation

$$
\mathbf{r}_1(x_1, y_1, z_1, 1) = \mathbf{M}_{12}(\phi)\mathbf{r}_2(x_2, y_2, z_2, 1) \tag{2.2.12}
$$

where

$$
\mathbf{M}_{12}(\phi) = \begin{bmatrix} \cos\phi & \sin\phi & 0 & \rho(\sin\phi - \phi\cos\phi) \\ -\sin\phi & \cos\phi & 0 & \rho(\cos\phi + \phi\sin\phi) \\ 0 & 0 & 1 & 0 \\ 0 & 0 & 0 & 1 \end{bmatrix}, \tag{2.2.13}
$$

we can represent the sliding velocity $\mathbf{v}_2^{(12)}$ in terms of position vector $\mathbf{r}_2(x_2, y_2, z_2, 1)$ as

$$
\mathbf{v}_2^{(12)} = \omega^{(1)} \begin{bmatrix} -y_2 \\ x_2 - \rho\phi \\ 0 \end{bmatrix}. \tag{2.2.14}
$$

2.3 APPLICATION OF SKEW-SYMMETRIC MATRICES

Equations (2.2.5) and (2.2.8) may be used directly for computerized operations on matrices. It may also be shown that these equations express the representation of $\mathbf{v}^{(12)}$ in terms of skew-symmetric matrices.

Let us recall that a cross product

$$
\mathbf{v} = \boldsymbol{\omega} \times \mathbf{r} \tag{2.3.1}
$$

may be represented in matrix form as

$$
\mathbf{v} = \boldsymbol{\omega}^s \mathbf{r} \tag{2.3.2}
$$

where the skew-symmetric matrix ω^s is represented as

$$\omega^s = \begin{bmatrix} 0 & -\omega_z & \omega_y \\ \omega_z & 0 & -\omega_x \\ -\omega_y & \omega_x & 0 \end{bmatrix}. \tag{2.3.3}$$

It is easy to verify that

$$\{L_{12}(\phi)\dot{L}_{21}(\phi)\}\dot{\phi} = \begin{bmatrix} 0 & -\omega^{(1)} & 0 \\ \omega^{(1)} & 0 & 0 \\ 0 & 0 & 0 \end{bmatrix} = \left(\omega_1^{(1)}\right)^s \tag{2.3.4}$$

represents in S_1 the skew-symmetric matrix for the case in which (Figs. 1.5.5 and 2.1.1)

$$\omega_1^{(1)} = \omega^{(1)}\mathbf{k}_1. \tag{2.3.5}$$

The final expression of the sliding velocity $\mathbf{v}^{(12)}$ in terms of the skew-symmetric matrix in coordinate systems S_1 is represented as

$$\mathbf{v}_1^{(12)} = \left(\omega_1^{(1)}\right)^s \rho_1(x_1, y_1, z_1) + \{L_{12}(\phi)\left[\dot{a}_{14}(\phi) \quad \dot{a}_{24}(\phi) \quad \dot{a}_{34}(\phi)\right]^T\}\dot{\phi}. \tag{2.3.6}$$

Problem 2.3.1
Consider the coordinate transformation represented in Fig. 2.1.3. Derive and represent the sliding velocity $\mathbf{v}_1^{(12)}$ using the skew-symmetric matrix for the vector of angular velocity.

Solution
Matrix $\mathbf{M}_{21}$ is represented by Eq. (2.2.9). From Eq. (2.2.9), we obtain

$$L_{21}(\phi) = \begin{bmatrix} \cos\phi & -\sin\phi & 0 \\ \sin\phi & \cos\phi & 0 \\ 0 & 0 & 1 \end{bmatrix} \tag{2.3.7}$$

$$L_{12}(\phi) = L_{21}^{-1}(\phi) = \begin{bmatrix} \cos\phi & \sin\phi & 0 \\ -\sin\phi & \cos\phi & 0 \\ 0 & 0 & 1 \end{bmatrix} \tag{2.3.8}$$

and

$$\dot{a}_{14}(\phi) = \rho\dot{\phi} \tag{2.3.9}$$

$$\dot{a}_{24}(\phi) = 0 \tag{2.3.10}$$

$$\dot{a}_{34}(\phi) = 0.$$

The skew-symmetric matrix for the vector of angular velocity $(\boldsymbol{\omega}_1^{(1)})^s$ is given by

$$\left(\boldsymbol{\omega}_1^{(1)}\right)^s = \omega^{(1)} \begin{bmatrix} 0 & -1 & 0 \\ 1 & 0 & 0 \\ 0 & 0 & 0 \end{bmatrix}. \qquad (2.3.11)$$

Using Eq. (2.3.6), we obtain

$$\mathbf{v}_1^{(12)} = \omega^{(1)} \begin{bmatrix} -y_1 + \rho \cos\phi \\ x_1 - \rho \sin\phi \\ 0 \end{bmatrix}. \qquad (2.3.12)$$

3 Centrodes, Axodes, and Operating Pitch Surfaces

3.1 THE CONCEPT OF CENTRODES

Consider that two bodies, 1 and 2, perform planar motions with respect to a fixed reference frame, f. We consider three cases:

(a) Both bodies perform rotational motion in *opposite* direction about parallel axes O_1 and O_2 with instantaneous angular velocities $\omega^{(1)}$ and $\omega^{(2)}$ (Fig. 3.1.1).
(b) Both bodies perform rotational motions in the *same* direction with angular velocities $\omega^{(1)}$ and $\omega^{(2)}$ (Fig. 3.1.2).
(c) One of the bodies, say 1, performs rotational motion with angular velocity ω, and the other body performs translational motion in the plane of motion with linear velocity $\mathbf{v}$ (Fig. 3.1.3).

The instantaneous center of rotation, designated I, is the point in the fixed coordinate system where the relative velocity $\mathbf{v}^{(12)}$ is equal to zero, that is,

$$\mathbf{v}^{(12)} = \mathbf{v}^{(1)} - \mathbf{v}^{(2)} = \mathbf{0}. \tag{3.1.1}$$

Vector equation

$$\mathbf{v}^{(1)} = \mathbf{v}^{(2)} \tag{3.1.2}$$
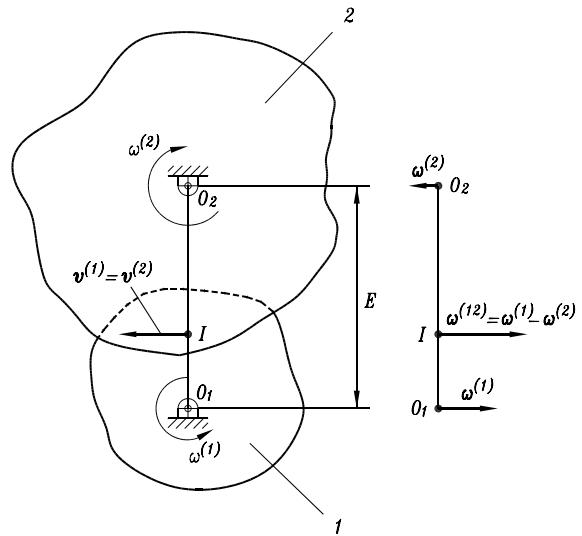
can be observed only at such a point I that lies on the shortest distance $O_1 O_2$ and satisfies the equation

$$\frac{\omega^{(1)}}{\omega^{(2)}} = \frac{O_2 I}{O_1 I}. \tag{3.1.3}$$

The location I on the center distance $O_1 O_2$ provides the same direction for vectors $\mathbf{v}^{(1)}$ and $\mathbf{v}^{(2)}$. Equation (3.1.3) provides that vectors $\mathbf{v}^{(1)}$ and $\mathbf{v}^{(2)}$ not only are of the same direction but also have the same magnitude.

For the most common case, the gear ratio

$$m_{21} = \frac{\omega^{(2)}}{\omega^{(1)}} \tag{3.1.4}$$
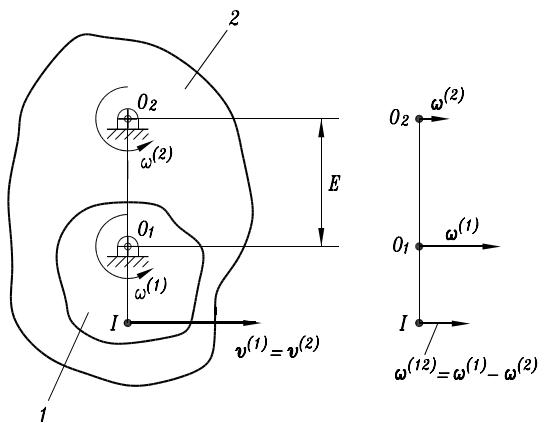
Figure 3.1.1: Rotation between parallel axes in opposite direction.

is constant and the instantaneous center I of rotation keeps its position on $O_1 O_2$. In some cases, the gear ratio is given by a function
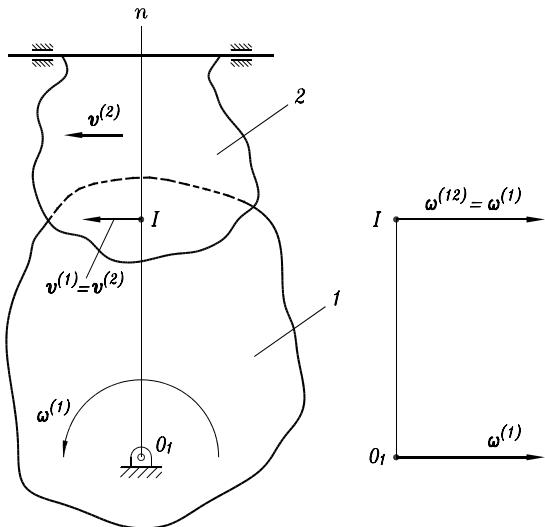
$$m_{21} = f(\phi_1)$$

where ϕ_1 is the input parameter, the angle of rotation of body 1. Then, the instantaneous center of rotation translates along $O_1 O_2$ in the process of transformation of rotation.

The centrode i is the *locus* of instantaneous centers of rotation in coordinate system S_i ($i = 1,2$). We may imagine that point I (it translates along $O_1 O_2$ or it is at rest) traces out the centrode while coordinate system S_i rotates about O_i. For the case in which

Figure 3.1.2: Rotation between parallel axes in the same direction.

Figure 3.1.3: Transformation of rotation into translation.

m_{12} is constant, the centrodes are circles of radii ρ_1 and ρ_2 that are determined from the following equations:

(i) The rotation is performed in opposite directions (Fig. 3.1.4)
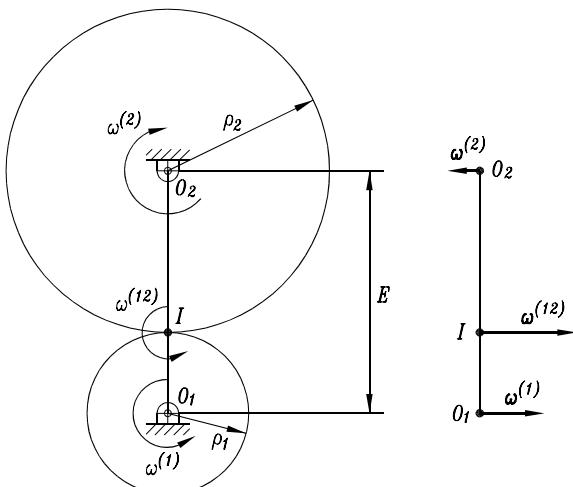
$$\rho_1 = \frac{E}{1 + m_{12}}, \quad \rho_2 = \frac{E}{1 + m_{21}} = \frac{m_{12}E}{1 + m_{12}} \tag{3.1.5}$$

where
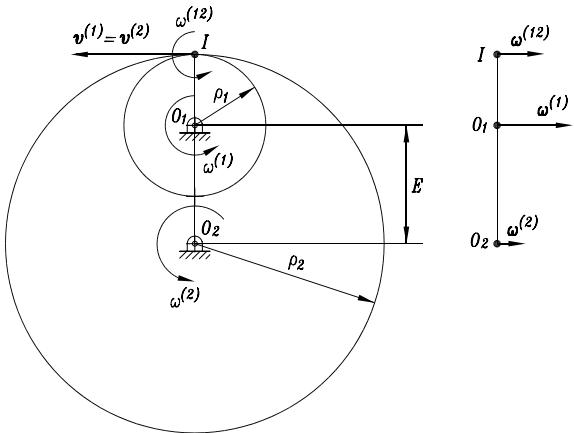
$$m_{12} = \frac{1}{m_{21}}.$$

(ii) The rotation is performed in opposite directions (Fig. 3.1.5)

$$\rho_1 = \frac{E}{|1 - m_{12}|}, \quad \rho_2 = \frac{E}{|1 - m_{21}|} = \frac{m_{12}E}{|1 - m_{12}|}. \tag{3.1.6}$$

Figure 3.1.4: Centrodes in external tangency.
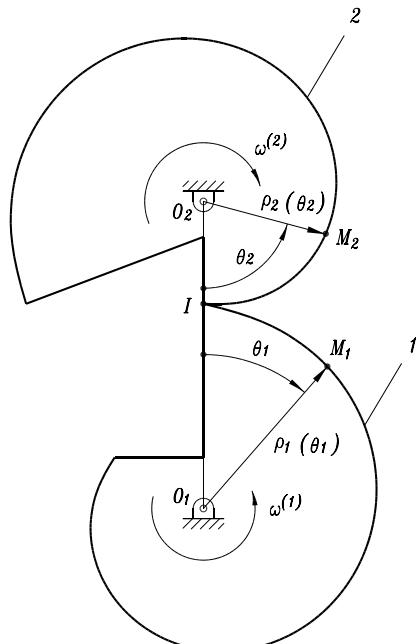
Figure 3.1.5: Centrodes in internal tangency.

The relative motion of centrode 1 with respect to centrode 2 is pure rolling about I with angular velocity

$$\boldsymbol{\omega}^{(12)} = \boldsymbol{\omega}^{(1)} - \boldsymbol{\omega}^{(2)}. \tag{3.1.7}$$

For the case in which $m_{21} \neq$ constant, the centrodes are noncircular curves, either closed or unclosed. Gears with such centrodes are called noncircular gears (See Chapter 12 and Litvin, 1956, 1968).

Figure 3.1.6 shows two unclosed centrodes that are in tangency at point I. We recall that the relative motion of the centrodes is pure rolling. Respective points M_1 and M_2

Figure 3.1.6: Noncircular centrodes of mating gears.

of the centrodes that will become the points of tangency satisfy the equations

$$\widehat{I M_1} = \widehat{I M_2}, \quad \rho_1(\theta_1) + \rho_2(\theta_2) = E. \tag{3.1.8}$$

Function $\rho_i(\theta_i)$ $(i = 1, 2)$, where θ_i is the polar angle, determines the centrodes. We emphasize that for noncircular centrodes, angles θ_1 and θ_2 are related as follows:

$$\theta_2 = \int_0^{\theta_1} m_{21}(\phi_1)d\theta_1 = \int_0^{\theta_1} m_{21}(\theta_1)d\theta_1. \tag{3.1.9}$$

Here, $\theta_i = \phi_i$, where ϕ_i is the angle of rotation, but the polar angle θ_i is measured in a direction that is opposite to the direction of rotation.

It is evident that

$$\phi_2 = \int_0^{\phi_1} m_{21}(\phi_1)d\phi_1. \tag{3.1.10}$$
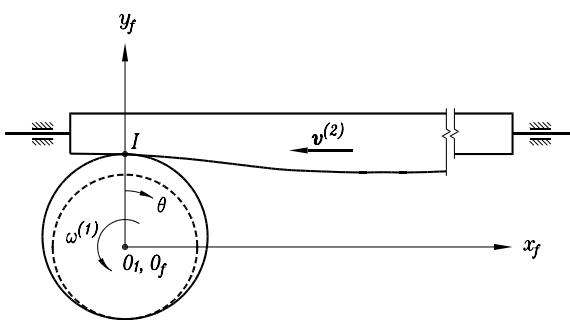
We recall that for the case where m_{21} is constant, we have

$$\frac{\phi_2}{\phi_1} = m_{21}. \tag{3.1.11}$$
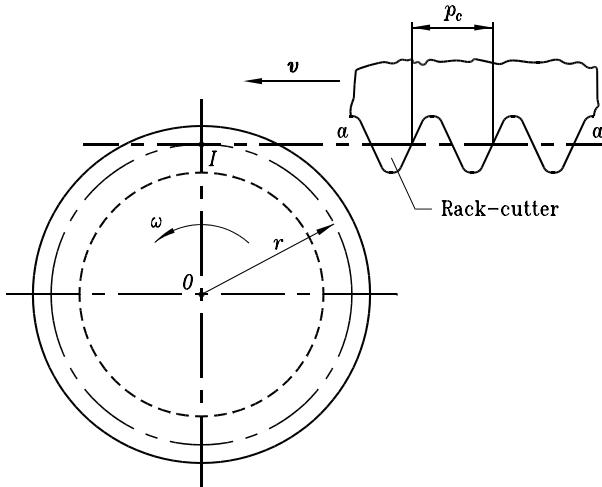
Let us consider now the case where rotation is transformed into translation and vice versa (Fig. 3.1.3). The instantaneous center of rotation I lies on line $O_1 n$ that is drawn from O_1 perpendicular to the velocity $\mathbf{v}$ of translation. The location of I satisfies the equation

$$O_1 I = \frac{v}{\omega}. \tag{3.1.12}$$

The relative motion of body 1 with respect to body 2 is pure rolling about I with angular velocity $\omega^{(12)} = \omega$. For the case where the ratio v/ω is given as function $v/\omega = f(\phi)$ where ϕ is the angle of rotation of body 1, the instantaneous center of rotation moves along $O_1 n$ in the process of transformation of motion. Figure 3.1.7 shows the centrodes for such a case. Usually the ratio v/ω is constant, the magnitude of segment OI is also constant, and the centrodes represent respectively a circle of radius $r = v/\omega$ and a straight line $a-a$ that is tangent to the circle (Fig. 3.2.1).

Figure 3.1.7: Centrodes of noncircular gear and rack.

Figure 3.2.1: Centrodes of rack-cutter and spur gear.

3.2 PITCH CIRCLE

The pitch circle is the *reference* circle that is used for determination of tooth element proportions. The tooth addendum and dedendum are measured from the pitch circle. The tooth thickness and the distance between the teeth are also referred to the pitch circle.

Another definition of the pitch circle is based on the fact that the pitch circle is the centrode of the gear, which is in mesh with the rack-cutter (Fig. 3.2.1). The pitch circle of radius r is the gear centrode in the process of generation because the angular velocity of the gear being generated and the linear velocity of the rack-cutter satisfy the equation

$$\frac{v}{\omega} = r. \tag{3.2.1}$$

The rack-cutter centrode is the straight line a–a that is tangent to the pitch circle. The radius r of the gear pitch circle can be expressed in terms of the number N of gear teeth and the distance p_c between two neighboring teeth of the rack-cutter. Due to pure rolling of the rack-cutter and the gear centrode, the distance along the pitch circle between two neighboring gear teeth is equal to p_c and

$$r = \frac{Np_c}{2\pi}. \tag{3.2.2}$$

The ratio π/p_c is called diametral pitch, P, and its unit is 1/in. The magnitude of P is standardized to decrease the number of applied tools. The diameter of the pitch circle can be expressed as

$$d = \frac{N}{P}. \tag{3.2.3}$$

The term – diametral pitch – is based on the consideration that the ratio

$$P = \frac{N}{d} \tag{3.2.4}$$

indicates the number of teeth corresponding to one inch of the diameter of the gear pitch circle.

3.3 OPERATING PITCH CIRCLES

The gear pitch circle can be identified uniquely by knowing the number N of gear teeth and the diametral pitch P (or the circular pitch p_c). The centrodes of gears can be identified considering as given the ratio $m_{12} = \omega^{(1)}/\omega^{(2)}$ and the actual center distance E. This means that if m_{12} is of the same magnitude but the designed value E has been changed, then the radii of the centrodes ρ_1 and ρ_2 will also be changed [see Eqs. (3.1.5) and (3.1.6)].
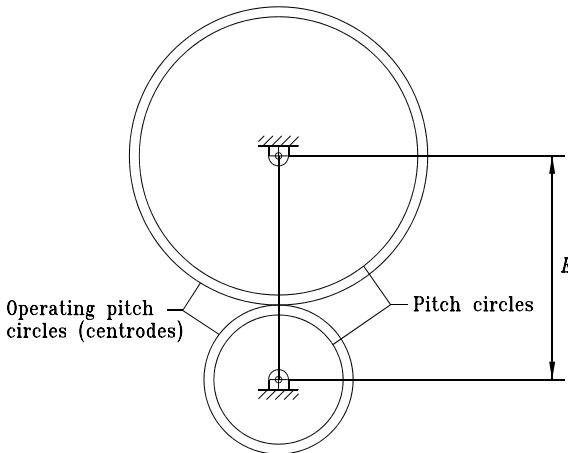
Usually, a change in the gear center distance is accompanied by a change in the gear ratio m_{12} due to the caused transmission errors. Involute spur and helical gears are exceptions to this rule. We have to differentiate two cases of design of involute gears: those with standard and those with nonstandard center distances (see more details in Chapter 10). The standard center distance is determined as

$$E_o = \frac{N_1 + N_2}{2P} \tag{3.3.1}$$
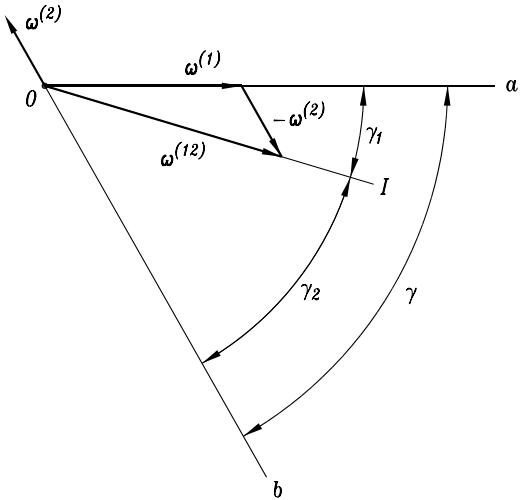
and the gear centrodes coincide with the pitch circles.

If the center distance E differs from E_o, the gear centrodes do not coincide with the pitch circles. The term "operating pitch circles" that is used in the technical literature is just a synonym of gear centrodes. Figure 3.3.1 shows the gear centrodes and the pitch circles for the case when $E > E_o$. It is evident from Eqs. (3.1.5) and (3.1.6) that the ratio between the radii of pitch circles and operating circles is related as follows:

$$\frac{\rho_i^{(0)}}{\rho_i} = \frac{E_o}{E}. \tag{3.3.2}$$

Figure 3.3.1: Pitch circles and centrodes.

Figure 3.4.1: Axodes: rotation between intersected axes.

3.4 AXODES IN ROTATION BETWEEN INTERSECTED AXES

Figure 3.4.1 shows that the rotation is transformed between two intersected axes Oa and Ob that form the angle γ. The gears rotate in opposite directions. The *instantaneous axis of rotation* OI is the line of action of the angular velocity $\boldsymbol{\omega}^{(12)}$ in relative motion of gear 1 with respect to 2 (or 2 with respect to 1). Here,

$$\boldsymbol{\omega}^{(12)} = \boldsymbol{\omega}^{(1)} - \boldsymbol{\omega}^{(2)}. \tag{3.4.1}$$

Similarly,

$$\boldsymbol{\omega}^{(21)} = \boldsymbol{\omega}^{(2)} - \boldsymbol{\omega}^{(1)}. \tag{3.4.2}$$

The orientation of OI with respect to the gear axes is determined with angles γ_1 and γ_2 that are represented as

$$\tan \gamma_1 = \frac{\sin \gamma}{m_{12} + \cos \gamma}, \quad \tan \gamma_2 = \frac{\sin \gamma}{m_{21} + \cos \gamma}. \tag{3.4.3}$$

Here,

$$\gamma = \gamma_1 + \gamma_2 \tag{3.4.4}$$

$$m_{12} = \frac{\omega^{(1)}}{\omega^{(2)}}, \quad m_{21} = \frac{1}{m_{12}} = \frac{\omega^{(2)}}{\omega^{(1)}} \tag{3.4.5}$$

where m_{12} (or m_{21}) is the gear ratio. The gear ratio can also be expressed in terms of angles of the pitch cones and the numbers of gear teeth

$$m_{12} = \frac{\sin \gamma_2}{\sin \gamma_1} = \frac{N_2}{N_1}. \tag{3.4.6}$$

The locus of instantaneous axes of rotation in the movable reference frame, S_i ($i=1,2$), which is rigidly connected to rotating gear i, forms the axode. In the case of transformation of rotation between the intersected axes, the axodes are two circular cones with apex angles γ_1 and γ_2 (Fig. 3.4.2). These cones are called *pitch cones*, their
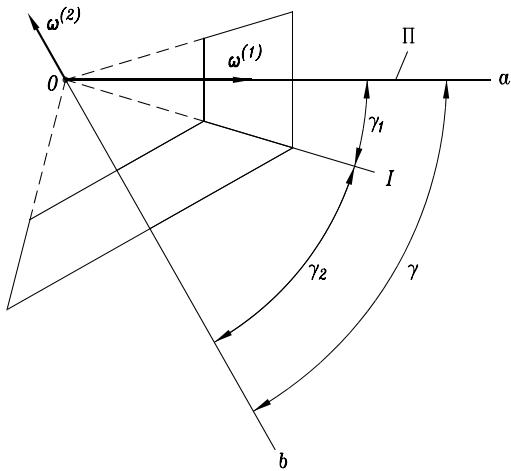
Figure 3.4.2: Plane and cone as axodes.

line of tangency is OI, and the relative motion is pure rolling – rotation about OI. The angular velocity $\omega^{(12)} = \omega^{(1)} - \omega^{(2)}$ represents the angular velocity of pitch cone 1 when it is rotated about OI while cone 2 is held at rest.

Problem 3.4.1

Consider that the transformation of rotation is performed between intersected axes under the condition that the pitch cone of gear 1 is turned out into a plane Π (Fig. 3.4.2). The gear ratio is m_{12} and the gears rotate in opposite directions. (i) Determine the angle of pitch cone of gear 2; (ii) express the angle γ between the intersected axes in terms of γ_2.

Solution

(i) Equation (3.4.6) yields

$$\sin \gamma_2 = m_{12}. \tag{3.4.7}$$

(ii) Using the expression for $\tan \gamma_1$ in Eq. (3.4.3), we obtain
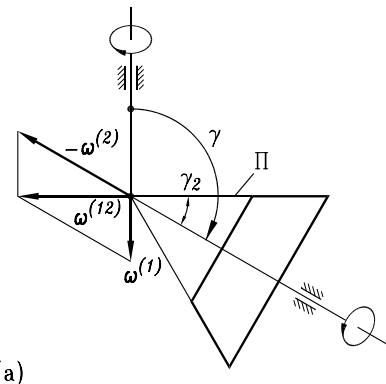
$$\cos \gamma = -m_{12} = -\sin \gamma_2. \tag{3.4.8}$$

The equation provides two solutions for γ that are represented in Fig. 3.4.3,

$$\gamma = 90° + \gamma_2 \quad \text{and} \quad \gamma = 270° - \gamma_2.$$
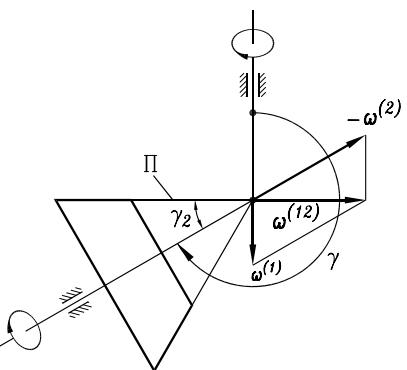
3.5 AXODES IN ROTATION BETWEEN CROSSED AXES

Consider two bodies rotating about crossed axes with the angular velocities $\omega^{(1)}$ and $\omega^{(2)}$, respectively (Fig. 3.5.1). The axes of rotation form the twist angle γ, and the shortest distance between the axes is E. The relative motion of body 1 with respect to body 2 may be represented as a motion of two components: (a) rotation about axis z_2 with angular velocity $(-\omega^{(2)})$ and (b) rotation about axis z_f with angular velocity $\omega^{(1)}$.
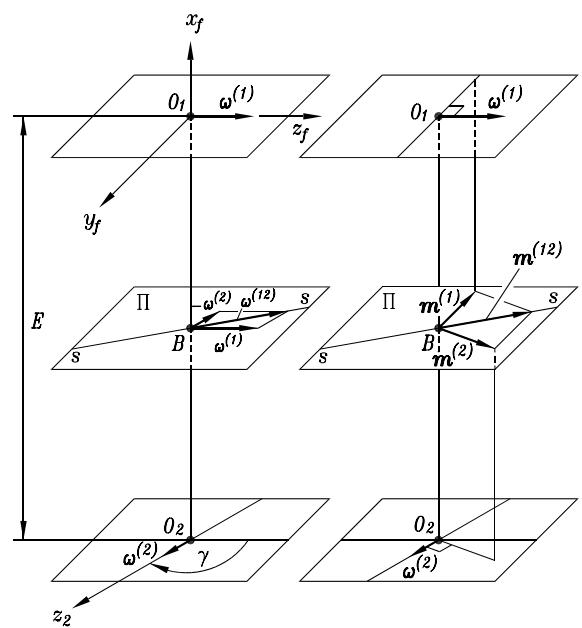
(a)

Figure 3.4.3: Two locations of cone-axode with respect to plane Π.

(b)

Figure 3.5.1: Rotation between crossed axes: substitution of vectors of angular velocities.

Our goal is to prove that the described relative motion may be represented as *screw motion* about an axis *s–s*. This axis and the lines of action of $\boldsymbol{\omega}^{(1)}$ and $\boldsymbol{\omega}^{(2)}$ lie in parallel planes that are perpendicular to the line of shortest distance $O_1 - O_2$. The proof is based on the concept that a given sliding vector may be substituted with an equal vector with a parallel line of action and a corresponding vector moment. Figure 3.5.1 shows that vector $\boldsymbol{\omega}^{(1)}$ that passes through O_1 is substituted with an equal vector that passes through B and the moment

$$\mathbf{m}^{(1)} = \overline{BO_1} \times \boldsymbol{\omega}^{(1)}.$$

Similarly, vector $(-\boldsymbol{\omega}^{(2)})$ that passes through O_2 is substituted with an equal vector that passes through point B and the moment

$$\mathbf{m}^{(2)} = \overline{BO_2} \times (-\boldsymbol{\omega}^{(2)}).$$

Then, the relative motion of body 1 with respect to body 2 may again be represented in two components: (i) rotation about *s–s* with the angular velocity

$$\boldsymbol{\omega}^{(12)} = \boldsymbol{\omega}^{(1)} + (-\boldsymbol{\omega}^{(2)}) = \boldsymbol{\omega}^{(1)} - \boldsymbol{\omega}^{(2)} \tag{3.5.1}$$

and (ii) translation with the velocity

$$\mathbf{m}^{(12)} = \mathbf{m}^{(1)} + \mathbf{m}^{(2)} = \left(\overline{BO_1} \times \boldsymbol{\omega}^{(1)}\right) + \left[\overline{BO_2} \times (-\boldsymbol{\omega}^{(2)})\right]. \tag{3.5.2}$$

Choosing a certain location of point B, we can provide the collinearity of vector $\boldsymbol{\omega}^{(12)}$ and $\mathbf{m}$. This means that the relative motion of body 1 with respect to body 2 will be a screw motion about axis *s–s*.

Henceforth, we consider three reference frames 1, 2, and f that are rigidly connected to the bodies and the housing of the gear train. We employ in the reference frame f, the fixed coordinate system $S_f(x_f, y_f, z_f)$ whose axis x_f is collinear to the vector of the shortest distance $\overline{O_1 O_2} = \mathbf{E}$ and the z_f axis is the axis of rotation of body 1. Vectors $\boldsymbol{\omega}^{(12)}$ and $\mathbf{m}^{(12)}$ are represented in S_f by the following equations:

$$\boldsymbol{\omega}_f^{(12)} = \begin{bmatrix} 0 & -\omega^{(2)} \sin\gamma & (\omega^{(1)} - \omega^{(2)} \cos\gamma) \end{bmatrix}^{\mathrm{T}} \tag{3.5.3}$$

$$\mathbf{m}_f^{(12)} = \begin{bmatrix} 0 \\ X_f \omega^{(1)} - (X_f + E)\omega^{(2)} \cos\gamma \\ (X_f + E)\omega^{(2)} \sin\gamma \end{bmatrix}. \tag{3.5.4}$$

Here, X_f is considered as an algebraic value and determines the location of point B on axis x_f. The direction of vector-moment $\mathbf{m}^{(12)}$ depends on the sign of X_f.

We may require the collinearity of $\mathbf{m}^{(12)}$ and $\boldsymbol{\omega}^{(12)}$, which means the relative motion will be a screw one. Using the equation

$$\mathbf{m}^{(12)} = \lambda \boldsymbol{\omega}^{(12)} \tag{3.5.5}$$

and Eqs. (3.5.3) and (3.5.4), we obtain the equations of the axis of screw motion, s–s (Fig. 3.5.1),

$$X_f = \frac{E m_{21}(\cos \gamma - m_{21})}{1 - 2m_{21} \cos \gamma + m_{21}^2} \tag{3.5.6}$$

$$\frac{Y_f}{Z_f} = -\frac{m_{21} \sin \gamma}{1 - m_{21} \cos \gamma} \tag{3.5.7}$$

where

$$m_{21} = \frac{\omega^{(2)}}{\omega^{(1)}}.$$

Equation (3.5.6) determines the location of plane Π where lies s–s; the negative value of X_f indicates that the plane intersects the negative axis x_f. Equation (3.5.7) determines the orientation of s–s in plane Π.

For the case when body 2 rotates in the direction opposite to that shown in Fig. 3.5.1, it is necessary to change the sign of m_{21} in Eqs. (3.5.6) and (3.5.7). Due to the collinearity of $\mathbf{m}^{(12)}$ and $\boldsymbol{\omega}^{(12)}$, we may represent $\mathbf{m}^{(12)}$ as

$$\mathbf{m}^{(12)} = p\boldsymbol{\omega}^{(12)}. \tag{3.5.8}$$

Here, p is the screw parameter that relates the angular velocity $\boldsymbol{\omega}^{(12)}$ and the linear velocity $\mathbf{m}^{(12)}$ in the screw motion. Parameter p is determined by the equation

$$p = E \frac{m_{21} \sin \gamma}{1 - 2m_{21} \cos \gamma + m_{21}^2}. \tag{3.5.9}$$

The instantaneous axis of screw motion does not change its location or orientation if m_{21}, γ, and E are constants. While bodies 1 and 2 are rotated, the instantaneous axis of screw motion, s–s, generates in reference frames 1 and 2 two surfaces – the *hyperboloids of revolution*. These surfaces are the *axodes* for the case of transformation of rotation between crossed axes. The axode represents the locus of the instantaneous axis of screw motion that is generated in coordinate system S_i ($i = 1, 2$).

The derivation of axodes is based on the following considerations:
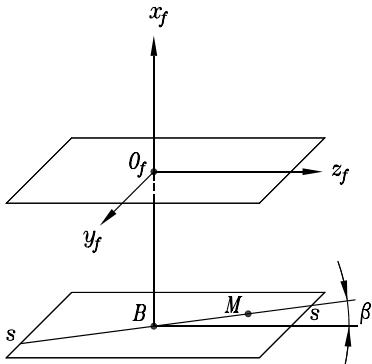
(i) Using Eqs. (3.5.6) and (3.5.7) we may represent in S_f the axis of screw motion by the following equations:

$$x_f = \frac{E m_{21}(\cos \gamma - m_{21})}{1 - 2m_{21} \cos \gamma + m_{21}^2}, \qquad y_f = -u \sin \beta, \qquad z_f = u \cos \beta. \tag{3.5.10}$$

Here, $u = BM$ is the variable parameter that determines the location of a point on s–s (Fig. 3.5.2); β is a constant parameter and indicates the angle that is formed by s–s and axis z_f and is determined with the equations

$$\sin \beta = -\frac{m_{21} \sin \gamma}{(1 - 2m_{21} \cos \gamma + m_{21}^2)^{1/2}},$$

$$\cos \beta = \frac{1 - m_{21} \cos \gamma}{(1 - 2m_{21} \cos \gamma + m_{21}^2)^{1/2}}. \tag{3.5.11}$$

Figure 3.5.2: Representation of axis of screw motion in S_f.

(ii) The coordinate transformations from S_f to S_1 and S_2, respectively, yield the following equations of hyperboloids in S_1 and S_2:

$$x_1 = -r_o \cos \phi_1 - u \sin \beta \sin \phi_1$$
$$y_1 = r_o \sin \phi_1 - u \sin \beta \cos \phi_1 \qquad (3.5.12)$$
$$z_1 = u \cos \beta$$

$$x_2 = (E - r_o) \cos \phi_2 - u \sin(\beta + \gamma) \sin \phi_2$$
$$y_2 = -(E - r_o) \sin \phi_2 - u \sin(\beta + \gamma) \cos \phi_2 \qquad (3.5.13)$$
$$z_2 = u \cos(\beta + \gamma).$$
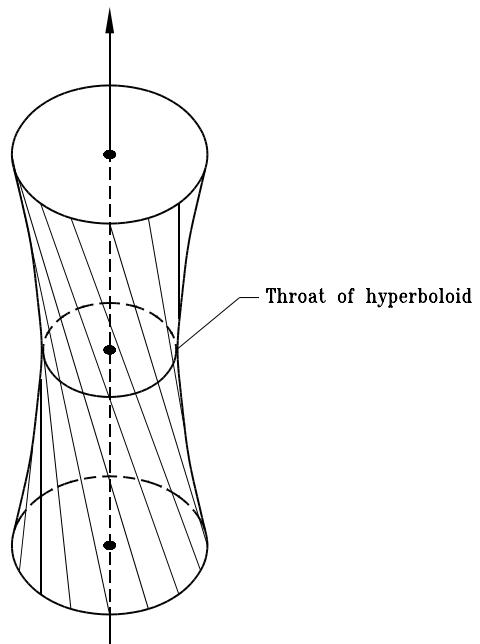
Here, $r_o = -X_f$, and u and ϕ_i $(i = 1, 2)$ are the surface coordinates (see the definition of surface coordinates in Section 5.2). A hyperboloid of revolution is shown in Fig. 3.5.3. Two mating hyperboloids contact each other along a straight line that is the axis of screw motion (Fig. 3.5.4). The relative motion of hyperboloids is rolling with sliding (*about* and *along* the axis of screw motion).

There are three types of gear trains that perform rotation between crossed axes: hypoid gears, worm-gear drives, and crossed helical gears.

3.6 OPERATING PITCH SURFACES FOR GEARS WITH CROSSED AXES

The idea of gear axodes is useful for visualization of the sliding velocity but it has not found application in design. The reason is that the dimensions of the driving and driven gears must satisfy many requirements that cannot be observed with the dimensions that are chosen for gear axodes. Therefore, the design of gears with crossed axes is based on the idea of *operating pitch surfaces* but not on the concept of axodes.
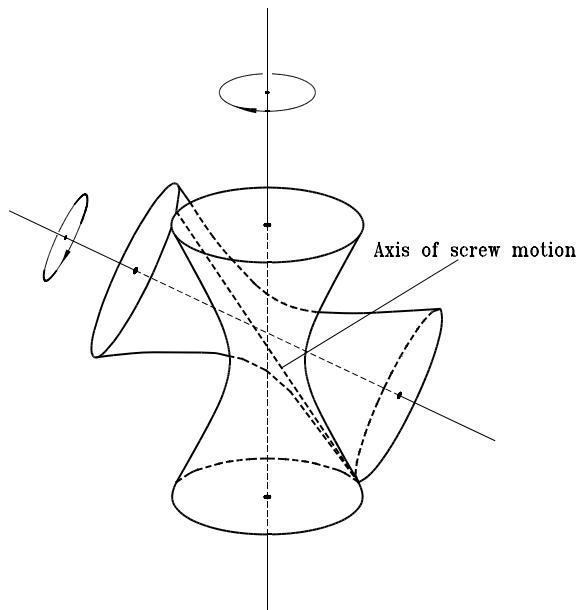
The operating pitch surfaces represent (i) two cylinders for a worm-gear drive and helical gears with crossed axes, and (ii) two cones for spiral and hypoid gear drives. The

Figure 3.5.3: Hyperboloid of revolution.

Throat of hyperboloid

chosen surfaces, which are called "operating pitch surfaces" in the technical literature, must satisfy the following requirements:

 (i) The axes of cylinders (cones) have to form the same twist angle and be at the same shortest distance as the gears to be designed.
(ii) The cylinders (cones) must be in tangency at the mean point of contact of the surfaces of the gears to be designed.

Figure 3.5.4: Mating hyperboloids.

Axis of screw motion

(iii) The relative sliding velocity $\mathbf{v}^{(12)}$ at point P of tangency of the cylinders (cones) must lie in the plane that is tangent to the cylinders (cones), and $\mathbf{v}^{(12)}$ must be directed along the common tangent to the helices of the gears to be designed. The term "helix" is a conventional one. Actually, we have to consider a spatial curve that belongs to the operating cylinders (cones) and represents the line of intersection of the gear tooth surface with the operating cylinders (cones). For the case of a helical gear, a cylinder worm, this line of intersection is indeed a helix. For the case of spiral bevel gears and hypoid gears, the line of intersection is a spatial curve that differs from a helix and might be represented with complicated equations.

(iv) Point P of tangency of operating pitch cylinders (cones) will be simultaneously the point of tangency of gear tooth surfaces if the surfaces have a common normal $\mathbf{N}$ at P and $\mathbf{N}$ is perpendicular to $\mathbf{v}^{(12)}$ (see Section 6.1).

It is shown below that the ratio of radii of two cylinders (cones) at point of contact P is not unique for the given gear ratio m_{12}. Therefore the previously mentioned requirements for the operating pitch surfaces must be complemented with additional relations between their parameters. The idea of operating pitch surfaces will be illustrated in following chapters for (i) helical gears with crossed axes, (ii) a worm-gear drive, and (iii) hypoid gears.

4 Planar Curves

4.1 PARAMETRIC REPRESENTATION

Consider a coordinate system $S(x, y)$. A position vector that is drawn from the origin of coordinate system S to a current point of the curve is represented by vector function

$$\mathbf{r}(\theta) = x(\theta)\mathbf{i} + y(\theta)\mathbf{j}, \quad \mathbf{r}(\theta) \in C^0, \quad \theta \in G \tag{4.1.1}$$

where $\mathbf{i}$ and $\mathbf{j}$ are the unit vectors of coordinate axes. The symbol C^0 means that $x(\theta)$ and $y(\theta)$ are continuous functions; G designates the open interval $a < \theta < b$ for the variable parameter θ. Functions $x(\theta)$ and $y(\theta)$ associate the point of the curve with the variable parameter θ.

A *simple* curve means that there is one-to-one correspondence between the point of the curve and parameter θ. A simple curve does not have points of self-intersection. Examples of self-intersecting curves are an extended involute curve (Fig. 1.6.2) and an extended epicycloid (Fig. 1.6.1). In some cases, to avoid the appearance of a point of self-intersection it is sufficient to just limit the interval (a, b) for the variable parameter θ.

A parametric curve is a *regular* curve if

$$\mathbf{r}(\theta) \in C^1, \quad \mathbf{r}_\theta \neq \mathbf{0}, \quad \theta \in G. \tag{4.1.2}$$

Here,

$$\mathbf{r}_\theta = \frac{d\mathbf{r}}{d\theta} = x_\theta \mathbf{i} + y_\theta \mathbf{j} \tag{4.1.3}$$

where

$$x_\theta = \frac{dx}{d\theta}, \quad y_\theta = \frac{dy}{d\theta}.$$

The inequality $\mathbf{r}_\theta \neq \mathbf{0}$ means that

$$|x_\theta| + |y_\theta| \neq 0 \quad \text{or} \quad x_\theta^2 + y_\theta^2 \neq 0.$$

Symbol C^1 means that functions $x(\theta)$ and $y(\theta)$ have continuous derivatives to the first order at least.

4.2 REPRESENTATION BY IMPLICIT FUNCTION

An equation

$$\phi(x, y) = 0, \qquad (x, y) \in G \tag{4.2.1}$$

does not necessarily represent a planar curve. Rather it merely represents a set of points in the (x, y) plane. Some of these points may be just isolated points and some may form a curve.

Consider that Eq. (4.2.1) is given. There is a set of parameters

$$P = (x_o, y_o) \tag{4.2.2}$$

that satisfies Eq. (4.2.1). The existence of a simple and regular curve in a local sense, in the neighborhood of P, is guaranteed if the curve is represented by

$$\phi(x, y) = 0, \qquad \phi \in C^1, \qquad |\phi_x| + |\phi_y| \neq 0. \tag{4.2.3}$$

The inequality in expressions (4.2.3) may also be represented by

$$\phi_x^2 + \phi_y^2 \neq 0. \tag{4.2.4}$$

Inequality (4.2.3) means that both partial derivatives cannot be equal to zero simultaneously. Consider that inequality (4.2.4) is observed just because $\phi_y \neq 0$. Then in the neighborhood of point P [see Eq. (4.2.2)] Eq. (4.2.1) may be solved by function $y(x)$ and this function represents a simple and regular curve.

4.3 TANGENT AND NORMAL TO A PLANAR CURVE

The concept of a tangent to a planar curve is based on the so-called *limiting* positions of rays [Zalgaller, 1975]. Consider a set of rays that are drawn through a curve point M and its neighboring curve points M_i ($i = 1, 2, \ldots, n$). As points M_i approach point M, all rays come to some limit position. In the case shown in Fig. 4.3.1(a), there are two limiting rays with coinciding lines of action. These two rays form the tangent to the curve at point M. Point M is identified as a *regular* point of the curve. Only one limiting ray exists at curve point M, as shown in Figs. 4.3.1(b) and 4.3.1(c). Thus, only a "*half*" *tangent* exists at these points. Point M shown in Figs. 4.3.1(b) and 4.3.1(c) is called the *point of regression*, which is of the variety of singular points. A tangent **T** exists only at a regular point of a curve. A curve point where the tangent **T** does not exist or is equal to zero is identified as a *singular* point.
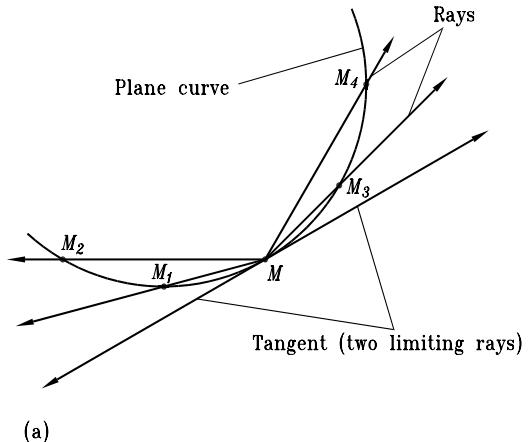
Consider two cases for determination of tangent **T**:

(a) The curve is represented in parametric form by
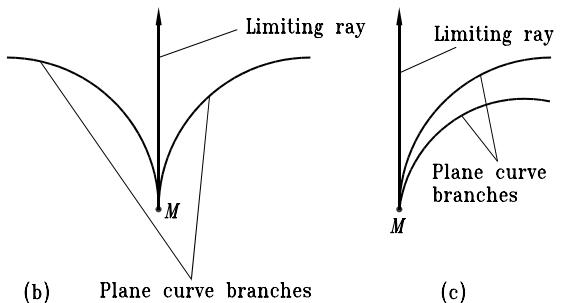
$$\mathbf{r}(\theta) \in C^1, \qquad \mathbf{r}_\theta \neq \mathbf{0}, \qquad \theta \in G.$$

Then,

$$\mathbf{T} = \mathbf{r}_\theta = x_\theta \mathbf{i} + y_\theta \mathbf{j}. \tag{4.3.1}$$

Figure 4.3.1: Limiting rays and tangent: (a) illustration of rays and tangent; (b) and (c) illustration of limiting ray, tangent, and two branches of a planar curve.

(b)   The curve is represented by an implicit function,

$$\phi(x, y) = 0, \quad \phi \in C^1, \quad (x, y) \in G, \quad \phi_x^2 + \phi_y^2 \neq 0.$$

Then, the tangent is represented by the equation,

$$T_x \phi_x + T_y \phi_y = 0. \tag{4.3.2}$$

Curve singular points are determined with $r_\theta = 0$ and $\phi_x^2 + \phi_y^2 = 0$ for the previously mentioned two cases, respectively. A point of regression is a particular case of a singular point where a "half" tangent exists [Figs. 4.3.1(b) and 4.3.1(c)]. Limiting the discussions to parametric curves, we say [Rashevski, 1956]:

(a)   a point of regression exists if

$$\mathbf{r}_\theta = 0, \quad \mathbf{r}_{\theta\theta} \neq 0;$$

(b)   the direction of the tangent at the point of regression is determined by vector $\mathbf{r}_{\theta\theta}$.

Henceforth, we consider regular points. The unit tangent to the curve, $\mathbf{t}$, is determined with the equation

$$\mathbf{t} = \frac{\mathbf{T}}{|\mathbf{T}|} = \frac{1}{m}(T_x \mathbf{i} + T_y \mathbf{j}) \tag{4.3.3}$$

where $m = (T_x^2 + T_y^2)^{1/2}$. The normal to a planar curve is perpendicular to its tangent and is represented by the equation

$$\mathbf{N} = \mathbf{T} \times \mathbf{k} \quad \text{or} \quad \mathbf{N}^* = \mathbf{k} \times \mathbf{T}. \tag{4.3.4}$$

Here, $\mathbf{k}$ is the unit vector of the z axis; vectors $\mathbf{N}$ and $\mathbf{N}^*$ are of opposite direction. Henceforth, we use the equation
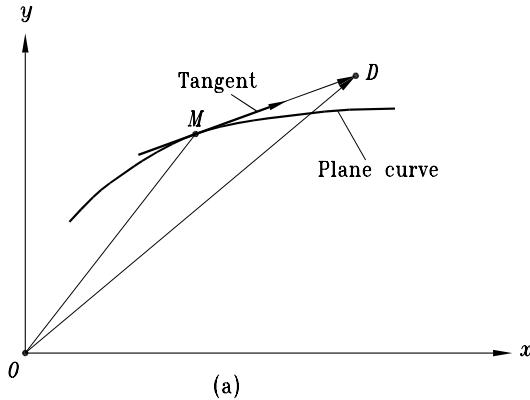
$$\mathbf{N} = \mathbf{T} \times \mathbf{k} = \begin{vmatrix} \mathbf{i} & \mathbf{j} & \mathbf{k} \\ T_x & T_y & 0 \\ 0 & 0 & 1 \end{vmatrix} = \begin{bmatrix} T_y \\ -T_x \\ 0 \end{bmatrix}. \tag{4.3.5}$$

The unit vector is determined by

$$\mathbf{n} = \frac{\mathbf{N}}{|\mathbf{N}|} = \frac{1}{\sqrt{T_x^2 + T_y^2}}(T_y\mathbf{i} - T_x\mathbf{j}) \quad (\text{provided } \mathbf{N} \neq \mathbf{0}). \tag{4.3.6}$$
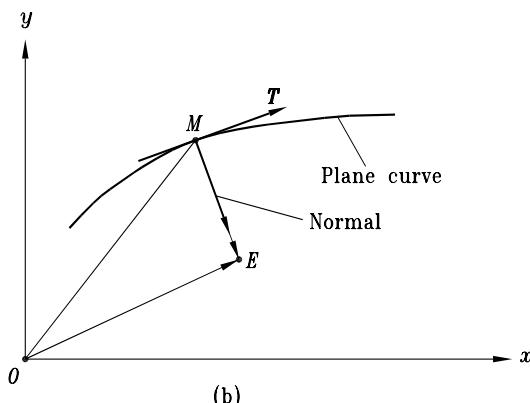
It is also necessary to derive the equation of a tangent or a normal that is drawn to the curve from a *given* point. Consider that the tangent to the curve is drawn from point $D(X, Y)$ [Fig. 4.3.2(a)] and the position vector for point D is

$$\overline{OD} = \overline{OM} + \overline{MD} = x\mathbf{i} + y\mathbf{j} + \lambda_T(T_x\mathbf{i} + T_y\mathbf{j}). \tag{4.3.7}$$

(a)

(b)

Figure 4.3.2: Tangent (a), and tangent and normal (b) to a planar curve.

Here, point $M(x, y)$ is the point of tangency of line MD with the curve; λ_T is a scalar and relates the length of $\overline{MD}$ and $\mathbf{T}(\overline{MD} = \lambda_T \mathbf{T})$. Equations (4.3.7) yield

$$\frac{X - x}{T_x} - \frac{Y - y}{T_y} = 0. \tag{4.3.8}$$

We may obtain the following equations for tangents to curves represented in parametric form [Eq. (4.1.2)] and by an implicit function [Eq. (4.2.3)], respectively:

$$\frac{X - x(\theta)}{x_\theta} - \frac{Y - y(\theta)}{y_\theta} = 0 \tag{4.3.9}$$

$$(X - x)\phi_x + (Y - y)\phi_y = 0. \tag{4.3.10}$$

Similarly, we may derive the equations of a normal that is drawn to the curve from point E [Fig. 4.3.2(b)]. These equations are represented for the two previously mentioned cases as follows:

$$\frac{X - x(\theta)}{y_\theta} + \frac{Y - y(\theta)}{x_\theta} = 0 \tag{4.3.11}$$

$$\frac{X - x}{\phi_x} - \frac{Y - y}{\phi_y} = 0. \tag{4.3.12}$$

Some curves that are applied as gear tooth shapes are generated by the rolling of a circle or a straight line over another circle. It is evident that the curve normal must pass through the instantaneous center of rotation, I.

Figure 4.3.3 shows a plane curve – an extended epicycloid – that is generated by point M; M is rigidly connected to circle 2. At every instant, the relative motion of circle 2 with respect to circle 1 may be represented as rotation about the instantaneous center I with the angular velocity,

$$\omega^{(21)} = \omega^{(2)} + \omega^{(1)} \qquad \left(\omega^{(2)} = \frac{d\psi}{dt}, \quad \omega^{(1)} = \frac{d\theta}{dt}\right).$$
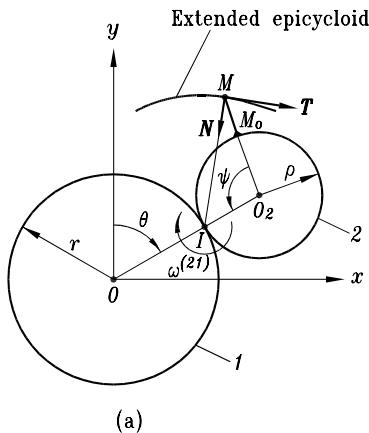
We may easily determine tangent $\mathbf{T}$ and normal $\mathbf{N}$ to the curve at point M using the following considerations:

(1) While circle 2 rotates about I, point M moves along tangent $\mathbf{T}$ to the curve. Thus $\mathbf{T}$ is perpendicular to MI.
(2) The direction of normal $\mathbf{N}$ at point M coincides with MI and is directed from M to I according to the cross product,

$$\mathbf{N} = \mathbf{T} \times \mathbf{k}.$$
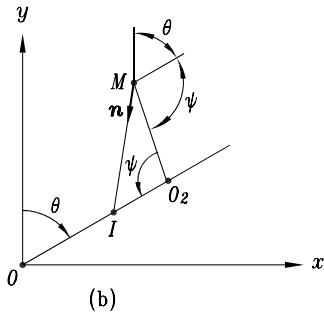
Problem 4.3.1

An involute curve is generated by point M of a straight line that rolls over a circle of radius r_b – the base circle. There are two possible parametric representations of an involute curve (see Section 10.2).

Figure 4.3.3: Derivation of extended epicycloid: (a) illustration of tangent $\mathbf{T}$ and normal $\mathbf{N}$; (b) illustration of relation of θ and ψ.

Solution

REPRESENTATION 1. [Fig. 4.3.4(a)]:
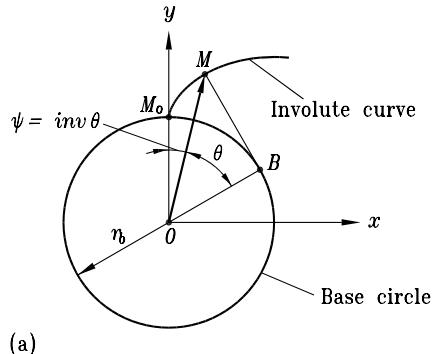
$$\mathbf{r}(\theta) = \frac{r_b}{\cos\theta}[\sin(\text{inv}\,\theta)\mathbf{i} + \cos(\text{inv}\,\theta)\mathbf{j}]$$

$$\text{inv}\,\theta = \tan\theta - \theta, \quad -\frac{\pi}{2} < \theta < \frac{\pi}{2}. \tag{4.3.13}$$

Equation (4.3.13) may be derived as follows:
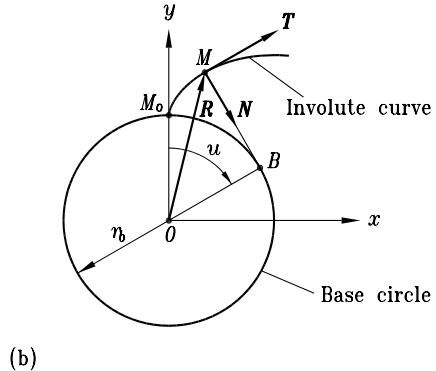
$$OM = \frac{r_b}{\cos\theta}, \quad x = OM\sin\psi, \quad y = OM\cos\psi,$$

$$\stackrel{\frown}{M_o B} = r_b(\psi + \theta), \quad MB = r_b\tan\theta,$$

$$\stackrel{\frown}{M_o B} = MB, \quad \text{and} \quad \psi = \tan\theta - \theta = \text{inv}\,\theta.$$

REPRESENTATION 2. [Fig. 4.3.4(b)]:

$$\mathbf{R}(u) = r_b[(\sin u - u\cos u)\mathbf{i} + (\cos u + u\sin u)\mathbf{j}], \quad -\infty < u < \infty. \tag{4.3.14}$$

(a)

Figure 4.3.4: Parametric representation of involute curve: (a) in terms of θ, and (b) in terms of u.

(b)

To derive this equation we use the following relations:

$$\overline{OM} = \overline{OB} + \overline{BM}, \quad x = \overline{OB} \cdot \mathbf{i} + \overline{BM} \cdot \mathbf{i}$$

$$y = \overline{OB} \cdot \mathbf{j} + \overline{BM} \cdot \mathbf{j}, \quad MB = \overparen{M_o B} = r_b u.$$

Parametric representation (4.3.14) may be derived from Eq. (4.3.13) by changing the parameter θ to parameter u using a continuous strongly monotonic function,

$$\theta(u) = \arctan u, \quad -\infty < u < \infty. \tag{4.3.15}$$

Relation (4.3.15) may be verified by the drawings in Fig. 4.3.4, which yield

$$MB = r_b \tan \theta \qquad \text{[Fig. 4.3.4(a)]}$$

$$MB = \overparen{M_o B} = r_b u \qquad \text{[Fig. 4.3.4(b)]}.$$

Problem 4.3.2

An involute curve $\mathbf{R}(u)$ represented by Eq. (4.3.14) is considered.

(i) Derive the equation of tangent $\mathbf{T}$, the unit tangent $\mathbf{t}$, the normal $\mathbf{N} = \mathbf{T} \times \mathbf{k}$, and the unit normal $\mathbf{n}$.

(ii) Interpret geometrically the direction of normal $\mathbf{N}$.

(iii) Determine the point of regression and the direction of the "half" tangent at this point.

Solution

(i)

$$\mathbf{T} = \mathbf{R}_u = r_b u(\sin u \, \mathbf{i} + \cos u \, \mathbf{j}) \tag{4.3.16}$$

$$\mathbf{t} = \sin u \, \mathbf{i} + \cos u \, \mathbf{j} \quad (\text{provided } u \neq 0) \tag{4.3.17}$$

$$\mathbf{N} = r_b u(\cos u \, \mathbf{i} - \sin u \, \mathbf{j}) \tag{4.3.18}$$

$$\mathbf{n} = \cos u \, \mathbf{i} - \sin u \, \mathbf{j} \quad (\text{provided } u \neq 0). \tag{4.3.19}$$

(ii) The direction of normal $\mathbf{N}$ at the instantaneous point M coincides with the direction of tangent MB to the base circle.

(iii) The point of regression is determined with $\mathbf{R}_u = 0$ and $\mathbf{R}_{uu} \neq 0$, where

$$\mathbf{R}_{uu} = r_b[(\sin u + u \cos u)\mathbf{i} + (\cos u - u \sin u)\mathbf{j}]. \tag{4.3.20}$$

Equations (4.3.16) and (4.3.20) yield that $u = 0$ corresponds to the point of regression. Equation (4.3.20) with $u = 0$ gives $\mathbf{R}_{uu} = r_b\mathbf{j}$. Thus the half tangent at point M_0 is directed along the positive y axis.

Problem 4.3.3

The derivation of the extended epicycloid is shown in Fig. 4.3.3. Position vector $\overline{OM}$ for a current point M of the curve is represented by

$$\overline{OM} = \overline{OO_2} + \overline{O_2M}.$$

It is necessary to (i) represent the extended epicycloid in coordinate system $S(x, y)$; (ii) derive the equations of the tangent $\mathbf{T}$, unit tangent $\mathbf{t}$, normal $\mathbf{N}$, and the unit normal $\mathbf{n}$; and (iii) investigate the existence of singular points.

Solution

(i) Equations of the extended epicycloid are

$$x = (r + \rho) \sin \theta - a \sin(\theta + \psi)$$
$$y = (r + \rho) \cos \theta - a \cos(\theta + \psi) \tag{4.3.21}$$

where

$$a = O_2 M, \quad \psi = \frac{r}{\rho} \theta.$$

(ii) The components of tangent T are represented as

$$T_x = x_\theta = (r + \rho)[\cos \theta - m \cos(\theta + \psi)]$$
$$T_y = y_\theta = -(r + \rho)[\sin \theta - m \sin(\theta + \psi)] \tag{4.3.22}$$

where

$$m = \frac{a}{\rho}.$$

The unit tangent is

$$\mathbf{t} = (1 - 2m\cos\psi + m^2)^{-1/2}\{[\cos\theta - m\cos(\theta + \psi)]\mathbf{i}$$
$$-[\sin\theta - m\sin(\theta + \psi)]\mathbf{j}\}. \tag{4.3.23}$$

The components of the normal N are

$$N_x = T_y, \quad N_y = -T_x. \tag{4.3.24}$$

The components of the unit normal n are

$$n_x = t_y, \quad n_y = -t_x. \tag{4.3.25}$$

(iii) The extended epicycloid does not have singular points because $\mathbf{T} \neq 0$.

Problem 4.3.4
Consider an ordinary epicycloid that is generated by point M_o [Fig. 4.3.3(a)].

(i) Derive the equations that represent the curve in coordinate system $S(x, y)$ [Fig 4.3.3(a)].
(ii) Derive the equation of tangent $\mathbf{T} = \mathbf{r}_\theta$ and the equation for $\mathbf{r}_{\theta\theta}$.
(iii) Investigate the existence of singular points and points of regression.

Solution
(i) The ordinary epicycloid is represented by the following equations:

$$x = (r + \rho)\sin\theta - \rho\sin(\theta + \psi), \quad y = (r + \rho)\cos\theta - \rho\cos(\theta + \psi).$$

(ii) The tangent $\mathbf{T}$ is

$$\mathbf{T} = \mathbf{r}_\theta = (r + \rho)\{[\cos\theta - \cos(\theta + \psi)]\mathbf{i} - [\sin\theta - \sin(\theta + \psi)]\mathbf{j}\}.$$

The derivative $\mathbf{r}_{\theta\theta}$ is
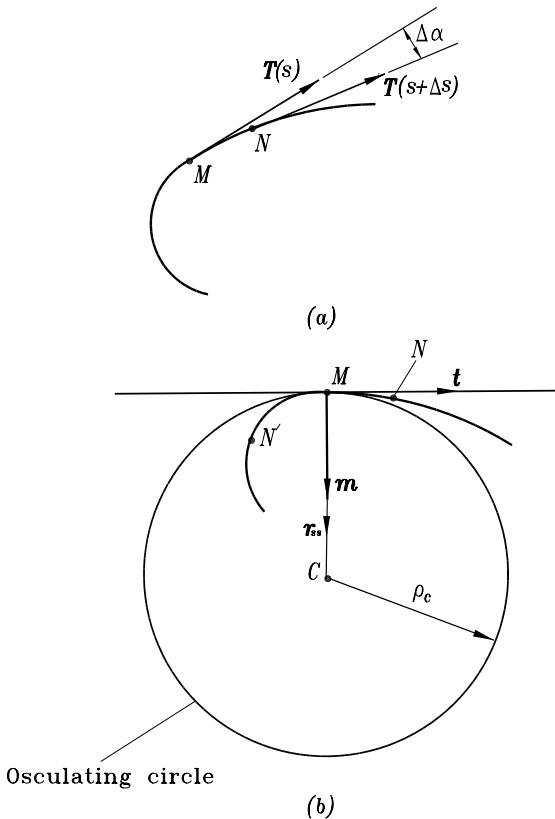
$$\mathbf{r}_{\theta\theta} = (r + \rho)\left\{\left[-\sin\theta + \left(1 + \frac{r}{\rho}\right)\sin(\theta + \psi)\right]\mathbf{i}\right.$$
$$\left.- \left[\cos\theta - \left(1 + \frac{r}{\rho}\right)\cos(\theta + \psi)\right]\mathbf{j}\right\}.$$

(iii) The equation of singular points is $\mathbf{r}_\theta = 0$. Such points occur at positions where $\psi = 2\pi n$ $(n = 0, 1, 2, \ldots)$ and $\theta = \frac{2\pi n\rho}{r}$. The above-mentioned singular points are points of regression because $\mathbf{r}_{\theta\theta} \neq 0$.

The direction of the "half" tangent is determined with

$$\mathbf{r}_{\theta\theta} = \frac{(r + \rho)r}{\rho}\left[\sin\left(\frac{2\pi n\rho}{r}\right)\mathbf{i} + \cos\left(\frac{2\pi n\rho}{r}\right)\mathbf{j}\right] \quad (n = 0, 1, 2, \ldots).$$

The half tangent coincides with the position vector that makes the angle $\theta = 2\pi n\rho/r$ with the y axis.

(a)

(b)

Osculating circle

Figure 4.4.1: For derivation of curvature of a planar curve: (a) illustration of two tangents at neighboring points M and N; (b) osculating circle at point M.

4.4 CURVATURE OF PLANAR CURVES

Introduction

To simplify the following derivations, we consider that the curve is represented by vector function

$$\mathbf{r}(s) \in C^2, \quad s \in E \tag{4.4.1}$$

where s is the length of the curve arc. Consider two neighboring points M and N of the curve that correspond to s and $(s + \Delta s)$, respectively [Fig. 4.4.1(a)]. The length of the arc between points M and N is Δs, and $\Delta \alpha$ is the angle between the tangents at M and N.

The limit of the ratio $\Delta \alpha / \Delta s$ as point N approaches point M is known as the *curvature* of the curve at point M (denoted as κ). We may also consider the limit of the inverse ratio $\Delta s / \Delta \alpha$, which is known as the radius of curvature (denoted as ρ_c) of the curve at point M. Here, ρ_c is the radius of the limiting (osculating) circle which is drawn through point M and two neighboring points N and N' as they approach point M [Fig. 4.4.1(b)]. Center C of the circle is called the center of curvature. The deviation of the curve from the osculating circle can be determined by application of Taylor's expansion

(see below). It is proven in differential geometry that the curve and the osculating circle have tangency of the second order at current point M (see below).

Frenet Trihedron

The right-hand Frenet trihedron is formed by three unit vectors $\mathbf{t}$, $\mathbf{m}$, and $\mathbf{b}$ shown in Fig. 4.4.2. Here,

$$\mathbf{t} = \mathbf{m} \times \mathbf{b}, \quad \mathbf{m} = \mathbf{b} \times \mathbf{t}, \quad \mathbf{b} = \mathbf{t} \times \mathbf{m}. \tag{4.4.2}$$

Unit vector $\mathbf{t}$ is determined as

$$\mathbf{t}(s) = \frac{d\mathbf{r}}{ds} = \mathbf{r}_s. \tag{4.4.3}$$

Vector $\mathbf{t}$ is the unit tangent vector to the curve at its current point M; $\mathbf{t}$ is a unit vector because $|d\mathbf{r}| = ds$. Unit vector $\mathbf{m}$ is determined as

$$\mathbf{m} = \frac{\mathbf{r}_{ss}}{|\mathbf{r}_{ss}|} \tag{4.4.4}$$

where $\mathbf{r}_{ss} = \partial^2 \mathbf{r}/\partial s^2$.

Our intermediate goal is to prove the following properties of unit vector $\mathbf{m}(s)$:

(a) Unit vector $\mathbf{m}(s)$ is located in the plane where the curve is represented, and $\mathbf{m}(s)$ is the unit normal to the planar curve.

(b) Unit vector $\mathbf{m}(s)$ is such a unit normal to the planar curve that is directed from current point M of the curve to the curvature center C [Fig. 4.4.1(b)].
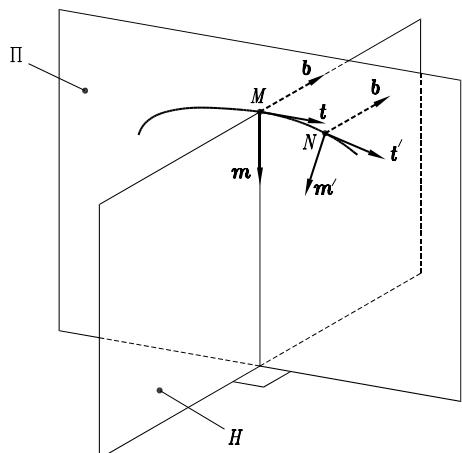
The proof of this statement is based on the following procedure:

Step 1: The derivative $\mathbf{a}_\theta = (d/d\theta)(\mathbf{a}(\theta))$ of a unit vector $\mathbf{a}(\theta)$ is perpendicular to $\mathbf{a}(\theta)$. Here, θ is the variable of vector function $\mathbf{a}(\theta)$.

The proof of this statement is based on the following considerations:

(i)

$$[\mathbf{a}(\theta)]^2 = \mathbf{a}(\theta) \cdot \mathbf{a}(\theta) = 1 \tag{4.4.5}$$

Figure 4.4.2: Frenet's trihedron for a planar curve.

because $\mathbf{a}(\theta)$ is a unit vector. Differentiating both parts of Eq. (4.4.5), we obtain

$$\mathbf{a} \cdot \mathbf{a}_\theta = 0. \tag{4.4.6}$$

(ii) Equation (4.4.6) confirms that the derivative $\mathbf{a}_\theta$ of unit vector $\mathbf{a}(\theta)$ is perpendicular to $\mathbf{a}(\theta)$.

Step 2: Consider vector equation $\mathbf{r}(s)$ of a planar curve. The unit tangent to the curve is represented as

$$\mathbf{t} = \frac{d}{ds}(\mathbf{r}(s)) = \mathbf{r}_s. \tag{4.4.7}$$

Vector

$$\mathbf{r}_{ss} = \frac{d}{ds}(\mathbf{t}(s)) = \mathbf{t}_s \tag{4.4.8}$$

is the derivative of unit vector $\mathbf{t}$. Thus, similar to Eq. (4.4.5), we have

$$\mathbf{r}_{ss} \cdot \mathbf{t} = 0. \tag{4.4.9}$$

Unit vector $\mathbf{m}$ has the same direction as $\mathbf{r}_{ss}$ [see Eq. (4.4.4)] and therefore $\mathbf{m}$ is perpendicular to the unit tangent $\mathbf{t}$.

Step 3: Vector $\mathbf{b}$ in the Frenet trihedron is perpendicular to plane Π of the curve (Fig. 4.4.2) and is represented as follows:

$$\mathbf{b} = \mathbf{t} \times \mathbf{m} = \frac{\mathbf{r}_s \times \mathbf{r}_{ss}}{|\mathbf{r}_{ss}|} = \frac{\mathbf{r}_s \times \mathbf{r}_{ss}}{|\mathbf{r}_s \times \mathbf{r}_{ss}|}. \tag{4.4.10}$$

Vector $\mathbf{r}_s$ lies in plane Π already. It was proven in Step 2 that $\mathbf{r}_{ss}$ is perpendicular to $\mathbf{t}$. Equation (4.4.10) is observed indeed if vector $\mathbf{r}_{ss}$ lies in plane Π as well. Vector $\mathbf{m}$ is the unit normal to the planar curve because it is perpendicular to the unit tangent $\mathbf{t}$ and lies in plane Π where the curve is represented. Statement (b) emphasizes that the unit normal $\mathbf{m}$ is directed from M to center C of the osculating circle. The proof is based on application of Taylor's expansion and the following discussion:

Step 1: Consider that the curve is represented by the vector function $\mathbf{r}(s)$. Points M and N are neighboring points of the curve, and $\overline{MN}$ is the vector of the displacement of N with respect to M [Fig. 4.4.1(b)].

Step 2: The displacement vector $\overline{MN}$ may be represented by Taylor's expansion as

$$\overline{MN} = \mathbf{r}(s + \Delta s) - \mathbf{r}(s) = \mathbf{r}_s \, \Delta s + \mathbf{r}_{ss} \frac{\Delta s^2}{2} + \mathbf{r}_{sss} \frac{\Delta s^3}{6} + \cdots . \tag{4.4.11}$$

The derivatives $\mathbf{r}_s$, $\mathbf{r}_{ss}$, and $\mathbf{r}_{sss}$ are taken at point M of the curve.

Step 3: It is known from differential geometry that the planar curve and the osculating circle are in tangency of second order at curve current point M [Fig. 4.4.1(b)]. Thus, we can take only the first two members of Taylor's expansion while considering the displacement vector $\overline{MN}$.

Vector $\mathbf{r}_s \, \Delta s$ is directed along the tangent to the curve. Vector $\mathbf{r}_{ss}(\Delta s^2/2)\,(\Delta s^2 > 0)$ is directed along the normal to the curve and determines the deviation of the curve from the tangent. The curve and the osculating circle are in tangency of second order and therefore the deviation of the osculating circle and the curve from the tangent are the

same. Therefore, the deviation of the curve from the tangent is directed to point C, the center of curvature of the curve.

Step 4: Vector $\mathbf{m}$ has the same direction as $\mathbf{r}_{ss}(\Delta s^2/2)$. Thus, $\mathbf{m}$ is such a unit normal to the planar curve that is always directed to the curvature center of the curve at a regular point of the curve. Statement (b) is proven.

Using Taylor's expansion (4.4.11) with at least three members, we can visualize the deviation of the curve from the osculating circle. Such a deviation is represented by vector $\mathbf{r}_{sss}(\Delta s^3/6)$, where Δs is positive for point N and negative for point N' [Fig. 4.4.1(b)]. This means that the deviation of the curve from the osculating circle is of different sign for points N and N'. The deviation is zero at point M.

Frenet Equations

Consider two trihedrons $(\mathbf{t}, \mathbf{m}, \mathbf{b})$ and $(\mathbf{t}', \mathbf{m}', \mathbf{b})$ that are located at neighboring points M and N of the curve (Fig. 4.4.2). The motion of trihedron $(\mathbf{t}, \mathbf{m}, \mathbf{b})$ which has to coincide with trihedron $(\mathbf{t}', \mathbf{m}', \mathbf{b})$ may be represented as a motion of two components: (1) translation along the curve from M to N (unit vectors $\mathbf{t}, \mathbf{m}, \mathbf{b}$ of the trihedron keep their original directions), and (2) rotation about $\mathbf{b}$ (then, trihedron $\mathbf{t}, \mathbf{m}, \mathbf{b}$ will coincide with trihedron $\mathbf{t}', \mathbf{m}', \mathbf{b}$).

We designate the angle of rotation about $\mathbf{b}$ as

$$d\boldsymbol{\alpha} = d\alpha \, \mathbf{b}. \tag{4.4.12}$$

The displacement of the tips of vectors $\mathbf{m}$ and $\mathbf{t}$ is represented by the following equations:

$$d\mathbf{m} = d\boldsymbol{\alpha} \times \mathbf{m} = \begin{vmatrix} \mathbf{t} & \mathbf{m} & \mathbf{b} \\ 0 & 0 & d\alpha \\ 0 & 1 & 0 \end{vmatrix} = -d\alpha \, \mathbf{t} \tag{4.4.13}$$

$$d\mathbf{t} = d\boldsymbol{\alpha} \times \mathbf{t} = \begin{vmatrix} \mathbf{t} & \mathbf{m} & \mathbf{b} \\ 0 & 0 & d\alpha \\ 1 & 0 & 0 \end{vmatrix} = d\alpha \, \mathbf{m}. \tag{4.4.14}$$

Equations (4.4.13) and (4.4.14), taking into account that $d\alpha/ds = \kappa$, yield

$$\mathbf{m}_s = -\kappa \, \mathbf{t} \tag{4.4.15}$$

$$\mathbf{t}_s = \kappa \, \mathbf{m}. \tag{4.4.16}$$

Equations (4.4.15) and (4.4.16) are known as Frenet's equations.

Curvature of curve represented by vector function r(s)

Henceforth, we consider that the curve is represented in plane (x, y) and vectors of Eqs. (4.4.15) and (4.4.16) can be represented as

$$\begin{aligned} \mathbf{m}_s &= m_{sx} \, \mathbf{i} + m_{sy} \, \mathbf{j}, \quad \mathbf{t} = \mathbf{r}_s = x_s \, \mathbf{i} + y_s \, \mathbf{j} \\ \mathbf{t}_s &= \mathbf{r}_{ss} = x_{ss} \, \mathbf{i} + y_{ss} \, \mathbf{j}, \quad \mathbf{m} = m_x \, \mathbf{i} + m_y \, \mathbf{j} \end{aligned} \tag{4.4.17}$$

where $\mathbf{i}$ and $\mathbf{j}$ are the unit vectors of axes x and y, respectively.

Equation (4.4.15) yields the following equations for determination of the curve curvature:

$$\kappa = -\mathbf{m}_s \cdot \mathbf{t} \tag{4.4.18}$$

(recall that $\mathbf{t}$ is a unit vector)

$$\kappa = -\frac{m_{sx}}{x_s} = -\frac{m_{sy}}{y_s}. \tag{4.4.19}$$

Equation (4.4.16) yields the following equations for determination of curvature κ:

$$\kappa = \mathbf{r}_{ss} \cdot \mathbf{m} \tag{4.4.20}$$

$$\kappa = |\mathbf{r}_{ss}| = |\mathbf{r}_s \times \mathbf{r}_{ss}|. \tag{4.4.21}$$

The derivation of Eq. (4.4.20) is based on the following procedure.

(i) Consider Eq. (4.4.16) and take into account that $\mathbf{m}$ is a unit vector. Then, we obtain

$$\kappa = \mathbf{t}_s \cdot \mathbf{m} = \frac{d}{ds}(\mathbf{t}) \cdot \mathbf{m}. \tag{4.4.22}$$

Here,

$$\mathbf{t} = \mathbf{r}_s, \quad \frac{d}{ds}(\mathbf{t}) = \mathbf{r}_{ss}. \tag{4.4.23}$$

(ii) Equations (4.4.22) and (4.4.23) yield Eq. (4.4.20).
The derivation of Eqs. (4.4.21) is based on the following considerations.

(a) Taking into account that $\mathbf{m}$ is a unit vector, we obtain from Eq. (4.4.16) that

$$\kappa = |\mathbf{t}_s| = |\mathbf{r}_{ss}|. \tag{4.4.24}$$

(b) Equations (4.4.10) for determination of unit vector $\mathbf{b}$ yield

$$|\mathbf{r}_{ss}| = |\mathbf{r}_s \times \mathbf{r}_{ss}|. \tag{4.4.25}$$

(c) Equations (4.4.24) and (4.4.25) confirm Eq. (4.4.21).

We emphasize that the curve curvature determined by Eqs. (4.4.18), (4.4.19), (4.4.20), and (4.4.21) is always positive. The direction of the curvature radius $\overline{MC}$ [Fig. 4.4.1(b)] is the same as that of the unit normal $\mathbf{m}(s)$.

Curvature of parametric curve represented by vector function r(θ)
Usually, a planar curve is represented in parametric form by the vector function $\mathbf{r}(\theta)$. Our goal is to derive equations for the direct determination of the curve curvature $\kappa(\theta)$ and the unit vectors $\mathbf{t}(\theta)$, $\mathbf{m}(\theta)$, and $\mathbf{b}(\theta)$.

It can be proven that the curvature of the curve $\mathbf{r}(\theta)$ may be represented by the following equations:

$$\kappa(\theta) = -\frac{\mathbf{m}_\theta \cdot \mathbf{r}_\theta}{\mathbf{r}_\theta^2} \tag{4.4.26}$$

$$\kappa(\theta) = -\frac{m_{\theta x}}{x_\theta} = -\frac{m_{\theta y}}{y_\theta} \tag{4.4.27}$$

$$\kappa(\theta) = \frac{\mathbf{t}_\theta \cdot \mathbf{m}(\theta)}{|\mathbf{r}_\theta|} \tag{4.4.28}$$

$$\kappa(\theta) = \frac{t_{\theta x}}{|\mathbf{r}_\theta| m_x} = \frac{t_{\theta y}}{|\mathbf{r}_\theta| m_y} \tag{4.4.29}$$

$$\kappa(\theta) = \frac{|\mathbf{r}_\theta \times \mathbf{r}_{\theta\theta}|}{|\mathbf{r}_\theta|^3} \tag{4.4.30}$$

$$\kappa(\theta) = \frac{\mathbf{r}_{\theta\theta} \cdot \mathbf{m}(\theta)}{r_\theta^2}. \tag{4.4.31}$$

The derivation of Eqs. (4.4.26) to (4.4.31) is based on the following procedure.

(i) We consider that the planar curve is represented by vector function $\mathbf{r}(s(\theta))$, where s is the arc length.

(ii) Differentiating the previously mentioned vector function, we obtain the auxiliary relations

$$\mathbf{r}_\theta = \mathbf{r}_s \frac{ds}{d\theta}. \tag{4.4.32}$$

Here,

$$\frac{ds}{d\theta} = |\mathbf{r}_\theta| \quad \text{because} \quad |\mathbf{r}_s| = 1 \tag{4.4.33}$$

$$\mathbf{r}_{\theta\theta} = \mathbf{r}_{ss}\left(\frac{ds}{d\theta}\right)^2 + \mathbf{r}_s\left(\frac{d^2s}{d\theta^2}\right). \tag{4.4.34}$$

It is easy to verify that

$$\mathbf{r}_s \times \mathbf{r}_{ss} = \frac{\mathbf{r}_\theta \times \mathbf{r}_{\theta\theta}}{\left(\dfrac{ds}{d\theta}\right)^3} = \frac{\mathbf{r}_\theta \times \mathbf{r}_{\theta\theta}}{|\mathbf{r}_\theta|^3}. \tag{4.4.35}$$

(iii) Using Eqs. (4.4.15) and (4.4.16), and auxiliary relations (4.4.32) to (4.4.35), we obtain after transformation the represented Eqs. (4.4.26) to (4.4.31).

We emphasize that curvature κ in the derived equations is always positive, and the orientation of vector $\overline{MC}$ of the curvature radius is the same as that of vector $\mathbf{m}(\theta)$. The orientation of unit vectors $\mathbf{t}(\theta)$, $\mathbf{b}(\theta)$, and $\mathbf{m}(\theta)$ for the Frenet trihedron is represented by the following equations:

$$\mathbf{t}(\theta) = \frac{\mathbf{r}_\theta}{|\mathbf{r}_\theta|} \tag{4.4.36}$$

$$\mathbf{b}(\theta) = \frac{\mathbf{r}_\theta \times \mathbf{r}_{\theta\theta}}{|\mathbf{r}_\theta \times \mathbf{r}_{\theta\theta}|} \tag{4.4.37}$$

$$\mathbf{m}(\theta) = \mathbf{b}(\theta) \times \mathbf{t}(\theta) = \frac{(\mathbf{r}_\theta \times \mathbf{r}_{\theta\theta}) \times \mathbf{r}_\theta}{|\mathbf{r}_\theta \times \mathbf{r}_{\theta\theta}||\mathbf{r}_\theta|}. \tag{4.4.38}$$

We have used for derivation of equation $\mathbf{b}(\theta)$ expression (4.4.35) and Eq. (4.4.10).

It is important to recognize for further discussions that vector $\mathbf{m}(\theta)$ has the same direction as $\mathbf{r}_{ss}$ and forms an acute angle with $\mathbf{r}_{\theta\theta}$. The inequality

$$\mathbf{r}_{\theta\theta} \cdot \mathbf{m}(\theta) > 0 \quad (\mathbf{r}_{\theta\theta} \neq 0, \ \mathbf{m}(\theta) \neq 0) \tag{4.4.39}$$

follows from Eq. (4.4.34) which yields

$$\mathbf{r}_{\theta\theta} \cdot \mathbf{r}_{ss} = \mathbf{r}_{ss}^2 \left(\frac{ds}{d\theta}\right)^2 = (\mathbf{r}_{ss}^2) \cdot (\mathbf{r}_\theta^2) > 0. \tag{4.4.40}$$

Recall that $\mathbf{r}_s \cdot \mathbf{r}_{ss} = 0$ because these vectors are perpendicular. Vector $\mathbf{m}$ has the same direction as $\mathbf{r}_{ss}$.

The most effective equations for determination of the curve curvature are Eq. (4.4.30) and the modified Eq. (4.4.31) (see below). Other equations from the set of (4.4.26) to (4.4.29) are more complex because they require the determination of complex derivatives $\mathbf{m}_\theta = (d/d\theta)(\mathbf{m})$, $\mathbf{t}_\theta = (d/d\theta)(\mathbf{t})$.

Modification of Eq. (4.4.31)

The modification is based on representation of the unit normal $\mathbf{n}$ to the planar curve by the vector equation

$$\mathbf{n} = \frac{\mathbf{k} \times \mathbf{r}_\theta}{|\mathbf{r}_\theta|} \tag{4.4.41}$$

or by

$$\mathbf{n} = \frac{\mathbf{r}_\theta \times \mathbf{k}}{|\mathbf{r}_\theta|}. \tag{4.4.42}$$

Here, $\mathbf{k}$ is the unit vector that is perpendicular to plane (x, y) where the curve is represented. Vector Eqs. (4.4.41) [or (4.4.42)] determine the unit normal to the planar curve as a unit vector that is perpendicular to the tangent to the curve and lies in plane (x, y). Vector $\mathbf{n}$ may coincide with $\mathbf{m}$ or be opposite to $\mathbf{m}$. This means that the direction of $\mathbf{n}$ might coincide or be opposite to the curvature radius $\overline{MC}$ [Fig. 4.4.1(b)]. The modified Eq. (4.4.31) is represented as

$$\kappa(\theta) = \frac{\mathbf{r}_{\theta\theta} \cdot \mathbf{n}}{\mathbf{r}_\theta^2}. \tag{4.4.43}$$

Equation (4.4.43) determines the curvature κ as an algebraic value. The positive (negative) value of κ indicates that the curvature center lies on the positive (negative) value of the unit normal $\mathbf{n}$. This rule works for both representations of the unit normal $\mathbf{n}$ by vector Eqs. (4.4.41) or (4.4.42).

It is easy to verify that the direction of $\mathbf{n}$ with respect to $\mathbf{m}$ can be determined with the sign of the scalar product $\mathbf{m} \cdot \mathbf{n}$: the positive (negative) sign of $\mathbf{n}$ indicates that $\mathbf{n}$ has the same (opposite) direction as $\mathbf{m}$. Let us assume that the unit normal $\mathbf{n}$ is determined with vector Eq. (4.4.42). Using Eqs. (4.4.42) and (4.4.38) we obtain

$$\mathbf{m} \cdot \mathbf{n} = \frac{[(\mathbf{r}_\theta \times \mathbf{r}_{\theta\theta}) \times \mathbf{r}_\theta] \cdot (\mathbf{r}_\theta \times \mathbf{k})}{|\mathbf{r}_\theta \times \mathbf{r}_{\theta\theta}|\mathbf{r}_\theta^2}. \tag{4.4.44}$$

Equation (4.4.44) yields (see vector algebra)

$$\mathbf{m} \cdot \mathbf{n} = \frac{\mathbf{r}_{\theta\theta} \cdot (\mathbf{r}_\theta \times \mathbf{k})}{|\mathbf{r}_\theta \times \mathbf{r}_{\theta\theta}|} = \frac{x_{\theta\theta} y_\theta - y_{\theta\theta} x_\theta}{|y_{\theta\theta} x_\theta - x_{\theta\theta} y_\theta|}. \tag{4.4.45}$$

The direction of $\mathbf{n}$ determined by Eq. (4.4.42) coincides with the direction of $\mathbf{m}$, if

$$x_{\theta\theta} y_\theta - y_{\theta\theta} x_\theta > 0. \tag{4.4.46}$$

Representation of Eq. (4.4.43) in terms of velocity and acceleration
Consider that the planar curve is represented by vector equation $\mathbf{r}(\theta)$. The velocity $\mathbf{v}_r$ and acceleration $\mathbf{a}_r$ of a point that moves along the curve are represented by the following equations:

$$\mathbf{v}_r = (x_\theta\, \mathbf{i} + y_\theta\, \mathbf{j}) \frac{d\theta}{dt} \tag{4.4.47}$$

$$\mathbf{a}_r = (x_{\theta\theta}\, \mathbf{i} + y_{\theta\theta}\, \mathbf{j}) \left(\frac{d\theta}{dt} \right)^2 + (x_\theta\, \mathbf{i} + y_\theta\, \mathbf{j}) \frac{d^2\theta}{dt^2} = \mathbf{a}_r^{(n)} + \mathbf{a}_r^{(t)}. \tag{4.4.48}$$

The subscript "r" indicates that the point moves *along* the curve, performing a relative motion with respect to the curve. The superscripts "n" and "t" indicate the *normal* and *tangential* components of the acceleration. Equations (4.4.43), (4.4.47), and (4.4.48) yield as the equation for the determination of the curve curvature,

$$\kappa = \frac{\mathbf{a}_r \cdot \mathbf{n}}{\mathbf{v}_r^2} = \frac{\mathbf{a}_r^{(n)} \cdot \mathbf{n}}{\mathbf{v}_r^2}, \tag{4.4.49}$$

because $\mathbf{a}_r^{(t)} \cdot \mathbf{n} = 0$. It is easy to verify that Eqs. (4.4.43) and (4.4.49) are identical.

Curvature of curves represented by explicit or implicit functions
Consider that the curve is represented as

$$y(x) \in C^2, \quad x_1 < x < x_2 \tag{4.4.50}$$

or

$$F(x, y) = 0, \quad F \in C^2, \quad |F_x| + |F_y| \neq 0. \tag{4.4.51}$$

Recall that the curvature is represented by

$$\kappa = \frac{d\alpha}{ds}. \tag{4.4.52}$$

For the curve given by function (4.4.50), we have

$$\tan \alpha = \frac{dy}{dx} = y_x \tag{4.4.53}$$

$$ds = \sqrt{dx^2 + dy^2} = \sqrt{1 + y_x^2}\, dx. \tag{4.4.54}$$

Differentiating Eq. (4.4.53), we get

$$\frac{1}{\cos^2 \alpha} d\alpha = \frac{d^2 y}{dx^2} dx = y_{xx} dx$$

and

$$d\alpha = \cos^2 \alpha \, y_{xx} dx = \frac{1}{1 + \tan^2 \alpha} y_{xx} dx = \frac{y_{xx}}{(1 + y_x^2)} dx. \tag{4.4.55}$$

Equations (4.4.52), (4.4.54), and (4.4.55) yield

$$\kappa = \frac{y_{xx}}{(1 + y_x^2)^{(3/2)}}. \tag{4.4.56}$$

For the curve represented by Eq. (4.4.51), we get

$$F_x dx + F_y dy = 0.$$

Assuming that $F_y \neq 0$, we get

$$\frac{dy}{dx} = -\frac{F_x}{F_y} \tag{4.4.57}$$

$$\frac{d^2 y}{dx^2} = \frac{2 F_x F_y F_{xy} - F_x^2 F_{yy} - F_{xx} F_y^2}{F_y^3} \tag{4.4.58}$$

$$\kappa = \frac{2 F_x F_y F_{xy} - F_x^2 F_{yy} - F_{xx} F_y^2}{\left(F_x^2 + F_y^2\right)^{3/2}}. \tag{4.4.59}$$

While differentiating Eq. (4.4.57), we have considered that

$$F_x = F_x(x, y), \quad F_y = F_y(x, y)$$

and

$$\frac{\partial}{\partial x}(F_x) = F_{xx} + F_{xy} \frac{dy}{dx} = F_{xx} - F_{xy} \frac{F_x}{F_y}$$

$$\frac{\partial}{\partial x}(F_y) = F_{yx} + F_{yy} \frac{dy}{dx} = F_{yx} - F_{yy} \frac{F_x}{F_y}.$$

Problem 4.4.1

An involute curve is represented by the equations

$$x_1 = \rho(\sin \phi - \phi \cos \phi), \quad y_1 = \rho(\cos \phi + \phi \sin \phi) \tag{4.4.60}$$

where ϕ is the curve parameter. These equations can be derived from Eqs. (1.6.4) for an extended involute curve taking that the tracing point M belongs to the rolling straight line and $a = |\overline{AM_o}| = 0$ (Fig. 1.6.2); ρ is the radius of the base cylinder. The unit normal to the involute curve is represented as

$$\mathbf{n} = \mathbf{t} \times \mathbf{k} \tag{4.4.61}$$

where $\mathbf{k}$ is the unit vector of the z axis; $\mathbf{t}$ is the unit tangent to the planar curve. Determine the curvature of the involute curve by using Eq. (4.4.43).

Solution

$$\kappa = \frac{1}{\rho\phi} \quad (\text{provided } \phi \neq 0).$$

Problem 4.4.2

An extended epicycloid (Fig. 1.6.1) is represented by Eqs. (1.6.2). Consider an ordinary epicycloid [take $a = |\overline{O_2 M}| = \rho_2$ in Eqs. (1.6.2)]. The unit normal to the epicycloid is represented by Eq. (4.4.61). Determine the curvature using Eq. (4.4.43).

DIRECTION: Express after transformations the tangent $\mathbf{T}_1$ to the epicycloid as follows:

$$T_{x1} = 2 \sin \frac{\phi_2}{2} \left[\sin \left(\phi_1 + \frac{\phi_2}{2} \right) \right] E$$

$$T_{y1} = 2 \sin \frac{\phi_2}{2} \left[\cos \left(\phi_1 + \frac{\phi_2}{2} \right) \right] E.$$

(4.4.62)

Solution

$$\kappa = \frac{\rho_1 + 2\rho_2}{4\rho_2(\rho_1 + \rho_2) \sin \frac{\phi_2}{2}} \quad (\text{provided } \phi_2 \neq 0).$$

5 Surfaces

5.1 PARAMETRIC REPRESENTATION OF SURFACES

Parametric representation of a surface means that the position vector of a current surface point is associated with two variable parameters u and θ and is represented by the following vector equation:

$$\mathbf{r}(u, \theta) = f(u, \theta)\mathbf{i} + g(u, \theta)\mathbf{j} + s(u, \theta)\mathbf{k}. \tag{5.1.1}$$

Here, $\mathbf{i}$, $\mathbf{j}$, and $\mathbf{k}$ are the unit vectors of the coordinate axes; functions

$$f(u, \theta) = x(u, \theta), \qquad g(u, \theta) = y(u, \theta), \qquad s(u, \theta) = z(u, \theta) \tag{5.1.2}$$

determine the Cartesian coordinates of the surface points if u and θ are given.
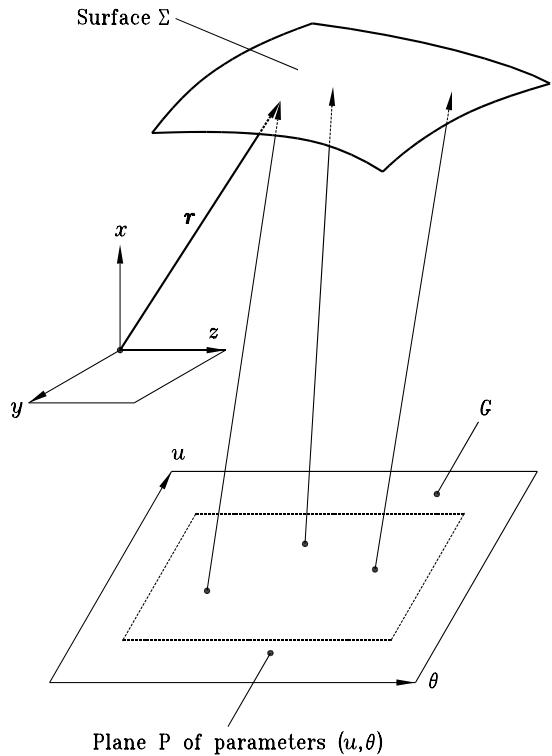
We may imagine a rectangle G in the plane of parameters (u, θ) (Fig. 5.1.1). Vector equation (5.1.1) sets the correspondence between the given point of the rectangle G and the single point $\mathbf{r}(u, \theta)$ of the surface. Generally, one-to-one correspondence is not guaranteed; it may happen that the given surface point $\mathbf{r}(u, \theta)$ corresponds to more than one point of the rectangle G. A surface with one-to-one correspondence between the set of parameters (u, θ) and the position vector $\mathbf{r}(u, \theta)$ is called a *simple surface*. Such a surface does not have points of self-intersection.

5.2 CURVILINEAR COORDINATES

Parameters (u, θ) are called curvilinear coordinates (Gaussian coordinates) on the surface. Consider that one of the curvilinear coordinates is fixed, for instance $\theta = \theta_0$, and the other one (u) is varied. Then, equation

$$\mathbf{r}(u, \theta_0) = x(u, \theta_0)\mathbf{i} + y(u, \theta_0)\mathbf{j} + z(u, \theta_0)\mathbf{k} \tag{5.2.1}$$
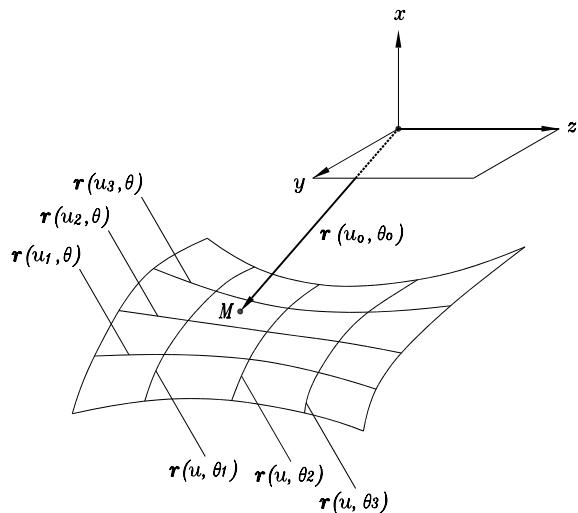
represents a line on the surface that is called the u line. Similarly, by setting $u = u_0$, we may determine by $\mathbf{r}(u_0, \theta)$ the θ line on the surface. Thus, the surface may be covered with u lines and θ lines, as shown in Fig. 5.2.1.
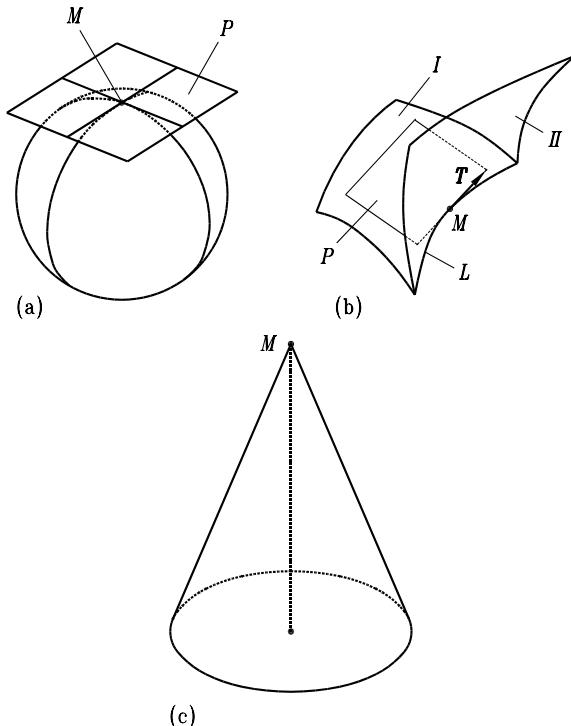
Figure 5.1.1: Mapping of a surface.

5.3 TANGENT PLANE AND SURFACE NORMAL

Consider that point M_0 is fixed on the surface and the position vector of this point is represented by $\mathbf{r}(u_0, \theta_0)$. A neighboring point M is represented by

$$\mathbf{r}(u, \theta) = \mathbf{r}(u_0 + \Delta u, \ \theta_0 + \Delta \theta).$$

Figure 5.2.1: Coordinate lines on a surface.
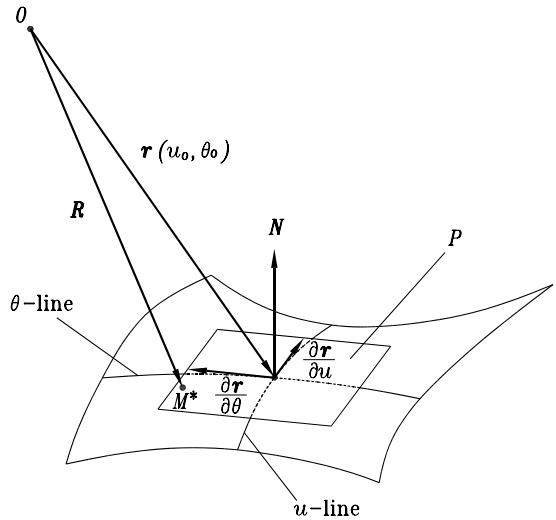
Figure 5.3.1: Regular and singular surface points.

The location of M with respect to M_0 depends on the chosen set of $\triangle u$ and $\triangle \theta$. Draw a ray from point M_0 to point M. This ray intersects the surface, and the orientation of this ray depends on the ratio $\triangle u / \triangle \theta$. The position of the ray when point M approaches M_0 [when (u, θ) approaches (u_0, θ_0)] is called the *limiting* position of the ray [Zalgaller, 1975]. The ray at its limiting position is tangent to the surface. Because the location of M with respect to M_0 depends on $(\triangle u, \triangle \theta)$, there is a set of points M within the neighborhood of M_0; there is also a set of limiting rays that are drawn from M_0 and that are tangents to the surface. We say that a surface has a tangent plane at M_0 if the set of limiting rays fills in a *plane*.

Figure 5.3.1 shows three types of sets of limiting rays. In the first case, the set of limiting rays fills in a plane P that is tangent to the surface at point M [Fig. 5.3.1(a)]. In the second case [Fig. 5.3.1(b)], two branches of the surface have a common line, L, the so-called *edge of regression*. The set of limiting rays that are drawn from point M of L fills in only a half-plane that is limited with the tangent $\mathbf{T}$ drawn to L at point M. In the third case [Fig. 5.3.1(c)], point M is the cone apex, and the set of limiting rays fills in the cone surface; the tangent plane at M does not exist.

A surface point at which the set of limiting rays fills in a full plane is called a *regular* point. The surface at such a point has a tangent plane. A surface point at which a tangent plane does not exist is called a *singular* point. The tangent plane P to a surface (if such a plane exists) is determined by the pair of vectors $\mathbf{r}_u$ and $\mathbf{r}_\theta$ that are tangents to the u-line and the θ-line, respectively (Fig. 5.3.2). It is assumed that $\mathbf{r}_u \neq 0$ and $\mathbf{r}_\theta \neq 0$ and

Figure 5.3.2: Surface tangent plane.

that vectors $\mathbf{r}_u$ and $\mathbf{r}_\theta$ are not collinear. The tangent plane P at the surface point $\mathbf{r}(u_0, \theta_0)$ is represented by the equation

$$\mathbf{A} \cdot (\mathbf{r}_u \times \mathbf{r}_\theta) = 0. \tag{5.3.1}$$

Here,

$$\mathbf{A} = \mathbf{R} - \mathbf{r}(u_0, \theta_0) = \overline{MM}^*.$$

Position vector $\mathbf{R}$ is drawn from the same origin as $\mathbf{r}(u_0, \theta_0)$ to an arbitrary point M^* of the tangent plane. Equation (5.3.1) yields that vector $\mathbf{A} = \overline{MM}^*$ lies in the plane drawn through vectors $\mathbf{r}_u$ and $\mathbf{r}_\theta$ taken at point $\mathbf{r}(u_0, \theta_0)$. The surface normal $\mathbf{N}$ is perpendicular to the tangent plane P and is represented by the equation

$$\mathbf{N} = \mathbf{r}_u \times \mathbf{r}_\theta. \tag{5.3.2}$$

The direction of the surface normal depends on the order of factors in the cross product (5.3.2). The surface normal may be expressed in terms of projections on the coordinate axis by

$$\mathbf{N} = \begin{vmatrix} \mathbf{i} & \mathbf{j} & \mathbf{k} \\ x_u & y_u & z_u \\ x_\theta & y_\theta & z_\theta \end{vmatrix} = \begin{vmatrix} y_u & z_u \\ y_\theta & z_\theta \end{vmatrix} \mathbf{i} + \begin{vmatrix} z_u & x_u \\ z_\theta & x_\theta \end{vmatrix} \mathbf{j} + \begin{vmatrix} x_u & y_u \\ x_\theta & y_\theta \end{vmatrix} \mathbf{k}. \tag{5.3.3}$$

The unit normal is represented by

$$\mathbf{n} = \frac{\mathbf{N}}{|\mathbf{N}|} = \frac{N_x}{|\mathbf{N}|}\mathbf{i} + \frac{N_y}{|\mathbf{N}|}\mathbf{j} + \frac{N_z}{|\mathbf{N}|}\mathbf{k} \tag{5.3.4}$$

provided $|\mathbf{N}| = (N_x^2 + N_y^2 + N_z^2)^{1/2} \neq 0$. The surface point $\mathbf{r}(u_0, \theta_0)$ is a singular one if

$$\mathbf{r}_u \times \mathbf{r}_\theta = 0. \tag{5.3.5}$$

A singular point at a surface appears if at least one of the vectors in the cross product (5.3.5) is equal to zero or if the vectors are collinear.

5.4 REPRESENTATION OF A SURFACE BY IMPLICIT FUNCTION

The equation

$$F(x, y, z) = 0 \qquad (5.4.1)$$

may represent a surface or just a set of points. To represent a surface, Eq. (5.4.1) must be complemented with the following additional requirements:

$$F \in C^1, \qquad |F_x| + |F_y| + |F_z| \neq 0 \qquad (5.4.2)$$

or

$$F \in C^1, \qquad F_x^2 + F_y^2 + F_z^2 \neq 0. \qquad (5.4.3)$$

Equation (5.4.1) with requirements (5.4.2) or (5.4.3) represents a simple and regular surface *locally*, in the neighborhood of point $M_o(x_o, y_o, z_o)$, whose coordinates satisfy Eq. (5.4.1). A surface point is singular if

$$F_x = F_y = F_z = 0. \qquad (5.4.4)$$

A tangent plane at a regular surface point is represented by the equation

$$F_x(x_0, y_0, z_0)(X - x_0) + F_y(x_0, y_0, z_0)(Y - y_0) + F_z(x_0, y_0, z_0)(Z - z_0) = 0. \quad (5.4.5)$$

Here, X, Y, and Z are the coordinates of a point in the tangent plane P (point M^* in Fig. 5.3.2); x_0, y_0, and z_0 are the coordinates of the surface point M; the derivatives F_x, F_y, and F_z are taken at M.

The surface normal $\mathbf{N}$ at the point (x_0, y_0, z_0) is

$$\mathbf{N} = F_x(x_0, y_0, z_0)\,\mathbf{i} + F_y(x_0, y_0, z_0)\,\mathbf{j} + F_z(x_0, y_0, z_0)\,\mathbf{k}. \qquad (5.4.6)$$

The surface unit normal $\mathbf{n}$ is
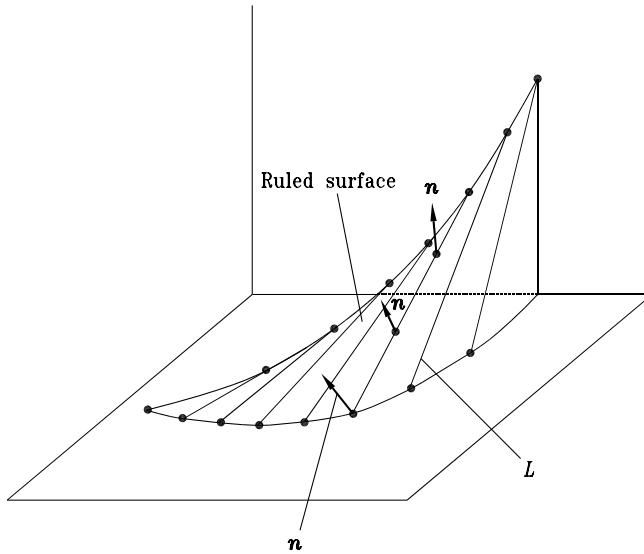
$$\mathbf{n} = \frac{F_x\mathbf{i} + F_y\mathbf{j} + F_z\mathbf{k}}{m} \qquad (5.4.7)$$

where $m = (F_x^2 + F_y^2 + F_z^2)^{1/2}$.

5.5 EXAMPLES OF SURFACES

A *ruled* surface represents a family of straight lines. Such a surface may be generated by a certain motion of the generating straight line (Fig. 5.5.1). The simplest cases of ruled surfaces are: a cone surface and a cylinder surface (they are generated by a straight line that rotates about a fixed axis), the surface of a screw (the Archimedes screw surface), and the surface of a helical involute gear (the involute screw surface). The last two surfaces are generated by the screw motion of a straight line (see below).

Generally, the direction of a unit normal to a ruled surface changes its orientation while the surface point moves along the straight line L (Fig. 5.5.1). An exception to this rule is a developable ruled surface that may be developed on a plane.

Figure 5.5.1: Ruled surface.

The direction of the surface unit normal for a developable ruled surface is the same for all points of a surface straight line. Typical examples of ruled developable surfaces are the cone surface, the cylinder surface, and the involute screw surface (see below).

Surface of Revolution

This surface (Fig. 5.5.2) may be generated by rotation of a planar curve L about the z axis; curve L is located in a plane drawn through the z axis. Consider that the planar curve L, which generates the surface of revolution, is represented in the auxiliary coordinate system S_a [Fig. 5.5.3(a)] by the equations

$$x_a = f(\theta), \qquad y_a = 0, \qquad z_a = g(\theta). \tag{5.5.1}$$
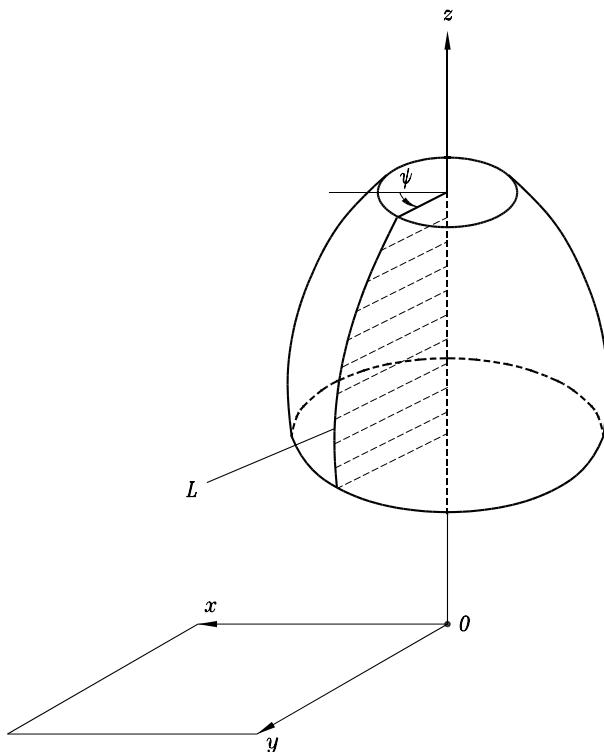
The auxiliary coordinate system rotates about the z axis and the coordinate transformation from $S_a(x_a, y_a, z_a)$ to $S(x, y, z)$ [Fig. 5.5.3(b)] is represented by the matrix equation

$$\begin{bmatrix} x \\ y \\ z \\ 1 \end{bmatrix} = \begin{bmatrix} \cos\psi & -\sin\psi & 0 & 0 \\ \sin\psi & \cos\psi & 0 & 0 \\ 0 & 0 & 1 & 0 \\ 0 & 0 & 0 & 1 \end{bmatrix} \begin{bmatrix} x_a \\ y_a \\ z_a \\ 1 \end{bmatrix}. \tag{5.5.2}$$

Equations (5.5.1) and (5.5.2) yield

$$x = f(\theta)\cos\psi, \qquad y = f(\theta)\sin\psi, \qquad z = g(\theta) \tag{5.5.3}$$

where $\theta_1 < \theta < \theta_2$ and $0 \le \psi \le 2\pi$.

Figure 5.5.2: Surface of revolution.

Problem 5.5.1

Consider the surface of revolution represented by Eqs. (5.5.3). Determine (1) equations of the θ lines and ψ lines and explain their geometric essence, and (2) equations of the surface normal $\mathbf{N}$ and the surface unit normal $\mathbf{n}$.

Solution

(1) The θ line is represented by the equations

$$x = f(\theta)\cos\psi_0, \qquad y = f(\theta)\sin\psi_0, \qquad z = g(\theta) \qquad (5.5.4)$$

(here, $\psi_o = $ constant) and is located in the plane that passes through the z axis and makes an angle $\psi = \psi_0$ with the x axis (Fig. 5.5.2). The ψ line is represented by the equations

$$x = f(\theta_0)\cos\psi, \qquad y = f(\theta_0)\sin\psi, \qquad z = g(\theta_0). \qquad (5.5.5)$$
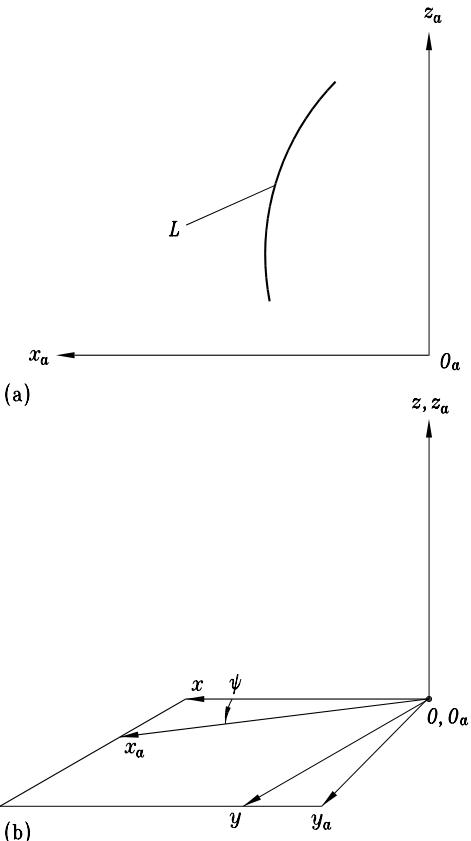
Equations (5.5.5) represent a circle of radius

$$\rho = (x^2 + y^2)^{1/2} = f(\theta_0)$$

which is located in the plane $z = g(\theta_0)$ and centered on the z axis.

(2) Using the cross product $\mathbf{r}_\theta \times \mathbf{r}_\psi$, the surface normal may be represented as follows:

$$N_x = -f(\theta)g'(\theta)\cos\psi, \qquad N_y = -f(\theta)g'(\theta)\sin\psi, \qquad N_z = f(\theta)f'(\theta). \qquad (5.5.6)$$

Figure 5.5.3: Generation of surface of revolution: (a) representation of planar curve L; (b) coordinate systems S_a and S.

The unit normal is (provided $f(\theta) \neq 0$)

$$n_x = -\frac{g'(\theta)\cos\psi}{A}, \qquad n_y = -\frac{g'(\theta)\sin\psi}{A}, \qquad n_z = \frac{f'(\theta)}{A} \qquad (5.5.7)$$

where
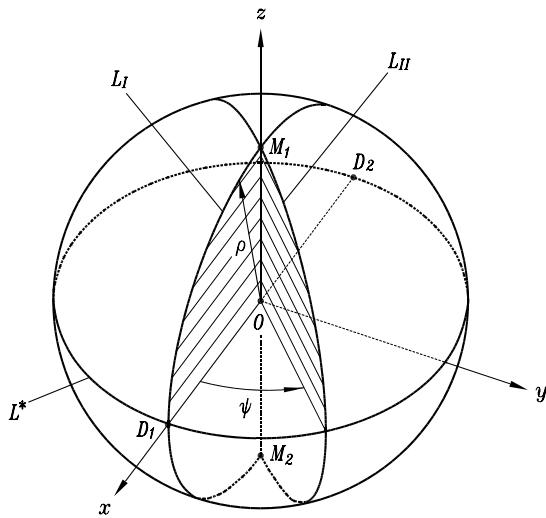
$$A^2 = [f'(\theta)]^2 + [g'(\theta)]^2, \qquad f'(\theta) = \frac{d}{d\theta}f(\theta), \qquad g'(\theta) = \frac{d}{d\theta}g(\theta).$$

Spherical Surface

This surface (Fig. 5.5.4) is a particular case of the surface of revolution. The generating planar curve L is a circle of radius ρ centered at the origin O of the coordinate system $S(x, y, z)$. The spherical surface is generated by the circle in rotational motion about the z axis; L_I and L_{II} are two positions of the generating circle, and ψ is the angle of rotation about the z axis.

Consider again an auxiliary coordinate system S_a, rigidly connected to the generating circle (Fig. 5.5.5). The generating circle is represented in the coordinate system S_a by the equations

$$x_a = \rho\cos\theta, \qquad y_a = 0, \qquad z_a = \rho\sin\theta. \qquad (5.5.8)$$

Figure 5.5.4: Spherical surface.

Using matrix equation (5.5.2) and Eq. (5.5.8), we represent the equations of the spherical surface as
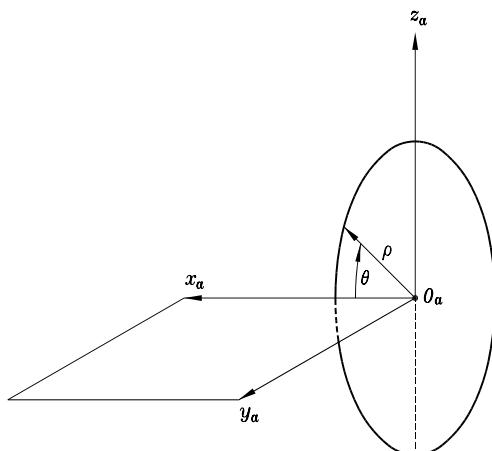
$$x_a = \rho \cos\theta \cos\psi, \qquad y_a = \rho \cos\theta \sin\psi, \qquad z_a = \rho \sin\theta \qquad (5.5.9)$$

where $0 < \theta < 2\pi$ and $0 < \psi < 2\pi$. The surface normal vector $\mathbf{N} = \mathbf{r}_\theta \times \mathbf{r}_\psi$ is given by
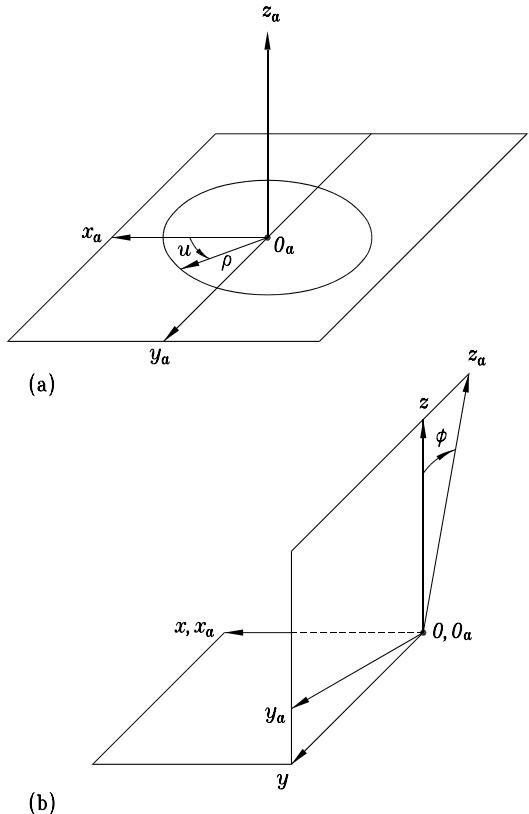
$$N_x = -\rho^2 \cos^2\theta \cos\psi, \quad N_y = -\rho^2 \cos^2\theta \sin\psi, \quad N_z = -\rho^2 \cos\theta \sin\theta. \quad (5.5.10)$$

The normal $\mathbf{N}$ is equal to zero with $\cos\theta = 0$. Thus, points M_1 and M_2 (Fig. 5.5.4) are singular.

We must differentiate between singular and pseudosingular points of a surface. Pseudosingular points appear only as a result of the chosen parametric representation, and they become regular by changing the parameters of representation. To prove this, let us consider that the spherical surface is generated by circle L^* in rotational motion about

Figure 5.5.5: Generating circle.

Figure 5.5.6: Generation of spherical surface: (a) representation of circle of radius ρ in S_a; (b) coordinate systems S_a and S.

the x axis (Fig. 5.5.4). Circle L^* is represented in the coordinate system S_a [Fig. 5.5.6(a)] by the equations

$$x_a = \rho \cos u, \quad y_a = \rho \sin u, \quad z_a = 0. \tag{5.5.11}$$

The coordinate transformation in transition from S_a to S [Fig. 5.5.6(b)] is represented by the matrix

$$\begin{bmatrix} x \\ y \\ z \\ 1 \end{bmatrix} = \begin{bmatrix} 1 & 0 & 0 & 0 \\ 0 & \cos\phi & -\sin\phi & 0 \\ 0 & \sin\phi & \cos\phi & 0 \\ 0 & 0 & 0 & 1 \end{bmatrix} \begin{bmatrix} x_a \\ y_a \\ z_a \\ 1 \end{bmatrix}. \tag{5.5.12}$$

Equations (5.5.11) and (5.5.12) yield

$$x = \rho \cos u, \qquad y = \rho \sin u \cos \phi, \qquad z = \rho \sin u \sin \phi. \tag{5.5.13}$$

The surface normal $\mathbf{N}^*$ is given by

$$\mathbf{N}^* = \mathbf{r}_u \times \mathbf{r}_\phi = \rho^2 \sin u (\cos u \mathbf{i} + \sin u \cos \phi \mathbf{j} + \sin u \sin \phi \mathbf{k}). \tag{5.5.14}$$

Surface points D_1 and D_2 (Fig. 5.5.4), which correspond to $\sin u = 0$, are singular because at these points $\mathbf{N}^* = \mathbf{0}$. All other surface points, including points M_1 and M_2 (Fig. 5.5.4), are regular. We may see that the singularity of surface points M_1 and M_2, which results from the parametric representation (Eq. 5.5.9), disappears when the new parametric representation (Eq. 5.5.14) is employed. But, at the same time, the singularity of surface points D_1 and D_2 occurs.

Actually, a spherical surface does not have singular points; that is, the normal to the surface has a definite direction at all surface points. This direction of the normal at pseudosingular points such as M_1 and M_2 and D_1 and D_2 may be determined by using a new parametric representation.

Considering the parametric representation (Eq. 5.5.13) and the equation of the surface normal (Eq. 5.5.14), we find that the surface unit normal is (provided $\sin u \neq 0$)

$$\mathbf{n}^* = \frac{\mathbf{N}^*}{|\mathbf{N}^*|} = \cos u \mathbf{i} + \sin u \cos \phi \mathbf{j} + \sin u \sin \phi \mathbf{k}. \qquad (5.5.15)$$

Cone Surface

This surface may be generated by a straight line L in rotation about an axis with which line L forms an angle ψ_c (the x axis in Fig. 5.5.7). Curvilinear coordinates of the cone surface are θ and $u = |\overline{AM}|$, where A is the cone apex. Equations of the cone surface are

$$x = \rho \cot \psi_c - u \cos \psi_c, \qquad y = u \sin \psi_c \sin \theta, \qquad z = u \sin \psi_c \cos \theta \qquad (5.5.16)$$

where $0 \leq u \leq u_1$ and $0 \leq \theta \leq 2\pi$.
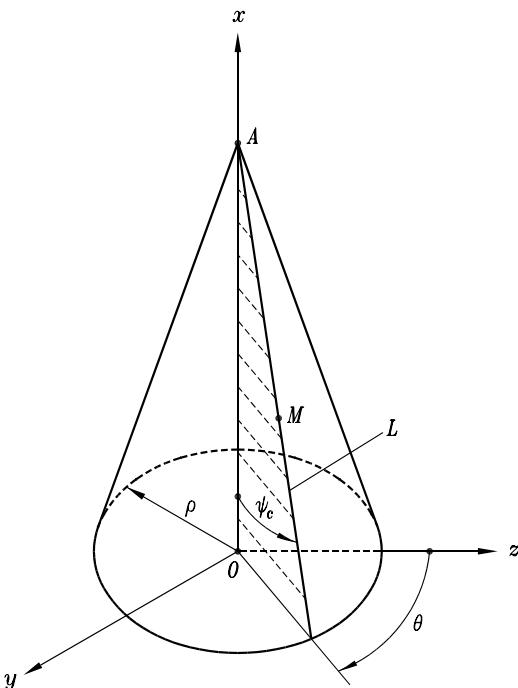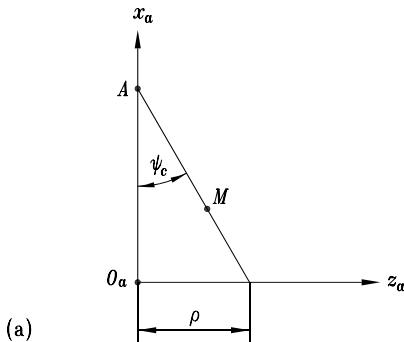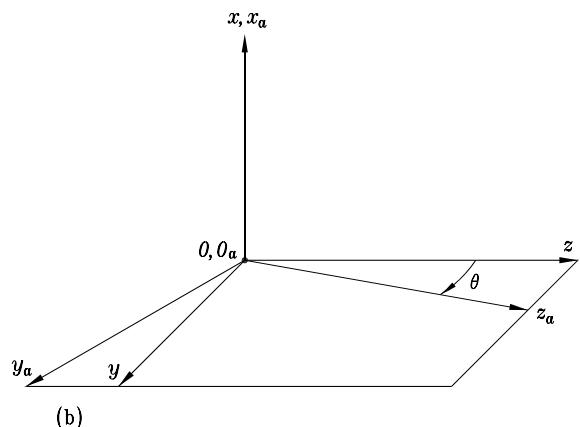
Figure 5.5.7: Cone surface.

Figure 5.5.8: Cone generation: (a) representation of generating straight line L in S_a; (b) coordinate systems S_a and S.

Equations (5.5.16) may also be derived using the following considerations:

(1) The generating straight line L is represented in the auxiliary coordinate system S_a [Fig. 5.5.8(a)] by the equations

$$x_a = \rho \cot \psi_c - u \cos \psi_c, \qquad y_a = 0, \qquad z_a = u \sin \psi_c. \qquad (5.5.17)$$

(2) The coordinate transformation in transition from S_a to S [Fig. 5.5.8(b)] is

$$\begin{bmatrix} x \\ y \\ z \\ 1 \end{bmatrix} = \begin{bmatrix} 1 & 0 & 0 & 0 \\ 0 & \cos\theta & \sin\theta & 0 \\ 0 & -\sin\theta & \cos\theta & 0 \\ 0 & 0 & 0 & 1 \end{bmatrix} \begin{bmatrix} x_a \\ y_a \\ z_a \\ 1 \end{bmatrix}. \qquad (5.5.18)$$

Equations (5.5.17) and (5.5.18) yield Eqs. (5.5.16).

A cone surface is an example of a developable ruled surface. The cone normal and its unit normal may be represented by

$$\mathbf{N} = \mathbf{r}_u \times \mathbf{r}_\theta = -u \sin \psi_c (\sin \psi_c \mathbf{i} + \cos \psi_c \sin\theta \mathbf{j} + \cos \psi_c \cos\theta \mathbf{k}) \qquad (5.5.19)$$

$$\mathbf{n} = \frac{\mathbf{N}}{|\mathbf{N}|} = -(\sin \psi_c \mathbf{i} + \cos \psi_c \sin\theta \mathbf{j} + \cos \psi_c \cos\theta \mathbf{k}) \quad \text{(by } u \sin \psi_c \neq 0\text{).} \qquad (5.5.20)$$

Equations (5.5.20) yield that the surface unit normal **n** is a function of only one curvilinear coordinate, θ. Consequently, the surface unit normals are the same for all points of the straight line L (Fig. 5.5.7). The cone apex, which corresponds to $u = 0$, is the singular surface point. This result comes from Eq. (5.5.19), where $\mathbf{N} = 0$ when $u = 0$.

Helicoid
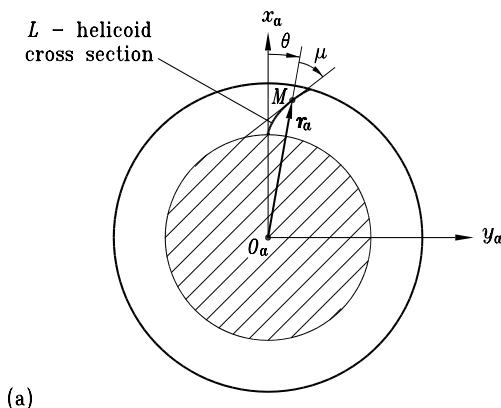
A helicoid is a surface that is generated by a line in a screw motion. The generating line may be a curve or a straight line. Helicoids are widespread in the field of gears. Surfaces of helical gears and cylindrical worms of worm-gear drives are helicoids.

General Equations of a Helicoid

Consider a screw motion of a planar curve L such that the axis of screw motion is perpendicular to the plane of L. In this motion, curve L generates a helicoid. Let us represent curve L in an auxiliary coordinate system S_a by the equations [Fig. 5.5.9(a)]
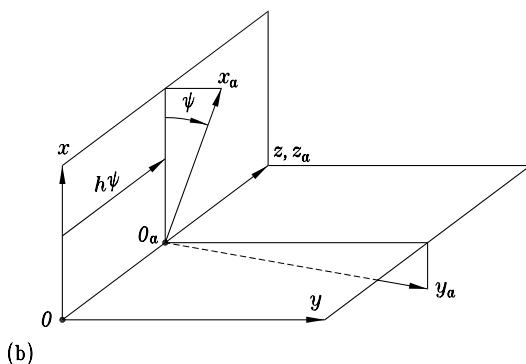
$$x_a = r_a(\theta) \cos \theta, \qquad y_a = r_a(\theta) \sin \theta, \qquad z_a = 0 \qquad (5.5.21)$$

where $r_a = |\overline{O_a M}|$ and $\theta_1 < \theta < \theta_2$. The axis of screw motion is the z axis [Fig. 5.5.9(b)], and the screw parameter is h. The screw parameter h represents the displacement along

(a)

(b)

Figure 5.5.9: Generation of helicoid: (a) representation of planar curve L in S_a; (b) coordinate systems S_a and S.

the z axis, which corresponds to the rotation about z through an angle of one radian. The sign of h is positive for a right-hand screw motion.

Coordinate transformation in transition from S_a to S is represented by the matrix equation

$$
\begin{bmatrix} x \\ y \\ z \\ 1 \end{bmatrix} = \begin{bmatrix} \cos\psi & -\sin\psi & 0 & 0 \\ \sin\psi & \cos\psi & 0 & 0 \\ 0 & 0 & 1 & h\psi \\ 0 & 0 & 0 & 1 \end{bmatrix} \begin{bmatrix} x_a \\ y_a \\ z_a \\ 1 \end{bmatrix}. \tag{5.5.22}
$$

Equations (5.5.21) and (5.5.22) yield

$$ x = r_a(\theta)\cos(\theta + \psi), \qquad y = r_a(\theta)\sin(\theta + \psi), \qquad z = h\psi \tag{5.5.23} $$

where $\theta_1 < \theta < \theta_2$ and $0 < \psi < 2\pi$.

The helicoid normal is

$$ \mathbf{N} = \frac{\partial\mathbf{r}}{\partial\theta} \times \frac{\partial\mathbf{r}}{\partial\psi} = \frac{r_a(\theta)}{\sin u}[h\sin(\theta + \psi_c + \mu)\mathbf{i} - h\cos(\theta + \psi_c + \mu)\mathbf{j} + r_a(\theta)\cos\mu\mathbf{k}] $$

$$ \tag{5.5.24} $$

where

$$ \mu = \arctan\left(\frac{r_a(\theta)}{dr_a(\theta)/d\theta}\right). $$

The helicoid unit normal is [provided $r_a(\theta) \neq 0$]
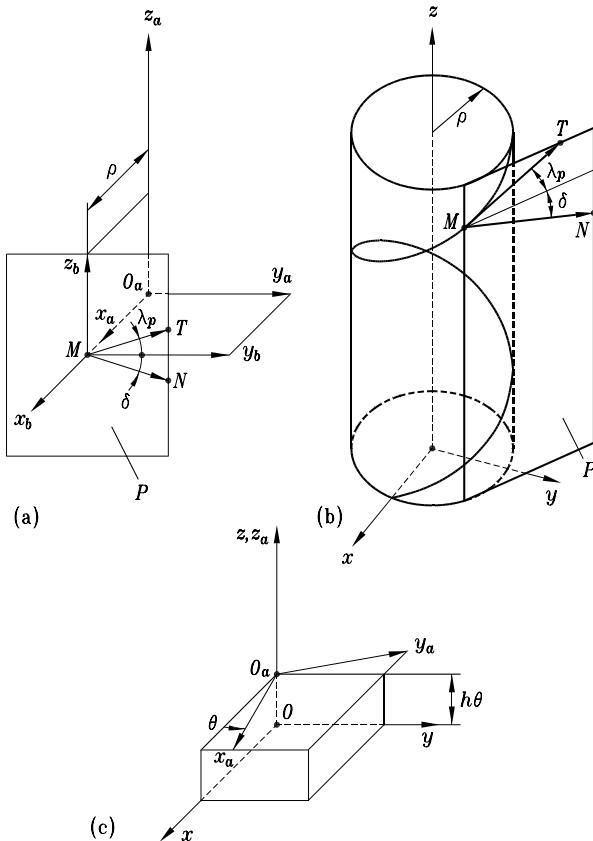
$$ \mathbf{n} = \frac{\mathbf{N}}{|\mathbf{N}|} = \frac{1}{\sqrt{h^2 + r_a^2\cos^2\mu}}[h\sin(\theta + \psi + \mu)\mathbf{i} - h\cos(\theta + \psi + \mu)\mathbf{j} + r_a(\theta)\cos\mu\mathbf{k}]. $$

$$ \tag{5.5.25} $$

Helicoid with Ruled Surface

A helicoid with a ruled surface is generated by a screw motion of a straight line L. The axis of screw motion and the generating line may form a crossed angle or they may intersect each other. Two coordinate systems S_a and S_b rigidly connected to the generating line L [Fig. 5.5.10(a)] and a coordinate system S in which the helicoid is represented [Figs. 5.5.10(b) and 5.5.10(c)] are given. The coordinate system S_a performs a screw motion with respect to S, and z is the axis of the screw motion. Each point of coordinate system S_a generates in the screw motion a helix on a cylinder. Point M generates a helix on the cylinder of radius $O_a M = \rho$, and MT is the tangent to the helix at point M [Figs. 5.5.10(a) and 5.5.10(b)]. We consider two lines MT and MN rigidly connected with each other. Line MN is the generating line which, while performing a screw motion, generates the helicoid.

We may derive the helicoid equations by using the rules of coordinate transformation. Consider that the generating line is represented in coordinate system S_b by the equations

$$ x_b = 0, \qquad y_b = u\cos\delta, \qquad z_b = -u\sin\delta \tag{5.5.26} $$

Figure 5.5.10: Generation of ruled helicoid: (a) representation of generating line L in S_a and S_b; (b) representation of helix on cylinder of radius ρ and tangent $\overline{MT}$ to helix and generating line $\overline{MN}$; (c) coordinate systems S_a and S.

where $u = MN$. The coordinate transformation from S_b to S is represented by the matrix equation

$$\mathbf{r} = \mathbf{M}_{0a}\mathbf{M}_{ab}\mathbf{r}_b$$

$$\begin{bmatrix} x \\ y \\ z \\ 1 \end{bmatrix} = \begin{bmatrix} \cos\theta & -\sin\theta & 0 & 0 \\ \sin\theta & \cos\theta & 0 & 0 \\ 0 & 0 & 1 & h\theta \\ 0 & 0 & 0 & 1 \end{bmatrix} \begin{bmatrix} 1 & 0 & 0 & \rho \\ 0 & 1 & 0 & 0 \\ 0 & 0 & 1 & 0 \\ 0 & 0 & 0 & 1 \end{bmatrix} \begin{bmatrix} x_b \\ y_b \\ z_b \\ 1 \end{bmatrix}. \qquad (5.5.27)$$

Equations (5.5.26) and (5.5.27) represent the equations of the helicoid surface as follows:

$$\mathbf{r} = (\rho\cos\theta - u\cos\delta\sin\theta)\mathbf{i} + (\rho\sin\theta + u\cos\delta\cos\theta)\mathbf{j} + (h\theta - u\sin\delta)\mathbf{k}. \qquad (5.5.28)$$

Vector equation (5.5.28) represents a ruled surface. The u line (surface parameter θ is considered fixed) represents a straight line, and the θ line represents a helix. Vector equation (5.5.28) is a general equation of a helicoid. In a particular case, Eq. (5.5.28)

may represent a helicoid with a ruled surface if the generating plane curve L is given as a cross section of a helicoid with a ruled surface.

The normal to the helicoid with the ruled surface (Eq. 5.5.28) is

$$\mathbf{N} = \frac{\partial \mathbf{r}}{\partial u} \times \frac{\partial \mathbf{r}}{\partial \theta} = [(h \cos \delta + \rho \sin \delta) \cos \theta - u \cos \delta \sin \delta \sin \theta]\mathbf{i}$$

$$+ [(h \cos \delta + \rho \sin \delta) \sin \theta + u \cos \delta \sin \delta \cos \theta]\mathbf{j} + u \cos^2 \delta \, \mathbf{k}. \quad (5.5.29)$$

The unit normal is

$$\mathbf{n} = \frac{\mathbf{N}}{|\mathbf{N}|} = \frac{\mathbf{N}}{m} \quad (5.5.30)$$

where

$$m^2 = (h \cos \delta + \rho \sin \delta)^2 + u^2 \cos^2 \delta. \quad (5.5.31)$$

There are two particular but important cases of helicoids with ruled surfaces. In the first case, the generating line L coincides with the tangent $\mathbf{T}$ to the helix on the cylinder surface. The straight line L generates a helicoid, an involute screw surface. We may obtain equations of such a surface from Eq. (5.5.28) by setting $\delta = -\lambda_\rho$ [Fig. 5.5.10(a)]. This yields

$$\mathbf{r} = (\rho \cos \theta - u \cos \lambda_\rho \sin \theta) \, \mathbf{i} + (\rho \sin \theta + u \cos \lambda_\rho \cos \theta) \, \mathbf{j} + (h\theta + u \sin \lambda_\rho) \, \mathbf{k}. \quad (5.5.32)$$

Equations of the normal $\mathbf{N}$ and unit normal $\mathbf{n}$ to this surface may be derived from Eqs. (5.5.29), (5.5.30), and (5.5.31) by making $\delta = -\lambda_\rho$ where $\tan \lambda_\rho = h/\rho$. We then obtain

$$h \cos \delta + \rho \sin \delta = h \cos \lambda_\rho - \rho \sin \lambda_\rho = 0 \quad (5.5.33)$$

$$m^2 = (h \cos \delta + \rho \sin \delta)^2 + u^2 \cos^2 \delta = u^2 \cos^2 \lambda_\rho \quad (5.5.34)$$

and

$$\mathbf{N} = u \cos \lambda_\rho (\sin \lambda_\rho \sin \theta \, \mathbf{i} - \sin \lambda_\rho \cos \theta \, \mathbf{j} + \cos \lambda_\rho \mathbf{k}). \quad (5.5.35)$$

With $u \cos \lambda_\rho \neq 0$, all points of the screw involute surface are regular, and the equation of the unit normal at these points is

$$\mathbf{n} = \sin \lambda_\rho (\sin \theta \, \mathbf{i} - \cos \theta \, \mathbf{j}) + \cos \lambda_\rho \mathbf{k}. \quad (5.5.36)$$

The direction of the unit normal $\mathbf{n}$ does not depend on the surface parameter u. This means that the unit normals have the same direction for all points of the generating straight line L, and the involute screw surface is a ruled developable surface.

The second particular case of a helicoid with a ruled surface is the Archimedes screw surface. This surface is generated by a straight line that does not cross but does intersect the axis of screw motion. The Archimedes screw surface is applied not only for worms but also for screws that are cut by straight-edged blades. The equation of

the Archimedes screw surface may be derived from Eq. (5.5.28) by setting $\rho = 0$. This yields

$$\mathbf{r} = u \cos \delta(-\sin\theta\, \mathbf{i} + \cos\theta\, \mathbf{j}) + (h\theta - u\sin\delta)\, \mathbf{k}. \qquad (5.5.37)$$

Equations of the normal $\mathbf{N}$ may be derived from Eq. (5.5.29) by setting $\rho = 0$ and dividing all three normal projections by a common factor $\cos\delta$ (with the assumption that $\delta \neq 90°$). This yields

$$\mathbf{N} = (h\cos\theta - u\sin\delta\sin\theta)\, \mathbf{i} + (h\sin\theta + u\sin\delta\cos\theta)\, \mathbf{j} + u\cos\delta\, \mathbf{k}. \qquad (5.5.38)$$

The unit normal $\mathbf{n}$ is

$$\mathbf{n} = \frac{\mathbf{N}}{m} \qquad (5.5.39)$$

where

$$m = (h^2 + u^2)^{1/2}. \qquad (5.5.40)$$

The orientation of normal $\mathbf{N}$ to the Archimedes screw surface depends on the location of the point on the generating straight line (depends on u). The Archimedes screw surface is not a developed surface but a ruled surface.

Relationship Between Helicoid Coordinates and the Surface Normal Projections

This relationship proposed by Litvin [1968, 1989] may be represented as follows:

$$y N_x - x N_y - h N_z = 0 \qquad (5.5.41)$$

$$y n_x - x n_y - h n_z = 0. \qquad (5.5.42)$$

This statement may be confirmed by substituting in Eqs. (5.5.41) and (5.5.42) the helicoid coordinates and projections of the surface normal $\mathbf{N}$ and the surface unit normal $\mathbf{n}$ with the previously derived expressions of helicoids.

The kinematic interpretation of Eqs. (5.5.41) and (5.5.42) is based on the following suggestions. Consider the screw motion of a helicoid. The screw parameter h in this motion is the same as the screw parameter of the helicoid. A fixed point of the helicoid traces out a helix, and the velocity vector in screw motion $\mathbf{v}$ is a tangent to the helix. The helix belongs to the helicoid, and the velocity vector $\mathbf{v}$ is a tangent to the helicoid. Consequently, the following equation must be observed:

$$\mathbf{n} \cdot \mathbf{v} = \mathbf{N} \cdot \mathbf{v} = 0. \qquad (5.5.43)$$

The velocity vector in screw motion may be determined by the equation

$$\mathbf{v} = (\boldsymbol{\omega} \times \mathbf{r}) + h\boldsymbol{\omega} = \begin{vmatrix} \mathbf{i} & \mathbf{j} & \mathbf{k} \\ 0 & 0 & \omega \\ x & y & z \end{vmatrix} + h\omega\mathbf{k} = \omega(-y\,\mathbf{i} + x\,\mathbf{j} + h\,\mathbf{k}). \qquad (5.5.44)$$

The surface normal and the surface unit normal are represented as

$$\mathbf{N} = N_x\,\mathbf{i} + N_y\,\mathbf{j} + N_z\,\mathbf{k}, \qquad \mathbf{n} = n_x\,\mathbf{i} + n_y\,\mathbf{j} + n_z\,\mathbf{k}. \qquad (5.5.45)$$

Equations (5.5.43), (5.5.44), and (5.5.45) yield relations (5.5.41) and (5.5.42). In the case of a surface of revolution with the z axis as an axis of rotation, we have to use in Eqs. (5.5.41) and (5.5.42) the screw parameter $h = 0$.

Cross Section of a Helicoid

The cross section of a helicoid is formed by cutting the surface with a plane perpendicular to the z axis, the axis of screw motion. This section may be represented by the equations of the helicoid and the equation $z = c$, where c is a constant. To simplify transformations, we may set $z = 0$. The cross sections of a helicoid corresponding to $z = 0$ and $z = c$ represent the *same* plane curve in two positions. One cross section will coincide with the other after rotation about the z axis through the angle

$$\psi = \frac{c}{h}. \tag{5.5.46}$$

Let us determine the cross section of the helicoid (Eq. 5.5.28) that is cut by the plane $z = 0$. Using the relation

$$u = \frac{h}{\sin \delta} \theta \tag{5.5.47}$$

we get

$$x = \rho \cos \theta - \theta \sin \theta h \cot \delta, \qquad y = \rho \sin \theta + \theta \cos \theta h \cot \delta, \qquad z = 0. \tag{5.5.48}$$

In polar form the cross section may be represented as

$$r(\theta) = (x^2 + y^2)^{1/2} = [\rho^2 + (\theta h \cot \delta)^2]^{1/2}$$

$$\tan q = \frac{y}{x} = \frac{\rho \tan \theta + \theta h \cot \delta}{\rho - \theta \tan \theta h \cot \delta}. \tag{5.5.49}$$

Here, q is the angle that is formed by the position vector $\mathbf{r}(\theta)$ and axis x.

The cross section is an extended involute. The generation of such a curve is shown in Fig. 5.5.11. Consider that a straight line S rolls over a circle of radius $OA = h \cot \delta$. Point B, whose location is determined by

$$|\overline{AB}| = |\overline{AO}| + |\overline{OB}| = h \cot \delta + \rho$$
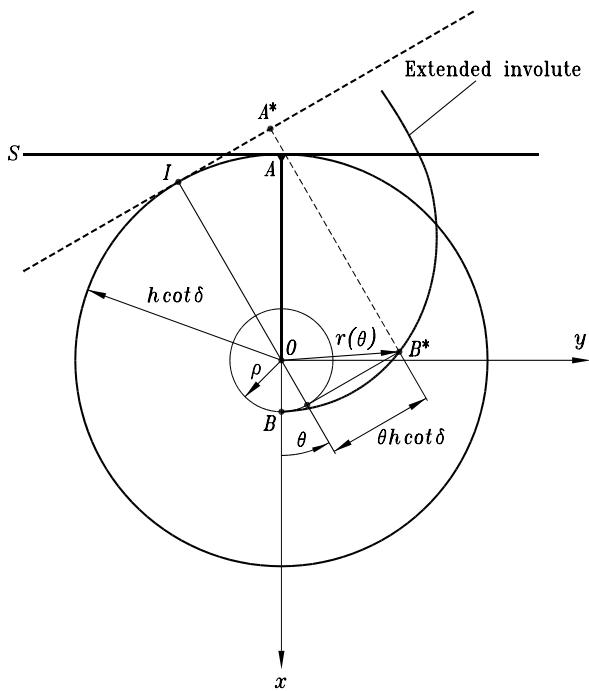
is rigidly connected to the straight line S (Fig. 5.5.11). The instantaneous position of the rolling straight line S is IA^*; B^* is a point of the extended involute that is traced out by point B considered above.

Problem 5.5.2

Consider the cross section of an involute screw surface (Eq. 5.5.32) formed by cutting the surface with plane $z = 0$. Prove that the cross section represents an involute curve corresponding to the base circle of radius ρ, and express the polar radius $r(\theta)$ in terms of θ and ρ.

Solution

$$r(\theta) = \rho(1 + \theta^2)^{1/2} \qquad (\rho \tan \lambda_\rho = h).$$

Figure 5.5.11: Generation of extended involute.

Problem 5.5.3

Consider the cross section of an Archimedes screw surface (Eq. 5.5.37) cut by the plane $z = 0$. Prove that the cross section represents Archimedes spiral, and express the polar radius $r(\theta)$ in terms of θ, h, and δ.

Solution

$$r(\theta) = \theta h \cot \delta.$$

6 Conjugated Surfaces and Curves

6.1 ENVELOPE TO A FAMILY OF SURFACES: NECESSARY CONDITIONS OF EXISTENCE

Introduction

Consider coordinate systems S_1, S_2, and S_f that are rigidly connected to gears 1, 2, and frame f (gear housing), respectively. Gear 1 is provided with a *regular* surface Σ_1 that is represented in S_1 as follows:

$$\mathbf{r}_1(u, \theta), \quad \frac{\partial \mathbf{r}_1}{\partial u} \times \frac{\partial \mathbf{r}_1}{\partial \theta} \neq \mathbf{0}, \quad (u, \theta) \in E. \tag{6.1.1}$$

The gears must transform prescribed motions (say, rotations about crossed axes) and stay in line contact at every instant. The location and orientation of gear axes and function $\phi_2(\phi_1)$ are given. Here, ϕ_2 and ϕ_1 are the angles of rotation of the driven and driving gears. The required type of contact of gear tooth surfaces (at a line at every instant) can be provided if the tooth surface of gear 2 is determined as the *envelope* to the family of surfaces, Σ_ϕ, that is generated in S_2 by surface Σ_1.

The theory of enveloping is represented in differential geometry by Favard [1957] and Zalgaller [1975], and in the theory of gearing by Litvin [1968, 1989, 1994] and Sheveleva [1999].

Henceforth, we consider the *necessary* and *sufficient* conditions of existence of Σ_2. The necessary conditions of existence of Σ_2 provide that Σ_2 (if it exists) is in tangency with Σ_1. The sufficient conditions of existence of Σ_2 provide that Σ_2 is *indeed* in tangency with Σ_1 and that Σ_2 is a *regular* surface. We have to emphasize that an instantaneous line contact is also typical for the case where Σ_1 is the tool surface and generates Σ_2.

In this section, only the necessary conditions of existence of Σ_2 are discussed. The sufficient conditions are discussed in Section 6.4. Two approaches to the solution of the discussed problem are presented: (i) the classical approach that has been developed in differential geometry, and (ii) the simpler approach that has been developed in the theory of gearing.

Parametric Representation of Family of Surfaces Σ_ϕ

The determination of Σ_ϕ is based on the following matrix equation:

$$\mathbf{r}_2 = \mathbf{M}_{21}\mathbf{r}_1 = \mathbf{M}_{2f}\mathbf{M}_{f1}\mathbf{r}_1. \tag{6.1.2}$$

Here, elements of matrices $\mathbf{M}_{2f}$ and $\mathbf{M}_{f1}$ are functions of related parameters ϕ_2 and ϕ_1, and coordinates of $\mathbf{r}_1$ are functions of u and θ. Matrix equation (6.1.2) yields that Σ_2 is represented by the vector equation

$$\mathbf{r}_2 = \mathbf{r}_2(u, \theta, \phi) \tag{6.1.3}$$

where $\phi_1 \equiv \phi$ is the generalized parameter of motion and $\phi_2 = \phi_2(\phi_1) = \phi_2(\phi)$. Equation (6.1.3) with a given value of ϕ represents a surface of the family Σ_ϕ.

Partial derivatives $\partial\mathbf{r}_2/\partial u$ and $\partial\mathbf{r}_2/\partial\theta$ represent in coordinate system S_2 the tangents to coordinate lines on surface Σ_1 that belongs to the family of surfaces Σ_ϕ. The location and orientation of Σ_1 in S_2 depend on the chosen parameter ϕ.

The normal $\mathbf{N}_2^{(1)}$ to surface Σ_1 is represented in S_2 as follows:

$$\mathbf{N}_2^{(1)} = \frac{\partial\mathbf{r}_2}{\partial u} \times \frac{\partial\mathbf{r}_2}{\partial\theta}. \tag{6.1.4}$$

The subscript "2" in $\mathbf{N}_2^{(1)}$ indicates that the normal is represented in S_2 and the superscript "1" designates that the normal to Σ_1 is considered. The direction of the normal can be changed to the opposite one by inverting the order of cofactors in the cross product.

Approach Used in Differential Geometry

The approach developed in differential geometry provides the necessary conditions of existence of Σ_2 by the following equation

$$f(u, \theta, \phi) = \left(\frac{\partial\mathbf{r}_2}{\partial u} \times \frac{\partial\mathbf{r}_2}{\partial\theta}\right) \cdot \frac{\partial\mathbf{r}_2}{\partial\phi} = 0. \tag{6.1.5}$$

Equation (6.1.5) relates the curvilinear coordinates (u, θ) of Σ_1 with the generalized parameter of motion, ϕ. This is the reason why this equation may be called the *equation of meshing*. Equation (6.1.5) is the *necessary* condition of existence of the envelope to the family of surfaces (6.1.3). If this equation is satisfied and the envelope indeed exists, the envelope can be represented in S_2 by Eqs. (6.1.3) and (6.1.5) considered simultaneously. These equations represent the envelope by three related surface parameters (u, θ, ϕ).

Engineering Approach

It is easy to verify that vector $\partial\mathbf{r}_2/\partial\phi$ has the same direction as vector $\mathbf{v}_2^{(12)}$ which represents the velocity of point M_1 on surface Σ_1 with respect to point M_2 on surface Σ_2. (Points M_1 and M_2 coincide with each other and form the point of tangency of surfaces Σ_1 and Σ_2.)

It is obvious that equations

$$\left(\frac{\partial\mathbf{r}_2}{\partial u} \times \frac{\partial\mathbf{r}_2}{\partial\theta}\right) \cdot \mathbf{v}_2^{(12)} = \left(\frac{\partial\mathbf{r}_2}{\partial u} \times \frac{\partial\mathbf{r}_2}{\partial\theta}\right) \cdot \mathbf{v}_2^{(21)} = 0 \tag{6.1.6}$$

can be applied instead of Eq. (6.1.5). Using new designations, we may represent Eqs. (6.1.6) as follows:

$$f(u, \theta, \phi) = \mathbf{N}_2^{(1)} \cdot \mathbf{v}_2^{(12)} = \mathbf{N}_2^{(1)} \cdot \mathbf{v}_2^{(21)} = 0. \tag{6.1.7}$$

The scalar product in Eqs. (6.1.7) does not depend on the chosen coordinate system and we may represent the equation of meshing as

$$\mathbf{N}_i^{(12)} \cdot \mathbf{v}_i^{(12)} = \mathbf{N}_i \cdot \mathbf{v}_i^{(21)} = f(u, \theta, \phi) = 0, \quad (i = 1, 2, f). \tag{6.1.8}$$

Vector $\mathbf{v}_i^{(12)}$ (similarly, $\mathbf{v}_i^{(21)} = -\mathbf{v}_i^{(12)}$) may be determined kinematically or by matrix operations (see Chapter 2). The normal to surface Σ_1 is represented in S_1 by

$$\mathbf{N}_1^{(1)} = \frac{\partial \mathbf{r}_1}{\partial u} \times \frac{\partial \mathbf{r}_1}{\partial \theta}. \tag{6.1.9}$$

To represent the normal in coordinate system S_j ($j = f, 2$), we use the matrix equation

$$\mathbf{N}_j^{(1)} = \mathbf{L}_{j1} \mathbf{N}_1^{(1)}. \tag{6.1.10}$$

To simplify the derivations of the equation of meshing (6.1.8), it is preferable to use coordinate system S_1 or S_f over S_2.

The discussed approach for the derivation of the equation of meshing is a substantial simplification in comparison with the derivation based on Eq. (6.1.5).

NOTE: The equation of meshing (6.1.8) becomes an identity in the case when a helicoid performs a screw motion about the axis of the helicoid. In such a screw motion, the helicoid does not generate a family of surfaces but rather a single surface that is identical to the generating helicoid.

Particular Cases
For the case where gears 1 and 2 perform rotation about parallel or intersected axes, the sliding velocity $\mathbf{v}^{(12)}$ (or $\mathbf{v}^{(21)}$) may be represented as the velocity in rotation about the instantaneous axis of rotation. Equation (6.1.8) yields that the common normal to surfaces Σ_1 and Σ_2 at their point of tangency passes through the instantaneous axis of rotation. Then, the equation of meshing may be derived as follows:

$$\frac{X_1 - x_1(u, \theta)}{N_{x1}(u, \theta)} = \frac{Y_1 - y_1(u, \theta)}{N_{y1}(u, \theta)} = \frac{Z_1 - z_1(u, \theta)}{N_{z1}(u, \theta)}. \tag{6.1.11}$$

Here, X_1, Y_1, and Z_1 are the Cartesian coordinates of a point that lies on the instantaneous axis of rotation. The instantaneous axis of rotation lies in the plane that is drawn through the axes of gear rotation, designated by z_1 and z_2, respectively. Knowing the orientation of the instantaneous axis of rotation, we may relate X_1, Y_1, and Z_1 and then derive the equation of meshing.

Representation of Σ_1 by an Implicit Function

Consider that the generating surface Σ_1 is represented by implicit function

$$F(x_1, y_1, z_1) = 0, \qquad F \in C^1,$$

$$\left(\frac{\partial F}{\partial x_1}\right)^2 + \left(\frac{\partial F}{\partial y_1}\right)^2 + \left(\frac{\partial F}{\partial z_1}\right)^2 \neq 0. \tag{6.1.12}$$

To derive the family of surfaces Σ_ϕ, which is generated in S_2, it is necessary to substitute x_1, y_1, and z_1 in Eq. (6.1.12) by

$$
\begin{aligned}
x_1 &= x_1(x_2, y_2, z_2, \phi), \\
y_1 &= y_1(x_2, y_2, z_2, \phi), \\
z_1 &= z_1(x_2, y_2, z_2, \phi)
\end{aligned}
\tag{6.1.13}
$$

where ϕ is the generalized parameter of motion. Equations (6.1.13) may be derived by using the matrix equation

$$\mathbf{r}_1 = \mathbf{M}_{12}\mathbf{r}_2. \tag{6.1.14}$$

Using Eqs. (6.1.12) and (6.1.13), we may represent the equation of family of surfaces Σ_ϕ as follows:

$$G(x_2, y_2, z_2, \phi) = F(x_1(x_2, y_2, z_2, \phi), y_1(x_2, y_2, z_2, \phi), z_1(x_2, y_2, z_2, \phi)) = 0$$

$$G \in C^1, \qquad \left(\frac{\partial G}{\partial x_2}\right)^2 + \left(\frac{\partial G}{\partial y_2}\right)^2 + \left(\frac{\partial G}{\partial z_2}\right)^2 \neq 0. \tag{6.1.15}$$

The *necessary* conditions of existence of the envelope to the family of surfaces are [Zalgaller, 1975; Litvin, 1968, 1989]

$$\frac{\partial G}{\partial \phi} = 0. \tag{6.1.16}$$

Planar Gearing

The discussed approach for derivation of the equation of meshing also works for planar gears. In the case of parametric representation, the tooth profile Σ_1 for gear 1 is represented by

$$\mathbf{r}_1(\theta), \qquad \frac{\partial \mathbf{r}_1}{\partial \theta} \neq 0. \tag{6.1.17}$$
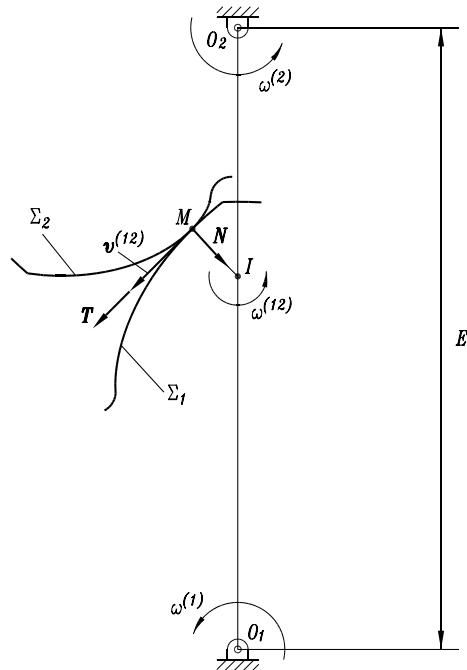
The normal $\mathbf{N}_1^{(1)}$ to Σ_1 is

$$\mathbf{N}_1^{(1)} = \frac{\partial \mathbf{r}_1}{\partial \theta} \times \mathbf{k}_1 \tag{6.1.18}$$

where $\mathbf{k}_1$ is the unit vector of gear axis z_1.

We consider that the tooth profile is represented in plane $z_1 = 0$, and the equation of meshing may be derived as follows:

$$f(\theta, \phi) = \left(\frac{\partial \mathbf{r}_1}{\partial \theta} \times \mathbf{k}_1\right) \cdot \mathbf{v}_1^{(12)} = \left(\frac{\partial \mathbf{r}_1}{\partial \theta} \times \mathbf{k}_1\right) \cdot \mathbf{v}_1^{(21)} = 0. \tag{6.1.19}$$

Figure 6.1.1: Visualization of Lewis theorem.

The alternative method of derivation of the equation of meshing is based on the equation

$$\frac{X_1 - x_1}{N_{x1}} = \frac{Y_1 - y_1}{N_{y1}} \tag{6.1.20}$$

where (X_1, Y_1) are the Cartesian coordinates of the *instantaneous center of rotation* in S_1. The kinematic interpretation of Eq. (6.1.20) is based on the *Lewis* theorem which states:

Conjugate tooth shapes must be such that their common normal at point of tangency intersects the line $\overline{O_1 O_2}$ of rotation centers (Fig. 6.1.1) and divides $\overline{O_1 O_2}$ into two segments $\overline{O_1 I}$ and $\overline{O_2 I}$ that are related as follows:

$$\frac{\overline{O_2 I}}{\overline{O_1 I}} = \frac{\omega^{(1)}}{\omega^{(2)}} = m_{12}, \qquad (\overline{O_1 I} + \overline{O_2 I} = E). \tag{6.1.21}$$

Here, $m_{12} = m_{12}(\phi)$ is (i) the prescribed function of gear ratio for the case of noncircular gears, and (ii) constant for circular gears.
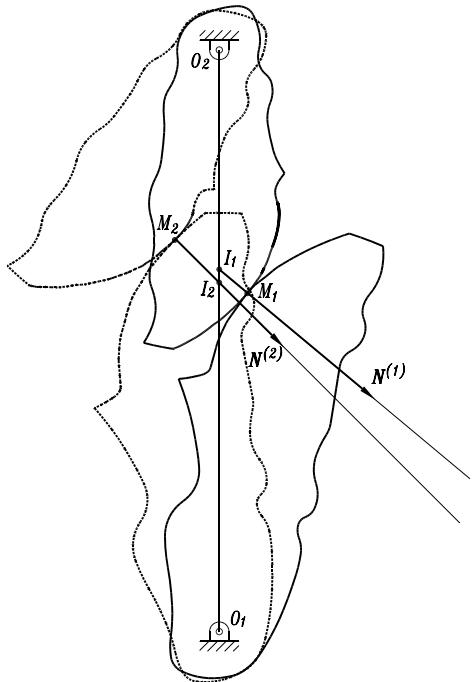
Figure 6.1.2 shows shapes of gear teeth that transform rotation with inconstant gear ratio m_{12}. Point I of intersection of normal $\mathbf{N}$ with center distance $\overline{O_1 O_2}$ moves along $\overline{O_1 O_2}$ in the process of motion.

Equation (6.1.19) or (6.1.20) provides the equation of meshing as

$$f(\theta, \phi) = 0. \tag{6.1.22}$$

Shape Σ_2 of the tooth profile of the driven gear is represented in S_2 by equations

$$\mathbf{r}_2 = \mathbf{M}_{21} \mathbf{r}_1, \qquad f(\theta, \phi) = 0. \tag{6.1.23}$$

Figure 6.1.2: Transformation of rotation with in-constant gear ratio.

Considering the case where the planar curve Σ_1 is located in plane $z_1 = 0$ and is represented by an implicit function, we can determine Σ_2 using Eqs. (6.1.12) and (6.1.16) and assuming that $z_1 = z_2 = 0$.

6.2 BASIC KINEMATIC RELATIONS

Basic kinematic relations proposed by Litvin [1968, 1969, 1989] relate the velocities (displacements) of the contact point and contact normal for a pair of gears that are in mesh.

We consider again coordinate systems S_1, S_2, and S_f that are rigidly connected to gear 1, gear 2, and frame f. Henceforth, we consider that the velocity of a contact point may be represented in two components: (i) in *transfer* motion, *with* the gear, designating this component by $\mathbf{v}_{tr}^{(i)}$; and (ii) in *relative* motion, *over* the tooth surface Σ_1, designating it by $\mathbf{v}_r^{(i)}$ ($i = 1, 2$). Due to the continuity of contact of gear tooth surfaces, the resulting velocity of the contact point must be the same for both gears. Thus

$$\mathbf{v}^{(abs)} = \mathbf{v}_{tr}^{(1)} + \mathbf{v}_r^{(1)} = \mathbf{v}_{tr}^{(2)} + \mathbf{v}_r^{(2)}. \tag{6.2.1}$$

Equations (6.2.1) yield

$$\mathbf{v}_r^{(2)} = \mathbf{v}_r^{(1)} + \mathbf{v}_{tr}^{(1)} - \mathbf{v}_{tr}^{(2)} = \mathbf{v}_r^{(1)} + \mathbf{v}^{(12)} \tag{6.2.2}$$

where $\mathbf{v}^{(12)}$ is the sliding velocity (see Section 2.1).

Using similar considerations, we obtain the following relation between the velocities of the tip of the contact normal

$$\dot{\mathbf{n}}_r^{(2)} = \dot{\mathbf{n}}_r^{(1)} + \left(\boldsymbol{\omega}^{(12)} \times \mathbf{n}\right). \tag{6.2.3}$$

Here, $\dot{\mathbf{n}}_r^{(i)}$ is the velocity of the tip of the contact normal in relative motion (over the tooth surface), in addition to the translational velocity of the normal; $\boldsymbol{\omega}^{(12)} = \boldsymbol{\omega}^{(1)} - \boldsymbol{\omega}^{(2)}$; $\mathbf{n}$ is the surface unit normal.

The advantage of Eqs. (6.2.2) and (6.2.3) is that they allow us to determine $\mathbf{v}_r^{(2)}$ and $\dot{\mathbf{n}}_r^{(2)}$ even though the equations of surfaces Σ_2 are not yet known or are too complicated for direct application. It is shown below that using Eqs. (6.2.2) and (6.2.3) we are able to (i) develop a simple solution to the problem of gear undercutting and (ii) relate the curvatures of surfaces of mating gears.

6.3 CONDITIONS OF NONUNDERCUTTING

The general conditions of nonundercutting have been determined in the literature [Litvin, 1968, 1975, 1989]. Two cases are considered: (i) the generating surface Σ_1 is represented in two-parameter form directly, and (ii) surface Σ_1 is the envelope to a family of surfaces and therefore it is represented by three related parameters.

Case 1: Consider that Σ_1 is the tool surface represented in two-parameter form. Surface Σ_1 generates the gear tooth surface Σ_2. Appearance of singular points on Σ_2 is the warning that the surface may be undercut in the process of generation. The mathematical definition of singularity of Σ_2, which occurs in the process of generation, may be represented by equation $\mathbf{v}_r^{(2)} = 0$ which yields [see Eq. (6.2.2)]

$$\mathbf{v}_r^{(1)} + \mathbf{v}^{(12)} = 0. \tag{6.3.1}$$

Equation (6.3.1) and differentiated equation of meshing

$$\frac{d}{dt}[f(u, \theta, \phi)] = 0 \tag{6.3.2}$$

allow us to determine a line (L) on surface Σ_1 that generates singular points on Σ_2. Limiting Σ_1 with line L, we may avoid the appearance of singular points on Σ_2. The derivation of this line is based on the following considerations:

(i) Equation (6.3.1) yields

$$\frac{\partial \mathbf{r}_1}{\partial u} \frac{du}{dt} + \frac{\partial \mathbf{r}_1}{\partial \theta} \frac{d\theta}{dt} = -\mathbf{v}_1^{(12)}. \tag{6.3.3}$$

Here, $\partial \mathbf{r}_1 / \partial u$, $\partial \mathbf{r}_1 / \partial \theta$, and $\mathbf{v}_1^{(12)}$ are three- or two-dimensional vectors for spatial and planar gearing, respectively. These vectors are represented in coordinate system S_1.

(ii) Equation (6.3.2) yields

$$\frac{\partial f}{\partial u} \frac{du}{dt} + \frac{\partial f}{\partial \theta} \frac{d\theta}{dt} = -\frac{\partial f}{\partial \phi} \frac{d\phi}{dt}. \tag{6.3.4}$$

(iii) Equations (6.3.3) and (6.3.4) represent a system of four linear equations in two unknowns: du/dt and $d\theta/dt$; $d\phi/dt$ is considered as given. This system has a certain solution for the unknowns if the matrix

$$\mathbf{A} = \begin{bmatrix} \dfrac{\partial \mathbf{r}_1}{\partial u} & \dfrac{\partial \mathbf{r}_1}{\partial \theta} & -\mathbf{v}_1^{(12)} \\[2ex] \dfrac{\partial f}{\partial u} & \dfrac{\partial f}{\partial \theta} & -\dfrac{\partial f}{\partial \phi}\dfrac{d\phi}{dt} \end{bmatrix} \tag{6.3.5}$$

has the rank $r = 2$. This yields

$$\Delta_1 = \begin{vmatrix} \dfrac{\partial x_1}{\partial u} & \dfrac{\partial x_1}{\partial \theta} & -v_{x1}^{(12)} \\[2ex] \dfrac{\partial y_1}{\partial u} & \dfrac{\partial y_1}{\partial \theta} & -v_{y1}^{(12)} \\[2ex] f_u & f_\theta & -f_\phi\dfrac{d\phi}{dt} \end{vmatrix} = 0 \tag{6.3.6}$$

$$\Delta_2 = \begin{vmatrix} \dfrac{\partial x_1}{\partial u} & \dfrac{\partial x_1}{\partial \theta} & -v_{x1}^{(12)} \\[2ex] \dfrac{\partial z_1}{\partial u} & \dfrac{\partial z_1}{\partial \theta} & -v_{z1}^{(12)} \\[2ex] f_u & f_\theta & -f_\phi\dfrac{d\phi}{dt} \end{vmatrix} = 0 \tag{6.3.7}$$
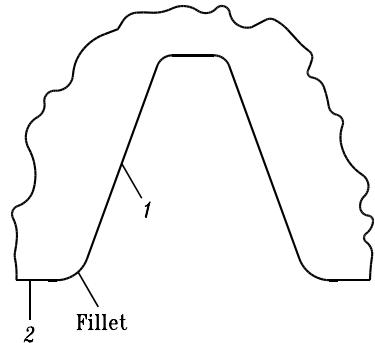
$$\Delta_3 = \begin{vmatrix} \dfrac{\partial y_1}{\partial u} & \dfrac{\partial y_1}{\partial \theta} & -v_{y1}^{(12)} \\[2ex] \dfrac{\partial z_1}{\partial u} & \dfrac{\partial z_1}{\partial \theta} & -v_{z1}^{(12)} \\[2ex] f_u & f_\theta & -f_\phi\dfrac{d\phi}{dt} \end{vmatrix} = 0 \tag{6.3.8}$$

$$\Delta_4 = \begin{vmatrix} \dfrac{\partial x_1}{\partial u} & \dfrac{\partial x_1}{\partial \theta} & -v_{x1}^{(12)} \\[2ex] \dfrac{\partial y_1}{\partial u} & \dfrac{\partial y_1}{\partial \theta} & -v_{y1}^{(12)} \\[2ex] \dfrac{\partial z_1}{\partial u} & \dfrac{\partial z_1}{\partial \theta} & -v_{z1}^{(12)} \end{vmatrix} = 0. \tag{6.3.9}$$

Equation (6.3.9) yields that

$$\left(\frac{\partial \mathbf{r}_1}{\partial u} \times \frac{\partial \mathbf{r}_1}{\partial \theta}\right) \cdot \mathbf{v}_1^{(12)} = \mathbf{N}_1^{(1)} \cdot \mathbf{v}_1^{(1)} = f(u, \theta, \phi) = 0. \tag{6.3.10}$$

Equation (6.3.10) is just the equation of meshing [see Eq. (6.1.8)] and it is satisfied because points of tangency of surfaces Σ_1 and Σ_2 are considered. Thus, only Eqs. (6.3.6) to (6.3.8) should be applied for determination of conditions of singularity for surface Σ_2.

Figure 6.3.1: Profiles of rack-cutter tooth.

The requirement of simultaneous satisfaction of the system of Eqs. (6.3.6) to (6.3.8) may be represented as

$$\mathbf{m} = f_u \left[\frac{\partial \mathbf{r}_1}{\partial \theta} \times \mathbf{v}^{(12)} \right] - f_\theta \left[\frac{\partial \mathbf{r}_1}{\partial u} \times \mathbf{v}^{(12)} \right] + f_\phi \frac{d\phi}{dt} \left[\frac{\partial \mathbf{r}_1}{\partial u} \times \frac{\partial \mathbf{r}_1}{\partial \theta} \right] = 0. \quad (6.3.11)$$

The satisfaction of vector Eq. (6.3.11) is guaranteed if (i) at least one equation from (6.3.6) to (6.3.8) is observed, and (ii) vector $\mathbf{m}$ is not perpendicular to any of the S_1 coordinate axes.

A sufficient condition for singularity of Σ_2 can be represented by

$$\Delta_1^2 + \Delta_2^2 + \Delta_3^2 = F(u, \theta, \phi) = 0. \quad (6.3.12)$$

There is a simple way to avoid singularity and undercutting of a generated surface (Σ_2). The equations

$$\mathbf{r}_1 = \mathbf{r}_1(u, \theta), \quad f(u, \theta, \phi) = 0, \quad F(u, \theta, \phi) = 0 \quad (6.3.13)$$
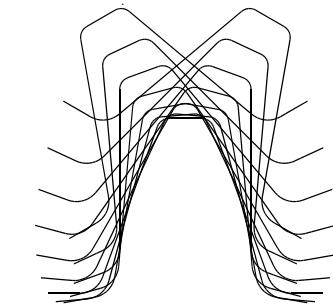
determine a line (L) which has to limit the generating surface Σ_1. In many cases this can be achieved by choosing appropriate settings for surface Σ_1 that generates Σ_2.

Figures 6.3.1 and 6.3.2 illustrate the phenomenon of undercutting with the example of generation of a spur involute gear by a rack-cutter. The shape of the rack-cutter (Fig. 6.3.1) consists of a straight line 1 that generates the involute curve of the gear, a straight line 2 that generates the dedendum circle of the gear, and the rack fillet that generates the gear fillet.
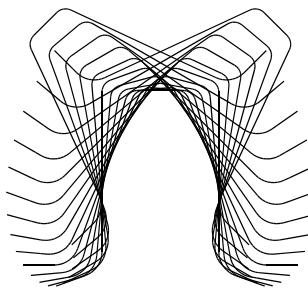
Figure 6.3.2(a) shows the family of shapes of the rack-cutter and the tooth profiles of the generated gear. The involute part of the gear tooth profile is free from a singular point; the gear fillet and the involute curve are in tangency; and the gear tooth is not undercut. Figure 6.3.2(b) shows that the fillet of the rack-cutter has undercut the gear involute shape: the gear fillet and involute shape are no longer in tangency but intersect each other. The undercutting was caused by settings of the rack-cutter that did not exclude the appearance of a singular point on the gear involute profile. Examples of how Eq. (6.3.13) can be applied to avoid undercutting are presented in Section 6.13.

Case 2: We consider that the generating surface Σ_1 is represented as the envelope to the family of surfaces as

$$\mathbf{r}_1(u, \theta, \psi), \quad f(u, \theta, \psi) = 0 \quad (6.3.14)$$

(a)

Figure 6.3.2: Generation of involute curve by rack-cutter.

(b)

where ψ is the generalized parameter of motion in the process of generation of Σ_1 and $f(u, \theta, \psi) = 0$ is the equation of meshing of Σ_1 with the surface that generates Σ_1.

Surface Σ_1 generates surface Σ_2 and our goal is determination of singularities of Σ_2. The computational procedure is based on the following considerations.

Step 1: We consider that (see Section 6.4)

$$|f_u| + |f_\theta| \neq 0, \tag{6.3.15}$$

and this inequality is observed, let us say, because $f_\theta = 0$. Then, as follows from the theorem of implicit function system existence [Korn & Korn, 1968], equation $f(u, \theta, \psi) = 0$ may be solved by function

$$\theta = \theta(u, \psi), \tag{6.3.16}$$

and surface Σ_1 may be represented as

$$\mathbf{r}_1(u, \theta(u, \psi), \psi) = \mathbf{R}_1(u, \psi). \tag{6.3.17}$$

Step 2: Surface Σ_2 is the envelope to the family of surfaces $\mathbf{R}_1(u, \psi)$. Surface Σ_2 is represented as

$$\mathbf{r}_2(u, \psi, \mu) = \mathbf{M}_{21}(\mu)\,\mathbf{R}_1(u, \psi) \tag{6.3.18}$$

$$\left(\frac{\partial \mathbf{r}_2}{\partial u} \times \frac{\partial \mathbf{r}_2}{\partial \psi}\right) \cdot \frac{\partial \mathbf{r}_2}{\partial \mu} = q(u, \psi, \mu) = 0. \tag{6.3.19}$$

Partial derivative $\partial \mathbf{r}_2/\partial \mu$ is equivalent to the sliding velocity $\mathbf{v}^{(12)}$.

Step 3: Considerations similar to those applied in Case 1 yield the following conclusion.

Singularities of Σ_2 occur at points where matrix

$$
\mathbf{B} = \begin{bmatrix} \dfrac{\partial \mathbf{R}_1}{\partial u} & \dfrac{\partial \mathbf{R}_1}{\partial \psi} & -\mathbf{v}_1^{(12)} \\[2ex] \dfrac{\partial q}{\partial u} & \dfrac{\partial q}{\partial \psi} & -\dfrac{\partial q}{\partial \mu}\dfrac{d\mu}{dt} \end{bmatrix} \tag{6.3.20}
$$

has the rank $r = 2$. Here,

$$
\frac{\partial \mathbf{R}_1}{\partial u} = \frac{\partial \mathbf{r}_1}{\partial u} + \frac{\partial \mathbf{r}_1}{\partial \theta}\frac{\partial \theta}{\partial u} = \frac{\partial \mathbf{r}_1}{\partial u} - \frac{\partial \mathbf{r}_1}{\partial \theta}\frac{f_u}{f_\theta} \tag{6.3.21}
$$

$$
\frac{\partial \mathbf{R}_1}{\partial \psi} = \frac{\partial \mathbf{r}_1}{\partial \psi} + \frac{\partial \mathbf{r}_1}{\partial \theta}\frac{\partial \theta}{\partial \psi} = \frac{\partial \mathbf{r}_1}{\partial \psi} - \frac{\partial \mathbf{r}_1}{\partial \theta}\frac{f_\psi}{f_\theta} \tag{6.3.22}
$$

where f_u, f_θ, and f_ψ are the derivatives of $f(u, \theta, \psi) = 0$ [see Eq. (6.3.14)]. Relations

$$
\frac{\partial \theta}{\partial u} = -\frac{f_u}{f_\theta}, \qquad \frac{\partial \theta}{\partial \psi} = -\frac{f_\psi}{f_\theta} \tag{6.3.23}
$$

are determined by derivations similar to those applied in Section 6.4.

Step 4: The requirement that matrix $\mathbf{B}$ have rank $r = 2$ enables us to determine a function

$$
p(u, \theta, \mu) = 0. \tag{6.3.24}
$$

Equations (6.3.24), (6.3.18), and (6.3.19) enable us to determine on surface Σ_1 a line L of regular points that generate singular points on surface Σ_2. Limitations of surface Σ_1 by line L enables undercutting of Σ_2 to be avoided. Singular points on generated surface Σ_2 may be determined by transformation of coordinates of line L from S_1 to S_2.

6.4 SUFFICIENT CONDITIONS FOR EXISTENCE OF AN ENVELOPE TO A FAMILY OF SURFACES

Classical Approach
The sufficient conditions of existence of an envelope of a family of surfaces (represented parametrically) guarantee that the envelope *indeed exists*, that it is in *tangency* with the surfaces of the family, and that the envelope is a *regular* surface. These conditions are set forth in the following theorem proposed by Zalgaller [1975]; see also the publication of this theorem in English [Litvin, 1989].

THEOREM. Given a *regular* generating surface Σ_1 that is represented in S_1 by

$$
\mathbf{r}_1(u, \theta) \in C^2, \qquad \frac{\partial \mathbf{r}_1}{\partial u} \times \frac{\partial \mathbf{r}_1}{\partial \theta} \neq 0, \qquad (u, \theta) \in E. \tag{6.4.1}
$$

Let the family Σ_ϕ of surfaces Σ_1 that is generated in S_2 be represented by $\mathbf{r}_2(u, \theta, \phi)$.

Suppose that at a point $M(u_o, \theta_o, \phi_o)$ the following conditions hold:

$$(\mathbf{r}_u \times \mathbf{r}_\theta) \cdot \mathbf{r}_\phi = f(u, \theta, \phi) = 0, \qquad f \in C^1 \tag{6.4.2}$$

$$f_u^2 + f_\theta^2 \neq 0 \tag{6.4.3}$$

and

$$\mathbf{N} = f_u(\mathbf{r}_\theta \times \mathbf{r}_\phi) - f_\theta(\mathbf{r}_u \times \mathbf{r}_\phi) + f_\phi(\mathbf{r}_u \times \mathbf{r}_\theta) \neq \mathbf{0} \tag{6.4.4}$$

where

$$\mathbf{r}_u = \frac{\partial \mathbf{r}_2}{\partial u}, \qquad \mathbf{r}_\theta = \frac{\partial \mathbf{r}_2}{\partial \theta}, \qquad \mathbf{r}_\phi = \frac{\partial \mathbf{r}_2}{\partial \phi}$$

$$f_u = \frac{\partial f}{\partial u}, \qquad f_\theta = \frac{\partial f}{\partial \theta}, \qquad f_\phi = \frac{\partial f}{\partial \phi}.$$

Then, the envelope to the family of surfaces exists in the neighborhood of point M and may be represented by

$$\mathbf{r}_2(u, \theta, \phi), \qquad f(u, \theta, \phi) = 0. \tag{6.4.5}$$

NOTE: Vector $\mathbf{N}$ is the normal to the envelope and the inequality (6.4.4) provides that the envelope is a *regular* surface. The theorem provides the sufficient conditions of the *local* existence of the envelope, in the neighborhood of a point. The whole envelope may be determined as the set of pieces of the envelope that have been found locally.

The derivation of $\mathbf{N}$ is based on the following considerations.

Step 1: Assume that inequality (6.4.3) is observed because $f_\theta \neq 0$. Then, as follows from the theorem of implicit function system existence [Korn & Korn, 1968], equation of meshing $f(u, \theta, \phi) = 0$ may be solved in the neighborhood of M by function

$$\theta = \theta(u, \phi) \in C'. \tag{6.4.6}$$

Step 2: Vector function $\mathbf{r}_2(u, \theta, \phi)$ and equation $f(u, \theta, \phi) = 0$, if considered simultaneously, represent the envelope by three related parameters (u, θ, ϕ). Using Eq. (6.4.6), we may represent the envelope as

$$\mathbf{r}(u, \theta(u, \phi), \phi) = \mathbf{R}(u, \phi). \tag{6.4.7}$$

Step 3: The normal to the envelope may be represented as

$$\mathbf{N} = \mathbf{R}_u \times \mathbf{R}_\phi = (\mathbf{r}_u \times \mathbf{r}_\phi) + (\mathbf{r}_\theta \times \mathbf{r}_\phi)\frac{\partial \theta}{\partial u} + (\mathbf{r}_u \times \mathbf{r}_\theta)\frac{\partial \theta}{\partial \phi}. \tag{6.4.8}$$

Step 4: Differentiating equation of meshing $f(u, \theta, \phi) = 0$ and Eq. (6.4.6), we obtain

$$f_u du + f_\theta d\theta + f_\phi d\phi = 0 \tag{6.4.9}$$

$$\frac{\partial \theta}{\partial u} du - d\theta + \frac{\partial \theta}{\partial \phi} d\phi = 0, \tag{6.4.10}$$

which yield

$$\frac{f_u}{\dfrac{\partial \theta}{\partial u}} = -\frac{f_\theta}{1} = \frac{f_\phi}{\dfrac{\partial \theta}{\partial \phi}}. \tag{6.4.11}$$

Equations (6.4.8) and (6.4.11), while taking into account that $f_\theta \neq 0$, yield the inequality of Eq. (6.4.4).

Engineering Approach (proposed by Litvin [1968, 1989])
The generating surface Σ_1 is represented by two independent parameters. Sufficient conditions for the existence of an envelope to the family of surfaces Σ_1 are formulated as follows.

THEOREM. A *regular* generating surface Σ_1 is represented by

$$\mathbf{r}_1(u, \theta) \in C^2, \qquad \frac{\partial \mathbf{r}_1}{\partial u} \times \frac{\partial \mathbf{r}_1}{\partial \theta} \neq \mathbf{0}, \qquad (u, \theta) \in E. \tag{6.4.12}$$

The family of surfaces Σ_1 that is generated in coordinate system S_2 is represented as

$$\mathbf{r}_2(u, \theta, \phi) = \mathbf{M}_{21}(\phi)\mathbf{r}_1(u, \theta) \tag{6.4.13}$$

where matrix $\mathbf{M}_{21}$ describes the coordinate transformation from S_1 to S_2 and ϕ is the generalized parameter of motion.

Assume that at a point $M(u_0, \theta_0, \phi_0)$, the following conditions are observed:

$$\mathbf{N}_1 \cdot \mathbf{v}_1^{(12)} = \left(\frac{\partial \mathbf{r}_1}{\partial u} \times \frac{\partial \mathbf{r}_1}{\partial \theta} \right) \cdot \mathbf{v}_1^{(12)} = f(u, \theta, \phi) = 0 \tag{6.4.14}$$

$$f_u^2 + f_\theta^2 \neq 0 \tag{6.4.15}$$

where $f_u = \partial f / \partial u$, $\partial f / \partial \theta$, and $\mathbf{v}_1^{(12)}$ is the relative velocity determined by differentiation of matrix $\mathbf{M}_{21}$ and respective transformations (see Section 2.2).
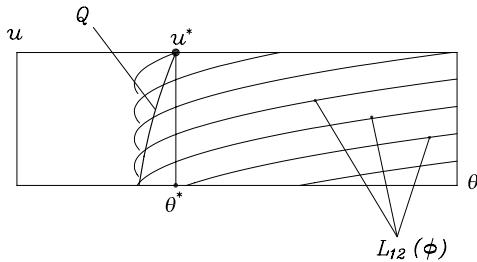
The rank of 4×3 matrix

$$A = \begin{bmatrix} \dfrac{\partial \mathbf{r}_1}{\partial u} & \dfrac{\partial \mathbf{r}_1}{\partial \theta} & \mathbf{v}_1^{(12)} \\ f_u & f_\theta & f_\phi \end{bmatrix} \tag{6.4.16}$$

is $r = 3$. This means that determinants Δ_i $(i = 1, 2, 3)$ of the third order of matrix A differ from zero $(\Delta_1^2 + \Delta_2^2 + \Delta_3^2 \neq 0)$ and envelope Σ_2 is a regular surface (see Eqs. (6.3.6) to (6.3.8) of Δ_1, Δ_2, and Δ_3 in Section 6.3.)

When the conditions of the theorem are observed, the envelope Σ_2 indeed exists in the neighborhood of M; it is a regular surface and may be represented in S_2 by expressions (6.4.5).

NOTE: Avoidance of singularities and observation of inequality (6.4.16) are based on the following procedure.

Figure 6.4.1: Determination of sub-area free of singularities of envelope Σ_2.

Step 1: Singularities of envelope Σ_2 occur if (see Section 6.3)

$$\Delta_1^2 + \Delta_2^2 + \Delta_3^2 = F(u, \theta, \phi) = 0. \tag{6.4.17}$$

Step 2: We consider now in the space of surface parameters (u, θ) lines of tangency $L_{12}(\phi)$ of Σ_1 and Σ_2 obtained by taking in equation of meshing $\phi = $ const. (Fig. 6.4.1).

Step 3: Equation $F(u, \theta, \phi) = 0$ enables us to obtain a line $Q(u, \theta, \phi)$ (Fig. 6.4.1).

Step 4: There is a sub-area $B \in (u, \theta)$ where line $Q(u, \theta, \phi)$ does not intersect lines $L_{12}(u, \theta, \phi)$ of tangency of Σ_1 and Σ_2, and Σ_2 has regular points. This is illustrated by Fig. 6.4.1, which is based on generation of face-gears by a shaper (see Section 18.6). Singularities of face-gears are avoided in the area $\theta > \theta^*$, $u < u^*$.

Sufficient Condition of Existence of Envelope Represented in Implicit Form

The family of generating surfaces is represented in S_2 as follows:

$$G(x, y, z, \phi) = 0, \qquad G \in C^2, \qquad (G_x)^2 + (G_y)^2 + (G_z)^2 \neq 0$$

$$(x, y, z) \in A, \qquad\qquad a < \phi < b. \tag{6.4.18}$$

The theorem of sufficient condition of envelope existence states [Zalgaller, 1975]:

Consider that at point $M(u_0, \theta_0, \phi_0)$, the following requirements are observed:
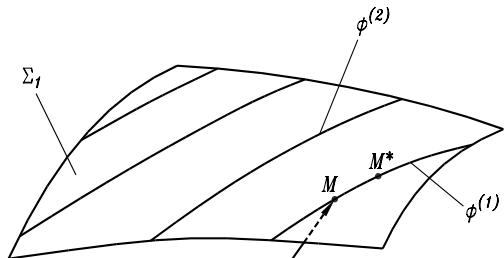
$$G(x_0, y_0, z_0, \phi_0) = 0, \qquad G_\phi = 0, \qquad G_{\phi\phi} \neq 0$$

$$\Delta = \left| \frac{D(G, G_\phi)}{D(x, y)} \right| + \left| \frac{D(G, G_\phi)}{D(x, z)} \right| + \left| \frac{D(G, G_\phi)}{D(y, z)} \right| \neq 0. \tag{6.4.19}$$

Then, the envelope exists *locally*, in the neighborhood of point M; the envelope is a regular surface that can be represented by the equation
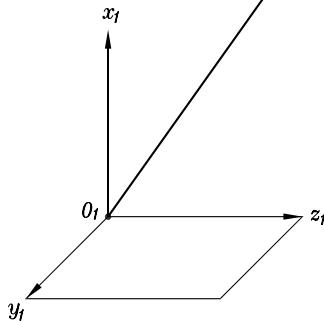
$$G(x, y, z, \phi) = 0, \qquad G_\phi(x, y, z, \phi) = 0. \tag{6.4.20}$$

6.5 CONTACT LINES; SURFACE OF ACTION

The mating surfaces Σ_1 and Σ_2 contact each other at every instant along a line called *contact line* or *characteristic*. The location of the instantaneous contact line on the gear tooth surface depends on the parameter of motion ϕ.

Figure 6.5.1: Contact lines on tooth surface.

Contact lines on surface Σ_1 may be represented by the expressions

$$\mathbf{r}_1(u, \theta) = x_1(u, \theta)\mathbf{i}_1 + y_1(u, \theta)\mathbf{j}_1 + z_1(u, \theta)\mathbf{k}_1, \quad f\left(u, \theta, \phi^{(i)}\right) = 0 \qquad (6.5.1)$$

where $\phi^{(i)}$ is the parameter of motion ($i = 1, 2, \ldots$). To determine a current point M of the instantaneous line of contact (Fig. 6.5.1), the following procedure must be applied.

Step 1: Fix the parameter of motion ϕ; for instance, take $\phi = \phi^{(1)}$.

Step 2: Choose one of the surface parameters, for instance θ, and determine u from the equation

$$f\left(u, \theta, \phi^{(1)}\right) = 0.$$

Step 3: Determine in S_1 coordinates (x_1, y_1, z_1) of point M using the vector-function

$$\mathbf{r}_1(u, \theta) = x_1(u, \theta)\mathbf{i}_1 + y_1(u, \theta)\mathbf{j}_1 + z_1(u, \theta)\mathbf{k}_1.$$

Step 4: To determine another point $M^\star$ on the same contact line, keep the same magnitude $\phi = \phi^{(1)}$ but change the surface parameter θ, determine u, and apply the procedure described previously.

A similar procedure can be applied for determination of other instantaneous contact lines on surface Σ_2.

Instantaneous contact lines on surface Σ_2 are represented by the equations

$$\mathbf{r}_2 = \mathbf{r}_2\left(u, \theta, \phi^{(i)}\right), \quad f\left(u, \theta, \phi^{(i)}\right) = 0 \qquad (6.5.2)$$

where

$$\mathbf{r}_2 = \mathbf{M}_{21}\mathbf{r}_1.$$

Here, $\phi^{(i)}$ is the chosen value of parameter of motion ϕ; $\mathbf{M}_{21}$ is the 4×4 matrix that represents the coordinate transformation from S_1 to S_2. The method for computation of points of the contact lines is similar to that discussed above.

The *surface of action* is the family of contact lines that are represented in the *fixed* coordinate system S_f that is rigidly connected to the frame. The surface of action is represented by the equations

$$\mathbf{r}_f = \mathbf{r}_f(u, \theta, \phi), \qquad f(u, \theta, \phi) = 0 \qquad (6.5.3)$$

where
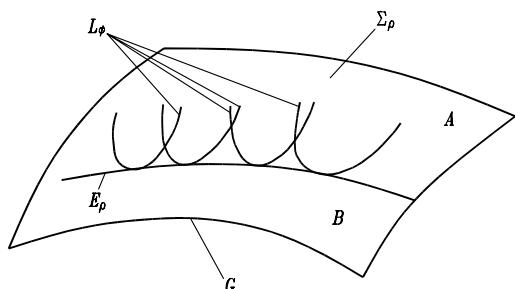
$$\mathbf{r}_f = \mathbf{M}_{f1}\mathbf{r}_1.$$

Here, 4×4 matrix $\mathbf{M}_{f1}$ describes the coordinate transformation in transition from S_1 to S_f.

6.6 ENVELOPE TO FAMILY OF CONTACT LINES ON GENERATING SURFACE Σ_1

Usually contact lines on generating surface Σ_ρ cover the entire working part of the surface. However, there are cases (they are not so rare) when contact lines on the generating surface have an envelope and therefore cover only a part of the generating surface. Figure 6.6.1 shows a family of contact lines, L_ϕ, on the generating surface Σ_ρ. Line E_ρ is the *envelope* to contact lines that divides Σ_ρ into two parts: (1) part A, which contains the contact lines and their envelope E_ρ, and (2) part B, which is free of contact lines. Line G is the edge of surface Σ_ρ that generates the fillet of the generated gear tooth surface Σ_r. The conditions of lubrication and heat transfer become unfavorable near the envelope E_ρ. This is why the envelope should be excluded from meshing. This can be achieved by choosing appropriate gear design parameters.

The existence of envelope E_ρ is accompanied by formation of generated surface Σ_r by two branches (see Section 6.7), where Σ_r is the envelope to the family of generating surfaces Σ_ρ. The necessary and sufficient conditions of existence of E_ρ on generating surface Σ_ρ are formulated by the following theorem (proposed by Litvin *et al.* [2001b]).

Figure 6.6.1: Envelope to contact lines.

THEOREM. The generating surface Σ_ρ is represented as

$$\rho(u, \theta) \in C^3, \qquad \rho_u \times \rho_\theta = 0, \qquad (u, \theta) \in G, \qquad a < \phi < b. \qquad (6.6.1)$$

The following conditions are observed at a point (u_0, θ_0, ϕ_0)(designated as M):

$$f(u, \theta, \phi) = (\rho_u \times \rho_\theta) \cdot v^{(\rho r)} = 0 \qquad (6.6.2)$$

$$f_\phi(u, \theta, \phi) = 0 \qquad (6.6.3)$$

$$f_{\phi\phi} \neq 0 \qquad (6.6.4)$$

$$\begin{vmatrix} f_u & f_\theta \\ f_{\phi u} & f_{\phi\theta} \end{vmatrix} \neq 0. \qquad (6.6.5)$$

If the conditions above are observed, the envelope E_ρ exists, it is a regular curve, and it is determined by

$$\rho(u, \theta), \qquad f(u, \theta, \phi) = 0, \qquad f_\phi(u, \theta, \phi) = 0. \qquad (6.6.6)$$

The proof of the theorem is based on the following considerations.

Step 1: Assuming that inequality (6.6.5) is observed and $|f_u| + |f_\theta| \neq 0$, we may determine on surface Σ_ρ a curve represented as

$$\mathbf{R}(\phi) = \rho[u(\phi), \theta(\phi)]. \qquad (6.6.7)$$

The tangent to the curve is represented as

$$\mathbf{R}_\phi = \frac{f_{\phi\phi}}{\begin{vmatrix} f_u & f_\theta \\ f_{\phi u} & f_{\phi\theta} \end{vmatrix}} (\rho_u f_\theta - \rho_\theta f_u). \qquad (6.6.8)$$

Here,

$$\rho_u f_\theta - \rho_\theta f_u = \mathbf{T}_\rho \qquad (6.6.9)$$

where $\mathbf{T}_\rho$ is the tangent to the contact line on generating surface Σ_ρ.
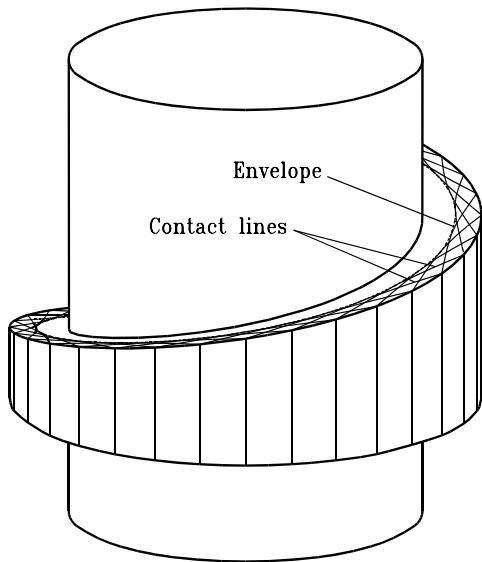
Step 2: The observation of inequalities (6.6.4) and (6.6.5) provides that $\mathbf{R}_\phi \neq 0$ and is collinear to the tangent to the contact line. Thus, $\mathbf{R}(\phi)$ is a regular curve and is an envelope to the contact lines on Σ_ρ.

We illustrate the existence of an envelope to contact lines in the case of a conventional worm-gear drive with an involute worm. The performed investigation shows that envelope E_ρ does exist. Figure 6.6.2 shows E_ρ on the surface of an involute worm.

The envelope to the family of contact lines can be easily represented in the plane of surface parameters, u and θ, as well. The *sufficient* conditions of envelope existence in such a plane are represented by the equation

$$f(u, \theta, \phi) = 0, \qquad f_\phi = q(u, \theta, \phi) = 0$$

$$\frac{D(f, q)}{D(u, \theta)} \neq 0, \qquad f_{\phi\phi} \neq 0. \qquad (6.6.10)$$
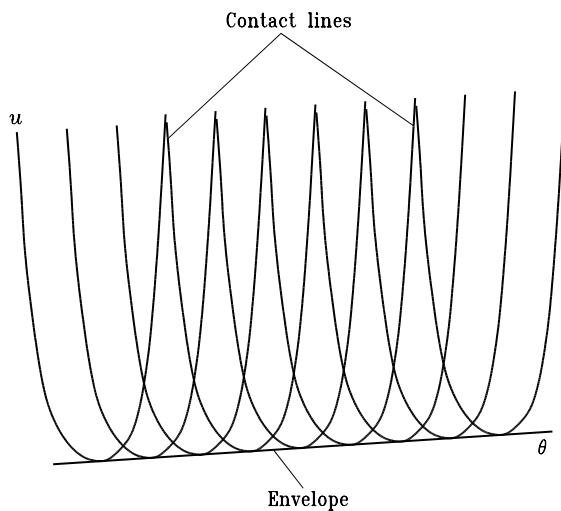
Figure 6.6.3 shows in the plane of parameters (u, θ) the contact lines and their envelope for an involute worm. The drawings are based on the investigation performed in Litvin & Kin [1992].
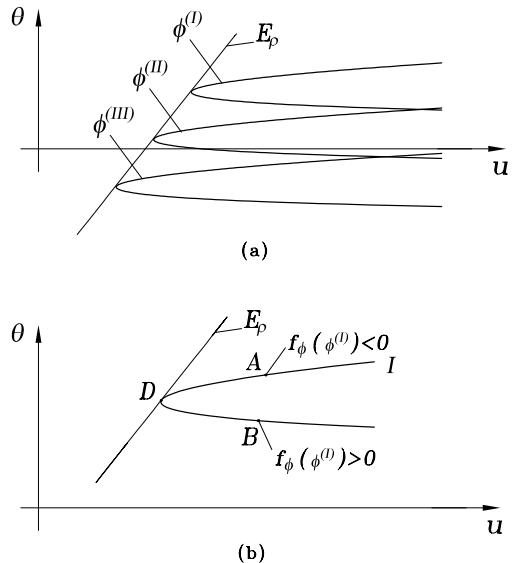
Figure 6.6.2: Envelope to contact lines on worm surface.

6.7 FORMATION OF BRANCHES OF ENVELOPE TO PARAMETRIC FAMILIES OF SURFACES AND CURVES

Formation of a generated surface (curve) by branches means that computerized simulation of meshing has to be performed for both branches separately. Detailed solutions to this problem are presented in Litvin *et al*. [2001b]. We limit the discussion to conceptual considerations.

Figure 6.6.3: Contact lines in the space of surface parameters.

Figure 6.7.1: Envelope E_ρ to contact lines in the space of parameters (θ, u): (a) contact lines and envelope E_ρ; (b) illustration of two branches, A and B, of each contact line.
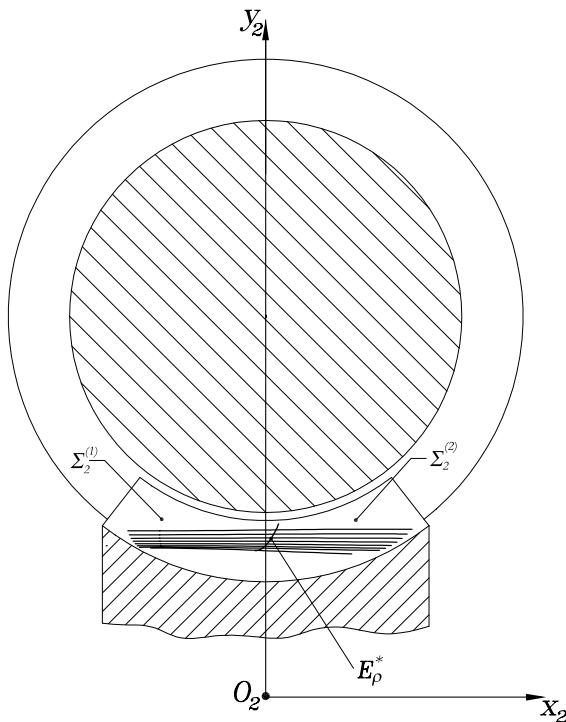
Branches of Worm-Gear Tooth Surface

A conventional worm-gear drive with an involute worm is considered. It is proven in Section 6.6 that the contact lines on the worm surface have an envelope E_ρ. Figure 6.7.1(a) shows the envelope E_ρ in the plane of worm surface parameters (θ, u) that is a straight line. Point D is the point of tangency of a current line of contact with the envelope E_ρ [Fig. 6.7.1(b)]. The derivative f_ϕ of the equation of meshing $f(u, \theta, \phi) = 0$ becomes equal to zero at D. Parameter ϕ is the generalized parameter of motion in the equation $f = 0$. We may consider that each current contact line has two branches that are recognized by the sign of derivative f_ϕ [Fig. 6.7.1(b)]. The worm-gear tooth surface Σ_2 (it is the envelope to the family of worm tooth surfaces Σ_1) is formed by two branches designated by $\Sigma_2^{(1)}$ and $\Sigma_2^{(2)}$ (Fig. 6.7.2). The common line of the branches is E_ρ^*, which is represented on the worm-gear tooth surface Σ_2 as the image of E_ρ.
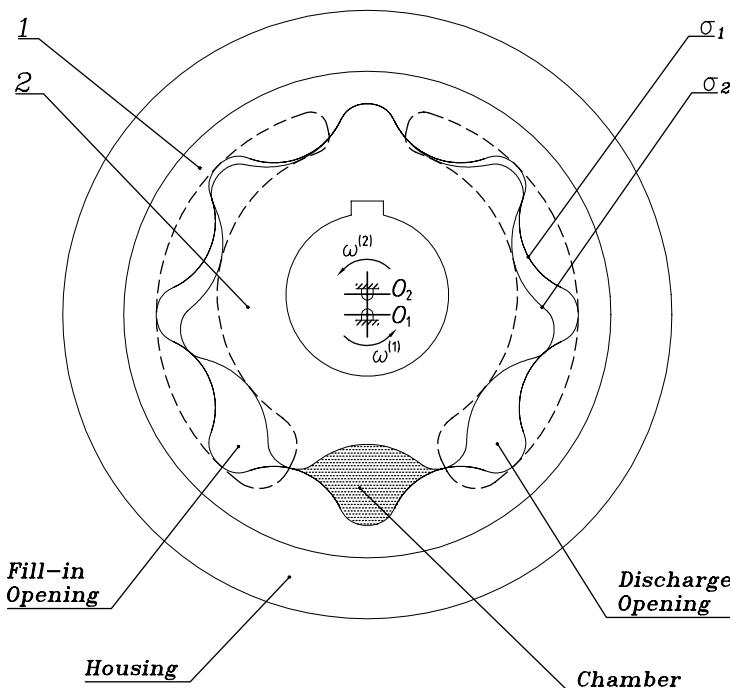
Branches of Tooth Profiles in a Cycloidal Pump

The schematic of the cycloidal gearing pump is shown in Fig. 6.7.3. Figure 6.7.4 shows the centrodes of rotors 1 and 2 as circles of radii r_1 and r_2 in internal tangency. The generating profile is a circle of radius ρ. Figure 6.7.5 shows that the generating profile of rotor 1 (it is the circle of radius ρ) forms on rotor 2 the generated profile by two branches designated $\sigma_2^{(1)}$ and $\sigma_2^{(2)}$. The common point of the two branches is designated as M. We may represent the equation of meshing of rotors 1 and 2 by $f(\theta, \phi) = 0$ where θ is the parameter of the generating profile of rotor 1 (Fig. 6.7.4) and ϕ is the generalized parameter of motion.
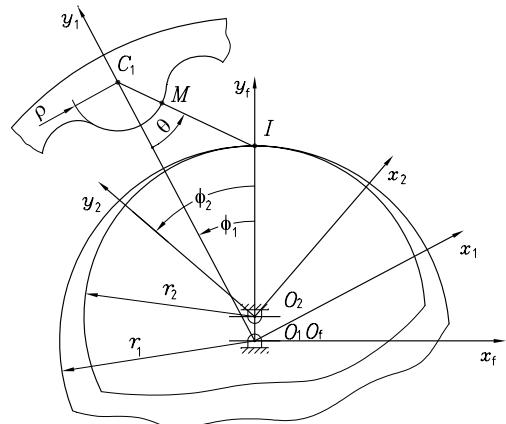
The performed investigation has led to the following results [Vecchiato *et al.*, 2001; Demenego *et al.*, 2002]:

Figure 6.7.2: Branches of envelope Σ_2.
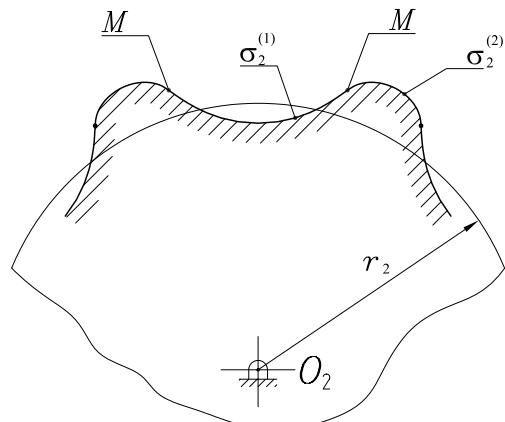
Figure 6.7.3: Schematic of a cycloidal pump.
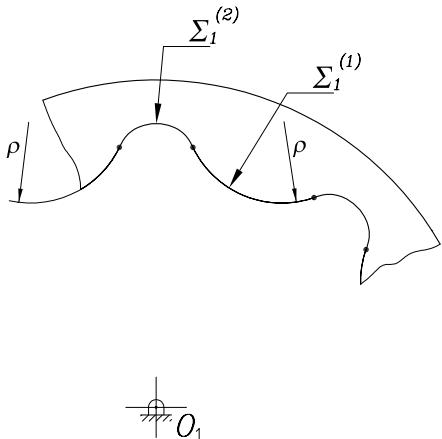
Figure 6.7.4: Generating profile $\Sigma_1^{(1)}$ of gear 1 and applied coordinate systems.

(i) Partial derivative f_ϕ of the equation of meshing is equal to zero at the common point M of the two branches $\sigma_2^{(1)}$ and $\sigma_2^{(2)}$ (Fig. 6.7.5).

(ii) The point of tangency of profiles of rotors 1 and 2 performs a reciprocative motion over the generating profile $\Sigma_1^{(1)}$ (Fig. 6.7.6). The velocity of motion of the point of tangency in its motion over $\Sigma_1^{(1)}$ becomes equal to zero at the beginning of reciprocation.

We have to emphasize that rotor 1 is provided by two profiles designated as $\Sigma_1^{(1)}$ (it is a circle of radius ρ) and profile $\Sigma_1^{(2)}$ (Fig. 6.7.6). We may consider profiles $\Sigma_1^{(1)}$ and $\Sigma_1^{(2)}$ as two branches of an envelope. This envelope is obtained by considering an imaginary generating process wherein profile $\sigma_2^{(2)}$ of rotor 2 is a generating profile. Then, the envelope to the family of profiles $\sigma_2^{(2)}$ will be formed as a combination of two branches, by profile $\Sigma_1^{(1)}$ and $\Sigma_1^{(2)}$ (Fig. 6.7.6). Profile $\Sigma_1^{(2)}$ has to be applied in real design as a connection of circular arc profiles $\Sigma_1^{(1)}$.

Figure 6.7.5: Illustration of formation of envelope σ_2 by branches $\sigma_2^{(1)}$ and $\sigma_2^{(2)}$.

Figure 6.7.6: Profiles $\Sigma_1^{(1)}$ and $\Sigma_1^{(2)}$ of addendum and dedendum of gear 1.

6.8 WILDHABER'S CONCEPT OF LIMIT CONTACT NORMAL

The theory developed in this book allows us to build a bridge between the concepts of undercutting and the envelope to the family of contact lines, "on one side of the river," and Wildhaber's concept of the limit contact normal, "on the other side of the river." Wildhaber's concept of the limit contact normal (limit pressure angle) has been developed on the basis of specific conditions of force transmission by gear tooth surfaces [Wildhaber, 1956]. However, Wildhaber's equation may be and should be interpreted geometrically, and this can be done on the basis of the concept of the envelope to the family of contact lines on Σ_1 and the concept of singularity of Σ_2. Here, Σ_1 and Σ_2 are the generating and the generated surfaces, respectively.

Generally, the limiting line L on Σ_1, which generates the singular point on Σ_2, and the envelope E of contact lines on Σ_1 do not intersect each other, that is, they do not have a common point. We have proven that Wildhaber's approach yields such a specific and rare case when *both* lines, L and E, have a common point, M, that is a point of contact of surfaces Σ_1 and Σ_2 as well. The determination of point M in our interpretation is based on the following considerations. Because M is a point of contact, the equation of meshing is satisfied at point M and within the neighborhood of M. Thus

$$\mathbf{n}^{(i)} \cdot \mathbf{v}^{(12)} = \mathbf{n}^{(i)} \cdot \left\{ \left[\left(\boldsymbol{\omega}^{(1)} - \boldsymbol{\omega}^{(2)} \right) \times \mathbf{r}^{(i)} \right] - \left(\mathbf{R} \times \boldsymbol{\omega}^{(2)} \right) \right\} = 0 \qquad (6.8.1)$$

$$\frac{d}{dt} \left(\mathbf{n}^{(i)} \cdot \mathbf{v}^{(12)} \right) = 0 \qquad (6.8.2)$$

where $i = 1, 2$. The derivation of $\mathbf{v}^{(12)}$ was discussed in Chapter 2.

While deriving Eq. (6.8.2), we consider two cases: (a) $v_r^{(1)} = 0$ and $\dot{\mathbf{n}}_r^{(1)} = 0$ on any direction that differs from the tangent to the envelope, and (b) $v_r^{(2)} = 0$ and $\dot{\mathbf{n}}_r^{(2)} = 0$ for a singular point of Σ_2. Requirements (a) and (b) considered simultaneously provide that M is the point of the envelope to the family of contact lines and a singular point on Σ_2 as well. Equation (6.8.2) considered with these requirements yields the equation

$$\mathbf{n} \cdot \left[\left(\boldsymbol{\omega}^{(1)} \times \mathbf{v}_{tr}^{(2)} \right) - \left(\boldsymbol{\omega}^{(2)} \times \mathbf{v}_{tr}^{(1)} \right) \right] = 0 \qquad (6.8.3)$$

where $v_{tr}^{(i)}$ ($i = 1, 2$) is the velocity of the contact point in transfer motion with the surface (see Section 6.2).

Equations (6.8.1) and (6.8.3) determine the orientation of the *limit contact normal*. This normal is perpendicular to the plane that is formed by vectors **a** and **b** where

$$\mathbf{a} = \mathbf{v}^{(12)} = \mathbf{v}_{tr}^{(1)} - \mathbf{v}_{tr}^{(2)} \tag{6.8.4}$$

$$\mathbf{b} = \left(\boldsymbol{\omega}^{(1)} \times \mathbf{v}_{tr}^{(2)} \right) - \left(\boldsymbol{\omega}^{(2)} \times \mathbf{v}_{tr}^{(1)} \right). \tag{6.8.5}$$
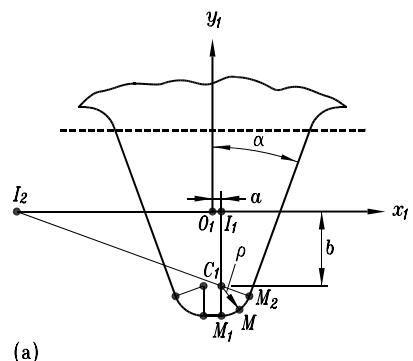
Wildhaber's concept of limit contact normal has been successfully applied for the design of face-milled hypoid gears with tapered teeth. These gears are designed with unequal pressure angles for the driving and coast tooth sides because equal deviations from the limit pressure angle are provided. The disadvantage of Wildhaber's approach is the impossibility of separately determining the envelope to the family of contact lines on Σ_1 and the singularities of Σ_2.

6.9 FILLET GENERATION

Planar Gearing
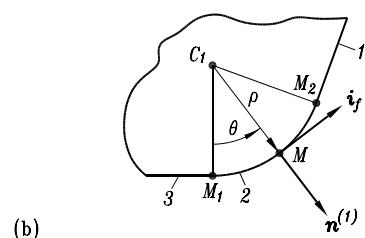
The fillet of the gear is a curve that interconnects the working part of the tooth profile of the gear with the dedendum circle.

Figure 6.9.1 shows the tooth of a rack-cutter for generation of involute spur gears. Part 1 of the tool profile generates the involute profile of the gear; part 3 of the tool profile is a straight line and generates the dedendum circle of the gear; and part 2 of the
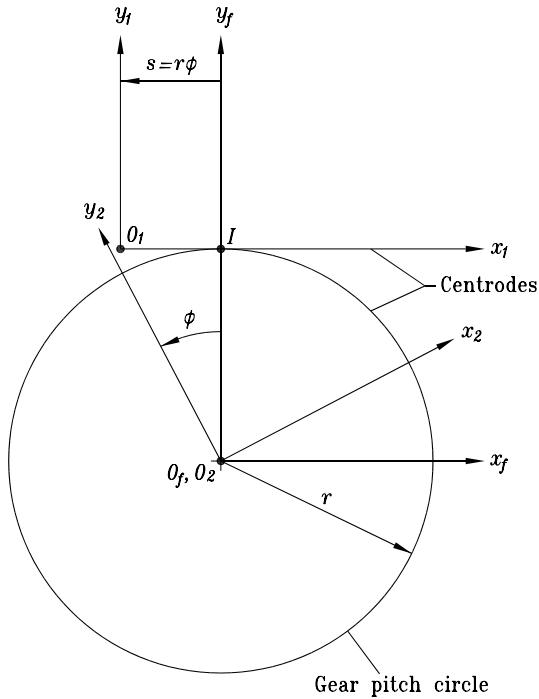
Figure 6.9.1: Rack-cutter and its fillet: (a) rack-cutter tooth and coordinate axes x_f and y_f; (b) representation of fillet circle of radius ρ.

Figure 6.9.2: Centrodes of rack-cutter and gear.
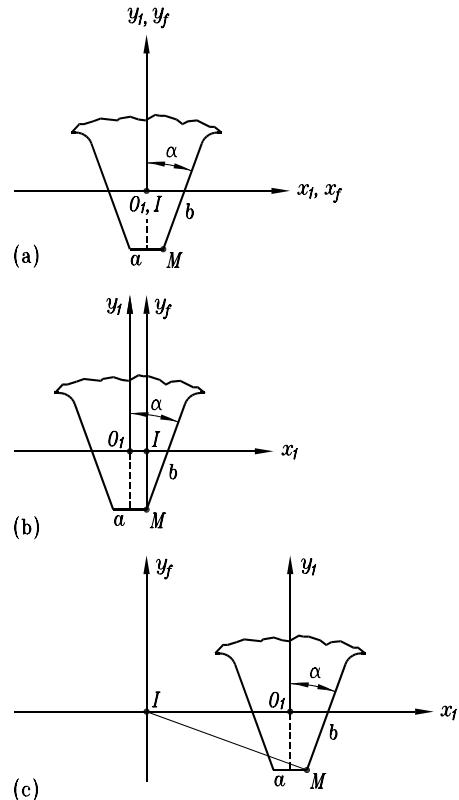
tool profile is an arc of radius ρ that generates the fillet of the gear. The gear fillet is the envelope to the family of circular arcs that is generated in coordinate system S_2 rigidly connected to the gear (Fig. 6.9.2).

To determine the positions of the rack-cutter where the limiting arc points M_1 and M_2 (Fig. 6.9.1) generate the respective points of the gear fillet, we have to derive the equation of meshing of the rack-cutter and the gear. The derivation of this equation may be based on the theorem that a point of the rack-cutter generates the respective point of the gear at a position where the normal to the shape of the rack-cutter passes through the instantaneous center of rotation, I (Fig. 6.9.2). The equation of meshing may be represented by

$$f(\phi, \theta) = 0 \qquad\qquad (6.9.1)$$

where θ is the arc parameter [Fig. 6.9.1(b)] and ϕ is the angle of gear rotation (Fig. 6.9.2). Taking $\theta = 0$ and $\theta = 90° - \alpha$ in Eq. (6.9.1), we may determine the respective values of ϕ and the respective positions of the rack-cutter where points M_1 and M_2 generate the limiting points of the gear fillet. It is evident from Fig. 6.9.1(a) that points M_1 and M_2 generate the gear fillet at the rack-cutter positions where points I_1 and I_2 [see Fig. 6.9.1(a)] will coincide with the instantaneous center of rotation I that is shown in Fig. 6.9.2.

Let us now consider the case where the gear fillet is generated by point M – the edge of the rack-cutter (Fig. 6.9.3). The equation of the gear fillet may be derived as the trajectory of edge M that is traced out in coordinate system S_2. This trajectory may be

Figure 6.9.3: Generation of gear fillet by edge point M: (a) initial position of coordinate system S_1 and generating point M; (b) second position of S_1 and generating point M with respect to S_f; (c) third position of S_1 and point M with respect to S_f.

represented by the matrix equation

$$\mathbf{r}_2 = \mathbf{M}_{21}\mathbf{r}_1^{(M)}. \tag{6.9.2}$$

Here, $\mathbf{r}_1^{(M)}$ is the column matrix that represents in S_1 the coordinates of edge M.

Figure 6.9.3 shows three positions of the rack-cutter in coordinate system S_f that is rigidly connected to the frame. At the initial position [Fig. 6.9.3(a)], the origin O_1 of the movable coordinate system S_1 coincides with the instantaneous center of rotation, I. Figure 6.9.3(b) shows the position of the rack-cutter where the gear fillet is in tangency with the dedendum circle that is generated by the straight-line a. At the position that is shown in Fig. 6.9.3(c) the gear fillet is in tangency with the involute curve that is generated by straight-line b.

Spatial Gearing
We have to differentiate between two cases where the gear fillet is generated by (i) a surface of a tool, or (ii) a line – the edge of the tool. For instance, in the case of generation of a worm-gear, the gear fillet surface is generated by a helix – the edge of the hob. Respectively, in the case of generation of spiral bevel gears and hypoid gears, the tool is a cone (Fig. 6.9.4), and the gear fillet surface is generated by the tool circle of radius r_c. The generation of the gear fillet surface that is generated by a tool surface may be investigated as the generation of an envelope to a family of surfaces (see Section 6.1).
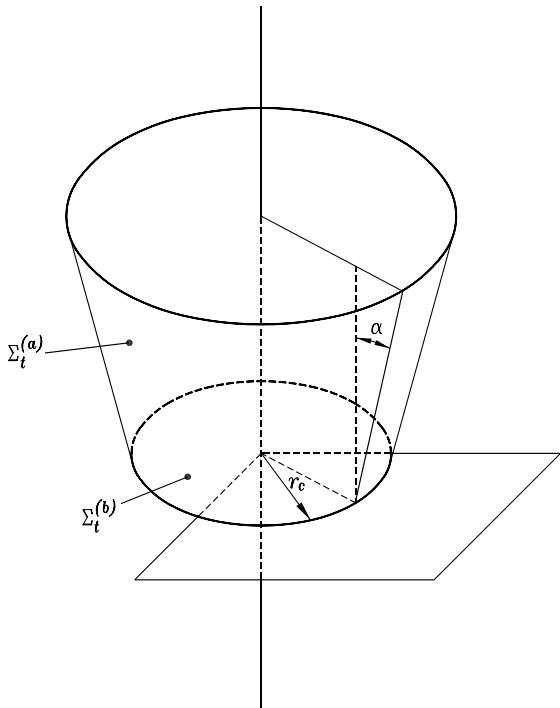
Figure 6.9.4: Generating cone.

Let us consider the generation of the gear fillet surface by the edge of the tool. The surface of the gear fillet may be represented in coordinate system S_g, which is rigidly connected to the gear, by the following matrix equation:

$$\mathbf{r}_g(\theta, \phi) = \mathbf{M}_{gt}(\phi)\mathbf{r}_t(\theta). \tag{6.9.3}$$

Here, $\mathbf{r}_t(\theta)$ represents in coordinate system S_t the edge of the tool; matrix $\mathbf{M}_{gt}(\phi)$ describes the coordinate transformation in transition from S_t to S_g (elements of the matrix depend on the generalized parameter of motion, ϕ); $\mathbf{r}_g(\theta, \phi)$ represents in coordinate system S_g the gear fillet surface with θ and ϕ as surface coordinates.

There are two alternative approaches for the determination of the normal to the gear fillet surface. The first approach is based on the equation
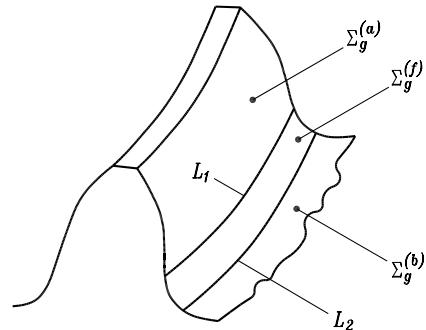
$$\mathbf{N}_g^{(g)} = \frac{\partial \mathbf{r}_g}{\partial \theta} \times \frac{\partial \mathbf{r}_g}{\partial \phi}. \tag{6.9.4}$$

The second approach allows us to represent in coordinate system S_t the normal to the gear fillet surface by the equation

$$\mathbf{N}_t^{(g)} = \frac{\partial \mathbf{r}_t}{\partial \theta} \times \mathbf{v}_t^{(tg)}. \tag{6.9.5}$$

Here,

$$\mathbf{v}_t^{(tg)} = \mathbf{v}_t^{(t)} - \mathbf{v}_t^{(g)}$$

Figure 6.9.5: Three subsurfaces of gear tooth.

is the sliding vector at a point of tangency of surfaces Σ_t and Σ_g. The subscript t indicates that the vectors are represented in S_t. The superscripts t and g designate surfaces Σ_t and Σ_g, respectively.
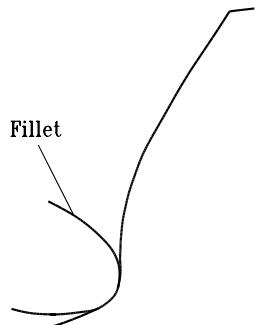
To represent the normal to the gear fillet surface in coordinate system S_g, it is necessary to use the following matrix equation:

$$\mathbf{N}_g^{(g)} = \mathbf{L}_{gt} \mathbf{N}_t^{(g)}. \tag{6.9.6}$$
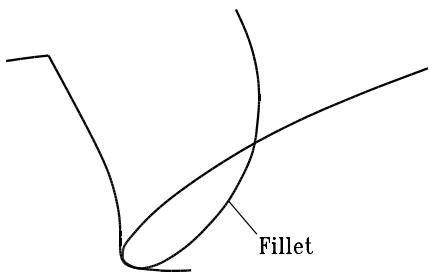
Here, $\mathbf{L}_{gt}$ is the 3×3 matrix that describes the transformation of vectors in transition from S_t to S_g.

The generating line of the tool is the line of intersection of two tool surfaces, $\Sigma_t^{(a)}$ and $\Sigma_t^{(b)}$. For instance, in the case of generation of hypoid and spiral bevel gears, the generating line, which is a circle of radius r_c, is the line of intersection of the cone surface $\Sigma_t^{(a)}$ and the plane $\Sigma_t^{(b)}$ that is perpendicular to the cone axis; this plane is limited by the circle of radius r_c (Fig. 6.9.4). The gear tooth surface (Fig. 6.9.5) consists of three parts: (i) $\Sigma_g^{(a)}$ which is generated by $\Sigma_t^{(a)}$, (ii) $\Sigma_g^{(b)}$ which is generated by the tool surface $\Sigma_t^{(b)}$, and (iii) the fillet surface $\Sigma_g^{(f)}$. Lines L_1 and L_2 represent the lines of tangency of the gear fillet with surfaces $\Sigma_g^{(a)}$ and $\Sigma_g^{(b)}$, respectively. (It is assumed that undercutting has been avoided.) At the line of tangency L_i $(i = 1, 2)$ of the gear fillet surface with surfaces $\Sigma_g^{(a)}$ and $\Sigma_g^{(b)}$ the normals to the gear fillet surface and the neighboring surface are collinear. Thus

$$\dot{\mathbf{r}}_t(\theta) \times \mathbf{v}_t^{(tg)} = \lambda \mathbf{N}_t^{(i)}, \qquad (i = a, b). \tag{6.9.7}$$

Figure 6.9.6: Fillet and surface section: hypoid pinion convex side.

Figure 6.9.7: Fillet and surface section: hypoid pinion concave side.

Fillet

Equations (6.9.7) and (6.9.3) determine the lines of tangency L_1 and L_2 on the gear surface.

Using the described method, the fillet surface for a hypoid pinion has been determined [Litvin, 1989]. The mean cross sections for both sides of the pinion tooth are represented in Figs. 6.9.6 and 6.9.7. Figure 6.9.8 shows the cross sections of the pinion tooth surface $\Sigma_g^{(a)}$ for both sides of the tooth. The shapes are asymmetrical because the tooth sides are generated by blades with different blade angles.

6.10 TWO-PARAMETER ENVELOPING
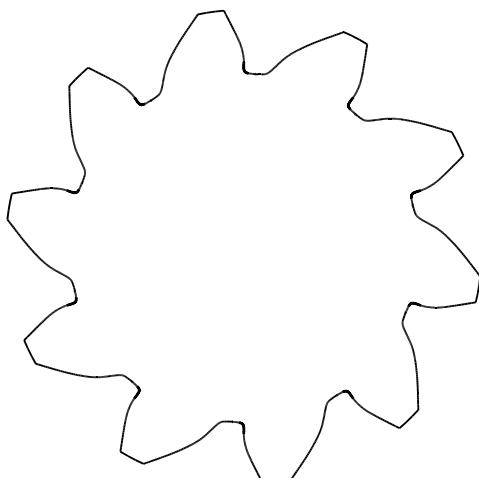
Introduction

The generating surface Σ_1 is represented in S_1 as
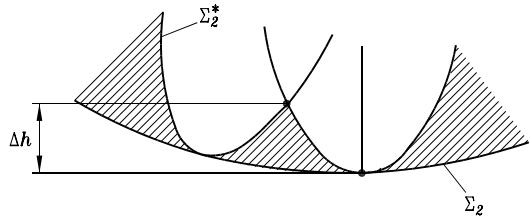
$$\mathbf{r}_1(u, \theta), \qquad \frac{\partial \mathbf{r}_1}{\partial u} \times \frac{\partial \mathbf{r}_1}{\partial \theta} \neq \mathbf{0}, \qquad (u, \theta) \in E. \qquad (6.10.1)$$

The motion of Σ_1 with respect to coordinate system S_2 is determined with *two indepen-dent* parameters ϕ and ψ. The family of surfaces Σ_1 that is generated in S_2 is represented as

$$\mathbf{r}_2(u, \theta, \phi, \psi) = \mathbf{M}_{21}(\phi, \psi)\, \mathbf{r}_1(u, \theta). \qquad (6.10.2)$$

Figure 6.9.8: Cross section of hypoid pinion.

Figure 6.10.1: Surface deviations.

Matrix $\mathbf{M}_{21}$ describes the coordinate transformation from S_1 to S_2. The goal is to determine surface Σ_2 as the envelope to the two-parameter family of surfaces (6.10.2).

The case of two-parameter enveloping had been considered in differential geometry and was of theoretical interest only. We may visualize the two-parameter enveloping considering the simplest case when Σ_1 is a spherical surface whose center performs independent translational motions ψ and ϕ along the x_2 and y_2 axes. The envelope to the two-parameter family generated by Σ_1 in S_2 is the set of two planes $z_2 = \pm\rho$ where ρ is the radius of spherical surface Σ_1.

There is a certain advantage in applying the method of two-parameter enveloping to generation of surfaces with the feed motion of the tool, for instance, in the milling (grinding) of spur and helical gears by a hob (grinding worm) or the generation of face-hobbed spiral bevel and hypoid pinions. We have to emphasize that *in reality* the generation of surfaces with feed motion is a one-parameter enveloping process because the two parameters of motion, ψ and ϕ, are not independent but related. This results from the fact that the kinematic chains of the machine that execute the motions of ψ and ϕ are run from one source. Therefore, there is a function $\psi(\phi)$ that relates the input parameters.

We may imagine two types of generated surface: (i) Σ_2^*, the envelope to the one-parameter family of surfaces that is generated when the parameters of motion are *dependent* and related by function $\psi(\phi)$; and (ii) Σ_2, the envelope to the two-parameter family of surfaces generated when the parameters of motion, ψ and ϕ, are *independent*. Surface Σ_2 is an imaginary surface, the result of an abstraction, and the real surface Σ_2^* deviates from Σ_2 as shown in Fig. 6.10.1. The deviation Δh depends on the applied feed motion ψ with respect to ϕ, where ϕ is the generalized parameter of the main generating motion. Thus, Δh depends on the slope of function $\psi(\phi)$. Usually, $\psi(\phi)$ is a linear function with a very small slope.

Equation of Meshing

Consider as given the generating surface Σ_1 and the normal $\mathbf{N}_1$ to Σ_1, which is represented as

$$\mathbf{N}_1 = \frac{\partial \mathbf{r}_1}{\partial u} \times \frac{\partial \mathbf{r}_1}{\partial \theta}. \tag{6.10.3}$$

We designate with $\mathbf{v}^{(12,\phi)}$ and $\mathbf{v}^{(12,\psi)}$ the sliding velocity $\mathbf{v}^{(12,q)}$ where $q = \phi, \psi$ is the varied parameter. While deriving $\mathbf{v}^{(12,\phi)}$ we will consider that ϕ is the varied parameter and ψ is fixed. The designation $\mathbf{v}^{(12,\psi)}$ has to be interpreted similarly.

Two-parameter enveloping has been the subject of research by Litvin *et al.* [1975] and Litvin & Seol [1996]. It was proven that the *necessary* conditions of existence of the two-parameter envelope Σ_2 are as follows:

$$\mathbf{N}_1 \cdot \mathbf{v}_1^{(12,\phi)} = 0, \qquad \mathbf{N}_1 \cdot \mathbf{v}_1^{(12,\psi)} = 0. \tag{6.10.4}$$

The subscript "1" in (6.10.4) indicates that the vectors are represented in S_1. Equations (6.10.4) and vector function $\mathbf{r}_1(u,\theta)$ represent on Σ_1 the current point of tangency of Σ_1 with the sought-for envelope Σ_2.

Not losing the generality, we assume that $\mathbf{v}_1^{(12,\phi)}$ is determined with $d\phi/dt = 1$, and $\mathbf{v}_1^{(12,\psi)}$ with $d\psi/dt = 1$. For purposes of simplification, we designate $\mathbf{v}_1^{(12,\phi)}$ and $\mathbf{v}_1^{(12,\psi)}$ as $\mathbf{v}_1^{(\phi)}$ and $\mathbf{v}_1^{(\psi)}$, respectively. Equations

$$\mathbf{N}_1 \cdot \mathbf{v}_1^{(\phi)} = 0, \qquad \mathbf{N}_1 \cdot \mathbf{v}_1^{(\psi)} = 0 \tag{6.10.5}$$

considered simultaneously with (6.10.1) and (6.10.3) yield two *equations of meshing*:

$$f(u,\theta,\phi,\psi) = 0, \qquad g(u,\theta,\phi,\psi) = 0. \tag{6.10.6}$$

Equations of Envelope Σ_2

Envelope Σ_2 to the family of surfaces (6.10.2) is represented by the equations

$$\mathbf{r}_2(u,\theta,\phi,\psi) = \mathbf{M}_{21}(\phi,\psi)\,\mathbf{r}_1(u,\theta)$$
$$f(u,\theta,\phi,\psi) = 0, \qquad g(u,\theta,\phi,\psi) = 0. \tag{6.10.7}$$

Line of Action

The line of action is the locus of points of contact between Σ_1 and Σ_2 that are represented in the *fixed* coordinate system S_f. The line of action is represented by the equations

$$\mathbf{r}_f(u,\theta,\phi,\psi) = \mathbf{M}_{f1}(\phi,\psi)\,\mathbf{r}_1(u,\theta)$$
$$f(u,\theta,\phi,\psi) = 0, \qquad g(u,\theta,\phi,\psi) = 0. \tag{6.10.8}$$

Here, matrix $\mathbf{M}_{f1}$ describes the coordinate transformation from S_1 to S_f.

Conditions of Nonundercutting

The velocity $\mathbf{v}_r^{(2)}$ of a contact point in its motion over Σ_2 is represented by an equation similar to Eq. (6.2.2):

$$\mathbf{v}_{r1}^{(2)} = \mathbf{v}_{r1}^{(1)} + \mathbf{v}_1^{(\phi)} \frac{d\phi}{dt} + \mathbf{v}_1^{(\psi)} \frac{d\psi}{dt} \tag{6.10.9}$$

where

$$\mathbf{v}_{r1}^{(1)} = \frac{\partial \mathbf{r}_1}{\partial u} \frac{du}{dt} + \frac{\partial \mathbf{r}_1}{\partial \theta} \frac{d\theta}{dt}.$$

Singularity of Σ_2 occurs if $\mathbf{v}_{r1}^{(2)} = 0$. The equation

$$\frac{\partial \mathbf{r}_1}{\partial u} \frac{du}{dt} + \frac{\partial \mathbf{r}_1}{\partial \theta} \frac{d\theta}{dt} + \mathbf{v}_1^{(\phi)} \frac{d\phi}{dt} + \mathbf{v}_1^{(\psi)} \frac{d\psi}{dt} = 0 \tag{6.10.10}$$

represents such a *regular* point on Σ_1 that will generate a *singular* point on Σ_2. Equations of meshing (6.10.6) are satisfied at the previously mentioned point and within its neighborhood. Therefore, we may differentiate (6.10.6) and obtain

$$f_u \frac{du}{dt} + f_\theta \frac{d\theta}{dt} + f_\phi \frac{d\phi}{dt} + f_\psi \frac{d\psi}{dt} = 0 \tag{6.10.11}$$

$$g_u \frac{du}{dt} + g_\theta \frac{d\theta}{dt} + g_\phi \frac{d\phi}{dt} + g_\psi \frac{d\psi}{dt} = 0. \tag{6.10.12}$$

Equations (6.10.10) to (6.10.12) represent a system of five dependent homogeneous equations in four unknowns: du/dt, $d\theta/dt$, $d\phi/dt$, and $d\psi/dt$. The matrix of coefficients for these equations is of the order of 5×4. The previously mentioned system of equations exists and provides nontrivial solutions for the unknowns if all five determinants of order four for the coefficient matrix are equal to zero simultaneously. It can be proven that two of five determinants are equal to zero simultaneously, and the additional requirement is

$$\Delta_1^2 + \Delta_2^2 + \Delta_3^2 = 0. \tag{6.10.13}$$

Here,

$$\Delta_1 = \begin{vmatrix} \dfrac{\partial x_1}{\partial u} & \dfrac{\partial x_1}{\partial \theta} & v_{x1}^{(\phi)} & v_{x1}^{(\psi)} \\[2mm] \dfrac{\partial y_1}{\partial u} & \dfrac{\partial y_1}{\partial \theta} & v_{y1}^{(\phi)} & v_{y1}^{(\psi)} \\[2mm] f_u & f_\theta & f_\phi & f_\psi \\[1mm] g_u & g_\theta & g_\phi & g_\psi \end{vmatrix} \tag{6.10.14}$$
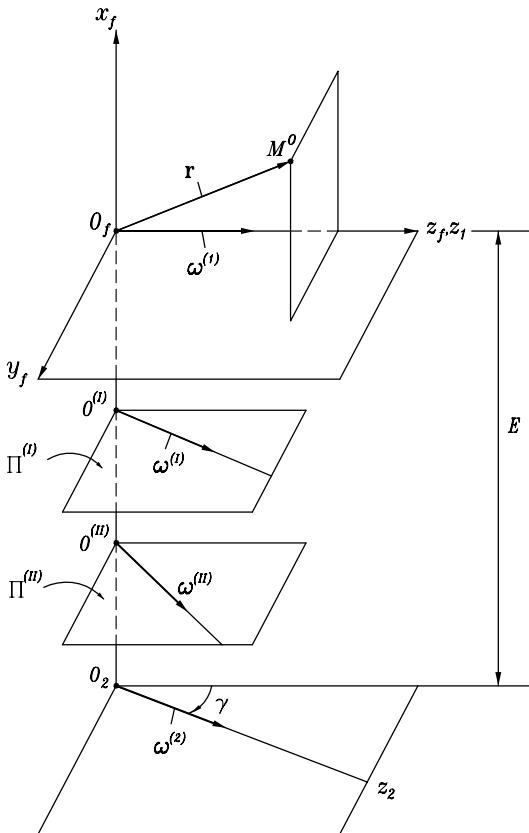
$$\Delta_2 = \begin{vmatrix} \dfrac{\partial x_1}{\partial u} & \dfrac{\partial x_1}{\partial \theta} & v_{x1}^{(\phi)} & v_{x1}^{(\psi)} \\[2mm] \dfrac{\partial z_1}{\partial u} & \dfrac{\partial z_1}{\partial \theta} & v_{z1}^{(\phi)} & v_{z1}^{(\psi)} \\[2mm] f_u & f_\theta & f_\phi & f_\psi \\[1mm] g_u & g_\theta & g_\phi & g_\psi \end{vmatrix} \tag{6.10.15}$$

$$\Delta_3 = \begin{vmatrix} \dfrac{\partial y_1}{\partial u} & \dfrac{\partial y_1}{\partial \theta} & v_{y1}^{(\phi)} & v_{y1}^{(\psi)} \\[2mm] \dfrac{\partial z_1}{\partial u} & \dfrac{\partial z_1}{\partial \theta} & v_{z1}^{(\phi)} & v_{z1}^{(\psi)} \\[2mm] f_u & f_\theta & f_\phi & f_\psi \\[1mm] g_u & g_\theta & g_\phi & g_\psi \end{vmatrix}. \tag{6.10.16}$$

Equation (6.10.13) provides the relation

$$F(u, \theta, \phi, \psi) = 0. \tag{6.10.17}$$

Equations (6.10.17) and (6.10.6) and vector function $\mathbf{r}_1(u, \theta)$ considered simultaneously determine on Σ_1 line L that generates singular points on surface Σ_2. Undercutting

Figure 6.11.1: For derivation of axes of meshing.

of Σ_2 can be avoided by limitations of Σ_1 in order to exclude the limiting line L from the working part of Σ_1.

6.11 AXES OF MESHING
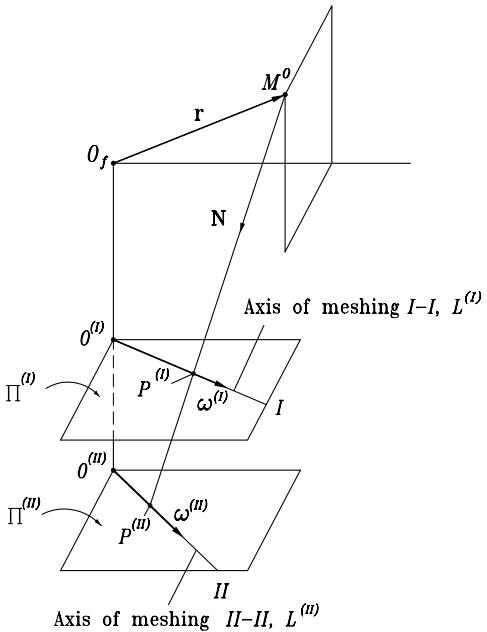
Basic Concept
The application of axes of meshing is useful for illustration of some cases of tangency of mating surfaces that are in line contact (see below). The definition of axes of meshing is based on the following considerations [Litvin, 1968; Litvin, 1969; Argyris *et al.*, 1998].

Step 1: Assume that rotation is provided for crossed axes z_1 and z_2 that form a crossing angle γ and shortest distance E (Fig. 6.11.1). The instantaneous angular velocities are $\omega^{(1)}$ and $\omega^{(2)}$. The generating gear tooth surface Σ_1 is given. Using the approach represented in Section 6.1, we may determine the equation of meshing $f(u, \theta, \phi) = 0$ and instantaneous lines of tangency $L_{12}(\phi)$ for any position determined by general parameter of motion ϕ. Point M belongs to line of tangency $L_{12}(\phi^{(1)})$.

Step 2: The relative velocity of gear 1 with respect to gear 2 may be determined by sliding vector $\omega^{(12)}$ and vector moment **m** as follows:

$$\boldsymbol{\omega}^{(12)} = \boldsymbol{\omega}^{(1)} - \boldsymbol{\omega}^{(2)}. \qquad (6.11.1)$$

Figure 6.11.2: Intersection of axes of meshing by the normal to the contacting surfaces.

Vector $\boldsymbol{\omega}^{(12)}$ passes through origin O_f of coordinate system S_1.

$$\mathbf{m}\left(-\mathbf{m}^{(2)}\right) = \overline{O_f O_2} \times \boldsymbol{\omega}^{(1)}. \tag{6.11.2}$$

Step 3: It is known from kinematics that there is a manifold of vectors $\boldsymbol{\omega}^{(I)}$ and $\boldsymbol{\omega}^{(II)}$ (Figs. 6.11.1 and 6.11.2) that may provide the same relative motion if $\boldsymbol{\omega}^{(I)}$ and $\boldsymbol{\omega}^{(II)}$ satisfy the following equations:

$$\boldsymbol{\omega}^{(I)} - \boldsymbol{\omega}^{(II)} = \boldsymbol{\omega}^{(12)} \tag{6.11.3}$$

$$\overline{O_f O^{(I)}} \times \boldsymbol{\omega}^{(I)} + \overline{O_f O^{(II)}} \times \left(-\boldsymbol{\omega}^{(II)}\right) = \overline{O_f O_2} \times \left(-\boldsymbol{\omega}^{(2)}\right). \tag{6.11.4}$$

Step 4: We now consider a sub-manifold of vectors $\boldsymbol{\omega}^{(I)}$ and $\boldsymbol{\omega}^{(II)}$ that in addition satisfies the following requirement: *common normal* $\mathbf{N}$ *at a point of tangency* M^0 *of contacting surfaces intersects lines* $L^{(I)}$ *and* $L^{(II)}$, *the lines of action of angular velocities* $\boldsymbol{\omega}^{(I)}$ *and* $\boldsymbol{\omega}^{(II)}$. This requirement is represented by the equations

$$\frac{X^{(i)} - x}{N_x} = \frac{Y^{(i)} - y}{N_y} = \frac{Z^{(i)} - z}{N_z} \qquad (i = I, II). \tag{6.11.5}$$
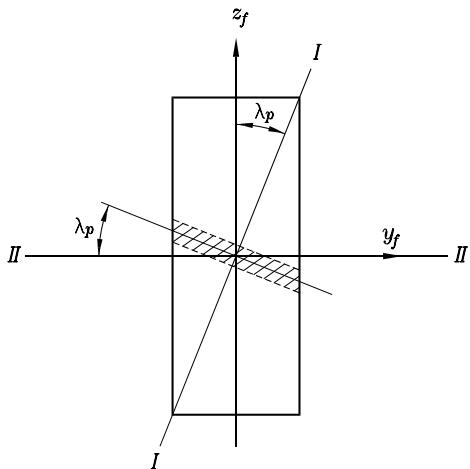
Here (see Figs. 6.11.1 and 6.11.2),

$$\overline{O_f P^{(i)}} = \left(X^{(i)}, Y^{(i)}, Z^{(i)}\right) \tag{6.11.6}$$
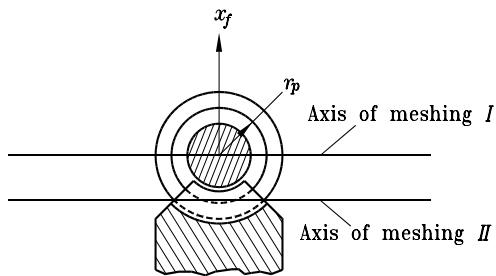
$$\overline{O_f M} = r(x, y, z) \tag{6.11.7}$$

$$\mathbf{N} = (N_x, N_y, N_z). \tag{6.11.8}$$

It is proven [Litvin, 1968; Litvin, 1989] that if normal $\mathbf{N}$ at contact point M^0 intersects the axes of meshing, then the necessary condition of envelope existence is satisfied and

Figure 6.11.3: Axes of meshing for orthogonal drive.

$$\mathbf{N} \cdot \left(\mathbf{v}^{(I)} - \mathbf{v}^{(II)}\right) = 0. \tag{6.11.9}$$
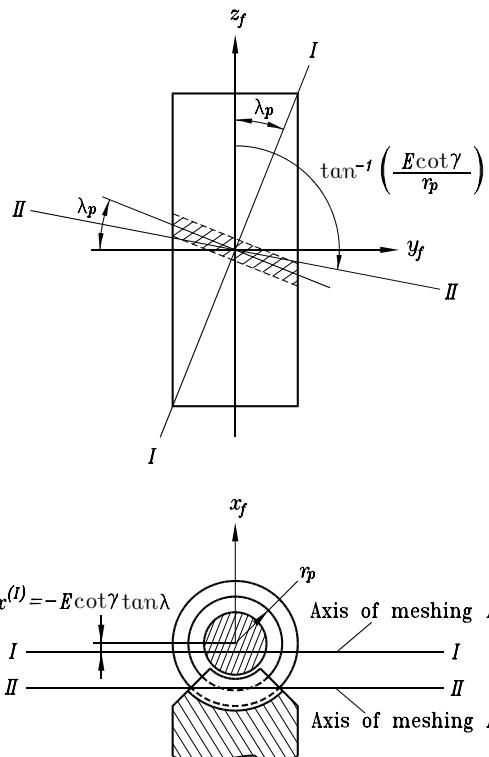
However, the equations represented above are observed at a sole point M^0 of tangency of surfaces Σ_1 and Σ_2.

Step 5: Lines of action $L^{(I)}$ and $L^{(II)}$ are called *axes of meshing* if Eqs. (6.11.4) to (6.11.8) are observed at *any* point of tangency of Σ_1 and Σ_2, not only at a point M^0. However, axes of meshing exist only in particular cases represented in this section: (i) worm-gear drives with cylindrical and conical worms when the worm is a helicoid, and (ii) generation of a helicoid by a peripheral tool.

Worm-Gear Drive with Cylindrical Worm

Figures 6.11.3 and 6.11.4 show in coordinate system S_f the location and orientation of axes of meshing I–I and II–II for the cases when the crossing angle is $\gamma = \pi/2$ and $\gamma \neq \pi/2$, respectively. Axis z_f is the axis of the worm rotation, and x_f coincides with the line of the shortest distance E between the worm and gear axes. Coordinates of axes of meshing for a standard worm-gear drive are given in Table 6.11.1.

Designations $K^{(i)}$ and $X^{(i)}$ in Table 6.11.1 indicate the orientation of the axis of meshing and the location of the point of intersection with the x_f axis. Here, $K^{(i)} = Z^{(i)}/Y^{(i)}$, where $Z^{(i)}$ and $Y^{(i)}$ ($i = I, II$) are coordinates of a current point of the axis of meshing. Axes of meshing lie in parallel planes that are perpendicular to the shortest distance between the axes of the worm and the worm-gear. Figure 6.11.5 shows the
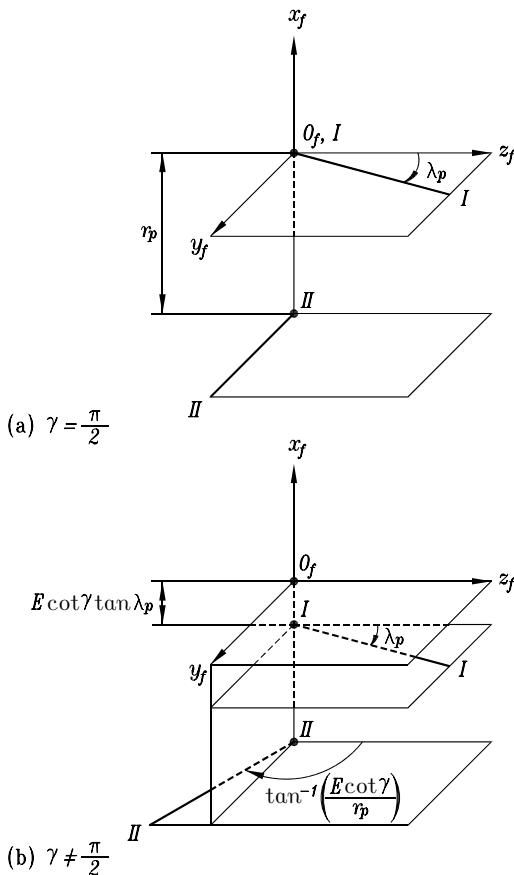
Figure 6.11.4: Axes of meshing for non-orthogonal drive.

location and orientation of axes of meshing in the 3D-space when the worm is right-handed.

We limit this discussion to the conventional worm-gear drive with a cylindrical worm. However, the axes of meshing exist as well in face-worm gear drives with conical and cylindrical worms. The concept of axes of meshing should be applied for the cases of generation of worm-gears and face-worm gears by a hob when the hob is a helicoid. The new tendency in design of face-gear drives (including worm gear drives and face-worm gear drives) is to modify the worm surface by double crowning, and the worm surface deviates from a helicoid surface. Therefore, the concept of axes of meshing cannot be

Table 6.11.1: Coordinates of axes of meshing for a standard worm-gear drive

γ	Worm thread	$K^{(I)}$	$X^{(I)}$	$K^{(II)}$	$X^{(II)}$
$\gamma \neq \dfrac{\pi}{2}$	Right-handed	$\cot \lambda_p$	$-E \cot \gamma \tan \lambda_p$	$\dfrac{E \cot \gamma}{r_p}$	$-r_p$
	Left-handed	$-\cot \lambda_p$	$E \cot \gamma \tan \lambda_p$	$\dfrac{E \cot \gamma}{r_p}$	$-r_p$
$\gamma = \dfrac{\pi}{2}$	Right-handed	$\cot \lambda_p$	0	0	$-r_p$
	Left-handed	$-\cot \lambda_p$	0	0	$-r_p$

Figure 6.11.5: Axes of meshing in 3D-space: (a) representation of axes of meshing $I–I$ and $II–II$ in orthogonal worm-gear drive ($\gamma = \pi/2$); (b) representation of axes of meshing $I–I$ and $II–II$ in nonorthogonal worm-gear drive ($\gamma \neq \pi/2$).
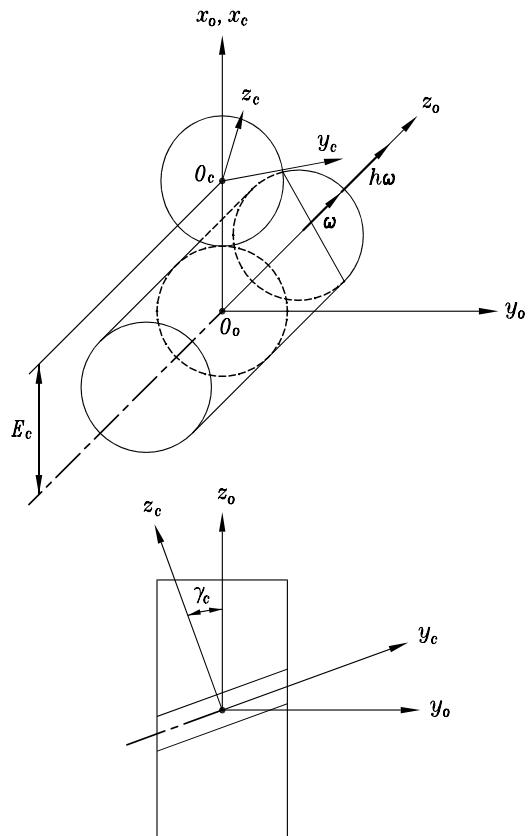
applied for meshing of the worm and the worm-gear (face-worm gear) but only for generation of the worm-gear (face-worm gear) by a hob-helicoid.

Generation of Worm by Peripheral Tool
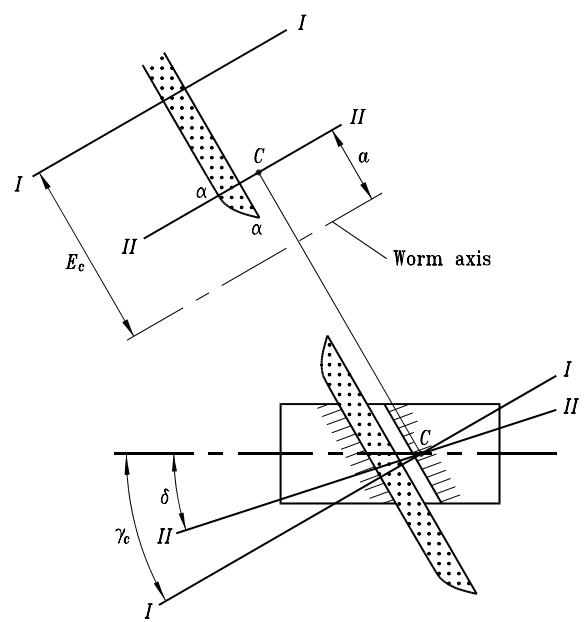
The installment of the tool is shown in Fig. 6.11.6. Coordinate system S_c is rigidly connected to the tool. Coordinate system S_o is rigidly connected to the frame. The worm in the process of generation performs a screw motion about the z_o axis with the screw parameter p. The rotation of the tool about its z_c axis provides the desired velocity of cutting but is not related to the process of generation. Thus, we may neglect the tool rotation and consider that systems S_c and S_o are rigidly connected. The crossing angle between the z_c axis and the z_o axis is γ_c; usually, $\gamma_c = \lambda_p$. The shortest distance is E_c.

There are two axes of meshing in this case: one, $I–I$, coincides with the z_c axis; the other one, $II–II$, lies in the plane that is perpendicular to the shortest distance (Fig. 6.11.7). The shortest distance between the worm axis and the axis of meshing $II–II$ is

$$a = X_o^{(II)} = p \cot \gamma_c. \tag{6.11.10}$$

Figure 6.11.6: Generation of worm by peripheral tool.

Figure 6.11.7: Axes of meshing in the case of worm generation.

Angle δ that is formed by the axis of meshing $II-II$ and the worm axis is represented by

$$\delta = \arctan\left(\frac{p}{E_c}\right). \tag{6.11.11}$$
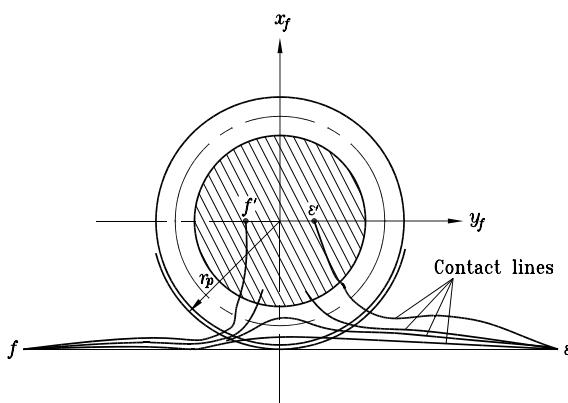
6.12 KNOTS OF MESHING

The surface of action may be represented as a locus of lines of contact of gear tooth surfaces in the fixed coordinate system rigidly connected to the frame. Generally a section of the surface of action cut by a plane represents a plane curve. There are special cases where such a section of the surface of action represents a straight line if the following conditions are satisfied (proven by Litvin [1968, 1989]).
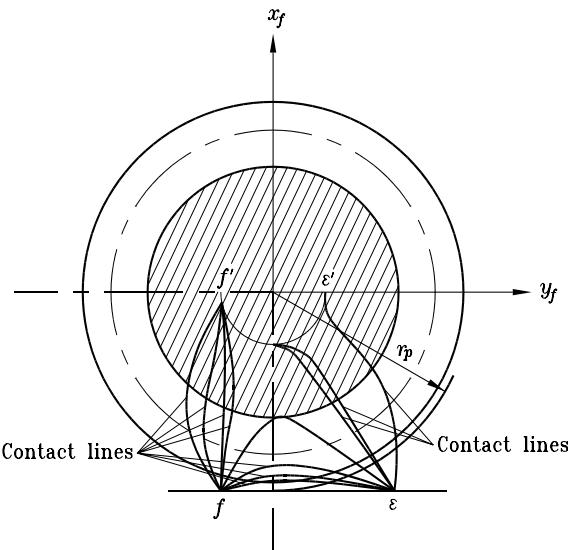
(1) The gears transform rotation between crossed axes with a constant angular velocity ratio.
(2) The tooth surface of one of the mating gears is a helicoid.
(3) The surface of action is cut by a plane that is parallel to the shortest distance **E** between the axes of gear rotation and is located at a definite distance from **E**.

When the preceding conditions are observed, there are straight lines on the surface of action, and the contact lines of gear tooth surfaces intersect these straight lines. These points of intersection are called the *knots of meshing*, because we may imagine that the lines of contact are attached to the straight lines, which are obtained as sections of the surface of action.

Figures 6.12.1 and 6.12.2 show projections of contact lines of the worm and the worm-gear surfaces on plane (x_f, y_f). These contact lines are determined for the worm-gear drives with the concave–convex surfaces of FI and FII worms (see Chapter 19) generated by the methods proposed by Niemann & Heyer [1953] (Fig. 6.12.1) and by Litvin [1968, 1989] (Fig. 6.12.2), respectively. Points ε, f, ε', and f' represent

Figure 6.12.1: Worm FI: contact lines.

Figure 6.12.2: Worm FII: contact lines.

projections of the lines of knots of meshing. Changing the location of the lines of knots, we can improve the shape of contact lines to obtain better conditions of lubrication.

The evidence of the existence of lines of knots is based on the following considerations:

(1) Because the worm surface is a helicoid, two axes of meshing exist. The normal at any point of contact of the worm and the worm-gear surfaces intersects both axes of meshing (see Section 6.11).
(2) There might be a limiting case when the common surface normal intersects one of the two axes of meshing and is parallel to the other one. (The normal intersects the other axis of meshing at infinity.)

Figure 6.12.3 shows a cross section of the worm surface at two positions for a worm of a worm-gear drive with a crossing angle of $90°$. The normal n–n to the worm surface intersects the I–I axis of meshing and is parallel to the II–II axis of meshing. The upper lines of knots of meshing are f'–f' and ε'–ε', respectively.

Figure 6.12.4 shows a cross section of the worm surface at two other positions. The normal n–n to the worm surface intersects the II–II axis of meshing. The bottom lines of the knots are f–f and ε–ε, respectively.
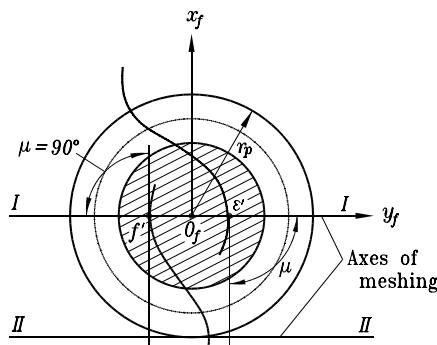
Considering the general case of the crossing angle $\gamma \neq 90°$, we represent the lines of knots by the following equations (see Table 6.11.1).

(1) The upper lines of knots of meshing are determined by
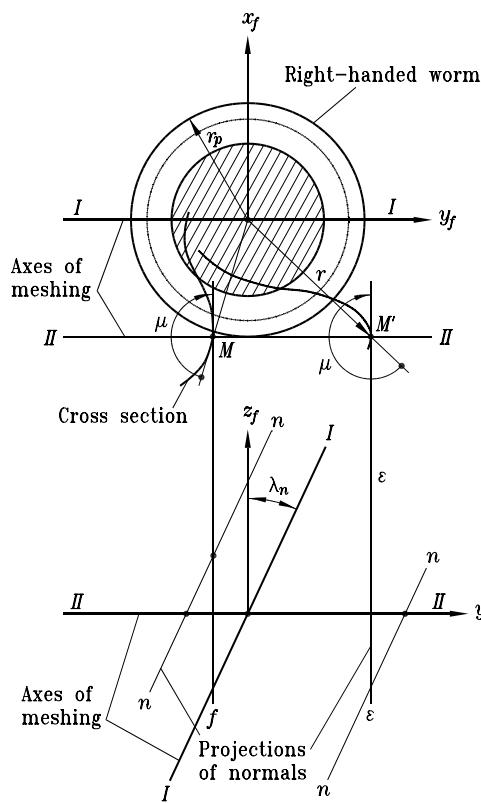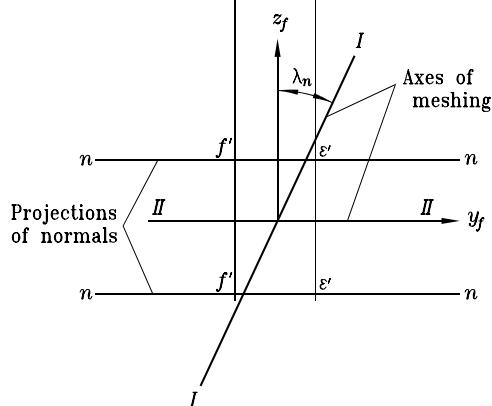
$$x_f = X_f^{(I)} = \mp E \cot \gamma \tan \lambda_p \tag{6.12.1}$$

$$n_{xf} = 0 \tag{6.12.2}$$

$$\frac{n_{zf}}{n_{yf}} = K^{(II)} = \frac{E \cot \gamma}{r_p}. \tag{6.12.3}$$

Figure 6.12.3: Knots of meshing: case 1.

Figure 6.12.4: Knots of meshing: case 2.

Here, (x_f, y_f, z_f) are the coordinates of the point of contact of the worm and the worm-gear surfaces; (n_{xf}, n_{yf}, n_{zf}) are the projections of the common normal to the surfaces; (x_f, y_f, z_f) and (n_{xf}, n_{yf}, n_{zf}) are determined for an angle of the worm rotation when one point of the instantaneous line of contact of mating surfaces is the point of the upper line of knots simultaneously.

The result of equation (6.12.1) is that the upper line of knots intersects the $I-I$ axis of meshing. Equations (6.12.2) and (6.12.3) yield that the common normal to the mating surfaces is parallel to the $II-II$ axis of meshing.

(2) The bottom lines of knots are represented by

$$x_f = X_f^{(II)} = -r_p \tag{6.12.4}$$

$$n_{xf} = 0 \tag{6.12.5}$$

$$\frac{n_{zf}}{n_{yf}} = K^{(I)} = \pm \cot \lambda_P. \tag{6.12.6}$$

Equations (6.12.4) to (6.12.6) are based on the same considerations. The upper and lower signs in Eqs. (6.12.1) and (6.12.6) correspond to the right-handed and left-handed worm thread, respectively.

6.13 PROBLEMS

The problems presented in this section are directed at study of the derivation of the equation of meshing, the line of action (meshing), the envelope (the generated shape), and the conditions of undercutting. We limit the discussion in most cases to examples of planar gears, for the purpose of simplification.

Problem 6.13.1

Coordinate systems S_1, S_2, and S_f are rigidly connected to the rack-cutter, the spur gear being generated, and the frame, respectively (Fig. 6.13.1). The shape of the rack-cutter is a straight line that is represented in S_1 by the equations
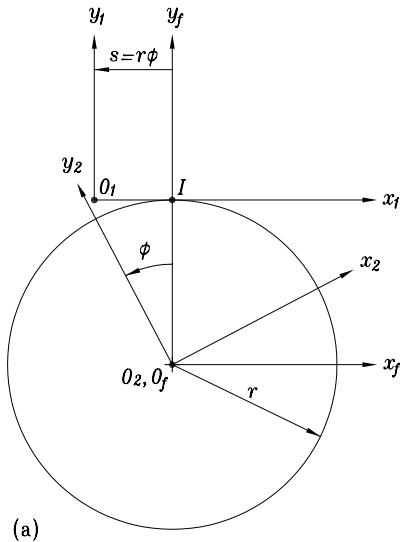
$$x_1 = u \sin \alpha, \qquad y_1 = u \cos \alpha, \qquad -u_1 < u < u_2. \tag{6.13.1}$$

Here, α is the shape angle (pressure angle); u is the variable parameter that determines the location of a current point on the shape of the rack-cutter ($u > 0$ for point M, and $u < 0$ for M^*). The instantaneous center of rotation is I. The gear centrode is the circle of radius r and the rack-cutter centrode coincides with the x_1 axis (Fig. 6.13.1). The displacement s of the rack-cutter and the angle ϕ of gear rotation are related by

$$s = r\phi. \tag{6.13.2}$$
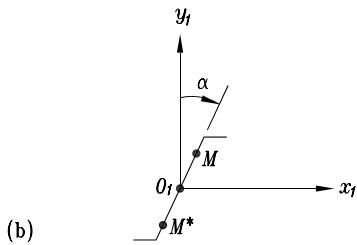
The problem is to derive the equation of meshing

$$f(u, \phi) = 0 \tag{6.13.3}$$

(a)

(b)

Figure 6.13.1: Applied coordinate systems for spur gear generation: (a) coordinate systems S_1 and S_2; (b) illustration of $u > 0$ for point M and $u < 0$ for point M^*.

using two approaches, considering that:

  (i) The normal to the generating shape at the point of contact must pass through the instantaneous center of rotation I.
 (ii) The current point of contact is determined with the equation

$$\mathbf{N}_1 \cdot \mathbf{v}_1^{(12)} = 0. \tag{6.13.4}$$

Here, $\mathbf{N}_1$ is the normal to the generating shape and $\mathbf{v}_1^{(12)}$ is the sliding velocity; both vectors are represented in S_1.

Solution

APPROACH 1. We consider the equation

$$\frac{X_1 - x_1}{N_{x1}} - \frac{Y_1 - y_1}{N_{y1}} = 0. \tag{6.13.5}$$

Here,

$$X_1 = r\phi, \qquad Y_1 = 0 \tag{6.13.6}$$

are the coordinates of I that are represented in S_1.

$$N_1 = T_1 \times k_1 = [\cos\alpha \quad -\sin\alpha \quad 0]^T \tag{6.13.7}$$

where T_1 and N_1 are the tangent and the normal to the generating shape, and k_1 is the unit vector of the z_1 axis. Equations (6.13.5) to (6.13.7) yield the following expression for the equation of meshing:

$$f(u,\phi) = u - r\phi\sin\alpha = 0. \tag{6.13.8}$$

APPROACH 2. The sliding vector $v_1^{(12)}$ is represented by the equation

$$v_1^{(12)} = v_1^{(1)} - v_1^{(2)} = -r\omega i_1 - [(\omega_1 \times r_1) + (R_1 \times \omega_1)]$$

$$= \begin{bmatrix} -r\omega \\ 0 \\ 0 \end{bmatrix} - \begin{bmatrix} -\omega u\cos\alpha \\ \omega u\sin\alpha \\ 0 \end{bmatrix} - \begin{bmatrix} -\omega r \\ -\omega r\phi \\ 0 \end{bmatrix} = \begin{bmatrix} \omega u\cos\alpha \\ \omega(-u\sin\alpha + r\phi) \\ 0 \end{bmatrix} \tag{6.13.9}$$

where

$$R_1 = [r\phi \quad -r \quad 0]^T$$

represents in S_1 coordinates of point O_2. Equations (6.13.4), (6.13.7), and (6.13.9) yield the same expression for the equation of meshing represented by (6.13.8).

Problem 6.13.2
With the conditions of Problem 6.13.1 derive equations of the line of action in meshing of the rack-cutter and the gear being generated.

Solution
The line of action is represented by the equations

$$r_f = M_{f1}r_1, \qquad f(u,\phi) = u - r\phi\sin\alpha = 0. \tag{6.13.10}$$

Then we obtain

$$x_f = u\sin\alpha - r\phi, \qquad y_f = u\cos\alpha + r, \qquad u - r\phi\sin\alpha = 0. \tag{6.13.11}$$

Equations (6.13.11) yield

$$x_f = -r\phi\cos^2\alpha, \qquad y_f = r + r\phi\sin\alpha\cos\alpha. \tag{6.13.12}$$

Line of action LK (Fig. 6.13.2) is a straight line that passes through I and forms the angle $(\pi - \alpha)$ with the x axis. Points of segment IK correspond to $\phi \geq 0$; points of segment IL correspond to $\phi \leq 0$.

Problem 6.13.3
With the conditions of Problem 6.13.1, derive the equations of the tooth shape for the generated gear.
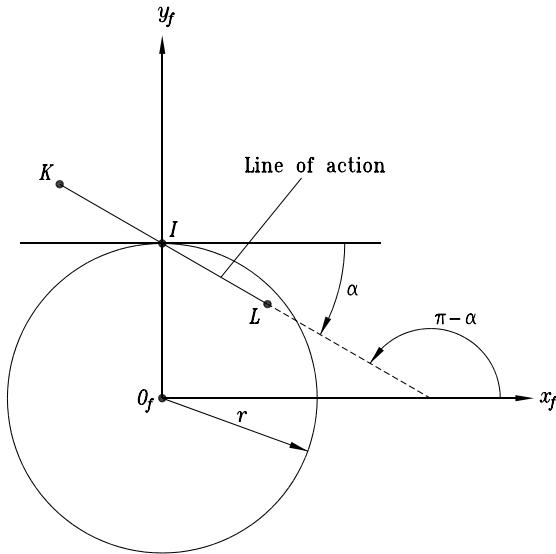
Figure 6.13.2: Line of action.

Solution

The tooth shape of the generated gear is represented by the equations

$$\mathbf{r}_2 = \mathbf{M}_{21}\mathbf{r}_1 = \mathbf{M}_{2f}\mathbf{M}_{f1}\mathbf{r}_1 \tag{6.13.13}$$

$$f(u, \phi) = u - r\phi \sin\alpha = 0 \tag{6.13.14}$$

where

$$\mathbf{M}_{21} = \begin{bmatrix} \cos\phi & \sin\phi & r(-\phi\cos\phi + \sin\phi) \\ -\sin\phi & \cos\phi & r(\phi\sin\phi + \cos\phi) \\ 0 & 0 & 1 \end{bmatrix}. \tag{6.13.15}$$
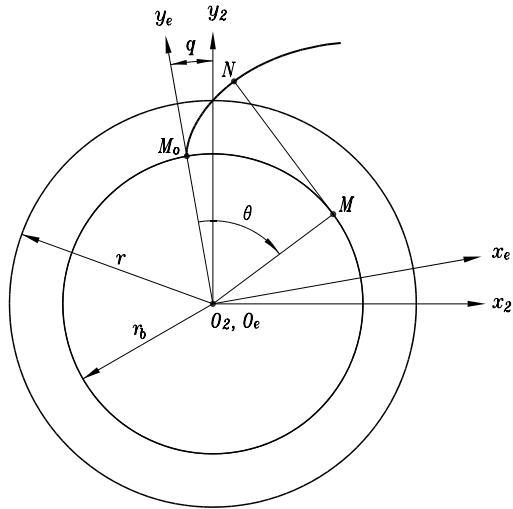
Here, matrix equation (6.13.13) describes the coordinate transformation from S_1 to S_2; Eq. (6.13.14) is the equation of meshing.

Equations (6.13.13) to (6.13.15) yield the following expressions for the generated shape of the gear tooth:

$$x_2 = u\sin(\phi + \alpha) + r(\sin\phi - \phi\cos\phi)$$

$$y_2 = u\cos(\phi + \alpha) + r(\cos\phi + \phi\sin\phi) \tag{6.13.16}$$

$$u - r\phi\sin\alpha = 0.$$

Equations (6.13.16) represent the generated shape (it is a planar curve) in two-parameter form by related parameters u and ϕ. However, in this particular case, because the equation of meshing is linear for parameter u, it is possible to eliminate u from Eqs. (6.13.16) and represent the generated shape in one-parameter form as follows:

$$x_2 = r\sin\phi - r\phi\cos\alpha\cos(\phi + \alpha)$$
$$y_2 = r\cos\phi + r\phi\cos\alpha\sin(\phi + \alpha). \tag{6.13.17}$$

Figure 6.13.3: Representation of generated involute curve.

We may verify that Eqs. (6.13.17) represent an involute curve that corresponds to the base circle $r_b = r \cos \alpha$. To prove it, let us set up a coordinate system $S_e(x_e, y_e)$ whose axis x_e (Fig. 6.13.3) forms with the x_2 axis the constant angle

$$q = \mathrm{inv}(\alpha) = \tan \alpha - \alpha.$$

The matrix representation of coordinate transformation is

$$\mathbf{r}_e = \mathbf{M}_{e2}\mathbf{r}_2 \tag{6.13.18}$$

where

$$\mathbf{M}_{e2} = \begin{bmatrix} \cos q & \sin q & 0 \\ -\sin q & \cos q & 0 \\ 0 & 0 & 1 \end{bmatrix}. \tag{6.13.19}$$

Equations (6.13.17) to (6.13.19) yield

$$x_e = r \sin(\phi + q) - r\phi \cos \alpha \cos(\phi + \alpha + q)$$
$$y_e = r \cos(\phi + q) + r\phi \cos \alpha \sin(\phi + \alpha + q).$$

Using substitutions
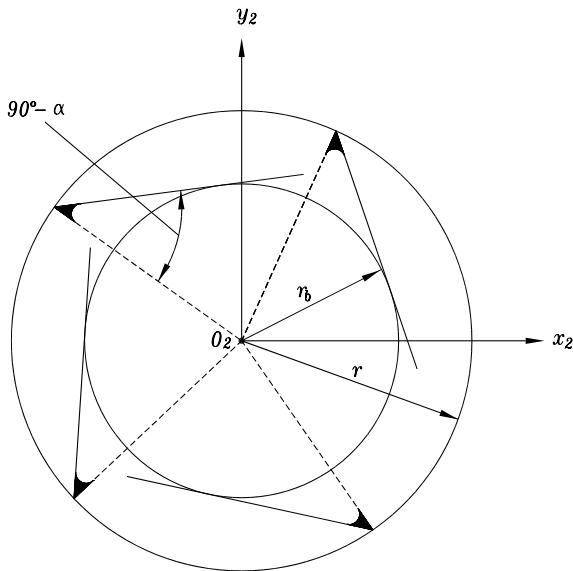
$$\phi + \alpha + q = \phi + \alpha + \mathrm{inv}(\alpha) = \phi + \tan \alpha = \theta, \quad \phi = \theta - \tan \alpha$$
$$\phi + q = \theta - \alpha, \quad r_b = r \cos \alpha,$$

we obtain

$$x_e = r_b(\sin \theta - \theta \cos \theta), \quad y_e = r_b(\cos \theta + \theta \sin \theta). \tag{6.13.20}$$

Equations (6.13.20) represent an involute curve (Fig. 6.13.3). This result – that the rack-cutter that is shown in Fig. 6.13.1 generates an involute curve – can be interpreted with the following considerations:

Figure 6.13.4: Contact normals in co-ordinate system S_2.

(i) The line of action by meshing of the rack-cutter with the gear is a straight line (Fig. 6.13.2).

(ii) The current contact normal has a constant orientation in the fixed coordinate S_f and coincides with the line of action.

(iii) The contact normals being represented in the coordinate system S_2 form a family of straight lines (Fig. 6.13.4); the envelope to the family of those straight lines is the circle of radius r_b, and the contact normals are tangent to their envelope.

(iv) The family of straight lines that is shown in Fig. 6.13.4 is also the family of contact normals to the tooth shape of the generated gear; the envelope of those straight lines is the *evolute* for the generated shape, and the generated shape is the *involute* with respect to the circle of radius r_b.

Problem 6.13.4

With the conditions of Problem 6.13.1, derive equations of the generated shape using the approach developed in differential geometry (see Section 6.1).

Solution

Step 1: Represent in S_2 equations of the family of the generating shapes using matrix equation

$$\mathbf{r}_2 = \mathbf{M}_{21}\mathbf{r}_1. \tag{6.13.21}$$

Equations (6.13.21) and (6.13.1) yield

$$\begin{aligned}
x_2 &= u\sin(\phi + \alpha) + r(\sin\phi - \phi\cos\phi) \\
y_2 &= u\cos(\phi + \alpha) + r(\cos\phi + \phi\sin\phi).
\end{aligned} \tag{6.13.22}$$

Step 2: Derive the equation of meshing as

$$\left(\frac{\partial \mathbf{r}_2}{\partial u} \times \mathbf{k}_2\right) \cdot \frac{\partial \mathbf{r}_2}{\partial \phi} = 0. \tag{6.13.23}$$

The cross product $\partial \mathbf{r}_2/\partial u \times \mathbf{k}_2$ represents in S_2 the normal to the generating shape, and $\partial \mathbf{r}_2/\partial \phi$ is collinear to $\mathbf{v}_2^{(12)}$.

Equations (6.13.22) and (6.13.23) after transformations will provide the equation of meshing as

$$f(u, \phi) = u - r\phi \sin \alpha = 0.$$

The generated shape is represented with the equations

$$x_2 = u \sin(\phi + \alpha) + r(\sin \phi - \phi \cos \phi)$$

$$y_2 = u \cos(\phi + \alpha) + r(\cos \phi + \phi \sin \phi) \tag{6.13.24}$$

$$f(u, \phi) = u - r\phi \sin \alpha = 0,$$

which coincide with previously derived Eqs. (6.13.16) (see Problem 6.13.3).

Problem 6.13.5

With the conditions of Problem 6.13.1, determine the limiting setting of the rack-cutter that will allow undercutting of the generated shape of the gear tooth to be avoided.

Solution

The limiting point of the shape of the rack-cutter is the point that generates the singular point on the gear tooth shape. The rack-cutter limiting point is determined with the equation of meshing,

$$f(u, \phi) = u - r\phi \sin \alpha = 0, \tag{6.13.25}$$

and the equation of undercutting,

$$F(u, \phi) = 0, \tag{6.13.26}$$

which can be obtained by using equations (see Section 6.3)
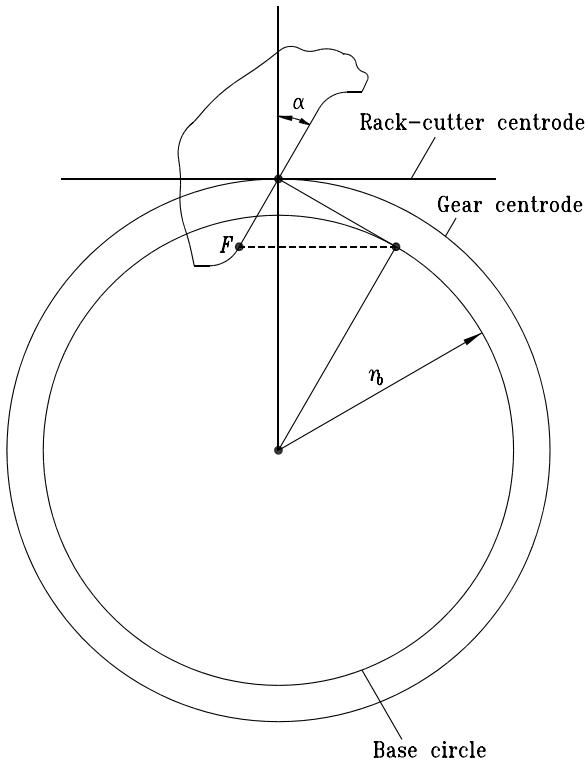
$$\begin{vmatrix} \dfrac{\partial x_1}{\partial u} & v_{x1}^{(12)} \\ f_u & f_\phi \dfrac{d\phi}{dt} \end{vmatrix} = \begin{vmatrix} \dfrac{\partial y_1}{\partial u} & v_{y1}^{(12)} \\ f_u & f_\phi \dfrac{d\phi}{dt} \end{vmatrix} = 0. \tag{6.13.27}$$

Equations (6.13.1), (6.13.9), (6.13.25), and (6.13.27) yield

$$\begin{vmatrix} \dfrac{\partial x_1}{\partial u} & v_{x1}^{(12)} \\ f_u & f_\phi \dfrac{d\phi}{dt} \end{vmatrix} = \begin{vmatrix} \sin \alpha & \omega u \cos \alpha \\ 1 & -\omega r \sin \alpha \end{vmatrix} = 0. \tag{6.13.28}$$

Then, we obtain that the limiting value for u is

$$u = -r \tan \alpha \sin \alpha. \tag{6.13.29}$$

Figure 6.13.5: Limiting setting of rack-cutter.

Similarly, using Eqs. (6.13.1), (6.13.9), (6.13.25), and (6.13.27), we obtain

$$
\begin{vmatrix}
\dfrac{\partial y_1}{\partial u} & v_{y1}^{(12)} \\[2mm]
f_u & f_\phi \dfrac{d\phi}{dt}
\end{vmatrix}
=
\begin{vmatrix}
\cos\alpha & \omega(-u\sin\alpha + r\phi) \\[1mm]
1 & -\omega r\sin\alpha
\end{vmatrix}
= 0.
$$

Then, taking into account Eq. (6.13.25), we obtain the same limiting value for u as given by Eq. (6.13.29).

Figure 6.13.5 illustrates the limiting setting of the rack-cutter when point F generates the singular point of the gear shape. Parameter u for point F is negative (recall the rule of signs for M and $M^\star$ in Fig. 6.13.1) and is determined with Eq. (6.13.29).

Problem 6.13.6

The fillet of the gear is generated by the circular arc of the rack-cutter centered at C_1 (Fig. 6.9.1). Coordinate systems S_1, S_2, and S_f are rigidly connected to the rack-cutter, the gear, and the frame, respectively (Fig. 6.13.1). Derive the equations of the gear fillet using the following procedure: (i) represent the circular arc of the rack-cutter (Σ_1) in coordinate system S_1; (ii) derive the equation of meshing using the rule that the contact normal passes through the instantaneous center of rotation, I; and (iii) represent equations of gear fillet (Σ_2) in coordinate system S_2.

Solution

Step 1: (Derivation of equations of shape Σ_1). The position vector of a current point M of the circular arc (Fig. 6.9.1) is represented by

$$\overline{O_1 M} = \overline{O_1 C_1} + \overline{C_1 M} \tag{6.13.30}$$

which yields

$$x_1 = a + \rho \sin \theta, \qquad y_1 = -b - \rho \cos \theta. \tag{6.13.31}$$

Here,

$$a = \frac{\pi - 5 \tan \alpha}{4P} - \frac{\rho(1 - \sin \alpha)}{\cos \alpha}, \qquad b = \frac{1.25}{P} - \rho$$

where P is the diametral pitch and $1.25/P$ is the addendum of the rack-cutter.

The normal to the generating shape Σ_1 is

$$\mathbf{N}_1 = \frac{\partial \mathbf{r}_1}{\partial \theta} \times \mathbf{k}_1 = \rho(\sin \theta \mathbf{i}_1 - \cos \theta \mathbf{j}_1) \tag{6.13.32}$$

where $\mathbf{i}_1$, $\mathbf{j}_1$, and $\mathbf{k}_1$ are the unit vectors of the coordinate axes of S_1.

Step 2: The equation of meshing is represented as

$$f(\theta, \phi) = \frac{X_1(\phi) - x_1(\theta)}{N_{x1}} - \frac{Y_1(\phi) - y_1(\theta)}{N_{y1}} = 0 \tag{6.13.33}$$

where (Fig. 6.13.1)

$$X_1(\phi) = r\phi, \qquad Y_1(\phi) = 0.$$

Equations (6.13.31), (6.13.32), and (6.13.33) yield

$$f(\theta, \phi) = r\phi - a + b \tan \theta = 0. \tag{6.13.34}$$

Step 3: (Equations of gear fillet). The generated gear fillet is represented by

$$\mathbf{r}_2 = \mathbf{M}_{21}\mathbf{r}_1 = \mathbf{M}_{2f}\mathbf{M}_{f1}\mathbf{r}_1, \qquad f(\theta, \phi) = 0. \tag{6.13.35}$$

These equations yield

$$x_2 = \rho \sin(\theta - \phi) + a \cos \phi - b \sin \phi + r(\sin \phi - \phi \cos \phi)$$

$$y_2 = -\rho \cos(\theta - \phi) - a \sin \phi - b \cos \phi + r(\cos \phi + \phi \sin \phi) \tag{6.13.36}$$
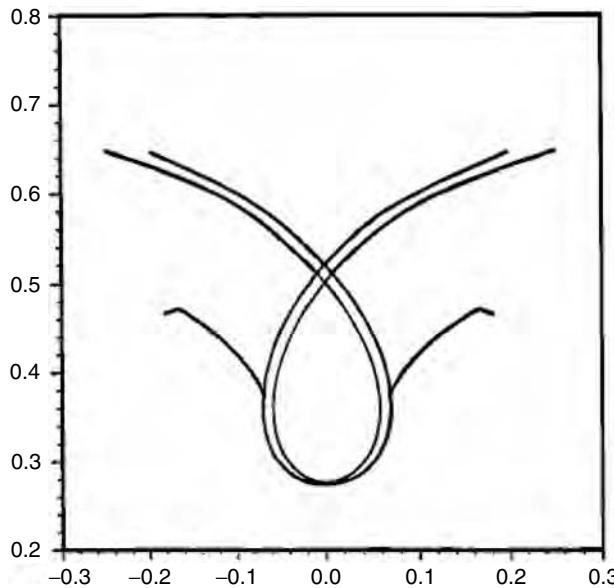
$$r\phi - a + b \tan \theta = 0.$$

The gear fillet for the case when the number of gear teeth is 10 and the profile angle of the rack-cutter is $20°$ is shown in Fig. 6.13.6. The gear is undercut, but undercutting can be avoided with special setting of the rack-cutter with respect to the gear (see Chapter 10).

Problem 6.13.7
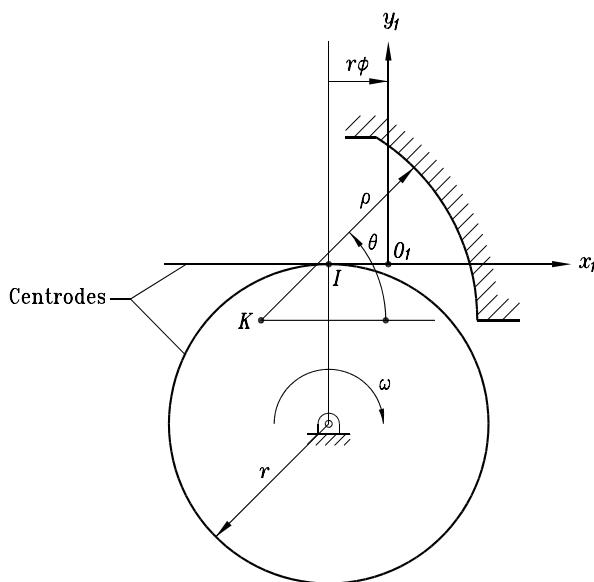
Consider the same coordinate systems as in Problem 6.13.1 (Fig. 6.13.1). Shape Σ_1 of the rack-cutter is a circular arc (Fig. 6.13.7) represented by equation

$$\mathbf{r}_1(\theta) = (a + \rho \cos \theta)\mathbf{i}_1 + (b + \rho \sin \theta)\mathbf{j}_1 \tag{6.13.37}$$
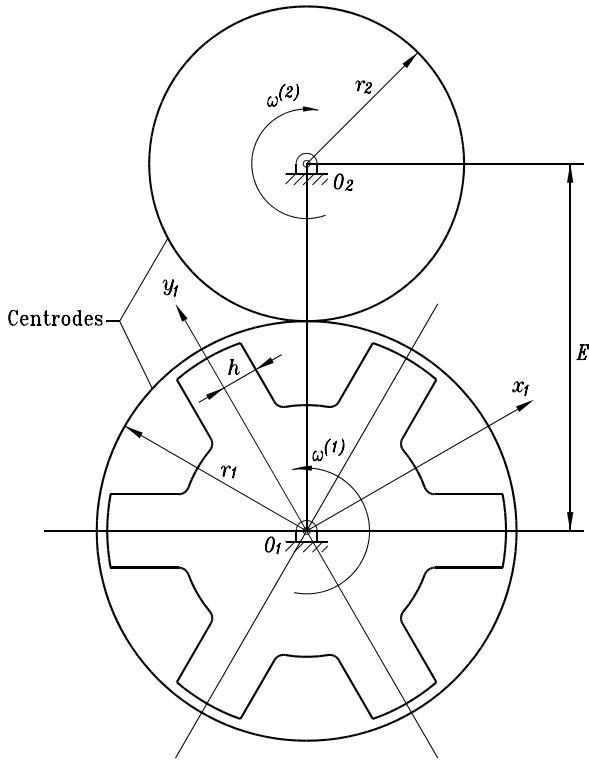
Figure 6.13.6: Involute profiles and gear fillets.

where a and b are the coordinates of point K – the center of the circular arc. Depending on the location of point K, parameters a and b may be positive or negative. Shape Σ_1 generates gear tooth shape Σ_2. Determine the limiting point of Σ_1 that generates the singular point of Σ_2.

Figure 6.13.7: Rack-cutter with circular arc profile.

Figure 6.13.8: Generation of multi-spline shaft.

DIRECTIONS. (a) Derive the equation of meshing. (b) Develop the relative velocity $\mathbf{v}_1^{(12)}$. (c) Determine the limiting point using the equation of nonundercutting (see Problem 6.13.5) and the equation of meshing.

Solution

$$(\sin\theta)^3 - \frac{b\sin\theta}{r} - \frac{b^2}{\rho r} = 0. \tag{6.13.38}$$

Problem 6.13.8

A multi-spline shaft is generated by a shaper. The shaft shape Σ_1 is represented by the equation (Fig. 6.13.8)

$$\mathbf{r}_1(\theta) = b\mathbf{i}_1 + \theta\mathbf{j}_1, \qquad \theta_{min} \leq \theta \leq \theta_{max}. \tag{6.13.39}$$

The angular velocity ratio by cutting is

$$m_{21} = \frac{\omega^{(2)}}{\omega^{(1)}} = \frac{r_1}{r_2} = \frac{N_1}{N_2}.$$

Here, r_1 and r_2 are the radii of the centrodes; N_1 and N_2 are the numbers of "teeth" of the shaft and the tool, respectively. The "undercutting" of the tool shape Σ_2 by shape Σ_1 (the interference of Σ_1 and Σ_2) does not occur if the tool shape is a regular curve

(it does not have singular points). Develop an equation that relates the limiting value of θ, the radius r_1 of the shaft centrode, and the angular velocity ratio m_{21}.

DIRECTIONS. (a) Develop the equation of meshing. (b) Derive the equation of relative velocity $\mathbf{v}_1^{(12)}$. (c) Determine the limiting point of Σ_1 using the equations of meshing and nonundercutting (see Problem 6.13.5).

Solution

$$r_1^2 - \theta^2 - \left(\frac{1+m_{21}}{2+m_{21}}\right)^2 h^2 = 0.$$

Consider m_{21} as given. To avoid undercutting, observe the following inequality:

$$r_1^2 \geq \theta_{max}^2 + \left(\frac{1+m_{21}}{2+m_{21}}\right)^2 h^2.$$

Here,

$$\theta_{max}^2 = r_a^2 - h^2$$

where r_a is the radius of the shaft addendum circle.

Problem 6.13.9

Interaction of a screw surface with a surface of revolution is the subject of this problem. The screw surface can be identified as the envelope to the family of surfaces of revolution that is generated in a relative screw motion that is performed with a constant or varied screw parameter. The surface of revolution might be a cylinder, a cone, a spherical surface, a toroid, or another surface.
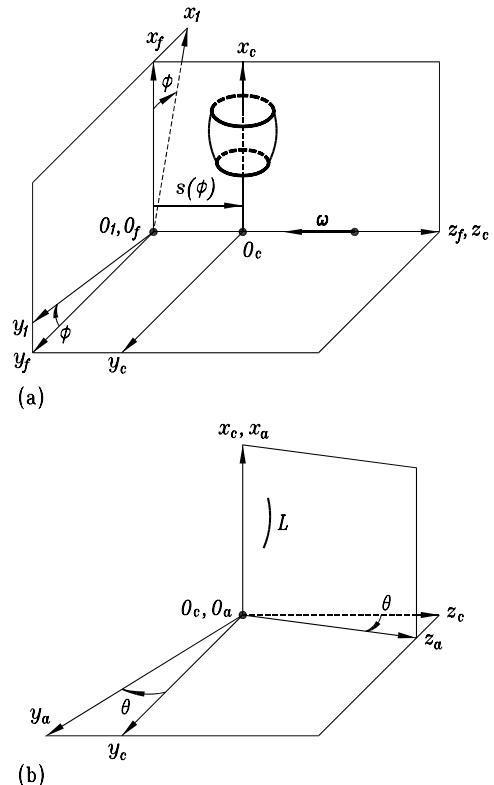
The discussed problem is related to the interaction of a spatial cam and a follower, in the generation of a screw by a tool. The follower (the tool) is provided with a surface of revolution and performs the prescribed screw motion with respect to the cam (the screw).

Figure 6.13.9(a) shows coordinate systems S_1, S_c, and S_f that are rigidly connected to the blank, the tool, and the frame, respectively; axis z_1 is the axis of the screw. While the blank rotates through angle ϕ, the tool translates along the z_f axis on the distance $s(\phi)$, where $s(\phi)$ is a prescribed function. The derivative ds/dt is represented as

$$\frac{ds}{dt} = p(\phi)\omega$$

where $p(\phi)$ is the varied screw parameter; ϕ is the angle of rotation. In a particular case, $p(\phi)$ is a constant and represents the ordinary screw parameter $p = H/2\pi$, where H is the lead – the axial displacement in a screw motion that corresponds to one revolution.

The solution to this problem is represented in a general form and covers the derivation of: (a) equations of tool surface, Σ_c; (b) the equation of meshing; (c) equations of the generated screw surface, Σ_1; and (d) equations of nonundercutting of Σ_1.

Figure 6.13.9: Generation of screw surface by finger-shaped cutter: (a) illustration of coordinate system S_f, S_1, and S_c; (b) illustration of generation of tool surface Σ_c by planar curve L, and illustration of coordinate system S_c of the tool and auxiliary coordinate system S_a.

Solution

EQUATIONS OF TOOL SURFACE. We can imagine that the tool surface Σ_c is generated by a planar curve L that is rotated about the x_c axis. Curve L is represented in auxiliary coordinate system S_a [Fig. 6.13.9(b)] by equations

$$x_a = f_1(u), \qquad y_a = 0, \qquad z_a = f_2(u)$$

where u is the varied parameter that determines the current point on L.

Using equations of coordinate transformation from S_a to S_c, we obtain the following equations of Σ_c:

$$x_c = f_1(u), \qquad y_c = f_2(u)\sin\theta, \qquad z_c = f_2(u)\cos\theta. \tag{6.13.40}$$

The normal to Σ_c is

$$\mathbf{N}_c = \frac{\partial \mathbf{r}_c}{\partial u} \times \frac{\partial \mathbf{r}_c}{\partial \theta} = \begin{bmatrix} -\dfrac{\partial f_2}{\partial u} \\[2mm] \dfrac{\partial f_1}{\partial u}\sin\theta \\[2mm] \dfrac{\partial f_1}{\partial u}\cos\theta \end{bmatrix}. \tag{6.13.41}$$

NOTE. The common factor $f_2(u)$ has been eliminated from the final expression for $\mathbf{N}_c$.

RELATIVE VELOCITY. The relative velocity $\mathbf{v}^{(c1)}$ is represented in S_c by the equation

$$\mathbf{v}_c^{(c1)} = \mathbf{v}_c^{(c)} - \mathbf{v}_c^{(1)} = p(\phi)\omega\mathbf{k}_c - \boldsymbol{\omega}_c \times \mathbf{r}_c = \omega \begin{bmatrix} -f_2(u)\sin\theta \\ f_1(u) \\ p(\phi) \end{bmatrix}. \quad (6.13.42)$$

EQUATION OF MESHING. Using the equation

$$\mathbf{N}_c \cdot \mathbf{v}_c^{(c1)} = 0$$

we obtain

$$\left[f_2(u)\frac{\partial f_2}{\partial u} + f_1(u)\frac{\partial f_1}{\partial u} \right]\sin\theta + p(\phi)\frac{\partial f_1}{\partial u}\cos\theta = f(u,\theta,\phi) = 0. \quad (6.13.43)$$

EQUATIONS OF GENERATED SCREW SURFACE Σ_1. Using the coordinate transformation from S_c to S_1 and the equation of meshing, we obtain

$$\begin{aligned}
x_1 &= f_1(u)\cos\phi - f_2(u)\sin\phi\sin\theta \\
y_1 &= f_1(u)\sin\phi + f_2(u)\cos\phi\sin\theta \\
z_1 &= f_2(u)\cos\theta + s(\phi) \\
f(u,\theta,\phi) &= 0.
\end{aligned} \quad (6.13.44)$$

CONDITIONS OF NONUNDERCUTTING. Using equations

$$\begin{vmatrix} \dfrac{\partial x_c}{\partial u} & \dfrac{\partial x_c}{\partial \theta} & v_{xc}^{(c1)} \\[2mm] \dfrac{\partial y_c}{\partial u} & \dfrac{\partial y_c}{\partial \theta} & v_{yc}^{(c1)} \\[2mm] f_u & f_\theta & f_\phi\dfrac{d\phi}{dt} \end{vmatrix} = \begin{vmatrix} \dfrac{\partial x_c}{\partial u} & \dfrac{\partial x_c}{\partial \theta} & v_{xc}^{(c1)} \\[2mm] \dfrac{\partial z_c}{\partial u} & \dfrac{\partial z_c}{\partial \theta} & v_{zc}^{(c1)} \\[2mm] f_u & f_\theta & f_\phi\dfrac{d\phi}{dt} \end{vmatrix} = \begin{vmatrix} \dfrac{\partial y_c}{\partial u} & \dfrac{\partial y_c}{\partial \theta} & v_{yc}^{(c1)} \\[2mm] \dfrac{\partial z_c}{\partial u} & \dfrac{\partial z_c}{\partial \theta} & v_{zc}^{(c1)} \\[2mm] f_u & f_\theta & f_\phi\dfrac{d\phi}{dt} \end{vmatrix} = 0 \quad (6.13.45)$$

we obtain the equation

$$F(u,\theta,\phi) = 0. \quad (6.13.46)$$

To avoid undercutting of Σ_1, the generating surface Σ_c must be limited with the line determined as

$$\mathbf{r}_c(u,\theta), \qquad f(u,\theta,\phi) = 0, \qquad F(u,\theta,\phi) = 0. \quad (6.13.47)$$

Problem 6.13.10
Using the general approach represented in Problem 6.13.9, consider the generation of a screw surface by a cylinder. Function $s(\phi)$ is a linear function and $ds/d\phi = p$ where p is a constant (the screw parameter). Derive equations of generating surface

Σ_c, the equation of meshing, and equations of generated surface Σ_1, and determine conditions of nonundercutting.

DIRECTIONS. Consider that the tool surface is generated by a straight line that is represented in S_a by equations

$$x_a = f_1(u) = u, \qquad y_a = 0, \qquad z_a = f_2(u) = \rho \qquad (6.13.48)$$

where ρ is the radius of the cylinder.

Solution
Equations of generating surface Σ_c are

$$x_c = u, \qquad y_c = \rho \sin \theta, \qquad z_c = \rho \cos \theta. \qquad (6.13.49)$$

The normal to Σ_c is

$$\mathbf{N}_c = [0 \quad \sin \theta \quad \cos \theta]^{\mathsf{T}}. \qquad (6.13.50)$$

The relative velocity is

$$\mathbf{v}_c^{(c1)} = \omega[-\rho \sin \theta \quad u \quad p]^{\mathsf{T}}. \qquad (6.13.51)$$

The equation of meshing is

$$\mathbf{n}_c \cdot \mathbf{v}_c^{(c1)} = \omega(u \sin \theta + p \cos \theta) = f(u, \theta) = 0. \qquad (6.13.52)$$
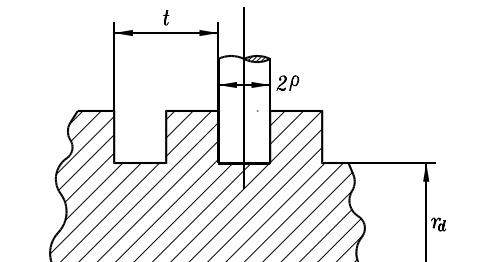
In this particular case, the equation of meshing does not contain the parameter of motion ϕ. The equation of meshing provides two solutions, one for each side of the surface being generated.

The generated surface can be represented in this particular case in two-parameter form because the equation of meshing is linear with respect to u. Thus, we obtain

$$x_1 = -p \cot \theta \cos \phi - \rho \sin \phi \sin \theta$$
$$y_1 = -p \cot \theta \sin \phi + \rho \cos \phi \sin \theta \qquad (6.13.53)$$
$$z_1 = \rho \cos \theta + p\phi.$$

Equations (6.13.45) result in

$$p^2 - \rho^2 \sin^4 \theta = 0, \qquad (6.13.54)$$

Figure 6.13.10: Design parameters of screw generated by cylindrical cutter.

which yields

$$\cos 2\theta = 1 - \frac{2p}{\rho}. \tag{6.13.55}$$

Equation (6.13.54) and equation of meshing (6.13.52) considered together enable us to determine the limiting value of u from the equation

$$u = \pm\frac{\rho}{2}\sin 2\theta. \tag{6.13.56}$$

Only the positive value of u should be taken into account.

We may transform Eqs. (6.13.54) and (6.13.56) taking into account the following relations (Fig. 6.13.10): (a) the screw parameter $p = H/2\pi$ where H is the lead; (b) the axial distance $t = H/N$ where N is the number of threads of the screw; and (c) (we may choose) $\rho = t/4 = H/4N$. Then we obtain the following limiting value for θ:

$$\cos 2\theta = 1 - \frac{4N}{\pi}. \tag{6.13.57}$$

A real solution for θ exists if $\cos 2\theta \geq -1$ and yields $2N/\pi \leq 1$. This means that undercutting can only occur for single-thread screws ($N = 1$).

Equations (6.13.57) and (6.13.56) with $N = 1$ and $\rho = H/4$ yield the following limiting value for u:

$$u = \frac{H}{2\pi}\left(\frac{\pi - 2}{2}\right)^{1/2}. \tag{6.13.58}$$

Equation (6.13.58) determines the limiting value of the radius r_d of the dedendum circle (Fig. 6.13.10). Undercutting will not occur even for single-thread screws if

$$r_d > \frac{H}{\pi}\left(\frac{\pi - 2}{2}\right)^{1/2}. \tag{6.13.59}$$

7 Curvatures of Surfaces and Curves

7.1 INTRODUCTION

The information on surface curvatures is required for computerized simulation of contact of gear tooth surfaces (see Chapter 9), and grinding of ruled undeveloped surfaces (see Chapter 26). The main ideas of surface curvatures have been developed in differential geometry by many distinguished scientists. This chapter provides condensed information about the basic equations of surface curvatures. For more details, we refer the reader to Nutbourne & Martin [1988], Finikov [1961], Favard [1957], Rashevski [1956], and Vigodsky [1949]. The chapter covers the following basic topics:

(1) Representation of a spatial curve in 3D-space and on a surface
(2) Geodesic and normal curvatures
(3) Curve and surface torsions
(4) First and second fundamental forms
(5) Principal curvatures and directions and three types of surface points.

7.2 SPATIAL CURVE IN 3D-SPACE
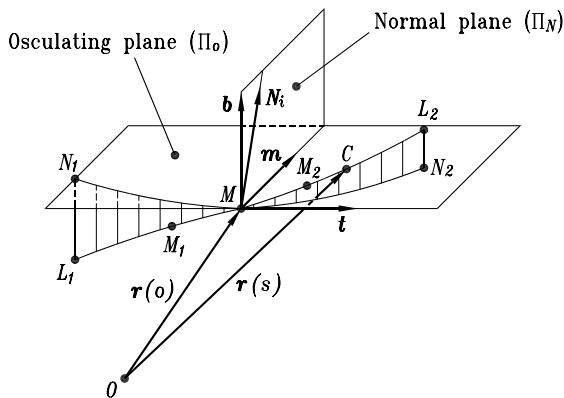
Osculating Plane
Figure 7.2.1 shows spatial curve $L_1 M L_2$. The *osculating* plane is the limiting position of such a plane that passes through curve points M_1, M, and M_2 as M_1 and M_2 approach M. The osculating plane for a curve at its regular point M is formed by the *tangent* to the curve and the *acceleration* vector for the same point.

The osculating plane and the curve are in tangency of *second* order. The osculating plane is an exceptional tangent plane: the deviations of the curve from the osculating plane are of different signs at two sides from the point of tangency, and the curve is above and below the plane (see points L_1 and L_2 in Fig. 7.2.1). An exception is the case when the point of tangency is a *rectification* point at which the second derivative $\mathbf{r}_{ss}$ of a curve represented by $\mathbf{r}(s)$ is equal to zero. Here, s is the arc length of the curve.

Space Curve Trihedron
We consider a coordinate system that is rigidly connected to the curve. Position vector $\overline{OC} = \mathbf{r}(s)$ determines the *current* point C of the curve (Fig. 7.2.1); $s = \overset{\frown}{MC}$ is the length
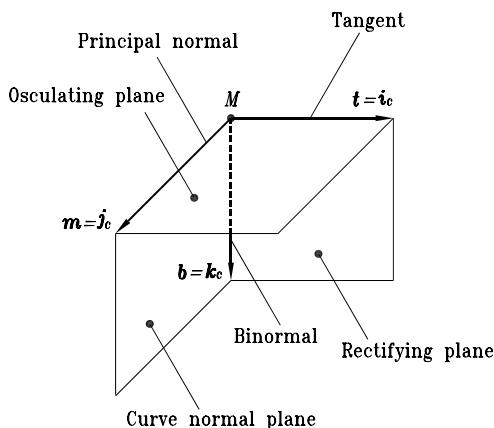
Figure 7.2.1: Osculating and normal planes.

of the curve arc; M is the *starting* point. Consider that a small piece of curve $L_1 M L_2$ is located in the osculating plane Π_o (Fig. 7.2.1). Plane Π_N is perpendicular to plane Π_o and passes through point M of the curve.

We define the normal $\mathbf{N}$ to the curve as a vector that is perpendicular to the tangent to the curve. There is an infinite number of normals $\mathbf{N}$ to the curve at its point M. All of the normals $\mathbf{N}$ belong to plane Π_N because the unit tangent $\mathbf{t}$ is perpendicular to Π_N. For instance, vector $\mathbf{N}_i$ is one of the set of curve normals (Fig. 7.2.1). Two normals of the set of normals must be specified:

 (i)   The *principal* normal with the unit vector $\mathbf{m}$ that lies in the osculating plane Π_o and is the line of intersection of Π_o and Π_N (Fig. 7.2.1)
(ii)   The *binormal* $\mathbf{b}$ that is perpendicular to $\mathbf{t}$ and $\mathbf{m}$ simultaneously.

We may identify at each *current* point of the curve three mutually orthogonal vectors (Fig. 7.2.1): the *tangent* vector $\mathbf{t}$, the *principal normal* $\mathbf{m}$, and the *binormal* $\mathbf{b}$. The orientation of these vectors in a fixed coordinate system varies, depending on the location of the point on the curve. We may consider now a trihedron S_c as a rigid body with three mutually perpendicular vectors $\mathbf{e}_c(\mathbf{i}_c,\ \mathbf{j}_c,\ \mathbf{k}_c)$ that form a right trihedron (Fig. 7.2.2). The origin of the trihedron moves along the curve, and the unit vectors $\mathbf{i}_c, \mathbf{j}_c$, and $\mathbf{k}_c$ represent

Figure 7.2.2: Curve trihedron.

t, m, and **b,** respectively. Unit vectors **t, m,** and **b** are taken at the current point of the curve where the origin of trihedron S_c is located at this instant.

The representation of unit vectors **t, m,** and **b** in terms of derivatives of vector function **r**(s) is based on the following considerations:

(i) Unit vectors **t, m,** and **b** form a right-hand trihedron (Figs. 7.2.1 and 7.2.2). Thus

$$\mathbf{t} = \mathbf{m} \times \mathbf{b}, \quad \mathbf{m} = \mathbf{b} \times \mathbf{t}, \quad \mathbf{b} = \mathbf{t} \times \mathbf{m}. \tag{7.2.1}$$

(ii) Unit vector **t** is directed along the tangent to the curve and therefore

$$\mathbf{t}(s) = \frac{d\mathbf{r}}{ds} = \mathbf{r}_s. \tag{7.2.2}$$

Vector $\mathbf{r}_s$ is a unit vector because $|d\mathbf{r}| = ds$.

(iii) The principal normal to the curve is perpendicular to the curve tangent $\mathbf{t} = \mathbf{r}_s$. The derivative $\mathbf{r}_{ss} = (d/ds)(\mathbf{r}_s)$ is perpendicular to $\mathbf{r}_s$ and lies in the osculating plane. Therefore, the unit vector **m** of the principal normal is represented as

$$\mathbf{m}(s) = \frac{\mathbf{r}_{ss}}{|\mathbf{r}_{ss}|}. \tag{7.2.3}$$

(iv) Taking into account the expression for **b** in Eqs. (7.2.1), we obtain the following equation for the binormal:

$$\mathbf{b}(s) = \mathbf{t} \times \mathbf{m} = \frac{\mathbf{r}_s \times \mathbf{r}_{ss}}{|\mathbf{r}_{ss}|}.$$

Because the direction of **b** is the same as that of vector $(\mathbf{r}_s \times \mathbf{r}_{ss})$, and **b** is a unit vector, we also obtain that

$$\mathbf{b}(s) = \frac{\mathbf{r}_s \times \mathbf{r}_{ss}}{|\mathbf{r}_s \times \mathbf{r}_{ss}|}.$$

The final expressions for **b** are

$$\mathbf{b}(s) = \frac{\mathbf{r}_s \times \mathbf{r}_{ss}}{|\mathbf{r}_{ss}|} = \frac{\mathbf{r}_s \times \mathbf{r}_{ss}}{|\mathbf{r}_s \times \mathbf{r}_{ss}|}. \tag{7.2.4}$$

Equations (7.2.4) yield

$$|\mathbf{r}_{ss}| = |\mathbf{r}_s \times \mathbf{r}_{ss}|, \tag{7.2.5}$$

and this relation is used in derivations below.

The designation of $\mathbf{t}(s)$, $\mathbf{m}(s)$, and $\mathbf{b}(s)$ indicates that the unit vectors are functions of s, the length of the curve arc. The change of direction of measurement for s causes the directions of **t** and **b** to change to their opposites, but not the direction of **m**. At a point of rectification the deviation of the curve from the tangent is not less than third order, because $\mathbf{r}_{ss} = 0$ at such a point. The orientation of **m** must be based on derivative $\mathbf{r}_{sss}$ or even $\mathbf{r}_{ssss}$.

Frenet–Serret Equations

These equations enable us to derive the matrix equation

$$\mathbf{e}_{sc} = \mathbf{L}_c \mathbf{e}_c \qquad (7.2.6)$$

where

$$\mathbf{e}_c = [\mathbf{t}_c \quad \mathbf{m}_c \quad \mathbf{b}_c]^\mathrm{T}, \qquad \mathbf{e}_{sc} = \frac{d}{ds}(\mathbf{e}_c) = [\mathbf{t}_{sc} \quad \mathbf{m}_{sc} \quad \mathbf{b}_{sc}]^\mathrm{T}.$$

The designation "c" indicates that the vectors are represented in S_c. The designation "sc" for a vector, say $\mathbf{t}_{sc}$, means that the derivative $(d/ds)(\mathbf{t}_c)$ is considered and represented in S_c. Matrix $\mathbf{L}_c$ is a 3×3 skew-symmetric matrix whose elements are represented in terms of the *curvature* and the *torsion* of the spatial curve (see below). The procedure for derivation of $\mathbf{e}_{sc}$ and $\mathbf{L}_c$ is as follows.

Step 1: [Determination of $\mathbf{t}_s$ (the subscript "c" has been dropped)].

The curvature κ_o of a spatial curve is determined as

$$\kappa_o = \lim \left| \frac{\Delta\phi}{\Delta s} \right|_{\Delta s \to 0} \qquad (7.2.7)$$

where $\Delta\phi$ is the angle formed by the tangents taken at the given and neighboring curve points; Δs is the arc length between the neighboring points; the subscript "o" in κ_o indicates that the curvature is considered for a small piece of the curve located in the osculating plane.

It is known from vector analysis that because $\mathbf{t}(s)$ is a unit vector, the derivative $\mathbf{t}_s$ is perpendicular to $\mathbf{t}$, and the magnitude of $\mathbf{t}_s$ is represented by the equation

$$|\mathbf{t}_s| = \lim \left| \frac{\Delta\phi}{\Delta s} \right|_{\Delta s \to 0} \qquad (7.2.8)$$

where $\Delta\phi$ is the angle formed by unit vectors $\mathbf{t}(s)$ and $\mathbf{t}(s + \Delta s)$. We may illustrate Eq. (7.2.8) with the following considerations:

(i) Figure 7.2.3(a) shows that unit vectors $\mathbf{t}(s)$ and $\mathbf{t}(s + \Delta s)$ (the tangents to the curve at neighboring points M_1 and M_2) form angle $\Delta\phi$.

(ii) Figure 7.2.3(b) shows vectors $\mathbf{t}(s)$ and $\mathbf{t}(s + \Delta s)$ that are drawn from the same origin O, where

$$\mathbf{t}(s + \Delta s) = \mathbf{t}(s) + \Delta\mathbf{t}. \qquad (7.2.9)$$
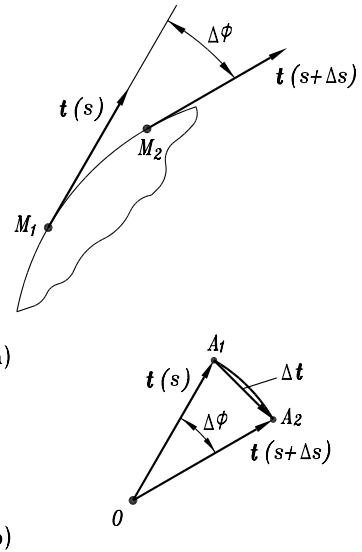
(iii) It is obvious that $\overset{\frown}{A_1 A_2} = \Delta\phi$ because $|\overline{OA_1}| = |\overline{OA_2}| = 1$, and $|\Delta\mathbf{t}| \approx \Delta\phi$. Then, we obtain

$$|\mathbf{t}_s| = \left| \frac{d\mathbf{t}}{ds} \right| = \lim \left| \frac{\Delta\phi}{\Delta s} \right|_{\Delta s \to 0}. \qquad (7.2.10)$$

Equations (7.2.7), (7.2.8), and (7.2.10) yield

$$|\mathbf{t}_s| = \kappa_o. \qquad (7.2.11)$$

It was mentioned above that $\mathbf{t}_s$ is perpendicular to $\mathbf{t}$; it has the same direction as $\mathbf{r}_{ss}$ and

Figure 7.2.3: For derivation of derivative $\dfrac{d}{ds}(\mathbf{t}_c)$.

(a)

(b)

$\mathbf{m}$. Thus, the final expression for $\mathbf{t}_s$ is

$$\mathbf{t}_s = \kappa_o \mathbf{m}. \qquad (7.2.12)$$

Step 2: (Determination of $\mathbf{b}_s$).
Consider the cross product for $\mathbf{b}$ in Eq. (7.2.1). After differentiation, we obtain

$$\mathbf{b}_s = \frac{d}{ds}(\mathbf{b}) = (\mathbf{t}_s \times \mathbf{m}) + (\mathbf{t} \times \mathbf{m}_s). \qquad (7.2.13)$$

Taking into account Eq. (7.2.12), and that $\mathbf{m}_s \cdot \mathbf{m} = 0$, we obtain

$$\mathbf{b}_s = \mathbf{t} \times \mathbf{m}_s = (\mathbf{m} \times \mathbf{b}) \times \mathbf{m}_s = -(\mathbf{m}_s \cdot \mathbf{b})\mathbf{m}. \qquad (7.2.14)$$

Equation (7.2.14) yields that the derivative $\mathbf{b}_s$ is directed opposite to $\mathbf{m}$ and that $|\mathbf{b}_s| = |\mathbf{m}_s \cdot \mathbf{b}|$.

We may interpret $|\mathbf{b}_s|$ as the *torsion* τ of the curve using considerations that are similar to those discussed in Step 1:

(i)

$$\tau = \lim \left| \frac{\Delta\theta}{\Delta s} \right|_{\Delta s \to 0} \qquad (7.2.15)$$

where $\Delta\theta$ is the angle formed between two osculating planes (or vectors $\mathbf{b}$) determined at two neighboring points.

(ii) It is known from linear algebra (see Step 1 and drawings similar to Fig. 7.2.3) that

$$\lim \left| \frac{\Delta\theta}{\Delta s} \right|_{\Delta s \to 0} = |\mathbf{b}_s|. \qquad (7.2.16)$$

Equations (7.2.14) to (7.2.16) yield the following equation:

$$\mathbf{b}_s = -\tau\mathbf{m}. \qquad (7.2.17)$$

Step 3: We consider the cross product for **m** in Eq. (7.2.1). After differentiation, we obtain

$$\mathbf{m}_s = \frac{d}{ds}(\mathbf{m}) = (\mathbf{b}_s \times \mathbf{t}) + (\mathbf{b} \times \mathbf{t}_s) = \mathbf{b}_s \times (\mathbf{m} \times \mathbf{b}) + (\mathbf{t} \times \mathbf{m}) \times \mathbf{t}_s$$

$$= -(\mathbf{b}_s \cdot \mathbf{m})\mathbf{b} - (\mathbf{t}_s \cdot \mathbf{m})\mathbf{t}. \tag{7.2.18}$$

Equations (7.2.12), (7.2.17), and (7.2.18) yield

$$\mathbf{m}_s = \tau\mathbf{b} - \kappa_o\mathbf{t}. \tag{7.2.19}$$

Step 4: Summary of obtained results:

$$\mathbf{e}_s = \begin{bmatrix} \mathbf{t}_s \\ \mathbf{m}_s \\ \mathbf{b}_s \end{bmatrix} = \begin{bmatrix} \kappa_o\mathbf{m} \\ \tau\mathbf{b} - \kappa_o\mathbf{t} \\ -\tau\mathbf{m} \end{bmatrix}. \tag{7.2.20}$$

Step 5: [Final expression for matrix equation (7.2.6)].
Equations (7.2.6) and (7.2.20) yield

$$\begin{bmatrix} \mathbf{t}_{sc} \\ \mathbf{m}_{sc} \\ \mathbf{b}_{sc} \end{bmatrix} = \begin{bmatrix} \kappa_o\mathbf{m}_c \\ \tau\mathbf{b}_c - \kappa_o\mathbf{t}_c \\ -\tau\mathbf{m}_c \end{bmatrix} = \begin{bmatrix} 0 & \kappa_o & 0 \\ -\kappa_o & 0 & \tau \\ 0 & -\tau & 0 \end{bmatrix} \begin{bmatrix} \mathbf{t}_c \\ \mathbf{m}_c \\ \mathbf{b}_c \end{bmatrix}. \tag{7.2.21}$$

Determination of κ_o and τ for a Curve Represented by r(s)

Our goal is to represent κ_o and τ in terms of derivatives of vector function $\mathbf{r}(s)$. Recall that the unit vectors of trihedron $\mathbf{e}_c$ have been represented by Eqs. (7.2.2), (7.2.3), and (7.2.4), respectively. The determination of curve curvature κ_o is based on the following considerations: Equation (7.2.11) yields

$$|\mathbf{t}_s| = \left|\frac{d}{ds}(\mathbf{t})\right| = \left|\frac{d}{ds}(\mathbf{r}_s)\right| = |\mathbf{r}_{ss}| = \kappa_o.$$

Taking Eq. (7.2.5) into account as well, we obtain that

$$\kappa_o = |\mathbf{r}_{ss}| = |\mathbf{r}_s \times \mathbf{r}_{ss}|. \tag{7.2.22}$$

It is easy to verify that the curvature κ_o may also be represented by the equation

$$\kappa_o = |\mathbf{r}_{ss}| = \frac{\mathbf{r}_{ss}^2}{|\mathbf{r}_{ss}|} = \mathbf{r}_{ss} \cdot \frac{\mathbf{r}_{ss}}{|\mathbf{r}_{ss}|} = \mathbf{r}_{ss} \cdot \mathbf{m}. \tag{7.2.23}$$

Equation (7.2.23) will be used in further derivations.

The derivation of torsion τ in terms of derivatives of vector function $\mathbf{r}(s)$ is based on the following considerations:

Step 1: (Derivation of $\mathbf{r}_{ss}$).
Equation (7.2.23) yields

$$\mathbf{r}_{ss} = \kappa_o\mathbf{m}. \tag{7.2.24}$$

Step 2: (Derivation of $\mathbf{r}_{sss}$).
Differentiation of Eq. (7.2.24) yields

$$\mathbf{r}_{sss} = \kappa_s\mathbf{m} + \kappa_o\mathbf{m}_s \tag{7.2.25}$$

where $\kappa_s = (d/ds)(\kappa_o)$. Using Eqs. (7.2.19) and (7.2.25), we obtain

$$\mathbf{r}_{sss} = \kappa_s \mathbf{m} + \kappa_o(\tau \mathbf{b} - \kappa_o \mathbf{t}). \tag{7.2.26}$$

Step 3: (Derivation of $\mathbf{r}_s \times \mathbf{r}_{ss}$).
Using Eq. (7.2.24) and taking into account that

$$\mathbf{r}_s = \mathbf{t}, \qquad \mathbf{t} \times \mathbf{m} = \mathbf{b},$$

we obtain

$$\mathbf{r}_s \times \mathbf{r}_{ss} = \mathbf{t} \times \kappa_o \mathbf{m} = \kappa_o \mathbf{b}. \tag{7.2.27}$$

Step 4: [Derivation of $\mathbf{r}_{sss} \cdot (\mathbf{r}_s \times \mathbf{r}_{ss})$].
Equations (7.2.26) and (7.2.27) yield

$$\mathbf{r}_{sss} \cdot (\mathbf{r}_s \times \mathbf{r}_{ss}) = \kappa_o^2 \tau. \tag{7.2.28}$$

Step 5: (Final expression of τ).
Equations (7.2.22), (7.2.27), and (7.2.28) yield

$$\tau = \frac{\mathbf{r}_{sss} \cdot (\mathbf{r}_s \times \mathbf{r}_{ss})}{\mathbf{r}_{ss}^2} = \frac{\mathbf{r}_{sss} \cdot \mathbf{b}}{\kappa_o}. \tag{7.2.29}$$

Equations (7.2.22) and (7.2.29) enable us to determine the curvature κ_o and the torsion τ for a curve represented by vector function $\mathbf{r}(s)$.

Determination of κ_o and τ for a Curve Represented by Vector Function $\mathbf{r}(\theta)$

Representation of a spatial curve by vector function $\mathbf{r}(s)$ enables us to simplify the derivation of Frenet–Serret equations. Usually, a spatial curve is represented by vector function $\mathbf{r}(\theta)$, where θ is the curve parameter. Our goal is to derive equations for determination of the curve curvature κ_o and curve torsion τ for such curve representation. We may use for this purpose the equations that have been derived for the curve $\mathbf{r}(s)$, considering that s and θ are related by function $s(\theta)$. Then, the curve to be discussed can be represented as $\mathbf{r}(s(\theta))$. Differentiation of this vector function yields

$$\mathbf{r}_\theta = \mathbf{r}_s \frac{ds}{d\theta}. \tag{7.2.30}$$

Here,

$$\frac{ds}{d\theta} = |\mathbf{r}_\theta| \quad \text{because} \quad |\mathbf{r}_s| = 1 \tag{7.2.31}$$

$$\mathbf{r}_{\theta\theta} = \mathbf{r}_{ss} \left(\frac{ds}{d\theta}\right)^2 + \mathbf{r}_s \left(\frac{d^2 s}{d\theta^2}\right) \tag{7.2.32}$$

$$\mathbf{r}_{\theta\theta\theta} = \mathbf{r}_{sss} \left(\frac{ds}{d\theta}\right)^3 + 3\mathbf{r}_{ss} \left(\frac{ds}{d\theta}\right) \left(\frac{d^2 s}{d\theta^2}\right) + \mathbf{r}_s \left(\frac{d^3 s}{d\theta^3}\right). \tag{7.2.33}$$

Equations (7.2.30) to (7.2.33) yield

$$\mathbf{r}_s \times \mathbf{r}_{ss} = \frac{\mathbf{r}_\theta \times \mathbf{r}_{\theta\theta}}{\left(\dfrac{ds}{d\theta}\right)^3} = \frac{\mathbf{r}_\theta \times \mathbf{r}_{\theta\theta}}{|\mathbf{r}_\theta|^3}. \tag{7.2.34}$$

Equations (7.2.33), (7.2.34), and (7.2.31) yield

$$\mathbf{r}_s \cdot (\mathbf{r}_{ss} \times \mathbf{r}_{sss}) = \frac{\mathbf{r}_\theta \cdot (\mathbf{r}_{\theta\theta} \times \mathbf{r}_{\theta\theta\theta})}{\left(\dfrac{ds}{d\theta}\right)^6} = \frac{\mathbf{r}_\theta \cdot (\mathbf{r}_{\theta\theta} \times \mathbf{r}_{\theta\theta\theta})}{|\mathbf{r}_\theta|^6}. \tag{7.2.35}$$

Equations (7.2.30), (7.2.34), and (7.2.35) are the basis for determination of unit vectors $\mathbf{t}$, $\mathbf{m}$, and $\mathbf{b}$ and for the derivation of κ_o and τ for a curve given by $\mathbf{r}(\theta)$. The representation of unit vectors $\mathbf{t}$, $\mathbf{m}$, and $\mathbf{b}$ in terms of derivatives of vector function $\mathbf{r}(\theta)$ is based on the following derivations.

Step 1: Unit vector $\mathbf{t}$ may be represented as

$$\mathbf{t} = \frac{\mathbf{r}_\theta}{|\mathbf{r}_\theta|}. \tag{7.2.36}$$

Step 2: For derivations of $\mathbf{b}$ we use equations (7.2.4) and (7.2.34) which yield

$$\mathbf{b} = \frac{\mathbf{r}_\theta \times \mathbf{r}_{\theta\theta}}{|\mathbf{r}_\theta \times \mathbf{r}_{\theta\theta}|}. \tag{7.2.37}$$

Step 3: Unit vector $\mathbf{m}$ is represented as

$$\mathbf{m} = \mathbf{b} \times \mathbf{t}. \tag{7.2.38}$$

Equations (7.2.36), (7.2.37), and (7.2.38) yield

$$\mathbf{m} = \mathbf{b} \times \mathbf{t} = \frac{(\mathbf{r}_\theta \times \mathbf{r}_{\theta\theta}) \times \mathbf{r}_\theta}{|\mathbf{r}_\theta \times \mathbf{r}_{\theta\theta}||\mathbf{r}_\theta|}. \tag{7.2.39}$$

It is important to recognize for further discussions that vector $\mathbf{m}$ has the same direction as $\mathbf{r}_{ss}$ and forms an acute angle with $\mathbf{r}_{\theta\theta}$. The inequality

$$\mathbf{r}_{\theta\theta} \cdot \mathbf{m} > 0 \qquad (\mathbf{r}_{\theta\theta} \neq \mathbf{0}) \tag{7.2.40}$$

is based on Eq. (7.2.32) which yields

$$\mathbf{r}_{\theta\theta} \cdot \mathbf{r}_{ss} = \mathbf{r}_{ss}^2 \left(\frac{ds}{d\theta}\right)^2. \tag{7.2.41}$$

Recall that we have designated by $\mathbf{e}_s(s)$ the 3D vector represented as [see Eq. (7.2.20)]

$$\mathbf{e}_s(s) = [\mathbf{t}_s \quad \mathbf{m}_s \quad \mathbf{b}_s]^{\mathrm{T}}.$$

A similar 3D vector $\mathbf{e}_\theta(\theta)$ can be represented as

$$\mathbf{e}_\theta(\theta) = [\mathbf{t}_\theta \quad \mathbf{m}_\theta \quad \mathbf{b}_\theta]^{\mathrm{T}} = \frac{ds}{d\theta}\mathbf{e}_s = |\mathbf{r}_\theta| [\mathbf{t}_s \quad \mathbf{m}_s \quad \mathbf{b}_s]^{\mathrm{T}}. \tag{7.2.42}$$

Our final goal is to derive equations for determination of κ_o and τ for a spatial curve represented by vector function $\mathbf{r}(\theta)$. The derivation of such equations is based on the following procedure.

Determination of κ_o

Equations (7.2.22), (7.2.23), (7.2.31), (7.2.32), and (7.2.39) yield

$$\kappa_o = \frac{\mathbf{r}_{\theta\theta} \cdot \mathbf{m}}{\mathbf{r}_\theta^2} = \frac{|\mathbf{r}_\theta \times \mathbf{r}_{\theta\theta}|}{|\mathbf{r}_\theta|^3}$$

$$= \frac{[(x_\theta y_{\theta\theta} - x_{\theta\theta} y_\theta)^2 + (x_\theta z_{\theta\theta} - x_{\theta\theta} z_\theta)^2 + (y_\theta z_{\theta\theta} - y_{\theta\theta} z_\theta)^2]^{1/2}}{\left(x_\theta^2 + y_\theta^2 + z_\theta^2\right)^{3/2}}. \quad (7.2.43)$$

We may also represent κ_o in terms of $\mathbf{m}$, $\mathbf{v}_r$, and $\mathbf{a}_r$. Here, $\mathbf{v}_r$ and $\mathbf{a}_r$ are the velocity and acceleration of a point that moves along the spatial curve and are represented by the equations

$$\mathbf{v}_r = \mathbf{r}_\theta \frac{d\theta}{dt} \quad (7.2.44)$$

$$\mathbf{a}_r = \mathbf{r}_{\theta\theta} \left(\frac{d\theta}{dt}\right)^2 + \mathbf{r}_\theta \left(\frac{d^2\theta}{dt^2}\right). \quad (7.2.45)$$

The subscript "r" indicates that the *relative* point motion, *along* the curve, is considered to differentiate it from the *transfer* point motion when the point moves together *with* the curve.
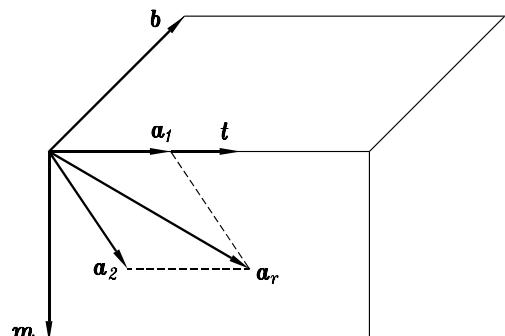
Our goal is to prove that the curvature can be represented by the equation

$$\kappa_o = \frac{\mathbf{a}_r \cdot \mathbf{m}}{\mathbf{v}_r^2}. \quad (7.2.46)$$

Equations (7.2.44), (7.2.45), and (7.2.46) yield

$$\kappa_o = \frac{\mathbf{r}_{\theta\theta} \cdot \mathbf{m}}{\mathbf{r}_\theta^2},$$

which coincides with the expression in (7.2.43), and this is the proof of the correctness of Eq. (7.2.46). Acceleration vector $\mathbf{a}_r$ [see Eq. (7.2.45)] has two components: $\mathbf{a}_1 = \mathbf{r}_\theta (d^2\theta/dt^2)$ and $\mathbf{a}_2 = \mathbf{r}_{\theta\theta}(d\theta/dt)^2$. Component $\mathbf{a}_1$ is collinear to the tangent vector $\mathbf{t}$, and its direction is the same as $\mathbf{t}$ or opposite to $\mathbf{t}$ depending on the sign of $d^2\theta/dt^2$. The second component lies in the osculating plane and forms an acute angle with $\mathbf{m}$ (Fig. 7.2.4).

Figure 7.2.4: Representation of acceleration vector for spatial curve.

Derivation of τ

We have represented the curve torsion τ by [see Eq. (7.2.29)]

$$\tau(s) = \frac{\mathbf{r}_{sss} \cdot \mathbf{b}}{\kappa_o} \qquad (7.2.47)$$

where [see Eq. (7.2.43)]

$$\kappa_o = \frac{|\mathbf{r}_\theta \times \mathbf{r}_{\theta\theta}|}{|\mathbf{r}_\theta|^3}.$$
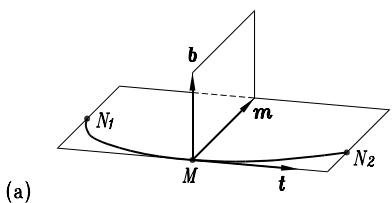
Equations (7.2.4), (7.2.34), (7.2.35), (7.2.43), and (7.2.47) yield

$$\tau(\theta) = \frac{(\mathbf{r}_\theta \times \mathbf{r}_{\theta\theta}) \cdot \mathbf{r}_{\theta\theta\theta}}{(\mathbf{r}_\theta \times \mathbf{r}_{\theta\theta})^2}. \qquad (7.2.48)$$
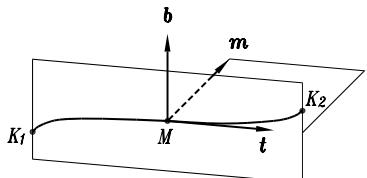
The sign of torsion can be positive or negative (see below).

Structure of Spatial Curve at the Curve Point

The osculating plane divides the space curve L_1ML_2 into two parts that are *above* and *below* the osculating plane (Fig. 7.2.1); only curve point M lies in the osculating plane. Projections of the curve on the planes of the trihedron are shown in Fig. 7.2.5. When the point moves along the curve counterclockwise, from M to C (Fig. 7.2.1), and the torsion is *positive*, the part L_1M of the curve is *below* the osculating plane, and ML_2 is *above* the osculating plane. The terms "below" and "above" are used for observation from $\mathbf{b}$. In the case of a *negative* torsion, but with the same direction of s, curve part L_1M will be *above* the osculating plane, and ML_2 will be
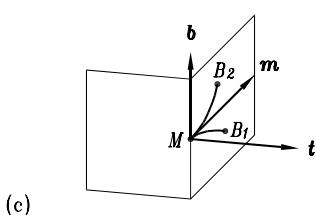
(a)

(b)

Figure 7.2.5: Representation of spatial curve in planes of trihedron.

(c)

below the osculating plane. It is obvious that the torsion is zero at any point of a planar curve. Positive and negative torsions are equivalent to the terms *right-hand* and *left-hand* screws (see Problem 7.2.1 below).

Equation of Osculating Plane

Consider that the curve is represented by vector function $\mathbf{r}(\theta)$ and that $\mathbf{r}(\theta_o)$ is the position vector of the starting point. Vectors $\mathbf{r}_\theta$ and $\mathbf{r}_{\theta\theta}$ form the osculating plane. Vector $\mathbf{R} = \mathbf{r}(\theta) - \mathbf{r}(\theta_o)$ lies in the osculating plane as well, and $\mathbf{R}$, $\mathbf{r}_\theta$, and $\mathbf{r}_{\theta\theta}$ are coplanar. Thus, the equation

$$[\mathbf{r}(\theta) - \mathbf{r}(\theta_o)] \cdot (\mathbf{r}_\theta \times \mathbf{r}_{\theta\theta}) = 0 \tag{7.2.49}$$

represents the osculating plane at curve point $\mathbf{r}(\theta_o)$.

Problem 7.2.1

Consider a right-hand helix that is represented in coordinate system S_o by equations

$$x_o = \rho \cos\theta, \qquad y_o = \rho \sin\theta, \qquad z_o = p\theta$$

where $p > 0$. Here, $p = \rho \tan\lambda$; λ is the lead angle. The starting curve point is determined with $\theta = 0$.

Determine:

(i) The unit vectors $\mathbf{t}_o$, $\mathbf{m}_o$, and $\mathbf{b}_o$ [use Eqs. (7.2.36), (7.2.37), and (7.2.39), respectively, and represent the vectors in coordinate system S_o].
(ii) Curvature κ_o and torsion τ [use Eqs. (7.2.43) and (7.2.48)].
(iii) Derive the matrix equation for coordinate transformation from S_o to S_c ($\mathbf{t}_c$, $\mathbf{m}_c$, $\mathbf{b}_c$), where S_c is the curve trihedron; the origin of S_c is placed into a point determined by $\mathbf{r}_o(\theta_o)$.

   Direction: use matrix equation

$$\mathbf{r}_c = \mathbf{M}_{cp}\mathbf{M}_{po}\mathbf{r}_o.$$

   Matrix $\mathbf{M}_{po}$ describes coordinate transformation from S_o to S_p; coordinate axes of S_p are parallel to axes of S_o; the origin O_p is located at the point determined by $\mathbf{r}_o(\theta_o)$.
(iv) Derive equations of the helix in S_c, and plot projections of the helix on coordinate planes of S_c. Verify that the structure of the helix in the neighborhood of O_c is similar to the structure represented in Fig. 7.2.5.

Solution
(i)

$$\mathbf{t}_o = [0 \quad \cos\lambda \quad \sin\lambda]^\mathsf{T}; \qquad \mathbf{m}_o = [-1 \quad 0 \quad 0]^\mathsf{T}; \qquad \mathbf{b}_o = [0 \quad -\sin\lambda \quad \cos\lambda]^\mathsf{T}.$$

(ii)

$$\kappa_o = \frac{\rho}{\rho^2 + p^2} = \frac{\cos^2\lambda}{\rho}; \qquad \tau = \frac{p}{\rho^2 + p^2} = \frac{\sin^2\lambda}{p}$$

($\tau > 0$ for a right-hand helix because $p > 0$; $\tau < 0$ for a left-hand helix because $p < 0$).

(iii) Matrix $\mathbf{M}_{co}$ is

$$\mathbf{M}_{co} = \begin{bmatrix} 0 & \cos \lambda & \sin \lambda & 0 \\ -1 & 0 & 0 & \rho \\ 0 & -\sin \lambda & \cos \lambda & 0 \\ 0 & 0 & 0 & 1 \end{bmatrix}.$$

(iv)

$$x_c = \rho \sin \theta \cos \lambda + p\theta \sin \lambda$$
$$y_c = \rho(1 - \cos \theta)$$
$$z_c = -\rho \sin \theta \sin \lambda + p\theta \cos \lambda.$$

Verify that within the neighborhood of $\theta = 0$ the curve is similar to that shown in Fig. 7.2.5.

7.3 SURFACE CURVES

We have to differentiate two cases of spatial curves: (a) the spatial curve that is determined in the 3D-space in one-parameter form (see Section (7.2)), and (b) the spatial curve that is represented in the 3D-space belongs to the given surface (see below). In the second case the spatial curve is determined in two-parameter form but the parameters are related. Some of the curve features in this case depend on the properties of the given surface (see below).

Surface Curve Trihedron
Consider a regular surface Σ that is represented by
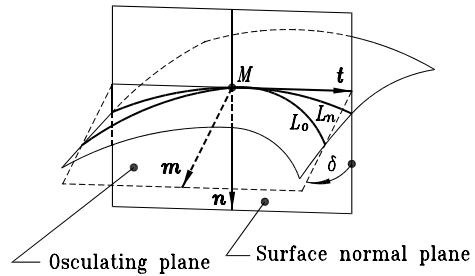
$$\mathbf{r}(u, \theta) \in C^2, \qquad \mathbf{r}_u \times \mathbf{r}_\theta \neq \mathbf{0}, \qquad (u, \theta) \in A. \qquad (7.3.1)$$

A curve on Σ is determined if in vector function $\mathbf{r}(u, \theta)$ surface parameters are related with the equation
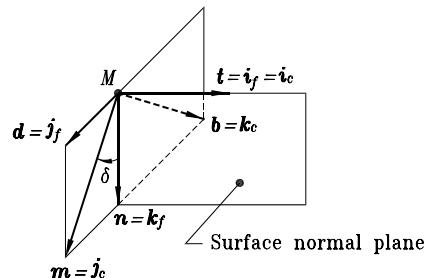
$$f(u, \theta) = 0, \quad \text{provided } (f_u^2 + f_\theta^2 \neq 0) \qquad (7.3.2)$$

Figure 7.3.1 shows two curves, L_n and L_o, that pass through the *same* surface point M and have the *same* tangent. Curve L_n is a planar curve obtained by intersection of the surface by the surface normal plane that is drawn through the unit tangent $\mathbf{t}$ and the surface unit normal $\mathbf{n}$. Curve L_o is a spatial curve identified *locally* with the orientation of the osculating plane, the curvature, and the torsion of the curve (see Section 7.2). Considering that a spatial curve belongs to a surface, we may determine more parameters for the local identification of the curve.

We introduced in Section 7.2 the curve trihedron $S_c(\mathbf{i}_c, \mathbf{j}_c, \mathbf{k}_c)$ where $\mathbf{i}_c = \mathbf{t}$ is the unit tangent, $\mathbf{j}_c = \mathbf{m}$ is the curve principal normal, and $\mathbf{k}_c = \mathbf{b}$ is the curve binormal [Figs. 7.2.2 and 7.3.1(b)]. In addition, we set up the surface trihedron $S_f(\mathbf{i}_f, \mathbf{j}_f, \mathbf{k}_f)$ shown in Fig. 7.3.1(b). Here, $\mathbf{i}_f = \mathbf{t}$ is the unit tangent to the spatial curve; $\mathbf{j}_f = \mathbf{d}$ is

Figure 7.3.1 (a): Osculating plane — Surface normal plane

(a)

Figure 7.3.1: Surface trihedron.

(b)

the unit vector that is perpendicular to $\mathbf{t}$ and lies in the plane tangent to the surface at point M; $\mathbf{k}_f = \mathbf{n}$ is the surface unit normal. The subscript " f " indicates that the surface ("fläche" in German) trihedron and its axes are considered.

The unit tangent $\mathbf{i}_f = \mathbf{i}_c = \mathbf{t}$ is determined as

$$\mathbf{t} = \frac{\mathbf{T}}{|\mathbf{T}|}, \quad \mathbf{T} = \mathbf{r}_u + \mathbf{r}_\theta \frac{d\theta}{du} = \mathbf{r}_u - \mathbf{r}_\theta \frac{f_u}{f_\theta}, \quad (f_\theta \neq 0) \tag{7.3.3}$$

[see Eqs. (7.3.1) and (7.3.2)]. The surface unit normal is represented as

$$\mathbf{n} = \frac{\mathbf{N}}{|\mathbf{N}|}, \quad \mathbf{N} = \mathbf{r}_u \times \mathbf{r}_\theta, \quad (\mathbf{n} = \mathbf{k}_f). \tag{7.3.4}$$

Changing the order in the cross product in Eq. (7.3.4), we can change the direction of $\mathbf{n}$ for the opposite one and provide that $\delta < 90°$, where δ is formed by $\mathbf{n}$ and $\mathbf{m}$. Recall that the direction of $\mathbf{m}$ is the same as $\mathbf{r}_{ss}$ and cannot be chosen arbitrarily. Unit vectors $\mathbf{t}$, $\mathbf{d}$, and $\mathbf{n}$ form the right trihedron S_f.

Determination of Derivatives $\mathbf{t}_s$, $\mathbf{d}_s$, $\mathbf{n}_s$

Consider that the common origin of the two trihedrons moves along the given surface curve. The 3D vectors $\mathbf{e}_f(\mathbf{t}, \mathbf{d}, \mathbf{n})$ and $\mathbf{e}_c(\mathbf{t}, \mathbf{m}, \mathbf{b})$ are functions of the arc lengths of the curve; angle δ is also a function of s. Our goal is to determine the derivatives $\mathbf{t}_s$, $\mathbf{d}_s$, and $\mathbf{n}_s$. The procedure of derivation is as follows.

Step 1: Coordinate transformation in transition from S_c to S_f is represented by matrix equation

$$\mathbf{e}_f = \mathbf{L}_{fc}\mathbf{e}_c. \tag{7.3.5}$$

Here [Fig. 7.3.1(b)],

$$\mathbf{L}_{fc} = \begin{bmatrix} 1 & 0 & 0 \\ 0 & \sin\delta & -\cos\delta \\ 0 & \cos\delta & \sin\delta \end{bmatrix}. \tag{7.3.6}$$

Step 2: Differentiation of Eq. (7.3.5) yields

$$\frac{d}{ds}(\mathbf{e}_f) = \frac{d}{ds}(\mathbf{L}_{fc})\mathbf{e}_c + \mathbf{L}_{fc}\frac{d}{ds}(\mathbf{e}_c). \tag{7.3.7}$$

Here,

$$\frac{d}{ds}(\mathbf{L}_{fc}) = \begin{bmatrix} 0 & 0 & 0 \\ 0 & \delta_s\cos\delta & \delta_s\sin\delta \\ 0 & -\delta_s\sin\delta & \delta_s\cos\delta \end{bmatrix} \tag{7.3.8}$$

where $\delta_s = (d/ds)(\delta)$.

Step 3: We take into account [see Eq. (7.2.6)] that

$$\frac{d}{ds}(\mathbf{e}_c) = \mathbf{e}_{sc} = \mathbf{L}_c\mathbf{e}_c \tag{7.3.9}$$

and

$$\mathbf{e}_c = \mathbf{L}_{cf}\mathbf{e}_f \tag{7.3.10}$$

where

$$\mathbf{L}_{cf} = (\mathbf{L}_{fc})^{\mathsf{T}}. \tag{7.3.11}$$

Equations (7.3.7), (7.3.9), and (7.3.10) yield

$$\mathbf{e}_{sf} = \left[\frac{d}{ds}(\mathbf{L}_{fc}) + \mathbf{L}_{fc}\mathbf{L}_c\right]\mathbf{L}_{cf}\mathbf{e}_f = \mathbf{L}_f\mathbf{e}_f. \tag{7.3.12}$$

Here,

$$\mathbf{L}_f = \left[\frac{d}{ds}(\mathbf{L}_{fc}) + \mathbf{L}_{fc}\mathbf{L}_c\right]\mathbf{L}_{cf} \tag{7.3.13}$$

is the curvature matrix for the surface curve trihedron.

Step 4: Matrix $\mathbf{L}_f$ is a skew-symmetric one and is represented as

$$\mathbf{L}_f = \begin{bmatrix} 0 & \kappa_o\sin\delta & \kappa_o\cos\delta \\ -\kappa_o\sin\delta & 0 & \tau+\delta_s \\ -\kappa_o\cos\delta & -(\tau+\delta_s) & 0 \end{bmatrix} = \begin{bmatrix} 0 & \kappa_g & \kappa_n \\ -\kappa_g & 0 & t \\ -\kappa_n & -t & 0 \end{bmatrix}. \tag{7.3.14}$$

Here, $\kappa_g = \kappa_o\sin\delta$ is the *geodesic curvature*, $\kappa_n = \kappa_o\cos\delta$ is the *normal curvature*, and $t = \tau + \delta_s$ is the *surface torsion*. The concepts of geodesic curvature and normal curvature are discussed below.

Step 5: Equations (7.3.12) and (7.3.14) yield the following final expressions for $(d/ds)(\mathbf{e}_f)$:

$$
\begin{aligned}
\mathbf{t}_s &= \kappa_g \mathbf{d} + \kappa_n \mathbf{n} = \kappa_g \mathbf{j}_f + \kappa_n \mathbf{k}_f \\
\mathbf{d}_s &= -\kappa_g \mathbf{t} + t\mathbf{n} = -\kappa_g \mathbf{i}_f + t\mathbf{k}_f \\
\mathbf{n}_s &= -\kappa_n \mathbf{t} - t\mathbf{d} = -\kappa_n \mathbf{i}_f - t\mathbf{j}_f.
\end{aligned}
\tag{7.3.15}
$$

Equations (7.3.15) are known as the Bonnet–Kovalevski relations (see Favard [1957]).

We have to emphasize that the normal curvature κ_n and the surface torsion t must be considered as the properties of the surface where the spatial curve is located. Only the geodesic curvature κ_g of the curve can be considered as the parameter that specifies the spatial curve uniquely but in a local sense (within the neighborhood of a given point).

Figure 7.3.3 shows a set of spatial curves L_o that are on the surface Σ and are in tangency with each other at the surface point M. Surface Σ is considered as given. Vector $\mathbf{t}$ is the unit vector of the common tangent to the set of curves L_o. All of these curves have the same normal curvature κ_n as stated in Meusnier's theorem (see curvature of spatial curve below and Fig. 7.3.4) and the same surface torsion as stated in Bonnet's theorem [see Section 7.9, Eq. (7.9.17)]. Curves of the set of L_o differ from each other only by the geodesic curvature. It is shown below that κ_n and t can be determined for the given surface if the surface point M and the direction of the unit tangent $\mathbf{t}$ are specified.

Equations for determination of κ_n and t are represented in Sections 7.4 and 7.9, respectively. The information about κ_g and t is required when grinding with optimal approximation is considered (Chapter 26). The information about t is required as well when the meshing of misaligned surfaces that are initially in line contact is considered (see Section 9.6). The visualization of geodesic curvature κ_g is discussed in this section (see below). The visualization of surface torsion is based on the concept of geodesic line and is discussed in Section 7.9.

Velocity and Acceleration

Consider that a point moves along a surface curve. Expressions of velocity and acceleration for the point motion are used in equations for determination of curve curvature. The surface curve is determined with Eqs. (7.3.1) and (7.3.2); function $\theta(u) \in C^2$ that relates surface parameters is known at curve point M and within its neighborhood.

The velocity $\mathbf{v}_r$ is represented by the equation

$$
\mathbf{v}_r = \mathbf{r}_u \frac{du}{dt} + \mathbf{r}_\theta \frac{d\theta}{dt} = \left(\mathbf{r}_u + \mathbf{r}_\theta \frac{d\theta}{du} \right) \frac{du}{dt} = \mathbf{T} \frac{du}{dt}
\tag{7.3.16}
$$

where

$$
\mathbf{T} = \mathbf{r}_u + \mathbf{r}_\theta \frac{d\theta}{du}
$$

is the curve tangent at M. The acceleration is represented by the equation

$$
\begin{aligned}
\mathbf{a}_r &= \frac{d}{dt}(\mathbf{v}_r) \\
&= \left[\mathbf{r}_{uu} + 2\mathbf{r}_{u\theta} \frac{d\theta}{du} + \mathbf{r}_{\theta\theta} \left(\frac{d\theta}{du} \right)^2 \right] \left(\frac{du}{dt} \right)^2 + \mathbf{T}\frac{d^2u}{dt^2} + \mathbf{r}_\theta \frac{d^2\theta}{du^2} \left(\frac{du}{dt} \right)^2 \\
&= (\mathbf{a} + \mathbf{c}) \left(\frac{du}{dt} \right)^2 + \mathbf{T}\frac{d^2u}{dt^2}.
\end{aligned}
\tag{7.3.17}
$$

Here,
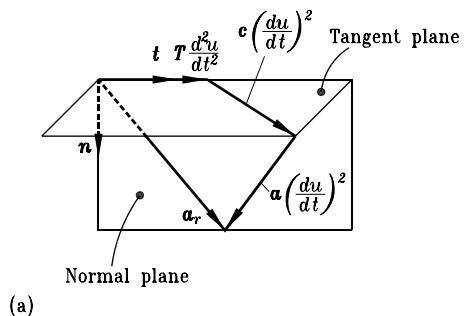
$$
\mathbf{a} = \mathbf{r}_{uu} + 2\mathbf{r}_{u\theta}\frac{d\theta}{du} + \mathbf{r}_{\theta\theta}\left(\frac{d\theta}{du} \right)^2
\tag{7.3.18}
$$

$$
\mathbf{c} = \mathbf{r}_\theta \frac{d^2\theta}{du^2}.
\tag{7.3.19}
$$
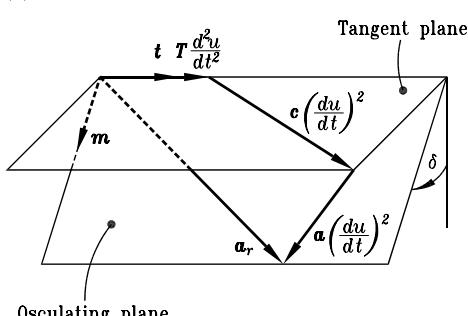
The direction of tangent $\mathbf{T}$ depends on the derivative $d\theta/du$. Our goal is to determine the derivative $d^2\theta/du^2$ considering as given the direction of the tangent $\mathbf{T}$ to the spatial curve and angle δ that is formed by the normal and the osculating plane (Fig. 7.3.1).

The requirement that the acceleration vector must lie in the osculating plane can be represented by the equation (Fig. 7.3.2)

$$
\mathbf{a}_r \cdot (\mathbf{t} \times \mathbf{m}) = \mathbf{a}_r \cdot \mathbf{b} = 0.
\tag{7.3.20}
$$

(a)

(b)

Figure 7.3.2: Representation of acceleration vector for surface spatial curve.

The component $\mathbf{T}(d^2u/dt^2)$ of the acceleration vector is perpendicular to $\mathbf{b}$ (Fig. 7.3.1). Thus

$$(\mathbf{a} + \mathbf{c}) \cdot \mathbf{b} = 0. \tag{7.3.21}$$

For further derivations, we use matrix equation (7.3.5), matrix (7.3.6), and the inverse matrix equation that relates trihedrons $\mathbf{e}_c = [\mathbf{t} \quad \mathbf{m} \quad \mathbf{b}]^T$ and $\mathbf{e}_f = [\mathbf{t} \quad \mathbf{d} \quad \mathbf{n}]^T$ [Fig. 7.3.1(b)]. Thus

$$\begin{bmatrix} \mathbf{t} \\ \mathbf{d} \\ \mathbf{n} \end{bmatrix} = \begin{bmatrix} 1 & 0 & 0 \\ 0 & \sin\delta & -\cos\delta \\ 0 & \cos\delta & \sin\delta \end{bmatrix} \begin{bmatrix} \mathbf{t} \\ \mathbf{m} \\ \mathbf{b} \end{bmatrix} \tag{7.3.22}$$

$$\begin{bmatrix} \mathbf{t} \\ \mathbf{m} \\ \mathbf{b} \end{bmatrix} = \begin{bmatrix} 1 & 0 & 0 \\ 0 & \sin\delta & \cos\delta \\ 0 & -\cos\delta & \sin\delta \end{bmatrix} \begin{bmatrix} \mathbf{t} \\ \mathbf{d} \\ \mathbf{n} \end{bmatrix}. \tag{7.3.23}$$

Matrix equation (7.3.23) yields

$$\mathbf{b} = -\cos\delta \mathbf{d} + \sin\delta \mathbf{n} = \cos\delta(\mathbf{t} \times \mathbf{n}) + \sin\delta \mathbf{n}. \tag{7.3.24}$$

Using Eqs. (7.3.21) and (7.3.24), and taking into account that

$$\mathbf{c} = \mathbf{r}_\theta \left(\frac{d^2\theta}{du^2} \right)$$

is perpendicular to $\mathbf{n}$, we obtain

$$\frac{d^2\theta}{du^2} = -\frac{\cos\delta \mathbf{a} \cdot (\mathbf{t} \times \mathbf{n}) + \sin\delta(\mathbf{a} \cdot \mathbf{n})}{\cos\delta[\mathbf{r}_\theta \cdot (\mathbf{t} \times \mathbf{n})]}. \tag{7.3.25}$$

There is a particular case when the spatial curve is a geodesic line (see Section 7.9). In this case $\delta = 0$, the osculating plane coincides with the normal plane, the acceleration vector lies in the normal plane, and the derivative $(d^2\theta/du^2)$ is determined as

$$\frac{d^2\theta}{du^2} = -\frac{\mathbf{a} \cdot (\mathbf{t} \times \mathbf{n})}{\mathbf{r}_\theta \cdot (\mathbf{t} \times \mathbf{n})} = -\frac{\mathbf{a} \cdot (\mathbf{T} \times \mathbf{N})}{\mathbf{r}_\theta \cdot (\mathbf{T} \times \mathbf{N})}. \tag{7.3.26}$$

We emphasize that Eqs. (7.3.25) and (7.3.26) provide different values of $(d^2\theta/du^2)$.

Figures 7.3.2(a) and (b) illustrate the orientation and components of the vector of acceleration for both cases discussed above. The change of orientation of the acceleration vector is caused by the change of the derivative $d^2\theta/du^2$ that affects the magnitude of vector $\mathbf{c}$ [see Eq. (7.3.19)].

It is shown below that the determination of the normal curvature of a surface curve is based on the scalar product $\mathbf{a}_r \cdot \mathbf{n}$. Equation (7.3.17) yields that

$$\mathbf{a}_r \cdot \mathbf{n} = \mathbf{a} \cdot \mathbf{n} \left(\frac{du}{dt} \right)^2 \tag{7.3.27}$$

because

$$\mathbf{c} \cdot \mathbf{n} = \left(\mathbf{r}_\theta \frac{d^2\theta}{du^2} \right) \cdot \mathbf{n} = 0, \quad \mathbf{T} \cdot \mathbf{n} = 0.$$

This means that fortunately the derivative $d^2u/d\theta^2$ is not involved in the process of determination of the curve normal curvature.

Normal Curvature

Curve L_n is a planar curve (Fig. 7.3.1) and is obtained by the intersection of the surface by a normal plane that is determined by the surface normal and the curve tangent. We may consider curve L_n as a particular case of a spatial curve, taking into account that the osculating plane for curve L_n coincides with the surface normal plane. The normal curvature for curve L_n may be represented by an equation that is similar to (7.2.46):

$$\kappa_n = \frac{\mathbf{a}_{rn} \cdot \mathbf{n}}{\mathbf{v}_r^2}. \tag{7.3.28}$$

Taking into account that vectors $\mathbf{T}(d^2u/dt^2)$ and $\mathbf{c}_n$ (the two of three components of $\mathbf{a}_{rn}$) are perpendicular to $\mathbf{n}$, we obtain

$$\kappa_n = \frac{\mathbf{a} \cdot \mathbf{n}}{\mathbf{T}^2} \tag{7.3.29}$$

where $\mathbf{a}$ is represented by (7.3.18) and

$$\mathbf{T} = \mathbf{r}_u + \mathbf{r}_\theta \frac{d\theta}{du} \tag{7.3.30}$$

is the tangent to the curve surface. The positive (negative) sign of κ_n shows that the curvature center lies on the positive (negative) direction of $\mathbf{n}$.

Curvature of Spatial Curve

The curvature κ_o of a surface curve can be determined with Eq. (7.2.46) which was derived for a curve represented in 3D-space. Thus

$$\kappa_o = \frac{\mathbf{a}_r \cdot \mathbf{m}}{\mathbf{v}_r^2}. \tag{7.3.31}$$

The component of acceleration represented as $\mathbf{T}(d^2u/dt^2)$ is perpendicular to $\mathbf{m}$, and we obtain that

$$\kappa_o = \frac{(\mathbf{a} + \mathbf{c}_o) \cdot \mathbf{m}}{\mathbf{T}^2}. \tag{7.3.32}$$

Our goal is to represent κ_o in terms of the normal curvature of curve L_n and angle δ that is formed by vectors $\mathbf{m}$ and $\mathbf{n}$ (Fig. 7.3.1). Curves L_n and L_o have a common tangent at point M. The procedure of derivations is as follows.

   Step 1: Matrix equation (7.3.23) yields
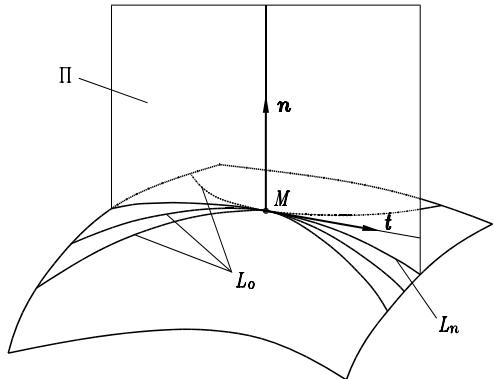
$$\mathbf{m} = \sin \delta \mathbf{d} + \cos \delta \mathbf{n}. \tag{7.3.33}$$

Matrix equation (7.3.22) yields

$$\mathbf{d} = \sin \delta \mathbf{m} - \cos \delta \mathbf{b}. \tag{7.3.34}$$

Using Eqs. (7.3.33) and (7.3.34), we obtain

$$\mathbf{m} = \frac{-\sin \delta \mathbf{b} + \mathbf{n}}{\cos \delta}. \tag{7.3.35}$$

Figure 7.3.3: Surface normal section and surface spatial curves.

Step 2: We consider Eqs. (7.3.32) and (7.3.35) simultaneously and take into account that vector $(\mathbf{a} + \mathbf{c}_o)$ lies in the osculating plane and therefore

$$(\mathbf{a} + \mathbf{c}_o) \cdot \mathbf{b} = 0.$$

Then we obtain

$$\frac{(\mathbf{a} + \mathbf{c}_o) \cdot \mathbf{m}}{\mathbf{T}^2} = \frac{(\mathbf{a} + \mathbf{c}_o) \cdot \mathbf{n}}{\cos \delta \mathbf{T}^2} = \frac{\mathbf{a} \cdot \mathbf{n}}{\cos \delta \mathbf{T}^2}. \tag{7.3.36}$$

Equations (7.3.29) and (7.3.36) yield
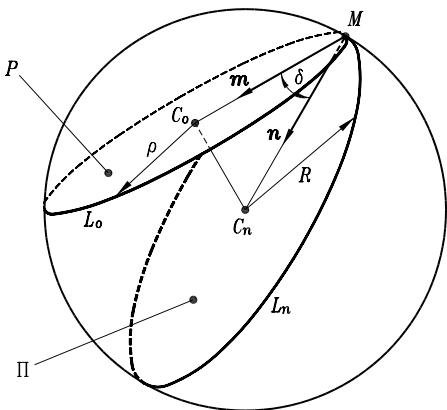
$$\kappa_o = \left| \frac{\kappa_n}{\cos \delta} \right|. \tag{7.3.37}$$

We emphasize [see Eq. (7.3.37)] that the curvature κ_o is always positive whereas the curvature κ_n can be positive or negative depending on the location of the curvature center on the positive or negative side of the normal. Equation (7.3.37) enables us to determine the curvature of spatial curve L_o through the normal curvature of L_n and the angle δ that is formed by the osculating plane and the surface normal.

Figure 7.3.3 shows a set of surface spatial curves L_o and the plane curve L_n obtained by intersection of the surface by normal plane Π. All curves have the same tangent $\mathbf{t}$ at point M. Meusnier's theorem states that the product $\kappa_o |\cos \delta|$ is the same for a set of curves identified as follows: (i) all of the curves pass through the same surface point M and have a common unit tangent $\mathbf{t}$ at M; (ii) the curves have different osculating planes but all of the planes pass through $\mathbf{t}$.

A spherical surface is the simplest example for illustration of Meusnier's theorem. Figure 7.3.4 shows the normal plane Π and the osculating plane P that pass through common point M. The intersections of the spherical surface by planes Π and P are circles L_n and L_o of radii R and ρ, respectively. Angle δ is formed by the surface normal $\mathbf{n}$ and the principal normal $\mathbf{m}$ to curve L_o. Figure 7.3.4 shows that

$$\cos \delta = \frac{\rho}{R}, \qquad \sin \delta = \frac{e}{R} = \frac{(R^2 - \rho^2)^{1/2}}{R} \tag{7.3.38}$$

Figure 7.3.4: Application of Meusnier's theorem to a spherical surface.

where $e = |\overline{C_o C_n}|$ is the length of the perpendicular that is drawn from center C_n of the spherical surface to plane P. Equation (7.3.38) confirms that

$$\kappa_o = \frac{\kappa_n}{\cos \delta}.$$

Here,

$$\kappa_o = \frac{1}{\rho}, \qquad \kappa_n = \frac{1}{R}.$$

Geodesic Curvature
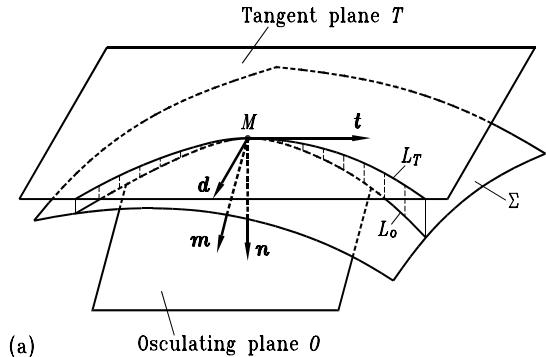
The first equation of system (7.3.15) yields that the curvature of a curve located in the osculating plane can be represented by two components: κ_g and κ_n. We may represent this equation in the form

$$\mathbf{r}_{ss} = \kappa_g \mathbf{d} + \kappa_n \mathbf{n}, \tag{7.3.39}$$
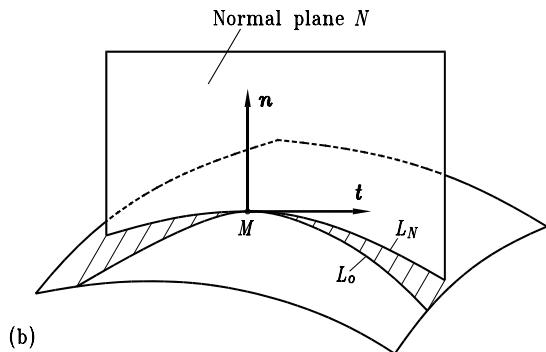
taking into account that $\mathbf{t}_s = \mathbf{r}_{ss}$.

This equation may be interpreted using the following considerations:

(1) Figure 7.3.5 shows a spatial curve L_o on surface Σ. Unit vectors $\mathbf{t}$, $\mathbf{d}$, and $\mathbf{n}$ represent the surface trihedron [Figs. 7.3.5(a) and 7.3.1(b)]. Here, $\mathbf{t}$ is the tangent to curve L_o; $\mathbf{d}$ lies in the tangent plane and is perpendicular to $\mathbf{t}$; $\mathbf{n}$ is the surface unit normal. Unit vector $\mathbf{m}$ is the principal normal to L_o and lies in the osculating plane. Vector $\mathbf{r}_{ss} = \kappa_o \mathbf{m}$ (see Section 7.2).

(2) Consider now that the spatial curve L_o is projected onto the tangent plane T and the normal plane N, respectively. The projections are designated by L_T and L_N. We emphasize that there is no difference between L_N [Fig. 7.3.5(b)] and L_n (Fig. 7.3.3) if they are considered locally. Both curves have the same normal curvature at the point of tangency M.

(3) Vector $\kappa_o \mathbf{m}$ is represented as the sum of two vectors: $\kappa_g \mathbf{d}$ and $\kappa_n \mathbf{n}$. The scalar κ_g represents the curvature of curve L_T, and the scalar κ_n represents the curvature of curve L_n.

Figure 7.3.5: Normal and geodesic curvatures.

(4) Equation (7.3.39) yields two relations:

$$\kappa_o(\mathbf{m} \cdot \mathbf{n}) = \kappa_o \cos \delta = \kappa_n \tag{7.3.40}$$

$$\kappa_g = \mathbf{r}_{ss} \cdot \mathbf{d} = \kappa_o \sin \delta. \tag{7.3.41}$$

Equation (7.3.40) relates the normal curvature κ_n and the curvature κ_o of the osculating plane. This equation was obtained above [see Eq. (7.3.37)]. Equation (7.3.41) relates the geodesic curvature κ_g and the curve curvature κ_o in the osculating plane. The direct computation of κ_g is based on the following equation:

(i) Using Eq. (7.3.41), we obtain

$$\kappa_g = \mathbf{r}_{ss} \cdot \mathbf{d} = \mathbf{r}_{ss} \cdot (\mathbf{n} \times \mathbf{t}) = \mathbf{r}_s \cdot (\mathbf{r}_{ss} \times \mathbf{n}) \tag{7.3.42}$$

because $\mathbf{t} = \mathbf{r}_s$.
This equation can be applied if curve L_o is represented by vector function $\mathbf{r}(s)$, where s is the arc length.

(ii) We consider now that the curve is represented by vector function $\mathbf{r}(t)$, where t is a chosen parameter. We may consider function $t(s)$ and then obtain

$$\mathbf{r}_s = \mathbf{r}_t \frac{dt}{ds}. \tag{7.3.43}$$

Taking into account that $|\mathbf{r}_s| = 1$ (see Section 7.2), we get

$$\mathbf{r}_s = \frac{\mathbf{r}_t}{|\mathbf{r}_t|}. \tag{7.3.44}$$

The derivative $\mathbf{r}_{ss}$ is represented as

$$\mathbf{r}_{ss} = \mathbf{r}_{tt} \left(\frac{dt}{ds}\right)^2 + \mathbf{r}_t \frac{d^2 t}{ds^2} = \frac{\mathbf{r}_{tt}}{|\mathbf{r}_t|^2} + \mathbf{r}_t \frac{d^2 t}{ds^2}. \tag{7.3.45}$$

Using Eqs. (7.3.42), (7.3.44), and (7.3.45), we derive

$$\kappa_g = \frac{\mathbf{r}_t \cdot (\mathbf{r}_{tt} \times \mathbf{n})}{|\mathbf{r}_t|^3}. \tag{7.3.46}$$

(iii) We consider now a curve that is represented on a surface $\mathbf{r}(u, \theta)$. The curve is represented by the equation

$$\mathbf{r} = \mathbf{r}(u(t), \theta(t)). \tag{7.3.47}$$

We may use Eq. (7.3.46) for determination of geodesic curvature κ_g, considering that

$$\mathbf{r}_t = \mathbf{r}_u \frac{du}{dt} + \mathbf{r}_\theta \frac{d\theta}{dt} \tag{7.3.48}$$

$$\mathbf{r}_{tt} = \mathbf{r}_{uu} \left(\frac{du}{dt}\right)^2 + 2\mathbf{r}_{u\theta} \left(\frac{d\theta}{dt}\right) \left(\frac{du}{dt}\right) + \mathbf{r}_{\theta\theta} \left(\frac{d\theta}{dt}\right)^2 + \mathbf{r}_u \frac{d^2 u}{dt^2} + \mathbf{r}_\theta \frac{d^2 \theta}{dt^2}. \tag{7.3.49}$$

Equations (7.3.46), (7.3.48), and (7.3.49) yield

$$\kappa_g = \frac{\dfrac{\mathbf{N}}{|\mathbf{N}|} \cdot (\mathbf{T} \times \mathbf{a}) + |\mathbf{N}| \left[\left(\dfrac{du}{dt}\right)\left(\dfrac{d^2 \theta}{dt^2}\right) - \left(\dfrac{d\theta}{dt}\right)\left(\dfrac{d^2 u}{dt^2}\right)\right]}{|\mathbf{T}|^3}. \tag{7.3.50}$$

Here,

$$\mathbf{T} = \mathbf{r}_u \frac{du}{dt} + \mathbf{r}_\theta \frac{d\theta}{dt}; \qquad \mathbf{a} = \mathbf{r}_{uu} \left(\frac{du}{dt}\right)^2 + 2\mathbf{r}_{u\theta} \left(\frac{d\theta}{dt}\right) \left(\frac{du}{dt}\right) + \mathbf{r}_{\theta\theta} \left(\frac{d\theta}{dt}\right)^2;$$

$$\mathbf{N} = \mathbf{r}_u \times \mathbf{r}_\theta; \qquad \mathbf{n} = \frac{\mathbf{N}}{|\mathbf{N}|}.$$

Considering that parameter t represents time, we obtain from Eq. (7.3.46) that

$$\kappa_g = \frac{\mathbf{v}_r \cdot (\mathbf{a}_r \times \mathbf{n})}{|\mathbf{v}_r|^3}. \tag{7.3.51}$$

Spatial curve L_o may represent in some cases the path of contact on the gear tooth surface. Curve L_o will be a geodesic curve locally, at the main point of contact, if $\kappa_g = 0$ at this point.

Problem 7.3.1
A cylinder surface is represented by

$$x = \rho \cos \theta, \qquad y = \rho \sin \theta, \qquad z = u. \tag{7.3.52}$$

Consider a helix on the cylinder surface given by the equation

$$u = h\theta \tag{7.3.53}$$

where

$$h = \rho \tan \lambda, \tag{7.3.54}$$

with λ being the lead angle of the helix.

  (i) Derive the equations for $\mathbf{n}$, $\mathbf{v}_r$, and $\mathbf{a}_r$.
 (ii) Determine the geodesic curvature κ_g [see Eq. (7.3.51)].

Solution
 (i)

$$\mathbf{n} = \frac{\mathbf{r}_u \times \mathbf{r}_\theta}{|\mathbf{r}_u \times \mathbf{r}_\theta|} = -\cos\theta\mathbf{i} - \sin\theta\mathbf{j}$$

$$\mathbf{v}_r = \rho\frac{d\theta}{dt}(-\sin\theta\mathbf{i} + \cos\theta\mathbf{j} + \tan\lambda\mathbf{k})$$

$$\mathbf{a}_r = \rho\left(\frac{d\theta}{dt}\right)^2(-\cos\theta\mathbf{i} - \sin\theta\mathbf{j}) + \rho\frac{d^2\theta}{dt^2}(-\sin\theta\mathbf{i} + \cos\theta\mathbf{j} + \tan\lambda\mathbf{k}).$$

 (ii) $\kappa_g = 0$.

7.4 FIRST AND SECOND FUNDAMENTAL FORMS

The concept of surface *first* and *second fundamental forms* (proposed by the famous mathematician Gauss) is important for determination of surface normal curvature, principal curvatures, and principal directions.

First Fundamental Form
Consider a regular surface given by vector function (7.3.1). The surface unit normal is represented by

$$\mathbf{n}(u, \theta) = \frac{\mathbf{r}_u \times \mathbf{r}_\theta}{|\mathbf{r}_u \times \mathbf{r}_\theta|}. \tag{7.4.1}$$

The first fundamental form of a surface is defined as

$$I = d\mathbf{r}^2 = (\mathbf{r}_u du + \mathbf{r}_\theta d\theta)^2 = \mathbf{r}_u^2 du^2 + 2(\mathbf{r}_u \cdot \mathbf{r}_\theta)du\,d\theta + \mathbf{r}_\theta^2 d\theta^2$$
$$= E du^2 + 2F du\,d\theta + G d\theta^2. \tag{7.4.2}$$

Here,

$$d\mathbf{r} = \mathbf{r}_u du + \mathbf{r}_\theta d\theta \tag{7.4.3}$$

$$E = \mathbf{r}_u^2, \qquad F = \mathbf{r}_u \cdot \mathbf{r}_\theta, \qquad G = \mathbf{r}_\theta^2. \tag{7.4.4}$$

The far right-hand side of Eq. (7.4.2) is a quadratic form in differentials du and $d\theta$.

Second Fundamental Form

The second fundamental form of a surface is defined by

$$II = d^2\mathbf{r} \cdot \mathbf{n} = -d\mathbf{r} \cdot d\mathbf{n}. \tag{7.4.5}$$

The equality of scalar products

$$d^2\mathbf{r} \cdot \mathbf{n} = -d\mathbf{r} \cdot d\mathbf{n} \tag{7.4.6}$$

results from differentiation of the equation

$$d\mathbf{r} \cdot \mathbf{n} = 0 \tag{7.4.7}$$

while taking into account that $d\mathbf{r}$ belongs to the tangent plane.

   Let us develop the expression for the second fundamental form using the equation

$$II = d^2\mathbf{r} \cdot \mathbf{n}. \tag{7.4.8}$$

The differentiation of Eq. (7.4.3) yields

$$d^2\mathbf{r} = d(\mathbf{r}_u du + \mathbf{r}_\theta d\theta) = \mathbf{r}_{uu} du^2 + 2\mathbf{r}_{u\theta} du\, d\theta + \mathbf{r}_{\theta\theta} d\theta^2 + \mathbf{r}_u d^2 u + \mathbf{r}_\theta d^2\theta$$

and

$$\begin{aligned}
II &= d^2\mathbf{r} \cdot \mathbf{n} \\
&= (\mathbf{r}_{uu} \cdot \mathbf{n})du^2 + 2(\mathbf{r}_{u\theta} \cdot \mathbf{n})du\, d\theta + (\mathbf{r}_{\theta\theta} \cdot \mathbf{n})d\theta^2 + (\mathbf{r}_u \cdot \mathbf{n})d^2 u + (\mathbf{r}_\theta \cdot \mathbf{n})d^2\theta \\
&= Ldu^2 + 2Mdu\, d\theta + Nd\theta^2, \quad (\mathbf{r}_u \cdot \mathbf{n} = 0, \quad \mathbf{r}_\theta \cdot \mathbf{n} = 0) \tag{7.4.9}
\end{aligned}$$

where

$$L = \mathbf{r}_{uu} \cdot \mathbf{n}, \qquad M = \mathbf{r}_{u\theta} \cdot \mathbf{n}, \qquad N = \mathbf{r}_{\theta\theta} \cdot \mathbf{n}. \tag{7.4.10}$$

The right side of Eq. (7.4.9) is a quadratic form in differentials du and $d\theta$. Expression (7.4.9) can also be obtained by using the equation

$$II = -d\mathbf{r} \cdot d\mathbf{n}. \tag{7.4.11}$$

Interpretation of Fundamental Forms

The first fundamental form is always positive and is related with the velocity $\mathbf{v}_r$ in the motion along the curve as
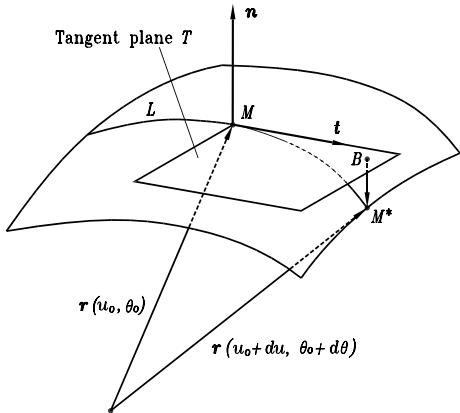
$$\mathbf{v}_r^2 = \frac{I}{dt^2} \tag{7.4.12}$$

where t is the time. The second fundamental form represents the deviation of the curve point M^* from the tangent plane (Fig. 7.4.1). The deviation is represented by vector

$$\overrightarrow{BM^*} = l\mathbf{n}.$$

Here, l is a signed value, and l is positive if vectors $\overrightarrow{BM^*}$ and $\mathbf{n}$ are of the same direction. It can be proven that

$$l = \frac{II}{2}. \tag{7.4.13}$$

Figure 7.4.1: Deviation of surface point.

The second fundamental form, the acceleration in motion along the curve, and the surface unit normal are related to the equation

$$\mathbf{a}_r \cdot \mathbf{n} = \frac{\text{II}}{dt^2} \tag{7.4.14}$$

where t is the time.

Determination of Normal Curvature

The normal curvature is determined by the equation

$$\kappa_n = \frac{\text{II}}{\text{I}}. \tag{7.4.15}$$

The geometric interpretation of Eq. (7.4.15) may be based on the following derivations.

Step 1: The curvature of a planar curve [Fig. 7.4.2(a)] is initially considered. The curve is represented by vector function $\mathbf{r}(s)$ where s is the arc length. Points M and N are the infinitesimally close curve points; $\overline{OM} = \mathbf{r}(s)$; $\overline{ON} = \mathbf{r}(s + ds)$; $d\mathbf{r} = \mathbf{r}(s + ds) - \mathbf{r}(s)$; $ds = \overset{\frown}{MN}$. The curve unit normals at M and N are $\mathbf{a}(s)$ and $\mathbf{a}(s + ds)$, respectively. The definition of curve curvature at M is

$$k = \frac{d\alpha}{ds} = \frac{1}{\rho}, \qquad (\rho = MC). \tag{7.4.16}$$

Step 2: While point M moves to N along the curve, normal $\mathbf{a}(s)$ will take the position of $\mathbf{a}(s + ds)$ by translation and rotation through angle $d\alpha$ about $\mathbf{b}$ [Fig. 7.4.2.(b)]. The vector of rotation of the tip of the unit normal $\mathbf{a}(s)$ is
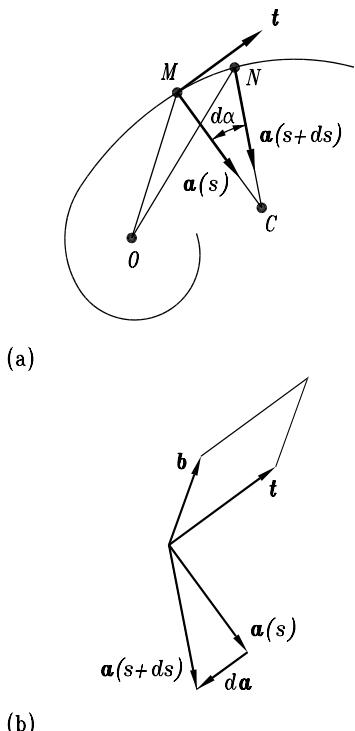
$$d\mathbf{a} = d\alpha(\mathbf{b} \times \mathbf{a}). \tag{7.4.17}$$

Vector $\mathbf{t}$, $\mathbf{b}$, and $\mathbf{a}$ are mutually perpendicular and form a fixed right-hand trihedron whose origin is M. Vector $\mathbf{t}$ is the curve unit tangent and is represented as

$$\mathbf{t} = \frac{d\mathbf{r}}{ds} \qquad (ds = |d\mathbf{r}|). \tag{7.4.18}$$

Vector $\mathbf{b}$ can be represented as

$$\mathbf{b} = \mathbf{t} \times \mathbf{a}. \tag{7.4.19}$$

(a)

Figure 7.4.2: For derivation of curvature of planar curve.

(b)

Equations (7.4.17) and (7.4.19) yield

$$d\mathbf{a} = d\alpha \, [(\mathbf{t} \times \mathbf{a}) \times \mathbf{a}] = -d\alpha \mathbf{t}. \tag{7.4.20}$$

Step 3: It is easy to verify that Eqs. (7.4.18) and (7.4.20) yield
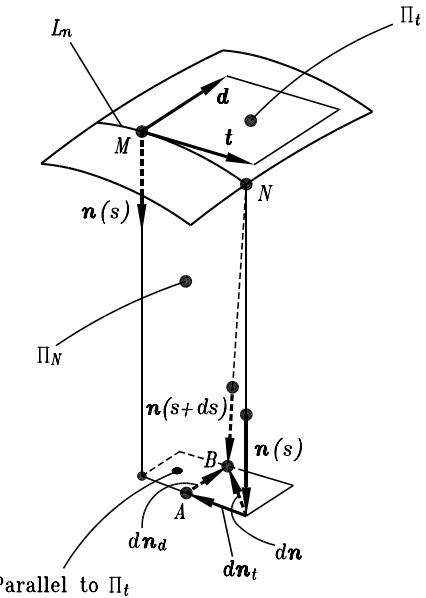
$$d\mathbf{a} \cdot d\mathbf{r} = -(d\alpha)(ds), \tag{7.4.21}$$

and the curve curvature can be represented as

$$k = -\frac{d\mathbf{a} \cdot d\mathbf{r}}{d\mathbf{r}^2} = \frac{d\alpha}{ds}. \tag{7.4.22}$$

Step 4: Consider now the normal section L_n of a surface (Fig. 7.4.3). Plane Π_t is tangent to the surface at point M, and vector $\mathbf{t}$ is the unit tangent chosen in Π_t. Vector $\mathbf{n}$ is the surface unit normal at M. Planar curve L_n is obtained by intersection of the surface by the normal plane that is formed by vectors $\mathbf{n}$ and $\mathbf{t}$. MN is an infinitesimally small piece of L_n.

Henceforth, we differentiate the unit normal $\mathbf{a}$ to the planar curve and the unit normal $\mathbf{n}$ to the surface. $\overline{NA}$ is the normal to the planar curve at N; $\overline{NB}$ is the surface normal at N. It is obvious that $\mathbf{a} = \mathbf{n}$ at point M. However, the surface normal $\overline{NB}$ and the curve normal $\overline{NA}$ generally do not coincide with each other. We designate the surface unit normals at points M and N by $\mathbf{n}(s)$ and $\mathbf{n}(s + ds)$, respectively. Because $\mathbf{n}(s)$ is a unit normal, the differential $d\mathbf{n}$ is perpendicular to $\mathbf{n}$. Thus, $d\mathbf{n}$ lies in the tangent plane and

Figure 7.4.3: For derivation of normal curvature.

may be represented as

$$dn = dn_t + dn_d.$$

Here, **t** and **d** are the orthogonal vectors that form the tangent plane.

The normal curvature κ_n of the surface is the curvature of normal section L_n and is represented by an equation that is similar to (7.4.22). Thus

$$\kappa_n = -\frac{d\mathbf{n}_t \cdot d\mathbf{r}}{d\mathbf{r}^2} \qquad (7.4.23)$$

where $d\mathbf{r} = ds\ \mathbf{t}$ ($ds = \widehat{MN}$). Taking into account that $d\mathbf{n}_d$ is perpendicular to **t**, we may represent κ_n by the equation

$$\kappa_n = -\frac{d\mathbf{n} \cdot d\mathbf{r}}{d\mathbf{r}^2}. \qquad (7.4.24)$$

Step 5: The transformation of Eq. (7.4.24) is based on the following considerations:

(i) The infinitesimal displacement $d\mathbf{r}$ of a surface point is performed in the tangent plane. Thus,

$$d\mathbf{r} \cdot \mathbf{n} = 0. \qquad (7.4.25)$$

(ii) Equation (7.4.25) is observed in the neighborhood of M and therefore we may differentiate it. Then we obtain

$$d\mathbf{r} \cdot d\mathbf{n} + d^2\mathbf{r} \cdot \mathbf{n} = 0. \qquad (7.4.26)$$

Equations (7.4.24) and (7.4.26) yield

$$\kappa_n = \frac{d^2\mathbf{r} \cdot \mathbf{n}}{d\mathbf{r}^2}, \qquad (7.4.27)$$

and Eq. (7.4.15) is confirmed.

7.5 PRINCIPAL DIRECTIONS AND CURVATURES

We recall that the determination of normal curvature of a tooth surface Σ is based on the following considerations:

(i) The tooth surface Σ is determined by vector function $\mathbf{r}(u, \theta)$.
(ii) The normal to Σ at a point M is determined as

$$\mathbf{N} = \mathbf{r}_u \times \mathbf{r}_\theta \quad \text{or as} \quad \mathbf{N} = \mathbf{r}_\theta \times \mathbf{r}_u$$

where the derivatives are taken at M.

(iii) The tangent to surface Σ at point M is determined as

$$\mathbf{T} = \mathbf{r}_u du + \mathbf{r}_\theta d\theta.$$

The orientation of $\mathbf{T}$ depends on the ratio $d\theta/du$.

(iv) The normal curvature of Σ is the curvature of a planar curve obtained by the intersection of Σ by plane Π that is formed by $\mathbf{N}$ and $\mathbf{T}$. The orientation of plane Π at point M depends on the orientation of tangent $\mathbf{T}$ to surface Σ. Therefore, the orientation of Π depends on the ratio $d\theta/du$.

(v) There is a set of planar curves L_n at point M of surface Σ obtained by the intersection of Σ by the set of normal planes Π. The normal curvature κ_n of each curve L_n may be determined by Eqs. (7.4.2), (7.4.9), and (7.4.15), which are based on the application of first and second fundamental forms (see Section 7.4).

(vi) The extreme values of normal curvature κ_n are called the *principal curvatures*, and the respective two directions of unit vector $\mathbf{t}$ (of tangent $\mathbf{T}$) are called the *principal directions*. It is proven that unit vectors $\mathbf{t}$ of principal directions are mutually perpendicular (see below). Another important property of the principal directions is that vectors $\mathbf{v}_r$ and $\dot{\mathbf{n}}_r$ (see below) are collinear on principal directions (Rodrigues' formula).

Two approaches for determination of principal curvatures and directions are represented as follows.

Approach I

Consider point M on a regular surface [Fig. 7.5.1(a)]. Vectors $\mathbf{r}_u$ and $\mathbf{r}_\theta$ are tangents to the coordinate lines on the surface, and $\mathbf{T}$ is the direction of an infinitesimally small displacement of a point over the surface. Angle μ (or λ) is a varied parameter but $\nu = \mu + \lambda$ is constant for the chosen point M. Our goals are (i) to prove that the principal directions are mutually perpendicular, and (ii) to derive equations for determination of the principal curvatures and directions.
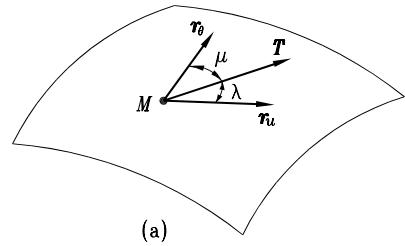
Step 1: (Expression for unit tangent $\mathbf{t}$).

The tangent $\mathbf{T}$ can be represented by [Fig 7.5.1(b)]

$$\mathbf{T} = a\mathbf{e}_u + b\mathbf{e}_\theta \tag{7.5.1}$$

where

$$\mathbf{e}_u = \frac{\mathbf{r}_u}{|\mathbf{r}_u|}, \qquad \mathbf{e}_\theta = \frac{\mathbf{r}_\theta}{|\mathbf{r}_\theta|}.$$

Figure 7.5.1: For determination of principal directions: (a) representation of tangents $\mathbf{r}_\theta$ and $\mathbf{r}_u$ to surface coordinate lines at point M; (b) for derivation of relations between magnitudes a and b of unit vectors $\mathbf{e}_u$ and $\mathbf{e}_\theta$.
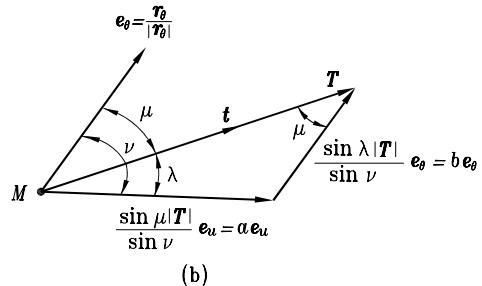
Figure 7.5.1(b) yields

$$\frac{a}{|\mathbf{T}|} = \frac{\sin \mu}{\sin v}, \qquad \frac{b}{|\mathbf{T}|} = \frac{\sin \lambda}{\sin v} \tag{7.5.2}$$

where $v = \mu + \lambda$. Using Eqs. (7.5.1) and (7.5.2), we obtain

$$\mathbf{t} = \frac{\mathbf{e}_u \sin \mu + \mathbf{e}_\theta \sin(v - \mu)}{\sin v}. \tag{7.5.3}$$

Here,

$$\mathbf{t} = \frac{\mathbf{T}}{|\mathbf{T}|}, \qquad \cos v = \mathbf{e}_u \cdot \mathbf{e}_\theta, \qquad \sin v = |\mathbf{e}_u \times \mathbf{e}_\theta|. \tag{7.5.4}$$

Step 2: Expressions for $\mathbf{v}$ and $\mathbf{t} = \mathbf{v}/|\mathbf{v}|$ are as follows:

$$\mathbf{v} = \mathbf{r}_u \frac{du}{dt} + \mathbf{r}_\theta \frac{d\theta}{dt} \tag{7.5.5}$$

$$\mathbf{t} = \left(\mathbf{r}_u \frac{du}{dt} + \mathbf{r}_\theta \frac{d\theta}{dt} \right) \frac{1}{|\mathbf{v}|}. \tag{7.5.6}$$

Step 3: (Expressions for du/dt and $d\theta/dt$).
Equations (7.5.3) and (7.5.6) yield

$$\mathbf{r}_u \left[\left(\frac{du}{dt} \right) \left(\frac{1}{|\mathbf{v}|} \right) - \left(\frac{\sin \mu}{\sin v} \right) \left(\frac{1}{|\mathbf{r}_u|} \right) \right] + \mathbf{r}_\theta \left[\left(\frac{d\theta}{dt} \right) \left(\frac{1}{|\mathbf{v}|} \right) - \left(\frac{\sin(v - \mu)}{\sin v} \right) \frac{1}{|\mathbf{r}_\theta|} \right] = 0. \tag{7.5.7}$$

Equation (7.5.7) must be satisfied with any values of $\mathbf{r}_u$ and $\mathbf{r}_\theta$, and this results in

$$\frac{du}{dt} = \frac{\sin \mu}{\sin v} \frac{|\mathbf{v}|}{|\mathbf{r}_u|}, \qquad \frac{d\theta}{dt} = \frac{\sin(v - \mu)}{\sin v} \frac{|\mathbf{v}|}{|\mathbf{r}_\theta|}. \tag{7.5.8}$$

Step 4: (Expression for acceleration $\mathbf{a}_r$).

$$\mathbf{a}_r = \mathbf{r}_{uu}\left(\frac{du}{dt}\right)^2 + 2\mathbf{r}_{u\theta}\left(\frac{du}{dt}\right)\left(\frac{d\theta}{dt}\right) + \mathbf{r}_{\theta\theta}\left(\frac{d\theta}{dt}\right)^2 + \mathbf{r}_u\frac{d^2u}{dt^2} + \mathbf{r}_\theta\frac{d^2\theta}{dt^2}. \quad (7.5.9)$$

Step 5: (Equation for normal curvature).

$$\kappa_n = \frac{\mathbf{a}_r \cdot \mathbf{n}}{\mathbf{v}_r^2} = \left[L\left(\frac{du}{dt}\right)^2 + 2M\left(\frac{du}{dt}\right)\left(\frac{d\theta}{dt}\right) + N\left(\frac{d\theta}{dt}\right)^2\right]\frac{1}{\mathbf{v}^2} \quad (7.5.10)$$

where

$$L = \mathbf{r}_{uu}\cdot\mathbf{n}, \qquad M = \mathbf{r}_{u\theta}\cdot\mathbf{n}, \qquad N = \mathbf{r}_{\theta\theta}\cdot\mathbf{n}.$$

Equations (7.5.8) and (7.5.10) yield

$$\kappa_n = A\sin^2\mu + 2B\sin(\nu-\mu)\sin\mu + C\sin^2(\nu-\mu) \quad (7.5.11)$$

where

$$A = \frac{L}{\mathbf{r}_u^2\sin^2\nu}, \qquad B = \frac{M}{|\mathbf{r}_u||\mathbf{r}_\theta|\sin^2\nu}, \qquad C = \frac{N}{\mathbf{r}_\theta^2\sin^2\nu}. \quad (7.5.12)$$

Step 6: (Determination of extreme values of κ_n).
Equation (7.5.11) and equation

$$\frac{d\kappa_n}{d\mu} = 0 \quad (7.5.13)$$

yield

$$\tan 2\mu = \frac{C\sin 2\nu - 2B\sin\nu}{A - 2B\cos\nu + C\cos 2\nu}. \quad (7.5.14)$$

Equation (7.5.14) yields two solutions for μ: μ_I and $\mu_{II} = \mu_I + \pi/2$. This means that the principal directions are indeed perpendicular.

Step 7: (Determination of principal curvatures).
Using the solutions for μ and Eq. (7.5.11), we obtain the sought-for principal curvatures.

Step 8: (Representation of principal directions).
The previously mentioned two solutions for μ and Eq. (7.5.3) allow us to represent analytically the unit vectors of principal directions. We emphasize that, in general, two orthogonal principal directions exist at each point of the surface with different values of principal curvatures. A spherical surface is an exception; each direction on the surface may be considered as the principal direction and the normal curvature is the same for all normal sections of the surface. Another exception is the case when the normal curvature of the surface is equal to zero for all directions. This is true for a plane or for a surface that turns into a plane at a certain point (called a flat point).

Rodrigues' Formula
According to Rodrigues' formula, vectors $\mathbf{v}_r$ and $\dot{\mathbf{n}}_r$ are collinear for the principal directions. The principal curvatures κ_I and κ_{II} satisfy the equation

$$\kappa_{I,II}\,\mathbf{v}_r = -\dot{\mathbf{n}}_r. \quad (7.5.15)$$

Consider that a regular surface and its unit normal are represented by Eqs. (7.3.1) and (7.4.1). Vectors $\mathbf{v}_r$ and $\dot{\mathbf{n}}_r$ are represented as follows:

$$\mathbf{v}_r = \mathbf{r}_u \frac{du}{dt} + \mathbf{r}_\theta \frac{d\theta}{dt} \qquad (7.5.16)$$

$$\dot{\mathbf{n}}_r = \mathbf{n}_u \frac{du}{dt} + \mathbf{n}_\theta \frac{d\theta}{dt}. \qquad (7.5.17)$$

We consider that the unit normal is determined as

$$\mathbf{n} = \mathbf{n}(u, \theta). \qquad (7.5.18)$$

Rodrigues' formula yields

$$\frac{n_{xu}\frac{du}{dt} + n_{x\theta}\frac{d\theta}{dt}}{x_u\frac{du}{dt} + x_\theta\frac{d\theta}{dt}} = \frac{n_{yu}\frac{du}{dt} + n_{y\theta}\frac{d\theta}{dt}}{y_u\frac{du}{dt} + y_\theta\frac{d\theta}{dt}} = \frac{n_{zu}\frac{du}{dt} + n_{z\theta}\frac{d\theta}{dt}}{z_u\frac{du}{dt} + z_\theta\frac{d\theta}{dt}} = -\kappa_{I,II}. \quad (7.5.19)$$

Approach 2

The direct application of Rodrigues' formula needs the differentiation of the radical,

$$|\mathbf{N}| = \left(N_x^2 + N_y^2 + N_z^2\right)^{0.5},$$

for determination of $\dot{\mathbf{n}}_r$. This can be avoided for rare cases when a developable surface is considered (cone surface, involute helicoid, etc). In a general case there is the need for simplification of derivations and this can be done by using the following procedure.

Step 1: In accordance with Rodrigues' formula we have

$$\mathbf{n}_u du + \mathbf{n}_\theta d\theta = -\kappa_{I,II}(\mathbf{r}_u du + \mathbf{r}_\theta d\theta). \qquad (7.5.20)$$

Step 2: Vectors $\mathbf{n}_u$, $\mathbf{n}_\theta$, $\mathbf{r}_u$, and $\mathbf{r}_\theta$ lie in the tangent plane, and vector Eq. (7.5.20) can be substituted by the two following scalar equations:

$$(\mathbf{n}_u \cdot \mathbf{r}_u)du + (\mathbf{n}_\theta \cdot \mathbf{r}_u)d\theta = -\kappa_{I,II} \left[(\mathbf{r}_u \cdot \mathbf{r}_u)du + (\mathbf{r}_\theta \cdot \mathbf{r}_u)d\theta\right] \qquad (7.5.21)$$

$$(\mathbf{n}_u \cdot \mathbf{r}_\theta)du + (\mathbf{n}_\theta \cdot \mathbf{r}_\theta)d\theta = -\kappa_{I,II} \left[(\mathbf{r}_u \cdot \mathbf{r}_\theta)du + (\mathbf{r}_\theta \cdot \mathbf{r}_\theta)d\theta\right]. \qquad (7.5.22)$$

Step 3: It is obvious that

$$\mathbf{r}_u \cdot \mathbf{n} = 0, \qquad \mathbf{r}_\theta \cdot \mathbf{n} = 0, \qquad (7.5.23)$$

and

$$\frac{\partial}{\partial u}(\mathbf{r}_u \cdot \mathbf{n}) = \mathbf{r}_{uu} \cdot \mathbf{n} + \mathbf{r}_u \cdot \mathbf{n}_u = 0 \qquad (7.5.24)$$

$$\frac{\partial}{\partial \theta}(\mathbf{r}_u \cdot \mathbf{n}) = \mathbf{r}_{u\theta} \cdot \mathbf{n} + \mathbf{r}_u \cdot \mathbf{n}_\theta = 0 \qquad (7.5.25)$$

$$\frac{\partial}{\partial \theta}(\mathbf{r}_\theta \cdot \mathbf{n}) = \mathbf{r}_{\theta\theta} \cdot \mathbf{n} + \mathbf{r}_\theta \cdot \mathbf{n}_\theta = 0 \qquad (7.5.26)$$

$$\frac{\partial}{\partial u}(\mathbf{r}_\theta \cdot \mathbf{n}) = \mathbf{r}_{u\theta} \cdot \mathbf{n} + \mathbf{r}_\theta \cdot \mathbf{n}_u = 0. \qquad (7.5.27)$$

Then we obtain

$$\mathbf{r}_{uu} \cdot \mathbf{n} = -(\mathbf{r}_u \cdot \mathbf{n}_u) \tag{7.5.28}$$

$$\mathbf{r}_{u\theta} \cdot \mathbf{n} = -(\mathbf{r}_u \cdot \mathbf{n}_\theta) = -(\mathbf{r}_\theta \cdot \mathbf{n}_u) \tag{7.5.29}$$

$$\mathbf{r}_{\theta\theta} \cdot \mathbf{n} = -(\mathbf{r}_\theta \cdot \mathbf{n}_\theta). \tag{7.5.30}$$

We recall also [see Eqs. (7.4.10)] that

$$\mathbf{r}_{uu} \cdot \mathbf{n} = L(u, \theta), \qquad \mathbf{r}_{u\theta} \cdot \mathbf{n} = M(u, \theta), \qquad \mathbf{r}_{\theta\theta} \cdot \mathbf{n} = N(u, \theta) \tag{7.5.31}$$

and [see Eqs. (7.4.4)]

$$\mathbf{r}_u \cdot \mathbf{r}_u = E, \qquad \mathbf{r}_u \cdot \mathbf{r}_\theta = F, \qquad \mathbf{r}_\theta \cdot \mathbf{r}_\theta = G. \tag{7.5.32}$$

Equations (7.5.21), (7.5.22), and (7.5.28) through (7.5.32) yield two basic equations:

$$L\,du + M\,d\theta = \kappa_{I,II}(E\,du + F\,d\theta) \tag{7.5.33}$$

$$M\,du + N\,d\theta = \kappa_{I,II}(F\,du + G\,d\theta). \tag{7.5.34}$$

Step 4: Excluding $\kappa_{I,II}$ from Eqs. (7.5.33) and (7.5.34), we obtain

$$(LF - ME)\left(\frac{du}{d\theta}\right)^2 + (LG - NE)\frac{du}{d\theta} + (MG - NF) = 0 \qquad \text{(provided } d\theta \neq 0\text{)} \tag{7.5.35}$$

or

$$(MG - NF)\left(\frac{d\theta}{du}\right)^2 + (LG - NE)\frac{d\theta}{du} + (LF - ME) = 0 \qquad \text{(provided } du \neq 0\text{)}. \tag{7.5.36}$$

Generally, Eq. (7.5.35) [Eq. (7.5.36)] provides two solutions for $du/d\theta$ ($d\theta/du$) that correspond to two principal directions at the surface point with the known values of L, M, N, F, G, and E. Then, using Eqs. (7.5.33) and (7.5.34), we obtain the principal curvatures. The unit vectors of principal directions can be obtained by using equations

$$\mathbf{e}_i = \frac{\mathbf{r}_u \dfrac{du}{d\theta} + \mathbf{r}_\theta}{\left|\mathbf{r}_u \dfrac{du}{d\theta} + \mathbf{r}_\theta\right|} \qquad \text{(provided } d\theta \neq 0\text{)} \quad (i = I, II) \tag{7.5.37}$$

or

$$\mathbf{e}_i = \frac{\mathbf{r}_u + \mathbf{r}_\theta \dfrac{d\theta}{du}}{\left|\mathbf{r}_u + \mathbf{r}_\theta \dfrac{d\theta}{du}\right|} \qquad \text{(provided } du \neq 0\text{)} \quad (i = I, II). \tag{7.5.38}$$

There are some difficulties in application of this procedure in those particular cases when at least one of the principal directions coincides with the tangent to the respective coordinate line. The following two particular cases illustrate the determination of the principal directions and curvatures in those particular cases previously mentioned.

Particular Case 1

Consider a screw involute surface that is a ruled developed surface represented as $\mathbf{r}(u, \theta)$; $\mathbf{r}(u, \theta_o)$ (θ_o is constant) is the generating line. The investigation shows that one of the principal directions coincides with the generating line, and therefore $d\theta = 0$. It may also be proven that in this case $L = 0$, $M = 0$. Two principal directions can be determined by application of Eq. (7.5.36), which yields the two following solutions for $d\theta/du$:

$$\left(\frac{d\theta}{du}\right)_I = 0, \qquad \left(\frac{d\theta}{du}\right)_{II} = -\frac{E}{F}.$$

Using Eqs. (7.5.33) and (7.5.34), we obtain

$$\kappa_I = 0 \ \text{ for } \ \frac{d\theta}{du} = 0, \qquad \kappa_{II} = \frac{NE}{GE - F^2} \quad \text{for} \quad \frac{d\theta}{du} = -\frac{E}{F}.$$

Particular Case 2

A surface of revolution is represented by $\mathbf{r}(u, \theta)$; $\mathbf{r}(u, \theta_o)$ (θ_o is constant) is the generating line. The tangents to the coordinate lines are mutually perpendicular, and therefore $F = \mathbf{r}_u \cdot \mathbf{r}_\theta = 0$. The investigation also shows that $M = \mathbf{r}_{u\theta} \cdot \mathbf{n} = 0$.

In this particular case the principal directions coincide with the tangents to the coordinate lines. This can be proven by application of Eq. (7.5.35), which yields $du = 0$. The other principal direction corresponds to $d\theta = 0$, and this result is based on the following considerations: (i) it is known that the principal directions are mutually perpendicular; (ii) the solution $du = 0$ for the principal direction means that the unit vector of the principal direction is collinear to $\mathbf{r}_\theta$; (iii) the unit vector of the other principal direction is collinear to $\mathbf{r}_u$, because $F = \mathbf{r}_u \cdot \mathbf{r}_\theta = 0$, and the principal directions are mutually perpendicular. The same results may be obtained by application of Eq. (7.5.36) and the equation $F = 0$.

The principal curvatures of the surface of revolution can be obtained by application of basic Eqs. (7.5.33) and (7.5.34), which yield

$$\kappa_I = \frac{N}{G} \quad \text{(provided } d\theta \neq 0)$$

$$\kappa_{II} = \frac{L}{E} \quad \text{(provided } du \neq 0).$$

Problem 7.5.1

Consider a cone surface that is represented by equations (Fig. 7.5.2)

$$x = u \cos \alpha, \quad y = u \sin \alpha \cos \theta, \quad z = u \sin \alpha \sin \theta \qquad (7.5.39)$$

where (u, θ) are the surface coordinates, $u = |\overline{OM}|$, and α is the apex angle. The surface unit normal is determined with the equation

$$\mathbf{n} = \frac{\mathbf{r}_u \times \mathbf{r}_\theta}{|\mathbf{r}_u \times \mathbf{r}_\theta|} = [\sin \alpha \quad -\cos \alpha \cos \theta \quad -\cos \alpha \sin \theta]^T \qquad (7.5.40)$$

(provided $u \sin \alpha \neq 0$).
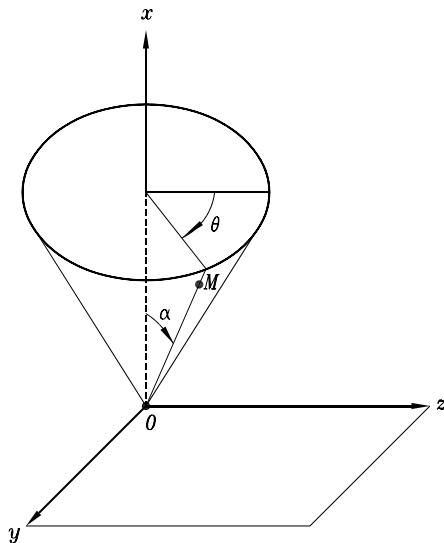
Figure 7.5.2: Cone surface.

(a) Determine auxiliary parameters (i) v [use Eqs. (7.5.4)], and (ii) coefficients A, B, and C [use Eqs. (7.5.12)].
(b) Determine solutions of μ for principal directions [use Eq. (7.5.14)], and unit vectors for principal directions [use Eq. (7.5.37)].
(c) Determine principal curvatures κ_I and κ_{II}.

Solution

(a) $v = 90°$, $A = 0$, $B = 0$, $C = \dfrac{1}{u \tan \alpha}$.

(b) $\mu_I = 90°$, $\mathbf{e}_I = \mathbf{e}_u = \dfrac{\mathbf{r}_u}{|\mathbf{r}_u|} = [\cos \alpha \quad \sin \alpha \cos \theta \quad \sin \alpha \sin \theta]^{\mathrm{T}}$

$\mu_{II} = 0$, $\mathbf{e}_{II} = \mathbf{e}_\theta = \dfrac{\mathbf{r}_\theta}{|\mathbf{r}_\theta|} = [0 \quad -\sin \theta \quad \cos \theta]^{\mathrm{T}}$.

(c) $\kappa_I = 0$, $\kappa_{II} = \dfrac{1}{u \tan \alpha}$.

Problem 7.5.2

Consider a spherical surface that is represented by

$$\mathbf{r} = [\rho \cos \theta \cos u \quad \rho \cos \theta \sin u \quad \rho \sin \theta]^{\mathrm{T}}. \tag{7.5.41}$$

The surface unit normal is represented by

$$\mathbf{n} = \dfrac{\mathbf{r}_u \times \mathbf{r}_\theta}{|\mathbf{r}_u \times \mathbf{r}_\theta|} = [\cos u \cos \theta \quad \sin u \cos \theta \quad \sin \theta]^{\mathrm{T}} \tag{7.5.42}$$

(provided $\rho \cos u \neq 0$). The surface normal $\mathbf{N}$ is equal to zero at two points where $\cos u = 0$, but such points are just pseudosingular points [see Section (5.5)].

(a) Determine auxiliary expressions for (i) v [use Eqs. (7.5.4)], and (ii) coefficients A, B, and C [use Eqs. (7.5.12)].

(b) Determine solutions of μ for principal directions if such exist [use Eq. (7.5.14)].
(c) Derive the equation for normal curvature [use Eq. (7.5.11)].

Solution

(a) $v = 90°$, $\quad A = -\dfrac{1}{\rho}$, $\quad B = 0$, $\quad C = -\dfrac{1}{\rho}$.

(b) The values of μ for principal directions are undetermined.

(c) The normal curvature is $\kappa_n = -\dfrac{1}{\rho}$ and does not depend on μ.

Problem 7.5.3

Consider the surface of an Archimedes worm that is represented by the equations

$$x = u \cos \alpha \cos \theta, \qquad y = u \cos \alpha \sin \theta, \qquad z = p\theta - u \sin \alpha \qquad (7.5.43)$$

where (u, θ) are the surface coordinates, p is the screw parameter, and α is a constant design parameter. The worm surface is a ruled one and is generated by a straight line that performs a screw motion about the worm axis (the z axis). The surface unit normal is represented by the equations

$$\mathbf{n} = \frac{\mathbf{N}}{|\mathbf{N}|} = \frac{\mathbf{r}_u \times \mathbf{r}_\theta}{|\mathbf{r}_u \times \mathbf{r}_\theta|} = (u^2 + p^2)^{-0.5} \begin{bmatrix} u \sin \alpha \cos \theta + p \sin \theta \\ u \sin \alpha \sin \theta - p \cos \theta \\ u \cos \alpha \end{bmatrix} \qquad (7.5.44)$$

(provided $\cos \alpha \neq 0$).
   Using approach 1, derive equations for:

  (i) angle v and $v/2$ [use Eqs. (7.5.4)];
 (ii) coefficients A, B, and C [use Eqs. (7.5.12)];
(iii) angle μ that determines the principal directions on the worm surface [use Eq. (7.5.14)];
(iv) unit vector $\mathbf{t}$ of principal directions [use Eq. (7.5.3)];
 (v) principal curvatures [use Eq. (7.5.11)].

Solution

(i) $\cos v = -\dfrac{p \sin \alpha}{\sqrt{u^2 \cos^2 \alpha + p^2}}$, $\qquad \sin v = \dfrac{\cos \alpha \sqrt{u^2 + p^2}}{\sqrt{u^2 \cos^2 \alpha + p^2}}$

$\tan \dfrac{v}{2} = \dfrac{p \sin \alpha + \sqrt{u^2 \cos^2 \alpha + p^2}}{\cos \alpha \sqrt{u^2 + p^2}}.$

(ii) $A = 0$, $\qquad B = -\dfrac{p(u^2 \cos^2 \alpha + p^2)^{0.5}}{(u^2 + p^2)^{\frac{3}{2}} \cos \alpha}$

$C = -\dfrac{u^2 \tan \alpha}{(u^2 + p^2)^{\frac{3}{2}}}.$

(iii) $\tan 2\mu = \dfrac{2[p(u^2 \cos^2\alpha + p^2)^{0.5} - u^2 \sin\alpha \cos v] \sin v}{2[p(u^2 \cos^2\alpha + p^2)^{0.5} - u^2 \sin\alpha \cos v] \cos v + u^2 \sin\alpha}$

$$= \dfrac{2p(u^2 + p^2)^{\frac{3}{2}}}{\tan\alpha[u^2(u^2 \cos^2\alpha + p^2) - 2p^2(u^2 + p^2)]}.$$

These equations provide two solutions for μ: μ_I and $\mu_{II} = \mu_I + \pi/2$.

(iv) $e_i = \dfrac{e_u \sin\mu_i + e_\theta \sin(v - \mu_i)}{\sin v}$ $(i = I, II)$.

(v) $\kappa_i = [2B \sin\mu_i + C \sin(v - \mu_i)] \sin(v - \mu_i)$ $(i = I, II)$.

Problem 7.5.4

With the conditions of Problem (7.5.3), using approach 2, derive equations for:

(i) coefficients E, F, G, L, M, and N for the first and second fundamental form [use Eqs. (7.4.4) and (7.4.10), respectively];
(ii) $(du/d\theta)_i = b_i$ ($i = I, II$) that correspond to principal directions [use Eq. (7.5.35)];
(iii) principal curvatures [use Eqs. (7.5.33) and (7.5.34)];
(iv) expressions for the unit vectors of principal directions [use Eqs. (7.5.37)].

Solution

(i) $E = 1$, $F = -p \sin\alpha$, $G = u^2 \cos^2\alpha + p^2$

$L = 0$, $M = -\dfrac{p \cos\alpha}{(u^2 + p^2)^{\frac{1}{2}}}$, $N = -\dfrac{u^2 \sin\alpha \cos\alpha}{(u^2 + p^2)^{\frac{1}{2}}}$.

(ii) $b_i = \dfrac{-u^2 \sin\alpha \pm (u^4 \sin^2\alpha + 4p^2u^2 + 4p^4)^{0.5}}{2p}$ $(i = I, II)$.

The upper and lower signs correspond to $i = I, II$, respectively.

(iii) $\kappa_i = \dfrac{Lb_i + M}{Eb_i + F}$ $(i = I, II)$.
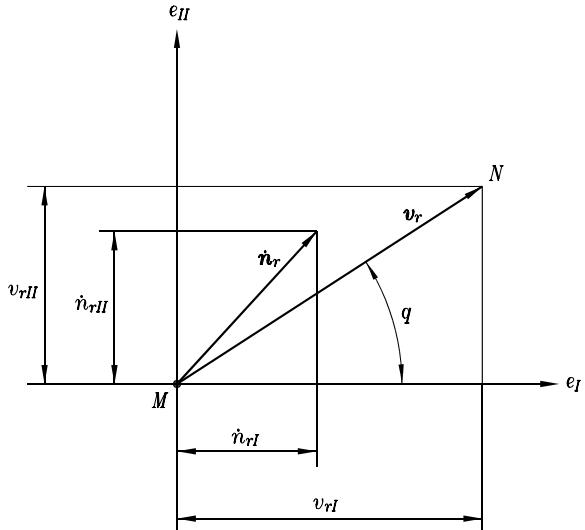
(iv) $e_i = \dfrac{r_u b_i + r_\theta}{|r_u b_i + r_\theta|}$ $(i = I, II)$.

7.6 EULER'S EQUATION

Euler's equation relates the normal and principal curvatures of a surface and is represented as

$$\kappa_n = \kappa_I \cos^2 q + \kappa_{II} \sin^2 q \tag{7.6.1}$$

where q is formed by vector $\overrightarrow{MN}$ and the unit vector e_I (Fig. 7.6.1). Vector $\overrightarrow{MN}$ represents the direction chosen in the tangent plane to the surface, and κ_n is the surface normal curvature on this direction. Unit vectors e_I and e_{II} are directed along the principal directions, and κ_I and κ_{II} are the principal curvatures.

Figure 7.6.1: Decomposition of vectors $\dot{\mathbf{n}}_r$ and $\mathbf{v}_r$.

The derivation of Eq. (7.6.1) is based on the following considerations:

(i) Directions of vectors $\mathbf{v}_r$ and $\dot{\mathbf{n}}_r$ [see Eq. (7.5.15)] are not collinear at any direction that differs from $\mathbf{e}_I$ and $\mathbf{e}_{II}$ (Fig. 7.6.1).

(ii) Using Eq. (7.4.24) for normal curvature, after transformations, we obtain

$$\kappa_n = -\frac{\dot{\mathbf{n}}_r \cdot \mathbf{v}_r}{(\mathbf{v}_r)^2} = -\frac{\dot{n}_{r\,I}\, v_{r\,I} + \dot{n}_{r\,II}\, v_{r\,II}}{(v_{r\,I})^2 + (v_{r\,II})^2}. \tag{7.6.2}$$

(iii) According to Rodrigues' formula, vectors $\mathbf{v}_{ri}$ and $\dot{\mathbf{n}}_{ri}$ $(i = I, II)$ are collinear at principal directions and

$$\kappa_i\, v_{ri} = -\dot{n}_{ri} \qquad (i = I, II). \tag{7.6.3}$$

(iv) Equations (7.6.2) and (7.6.3) yield

$$\kappa_n = \frac{\kappa_I (v_{r\,I})^2 + \kappa_{II} (v_{r\,II})^2}{(v_{r\,I})^2 + (v_{r\,II})^2}. \tag{7.6.4}$$

(v) In accordance with Fig. 7.6.1, we have

$$\cos q = \frac{v_{r\,I}}{[(v_{r\,I})^2 + (v_{r\,II})^2]^{0.5}}, \qquad \sin q = \frac{v_{r\,II}}{[(v_{r\,I})^2 + (v_{r\,II})^2]^{0.5}}. \tag{7.6.5}$$

(vi) Considering Eqs. (7.6.4) and (7.6.5) simultaneously, we obtain Euler's equation (7.6.1).

7.7 GAUSSIAN CURVATURE; THREE TYPES OF SURFACE POINTS

The *Gaussian curvature K* at a point of a surface is represented by

$$K = \kappa_I \kappa_{II} = \frac{LN - M^2}{EG - F^2}.$$
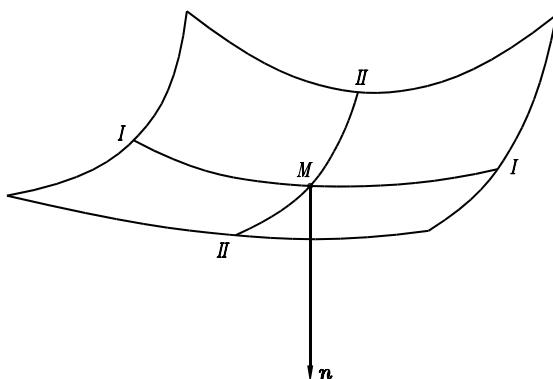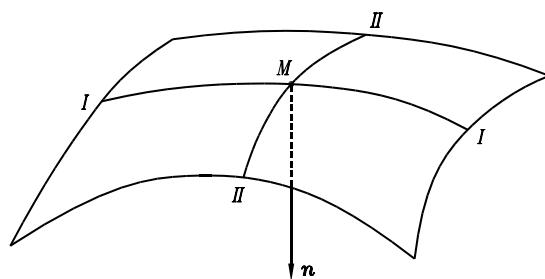
Figure 7.7.1: Surface elliptic point.

The sign of K depends on the signs of principal curvatures κ_I and κ_{II}. We can also determine the sign of K through the sign of $(LN - M^2)$ because $(EG - F^2)$ is always positive.

There are three types of surface points:

(1) The *elliptic* point – when the principal curvatures are of the same sign and the Gaussian curvature $K > 0$ (Fig. 7.7.1).
(2) The *hyperbolic* point – when the principal curvatures are of different signs and the Gaussian curvature $K < 0$ (Fig. 7.7.2). The surface has the form of a saddle near the considered point M. There are two such directions at M where the normal curvature is zero. These directions are called *asymptotic*.
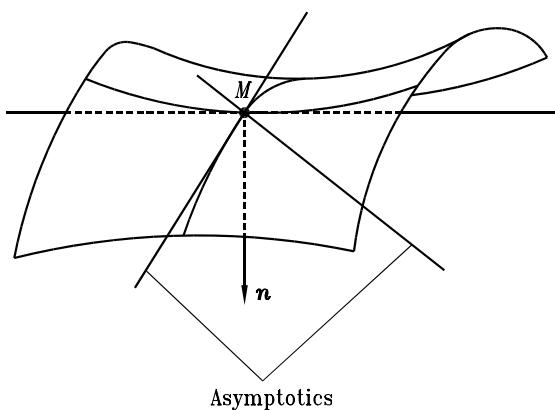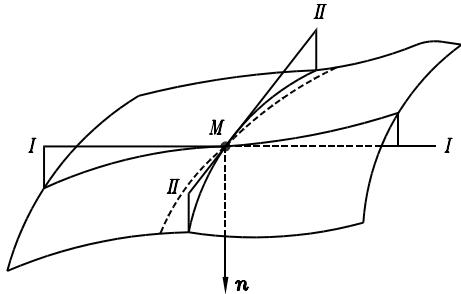
Figure 7.7.2: Surface hyperbolic point.

Figure 7.7.3: Surface parabolic point.

(3) The *parabolic* point – when one of the principal curvatures is zero (direction I in Fig. 7.7.3).

There are two approaches for determination of asymptotic directions. The first one is based on Euler's equation (7.6.1), which for the case when $\kappa_n = 0$ yields

$$\tan q = \pm \sqrt{-\frac{\kappa_I}{\kappa_{II}}}. \tag{7.7.1}$$

Equation (7.7.1) provides two real solutions for the asymptotic directions. Solutions for q that differ for π determine the same directions. The other approach is based on application of Eq. (7.5.11), which for the case when $\kappa_n = 0$ yields

$$\tan \mu = \frac{\sin v}{\cos v - \dfrac{B \mp (B^2 - AC)^{0.5}}{C}}. \tag{7.7.2}$$

Equation (7.7.2) provides two solutions of μ for asymptotic directions (solutions of μ that differ for $180°$ are not taken into account).

There is a specific interest in determining curvatures of *ruled* surfaces. Such surfaces are generated by a certain motion of a straight line. The surface parameter u in vector equation $\mathbf{r}(u, \theta)$ for a ruled surface determines the location of a point on the generating straight line. The second derivative $\mathbf{r}_{uu}$ and coefficients L and A on this direction are equal to zero.

There are two types of ruled surfaces: (i) those with a hyperbolic point, and (ii) those with a parabolic point. It is evident from Eq. (7.7.2) that there are two asymptotic directions for a ruled surface with a hyperbolic point that are determined with the following values of μ:

$$\mu_I = v \tag{7.7.3}$$

$$\tan \mu_{II} = \frac{\sin v}{\cos v - \dfrac{2B}{C}} \tag{7.7.4}$$

(provided $B \neq 0$).

Let us now consider such ruled surfaces for which $A = B = 0$. The analysis of Eqs. (7.5.11) and (7.5.12) yields the following results:

(i) Two principal directions on the ruled surface are determined with the conditions

$$v - \mu_I = 0 \qquad |v - \mu_{II}| = 90°. \qquad (7.7.5)$$

(ii) The principal curvatures are

$$\kappa_I = 0 \qquad \kappa_{II} = C. \qquad (7.7.6)$$

It can be proven that the condition $B = 0$ is satisfied for a *developed* ruled surface, taking into account the following considerations:

(a) Equation $B = 0$ yields

$$M = \mathbf{r}_{u\theta} \cdot \mathbf{n} = 0 \qquad (7.7.7)$$

and

$$\mathbf{r}_{u\theta} = \mathbf{0}, \qquad (7.7.8)$$

or $\mathbf{r}_{u\theta}$ lies in the tangent plane; $\mathbf{n} \neq \mathbf{0}$ because a regular surface is considered.

(b) It is evident that

$$\mathbf{r}_\theta \cdot \mathbf{n} = 0 \qquad (7.7.9)$$

and

$$\frac{\partial}{\partial u}(\mathbf{r}_\theta \cdot \mathbf{n}) = \mathbf{r}_{\theta u} \cdot \mathbf{n} + \mathbf{r}_\theta \cdot \mathbf{n}_u = 0. \qquad (7.7.10)$$

(c) Equations (7.7.8) and (7.7.10) yield that $\mathbf{n}_u = \mathbf{0}$ ($\mathbf{r}_\theta \neq \mathbf{0}$ for a regular surface). This means that the unit normals to the surface along the generating line are equal. Such a surface is a developable ruled surface.

A cone and an involute helicoid are examples of a developed ruled surface, and the point of the surface is a parabolic one. The surface of an Archimedes worm is an undeveloped ruled surface, the point of the surface is a hyperbolic one, and there are two asymptotic directions on such a surface.
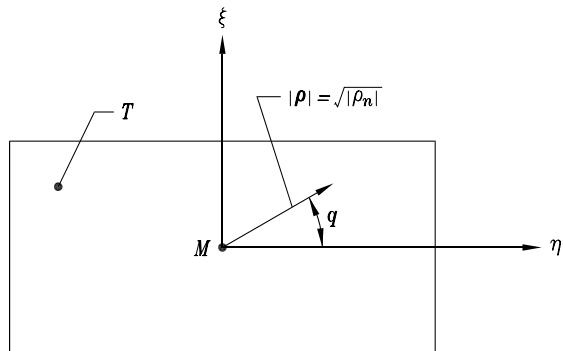
Problem 7.7.1
Consider a straight helicoid that represents the surface of a square screw. We may obtain equations of a straight helicoid taking in Eqs. (7.5.43) $\alpha = 0$. Verify that in this particular case $A = 0$, $C = 0$, and $v = 90°$, and determine the asymptotic directions [use Eq. (7.5.11)].

Solution

$$\mu_I = 90° \quad \text{and} \quad \mu_{II} = 0°.$$

The asymptotic directions coincide with the tangents to coordinate lines.

Figure 7.8.1: For derivation of Dupin's indicatrix.

7.8 DUPIN'S INDICATRIX

Dupin's indicatrix is a planar curve that illustrates the change of surface normal curvature in the neighborhood of surface point M. The position vector of a point of such a curve is designated with ρ where $|\rho| = \sqrt{|\rho_n|}$ and $|\rho_n|$ is the radius of normal curvature (Fig. 7.8.1). Axes η and ξ lie in plane T that is tangent to the surface and are directed along the unit vectors e_I and e_{II} of principal directions. The normal curvature κ_n and the principal curvatures κ_I and κ_{II} are related by Euler's equation (7.6.1) and $|\kappa_n| = 1/\rho$. The Dupin's indicatrix can be represented in coordinate system (η, ξ) as follows:

$$\eta = \sqrt{|\rho|}\cos q, \qquad \xi = \sqrt{|\rho|}\sin q. \tag{7.8.1}$$

We consider the Dupin's indicatrix for elliptic, hyperbolic, and parabolic points of a surface.

Elliptic Point
Equations (7.8.1) and (7.6.1) yield

$$\frac{\eta^2}{\rho_I} + \frac{\xi^2}{\rho_{II}} = 1 \tag{7.8.2}$$
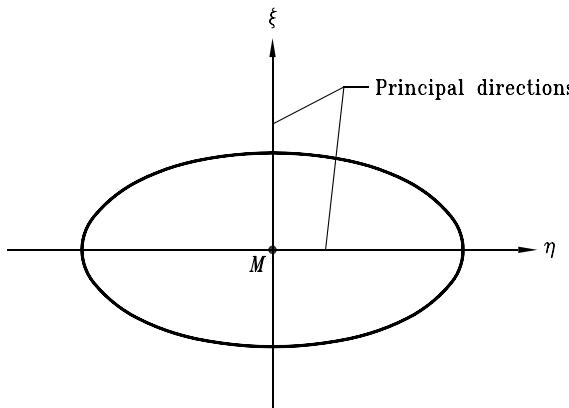
where $\rho_I = 1/\kappa_I$, $\rho_{II} = 1/\kappa_{II}$. The Gaussian curvature $K = \kappa_I\kappa_{II}$ is positive, and choosing appropriately the direction of the surface normal, we may consider that ρ_I and ρ_{II} are positive. Equation (7.8.2) represents an ellipse with axes $a = \sqrt{\rho_I}$ and $b = \sqrt{\rho_{II}}$ (Fig. 7.8.2).

Hyperbolic Point
The Gaussian curvature $K = \kappa_I\kappa_{II}$ is negative. We may assume that the chosen direction of the surface normal provides that κ_I is positive. Equations (7.8.1) and (7.6.1) yield the following equation of the indicatrix:

$$\frac{\eta^2}{a^2} - \frac{\xi^2}{b^2} = \pm 1,$$

which is the equation of two conjugate hyperboles (Fig. 7.8.3). Here, $a = \sqrt{\rho_I}$ and

Figure 7.8.2: Dupin's indicatrix for a surface elliptic point.

$b = \sqrt{\rho_{II}}$. The hyperboles have the same asymptotes whose directions are determined with Eq. (7.7.1).

Parabolic Point

The Gaussian curvature is zero. Assuming that $K = \kappa_I \kappa_{II} = 0$ because $\kappa_{II} = 0$ we obtain that the indicatrix is represented by the equation
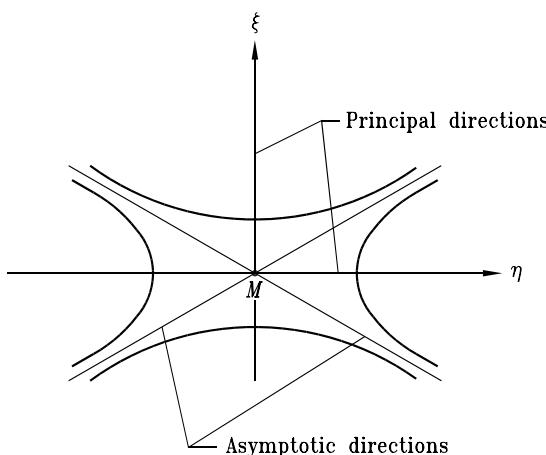
$$\frac{\eta^2}{\rho_I} = 1,$$

and the indicatrix is a set of two straight lines (Fig. 7.8.4).
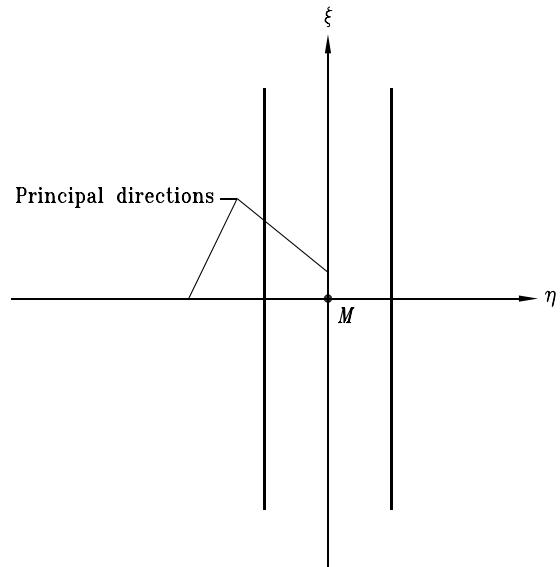
7.9 GEODESIC LINE; SURFACE TORSION

Geodesic Line

The geometric interpretation of surface torsion is based on the concept of the *geodesic lines* on a surface. A line on a surface is a geodesic one if the principal normal to the

Figure 7.8.3: Dupin's indicatrix for a surface hyperbolic point.

Figure 7.8.4: Dupin's indicatrix for a surface hyperbolic point.

curve at any curve point M coincides with the surface normal at M, or if the surface line is a straight one. It follows from this definition that the geodesic curvature of a geodesic line at any curve point is equal to zero.

When a set of curves on a surface is considered (Fig. 7.3.3) that pass through surface point M and have a common unit tangent $\mathbf{t}$ at M, there is a single curve of such a set that has the properties of a geodesic line. This line corresponds to the considered tangent vector. This means that because there is an infinite number of vectors $\mathbf{t}$ at the surface regular point M, there is an infinite number of geodesic lines that pass through M.
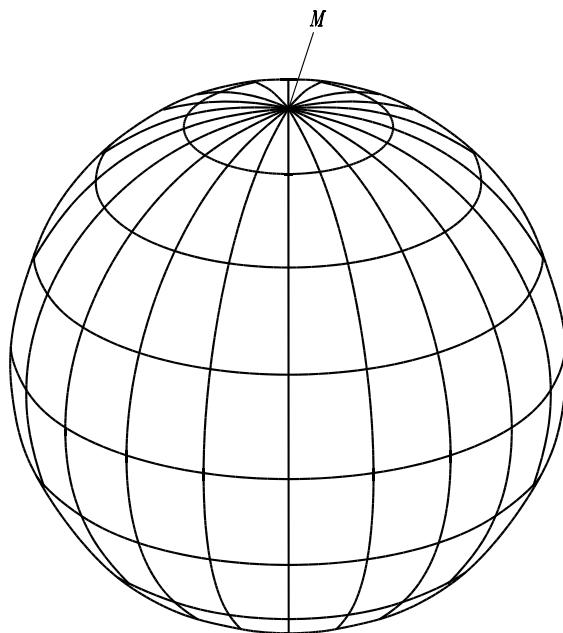
It has been proven in differential geometry that the geodesic line G that passes through the surface points M and N is the shortest distance between M and N. However, if G is a closed curve, the smaller arc $\overset{\frown}{MN}$ should be considered.

Figures (7.9.1) through (7.9.3) illustrate various examples of geodesic curves. In the case of a spherical surface any line of its large circle that passes through surface point M is a geodesic line. Figure 7.9.1 shows the infinite number of geodesic lines that pass through surface point M.

In the case of a surface of revolution (Fig. 7.9.2) the geodesic lines with common surface point M are the generatrix G that passes through M, and an infinite large number of lines L. The current point M_i of L is determined with the following equation based on Clariaut's theorem [Favard, 1957]:

$$\rho_i \sin \beta_i = \text{constant} \tag{7.9.1}$$

where ρ_i is the distance of point M_i from the axis of the surface of revolution. A particular case of a surface of revolution is the surface of a circular cylinder (Fig. 7.9.3). The geodesic lines at point M are the generatrix, the cylinder circle, and an infinitely large number of helices with angles β_i; two of these helices are shown in Fig. 7.9.3. In the case of a ruled surface (developed or undeveloped) one of the geodesic lines that
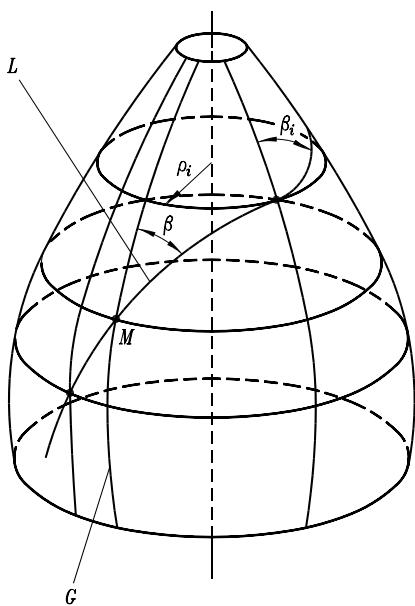
Figure 7.9.1: Geodesic lines on a spherical surface.
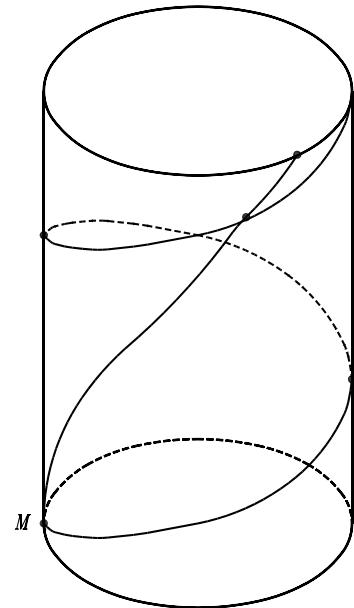
passes through surface point M is the generatrix (it is a straight line) that generates the ruled surface.

Surface Torsion as the Curve Torsion of a Geodesic Line

In accordance with Bonnet's theorem (see Favard [1957]) the surface torsion is the same for the whole set of curves that are in tangency with each other at surface point M

Figure 7.9.2: Geodesic lines on a surface of revolution.

Figure 7.9.3: Geodesic lines on a cylinder surface.

(Fig. 7.3.3). One of these curves is the geodesic line that is unique for the considered common unit tangent **t**. Thus, the curve torsion of the geodesic line is the same as the surface torsion of any surface curve that is in tangency with the geodesic line.

We have found above [see expressions (7.3.14)] that the surface torsion t is represented as

$$t = \tau + \delta_s \qquad \left(\delta_s = \frac{d}{ds}(\delta) \right) \tag{7.9.2}$$
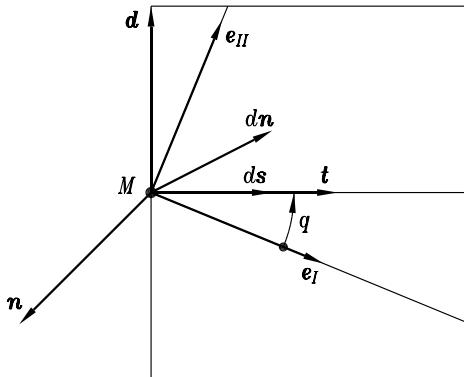
where δ is the angle that is formed by the principal normal to the curve and the surface normal. In the case of a geodesic line, δ is equal to zero or $180°$ at any point of the curve, and $\delta_s = 0$. Thus, $t = \tau_g$ where τ_g is the torsion of the geodesic line. This means that the surface torsion is equal to the torsion of the geodesic line.

The surface torsion and the torsion of the geodesic line may be interpreted as well as the measure of how the surface normal plane (it is drawn through the tangent to the geodesic line) is twisting as a point moves along the geodesic line. (Recall that the current osculating plane for a geodesic line coincides with the respective surface normal plane.)

Analytically, this can be proven with the following considerations:

(i) Equations (7.2.17) and (7.2.14) yield that the torsion for a spatial curve may be represented as

$$\tau = -\mathbf{b}_s \cdot \mathbf{m} = \mathbf{m}_s \cdot \mathbf{b}. \tag{7.9.3}$$

Figure 7.9.4: For interpretation of surface torsion.

(ii) When the spatial curve is the geodesic line on the surface, $\mathbf{b} = -\mathbf{d}$ because $\mathbf{m}$ and $\mathbf{n}$ coincide for a geodesic line, and the torsion of the geodesic line is

$$\tau_g = -\mathbf{n}_s \cdot \mathbf{d}. \tag{7.9.4}$$

The derivative $\mathbf{n}_s$ in accordance with Fig. 7.9.4 can be represented as follows:

$$\mathbf{n}_s = a\mathbf{t} + b\mathbf{d}. \tag{7.9.5}$$

Here, a and b are the projections of $\mathbf{n}_s$ on the unit vectors $\mathbf{t}$ and $\mathbf{d}$, determined as

$$a = \mathbf{n}_s \cdot \mathbf{t}, \qquad b = \mathbf{n}_s \cdot \mathbf{d}. \tag{7.9.6}$$

Equations (7.9.5) and (7.9.4) yield

$$t = \tau_g = -\mathbf{n}_s \cdot \mathbf{d} = -b \tag{7.9.7}$$

where b is the measure of how the surface normal plane twists when a point moves along the unit tangent $\mathbf{t}$ to the curve.
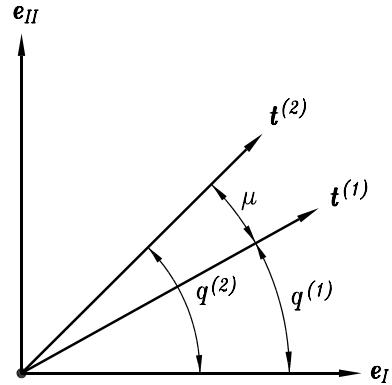
Relations Between Surface Torsion and Surface Principal Curvatures

We consider two cases:

(i) The principal curvatures and directions at surface point M are known. The unit vector $\mathbf{t}$ is determined with angle q (Fig. 7.9.4). The goal is to determine the surface torsion in the direction of $\mathbf{t}$.

(ii) Two directions in the tangent plane determined by the unit vectors $\mathbf{t}^{(1)}$ and $\mathbf{t}^{(2)}$ that form angle μ (Fig. 7.9.5) are given. The surface normal curvatures $(\kappa_n^{(1)}, \kappa_n^{(2)})$ and surface torsion $t^{(1)}$ are known. The goal is to determine the surface principal curvatures (κ_I, κ_{II}) and angle $q^{(1)}$ (or $q^{(2)}$).

Case I

Figure 7.9.4 shows the surface trihedron $\mathbf{e}_f(\mathbf{t}, \mathbf{d}, \mathbf{n})$, where $\mathbf{t}$ is the unit tangent to the surface curve; $\mathbf{n}$ is the surface normal; unit vectors $\mathbf{t}$ and $\mathbf{d}$ form a tangent plane; the

Figure 7.9.5: Surface principal directions and directions of tangents to two surface curves.

origin of the trihedron is the current point M of the surface curve; unit vectors $\mathbf{e}_I$ and $\mathbf{e}_{II}$ represent the principal directions; the principal curvatures are κ_I and κ_{II}; and angle q is formed by the unit vectors $\mathbf{e}_I$ and $\mathbf{t}$.

Our goal is to represent the surface torsion t in terms of κ_I, κ_{II}, and q. The derivations are based on the third equation of system (7.3.15).

Consider that the trihedron moves along the surface curve and vector $d\mathbf{s}$ represents the displacement along $\mathbf{t}$. The displacement of the trihedron is accompanied with the change of orientation of the surface normal $\mathbf{n}$ that is represented by $d\mathbf{n}$ (Fig. 7.9.4). Generally, $d\mathbf{n}$ and $d\mathbf{s}$ are not collinear. The third equation of system (7.3.15) is represented as

$$\mathbf{n}_s = \frac{d\mathbf{n}}{ds} = -\kappa_n \mathbf{t} - t\mathbf{d}. \tag{7.9.8}$$

The procedure for derivation of t in terms of principal curvatures is as follows:

Step 1: Multiplying both parts of Eq. (7.9.8) by $\mathbf{e}_I$ and $\mathbf{e}_{II}$, we obtain (Fig. 7.9.4)

$$dn_I = (-\kappa_n \cos q + t \sin q)ds \tag{7.9.9}$$

$$dn_{II} = (-\kappa_n \sin q - t \cos q)ds. \tag{7.9.10}$$

Step 2: The displacement vector $d\mathbf{s}$ can be represented as

$$d\mathbf{s} = (\cos q \, \mathbf{e}_I + \sin q \, \mathbf{e}_{II})ds = ds_I \mathbf{e}_I + ds_{II}\mathbf{e}_{II} \tag{7.9.11}$$

where

$$ds_I = ds \cos q, \quad ds_{II} = ds \sin q. \tag{7.9.12}$$

Step 3: In accordance with Rodrigues' theorem, we have

$$\frac{dn_I}{ds_I} = -\kappa_I, \quad \frac{dn_{II}}{ds_{II}} = -\kappa_{II}. \tag{7.9.13}$$

Thus

$$dn_I = -\kappa_I \cos q \, ds, \quad dn_{II} = -\kappa_{II} \sin q \, ds. \tag{7.9.14}$$

Step 4: Equations (7.9.9), (7.9.10), and (7.9.14) represent the following system of two linear equations in unknowns κ_n and t:

$$-\kappa_I \cos q = -\kappa_n \cos q + t \sin q \tag{7.9.15}$$

$$-\kappa_{II} \sin q = -\kappa_n \sin q - t \cos q. \tag{7.9.16}$$

Step 5: The solution of these equations for the surface torsion t yields

$$t = 0.5(\kappa_{II} - \kappa_I) \sin 2q. \tag{7.9.17}$$

Equation (7.9.17) has been proposed by Sophia Germain (see Nutbourne & Martin [1988]) and by O. Bonnet (see Favard [1957]). It is obvious that the surface torsion is equal to zero when the tangent coincides with the principal direction (when q is zero or $90°$).

NOTE. The solution of the system of linear equations (7.9.15) and (7.9.16) for κ_n represents the Euler equation introduced as

$$\kappa_n = \kappa_I \cos^2 q + \kappa_{II} \sin^2 q \tag{7.9.18}$$

where κ_n is the surface normal curvature in the direction of **t**.

Case 2

The input data are the normal curvatures $\kappa_n^{(1)}$, $\kappa_n^{(2)}$ given in directions of $\mathbf{t}^{(1)}$ and $\mathbf{t}^{(2)}$, and surface torsion $t^{(1)}$ given for $\mathbf{t}^{(1)}$; angle μ is formed by $\mathbf{t}^{(1)}$ and $\mathbf{t}^{(2)}$ (Fig. 7.9.5). The goal is to determine the principal curvatures κ_I and κ_{II} and angle $q^{(1)}$ (or $q^{(2)}$) (Fig. 7.9.5). The solution to this problem is based on the Euler equation for normal curvatures $\kappa_n^{(1)}$ and $\kappa_n^{(2)}$ and Eq. (7.9.17). Then we obtain the following system of three equations:

$$\kappa_I \left(1 + \cos 2q^{(1)}\right) + \kappa_{II} \left(1 - \cos 2q^{(1)}\right) = 2\kappa_n^{(1)}$$

$$\kappa_I \left[1 + \cos 2 \left(q^{(1)} + \mu\right)\right] + \kappa_{II} \left[1 - \cos 2 \left(q^{(1)} + \mu\right)\right] = 2\kappa_n^{(2)} \tag{7.9.19}$$

$$\kappa_I - \kappa_{II} = -\frac{2t^{(1)}}{\sin 2q^{(1)}}.$$

We may consider equation system (7.9.19) as a system of three dependent linear equations in two unknowns κ_I and κ_{II}. The rank of the augmented matrix must be equal to two, and this yields

$$\tan 2q^{(1)} = \frac{t^{(1)}(1 - \cos 2\mu)}{\kappa_n^{(2)} - \kappa_n^{(1)} - t^{(1)} \sin 2\mu}. \tag{7.9.20}$$

The solution of equations (7.9.19) for κ_I and κ_{II} is

$$\kappa_I = \kappa_n^{(1)} - t^{(1)} \tan q^{(1)} \tag{7.9.21}$$

$$\kappa_{II} = \kappa_n^{(1)} + t^{(1)} \cot q^{(1)}. \tag{7.9.22}$$

Equations (7.9.20) to (7.9.22) enable us to determine the principal curvatures of the surface and the principal directions (Fig. 7.9.5).

Relation Between Surface Normal Curvatures and Torsions in Directions of $t^{(1)}$ and $t^{(2)}$ (Fig. 7.9.5)

Equation (7.9.17) yields that

$$\frac{t^{(2)}}{t^{(1)}} = \frac{\sin 2\left(q^{(1)} + \mu\right)}{\sin 2q^{(1)}}.$$
(7.9.23)

Then, using equations (7.9.23) and (7.9.20), we obtain the sought-for relation

$$\frac{t^{(1)} + t^{(2)}}{\kappa_n^{(2)} - \kappa_n^{(1)}} - \cot \mu = 0.$$
(7.9.24)

8 Mating Surfaces: Curvature Relations, Contact Ellipse

8.1 INTRODUCTION

Consider that two solids (1 and 2) are provided with interacting surfaces Σ_1 and Σ_2, and perform the prescribed transformation of motion. Surfaces Σ_1 and Σ_2 are in continuous tangency. These conditions are typical for the case of generation of surfaces by a tool, and for transformation of motion by gear tooth surfaces.

Henceforth, we differentiate two cases of tangency: (i) the interacting surfaces Σ_1 and Σ_2 are in *line contact* at every instant, and Σ_2 is the *envelope* to the family of surfaces that is generated by Σ_1 in coordinate system S_2; and (ii) surfaces Σ_1 and Σ_2 are in *point* contact at every instant (the contact of Σ_1 and Σ_2 is localized).

We consider as given surface Σ_1 and the location of point P of surface tangency (P is the point of the *characteristic* on Σ_1 in the case in which Σ_2 is the envelope, or the single point of tangency of Σ_1 and Σ_2); given as well are the value of transmission function $\phi_2(\phi_1)$ at point P and the derivative $\partial/\partial\phi_1(\phi_2(\phi_1))$ at P. (The characteristic is the instantaneous line of contact of enveloping surfaces). Our goals are to determine (i) direct relations between the principal curvatures and directions of contacting surfaces at P, (ii) relations between the normal curvatures of surfaces Σ_1 and Σ_2, and (iii) the relative normal curvatures.

The solution to these problems is important for computerized simulation of bearing contact of interacting surfaces. The solution is based on the following ideas: (i) the velocity of a contact point in a fixed coordinate system (the reference frame for the movable solids) is represented in two components: (a) transfer motion *with* surface Σ_i, and (b) relative motion *over* surface Σ_i ($i = 1, 2$); and (ii) the displacement over the surface may be decomposed and represented by two components in separate motions along the principal directions of the respective surface; and (iii) a similar idea of decomposition is applied for representation of motion in two perpendicular directions in the tangent plane, particularly when one of these directions is the tangent to the contact line (for enveloping surfaces).

Decomposition of motion along the principal directions for a *single* surface was applied by Sophia Germain (see Nutbourne & Martin [1988]) for presentation of the surface torsion in terms of principal curvatures of the surface. Decomposition of motions along principal directions for interacting surfaces has been applied by Litvin [1969].

An extended approach, in a more general form, has been developed by Litvin & Hsiao [1993] and is presented in this book.

8.2 BASIC EQUATIONS

Conditions of continuous tangency of interacting surfaces yield the following relations between the velocities of the contact point (see Section 6.2):

$$\mathbf{v}_{tr}^{(1)} + \mathbf{v}_r^{(1)} = \mathbf{v}_{tr}^{(2)} + \mathbf{v}_r^{(2)}. \tag{8.2.1}$$

Thus,

$$\mathbf{v}_r^{(2)} = \mathbf{v}_r^{(1)} + \mathbf{v}_{tr}^{(1)} - \mathbf{v}_{tr}^{(2)} = \mathbf{v}_r^{(1)} + \mathbf{v}^{(12)}. \tag{8.2.2}$$

The subscripts "r" and "tr" indicate the velocity of the contact point in *relative* motion (*over* the surface) and in *transfer* motion (*with* the surface), respectively; $\mathbf{v}^{(12)}$ is the *sliding* velocity at the point of surface tangency, which is determined with the equation

$$\mathbf{v}^{(12)} = \boldsymbol{\omega}^{(12)} \times \mathbf{r}^{(1)} - \mathbf{R} \times \boldsymbol{\omega}^{(2)}. \tag{8.2.3}$$

Here, $\mathbf{r}^{(1)}$ is a position vector that is drawn from a point of the line of action of $\boldsymbol{\omega}^{(1)}$ to the point of tangency, and $\mathbf{R}$ is a position vector that is drawn from a point of the line of action of $\boldsymbol{\omega}^{(1)}$ to a point of the line of action of $\boldsymbol{\omega}^{(2)}$.

Similarly, we obtain

$$\dot{\mathbf{n}}_r^{(2)} = \dot{\mathbf{n}}_r^{(1)} + \left(\boldsymbol{\omega}^{(1)} - \boldsymbol{\omega}^{(2)}\right) \times \mathbf{n} = \dot{\mathbf{n}}_r^{(1)} + \left(\boldsymbol{\omega}^{(12)} \times \mathbf{n}\right). \tag{8.2.4}$$

Here, $\dot{\mathbf{n}}_r^{(i)}$ is the velocity of the tip of the surface unit normal in its motion *over* the surface (in addition to the translational motion), $\mathbf{n}$ is the surface unit normal, and $\boldsymbol{\omega}^{(i)}$ is the angular velocity of solid i (it is assumed that the solids with the interacting surfaces perform rotational motions). The advantage of Eqs. (8.2.2) and (8.2.4) is the possibility of determining $\mathbf{v}_r^{(2)}$ and $\dot{\mathbf{n}}_r^{(2)}$ for surface Σ_2, although the equations of Σ_2 are not known yet.

For further derivations, in addition to Eqs. (8.2.2) and (8.2.4), we use the differentiated equation of meshing

$$\frac{d}{dt}\left(\mathbf{n} \cdot \mathbf{v}^{(12)}\right) = 0. \tag{8.2.5}$$

The equation of meshing

$$\mathbf{n} \cdot \mathbf{v}^{(12)} = 0 \tag{8.2.6}$$

is the *necessary* condition of the existence of the envelope to the family of surfaces (see Section 6.1). Using Eqs. (8.2.3) to (8.2.6), we obtain after transformations the following differentiated equation of meshing:

$$\left(\dot{\mathbf{n}}_r^{(i)} \cdot \mathbf{v}^{(12)}\right) - \left[\mathbf{v}_r^{(i)} \cdot \left(\boldsymbol{\omega}^{(12)} \times \mathbf{n}\right)\right] + \mathbf{n} \cdot \left[\left(\boldsymbol{\omega}^{(1)} \times \mathbf{v}_{tr}^{(2)}\right) - \left(\boldsymbol{\omega}^{(2)} \times \mathbf{v}_{tr}^{(1)}\right)\right]$$

$$- \left(\omega^{(1)}\right)^2 m_{21}' \mathbf{n} \cdot \left[\mathbf{k}_2 \times \left(\mathbf{r}^{(1)} - \mathbf{R}\right)\right] = 0 \quad (i = 1, 2). \tag{8.2.7}$$

Here,

$$m_{21}(\phi_1) = \frac{\omega^{(2)}}{\omega^{(1)}}, \qquad m'_{21} = \frac{\partial}{\partial \phi_1}[m_{21}(\phi_1)].$$

8.3 PLANAR GEARING: RELATION BETWEEN CURVATURES

The equations of the envelope to a family of planar curves are more complicated than the equations of the curve that generates the curve family. Thus, it is an attractive prospect to determine the curvature of the envelope having only the equations of the generating curve and parameters of motion of the process for envelope generation. Such a method was first proposed by Litvin [1969].

Planar gearing may be considered as a particular case of spatial gearing, which is discussed below in Sections 8.4 to 8.6. For the purpose of simplification of study, the case of planar gearing is considered first and independent of these sections.

Consider the following conditions:

(1) Three coordinate systems S_1, S_2, and S_f are applied. Coordinate systems S_1 and S_2 are rigidly connected to the driving and driven gears 1 and 2; coordinate system S_f is rigidly connected to the frame.

(2) The shape Σ_1 is represented by

$$\mathbf{r}_1(\theta_1) \in C^2, \quad \theta_1 \in G, \quad \frac{d\mathbf{r}_1}{d\theta_1} \neq 0. \tag{8.3.1}$$

(3) The angles of gear rotation ϕ_1 and ϕ_2 are related by the function

$$\phi_2(\phi_1) \in C^2, \quad a < \phi_1 < b. \tag{8.3.2}$$

(4) The equation of meshing is determined by the equation

$$\mathbf{n}_f^{(1)} \cdot \mathbf{v}_f^{(12)} = \mathbf{n}_f^{(1)} \cdot \left[\left(\boldsymbol{\omega}_f^{(12)} \times \mathbf{r}_f^{(1)} \right) - \left(\overline{O_1 O_2} \times \boldsymbol{\omega}_f^{(2)} \right) \right] = f(\theta_1, \phi_1) = 0. \tag{8.3.3}$$

(5) The curvature of shape Σ_1 is represented by the equation

$$\kappa_1 \mathbf{v}_r^{(1)} = -\dot{\mathbf{n}}_r^{(1)}. \tag{8.3.4}$$

The curvature of shape Σ_2 is represented as

$$\kappa_2 \mathbf{v}_r^{(2)} = -\dot{\mathbf{n}}_r^{(2)}. \tag{8.3.5}$$

The problem is to determine the curvature κ_2 of shape Σ_2 in terms of κ_1 and the parameters of motion. The solution to this problem is based on Eqs. (8.2.2), (8.2.4), and (8.2.5), which we represent as follows:

$$\mathbf{v}_r^{(2)} = \mathbf{v}_r^{(1)} + \mathbf{v}^{(12)} \tag{8.3.6}$$

$$\dot{\mathbf{n}}_r^{(2)} = \dot{\mathbf{n}}_r^{(1)} + \left(\boldsymbol{\omega}^{(12)} \times \mathbf{n}^{(1)} \right) \tag{8.3.7}$$

$$\frac{d}{dt} \left(\mathbf{n}^{(1)} \cdot \mathbf{v}^{(12)} \right) = 0. \tag{8.3.8}$$

Equation (8.3.8) is just the equation of meshing differentiated with respect to time. The subscript f in Eq. (8.3.8) [see Eq. (8.3.3)] is dropped for simplification.

Let us transform Eq. (8.3.8) as follows:

$$\frac{d}{dt}\left(\mathbf{n}^{(1)} \cdot \mathbf{v}^{(12)}\right) = \left(\dot{\mathbf{n}}^{(1)} \cdot \mathbf{v}^{(12)}\right) + \left(\mathbf{n}^{(1)} \cdot \frac{d}{dt}\left(\mathbf{v}^{(12)}\right)\right) = 0. \tag{8.3.9}$$

Here,

$$\dot{\mathbf{n}}^{(1)} = \dot{\mathbf{n}}_{tr}^{(1)} + \dot{\mathbf{n}}_{r}^{(1)} = \left(\boldsymbol{\omega}^{(1)} \times \mathbf{n}^{(1)}\right) + \dot{\mathbf{n}}_{r}^{(1)}. \tag{8.3.10}$$

We represent the derivative $(d/dt)\,(\mathbf{v}^{(12)})$ by

$$\frac{d}{dt}\left(\mathbf{v}^{(12)}\right) = \frac{d}{dt}\left\{\left[\left(\boldsymbol{\omega}^{(1)} - \boldsymbol{\omega}^{(2)}\right) \times \mathbf{r}^{(1)}\right] - \left(\mathbf{E} \times \boldsymbol{\omega}^{(2)}\right)\right\} \tag{8.3.11}$$

where $\mathbf{E} = \overline{O_f O_2}$. Not losing generality in our solution, we assume that gear 1 rotates counterclockwise with constant angular velocity $\omega^{(1)}$. The angular velocity of gear 2 is

$$\boldsymbol{\omega}^{(2)} = \mp \omega^{(2)}\mathbf{k} = \mp \frac{\omega^{(1)}}{m_{12}(\phi_1)}\mathbf{k} \tag{8.3.12}$$

where

$$m_{12}(\phi_1) = \frac{d\phi_1}{d\phi_2} = \frac{1}{\dfrac{d}{d\phi_1}(\phi_2(\phi_1))}.$$

The time derivative $\dot{\boldsymbol{\omega}}^{(2)}$ is

$$\dot{\boldsymbol{\omega}}^{(2)} = \mp \frac{d}{d\phi_1}\left(\frac{\omega^{(1)}}{m_{12}(\phi_1)}\right)\frac{d\phi_1}{dt}\mathbf{k} = \pm \frac{m_{12}'\left(\omega^{(1)}\right)^2}{(m_{12})^2}\mathbf{k}$$

$$= \pm \frac{m_{12}'\omega^{(1)}\omega^{(2)}}{m_{12}}\mathbf{k} = -\frac{m_{12}'\omega^{(1)}}{m_{12}}\boldsymbol{\omega}^{(2)}. \tag{8.3.13}$$

Here, the upper (lower) sign in Eqs. (8.3.12) and (8.3.13) corresponds to gear rotations in opposite (same) directions; $m_{12}' = (d/d\phi_1)(m_{12}(\phi_1))$; and $\mathbf{k}$ is the unit vector of axis z_f.

Let us now transform Eq. (8.3.11):

$$\frac{d}{dt}\left(\mathbf{v}^{(12)}\right) = \left(-\dot{\boldsymbol{\omega}}^{(2)} \times \mathbf{r}^{(1)}\right) + \left(\boldsymbol{\omega}^{(12)} \times \dot{\mathbf{r}}^{(1)}\right) - \left(\mathbf{E} \times \dot{\boldsymbol{\omega}}^{(2)}\right)$$

$$= \left(-\dot{\boldsymbol{\omega}}^{(2)} \times \mathbf{r}^{(1)}\right) + \left(\boldsymbol{\omega}^{(12)} \times \left(\mathbf{v}_{tr}^{(1)} + \mathbf{v}_{r}^{(1)}\right)\right) - \left(\mathbf{E} \times \dot{\boldsymbol{\omega}}^{(2)}\right). \tag{8.3.14}$$

Note that $\dot{\mathbf{r}}^{(1)} = \mathbf{v}_{abs}^{(1)} = \mathbf{v}_{tr}^{(1)} + \mathbf{v}_{r}^{(1)}$. Substituting $\dot{\boldsymbol{\omega}}^{(2)}$ from (8.3.13), we get

$$\frac{d}{dt}\left(\mathbf{v}^{(12)}\right) = \frac{m_{12}'}{m_{12}}\omega^{(1)}\left(\left(\boldsymbol{\omega}^{(2)} \times \mathbf{r}^{(1)}\right) + \left(\mathbf{E} \times \boldsymbol{\omega}^{(2)}\right)\right)$$

$$+ \left(\boldsymbol{\omega}^{(12)} \times \mathbf{v}_{r}^{(1)}\right) + \left(\boldsymbol{\omega}^{(12)} \times \mathbf{v}_{tr}^{(1)}\right)$$

$$= \frac{m_{12}'}{m_{12}}\omega^{(1)}\mathbf{v}_{tr}^{(2)} + \left(\boldsymbol{\omega}^{(12)} \times \mathbf{v}_{r}^{(1)}\right) + \left(\boldsymbol{\omega}^{(12)} \times \mathbf{v}_{tr}^{(1)}\right). \tag{8.3.15}$$

Equations (8.3.9), (8.3.10), and (8.3.15) yield

$$\frac{d}{dt}\left(\mathbf{n}^{(1)} \cdot \mathbf{v}^{(12)}\right) = \dot{\mathbf{n}}_r^{(1)} \cdot \mathbf{v}^{(12)} + \boldsymbol{\omega}^{(1)} \cdot \left(\mathbf{n}^{(1)} \times \mathbf{v}^{(12)}\right)$$

$$+ \mathbf{n}^{(1)} \cdot \left(\boldsymbol{\omega}^{(12)} \times \mathbf{v}_r^{(1)}\right) + \mathbf{n}^{(1)} \cdot \left(\boldsymbol{\omega}^{(12)} \times \mathbf{v}_{tr}^{(1)}\right)$$

$$+ \frac{m_{12}'}{m_{12}}\omega^{(1)}\left(\mathbf{n}^{(1)} \cdot \mathbf{v}_{tr}^{(2)}\right) = 0. \tag{8.3.16}$$

We may transform Eq. (8.3.16) further by taking into account the following relations:

$$\boldsymbol{\omega}^{(1)} \cdot \left(\mathbf{n}^{(1)} \times \mathbf{v}^{(12)}\right) = -\mathbf{n}^{(1)} \cdot \left(\boldsymbol{\omega}^{(1)} \times \mathbf{v}_{tr}^{(1)}\right) + \mathbf{n}^{(1)} \cdot \left(\boldsymbol{\omega}^{(1)} \times \mathbf{v}_{tr}^{(2)}\right) \tag{8.3.17}$$

$$\mathbf{n}^{(1)} \cdot \left(\boldsymbol{\omega}^{(12)} \times \mathbf{v}_{tr}^{(1)}\right) = \mathbf{n}^{(1)} \cdot \left[\left(\boldsymbol{\omega}^{(1)} \times \mathbf{v}_{tr}^{(1)}\right) - \left(\boldsymbol{\omega}^{(2)} \times \mathbf{v}_{tr}^{(1)}\right)\right]. \tag{8.3.18}$$

Equations (8.3.17) and (8.3.18) yield

$$\boldsymbol{\omega}^{(1)} \cdot \left(\mathbf{n}^{(1)} \times \mathbf{v}^{(12)}\right) + \mathbf{n}^{(1)} \cdot \left(\boldsymbol{\omega}^{(12)} \times \mathbf{v}_{tr}^{(1)}\right)$$

$$= \mathbf{n}^{(1)} \cdot \left[\left(\boldsymbol{\omega}^{(1)} \times \mathbf{v}_{tr}^{(2)}\right) - \left(\boldsymbol{\omega}^{(2)} \times \mathbf{v}_{tr}^{(1)}\right)\right]. \tag{8.3.19}$$

Further transformation of Eq. (8.3.19) yields

$$\boldsymbol{\omega}^{(1)} \times \mathbf{v}_{tr}^{(2)} = \left(\boldsymbol{\omega}^{(1)} \times \left(\boldsymbol{\omega}^{(2)} \times \mathbf{r}^{(1)}\right)\right) + \left(\boldsymbol{\omega}^{(1)} \times \left(\mathbf{E} \times \boldsymbol{\omega}^{(2)}\right)\right)$$

$$= \boldsymbol{\omega}^{(2)}\left(\boldsymbol{\omega}^{(1)} \cdot \mathbf{r}^{(1)}\right) - \mathbf{r}^{(1)}\left(\boldsymbol{\omega}^{(1)} \cdot \boldsymbol{\omega}^{(2)}\right) + \mathbf{E}\left(\boldsymbol{\omega}^{(1)} \cdot \boldsymbol{\omega}^{(2)}\right)$$

$$- \boldsymbol{\omega}^{(2)}\left(\boldsymbol{\omega}^{(1)} \cdot \mathbf{E}\right)$$

$$= \left(\mathbf{E} - \mathbf{r}^{(1)}\right)\left(\boldsymbol{\omega}^{(1)} \cdot \boldsymbol{\omega}^{(2)}\right). \tag{8.3.20}$$

Here, $\boldsymbol{\omega}^{(1)} \cdot \mathbf{r}^{(1)} = 0$ and $\boldsymbol{\omega}^{(1)} \cdot \mathbf{E} = 0$ due to the perpendicularity of vectors in these scalar products. Similarly,

$$\boldsymbol{\omega}^{(2)} \times \mathbf{v}_{tr}^{(1)} = \boldsymbol{\omega}^{(2)} \times \left(\boldsymbol{\omega}^{(1)} \times \mathbf{r}^{(1)}\right)$$

$$= \boldsymbol{\omega}^{(1)}\left(\boldsymbol{\omega}^{(2)} \cdot \mathbf{r}^{(1)}\right) - \mathbf{r}^{(1)}\left(\boldsymbol{\omega}^{(1)} \cdot \boldsymbol{\omega}^{(2)}\right)$$

$$= -\mathbf{r}^{(1)}\left(\boldsymbol{\omega}^{(1)} \cdot \boldsymbol{\omega}^{(2)}\right). \tag{8.3.21}$$

Equations (8.3.19) to (8.3.21) yield

$$\mathbf{n}^{(1)} \cdot \left[\left(\boldsymbol{\omega}^{(1)} \times \mathbf{v}_{tr}^{(2)}\right) - \left(\boldsymbol{\omega}^{(2)} \times \mathbf{v}_{tr}^{(1)}\right)\right] = \left(\mathbf{n}^{(1)} \cdot \mathbf{E}\right)\left(\boldsymbol{\omega}^{(1)} \cdot \boldsymbol{\omega}^{(2)}\right). \tag{8.3.22}$$

The final expression of Eq. (8.3.16) is as follows:

$$\frac{d}{dt}\left(\mathbf{n}^{(1)} \cdot \mathbf{v}^{(12)}\right) = \dot{\mathbf{n}}_r^{(1)} \cdot \mathbf{v}^{(12)} + \mathbf{n}^{(1)} \cdot \left(\boldsymbol{\omega}^{(12)} \times \mathbf{v}_r^{(1)}\right)$$

$$+ \left(\mathbf{n}^{(1)} \cdot \mathbf{E}\right)\left(\boldsymbol{\omega}^{(1)} \cdot \boldsymbol{\omega}^{(2)}\right) + \frac{m_{12}'}{m_{12}}\omega^{(1)}\left(\mathbf{n}^{(1)} \cdot \mathbf{v}_{tr}^{(2)}\right) = 0. \tag{8.3.23}$$

To get the direct relation between curvatures of conjugate shapes κ_1 and κ_2, we apply a system of equations formed by (8.3.23) and from (8.3.4) to (8.3.7). We may transform this system and obtain a system of three equations in two unknowns, $v_r^{(1)}$ and $v_r^{(2)}$. For

these transformations, we represent that

$$v_r^{(1)} = \mathbf{v}_r^{(1)} \cdot \mathbf{i}_t, \quad v_r^{(2)} = \mathbf{v}_r^{(2)} \cdot \mathbf{i}_t, \quad v^{(12)} = \mathbf{v}^{(12)} \cdot \mathbf{i}_t. \tag{8.3.24}$$

Here, $\mathbf{i}_t$ is the unit vector of the common tangent to the conjugate shapes; vectors $\mathbf{v}_r^{(2)}$ and $\mathbf{v}^{(12)}$ are collinear at the point of shape tangency; and $v_r^{(1)}$, $v_r^{(2)}$, and $v^{(12)}$ must be considered as algebraic quantities (they may be positive or negative).

Next, we substitute vector $\dot{\mathbf{n}}_r^{(1)}$ by using Eq. (8.3.24). Equations (8.3.23) and (8.3.24) yield

$$-\kappa_1 v_r^{(1)} \left(\mathbf{v}^{(12)} \cdot \mathbf{i}_t \right) + v_r^{(1)} \mathbf{i}_t \cdot \left(\mathbf{n}^{(1)} \times \boldsymbol{\omega}^{(12)} \right)$$

$$= - \left(\mathbf{n}^{(1)} \cdot \mathbf{E} \right) \left(\boldsymbol{\omega}^{(1)} \cdot \boldsymbol{\omega}^{(2)} \right) - \frac{m'_{12}}{m_{12}} \omega^{(1)} \left(\mathbf{n}^{(1)} \cdot \mathbf{v}_{tr}^{(2)} \right). \tag{8.3.25}$$

We may represent the unit normal vector as

$$\mathbf{n}^{(1)} = \mathbf{i}_t \times \mathbf{k},$$

which yields

$$
\begin{aligned}
\mathbf{i}_t \cdot \left(\mathbf{n}^{(1)} \times \boldsymbol{\omega}^{(12)} \right) &= -\mathbf{i}_t \cdot \left[\boldsymbol{\omega}^{(12)} \times \left(\mathbf{i}_t \times \mathbf{k} \right) \right] \\
&= -\mathbf{i}_t \cdot \left[\mathbf{i}_t \left(\boldsymbol{\omega}^{(12)} \cdot \mathbf{k} \right) - \mathbf{k} \left(\boldsymbol{\omega}^{(12)} \cdot \mathbf{i}_t \right) \right] \\
&= -\boldsymbol{\omega}^{(12)} \cdot \mathbf{k}.
\end{aligned}
\tag{8.3.26}
$$

Here, $\mathbf{k}$ is the unit vector of the z axis, and

$$\boldsymbol{\omega}^{(12)} \cdot \mathbf{i}_t = 0$$

due to the perpendicularity of these vectors.

Equations (8.3.24) to (8.3.26) yield

$$\left[\kappa_1 \left(\mathbf{v}^{(12)} \cdot \mathbf{i}_t \right) + \left(\boldsymbol{\omega}^{(12)} \cdot \mathbf{k} \right) \right] v_r^{(1)} = b_1 \tag{8.3.27}$$

where

$$b_1 = \left(\mathbf{n}^{(1)} \cdot \mathbf{E} \right) \left(\boldsymbol{\omega}^{(1)} \cdot \boldsymbol{\omega}^{(2)} \right) + \frac{m'_{12}}{m_{12}} \omega^{(1)} \left(\mathbf{n}^{(1)} \cdot \mathbf{v}_{tr}^{(2)} \right).$$

Equation (8.3.6) yields

$$-v_r^{(1)} + v_r^{(2)} = \mathbf{v}^{(12)} \cdot \mathbf{i}_t. \tag{8.3.28}$$

Equations (8.3.7), (8.3.4), (8.3.5), and (8.3.26) yield

$$\kappa_1 v_r^{(1)} - \kappa_2 v_r^{(2)} = \boldsymbol{\omega}^{(12)} \cdot \mathbf{k}. \tag{8.3.29}$$

Equations (8.3.27) to (8.3.29) represent a system of three linear equations in two unknowns,

$$a_{i1} x_1 + a_{i2} x_2 = b_i \quad (i = 1, 2, 3) \tag{8.3.30}$$

where

$$a_{11} = \kappa_1 \left(\mathbf{v}^{(12)} \cdot \mathbf{i}_t \right) + \left(\boldsymbol{\omega}^{(12)} \cdot \mathbf{k} \right), \quad a_{12} = 0$$

$$b_1 = \left(\mathbf{n}^{(1)} \cdot \mathbf{E} \right) \left(\boldsymbol{\omega}^{(1)} \cdot \boldsymbol{\omega}^{(2)} \right) + \frac{m'_{12}}{m_{12}} \omega^{(1)} \left(\mathbf{n}^{(1)} \cdot \mathbf{v}_{tr}^{(2)} \right)$$

$$a_{21} = -1, \quad a_{22} = 1, \quad b_2 = \mathbf{v}^{(12)} \cdot \mathbf{i}_t$$

$$a_{31} = \kappa_1, \quad a_{32} = -\kappa_2, \quad b_3 = \boldsymbol{\omega}^{(12)} \cdot \mathbf{k}$$

$$x_1 = v_r^{(1)}, \quad x_2 = v_r^{(2)}.$$

It is known from linear algebra that the system of Eqs. (8.3.30) possesses a unique solution if and only if the system matrix

$$\begin{bmatrix} a_{11} & a_{12} \\ a_{21} & a_{22} \\ a_{31} & a_{32} \end{bmatrix}$$

and the augmented matrix

$$\begin{bmatrix} a_{11} & a_{12} & b_1 \\ a_{21} & a_{22} & b_2 \\ a_{31} & a_{32} & b_3 \end{bmatrix}$$

are of the same rank. This results in the requirement that

$$\begin{vmatrix} a_{11} & a_{12} & b_1 \\ a_{21} & a_{22} & b_2 \\ a_{31} & a_{32} & b_3 \end{vmatrix} = \begin{vmatrix} a_{11} & 0 & b_1 \\ -1 & 1 & b_2 \\ \kappa_1 & -\kappa_2 & b_3 \end{vmatrix} = 0. \tag{8.3.31}$$

Substituting coefficients of the determinant (8.3.31) with the above expressions, we get

$$\kappa_2 = \frac{\kappa_1 \left[b_1 - \left(\mathbf{v}^{(12)} \cdot \mathbf{i}_t \right) \left(\boldsymbol{\omega}^{(12)} \cdot \mathbf{k} \right) \right] - \left(\omega^{(12)} \right)^2}{\kappa_1 \left(v^{(12)} \right)^2 + \left(\boldsymbol{\omega}^{(12)} \cdot \mathbf{k} \right) \left(\mathbf{v}^{(12)} \cdot \mathbf{i}_t \right) + b_1}. \tag{8.3.32}$$
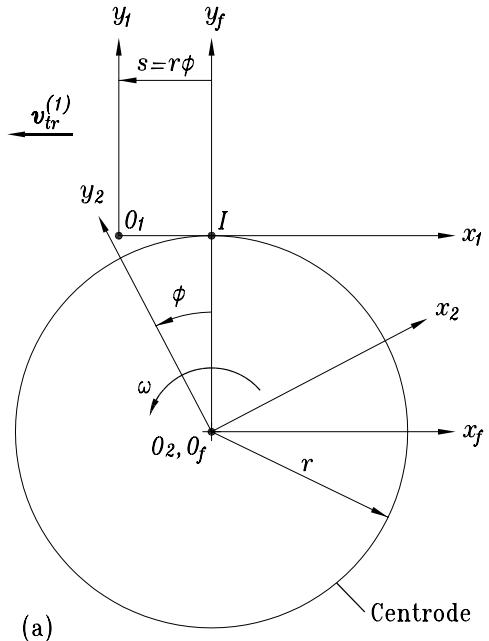
The expression for the coefficient b_1 was presented above. Equation (8.3.32) is the basic equation that relates the curvatures of tooth shapes in planar gearings.

Consider a particular case when shapes Σ_1 and Σ_2 are in contact at the pitch point. At this point $\mathbf{v}^{(12)} = 0$, and the curvature of shape Σ_2 is
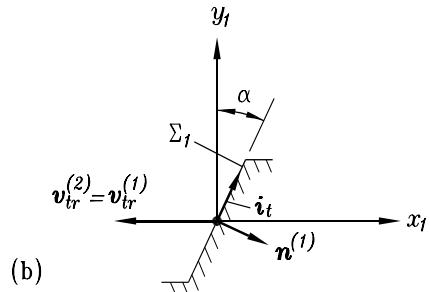
$$\kappa_2 = \kappa_1 - \frac{\left(\omega^{(12)} \right)^2}{b_1}. \tag{8.3.33}$$

Transformation of Translation into Rotation and Rotation into Translation

Consider that a rack-cutter 1 generates a gear 2. Shape Σ_1 is given, and it is necessary to determine relations between the curvatures of shapes Σ_1 and Σ_2. We set up three

Figure 8.3.1: Transformation of translation into rotation.

coordinate systems S_1, S_2, and S_f, as shown in Fig. 8.3.1(a). It is assumed that

$$\frac{v_{tr}^{(1)}}{\omega} = r = \text{constant}.$$

Here, $v_{tr}^{(1)}$ is the velocity of the rack translation, ω is the angular velocity of gear rotation, and r is the radius of the gear centrode. The relation between curvatures of shapes Σ_1 and Σ_2 is based on Eqs. (8.3.4) to (8.3.7) and (8.3.16). But for the considered case, new equations must be developed instead of Eqs. (8.3.7) and (8.3.16) due to new conditions of motion transformation. Taking into account that translation is transformed into rotation, we have

$$\omega^{(1)} = 0, \quad \omega^{(2)} = \omega, \quad \omega^{(12)} = \omega^{(1)} - \omega^{(2)} = -\omega.$$

The equations we apply instead of Eqs. (8.3.7) and (8.3.16) are represented by

$$\dot{\mathbf{n}}_r^{(2)} = \dot{\mathbf{n}}_r^{(1)} - \left(\boldsymbol{\omega} \times \mathbf{n}^{(1)}\right). \tag{8.3.34}$$

Here, $\dot{\mathbf{n}}_r^{(1)} \neq 0$ if the profile of the rack-cutter is not a straight line.

$$\dot{\mathbf{n}}_r^{(1)} \cdot \mathbf{v}^{(12)} - \mathbf{n}^{(1)} \cdot \left(\boldsymbol{\omega} \times \mathbf{v}_r^{(1)}\right) - \mathbf{n}^{(1)} \cdot \left(\boldsymbol{\omega} \times \mathbf{v}_{tr}^{(1)}\right) = 0. \qquad (8.3.35)$$

Developing Eq. (8.3.35), we assume that $\mathbf{v}_{tr}^{(1)}$ and $\boldsymbol{\omega}$ are constant vectors. The triple product $\mathbf{n}^{(1)} \cdot (\boldsymbol{\omega} \times \mathbf{v}_{tr}^{(1)})$ may be represented as

$$\mathbf{n}^{(1)} \cdot \left(\boldsymbol{\omega} \times \mathbf{v}_{tr}^{(1)}\right) = \left(\mathbf{i}_t \times \mathbf{k}\right) \cdot \left(\boldsymbol{\omega} \times \mathbf{v}_{tr}^{(1)}\right)$$

$$= \begin{vmatrix} \left(\mathbf{i}_t \cdot \boldsymbol{\omega}\right) & \left(\mathbf{i}_t \cdot \mathbf{v}_{tr}^{(1)}\right) \\ \left(\mathbf{k} \cdot \boldsymbol{\omega}\right) & \left(\mathbf{k} \cdot \mathbf{v}_{tr}^{(1)}\right) \end{vmatrix}$$

$$= -\left(\mathbf{i}_t \cdot \mathbf{v}_{tr}^{(1)}\right)(\boldsymbol{\omega} \cdot \mathbf{k}) \qquad (8.3.36)$$

because $\mathbf{i}_t \cdot \boldsymbol{\omega} = 0$ and $\mathbf{k} \cdot \mathbf{v}_{tr}^{(1)} = 0$ due to the perpendicularity of vectors. Thus,

$$\dot{\mathbf{n}}_r^{(1)} \cdot \mathbf{v}^{(12)} - \mathbf{n}^{(1)} \cdot \left(\boldsymbol{\omega} \times \mathbf{v}_r^{(1)}\right) = -\left(\mathbf{i}_t \cdot \mathbf{v}_{tr}^{(1)}\right)(\mathbf{k} \cdot \boldsymbol{\omega}). \qquad (8.3.37)$$

Equations (8.3.4) to (8.3.6), (8.3.34), and (8.3.37) yield a system of three linear equations in two unknowns,

$$a_{i1}x_1 + a_{i2}x_2 = b_i \quad (i = 1, 2, 3). \qquad (8.3.38)$$

Here,

$$x_1 = v_r^{(1)}, \quad x_2 = v_r^{(2)}$$

$$a_{11} = \kappa_1 \left(\mathbf{v}^{(12)} \cdot \mathbf{i}_t\right) - (\boldsymbol{\omega} \cdot \mathbf{k}), \quad a_{12} = 0, \quad b_1 = \left(\mathbf{v}_{tr}^{(1)} \cdot \mathbf{i}_t\right)(\boldsymbol{\omega} \cdot \mathbf{k})$$

$$a_{21} = -1, \quad a_{22} = 1, \quad b_2 = \left(\mathbf{v}^{(12)} \cdot \mathbf{i}_t\right)$$

$$a_{31} = \kappa_1, \quad a_{32} = -\kappa_2, \quad b_3 = -(\boldsymbol{\omega} \cdot \mathbf{k}).$$

Discussions regarding the system of linear equations (8.3.38), similar to those above, result in

$$\begin{vmatrix} a_{11} & 0 & b_1 \\ -1 & 1 & b_2 \\ \kappa_1 & -\kappa_2 & b_3 \end{vmatrix} = 0.$$

This yields

$$\kappa_2 = \frac{\kappa_1 b_1 - a_{11}b_3}{a_{11}b_2 + b_1} = \frac{\kappa_1\left[(\boldsymbol{\omega} \cdot \mathbf{k})\left(\mathbf{v}_{tr}^{(1)} + \mathbf{v}^{(12)}\right) \cdot \mathbf{i}_t\right] - \omega^2}{\kappa_1\left(v^{(12)}\right)^2 + (\boldsymbol{\omega} \cdot \mathbf{k})\left(\mathbf{v}_{tr}^{(2)} \cdot \mathbf{i}_t\right)}. \qquad (8.3.39)$$

Consider a case when the contact point coincides with the pitch point I [Fig. 8.3.1(a)]. Then, $\mathbf{v}^{(12)} = 0$,

$$\mathbf{v}_{tr}^{(1)} = \mathbf{v}_{tr}^{(2)},$$

and Eq. (8.3.39) yields

$$\kappa_2 = \kappa_1 - \frac{\omega^2}{(\boldsymbol{\omega} \cdot \mathbf{k})\left(\mathbf{v}_{tr}^{(2)} \cdot \mathbf{i}_t\right)}. \qquad (8.3.40)$$

If the rack-cutter is applied for cutting of involute gears, its shape Σ_1 is a straight line [Fig. 8.3.1(b)] and its curvature is $\kappa_1 = 0$. Equation (8.3.40) yields [Fig. 8.3.1(b)]

$$\kappa_2 = -\frac{\omega^2}{(\boldsymbol{\omega} \cdot \mathbf{k})(\mathbf{v}_{tr}^{(2)} \cdot \mathbf{i}_t)} = \frac{1}{r \sin \alpha}. \tag{8.3.41}$$

The positive sign of the curvature κ_2 means that the curvature center is located on the positive direction of unit normal

$$\mathbf{n}^{(1)} = \mathbf{i}_t \times \mathbf{k}.$$

A more complicated case dealing with the curvature of generated shape Σ_2 is discussed in Problem 8.3.3.

Problem 8.3.1
Consider that the shape of gear 1 is an involute curve corresponding to the base circle of radius r_{b1}. The centrode of gear 1 is the circle of radius r_1. The ratio of these radii is

$$\frac{r_{b1}}{r_1} = \cos \alpha.$$

We consider the particular case wherein the contact point coincides with the pitch point I (Fig. 8.3.2). The angular velocity ratio m_{12} is constant and is represented as

$$m_{12} = \frac{\omega^{(1)}}{\omega^{(2)}} = \frac{r_2}{r_1} \tag{8.3.42}$$

where r_1 and r_2 are the gear centrode radii. Determine the curvature of gear shape Σ_2 at the contact point, assuming that the curvature κ_1 of the shape Σ_1 is given.

Solution
At the pitch point I, we have that the velocity of sliding vector $\mathbf{v}^{(12)} = 0$, and the shape curvatures are related by Eq. (8.3.33). The derivative $m'_{12} = 0$ because the angular velocity ratio is constant, and

$$b_1 = \left(\mathbf{n}^{(1)} \cdot \mathbf{E}\right)\left(\boldsymbol{\omega}^{(1)} \cdot \boldsymbol{\omega}^{(2)}\right).$$

Vectors $\mathbf{n}^{(1)}$ and $\mathbf{E}$ form the angle $90° + \alpha$. Gears rotate in opposite directions, and

$$\boldsymbol{\omega}^{(1)} \cdot \boldsymbol{\omega}^{(2)} = -\omega^{(1)}\omega^{(2)}, \quad \boldsymbol{\omega}^{(12)} = \boldsymbol{\omega}^{(1)} - \boldsymbol{\omega}^{(2)}, \quad \left|\boldsymbol{\omega}^{(12)}\right| = \omega^{(1)} + \omega^{(2)}.$$

At point I the curvature radius of shape Σ_1 is IK, and the curvature is

$$\kappa_1 = \frac{1}{r_1 \sin \alpha}.$$

The curvature $\kappa_1 > 0$ because the center of curvature κ_1 is located on the positive direction of the normal.

The coefficient b_1 may be expressed as follows:

$$b_1 = \left(\mathbf{n}^{(1)} \cdot \mathbf{E}\right)\left(\boldsymbol{\omega}^{(1)} \cdot \boldsymbol{\omega}^{(2)}\right) = \omega^{(1)}\omega^{(2)}(r_1 + r_2) \sin \alpha.$$
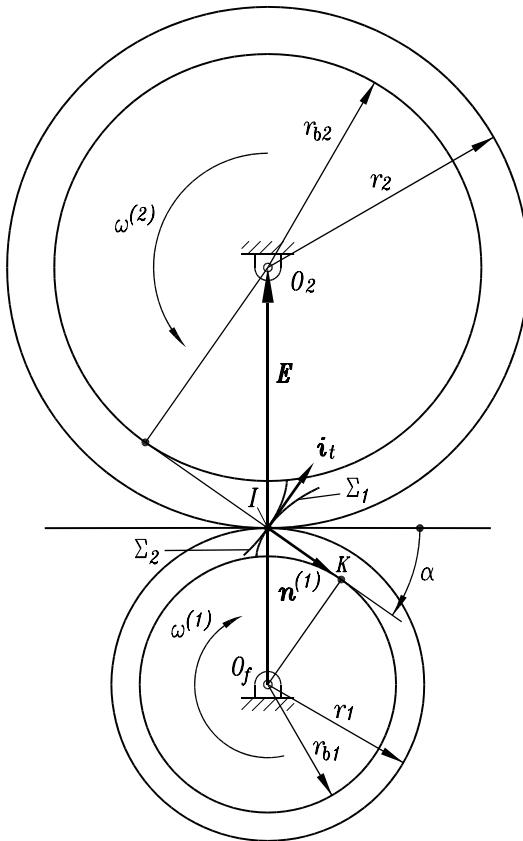
Figure 8.3.2: Tangency of involute profiles.

Then, we get

$$
\frac{\left(\omega^{(12)}\right)^2}{b_1} = \frac{\left(\omega^{(1)} + \omega^{(2)}\right)^2}{\omega^{(1)}\omega^{(2)}(r_1 + r_2)\sin\alpha} = \frac{r_1 + r_2}{r_1 r_2 \sin\alpha}
$$

and [see Eq. (8.3.33)]
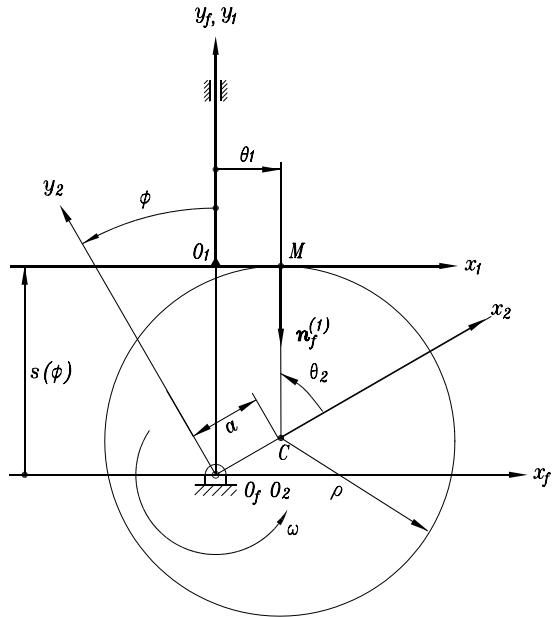
$$
\kappa_2 = \frac{1}{r_1 \sin\alpha} - \frac{r_1 + r_2}{r_1 r_2 \sin\alpha} = -\frac{1}{r_2 \sin\alpha}. \tag{8.3.43}
$$

The negative sign for curvature κ_2 means that the curvature center of shape Σ_2 is located on the negative direction of the normal. Equation (8.3.43) may be obtained by using simpler methods; however, the application of general equations (8.3.32) and (8.3.33) illustrates the power of those equations even for this particular case.

Problem 8.3.2

Consider a cam mechanism with a flat-faced follower (Fig. 8.3.3). We set up coordinate systems S_1, S_2, and S_f rigidly connected to the follower, cam, and frame, respectively. Given are the displacement function

$$
s(\phi) \in C^2, \quad 0 < \phi < 2\pi, \tag{8.3.44}
$$

Figure 8.3.3: Cam with a flat-faced follower.

and the shape Σ_1 represented by the equations

$$x_1 = \theta_1, \quad y_1 = 0 \tag{8.3.45}$$

where $a < \theta_1 < b$. Determine (1) the equations of the cam shape Σ_2, (2) the line of action, and (3) the curvature $\kappa_2(\phi)$ of the cam.

Solution

EQUATION OF MESHING. We represent shape Σ_1 in the coordinate system S_f by

$$\mathbf{r}_f^{(1)} = \theta_1 \mathbf{i}_f + s(\phi)\mathbf{j}_f. \tag{8.3.46}$$

The normal to the shape Σ_1 is

$$\mathbf{N}_f^{(1)} = \frac{\partial \mathbf{r}_f^{(1)}}{\partial \theta_1} \times \mathbf{k}_f = -\mathbf{j}_f. \tag{8.3.47}$$

The sliding velocity is represented by

$$\mathbf{v}_f^{(12)} = \mathbf{v}_{tr}^{(1)} - \mathbf{v}_{tr}^{(2)} = \frac{d\mathbf{s}}{dt} - \boldsymbol{\omega} \times \mathbf{r}_f^{(1)} = \frac{ds}{d\phi}\omega \mathbf{j}_f - \begin{vmatrix} \mathbf{i}_f & \mathbf{j}_f & \mathbf{k}_f \\ 0 & 0 & \omega \\ x_f^{(1)} & y_f^{(1)} & 0 \end{vmatrix}$$

$$= \omega \left[s(\phi)\mathbf{i}_f + \left(\frac{ds}{d\phi} - \theta_1 \right)\mathbf{j}_f \right]. \tag{8.3.48}$$

The equation of meshing may be determined by

$$\mathbf{N}_f^{(1)} \cdot \mathbf{v}_f^{(12)} = f(\theta_1, \phi) = -\omega \left(\frac{ds}{d\phi} - \theta_1 \right) = 0. \tag{8.3.49}$$

Equation (8.3.49) yields that

$$f(\theta_1, \phi) = \theta_1 - \frac{ds}{d\phi} = 0. \tag{8.3.50}$$

This equation determines the location of the contact point M (Fig. 8.3.3) as a function of parameter ϕ.

EQUATION OF SHAPE Σ_2. Shape Σ_2 is determined as follows:

$$\mathbf{r}_2 = \mathbf{M}_{21}\mathbf{r}_1 = \mathbf{M}_{2f}\mathbf{r}_f^{(1)}, \quad f(\theta_1, \phi) = 0. \tag{8.3.51}$$

Here,

$$\mathbf{M}_{21} = \mathbf{M}_{2f}\mathbf{M}_{f1} = \begin{bmatrix} \cos\phi & \sin\phi & s(\phi)\sin\phi \\ -\sin\phi & \cos\phi & s(\phi)\cos\phi \\ 0 & 0 & 1 \end{bmatrix}.$$

Equations (8.3.50), (8.3.51), and (8.3.45) yield

$$x_2 = \theta_1\cos\phi + s(\phi)\sin\phi, \quad y_2 = -\theta_1\sin\phi + s(\phi)\cos\phi, \quad \theta_1 - \frac{ds}{d\phi} = 0. \tag{8.3.52}$$

Substituting θ_1 by $ds/d\phi$ in x_2 and y_2, we get the following equations of shape Σ_2:

$$x_2 = s(\phi)\sin\phi + \frac{ds}{d\phi}\cos\phi, \quad y_2 = s(\phi)\cos\phi - \frac{ds}{d\phi}\sin\phi. \tag{8.3.53}$$

LINE OF ACTION. We represent the line of action by the expressions

$$\mathbf{r}_f(\theta_1, \phi), \quad f(\theta_1, \phi) = 0, \tag{8.3.54}$$

which yield

$$\mathbf{r}_f = \frac{ds}{d\phi}\mathbf{i}_f + s(\phi)\mathbf{j}_f. \tag{8.3.55}$$

CAM CURVATURE. To determine the cam curvature, we apply Eqs. (8.3.4) to (8.3.7), which yield

$$-\kappa_2\left(\mathbf{v}_r^{(1)} + \mathbf{v}^{(12)}\right) = -\kappa_1\mathbf{v}_r^{(1)} + \left(\boldsymbol{\omega}^{(12)} \times \mathbf{n}^{(1)}\right).$$

For the considered case, $\kappa_1 = 0$ (shape Σ_1 is a straight line), $\boldsymbol{\omega}^{(12)} = -\boldsymbol{\omega}$, and we get

$$\kappa_2\left(\mathbf{v}_r^{(1)} + \mathbf{v}^{(12)}\right) = \boldsymbol{\omega} \times \mathbf{n}^{(1)}. \tag{8.3.56}$$

Equation (8.3.46) yields

$$\mathbf{v}_r^{(1)} = \frac{\partial\mathbf{r}_f^{(1)}}{\partial\theta_1}\frac{d\theta_1}{dt} = \frac{d\theta_1}{dt}\mathbf{i}_f. \tag{8.3.57}$$

Differentiation of Eq. (8.3.50) gives

$$\frac{d\theta_1}{dt} = \frac{d^2s}{d\phi^2}\omega. \tag{8.3.58}$$

Then

$$\mathbf{v}_r^{(1)} = \omega \frac{d^2 s}{d\phi^2} \mathbf{i}_f. \tag{8.3.59}$$

Equations (8.3.48) and (8.3.50) yield

$$\mathbf{v}_f^{(12)} = \omega \, s \, (\phi) \mathbf{i}_f. \tag{8.3.60}$$

Equations (8.3.56) to (8.3.60) yield that

$$\kappa_2 \, \omega \left[\frac{d^2 s}{d\phi^2} + s \, (\phi) \right] \mathbf{i}_f = \begin{vmatrix} \mathbf{i}_f & \mathbf{j}_f & \mathbf{k}_f \\ 0 & 0 & \omega \\ 0 & -1 & 0 \end{vmatrix} = \omega \mathbf{i}_f$$

and

$$\kappa_2 = \frac{1}{\dfrac{d^2 s}{d\phi^2} + s \, (\phi)}. \tag{8.3.61}$$

Cam shape Σ_2 must be a convex curve with the curvature center located on the positive unit normal $\mathbf{n}_f^{(1)}$ (Fig. 8.3.3). The curvature κ_2 is positive if the following inequality is observed:

$$s \, (\phi) + \frac{d^2 s}{d\phi^2} > 0. \tag{8.3.62}$$

Problem 8.3.3

Figure 8.3.4(a) shows a rack-cutter tooth that generates spur involute gears. The straight-lined edge of the rack-cutter generates the involute curve, and the arc of the circle of radius ρ, centered at point C_1 [Figs. 8.3.4(a) and (b)], generates the fillet of the gear. The displacement of the rack-cutter s and the angle of gear rotation ϕ are related by

$$s = r\phi \tag{8.3.63}$$

where r is the radius of the gear pitch circle. Develop equations of the gear fillet and its curvature. Apply the coordinate systems shown in Fig. 8.3.1(a).

Solution

EQUATIONS OF SHAPE Σ_1. The position vector of a current point M of shape Σ_1 [Fig. 8.3.4(a)] is

$$\mathbf{r}_1(\theta_1) = \overline{O_1 M} = \overline{O_1 C_1} + \overline{C_1 M}. \tag{8.3.64}$$

Projecting this vector equation on the x_1 and y_1 axes [Figs. 8.3.4(a) and (b)], we get for the equations for shape Σ_1,

$$x_1 = a + \rho \sin \theta_1, \quad y_1 = b - \rho \cos \theta_1 \tag{8.3.65}$$

(a)
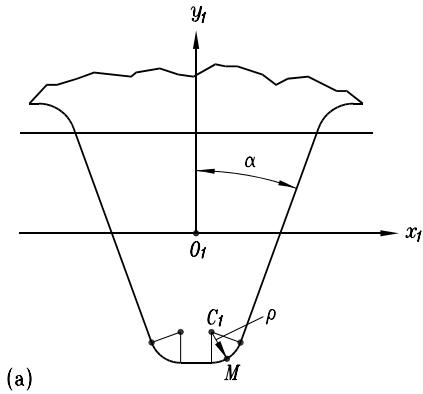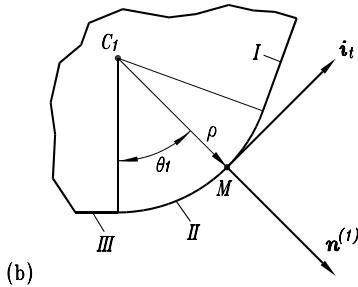
Figure 8.3.4: Rack-cutter fillet.

(b)

where

$$\{x_1(\theta_1), y_1(\theta_1)\} \in C^1, \quad 0 < \theta_1 < 90° - \alpha$$

Here, $a = x_c^{(C_1)}$ and $b = y_1^{(C_1)}$ are the coordinates of point C_1.

Shape Σ_1 is a simple and regular curve. The unit normal $\mathbf{n}_1$ to shape Σ_1 is

$$\mathbf{n}_1 = \frac{\dfrac{\partial \mathbf{r}_1}{\partial \theta_1} \times \mathbf{k}_1}{\left| \dfrac{\partial \mathbf{r}_1}{\partial \theta_1} \times \mathbf{k}_1 \right|} = \sin \theta_1 \mathbf{i}_1 - \cos \theta_1 \mathbf{j}_1. \tag{8.3.66}$$

EQUATION OF MESHING. We apply the equation of meshing that expresses that the unit normal at the contact point passes through the instantaneous center of rotation (pitch point) I:

$$\frac{X_1(\phi) - x_1(\theta_1)}{n_{x1}(\theta_1)} - \frac{Y_1(\phi) - y_1(\theta_1)}{n_{y1}(\theta_1)} = f(\theta_1, \phi) = 0. \tag{8.3.67}$$

Here [Fig. 8.3.1(a)],

$$X_1(\phi) = r\phi, \quad Y_1 = 0. \tag{8.3.68}$$

Equations (8.3.65) to (8.3.68) yield

$$f(\theta_1, \phi) = r\phi - a - b \tan \theta_1 = 0. \tag{8.3.69}$$

EQUATIONS OF SHAPE Σ_2. Shape Σ_2 is represented by the following equations:

$$\mathbf{r}_2 = \mathbf{M}_{21}\mathbf{r}_1, \quad f(\theta_1, \phi) = 0. \tag{8.3.70}$$

Here [Fig. 8.3.1(a)],

$$\mathbf{M}_{21} = \mathbf{M}_{2f}\mathbf{M}_{f1} = \begin{bmatrix} \cos\phi & \sin\phi & -r\phi\cos\phi + r\sin\phi \\ -\sin\phi & \cos\phi & r\phi\sin\phi + r\cos\phi \\ 0 & 0 & 1 \end{bmatrix}.$$

Equations (8.3.65), (8.3.69), and (8.3.70) yield

$$
\begin{aligned}
x_2 &= a\cos\phi + b\sin\phi - \rho\sin(\phi - \theta_1) - r\phi\cos\phi + r\sin\phi \\
y_2 &= -a\sin\phi + b\cos\phi - \rho\cos(\phi - \theta_1) + r\phi\sin\phi + r\cos\phi \\
r\phi &- a - b\tan\theta_1 = 0.
\end{aligned} \tag{8.3.71}
$$

LINE OF ACTION. We represent the line of action by the equations

$$\mathbf{r}_f = \mathbf{M}_{f1}\mathbf{r}_1, \quad f(\theta_1, \phi) = 0,$$

which yield

$$\mathbf{r}_f = (a + \rho\sin\theta_1 - r\phi)\mathbf{i}_f + (b - \rho\cos\theta_1 + r)\mathbf{j}_f, \quad r\phi - a - b\tan\theta_1 = 0. \tag{8.3.72}$$

CURVATURE OF SHAPE Σ_2. To determine the curvature κ_2, we apply Eq. (8.3.39). Here,

$$\kappa_1 = -\frac{1}{\rho}, \quad \mathbf{i}_t = \frac{\dfrac{\partial \mathbf{r}_f}{\partial \theta_1}}{\left| \dfrac{\partial \mathbf{r}_f}{\partial \theta_1} \right|} = \cos\theta_1 \mathbf{i}_f + \sin\theta_1 \mathbf{j}_f$$

$$\mathbf{v}_{tr}^{(1)} = -r\omega\mathbf{i}_f$$

$$\mathbf{v}^{(12)} = \mathbf{v}_{tr}^{(1)} - \mathbf{v}_{tr}^{(2)} = -r\omega\mathbf{i}_f - (\boldsymbol{\omega} \times \mathbf{r}_f)$$

$$= -r\omega\mathbf{i}_f - \begin{vmatrix} \mathbf{i}_f & \mathbf{j}_f & \mathbf{k}_f \\ 0 & 0 & \omega \\ x_f & y_f & 0 \end{vmatrix}$$

$$= \omega[(b - \rho\cos\theta_1)\mathbf{i}_f + (b\tan\theta_1 - \rho\sin\theta_1)\mathbf{j}_f]$$

$$\left(v^{(12)}\right)^2 = \omega^2 \left(\frac{b}{\cos\theta_1} - \rho \right)^2.$$

Deriving the equation for $\mathbf{v}^{(12)}$, we eliminated $r\phi$ by using equation of meshing (8.3.69). Thus, we have [see Eq. (8.3.39)]

$$\kappa_2(\theta_1) = -\frac{r\cos^3\theta_1 - b\cos\theta_1}{b^2 + \rho(r\cos^3\theta_1 - b\cos\theta_1)} \tag{8.3.73}$$

$$0 < \theta_1 < 90° - \alpha \quad (b \text{ is negative}).$$

The negative sign of κ_2 indicates that the center of curvature of the generated fillet is located on the negative direction of the normal [Fig. 8.3.4(b)]. Consequently, the rack-cutter and the gear fillet are in internal tangency by cutting.

The rack-cutter shape Σ_1, shown in Fig. 8.3.4(b), generates shape Σ_2 which contains three curves. These curves are (1) the involute curve, generated by the straight line I; (2) the fillet, generated by the arc of circle II; and (3) a circle which belongs to the dedendum, generated by the straight line III. The fillet curvature at the point of tangency of the involute curve and the fillet corresponds to the parameter $\theta_1 = 90° - \alpha$. The curvature of the fillet at the point of its tangency with the dedendum circle corresponds to $\theta_1 = 0$.
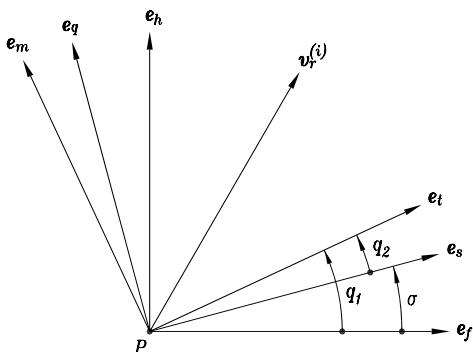
8.4 DIRECT RELATIONS BETWEEN PRINCIPAL CURVATURES OF MATING SURFACES

The derivations of the curvature matrix are based on the following ideas: (i) the displacement velocities of contact points and the tip of the surface unit normals in their motions over the surfaces are related with Eqs. (8.2.2) and (8.2.4), and (ii) the displacement motions are decomposed and the displacements along the principal directions on the interacting surfaces are considered. Point P is the point of tangency of Σ_1 and Σ_2 (Fig. 8.4.1). The unit vectors of principal directions on Σ_1 at point P are designated by $\mathbf{e}_f$ and $\mathbf{e}_h$; κ_f and κ_h are the respective principal curvatures of Σ_1. Unit vectors $\mathbf{e}_s$ and $\mathbf{e}_q$ represent the principal directions on Σ_2; κ_s and κ_q are the respective principal curvatures of Σ_2. Angle σ is formed between $\mathbf{e}_f$ and $\mathbf{e}_s$ and is measured counterclockwise from $\mathbf{e}_f$ to $\mathbf{e}_s$.

Auxiliary Equations

Henceforth, we consider in the 2D-space coordinate systems S_a ($\mathbf{e}_f$, $\mathbf{e}_h$) and S_b ($\mathbf{e}_s$, $\mathbf{e}_q$) that are rigidly connected to gears 1 and 2 (surfaces Σ_1 and Σ_2), respectively. The coordinate transformation between these coordinate systems is based on application of the following matrices:

$$\mathbf{L}_{ba} = \begin{bmatrix} \cos\sigma & \sin\sigma \\ -\sin\sigma & \cos\sigma \end{bmatrix}, \quad \mathbf{L}_{ab} = \begin{bmatrix} \cos\sigma & -\sin\sigma \\ \sin\sigma & \cos\sigma \end{bmatrix}. \quad (8.4.1)$$


Figure 8.4.1: Unit vectors in tangent plane.

In the derivations below we use the designations

$$\mathbf{v}_r^{(1)} = \begin{bmatrix} v_f^{(1)} \\ v_h^{(1)} \end{bmatrix}, \qquad \dot{\mathbf{n}}_r^{(1)} = \begin{bmatrix} \dot{n}_f^{(1)} \\ \dot{n}_h^{(1)} \end{bmatrix},$$

(8.4.2)

which means that vectors $\mathbf{v}_r^{(1)}$ and $\dot{\mathbf{n}}_r^{(1)}$ are represented in coordinate system S_a ($\mathbf{e}_f$, $\mathbf{e}_h$) which is rigidly connected to surface Σ_1. We also need the representation of vectors $\mathbf{v}_r^{(1)}$ and $\dot{\mathbf{n}}_r^{(1)}$ in coordinate system S_b ($\mathbf{e}_s$, $\mathbf{e}_q$) which is rigidly connected to gear 2. It is obvious that

$$\begin{bmatrix} v_s^{(1)} \\ v_q^{(1)} \end{bmatrix} = \mathbf{L}_{ba} \begin{bmatrix} v_f^{(1)} \\ v_h^{(1)} \end{bmatrix}, \qquad \begin{bmatrix} \dot{n}_s^{(1)} \\ \dot{n}_q^{(1)} \end{bmatrix} = \mathbf{L}_{ba} \begin{bmatrix} \dot{n}_f^{(1)} \\ \dot{n}_h^{(1)} \end{bmatrix}.$$

(8.4.3)

The superscript "1" indicates that the displacement over surface Σ_1 is considered; the pairs of subscripts "f" and "h" and "s" and "q" indicate that the respective vectors are considered in coordinate systems S_a ($\mathbf{e}_f$, $\mathbf{e}_h$) and S_b ($\mathbf{e}_s$, $\mathbf{e}_q$), respectively.

Similarly, we use the designations

$$\mathbf{v}_r^{(2)} = \begin{bmatrix} v_s^{(2)} \\ v_q^{(2)} \end{bmatrix}, \qquad \dot{\mathbf{n}}_r^{(2)} = \begin{bmatrix} \dot{n}_s^{(2)} \\ \dot{n}_q^{(2)} \end{bmatrix}$$

(8.4.4)

and

$$\begin{bmatrix} v_f^{(2)} \\ v_h^{(2)} \end{bmatrix} = \mathbf{L}_{ab} \begin{bmatrix} v_s^{(2)} \\ v_q^{(2)} \end{bmatrix}, \qquad \begin{bmatrix} \dot{n}_f^{(2)} \\ \dot{n}_h^{(2)} \end{bmatrix} = \mathbf{L}_{ab} \begin{bmatrix} \dot{n}_s^{(2)} \\ \dot{n}_q^{(2)} \end{bmatrix}.$$

(8.4.5)

In Section (8.2) we represented the basic relations between the velocities of displacements by Eqs. (8.2.2) and (8.2.4) as follows:

$$\mathbf{v}_r^{(2)} = \mathbf{v}_r^{(1)} + \mathbf{v}^{(12)}, \qquad \dot{\mathbf{n}}_r^{(2)} = \dot{\mathbf{n}}_r^{(1)} + (\boldsymbol{\omega}^{(12)} \times \mathbf{n}).$$

Considering that all vectors in these equations are represented in the same coordinate system, say S_a, we obtain

$$\begin{bmatrix} v_f^{(2)} \\ v_h^{(2)} \end{bmatrix} = \begin{bmatrix} v_f^{(1)} \\ v_h^{(1)} \end{bmatrix} + \begin{bmatrix} v_f^{(12)} \\ v_h^{(12)} \end{bmatrix}$$

(8.4.6)

$$\begin{bmatrix} \dot{n}_f^{(2)} \\ \dot{n}_h^{(2)} \end{bmatrix} = \begin{bmatrix} \dot{n}_f^{(1)} \\ \dot{n}_h^{(1)} \end{bmatrix} + \begin{bmatrix} (\boldsymbol{\omega}^{(12)} \times \mathbf{n}) \cdot \mathbf{e}_f \\ (\boldsymbol{\omega}^{(12)} \times \mathbf{n}) \cdot \mathbf{e}_h \end{bmatrix}.$$

(8.4.7)

Similar equations can be derived when all vectors of Eqs. (8.2.2) and (8.2.4) are represented in coordinate system S_b $(\mathbf{e}_s, \mathbf{e}_q)$, that is,

$$
\begin{bmatrix} v_s^{(2)} \\ v_q^{(2)} \end{bmatrix} = \begin{bmatrix} v_s^{(1)} \\ v_q^{(1)} \end{bmatrix} + \begin{bmatrix} v_s^{(12)} \\ v_q^{(12)} \end{bmatrix} \tag{8.4.8}
$$

$$
\begin{bmatrix} \dot{n}_s^{(2)} \\ \dot{n}_q^{(2)} \end{bmatrix} = \begin{bmatrix} \dot{n}_s^{(1)} \\ \dot{n}_q^{(1)} \end{bmatrix} + \begin{bmatrix} (\boldsymbol{\omega}^{(12)} \times \mathbf{n}) \cdot \mathbf{e}_s \\ (\boldsymbol{\omega}^{(12)} \times \mathbf{n}) \cdot \mathbf{e}_q \end{bmatrix}. \tag{8.4.9}
$$

Components of vectors $\mathbf{v}_r^{(i)}$ and $\dot{\mathbf{n}}_r^{(i)}$ are related by Rodrigues' formula (see Section 7.5) as

$$
\dot{\mathbf{n}}_r^{(i)} = -\kappa_{I,II}^{(i)} \mathbf{v}_r^{(i)} \qquad (i = 1, 2) \tag{8.4.10}
$$

where $\kappa_{I,II}^{(i)}$ are the principal curvatures of surface Σ_i [designated above by (κ_f, κ_b) and (κ_s, κ_q)]. Equation (8.4.10) yields

$$
\begin{bmatrix} \dot{n}_f^{(1)} \\ \dot{n}_b^{(1)} \end{bmatrix} = \mathbf{K}_1 \begin{bmatrix} v_f^{(1)} \\ v_b^{(1)} \end{bmatrix} = \begin{bmatrix} -\kappa_f & 0 \\ 0 & -\kappa_b \end{bmatrix} \begin{bmatrix} v_f^{(1)} \\ v_b^{(1)} \end{bmatrix}. \tag{8.4.11}
$$

Vectors $\dot{\mathbf{n}}_r^{(1)}$ and $\mathbf{v}_r^{(1)}$ are represented in coordinate system S_a $(\mathbf{e}_f, \mathbf{e}_b)$, and Eqs. (8.4.11) relate the components of these vectors. Similarly, we obtain

$$
\begin{bmatrix} \dot{n}_s^{(2)} \\ \dot{n}_q^{(2)} \end{bmatrix} = \mathbf{K}_2 \begin{bmatrix} v_s^{(2)} \\ v_q^{(2)} \end{bmatrix} = \begin{bmatrix} -\kappa_s & 0 \\ 0 & -\kappa_q \end{bmatrix} \begin{bmatrix} v_s^{(2)} \\ v_q^{(2)} \end{bmatrix}. \tag{8.4.12}
$$

Here, $\mathbf{K}_i$ $(i = 1, 2)$ is the matrix of curvature of surface Σ_i.

Our next goal is to derive equations that relate (i) components of vectors $\dot{\mathbf{n}}_r^{(1)}$ and $\mathbf{v}_r^{(1)}$ that are represented in S_b $(\mathbf{e}_s, \mathbf{e}_q)$, and (ii) components of vectors $\dot{\mathbf{n}}_r^{(2)}$ and $\mathbf{v}_r^{(2)}$ that are represented in S_a $(\mathbf{e}_f, \mathbf{e}_b)$. This goal can be achieved by application of coordinate transformations. The transformation of Eqs. (8.4.3) and (8.4.11) yields

$$
\begin{bmatrix} \dot{n}_s^{(1)} \\ \dot{n}_q^{(1)} \end{bmatrix} = \mathbf{L}_{ba} \mathbf{K}_1 \mathbf{L}_{ab} \begin{bmatrix} v_s^{(1)} \\ v_q^{(1)} \end{bmatrix}. \tag{8.4.13}
$$

Similar transformations of Eqs. (8.4.12) yield

$$
\begin{bmatrix} \dot{n}_f^{(2)} \\ \dot{n}_b^{(2)} \end{bmatrix} = \mathbf{L}_{ab} \mathbf{K}_2 \mathbf{L}_{ba} \begin{bmatrix} v_f^{(2)} \\ v_b^{(2)} \end{bmatrix}. \tag{8.4.14}
$$

Basic System of Linear Equations
Our next goal is to derive the system of four linear equations

$$
\mathbf{AX} = \mathbf{B} \tag{8.4.15}
$$

where

$$\mathbf{X} = \begin{bmatrix} v_f^{(2)} & v_h^{(2)} & v_s^{(1)} & v_q^{(1)} \end{bmatrix}^{\mathrm{T}}. \tag{8.4.16}$$

Here,

$$v_f^{(2)} = \mathbf{v}_r^{(2)} \cdot \mathbf{e}_f, \quad v_h^{(2)} = \mathbf{v}_r^{(2)} \cdot \mathbf{e}_h, \quad v_s^{(1)} = \mathbf{v}_r^{(1)} \cdot \mathbf{e}_s, \quad \text{and} \quad v_q^{(1)} = \mathbf{v}_r^{(1)} \cdot \mathbf{e}_q.$$

The expressions of the (4×4) matrix $\mathbf{A}$ and the (4×1) matrix $\mathbf{B}$ are given below.

We may consider that equation system (8.4.15) consists of two subsystems, in two linear equations each. The derivation of the first subsystem in the unknowns $v_f^{(2)}$ and $v_h^{(2)}$ is based on the following procedure:

Step 1: Considering Eqs. (8.4.7) and (8.4.14) simultaneously, we obtain

$$\begin{bmatrix} \dot{n}_f^{(1)} \\ \dot{n}_h^{(1)} \end{bmatrix} + \begin{bmatrix} (\boldsymbol{\omega}^{(12)} \times \mathbf{n}) \cdot \mathbf{e}_f \\ (\boldsymbol{\omega}^{(12)} \times \mathbf{n}) \cdot \mathbf{e}_h \end{bmatrix} = \mathbf{L}_{ab} \mathbf{K}_2 \mathbf{L}_{ba} \begin{bmatrix} v_f^{(2)} \\ v_h^{(2)} \end{bmatrix}. \tag{8.4.17}$$

Step 2: Using Eqs. (8.4.11) and (8.4.6), we obtain

$$\begin{bmatrix} \dot{n}_f^{(1)} \\ \dot{n}_h^{(1)} \end{bmatrix} = \mathbf{K}_1 \begin{bmatrix} v_f^{(1)} \\ v_h^{(1)} \end{bmatrix} = \mathbf{K}_1 \begin{bmatrix} v_f^{(2)} \\ v_h^{(2)} \end{bmatrix} - \mathbf{K}_1 \begin{bmatrix} v_f^{(12)} \\ v_h^{(12)} \end{bmatrix}. \tag{8.4.18}$$

Step 3: Equations (8.4.17) and (8.4.18) yield the first subsystem of two linear equations in the unknowns $(v_f^{(2)}, v_h^{(2)})$ as follows:

$$(\mathbf{K}_1 - \mathbf{L}_{ab} \mathbf{K}_2 \mathbf{L}_{ba}) \begin{bmatrix} v_f^{(2)} \\ v_h^{(2)} \end{bmatrix} = \mathbf{K}_1 \begin{bmatrix} v_f^{(12)} \\ v_h^{(12)} \end{bmatrix} + \begin{bmatrix} (\mathbf{n} \times \boldsymbol{\omega}^{(12)}) \cdot \mathbf{e}_f \\ (\mathbf{n} \times \boldsymbol{\omega}^{(12)}) \cdot \mathbf{e}_h \end{bmatrix}. \tag{8.4.19}$$

The derivation of the second subsystem of two linear equations in the unknowns $(v_s^{(1)}, v_q^{(1)})$ is based on a procedure similar to that used above.

Step 1: Equations (8.4.13) and (8.4.9) yield

$$\begin{bmatrix} \dot{n}_s^{(2)} \\ \dot{n}_q^{(2)} \end{bmatrix} - \begin{bmatrix} (\boldsymbol{\omega}^{(12)} \times \mathbf{n}) \cdot \mathbf{e}_s \\ (\boldsymbol{\omega}^{(12)} \times \mathbf{n}) \cdot \mathbf{e}_q \end{bmatrix} = \mathbf{L}_{ba} \mathbf{K}_1 \mathbf{L}_{ab} \begin{bmatrix} v_s^{(1)} \\ v_q^{(1)} \end{bmatrix}. \tag{8.4.20}$$

Step 2: Using Eqs. (8.4.12) and (8.4.8), we obtain

$$\begin{bmatrix} \dot{n}_s^{(2)} \\ \dot{n}_q^{(2)} \end{bmatrix} = \mathbf{K}_2 \begin{bmatrix} v_s^{(2)} \\ v_q^{(2)} \end{bmatrix} = \mathbf{K}_2 \begin{bmatrix} v_s^{(1)} \\ v_q^{(1)} \end{bmatrix} + \mathbf{K}_2 \begin{bmatrix} v_s^{(12)} \\ v_q^{(12)} \end{bmatrix}. \tag{8.4.21}$$

Step 3: Equations (8.4.20) and (8.4.21) enable us to represent the second subsystem of two linear equations in the unknowns $(v_s^{(1)}, v_q^{(1)})$, as follows:

$$(\mathbf{L}_{ba} \mathbf{K}_1 \mathbf{L}_{ab} - \mathbf{K}_2) \begin{bmatrix} v_s^{(1)} \\ v_q^{(1)} \end{bmatrix} = \mathbf{K}_2 \begin{bmatrix} v_s^{(12)} \\ v_q^{(12)} \end{bmatrix} - \begin{bmatrix} (\boldsymbol{\omega}^{(12)} \times \mathbf{n}) \cdot \mathbf{e}_s \\ (\boldsymbol{\omega}^{(12)} \times \mathbf{n}) \cdot \mathbf{e}_q \end{bmatrix}. \tag{8.4.22}$$

The final result of the discussion above is that Eqs. (8.4.19) and (8.4.22) considered simultaneously represent the desired system (8.4.15) of four linear equations in four unknowns represented by the matrix (8.4.16).

Matrix **A** is symmetric and is represented in terms of principal curvatures of contacting surfaces Σ_1 and Σ_2, and angle σ that is formed between the principal directions on Σ_1 and Σ_2.

$$\mathbf{A} = \begin{bmatrix} b_{11} & b_{12} & 0 & 0 \\ b_{21} & b_{22} & 0 & 0 \\ 0 & 0 & b_{33} & b_{34} \\ 0 & 0 & b_{43} & b_{44} \end{bmatrix}. \tag{8.4.23}$$

Using Eqs. (8.4.19) and (8.4.22), we obtain after transformations

$$b_{11} = -\kappa_f + 0.5(\kappa_s + \kappa_q) + 0.5(\kappa_s - \kappa_q)\cos 2\sigma \tag{8.4.24}$$

$$b_{12} = b_{21} = 0.5(\kappa_s - \kappa_q)\sin 2\sigma \tag{8.4.25}$$

$$b_{22} = -\kappa_h + 0.5(\kappa_s + \kappa_q) - 0.5(\kappa_s - \kappa_q)\cos 2\sigma \tag{8.4.26}$$

$$b_{33} = \kappa_s - 0.5(\kappa_f + \kappa_h) - 0.5(\kappa_f - \kappa_h)\cos 2\sigma \tag{8.4.27}$$

$$b_{34} = b_{43} = 0.5(\kappa_f - \kappa_h)\sin 2\sigma \tag{8.4.28}$$

$$b_{44} = \kappa_q - 0.5(\kappa_f + \kappa_h) + 0.5(\kappa_f - \kappa_h)\cos 2\sigma. \tag{8.4.29}$$

The column vector **B** is represented as

$$\mathbf{B} = [\, b_{15} \quad b_{25} \quad b_{35} \quad b_{45}\,]^{\mathrm{T}} \tag{8.4.30}$$

where

$$b_{15} = -\left(\boldsymbol{\omega}^{(12)} \cdot \mathbf{e}_h\right) - \kappa_f\left(\mathbf{v}^{(12)} \cdot \mathbf{e}_f\right) \tag{8.4.31}$$

$$b_{25} = \left(\boldsymbol{\omega}^{(12)} \cdot \mathbf{e}_f\right) - \kappa_h\left(\mathbf{v}^{(12)} \cdot \mathbf{e}_h\right) \tag{8.4.32}$$

$$b_{35} = -\left(\boldsymbol{\omega}^{(12)} \cdot \mathbf{e}_q\right) - \kappa_s\left(\mathbf{v}^{(12)} \cdot \mathbf{e}_s\right) \tag{8.4.33}$$

$$b_{45} = \left(\boldsymbol{\omega}^{(12)} \cdot \mathbf{e}_s\right) - \kappa_q\left(\mathbf{v}^{(12)} \cdot \mathbf{e}_q\right). \tag{8.4.34}$$

In the following discussion, we consider three cases:

Case 1: Surfaces Σ_1 and Σ_2 are in *line* contact at every instant, and point P lies on the instantaneous line of tangency. Principal curvatures κ_f and κ_h are given, and the parameters of motion at point P are known. The goal is to determine κ_s, κ_q, and σ for Σ_2.

Case 2: Surfaces Σ_1 and Σ_2 are again in *line* contact, but we consider the principal curvatures κ_s and κ_q of surface Σ_2 as given. The goal is to determine κ_f, κ_h, and σ.

Case 3: Surfaces Σ_1 and Σ_2 are in *point* contact at every instant, and P is the current point of tangency. The goal is to determine an equation that relates κ_f, κ_h, κ_s, κ_q, and σ.

Case I

We use for this case a system of three linear equations in the unknowns $v_f^{(2)}$ and $v_h^{(2)}$. This system contains the first two linear equations of system (8.4.15). The third linear

equation is the differentiated equation of meshing (8.2.7), in which we take $i = 1$ and represent it as follows:

$$\dot{\mathbf{n}}_r^{(1)} \cdot \mathbf{v}^{(12)} - \left[\mathbf{v}_r^{(1)} \cdot \left(\boldsymbol{\omega}^{(12)} \times \mathbf{n}\right)\right]$$
$$+ \mathbf{n} \cdot \left[\left(\boldsymbol{\omega}^{(1)} \times \mathbf{v}_{tr}^{(2)}\right) - \left(\boldsymbol{\omega}^{(2)} \times \mathbf{v}_{tr}^{(1)}\right)\right]$$
$$- \left(\boldsymbol{\omega}^{(1)}\right)^2 m'_{21} \mathbf{n} \cdot \left[\mathbf{k}_2 \times \left(\mathbf{r}^{(1)} - \mathbf{R}\right)\right] = 0. \tag{8.4.35}$$

We transform Eq. (8.4.35) using the following procedure:

Step 1: Representing vectors of the scalar product $\dot{\mathbf{n}}_r^{(1)} \cdot \mathbf{v}^{(12)}$ in coordinate system S_a $(\mathbf{e}_f, \mathbf{e}_h)$, we obtain

$$\mathbf{v}^{(12)} \cdot \dot{\mathbf{n}}_r^{(1)} = \begin{bmatrix} v_f^{(12)} \\ v_h^{(12)} \end{bmatrix}^\mathrm{T} \begin{bmatrix} \dot{n}_f^{(1)} \\ \dot{n}_h^{(1)} \end{bmatrix}. \tag{8.4.36}$$

Step 2: Using Eqs. (8.4.11), we obtain

$$\mathbf{v}^{(12)} \cdot \dot{\mathbf{n}}_r^{(1)} = \begin{bmatrix} v_f^{(12)} \\ v_h^{(12)} \end{bmatrix}^\mathrm{T} \mathbf{K}_1 \begin{bmatrix} v_f^{(1)} \\ v_h^{(1)} \end{bmatrix}. \tag{8.4.37}$$

Step 3: Equations (8.4.37) and (8.4.6) yield

$$\mathbf{v}^{(12)} \cdot \dot{\mathbf{n}}_r^{(1)} = \begin{bmatrix} v_f^{(12)} \\ v_h^{(12)} \end{bmatrix}^\mathrm{T} \mathbf{K}_1 \begin{bmatrix} v_f^{(2)} \\ v_h^{(2)} \end{bmatrix} - \begin{bmatrix} v_f^{(12)} \\ v_h^{(12)} \end{bmatrix}^\mathrm{T} \mathbf{K}_1 \begin{bmatrix} v_f^{(12)} \\ v_h^{(12)} \end{bmatrix}$$
$$= \begin{bmatrix} v_f^{(12)} \\ v_h^{(12)} \end{bmatrix}^\mathrm{T} \mathbf{K}_1 \begin{bmatrix} v_f^{(2)} \\ v_h^{(2)} \end{bmatrix} + \kappa_f \left(v_f^{(12)}\right)^2 + \kappa_h \left(v_h^{(12)}\right)^2. \tag{8.4.38}$$

Step 4: Our next step is directed at the transformation of the triple product $\{-\mathbf{v}_r^{(1)} \cdot (\boldsymbol{\omega}^{(12)} \times \mathbf{n})\}$. Representing vectors of the triple product in coordinate system S_a $(\mathbf{e}_f, \mathbf{e}_h)$, we obtain

$$- \mathbf{v}_r^{(1)} \cdot \left(\boldsymbol{\omega}^{(12)} \times \mathbf{n}\right) = \begin{bmatrix} \left(\mathbf{n} \times \boldsymbol{\omega}^{(12)}\right) \cdot \mathbf{e}_f \\ \left(\mathbf{n} \times \boldsymbol{\omega}^{(12)}\right) \cdot \mathbf{e}_h \end{bmatrix}^\mathrm{T} \begin{bmatrix} v_f^{(1)} \\ v_h^{(1)} \end{bmatrix}. \tag{8.4.39}$$

Step 5: Equations (8.4.39) and (8.4.6) yield

$$- \mathbf{v}_r^{(1)} \cdot \left(\boldsymbol{\omega}^{(12)} \times \mathbf{n}\right) = \begin{bmatrix} \left(\mathbf{n} \times \boldsymbol{\omega}^{(12)}\right) \cdot \mathbf{e}_f \\ \left(\mathbf{n} \times \boldsymbol{\omega}^{(12)}\right) \cdot \mathbf{e}_h \end{bmatrix}^\mathrm{T} \begin{bmatrix} v_f^{(2)} \\ v_h^{(2)} \end{bmatrix} - \left(\mathbf{n} \times \boldsymbol{\omega}^{(12)}\right) \cdot \mathbf{v}^{(12)}. \tag{8.4.40}$$

Step 6: Using Eqs. (8.4.38) and (8.4.40), we represent Eq. (8.4.35) as follows:

$$\left\{ \begin{bmatrix} v_f^{(12)} \\ v_b^{(12)} \end{bmatrix}^{\mathrm{T}} \mathbf{K}_1 + \begin{bmatrix} (\mathbf{n} \times \boldsymbol{\omega}^{(12)}) \cdot \mathbf{e}_f \\ (\mathbf{n} \times \boldsymbol{\omega}^{(12)}) \cdot \mathbf{e}_b \end{bmatrix}^{\mathrm{T}} \right\} \begin{bmatrix} v_f^{(2)} \\ v_b^{(2)} \end{bmatrix}$$

$$= -\mathbf{n} \cdot \left[(\boldsymbol{\omega}^{(1)} \times \mathbf{v}_{tr}^{(2)}) - (\boldsymbol{\omega}^{(2)} \times \mathbf{v}_{tr}^{(1)}) \right]$$

$$+ (\omega^{(1)})^2 \, m_{21}' (\mathbf{n} \times \mathbf{k}_2) \cdot (\mathbf{r}^{(1)} - \mathbf{R})$$

$$+ (\mathbf{n} \times \boldsymbol{\omega}^{(12)}) \cdot \mathbf{v}^{(12)} - \kappa_f (v_f^{(12)})^2 - \kappa_b (v_b^{(12)})^2. \tag{8.4.41}$$

Finally, using Eq. (8.4.41) and the first two equations of equation system (8.4.15), we obtain the following system of three linear equations in the unknowns $v_f^{(2)}$ and $v_b^{(2)}$:

$$t_{i1} v_f^{(2)} + t_{i2} v_b^{(2)} = t_{i3} \qquad (i = 1, 2, 3). \tag{8.4.42}$$

Here,

$$t_{11} \equiv b_{11}, \quad t_{12} = t_{21} \equiv b_{12}, \quad t_{22} \equiv b_{22}$$

$$t_{13} = t_{31} \equiv b_{15}, \quad t_{23} \equiv t_{32} \equiv b_{25}$$

$$t_{33} = -\mathbf{n} \cdot \left[(\boldsymbol{\omega}^{(1)} \times \mathbf{v}_{tr}^{(2)}) - (\boldsymbol{\omega}^{(2)} \times \mathbf{v}_{tr}^{(1)}) \right] \tag{8.4.43}$$

$$+ (\omega^{(1)})^2 \, m_{21}' (\mathbf{n} \times \mathbf{k}_2) \cdot (\mathbf{r}^{(1)} - \mathbf{R})$$

$$+ (\mathbf{n} \times \boldsymbol{\omega}^{(12)}) \cdot \mathbf{v}^{(12)} - \kappa_f (v_f^{(12)})^2 - \kappa_b (v_b^{(12)})^2.$$

For further derivations, it is important to recognize that the rank of the system matrix and the augment matrix for equation system (8.4.42) is 1. This follows from the fact that the contacting surfaces are in line contact at every instant, the displacement of a contact point over the surface is not unique, and therefore the solution of system equation (8.4.42) for the unknowns $v_f^{(2)}$ and $v_b^{(2)}$ is not unique either. The requirement that the rank of the system matrix and the augmented matrix be 1 enables us to derive the following equations for determination of principal directions on Σ_2 and the principal curvatures of this surface:

$$\tan 2\sigma = \frac{-2 t_{13} t_{23}}{t_{23}^2 - t_{13}^2 - (\kappa_f - \kappa_b) t_{33}} \tag{8.4.44}$$

$$\kappa_q - \kappa_s = \frac{-2 t_{13} t_{23}}{t_{33} \sin 2\sigma} = \frac{t_{23}^2 - t_{13}^2 - (\kappa_f - \kappa_b) t_{33}}{t_{33} \cos 2\sigma} \tag{8.4.45}$$

$$\kappa_q + \kappa_s = \kappa_f + \kappa_b + \frac{t_{13}^2 + t_{23}^2}{t_{33}}. \tag{8.4.46}$$

The advantage of Eqs. (8.4.44) to (8.4.46) is the opportunity to determine the principal curvatures and directions on surface Σ_2 knowing the principal curvatures and directions on Σ_1 and the parameters of motion of the mating surfaces. The knowledge of principal curvatures and directions of contacting surfaces is necessary for determination of the instantaneous contact ellipse for elastic surfaces.

Case 2

The derivations are similar to those discussed in Case 1. We consider the following system of three linear equations:

$$a_{i1}v_s^{(1)} + a_{i2}v_q^{(1)} = a_{i3} \qquad (i = 1, 2, 3).$$ (8.4.47)

The first two equations of system (8.4.47) have been represented as the third and fourth equations in the system of linear equations (8.4.15). The third equation in the system (8.4.47) is the differentiated equation of meshing (8.2.7) ($i = 2$) that we express in terms of $\mathbf{v}_r^{(1)}$ and $\dot{\mathbf{n}}_r^{(1)}$. Here,

$$a_{11} = b_{33}, \; a_{12} = a_{21} = b_{34}, \; a_{22} = b_{44}$$

$$a_{13} = a_{31} = -\kappa_s v_s^{(12)} - \boldsymbol{\omega}^{(12)} \cdot (\mathbf{n} \times \mathbf{e}_s)$$

$$a_{23} = a_{32} = -\kappa_q v_q^{(12)} - \boldsymbol{\omega}^{(12)} \cdot (\mathbf{n} \times \mathbf{e}_q)$$

$$a_{33} = -\mathbf{n} \cdot \left[(\boldsymbol{\omega}^{(1)} \times \mathbf{v}_{tr}^{(2)}) - (\boldsymbol{\omega}^{(2)} \times \mathbf{v}_{tr}^{(1)}) \right]$$ (8.4.48)

$$+ \left\{ \left[(\boldsymbol{\omega}^{(1)})^2 m_{21}' (\mathbf{n} \times \mathbf{k}_2) \right] \cdot (\mathbf{r}^{(1)} - \mathbf{R}) \right\}$$

$$- \mathbf{n} \cdot (\boldsymbol{\omega}^{(12)} \times \mathbf{v}^{(12)}) + \kappa_s \left(v_s^{(12)} \right)^2 + \kappa_q \left(v_q^{(12)} \right)^2.$$

The rank of the system matrix and the augmented matrix is 1, as explained for case 1. The solution for κ_f, κ_h, and σ is as follows:

$$\tan 2\sigma = \frac{2a_{13}a_{23}}{a_{23}^2 - a_{13}^2 + (\kappa_s - \kappa_q)a_{33}}$$ (8.4.49)

$$\kappa_f - \kappa_h = \frac{2a_{13}a_{23}}{a_{33}\sin 2\sigma} = \frac{a_{23}^2 - a_{13}^2 + (\kappa_s - \kappa_q)a_{33}}{a_{33}\cos 2\sigma}$$ (8.4.50)

$$\kappa_f + \kappa_h = (\kappa_s + \kappa_q) - \frac{a_{13}^2 + a_{23}^2}{a_{33}}.$$ (8.4.51)

Case 3

Surfaces Σ_1 and Σ_2 are in point contact at every instant. The velocity of the point of contact in its motion over the surface has a definite direction; equation system (8.4.47) must possess a unique solution; and the rank of the system matrix is 2. This condition yields that

$$\begin{vmatrix} a_{11} & a_{12} & a_{13} \\ a_{12} & a_{22} & a_{23} \\ a_{13} & a_{23} & a_{33} \end{vmatrix} = F\left(\kappa_f, \; \kappa_h, \; \kappa_s, \; \kappa_q, \; \sigma, \; m_{21}'\right) = 0.$$ (8.4.52)

There is only one relation between the principal curvatures and directions for the contacting surfaces. Considering that the principal curvatures are given for one surface, say Σ_1, we can synthesize an infinitely large number of matching surfaces Σ_2 that will satisfy the same value of m_{12}' and other motion parameters. More details are given in Litvin & Zhang [1991].

8.5 DIRECT RELATIONS BETWEEN NORMAL CURVATURES OF MATING SURFACES

We consider again two cases when the interacting surfaces Σ_1 and Σ_2 are in line contact, or in point contact. The plane in which unit vectors of principal directions are shown in Fig. 8.4.1 is the tangent plane to Σ_1 and Σ_2, and P is the point of tangency of these surfaces. Point P belongs to the instantaneous characteristic (instantaneous line of tangency) in the case of line contact and is the single point of tangency in the case of point contact. We consider three trihedrons: $S_c(\mathbf{e}_t, \mathbf{e}_m, \mathbf{e}_n)$, $S_a(\mathbf{e}_f, \mathbf{e}_h, \mathbf{e}_n)$, and $S_b(\mathbf{e}_s, \mathbf{e}_q, \mathbf{e}_n)$, where $\mathbf{e}_n \equiv \mathbf{n}$ is the surface unit normal; $\mathbf{e}_f$ and $\mathbf{e}_h$ are the unit vectors of principal directions on Σ_1; $\mathbf{e}_s$ and $\mathbf{e}_q$ are the unit vectors of principal directions on Σ_2; and $\mathbf{e}_t$ and $\mathbf{e}_m$ are two mutually perpendicular directions that are chosen in the tangent plane. Angles q_1, q_2, and $\sigma = q_1 - q_2$ designate the angles that are formed between the above-mentioned respective unit vectors.

Our goal is to determine the relations between the normal curvatures $\kappa_t^{(i)}$, $\kappa_m^{(i)}$ $(i = 1, 2)$ along $\mathbf{e}_t$ and $\mathbf{e}_m$ for surfaces Σ_1 and Σ_2. Our approach to the solution of this problem is based on two steps of decomposition of motions: the first one is performed along the principal directions, and the second one is in the directions of $\mathbf{e}_t$ and $\mathbf{e}_m$. The derivations are based on application of Eqs. (8.2.2), (8.2.4), and (8.2.7). For the purpose of simplification, we designate $\mathbf{v}_r^{(i)} = \mathbf{v}^{(i)}$, $\dot{\mathbf{n}}_r^{(i)} = \dot{\mathbf{n}}^{(i)}$, $\mathbf{v}^{(12)} = \mathbf{v}$, and $\boldsymbol{\omega}^{(12)} = \boldsymbol{\omega}$, and we represent Eqs. (8.2.2) and (8.2.4) as follows:

$$\mathbf{v}^{(1)} - \mathbf{v}^{(2)} = -\mathbf{v}, \qquad \dot{\mathbf{n}}^{(1)} - \dot{\mathbf{n}}^{(2)} = -(\boldsymbol{\omega} \times \mathbf{n}). \qquad (8.5.1)$$

We may represent vectors $\mathbf{v}^{(i)}$ and $\dot{\mathbf{n}}^{(i)}$ $(i = 1, 2)$ in coordinate systems S_c, S_a, and S_b as follows:

$$\mathbf{a}^{(1)} = a_t^{(1)}\mathbf{e}_t + a_m^{(1)}\mathbf{e}_m = a_f^{(1)}\mathbf{e}_f + a_h^{(1)}\mathbf{e}_h = a_s^{(1)}\mathbf{e}_s + a_q^{(1)}\mathbf{e}_q$$

$$\left(\mathbf{a}^{(1)} = \mathbf{v}^{(1)}, \text{ or } \mathbf{a}^{(1)} = \dot{\mathbf{n}}^{(1)}\right) \qquad (8.5.2)$$

$$\mathbf{b}^{(2)} = b_t^{(2)}\mathbf{e}_t + b_m^{(2)}\mathbf{e}_m = b_f^{(2)}\mathbf{e}_f + b_h^{(2)}\mathbf{e}_h = b_s^{(2)}\mathbf{e}_s + b_q^{(2)}\mathbf{e}_q$$

$$\left(\mathbf{b}^{(2)} = \mathbf{v}^{(2)}, \text{ or } \mathbf{b}^{(2)} = \dot{\mathbf{n}}^{(2)}\right). \qquad (8.5.3)$$

In addition to Eqs. (8.5.1), we also consider the differentiated equation of meshing (8.2.7). The following is an application of these equations for the following three cases.

Case I

Surfaces Σ_1 and Σ_2 are in line contact, and point P is the point of the instantaneous line of contact. Given are the normal curvatures $\kappa_t^{(1)}$ and $\kappa_m^{(1)}$ of Σ_1 at point P, and angle q_1. Our goal is to derive the equations for determination of normal curvatures $\kappa_t^{(2)}$, $\kappa_m^{(2)}$, and angle q_2 (Fig. 8.4.1).

It is shown below that the solution to this problem requires the derivation of three linear equations in unknowns $v_t^{(2)}$ and $v_m^{(2)}$. This system is represented as

$$\begin{bmatrix} c_{11} & c_{12} \\ c_{21} & c_{22} \\ c_{31} & c_{32} \end{bmatrix} \begin{bmatrix} v_t^{(2)} \\ v_m^{(2)} \end{bmatrix} = \begin{bmatrix} d_1 \\ d_2 \\ d_3 \end{bmatrix}. \qquad (8.5.4)$$

We may derive this system, using equation system (8.4.42) in unknowns $v_f^{(2)}$ and $v_h^{(2)}$. It is also shown that the coefficients c_{kl} ($k = 1, 2, 3; l = 1, 2$) and d_k ($k = 1, 2, 3$) are represented as follows:

$$c_{11} = \kappa_t^{(2)} - \kappa_t^{(1)} \tag{8.5.5}$$

$$c_{12} = c_{21} = t^{(2)} - t^{(1)} \tag{8.5.6}$$

$$c_{22} = \kappa_m^{(2)} - \kappa_m^{(1)} \tag{8.5.7}$$

$$c_{31} = d_1 = -t^{(1)}v_m^{(12)} - \kappa_t^{(1)}v_t^{(12)} - \left(\boldsymbol{\omega}^{(12)} \cdot \mathbf{e}_m\right) \tag{8.5.8}$$

$$c_{32} = d_2 = -t^{(1)}v_t^{(12)} - \kappa_m^{(1)}v_m^{(12)} + \left(\boldsymbol{\omega}^{(12)} \cdot \mathbf{e}_t\right) \tag{8.5.9}$$

$$d_3 = -\kappa_t^{(1)}(v_t^{(12)})^2 - \kappa_m^{(1)}\left(v_m^{(12)}\right)^2 - 2t^{(1)}v_t^{(12)}v_m^{(12)}$$
$$+ \left(\mathbf{n} \times \boldsymbol{\omega}^{(12)}\right) \cdot \mathbf{v}^{(12)} - \mathbf{n} \cdot \left[\left(\boldsymbol{\omega}^{(1)} \times \mathbf{v}_{tr}^{(2)}\right) - \left(\boldsymbol{\omega}^{(2)} \times \mathbf{v}_{tr}^{(1)}\right)\right]$$
$$+ \left(\omega^{(1)}\right)^2 m_{21}' \left(\mathbf{n} \times \mathbf{k}_2\right) \cdot \left(\mathbf{r}^{(1)} - \mathbf{R}\right). \tag{8.5.10}$$

The designation $t^{(1)}$ indicates the surface torsion of Σ_1 for the displacement along $\mathbf{e}_t$ and is represented as (see Section 7.9)

$$t^{(1)} = 0.5\left(\kappa_m^{(1)} - \kappa_t^{(1)}\right) \cdot \tan 2q_1. \tag{8.5.11}$$

The following is the explanation of the derivation of Eqs. (8.5.5) to (8.5.11).

Derivation of First Two Equations of System (8.5.4)

The derivation is based on the following procedure:

Step 1: Consider the first two equations of system (8.4.42) that have been represented as

$$\begin{bmatrix} t_{11} & t_{12} \\ t_{12} & t_{22} \end{bmatrix} \begin{bmatrix} v_f^{(2)} \\ v_b^{(2)} \end{bmatrix} = \begin{bmatrix} t_{13} \\ t_{23} \end{bmatrix}. \tag{8.5.12}$$

Here [see Eqs. (8.4.42)], $t_{11} = b_{11}$, $t_{12} = b_{12}$, $t_{22} = b_{22}$, $t_{13} = b_{15}$, and $t_{23} = b_{25}$. The b_{ml} coefficients ($m = 1, 2; l = 1, 2, 5$) have been represented by Eqs. (8.4.24), (8.4.25), (8.4.26), (8.4.31), and (8.4.32).

Step 2: The coordinate transformation in the 2D-space from S_c ($\mathbf{e}_t$, $\mathbf{e}_m$) to S_a ($\mathbf{e}_f$, $\mathbf{e}_h$) (Fig. 8.4.1) is based on the matrix equation

$$\begin{bmatrix} v_f^{(2)} \\ v_t^{(2)} \end{bmatrix} = \mathbf{L}_{ac} \begin{bmatrix} v_t^{(2)} \\ v_m^{(2)} \end{bmatrix} \tag{8.5.13}$$

where

$$\mathbf{L}_{ac} = \begin{bmatrix} \cos q_1 & -\sin q_1 \\ \sin q_1 & \cos q_1 \end{bmatrix}. \tag{8.5.14}$$

Step 3: Using Eqs. (8.5.12), (8.4.43), (8.5.13), and (8.5.14), we obtain after transformations

$$\mathbf{L}_{ca} \begin{bmatrix} b_{11} & b_{12} \\ b_{12} & b_{22} \end{bmatrix} \mathbf{L}_{ac} \begin{bmatrix} v_t^{(2)} \\ v_m^{(2)} \end{bmatrix} = \mathbf{L}_{ca} \begin{bmatrix} b_{15} \\ b_{25} \end{bmatrix} \tag{8.5.15}$$

where

$$\mathbf{L}_{ca} = \mathbf{L}_{ac}^{\mathrm{T}}.$$

Step 4: We now use the following designations:

$$\mathbf{L}_{ca}\begin{bmatrix} b_{11} & b_{12} \\ b_{12} & b_{22} \end{bmatrix}\mathbf{L}_{ac} = \begin{bmatrix} c_{11} & c_{12} \\ c_{12} & c_{22} \end{bmatrix} \tag{8.5.16}$$

$$\mathbf{L}_{ca}\begin{bmatrix} b_{15} \\ b_{25} \end{bmatrix} = \begin{bmatrix} d_1 \\ d_2 \end{bmatrix}. \tag{8.5.17}$$

Step 5: Using Eqs. (8.5.16) and (8.5.17) and Euler's equations that relate the principal and normal curvatures (see Section 7.6), we obtain the above-mentioned equations for c_{11}, c_{12}, c_{22}, d_1, and d_2.

Derivation of Third Equation of System (8.5.4)

We use for this purpose the third equation of system (8.4.42) that is represented as

$$t_{31}v_f^{(2)} + t_{32}v_h^{(2)} = b_{15}v_f^{(2)} + b_{25}v_h^{(2)} = t_{33} \tag{8.5.18}$$

[see Eqs. (8.4.43) for t_{31} and t_{32}]. The transformation of Eq. (8.5.18) is based on the following procedure:

Step 1: Using Eqs. (8.5.18) and (8.5.13), we obtain

$$[b_{15} \quad b_{25}]\,\mathbf{L}_{ac}\begin{bmatrix} v_t^{(2)} \\ v_m^{(2)} \end{bmatrix} = t_{33}. \tag{8.5.19}$$

Step 2: The matrix product $[b_{15} \quad b_{25}]\,\mathbf{L}_{ac}$ can be transformed as follows:

$$[b_{15} \quad b_{25}]\,\mathbf{L}_{ac} = [b_{15} \quad b_{25}]\,\mathbf{L}_{ca}^{\mathrm{T}} = \left\{\mathbf{L}_{ca}\begin{bmatrix} b_{15} \\ b_{25} \end{bmatrix}\right\}^{\mathrm{T}}$$

$$= \left\{\begin{bmatrix} \cos q_1 & \sin q_1 \\ -\sin q_1 & \cos q_1 \end{bmatrix}\begin{bmatrix} b_{15} \\ b_{25} \end{bmatrix}\right\}^{\mathrm{T}}. \tag{8.5.20}$$

Step 3: Matrix product (8.5.20) results in a row matrix whose elements we designate as c_{31}, c_{32}. Thus,

$$\left\{\begin{bmatrix} \cos q_1 & \sin q_1 \\ -\sin q_1 & \cos q_1 \end{bmatrix}\begin{bmatrix} b_{15} \\ b_{25} \end{bmatrix}\right\}^{\mathrm{T}} = [c_{31} \quad c_{32}]. \tag{8.5.21}$$

Step 4: Equations (8.5.21) and (8.5.19) enable us to represent Eq. (8.5.18) as

$$[c_{31} \quad c_{32}]\begin{bmatrix} v_t^{(2)} \\ v_m^{(2)} \end{bmatrix} = d_3 \tag{8.5.22}$$

where $d_3 \equiv t_{33}$.

Step 5: Using Eqs. (8.4.31) and (8.4.32) for b_{15} and b_{25}, respectively, and the Euler equations that relate the principal and normal curvatures, we obtain Eqs. (8.5.8) and (8.5.9) for c_{31} and c_{32}.

Step 6: To derive the expression for d_3, we have to transform the expressions for κ_f, κ_b, $v_f^{(12)}$, and $v_b^{(12)}$ in the equation for t_{33} that has been represented in equation system (8.4.43). We use for this purpose the following equations:

$$\begin{bmatrix} v_f^{(12)} \\ v_b^{(12)} \end{bmatrix} = \mathbf{L}_{ac} \begin{bmatrix} v_t^{(12)} \\ v_m^{(12)} \end{bmatrix} = \begin{bmatrix} \cos q_1 & -\sin q_1 \\ \sin q_1 & \cos q_1 \end{bmatrix} \begin{bmatrix} v_t^{(12)} \\ v_m^{(12)} \end{bmatrix} \tag{8.5.23}$$

$$\kappa_f = \frac{\kappa_t^{(1)} \cos^2 q_1 - \kappa_m^{(1)} \sin^2 q_1}{\cos 2q_1} \tag{8.5.24}$$

$$\kappa_b = \frac{\kappa_m^{(1)} \cos^2 q_1 - \kappa_t^{(1)} \sin^2 q_1}{\cos 2q_1}. \tag{8.5.25}$$

Matrix equation (8.5.23) is similar to Eq. (8.5.13). Equations (8.5.24) and (8.5.25) are based on the Euler equations that relate the surface principal and normal curvatures (see Section 7.6). Using the equation for t_{33} and Eqs. (8.5.23) to (8.5.25), we obtain the represented equation (8.5.10) for d_3.

Derivation of Direct Relations Between the Normal Curvatures of Mating Surfaces

The derivation is based on the investigation of the overdetermined system (8.5.4) of three linear equations in two unknowns. The augmented matrix is

$$\mathbf{C} = \begin{bmatrix} c_{11} & c_{12} & d_1 \\ c_{12} & c_{22} & d_2 \\ d_1 & d_2 & d_3 \end{bmatrix}. \tag{8.5.26}$$

Matrix $\mathbf{C}$ is symmetric and its rank is 1, because the surfaces are in line contact and the displacement of a contact point over the surface is indefinite. Therefore, we have

$$\frac{c_{11}}{c_{12}} = \frac{c_{12}}{c_{22}} = \frac{d_1}{d_2}; \quad \frac{c_{11}}{d_1} = \frac{c_{12}}{d_2} = \frac{d_1}{d_3}; \quad \frac{c_{12}}{d_1} = \frac{c_{22}}{d_2} = \frac{d_2}{d_3}. \tag{8.5.27}$$

After transformations, we obtain the following relations:

$$\kappa_t^{(2)} = \kappa_t^{(1)} + \frac{d_1^2}{d_3} \tag{8.5.28}$$

$$\kappa_m^{(2)} = \kappa_m^{(1)} + \frac{d_2^2}{d_3} \tag{8.5.29}$$

$$\tan 2q_2 = \frac{1}{\kappa_m^{(2)} - \kappa_t^{(2)}} \left[\tan 2q_1 \left(\kappa_m^{(1)} - \kappa_t^{(1)} \right) + \frac{2d_1 d_2}{d_3} \right]. \tag{8.5.30}$$

[See expressions (8.5.8), (8.5.9), and (8.5.10) for d_1, d_2, and d_3.] Equations (8.5.28), (8.5.29), and (8.5.30) enable us to determine the normal curvatures $\kappa_t^{(2)}$, $\kappa_m^{(2)}$, and q_2 for surface Σ_2.

Case 2

Surfaces Σ_1 and Σ_2 are in line contact, and L is the instantaneous line of contact. Given are $\kappa_t^{(2)}$, $\kappa_m^{(2)}$, q_2, and m'_{21} for point P of L. Our goal is to determine $\kappa_t^{(1)}$, $\kappa_m^{(1)}$, and q_1.

In this case, we consider initially system (8.4.47) of three linear equations in the unknowns $v_s^{(1)}$ and $v_q^{(1)}$. Using an approach that is similar to that discussed in Case 1, we obtain

$$\kappa_t^{(1)} = \kappa_t^{(2)} - \frac{l_1^2}{l_3} \tag{8.5.31}$$

$$\kappa_m^{(1)} = \kappa_m^{(2)} - \frac{l_2^2}{l_3} \tag{8.5.32}$$

$$\tan 2q_1 = \frac{1}{\kappa_t^{(1)} - \kappa_m^{(1)}} \left[\tan 2q_2 \left(\kappa_t^{(2)} - \kappa_m^{(2)} \right) + \frac{2 l_1 l_2}{l_3} \right]. \tag{8.5.33}$$

Here,

$$l_1 = -t^{(2)} v_m^{(12)} - \kappa_t^{(2)} v_t^{(12)} - \left(\boldsymbol{\omega}^{(12)} \cdot \mathbf{e}_m \right) \tag{8.5.34}$$

$$l_2 = -t^{(2)} v_t^{(12)} - \kappa_m^{(2)} v_m^{(12)} + \left(\boldsymbol{\omega}^{(12)} \cdot \mathbf{e}_t \right) \tag{8.5.35}$$

$$l_3 = \kappa_t^{(2)} \left(v_t^{(12)} \right)^2 + \kappa_m^{(2)} \left(v_m^{(12)} \right)^2 + 2 t^{(2)} v_t^{(12)} v_m^{(12)}$$
$$- \left(\mathbf{n} \times \boldsymbol{\omega}^{(12)} \right) \cdot \mathbf{v}^{(12)} - \mathbf{n} \cdot \left[\left(\boldsymbol{\omega}^{(1)} \times \mathbf{v}_{tr}^{(2)} \right) - \left(\boldsymbol{\omega}^{(2)} \times \mathbf{v}_{tr}^{(1)} \right) \right]$$
$$+ \left(\boldsymbol{\omega}^{(1)} \right)^2 m_{21}' \left(\mathbf{n} \times \mathbf{k}_2 \right) \cdot \left(\mathbf{r}^{(1)} - \mathbf{R} \right) \tag{8.5.36}$$

$$t^{(2)} = 0.5 \left(\kappa_m^{(2)} - \kappa_t^{(2)} \right) \tan 2q_2. \tag{8.5.37}$$

Equations (8.5.31) to (8.5.33) enable us to determine the normal curvatures $\kappa_t^{(1)}$, $\kappa_m^{(1)}$ of surface Σ_1 and angle q_1.

Case 3

Surfaces Σ_1 and Σ_2 are in point contact at point P. There is a unique solution of the system of linear equations (8.5.4) for the unknowns $v_t^{(2)}$ and $v_m^{(2)}$. The rank of the augmented matrix is 2. The condition that the $\det(\mathbf{C}) = 0$ provides the relation

$$F \left(\kappa_t^{(1)}, \kappa_m^{(1)}, \kappa_t^{(2)}, \kappa_m^{(2)}, q_1, m_{12}' \right) = 0. \tag{8.5.38}$$

This means that there is only one constraint when surfaces with an instantaneous point of contact are synthesized.

Particular Case

Surfaces Σ_1 and Σ_2 are in line contact, but $\mathbf{e}_t$ is directed along the tangent $\mathbf{e}_t^*$ to the contact line at point P. In this case, we have [see Eqs. (8.5.31) to (8.5.33)]

$$l_1 = 0, \quad \kappa_t^{(1)} = \kappa_t^{(2)} = \kappa_t, \quad \kappa_m^{(2)} - \kappa_m^{(1)} = \frac{l_2^2}{l_3}, \quad \frac{\tan 2q_1}{\tan 2q_2} = \frac{\kappa_t - \kappa_m^{(2)}}{\kappa_t - \kappa_m^{(1)}} \tag{8.5.39}$$

$$t^{(2)} = t^{(1)} = -\frac{\kappa_t v_t^{(12)} + \boldsymbol{\omega}^{(12)} \cdot \mathbf{e}_m}{v_m^{(12)}}. \tag{8.5.40}$$

The side result of the performed investigation is the equality of the surface torsions in the displacement along the tangent $\mathbf{e}_t^*$ to the contact line. It also becomes possible to

determine the component $v_m^{(i)} = v_r^{(i)} \cdot e_m^*$ of the velocity of the contact point along e_m^* that is perpendicular to e_t^* (see Section 8.6). However, the component $v_t^{(i)}$ is indefinite.

8.6 DIAGONALIZATION OF CURVATURE MATRIX

We recall that matrix $\mathbf{A}$ of equation system (8.4.15) is symmetric and is represented by Eq. (8.4.23). Elements of matrix $\mathbf{A}$ are expressed in terms of principal curvatures of mating surfaces, and therefore we call it the curvature matrix. Our goal is to prove that the eigenvectors for matrix $\mathbf{A}$ are directed along the unit vectors e_t and e_m (Fig. 8.4.1), where e_t is the unit vector of the tangent to the contact line. It is also proven below that the eigenvalues are the extreme values of the relative normal curvature. A side effect of this investigation is that it becomes possible to determine the components of relative velocities $v_r^{(i)}$ $(i = 1, 2)$ that are directed along e_m (Fig. 8.4.1). However, the components of $v_r^{(i)}$ directed along the tangent to the contact line cannot be determined, because the direction of $v_r^{(1)}$ (or $v_r^{(2)}$) in the case of line contact of surfaces is indefinite.

The initial system of linear equations is Eq. (8.4.15). The diagonalization of matrix $\mathbf{A}$ is based on the matrix equation

$$\mathbf{U}^T \mathbf{A} \mathbf{U} = \mathbf{W}. \tag{8.6.1}$$

Here, $\mathbf{U}$ is the matrix of coordinate transformation that is represented by

$$\mathbf{U} = \begin{bmatrix} 0 & 0 & \cos q_1 & -\sin q_1 \\ 0 & 0 & \sin q_1 & \cos q_1 \\ \cos q_2 & -\sin q_2 & 0 & 0 \\ \sin q_2 & \cos q_2 & 0 & 0 \end{bmatrix}. \tag{8.6.2}$$

Then, we obtain that the diagonalized matrix is

$$\mathbf{W} = \begin{bmatrix} 0 & 0 & 0 & 0 \\ 0 & w_{22} & 0 & 0 \\ 0 & 0 & 0 & 0 \\ 0 & 0 & 0 & w_{44} \end{bmatrix}. \tag{8.6.3}$$

Here:
(i)

$$w_{11} = w_{33} = \kappa_t^{(2)} - \kappa_t^{(1)} = 0 \tag{8.6.4}$$

because since the normal curvature along the tangent to the contact line is the same for both surfaces.
(ii)

$$w_{12} = w_{21} = t^{(2)} - t^{(1)} = 0 \tag{8.6.5}$$

because the surface torsion in the direction along the tangent to the contact line is the same for both surfaces [see Eq. (8.5.40)].

(iii)

$$w_{33} = w_{11} = 0$$
$$w_{34} = w_{43} = t^{(2)} - t^{(1)} = 0. \tag{8.6.6}$$

(iv) In accordance with the results of transformation, we have that

$$w_{22} = w_{44} = \kappa_m^{(2)} - \kappa_m^{(1)} \tag{8.6.7}$$

where $\kappa_m^{(i)}$ is the normal curvature along e_m (Fig. 8.4.1).

It can be proven that the eigenvalues of the curvature matrix represent the extreme values of the relative normal curvature, κ_R. This can be done considering the equation for κ_R as

$$\kappa_R(q) = \kappa_n^{(2)}(q) - \kappa_n^{(1)}(q) \tag{8.6.8}$$

where

$$\kappa_n^{(2)} = \kappa_s \cos^2 q + \kappa_q \sin^2 q, \quad \kappa_n^{(1)} = \kappa_f \cos^2(q+\sigma) + \kappa_h \sin^2(q+\sigma), \quad (8.6.9)$$

and $\kappa_n^{(i)}$ designates the surface normal curvature. The varied angle q represents the direction in the tangent plane where the normal curvature is considered. The extreme values of κ_R are determined with $\partial \kappa_R / \partial q = 0$ which yields (i) that the directions of extreme values κ_R coincide with e_t^* and e_m^*, respectively; and (ii) that the extreme values of κ_R on these directions are $\kappa_R = 0$ along e_t^*, and $\kappa_R = \kappa_m^{(2)} - \kappa_m^{(1)}$ along e_m^*.

Using the diagonalized matrix, we may determine as well equations for determination of components $v_m^{(i)} = \mathbf{v}_r^{(i)} \cdot e_m^*$ $(i = 1, 2)$, where e_m^* is the unit vector that is perpendicular to the tangent to the characteristic. Vectors e_t^* and e_m^* are shown in Fig. 8.4.1 as e_t and e_m.

We mentioned above that the initial system of linear equations is [see Eq. (8.4.15)]

$$\mathbf{A}\,\mathbf{X} = \mathbf{B}.$$

We may transform equation system (8.4.15) using the transformations

$$\mathbf{X} = \mathbf{U}\mathbf{Y} \tag{8.6.10}$$

and

$$\mathbf{Y} = \mathbf{U}^{\mathrm{T}}\mathbf{X}. \tag{8.6.11}$$

Here, matrix $\mathbf{U}$ describes the coordinate transformation in the tangent plane (see Fig. 8.4.1) and is represented by Eq. (8.6.2). Using new designations, we represent matrix $\mathbf{X}$ as follows [see Eq. (8.4.16)]:

$$\mathbf{X} = \begin{bmatrix} \dot{s}_f^{(2)} & \dot{s}_h^{(2)} & \dot{s}_s^{(1)} & \dot{s}_q^{(1)} \end{bmatrix}^{\mathrm{T}}. \tag{8.6.12}$$

Equations (8.4.15) and (8.6.10) yield

$$\mathbf{A}\mathbf{U}\mathbf{Y} = \mathbf{B} \tag{8.6.13}$$

and

$$\mathbf{U}^{\mathrm{T}}\mathbf{A}\mathbf{U}\mathbf{Y} = \mathbf{U}^{\mathrm{T}}\mathbf{B}. \tag{8.6.14}$$

We recall [see Eq. (8.6.1)] that

$$\mathbf{U}^\mathrm{T}\mathbf{A}\mathbf{U} = \mathbf{W}. \tag{8.6.15}$$

Matrix $\mathbf{W}$ is represented above by Eqs. (8.6.3) and (8.6.7). The matrix product $\mathbf{U}^\mathrm{T}\mathbf{B}$ we designate by $\mathbf{E}$. Then we obtain

$$\mathbf{E} = \mathbf{W}\mathbf{Y} \tag{8.6.16}$$

where

$$\mathbf{E} = [\, e_1 \ e_2 \ e_3 \ e_4 \,]^\mathrm{T}. \tag{8.6.17}$$

Equations (8.6.16), (8.6.3), (8.6.7), (8.6.11), (8.6.2), and (8.6.12) yield

$$e_1 = e_3 = 0 \tag{8.6.18}$$

$$e_2 = \left(-\dot{s}_s^{(1)} \sin q_2 + \dot{s}_q^{(1)} \cos q_2\right)\left(\kappa_m^{(2)} - \kappa_m^{(1)}\right) \tag{8.6.19}$$

$$e_4 = \left(-\dot{s}_f^{(2)} \sin q_1 + \dot{s}_h^{(1)} \cos q_1\right)\left(\kappa_m^{(2)} - \kappa_m^{(1)}\right). \tag{8.6.20}$$

Here,

$$\cos q_2 = \mathbf{e}_t \cdot \mathbf{e}_s, \quad -\sin q_2 = \mathbf{e}_m \cdot \mathbf{e}_s \tag{8.6.21}$$

$$\cos q_1 = \mathbf{e}_t \cdot \mathbf{e}_f, \quad -\sin q_1 = \mathbf{e}_m \cdot \mathbf{e}_f. \tag{8.6.22}$$

It is easy to verify that

$$\dot{s}_m^{(1)} = \mathbf{v}_r^{(1)} \cdot \mathbf{e}_m = -\dot{s}_s^{(1)} \sin q_2 + \dot{s}_q^{(1)} \cos q_2 \tag{8.6.23}$$

using the following considerations:
(i) Let vector $\mathbf{v}_r^{(1)}$ be represented as

$$\mathbf{v}_r^{(1)} = \dot{s}_s^{(1)}\mathbf{e}_s + \dot{s}_q^{(1)}\mathbf{e}_q. \tag{8.6.24}$$

(ii) The coordinate transformation from coordinate system $(\mathbf{e}_s, \mathbf{e}_q)$ to coordinate system $(\mathbf{e}_t, \mathbf{e}_m)$ is represented by the following matrix equation (Fig. 8.4.1):

$$\begin{bmatrix} \dot{s}_t^{(1)} \\ \dot{s}_m^{(1)} \end{bmatrix} = \begin{bmatrix} \cos q_2 & \sin q_2 \\ -\sin q_2 & \cos q_2 \end{bmatrix} \begin{bmatrix} \dot{s}_s^{(1)} \\ \dot{s}_q^{(1)} \end{bmatrix}. \tag{8.6.25}$$

Using matrix equation (8.6.25), we may confirm Eq. (8.6.23).
Equations (8.6.19) and (8.6.23) yield

$$\dot{s}_m^{(1)} = \frac{e_2}{\kappa_m^{(2)} - \kappa_m^{(1)}}. \tag{8.6.26}$$

Similarly, we obtain that

$$\dot{s}_m^{(2)} = \frac{e_4}{\kappa_m^{(2)} - \kappa_m^{(1)}} = \dot{s}_m^{(1)} + \left(\mathbf{v}^{(12)} \cdot \mathbf{e}_m\right). \tag{8.6.27}$$

To derive equations for e_2 and e_4, we consider the matrix equation

$$\mathbf{E} = \mathbf{U}^\mathrm{T}\mathbf{B} \tag{8.6.28}$$

where $\mathbf{B}$ is represented by Eqs. (8.4.30) to (8.4.34). Further derivations are based on the following relations:

$$t = t^{(1)} = t^{(2)} \tag{8.6.29}$$

$$t^{(1)} = 0.5(\kappa_h - \kappa_f) \sin 2q_1 = 0.5\left(\kappa_m^{(1)} - \kappa_t\right) \tan 2q_1 \tag{8.6.30}$$

$$t^{(2)} = 0.5(\kappa_q - \kappa_s) \sin 2q_2 = 0.5\left(\kappa_m^{(2)} - \kappa_t\right) \tan 2q_2. \tag{8.6.31}$$

Finally, we obtain

$$e_2 = -\kappa_m^{(2)} \left(\mathbf{v}^{(12)} \cdot \mathbf{e}_m\right) - t \left(\mathbf{v}^{(12)} \cdot \mathbf{e}_t\right) + \left(\boldsymbol{\omega}^{(12)} \cdot \mathbf{e}_t\right) \tag{8.6.32}$$

$$e_4 = -\kappa_m^{(1)} \left(\mathbf{v}^{(12)} \cdot \mathbf{e}_m\right) - t \left(\mathbf{v}^{(12)} \cdot \mathbf{e}_t\right) + \left(\boldsymbol{\omega}^{(12)} \cdot \mathbf{e}_t\right). \tag{8.6.33}$$

Equations (8.6.26), (8.6.27), (8.6.32), and (8.6.33) represent the normal components of relative velocities $\mathbf{v}_r^{(1)}$ and $\mathbf{v}_r^{(2)}$. The solutions for $\dot{s}_t^{(1)}$ and $\dot{s}_t^{(2)}$ are indefinite.

8.7 CONTACT ELLIPSE
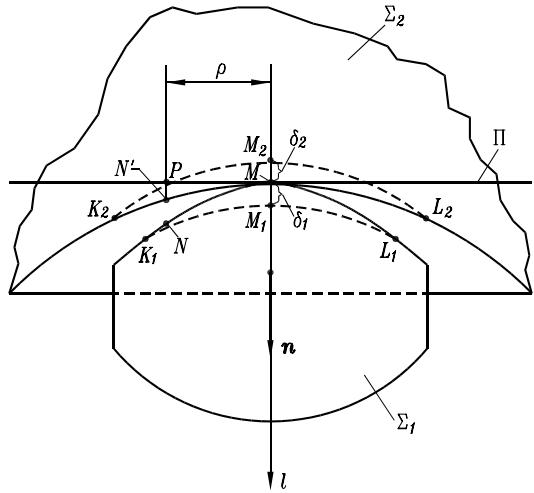
Basic Equation of Elastic Deformations

Due to elasticity of tooth surfaces, the instantaneous contact of surfaces at a point is spread over an elliptical area. The center of symmetry of the instantaneous contact ellipse coincides with the theoretical point of tangency. The bearing contact is formed as the set of contact ellipses. Our goal is to determine the orientation of the contact ellipse in the plane that is tangent to the contacting surfaces, and the dimensions of the contact ellipse. This can be done, considering as given: the principal curvatures of the contacting surfaces, angle σ that is formed between the unit vectors $\mathbf{e}_I^{(1)}$ and $\mathbf{e}_I^{(2)}$ that represent the principal directions on the surfaces, and the elastic deformation δ of the surfaces at the theoretical point of tangency M. The elastic deformation δ depends on the applied load, but we will consider δ a given value that is known from the experimental data. Usually, the contact ellipse is considered for the case when the gears are under a small load and δ is taken to be 0.00025 in. It is shown below that the *ratio* between the major and minor axes of the contact ellipse does not depend on δ.

Figure 8.7.1 shows that surfaces Σ_1 and Σ_2 are in tangency at point M. The unit surface normal and the tangent plane are designated by $\mathbf{n}$ and Π. The area of surface deformation is shown by a dashed line and designated by $K_1 M_1 L_1$ and $K_2 M_2 L_2$ for surfaces Σ_1 and Σ_2, respectively. The deformation of contacting surfaces at M is designated by δ_1 and δ_2, respectively, and the elastic approach at M is $\delta = \delta_1 + \delta_2$.

Designations N and N' indicate surface points, candidates for surface tangency *after* the elastic deformation (Fig. 8.7.1). There is a backlash between the surfaces at points N and N' *before* the elastic deformation as shown in Fig. 8.7.1. The location of N and N' with respect to M is determined with coordinates $(\rho, l^{(i)})$ $(i = 1, 2)$ as shown in Fig. 8.7.2. Here $l^{(i)}$ is the deviation of $N^{(i)}$ from M that depends on the curvature of the curve $K_i M L_i$ $(i = 1, 2)$ in the considered cross section of the surface (Fig. 8.7.1).

Consider now that surfaces Σ_1 and Σ_2 are deformed under the action of the contact force. We may consider for further derivations that surfaces Σ_1 and Σ_2 are deformed
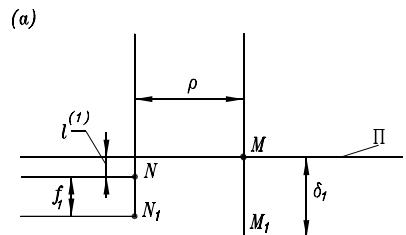
Figure 8.7.1: Area of elastic deformation.
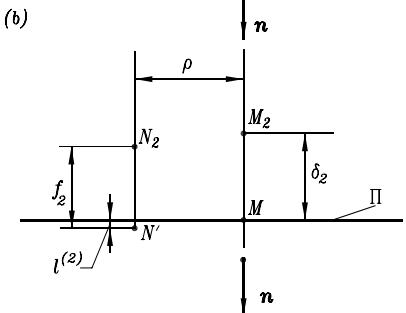
separately. Points M and N of surface Σ_1 will take positions M_1 and N_1, respectively, as shown in Fig. 8.7.2(a). Here, $|\overline{MM_1}| = \delta_1$, $|\overline{NN_1}| = f_1$, where δ_1 and f_1 are the elastic deformations of surface Σ_1 at points M and N, respectively; δ_1 and f_1 are measured along the surface unit normal $\mathbf{n}$. Similarly, considering the elastic deformation of surface Σ_2, we say that surface points M and N' will take positions M_2 and N_2, respectively [Fig. 8.7.2(b)].

The deviations of points M_1, M_2, N_1, and N_2 from the tangent plane are represented as follows:

$$\mathbf{\Delta}(M_1) = \delta_1\mathbf{n}, \qquad \mathbf{\Delta}(M_2) = -\delta_2\mathbf{n}, \qquad \mathbf{\Delta}(N_1) = \left(l^{(1)} + f_1\right)\mathbf{n}$$

$$\mathbf{\Delta}(N_2) = \left(l^{(2)} - f_2\right)\mathbf{n}. \qquad (8.7.1)$$

Figure 8.7.2: For derivation of basic equation of elastic deformation.

The backlash between the surfaces at points M_1 and M_2 is

$$\overline{M_2 M_1} = (\delta_1 + \delta_2)\, \mathbf{n}. \tag{8.7.2}$$

Surfaces Σ_1 and Σ_2 are in continuous tangency while gears 1 and 2 perform rotational motions. The imaginary backlash between the surfaces at points M_1 and M_2 will disappear if one of the mating gears, say gear 2, is rotated through a small angle $\Delta\phi_2$ about the gear axis of rotation. The condition of tangency of surfaces Σ_1 and Σ_2 at points M_1 and M_2 is as follows:

$$(\Delta\phi_2 \times \mathbf{r}_2) \cdot \mathbf{n} = \delta = \delta_1 + \delta_2. \tag{8.7.3}$$

Here, $\mathbf{r}_2$ is the position vector of M_2 that is drawn from any point of the axis of rotation of gear 2 to M_2. Rotation of gear 2 through the angle $\Delta\phi_2$ is equivalent to the displacement $(\delta_1 + \delta_2)\, \mathbf{n}$ of M_2 along the surface unit normal $\mathbf{n}$.

Taking into account that ρ is small with respect to $\mathbf{r}_2$, we may consider that the displacement of N_2 by the gear rotation is the same as M_2. Tangency of surfaces Σ_1 and Σ_2 at points N_1 and N_2 will be provided simultaneously with tangency at points M_1 and M_2, if the following equation is observed:

$$\mathbf{\Delta}(N_2) + \delta\mathbf{n} = \mathbf{\Delta}(N_1)$$

or

$$\left[(l^{(2)} - f_2) + (\delta_1 + \delta_2) \right]\, \mathbf{n} = \left(l^{(1)} + f_1 \right)\, \mathbf{n}. \tag{8.7.4}$$

Equation (8.7.4) yields

$$\left| l^{(1)} - l^{(2)} \right| = (\delta_1 + \delta_2) - (f_1 + f_2). \tag{8.7.5}$$

The right-hand side of Eq. (8.7.5) is always positive because $\delta_1 > f_1$ and $\delta_2 > f_2$. Equation (8.7.5) is satisfied for all mating points of contacting surfaces within the area of deformation and at the edge of this area. However, at the edge of this area $f_1 = 0$ and $f_2 = 0$, and therefore Eq. (8.7.5) becomes

$$\left| l^{(1)} - l^{(2)} \right| = \delta_1 + \delta_2 = \delta. \tag{8.7.6}$$

Outside of the area of deformation,

$$\left| l^{(1)} - l^{(2)} \right| > \delta, \tag{8.7.7}$$

and within this area,

$$\left| l^{(1)} - l^{(2)} \right| < \delta. \tag{8.7.8}$$

Determination of Contact Ellipse
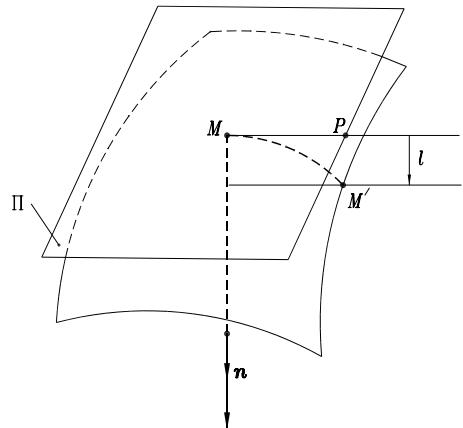
We can correlate deviation $l^{(i)}$ ($i = 1, 2$) with the surface curvature as follows. Consider that a surface Σ is represented by

$$\mathbf{r}(u, \theta) \in C^2, \quad \mathbf{r}_u \times \mathbf{r}_\theta \neq 0, \quad (u, \theta) \in E \tag{8.7.9}$$

where (u, θ) represent the surface coordinates. Curve $\overline{MM'}$ on surface Σ is represented by the equation

$$\mathbf{r} = \mathbf{r}\, [u(s),\ \theta(s)] \tag{8.7.10}$$

where s is the arc length.

Figure 8.7.3: For determination of deviation l.

Let us designate the length of the arc that connects two neighboring points M and M' of the curve by Δs, where $\Delta s = MM'$. The increment of the position vector $\mathbf{r}$ is designated by $\Delta \mathbf{r}$, where $\Delta \mathbf{r} = \overline{MM'}$. Expanding $\Delta \mathbf{r}$ with the Taylor-series expansion, we get

$$\overline{MM'} = \Delta \mathbf{r} = \frac{d\mathbf{r}}{ds}\Delta s + \frac{d^2\mathbf{r}}{ds^2}\frac{(\Delta s)^2}{2!} + \frac{d^3\mathbf{r}}{ds^3}\frac{(\Delta s)^3}{3!} + \cdots . \tag{8.7.11}$$

Here,

$$\frac{d\mathbf{r}}{ds} = \frac{\partial \mathbf{r}}{\partial u}\frac{du}{ds} + \frac{\partial \mathbf{r}}{\partial \theta}\frac{d\theta}{ds}$$

$$\frac{d^2\mathbf{r}}{ds^2} = \frac{\partial^2 \mathbf{r}}{\partial u^2}\left(\frac{du}{ds}\right)^2 + 2\frac{\partial^2 \mathbf{r}}{\partial u \partial \theta}\frac{du}{ds}\frac{d\theta}{ds} + \frac{\partial^2 \mathbf{r}}{\partial \theta^2}\left(\frac{d\theta}{ds}\right)^2 .$$

Plane Π shown in Fig. 8.7.3 is tangent to the surface at point M. Point P designates the projection of point M' onto plane Π. Vector

$$\overline{P M'} = l\mathbf{n} \tag{8.7.12}$$

is perpendicular to plane Π at point P, and l represents the deviation of the curve point M' from the tangent plane. The deviation l is positive if $\overline{P M'}$ and $\mathbf{n}$ are in the same direction. Equations $\overline{MM'} = \Delta \mathbf{r}$ and $\overline{MM'} = \overline{MP} + l\mathbf{n}$ yield
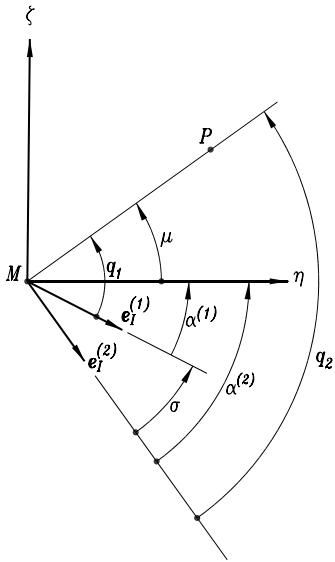
$$\overline{MP} + l\mathbf{n} = \frac{d\mathbf{r}}{ds}\Delta s + \frac{d^2\mathbf{r}}{ds^2}\frac{(\Delta s)^2}{2!} + \frac{d^3\mathbf{r}}{ds^3}\frac{(\Delta s)^3}{3!} + \cdots . \tag{8.7.13}$$

Vectors $\overline{MP}$ and $\mathbf{n}$ are mutually perpendicular. Taking the scalar product on both sides of Eq. (8.7.13) with $\mathbf{n}$, and limiting the expression for l up to terms of the third order, we obtain

$$l = \left(\frac{d^2\mathbf{r}}{ds^2}\cdot \mathbf{n}\right)\frac{\Delta s^2}{2}. \tag{8.7.14}$$

As mentioned in Chapter 7, the normal curvature of a surface may be represented by

$$\kappa_n = \frac{d^2\mathbf{r}}{ds^2}\cdot \mathbf{n}. \tag{8.7.15}$$

Figure 8.7.4: For derivation of contact ellipse.

Thus,

$$l = \kappa_n \frac{\Delta s^2}{2} = \frac{1}{2}\kappa_n \rho^2 \qquad (8.7.16)$$

considering that $\Delta s \approx \left| \overline{MP} \right| = \rho$.

The normal and principal curvatures of surface Σ_i ($i = 1, 2$) are related by Euler's equation (see Chapter 7). Thus,

$$\kappa_n^{(i)} = \kappa_I^{(i)} \cos^2 q_i + \kappa_{II}^{(i)} \sin^2 q_i \qquad (8.7.17)$$

where q_i is the angle that is formed by vectors $e_I^{(i)}$ and $\overline{MP}$ (Fig. 8.7.4).

We have designated points N and N' of contacting surfaces (Fig. 8.7.1) as the points of surface tangency after the elastic deformation. Point P is the projection of points N and N' on the tangent plane. The deviations of points N and N' from the tangent plane (before the elastic deformation) are determined with the following equations:

$$l^{(1)} = \frac{\rho^2}{2} \left(\kappa_I^{(1)} \cos^2 q_1 + \kappa_{II}^{(1)} \sin^2 q_1 \right) \qquad (8.7.18)$$

$$l^{(2)} = \frac{\rho^2}{2} \left(\kappa_I^{(2)} \cos^2 q_2 + \kappa_{II}^{(2)} \sin^2 q_2 \right). \qquad (8.7.19)$$

Angles q_1 and q_2 are formed by vectors $e_I^{(1)}$ and $\overline{MP}$, $e_I^{(2)}$ and $\overline{MP}$, respectively (Fig. 8.7.4); $\kappa_I^{(i)}$, $\kappa_{II}^{(i)}$ ($i = 1, 2$) are the principal curvatures of surfaces Σ_1 and Σ_2.

Let us choose in the tangent plane coordinate axes (η, ζ) (Fig. 8.7.4) as the axes of the to-be-determined contact ellipse. The orientation of vector $\overline{MP}$ in plane (η, ζ) is determined with angle μ. At the edge of the contact area, we have [see Eq. (8.7.6)]

$$l^{(1)} - l^{(2)} = \pm \delta. \qquad (8.7.20)$$

The determination of the dimensions of the contact ellipse and its orientation with respect to $e_I^{(1)}$ (or $e_I^{(2)}$) is based on Eqs. (8.7.18), (8.7.19), and (8.7.20), taking into

account the following relations (Fig. 8.7.4):

$$q_1 = \alpha^{(1)} + \mu, \quad q_2 = \alpha^{(2)} + \mu, \qquad \rho^2 = \eta^2 + \zeta^2,$$

$$\cos \mu = \frac{\eta}{\rho}, \quad \sin \mu = \frac{\zeta}{\rho}. \tag{8.7.21}$$

After transformations, we obtain

$$\eta^2 \left(\kappa^{(1)} \cos^2 \alpha^{(1)} + \kappa_{II}^{(1)} \sin^2 \alpha^{(1)} - \kappa_I^{(2)} \cos^2 \alpha^{(2)} - \kappa_{II}^{(2)} \sin^2 \alpha^{(2)} \right)$$

$$+ \zeta^2 \left(\kappa^{(1)} \sin^2 \alpha^{(1)} + \kappa_{II}^{(1)} \cos^2 \alpha^{(1)} - \kappa_I^{(2)} \sin^2 \alpha^{(2)} - \kappa_{II}^{(2)} \cos^2 \alpha^{(2)} \right)$$

$$- \eta \zeta \left(g_1 \sin 2\alpha^{(1)} - g_2 \sin 2\alpha^{(2)} \right) = \pm 2\delta \tag{8.7.22}$$

where

$$g_1 = \kappa_I^{(1)} - \kappa_{II}^{(1)}, \qquad g_2 = \kappa_I^{(2)} - \kappa_{II}^{(2)}.$$

Angle $\alpha^{(1)}$ that determines the orientation of the coordinate axes η and ζ with respect to $e_I^{(1)}$ may be chosen arbitrarily. For instance, $\alpha^{(1)}$ may be chosen as satisfying the equation

$$g_1 \sin 2\alpha^{(1)} - g_2 \sin 2\alpha^{(2)} = 0 \tag{8.7.23}$$

where (Fig. 8.7.4)

$$\alpha^{(2)} = \alpha^{(1)} + \sigma. \tag{8.7.24}$$

Equations (8.7.23) and (8.7.24) yield

$$\tan 2\alpha^{(1)} = \frac{g_2 \sin 2\sigma}{g_1 - g_2 \cos 2\sigma}. \tag{8.7.25}$$

Equation (8.7.25) provides two solutions for $2\alpha^{(1)}$. We choose the solution represented by equations

$$\cos 2\alpha^{(1)} = \frac{g_1 - g_2 \cos 2\sigma}{\left(g_1^2 - 2g_1 g_2 \cos 2\sigma + g_2^2 \right)^{1/2}} \tag{8.7.26}$$

$$\sin 2\alpha^{(1)} = \frac{g_2 \sin 2\sigma}{\left(g_1^2 - 2g_1 g_2 \cos 2\sigma + g_2^2 \right)^{1/2}}. \tag{8.7.27}$$

Equations (8.7.26), (8.7.27), and (8.7.24) determine the orientation of axes η and ζ with respect to the principal directions of the contacting surfaces. These equations yield

$$\cos^2 \alpha^{(1)} = 0.5 \left[1 + m(g_1 - g_2 \cos 2\sigma) \right] \tag{8.7.28}$$

$$\sin^2 \alpha^{(1)} = 0.5 \left[1 - m(g_1 - g_2 \cos 2\sigma) \right] \tag{8.7.29}$$

$$\cos^2 \alpha^{(2)} = 0.5 \left[1 + m(g_1 \cos 2\sigma - g_2) \right] \tag{8.7.30}$$

$$\sin^2 \alpha^{(2)} = 0.5 \left[1 - m(g_1 \cos 2\sigma - g_2) \right] \tag{8.7.31}$$
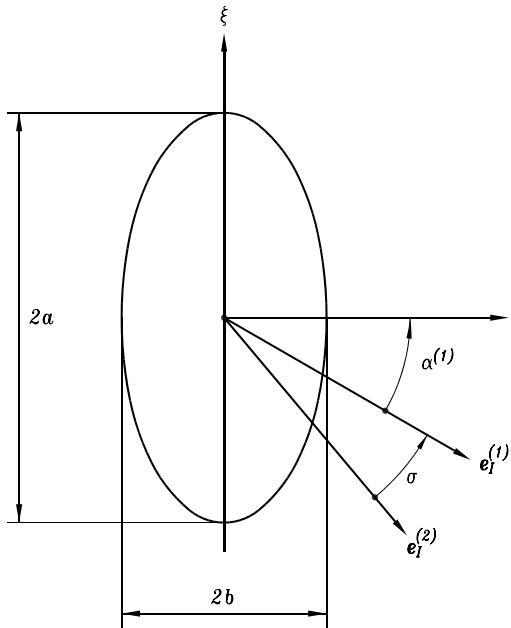
Figure 8.7.5: Contact ellipse.

where

$$m = \frac{1}{\left(g_1^2 - 2g_1 g_2 \cos 2\sigma + g_2^2\right)^{1/2}}. \tag{8.7.32}$$

Equations (8.7.22) and (8.7.23) confirm that the projection of contact area on the tangent plane is an ellipse. The contact ellipse is determined with the equation

$$B\eta^2 + A\zeta^2 = \pm\delta. \tag{8.7.33}$$

Ellipse axes are determined with the equations

$$2a = 2\left|\frac{\delta}{A}\right|^{1/2}, \qquad 2b = 2\left|\frac{\delta}{B}\right|^{1/2} \tag{8.7.34}$$

where

$$A = \frac{1}{4}\left[\kappa_\Sigma^{(1)} - \kappa_\Sigma^{(2)} - \left(g_1^2 - 2g_1 g_2 \cos 2\sigma + g_2^2\right)^{1/2}\right] \tag{8.7.35}$$

$$B = \frac{1}{4}\left[\kappa_\Sigma^{(1)} - \kappa_\Sigma^{(2)} + \left(g_1^2 - 2g_1 g_2 \cos 2\sigma + g_2^2\right)^{1/2}\right] \tag{8.7.36}$$

$$\kappa_\Sigma^{(i)} = \kappa_I^{(i)} + \kappa_{II}^{(i)}, \qquad g_i = \kappa_I^{(i)} - \kappa_{II}^{(i)}. \tag{8.7.37}$$

The orientation of the ellipse in the tangent plane is determined with Eqs. (8.7.26) and (8.7.27). The contact ellipse is shown in Fig. 8.7.5.

9 Computerized Simulation of Meshing and Contact

9.1 INTRODUCTION

Computerized simulation of meshing and bearing contact is a significant achievement that could substantially improve the technology and quality of gears. Computer programs known as tooth contact analysis (TCA) programs are directed at the solution of the following basic problem:

The equations of pinion and gear tooth surfaces, the crossing angle, and the shortest distance between the axes of rotation are given. The pinion and gear tooth surfaces are in point contact. It is necessary to determine (i) the transmission errors, (ii) the paths of contact points on the gear tooth surfaces, and (iii) the bearing contact as the set of instantaneous contact ellipses.

In the case of determination of the bearing contact, it is considered that due to the elasticity of gear tooth surfaces their contact is spread over an elliptic area, and the center of the contact ellipse is the theoretical point of contact. It is also considered that the surface elastic approach is known (for instance, from the experimental data), and the problem of bearing contact can be solved as a geometric problem (see Section 8.7).

The main idea of TCA is based on simulation of tangency of tooth surfaces that are in mesh. The determination of the instantaneous contact ellipse requires knowledge of the principal directions and curvatures of the tooth surfaces that are in tangency. A substantial simplification for the solution to this problem has been achieved due to the expression of principal curvatures and directions for the generated surface by the principal curvatures and directions of the generating tool (see Section 8.4).

The main goal of TCA is the analysis of gear meshing and bearing contact. The determination of machine-tool settings that provide improved conditions of meshing and contact is the goal of gear synthesis. The computerized search of such settings by the TCA program can require substantial computer time. This difficulty can be avoided by application of the local synthesis method that enables machine-tool settings to be determined directly (see Section 9.3). These machine-tool settings provide improved conditions of meshing and contact at the *mean* contact point and within its neighborhood. Local synthesis and tooth contact analysis (TCA) are applied simultaneously in the design of spiral bevel gears (see Chapter 21).

A specific problem occurs in the case of simulation of meshing and contact for gear tooth surfaces that are initially in line contact. Examples are spur gears, helical gears with

parallel axes, and worm-gear drives. However, the instantaneous line contact of gear tooth surfaces exists only theoretically, for an ideal gear train without misalignment or errors of manufacture. In practice, the surface line contact is substituted by point contact due to gear misalignment. The problem is to determine the *transition* point – the point on the theoretical contact line where the *real* point contact starts. After determination of the transition point, it becomes possible to determine a point in the neighborhood of the transition point that belongs to the path of point contact and then start the TCA computations.

This chapter covers computerized simulation of meshing and bearing contact, the local synthesis method, the application of finite element analysis for design of gear drives, and the analysis of edge contact of gear tooth surfaces.

9.2 PREDESIGN OF A PARABOLIC FUNCTION OF TRANSMISSION ERRORS
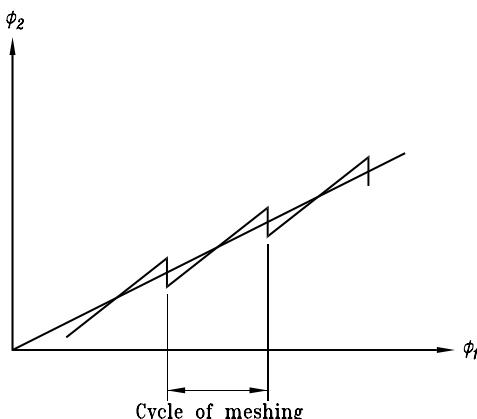
Application of a predesigned parabolic function of transmission errors enables the absorption of almost-linear discontinuous functions of transmission errors that are caused by misalignment. This is the key for reduction of noise and vibration of gear drives. The idea of the approach is based on the following considerations Litvin [1994]:

(i) The transmission function for an ideal gear train is linear and is represented as
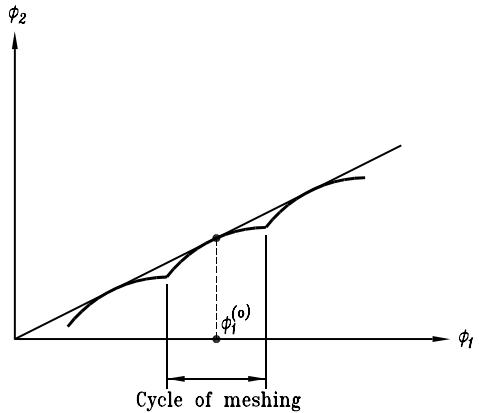
$$\phi_2 = \frac{N_1}{N_2}\phi_1 \tag{9.2.1}$$

where N_i and ϕ_i $(i = 1, 2)$ are the number of teeth and the rotation angle, respectively, for the pinion $(i = 1)$ and the gear $(i = 2)$.

(ii) Due to misalignment (change of crossing angle; change of shortest center distance in the case of noninvolute gears; axial displacement of spiral bevel gears, hypoid gears, worm-gears, and so on) the transmission function becomes a piecewise almost-linear one (Fig. 9.2.1) with a period of the cycle of meshing of a pair of teeth. This type of function of transmission errors is confirmed by simulation of meshing.

Figure 9.2.1: Transmission function as a sum of a linear function and a piecewise linear function of transmission errors.

Figure 9.2.2: Transmission function as a sum of a linear function and a predesigned parabolic function of transmission errors.

Due to the jump in the angular velocity at the junction of cycles, the acceleration approaches an infinitely large value and this causes large vibrations.
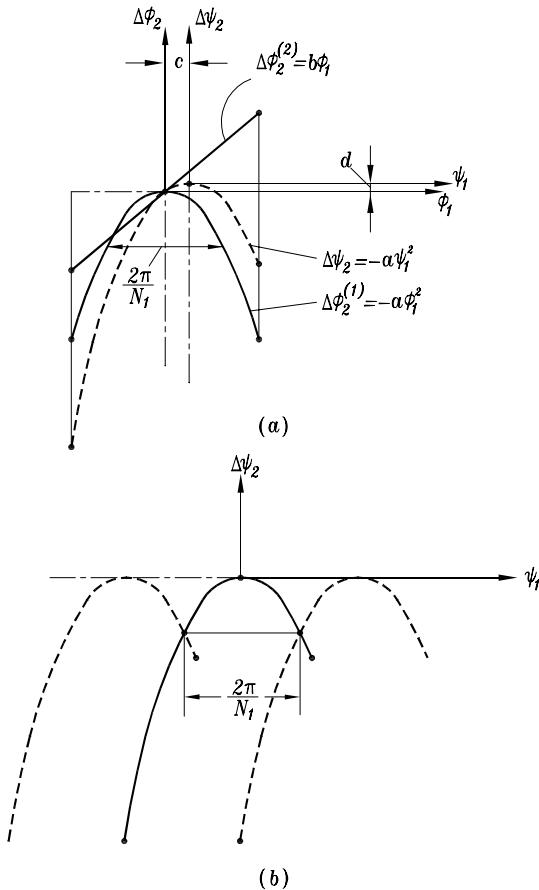
Due to absorption of linear functions of transmission errors by a predesigned parabolic function of transmission error, the transmission function is of the shape shown in Fig. 9.2.2. The transfer of meshing is not accompanied by a jump in acceleration as in the case shown in Fig. 9.2.1.

Effect of Application of a Predesigned Parabolic Function of Transmission Errors

We discuss the effect of application of a predesigned parabolic function of transmission errors by considering the interaction of a parabolic function $\Delta\phi_2^{(1)} = -a\phi_1^2$ with a linear function $\Delta\phi_2^{(2)} = b\phi_1$. Function $\Delta\phi_2^{(2)}$ is caused by misalignment of the gear drive. Function $\Delta\phi_2^{(1)}$ is predesigned for absorption of $\Delta\phi_2^{(2)}$.

It is easy to verify that the sum of functions $\Delta\phi_2^{(1)}(\phi_1)$ and $\Delta\phi_2^{(2)}(\phi_1)$ is a parabolic function of the same slope as $\Delta\phi_2^{(1)}(\phi_1)$. The new parabolic function designated as $\Delta\psi_2 = -a\psi_2^2$ (Fig. 9.2.3) is merely displaced by translation with respect to the initially given parabolic one. This means that a predesigned parabolic function of transmission errors can indeed *absorb* the linear function of transmission errors caused by gear misalignment. The displacement of function $\Delta\psi_2(\psi_1)$ with respect to $\Delta\phi_2^{(1)}(\phi_1)$ is determined by $c = b/2a$ and $d = b^2/4a$ [Fig. 9.2.3(a)]. We have to emphasize that the end points of function $\Delta\psi_2(\psi_1)$ are located asymmetrically in comparison with function $\Delta\phi_2^{(1)}(\phi_1)$ [Fig. 9.2.3(a)]. However, the function of transmission errors for each cycle of meshing [Fig. 9.2.3(b)] can be obtained as a continuous parabolic function.

In the process of computerized design of a misaligned gear drive, the resulting function of transmission errors is obtained by application of a tooth contact analysis (TCA) computer program. In some cases of design, it may happen that the obtained function of transmission errors is parabolic but discontinuous. This result indicates that the errors of alignment (simulated by coefficient b of function $\Delta\phi_2^{(2)} = b\phi_1$) are too large. Therefore, the predesigned parabolic function $\Delta\phi_2^{(1)}(\phi_1) = -a\phi_1^2$ with the existing parabola coefficient a cannot absorb the linear functions of transmission errors. Absorption will be achieved by increasing the parabola coefficient a, but it will be accompanied by an

Figure 9.2.3: Interaction of parabolic and linear functions.

increase of the maximal error

$$\left|\Delta\phi_2^{(1)}\right|_{\max} = a\left(\frac{\pi}{N_1}\right)^2. \tag{9.2.2}$$

Design of gear drives of high precision requires reduction of tolerances of errors of alignment.

NOTE. A *negative* parabolic function of transmission errors, not a positive one, should be applied for design so that the gear will lag with respect to the pinion and the elastic deformation will favor an increase in the contact ratio.

Determination of Derivative m'_{21}

We recall that the transmission function for an ideal gear drive is represented by linear function (9.2.1). The transmission function wherein a predesigned parabolic function of transmission errors is applied is determined as

$$\phi_2(\phi_1) = \frac{N_1}{N_2}\phi_1 - a\phi_1^2. \tag{9.2.3}$$

The first and second derivatives of $\phi_2(\phi_1)$ yield

$$m_{21}(\phi) = \frac{d}{d\phi_1}[\phi_2(\phi_1)] = \frac{N_1}{N_2} - 2a\phi_1 \qquad (9.2.4)$$

$$m'_{21}(\phi) = \frac{d^2}{d\phi_1^2}[\phi_2(\phi_1)] = -2a. \qquad (9.2.5)$$

The predesigned parabolic function may be represented as
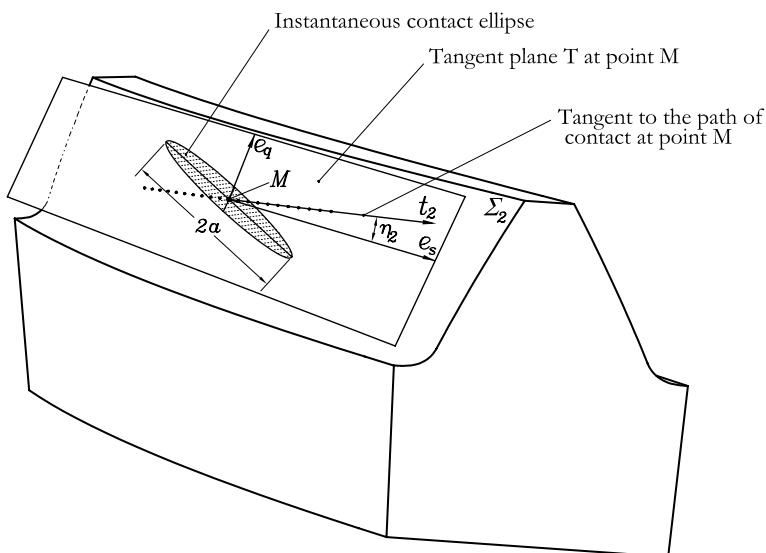
$$\Delta\phi_2(\phi_1) = -a\phi_1^2 = -\frac{1}{2}m'_{21}\phi_1^2. \qquad (9.2.6)$$

The derivative $m'_{21}(\phi_1)$ is used in the local synthesis procedure.
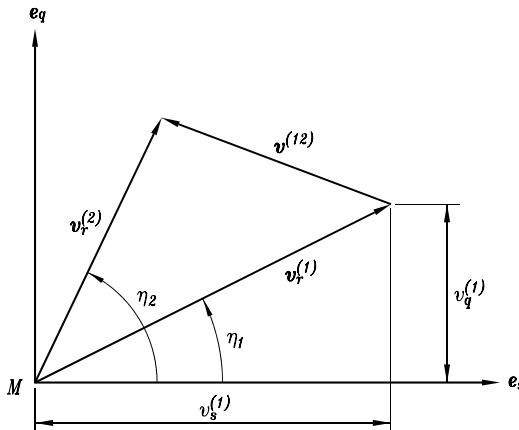
9.3 LOCAL SYNTHESIS

The approach of local synthesis was proposed by Litvin [1968] and then applied for synthesis of spiral bevel gears, hypoid gears, and face-worm gears. The *local* synthesis of gears must provide (i) the required gear ratio at the mean (selected) contact point M, (ii) the desired direction of tangent $\mathbf{t}$ to the contact path on the gear tooth surface determined by angle η_2 (Fig. 9.3.1), (iii) the desired length $2a$ of the major axis of the contact ellipse at M (Fig. 9.3.1), and (iv) a predesigned parabolic function of a controlled level of maximal transmission errors (say, 8 to 10 arc seconds). Angle η_2 in Fig. 9.3.1 is formed by tangent $\mathbf{t}_2$ to the path of contact and principal direction $\mathbf{e}_s$ on surface Σ_2. Detailed description of local synthesis is presented in Section 21.5 in relation to synthesis of spiral bevel gears.

Local synthesis is usually applied in combination with tooth contact analysis (TCA) and is developed as an iterative process. The local synthesis applied to spiral bevel gears and hypoid gears is based on the assumptions that the machine-tool settings for the gear are given already and the gear principal curvatures and directions at the mean contact

Figure 9.3.1: Illustration of parameters η_2 and a applied for local synthesis.

Figure 9.3.2: For derivation of tangents to paths of contact.

point are known as well. The local synthesis method enables determination of the pinion machine-tool settings that provide improved conditions of meshing and contact at the mean contact point M and within the neighborhood of M.

Relation Between Directions of Paths of Contact

We recall that velocities $\mathbf{v}_r^{(1)}$ and $\mathbf{v}_r^{(2)}$ are related by the equation (see Section 8.2)

$$\mathbf{v}_r^{(2)} = \mathbf{v}_r^{(1)} + \mathbf{v}^{(12)} \tag{9.3.1}$$

where $\mathbf{v}_r^{(i)} (i = 1, 2)$ is the velocity of the contact point in its motion over surface Σ_i. Vectors $\mathbf{v}_r^{(1)}$, $\mathbf{v}_r^{(2)}$, and $\mathbf{v}^{(12)}$ lie in the tangent plane; vectors $\mathbf{v}_r^{(1)}$ and $\mathbf{v}_r^{(2)}$ are tangent to the contact paths. Henceforth, we consider that the principal curvatures and principal directions on Σ_2 are known. Then, we may consider that the tangents to the contact paths form angles η_1 and η_2 with the unit vector $\mathbf{e}_s$ (Fig. 9.3.2), where $\mathbf{e}_s$ and $\mathbf{e}_q$ are the unit vectors of principal directions on Σ_2. Usually, the direction of the tangent to the contact path on surface Σ_2 is chosen. Our goal is to derive equations that enable us to determine angle η_1 and components $v_s^{(1)}$ and $v_q^{(1)}$ – projections of $\mathbf{v}_r^{(1)}$ on $\mathbf{e}_s$ and $\mathbf{e}_q$ (Fig. 9.3.2) – in terms of η_2 and principal curvatures of Σ_2 at M.

It is obvious that

$$v_s^{(2)} = v_s^{(1)} + v_s^{(12)}, \qquad v_q^{(2)} = v_q^{(1)} + v_q^{(12)} \tag{9.3.2}$$

and

$$v_q^{(i)} = v_s^{(i)} \tan \eta_i \qquad (i = 1, 2). \tag{9.3.3}$$

The differentiated equation of meshing (it is represented as Eq. (8.2.7) with $i = 2$) and Eqs. (9.3.2) and (9.3.3) yield

$$\tan \eta_1 = \frac{-a_{31} v_q^{(12)} + (a_{33} + a_{31} v_s^{(12)}) \tan \eta_2}{a_{33} + a_{32} (v_q^{(12)} - v_s^{(12)} \tan \eta_2)} \tag{9.3.4}$$

$$v_s^{(1)} = \frac{a_{33}}{a_{13} + a_{23} \tan \eta_1} \tag{9.3.5}$$

$$v_q^{(1)} = \frac{a_{33} \tan \eta_1}{a_{13} + a_{23} \tan \eta_1}. \tag{9.3.6}$$

Coefficients a_{31}, a_{32}, and a_{33} have been represented by Eqs. (8.4.48). Prescribing a certain value for η_2 (choosing the direction for a path of contact on Σ_2), we can determine $\tan \eta_1$, $v_s^{(1)}$, and $v_q^{(1)}$. We recall that coefficients a_{31}, a_{32}, and a_{33} depend only on the principal curvatures and principal directions on Σ_2.

Relations Between the Magnitude of the Major Axis of the Contact Ellipse, Its Orientation, and Principal Curvatures and Directions of Contacting Surfaces

Our goal is to relate parameters $\sigma^{(12)}$, κ_f, and κ_h of the pinion surface Σ_1 with the length of the major axis of the instantaneous contact ellipse. This ellipse is considered to be at the mean contact point, and the elastic approach δ of contacting surfaces is considered known from the experimental data. The derivation of the above-mentioned relations is based on the following procedure:

Step 1: We use for transformations the relations $a_{11} = b_{33}$, $a_{12} = b_{34}$, and $a_{22} = b_{44}$ (see Eqs. (8.4.48) and Eqs. (8.4.27), (8.4.28), and (8.4.29) which determine b_{33}, b_{34}, and b_{44}). Then, we obtain

$$a_{11} + a_{22} = \kappa_{\Sigma}^{(2)} - \kappa_{\Sigma}^{(1)} \equiv \kappa_{\Sigma}$$

$$a_{11} - a_{22} = g_2 - g_1 \cos 2\sigma^{(12)} \tag{9.3.7}$$

$$(a_{11} - a_{22})^2 + 4a_{12}^2 = g_2^2 - 2g_1 g_2 \cos 2\sigma^{(12)} + g_1^2.$$

Here, $\kappa_{\Sigma}^{(1)} = \kappa_f + \kappa_h$; $\kappa_{\Sigma}^{(2)} = \kappa_s + \kappa_q$; $g_1 = \kappa_f - \kappa_h$; and $g_2 = \kappa_s - \kappa_q$.

Step 2: It is known from Eqs. (8.7.34) and (8.7.35) that

$$a = \sqrt{\left| \frac{\delta}{A} \right|} \tag{9.3.8}$$

$$A = \frac{1}{4} \left[\kappa_{\Sigma}^{(1)} - \kappa_{\Sigma}^{(2)} - \sqrt{g_1^2 - 2g_1 g_2 \cos 2\sigma^{(12)} + g_2^2} \right] \tag{9.3.9}$$

where a is the major axis of the contact ellipse. Equations (9.3.7) and (9.3.9) yield

$$[(a_{11} + a_{22}) + 4A]^2 = (a_{11} - a_{22})^2 + 4a_{12}^2. \tag{9.3.10}$$

Step 3: We may consider now a system of three linear equations in unknowns a_{11}, a_{12}, and a_{22}:

$$v_s^{(1)} a_{11} + v_q^{(1)} a_{12} = a_{13}$$

$$v_s^{(1)} a_{12} + v_q^{(1)} a_{22} = a_{23} \tag{9.3.11}$$

$$a_{11} + a_{22} = \kappa_{\Sigma}.$$

Step 4: The solution of equation system (9.3.11) for the unknowns a_{11}, a_{12}, and a_{22} allows these unknowns to be expressed in terms of $a_{13}, a_{23}, \kappa_{\Sigma}, v_s^{(1)}$, and $v_q^{(1)}$. Then, using Eq. (9.3.10), we can get the following equation for κ_{Σ}:

$$\kappa_{\Sigma} = \frac{4A^2 - (n_1^2 + n_2^2)}{2A - (n_1 \cos 2\eta_1 + n_2 \sin 2\eta_1)}. \tag{9.3.12}$$

Here,

$$n_1 = \frac{a_{13}^2 - a_{23}^2 \tan^2 \eta_1}{(1 + \tan^2 \eta_1)a_{33}}$$

$$n_2 = \frac{(a_{13} \tan \eta_1 + a_{23})(a_{13} + a_{23} \tan \eta_1)}{(1 + \tan^2 \eta_1)a_{33}} \tag{9.3.13}$$

$$|A| = \frac{\delta}{a^2}.$$

The advantage of Eq. (9.3.12) is that we are able to determine κ_Σ, taking as given the major axis $2a$ of the contact ellipse and the elastic approach δ.

Step 5: The sought-for principal curvatures and directions for the pinion identified as κ_f, κ_h, and $\sigma^{(12)}$, respectively, can be determined from the following equations:

$$\kappa_\Sigma^{(1)} = \kappa_\Sigma^{(2)} - \kappa_\Sigma \tag{9.3.14}$$

$$\tan 2\sigma^{(12)} = \frac{2a_{22}}{g_2 - (a_{11} - a_{22})} = \frac{2n_2 - \kappa_\Sigma \sin 2\eta_1}{g_2 - 2n_1 + \kappa_\Sigma \cos 2\eta_1} \tag{9.3.15}$$

$$g_1 = \frac{2a_{12}}{\sin 2\sigma^{(12)}} = \frac{2n_2 - \kappa_\Sigma \sin 2\eta_1}{\sin 2\sigma^{(12)}} \tag{9.3.16}$$

$$\kappa_f \equiv \kappa_I^{(1)} = \frac{\kappa_\Sigma^{(1)} + g_1}{2} \tag{9.3.17}$$

$$\kappa_h \equiv \kappa_{II}^{(1)} = \frac{\kappa_\Sigma^{(1)} - g_1}{2}. \tag{9.3.18}$$

Step 6: The orientation of unit vectors e_f and e_h for the pinion principal directions can be represented with the following equations:

$$e_I^{(1)} = e_f = \cos \sigma^{(12)} e_s - \sin \sigma^{(12)} e_q \tag{9.3.19}$$

$$e_{II}^{(1)} = e_h = \sin \sigma^{(12)} e_s + \cos \sigma^{(12)} e_q. \tag{9.3.20}$$

The orientation of the contact ellipse with respect to e_f is determined with angle $\alpha^{(1)}$ (Fig. 9.3.3) that is represented with the equations
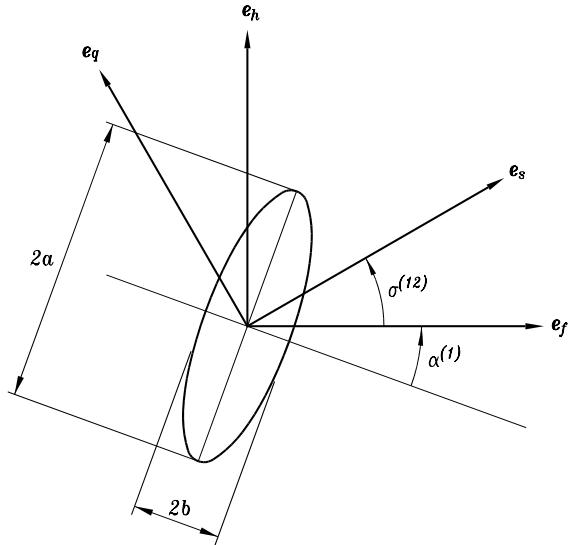
$$\cos 2\alpha^{(1)} = \frac{g_1 - g_2 \cos 2\sigma^{(12)}}{\left(g_1^2 - 2g_1g_2 \cos 2\sigma^{(12)} + g_2^2\right)^{1/2}} \tag{9.3.21}$$

$$\sin 2\alpha^{(1)} = \frac{g_2 \sin 2\sigma^{(12)}}{\left(g_1^2 - 2g_1g_2 \cos 2\sigma^{(12)} + g_2^2\right)^{1/2}}. \tag{9.3.22}$$

The minor axis $2b$ of the contact ellipse is determined with the equations

$$b = \sqrt{\left|\frac{\delta}{B}\right|} \tag{9.3.23}$$

$$B = \frac{1}{4}\left[\kappa_\Sigma^{(1)} - \kappa_\Sigma^{(2)} + \sqrt{g_1^2 - 2g_1g_2 \cos 2\sigma^{(12)} + g_2^2}\right]. \tag{9.3.24}$$

Figure 9.3.3: Orientation and dimensions of contact ellipse.

The following is an overview of the computational procedure that is to be used for the local synthesis. The input data are κ_s, κ_q, $\mathbf{e}_s$, $\mathbf{e}_q$, $\mathbf{r}^{(M)}$, $\omega^{(12)}$, $\mathbf{v}^{(12)}$, and δ. The to-be-chosen parameters are η_2, m'_{21}, and $2a$. The output data are κ_f, κ_h, $\sigma^{(12)}$, $\mathbf{e}_f$, and $\mathbf{e}_h$.

Step 1: Choose η_2 and determine η_1 from Eq. (9.3.4).

Step 2: Determine $v_s^{(1)}$ and $v_q^{(1)}$ from Eqs. (9.3.5) and (9.3.6).

Step 3: Determine A from the third equation of system (9.3.13).

Step 4: Determine κ_Σ from Eq. (9.3.12).

Step 5: Determine $\sigma^{(12)}$, κ_f, and κ_h by using Eqs. (9.3.14) to (9.3.18).

Step 6: Determine the orientation of the contact ellipse and its minor axis by using Eqs. (9.3.21) to (9.3.24).

To determine the pinion machine-tool settings, we have to consider the meshing of the pinion with the tool in line contact at every instant (see, for instance, Chapter 21).

9.4 TOOTH CONTACT ANALYSIS

The purpose of TCA computer programs is the simulation of meshing and contact of gear tooth surfaces with *localized* bearing contact, which provides the surface contact point at every instant. The main goals of TCA are to determine (i) the contact paths on gear tooth surfaces, (ii) the transmission errors caused by gear misalignment, and (iii) the bearing contact as the set of instantaneous contact ellipses. The gear tooth surfaces are considered to be known, and the location and orientation of gear axes are given, taking into account the misalignment.

Conditions of Continuous Tangency

We set up three coordinate systems S_1, S_2, and S_f, rigidly connected with gears 1 and 2 and the frame, respectively. An additional fixed coordinate system S_q is applied to

simulate the misalignment. The tooth surfaces Σ_1 and Σ_2 are represented in coordinate systems S_1 and S_2, respectively, as follows:

$$\mathbf{r}_i(u_i, \theta_i) \in C^2, \qquad \frac{\partial \mathbf{r}_i}{\partial u_i} \times \frac{\partial \mathbf{r}_i}{\partial \theta_i} \neq 0, \qquad (u_i, \theta_i) \in E_i \quad (i = 1, 2). \tag{9.4.1}$$

The surface unit normals are represented as follows:

$$\mathbf{n}_i = \frac{\dfrac{\partial \mathbf{r}_i}{\partial u_i} \times \dfrac{\partial \mathbf{r}_i}{\partial \theta_i}}{\left| \dfrac{\partial \mathbf{r}_i}{\partial u_i} \times \dfrac{\partial \mathbf{r}_i}{\partial \theta_i} \right|}. \tag{9.4.2}$$

Consider that gear 1 with the tooth surface Σ_1 rotates about a fixed axis located in S_f. Thus, a family of gear tooth surfaces is generated in the coordinate system S_f. The family of these surfaces may be determined by the matrix equation

$$\mathbf{r}_f^{(1)} = \mathbf{M}_{f1} \mathbf{r}_1. \tag{9.4.3}$$

The unit normal to surface Σ_1 is represented in S_f by the matrix equation

$$\mathbf{n}_f^{(1)} = \mathbf{L}_{f1} \mathbf{n}_1. \tag{9.4.4}$$

Gear 2 with surface Σ_2 rotates about another fixed axis located in S_q. We trace the errors of misalignment to gear 2, and the location and orientation of S_q with respect to S_f simulates the misalignment of the gear drive. Using matrix equations

$$\mathbf{r}_f^{(2)} = \mathbf{M}_{fq} \mathbf{M}_{q2} \mathbf{r}_2 \tag{9.4.5}$$

and

$$\mathbf{n}_f^{(2)} = \mathbf{L}_{fq} \mathbf{L}_{q2} \mathbf{n}_2, \tag{9.4.6}$$

we represent surface Σ_2 of the misaligned gear drive and the surface unit normal in coordinate system S_f. Matrices $\mathbf{L}$ are of the 3×3 order and they can be determined from respective matrices $\mathbf{M}$ by the elimination of the last row and column in $\mathbf{M}$.

The contacting surfaces must be in continuous tangency and this can be achieved if their position vectors and normals coincide at any instant (Fig. 9.4.1). Thus,

$$\mathbf{r}_f^{(1)}(u_1, \theta_1, \phi_1) = \mathbf{r}_f^{(2)}(u_2, \theta_2, \phi_2) \tag{9.4.7}$$

$$\mathbf{n}_f^{(1)}(u_1, \theta_1, \phi_1) = \mathbf{n}_f^{(2)}(u_2, \theta_2, \phi_2) \tag{9.4.8}$$
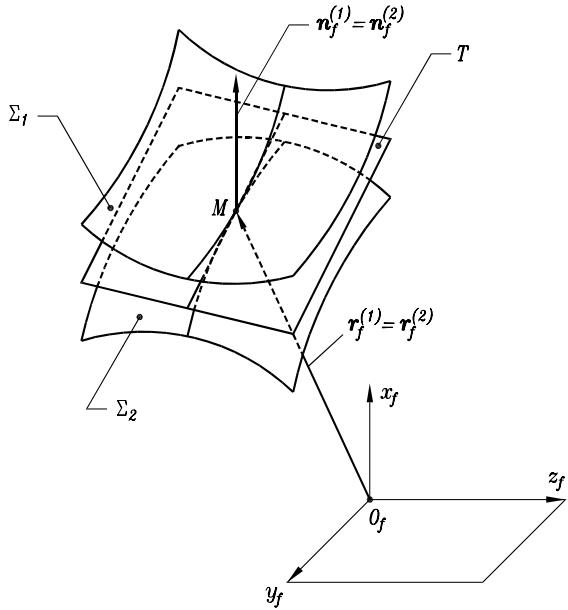
where ϕ_1 and ϕ_2 are the angles of gear rotation. Vector equation (9.4.7) yields three scalar equations, but Eq. (9.4.8) yields only two independent scalar equations because

$$\left| \mathbf{n}_f^{(1)} \right| = \left| \mathbf{n}_f^{(2)} \right| = 1. \tag{9.4.9}$$

We may require the collinearity of surface normals using the equation

$$\mathbf{N}^{(1)}(u_1, \theta_1, \phi_1) = \lambda \mathbf{N}^{(2)}(u_2, \theta_2, \phi_2) \tag{9.4.10}$$

instead of Eq. (9.4.8). However, Eq. (9.4.8) is preferable because it can be applied as a basis for important kinematic relations.

Figure 9.4.1: Tangency of surfaces in ideal gear train.

Analysis of Meshing

Equations (9.4.7) and (9.4.8) may be represented as

$$\mathbf{r}_f^{(1)}(u_1, \theta_1, \phi_1) - \mathbf{r}_f^{(2)}(u_2, \theta_2, \phi_2) = 0 \qquad (9.4.11)$$

$$\mathbf{n}_f^{(1)}(u_1, \theta_1, \phi_1) - \mathbf{n}_f^{(2)}(u_2, \theta_2, \phi_2) = 0. \qquad (9.4.12)$$

Vector equations (9.4.11) and (9.4.12) yield five independent scalar equations in six unknowns, u_1, θ_1, ϕ_1, u_2, θ_2, and ϕ_2. Here,

$$f_i(u_1, \theta_1, \phi_1, u_2, \theta_2, \phi_2) = 0, \quad f_i \in C^1 \quad (i = 1, 2, 3, 4, 5). \qquad (9.4.13)$$

The aim of gearing analysis is to obtain from Eqs. (9.4.13) the functions

$$\{u_1(\phi_1), \theta_1(\phi_1), u_2(\phi_1), \theta_2(\phi_1), \phi_2(\phi_1)\} \in C^1. \qquad (9.4.14)$$

According to the theorem of implicit function system existence (see Korn & Korn [1968] and Litvin [1989]), we may state that functions (9.4.14) exist in the neighborhood of a point

$$P^0 = \left(u_1^o, \theta_1^o, \phi_1^o, u_2^o, \theta_2^o, \phi_2^o\right) \qquad (9.4.15)$$

if the following are true: (i) functions $[f_1, f_2, f_3, f_4, f_5] \in C^1$; (ii) Eqs. (9.4.13) are

satisfied at point P^0; and (iii) the following Jacobian differs from zero, that is, if

$$\frac{D(f_1,\,f_2,\,f_3,\,f_4,\,f_5)}{D(u_1,\,\theta_1,\,u_2,\,\theta_2,\,\phi_2)} = \begin{vmatrix} \dfrac{\partial f_1}{\partial u_1} & \dfrac{\partial f_1}{\partial \theta_1} & \dfrac{\partial f_1}{\partial u_2} & \dfrac{\partial f_1}{\partial \theta_2} & \dfrac{\partial f_1}{\partial \phi_2} \\ \vdots & \vdots & \vdots & \vdots & \vdots \\ \dfrac{\partial f_5}{\partial u_1} & \dfrac{\partial f_5}{\partial \theta_1} & \dfrac{\partial f_5}{\partial u_2} & \dfrac{\partial f_5}{\partial \theta_2} & \dfrac{\partial f_5}{\partial \phi_2} \end{vmatrix} \neq 0. \qquad (9.4.16)$$

Functions (9.4.14) provide complete information about the conditions of meshing of gear tooth surfaces that are in point contact. Function $\phi_2(\phi_1)$ represents the relation between the angles of gear rotation (the law of motion). Functions

$$\mathbf{r}_1(u_1,\theta_1), \qquad u_1(\phi_1), \qquad \theta_1(\phi_1) \qquad\qquad (9.4.17)$$

determine the *path of contact points* on surface Σ_1. Similarly, functions

$$\mathbf{r}_2(u_2,\theta_2), \qquad u_2(\phi_2), \qquad \theta_2(\phi_2) \qquad\qquad (9.4.18)$$

determine the path of contact points on surface Σ_2. The path of contact points on surface Σ_i $(i = 1, 2)$ is the *working line* on the gear tooth surface. The gear tooth surface contacts the mating surface at points of the working line only. The line of action of gear tooth surfaces is represented by functions

$$\mathbf{r}_f^{(1)}(u_1,\theta_1,\phi_1), \qquad u_1(\phi_1), \qquad \theta_1(\phi_1) \qquad\qquad (9.4.19)$$

or by functions

$$\mathbf{r}_f^{(2)}(u_2,\theta_2,\phi_2), \qquad u_2(\phi_1), \qquad \phi_2(\phi_1), \qquad \theta_2(\phi_1). \qquad (9.4.20)$$

In some cases, a variable parameter other than ϕ_1, for instance u_1, may be chosen when solving Eqs. (9.4.13). We may solve these equations in the neighborhood of point P^0 that is determined by Eq. (9.4.15), if the respective Jacobian differs from zero, that is, if

$$\frac{D(f_1,\,f_2,\,f_3,\,f_4,\,f_5)}{D(\theta_1,\,\phi_1,\,u_2,\,\theta_2,\,\phi_2)} \neq 0.$$
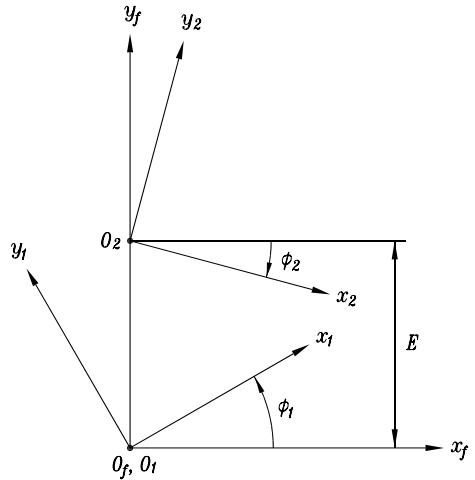
The solution of Eqs. (9.4.13) will be obtained by functions

$$\{\phi_1(u_1), \theta_1(u_1), u_2(u_1), \theta_2(u_1), \phi_2(u_1)\} \in C^1. \qquad (9.4.21)$$

In some cases, the gear tooth surface cannot be represented directly in two-parameter form but can be represented in three-parameter form with an additional relation between the parameters that is provided by the equation of meshing. For instance, the worm-gear surface for certain types of worm-gear drives is represented as

$$\mathbf{r}_2(u_2,\theta_2,\psi), \qquad f(u_2,\theta_2,\psi) = 0 \qquad\qquad (9.4.22)$$

where ψ is the parameter of motion in the process for generation. Then, the to-be-solved system of nonlinear equations will contain six independent equations in seven unknowns.
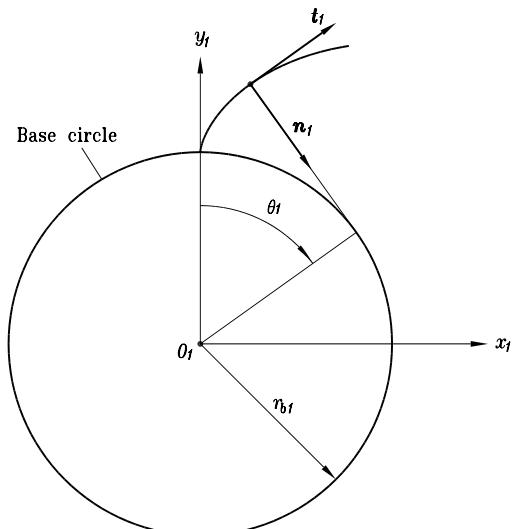
Figure 9.4.2: Applied coordinate systems.

    The numerical solution of the system of nonlinear equations is based on application of a respective subroutine; see, for instance, More *et al.* [1980] and Visual Numerics, Inc. [1998]. The first guess for the solution can be obtained from the data provided by the local synthesis. We illustrate the discussed method of TCA with the following simple problem of a planar gearing.
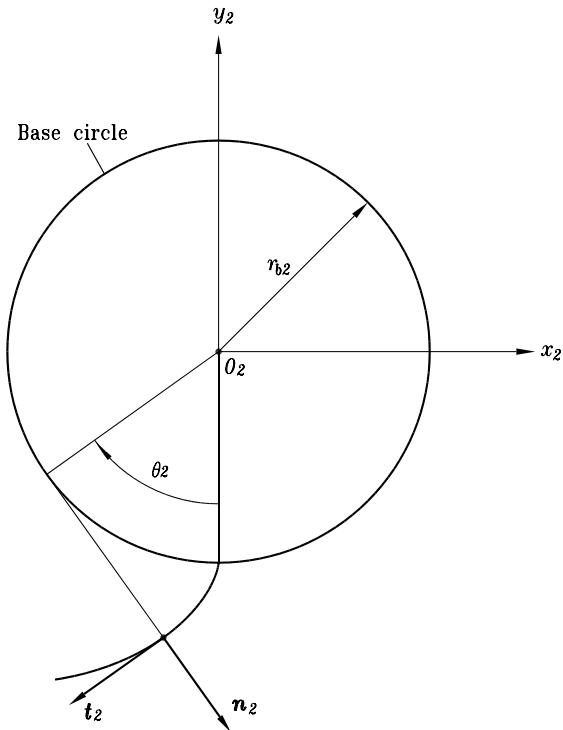
Problem 9.4.1

Consider three coordinate systems S_1, S_2, and S_f that are rigidly connected to driving gear 1, driven gear 2, and the frame f, respectively (Fig. 9.4.2). Gear 1 is provided with involute profile Σ_1 that is represented in S_1 by the following equations (Fig. 9.4.3):

$$x_1 = r_{b1}(\sin\theta_1 - \theta_1 \cos\theta_1), \quad y_1 = r_{b1}(\cos\theta_1 + \theta_1 \sin\theta_1), \quad z_1 = 0. \quad (9.4.23)$$

Figure 9.4.3: Profile Σ_1 of gear 1.

Figure 9.4.4: Profile Σ_2 of gear 2.

Gear 2 is provided with involute profile Σ_2 that is represented in S_2 by the equations (Fig. 9.4.4)

$$x_2 = r_{b2}(-\sin\theta_2 + \theta_2 \cos\theta_2), \quad y_2 = r_{b2}(-\cos\theta_2 - \theta_2 \sin\theta_2), \quad z_2 = 0. \quad (9.4.24)$$

Solution
The application of the basic principle of tooth contact analysis enables us to determine the conditions of meshing of Σ_1 and Σ_2 in coordinate system S_f using the following procedure:

(1) We determine the unit normals $\mathbf{n}_1$ and $\mathbf{n}_2$ to Σ_1 and Σ_2 in coordinate systems S_1 and S_2, respectively. The unit normals to Σ_1 and Σ_2 must be of the same orientation at the point of tangency of the profiles.
(2) Then, we represent profiles Σ_1 and Σ_2 in coordinate system S_f and derive the equations of their tangency.
(3) Using the equations of tangency we can obtain three equations of the following structure:

$$f_1[(\theta_1 - \phi_1), (\theta_2 + \phi_2)] = 0 \quad (9.4.25)$$

$$f_2[(\theta_1 - \phi_1), r_{b1}, r_{b2}, E] = 0 \quad (9.4.26)$$

$$f_3[\theta_1, \theta_2, r_{b1}, r_{b2}, E, (\theta_1 - \phi_1)] = 0. \quad (9.4.27)$$

(4) The analysis of the obtained equations shows that the ratio $d\phi_1/d\phi_2$ is constant and is represented as

$$\frac{d\phi_1}{d\phi_2} = -\frac{d\theta_1}{d\theta_2} = \frac{r_{b2}}{r_{b1}}.$$

(5) We can determine the line of action by the vector function $\mathbf{r}_f^{(1)}(\theta_1 - \phi_1)$ and prove that the line of action is a straight line. The orientation of the line of action can be determined by the scalar product $\mathbf{a}_f \cdot (-\mathbf{i}_f)$ where

$$\mathbf{a}_f = \frac{\dfrac{\partial \mathbf{r}_f^{(1)}}{\partial \theta_1}}{\left| \dfrac{\partial \mathbf{r}_f^{(1)}}{\partial \theta_1} \right|}$$

is the unit vector of the line of action.

The procedure of derivations is as follows:

Step 1: Equations (9.4.23) yield the following expressions for the unit normal to Σ_1:

$$\mathbf{n}_1 = \mathbf{t}_1 \times \mathbf{k}_1 = \cos\theta_1 \mathbf{i}_1 - \sin\theta_1 \mathbf{j}_1 \quad \text{(provided } \theta_1 \neq 0\text{).} \tag{9.4.28}$$

Here, $\mathbf{t}_1$ is the unit tangent to Σ_1; $\mathbf{k}_1$ is the unit vector of the z_1 axis.

Step 2: Similarly, using Eqs. (9.4.24) we obtain that

$$\mathbf{n}_2 = \mathbf{k}_2 \times \mathbf{t}_2 = \cos\theta_2 \mathbf{i}_2 - \sin\theta_2 \mathbf{j}_2. \tag{9.4.29}$$

Here, $\mathbf{t}_2$ is the unit tangent to Σ_2; $\mathbf{k}_2$ is the unit vector of the z_2 axis. The order of cofactors in Eq. (9.4.29) provides the orientation of $\mathbf{n}_2$ as shown in Fig. 9.4.4.

Step 3: Using matrix equations

$$\mathbf{r}_f^{(i)} = \mathbf{M}_{fi}\, \mathbf{r}_i(\theta_i), \qquad \mathbf{n}_f^{(i)} = \mathbf{L}_{fi}\, \mathbf{n}_i(\theta_i) \quad (i = 1, 2), \tag{9.4.30}$$

we derive the following equations of tangency:

$$\mathbf{r}_f^{(1)}(\theta_1, \phi_1) = \mathbf{r}_f^{(2)}(\theta_2, \phi_2), \qquad \mathbf{n}_f^{(1)}(\theta_1, \phi_1) = \mathbf{n}_f^{(2)}(\theta_2, \phi_2). \tag{9.4.31}$$

Step 4: Vector Eqs. (9.4.31) yield the following system of scalar equations:

$$r_{b1}\left[\sin(\theta_1 - \phi_1) - \theta_1 \cos(\theta_1 - \phi_1)\right]$$
$$-r_{b2}\left[-\sin(\theta_2 + \phi_2) + \theta_2 \cos(\theta_2 + \phi_2)\right] = 0 \tag{9.4.32}$$

$$r_{b1}\left[\cos(\theta_1 - \phi_1) + \theta_1 \sin(\theta_1 - \phi_1)\right]$$
$$-r_{b2}\left[-\cos(\theta_2 + \phi_2) - \theta_2 \sin(\theta_2 + \phi_2)\right] - E = 0 \tag{9.4.33}$$

$$\cos(\theta_1 - \phi_1) - \cos(\theta_2 + \phi_2) = 0 \tag{9.4.34}$$

$$\sin(\theta_1 - \phi_1) - \sin(\theta_2 + \phi_2) = 0. \tag{9.4.35}$$

Step 5: Analyzing Eqs. (9.4.34) and (9.4.35), we obtain

$$\theta_1 - \phi_1 = \theta_2 + \phi_2. \tag{9.4.36}$$

Equations (9.4.32) and (9.4.33), considered simultaneously, yield the following relations:

$$\cos(\theta_1 - \phi_1) - \frac{r_{b1} + r_{b2}}{E} = 0 \tag{9.4.37}$$

$$r_{b1}\theta_1 + r_{b2}\theta_2 - E\sin(\theta_1 - \phi_1) = 0. \tag{9.4.38}$$

The system of Eqs. (9.4.36) to (9.4.38) has the structure of the system of Eqs. (9.4.25) to (9.4.27) discussed above. Equations (9.4.36) to (9.4.38) yield

$$\theta_1 - \phi_1 = \theta_2 + \phi_2 = \text{const.} \tag{9.4.39}$$

$$r_{b1}\theta_1 + r_{b2}\theta_2 = \text{const.} \tag{9.4.40}$$

Step 6: Differentiating Eqs. (9.4.39) and (9.4.40), we obtain that the gear ratio is constant and can be represented as follows:

$$m_{12} = \frac{d\phi_1}{d\phi_2} = -\frac{d\theta_1}{d\theta_2} = \frac{r_{b2}}{r_{b1}}. \tag{9.4.41}$$

Step 7: The line of action is represented by the equation

$$\mathbf{r}_f^{(1)} = r_{b1}\left[\sin(\theta_1 - \phi_1) - \theta_1\cos(\theta_1 - \phi_1)\right]\mathbf{i}_f$$
$$+ r_{b1}\left[\cos(\theta_1 - \phi_1) + \theta_1\sin(\theta_1 - \phi_1)\right]\mathbf{j}_f \tag{9.4.42}$$

where $(\theta_1 - \phi_1)$ is constant [see Eq. (9.4.39)]. Vector function $\mathbf{r}_f^{(1)}(\theta_1)$ is a linear one because $(\theta_1 - \phi_1) = \text{constant}$, and the line of action is a straight line.

The unit vector of the line of action is represented as

$$\mathbf{a}_f = \frac{\dfrac{\partial \mathbf{r}_f^{(1)}}{\partial \theta_1}}{\left|\dfrac{\partial \mathbf{r}_f^{(1)}}{\partial \theta_1}\right|} = -\cos(\theta_1 - \phi_1)\mathbf{i}_f + \sin(\theta_1 - \phi_1)\mathbf{j}_f. \tag{9.4.43}$$

The orientation of the line of action is determined with the scalar product

$$\mathbf{a}_f \cdot (-\mathbf{i}_f) = \cos(\theta_1 - \phi_1) = \frac{r_{b1} + r_{b2}}{E}. \tag{9.4.44}$$
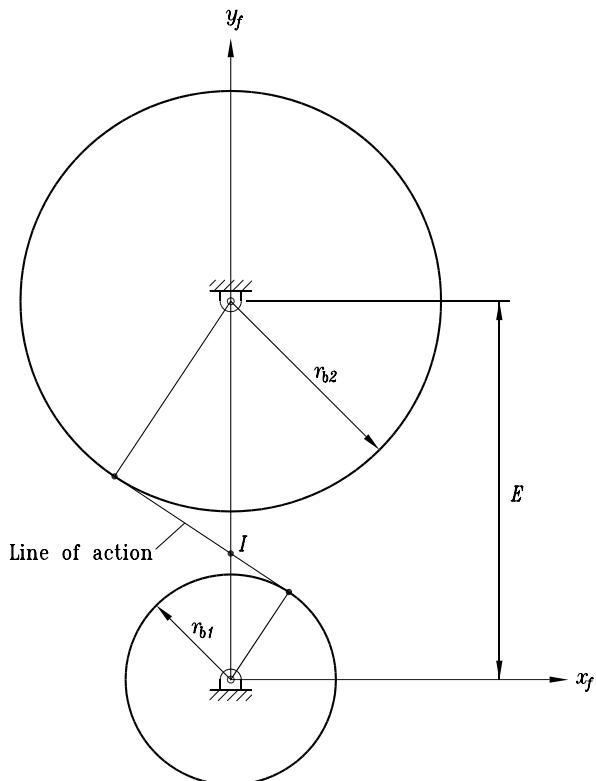
The line of action passes through point I that lies on the y_f axis. Equation (9.4.42) yields that when $x_f^{(I)} = 0$, we have

$$y_f^{(I)} = \frac{r_{b1}}{\cos(\theta_1 - \phi_1)}. \tag{9.4.45}$$

Using Eqs. (9.4.44) and (9.4.45), we obtain

$$y_f^{(I)} = \left(\frac{r_{b1}}{r_{b1} + r_{b2}}\right)E = \frac{E}{1 + m_{12}}. \tag{9.4.46}$$

The line of action is shown in Fig. 9.4.5. It is easy to verify that the line of action is tangent to the gear base circles. We emphasize that the location and orientation of the line of action depends on the chosen center distance E (considering the radii r_{b1} and r_{b2} of base circles as given).

Figure 9.4.5: Location and orientation of line of action.

9.5 APPLICATION OF FINITE ELEMENT ANALYSIS FOR DESIGN OF GEAR DRIVES

Application of finite element analysis allows us to perform (i) stress analysis, (ii) investigation of formation of bearing contact, and (iii) detection of severe areas of contact stresses inside the cycle of meshing.

Such an approach requires (i) development of the finite element mesh of the gear drive, (ii) definition of contacting surfaces, and (iii) establishment of boundary conditions for loading the gear drive.

This section covers the authors' approach to finite element analysis for gear design. The approach is based on application of the general purpose computer program presented by Hibbit, Karlsson & Sirensen, Inc. [1998].

The main features of the developed approach are as follows:

(a) The finite element mesh is generated automatically by using the equations of the tooth surfaces and the rim. Nodes of finite element mesh are obtained as points of gear tooth surfaces. Therefore, the loss of accuracy associated with development of solid models using CAD (computer aided design) computer programs is avoided. The boundary conditions for stress analysis of the pinion and the gear are set up automatically as well.

(b) Modules for automatic generation of finite element models are integrated into the developed computer programs. Therefore, the generation of finite element models can be accomplished easily and fast for any position of contact of the cycle of meshing. In addition, the formation of the bearing contact can be investigated and the appearance of edge contact and areas of severe contact can be detected.

Application of CAD computer programs for the development of finite element models is an intermediate stage of the existing approach for application of finite element analysis and has the following disadvantages:

(1) Determination of wire models formed by splines is obtained *numerically*. The wire models consist of planar sections of gear teeth and such sections are used for the development of solid models.
(2) Finite element meshes of solid models require application of computer programs for finite element analysis.
(3) Setting of boundary conditions for the finite element meshes have to be determined.
(4) The increase of planar sections of gear teeth improves the precision of wire models and solid models but is costly in terms of time.
(5) The developments described above have to be performed by skilled users of CAD computer programs, are costly in terms of time, and have to be accomplished for each assigned case of design of various gear geometries, for each position of meshing, and for various cases of investigation.

The modified approach presented in this section is free of the disadvantages mentioned above and may be summarized as follows:

Step 1: Using the equations of both sides of the pinion or gear tooth surfaces and the portions of the corresponding rim, we may represent *analytically* the volume of the designed body. Figure 9.5.1(a) shows the designed body for a one-tooth model of the pinion of a modified involute helical gear drive.
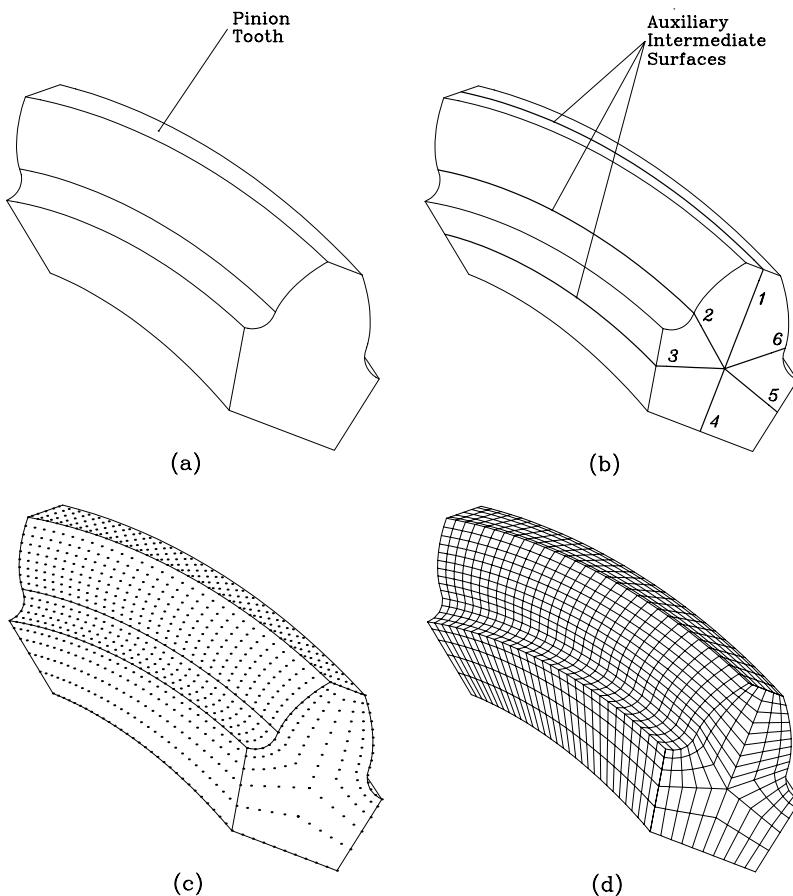
Step 2: Auxiliary intermediate surfaces 1 to 6 shown in Fig. 9.5.1(b) are determined *analytically* as well. Surfaces 1 to 6 enable us to divide the tooth into six parts and control the discretization of these tooth subvolumes into finite elements.

Step 3: Analytical determination of node coordinates is performed taking into account the number of desired elements in the longitudinal and profile directions [Fig. 9.5.1(c)]. We emphasize that all nodes of the finite element mesh are determined analytically and those lying on the intermediate surfaces of the tooth are indeed points belonging to the real surface.

Step 4: Discretization of the model by finite elements using nodes determined in previous step is accomplished as shown in Fig. 9.5.1(d).

Step 5: The setting of boundary conditions for gear and pinion is performed automatically as follows:
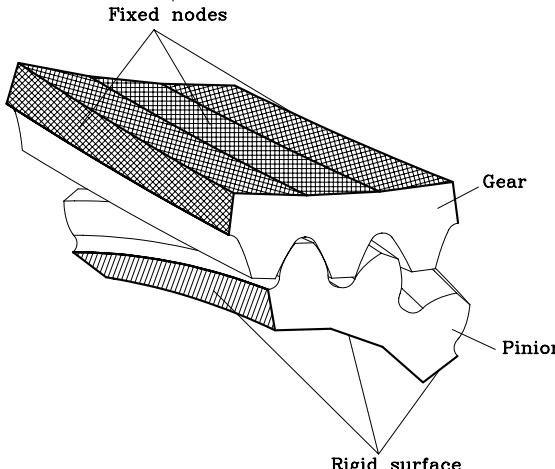
(i) Nodes on the sides and bottom part of the rim portion of the gear are considered fixed [Fig. 9.5.2(a)].
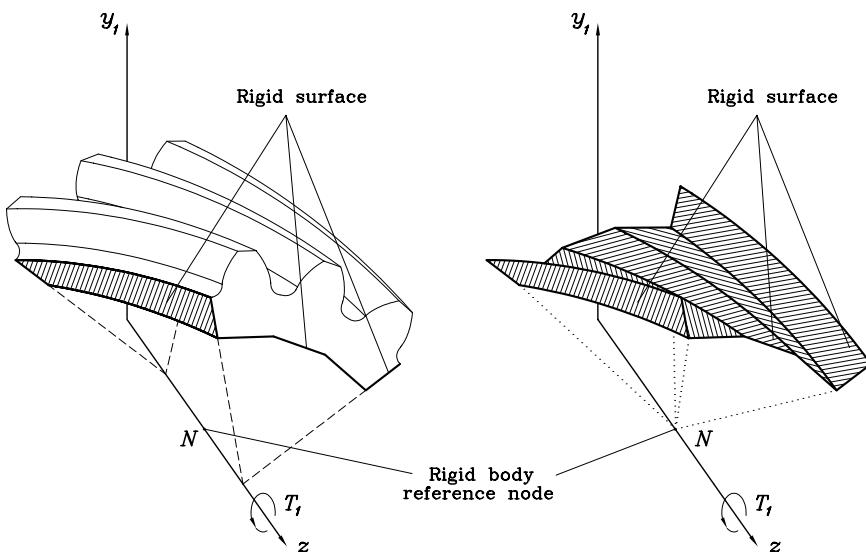
Figure 9.5.1: Illustration of (a) the volume of the designed body, (b) auxiliary intermediate surfaces, (c) determination of nodes for the whole volume, and (d) discretization of the volume by finite elements.

(ii) Nodes on the two sides and bottom part of the rim portion of the pinion build a rigid surface [Fig. 9.5.2(b)]. Rigid surfaces are three-dimensional geometric structures that cannot be deformed but can perform translation or rotation as rigid bodies (Hibbit, Karlsson & Sirensen, Inc. [1998]). They are also very cost effective because the variables associated with a rigid surface are the translations and rotations of a single node, known as the rigid body reference node [Fig. 9.5.2(b)]. The rigid body reference node is located on the pinion axis of rotation with all degrees of freedom except the rotation around the axis of rotation of the pinion fixed to zero. The torque is applied directly to the remaining degree of freedom of the rigid body reference node [Fig. 9.5.2(b)].

Step 6: Definition of contacting surfaces for the contact algorithm of the finite element computer program (Hibbit, Karlsson & Sirensen, Inc. [1998]) is performed automatically as well and requires definition of the master and slave surfaces. Generally, the master surface is chosen as the surface of the stiffer body or as the surface with the coarser mesh if the two surfaces are on structures with comparable stiffness.

(a)
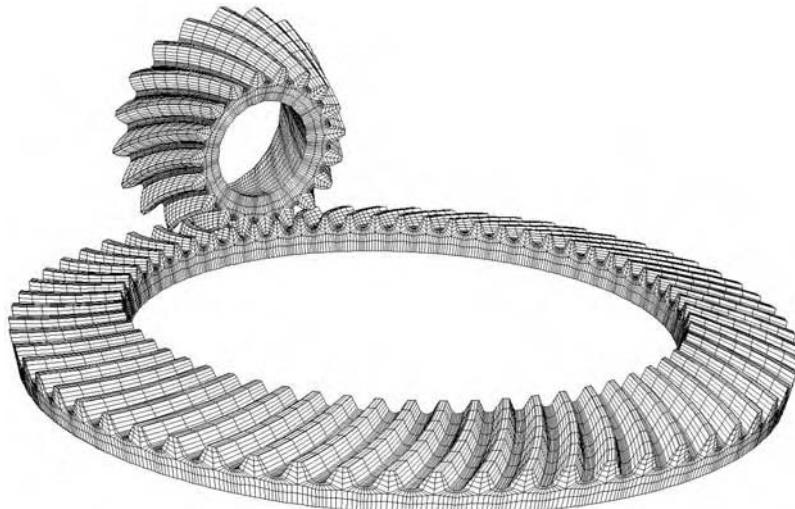
(b)

Figure 9.5.2: (a) Boundary conditions for the gear; (b) schematic representation of boundary conditions and application of torque for the pinion.

Figures 9.5.3 to 9.5.5 show examples of finite element models of a spiral bevel gear drive, a helical gear drive, and a face-worm gear drive with a conical worm, respectively.
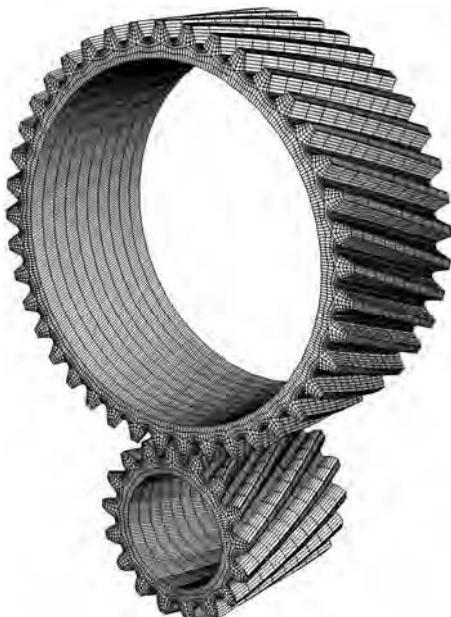
9.6 EDGE CONTACT

Most prospective gear design has to be based on localization of the bearing contact on gear tooth surfaces. Gear tooth surfaces with localized bearing contact are in point
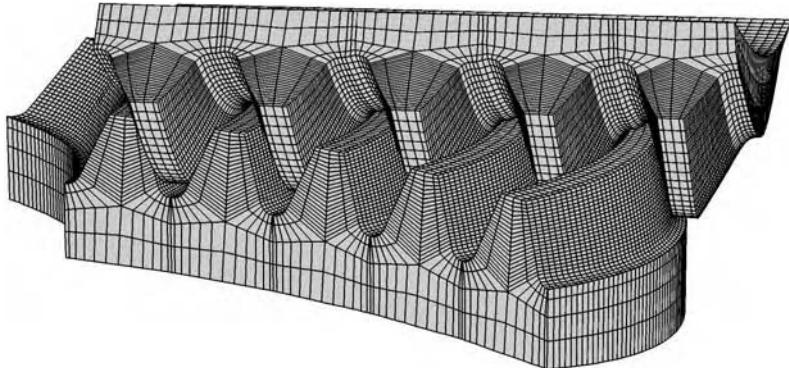
Figure 9.5.3: Finite element model of a whole spiral bevel gear drive.

contact at every instant but are not in line contact. However, there are at present some gear drives with tooth surfaces that are still in line contact. In fact, due to errors of alignment, the theoretical instantaneous contact at a line is turned over into a point contact, but it may be accompanied by an *edge contact* (see below). The simulation of meshing of tooth surfaces being in instantaneous point contact may be performed by TCA computer programs (see Section 9.4) based on continuous tangency of tooth surfaces that have a common normal at the instantaneous point contact.

Figure 9.5.4: Finite element model of a whole helical gear drive.

Figure 9.5.5: Finite element model of a face-worm gear drive with a conical worm.

Edge contact means that instead of tangency of surfaces, an edge of the tooth surface of one gear is in mesh with the tooth surface of the mating gear. Edge contact may be represented by the following equations:

$$\mathbf{r}_f^{(1)}(u_1(\theta_1), \theta_1, \phi_1) = \mathbf{r}_f^{(2)}(u_2, \theta_2, \phi_2) \tag{9.6.1}$$

$$\frac{\partial \mathbf{r}_f^{(1)}}{\partial \theta_1} \cdot \mathbf{N}_f^{(2)} = 0. \tag{9.6.2}$$
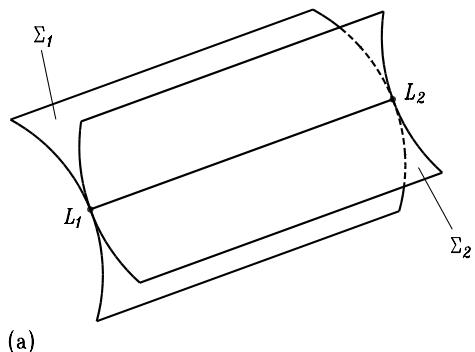
Here, $\mathbf{r}_f^{(1)}(u_1(\theta_1), \theta_1, \phi_1)$ represents the edge of the pinion tooth surface; $\partial \mathbf{r}_f^{(1)}/\partial \theta_1$ is the tangent to the edge. Equation system (9.6.1) and (9.6.2) represents a system of four nonlinear equations in four unknowns: $\theta_1, u_2, \theta_2, \phi_2$; ϕ_1 is the input parameter. Similar equations can be derived for the case of tangency of the edge of the gear tooth surface with the pinion tooth surface.

Edge contact may occur in two cases: (i) when the gear tooth surfaces are initially in line contact, and (ii) when the gear tooth surfaces are in point contact. Each case is discussed separately.

Edge Contact of Gear Tooth Surfaces That Are Initially in Line Contact
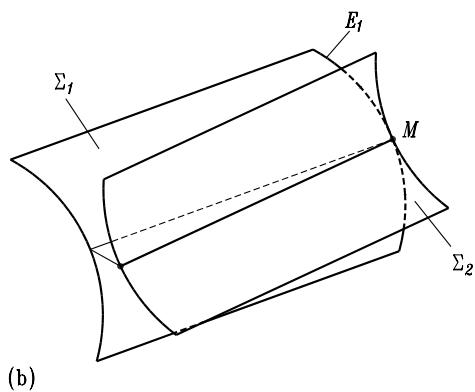
We start the discussion with the case of spur gears. Figure 9.6.1(a) shows that the gear tooth surfaces Σ_1 and Σ_2 of an ideal gear train are in tangency along the line L_1–L_2. Consider now that the gears are misaligned and the gear axes are crossed or intersected. Then, edge E_1 of the pinion tooth surface will be in tangency with the gear tooth surface Σ_2 at point M. The paths of contact on the gear tooth surfaces are shown in Fig. 9.6.2(a). The transformation of motion is accompanied by the function of transmission errors shown in Fig. 9.6.2(b). The transfer of meshing at the end of the cycle of meshing is accompanied by the jump in the angular velocity, and vibration and noise are inevitable. Similarly, the edge contact of helical gears with parallel axes caused by angular misalignment, such as the crossing angle of gear axes and the difference of gear helix angles, may be discussed.

Edge contact of misaligned gears whose tooth surfaces are initially in line contact can be avoided by application of a modified topology of tooth surfaces. Such a topology
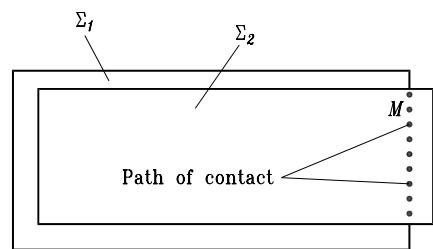
(a)

Figure 9.6.1: Edge contact of tooth surfaces of spur gears.
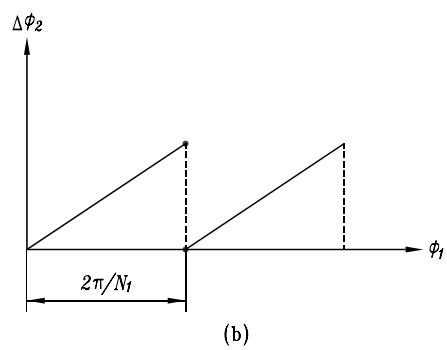
(b)
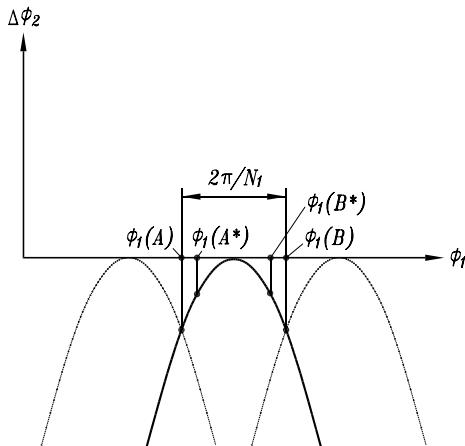
(a)

Figure 9.6.2: Path of contact and transmission errors for a gear drive with edge contact: (a) illustration of path of contact at the edge; (b) illustration of transmission errors in the case of edge contact.

(b)
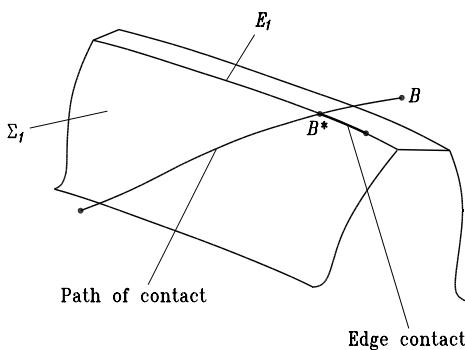
Figure 9.6.3: Function of transmission errors.

must provide the following: (i) a point contact of tooth surfaces but with the sufficient dimension of the major axis of the contact ellipse, (ii) a favorable direction of the path of contact on the gear tooth surface, and (iii) a predesigned parabolic type of function of transmission errors to absorb a discontinuous almost-linear function of transmission errors caused by misalignments (see Section 9.2).
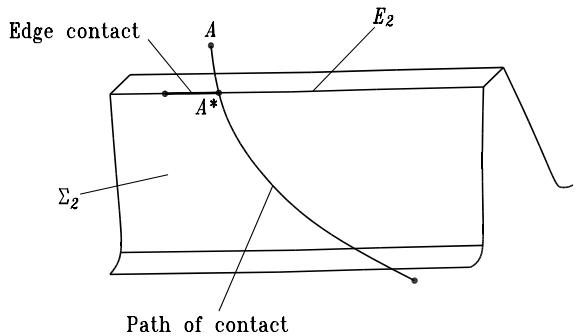
Edge Contact of Gear Tooth Surfaces That Are Initially in Point Contact

Instantaneous point contact of gear tooth surfaces is typical, for instance, for hypoid gear drives and spiral bevel gears. The possibility of edge contact for hypoid gears has been mentioned in the Gleason commercially available TCA programs for hypoid gear drives.

The edge contact in hypoid gear drives can be discovered if the function of transmission errors and the shape of contact paths on the gear tooth surfaces are considered simultaneously. We illustrate this statement in Figs. 9.6.3, 9.6.4, and 9.6.5, which show the function of transmission errors, and the paths of contact on the pinion and gear tooth surfaces, respectively. Points $\phi_1(A)$ and $\phi_1(B)$ on the ϕ_1 axis in Fig. 9.6.3 indicate the values of ϕ_1 for the beginning and the end of the cycle of meshing for one pair of teeth. These points also correspond to the points of intersection of the functions of transmission errors for three neighboring pairs of teeth. Figures 9.6.4 and 9.6.5 show the paths of contact on the pinion and gear tooth surfaces, respectively. The sufficient

Figure 9.6.4: Path of contact on pinion tooth surface.

Figure 9.6.5: Path of contact on gear tooth surface.
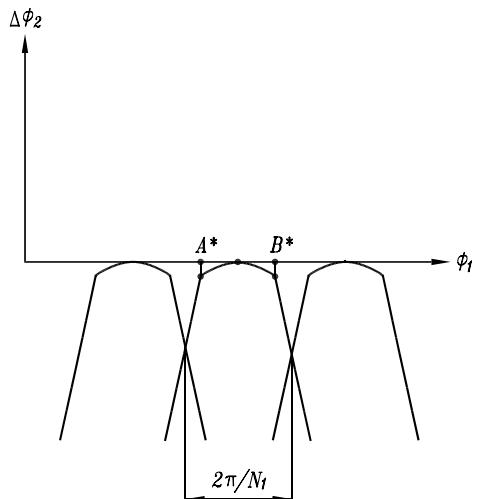
condition for avoidance of tangency of pinion edge E_1 with the gear tooth surface Σ_2 is that point B (Fig. 9.6.4) is *inside* of the dimensions of the pinion tooth. Similarly, the sufficient condition for avoidance of tangency of E_2 with Σ_1 can be formulated: point A must be *inside* of the dimensions of the gear tooth (Fig. 9.6.5). Figures 9.6.4 and 9.6.5 show that the conditions above are not satisfied and the edge contact of E_1 and E_2 will occur.

Figure 9.6.3 shows that the surface-to-surface contact will be only in the area

$$\phi_1(A^*) \leq \phi_1 \leq \phi_1(B^*). \tag{9.6.3}$$

Here, B^* and A^* are the points of intersection of the path of contact with the addendum edge of the pinion and the gear, respectively (Figs. 9.6.4 and 9.6.5); $\phi_1(A^*)$ and $\phi_1(B^*)$ designate the angles of rotation of the pinion with which the gear tooth surfaces will be in tangency at A^* and B^*, respectively. Edge contact at E_2 (Fig. 9.6.5) will occur when $\phi_1 < \phi_1(A^*)$. Respectively, edge contact at E_1 (Fig. 9.6.4) will occur when $\phi_1 > \phi_1(B^*)$.

Due to the edge contact, the resulting function of transmission errors is a combination of three functions that correspond to edge contacts at E_1 and E_2 and surface-to-surface tangency (Fig. 9.6.6).

Figure 9.6.6: Resulting function of transmission errors.

We have discussed the case when during the cycle of meshing the edge contact occurs twice. Similarly, we can consider the case when the edge contact occurs only once and the resulting transmission errors are determined by a combination of two functions.

The edge contact can be avoided by proper choice of machine-tool settings which can be accomplished by application of the local synthesis method and the TCA approach. The local synthesis method will enable us to obtain the most favorable direction of the tangent to the path of contact. The application of TCA is the final test of whether the objective, the avoidance of edge contact, is indeed achieved.

10 Spur Involute Gears
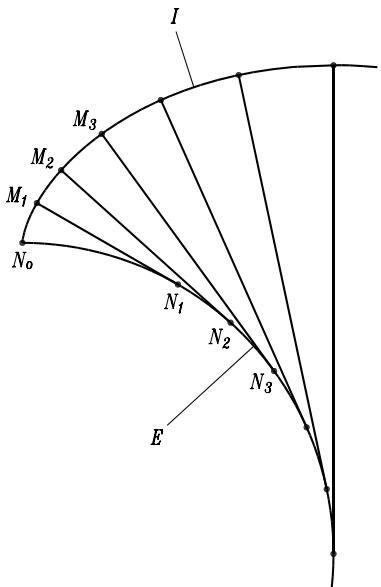
10.1 INTRODUCTION

The involute gearing, first proposed by Euler, has found widespread application in the industry due to its many advantages: (i) the tools for generation of involute gears can be produced with high precision, (ii) it is easy to vary the tooth thickness and provide a nonstandard center distance just by changing tool settings for gear generation, (iii) nonstandard involute gears can be generated by using standardized tools applied for standard gears, and (iv) the change of gear center distance does not cause transmission errors.

The invention of Novikov–Wildhaber gearing is very attractive in its theoretical aspect and has found application in some areas. However, this gearing is limited to application to helical gears and has not replaced the involute gearing. A new version of Novikov–Wildhaber gears based on the latest developments is presented in Chapter 17 of this book.

Spur involute gears are in line contact at every instant, and therefore they are sensitive to the misalignment of gear axes. For this reason, it is necessary to localize their bearing contact, and this can be achieved by crowning the surface of one of the mating gears. It is preferable to crown the pinion tooth surface rather than the gear tooth surface because the number of pinion teeth is smaller than the number of gear teeth. The tooth profile of the spur gears is generated as an involute curve. The meshing of a crowned pinion tooth surface and a conventional involute gear tooth surface should be the subject of a study directed at minimization of transmission errors and favorable location of the bearing contact. Modified spur involute gears with a localized bearing contact and a reduced level of transmission errors have been presented in the work of Litvin *et al.* [2000b].

For better understanding of the following chapters, a brief review of the basic concept of centrodes (Section 3.1), the geometry of planar curves (Chapter 4), the determination of the envelope to a family of planar curves and surfaces (Chapter 6), and the concept of relative velocity (Chapter 2) is recommended.

Figure 10.2.1: Involute and evolute.

10.2 GEOMETRY OF INVOLUTE CURVES

Henceforth, we consider *conventional*, *extended*, and *shortened* involute curves (see Section 1.6). We start with general definitions of the *evolute* and the *involute* of a planar curve.

Involute and Evolute
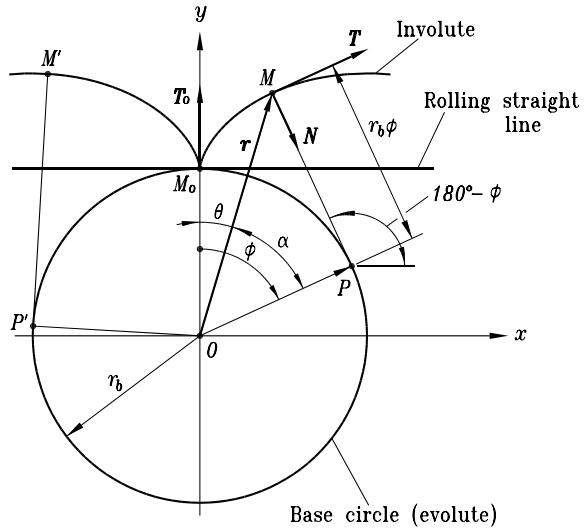
Consider that a planar curve I is given (Fig. 10.2.1). Segments $M_i N_i$ $(i = 1, 2, \ldots, n)$ represent the curvature radii of curve I at points M_i, where N_i is the curvature center. The locus of curvature centers N_i is the *evolute* E to curve I. The main features of E, evolute to curve I, are as follows:

 (i) The normal $M_i N_i$ at point M_i of curve I is the tangent to the evolute E.
(ii) The evolute to a regular curve I is the *envelope* to the family of normals $M_i N_i$ to I.

Considering E as given, we may determine the involute I for E as the result of development of E. Let us imagine an inextensible thread MN that is wrapped on curve E. Point M of the thread will trace out the involute I while the thread is wound on and off.

Involute Curve Used for Spur Gears

Consider the particular case when the evolute E is a circle. The involute I for such a case is the tooth profile for a spur gear. The evolute, the circle of radius r_b (Fig. 10.2.2), is called the *base circle*. Two branches of an involute curve are shown in Fig. 10.2.2. They are generated by point M_o of the straight line that rolls over the base circle clockwise and counterclockwise, respectively. Each branch represents its respective side of the tooth (Fig. 10.2.3).
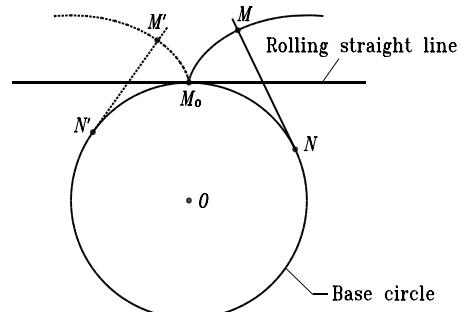
Figure 10.2.2: For derivation of the equation of an involute curve.

The analytical representation of an involute curve is based on the following considerations (Fig. 10.2.2).
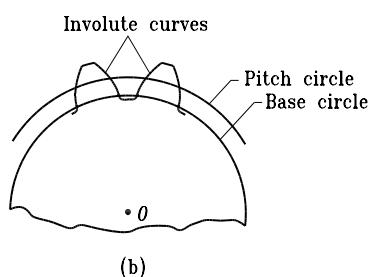
(i) A current point M of the involute curve is determined by the vector equation

$$\overline{OM} = \overline{OP} + \overline{PM} \qquad (10.2.1)$$

Figure 10.2.3: Two branches of an involute curve.

where

$$\overline{OP} = r_b [\sin \phi \quad \cos \phi]^{\mathrm{T}} \tag{10.2.2}$$

$$\overline{PM} = PM \, [-\cos \phi \quad \sin \phi]^{\mathrm{T}}. \tag{10.2.3}$$

(ii) Due to rolling without sliding, we have

$$PM = \overset{\frown}{M_o P} = r_b \phi. \tag{10.2.4}$$

Here, ϕ is the angle of rotation in rolling motion.

(iii) Equations (10.2.1) to (10.2.4) yield

$$x = r_b (\sin \phi - \phi \cos \phi), \qquad y = r_b (\cos \phi + \phi \sin \phi). \tag{10.2.5}$$

Another representation of an involute curve is based on application of variable parameter α (Fig. 10.2.2). The derivation of equations of the involute curve may be accomplished as follows:

$$x = r \sin \theta, \qquad y = r \cos \theta. \tag{10.2.6}$$

Here,

$$r = \frac{r_b}{\cos \alpha}, \qquad r_b (\theta + \alpha) = \overset{\frown}{M_o P}, \qquad \overset{\frown}{M_o P} = MP$$

$$MP = r_b \tan \alpha, \qquad \theta = \tan \alpha - \alpha. \tag{10.2.7}$$

Function $\theta(\alpha)$ is designated as inv α. Equations (10.2.6) and (10.2.7) yield

$$x = \frac{r_b}{\cos \alpha} \sin(\text{inv } \alpha), \qquad y = \frac{r_b}{\cos \alpha} \cos(\text{inv } \alpha). \tag{10.2.8}$$

Function

$$\text{inv } \alpha = \tan \alpha - \alpha \tag{10.2.9}$$

may be determined by direct computation considering α as given. The *inverse* operation, determination of α considering inv α as given, needs the solution of the nonlinear equation
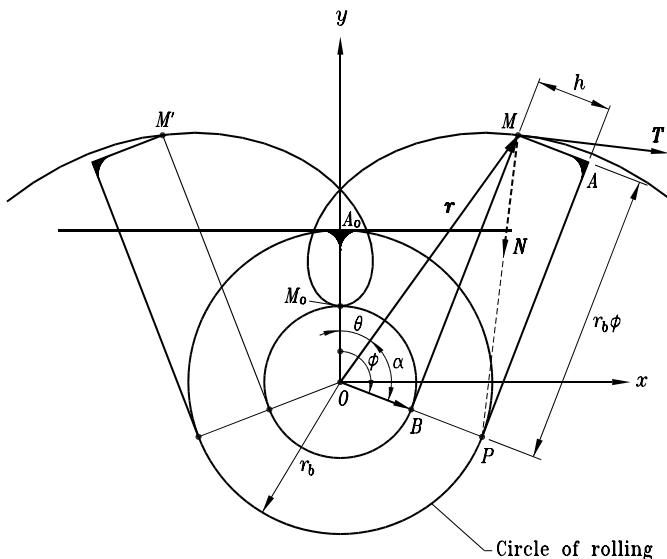
$$\alpha - \tan \alpha + \text{inv } \alpha = 0$$

where inv α is considered as given. The solution can be obtained using the IMSL library for solution of nonlinear equations (see More *et al.* [1980] or Visual Numerics, Inc. [1998]). An approximate representation but with high precision of the inverse function $\alpha(\theta)$ ($\theta = \tan \alpha - \alpha$) was proposed by Cheng [1992]:

$$\alpha = (3\theta)^{1/3} - \frac{2}{5}\theta + \frac{9}{175} 3^{2/3} \theta^{5/3} - \frac{2}{175} 3^{1/3} \theta^{7/3} + \cdots \qquad \text{for } \theta < 1.8 \tag{10.2.10}$$

Extended and Shortened Involute Curves

These curves are traced out by point M, which is offset with respect to the rolling straight line (Figs. 10.2.4 and 10.2.5). The straight line rolls over the circle of radius r_b.
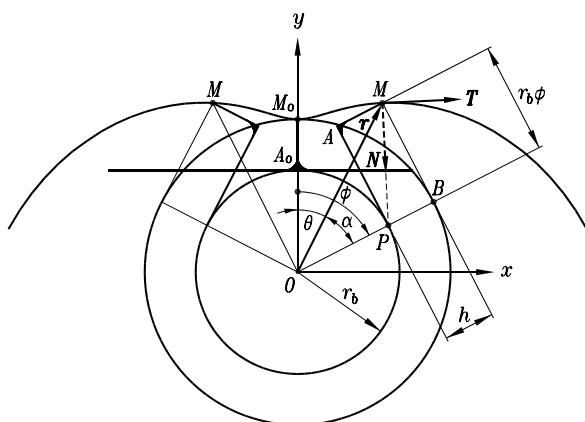
Figure 10.2.4: Extended involute curve.

Using an approach similar to that discussed above, we obtain the following equations:

$$x = (r_b \mp h) \sin \phi - r_b \phi \cos \phi$$
$$y = (r_b \mp h) \cos \phi + r_b \phi \sin \phi. \tag{10.2.11}$$

The upper sign in Eqs. (10.2.11) corresponds to the *extended* involute (Fig. 10.2.4), and the lower sign to the *shortened* involute (Fig. 10.2.5). Parameter h is the offset of the tracing point M with respect to the rolling straight line. Two branches are generated by rolling of the straight line clockwise and counterclockwise, respectively. The common point of the two branches is M_o, and M_o is a regular curve point (see Problem 10.2.2). Point P is the instantaneous center of rotation of the rolling straight line.

Figure 10.2.5: Shortened involute curve.
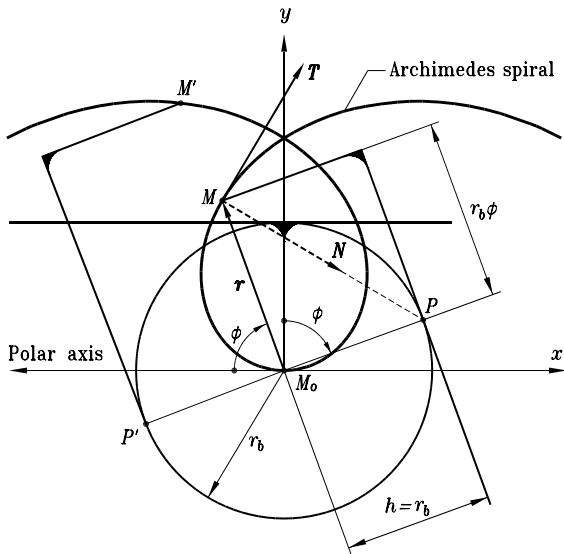
Figure 10.2.6: Archimedes spiral.

There is a particular case when $h = r_b$ and the extended involute curve turns out into the Archimedes spiral (Fig. 10.2.6) determined by the equation

$$M_o M = r = r_b \phi.$$

(See also Problem 1.6.1). Another particular case is when $h = 0$ and curve (10.2.11) is a conventional involute curve. An example of an extended involute curve is the trajectory that is traced out in relative motion by the center of the circular arc, the fillet of a rack-cutter (see Section 6.8).

Problem 10.2.1
Consider Eqs. (10.2.11) of extended and shortened involute curves. Derive equations of tangent $\mathbf{T}$ and normal $\mathbf{N} = \mathbf{T} \times \mathbf{k}$, where $\mathbf{k}$ is the unit vector of the z axis.

Solution

$$T_x = \mp h \cos \phi + r_b \phi \sin \phi, \qquad T_y = \pm h \sin \phi + r_b \phi \cos \phi$$
$$N_x = \pm h \sin \phi + r_b \phi \cos \phi, \qquad N_y = \pm h \cos \phi - r_b \phi \sin \phi.$$
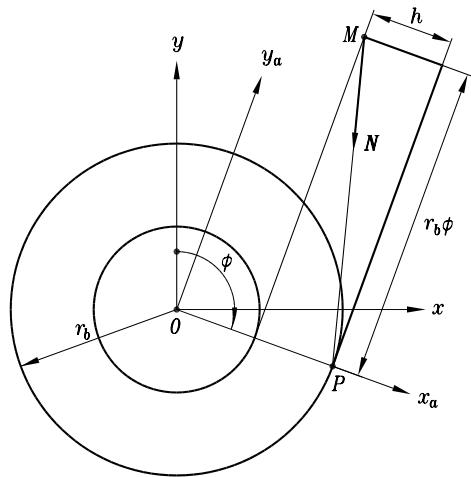
Problem 10.2.2
Represent the curve normal $\mathbf{N}$ in coordinate system S_a (Fig. 10.2.7) for an extended involute curve, and define the orientation of $\mathbf{N}$.

Solution

$$N_{xa} = h, \qquad N_{ya} = -r_b \phi.$$

The normal is directed from curve current point M to the instantaneous center of rotation P.

Figure 10.2.7: Geometric interpretation of normal to involute curve.

Problem 10.2.3

Consider equations of a conventional involute curve, taking, in Eqs. (10.2.11), $h = 0$. A singular point is determined with the condition that the tangent to a curve is $\mathbf{T} = \mathbf{0}$. Determine and visualize the singular point of the curve (see also Problem 4.3.2).

Solution

$$T_x = r_b \phi \sin \phi, \qquad T_y = r_b \phi \cos \phi.$$

$T_x = T_y = 0$ at the position where $\phi = 0$ (point M_o in Fig. 10.2.2).

NOTE. There is only a "half" tangent to the curve at M_o (see Section 4.3). The direction of the "half" tangent may be represented by the equations [Rashevski, 1956]

$$T_{x\phi} = \frac{\partial T_x}{\partial \phi} = r_b(\phi \cos \phi + \sin \phi), \qquad T_{y\phi} = \frac{\partial T_y}{\partial \phi} = r_b(-\phi \sin \phi + \cos \phi).$$

Taking into account that $\phi = 0$ at point M_o, we obtain that the "half" tangent $\mathbf{T}$ at M_o is directed opposite to the normal $\overline{M_o O}$ to the base circle (Fig. 10.2.2).
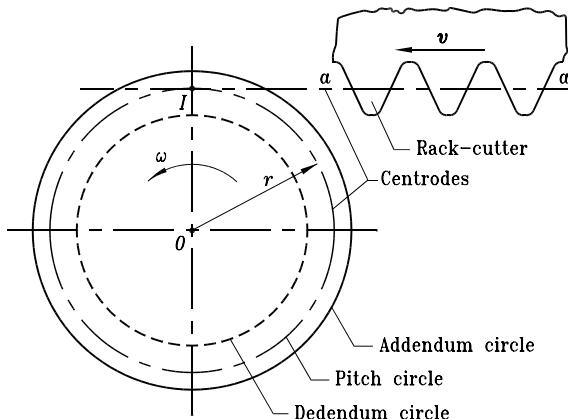
10.3 GENERATION OF INVOLUTE CURVES BY TOOLS

The generation of involute spur gears by a rack-cutter, hob, or shaper is a widespread practice in industry.

Generation by a Rack-Cutter

The generation of a spur involute gear by a rack-cutter is shown in Fig. 10.3.1. The gear to be cut rotates with angular velocity ω about O, and the rack-cutter translates with velocity $\mathbf{v}$. The velocity $|\mathbf{v}|$ and angular velocity ω are related by the equation

$$\frac{v}{\omega} = r_p = \frac{N}{2P}. \tag{10.3.1}$$
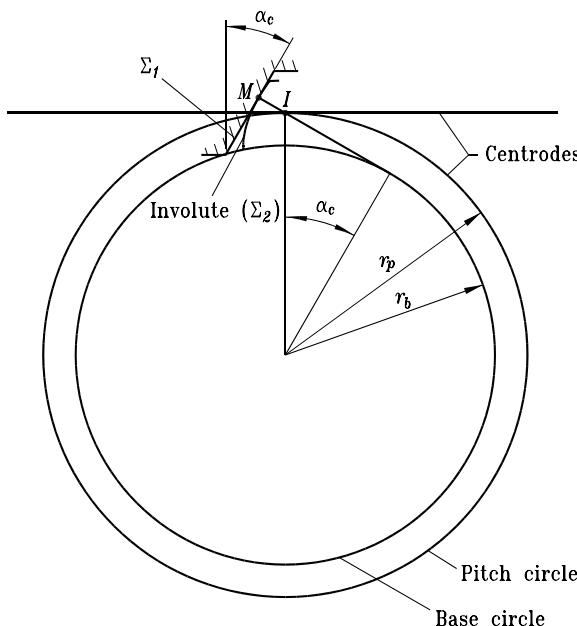
Figure 10.3.1: Generation of involute curve by rack-cutter.

Here, r_p is the radius of the pitch circle, N is the number of gear teeth, and P is the diametral pitch. The pitch circle is the gear centrode by cutting. The rack-cutter centrode by cutting is the straight line a–a that is tangent to the pitch circle and parallel to **v** (Fig. 10.3.1). Point I is the *instantaneous center of rotation*.

During tooth cutting, the rack-cutter reciprocates parallel to the gear axis of rotation. The gear tooth shape Σ_2 is generated as the *envelope* to the family of rack-cutter shapes Σ_1 that is represented in coordinate system S_2 rigidly connected to the gear being generated. Shape Σ_2 is a *conventional involute*. The evolute for Σ_2 is the base circle of radius r_b (Fig. 10.3.2) determined as

$$r_b = \frac{N \cos \alpha_c}{2P} = r_p \cos \alpha_c = \frac{v}{\omega} \cos \alpha_c \qquad (10.3.2)$$

where α_c is the profile angle of the rack-cutter.

Figure 10.3.2: Meshing of rack with involute gear.

We may prove that a rack-cutter with a straight-lined shape Σ_1 generates an involute curve Σ_2, by applying the theory of envelopes (see Section 6.1 and Problem 6.12.1). The *same* involute Σ_2 (with the same radius r_b of the base circle) can be generated using a rack-cutter with various profile angles α_c by changing the ratio of v/ω correspondingly [see Eq. (10.3.2)]. This is used in practice when an involute gear is ground by a plane and α_c is the tilt of the plane.

Figure 10.3.2 illustrates the meshing of the rack-cutter with the gear: I is the instantaneous center of rotation; M is the current point of tangency of Σ_1 and Σ_2; the common normal to Σ_1 and Σ_2 passes through I and is tangent to the base circle.
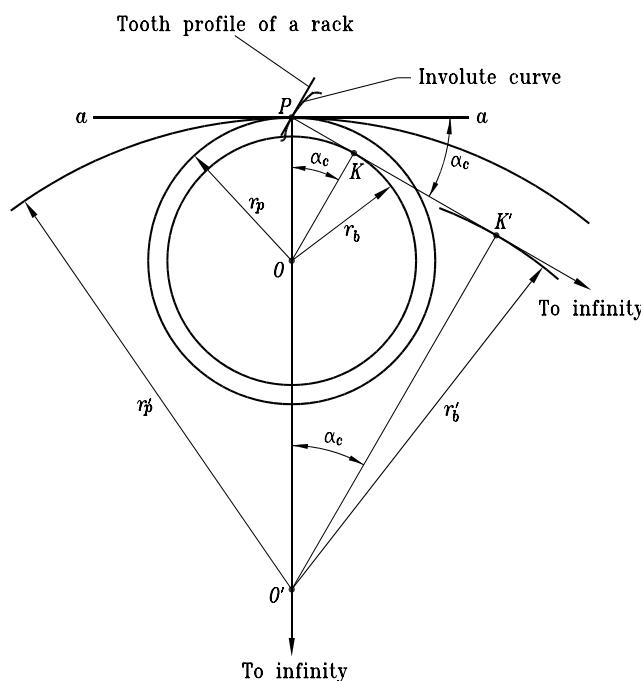
Design Parameters of Rack-Cutter
To visualize a rack it is useful to consider a rack as the limiting case of a gear with an infinite number of teeth. Figure 10.3.3 shows an involute spur gear. The radii of the pitch circle and the base circle, r_p and r_b, are related as [see Eq. (10.3.2)]

$$r_b = r_p \cos\alpha_c = \frac{N}{2P}\cos\alpha_c$$
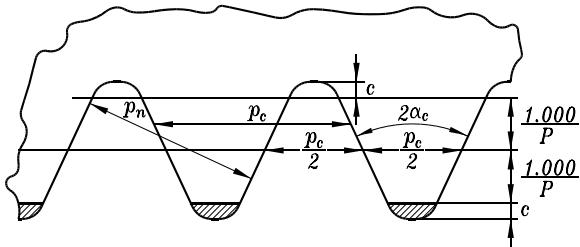
where α_c determines the orientation of the normal PK to the involute curve at point P. The curvature radius PK at P is

$$r_b \tan\alpha_c = PK = \frac{N}{2P}\sin\alpha_c. \tag{10.3.3}$$

Consider now that the number N of gear teeth has been increased but P and α_c are kept at the same values. With $N' > N$ the radii of the pitch circle and the base

Figure 10.3.3: Rack as a particular case of a gear.

Figure 10.3.4: Parameters of a rack-cutter.

circle are r'_p and r'_b, respectively; the center of these circles is O'. The curvature center is K', and the curvature radius $PK' = r'_b \tan \alpha_c$ is increased. It is evident that while the gear center O is moved to infinity along OO', the curvature center at P is also moved to infinity but along PK'; the gear involute profile is turned out into a straight line that is perpendicular to PK (Fig. 10.3.3). The gear pitch circle is turned out into the straight line $a-a$. Thus, when N approaches infinity, the gear is turned out into a rack.

The design parameters of rack-cutters are standardized to save the number of tools to be applied (Fig. 10.3.4). The standardized parameters are $P = \frac{\pi}{p_c}$ (see Section 10.4), α_c, the dimensions of the dedendum and addendum of the rack-cutter, and the clearance parameter c. We have to differentiate between a conventional rack designed to be in mesh with a spur gear, and a rack-cutter designated for generation of spur gears. The addendum of the rack-cutter is extended in comparison with the addendum of a conventional rack. Only the rack-cutter is provided with the shaded part of the tooth. The shape of the fillet of the rack-cutter is shown in Fig. 6.9.1. The same rack-cutter can be applied for generation of gears with the given values of P and α_c but with different numbers of teeth.
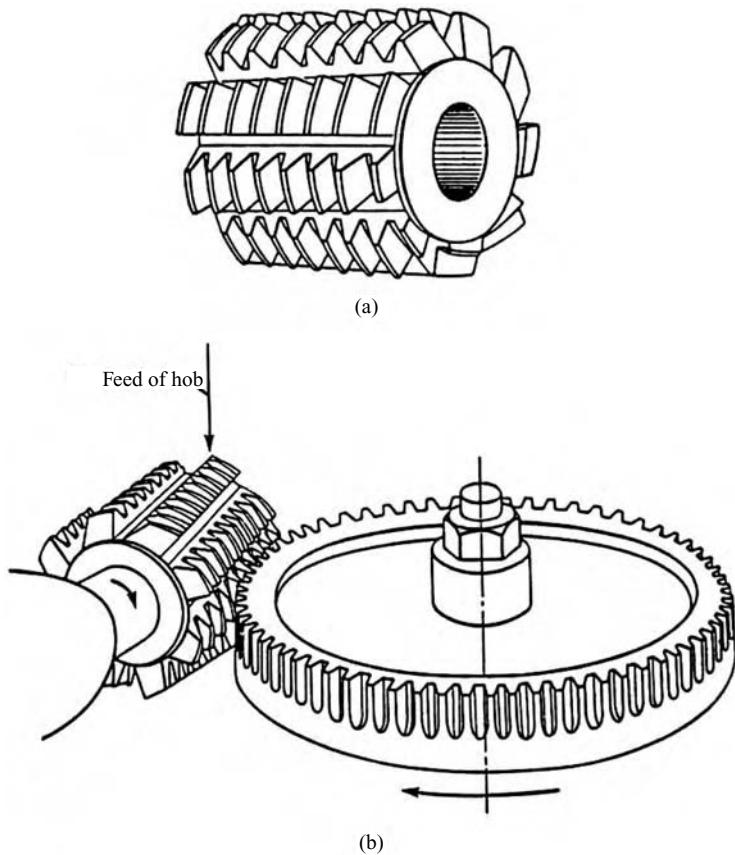
Generation by Hob

The generation of gears by a hob is shown in Fig. 10.3.5. The hob may be considered as a worm [usually a worm with a single thread, as in Fig. 10.3.5(a)]. The worm is slotted in the axial direction to form a series of cutting blades. The axial section of the worm may be considered to be a rack. The rotation of the hob simulates the translation of the imaginary rack. During cutting, the hob and the gear to be generated rotate about their respective axes [Fig. 10.3.5(b)]. The hob in addition to rotating translates parallel to the gear axis; this is the feed motion of the hob.
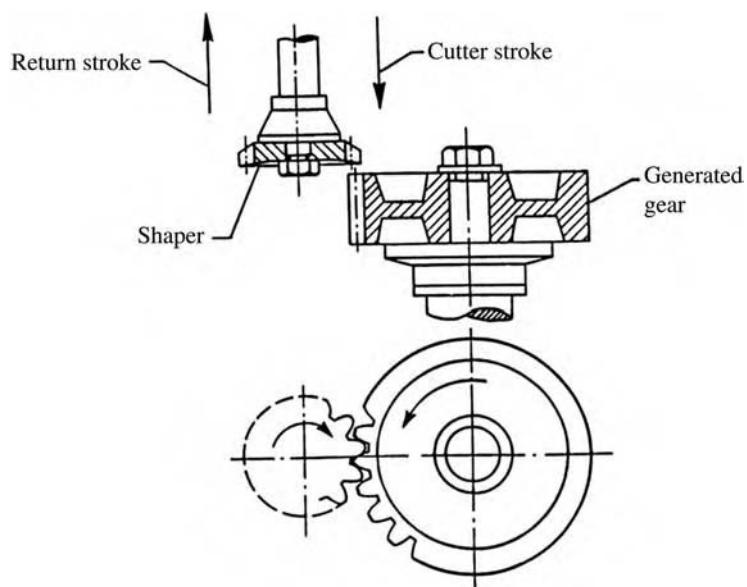
Angles ϕ_h and ϕ_g of hob and gear rotations are related as

$$\frac{\phi_h}{\phi_g} = \frac{N_g}{N_h} \tag{10.3.4}$$
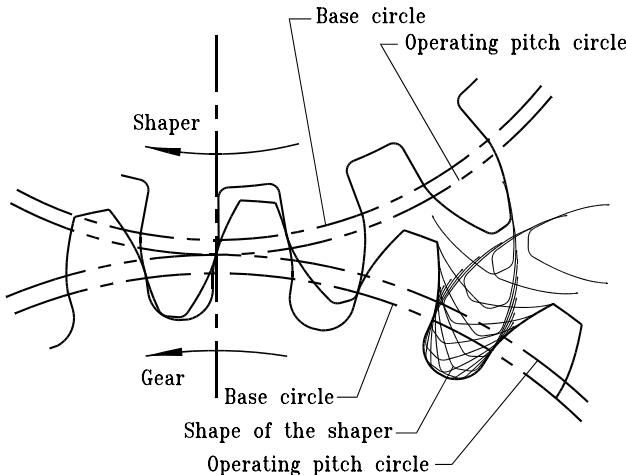
where N_g is the number of gear teeth and N_h is the number of hob threads. Usually $N_h = 1$. The meshing of the hob with the gear being generated may be considered as the rack-gear meshing. The rotation of the hob simulates the translation of the imaginary rack.

(a)

Feed of hob

(b)

Figure 10.3.5: Generation by hob.

Return stroke

Cutter stroke

Generated gear

Shaper

**Figure 10.3.6:** Generation by shaper.

Figure 10.3.7: Meshing of gear and shaper.

Generation by Shaper

Tooth generation by a shaper simulates the mesh of two gears, one of which is the shaper (Fig. 10.3.6). An involute shaper with a radius of base circle r_{bc} generates an involute spur gear with the radius of the base circle r_{bg} determined as

$$r_{bg} = \frac{N_g}{N_c} r_{bc} \qquad (10.3.5)$$

where N_c and N_g are the numbers of teeth of the shaper and of the generated gear, respectively. The shape Σ_2 of the gear teeth is the envelope to the family of shaper shape Σ_1, which is formed in relative motion (Fig. 10.3.7).

The great advantage of generation of gears by a shaper is the possibility of manufacturing of gears with internal teeth. Such gears have been widely applied in planetary trains due to higher efficiency of internal gearing.

10.4 TOOTH ELEMENT PROPORTIONS

The pitch circle is the reference circle for tooth element proportions (Fig. 10.4.1). The *circular pitch* p_c is the distance between two gear neighboring teeth measured along the pitch circle. The circular pitch is an arc of the pitch circle. The distance between two neighboring teeth of the rack-cutter (Fig. 10.3.4) is a segment of a straight line that is equal to p_c. (Recall that the pitch circle is the centrode in meshing with the rack-cutter.)

The *diametral pitch* is represented as

$$P = \frac{N}{d} = \frac{\pi}{p_c} \qquad (10.4.1)$$
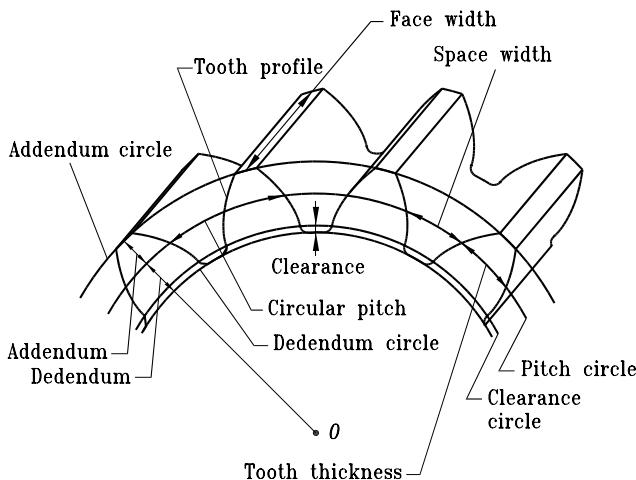
Figure 10.4.1: Gear tooth parameters.

and is defined as the number of teeth of the gear per inch of its diameter. Relations (10.4.1) are based on the following considerations:

Step 1: The circumference of the pitch circle is

$$L = p_c N = \pi d \qquad (10.4.2)$$

where N is the number of gear teeth.

Step 2: Equations (10.4.2) yield relation (10.4.1). The ratio N/d is called the diametral pitch.

The *module m* is represented as

$$m = \frac{p_c}{\pi} = \frac{d}{N}.$$

The unit for m is in millimeters, but the unit for P is (1/in.).

The *addendum a* is the *radial* distance between the addendum circle and the pitch circle.

The *dedendum b* is the *radial* distance between the pitch circle and the dedendum circle.

The tooth thickness t and the space width w are arcs measured *along* the pitch circle.

In the case of standard gears (with standard tooth element proportions) we have $a = 1/P$; $b = 1.250/P$ for coarse pitch gears (up to $P = 20$); $b = 1.200/P + 0.002$ in. for fine pitch gears; the clearance is $c = b - a$; and the nominal values of tooth thickness and space width are $t = w = p_c/2$.

Problem 10.4.1

Consider the following as known: the diameter of the addendum circle $d_a = 2.200$ in. (obtained by measurements); the teeth number $N = 20$; and the gear is generated by a rack-cutter with the profile angle $\alpha_c = 20°$ with the conventional setting of the tool.

Determine

(i) the diametral pitch P,
(ii) the circular pitch p_c,
(iii) the radius of the base circle r_b,
(iv) the base pitch p_b,
(v) the nominal value of tooth thickness t on the pitch circle.

Solution

(i) $P = 10 \dfrac{1}{\text{in.}}$.

(ii) $p_c = \dfrac{\pi}{10}$ in.

(iii) $r_b = r_p \cos 20° = 0.94$ in.

(iv) $p_b = \dfrac{\pi}{10} \cos 20°$ in. $= 0.094\pi$ in.

(v) $t = \dfrac{\pi}{20}$ in.

10.5 MESHING OF INVOLUTE GEAR WITH RACK-CUTTER
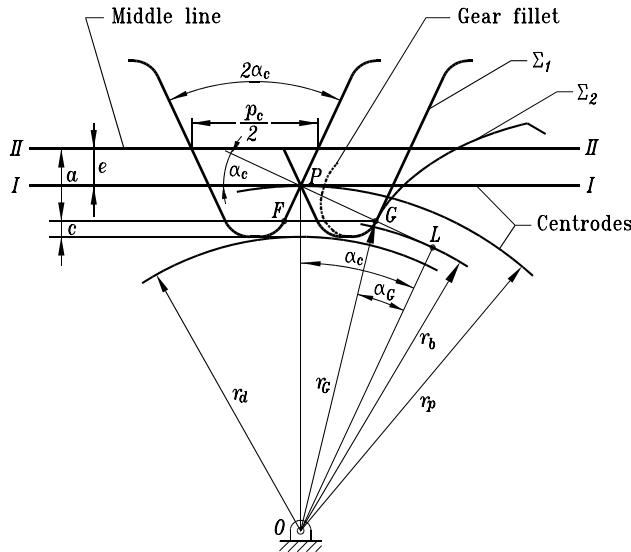
Conventional and Non-Conventional Settings of Rack-Cutter

Recall that the gear centrode by cutting is the pitch circle because the translational velocity v and the angular velocity ω are related by cutting with Eq. (10.3.1). The rack-cutter centrode is the straight line that is tangent to the gear centrode and is parallel to **v**.

We call the setting of the rack-cutter with respect to the gear the *conventional* setting when the middle-line of the rack-cutter is tangent to the gear pitch circle. Figure 10.5.1 shows that the rack-cutter was displaced at the distance e; the middle-line of the rack-cutter is designated as $II–II$, and the rack-cutter centrode is $I–I$. This setting of the rack-cutter we call the *non-conventional* setting. The displacement of the rack-cutter enables us to change the gear tooth thickness and avoid undercutting as well. We have to emphasize that the gear and rack-cutter centrodes are the same for conventional and non-conventional settings because the ratio v/ω is observed to be the same for both types of settings. Involute gears generated by the non-conventional setting of the rack-cutter are called *nonstandard* gears.

Conditions of Nonundercutting

Conditions of nonundercutting by a rack-cutter may be determined by using the general approach presented in Section 6.3 (see also Problems 10.5.1 to 10.5.3). An approach based on simple geometric considerations is introduced in this section to illustrate the case of undercutting of involute gears. We start the discussions with the concept of the limiting setting of a rack-cutter. We have to emphasize that generally speaking the initial

Figure 10.5.1: Generation of point G.

point of the involute curve that is generated by the rack-cutter may be located *upward* with respect to the base circle.

We designate by F the point of tangency of the straight line of the rack-cutter shape Σ_1 with the rack-cutter fillet. It is evident that the *initial* point of the involute curve Σ_2 is generated when Σ_1 and Σ_2 will be in tangency at point G of the line of action. Thus, initial point G of the involute curve belongs to the gear circle of radius $r_G = OG$, and $r_G \neq r_b$. This means that generally G does not coincide with the initial point M_o of the involute curve that belongs to the base circle (Fig. 10.2.2). *The real initial point of an involute curve generated by a rack-cutter is G but not M_o.*

Using Fig. 10.5.1 we may derive the following equations:

$$\tan \alpha_G = \frac{GL}{r_b} = \tan \alpha_c - \frac{4P(a-e)}{N \sin 2\alpha_c} \tag{10.5.1}$$

$$r_G = \frac{N \cos \alpha_c}{2P \cos \alpha_G}. \tag{10.5.2}$$

Equations (10.5.1) and (10.5.2) enable us to determine the radius r_G of the circle where the initial point of the involute curve is located. Using these equations we are able to determine as well the conditions of nonundercutting with the requirements that $r_G \geq r_b$ or $\alpha_G \geq 0$. Simpler expressions can be derived if we use the concept of minimal number of teeth free from undercutting. Figure 10.5.2 shows one such case when point F generates the *initial* point of the involute curve at point L of the line of action. This case may exist if and only if a pinion with a certain number of teeth is generated. It is assumed in our discussion that the setting of the rack-cutter is the conventional one (the middle rack-cutter line a–a is the tangent to the pitch circle). Equation (10.5.1) with $\alpha_G = 0$ and $e = 0$ yields

$$N_{\min} = \frac{2Pa}{\sin^2 \alpha_c}. \tag{10.5.3}$$
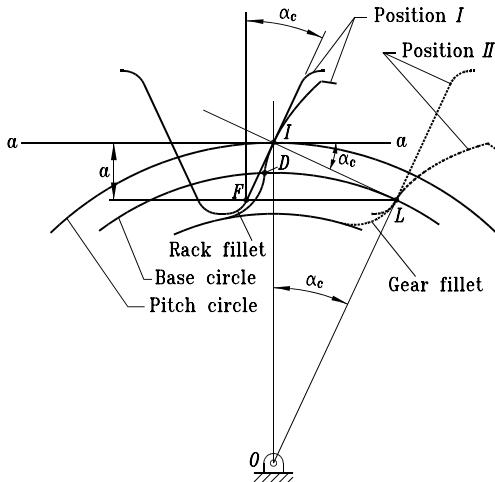
Figure 10.5.2: Limiting setting of rack-cutter.

For the case where $a = 1/P$, we obtain that

$$N_{\min} = \frac{2}{\sin^2 \alpha_c}. \tag{10.5.4}$$

The minimal number of pinion teeth, $N_{\min}$, indicates for the designer that when $N \geq N_{\min}$ the pinion may be generated with the conventional setting of the rack-cutter. Here, N is the number of teeth of the designed pinion. For the case where $N < N_{\min}$, a non-conventional setting of the rack-cutter must be provided. The respective displacement e of the rack-cutter (Fig. 10.5.1) can be determined from Eq. (10.5.1) with the requirement that $\alpha_G \geq 0$. Then we obtain

$$\tan \alpha_c - \frac{4P(a - e)}{N \sin 2\alpha_c} \geq 0. \tag{10.5.5}$$

Expression (10.5.5) with $a = 1/P$ yields

$$\frac{N \sin^2 \alpha_c - 2(1 - Pe)}{N \sin \alpha_c \cos \alpha_c} \geq 0. \tag{10.5.6}$$

Considering (10.5.6) and (10.5.4) simultaneously, we obtain

$$Pe \geq \frac{N_{\min} - N}{N_{\min}}. \tag{10.5.7}$$

Here, Pe is an algebraic unitless value. Designating Pe by ζ, we obtain

$$\zeta \geq \frac{N_{\min} - N}{N_{\min}}. \tag{10.5.8}$$

We may consider two cases:

(i) $N < N_{\min}$. Then $\zeta > 0$, and the rack-cutter must be displaced *outward* from the gear center. The minimal value of ζ is

$$\zeta_{\min} = \frac{N_{\min} - N}{N_{\min}}. \tag{10.5.9}$$

Choosing $\zeta > \zeta_{min}$, we have to limit ζ due to the possibility of tooth pointing (see Problem 10.6.2).

(ii) $N > N_{min}$. Then $\zeta \leq 0$, and the rack-cutter can be displaced *toward* the gear center, or the setting can be conventional ($\zeta = 0$).

Change of Gear Tooth Thickness and Dedendum Height

The displacement of the rack-cutter affects the gear tooth thickness and the dedendum dimension. Henceforth, we consider the change of tooth thickness (space width) that is measured along the gear pitch circle. The space width of the gear that is measured along the pitch circle is equal to the tooth thickness of the rack-cutter that is measured along $I–I$, the rack-cutter centrode. In the case of the conventional setting of the rack-cutter, the nominal value of the gear space width is

$$w = s_c = \frac{p_c}{2} = \frac{\pi}{2P} \qquad (10.5.10)$$

where s_c is the tooth thickness of the rack-cutter on the middle-line $a–a$. When a non-conventional setting of the rack-cutter is provided, the tooth thickness of the rack-cutter on its centrode $I–I$ is [Fig. 10.5.3(b)]

$$s_c^* = s_c - 2e \tan \alpha_c = \frac{p_c}{2} - 2e \tan \alpha_c. \qquad (10.5.11)$$

The gear space width is

$$w = s_c^* = \frac{p_c}{2} - 2e \tan \alpha_c. \qquad (10.5.12)$$

The radius of the dedendum circle is determined with the equation

$$r_d = r_p - b + e, \qquad (10.5.13)$$

and the dedendum height is $(b - e)$. To keep the total height at the gear tooth at the proper value it is necessary to change the radius of the addendum circle while preparing the gear blank for cutting.

Problem 10.5.1
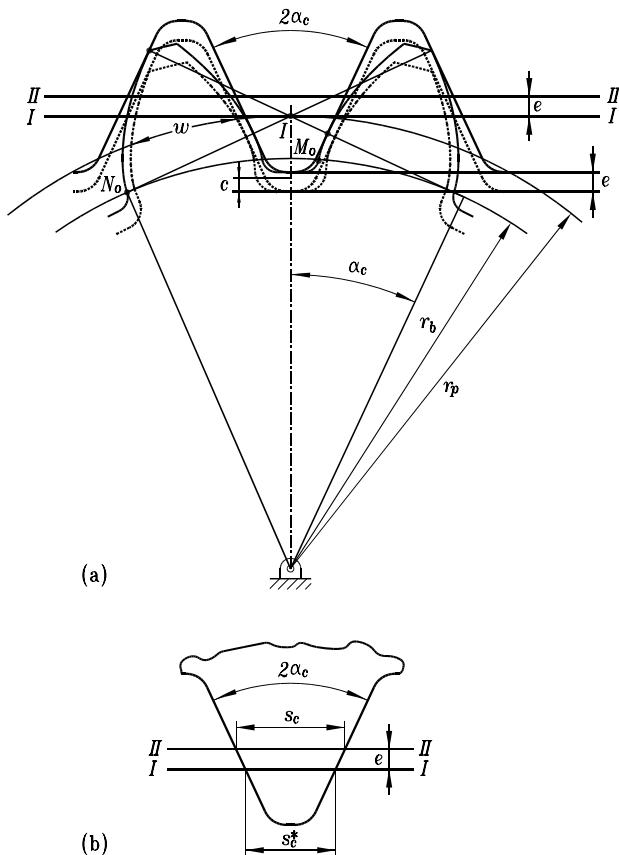
Consider a conventional setting of the rack-cutter ($e = 0$). The radius r_G of the circle where the initial point of the involute curve is located is represented by Eqs. (10.5.1) and (10.5.2). Represent radius r_G in terms of N, α_c, and P; take $a = 1/P$.

Solution

$$r_G = \frac{(N^2 \sin^2 \alpha_c - 4N \sin^2 \alpha_c + 4)^{\frac{1}{2}}}{2P \sin \alpha_c}. \qquad (10.5.14)$$

Problem 10.5.2

Consider that radius r_G is represented by Eq. (10.5.14). Derive an equation in terms of N and α_c when the initial point of the involute curve belongs to the base circle.

(a)

(b)

Figure 10.5.3: Illustration of (a) generation of standard and nonstandard gears and (b) tooth thickness of the rack-cutter.

Solution

$$N = \frac{2}{\sin^2 \alpha_c}.$$

Problem 10.5.3

Transform expression (10.5.8) by using Eq. (10.5.4). Represent ζ in terms of N and α_c.

Solution

$$\zeta \geq \frac{2 - N \sin^2 \alpha_c}{2}.$$

Problem 10.5.4

A gear with tooth number $N > N_{\min}$ is generated by a rack-cutter with the profile angle α_c; the diametral pitch is P; the addendum of the rack-cutter is $b = 1.25/P$; a non-conventional setting of the rack-cutter is used ($e < 0$). Represent in terms of N, α_c, and

P the minimal radius of the gear dedendum circle with which undercutting might still be avoided.

DIRECTIONS. Use Eq. (10.5.13) for r_d. Expression (10.5.7) yields that undercutting may still be avoided with

$$e = \frac{N_{min} - N}{P N_{min}} = \frac{2 - N \sin^2 \alpha_c}{2P}.$$

Solution

$$r_d = \frac{N \cos^2 \alpha_c - 0.5}{2P}. \qquad (10.5.15)$$

Problem 10.5.5

Equation (10.5.15) determines the radius of the dedendum circle when the non-conventional setting of the rack-cutter is applied. The radius of the dedendum circle when a conventional setting of the rack-cutter is applied is represented by the equation

$$r_d^* = r_p - \frac{1.25}{P}.$$

Determine N in terms of α_c when: (i) $r_d > r_d^*$, (ii) $r_d = r_d^*$, and (iii) $r_d < r_d^*$.

Solution

$$\text{(i)} \ \ N < \frac{2}{\sin^2 \alpha_c}; \quad \text{(ii)} \ \ N = \frac{2}{\sin^2 \alpha_c}; \quad \text{(iii)} \ \ N > \frac{2}{\sin^2 \alpha_c}.$$

10.6 RELATIONS BETWEEN TOOTH THICKNESSES MEASURED ON VARIOUS CIRCLES

Consider that the tooth thickness $t_p = \overset{\frown}{AA'}$ on the pitch circle is given (Fig. 10.6.1). The goal is to determine the tooth thickness $t_x = \overset{\frown}{BB'}$ on the circle of given radius r_x; t_x must be represented in terms of P, pressure angle α_c, tooth number N, and radius r_x.

The tooth half-thickness and the corresponding angle β (or β_x) are related by the following equations:

$$\beta = \frac{\overset{\frown}{AA'}}{2r_p} = \frac{t_p}{2r_p} \qquad (10.6.1)$$
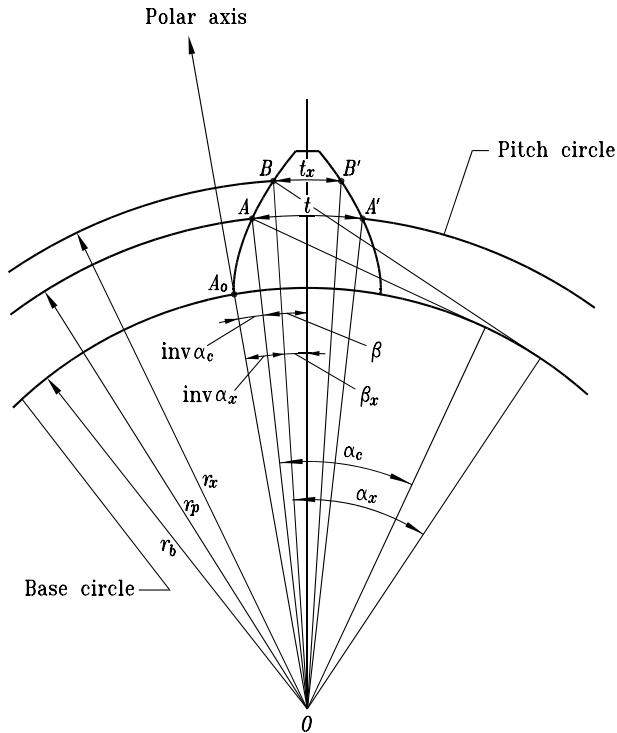
$$\beta_x = \frac{t_x}{2r_x} \qquad (10.6.2)$$

Figure 10.6.1 yields

$$\beta_x = \beta + \text{inv}\, \alpha_c - \text{inv}\, \alpha_x \qquad (10.6.3)$$

where $\text{inv}\, \alpha_c = \tan \alpha_c - \alpha_c$, $\text{inv}\, \alpha_x = \tan \alpha_x - \alpha_x$, and

$$\cos \alpha_x = \frac{r_b}{r_x} = \frac{N \cos \alpha_c}{2P r_x}. \qquad (10.6.4)$$

Figure 10.6.1: For derivation of tooth thickness.

The nominal value of t_p for a standard gear is

$$t_p = \frac{p_c}{2} = \frac{\pi}{2P}.$$ (10.6.5)

Equations (10.6.1) to (10.6.3) yield

$$t_x = r_x \left[\frac{t_p}{r_p} + 2(\text{inv}\,\alpha_c - \text{inv}\,\alpha_x) \right].$$ (10.6.6)

The procedure for computation of t_x is as follows:

Step 1: Determine $\cos\alpha_x$:

$$\cos\alpha_x = \frac{N\cos\alpha_c}{2Pr_x}.$$

Step 2: Determine inv α_x:

$$\text{inv}\,\alpha_x = \tan\alpha_x - \alpha_x.$$

Step 3: Determine t_x using Eq. (10.6.6).

Problem 10.6.1
Determine the tooth thickness on the base circle of a standard gear [use Eq. (10.6.6)].

Solution

$$t_b = r_b \left(\frac{\pi}{N} + 2 \text{ inv } \alpha_c \right). \tag{10.6.7}$$

Problem 10.6.2
Determine the radius of the circle where the teeth are pointed for: (i) a standard gear, and (ii) a nonstandard gear.

Solution
(i)

$$\text{inv } \alpha_x = \frac{\pi}{2N} + \text{inv } \alpha_c \tag{10.6.8}$$

$$r_x = \frac{N \cos \alpha_c}{2P \cos \alpha_x}. \tag{10.6.9}$$

(ii) In the case of a nonstandard gear we have [see Eq. (10.5.12)]

$$t_p = p_c - w = \frac{p_c}{2} + 2e \tan \alpha_c = \frac{\pi}{2P} + 2e \tan \alpha_c \tag{10.6.10}$$

$$\text{inv } \alpha_x = \frac{\pi}{2N} + \frac{2eP \tan \alpha_c}{N} + \text{inv } \alpha_c \tag{10.6.11}$$

$$r_x = \frac{N \cos \alpha_c}{2P \cos \alpha_x}.$$

10.7 MESHING OF EXTERNAL INVOLUTE GEARS
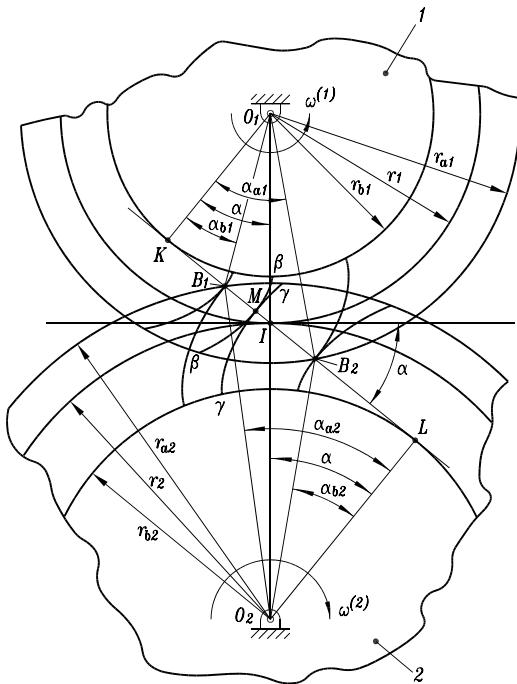
Figure 10.7.1 shows involute profiles β–β and γ–γ of the teeth of two mating gears. These curves have been obtained by the development of base circles of radii r_{b1} and r_{b2}, respectively.

Constancy of Gear Ratio
The transformation of motion is performed with a constant ratio of angular velocities because the common normal KL to the involute curve intersects the center distance O_1–O_2 at a point of constant location (point I in Fig. 10.7.1). This point is the instantaneous center of rotation. The proof of this statement is based on the basic theorem of planar gearing, Lewis' theorem (see Section 6.1).

Line of Action
The *line of action* is KL, the common tangent to the base circles. Straight line KL is the common normal to the gear tooth profiles as well.

Figure 10.7.1: Meshing of involute gears.

Gear Centrodes
Circles of radii $O_1 I$ and $O_2 I$ are the gear *centrodes*. Generally, the gear centrodes do not coincide with the gear pitch *circles* (see below).
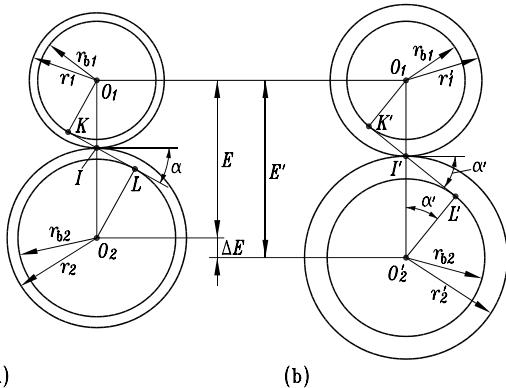
Pressure Angle
The pressure angle α is formed by the line of action KL and the tangent to the gear centrodes. Generally, the pressure angle α differs from the rack-cutter profile angle α_c. The equality $\alpha = \alpha_c$ can be observed in a particular case only (see below).

Change of Center Distance
The change of center distance does not affect the gear ratio m_{12}, but it is accompanied with a change of the pressure angle and the radii of gear centrodes. The proof of this statement is based on the following considerations:

(a) Considering that gear tooth profiles β–β and γ–γ are given, we have to consider that the corresponding base circles are also given (Fig. 10.7.1). Recall that β–β and γ–γ have been obtained by the development of base circles of radii r_{b1} and r_{b2}, respectively.

(b) Figure 10.7.2 shows that the gears with the *same* base circles have been assembled: initially with the center distance E [Fig. 10.7.2(a)], and then with the center distance $E' = E + \Delta E$ [Fig. 10.7.2(b)]. The common normal in the first case is KL and in the second case is $K'L'$. The point of intersection of the common normal with the center distance (I and I', respectively) does not change its location in the process

Figure 10.7.2: Influence of change of center distance.

(a) (b)

of transformation of motions. Thus, the gear ratio is constant in both previously mentioned cases.

(c) Due to the change of center distance, the new pressure angle is $\alpha' \neq \alpha$, and the radii of gear centrodes r_i' $(i = 1, 2)$ differ from the previous ones, r_i.

(d) It is easy to verify that the gear ratio is the *same* for both cases of assembly. This statement follows from the equations

$$m_{12} = \frac{\omega^{(1)}}{\omega^{(2)}} = \frac{r_2}{r_1} = \frac{r_{b2}}{r_{b1}} = \frac{r_2'}{r_1'}. \tag{10.7.1}$$

Involute Profiles as Equidistant Curves

The advantage of involute gearing is that the tooth profiles are equidistant curves (Fig. 10.7.3) because they are generated by a rack-cutter whose tooth profiles are parallel straight lines (Fig. 10.3.4). The distance p_b between the gear tooth profiles (Fig. 10.7.3) that is measured along the common normal to the profiles is equal to the distance p_n between the profiles of the rack-cutter (Fig. 10.3.4) and is determined as
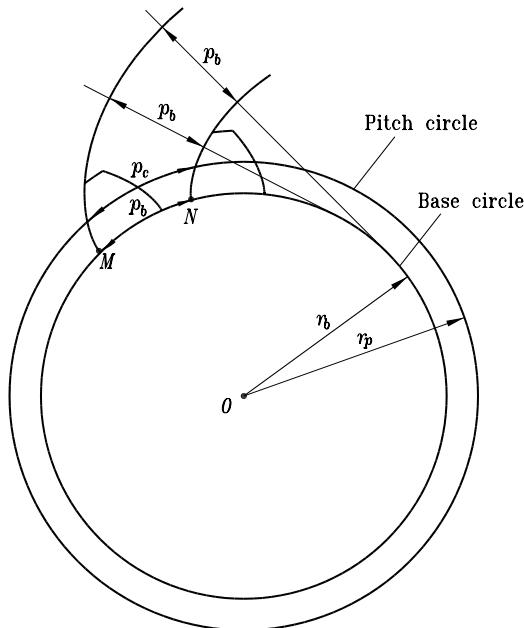
$$p_b = p_n = p_c \cos \alpha_c.$$

Taking into account how the involute curves are generated, we obtain (Fig. 10.7.3) that

$$p_b = \widehat{MN}$$

where arc $\widehat{MN}$ is the distance between two neighboring involute curves that is measured along the base circle.

The neighboring involute curves, because they are the equidistant ones, have a common normal at a position that is called the *transfer of meshing* when one pair of teeth is out of mesh and is substituted by another one. This is especially important in the case when gear eccentricity is an error of manufacturing (or assembly). The transmission function of eccentric gears is nonlinear, but if the profiles are involute curves the transmission function and its first derivative are continuous ones at the transfer point. This means that eccentricity of involute gears does not cause a *stroke* at the transfer point.

Figure 10.7.3: Involute profiles as equidistant curves.

Sliding of Involute Profiles

The involute profiles while they are in mesh are in tangency at a point that belongs to the line of action KL. The relative motion of one tooth profile with respect to the other one is pure rolling when they are in tangency at point I, the instantaneous center of rotation. The relative motion when the tooth profiles are in tangency at any point of KL that differs from I is rolling and sliding (Fig. 10.7.4). Our goal is to determine the sliding velocity.

Let the tooth profiles be in tangency at point M of line KL. This means that point M_1 of profile Σ_1 coincides with point M_2 of profile Σ_2. The velocity of point M_1 with respect to point M_2 is

$$\mathbf{v}^{(12)} = \mathbf{v}^{(1,M)} - \mathbf{v}^{(2,M)} = \left(\boldsymbol{\omega}^{(1)} \times \overline{O_1 M}\right) - \left(\boldsymbol{\omega}^{(2)} \times \overline{O_2 M}\right). \tag{10.7.2}$$
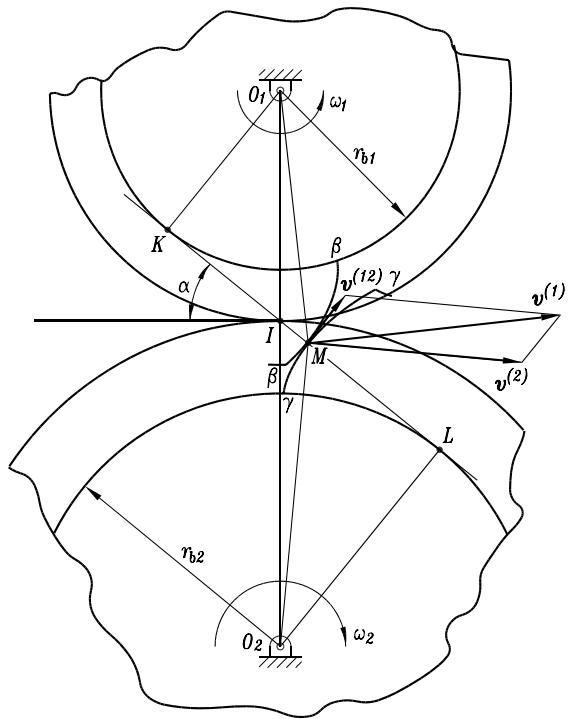
The sliding velocity at point I is equal to zero. When the point of tangency goes through I, the direction of sliding velocity will be changed in the neighborhood of I.

Interference

Interference means that an involute shape of one mating gear is in mesh with the fillet of the other gear. The determination of conditions of noninterference is based on the following considerations:

(i) Equation (10.5.1) determines parameter α_G for the point of tangency of the involute profile with the fillet. Here,

$$\tan \alpha_{Gi} = \tan \alpha_c - \frac{4P(a - e_i)}{N_i \sin 2\alpha_c} \quad (i = 1, 2). \tag{10.7.3}$$

Figure 10.7.4: For derivation of sliding velocity.

(ii) Figure 10.7.1 shows B_1–B_2, the working part of the line of action. Here, B_1 is the point of tangency of the tip of the driven profile γ–γ with the driving profile β–β; B_2 is the point of tangency of the tip of the driving profile β–β with the driven profile γ–γ. The pressure angles at points B_1 and B_2 are determined by the equations

$$\tan \alpha_{b1} = \frac{(r_{b1} + r_{b2}) \tan \alpha - r_{b2} \tan \alpha_{a2}}{r_{b1}}$$

$$= \tan \alpha - \frac{N_2}{N_1}(\tan \alpha_{a2} - \tan \alpha) \tag{10.7.4}$$

$$\tan \alpha_{b2} = \tan \alpha - \frac{N_1}{N_2}(\tan \alpha_{a1} - \tan \alpha) \tag{10.7.5}$$

where α_{ai} $(i = 1, 2)$ is the pressure angle at the tip of the involute profile (at the point of intersection of the involute profile with the addendum circle).

(iii) The interference will be avoided if the following inequality is observed:

$$\alpha_{Gi} \leq \alpha_{bi} \qquad (i = 1, 2). \tag{10.7.6}$$
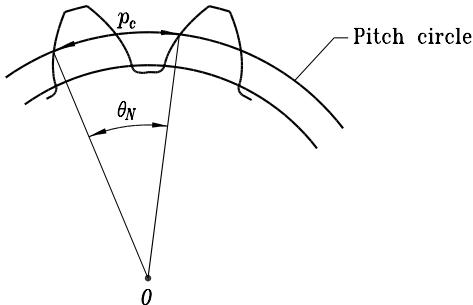
10.8 CONTACT RATIO

The contact ratio is an important criterion of load distribution between the teeth that are in mesh. We start the discussion with the definition of *angular pitch*, which is the angle θ_N that corresponds to the circular pitch p_c. Here (Fig. 10.8.1),

$$\theta_{Ni} = \frac{p_c}{r_{pi}} = \frac{2 p_c P}{N_i} = \frac{2\pi}{N_i} \qquad (i = 1, 2). \tag{10.8.1}$$

Figure 10.7.1 shows the tooth profiles β–β and γ–γ at three positions of meshing. Points B_1 and B_2 indicate the points of contact at the line of action in the *beginning* and at the *end* of meshing for the same pair of profiles, respectively. These points have been obtained as points of intersection of the line of action with (i) the gear addendum circle (point B_1), and (ii) the pinion addendum circle (point B_2). Point M is the current point of tangency of the tooth profiles.

Let us now consider the angles of rotation of mating gears for the *cycle* of meshing when one pair of profiles starts and finishes the meshing. It is evident that the pinion and gear angles of rotation for the cycle are $B_1\widehat{O_1}B_2$ and $B_1\widehat{O_2}B_2$, respectively. The tangency of neighboring tooth profiles is a continuous process if

$$B_1\widehat{O_1}B_2 \geq \frac{2\pi}{N_1}, \qquad B_1\widehat{O_2}B_2 \geq \frac{2\pi}{N_2}.$$

The contact ratio is represented by the equation

$$m_c = \frac{B_1\widehat{O_i}B_2}{\theta_{Ni}} \qquad (i = 1, 2). \tag{10.8.2}$$

Another representation of the contact ratio is based on the equation

$$m_c = \frac{l}{p_b} = \frac{l}{p_c \cos\alpha_c} = \frac{Pl}{\pi \cos\alpha_c} \tag{10.8.3}$$

where $l = B_1 B_2$ is the length of the working part of the line of action – the displacement of the contact point along the line of action during the cycle of meshing; p_b is the distance between the neighboring tooth profiles that is measured along their common normal.

Using Fig. 10.7.1, we obtain

$$KB_2 + B_1L = KL + l. \tag{10.8.4}$$

Thus,

$$l = KB_2 + B_1L - KL = \left(r_{a1}^2 - r_{b1}^2\right)^{\frac{1}{2}} + \left(r_{a2}^2 - r_{b2}^2\right)^{\frac{1}{2}} - E \sin \alpha \qquad (10.8.5)$$

or

$$l = r_{b1} \tan \alpha_{a1} + r_{b2} \tan \alpha_{a2} - (r_{b1} + r_{b2}) \tan \alpha. \qquad (10.8.6)$$

Thus, we can obtain two alternative expressions for m_c,

$$m_c = P \frac{\left(r_{a1}^2 - r_{b1}^2\right)^{\frac{1}{2}} + \left(r_{a2}^2 - r_{b2}^2\right)^{\frac{1}{2}} - E \sin \alpha}{\pi \cos \alpha_c} \qquad (10.8.7)$$

and

$$m_c = \frac{N_1(\tan \alpha_{a1} - \tan \alpha) + N_2(\tan \alpha_{a2} - \tan \alpha)}{2\pi} \qquad (10.8.8)$$
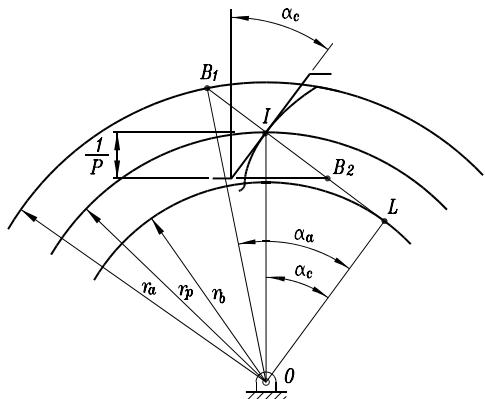
where

$$\cos \alpha_{ai} = \frac{r_{bi}}{r_{ai}} = \frac{N_i \cos \alpha_c}{2P r_{ai}} \qquad (i = 1, 2).$$

We must emphasize that $\alpha \neq \alpha_c$ if $E \neq (N_1 + N_2)/2P$ [see Eq. (10.9.16)]. The contact ratio increases as the number of teeth N_1 and N_2 increases. A pinion has the largest value of m_c when N_2 approaches infinity and the gear is a rack (see Problem 10.8.1). A high contact ratio can be obtained for a gear drive with teeth of increased height. In the case of an error of the base pitch p_b, the contact ratio is equal to 1, and the transfer of meshing is accompanied with a stroke.

Problem 10.8.1
Determine the contact ratio for a drive formed by a gear and a rack (Fig. 10.8.2). Given: the number N of gear teeth; $r_a = r_p + 1/P$; the rack addendum is $1/P$. Determine (i) the length $l = B_1 B_2$ of the working length of the line of action, and (ii) the contact ratio.

Figure 10.8.2: For derivation of contact ratio.

Solution

(i)

$$l = \frac{1}{P}\left[\frac{N\cos\alpha_c}{2}(\tan\alpha_a - \tan\alpha_c) + \frac{1}{\sin\alpha_c}\right]$$

where

$$\cos\alpha_a = \frac{r_b}{r_a} = \frac{N\cos\alpha_c}{N+2}.$$

(ii)

$$m_c = \frac{1}{\pi}\left[\frac{N(\tan\alpha_a - \tan\alpha_c)}{2} + \frac{2}{\sin 2\alpha_c}\right].$$

10.9 NONSTANDARD GEARS
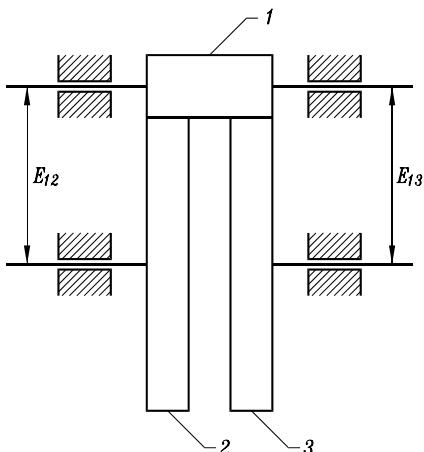
Nonstandard gears are applied in the following cases:

(1) To avoid undercutting of the pinion with the tooth number $N < 2/\sin^2\alpha_c$
(2) To obtain the contact ratio $m_c \geq 2$ by increasing the tooth height
(3) To design a gear train with a specific value of center distance
(4) To increase the tooth thickness and reduce the bending stresses.
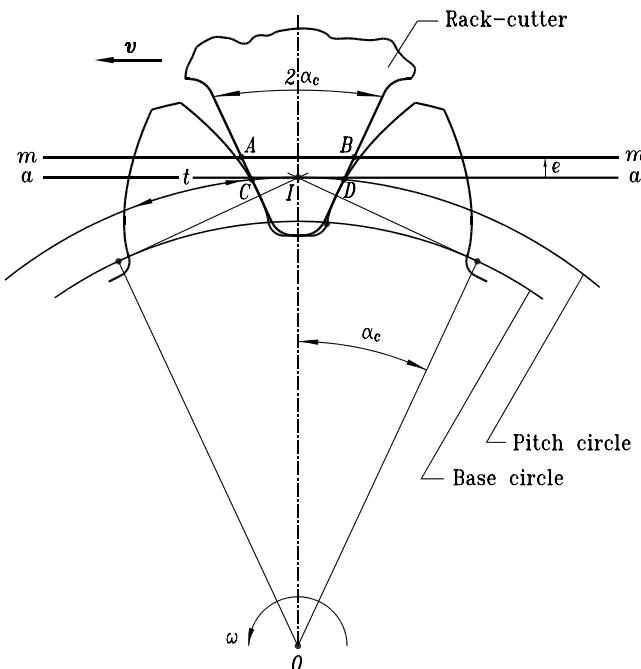
Nonstandard gears are generated by a standardized tool used for generation of standard gears but with modified settings of the tool with respect to the gear being generated.

The need for a specific value of the center distance for a gear train is illustrated in Fig. 10.9.1. Gears 1, 2, and 3 have the same circular pitch p_c, $N_2 \neq N_3$, but the center distance E_{12} must be equal to the center distance E_{13}. The requirement that $E_{12} = E_{13}$ can be observed if one of the two gears (2 or 3) is designed as a nonstandard gear, with a changed tooth thickness.

We recall that when a non-conventional setting of the rack-cutter is applied, its middle-line m–m is displaced at the distance e with respect to the tangent a–a to the pitch

Figure 10.9.1: Application of nonstandard gears in a gear train.

Figure 10.9.2: Non-conventional setting of rack-cutter.

circle (Fig. 10.9.2). The displacement e is performed perpendicular to $\mathbf{v}$ and must be considered as an algebraic value: $e > 0$ if the displacement is performed *outward* from the gear center O; $e < 0$ if the displacement is performed *toward* O; a conventional setting of the rack-cutter means that $e = 0$. The gear and rack-cutter centrodes are the same for all three types of rack-cutter setting (with $e > 0$, $e < 0$, and $e = 0$) because the same ratio v/ω is observed for the gear generation. A non-conventional setting of the rack-cutter results in a change of tooth thickness of the gear being generated: the space width is *decreased* and tooth thickness is *increased* if $e > 0$.

There are two systems of nonstandard gears:

(a) the *Long–Short Addendum System* that is characterized with the relation $e_p + e_g = 0$

(b) the *General Nonstandard Gear System* that is characterized with the relation $e_p + e_g \neq 0$.

The subscripts "p" and "g" indicate the rack-cutter displacements for pinion and gear generation, respectively.

Long–Short Addendum System
The main features of the system are as follows:

(i) $e_p + e_g = 0$, which means that the absolute values of the rack-cutter displacements e_p and e_g are the same but are performed in *opposite* directions with respect to the centers of the pinion and the gear, O_p and O_g.

(ii) The pressure angle is $\alpha = \alpha_c$.

(iii) The center distance is $E = (N_1 + N_2)/2P$.

(iv) The pinion and gear tooth thicknesses that are measured on the pitch circles differ from the standard ones.

(v) The pinion and gear addendums and dedendums differ from the standard ones.

(vi) The pinion and gear centrodes coincide with their pitch circles.

The discussed nonstandard system can be applied if the following inequality is observed:

$$N_p + N_g \geq 2N_{\min} = \frac{4}{\sin^2 \alpha_c}. \qquad (10.9.1)$$

This statement may be proven with the following considerations:

(i) The undercutting of the pinion and the gear can be avoided if [see expression (10.5.7)]

$$e_p \geq \frac{N_{\min} - N_p}{P N_{\min}} \qquad (10.9.2)$$

$$e_g \geq \frac{N_{\min} - N_g}{P N_{\min}}. \qquad (10.9.3)$$

(ii) Taking into account that $e_p + e_g = 0$, we obtain inequality (10.9.1).

Long–Short Addendum System: Computational Procedure

We assume (a) the pinion tooth number is $N_p < N_{\min}$, thus the pinion tooth undercutting must be avoided; and (b) the sum of the numbers of gear and pinion teeth is (Fig. 10.9.3)

$$N_p + N_g \geq 2N_{\min}.$$

Step 1: Determination of rack-cutter settings:

$$e_p = \frac{N_{\min} - N_p}{P N_{\min}} \qquad (10.9.4)$$

$$e_g = -e_p. \qquad (10.9.5)$$
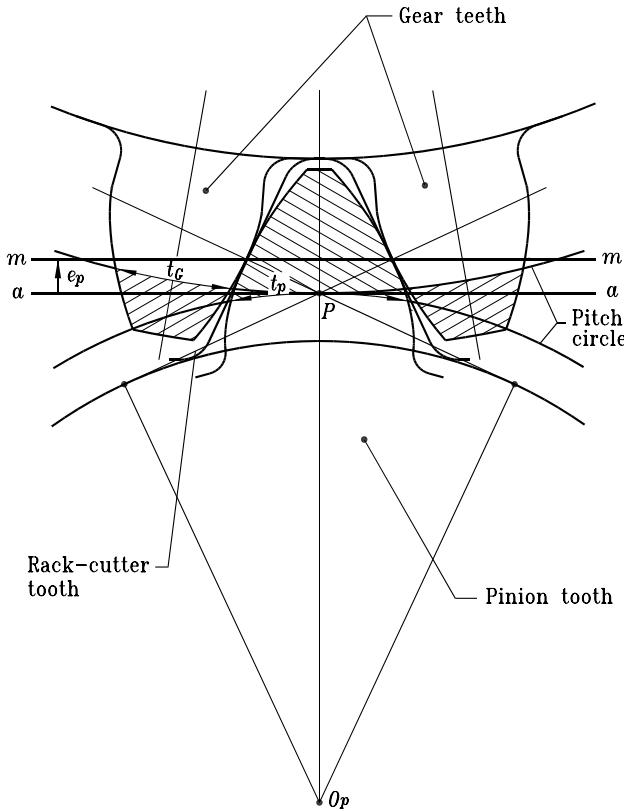
Step 2: Determination of tooth thicknesses on the pitch circle:

$$t_p = \frac{\pi}{2P} + 2e_p \tan \alpha_c \qquad (10.9.6)$$

$$t_g = \frac{\pi}{2P} + 2e_g \tan \alpha_c. \qquad (10.9.7)$$

It is easy to prove that

$$t_p = w_g$$

Figure 10.9.3: Long–short addendum system.

where w_g is the gear space width. This comes from the relations

$$w_g = p_c - t_g = \frac{\pi}{P} - \left(\frac{\pi}{2P} + 2e_g \tan \alpha_c \right)$$

$$= \frac{\pi}{2P} - 2e_g \tan \alpha_c = \frac{\pi}{2P} + 2e_p \tan \alpha_c.$$

because $e_g = -e_p$. Due to the relations

$$t_p = w_g, \qquad t_g = w_p,$$

the pinion and the gear may be assembled with a standard center distance

$$E = r_p + r_g = \frac{N_p}{2P} + \frac{N_g}{2P}. \tag{10.9.8}$$

Step 3: Determination of pinion and gear dedendums:

(a) for coarse diametral pitches (P from 1 up to 20)

$$b_p = \frac{1.250}{P} - e_p \tag{10.9.9}$$

$$b_g = \frac{1.250}{P} - e_g \tag{10.9.10}$$

(b) for fine diametral pitches (for $P = 20$–200)

$$b_p = \frac{1.200}{P} + 0.002 - e_p \tag{10.9.11}$$

$$b_g = \frac{1.200}{P} + 0.002 - e_g. \tag{10.9.12}$$

Step 4: Determination of pinion and gear addendums:

$$a_p = \frac{1}{P} + e_p \tag{10.9.13}$$

$$a_g = \frac{1}{P} + e_g. \tag{10.9.14}$$

General Nonstandard Gear System: Computational Procedure

The main features of this system are as follows: (i) $e_p + e_g \neq 0$; (ii) the center distance is $E' \neq \frac{N_1 + N_2}{2P}$; (iii) the pressure angle is $\alpha \neq \alpha_c$; (iv) the gear centrodes differ from pitch circles; and (v) the tooth element proportions and tooth thicknesses are modified. There is a particular case when one of the mating gears (say, the gear with tooth number N_g) is generated with the conventional setting of the rack-cutter ($e_g = 0$ but $e_p \neq 0$).

Step 1: Determination of the pressure angle α.

The pressure angle α is represented by the equation

$$\text{inv } \alpha = \text{inv } \alpha_c + \frac{2(e_p + e_g)P}{N_p + N_g} \tan \alpha_c. \tag{10.9.15}$$

The derivation of Eq. (10.9.15) is based on the following considerations:

(i) The pinion tooth thickness on the pitch circle is [see Eq. (10.6.10)]

$$t_p = \frac{\pi}{2P} + 2e_p \tan \alpha_c. \tag{10.9.16}$$

(ii) The pinion tooth thickness on the pinion centrode, the pinion operating pitch circle, is designated by t'_p (Fig. 10.9.4) and may be determined as [see Eq. (10.6.6) and Fig. 10.9.4]

$$\frac{t'_p}{r'_p} = \frac{t_p}{r_p} - 2(\text{inv } \alpha - \text{inv } \alpha_c)$$

$$= \frac{\pi + 4e_p P \tan \alpha_c}{N_p} - 2(\text{inv } \alpha - \text{inv } \alpha_c). \tag{10.9.17}$$

(iii) Similarly, using Fig. 10.9.5, we obtain

$$\frac{w'_g}{r'_g} = \frac{\pi - 4e_g P \tan \alpha_c}{N_g} + 2(\text{inv } \alpha - \text{inv } \alpha_c) \tag{10.9.18}$$

where w'_g is the gear space width on the gear centrode of radius r'_g. Here, r'_g is the expected centrode radius of the gear. Centrodes of radii r'_p and r'_g roll over each other and $t'_p = w'_g$. Consequently,

$$\frac{t'_p}{r'_p} : \frac{w'_g}{r'_g} = \frac{r'_g}{r'_p} = \frac{N_g}{N_p} = m_{pg} \tag{10.9.19}$$
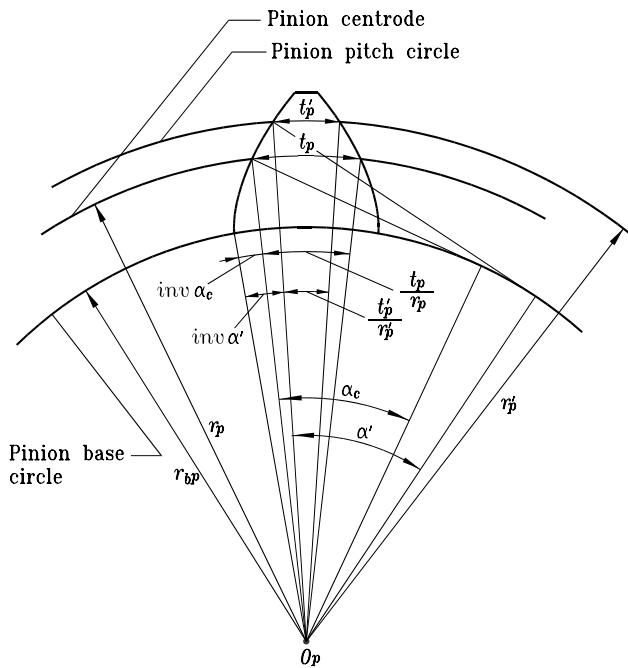
**Figure 10.9.4:** Tooth thickness on pinion centrode.
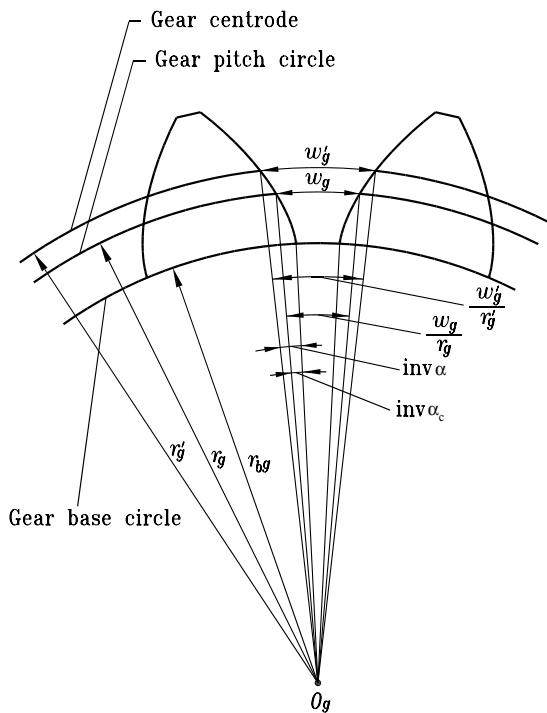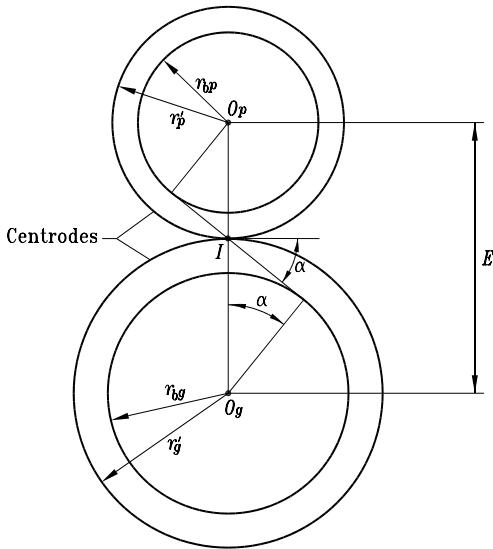
**Figure 10.9.5:** Space width on gear centrode.

Figure 10.9.6: Gear centrodes of nonstandard gears.

where m_{pg} is the angular velocity ratio by transformation of motion from the pinion to the gear. Equations (10.9.17), (10.9.18), and (10.9.19) yield Eq. (10.9.15).

Step 2: Determination of operating center distance. Figure 10.9.6 shows the pinion and gear assembled with operating center distance E' and operating pressure angle α. It is evident that

$$E' = r'_p + r'_g = \frac{r_{bp}}{\cos \alpha} + \frac{r_{bg}}{\cos \alpha} = \frac{(r_p + r_g)\cos \alpha_c}{\cos \alpha}$$

$$= \frac{(N_p + N_g)\cos \alpha_c}{2P \cos \alpha}. \tag{10.9.20}$$

It is easy to verify that [see Eq. (10.9.15)] $\alpha = \alpha_c$ with $e_p + e_g = 0$. In this case Eq. (10.9.20) yields that

$$E' = \frac{N_p + N_g}{2P}.$$

NOTE. the gear centrodes differ from the pitch circles and are determined as

$$r'_p = \frac{r_{b1}}{\cos \alpha}, \quad r'_g = \frac{r_{b2}}{\cos \alpha} \quad (\alpha \neq \alpha_c). \tag{10.9.21}$$
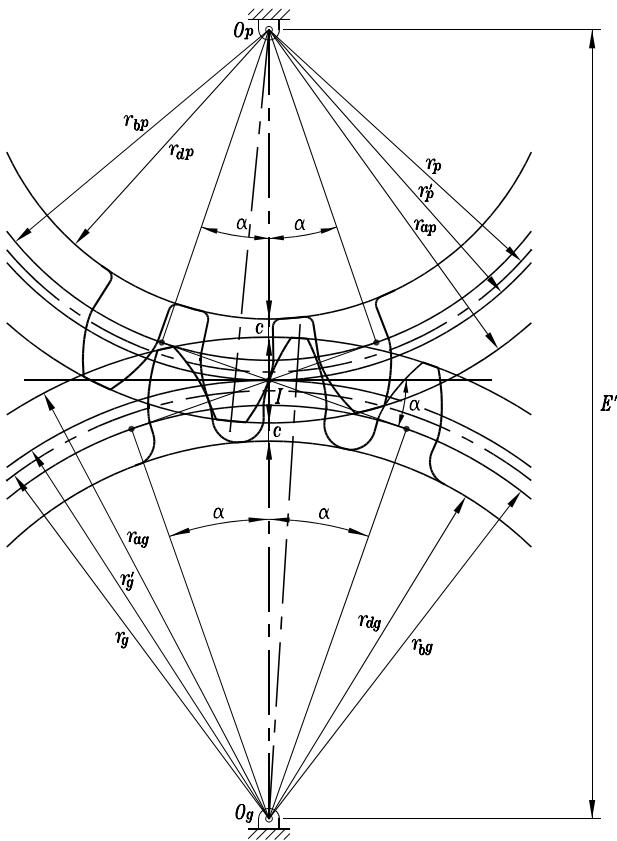
Step 3: Determination of radii of dedendum circles:

$$r_{di} = r_i - b + e_i \quad (i = p, g). \tag{10.9.22}$$

Here, b is the rack-cutter addendum represented as:

$$b = \frac{1.250}{P} \text{ (in inches) for coarse diametral pitches } (P \text{ from 1 up to 20});$$

$$b = \frac{1.200}{P} + 0.002 \text{ (in inches) for fine pitches.}$$

Figure 10.9.7: For derivation of the addendum radii of pinion and gear.

Step 4: Determination of radii of addendum circles.

The following derivations are directed at the observation of the standardized clearance c between the addendum circle of one gear and the dedendum circle of the other one. This requirement can be observed with the following equations (Fig. 10.9.7):

$$r_{ap} + r_{dg} + c = E', \qquad r_{ag} + r_{dp} + c = E'. \tag{10.9.23}$$

Equations (10.9.23) yield
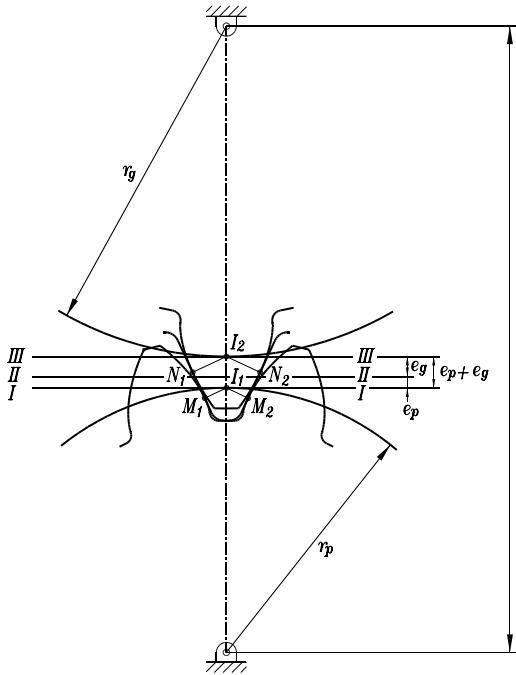
$$r_{ap} = E' - r_{dg} - c \tag{10.9.24}$$

$$r_{ag} = E' - r_{dp} - c. \tag{10.9.25}$$

The clearance is $c = 0.250/P$ for coarse pitch gears ($P < 20$) and $c = 0.200/P + 0.002$ in. for fine pitch gears ($P \geq 20$).

The observation of the standardized value of clearance is accompanied with the reduction of tooth height h in the case of a general nonstandard gear system. The derivation of h is based on the following equations (Fig. 10.9.7):

$$E' = r_{dp} + r_{dg} + h + c = r_{dp} + r_{dg} + h + (b - a). \tag{10.9.26}$$

Figure 10.9.8: Visualization of sum of settings $(e_p + e_g)$.

Here, r_{dp} and r_{dg} are represented by Eq. (10.9.22); a and b are the dedendum and addendum of the rack-cutter. We may represent Eq. (10.9.26) as

$$E' = E + \Delta E = r_p + r_g + \Delta E = \frac{N_p + N_g}{2P} + \Delta E \qquad (10.9.27)$$

where ΔE is the change of standard center distance E.

Equations (10.9.26), (10.9.22), and (10.9.27) yield

$$h = h_o - [(e_p + e_g) - \Delta E] \qquad (10.9.28)$$

where $h_o = a + b$ is the conventional tooth height. It may be proven that $e_p + e_g > \Delta E$. Figure 10.9.8 shows nonstandard gears that have been generated with the displacements of the rack-cutter e_p and e_g and then assembled with the center distance

$$E' = (r_p + r_g) + (e_p + e_g) = E + (e_p + e_g).$$

The rack-cutter is simultaneously in tangency with the pinion and the gear. Points I_1 and I_2 are the instantaneous centers of rotation of the rack-cutter with the pinion and the gear, respectively. The pinion and gear pitch circles are the centrodes in the process of meshing of the rack-cutter and the pinion and gear. Points M_1 and M_2, and N_1 and N_2, respectively, are the points of tangency of the rack-cutter with the pinion and the gear. However, the pinion and gear tooth profiles are not in tangency if the gears are assembled with the center distance

$$E' = r_p + r_g + e_p + e_g = \frac{N_1 + N_2}{2P} + \Delta E$$

where

$$\Delta E = e_p + e_g.$$

The gear tooth profiles will be in tangency if the center distance E' satisfies Eqs. (10.9.20) and (10.9.15). These equations provide $\Delta E < e_p + e_g$. This means [see Eq. (10.9.28)] that $h < h_o$, and generally the tooth height of nonstandard gears is less than the tooth height of standard gears. However, the tooth height of nonstandard gears is the same as that of standard gears if $e_p + e_g = 0$, as in the case of the long–short addendum system.

11 Internal Involute Gears

11.1 INTRODUCTION
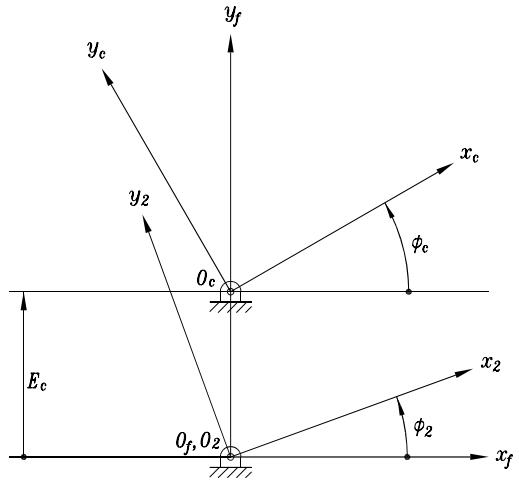
A gear drive composed of external and internal gears is considered. Application of such a train enables us to reduce the loss of power caused by sliding of tooth profiles. This effect is the result of the reduction of the relative angular velocity $\boldsymbol{\omega}^{(12)} = \boldsymbol{\omega}^{(1)} - \boldsymbol{\omega}^{(2)}$, where $|\boldsymbol{\omega}^{(12)}| = |\boldsymbol{\omega}^{(1)} - \boldsymbol{\omega}^{(2)}|$. (Recall that the gears perform rotation in the *same* direction). However, a high reduction of $|\boldsymbol{\omega}^{(12)}|$ requires a small difference ΔN of the numbers of teeth of the pinion and the internal gear. The possible interference of tooth profiles by the gear assembly, and the undercutting of the internal gear in the process of generation, should be investigated before designation of the desired value of ΔN. Another advantage of application of an internal gear train is the possibility of reducing the dimensions of the train. Trains with internal gears are applied in planetary transmissions, in transmissions of cranes, in excavators, and so on.

The problems of undercutting of internal involute spur gears in the process of generation and interference by their assembly with pinions have been studied by several researchers. The phenomenon of undercutting of internal involute gears was first discussed by Schreier [1961]. Polder [1991] has extended this research and contributed the idea of the envelope to a family of extended hypocycloids. Dudley [1962] has considered the interference for the cases of axial and radial assembly of an internal gear with the mating pinion and has published useful tables for the determination of the minimal difference $(N_2 - N_1)$, where N_2 and N_1 are the numbers of gear and pinion teeth, respectively.

The solutions to the problems discussed in this chapter are based on research by Litvin, Hsiao, Wang, and Zhou [1994] and cover the following:

(i) The kinematics of the process for generation of the gear fillet as a pseudohypocycloid, ordinary extended hypocycloid, and an envelope to the family of ordinary extended hypocycloids

(ii) Investigation of interference by radial assembly of the gear and pinion that is based on a tooth contact analysis (TCA) program for simulation of meshing.

The term pseudohypocycloid means that the generation of the gear fillet is performed with the following conditions: (a) the center distance E_c between the axes of rotation of the shaper and the internal gear is not constant; and (b) E_c and the angle of rotation of the gear, ϕ_2, are related by function $E_c(\phi_2)$ that simulates the radial feed motion of

Figure 11.2.1: Applied coordinate systems.

the shaper in the process of generation. The research mentioned above was performed for pressure angles of 20°, 25°, and 30°.

11.2 GENERATION OF GEAR FILLET

Consider coordinate systems S_c, S_2, and S_f that are rigidly connected to the cutter (shaper), the gear being generated, and the frame of the cutting machine, respectively (Fig. 11.2.1). Angles ϕ_c and ϕ_2 of rotation of the cutter and the gear are related with the equation
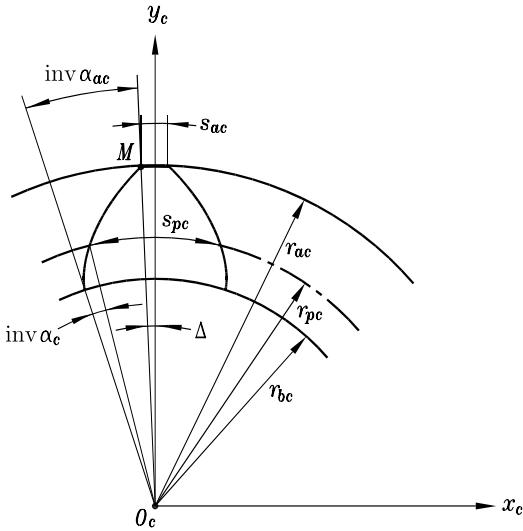
$$m_{c2} = \frac{\phi_c}{\phi_2} = \frac{N_2}{N_c}. \tag{11.2.1}$$

The center distance E_c is considered either constant or varied due to the following cases of generation:

(1) *Case 1, axial generation.* The center distance E_c is constant, and the cutter performs a reciprocative motion that is parallel to the gear axis. In this case

$$E_c = r_{p2} - r_{pc} = \frac{N_2 - N_c}{2P}. \tag{11.2.2}$$

(2) *Case 2, axial–radial generation.* The cutter performs the reciprocating motion described above as well as the continuous radial motion that is perpendicular to the axes of the cutter and the gear. The varied center distance in this case is represented by linear function $E_c(\phi_2)$.

(3) *Case 3, axial and step-by-step radial generation.* It is assumed that the generation of the internal gear is performed by k steps. During each step the center distance E_c is constant, and the angles of rotation are related to Eq. (11.2.1). The center distance E_c is installed as the minimal at the first step, and as the maximal at the kth step.

Figure 11.2.2: Representation of generating point.

In all the cases above, the gear root curve is generated in S_2 by the tip point M of the cutter (Fig. 11.2.2) and can be represented analytically by the following matrix equation:

$$\mathbf{r}_2^{(M)}(\phi_2, E_c) = \mathbf{M}_{2c}(\phi_2, E_c)\,\mathbf{r}_c^{(M)}. \tag{11.2.3}$$

Here,

$$\mathbf{M}_{2c} = \mathbf{M}_{2f}\mathbf{M}_{fc} = \begin{bmatrix} \cos(\phi_c - \phi_2) & -\sin(\phi_c - \phi_2) & 0 & E_c \sin\phi_2 \\ \sin(\phi_c - \phi_2) & \cos(\phi_c - \phi_2) & 0 & E_c \cos\phi_2 \\ 0 & 0 & 1 & 0 \\ 0 & 0 & 0 & 1 \end{bmatrix} \tag{11.2.4}$$

$$\mathbf{r}_c^{(M)} = r_{ac}[-\sin\Delta \quad \cos\Delta \quad 0 \quad 1]^{\mathrm{T}} \tag{11.2.5}$$

where

$$\Delta = \frac{s_{ac}}{2r_{ac}}. \tag{11.2.6}$$

Using Fig. 11.2.2, we can determine the following relations between the tooth element parameters of the shaper (see Nomenclature at the end of this chapter):

$$\frac{s_{ac}}{2r_{ac}} = \frac{s_{pc}}{2r_{pc}} - (\operatorname{inv}\alpha_{ac} - \operatorname{inv}\alpha_c) \tag{11.2.7}$$

$$\cos\alpha_{ac} = \frac{r_{bc}}{r_{ac}} = \frac{N_c \cos\alpha_c}{2r_{ac}P} \tag{11.2.8}$$

$$\operatorname{inv}\alpha_{ac} = \tan\alpha_{ac} - \alpha_{ac} \tag{11.2.9}$$

$$\cos\alpha_c = \frac{r_{bc}}{r_{pc}} = \frac{2r_{bc}P}{N_c}. \tag{11.2.10}$$

In the case of standard gears, we have

$$r_{ac} = \frac{N_c + 2.5}{2P}, \quad r_{pc} = \frac{N_c}{2P}, \quad r_{bc} = \frac{N_c}{2P}\cos\alpha_c, \quad s_{pc} = \frac{\pi}{2P}.$$

Equations (11.2.3), (11.2.4), and (11.2.5) yield

$$\mathbf{r}_2^{(M)}(\phi_2, E_c) = (-r_{ac}\sin(\phi_c - \phi_2 + \Delta) + E_c\sin\phi_2)\mathbf{i}_2$$
$$+ (r_{ac}\cos(\phi_c - \phi_2 + \Delta) + E_c\cos\phi_2)\mathbf{j}_2 \tag{11.2.11}$$

where $\phi_c = \phi_2(N_2/N_c)$.

Using vector-function $\mathbf{r}_2^{(M)}(\phi_2, E_c)$, we can represent the gear fillet for all three cases discussed above: (i) as an ordinary extended hypocycloid, (ii) as a pseudohypocycloid, and (iii) as an envelope to the family of ordinary extended hypocycloids (see below). Undercutting of the gear tooth profile is the result of intersection of the gear fillet with the working part of the gear tooth profile. The investigation of undercutting will be considered in Section 11.3 for these three cases.

Ordinary Extended Hypocycloid

The gear fillet is determined by Eq. (11.2.11) while considering that E_c is constant and is represented by Eq. (11.2.2).

Pseudohypocycloid

We consider that the center distance E_c is continuously varied in the process of generation. Function $E_c(\phi_c)$ is linear because only a linear relation between ϕ_c (or ϕ_2) and E_c can be provided by the transmission of the cutting machine. The pseudohypocycloid is represented by Eq. (11.2.11) while considering that the varied center distance E_c is represented as a linear function with respect to ϕ_2:

$$E_c(\phi_2) = E_c^{(1)} + \frac{2.25}{2P\pi a}\phi_2. \tag{11.2.12}$$

Here, $E_c^{(1)} = E_c(0)$ is the initial value of the center distance represented by

$$E_c^{(1)} = r_{a2} - r_{ac} = \left(r_{p2} - \frac{1}{P}\right) - \left(r_{pc} + \frac{1.25}{P}\right) = \frac{N_2 - N_c}{2P} - \frac{2.25}{P}. \tag{11.2.13}$$

Parameter a in Eq. (11.2.12) is the number of revolutions of gear 2 that will be performed for the whole process of generation.

The derivation of Eq. (11.2.12) is based on the following considerations:
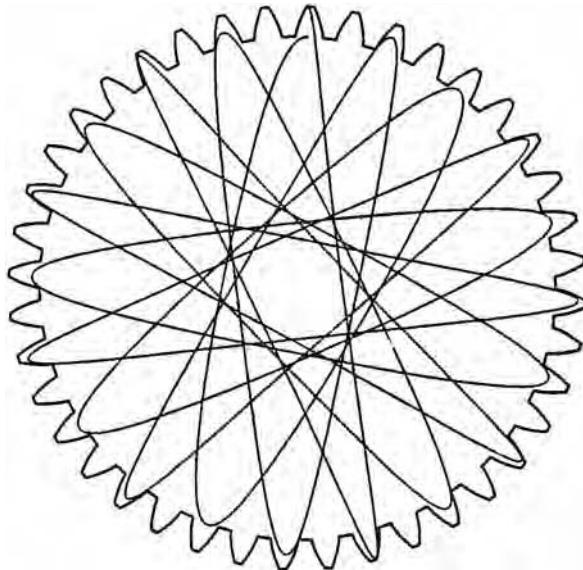
(i) The final value of $E_c(\phi_2)$ is

$$E_c^{(2)} = E_c(2\pi a) = r_{p2} - r_{pc} = \frac{N_2 - N_c}{2P}. \tag{11.2.14}$$

(ii) It is obvious that

$$\frac{E_c(\phi_2) - E_c^{(1)}}{E_c^{(2)} - E_c^{(1)}} = \frac{\phi_2}{2\pi a}. \tag{11.2.15}$$

(iii) Equations from (11.2.13) to (11.2.15) confirm Eq. (11.2.12).

Figure 11.2.3: Pseudohypocycloid.

The pseudohypocycloid is shown in Fig. 11.2.3. We emphasize that the initial and final points of the generated pseudohypocycloid are located in the same gear space as shown in Fig. 11.2.3 if the following conditions are observed: (i) the gear and the shaper perform a whole number of revolutions, a and b, during the process of generation; and (ii) a and b satisfy the equation

$$\frac{a}{b} = \frac{\phi_2}{\phi_c} = \frac{N_c}{N_2}.$$

(11.2.16)

Envelope to Family of Extended Hypocycloids
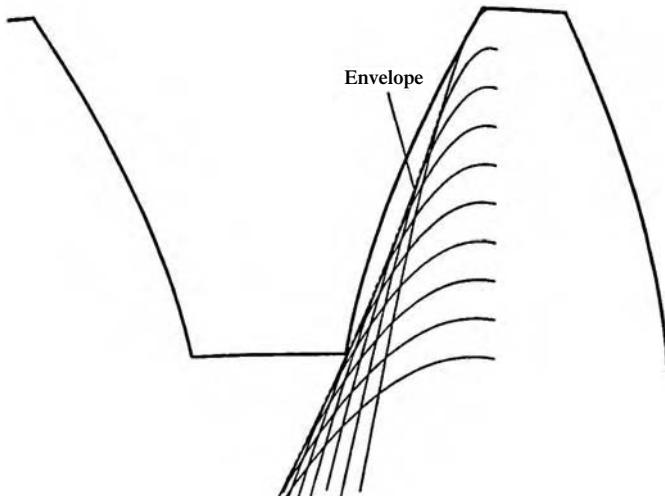
We consider that the internal gear is generated by k steps and the center distance E_c is constant at each step, but the magnitude of E_c for each step is different and is in the range $E_c^{(1)} \leq E_c \leq E_c^{(2)}$. Equation (11.2.11) with the conditions above represents a family of extended hypocycloids (Fig. 11.2.4). We interpret Eq. (11.2.11) as an equation with two independent parameters, ϕ_2 and E_c, where E_c is the parameter of the family of curves. Considering that the family of curves is represented in S_2 by the vector function $\mathbf{r}_2(\phi_2, E_c)$, we determine the envelope to the family of curves as (see Section 6.1)

$$\mathbf{r}_2 = \mathbf{r}_2^{(M)}(\phi_2, E_c), \qquad \frac{\partial \mathbf{r}_2}{\partial \phi_2} \times \frac{\partial \mathbf{r}_2}{\partial E_c} = 0.$$

(11.2.17)

Using Eqs. (11.2.11) and (11.2.17), we obtain the following equations of the envelope:

$$E_{x2} = \frac{r_{ac}}{N_c} \left[-N_c \sin(\phi_c + \Delta) \cos \phi_2 + N_2 \cos(\phi_c + \Delta) \sin \phi_2 \right]$$

$$E_{y2} = \frac{r_{ac}}{N_c} \left[N_c \sin(\phi_c + \Delta) \sin \phi_2 + N_2 \cos(\phi_c + \Delta) \cos \phi_2 \right]$$

(11.2.18)

Figure 11.2.4 shows the family of extended hypocycloids, the envelope to the family, and the location of these curves in the space of an internal involute gear.

Figure 11.2.4: Family of extended hypocycloids and their envelope.

11.3 CONDITIONS OF NONUNDERCUTTING

We consider the conditions of nonundercutting of the internal involute gear for two cases of generation: (i) axial generation when the center distance between the shaper and the gear is constant and installed as $E_c = E_c^{(2)}$, and (ii) parametric generation with two independent parameters ϕ_2 and E_c; E_c is changed (independently with respect to ϕ_2) in the range $E_c^{(1)} \le E_c \le E_c^{(2)}$. The conditions of nonundercutting are determined as conditions of nonintersection of the gear involute profile with the gear root curve.

Internal Gear Involute Profile
Figure 11.3.1 shows an involute profile represented in parametric form in an auxiliary coordinate system S_a; θ_i is the curve parameter. The derivation of equations of the involute profile is based on the relation that $MN = \widehat{M_0 N}$ (see Chapter 10). Figure 11.3.2 shows the gear involute profile with the y_2 axis as the axis of symmetry of the space. The equation of the involute profile is
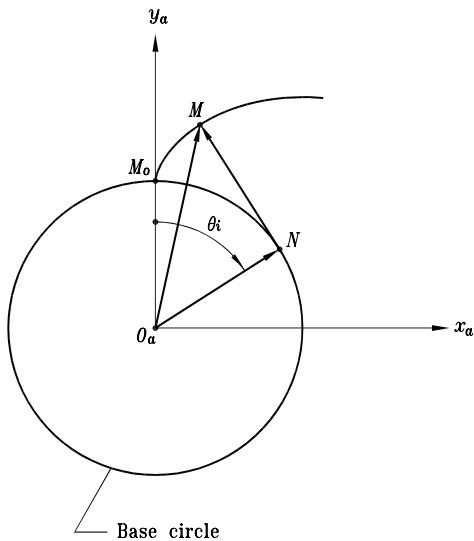
$$\mathbf{r}_2(\theta_2) = r_{b2} \begin{bmatrix} \sin(\theta_2 - q_2) - \theta_2 \cos(\theta_2 - q_2) \\ \cos(\theta_2 - q_2) + \theta_2 \sin(\theta_2 - q_2) \\ 0 \\ 1 \end{bmatrix} \qquad (11.3.1)$$

where
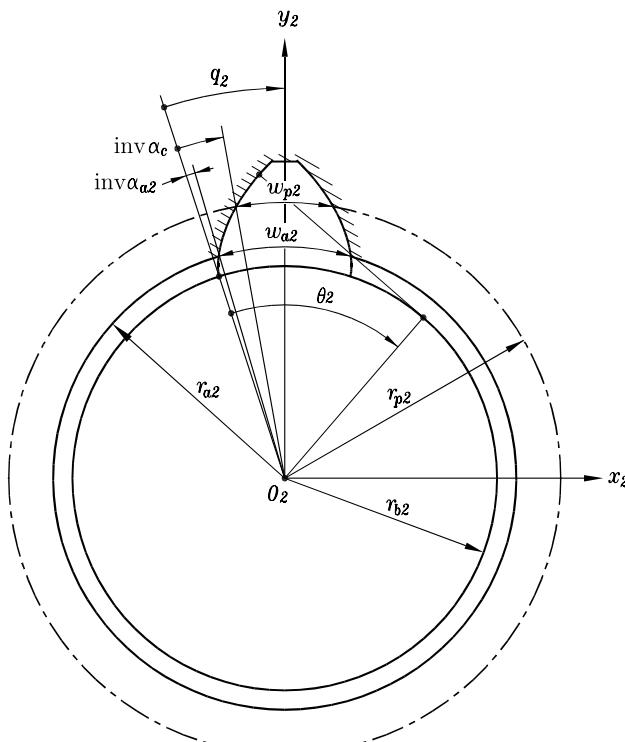
$$q_2 = \text{inv}\,\alpha_c + \frac{\pi}{2N_2}. \qquad (11.3.2)$$

For further derivations, we need the width w_{a2} of the space on the gear addendum circle. It is easy to verify that
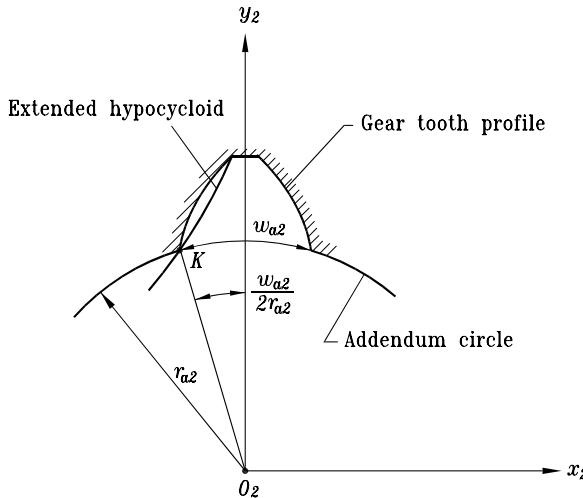
$$w_{a2} = 2r_{a2}(q_2 - \text{inv}\,\alpha_{a2}) \qquad (11.3.3)$$

Figure 11.3.1: Representation of involute profile in S_a.

Figure 11.3.2: Space of internal gear.

Figure 11.3.3: For determination of conditions of nonundercutting.

where

$$\cos \alpha_{a2} = \frac{r_{b2}}{r_{a2}} = \frac{N_2 \cos \alpha_c}{2 P r_{a2}} \tag{11.3.4}$$

$$\text{inv } \alpha_{a2} = \tan \alpha_{a2} - \alpha_{a2}. \tag{11.3.5}$$

Nonundercutting by Axial Generation
We consider the limiting case when the extended hypocycloid intersects the gear involute curve at the gear addendum circle. Coordinates of point K of the involute curve are represented as (Fig. 11.3.3)

$$x_2 = -r_{a2} \sin \left(\frac{w_{a2}}{2 r_{a2}} \right), \quad y_2 = r_{a2} \cos \left(\frac{w_{a2}}{2 r_{a2}} \right). \tag{11.3.6}$$

Using Eqs. (11.2.11), we represent the extended hypocycloid by the equations

$$x_2 = -r_{ac} \sin(\phi_c - \phi_2 + \Delta) + \frac{N_2 - N_c}{2P} \sin \phi_2$$

$$y_2 = r_{ac} \cos(\phi_c - \phi_2 + \Delta) + \frac{N_2 - N_c}{2P} \cos \phi_2 \tag{11.3.7}$$

where $\phi_c = \phi_2 \frac{N_2}{N_c}$.

Equations (11.3.6) and (11.3.7) represent a system of two nonlinear equations in unknowns ϕ_2, N_c (N_2 is given).

$$-r_{ac} \sin(\phi_c - \phi_2 + \Delta) + E_c \sin \phi_2 = -r_{a2} \sin \left(\frac{w_{a2}}{2 r_{a2}} \right)$$

$$r_{ac} \cos(\phi_c - \phi_2 + \Delta) + E_c \cos \phi_2 = r_{a2} \cos \left(\frac{w_{a2}}{2 r_{a2}} \right) \tag{11.3.8}$$

where

$$E_c = \frac{N_2 - N_c}{2P}.$$

The solution of this system for N_c determines the maximal number of cutter teeth allowed from the conditions of gear nonundercutting. The first guess for the solution is based on the following considerations:

Step 1: Transforming equation system (11.3.8), we obtain

$$\cos(\phi_c + \Delta) = \frac{r_{a2}^2 - r_{ac}^2 - E_c^2}{2E_c r_{ac}}. \qquad (11.3.9)$$
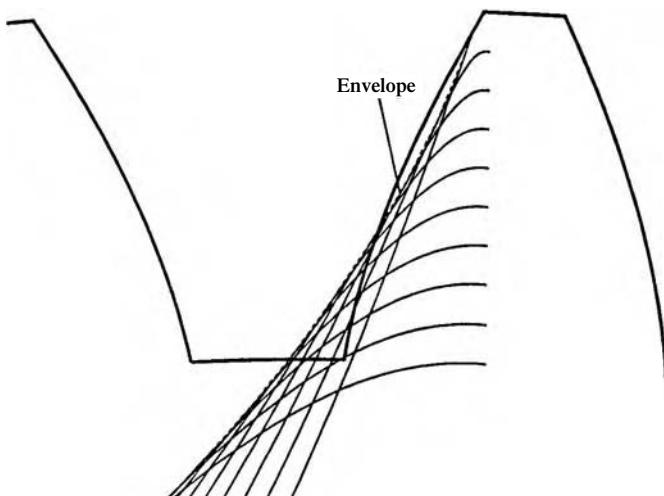
We take for the first guess that $N_c = 0.9N_2$ and determine ϕ_c from Eq. (11.3.9). Parameter ϕ_2 is determined as

$$\phi_2 = \phi_c \frac{N_c}{N_2}. \qquad (11.3.10)$$

Step 2: Knowing N_c, ϕ_c, and ϕ_2 for the first guess parameter, we can determine the exact solution of system (11.3.8) for N_c using a numerical method (see More *et al.* [1980] and Visual Numerics, Inc. [1998]).

Two-Parameter Generation

The generation of the internal gear is performed with the continuously varied value of E_c, and the gear root curve is determined as the envelope to the family of extended hypocycloids. Figure 11.3.4 shows the case when the envelope intersects the gear involute profile, and undercutting occurs. The limiting case of nonundercutting is when the envelope intersects the involute profile at point K (Fig. 11.3.3). Conditions of intersection at point K of the envelope and the involute profile yield the following system of two nonlinear equations formed by Eqs. (11.3.6) and (11.2.18) in the unknowns ϕ_2

Figure 11.3.4: Undercutting by two-parameter generation.

and N_c (N_2 is given):

$$\frac{r_{ac}}{N_c}[-N_c \sin(\phi_c + \Delta)\cos\phi_2 + N_2 \cos(\phi_c + \Delta)\sin\phi_2] = -r_{a2}\sin\left(\frac{w_{a2}}{2r_{a2}}\right)$$

$$\frac{r_{ac}}{N_c}[N_c \sin(\phi_c + \Delta)\sin\phi_2 + N_2 \cos(\phi_c + \Delta)\cos\phi_2] = r_{a2}\cos\left(\frac{w_{a2}}{2r_{a2}}\right).$$
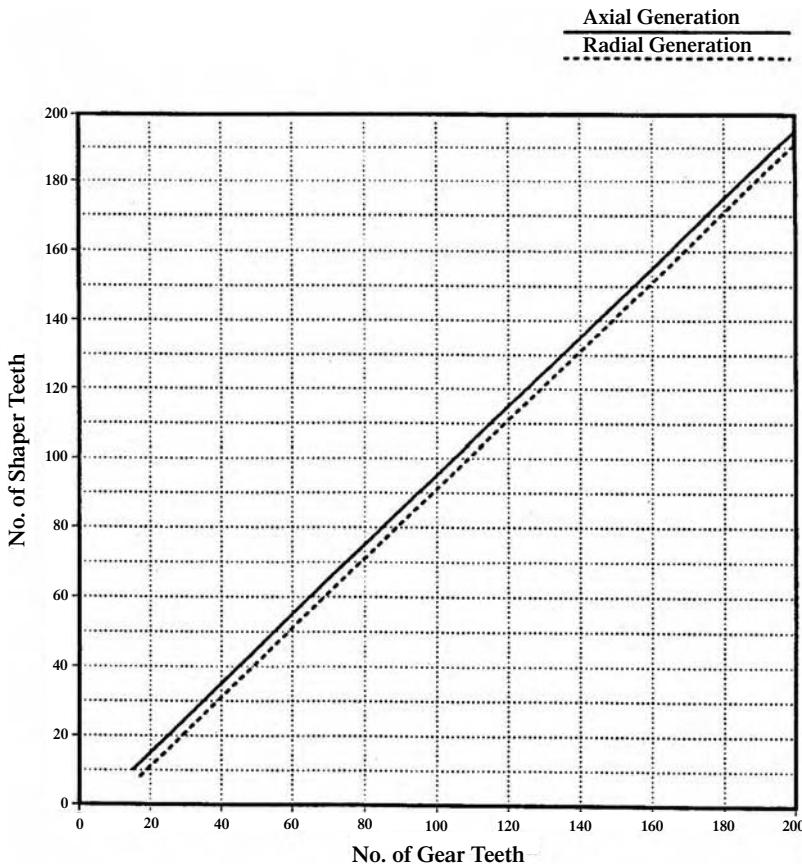
(11.3.11)

The first guess for the solution of system (11.3.11) is based on considerations similar to those previously discussed:

Step 1: Transforming equation system (11.3.11), we obtain

$$\cos^2(\phi_c + \Delta) = \frac{r_{a2}^2 - r_{ac}^2}{r_{ac}^2\left[\left(\frac{N_2}{N_c}\right)^2 - 1\right]}.$$

(11.3.12)

We take for the first guess $N_c = 0.8N_2$ and obtain $(\phi_c + \Delta)$ from Eq. (11.3.12). Parameter ϕ_2 is determined from Eq. (11.3.10).

Step 2: Knowing N_c, ϕ_c, and ϕ_2 for the first guess, and using the subroutine for the solutions of equation system (11.3.11), we can determine the exact solution for

Figure 11.3.5: Design chart for pressure angle $\alpha_c = 30°$.

Table 11.3.1: Maximal number of shaper teeth

Pressure angle	Generation method	Gear teeth	Shaper teeth
	Axial	$25 \leq N_2 \leq 31$	$N_c \leq 0.82 N_2 - 3.20$
$\alpha_c = 20°$	Axial	$32 \leq N_2 \leq 200$	$N_c \leq 1.004 N_2 - 9.162$
	Two-parameter	$36 \leq N_2 \leq 200$	$N_c \leq N_2 - 17.6$
	Axial	$17 \leq N_2 \leq 31$	$N_c \leq 0.97 N_2 - 5.40$
$\alpha_c = 25°$	Axial	$32 \leq N_2 \leq 200$	$N_c \leq N_2 - 6.00$
	Two-parameter	$23 \leq N_2 \leq 200$	$N_c \leq N_2 - 11.86$
$\alpha_c = 30°$	Axial	$15 \leq N_2 \leq 200$	$N_c \leq N_2 - 4.42$
	Two-parameter	$17 \leq N_2 \leq 200$	$N_c \leq N_2 - 8.78$

N_c. Computations based on the above algorithms allow us to develop charts for determination of the maximal number of shaper teeth, N_c, as a function of N_2 and the pressure angle α_c. An example of such a chart developed for axial generation and two-parameter generation is shown in Fig. 11.3.5. Table 11.3.1 (developed by Litvin *et al.* [1994]) allows us to determine the maximal number of shaper teeth for various pressure angles.

11.4 INTERFERENCE BY ASSEMBLY

We consider that the internal gear with the tooth number N_2 was generated by the shaper with tooth number N_c and the condition of nonundercutting was observed. Then, we consider that the internal gear is assembled with the pinion with the tooth number $N_1 > N_c$. The question is what is the limiting tooth number N_1 that allows us to avoid interference by assembly. Henceforth, we consider two possible cases of assembly – axial and radial.

Axial Assembly

Axial assembly is performed when the final center distance $E^{(2)} = (N_2 - N_1)/2P$ is initially installed and the pinion is put into mesh with the internal gear by the axial displacement of the pinion. Radial assembly means that the pinion is put into mesh with the internal gear by translational displacement along the center distance. The center distance E by the radial displacement of the pinion is changed from $(N_2 - N_1 - 4)/2P$ to $(N_2 - N_1)/2P$.

Interference in the axially assembled drive occurs if the tip of the pinion tooth generates in relative motion a trajectory that intersects the gear involute profile. The trajectory is an extended hypocycloid. The solution is based on the same approach that was applied for axial generation. The limiting number N_1 of pinion teeth is a little larger than N_c due to the lessened dimension of the pinion addendum in comparison with the shaper addendum.

Radial Assembly

The investigation of interference in the radial assembly is based on the following considerations:

(i) We represent in fixed coordinate system S_f equations of profiles of several gear spaces and pinion teeth by the following vector functions:

$$\mathbf{r}_f^{(2)}(\theta_2, j\delta_2, N_2), \quad \mathbf{r}_f^{(1)}(\theta_1, j\delta_1, E, N_1). \tag{11.4.1}$$

Here, θ_i is the parameter of the involute profile $(i = 1, 2)$; $\delta_i = (2\pi)/N_i$ is the angular pitch; j is the space (tooth) number; and E is the variable center distance that is installed by the assembly. The superscripts "1" and "2" indicate the pinion and the gear, respectively; N_2 is considered as given.
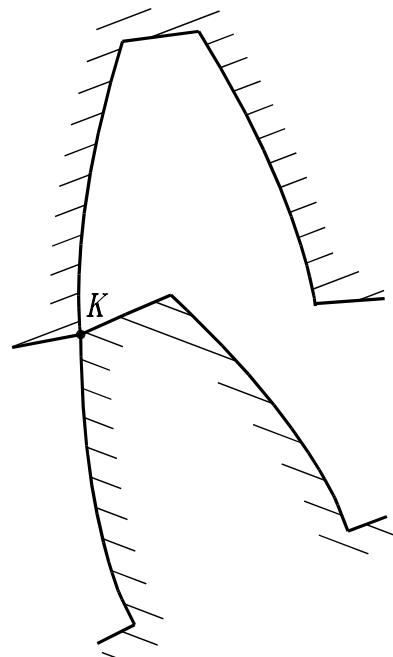
(ii) Interference of pinion and gear involute profiles occurs if

$$\mathbf{r}_f^{(2)}(\theta_2, j\delta_2, N_2) - \mathbf{r}_f^{(1)}(\theta_1, j\delta_1, E, N_1) = 0. \tag{11.4.2}$$
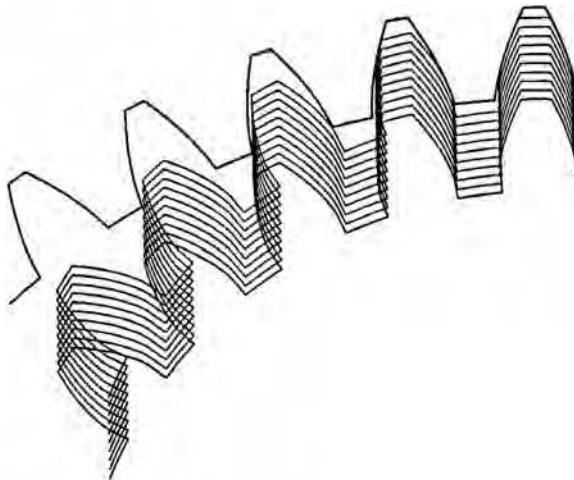
(iii) Equations (11.4.2) provide a system of two scalar equations

$$f_j(\theta_2, \theta_1, j\delta_2, j\delta_1, E, N_1, N_2) = 0 \quad (j = 0, 1, 2, \ldots, m). \tag{11.4.3}$$

We consider the most unfavorable case when the point of interference lies on the addendum circles of the pinion and the gear (Fig. 11.4.1), and therefore parameters θ_1 and θ_2 are known. We will determine (N_1, E) if the solution of equation system (11.4.3) exists. The solution for $N_1 = N_1^{(r)}$ determines the maximal number $N_1^{(r)}$ of the pinion that is allowed by radial assembly.

Figure 11.4.1: Interference by radial assembly.

Figure 11.4.2: Radial assembly.

After the gears are radially assembled and the final center distance $E^{(2)}$ is installed, the tip of the pinion generates an extended hypocycloid while the pinion and gear perform rotational motions. Interference of the hypocycloid with the gear involute profile is avoided by making the number of pinion teeth $N_1 \leq N_1^{(a)}$, where $N_1^{(a)}$ is the number of pinion teeth allowed by axial assembly. The designed number of pinion teeth should not exceed $N_1^{(a)}$ and $N_1^{(r)}$.

Figure 11.4.2 illustrates the computerized simulation of radial assembly of the pinion and gear. The computations were performed for a gear drive with $N_1 = 25$, $N_2 = 40$, diametral pitch $P = 8$, and pressure angle $\alpha_c = 20°$.

We can avoid the investigation of interference by radial assembly if the pinion tooth number $N_1^{(r)}$ satisfies the inequality $N_1^{(r)} \leq N_c^{(r)}$ where $N_c^{(r)}$ is the shaper tooth number allowed by radial–axial generation (see Table 11.3.1).

Nomenclature

E_c	distance between gear and cutter axes (Fig. 11.2.1)
N_1	pinion teeth number
N_2	gear teeth number
N_c	shaper teeth number
P	diametral pitch
j	tooth number
m_{ij}	transmission ratio of gear i to gear j
r_{a1}	radius of pinion addendum circle
r_{a2}	radius of gear addendum circle (Fig. 11.3.2)
r_{ac}	radius of cutter addendum circle (Fig. 11.2.2)
r_{b1}	radius of pinion base circle
r_{b2}	radius of gear base circle (Fig. 11.3.2)
r_{bc}	radius of cutter base circle (Fig. 11.2.2)
r_{p2}	radius of gear pitch circle (Fig. 11.3.2)

r_{pc} radius of cutter pitch circle (Fig. 11.2.2)
s_{ac} tooth thickness of the cutter on the addendum circle (Fig. 11.2.2)
s_{pc} tooth thickness of the cutter on the pitch circle (Fig. 11.2.2)
w_{a2} space width on the gear addendum circle (Fig. 11.3.2)
w_{p2} space width on the gear pitch circle (Fig. 11.3.2)
2Δ angle of tooth thickness on the cutter addendum circle (Fig. 11.2.2)
α_c pressure angle of cutter
θ_i parameter of gear involute profile ($i = 1, 2$) (Fig. 11.3.1)
ϕ_2 angle of gear rotation (Fig. 11.2.1)
ϕ_c angle of cutter rotation (Fig. 11.2.1)

12 **Noncircular Gears**

12.1 INTRODUCTION

Noncircular gears transform rotation between parallel axes with the prescribed *gear ratio function*

$$m_{12} = \frac{\omega^{(1)}}{\omega^{(2)}} = f(\phi_1)$$
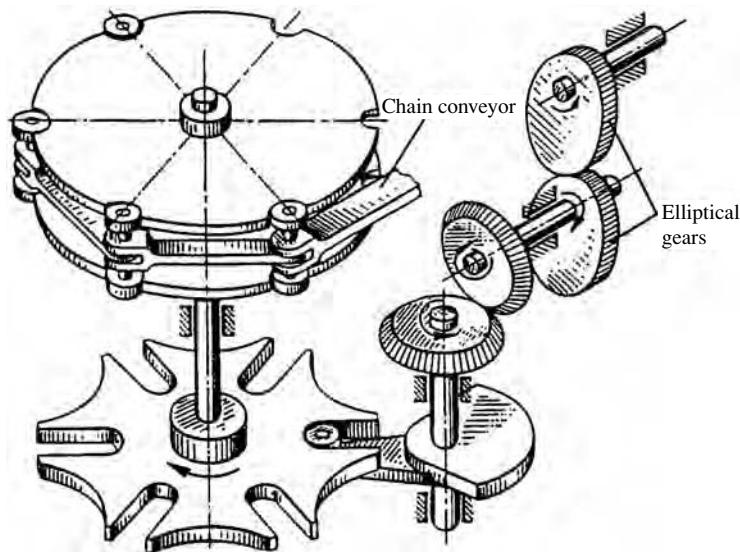
where ϕ_1 is the angle of rotation of the driving gear. The center distance between the axes of rotation is constant. The most typical examples of application of noncircular gears are (i) as the driving mechanism for a linkage to modify the displacement function or the velocity function, and (ii) for the generation of a prescribed function.

Figure 12.1.1 shows the Geneva mechanism that is driven by elliptical gears. The application of elliptical gears enables it to change the angular velocity of the crank of the mechanism during the crank revolution. A crank–slider linkage that is driven by elliptical gears is shown in Fig. 12.1.2. A kinematical sketch of the mechanism is shown in Fig. 12.1.3(a). Application of elliptical gears enables it to modify the velocity function $v(\phi)$ of the slider [Fig. 12.1.3(b)]. Oval gears (Fig. 12.1.4) are applied in the Bopp and Reuter meters for the measurement of the discharge of liquid; the oval gears are shown in the figure in three positions. Figure 12.1.5 shows noncircular gears with unclosed centrodes that are applied in instruments for the generation of functions. Figure 12.1.6 shows a noncircular gear of a drive that is able to transform rotation between parallel axes for a cycle that exceeds one gear revolution. During the cycle the gears perform axial translational motions in addition to rotational motions.

Noncircular gears have not yet found a broad application although modern manufacturing methods enable their makers to provide conjugate profiles using the same tools as are applied for spur circular gears. The following sections are based on work by Litvin [1956].

12.2 CENTRODES OF NONCIRCULAR GEARS

We consider two cases, assuming as given either (i) the gear ratio function $m_{12}(\phi_1)$, or (ii) the function $y(x)$ to be generated.

Figure 12.1.1: Conveyor driven by the Geneva mechanism and elliptical gears.
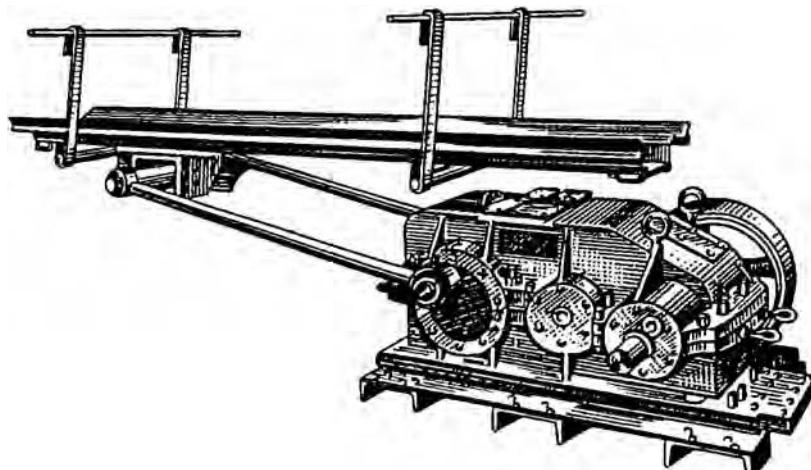
Case 1: The gear ratio function

$$m_{12}(\phi_1) \in C^1, \qquad 0 \leq \phi_1 \leq \phi_1^* \tag{12.2.1}$$
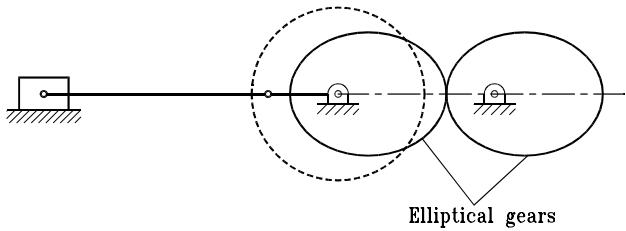
where ϕ_1 is the angle of rotation of the driving gear 1 is given. Here,

$$m_{12}(\phi_1) = \frac{\omega^{(1)}}{\omega^{(2)}} = \frac{d\phi_1}{d\phi_2}$$
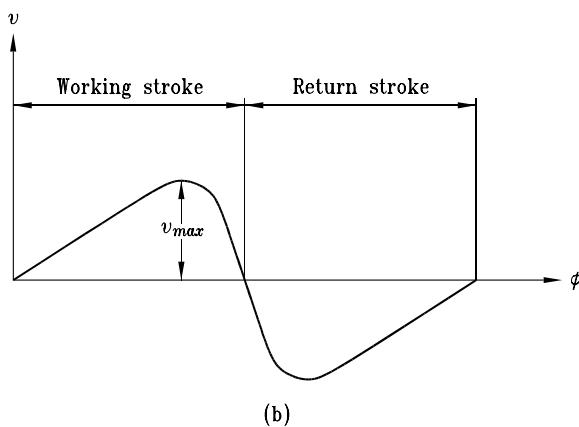
where $\omega^{(i)}$ $(i = 1, 2)$ is the gear angular velocity.

Figure 12.1.2: Conveyor based on application of the crank–slider linkage and elliptical gears.
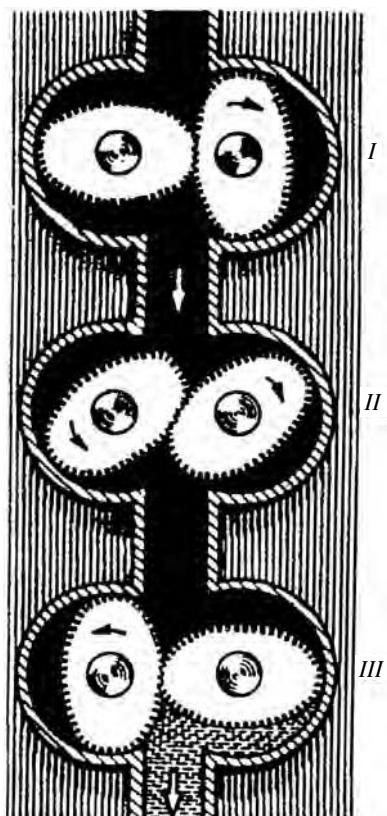
Elliptical gears

(a)
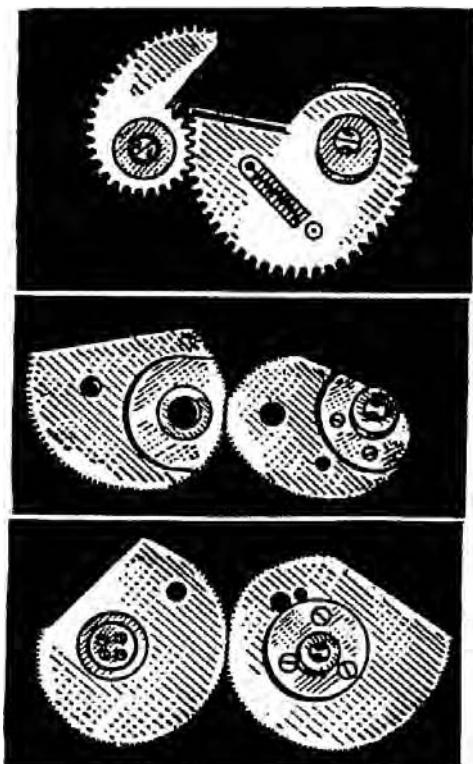
(b)
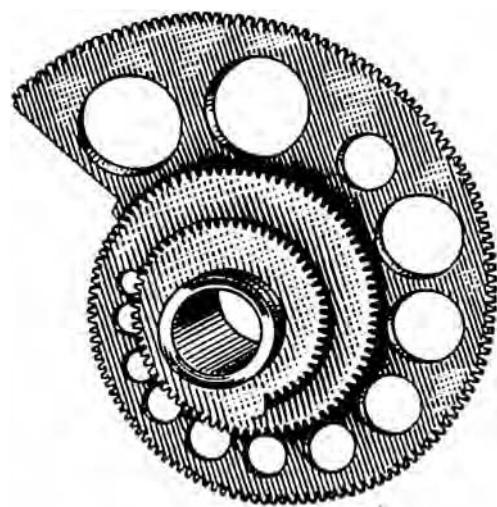
Figure 12.1.3: Combination of elliptical gears with a crank–slider linkage.

Figure 12.1.4: Oval gears of a liquid meter.

Figure 12.1.5: Noncircular gears applied in instruments.

Figure 12.1.6: Twisted noncircular gear.

The *centrode* of gear 1 is represented in polar form by the equation

$$r_1(\phi_1) = E \frac{1}{m_{12}(\phi_1) \pm 1} \tag{12.2.2}$$

where E is the center distance. The *centrode* of the driven gear 2 is determined with the equations

$$r_2(\phi_2) = E \frac{m_{12}(\phi_1)}{m_{12}(\phi_1) \pm 1}, \qquad \phi_2 = \int_0^{\phi_1} \frac{d\phi_1}{m_{12}(\phi_1)}. \tag{12.2.3}$$

Function $\phi_2(\phi_1) \in C^2$ is a monotonic increasing function, and the gear ratio function $m_{12}(\phi_1) \in C^1$ must be positive. The difference between $m_{12\,max}$ and $m_{12\,min}$ is to be limited to avoid undesirable pressure angles (see Section 12.12). We have to differentiate the angle of rotation ϕ_i of gear i from the polar angle θ_i that determines the position vector of the centrode $(i = 1, 2)$. Angles ϕ_i and θ_i are equal, but they are measured in opposite directions.

The orientation of the tangent with respect to the current position vector of the centrode is designated by angle μ, where

$$\tan \mu_i = \frac{r_i(\phi_i)}{\dfrac{dr_i}{d\phi_i}}. \tag{12.2.4}$$

Equations (12.2.1), (12.2.3), and (12.2.4) yield

$$\tan \mu_1 = -\frac{m_{12}(\phi_1) \pm 1}{m'_{12}(\phi_1)} \tag{12.2.5}$$

$$\tan \mu_2 = \pm \frac{m_{12}(\phi_1) \pm 1}{m'_{12}(\phi_1)}. \tag{12.2.6}$$

Here, $m'_{12} = (\partial/\partial\phi_1)[m_{12}(\phi_1)]$.

Function $\mu_i(\phi_1)(i = 1, 2)$ is used for determination of variations of the pressure angle in the process of meshing (see Section 12.12). The upper (lower) sign in the above expressions with double signs corresponds to the case of external (internal) gears. Angle μ_i is measured in the same direction as θ_i.

The following discussion is limited to the case of external noncircular gears. The subscripts "1" and "2" in expressions for μ_1 and μ_2 indicate gears 1 and 2, respectively.

Case 2: Function $y(x)$ to be generated is given

$$y(x) \in C^2, \qquad x_2 \ge x \ge x_1.$$

Rotation angles of the gears are determined as

$$\phi_1 = k_1(x - x_1), \qquad \phi_2 = k_2[y(x) - y(x_1)] \tag{12.2.7}$$

where k_1 and k_2 are the scale coefficients of constant values. Equations (12.2.7) represent in parametric form the displacement function of the gears.

The gear ratio function is

$$m_{12} = \frac{d\phi_1}{d\phi_2} = \frac{k_1}{k_2 y_x} \tag{12.2.8}$$

where $y_x = dy/dx$; $y_x(x) \in C^1$, and $x_1 \leq x \leq x_2$. The gear centrodes are represented by the equations

$$\phi_1 = k_1(x - x_1), \quad r_1 = E\frac{k_2 y_x}{k_1 + k_2 y_x} \tag{12.2.9}$$

$$\phi_2 = k_2[y(x) - y(x_1)], \quad r_2 = E\frac{k_1}{k_1 + k_2 y_x}. \tag{12.2.10}$$

In the case when the derivative y_x changes its sign in the area $x_1 \leq x \leq x_2$, the direct generation of $y(x)$ by noncircular gears becomes impossible. This obstacle can be overcome as follows:

(i) Consider that the noncircular gears generate instead of $y(x)$ the function

$$F_1(x) = y(x) + k_3 x \qquad (k_3 \text{ is constant}). \tag{12.2.11}$$

(ii) A pair of circular gears generates simultaneously the function

$$F_2(x) = k_3 x. \tag{12.2.12}$$

(iii) Functions $F_1(x)$ and $F_2(x)$ are transmitted to a differential gear mechanism, and then the given function $y(x)$ will be executed as the angle of rotation of the driven shaft of the differential mechanism.

The maximal values of the scale coefficients are determined by the equations

$$k_{1\,\text{max}} = \frac{\phi_{1\,\text{max}}}{x_2 - x_1}, \quad k_{2\,\text{max}} = \frac{\phi_{2\,\text{max}}}{y(x_2) - y(x_1)} \tag{12.2.13}$$

where $\phi_{i\,\text{max}} = 300° \sim 330°$ for gears with unclosed centrodes. Knowing function $y_x(x)$ and the coefficients k_1 and k_2, we are able to determine function $\mu_1(\phi_1)$ and estimate the variation of the pressure angle. In some cases, it becomes necessary to use a sequence of two pairs of noncircular gears to decrease the maximal value of the pressure angle (see Section 12.8).

12.3 CLOSED CENTRODES

Noncircular gears designated for continuous transformation of rotational motion must be provided with *closed* centrodes. This yields the following requirement for $m_{12}(\phi_1)$. The gear ratio function $m_{12}(\phi_1)$ must be a periodic one, and its period T is related with the periods T_1 and T_2 of the revolutions of gears 1 and 2 as

$$T = \frac{T_1}{n_2} = \frac{T_2}{n_1} \tag{12.3.1}$$

where n_1 and n_2 are whole numbers.

Let us now consider the following design case:

(i) The centrode of gear 1 is already designed as a closed curve.
(ii) Gears 1 and 2 must perform continuous rotations, and n_1 and n_2 are the numbers of revolutions of the gears.

The question is, what are the requirements to be satisfied to obtain that the gear 2 centrode is a closed curve as well. The solution is based on the following ideas:

(i) We consider that the centrode of gear 1 is represented as a closed curve by the periodic function $r_1(\phi_1) \in C^2$ and $r_1(2\pi) = r_1(2\pi/n_1) = r_1(0)$.
(ii) The angle of rotation of gear 2, $\phi_2 = 2\pi/n_2$, must be performed while gear 1 performs rotation of the angle $\phi_1 = 2\pi/n_1$.
(iii) Taking into account that

$$\frac{2\pi}{n_2} = \int_0^{\frac{2\pi}{n_1}} \frac{d\phi_1}{m_{12}(\phi_1)} \tag{12.3.2}$$

and

$$m_{12}(\phi_1) = \frac{r_2(\phi_1)}{r_1(\phi_1)} = \frac{E - r_1(\phi_1)}{r_1(\phi_1)}. \tag{12.3.3}$$

we obtain

$$\frac{2\pi}{n_2} = \int_0^{\frac{2\pi}{n_1}} \frac{r_1(\phi_1)}{E - r_1(\phi_1)} \, d\phi_1. \tag{12.3.4}$$
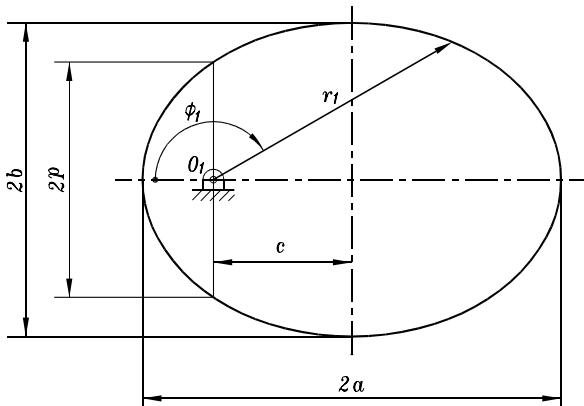
Equation (12.3.4) can be satisfied with a certain value of center distance E, with which the centrode of gear 2 will be a closed curve.

Problem 12.3.1

Consider that the centrode of gear 1 is an ellipse (Fig. 12.3.1) and the number of revolutions of the gears are $n_1 = 1$ and $n_2 = n$. The center of rotation of gear 1 is focus O_1 of the ellipse. The centrode of gear 1 is represented in polar form by the equation

$$r_1(\phi_1) = \frac{p}{1 + e\cos\phi}. \tag{12.3.5}$$

Here, $p = a(1 - e^2)$, $e = c/a$ (Fig. 12.3.1).

Figure 12.3.1: Elliptical centrode.

Equation (12.3.4) yields

$$\frac{2\pi}{n} = \int_0^{2\pi} \frac{p}{E - p + Ee\cos\phi_1} d\phi_1 = \frac{2\pi p}{[(E-p)^2 - E^2 e^2]^{\frac{1}{2}}}. \tag{12.3.6}$$

The derivation of Eq. (12.3.6) is based on the following considerations:

(i)

$$\int_0^{2\pi} \frac{d\phi}{a + b\cos\phi} = \int_{-\pi}^{\pi} \frac{d\phi}{a + b\cos\phi}$$

where $a = E - p$, $b = Ee$.

(ii) The substitution

$$\tan\frac{\phi}{2} = y$$

yields that

$$\int \frac{d\phi}{a + b\cos\phi} = \frac{2}{(a+b)} \int \frac{dy}{1 + \left[\left(\dfrac{a-b}{a+b}\right)^{0.5} y\right]^2}$$

$$= \frac{2}{(a^2 - b^2)^{0.5}} \int \frac{dz}{1 + z^2} = \frac{2}{(a^2 - b^2)^{0.5}} \tan^{-1} z$$

where

$$z = \left(\frac{a-b}{a+b}\right)^{0.5} y = \left(\frac{a-b}{a+b}\right)^{0.5} \tan\left(\frac{\phi}{2}\right).$$

(iii) Finally, we obtain

$$\int_{-\pi}^{\pi} \frac{d\phi}{a + b\cos\phi} = \frac{2}{(a^2 - b^2)^{0.5}} \left\{\tan^{-1}\left[\left(\frac{a-b}{a+b}\right)^{0.5} \tan\left(\frac{\phi}{2}\right)\right]\right\}\Bigg|_{-\pi}^{\pi}$$

$$= \frac{2\pi}{(a^2 - b^2)^{0.5}}.$$

The derivations above confirm Eq. (12.3.6).

Using Eq. (12.3.6), we obtain the following expression for E:

$$E = \frac{p}{1 - e^2} \left\{1 + [1 + (n^2 - 1)(1 - e^2)]^{\frac{1}{2}}\right\}. \tag{12.3.7}$$

For the case when $n = 1$, we obtain

$$E = \frac{2p}{1 - e^2} = 2a,$$

and the gear centrode is an ellipse as well.

12.4 ELLIPTICAL AND MODIFIED ELLIPTICAL GEARS

Modification of Elliptical Centrode

The modification of an elliptical centrode is based on the following ideas proposed by Litvin [1956]:
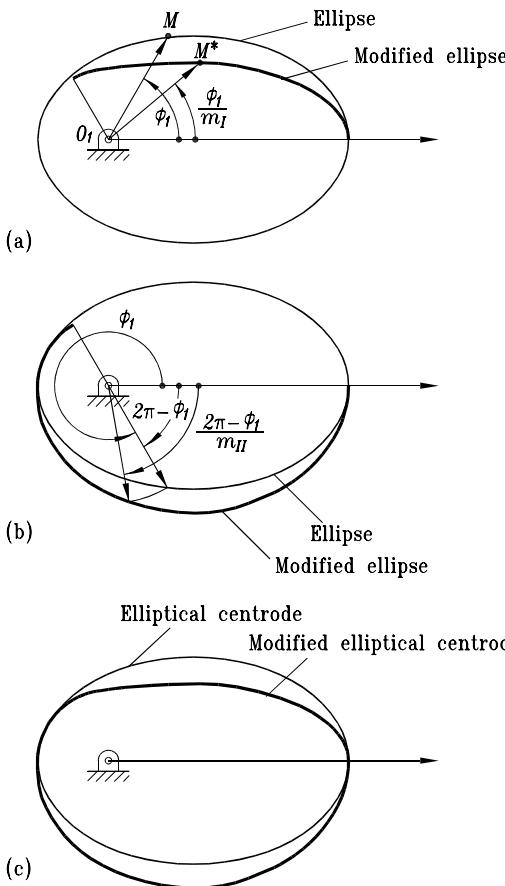
(i) Consider that a current point M of the elliptical centrode is determined with the position vector [Fig. 12.4.1(a)]

$$\overline{O_1 M} = \mathbf{r}_1(\phi_1), \qquad 0 \le \phi_1 \le \pi. \tag{12.4.1}$$
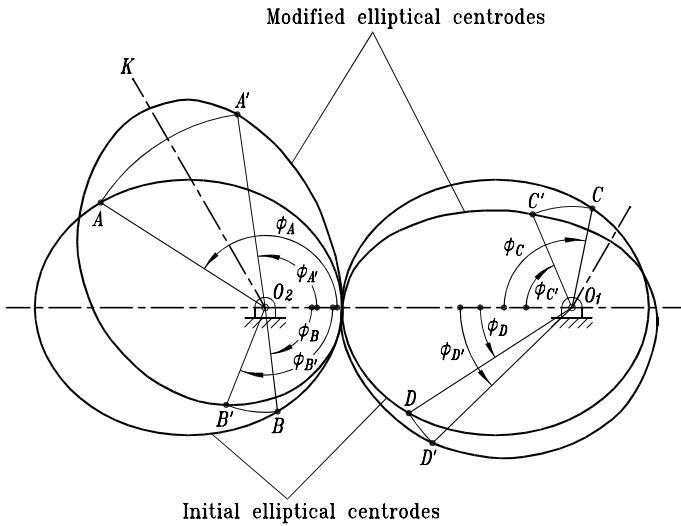
(ii) We determine the respective point M^* of the modified centrode as

$$\overline{O_1 M^*} = \mathbf{r}_1^* \left(\frac{\phi_1}{m_I} \right) \qquad 0 \le \phi_1 \le \pi, \qquad |\mathbf{r}_1^*| = |\mathbf{r}_1|. \tag{12.4.2}$$

(iii) The same principle of centrode modification is applied for the lower part of the ellipse [Fig. 12.4.1(b)]; the modification coefficient is m_{II}. Generally, $m_{II} \ne m_I$.

(iv) The initial elliptical centrode and the modified one are shown in Fig. 12.4.1(c).

(a)

(b)
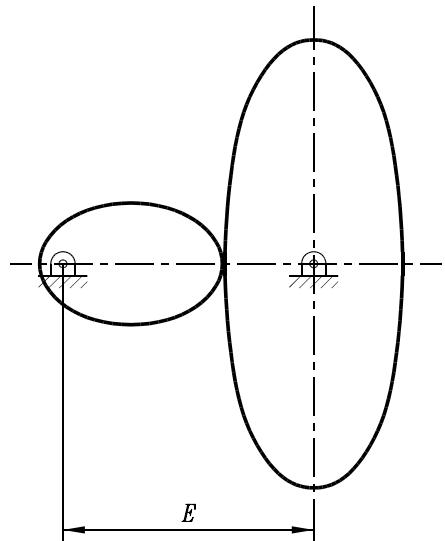
Figure 12.4.1: Modified elliptical centrode.

(c)
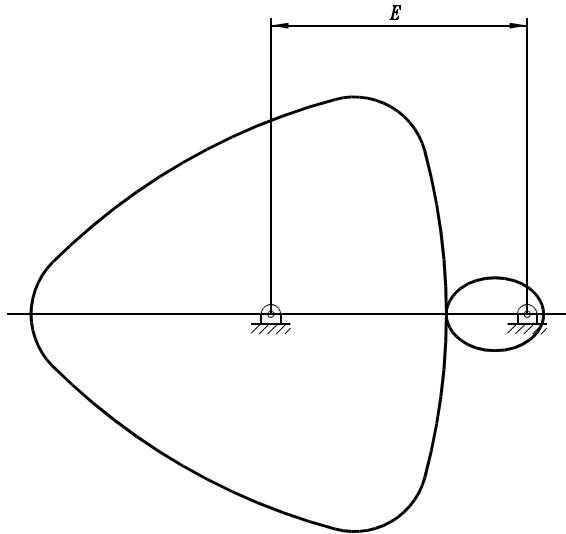
Figure 12.4.2: Ordinary and modified elliptical centrodes.

Figure 12.4.2 shows the modification of identical elliptical centrodes for the case where $m_I = 3/2$, $n_1 = n_2 = 1$, and $e_1 = 0.5$. Figure 12.4.2 illustrates the principle of centrode modification. Noncircular gears with modified elliptical centrodes transform rotation with a nonsymmetrical gear ratio function $m_{12}(\phi_1)$. This function is symmetrical for noncircular gears with elliptical centrodes.

Figures 12.4.3 and 12.4.4 illustrate noncircular gear drives whose driving gear is provided with an elliptical centrode. The driving gear performs two and three revolutions, respectively, while the driven gear performs one revolution. It was proven by Litvin [1956] that the centrodes of driven gears are modified ellipses.

Figure 12.4.3: Conjugation of an elliptical centrode and an oval centrode for two revolutions of the driving gear.
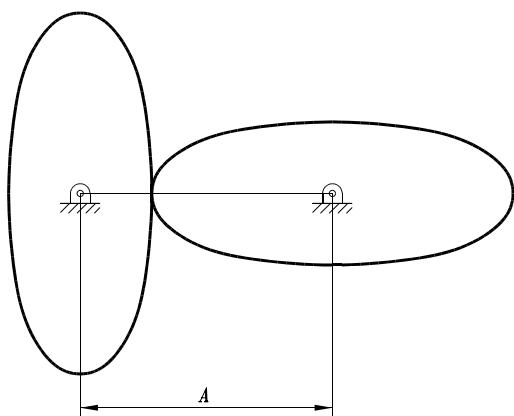
Figure 12.4.4: Conjugation of an elliptical centrode and a mating centrode for three revolutions of the driving gear.
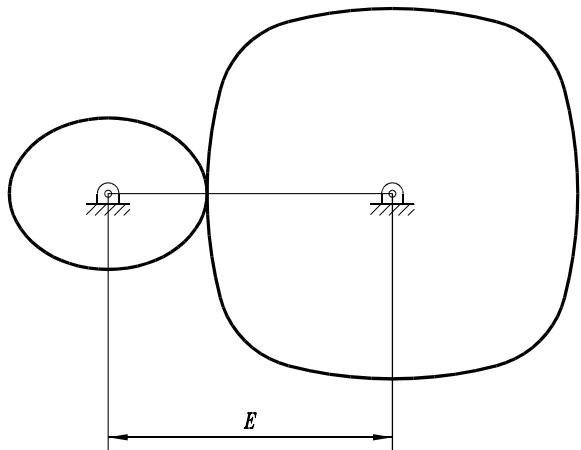
Two oval gears with identical centrodes (Fig. 12.4.5) are a particular case of modified elliptical gears when the coefficients of modification are $m_I = m_{II} = m = 2$ (see Fig. 12.4.1). The gear centrode is represented by the equation

$$r_1 = \frac{a(1 - e^2)}{1 - e\cos 2\phi_1} = \frac{p}{1 - e\cos 2\phi_1}. \tag{12.4.3}$$

The center of gear rotation is the center of symmetry of the oval. The oval gears are used in the meter for liquid discharge (Fig. 12.1.4). A gear drive formed by an oval centrode and a deformed ellipse is shown in Fig. 12.4.6. The driving gear performs two revolutions for one revolution of the driven gear.

Figure 12.4.5: Oval centrodes.

Figure 12.4.6: Conjugation of an elliptical centrode with the mating centrode for four revolutions of the driving link.

12.5 CONDITIONS OF CENTRODE CONVEXITY

Noncircular gears with convex–concave centrodes can be generated by a shaper but not by a hob. The condition of convexity of a gear centrode means that $\rho > 0$, where ρ is the centrode curvature radius. In the case of concave–convex centrodes, there is a point of the gear centrode where $\rho = \infty$.

The curvature radius of a gear centrode is represented by the equation

$$\rho = \frac{\left[r^2 + \left(\dfrac{dr}{d\phi}\right)^2\right]^{3/2}}{r^2 + 2\left(\dfrac{dr}{d\phi}\right)^2 - r\dfrac{d^2r}{d\phi^2}}. \tag{12.5.1}$$

The condition of centrode convexity ($\rho > 0$) yields

$$r^2 + 2\left(\frac{dr}{d\phi}\right)^2 - r\frac{d^2r}{d\phi^2} > 0. \tag{12.5.2}$$

Using Eqs. (12.2.2) and (12.2.3), we can represent the condition of centrode convexity in terms of function $m_{12}(\phi_1)$ and its derivatives:

(i) For the driving gear we have

$$1 + m_{12}(\phi_1) + m_{12}''(\phi_1) \geq 0. \tag{12.5.3}$$

(ii) For the driven gear we obtain

$$1 + m_{12}(\phi_1) + (m_{12}'(\phi_1))^2 - m_{12}(\phi_1)m_{12}''(\phi_1) \geq 0. \tag{12.5.4}$$

Here, $m_{12}' = (d/d\phi_1)(m_{12}(\phi_1))$, $m_{12}'' = (d^2/d^2\phi_1)(m_{12}(\phi_1))$. When the inequalities (12.5.3) and (12.5.4) turn into equalities, there is a centrode point where $\rho = \infty$.

In the case of generation of given function $f(x)$, we obtain the following conditions of convexity for the driving and driven gears, respectively:

(i)

$$k_1 k_2 [f'(x)]^3 + k_1^2 [f'(x)]^2 + 2[f''(x)]^2 - f'''(x) f'(x) \geq 0. \qquad (12.5.5)$$

(ii)

$$k_2 [f'(x)]^3 [k_1 + k_2 f'(x)] + f'(x) f'''(x) - [f''(x)]^2 \geq 0. \qquad (12.5.6)$$

Problem 12.5.1

Consider an oval centrode given as [see Eq. (12.4.3)]

$$r_1 = \frac{a(1 - e^2)}{1 - e \cos 2\phi_1}.$$

Determine the condition of centrode convexity.

Solution

The gear ratio function and its derivatives are

$$m_{12}(\phi_1) = \frac{E - r_1(\phi_1)}{r_1(\phi_1)} = \frac{1 - 2e \cos 2\phi_1 + e^2}{1 - e^2} \qquad (12.5.7)$$

because $E = 2a$.

$$m'_{12}(\phi_1) = \frac{4e \sin 2\phi_1}{1 - e^2}, \qquad m''_{12}(\phi_1) = \frac{8e \cos 2\phi_1}{1 - e^2}. \qquad (12.5.8)$$

Equations (12.5.3), (12.5.8), and (12.5.7) yield

$$1 + 3e \cos 2\phi_1 \geq 0, \qquad (12.5.9)$$

which yields $e \leq 1/3$.

12.6 CONJUGATION OF AN ECCENTRIC CIRCULAR GEAR WITH A NONCIRCULAR GEAR

Figure 12.6.1 shows that the center of rotation O_1 of the eccentric circular gear 1 does not coincide with the geometric center of the circle of radius a. The centrode of gear 2 must be conjugate with the eccentric circle, the centrode of gear 1. Such drives can be applied with $n = 1, 2, 3, \ldots, n$ where n is the total number of revolutions of gear 2.
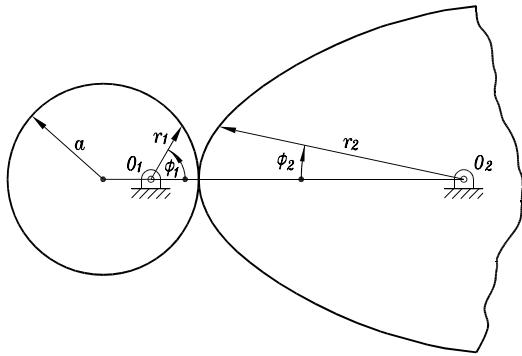
The centrode of the eccentric circular gear is represented by the equation

$$r_1(\phi_1) = (a^2 - e^2 \sin^2 \phi_1)^{1/2} - e \cos \phi_1 = a[(1 - \varepsilon^2 \sin^2 \phi_1)^{1/2} - \varepsilon \cos \phi_1] \qquad (12.6.1)$$

where $\varepsilon = e/a$, and e is the eccentricity. The gear ratio function $m_{21}(\phi_1)$ is

$$m_{21}(\phi_1) = \frac{r_1(\phi_1)}{E - r_1(\phi_1)} = \frac{c}{c - (1 - \varepsilon^2 \sin^2 \phi_1)^{1/2} + \varepsilon \cos \phi_1} - 1 \qquad (12.6.2)$$

where $c = E/a$, $m_{21\,\text{max}} = (1 + \varepsilon)/(c - (1 + \varepsilon))$, $m_{21\,\text{min}} = (1 - \varepsilon)/(c - (1 - \varepsilon))$.

Figure 12.6.1: Conjugation of an eccentric circular centrode with the mating centrode.

The centrode of gear 2 will be a closed curve if the following equation is observed [see Eq. (12.3.4)]:

$$\frac{2\pi}{n} = \int_0^{2\pi} \left(\frac{c}{c - (1 - \varepsilon^2 \sin^2 \phi_1)^{1/2} + \varepsilon \cos \phi_1} - 1 \right) d\phi_1. \tag{12.6.3}$$

The solution of Eq. (12.6.3) for c can be accomplished numerically, using an iterative process of computations. The first guess for c is [Litvin, 1968]

$$c = (1 + n) \left[1 - \frac{(n - 12)\varepsilon^2}{4n} \right]. \tag{12.6.4}$$

The centrode of gear 2 is determined with the following equations:

$$r_2 = E - r_1 = a[c - (1 - \varepsilon^2 \sin^2 \phi_1)^{1/2} + \varepsilon \cos \phi_1] \tag{12.6.5}$$

$$\phi_2 = \int_0^{\phi_1} \frac{(1 - \varepsilon^2 \sin^2 \phi_1)^{1/2} - \varepsilon \cos \phi_1}{c - (1 - \varepsilon^2 \sin^2 \phi_1)^{1/2} + \varepsilon \cos \phi_1} d\phi_1. \tag{12.6.6}$$

The curvature radius of the gear 2 centrode is

$$\rho_2 = \frac{a \, r_1(\phi_1)[E - r_1(\phi_1)]}{[r_1(\phi_1)]^2 + Ee \cos \phi_1}. \tag{12.6.7}$$

The condition of convexity of the gear 2 centrode is
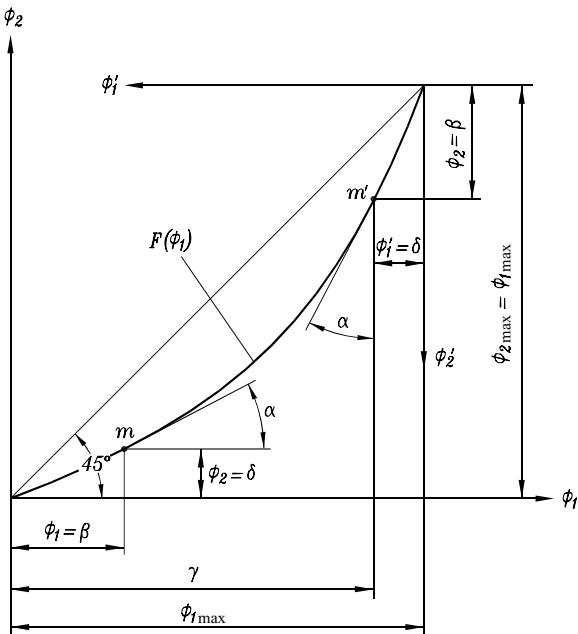
$$[r_1(\phi_1)]^2 + Ee \cos \phi_1 \geq 0. \tag{12.6.8}$$

12.7 IDENTICAL CENTRODES

In some rare cases the centrodes of mating gears can be designed to be identical. This goal can be achieved if the following requirements are satisfied:

(i)

$$\phi_{2\max} = F(\phi_{1\max}) = \phi_{1\max} \tag{12.7.1}$$

Figure 12.7.1: Displacement function for gears with identical centrodes.

where

$$F(\phi_1) = \phi_2$$

is the displacement function.

(ii)

$$F(\phi_{1\max} - F(\phi_1)) = \phi_{1\max} - \phi_1. \tag{12.7.2}$$

The displacement function $F(\phi_1)$ that satisfies Eqs. (12.7.1) and (12.7.2) is shown in Fig. 12.7.1. Points m and m' of the graph are conjugate points of the function. At these points we have

$$\phi_2' = \phi_1 = \beta, \quad \phi_1' = \phi_2 = \delta, \quad \tan\alpha = \frac{d\phi_2}{d\phi_1} = \frac{d\phi_1'}{d\phi_2'}. \tag{12.7.3}$$

It is easy to verify that elliptical gears that have identical centrodes satisfy the above requirements.

Another example of design of noncircular gears with identical centrodes is the case where the gears generate the function

$$y = \frac{1}{x}, \quad x_2 \geq x \geq x_1. \tag{12.7.4}$$

The design is based on the relations

$$\phi_1 = k_1(x - x_1), \qquad \phi_2 = k_2 \left(\frac{1}{x_1} - \frac{1}{x} \right) \qquad (12.7.5)$$

$$k_1 = \frac{\phi_{1\,\text{max}}}{x_2 - x_1}, \qquad k_2 = \frac{\phi_{2\,\text{max}}}{\dfrac{1}{x_1} - \dfrac{1}{x}} \qquad (12.7.6)$$

where $\phi_{1\,\text{max}} = \phi_{2\,\text{max}}$.

The displacement function of the gears is

$$\phi_2 = F(\phi_1) = \frac{a_2\phi_1}{a_3 + a_4\phi_1} \qquad (12.7.7)$$

where $a_2 = k_2$, $a_3 = k_1 x_1^2$, $a_4 = x_1$. Coefficients a_2, a_3, and a_4 are related as

$$\phi_{2\,\text{max}} = \phi_{1\,\text{max}} = \frac{a_2\phi_{1\,\text{max}}}{a_3 + a_4\phi_{1\,\text{max}}}, \qquad (12.7.8)$$

which yields

$$\frac{a_2 - a_3}{a_4} = \phi_{1\,\text{max}}. \qquad (12.7.9)$$

Using Eq. (12.7.7), we may represent the required functional relations (12.7.2) as follows:

$$\frac{a_2[\phi_{1\,\text{max}} - F(\phi_1)]}{a_3 + a_4[\phi_{1\,\text{max}} - F(\phi_1)]} = \phi_{1\,\text{max}} - \phi_1. \qquad (12.7.10)$$

It is easy to verify that Eq. (12.7.10) is satisfied with expressions (12.7.8) for $\phi_{1\,\text{max}}$ and (12.7.7) for $F(\phi_1)$. Thus, the requirement for the design of identical centrodes is observed, and function $y = 1/x$ can be generated by a noncircular gear with such centrodes.

12.8 DESIGN OF COMBINED NONCIRCULAR GEAR MECHANISM
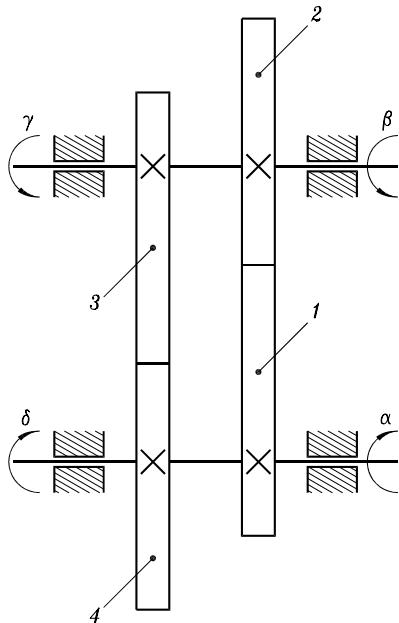
A combined mechanism of noncircular gears (Fig. 12.8.1) enables us to generate function $y(x)$ with substantial variation of the derivative $y_x(x)$. Application of a mechanism with only one pair of noncircular gears might cause undesirable pressure angles. There are important reasons to require that gears 1 and 3, respectively gears 2 and 4, be provided with identical centrodes. The design of such a combined mechanism of noncircular gears is considered in this section.

We designate with α and δ the angles of rotation of gears 1 and 4 (Fig. 12.8.1) and introduce the equations

$$\alpha = k_1(x - x_1), \qquad \delta = k_4(y - y_1) \qquad (12.8.1)$$

where

$$k_1 = \frac{\alpha_{\text{max}}}{x_2 - x_1}, \qquad k_4 = \frac{\delta_{\text{max}}}{y_2 - y_1}. \qquad (12.8.2)$$

Figure 12.8.1: Combined gear mechanism with identical centrodes for (i) gears 1 and 3, and (ii) gears 2 and 4.

Because the above identity of gear centrodes must be provided, it is required that

$$\alpha_{max} = \beta_{max} = \gamma_{max} = \delta_{max}. \tag{12.8.3}$$

It is obvious that $\beta = \gamma$ because gears 2 and 3 perform rotation as a rigid body. The requirement that the centrodes be identical can be represented by the following equation:

$$\psi(\alpha) = f(f(\alpha)). \tag{12.8.4}$$

Here,

$$\delta = \psi(\alpha) \tag{12.8.5}$$

is the function to be generated. Function
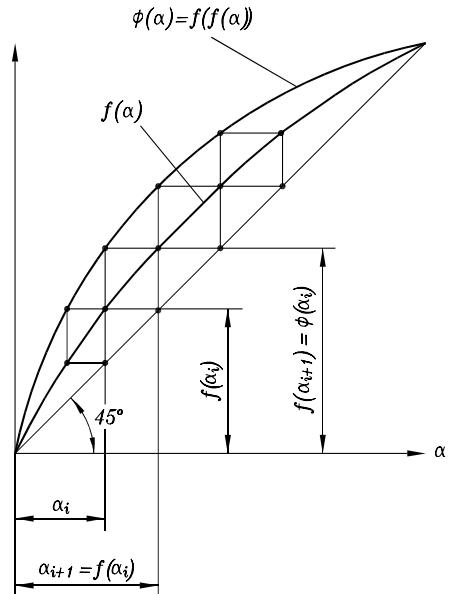
$$\beta = f(\alpha), \qquad \delta = f(\beta)$$

that relates the angles of rotation β and α (δ and β) is to be determined. In other words, considering function $\psi(\alpha)$ as given, we have to determine function $f(\alpha)$.

Generally, Eq. (12.8.4) can be solved only numerically, using an iterative process for computations. Such a process is based on the idea that if $f(\alpha_i)$ is known for a fixed value α_i, and $f(\alpha_i) \neq \alpha_i$, we can determine the desired function $f(\alpha)$ numerically, in discrete form, using the equations

$$\alpha_{i+1} = f(\alpha_i), \qquad f(\alpha_{i+1}) = \psi(\alpha_i). \tag{12.8.6}$$

The above procedure is illustrated graphically in Fig. 12.8.2; more details are given in Litvin [1968].

Figure 12.8.2: Iterative process of the solution of Eq. $\psi(\alpha) = f(f(\alpha))$.

The first guess for the numerical solution of Eq. (12.8.4) is based on the approximate solution

$$f(\alpha) \approx [\psi(\alpha)\alpha^n]^{1/(1+n)} \qquad (12.8.7)$$

where
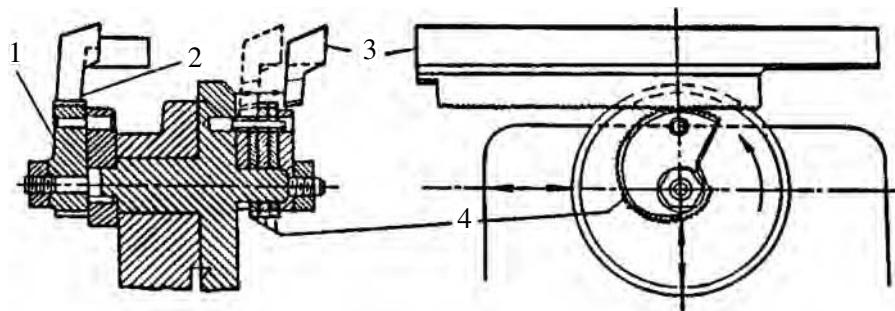
$$n = \left[\frac{\alpha\psi'(\alpha)}{\psi(\alpha)}\right]^{1/2}.$$

Another approximate solution for $f(\alpha)$ was proposed by Kislitsin [1955]:

$$f(\alpha) \approx \frac{\psi(\alpha) + \alpha[\psi'(\alpha)]^{1/2}}{1 + [\psi'(\alpha)]^{1/2}}. \qquad (12.8.8)$$

12.9 GENERATION BASED ON APPLICATION OF NONCIRCULAR MASTER-GEARS
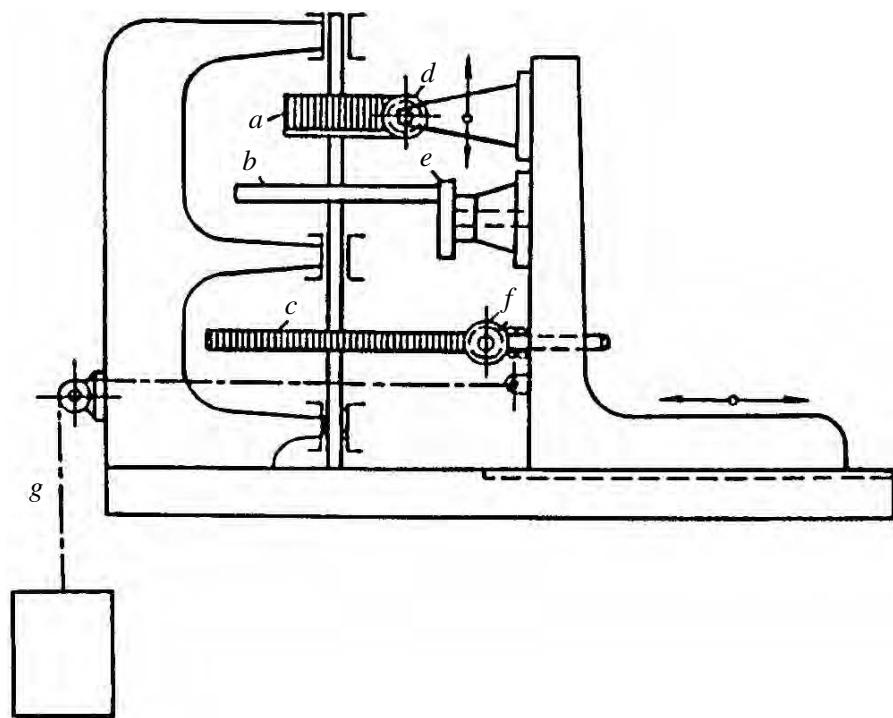
Initially, the generation of noncircular gears was based on application of devices that simulated the meshing of a noncircular gear with a tool. Figure 12.9.1 shows the Fellow device where the noncircular master-gear 1 is in mesh with a master-rack. The rack-cutter and gear being generated are designated by 3 and 4, respectively. The device developed by Bopp and Reuter is based on simulation of meshing of a noncircular master worm gear c with a worm f that is identical to the hob d (Fig. 12.9.2); a is the spur noncircular gear being generated; the cam b and the follower e form the cam mechanism designated for simulation of the required variable distance between c and f. Weight g maintains the continuous contact between the cam and the follower.
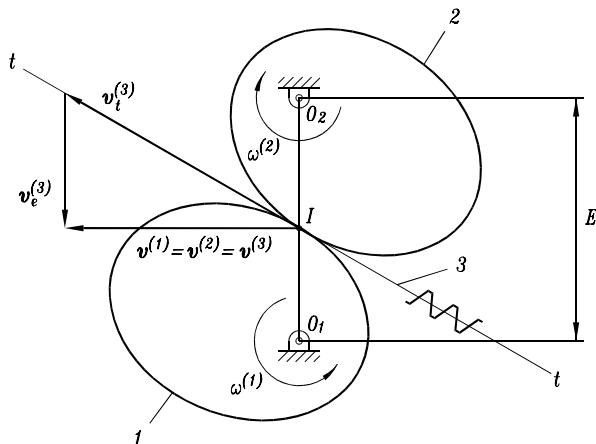
Figure 12.9.1: Generation of noncircular gears by application of the noncircular master-gear and the rack-cutter.

12.10 ENVELOPING METHOD FOR GENERATION

The main difficulty in application of the devices discussed above was the necessity of manufacturing noncircular master-gears. A general method for generation of noncircular gears that does not require master-gears is based on remodelling existing equipment designed for manufacture of circular gears or using computer-controlled machines, as proposed by Litvin [1956, 1968]. Patents based on this idea were claimed by Litvin and

Figure 12.9.2: Generation of a noncircular gear by application of a noncircular worm-gear.

Figure 12.10.1: General principle of generation of noncircular gears.

followers in 1949–1951. The proposed approach is based on the following ideas:

(a) The noncircular gears are generated by the same tools (rack-cutters, hobs, and shapers) that are used for manufacture of circular gears.
(b) Conjugate tooth profiles for noncircular gears are provided due to the imaginary rolling of the tool centrode over the given gear centrode.
(c) The imaginary rolling of the tool centrode over the centrode of the gear being generated is accomplished with proper relations between the motions of the tool and the gear in the process of cutting.

Figure 12.10.1 illustrates the principle of conjugation of tooth shapes for two mating noncircular gears that are generated by a rack-cutter. The gear centrodes 1 and 2 and the rack-cutter centrode 3 are in tangency at the instantaneous center of rotation I. The rack-cutter centrode is a straight line. Pure rolling of each centrode over the other one is provided if the instantaneous linear velocities of point I of each centrode are equal under the magnitude and direction. While the gears perform rotation about O_1 and O_2, respectively, the rack-cutter translates along the tangent t–t to the gear centrodes and along the center distance E and rotates about I. The pure rolling of the rack-cutter over the gear centrodes is provided if the following vector equations are observed (Fig. 12.10.1):

$$\mathbf{v}^{(3)} = \mathbf{v}^{(1)} = \mathbf{v}^{(2)}. \tag{12.10.1}$$

Here,

$$\mathbf{v}^{(i)} = \boldsymbol{\omega}^{(i)} \times \overline{O_i I} \quad (i = 1, 2)$$

is the gear velocity in rotation about O_i.

$$\mathbf{v}^{(3)} = \mathbf{v}_t^{(3)} + \mathbf{v}_e^{(3)}$$
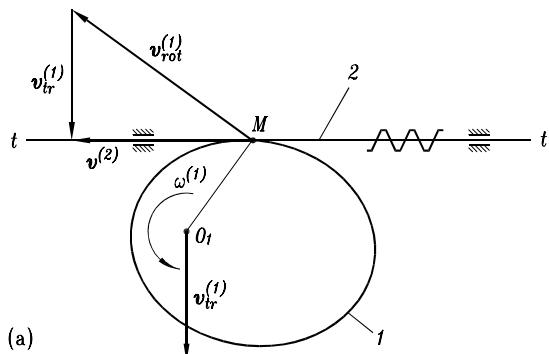
where $\mathbf{v}_t^{(3)}$ and $\mathbf{v}_e^{(3)}$ are the rack-cutter velocities in the direction of t–t and $O_1 O_2$, respectively. The velocity of the rack-cutter in rotational motion about I is equal to zero at point I. We have to emphasize that the instantaneous center of rotation I moves in the process of meshing along the center distance, and Eqs. (12.10.1) must be observed for any instantaneous position of I.

While the rack-cutter and the gears being generated perform the described related motions, the rack-cutter will generate conjugate tooth profiles for gears 1 and 2. This principle for generation also works for the case when a shaper (preferably an involute shaper) is used instead of a rack-cutter.
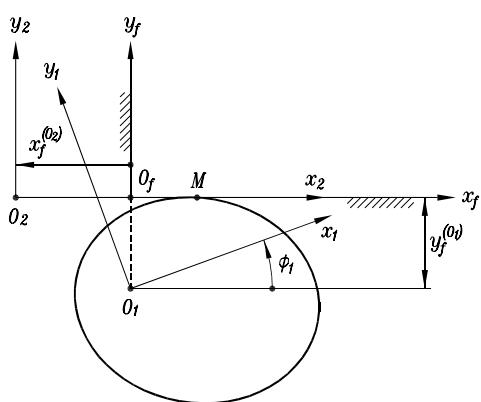
Generation by a Rack-Cutter: Relations Between Motions

While discussing the principle for generation, we have considered the pure rolling of three centrodes (Fig. 12.10.1). To determine the relations between the motions of the tool and the gears, we may consider the conditions of pure rolling of only two centrodes – the one of the rack-cutter and the one of the gear being generated.

Consider that the gear centrode 1 and the rack-cutter centrode 2 are in tangency at a current point M [Fig. 12.10.2(a)]. The rack-cutter translates along the common tangent t–t to the centrodes with velocity $\mathbf{v}^{(2)}$, and the gear rotates about point O_1 with angular velocity $\boldsymbol{\omega}^{(1)}$ and translates in a direction that is perpendicular to t–t. Pure rolling at point M of centrode tangency will be provided if M is the instantaneous center


(a)

(b)

Figure 12.10.2: Derivation of displacement functions for generation by a rack-cutter.

of rotation and the following relation between the velocities is observed:

$$\mathbf{v}^{(2)} = \mathbf{v}_{\text{rot}}^{(1)} + \mathbf{v}_{\text{tr}}^{(1)}. \tag{12.10.2}$$

Here,

$$\mathbf{v}_{\text{rot}}^{(1)} + \mathbf{v}_{\text{tr}}^{(1)} = \mathbf{v}^{(1)}, \qquad \mathbf{v}_{\text{rot}}^{(1)} = \boldsymbol{\omega}^{(1)} \times \overline{O_1 M}$$

where $\mathbf{v}^{(1)}$ is the resulting velocity of point M of centrode 1, $\mathbf{v}_{\text{rot}}^{(1)}$ is the gear velocity in rotational motion, and $\mathbf{v}_{\text{tr}}^{(1)}$ is the gear velocity in translational motion.

Consider now that we set up three coordinate systems [Fig. 12.10.2(b)]: the fixed coordinate system S_f that is rigidly connected to the frame of the cutting machine, S_1 that is rigidly connected to the gear, and S_2 that is rigidly connected to the rack-cutter. Axes x_f and x_2 coincide with the rack-cutter centrode. The governance of motions of the rack-cutter and gear being generated can be accomplished with functions

$$x_f^{(O_2)}(\theta_1), \ \phi_1(\theta_1), \ \text{and} \ y_f^{(O_1)}(\theta_1) \tag{12.10.3}$$

where the variable θ_1 is the parameter of the gear centrode, O_2 is the origin of S_2, and O_1 is the origin of S_1. The derivation of functions (12.10.3) is given in Appendix 12.A.

The manufacture of noncircular gears based on the principle above has been accomplished (i) by remodelled cutting machines complemented by two cam mechanisms (proposed by Litvin [1956, 1968]) and (ii) by numerically controlled machines (CNC) (proposed by F. Cunningham [Smith, 1995]). The design of such cam mechanisms and the development of computer programs for the CNC are based on the following considerations:

(i) Using functions (12.10.3), we can also determine functions (Fig. 12.10.3)

$$\phi_1\left(x_f^{(O_2)}\right) \ \text{and} \ y_f^{(O_1)}(\phi_1). \tag{12.10.4}$$
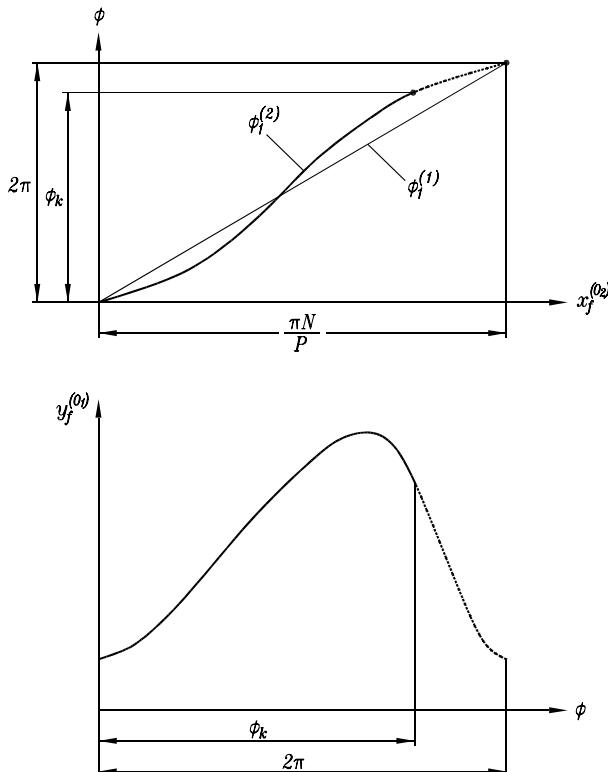
(ii) Function $\phi_1(x_f^{(O_2)})$ may be represented as a sum of linear function $\phi_1^{(1)}$ and nonlinear function

$$\phi_1^{(2)} = \phi_1\left(x_f^{(O_2)}\right) - \phi_1^{(1)} = \phi_1\left(x_f^{(O_2)}\right) - m\left(x_f^{(O_2)}\right). \tag{12.10.5}$$
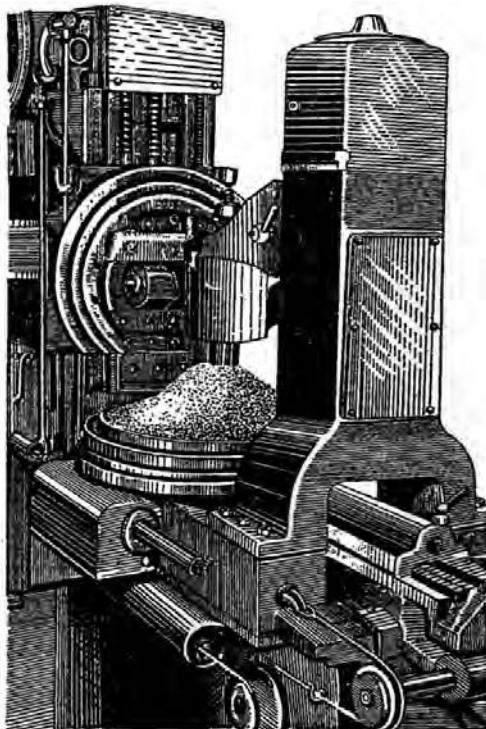
Here, $m = 2P/N$, P is the diametral pitch, and N is the number of gear teeth.

(iii) The proposed cam mechanisms generate functions $\phi_1^{(2)}(x_f^{(O_2)})$ and $y_f^{(O_1)}(\phi_1)$, respectively.

(iv) In the case when the gear centrode is an unclosed curve, Functions (12.10.4) can be determined for the range $0 < \phi_1 < \phi_k$, where $\phi_k < 2\pi$. However, because the generation of the gear by a hob requires several gear revolutions, it is necessary to extend Functions (12.10.4) and make functions $\phi_1^{(2)}(x_f^{(O_2)})$ and $y_f^{(O_1)}(\phi_1)$ periodic ones.
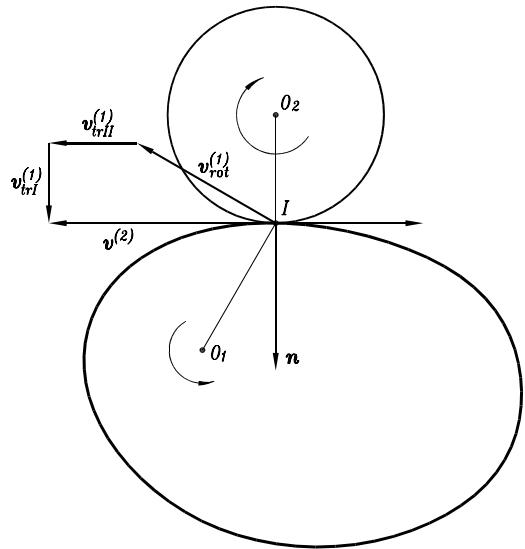
Figure 12.10.4 shows one of the first models of a cutting machine for generation of noncircular gears by a hob. The cutting machine represents a remodelled machine applied for generation of circular gears. The remodelling is based on application of two additional cam mechanisms (proposed by Litvin and Pavlov [1951]).

**Figure 12.10.3:** Extension of displacement functions used for generation.

Figure 12.10.4: One of the first models of a cutting machine for generation of noncircular gears.

Figure 12.10.5: Velocity polygon in the case of generation by a shaper.

Generation by a Shaper

Application of a shaper enables us to generate (i) gears with concave–convex centrodes, and (ii) internal noncircular gears. In the process of generation the shaper rotates about O_2 with angular velocity $\omega^{(2)}$, and the gear rotates about O_1 with angular velocity $\omega^{(1)}$ and translates into two perpendicular directions with velocities $\mathbf{v}_{trI}^{(1)}$ and $\mathbf{v}_{trII}^{(1)}$ that are collinear to the common normal $\mathbf{n}$ and the common tangent to the centrodes at point I, respectively (Fig. 12.10.5). The pure rolling of centrodes is provided by the following equation:
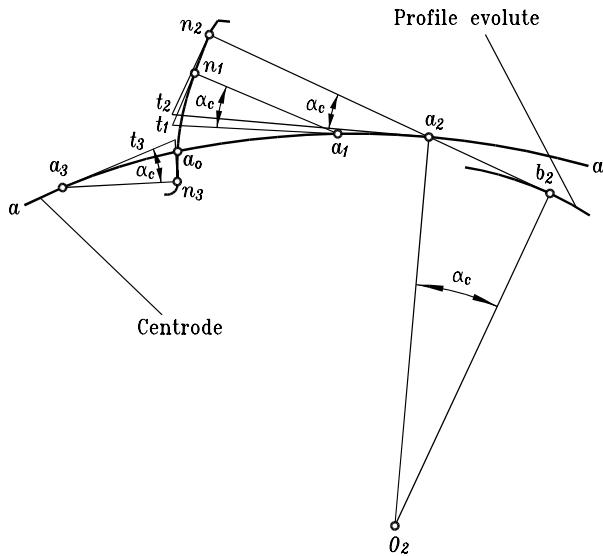
$$\mathbf{v}_{rot}^{(1)} + \mathbf{v}_{trI}^{(1)} + \mathbf{v}_{trII}^{(1)} = \mathbf{v}^{(1)} = \mathbf{v}^{(2)}. \tag{12.10.6}$$

Here, $\mathbf{v}^{(1)}$ is the resulting velocity of point I of the gear centrode that is represented as a sum of three components; $\mathbf{v}^{(2)}$ is the velocity of point I of the shaper centrode. Point I of centrode tangency does not change its location in the process of generation. The derivation of displacement functions for the gear and the shaper is given in Appendix 12.B.

12.11 EVOLUTE OF TOOTH PROFILES

The method described above for generation of noncircular gears (Section 12.10) provides that the normal $a_i n_i$ to the tooth profile and the tangent $a_i t_i$ to the gear centrode form angle α_c at their point of intersection a_i (Fig. 12.11.1) where α_c is the profile angle of the rack-cutter. Henceforth, we differentiate the *evolute* of the gear *centrode* from the *evolute* of the gear *tooth profile*.

Figure 12.11.2 shows the gear centrode b–b, and the evolute a–a of the centrode. Point C_i is the current point of the evolute of the gear tooth profile. It can be proven that the curvature radius $A_i C_i$ of the profile evolute and the curvature radius $A_i B_i$ of
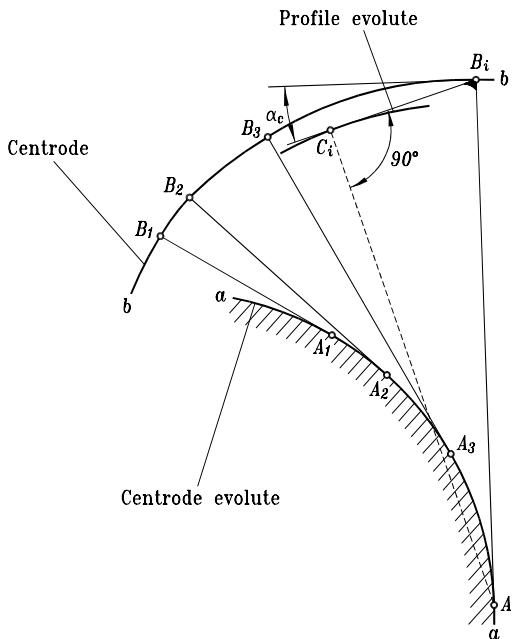
Figure 12.11.1: Orientation of the tooth profile with respect to the tangent of the gear centrode.

the gear centrode form angle α_c, and the radii above are related by the equation
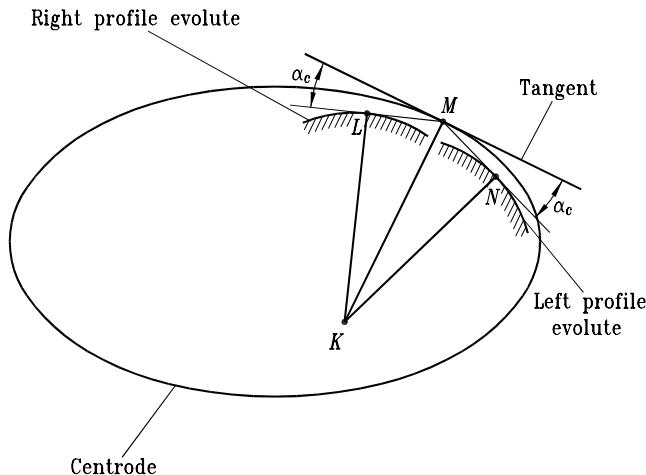
$$l_i = \rho_i \cos \alpha_c \tag{12.11.1}$$

where $l_i = A_i C_i$, $A_i B_i = \rho_i$.

In the case of a circular involute gear, the right-side involute tooth profiles and the left-side profiles have the same evolute, the base circle. The right-side and left-side involute profiles have different evolutes as shown in Fig. 12.11.3. Here, M is the current point
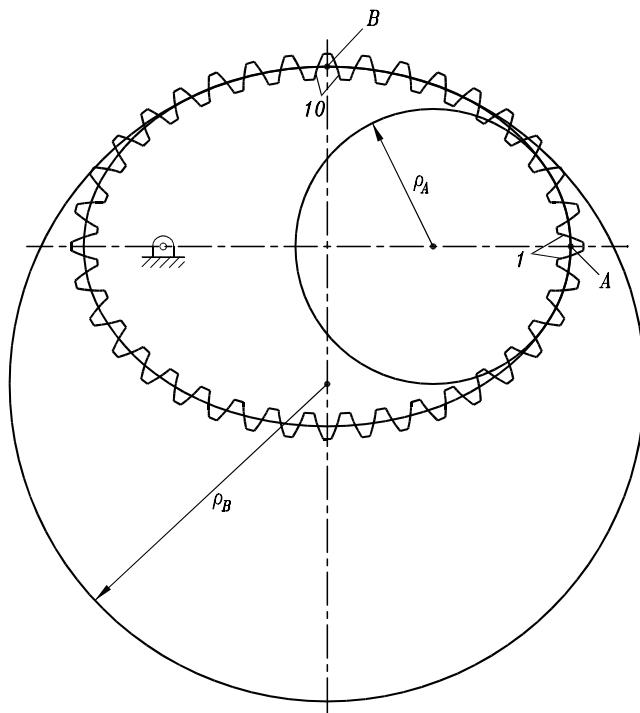

**Figure 12.11.2:** Gear centrode, centrode evolute, and tooth profile evolute.

Figure 12.11.3: Gear centrode and evolutes of left- and right-hand sides of tooth profile.

of the centrode; K is the curvature center at M; L and N are the current points of both profile evolutes.

An approximate representation of tooth profiles of a noncircular gear is based on the local substitution of the gear centrode by the pitch circle of a circular involute gear. Figure 12.11.4 shows that the profiles of tooth number 1 can be approximately represented


Figure 12.11.4: Local representation of a noncircular gear by the respective circular gear.

as tooth profiles of the circular involute gear with the pitch circle ρ_A, where ρ_A is the curvature radius of the noncircular gear centrode at point A. Similarly, tooth profiles of tooth number 10 are represented approximately as tooth profiles of the circular gear with the pitch circle of radius ρ_B.

The number of teeth of the substituting circular gear is determined as

$$N_i = 2P\rho_i \qquad (12.11.2)$$
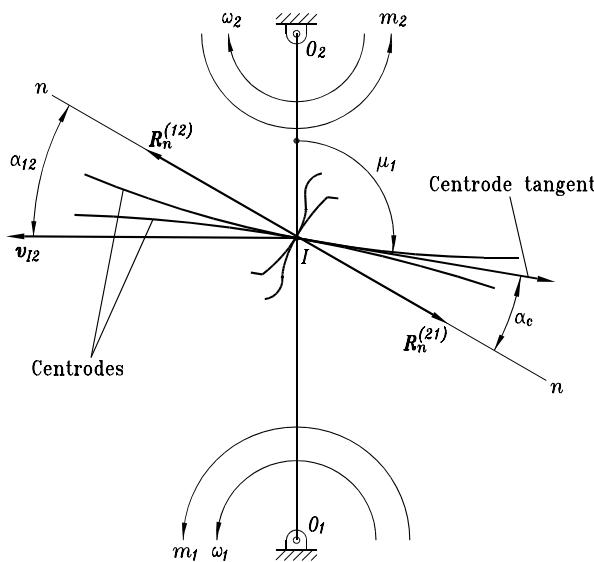
where ρ_i is the curvature radius of the centrode of the noncircular gear, and P is the diametral pitch of the tool applied for generation.

12.12 PRESSURE ANGLE

Consider Fig. 12.12.1 which shows conjugate tooth profiles of the noncircular gears. The rotation centers of the gears are O_1 and O_2; the driving and resisting torques are m_1 and m_2. The tooth profiles are in tangency at the instantaneous center of rotation I. The common normal to the tooth profiles is directed along n–n. The *pressure angle* α_{12} is formed by the velocity $\mathbf{v}_{I2}$ of driven point I and the reaction $\mathbf{R}_n^{(12)}$ that is transmitted from the driving gear 1 to driven gear 2. (Friction of profiles is neglected.) The pressure angle is determined with the following equations:

(i)   When the driving profile is the left-side one, as shown in Fig. 12.12.1, we have

$$\alpha_{12}(\theta_1) = \mu_1(\theta_1) + \alpha_c - \frac{\pi}{2}. \qquad (12.12.1)$$


Figure 12.12.1: Pressure angle of noncircular gears.

(ii) When the driving profile is the right-side one, we have

$$\alpha_{12}(\theta_1) = \mu_1(\theta_1) - \alpha_c - \frac{\pi}{2}. \tag{12.12.2}$$

The pressure angle $\alpha_{12}(\theta_1)$ is varied in the process of motion because μ_1 is not constant. The negative sign of α_{12} indicates that the profile normal passes through another quadrant in comparison with the case shown in Fig. 12.12.1.

APPENDIX 12.A: DISPLACEMENT FUNCTIONS FOR GENERATION BY RACK-CUTTER
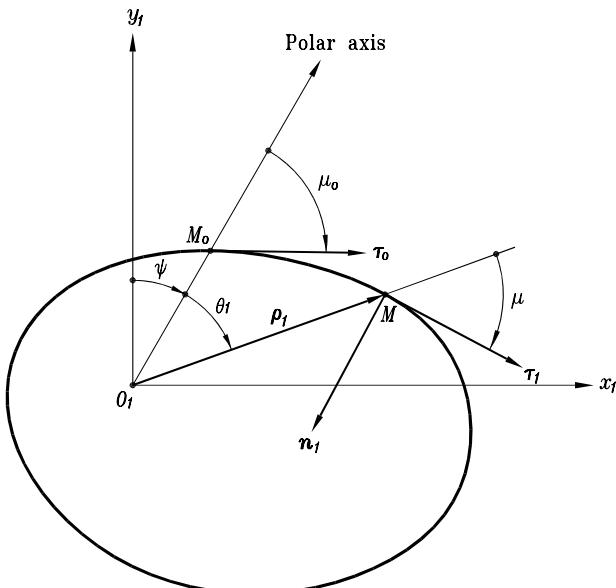
Gear Centrode

The gear centrode is represented in polar form by angle θ_1 and function $\rho_1(\theta_1) = |\boldsymbol{\rho}_1(\theta_1)|$, where $\boldsymbol{\rho}_1(\theta_1) = \overline{O_1 M}$ is the position vector of current point M (see Fig. 12.A.1). The tangent $\boldsymbol{\tau}_1$ to the centrode and $\boldsymbol{\rho}_1(\theta_1)$ form angle μ where

$$\tan \mu(\theta_1) = \frac{\rho_1(\theta_1)}{\rho_\theta}, \qquad \left(\rho_\theta = \frac{d\rho_1}{d\theta_1} \right). \tag{12.A.1}$$

Point M_0 and angle μ_0 are determined with $\theta_1 = 0$ and $\mu_0 = \mu(0)$. The coordinate axis x_1 is parallel to $\boldsymbol{\tau}_0$. The Cartesian coordinates of the centrode, the unit tangent $\boldsymbol{\tau}_1$, and the unit normal $\mathbf{n}_1$ are represented by the equations

$$x_1 = \rho_1(\theta_1) \cos(\theta_1 - \mu_0), \qquad y_1 = -\rho_1(\theta_1) \sin(\theta_1 - \mu_0) \tag{12.A.2}$$


Figure 12.A.1: Representation of gear centrode, its unit tangent, and its unit normal.

where $\mu_0 = 90° - \psi$.

$$\tau_1 = [\cos(\theta_1 + \mu - \mu_0) \quad -\sin(\theta_1 + \mu - \mu_0) \quad 0]^T \tag{12.A.3}$$

$$\mathbf{n}_1 = \tau_1 \times \mathbf{k}_1 = [-\sin(\theta_1 + \mu - \mu_0) \quad -\cos(\theta_1 + \mu - \mu_0) \quad 0]^T. \tag{12.A.4}$$

Rack-Cutter Centrode

The centrode of the rack-cutter coincides with the x_2 axis [Fig. 12.10.2(b)]. The rack-cutter centrode and its unit normal are represented in S_2 by the equations

$$\rho_2 = [u \quad 0 \quad 0 \quad 1]^T \tag{12.A.5}$$

$$\mathbf{n}_2 = [0 \quad -1 \quad 0]^T. \tag{12.A.6}$$

Coordinate Transformation

Our next goal is to represent the gear and rack-cutter centrodes in fixed coordinate system S_f. The coordinate transformation from S_i $(i = 1, 2)$ to S_f is based on the following matrix equations [Fig. 12.10.2(b)]:

$$\mathbf{r}_f^{(i)} = \mathbf{M}_{fi}\, \rho_i, \qquad \mathbf{n}_f^{(i)} = \mathbf{L}_{fi}\mathbf{n}_i. \tag{12.A.7}$$

After transformations we obtain

$$\mathbf{r}_f^{(1)} = [\rho_1(\theta_1)\cos q \quad -\rho_1(\theta_1)\sin q + y_f^{(O_1)} \quad 0 \quad 1]^T. \tag{12.A.8}$$

Here, $q = \theta_1 - \mu_0 - \phi_1$, where ϕ_1 is the angle of gear rotation; $y_f^{(O_1)} = (\overline{O_f O_1}) \cdot \mathbf{j}_f$;

$$\mathbf{n}_f^{(1)} = [-\sin\delta \quad -\cos\delta \quad 0]^T \tag{12.A.9}$$

where $\delta = \theta_1 + \mu - \mu_0 - \phi_1$.

$$\mathbf{r}_f^{(2)} = [u + x_f^{(O_2)} \quad 0 \quad 0 \quad 1]^T \tag{12.A.10}$$

where $x_f^{(O_2)} = (\overline{O_f O_2}) \cdot \mathbf{i}_2$.

$$\mathbf{n}_f^{(2)} = [0 \quad -1 \quad 0]^T. \tag{12.A.11}$$

Equations of Centrode Tangency

The gear and rack-cutter centrodes are in tangency at any instant. Thus

$$\mathbf{r}_f^{(1)} - \mathbf{r}_f^{(2)} = 0 \tag{12.A.12}$$

$$\mathbf{n}_f^{(1)} - \mathbf{n}_f^{(2)} = 0. \tag{12.A.13}$$

Equations (12.A.12) and (12.A.13) yield a system of only three independent scalar equations because $|\mathbf{n}_f^{(1)}| = |\mathbf{n}_f^{(2)}| = 1$. These equations are

$$\rho_1(\theta_1)\cos q - u - x_f^{(O_2)} = 0 \tag{12.A.14}$$

$$-\rho_1(\theta_1)\sin q + y_f^{(O_1)} = 0 \tag{12.A.15}$$

$$-\sin\delta = 0, \qquad -\cos\delta = -1. \tag{12.A.16}$$

Equations (12.A.16) yield

$$\phi_1(\theta_1) = \theta_1 + \mu - \mu_0 \tag{12.A.17}$$

where $\mu = \arctan(\rho_1(\theta_1)/\rho_\theta)$, $\mu_0 = \arctan(\rho_1(0)/\rho_\theta)$.

Transformations of Eqs. (12.A.14) are based on the following considerations:

(i) At the start of motion we have $\phi_1 = 0$, $\theta_1 = 0$, origins O_f and O_2 coincide with each other, and $x_f^{(O_2)}(0) = 0$. Then, we obtain

$$\rho_1(0)\cos\mu_0 = \rho_0\cos\mu_0 = u_0 \tag{12.A.18}$$

where u_0 determines the initial position of the point of tangency of the centrodes on the x_2 axis.

(ii) The displacement of the point of tangency of the centrodes along the rack-cutter centrode is

$$s_2 = u - u_0. \tag{12.A.19}$$

(iii) The displacement of the point of tangency along the gear centrode is determined as

$$s_1 = \int_0^{\theta_1} ds_1(\theta_1) = \int_0^{\theta_1} (dx_1^2 + dy_1^2)^{1/2} = \int_0^{\theta_1} \frac{\rho_1(\theta_1)}{\sin\mu} d\theta_1. \tag{12.A.20}$$

Due to pure rolling of the centrodes, we have that $s_1 = s_2$ and

$$u - u_0 = u - \rho_0\cos\mu_0 = \int_0^{\theta_1} \frac{\rho_1(\theta_1)}{\sin\mu} d\theta_1. \tag{12.A.21}$$

(iv) Equation (12.A.17) yields

$$q = \theta_1 - \mu_0 - \phi_1 = -\mu. \tag{12.A.22}$$

(v) Equations (12.A.14), (12.A.21), and (12.A.22) yield the following final expression for $x_f^{(O_2)}$:

$$x_f^{(O_2)}(\theta_1) = \rho_1(\theta_1)\cos\mu - \rho_0\cos\mu_0 - s_1. \tag{12.A.23}$$

Similar transformations of Eq. (12.A.15) yield

$$y_f^{(O_1)}(\theta_1) = -\rho_1(\theta_1)\sin\mu. \tag{12.A.24}$$

Computational Procedure

The final system of displacement equations is

$$\phi_1(\theta_1) = \theta_1 + \mu - \mu_0$$
$$x_f^{(O_2)} = \rho_1(\theta_1)\cos\mu - \rho_0\cos\mu_0 - s_1(\theta_1) \tag{12.A.25}$$
$$y_f^{(O_1)} = -\rho_1(\theta_1)\sin\mu.$$

Here,

$$\mu = \arctan\left(\frac{\rho_1(\theta_1)}{\rho_\theta}\right), \qquad \rho_\theta = \frac{d\rho_1}{d\theta_1}, \qquad s_1(\theta_1) = \int_0^{\theta_1} \frac{\rho_1(\theta_1)}{\sin\mu} d\theta_1.$$

Generally, $s_1(\theta_1)$ can be determined by numerical integration. Equation system (12.A.25) is used for the numerical control of motions of the cutting machine (or for the design of cams if a mechanical cutting machine is used).

APPENDIX 12.B: DISPLACEMENT FUNCTIONS FOR GENERATION BY SHAPER

The applied coordinate systems S_1, S_2, and S_f are rigidly connected to the gear being generated, the shaper, and the frame of the cutting machine, respectively. The orientation of these coordinate systems at the initial position is as shown in Fig. 12.B.1. The gear centrode and its unit normal are represented in S_1 by Eqs. (12.A.2) and (12.A.4), respectively. The shaper centrode is a circle of radius ρ_2, and this centrode and its normal are represented in S_2 by the equations
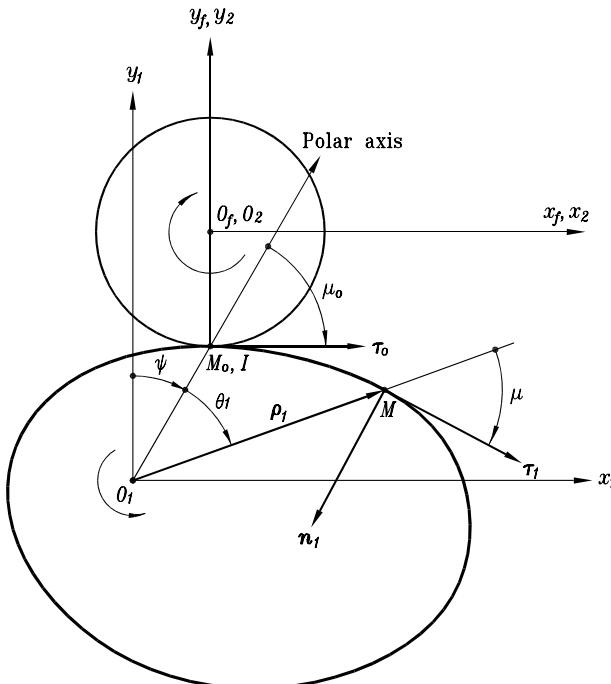
$$\boldsymbol{\rho}_2(\theta_2) = \rho_2[\sin\theta_2 \quad -\cos\theta_2 \quad 0 \quad 1]^{\mathrm{T}} \tag{12.B.1}$$

$$\mathbf{n}_2 = [\sin\theta_2 \quad -\cos\theta_2 \quad 0]^{\mathrm{T}}. \tag{12.B.2}$$
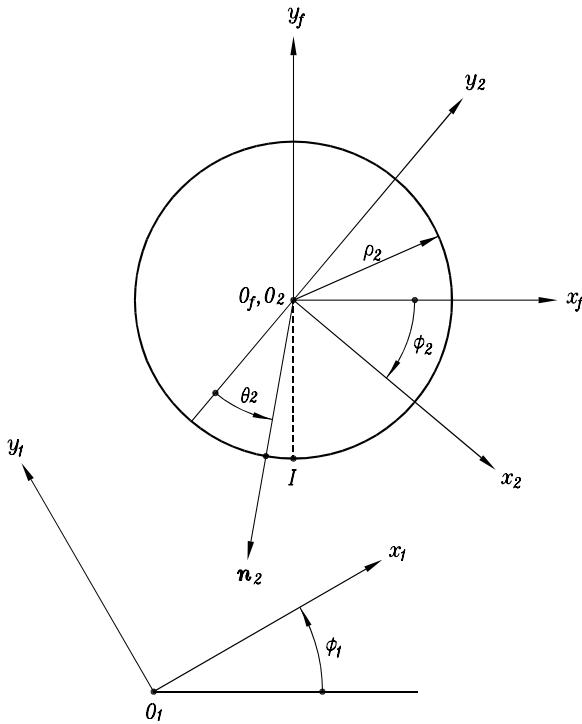
The coordinate transformations from S_1 and S_2 to S_f (Fig. 12.B.2) are based on the following equations:

$$\boldsymbol{\rho}_f^{(i)}(\theta_i, \phi_i) = \mathbf{M}_{fi}\,\boldsymbol{\rho}_i(\theta_i, \phi_i) \qquad (i = 1, 2) \tag{12.B.3}$$

$$\mathbf{n}_f^{(i)}(\theta_i, \phi_i) = \mathbf{L}_{fi}\,\mathbf{n}_i(\theta_i, \phi_i) \qquad (i = 1, 2). \tag{12.B.4}$$


Figure 12.B.1: Coordinate systems applied for generation by a shaper.

Figure 12.B.2: Derivation of displacement functions for generation by a shaper.

The centrodes of the gear and the shaper are in tangency with each other at point I, represented as $[\,0 \;\; -\rho_2 \;\; 0 \;\; 1\,]^{\mathrm{T}}$. Equations of centrode tangency provide the following displacement functions:

$$\phi_1(\theta_1) = \theta_1 + \mu - \mu_0 \tag{12.B.5}$$

$$x_f^{(O_1)}(\theta_1) = -\rho_1(\theta_1)\cos\mu \tag{12.B.6}$$

$$y_f^{(O_1)}(\theta_1) = -\rho_2 - \rho_1(\theta_1)\sin\mu \tag{12.B.7}$$

$$\phi_2(\theta_1) = \frac{1}{\rho_2}\int_0^{\theta_1} \frac{\rho_1(\theta_1)}{\sin\mu}d\theta_1. \tag{12.B.8}$$

Displacement functions (12.B.5)–(12.B.8) enable us to execute the motions of the shaper and gear being generated in the process for generation.

13 Cycloidal Gearing

13.1 INTRODUCTION

The predecessor of involute gearing is the cycloidal gearing that has been broadly used in watch mechanisms. Involute gearing has replaced cycloidal gearing in many areas but not in the watch industry. There are several examples of the application of cycloidal gearing not only in instruments but also in machines that show the strength of positions that are still kept by cycloidal gearing: Root's blower (see Section 13.8), rotors of screw compressors (Fig. 13.1.1), and pumps (Fig. 13.1.2).

This chapter covers (1) generation and geometry of cycloidal curves, (2) Camus' theorem and its application for conjugation of tooth profiles, (3) the geometry and design of pin gearing for external and internal tangency, (4) overcentrode cycloidal gearing with a small difference of numbers of teeth, and (5) the geometry of Root's blower.

13.2 GENERATION OF CYCLOIDAL CURVES

A *cycloidal* curve is generated as the trajectory of a point rigidly connected to the circle that rolls over another circle (over a straight line in a particular case). Henceforth, we differentiate ordinary, extended, and shortened cycloidal curves.
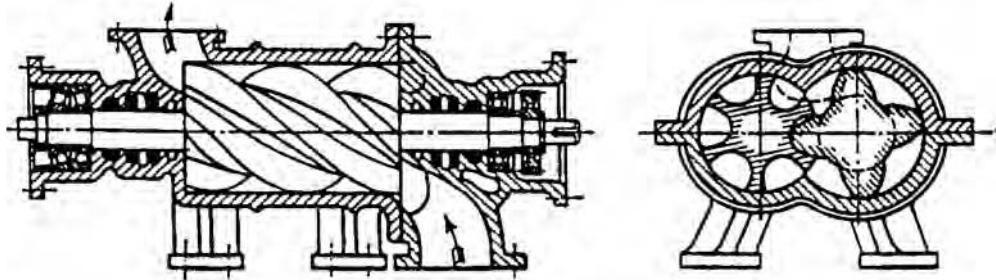
Figure 13.2.1 shows the generation of an *extended epicycloid* as the trajectory of point M that is rigidly connected to the rolling circle of radius r. In the case when generating point M is a point of the rolling circle, it will generate an *ordinary epicycloid*, but when M is inside of circle r it will generate a *shortened epicycloid*.

Point P of tangency of circles r and r_1 is the *instantaneous center of rotation*. The velocity $\mathbf{v}$ of point M of the rolling circle is determined as
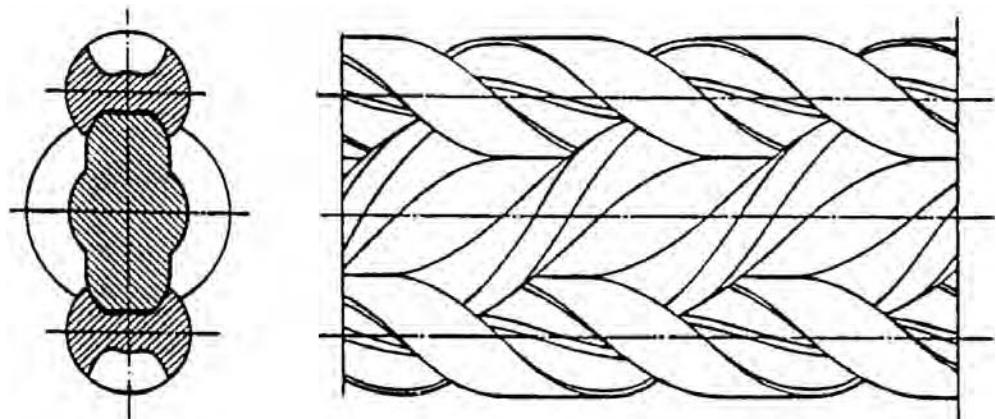
$$\mathbf{v} = \boldsymbol{\omega} \times \overline{PM}. \tag{13.2.1}$$

Vector $\mathbf{v}$ is directed along the tangent to the cycloidal curve Σ being generated, and $\overline{PM}$ is directed along the normal to Σ at point M.
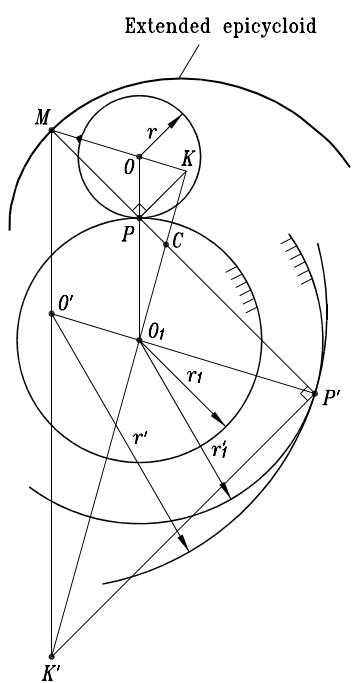
There is an alternative approach for generation of the same curve Σ. The generation is performed by the rolling of circle r' over the circle r'_1. The same tracing point M is rigidly connected now to circle r'. The new instantaneous center of rotation is P' which is determined as the point of intersection of two straight lines: (i) the extended straight

**Figure 13.1.1:** Screw rotors of a compressor.


Figure 13.1.2: Screw rotors of a pump.

Figure 13.2.1: Generation of extended epicycloid.

line PM – the normal to the generated curve, and (ii) line $O'P'$ that passes through point O_1 and is drawn parallel to OM. Point O_1 is the common center of circles r_1 and r'_1. Point O' is a vertex of parallelogram $OMO'O_1$ and is also the center of circle r'. The radii r' and r'_1 of the circles used in the alternative approach are determined with the equations

$$r' = a\frac{r_1 + r}{r} \tag{13.2.2}$$

$$r'_1 = a\frac{r_1}{r} \tag{13.2.3}$$

where $a = |\overline{OM}|$. The segments $|\overline{PM}|$ and $|\overline{P'M}|$ are related with the equation

$$\frac{PM}{P'M} = \frac{r}{r_1 + r}. \tag{13.2.4}$$

The velocity $\mathbf{v}$ of generating point M is the same in both approaches if the angular velocities ω_P and $\omega_{P'}$ are related as

$$\frac{\omega_P}{\omega_{P'}} = \frac{r_1 + r}{r}. \tag{13.2.5}$$

The Bobilier construction [Hall, 1966] enables us to determine the curvature center C of the generated curve. The theorem states:

Consider as known the centers of curvature of two centrodes and the centers of curvature of two conjugate profiles that are rigidly connected to the respective centrodes. Draw two straight lines such as those that interconnect the curvature center of the respective centrode and the curvature center of the profile rigidly connected to the centrode. These two straight lines intersect at point K of line PK that passes through the instantaneous center of rotation P and is perpendicular to the common normal to the conjugate profiles.

In our case, one of the mating profiles is the tracing point M, and the other mating profile is the generated extended epicycloid. The determination of curvature center C of the extended epicycloid in accordance with the Bobilier construction is based on the following procedure (Fig. 13.2.1):

Step 1: Identify as given (a) the centers of curvature O and O_1 of the centrodes r and r_1, (b) point M is one of the mating profiles that is rigidly connected to centrode r, (c) point P is the point of tangency of the centrodes r and r_1, and (d) the normal PM to the generated curve.
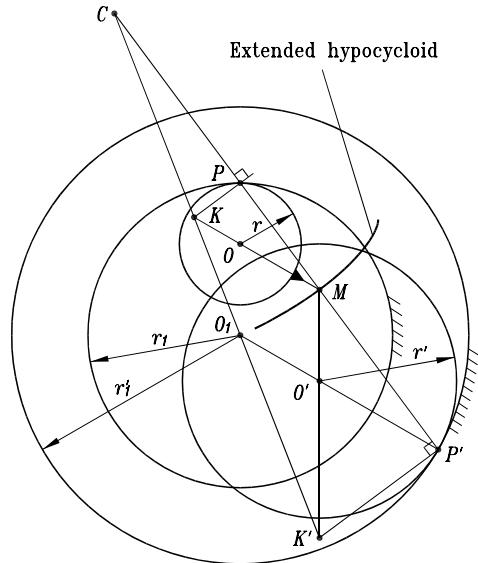
Step 2: Draw straight line MO that interconnects points M and O.

Step 3: Draw through point P line PK that is perpendicular to the normal PM.

Step 4: It is evident that the sought-for center of curvature of the extended epicycloid is point C. The two straight lines OM and O_1C intersect each other at point K.

Step 5: The Bobilier construction can be similarly applied for the alternative method of generation of the extended epicycloid where the rolling centrodes are the circles of radii r'_1 and r' (Fig. 13.2.1). The two straight lines $O'M$ and O_1C intersect each other at point K' of the straight line $P'K'$; line $P'K'$ passes through point P' and is perpendicular to the curve normal $P'M$.

Figure 13.2.2 shows the generation of an *extended hypocycloid* by two alternative approaches. In this case it is necessary to take $(r_1 - r)$ instead of $(r_1 + r)$ in equations
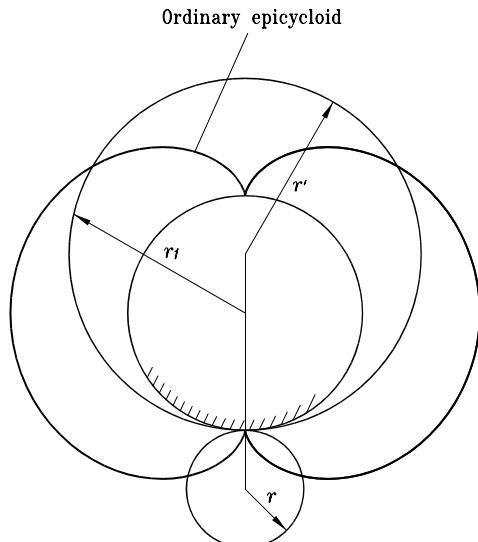
Figure 13.2.2: Generation of extended hypocycloid.

that are similar to (13.2.2), (13.2.4), and (13.2.5). The Bobilier construction has been applied in this case as well to illustrate the geometric way of determining the curvature center C for the extended hypocycloid.
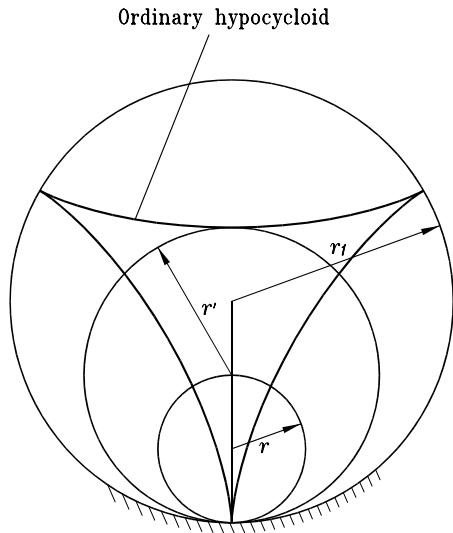
Figures 13.2.3 and 13.2.4 illustrate the generation of an ordinary epicycloid and an ordinary hypocycloid. Again, two alternative methods for generation can be applied. Here,

$$a = r, \quad r_1' = r_1, \quad r' = r_1 \pm r. \tag{13.2.6}$$

The upper (lower) sign corresponds to the case of generation of an ordinary epicycloid (hypocycloid).

**Figure 13.2.3:** Generation of ordinary epicycloid.

Ordinary hypocycloid

Figure 13.2.4: Generation of ordinary hypocycloid.

13.3 EQUATIONS OF CYCLOIDAL CURVES
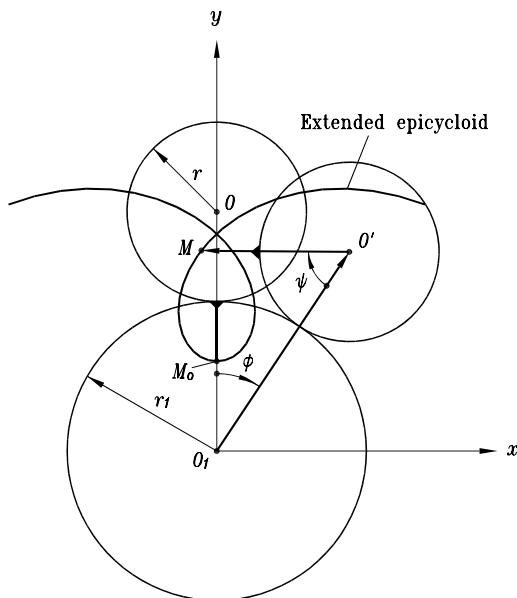
Extended Epicycloid

The position vector $\overline{O_1M}$ (Fig. 13.3.1) is represented as
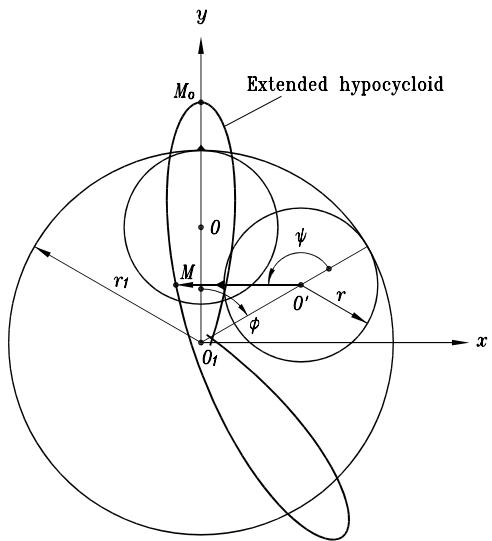
$$\overline{O_1M} = \overline{O_1O'} + \overline{O'M}. \tag{13.3.1}$$

Due to pure rolling, we have

$$\psi r = \phi r_1. \tag{13.3.2}$$

Figure 13.3.1: For derivation of equations of extended epicycloid.

Figure 13.3.2: For derivation of equations of extended hypocycloid.

After transformations we obtain the following equations:

$$x = (r_1 + r) \sin \phi - a \sin \left[\phi \left(1 + \frac{r_1}{r} \right) \right]$$

$$y = (r_1 + r) \cos \phi - a \cos \left[\phi \left(1 + \frac{r_1}{r} \right) \right].$$

(13.3.3)

In the case of an ordinary epicycloid, we have to take $a = r$.

Extended Hypocycloid
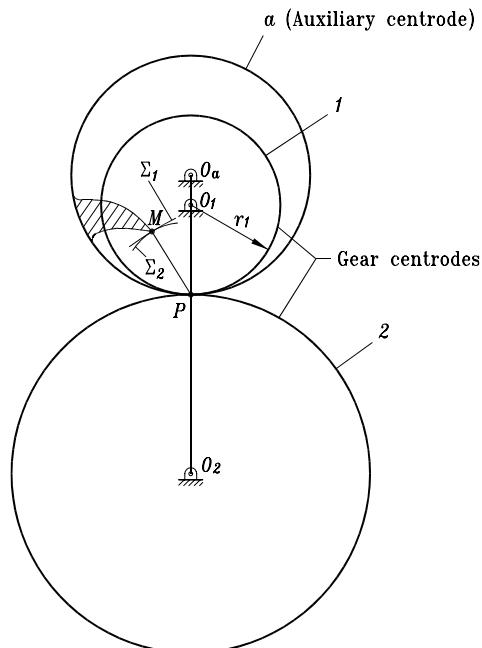
The derivations are based on an approach similar to the one discussed above. Using Fig. 13.3.2, we obtain

$$x = (r_1 - r) \sin \phi - a \sin \left[\phi \left(\frac{r_1}{r} - 1 \right) \right]$$

$$y = (r_1 - 1) \cos \phi + a \cos \left[\phi \left(\frac{r_1}{r} - 1 \right) \right].$$

(13.3.4)

In the case of an ordinary hypocycloid, we have to take $a = r$.

13.4 CAMUS' THEOREM AND ITS APPLICATION

Camus' theorem formulates the conditions of conjugation of two cycloidal curves. Consider that gear centrodes are given. An auxiliary centrode a (Fig. 13.4.1) is in tangency with centrodes 1 and 2, and P is their common instantaneous center of rotation. An arbitrarily chosen point M is rigidly connected to centrode a. Point M traces out in relative motion (with respect to centrodes 1 and 2) the curves Σ_1 and Σ_2, respectively. Camus' theorem states that curves Σ_1 and Σ_2 may be chosen as conjugated shapes for teeth of gears 1 and 2, respectively.

Figure 13.4.1: For illustration of Camus' theorem.

To prove this theorem, let us consider an instantaneous position of centrodes 1, 2, and a. Supposing that centrode 1 is fixed and centrode a rolls over centrode 1, we say that the motion of centrode a relative to centrode 1 is rotation about point P. Assume that centrode a rotates about point P through a small angle. Then point M of centrode a traces out in this motion a small piece of curve Σ_1 (point M moves along Σ_1). Line MP is the normal to Σ_1 at point M. Similarly, by rotation of centrode a about P with respect to centrode 2, point M traces out a small piece of curve Σ_2 (M moves along Σ_2). Line MP is also the normal to shape Σ_2 at point M.
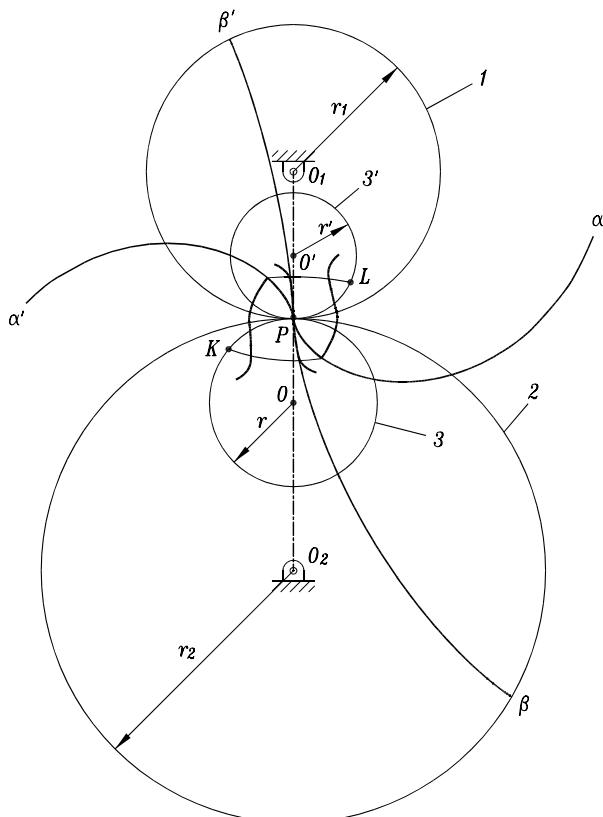
Thus, curves Σ_1 and Σ_2 have a common point M, they are in tangency at M, and their common normal MP passes through point P, the instantaneous center of rotation of centrodes 1 and 2. According to the general theorem of planar gearing (see Section 6.1), the generated curves Σ_1 and Σ_2 are the conjugate ones.

Tooth Addendum–Dedendum Profiles

Considering the synthesis of planar cycloidal gears, the Camus' theorem should be applied twice, for conjugation of profiles for the gear addendum and dedendum.

Figure 13.4.2 shows the gear centrodes 1 and 2 with radii r_1 and r_2. To generate the profiles of the gear addendum and dedendum, two auxiliary centrodes 3 and 3′, of radii r and r', are used. The generation of conjugate profiles for gears 1 and 2 may be represented as follows:

Step 1: Consider that the auxiliary centrode 3 rolls over the gear centrodes 1 and 2. Centrodes 3 and 1 are in external tangency and centrodes 3 and 2 are in internal tangency. Point P of auxiliary centrode 3 generates in coordinate system S_1 rigidly connected to gear 1 the epicycloid $P\alpha$ as the profile of the *addendum* of gear 1.
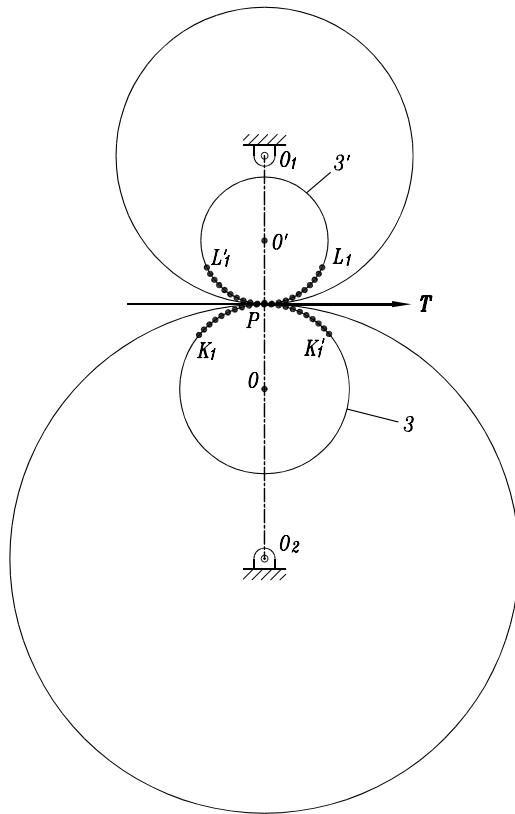
Figure 13.4.2: Generation of conjugate profiles for cycloidal gears.

Respectively, point P of auxiliary centrode 3 generates in coordinate system S_2 rigidly connected to gear 2 the hypocycloid $P\beta$ as the profile of the *dedendum* of gear 2. In accordance to Camus' theorem, curves $P\alpha$ and $P\beta$ are the conjugate profiles for gears 1 and 2.

   Step 2: We consider now that the other auxiliary centrode, circle $3'$, rolls over the gear centrodes 1 and 2. Centrodes 1 and $3'$ are in internal tangency, and centrodes 2 and $3'$ are in external tangency. Point P of circle $3'$ generates in S_1 the hypocycloid $P\beta'$ as the profile of the tooth *dedendum* of gear 1. Respectively, point P of circle $3'$ generates in S_2 the epicycloid $P\alpha'$ as the profile of the *addendum* of gear 2.

   Unlike involute planar gears, the addendum and dedendum profiles of a cycloidal gear are represented by two different curves, an epicycloid and a hypocycloid. The change of the center distance of cycloidal gears is accompanied with the breaking of conjugation of tooth profiles.

   The *line of action* of cycloidal gears is a combination of two circular arcs that belong to auxiliary centrodes 3 and $3'$ as shown in Fig. 13.4.3. Here, L_1PK_1 and $L'_1PK'_1$ represent the lines of action for both sides of tooth profiles. The tangent $\mathbf{T}$ to the line of action at P is perpendicular to the center distance $\overline{O_1O_2}$. Point P of the gear tooth profiles is a singular point. However, normal $\mathbf{N}$ to the tooth profiles at P can be determined. The line of action of $\mathbf{N}$ is the same as of $\mathbf{T}$. Thus, the pressure angle at P is equal to zero.
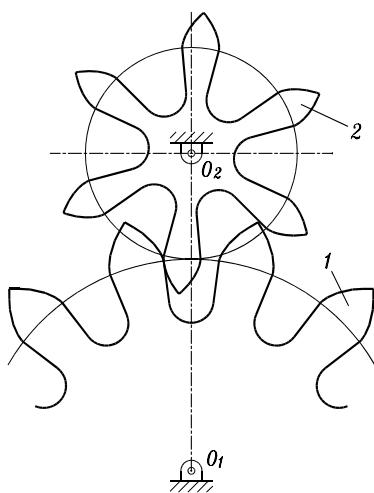
Figure 13.4.3: Lines of action of cycloidal gears.
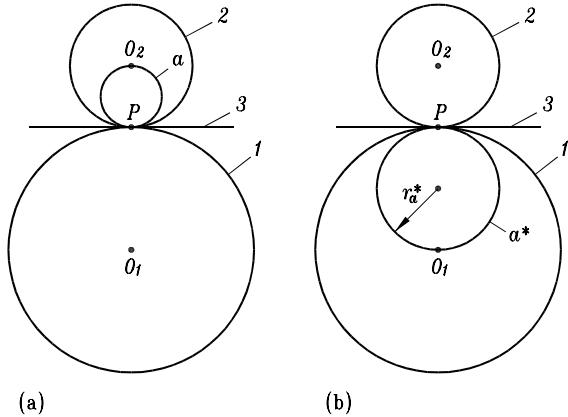
Watch Gearing

Cycloidal watch gearing that is still used in watch mechanisms is a particular case of a general cycloidal gearing. The main features of cycloidal watch gearing are as follows (Fig. 13.4.4):

(i) Driving gear 1 in a watch gear mechanism is provided with a larger number N_1 of teeth than the number of teeth N_2 of the driven gear. Therefore, the angular


Figure 13.4.4: Watch gearing.

Figure 13.4.5: Centrodes of gears 1 and 2, rack-cutter 3, and auxiliary centrodes a and a^*.

velocity $\omega^{(2)}$ of driven gear 2 is larger than the angular velocity of driving gear 1, and the gear ratio is

$$m_{21} = \frac{\omega^{(2)}}{\omega^{(1)}} = \frac{N_1}{N_2} > 1.$$

The watch gear mechanism is designated to *multiply* the angular velocity because the rotation is provided to the watch arrows. Recall that the main purpose of a reducer with involute gears is to *reduce* the angular velocity of the driven gear. In a reducer, we have that N_1 is less than N_2, and the gear ratio is $m_{21} < 1$.

(ii) The profile of the tooth dedendum is a straight line directed from P to O_i ($i = 1, 2$). Such straight lines are particular cases of hypocycloids $P\beta$ and $P\beta'$ (Fig. 13.4.2) that are generated when $r' = r_1/2$ and $r = r_2/2$. This statement can be proven with the analysis of Eqs. (13.3.4) for an extended hypocycloid.

Rack-Cutter Profiles for Watch Gears
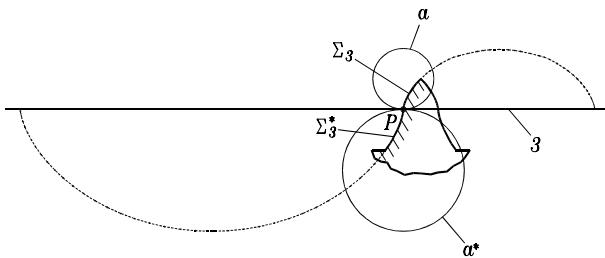
Figure 13.4.5 shows gear centrodes 1 and 2 and two auxiliary centrodes a and a^* that are used for generation of conjugate profiles of watch gears. The radii of the circles a and a^* are

$$r_a = \frac{r_2}{2}, \quad r_a^* = \frac{r_1}{2}$$

The rack-cutter centrode 3 is a straight line that is tangent to the gear centrodes at P. The rack-cutter profiles, Σ_3 and Σ_3^*, are ordinary cycloids that are generated in S_3 by point P of auxiliary centrodes a and a^* (Fig. 13.4.6).

13.5 EXTERNAL PIN GEARING

Pin gearing (Fig. 13.5.1) is a particular case of cycloidal gearing. The teeth of the pinion are cylinders and the gear tooth surface is conjugate to the cylinder surface. Pin gearing is used in reducers for cranes, in some planetary trains, and is still used as watch gearing. The main advantage of pin gearing is the possibility of avoiding the generation of the

Figure 13.4.6: Rack-cutter profiles.
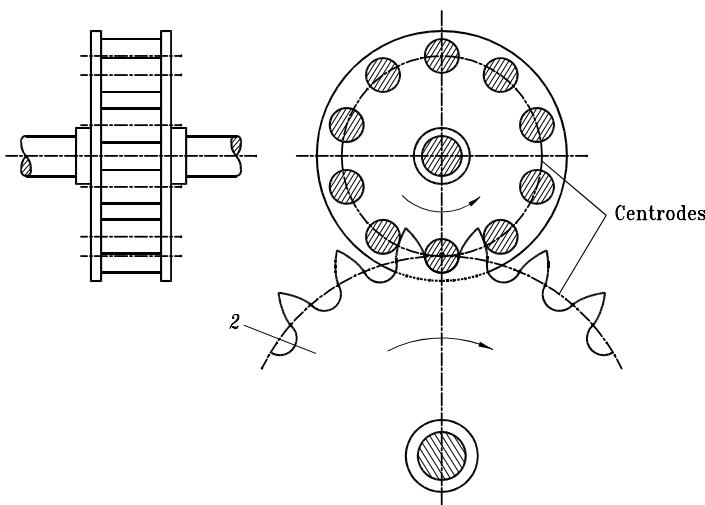
pinion teeth because the pinion is designed as an assembly of cylinders placed between two disks (Fig. 13.5.1).

The centrodes of pin gearing that are represented in Fig. 13.5.1 are in external tangency. In addition, we consider a pin gearing that has centrodes in internal tangency, and the pins are tooth profiles of the driven gear 2 but not the pinion 1 (see Section 13.6). The pin gearing is used for transformation of rotation between parallel axes and it can be considered as a planar gearing where the pinion tooth profile is a circle, and the gear tooth profile is a curve conjugate to such a circle.
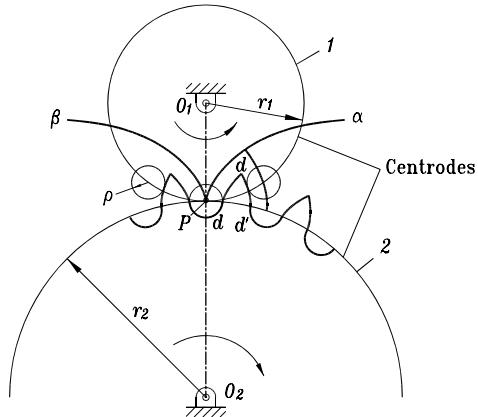
Conjugation of Tooth Profiles

Conjugation of tooth profiles of pin gearing may be considered as a particular case of application of Camus' theorem that is based on the following considerations:

Step 1: Figure 13.5.2 shows the pinion-gear centrodes, circles of radii r_1 and r_2. We may consider that the Camus auxiliary centrode coincides with the pinion centrode, the circle of radius r_1. Point P of this circle generates in coordinate system S_2 rigidly connected to gear 2 epicycloids $P\alpha$ and $P\beta$.


Figure 13.5.1: Pin gearing.

Figure 13.5.2: For conjugation of tooth profiles for pin gearing.

Step 2: We can imagine now that the conjugate pinion-gear tooth profiles are (i) point P of the pinion, and (ii) the two branches $P\alpha$ and $P\beta$ of the epicycloid of the tooth profiles of the gear.

Step 3: The interaction of a point and a curve as the conjugation of tooth profiles is not applicable in practice. The real conjugate profiles are (i) the circle of radius ρ as the pinion tooth profile, and (ii) curves $d–d$ and $d–d'$ (Fig. 13.5.2) that are equidistant to the epicycloids $P\alpha$ and $P\beta$.

Applied Coordinate Systems

The investigation below is directed at the determination of the equation of meshing, the line of action, the equations of the gear tooth profile, and the profile of the rack-cutter for gear generation. Movable coordinate systems S_1 and S_2 (Fig. 13.5.3) are rigidly connected to the pinion and the gear, respectively. Fixed coordinate system S_f is rigidly connected to the housing. Movable coordinate system S_t is rigidly connected to the tool, the rack-cutter.

Equation of Meshing

Consider that the pinion tooth profile, the circle of radius ρ, is represented in coordinate system S_1 (Fig. 13.5.4) by the equations
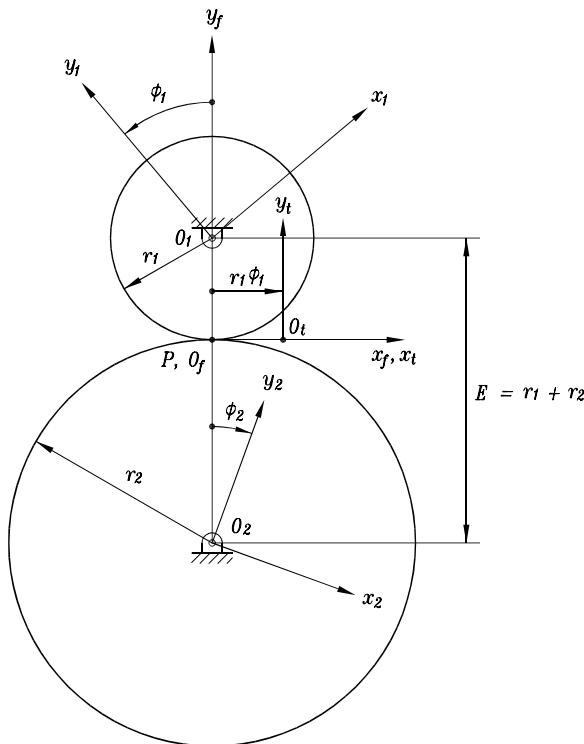
$$x_1 = -\rho \sin\theta, \qquad y_1 = -(r_1 + \rho\cos\theta) \tag{13.5.1}$$

where the variable parameter θ determines the location of a current point on the pin circle. The unit normal to the pinion tooth profile passes through center C and is represented as
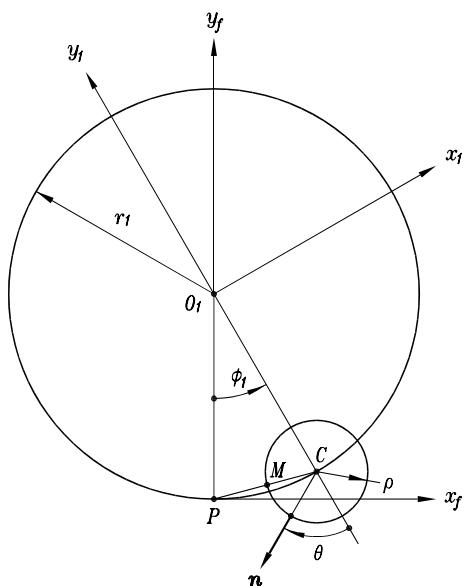
$$n_{x1} = -\sin\theta, \qquad n_{y1} = -\cos\theta. \tag{13.5.2}$$

The normal at point M of tangency of the pinion-gear tooth profiles must pass through the instantaneous center of rotation determined in S_1 as

$$X_1 = -r_1 \sin\phi_1, \qquad Y_1 = -r_1 \cos\phi_1. \tag{13.5.3}$$

**Figure 13.5.3:** Applied coordinate systems.

Figure 13.5.4: For derivation of equation of meshing.

Thus,

$$\frac{-r_1 \sin \phi_1 + \rho \sin \theta}{-\sin \theta} = \frac{-r_1 \cos \phi_1 + r_1 + \rho \cos \theta}{-\cos \theta}. \tag{13.5.4}$$

Using Eqs. (13.5.4), we can obtain the equation of meshing in the form

$$\sin(\theta - \phi_1) - \sin \theta = 0, \tag{13.5.5}$$

which yields two solutions for θ considering ϕ_1 as given:

(i) Any value of θ satisfies Eq. (13.5.5) when ϕ_1 is zero.
(ii) The other solution is

$$\theta = 90° + \frac{\phi_1}{2}. \tag{13.5.6}$$

The kinematic interpretation of the first solution is based on the following considerations:

(a) Center C of the circle of radius ρ coincides with the instantaneous center of rotation P when ϕ_1 is zero and any normal to this circle passes through P.
(b) Thus, circle ρ copies itself as a part of the profile of the gear 2 tooth.

Taking into account both solutions, it is easy to verify that the profile of one side of the gear 2 tooth is composed by two curves:

(i) a circular arc of radius ρ determined by $90° \geq \theta \geq 0$;
(ii) a curve that is conjugate to the pinion tooth profile, the circle of radius ρ (see below).

Line of Action
Figure 13.5.4 yields that M is the current point of the line of action at the current angle of pinion rotation determined by $\phi_1 \neq 0$. The position vector $\overline{PM}$ of the line of action is determined in S_f by the equations

$$x_f = \left(2r_1 \sin \frac{\phi_1}{2} - \rho\right) \cos \frac{\phi_1}{2},$$

$$\tag{13.5.7}$$

$$y_f = \left(2r_1 \sin \frac{\phi_1}{2} - \rho\right) \sin \frac{\phi_1}{2} \quad \text{(provided } \phi_1 \neq 0\text{)}.$$

At $\phi_1 = 0$, the pinion and gear tooth profiles are in instantaneous tangency at all points of the segment of the circle of radius ρ, where $90° \leq \theta \leq -90°$. It is easy to verify that in the case in which $\rho = 0$, the line of action is a circular arc of radius $r_1 = 0$.

Gear 2 Tooth Profile
It was mentioned above that the tooth profile of gear 2 is formed by two curves, I and II, that are represented in coordinate system S_2 (Fig. 13.5.5) as follows:

(i) Curve I is the circular arc of radius ρ centered at point $C(0, r_2)$ and determined by $90° \geq \theta \geq 0$.
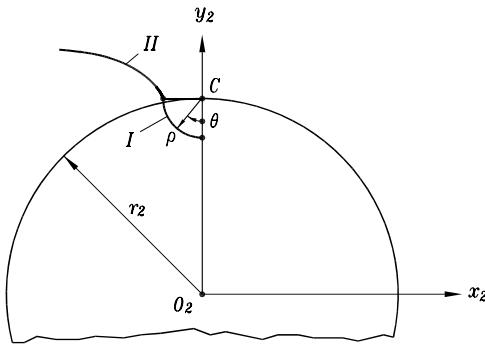
Figure 13.5.5: Gear 2 tooth profile.

(ii) Curve II is represented by the equations

$$\theta > 90°, \quad \phi_1 = 2(\theta - 90°), \quad \phi_2 = \phi_1 \frac{r_1}{r_2}$$

$$\mathbf{r}_2(\theta, \phi_1) = \mathbf{M}_{21}(\phi_1, \phi_2)\mathbf{r}_1(\theta). \tag{13.5.8}$$

Axis y_2 is the axis of symmetry of gear 2 space (Fig. 13.5.5).
Using Eqs. (13.5.8), we obtain after transformations

$$\theta > 90°, \quad \phi_1 = 2(\theta - 90°), \quad \phi_2 = \phi_1 \frac{r_1}{r_2}$$

$$x_2 = r_1 \sin(\phi_1 + \phi_2) - (r_1 + r_2) \sin \phi_2 - \rho \sin[\theta - (\phi_1 + \phi_2)] \tag{13.5.9}$$

$$y_2 = -r_1 \cos(\phi_1 + \phi_2) + (r_1 + r_2) \cos \phi_2 - \rho \cos[\theta - (\phi_1 + \phi_2)].$$

Taking θ as the input parameter, we determine ϕ, ϕ_2, x_2, and y_2. Equations (13.5.9) represent the left-side profile of the teeth of gear 2. Similarly, we may obtain the right-side profile of gear 2 teeth. Taking $\rho = 0$ in Eq. (13.5.9), we obtain equations of an epicycloid.
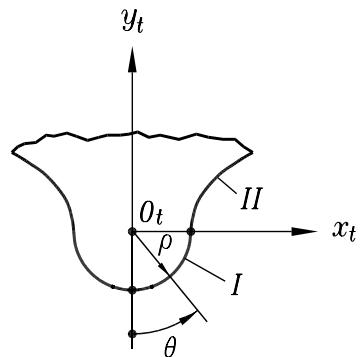
Rack-Cutter Tooth Profile

Gear 2 teeth are generated by a hob whose design is based on an imaginary rack-cutter being in mesh with the pinion and the gear. The rack-cutter tooth profile is also formed by two curves, I and II, that are represented in coordinate system S_t. Curve I is the circular arc of radius ρ centered at the origin of coordinate system S_t (Fig. 13.5.6). Curve I is determined with $90° \geq \theta \geq 0$. Curve II is determined with the equations

$$\theta > 90°, \quad \phi_1 = 2(\theta - 90°), \quad \mathbf{r}_t(\theta, \phi_1) = \mathbf{M}_{t1}(\phi_1)\mathbf{r}_1(\theta). \tag{13.5.10}$$

Axis y_t is the axis of symmetry of the tooth profiles for both tooth sides. Equations (13.5.10) yield

$$\theta > 90°, \quad \phi_1 = 2(\theta - 90°)$$

$$x_t = -r_1(\phi_1 - \sin \phi_1) - \rho \sin(\theta - \phi_1)$$

$$y_t = r_1(1 - \cos \phi_1) - \rho \cos(\theta - \phi_1). \tag{13.5.11}$$
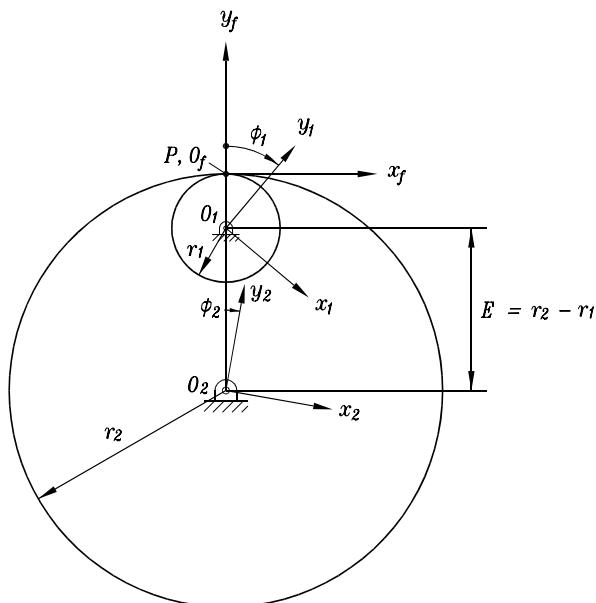
Figure 13.5.6: Rack-cutter tooth profile.

13.6 INTERNAL PIN GEARING
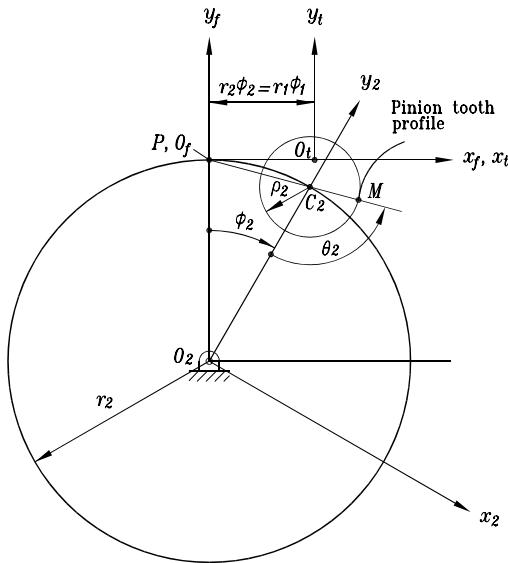
Internal pin gearing is applied in reducers of large dimensions. The pin-gearing centrodes are in internal tangency as shown in Fig. 13.6.1. Unlike in external pin gearing, gear 2 but not pinion 1 is provided with pins. This means gear 2 teeth do not have to be manufactured by a shaper, an important advantage given the large dimensions of gear 2. The tooth profiles of pinion 1 are generated as conjugate to the circle of radius ρ, which is the profile of the gear 2 tooth.

Applied Coordinate Systems

Movable coordinate systems S_1 and S_2 are rigidly connected to pinion 1 and gear 2, respectively. The fixed coordinate system is S_f. The following investigation covers the solution to the following problems: (i) determination of the equation of meshing,


Figure 13.6.1: Applied coordinate systems.

Figure 13.6.2: For derivation of equation of meshing.

(ii) derivation of equations of the line of action, (iii) determination of equations of the pinion tooth profile, and (iv) determination of the tooth profile for the imaginary rack-cutter to be used for generation of pinion 1 teeth. The approach applied for the solution of the above problems is similar to the one discussed in Section 13.5. The final results of the investigation are as follows.

Equation of Meshing

There are two solutions for determination of current point M of tangency of gear 2 tooth profile Σ_2 and pinion tooth profile Σ_1 (Fig. 13.6.2):

(i)   Solution 1 provides any value of θ_2 at the position $\phi_2 = 0$. The gear 2 pin of circle of radius ρ_2 copies the same circle in coordinate system S_1.

(ii) Solution 2 provides the relation

$$\phi_2 = 2(\theta_2 - 90°), \quad \theta_2 > 90°. \tag{13.6.1}$$

Line of Action

The current point of the line of action is M (Fig. 13.6.2), determined in S_f by the equations

$$\theta_2 \geq 90°, \quad \phi_2 = 2(\theta_2 - 90°)$$
$$x_f = r_2 \sin\phi_2 + \rho_2 \sin(\theta_2 - \phi_2) \tag{13.6.2}$$
$$y_f = r_2 \cos\phi_2 - \rho_2 \cos(\theta_2 - \phi_2).$$

It is easy to verify that if $\rho_2 = 0$, the line of action is a circular arc of radius r_2.

Pinion Tooth Profile

The pinion tooth profile is formed by two curves, I and II:

(i) Curve I in S_1 is an arc of the circle of radius ρ_2 and is represented by the equations

$$x_1 = \rho_2 \sin\theta_2, \quad y_1 = r_1 - \rho_2 \cos\theta_2 \quad (90° \geq \theta_2 \geq 0). \tag{13.6.3}$$

(ii) Curve II is represented in S_1 by the equations

$$\theta_2 \geq 90°, \quad \phi_2 = 2(\theta_2 - 90°), \quad \phi_1 = \frac{r_2}{r_1}\phi_2$$

$$x_1 = -r_2 \sin(\phi_1 - \phi_2) + (r_2 - r_1)\sin\phi_1 + \rho_2 \sin[\theta_2 + (\phi_1 - \phi_2)]$$

$$y_1 = r_2 \cos(\phi_1 - \phi_2) - (r_2 - r_1)\cos\phi_1 - \rho_2 \cos[\theta_2 + (\phi_1 - \phi_2)]. \tag{13.6.4}$$

Equations (13.6.4) represent the right-side profile of gear 1 teeth. Similarly, we may obtain the left-side profile of gear 1 teeth. Taking $\rho_2 = 0$ in Eq. (13.6.4), we obtain equations of an epicycloid that is generated in S_1 by the center of circle ρ_2.

Tooth Profile of an Imaginary Rack-Cutter

Pinion 1 can be generated by a hob designed on the basis of an imaginary rack-cutter. The tooth profile of the rack-cutter is formed in S_t (Fig. 13.6.2) by curves I and II:

(i) Curve I is a circular arc of radius ρ with center located at O_t.
(ii) The right-side profile of the rack-cutter tooth is represented by the matrix equation

$$\mathbf{r}_t(\theta_2, \phi_2) = \mathbf{M}_{t2}(\phi_2)\mathbf{r}_2(\theta_2), \tag{13.6.5}$$

which yields

$$\theta_2 \geq 90°, \quad \phi_2 = 2(\theta_2 - 90°)$$

$$x_t = -r_2(\phi_2 - \sin\phi_2) + \rho_2 \sin(\theta_2 - \phi_2)$$

$$y_t = -r_2(1 - \cos\phi_2) - \rho_2 \cos(\theta_2 - \phi_2). \tag{13.6.6}$$
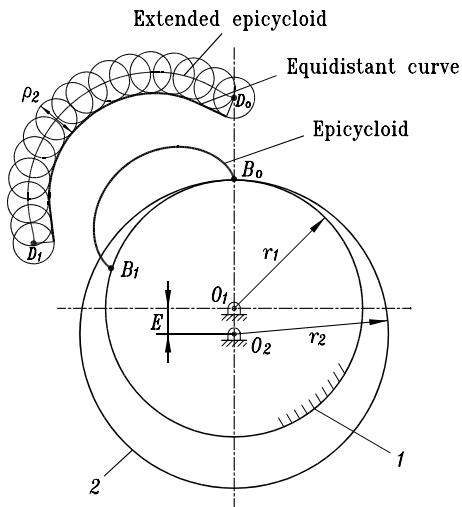
Axis y_t is the axis of symmetry of the tooth profile of the rack-cutter.

13.7 OVERCENTRODE CYCLOIDAL GEARING

Basic Idea

The term "overcentrode" means that the gear teeth are displaced with respect to the gear centrodes. Overcentrode cycloidal gearing has found application in planetary trains with a difference in the number of pinion-gear teeth equal to 1.

The idea of overcentrode cycloidal gearing is illustrated by Fig. 13.7.1. Here, r_1 and r_2 are the radii of gear centrodes that are in internal tangency. By rolling circle 2 over circle 1, point B_o which is rigidly connected to circle 2 will trace out in coordinate

Figure 13.7.1: Overcentrode cycloidal gearing.

system S_1 a conventional epicycloid B_o–B_1. Coordinate system S_1 is rigidly connected to gear 1.

Let us imagine now that point D_o instead of B_o is rigidly connected to centrode 2. Point D_o will trace out in S_1 the extended epicycloid D_o–D_1. Theoretically, we may consider the interaction of two "profiles": (i) point D_o as the tooth "profile" of gear 2, and (ii) the extended epicycloid as the tooth profile of gear 1. In reality, a pin of radius ρ_2 should be chosen as the tooth profile of gear 2. The tooth profile of gear 1 is the curve that is equidistant to the extended epicycloid D_o–D_1.

Relation Between Gear Tooth Numbers

The determination of the sought-for relation between the pinion-gear tooth numbers, N_1 and N_2, is based on the following considerations:

  (i) A full branch of the extended epicycloid is used as the tooth profile of gear 1 (Fig. 13.7.1). Gear 1 must be provided with a whole number N_1 of such branches.
 (ii) The generation of the extended epicycloid D_o–D_1 and the conventional epicycloid B_o–B_1 is performed for the same angle of rotation of centrode 2.
(iii) Consider now that while centrode 2 will make one revolution, point B_o of this centrode will generate in S_1 $(N_1 + 1)$ branches of conventional epicycloids. The common point of tangency of centrodes 1 and 2 will trace out on these centrodes two equal arcs determined as

$$L = 2\pi r_2 = 2\pi r_1 + mp_c. \tag{13.7.1}$$

Here, p_c is the circular pitch, the distance between points B_o and B_1 measured on centrode 1; $m \geq 1$ is a whole number.

 (iv) It is evident that

$$p_c = \frac{2\pi r_1}{N_1}. \tag{13.7.2}$$

(v) Equations (13.7.1) and (13.7.2) yield

$$r_2 = r_1 \left(1 + \frac{m}{N_1} \right). \tag{13.7.3}$$

(vi) Taking into account that

$$\frac{r_2}{r_1} = \frac{N_2}{N_1}, \tag{13.7.4}$$

we obtain that

$$N_2 = N_1 \left(1 + \frac{m}{N_1} \right) \tag{13.7.5}$$

where $m = 1, 2, 3, \ldots$.

For the case when $m = 1$, we obtain that

$$N_2 = N_1 + 1. \tag{13.7.6}$$

This means that the number N_2 of pins provided for gear 2 must be at least one larger than the number of branches N_1 provided for gear 1.

(vii) Consider that the number of branches on centrode 1 is N_1 and the center distance E is chosen. Then, taking into account that

$$r_2 = r_1 + E, \quad \frac{r_2}{r_1} = \frac{N_2}{N_1},$$

we obtain

$$r_1 = EN_1 \tag{13.7.7}$$

$$r_2 = EN_2 = E(N_1 + 1) \tag{13.7.8}$$

assuming that $N_2 = N_1 + 1$.

(viii) It is easy to verify as well that
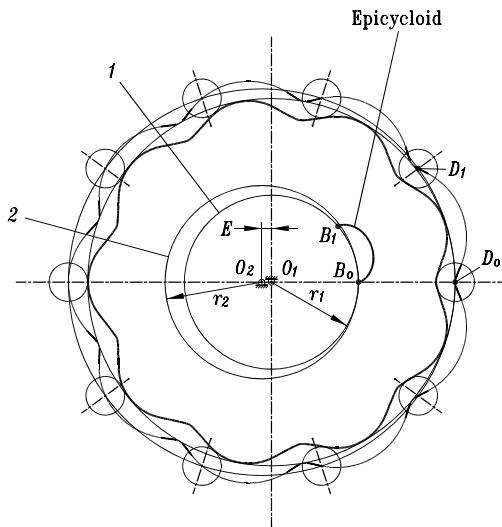
$$p_c = 2\pi E. \tag{13.7.9}$$

Examples of Overcentrode Cycloidal Gearing

Figure 13.7.2 illustrates that the pins are provided on gear 2, and the tooth profiles of gear 1 are extended epicycloids. Figure 13.7.3 illustrates a gear train when gear 1 but not gear 2 is provided with N_1 pins; the profiles of the N_2 teeth of gear 2 are extended hypocycloids ($N_2 = N_1 + 1$). In both cases all the pins are in tangency with all of the cycloidal curves (disregarding misalignment and errors of manufacture). However, only half of them can be under the load, and less than half can be due to misalignment.

13.8 ROOT'S BLOWER
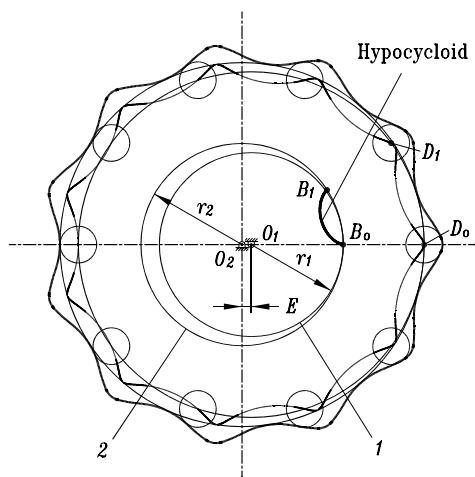
Root's blowers are used as air dischargers for diesel engines and other equipment. Rotors with two and three lobes are used in the industry (Fig. 13.8.1). The ratio of angular velocities of the rotors is 1, and their centrodes are circles of the same radius (Fig. 13.8.2). The rotors are driven by two equal gears mounted on the shafts of the rotors.
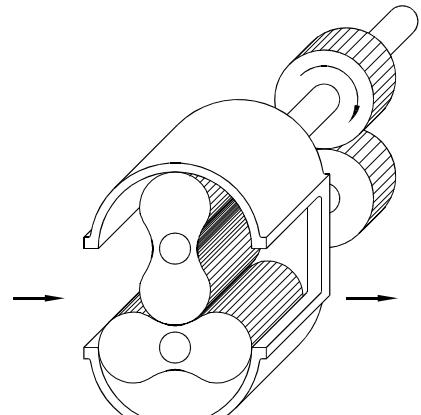
Figure 13.7.2: Overcentrode epicycloidal gear train.

Conjugation of Profiles
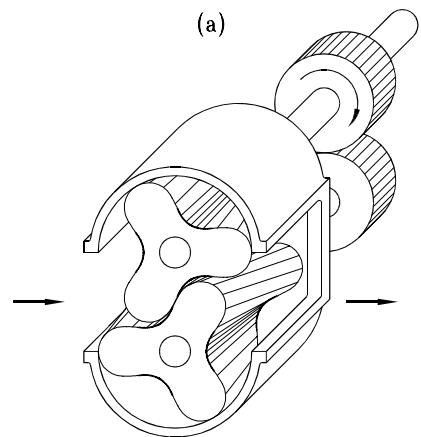
The tooth profile of blower 1 is a circle of radius ρ_1 centered at C; point C is located at distance a from the center of rotation O_1. Consider that the rotor centrode 1 is rolling over centrode 2 of the other rotor. Then, point C will trace out in coordinate system S_2 the shortened epicycloid (not shown in Fig. 13.8.2); S_2 is rigidly connected to rotor 2. Theoretically, we may consider the interaction of point C of rotor 1 with the shortened epicycloid of rotor 2. In reality, the following conjugate profiles are designed: (i) the circular arc Σ_1 of radius ρ_1 as the tooth profile of rotor 1, and (ii) curve Σ_2 that is equidistant to the shortened epicycloid as the tooth profile of rotor 2. Curves Σ_1 and Σ_2 are the profiles of the addendum of rotor 1 and the dedendum of rotor 2, respectively.

Figure 13.7.3: Overcentrode hypocycloidal gear train.

Figure 13.8.1: Root's blowers.

(a)

(b)
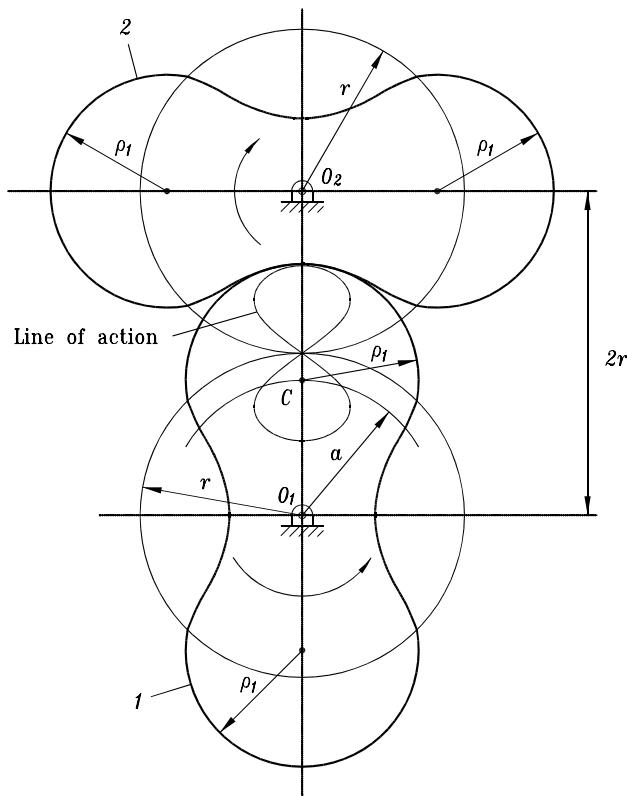
The lobe element proportions can be determined with Fig. 13.8.3. The addendum angle of Σ_1 of a rotor with two and three lobes is equal to 90° and 60°, respectively. The design parameters are related by the equation

$$r^2 + a^2 - 2ar \cos q = \rho^2. \tag{13.8.1}$$

Here, q is 45° and 30° for two and three lobe rotors, respectively.

Applied Coordinate Systems

Movable coordinate systems S_1 and S_2 are rigidly connected to rotors 1 and 2, respectively [Fig. 13.8.4(b)]. The fixed coordinate system, S_f, is rigidly connected to the housing. Our next goals are (i) derivation of the equation of meshing, (ii) determination of the line of action, and (iii) determination of curve Σ_2, the dedendum profile of rotor 2.

Figure 13.8.2: Rotor tooth profiles.

Equation of Meshing; Line of Action

The tooth profile of two-lobe rotor 1 is represented in S_1 (Fig. 13.8.4) by the equations

$$x_1 = \rho \sin\theta, \quad y_1 = a + \rho \cos\theta$$

$$-\frac{(a+\rho)^2 - r^2}{\sqrt{2ar}} \leq \tan\frac{\theta}{2} \leq \frac{(a+\rho)^2 - r^2}{\sqrt{2ar}}. \tag{13.8.2}$$
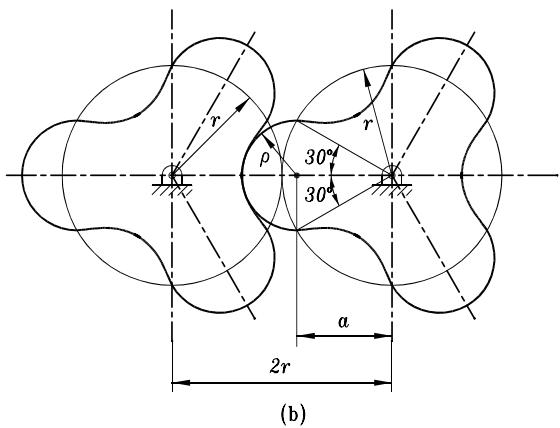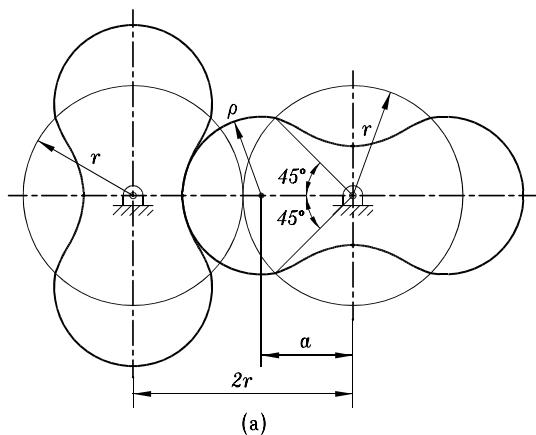
Using the approach for derivation of the equation of meshing discussed in Sections 13.5 and 13.6, we obtain

$$f(\theta, \phi) = r \sin(\theta - \phi) - a \sin\theta = 0. \tag{13.8.3}$$
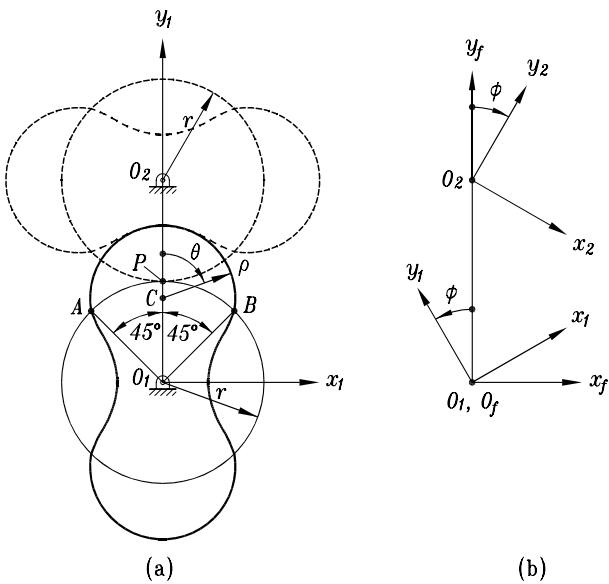
Consider a particular case when $a = r$ and $\phi = 0$. It is evident that in this case center C of the circular arc Σ_1 coincides with the instantaneous center of rotation P, any normal to Σ_1 passes through P, and Eq. (13.8.3) is satisfied for any value of θ. The relation $a = r$ should not be applied in practical design.

The line of action is represented in S_f by the equations

$$\mathbf{r}_f = \mathbf{M}_{f1}\mathbf{r}_1(\theta), \quad f(\theta, \phi) = 0, \tag{13.8.4}$$

Figure 13.8.3: For derivation of relation between the design parameters.

Figure 13.8.4: Applied coordinate systems.

Table 13.8.1: Properties of Σ_2

Lobe number	Convex	Concave–Convex	With singularities
2	$0 < \dfrac{a}{r} < 0.5$	$0.5 < \dfrac{a}{r} < 0.9288$	$\dfrac{a}{r} > 0.9288$
3	$0 < \dfrac{a}{r} < 0.5$	$0.5 < \dfrac{a}{r} < 0.9670$	$\dfrac{a}{r} > 0.9670$

which yield

$$x_f = \rho \sin(\theta - \phi) - a \sin \phi$$

$$y_f = \rho \cos(\theta - \phi) + a \cos \phi \qquad (13.8.5)$$

$$r \sin(\theta - \phi) - a \sin \theta = 0.$$

Equations of Dedendum Curve Σ_2 of Rotor 2

Profile Σ_2 is represented in S_2 by the equations

$$\mathbf{r}_2 = \mathbf{M}_{21}\mathbf{r}_1, \quad f(\theta, \phi) = 0, \qquad (13.8.6)$$

which yield

$$x_2 = \rho \sin(\theta - 2\phi) - a \sin 2\phi + 2r \sin \phi$$

$$y_2 = \rho \cos(\theta - 2\phi) + a \cos 2\phi - 2r \cos \phi \qquad (13.8.7)$$

$$r \sin(\theta - \phi) - a \sin \theta = 0.$$

Depending on the ratio a/r, profile Σ_2 may be represented by (i) a convex curve, (ii) a concave–convex curve, and (iii) a curve with singularities. The third case may be investigated by considering the conditions of "nonundercutting" of Σ_2 by Σ_1 (see Section 6.3). The first and second cases may be investigated by considering the relations between the curvatures of conjugate shapes (see Section 8.3). The results of the investigations are presented in Table 13.8.1.

14 Involute Helical Gears with Parallel Axes

14.1 INTRODUCTION

Cycloidal gears (Chapter 13) and involute gears (Chapters 10, 11, 14, 15, and 16) have different areas of application. This chapter covers involute gears with parallel axes, whose design is based on the assumption that the gear tooth surfaces are in instantaneous contact along a line (line contact) in the case of aligned gear drives. Although the influence of errors of alignment should be considered in the study of the real meshing (see Chapters 15, 16, and 17), in this chapter we consider a preliminary study limited to the theoretical study of meshing. This allows the reader to focus initially on the theoretical study of involute gears. However, we have to emphasize that the modern design of helical gear drives is directed at observation of localized bearing contact (obtained by tooth surfaces being in point contact instead of line contact), simulation of meshing of misaligned gear drives, and stress analysis (see Chapters 15, 16, and 17). The nomenclature used in this chapter is presented in Section 14.10.

14.2 GENERAL CONSIDERATIONS

Helical gears that transform rotation between parallel axes in opposite directions are in external meshing and are provided with screw tooth surfaces of opposite directions.

The *axodes* of nonstandard gears are two cylinders of radii r_{o1} and r_{o2} related as

$$\frac{r_{o2}}{r_{o1}} = \frac{\omega^{(1)}}{\omega^{(2)}} = m_{12}. \tag{14.2.1}$$

These cylinders are called the *operating pitch cylinders* as well. Henceforth, we differentiate standard and nonstandard helical gears. The operating pitch cylinders (the axodes) coincide with the pitch cylinders in the case of standard helical gears, and they differ from the pitch cylinders for nonstandard helical gears (see below). Axodes of standard gears are the gear pitch cylinders. The line of tangency of the axodes is the *instantaneous axis of rotation* of the gears in relative motion. The cylinders of radii r_{o1} and r_{o2} roll over each other without sliding. The helices on the operating pitch cylinders are of opposite direction but the magnitude of the lead angle (or the helix angle) is the same for both helices.

The tooth surface of a helical gear is a helicoid that is represented by Eq. (1.7.5). It was assumed in the derivation of this equation that the helicoid is generated by the screw motion of a cross profile about the gear axis. The cross profile is represented in a plane that is perpendicular to the gear axis. However, a helicoid may also be generated by the screw motion of the *axial* profile, which is a curve represented in the plane drawn through the axis of the helical gear.

Consider that the tooth surface is represented by the vector equation

$$\mathbf{r}_1 = x_1(u, \theta) \, \mathbf{i}_1 + y_1(u, \theta) \, \mathbf{j}_1 + z_1(u, \theta, p) \, \mathbf{k}_1 \tag{14.2.2}$$

where (u, θ) are the surface parameters (Gaussian coordinates); p is the screw parameter in the screw motion about the z_1 axis. The normal to the surface is represented as

$$\mathbf{N}_1 = \frac{\partial \mathbf{r}_1}{\partial \theta} \times \frac{\partial \mathbf{r}_1}{\partial u}, \tag{14.2.3}$$

and $\mathbf{N}_1 \neq 0$ is for a regular surface. The requirement for surface (14.2.2) to be a helicoid is expressed by the equation

$$x_1 N_{y1} - y_1 N_{x1} + p N_{z1} = x_1 n_{y1} - y_1 n_{x1} + p n_{z1} = 0. \tag{14.2.4}$$

Here, the screw parameter p in Eq. (14.2.4) is considered as an algebraic value;

$$\mathbf{n}_1 = \frac{\mathbf{N}_1}{|\mathbf{N}_1|}$$

is the surface unit normal; $p > 0$ for a right-hand gear.

Figure 14.2.1(a) shows a helicoid, an involute screw surface, which is generated by the screw motion of an involute curve; r_b is the radius of the base cylinder. The intersection of the helicoid by a cylinder of radius ρ is a helix [Fig. 14.2.1(b)]; H is the lead of the helicoid; λ_ρ is the lead angle on the cylinder of radius ρ.

Figure 14.2.1(c) shows that the cylinder of radius ρ and the helix have been developed on a plane. It is easy to verify that
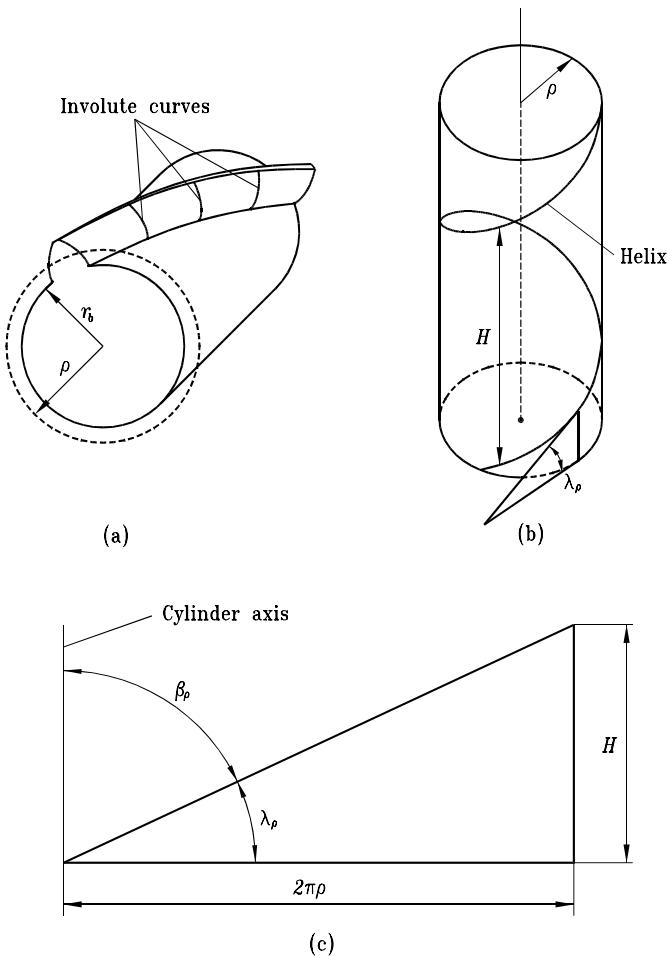
$$\tan \lambda_\rho = \cot \beta_\rho = \frac{H}{2\pi\rho} \tag{14.2.5}$$

where λ_ρ and β_ρ are the lead angle and the helix angle, respectively. The ratio $H/2\pi = p$ is the *screw parameter*, which is the axial displacement in screw motion corresponding to rotation through the angle of one radian. Equation (14.2.5) yields that the product

$$\rho \tan \lambda_\rho = p \tag{14.2.6}$$

is an invariant with respect to the radius ρ of the cylinder that intersects the helicoid being considered.

The investigation of meshing of helical gears with parallel axes requires solutions to the following problems (see Section 14.5): (i) determination of surface Σ_2 that is conjugate to given surface Σ_1, (ii) determination of the lines of contact between Σ_1 and Σ_2, and (iii) determination of the surface of action.
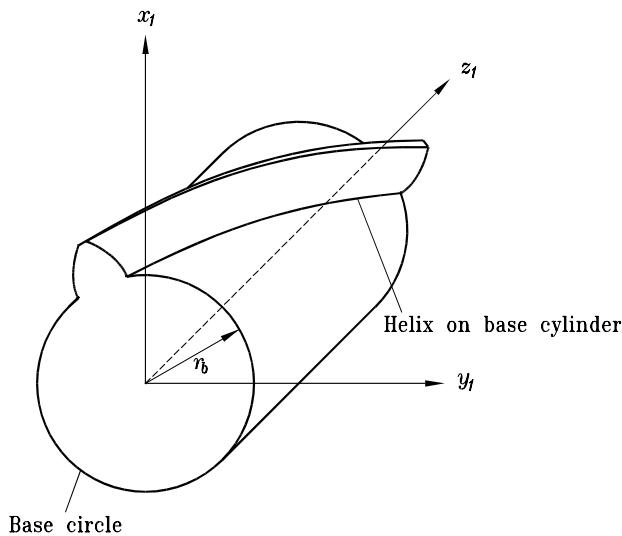
Figure 14.2.1: Development of a cylinder and its helix.

14.3 SCREW INVOLUTE SURFACE
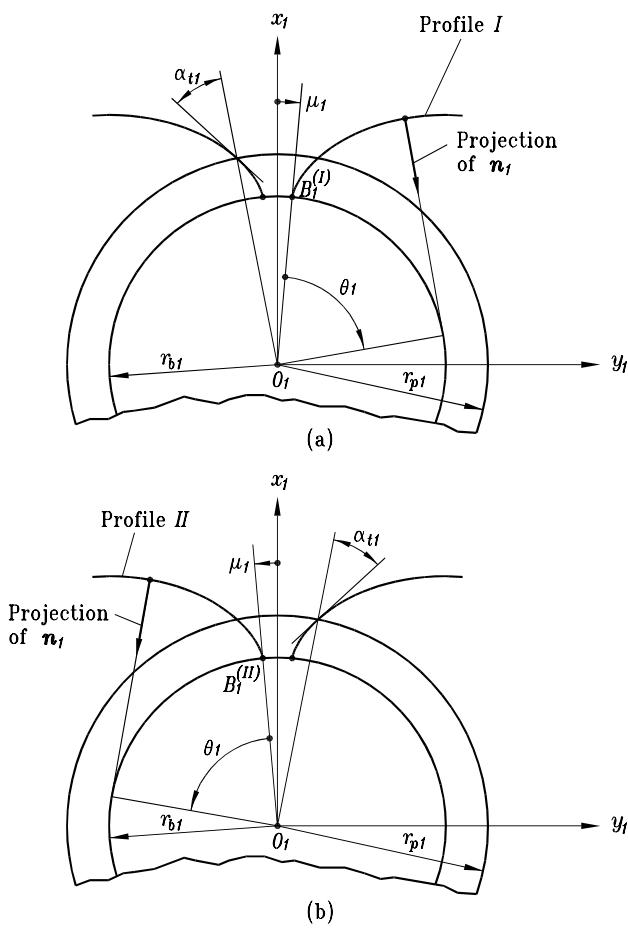
An involute helical gear may be considered as a multi-thread involute worm. Equations of tooth surfaces of an involute helical gear are the same as for an involute worm (see Section 19.6). The equations below describe tooth side I and II surfaces for right-hand and left-hand gears. Equations of the gear tooth surfaces are presented separately for the driving gear 1 and driven gear 2, in coordinate systems S_1 and S_2, respectively. A right-hand helical gear 1 is shown in Fig. 14.3.1.

Figure 14.3.2 shows the cross section of tooth surfaces of gear 1 obtained by intersection by plane $z_1 = 0$. Axis x_1 is the axis of symmetry of the *space*. Half of the angular width of the space on the base circle is formed by axis x_1 and the position vector $\overline{O_1 B_1}^{(k)}$ ($k = I, II$) and is determined with angle μ_1. Here (Fig. 14.3.2),
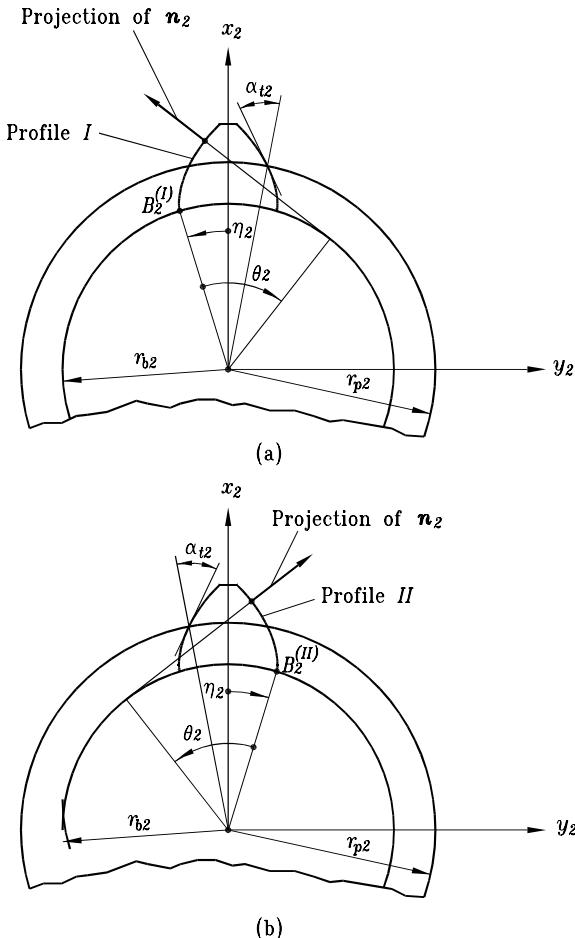
$$\mu_1 = \frac{w_{t1}}{2r_{p1}} - \text{inv}\alpha_{t1} \tag{14.3.1}$$

Figure 14.3.1: Right-hand helical gear.

Figure 14.3.2: Cross section of helical gear 1.

Figure 14.3.3: Cross section of helical gear 2.

where w_{t1} is the nominal value of space width on the pitch circle and α_{t1} is the profile angle in the cross section, at the point of intersection of the profile with the pitch circle.

The tooth surface equations are represented in terms of surface parameters (u_1, θ_1) (see Section 19.6). Parameter θ_1 is measured from position vector $\overline{O_1 B_1}^{(k)}$ $(k = I, II)$ in the direction shown in Fig. 14.3.2. The direction of measurements of θ_1 and μ_1 is clockwise for surface I and counterclockwise for surface II. It is assumed that the observer is located on the negative axis z_1.

Figure 14.3.3 shows the tooth profiles in the cross section of tooth surfaces of gear 2. The surface equations are represented in S_2 in terms of surface parameters u_2 and θ_2. The concept of parameters u_2 and θ_2 is based on considerations similar to those used in Section 19.6 for u_1 and θ_1. Parameter θ_2 is measured from the position vector $O_2 B_2^{(k)}$ $(k = I, II)$, clockwise for surface I and counterclockwise for surface II, as shown in Fig. 14.3.3. Recall that the observer is located on the negative axis z_2. Half of the angular tooth thickness on the base circle is represented by angle η_2 where

$$\eta_2 = \frac{s_{t2}}{2r_{p2}} + \text{inv}\alpha_{t2}. \tag{14.3.2}$$

Here, s_{t2} is the nominal value of tooth thickness on the pitch circle, and α_{t2} is the profile angle in the cross section, at the point of intersection of the profile with the pitch circle. The direction of measurements of η_2 is opposite to the direction of measurements of θ_2.

The gear tooth surfaces are represented in S_i by the vector function

$$\mathbf{r}_i(u_i, \theta_i) \quad (i = 1, 2). \tag{14.3.3}$$

The unit normals to the tooth surfaces of gear 1 are represented as

$$\mathbf{n}_1 = \mp \frac{\dfrac{\partial \mathbf{r}_1}{\partial u_1} \times \dfrac{\partial \mathbf{r}_1}{\partial \theta_1}}{\left| \dfrac{\partial \mathbf{r}_1}{\partial u_1} \times \dfrac{\partial \mathbf{r}_1}{\partial \theta_1} \right|}. \tag{14.3.4}$$

The upper and lower signs correspond to surfaces of gear 1 for a right-hand and left-hand orientation, respectively. The direction chosen below of the surface unit normal $\mathbf{n}_2$ enables us to provide the coincidence of $\mathbf{n}_1$ and $\mathbf{n}_2$ when the tangency of tooth surfaces of gears 1 and 2 is considered.

The u_i coordinate line on gear tooth surface (14.3.3) (θ_i is fixed) is a straight line, which generates the gear tooth surface while performing a screw motion (see Section 19.6). The θ_i line (u_i is fixed) is a helix on the gear tooth surface. The screw parameters p_1 and p_2 in the equations below are always considered as positive values for either right-hand gears or left-hand gears.

Here are the derived equations of gear tooth surfaces and the surface unit normals:

(i) Right-hand gear 1, side surface *I* (Fig. 14.3.2):

$$\begin{aligned}
x_1 &= r_{b1} \cos(\theta_1 + \mu_1) + u_1 \cos \lambda_{b1} \sin(\theta_1 + \mu_1) \\
y_1 &= r_{b1} \sin(\theta_1 + \mu_1) - u_1 \cos \lambda_{b1} \cos(\theta_1 + \mu_1) \\
z_1 &= -u_1 \sin \lambda_{b1} + p_1 \theta_1
\end{aligned} \tag{14.3.5}$$

$$\mathbf{n}_1 = [-\sin \lambda_{b1} \sin(\theta_1 + \mu_1) \quad \sin \lambda_{b1} \cos(\theta_1 + \mu_1) \quad -\cos \lambda_{b1}]^{\mathrm{T}}. \tag{14.3.6}$$

Angle θ_1 and μ_1 are measured clockwise.

(ii) Right-hand gear 1, side surface *II* (Fig. 14.3.2):

$$\begin{aligned}
x_1 &= r_{b1} \cos(\theta_1 + \mu_1) + u_1 \cos \lambda_{b1} \sin(\theta_1 + \mu_1) \\
y_1 &= -r_{b1} \sin(\theta_1 + \mu_1) + u_1 \cos \lambda_{b1} \cos(\theta_1 + \mu_1) \\
z_1 &= u_1 \sin \lambda_{b1} - p_1 \theta_1
\end{aligned} \tag{14.3.7}$$

$$\mathbf{n}_1 = [-\sin \lambda_{b1} \sin(\theta_1 + \mu_1) \quad -\sin \lambda_{b1} \cos(\theta_1 + \mu_1) \quad \cos \lambda_{b1}]^{\mathrm{T}}. \tag{14.3.8}$$

Angles θ_1 and μ_1 are measured counterclockwise.

(iii) Left-hand gear 1, side surface *II* (Fig. 14.3.2):

$$x_1 = r_{b1} \cos(\theta_1 + \mu_1) + u_1 \cos \lambda_{b1} \sin(\theta_1 + \mu_1)$$

$$y_1 = -r_{b1} \sin(\theta_1 + \mu_1) + u_1 \cos \lambda_{b1} \cos(\theta_1 + \mu_1) \tag{14.3.9}$$

$$z_1 = -u_1 \sin \lambda_{b1} + p_1 \theta_1$$

$$\mathbf{n}_1 = [-\sin \lambda_{b1} \sin(\theta_1 + \mu_1) \quad -\sin \lambda_{b1} \cos(\theta_1 + \mu_1) \quad -\cos \lambda_{b1}]^{\mathrm{T}}. \tag{14.3.10}$$

Angles θ_1 and μ_1 are measured counterclockwise.

(iv) Left-hand gear 1, side surface *I* (Fig. 14.3.2):

$$x_1 = r_{b1} \cos(\theta_1 + \mu_1) + u_1 \cos \lambda_{b1} \sin(\theta_1 + \mu_1)$$

$$y_1 = r_{b1} \sin(\theta_1 + \mu_1) - u_1 \cos \lambda_{b1} \cos(\theta_1 + \mu_1) \tag{14.3.11}$$

$$z_1 = u_1 \sin \lambda_{b1} - p_1 \theta_1$$

$$\mathbf{n}_1 = [-\sin \lambda_{b1} \sin(\theta_1 + \mu_1) \quad \sin \lambda_{b1} \cos(\theta_1 + \mu_1) \quad \cos \lambda_{b1}]^{\mathrm{T}}. \tag{14.3.12}$$

Angles θ_1 and μ_1 are measured clockwise.

Similarly, we represent equations of tooth surfaces of gear 2. We remind the reader that angle η_2 is measured in a direction opposite to the direction of measurements of θ_2 (Fig. 14.3.3).

(i) Right-hand gear 2, side-surface *I* (Fig. 14.3.3):

$$x_2 = r_{b2} \cos(\theta_2 - \eta_2) + u_2 \cos \lambda_{b2} \sin(\theta_2 - \eta_2)$$

$$y_2 = r_{b2} \sin(\theta_2 - \eta_2) - u_2 \cos \lambda_{b2} \cos(\theta_2 - \eta_2) \tag{14.3.13}$$

$$z_2 = -u_2 \sin \lambda_{b2} + p_2 \theta_2$$

$$\mathbf{n}_2 = [\sin \lambda_{b2} \sin(\theta_2 - \eta_2) \quad -\sin \lambda_{b2} \cos(\theta_2 - \eta_2) \quad \cos \lambda_{b2}]^{\mathrm{T}}. \tag{14.3.14}$$

Angle θ_2 is measured clockwise.

(ii) Right-hand gear 2, side-surface *II* (Fig. 14.3.3):

$$x_2 = r_{b2} \cos(\theta_2 - \eta_2) + u_2 \cos \lambda_{b2} \sin(\theta_2 - \eta_2)$$

$$y_2 = -r_{b2} \sin(\theta_2 - \eta_2) + u_2 \cos \lambda_{b2} \cos(\theta_2 - \eta_2) \tag{14.3.15}$$

$$z_2 = u_2 \sin \lambda_{b2} - p_2 \theta_2$$

$$\mathbf{n}_2 = [\sin \lambda_{b2} \sin(\theta_2 - \eta_2) \quad \sin \lambda_{b2} \cos(\theta_2 - \eta_2) \quad -\cos \lambda_{b2}]^{\mathrm{T}}. \tag{14.3.16}$$

Angle θ_2 is measured counterclockwise.

(iii) Left-hand gear 2, side-surface *II* (Fig. 14.3.3):

$$x_2 = r_{b2} \cos(\theta_2 - \eta_2) + u_2 \cos \lambda_{b2} \sin(\theta_2 - \eta_2)$$

$$y_2 = -r_{b2} \sin(\theta_2 - \eta_2) + u_2 \cos \lambda_{b2} \cos(\theta_2 - \eta_2) \tag{14.3.17}$$

$$z_2 = -u_2 \sin \lambda_{b2} + p_2 \theta_2$$

$$\mathbf{n}_2 = [\sin \lambda_{b2} \sin(\theta_2 - \eta_2) \quad \sin \lambda_{b2} \cos(\theta_2 - \eta_2) \quad \cos \lambda_{b2}]^{\mathrm{T}}. \tag{14.3.18}$$

Angle θ_2 is measured counterclockwise.

(iv) Left-hand gear 2, side-surface I (Fig. 14.3.3):

$$x_2 = r_{b2} \cos(\theta_2 - \eta_2) + u_2 \cos \lambda_{b2} \sin(\theta_2 - \eta_2)$$
$$y_2 = r_{b2} \sin(\theta_2 - \eta_2) - u_2 \cos \lambda_{b2} \cos(\theta_2 - \eta_2) \tag{14.3.19}$$
$$z_2 = u_2 \sin \lambda_{b2} - p_2 \theta_2$$
$$\mathbf{n}_2 = [\sin \lambda_{b2} \sin(\theta_2 - \eta_2) \quad -\sin \lambda_{b2} \cos(\theta_2 - \eta_2) \quad -\cos \lambda_{b2}]^{\mathrm{T}}. \tag{14.3.20}$$
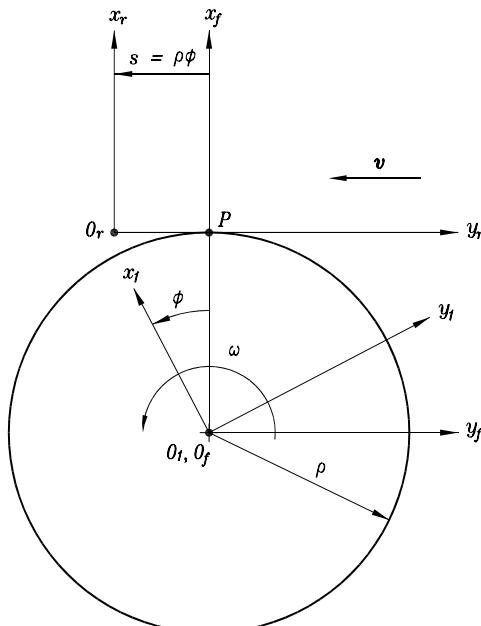
Angle θ_2 is measured clockwise.

14.4 MESHING OF A HELICAL GEAR WITH A RACK

We may consider the meshing of a screw involute gear, say gear 1, with the respective rack in plane $z_1 = 0$ that is perpendicular to the z_1 gear axis. The cross section of the gear tooth surface by plane $z_1 = 0$ is an involute curve. Then, we may consider that a spur gear with an infinitesimally small tooth length is in mesh with a rack whose tooth length is also infinitesimally small. It is known that the profile of such a rack is a straight line (see Chapter 10).

The derivation of tooth surface Σ_r of the rack is represented as the determination of the envelope to the family of screw involute surfaces Σ_1. Consider that movable coordinate systems S_1 and S_r are rigidly connected to the gear and the rack; coordinate system S_f is the fixed one (Fig. 14.4.1). The gear and the rack perform rotational and translational motions, respectively. The velocities of these motions are related as follows:

$$\frac{v}{\omega} = \rho. \tag{14.4.1}$$

Figure 14.4.1: For investigation of meshing of a helical gear with a rack.

The gear axode is the cylinder of radius ρ; the rack axode is the plane that is tangent to the cylinder mentioned above and is parallel to vector $\mathbf{v}$. The instantaneous axis of rotation, $P-P$, is parallel to the gear axis and is represented in S_f as

$$X_f = \rho, \quad Y_f = 0, \quad Z_f = l \tag{14.4.2}$$

where (X_f, Y_f, l) determine a current point of $P-P$; l is a varied parameter. The instantaneous axis of rotation is represented in coordinate system S_1 by the equation

$$[\, X_1 \quad Y_1 \quad Z_1 \,]^{\mathrm{T}} = \mathbf{M}_{1f}[\, X_f \quad Y_f \quad Z_f \,]^{\mathrm{T}} \tag{14.4.3}$$

which yields

$$X_1 = \rho \cos \phi, \quad Y_1 = \rho \sin \phi, \quad Z_1 = l. \tag{14.4.4}$$

We consider in the following derivations that Σ_1 is surface I of a right-hand helical gear and is represented by Eqs. (14.3.5). Our goal is to derive the equations of the rack tooth surface Σ_r that is conjugate to Σ_1. The derivation of Σ_r and its visualization is based on the following procedure.

Equation of Meshing

We derive the equation of meshing considering that *the normal to the screw involute surface Σ_1 at any point of the line of contact between Σ_1 and Σ_r passes through the instantaneous axis of rotation $P-P$.* Thus,

$$\frac{X_1 - x_1(u, \theta)}{n_{x1}(\theta)} = \frac{Y_1 - y_1(u, \theta)}{n_{y1}(\theta)} = \frac{Z_1 - z_1(u, \theta)}{n_{z1}(\theta)}. \tag{14.4.5}$$

Here, $x_1(u, \theta)$, $y_1(u, \theta)$, $z_1(u, \theta)$ are the coordinates of a point of screw involute surface Σ_1; (n_{x1}, n_{y1}, n_{z1}) are the components of the unit normal to Σ_1 at this point [see Eqs. (14.3.6)]. The subscript "1" in designations for u_1, θ_1, r_{b1}, ρ_1, α_{t1}, and ϕ_1 has been dropped. Equations (14.3.5), (14.3.6), (14.4.4), and (14.4.5) yield

$$\cos(\theta + \mu - \phi) = \frac{r_b}{\rho} = \cos \alpha_t \tag{14.4.6}$$

where α_t is the pressure angle in plane $z_1 = 0$ (see Chapter 10). Equation (14.4.6) provides two solutions for $(\theta + \mu - \phi)$ considering α_t and μ as given. We choose the solution

$$\theta + \mu - \phi - \alpha_t = f(\theta, \phi) = 0. \tag{14.4.7}$$

Equation (14.4.7) is the equation of meshing.

Rack Surface Σ_r

The sought-for surface Σ_r is represented by the equations

$$\mathbf{r}_r(\theta, \phi) = \mathbf{M}_{r1}\mathbf{r}_1(\theta), \quad f(\theta, \phi) = 0 \tag{14.4.8}$$

Here,

$$\mathbf{M}_{r1} = \begin{bmatrix} \cos\phi & \sin\phi & 0 & -\rho \\ -\sin\phi & \cos\phi & 0 & \rho\phi \\ 0 & 0 & 1 & 0 \\ 0 & 0 & 0 & 1 \end{bmatrix}. \tag{14.4.9}$$

Equations (14.3.5), (14.4.7), and (14.4.9) yield the following equations of Σ_r:

$$\begin{aligned} x_r &= r_b \cos\alpha_t + u\cos\lambda_b \sin\alpha_t - \rho \\ y_r &= r_b \sin\alpha_t - u\cos\lambda_b \cos\alpha_t + \rho\phi \\ z_r &= p(\alpha_t - \mu + \phi) - u\sin\lambda_b \end{aligned} \tag{14.4.10}$$

where (u, ϕ) are the surface parameters. The unit normal to surface Σ_r is represented by the equation

$$\mathbf{n}_r = \frac{\dfrac{\partial \mathbf{r}_r}{\partial \phi} \times \dfrac{\partial \mathbf{r}_r}{\partial u}}{\left| \dfrac{\partial \mathbf{r}_r}{\partial \phi} \times \dfrac{\partial \mathbf{r}_r}{\partial u} \right|} = [-\sin\lambda_b \sin\alpha_t \quad \sin\lambda_b \cos\alpha_t \quad -\cos\lambda_b]^{\mathrm{T}}. \tag{14.4.11}$$

Interpretation of Σ_r

Surface Σ_r of the rack is a plane because Eqs. (14.4.10) are represented in the surface parameters (u, ϕ) of the first order. We may represent this plane by the equation

$$x_r n_{xr} + y_r n_{yr} + z_r n_{zr} - m = 0. \tag{14.4.12}$$

Here,

$$\mathbf{n}_r = [n_{xr} \quad n_{yr} \quad n_{zr}]^{\mathrm{T}} \tag{14.4.13}$$

is the unit normal to plane Σ_r represented by Eqs. (14.4.11); m is the magnitude of the perpendicular that is drawn from the origin O_r of S_r to plane Σ_r. Further derivations do not require the determination of m. However, m can be easily determined, if necessary, considering the following system of three linear equations in three unknowns (u, ϕ, and m):

$$\begin{aligned} a_{11}u \quad\quad\quad + a_{13}m &= b_1 \\ a_{21}u + a_{22}\phi + a_{23}m &= b_2 \\ a_{31}u + a_{32}\phi + a_{33}m &= b_3. \end{aligned} \tag{14.4.14}$$

Here,

$$\begin{bmatrix} a_{11} \ a_{12} \ a_{13} \ b_1 \\ a_{21} \ a_{22} \ a_{23} \ b_2 \\ a_{31} \ a_{32} \ a_{33} \ b_3 \end{bmatrix} = \begin{bmatrix} \cos\lambda_b \sin\alpha_t & 0 & -n_{xr} & r_b \sin\alpha_t \tan\alpha_t \\ -\cos\lambda_b \cos\alpha_t & \rho & -n_{yr} & -r_b \sin\alpha_t \\ -\sin\lambda_b & p & -n_{zr} & -p(\alpha_t - \mu) \end{bmatrix}. \quad (14.4.15)$$

The derivation of Eqs. (14.4.14) from (14.4.10) is based on the following considerations:

(i) We have considered in Eqs. (14.4.10) that

$$x_r = m \, n_{xr}, \qquad y_r = m \, n_{yr}, \qquad z_r = m \, n_{zr} \qquad (14.4.16)$$

are the coordinates of the point of intersection of the surface normal with Σ_r. This normal is drawn to Σ_r from the origin O_r of coordinate system S_r.

(ii) The screw parameter p can be expressed as

$$p = \rho \tan\lambda_\rho = r_b \tan\lambda_b \qquad (14.4.17)$$

where λ_k $(k = \rho, b)$ are the lead angles on cylinders of radii ρ and r_b.

Sections of Σ_r

Using Eq. (14.4.12), we are able to determine the profile angles of the rack surface Σ_r in the sections of Σ_r by plane $z_r = 0$, plane $x_r = 0$, and the normal section of Σ_r. Intersection of Σ_r by plane $z_r = 0$ represents a straight line that is determined by the equation

$$x_r n_{xr} + y_r n_{yr} - m = 0. \qquad (14.4.18)$$

The unit vector of this straight line is determined as

$$\frac{1}{(dx_r^2 + dy_r^2)^{0.5}} [\, dx_r \quad dy_r \quad 0\,]^{\mathrm{T}}.$$

The profile angle α_t of the rack is determined as [Fig. 14.4.2(a)]
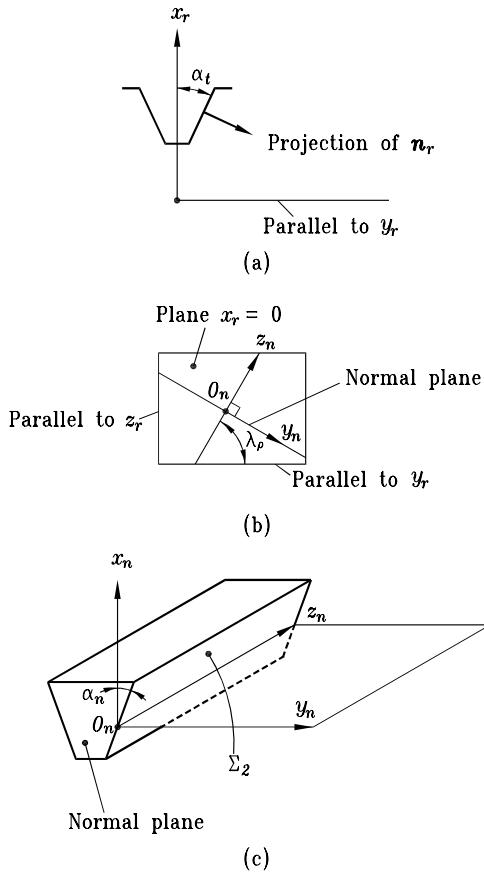
$$\tan\alpha_t = \frac{dy_r}{dx_r} = -\frac{n_{xr}}{n_{yr}}$$

where

$$\cos\alpha_t = \frac{r_b}{\rho} = \frac{\tan\lambda_\rho}{\tan\lambda_b}. \qquad (14.4.19)$$

We consider now the intersection of Σ_r by plane $x_r = 0$ that is tangent to the cylinder of radius ρ (Fig. 14.4.1). The intersection results in a straight line represented by the equation

$$y_r n_{yr} + z_r n_{zr} - m = 0. \qquad (14.4.20)$$

Figure 14.4.2: Profile angles and rack-cutter surface.

The unit vector of this straight line is represented as

$$\frac{1}{(dy_r^2 + dz_r^2)^{0.5}} [\,0 \quad dy_r \quad dz_r\,]^{\mathrm{T}}.$$

The orientation of this unit vector in plane $x_r = 0$ is determined by angle λ_ρ [Fig. 14.4.2(b)], where

$$\tan \lambda_\rho = \frac{dz_r}{dy_r} = -\frac{n_{yr}}{n_{zr}} = \tan \lambda_b \cos \alpha_t. \tag{14.4.21}$$

We consider now the normal section of rack tooth surface Σ_r as the intersection of Σ_r by the plane that passes through the normal to Σ_r and is perpendicular to plane $x_n = 0$ [Fig. 14.4.2(b)]. Coordinate system S_n is rigidly connected to the normal plane, and the origin of coordinate system S_n is located on the rack tooth surface Σ_r (recall that Σ_r is a plane represented by Eq. (14.4.12)). Plane Σ_r is represented in coordinate system S_n by the equation

$$x_n n_{xn} + y_n n_{yn} = 0 \tag{14.4.22}$$

because the origin O_n lies in plane Σ_r and $n_{zn} = 0$ because the normal to Σ_r is perpendicular to z_n [Fig. 14.4.2(c)].

Equation (14.4.22) represents a straight line and the profile angle of the rack tooth surface in the normal plane is represented by the equation

$$\tan \alpha_n = \frac{y_n}{x_n} = -\frac{n_{xn}}{n_{yn}}. \tag{14.4.23}$$

Using coordinate transformation from S_r to S_n, we obtain [see Eqs. (14.4.11)]

$$n_{xn} = n_{xr} = -\sin \lambda_b \sin \alpha_t, \quad n_{yn} = n_{yr} \sin \lambda_\rho - n_{zr} \cos \lambda_\rho$$

$$= \sin \lambda_b \cos \alpha_t \sin \lambda_\rho + \cos \lambda_b \cos \lambda_\rho = \frac{\sin \lambda_b \cos \alpha_t}{\sin \lambda_\rho}. \tag{14.4.24}$$

(Recall that $\tan \lambda_b = \tan \lambda_\rho / \cos \alpha_t$.)
Equations (14.4.23) and (14.4.24) yield

$$\tan \alpha_n = \tan \alpha_t \sin \lambda_\rho. \tag{14.4.25}$$

Lines of Contact on Σ_r

An instantaneous line L_{1r} of contact between Σ_1 and Σ_r is represented in S_r with Eqs. (14.4.10), taking ϕ as constant. Line L_{1r} is a straight line whose unit vector $\mathbf{a}$ is represented in S_r as
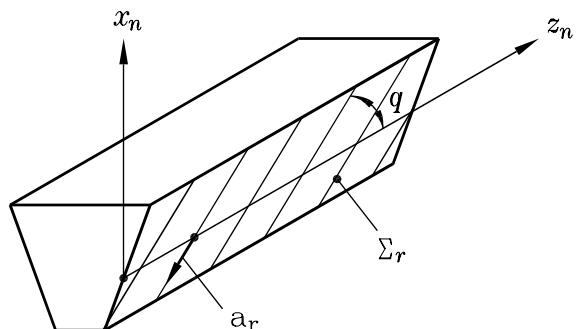
$$\mathbf{a}_r = \frac{\partial \mathbf{r}_r}{\partial u} = [\cos \lambda_b \sin \alpha_t \quad -\cos \lambda_b \cos \alpha_t \quad -\sin \lambda_b]^{\mathrm{T}}. \tag{14.4.26}$$

Using coordinate transformation from S_r to S_n, we represent the unit vector $\mathbf{a}_n$ as follows:

$$\begin{bmatrix} a_{xn} \\ a_{yn} \\ a_{zn} \end{bmatrix} = \begin{bmatrix} 1 & 0 & 0 \\ 0 & \sin \lambda_\rho & -\cos \lambda_\rho \\ 0 & \cos \lambda_\rho & \sin \lambda_\rho \end{bmatrix} \begin{bmatrix} a_{xr} \\ a_{yr} \\ a_{zr} \end{bmatrix}. \tag{14.4.27}$$

Angle q (Fig. 14.4.3) is determined by the equation

$$\cos q = -\mathbf{a}_n \cdot \mathbf{k}_n = \frac{\cos \alpha_t}{\cos \alpha_n}. \tag{14.4.28}$$
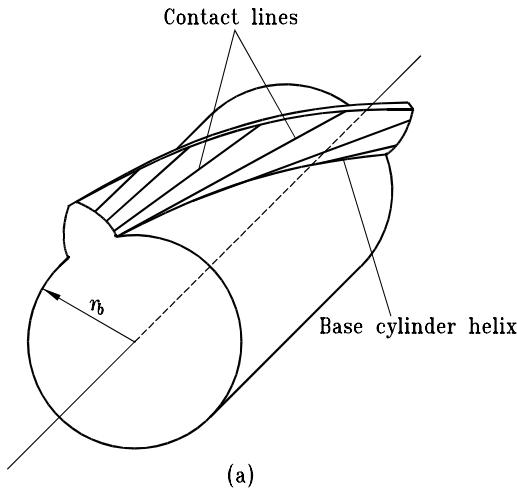
Figure 14.4.3: Contact lines on rack tooth surface.

Contact lines L_{1r} represent in plane Σ_r (the surface of the rack tooth) a family of parallel straight lines that form with axis z_n the angle q (Fig. 14.4.3).
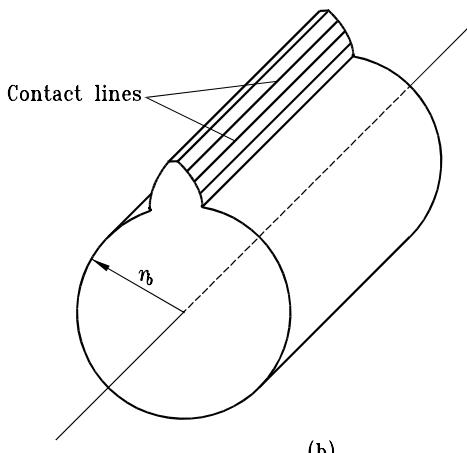
Lines of Contact L_{1r} on Surface Σ_1

Lines L_{1r} on surface Σ_1 of the helical gear are represented by surface Eqs. (14.3.5) and the equation of meshing (14.4.7) taking ϕ as a sequence of constant values. Lines of contact L_{1r} are represented in S_1 by the vector function $\mathbf{r}_1(u, \theta(\phi))$.

The equation of meshing (14.4.7) yields that θ is constant if ϕ is a constant value. Thus the instantaneous line of contact on Σ_1 is the u coordinate line that is tangent to the helix on the base cylinder of radius r_b [Fig. 14.4.4(a)]. We remind the reader that contact lines on the tooth surface of a spur gear are straight lines that are parallel to the gear axis [Fig. 14.4.4(b)].


Figure 14.4.4: Contact lines on tooth surfaces of a helical gear and a spur gear.

Surface of Action
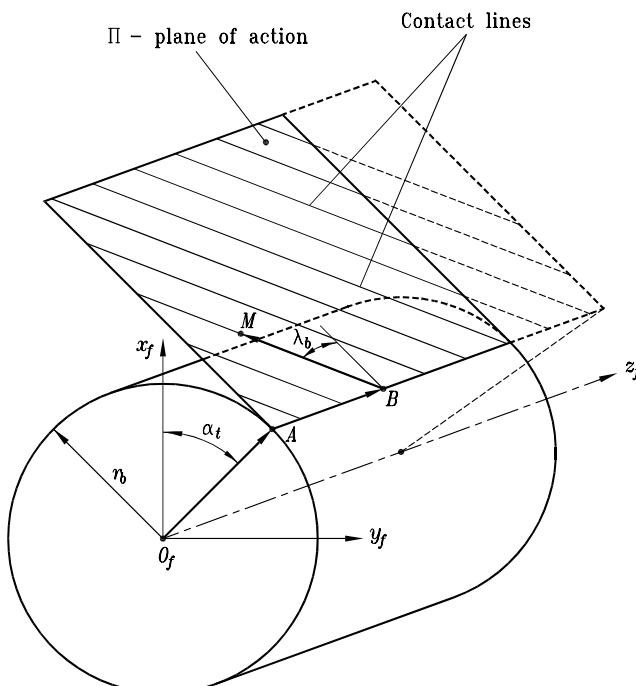
The *surface of action* is the family of contact lines L_{1r} that are represented in the fixed coordinate system S_f. The family of L_{1r} is represented in S_f by the equations

$$\mathbf{r}_f = \mathbf{M}_{f1}\mathbf{r}_1(u, \theta), \quad f(\theta, \phi) = 0. \tag{14.4.29}$$

Equations (14.3.5), (14.4.7), and (14.4.29) yield the following equations of the surface of action:

$$
\begin{aligned}
x_f &= r_b \cos \alpha_t + u \cos \lambda_b \sin \alpha_t \\
y_f &= r_b \sin \alpha_t - u \cos \lambda_b \cos \alpha_t \\
z_f &= -u \sin \lambda_b + p(\alpha_t + \phi - \mu)
\end{aligned} \tag{14.4.30}
$$

where u and ϕ are the surface parameters. Obviously, the surface of action is a plane. The instantaneous line of contact is determined by Eqs. (14.4.29) considering that ϕ is a fixed value. The family of contact lines on the surface of action is represented by parallel straight lines that belong to plane Π (Fig. 14.4.5). This plane is tangent to the base cylinder of radius r_b, and AB is the line of tangency of Π and the base cylinder. The position vector $\overline{O_f M}$ of current point M in the plane of action is represented as


Figure 14.4.5: Plane of action when a helical gear is in mesh with a rack.

follows (Fig. 14.4.5):

$$\overline{O_f M} = \overline{O_f A} + \overline{AB} + \overline{BM}. \tag{14.4.31}$$

Here,

$$\overline{O_f A} = [\, r_b \cos \alpha_t \quad r_b \sin \alpha_t \quad 0\,]^{\mathrm{T}}, \quad \overline{AB} = p(\alpha_t + \phi - \mu)\mathbf{k}_f$$

$$\overline{BM} = [\, u \cos \lambda_b \sin \alpha_t \quad -u \cos \lambda_b \cos \alpha_t \quad -u \sin \lambda_b\,]^{\mathrm{T}}$$

$$\overline{O_f M} = [\, x_f \quad y_f \quad z_f\,]^{\mathrm{T}} \tag{14.4.32}$$

where ϕ is taken as constant.

Relations Between Design Parameters

Henceforth, we consider that in the process of generation of a helical gear the gear axode is the pitch cylinder of radius $r_p = \rho$. We designate the lead angle and the helix angle on the gear pitch cylinder by λ_p and β_p, respectively.

Figure 14.4.6 illustrates the tooth profiles, design parameters, and tooth element proportions for two sections of an imaginary rack-cutter: the normal section $B-B$ and the transverse section $A-A$, respectively (Fig. 14.4.7). The designations $k = n, t$ in Fig. 14.4.6 correspond to these sections, respectively. We emphasize that the tooth height $2b$ for the rack-cutter is the same for both sections. The tooth height for an *ordinary* rack (but not a rack-cutter) is $(a + b)$. The designation $p_b^{(k)}$ $(k = n, t)$ indicates that the distance between the neighboring teeth of a rack is equal to the base circular pitch for a spur gear $(k = n)$ and for the helical gear $(k = n, t)$ in its cross section.

The design parameters of the normal section of the cutter are standardized. A standard helical gear is generated when the middle line $a-a$ of the rack-cutter lies in the plane that is tangent to the gear pitch cylinder. The input data for computation of the design parameters of a standard helical gear are α_n, P_n, λ_p, N, $a = 1/P_n$, and $b = 1.25/P_n$. The computation of design parameters is based on the following procedure:

Step 1: Determination of profile angle α_t:

$$\tan \alpha_t = \frac{\tan \alpha_n}{\sin \lambda_p} = \frac{\tan \alpha_n}{\cos \beta_p}. \tag{14.4.33}$$
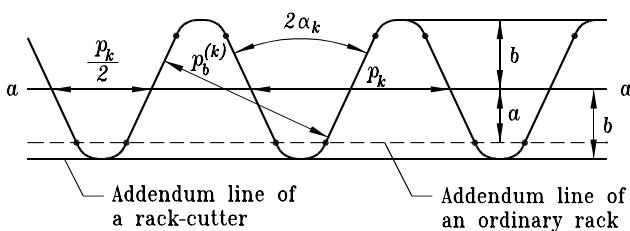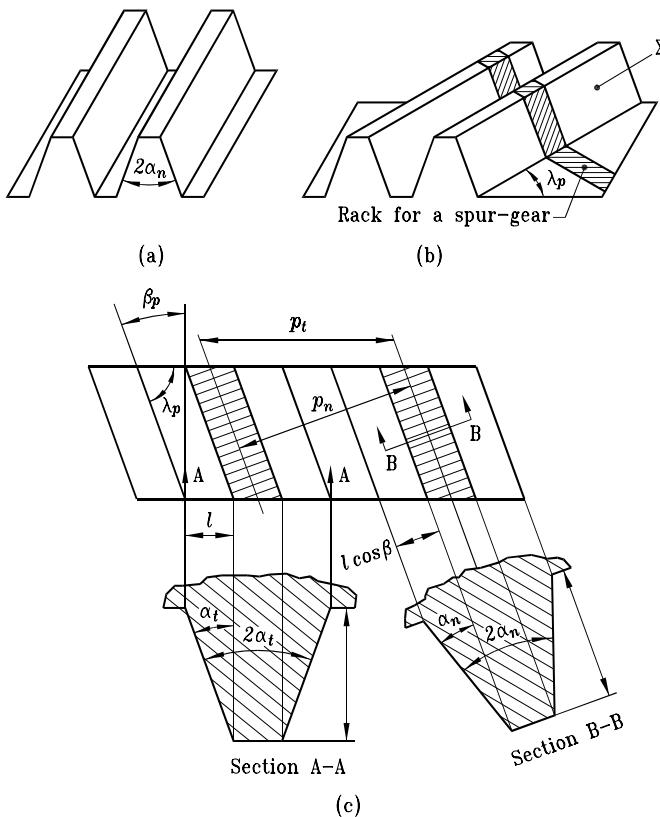

Figure 14.4.6: Design parameters of a rack-cutter in normal and transverse sections $(k = n, t)$.

Figure 14.4.7: Sections of a rack-cutter for a helical gear.

Step 2: Determination of p_t and P_t:

$$p_t = \frac{p_n}{\sin \lambda_p}, \quad P_t = P_n \sin \lambda_p. \tag{14.4.34}$$

Step 3: Determination of radius r_p of the pitch cylinder:

$$r_p = \frac{N}{2P_t} = \frac{N}{2P_n \sin \lambda_p}. \tag{14.4.35}$$

Step 4: Determination of radius r_b of the base cylinder:

$$r_b = r_p \cos \alpha_t = \frac{N \cos \alpha_t}{2P_n \sin \lambda_p}. \tag{14.4.36}$$

Step 5: Determination of the lead angle λ_b on the base cylinder:

$$\tan \lambda_b = \frac{p}{r_b} = \frac{r_p \tan \lambda_p}{r_b}. \tag{14.4.37}$$

An alternative equation for λ_b is

$$\cos \lambda_b = \cos \lambda_p \cos \alpha_n. \tag{14.4.38}$$

The derivation of Eq. (14.4.38) is based on application of Eqs. (14.4.17) and (14.4.33) with $\rho = r_p$.

Step 6: Determination of the addendum and dedendum cylinder radii:

$$r_a = r_p + a = \frac{N + 2 \sin \lambda_p}{2 P_n \sin \lambda_p} \tag{14.4.39}$$

$$r_d = r_p - b = \frac{N - 2.5 \sin \lambda_p}{2 P_n \sin \lambda_p}. \tag{14.4.40}$$

Step 7: The nominal values of tooth thickness and space width on the pitch circle (in the cross section) are determined as

$$s_t = w_t = \frac{p_t}{2} = \frac{p_n}{2 \sin \lambda_p} = \frac{\pi}{2 P_n \sin \lambda_p}. \tag{14.4.41}$$

14.5 MESHING OF MATING HELICAL GEARS

We apply movable coordinate systems S_1 and S_2 that are rigidly connected to gears 1 and 2, and the fixed coordinate system S_f (Fig. 14.5.1). The gear ratio m_{12} is constant and the rotation angles ϕ_1 and ϕ_2 are related as follows:

$$m_{12} = \frac{\omega^{(1)}}{\omega^{(2)}} = \frac{\rho_2}{\rho_1} = \frac{\phi_1}{\phi_2}. \tag{14.5.1}$$

The shortest distance between the gear axes is E. The instantaneous axis of rotation $P-P$ is parallel to the gear axis of rotation (Fig. 14.5.1), and its location in S_f is determined as

$$|\overline{O_f P}| = \rho_1 = E \frac{1}{1 + m_{12}}. \tag{14.5.2}$$
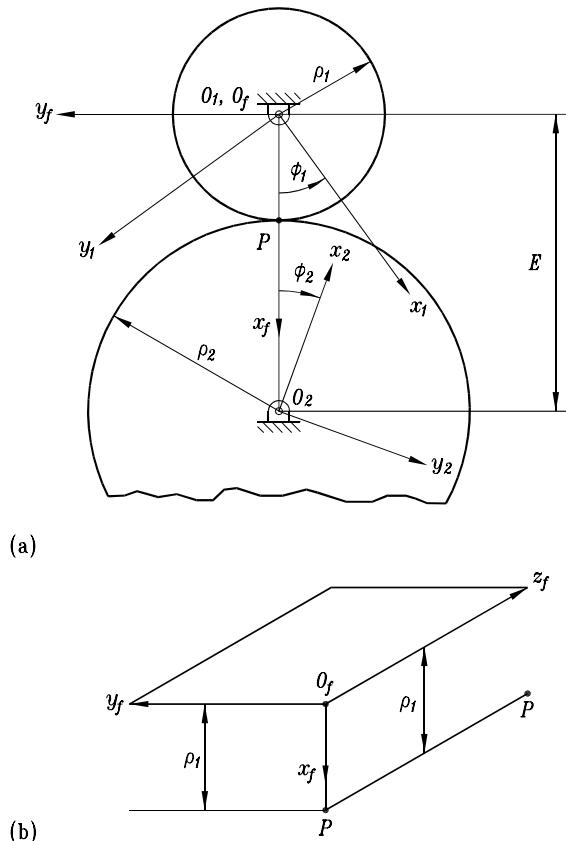
We consider that surface Σ_1 of helical gear 1 is a screw involute surface and our goals are to determine (i) surface Σ_2 as conjugate to Σ_1, (ii) lines of contact between surfaces Σ_1 and Σ_2, and (iii) the surface of action for conjugate surfaces Σ_1 and Σ_2. We assume for further derivations that surface Σ_1 and its unit normal are given by Eqs. (14.3.5) and (14.3.6).

Equation of Meshing

The derivation of the equation of meshing is based on the following theorem: *The normal to surfaces Σ_1 and Σ_2 at the current point of their tangency must intersect the instantaneous axis of rotation $P-P$.*

Derivations similar to that described in Section 14.4 result in the equation of meshing

$$\cos(\theta_1 + \mu_1 - \phi_1) = \frac{r_{b1}}{\rho_1} = \cos \alpha_o \tag{14.5.3}$$

(a)

(b)

Figure 14.5.1: Coordinate systems applied for a pair of helical gears.

where α_o is the pressure angle of helical gears. Equation (14.5.3) provides two solutions. We choose the solution

$$\theta_1 + \mu_1 - \phi_1 - \alpha_o = f(\theta_1, \phi_1) = 0, \qquad (14.5.4)$$

which represents the equation of meshing.

Derivation of Surface Σ_2

Surface Σ_2 is determined with the equations

$$\mathbf{r}_2(u_1, \theta_1, \phi_1) = \mathbf{M}_{21}(\phi_1)\mathbf{r}_1(u_1, \theta_1), \quad f(\theta_1, \phi_1) = 0. \qquad (14.5.5)$$

Here,

$$f(\theta_1, \phi_1) = 0$$

is the equation of meshing represented by (14.5.4). Matrix $\mathbf{M}_{21}$ represents the coordinate

transformation from S_1 to S_2 (Fig. 14.5.1) and is represented as

$$
\mathbf{M}_{21} =
\begin{bmatrix}
-\cos(\phi_1 + \phi_2) & -\sin(\phi_1 + \phi_2) & 0 & E\cos\phi_2 \\
\sin(\phi_1 + \phi_2) & -\cos(\phi_1 + \phi_2) & 0 & -E\sin\phi_2 \\
0 & 0 & 1 & 0 \\
0 & 0 & 0 & 1
\end{bmatrix}
\tag{14.5.6}
$$

where ϕ_1 and ϕ_2 are related by Eq. (14.5.1).

Figure 14.5.1 shows the radii ρ_1 and ρ_2 of two axodes of helical gears. Taking into account that

$$
E = \rho_1 + \rho_2, \quad m_{12} = \frac{\omega^{(1)}}{\omega^{(2)}} = \frac{\rho_2}{\rho_1}, \quad \rho_1 = \frac{r_{b1}}{\cos\alpha_o}
\tag{14.5.7}
$$

and using Eqs. (14.5.4), (14.5.5), (14.5.6), and (14.3.5), we obtain the following equations of Σ_2:

$$
\begin{aligned}
x_2 &= \frac{r_{b1}}{\cos\alpha_o}(m_{12}\cos\phi_2 - \sin\alpha_o\sin(\phi_2 - \alpha_o)) \\
&\quad + u_1\cos\lambda_{b1}\sin(\phi_2 - \alpha_o)
\end{aligned}
\tag{14.5.8}
$$

$$
\begin{aligned}
y_2 &= -\frac{r_{b1}}{\cos\alpha_o}(m_{12}\sin\phi_2 + \sin\alpha_o\cos(\phi_2 - \alpha_o)) \\
&\quad + u_1\cos\lambda_{b1}\cos(\phi_2 - \alpha_o)
\end{aligned}
\tag{14.5.9}
$$

$$
z_2 = -u_1\sin\lambda_{b1} + p_1(m_{12}\phi_2 + \alpha_o - \mu_1).
\tag{14.5.10}
$$

Equations (14.5.8) to (14.5.10) represent surface Σ_2 in terms of surface parameters (u_1, ϕ_2). The surface unit normal is represented as

$$
\mathbf{n}_2 = \frac{\mathbf{N}_2}{|\mathbf{N}_2|}, \quad \mathbf{N}_2 = \frac{\partial \mathbf{r}_2}{\partial \phi_2} \times \frac{\partial \mathbf{r}_2}{\partial u_1}
\tag{14.5.11}
$$

We obtain after derivations that

$$
\mathbf{n}_2 = -[\,\sin\lambda_{b1}\sin(\phi_2 - \alpha_o) \quad \sin\lambda_{b1}\cos(\phi_2 - \alpha_o) \quad \cos\lambda_{b1}\,]^{\mathrm{T}}
$$

(provided that $r_{b1}\tan\alpha_o(1 + m_{12}) - u_1\cos\lambda_{b1} \neq 0$).
$\qquad$ (14.5.12)

An alternative approach for derivation of $\mathbf{n}_2$ is based on application of the equation

$$
\mathbf{n}_2 = \mathbf{L}_{21}\mathbf{n}_1
\tag{14.5.13}
$$

and the equation of meshing (14.5.4). Here, $\mathbf{L}_{21}$ is the (3×3) submatrix of $\mathbf{M}_{21}$. Surface Σ_2 is a helicoid because the equation

$$
y_2 n_{x2} - x_2 n_{y2} - p_2 n_{z2} = 0
\tag{14.5.14}
$$

is satisfied. Here,

$$p_2 = -p_1 m_{12}. \qquad (14.5.15)$$

This surface is a developed ruled helicoid because the orientation of the unit normal does not depend on the surface parameter u_1. It is easy to verify that Σ_2 is a screw involute surface, and this conclusion is based on the following considerations:

(i) The cross section of Σ_1 by plane Π that is perpendicular to the gear axis is an involute curve.
(ii) The meshing of gears in plane Π can be represented as the meshing of two conjugate curves. Because one of these curves is an involute one, the other one is an involute curve as well (see Chapter 10).
(iii) The gear ratio of two involute gears is

$$m_{12} = \frac{\omega^{(1)}}{\omega^{(2)}} = \frac{r_{b2}}{r_{b1}}. \qquad (14.5.16)$$

Equations (14.5.15) and (14.5.16) yield that the direction of screw teeth for gear 2 is opposite to the direction of the screw teeth of gear 1. However, the magnitudes of lead angles λ_{b1} and λ_{b2} of the two gears are equal.

Surface of Action
The surface of action is represented in S_f by the equations

$$\mathbf{r}_f = \mathbf{M}_{f1}\mathbf{r}_1(u_1, \theta_1), \quad f(\theta_1, \phi_1) = \theta_1 + \mu_1 - \phi_1 - \alpha_o = 0. \qquad (14.5.17)$$
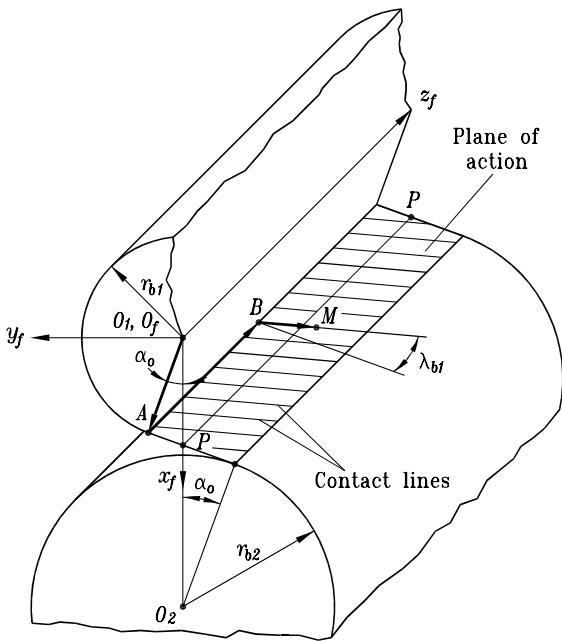
Equations (14.3.5) and (14.5.17) yield the following representation of the surface of action:

$$\begin{aligned}
x_f &= r_{b1} \cos\alpha_o + u_1 \cos\lambda_{b1} \sin\alpha_o \\
y_f &= r_{b1} \sin\alpha_o - u_1 \cos\lambda_{b1} \cos\alpha_o \\
z_f &= -u_1 \sin\lambda_{b1} + p_1(\alpha_o - \mu_1 + \phi_1).
\end{aligned} \qquad (14.5.18)$$

Equations (14.5.18) verify that the surface of action is a plane that is tangent to the base cylinders of radii r_{b1} and r_{b2}, oriented as shown in Fig. 14.5.2(a), and passes through the instantaneous axis of rotation P–P.

Equations (14.5.18) with the fixed value of parameter ϕ_1 represent in S_f the instantaneous line of contact L_{12} between surfaces Σ_1 and Σ_2. Contact lines L_{12} in the plane of action are represented as parallel straight lines. Position vector $\overline{O_f M}$ of current point M of contact is represented as

$$\overline{O_f M} = \overline{O_f A} + \overline{AB} + \overline{BM}. \qquad (14.5.19)$$

Figure 14.5.2: Plane of action of helical gears.

Here,

$$\overline{O_f A} = [\, r_{b1} \cos \alpha_o \quad r_{b1} \sin \alpha_o \quad 0\,]^{\mathrm{T}} \tag{14.5.20}$$

$$\overline{AB} = p_1(\alpha_o - \mu_1 + \phi_1)\mathbf{k}_f \tag{14.5.21}$$

$$\overline{BM} = [\, u_1 \cos \lambda_{b1} \sin \alpha_o \quad -u_1 \cos \lambda_{b1} \cos \alpha_o \quad -u_1 \sin \lambda_{b1}\,]^{\mathrm{T}}. \tag{14.5.22}$$

Analysis similar to that performed in Section 14.4 shows that the instantaneous line of contact L_{12} is represented in coordinate system S_i ($i = 1, 2$) as the tangent to the helix on the base cylinder of radius r_{bi} [Fig. 14.4.4(a)].

The pressure angle α_o for helical gears depends on the profile angle α_t of the rack-cutter and the shortest distance E. It is easy to verify that
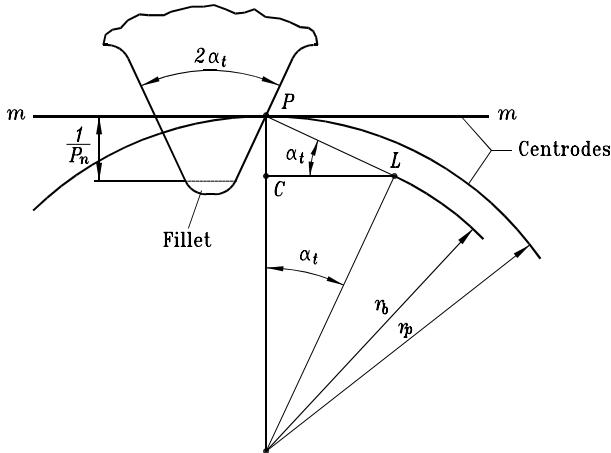
$$\cos \alpha_o = \frac{r_{b1} + r_{b2}}{E} = \frac{(r_{p1} + r_{p2}) \cos \alpha_t}{E} = \frac{(N_{p1} + N_{p2}) \cos \alpha_t}{2 P_t E}. \tag{14.5.23}$$

In the case of standard gears, we have

$$E = r_{p1} + r_{p2}, \quad \alpha_o = \alpha_t. \tag{14.5.24}$$

14.6 CONDITIONS OF NONUNDERCUTTING

Helical involute gears in comparison with spur involute gears are less sensitive to undercutting. The conditions of nonundercutting can be determined by considering the

Figure 14.6.1: For derivation of conditions of nonundercutting of helical involute gears.

meshing of a planar involute gear with the respective rack-cutter in a plane that is perpendicular to the axis of the helical gear (Fig. 14.6.1). The profile angle of the rack-cutter is α_t. The centrode of the planar gear is the pitch circle with the radius

$$r_p = \frac{N}{2P_t} = \frac{N}{2P_n \cos \beta_p}. \tag{14.6.1}$$

In the case of a *standard* helical gear, the middle line m–m of the rack-cutter is tangent to the pitch circle. Undercutting is avoided if

$$\frac{1}{P_n} \leq PC \tag{14.6.2}$$

$$PC = r_p \sin^2 \alpha_t = \frac{N}{2P_t} \sin^2 \alpha_t = \frac{N}{2P_n \cos \beta_p} \sin^2 \alpha_t. \tag{14.6.3}$$

Then, we obtain that undercutting is avoided if

$$N \geq \frac{2 \cos \beta_p}{\sin^2 \alpha_t} = \frac{2 \cos \beta_p (\cos^2 \beta_p + \tan^2 \alpha_n)}{\tan^2 \alpha_n}. \tag{14.6.4}$$

In the case of a spur gear, we have $\beta_p = 0$ and

$$N \geq \frac{2}{\sin^2 \alpha_n}. \tag{14.6.5}$$

A numerical example is considered for a helical gear with the following input data: $\beta_p = 45°$, $\alpha_n = 20°$. Inequality (14.6.4) yields that

$$N \geq 7.$$

Obviously, the number of gear teeth is considered as a whole number. We recall that for the case of a spur gear with $\alpha_n = 20°$, we have that

$$N \geq 17.$$

14.7 CONTACT RATIO

The contact ratio is determined as the sum of two components,
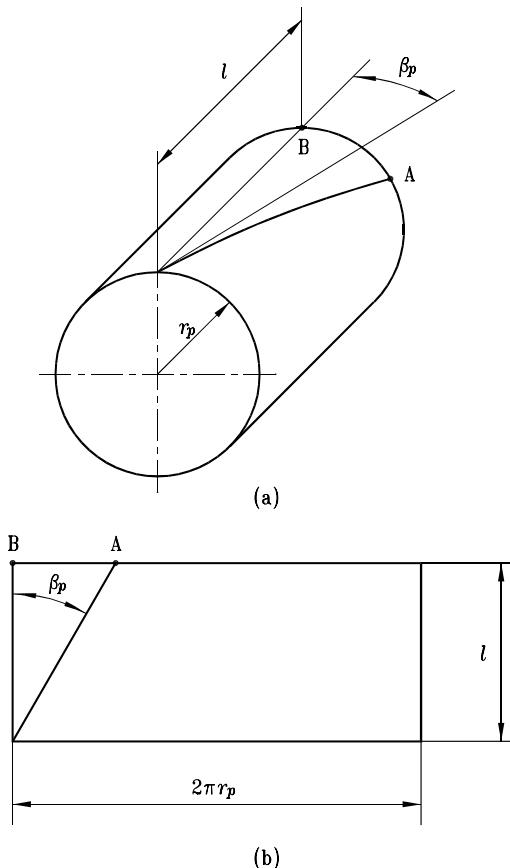
$$m_c = m_c^{(c)} + m_c^{(l)} \tag{14.7.1}$$

where the superscripts "c" and "l" indicate that the meshing is considered in the cross section and in the longitudinal direction, respectively. The contact ratio $m_c^{(c)}$ is determined in a manner similar to that for the contact ratio for respective spur gears but taking into account the specific relations between the design parameters for helical gears (see Section 14.4). The contact ratio $m_c^{(l)}$ is represented by the following equation [Fig. 14.7.1(a)]:

$$m_c^{(l)} = \frac{\overarc{AB}}{p_t}. \tag{14.7.2}$$

Figure 14.7.1(b) shows the development of the pitch cylinder on a plane. It is easy to verify that

$$\overarc{AB} = AB = l \tan \beta_p \tag{14.7.3}$$

Figure 14.7.1: For derivation of contact ratio.

where segment AB is the development of the arc $\overset{\frown}{AB}$, and l is the axial dimension of the helical gear. Equations (14.7.2) and (14.7.3) yield

$$m_c^{(l)} = \frac{l \tan \beta_p}{p_t} = \frac{P_t l \tan \beta_p}{\pi} = \frac{P_n l \sin \beta_p}{\pi}. \qquad (14.7.4)$$

The contact ratio of helical gears is larger in comparison to that of respective spur gears.

14.8 FORCE TRANSMISSION

The goal is to determine the components of the contact force at the mean tangency point P considering as given the resisting moment $\mathbf{M}_r$ applied to the driven gear. The derivations are based on the following procedure:

Step 1: Recall the derivation of a surface unit normal. Consider a surface Σ and two lines L_1 and L_2 on Σ (Fig. 14.8.1). Lines L_1 and L_2 intersect each other at point P; vectors $\mathbf{a}$ and $\mathbf{b}$ are the tangents to these lines at P and form the tangent plane Π to Σ at point P. The surface unit normal is determined with the following equations:

$$\mathbf{n} = \frac{\mathbf{N}}{|\mathbf{N}|}, \quad \mathbf{N} = \mathbf{a} \times \mathbf{b}. \qquad (14.8.1)$$

Step 2: The tooth surfaces of helical gears contact each other along a line at every instant. We consider such an instantaneous position of gear tooth surfaces when the instantaneous contact line passes through point P, the middle point of the line of tangency of the gear pitch cylinder (Fig. 14.8.2). Plane Π (not shown in Fig. 14.8.2) is tangent to the surface of gear 2 at the pitch cylinder. Vector $\mathbf{a}$ lies in plane Π and is tangent to the helix on the pitch cylinder with the radius r_{p2}; β_p is the helix angle; d–d is the trace of the plane that is perpendicular to vector $\mathbf{a}$ and passes through point P. The intersection of plane d–d with the pitch cylinder is an ellipse with axes $2r_{p2}$ and $2r_{p2}/\cos \beta_p$. Figure 14.8.2 also shows the normal section of the gear tooth surface Σ_2. Vector $\mathbf{b}$ is tangent to the surface Σ_2 normal section at point P.
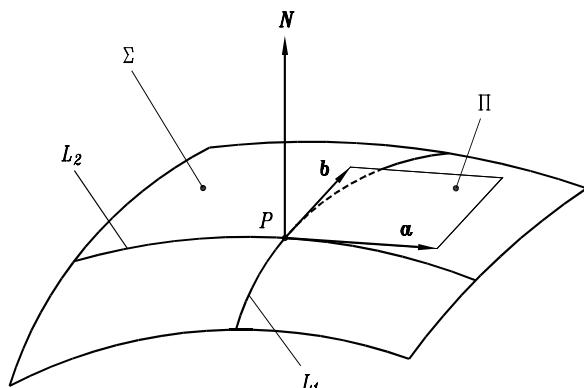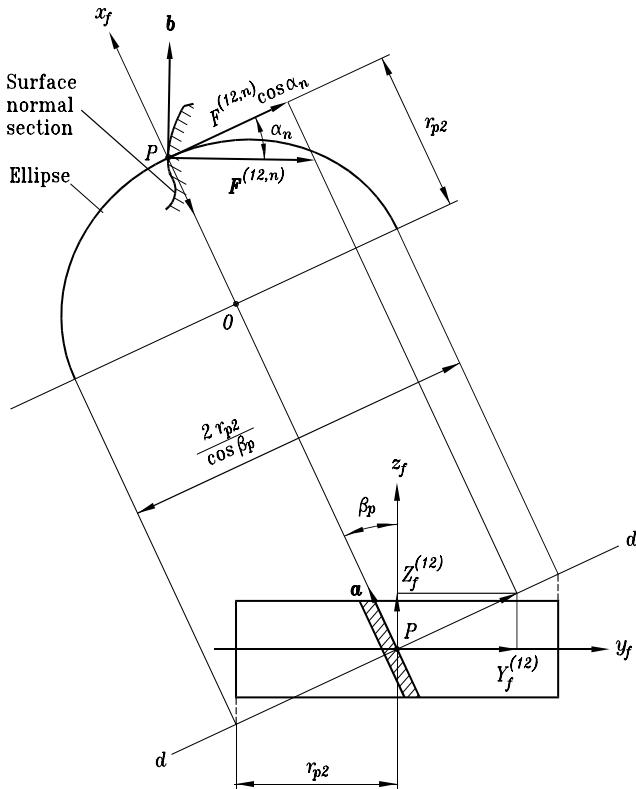

**Figure 14.8.1:** For derivation of surface normal.

Figure 14.8.2: Derivation of components of contact force.

Step 3: Vectors **a** and **b** are represented in S_f as follows:

$$\mathbf{a} = [0 \quad -\sin\beta_p \quad \cos\beta_p]^{\mathrm{T}} \tag{14.8.2}$$

$$\mathbf{b} = [\cos\alpha_n \quad \sin\alpha_n\cos\beta_p \quad \sin\alpha_n\sin\beta_p]^{\mathrm{T}}. \tag{14.8.3}$$

Equations (14.8.1) to (14.8.3) yield

$$\mathbf{n} = [-\sin\alpha_n \quad \cos\alpha_n\cos\beta_p \quad \cos\alpha_n\sin\beta_p]^{\mathrm{T}}. \tag{14.8.4}$$
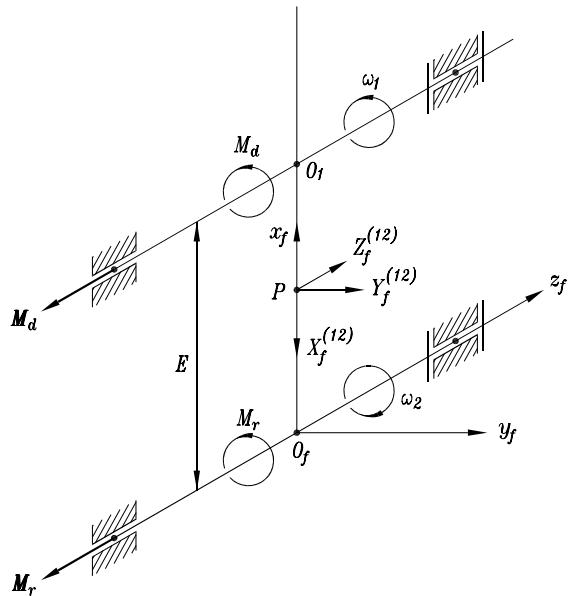
Step 4: The normal component of contact force $\mathbf{F}^{(12,n)}$ transmitted from gear 1 to gear 2 at point P is directed along the normal to the contacting surfaces. The tangential component, the force of friction, is neglected. Here,

$$\mathbf{F}^{(12,n)} = F^{(12,n)}\mathbf{n} \tag{14.8.5}$$

where

$$F^{(12,n)} = |\mathbf{F}^{(12,n)}|.$$

Projections of $\mathbf{F}^{(12,n)}$ on the coordinate axes of S_f are designated as $X_f^{(12)}$, $Y_f^{(12)}$, and

Figure 14.8.3: Components of contact force.

$Z_f^{(12)}$ (Fig. 14.8.3) and are shown in Fig. 14.8.3. Here,

$$X_f^{(12)} = -F^{(12,n)} \sin \alpha_n$$
$$Y_f^{(12)} = F^{(12,n)} \cos \alpha_n \cos \beta_p \qquad (14.8.6)$$
$$Z_f^{(12)} = F^{(12,n)} \cos \alpha_n \sin \beta_p.$$

It is evident that the force transmission is accompanied with an axial load and therefore at least one of the pair of bearings for each gear must be designed to be able to accept an axial load (Fig. 14.8.3).

Step 5: Considering the conditions of equilibrium of gear 2, we can determine the magnitude of the transmission force $Y_f^{(12)}$ as follows:

$$Y_f^{(12)} = \frac{M_r}{r_{p2}}. \qquad (14.8.7)$$
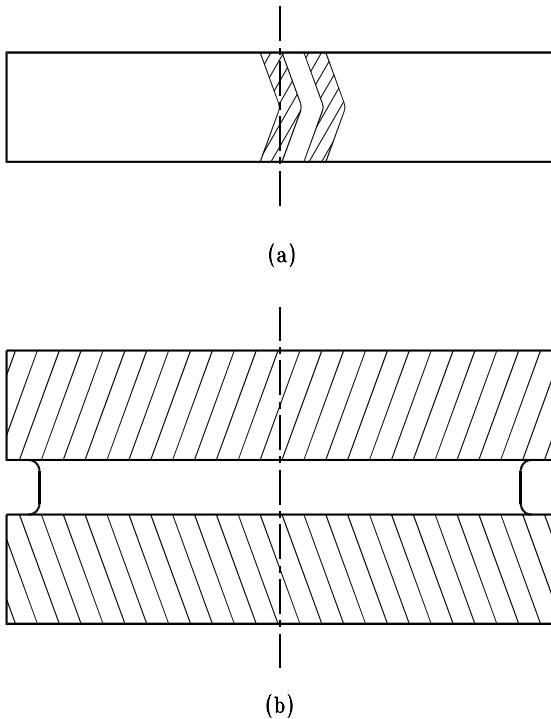
Equations (14.8.7) and (14.8.6) yield

$$F^{(12,n)} = \frac{M_r}{r_{p2} \cos \alpha_n \cos \beta_p} \qquad (14.8.8)$$

$$X_f^{(12)} = -\frac{M_r \tan \alpha_n}{r_{p2} \cos \beta_p} \qquad (14.8.9)$$

$$Z_f^{(12)} = \frac{M_r \tan \beta_p}{r_{p2}}. \qquad (14.8.10)$$

The axial component of contact force becomes equal to zero by application of herring-bone teeth [Fig. 14.8.4(a)] or when each of the mating gears is designed as a combination

(a)

Figure 14.8.4: Helical gears with zero axial load.

(b)

of two helical gears made from one piece and provided with helical teeth of opposite directions [Fig. 14.8.4(b)].

14.9 RESULTS OF TOOTH CONTACT ANALYSIS (TCA)

The results of computation show that the gears are very sensitive to angular errors of misalignment such as the crossing angle $\Delta\gamma$, the lead angle $\Delta\lambda_{pi}$ $(i = 1, 2)$ on the pinion (gear) pitch cylinder, and the error $\Delta\alpha_n$ of the profile angle of the hob; $\Delta\alpha_n$ means the difference of profile angles of two hobs that are used for generation of mating helical gears. The errors $\Delta\gamma$ and $\Delta\lambda_{pi}$ cause an edge contact and a piecewise almost-linear function of transmission errors similar to that shown in Fig. 9.2.1. The vibration of gears caused by $\Delta\gamma$ and $\Delta\lambda_{pi}$ is inevitable. The error $\Delta\alpha_n$ causes the edge contact.

To avoid the edge contact and reduce the vibration, a new topology of helical gears should be applied [Litvin *et al.*, 2003]. The modification of gear tooth surfaces should be based on the following principles: (i) point contact of tooth surfaces with controlled dimensions of the instantaneous contact ellipse instead of surface line contact should be provided; (ii) conjugation of double-crowned pinion with a conventional helical gear should be applied. Double crowning of the pinion means deviation of the cross profile from an involute curve and deviation of the surface in longitudinal direction from a helicoid surface [Litvin *et al.*, 2003]. The proposed modification enables us to obtain a

parabolic function of transmission errors that is able to absorb the linear functions of transmission errors caused by misalignments.

14.10 NOMENCLATURE

α_n	rack profile angle in normal section (Fig. 14.4.7)
α_t	rack profile angle in transverse section (Fig. 14.4.7)
β_k $(k = p, \rho)$	helix angle on pitch cylinder $(k = p)$, on cylinder of radius ρ $(k = \rho)$ (Figs. 14.2.1 and 14.4.7)
λ_i $(i = p, b, \rho)$	lead angle on the pitch cylinder $(i = p)$, on the base cylinder $(i = b)$, and on the cylinder of radius ρ (Figs. 14.2.1, 14.4.5 and 14.4.7)
μ_1	half of the angular width of the tooth space on the base circle of gear 1 (Fig. 14.3.2)
θ, θ_1, and θ_2	surface parameter of the screw involute surface (Figs. 14.3.2 and 14.3.3)
ϕ, ϕ_1, and ϕ_2	angle of gear rotation (Figs. 14.4.1 and 14.5.1)
η_2	half of the angular tooth thickness on pitch circle of gear 2
E	shortest axes distance (Fig. 14.5.1)
$\mathbf{F}^{(12,n)}$	normal component of contact force (Fig. 14.8.2)
H	lead (Fig. 14.2.1)
l	axial dimension of helical gear [Fig. 14.7.1(b)]
m_{12}	gear ratio
m_c	gear contact ratio
$\mathbf{N}$	surface normal
$\mathbf{n}$	surface unit normal
p_n	circular pitch measured perpendicular to the direction of skew teeth of the rack [Fig. 14.4.7(c)]
p_t	circular pitch in the cross section [Fig. 14.4.7(c)]
P_n and P_t	diametral pitches that correspond to p_n and p_t
$p = H/2\pi$	screw parameter
q	orientation angle of straight contact lines on rack tooth surface (Fig. 14.4.3)
r_b	radius of base cylinder (Fig. 14.4.4)
r_o	radius of operating pitch cylinder, axode
r_{pi}	radius of pitch cylinder i (Figs. 14.3.2 and 14.3.3)
s	rack displacement (Fig. 14.4.1)
s_t	tooth thickness on the pitch circle in the cross section
u	surface parameter of a screw involute surface
w_t	space width measured on the pitch circle in cross section
$X_f^{(12)}$, $Y_f^{(12)}$, $Z_f^{(12)}$	components of contact force (Figs. 14.8.2 and 14.8.3)

15 Modified Involute Gears

15.1 INTRODUCTION

Involute gears, spur and helical ones, are widely used in reducers, planetary gear trains, transmissions, and many other industrial applications. The level of sophistication in the design and manufacture of such gears (by hobbing, shaping, and grinding) is impressive. The geometry, design, and manufacture of helical gears was the subject of research presented in the works of Litvin *et al.* [1995, 1999, 2001a, 2003], Stosic [1998], and Feng *et al.* [1999].

The advantage of involute gearing in comparison with cycloidal gearing is that the change of center distance does not cause transmission errors. However, the practice of design and the test of bearing contact and transmission errors show the need for modification of involute gearing, particularly of helical gears. Figure 15.1.1 shows a 3D model of a modified involute helical gear drive.

The existing design and manufacture of involute helical gears provide instantaneous contact of tooth surfaces along a line. The instantaneous line of contact of conjugated tooth surfaces is a straight line L_0 that is the tangent to the helix on the base cylinder (Fig. 15.1.2). The normals to the tooth surface at any point of line L_0 are collinear and they intersect in the process of meshing with the instantaneous axis of relative motion that is the tangent to the pitch cylinders. The concept of pitch cylinders is discussed in Section 15.2.

The involute gearing is sensitive to the following errors of assembly and manufacture: (i) the change $\Delta\gamma$ of the shaft angle, and (ii) the variation of the screw parameter (of one of the mating gears). Angle $\Delta\gamma$ is formed by the axes of the gears when they are crossed, but not parallel, due to misalignment (see Fig. 15.4.4). Such errors cause discontinuous linear functions of transmission errors which result in vibration and noise, and these errors may also cause edge contact wherein meshing of a curve and a surface occurs instead of surface-to-surface contact (see Section 15.9). In a misaligned gear drive, the transmission function varies in each cycle of meshing (a cycle for each pair of meshing teeth). Therefore the function of transmission errors is interrupted at the transfer of meshing between two pairs of teeth [see Fig. 15.4.6(a)].
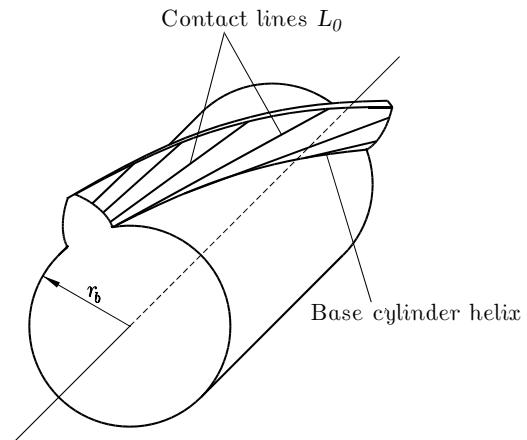
This chapter covers (i) computerized design, (ii) methods for generation, (iii) simulation of meshing, and (iv) enhanced stress analysis of modified involute helical gears.
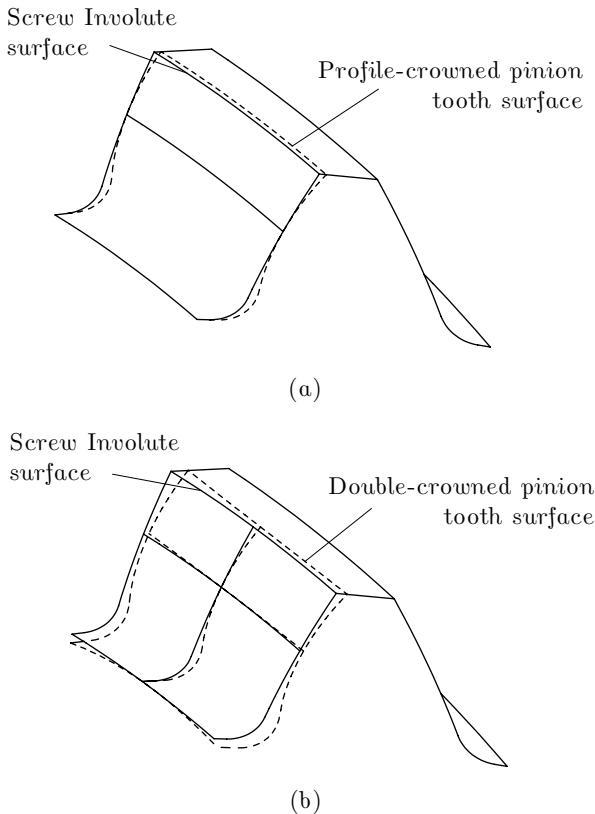
Figure 15.1.1: Modified involute helical gear drive.

The approaches proposed for modification of conventional involute helical gears are based on the following basic ideas:

(i) Line contact of tooth surfaces is substituted by instantaneous point contact.
(ii) The point contact of tooth surfaces is achieved by crowning of the pinion in the profile and longitudinal directions. The tooth surface of the gear is a conventional screw involute surface.
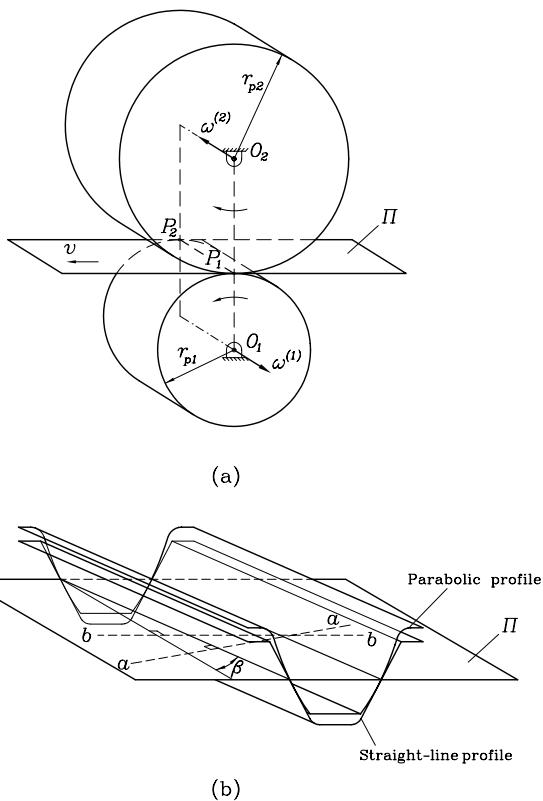
Figure 15.1.2: Contact lines on an involute helical tooth surface.

Contact lines L_0

Base cylinder helix

r_b

Screw Involute
surface

Profile-crowned pinion
tooth surface

(a)

Screw Involute
surface

Double-crowned pinion
tooth surface

(b)

Figure 15.1.3: Crowning of pinion tooth surface.

(iii) Profile crowning provides localization of bearing contact, and the path of contact on the tooth surface of the pinion or the gear is oriented longitudinally (see Section 15.4).

(iv) Longitudinal crowning enables us to provide a parabolic function of transmission errors of the gear drive. Such a function absorbs discontinuous linear functions of transmission errors caused by misalignment and therefore reduces noise and vibration (see Section 15.7). Figures 15.1.3(a) and 15.1.3(b) illustrate the profile-crowned and double-crowned pinion tooth surface.

(v) Profile crowning of the pinion tooth surface is achieved by deviation of the generating tool surface in the profile direction (see Section 15.2). Longitudinal crowning of the pinion tooth surface can be achieved by: (i) plunging of the tool, or (ii) application of modified roll (see Sections 15.5 and 15.6).

(vi) The effectiveness of the procedure of stress analysis is enhanced by automatization of development of the contacting model of several pairs of teeth. The derivation of the model is based on application of the equations of the tooth surfaces; CAD codes for building the model are not required. Details of application of the proposed approaches are presented in Section 15.9.

(a)

(b)

Figure 15.2.1: Axodes of pinion, gear, and rack-cutter: (a) axodes; (b) tooth surfaces of two skew rack-cutters.

15.2 AXODES OF HELICAL GEARS AND RACK-CUTTERS

The concept of generation of pinion and gear tooth surfaces is based on application of rack-cutters. The idea of the rack-cutters is the basis for design of such generating tools as disks and worms. The concept of axodes is applied when the meshing and generation of helical gears are considered.

Figure 15.2.1(a) shows the case wherein gears 1 and 2 perform rotation about parallel axes with angular velocities $\boldsymbol{\omega}^{(1)}$ and $\boldsymbol{\omega}^{(2)}$ with the ratio $\omega^{(1)}/\omega^{(2)} = m_{12}$ where m_{12} is the constant gear ratio. The axodes of the gears are two cylinders of radii r_{p1} and r_{p2}, and the line of tangency of the cylinders designated as P_1–P_2 is the instantaneous axis of rotation (see Chapter 3). The axodes roll over each other without sliding.

The rack-cutter and the gear being generated perform related motions:

(i) translational motion with velocity

$$\mathbf{v} = \boldsymbol{\omega}^{(1)} \times \overline{O_1 P} = \boldsymbol{\omega}^{(2)} \times \overline{O_2 P} \tag{15.2.1}$$

where P belongs to P_1–P_2

(ii) rotation with angular velocity $\boldsymbol{\omega}^{(i)}$ $(i = 1, 2)$ about the axis of the gear.

The axode of the rack-cutter that is meshing with gear i is plane Π that is tangent to the gear axodes.

In the existing design, one rack-cutter with a straight-line profile is applied for generation of pinion and gear tooth surfaces. Then, the tooth surfaces contact each other along a *line* and edge contact in a misaligned gear drive is *inevitable*.

Point contact in the proposed design (instead of line contact) is provided by application of two mismatched rack-cutters, as shown in Fig. 15.2.1(b), one of a straight-line profile for generation of the gear and the other of a parabolic profile for generation of the pinion. This method of generation provides a profile-crowned pinion.

It is shown below (see Sections 15.5 and 15.6) that the pinion in the proposed new design is double-crowned (longitudinal crowning is provided in addition to profile crowning). Double-crowning of the pinion (proposed in Litvin *et al.* [2001c]) allows edge contact to be avoided and provides a favorable function of transmission errors.

Normal and Transverse Sections

The normal section $a-a$ of the rack-cutter is obtained by a plane that is perpendicular to plane Π and whose orientation is determined by angle β [Fig. 15.2.1(b)]. The transverse section of the rack-cutter is determined as a section by a plane that has the orientation of $b-b$ [Fig. 15.2.1(b)].

Mismatched Rack-Cutters

Figure 15.2.2(a) shows the profiles of the normal sections of the mismatched rack-cutters. The profiles of the pinion and gear rack-cutters are shown in Figs. 15.2.2(b) and 15.2.2(c), respectively. Dimensions s_1 and s_2 are related by module m and parameter b as follows:

$$s_1 + s_2 = \pi m \tag{15.2.2}$$

$$s_{12} = \frac{s_1}{s_2}. \tag{15.2.3}$$

Parameter s_{12}, which might be chosen in the process of optimization, relates pinion and gear tooth thicknesses and it allows modification of the relative rigidity. In a conventional case of design, we choose $s_{12} = 1$.
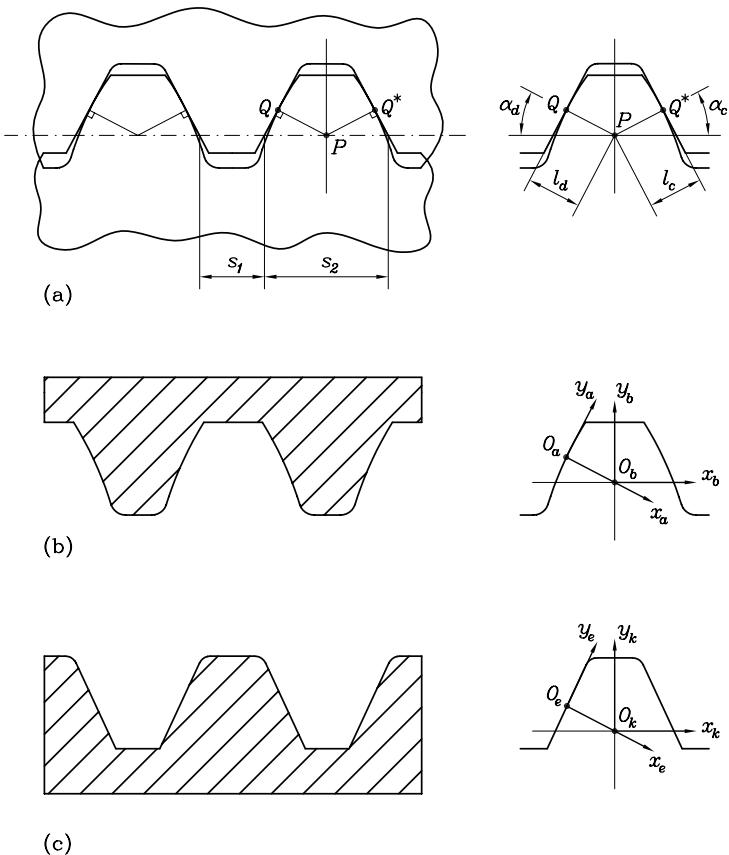
The rack-cutter for gear generation is a conventional one and has a straight-line profile in the normal section. The rack-cutter for pinion generation is provided with a parabolic profile. The profiles of the rack-cutters are in tangency at points Q and Q^* [Fig. 15.2.2(a)] that belong to the normal profiles of the driving and coast sides of the teeth, respectively. The common normal to the profiles passes through point P that belongs to the instantaneous axis of rotation P_1-P_2 [Fig. 15.2.1(a)].

Pinion Parabolic Rack-Cutter

The parabolic profile of the pinion rack-cutter is represented in parametric form in an auxiliary coordinate system $s_a(x_a, y_a)$ as (Fig. 15.2.3)

$$x_a = a_c u_c^2, \quad y_a = u_c \tag{15.2.4}$$

where a_c is the parabola coefficient. The origin of s_a coincides with Q.

Figure 15.2.2: Normal sections of pinion and gear rack-cutters: (a) mismatched profiles; (b) profiles of pinion rack-cutter in coordinate systems s_a and S_b; (c) profiles of gear rack-cutter in coordinate systems S_e and S_k.

The surface of the rack-cutter is denoted by Σ_c and is derived as follows:
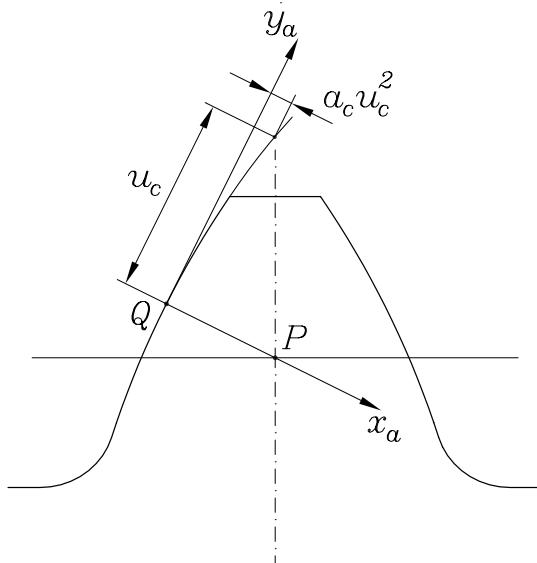
(i) The mismatched profiles of pinion and gear rack-cutters are represented in Fig. 15.2.2(a). The pressure angles are α_d for the driving profile and α_c for the coast profile. The locations of points Q and Q^* are denoted by $|\overline{QP}| = l_d$ and $|\overline{Q^*P}| = l_c$ where l_d and l_c are defined as

$$l_d = \frac{\pi m}{1 + s_{12}} \cdot \frac{\sin \alpha_d \cos \alpha_d \cos \alpha_c}{\sin(\alpha_d + \alpha_c)} \tag{15.2.5}$$

$$l_c = \frac{\pi m}{1 + s_{12}} \cdot \frac{\sin \alpha_c \cos \alpha_c \cos \alpha_d}{\sin(\alpha_d + \alpha_c)}. \tag{15.2.6}$$

(ii) Coordinate systems $s_a(x_a, y_a)$ and $S_b(x_b, y_b)$ are located in the plane of the normal section of the rack-cutter [Fig. 15.2.2(b)]. The normal profile is represented in S_b by the matrix equation

$$\mathbf{r}_b(u_c) = \mathbf{M}_{ba}\mathbf{r}_a(u_c) = \mathbf{M}_{ba}[a_c u_c^2 \quad u_c \quad 0 \quad 1]^{\mathrm{T}} \tag{15.2.7}$$
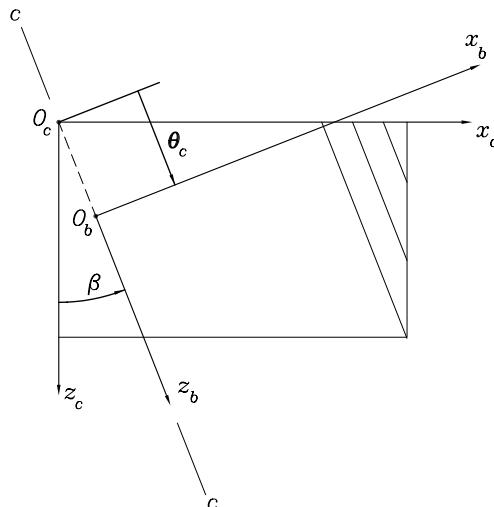
Figure 15.2.3: Parabolic profile of pinion rack-cutter in normal section.

(iii) The rack-cutter surface Σ_c is represented in coordinate system S_c (Fig. 15.2.4) wherein the normal profile performs translational motion along c–c. Then we obtain that surface Σ_c is determined by vector function

$$\mathbf{r}_c(u_c, \theta_c) = \mathbf{M}_{cb}(\theta_c)\mathbf{r}_b(u_c) = \mathbf{M}_{cb}(\theta_c)\mathbf{M}_{ba}\mathbf{r}_a(u_c). \tag{15.2.8}$$

Gear Rack-Cutter

We apply coordinate systems S_e and S_k [Fig. 15.2.2(c)] and coordinate system S_t [Fig. 15.3.1(b)]. The straight-line profile of the gear rack-cutter is represented in parametric


Figure 15.2.4: For derivation of pinion rack-cutter.

form in coordinate system $S_e(x_e, y_e)$ as:

$$x_e = 0, \quad y_e = u_t. \tag{15.2.9}$$

The coordinate transformation from S_k to S_t is similar to the transformation from S_b to S_c (Fig. 15.2.4), and the gear rack-cutter surface is represented by the following matrix equation:

$$\mathbf{r}_t(u_t, \theta_t) = \mathbf{M}_{tk}(\theta_t)\mathbf{M}_{ke}\mathbf{r}_e(u_t). \tag{15.2.10}$$
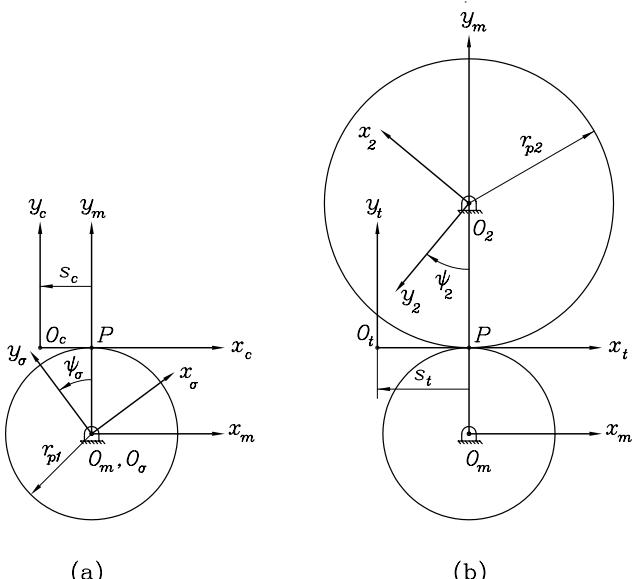
15.3 PROFILE-CROWNED PINION AND GEAR TOOTH SURFACES

Profile-crowned pinion and gear tooth surfaces are designated as Σ_σ and Σ_2, respectively, wherein Σ_1 indicates the pinion double-crowned surface.

Generation of Σ_σ

Profile-crowned pinion tooth surface Σ_σ is generated as the envelope to the pinion rack-cutter surface Σ_c. The derivation of Σ_σ is based on the following considerations:

(i) Movable coordinate systems $S_c(x_c, y_c)$ and $S_\sigma(x_\sigma, y_\sigma)$ are rigidly connected to the pinion rack-cutter and the pinion, respectively (Fig. 15.3.1(a)). The fixed coordinate system S_m is rigidly connected to the cutting machine.

(ii) The rack-cutter and the pinion perform related motions, as shown in Fig. 15.3.1(a),

(a)   (b)

Figure 15.3.1: Generation of profile-crowned tooth surfaces by application of rack-cutters: (a) for pinion generation by rack-cutter Σ_c; (b) for gear generation by rack-cutter Σ_t.

where $s_c = r_{p1}\psi_\sigma$ is the displacement of the rack-cutter in its translational motion, and ψ_σ is the angle of rotation of the pinion.

(iii) Using coordinate transformation from coordinate system S_c to coordinate system S_σ we obtain a family of generating surfaces Σ_σ represented in S_σ by the following matrix equation:

$$\mathbf{r}_\sigma(u_c, \theta_c, \psi_\sigma) = \mathbf{M}_{\sigma c}(\psi_\sigma)\mathbf{r}_c(u_c, \theta_c). \tag{15.3.1}$$

(iv) The pinion tooth surface Σ_σ is determined as the envelope to the family of surfaces $\mathbf{r}_\sigma(u_c, \theta_c, \psi_\sigma)$ and requires simultaneous application of vector function $\mathbf{r}_\sigma(u_c, \theta_c, \psi_\sigma)$ and the equation of meshing represented as follows (see Zalgaller [1975], Litvin [1994], and Litvin et al. [1995]):

$$\left(\frac{\partial \mathbf{r}_\sigma}{\partial u_c} \times \frac{\partial \mathbf{r}_\sigma}{\partial \theta_c} \right) \cdot \frac{\partial \mathbf{r}_\sigma}{\partial \psi_\sigma} = f_{c\sigma}(u_c, \theta_c, \psi_\sigma) = 0. \tag{15.3.2}$$

Equation $f_{c\sigma} = 0$ may be determined applying an alternative approach:

$$\mathbf{N}_c \cdot \mathbf{v}_c^{(c\sigma)} = 0. \tag{15.3.3}$$

Here, $\mathbf{N}_c$ is the normal to Σ_c represented in S_c; $\mathbf{v}_c^{(c\sigma)}$ is the relative velocity represented in S_c.

The coordinate transformation discussed above is based on application of homogeneous coordinates and 4x4 matrices (Chapter 1).

Generation of Gear Tooth Surface Σ_2
The schematic of generation of Σ_2 is shown in Fig. 15.3.1(b). Surface Σ_2 is represented by the following two equations considered simultaneously:

$$\mathbf{r}_2(u_t, \theta_t, \psi_2) = \mathbf{M}_{2t}(\psi_2)\mathbf{r}_t(u_t, \theta_t) \tag{15.3.4}$$

$$f_{t2}(u_t, \theta_t, \psi_2) = 0. \tag{15.3.5}$$

Here, vector equation $\mathbf{r}_t(u_t, \theta_t)$ represents the gear rack-cutter surface Σ_t; (u_t, θ_t) are the surface parameters of Σ_t; matrix $\mathbf{M}_{2t}(\psi_2)$ represents the coordinate transformation from S_t to S_2; ψ_2 is the generalized parameter of motion. It may be verified that the generated surface is a screw involute one. Equations (15.3.4) and (15.3.5) represent surface Σ_2 by three related parameters. The gear tooth surface may be represented as well in two-parameter form describing it as a ruled surface generated by a tangent to the helix on the base cylinder.

Necessary and Sufficient Conditions of Existence of an Envelope to a Parametric Family of Surfaces
Such conditions in the case of profile-crowned pinion tooth surface Σ_σ are formulated as follows (see Zalgaller [1975] and Litvin [1989, 1994]):

(i) Vector function $\mathbf{r}_\sigma(u_c, \theta_c, \psi_\sigma)$ of class C^2 is considered.
(ii) We designate by point $M(u_c^{(0)}, \theta_c^{(0)}, \psi_\sigma^{(0)})$ the set of parameters that satisfies the equation of meshing (15.3.2) at M and satisfies as well the following conditions [see items (iii)–(v)].

(iii) Generating surface Σ_c of the rack-cutter is a *regular* one, and we have at M that

$$\frac{\partial \mathbf{r}_c}{\partial u_c} \times \frac{\partial \mathbf{r}_c}{\partial \theta_c} \neq 0. \tag{15.3.6}$$

Vectors $\partial \mathbf{r}_c / \partial u_c$ and $\partial \mathbf{r}_c / \partial \theta_c$ represent in coordinate systems S_σ tangents to coordinate lines of rack-cutter surface Σ_c. Inequality (15.3.6) means that normal $\mathbf{N}_\sigma^{(c)}$ to surface Σ_c differs from zero. The designations of $\mathbf{N}_\sigma^{(c)}$ indicate that the normal to Σ_c is represented in coordinate system S_σ.

(iv) Partial derivatives of the equation of meshing (15.3.2) satisfy at M the inequality

$$\left| \frac{\partial f_{c\sigma}}{\partial u_c} \right| + \left| \frac{\partial f_{c\sigma}}{\partial \theta_c} \right| \neq 0. \tag{15.3.7}$$

(v) Singularities of surface Σ_σ are avoided by using the procedure described in Section 15.8.

By observation of conditions (i)–(v), the envelope Σ_σ is a *regular* surface, it contacts the generating surface Σ_c along a line, and the normal to Σ_σ is collinear to the normal of Σ_c. Vector function $\mathbf{r}_\sigma(u_c, \theta_c, \psi_\sigma)$ and Eq. (15.3.2) considered simultaneously represent surface Σ_σ in three-parameter form, by three related parameters $(u_c, \theta_c, \psi_\sigma)$.

Representation of Envelope Σ_σ in Two-Parameter Form
The profile-crowned surface Σ_σ may also be represented in two-parameter form, taking into account the following considerations:

(i) Assume that inequality (15.3.7) is observed, say, because

$$\frac{\partial f_{c\sigma}}{\partial \theta_c} \neq 0. \tag{15.3.8}$$

(ii) The theorem of implicit function system existence [Korn & Korn, 1968] yields that due to observation of inequality (15.3.8), equation of meshing (15.3.2) may be solved in the neighborhood of point M by function
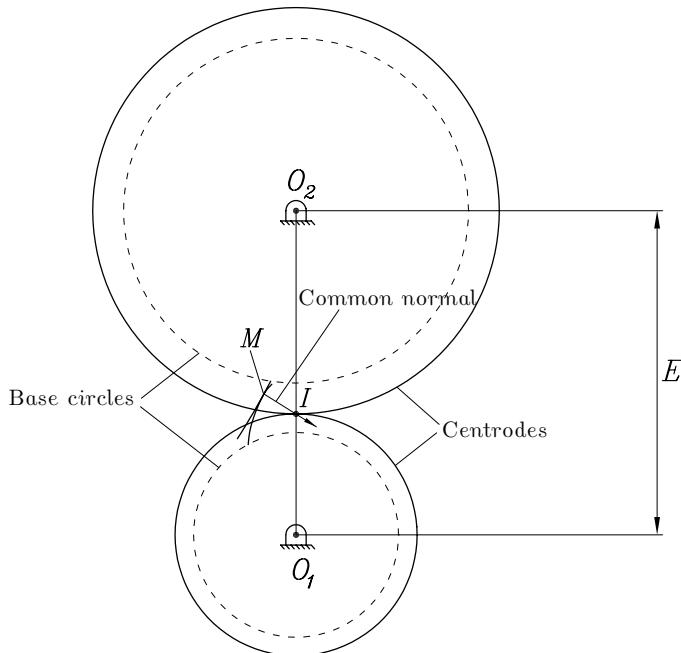
$$\theta_c = \theta_c(u_c, \psi_\sigma). \tag{15.3.9}$$

(iii) Then, surface Σ_σ can be represented as

$$\mathbf{R}_\sigma(u_c, \psi_\sigma) = \mathbf{r}_\sigma(u_c, \theta_c(u_c, \psi_\sigma), \psi_\sigma). \tag{15.3.10}$$

Similar representations of pinion tooth surfaces may be obtained for the case wherein inequality (15.3.7) is observed if $\partial f_{c\sigma} / \partial u_c \neq 0$ instead of inequality (15.3.8). The pinion profile-crowned tooth surface in this case may be represented as

$$\mathbf{R}_\sigma(\theta_c, \psi_\sigma) = \mathbf{r}_\sigma(u_c(\theta_c, \psi_\sigma), \theta_c, \psi_\sigma). \tag{15.3.11}$$

Figure 15.4.1: Illustration of cross-profiles of profile-crowned helicoids.

15.4 TOOTH CONTACT ANALYSIS (TCA) OF PROFILE-CROWNED PINION AND GEAR TOOTH SURFACES
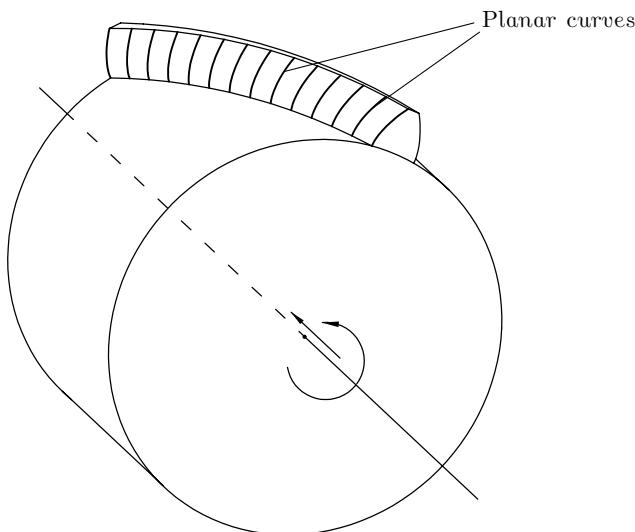
Meshing of Profile-Crowned Helicoids: Conceptual Considerations

Two profile-crowned helicoids are considered. The concept of the meshing is based on the following considerations discussed in Litvin [1962, 1989] and Litvin & Tsay [1985]:

(1) The helicoids transform rotation between parallel axes.

(2) The helicoid tooth surfaces are in point contact and this is achieved by the modification of the cross-profile of the pinion tooth surface. This statement is illustrated for the example in Fig. 15.4.1 in which an involute helicoid of the gear and pinion modified helicoid are shown. Profile crowning of the pinion is provided because the cross-profile deviates from the involute profile. The gear and the pinion tooth surfaces are in point contact provided by mismatched crossed profiles.

(3) The formation of each of the mating helicoids may be represented as the result of screw motion of the cross-profile. Figure 15.4.2 shows the formation of a helicoid by a family of planar curves that perform a screw motion about the axis of the helicoid.

(4) The screw parameters p_1 and p_2 of the profile-crowned helicoids have to be related as

$$\frac{p_1}{p_2} = \frac{\omega^{(2)}}{\omega^{(1)}} \qquad (15.4.1)$$

where $\omega^{(i)}$ ($i = 1, 2$) is the angular velocity of the helicoid.
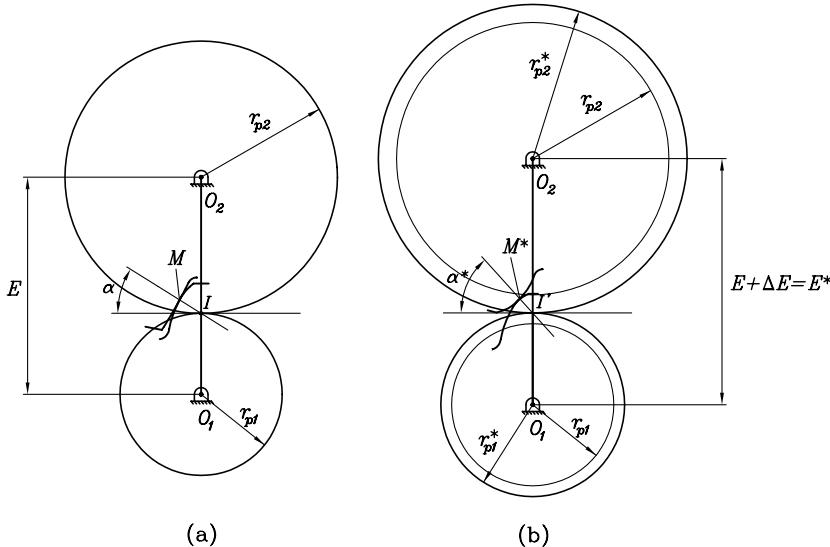
Figure 15.4.2: Illustration of formation of helicoid surface by screw motion of a cross-profile of the helicoid.

(5) The common normal to the cross-profiles at point M of tangency of profiles passes through point I of tangency of the centrodes (Fig. 15.4.1).

(6) It is easy to verify that during the process of meshing, point M of tangency of cross-profiles performs in the fixed coordinate system a translational motion along a straight line that passes through M and is parallel to the axes of aligned gears. The motion of a contact point along line M–M may be represented by two components:

   (i) transfer motion with gear i $(i = 1, 2)$ that is performed as rotation about the gear axis

  (ii) relative motion with respect to the helicoid surface that is a screw motion with parameter p_i.

The screw motion by its nature represents a combination of rotation about the gear axis with angular velocity designated as $\Omega^{(i)}$ and translational motion with the velocity $p_i \Omega^{(i)}$. The resulting motion of the contact point in the fixed coordinate system is a translational motion with the velocity $p_i \Omega^{(i)}$ along line M–M because rotations in transfer and relative motions are performed with $\Omega^{(i)} = -\omega^{(i)}$.

(7) It is easy to verify that the contact point moves over the helicoid surface along a helix that is generated by point M while it performs a screw motion over the surface of the helicoid. The path of contact on the surface of the helicoid is a helix in which radius ρ_i and the lead angle λ_i are related by $p_i = \rho_i \tan \lambda_i$ $(i = 1, 2)$.

(8) The meshing of the mating helicoids is not sensitive to the change of the center distance. Using Fig. 15.4.3, it is easy to verify that the change of the center distance does not cause transmission errors. We may assume that the crossing profiles form a center distance $E^* \neq E$. This involves that the point of tangency will be M^* instead of M and the pressure angle will be α^* instead of α. The new radii of centrodes will be r_i^* $(i = 1, 2)$. However, the line of action in the fixed coordinate
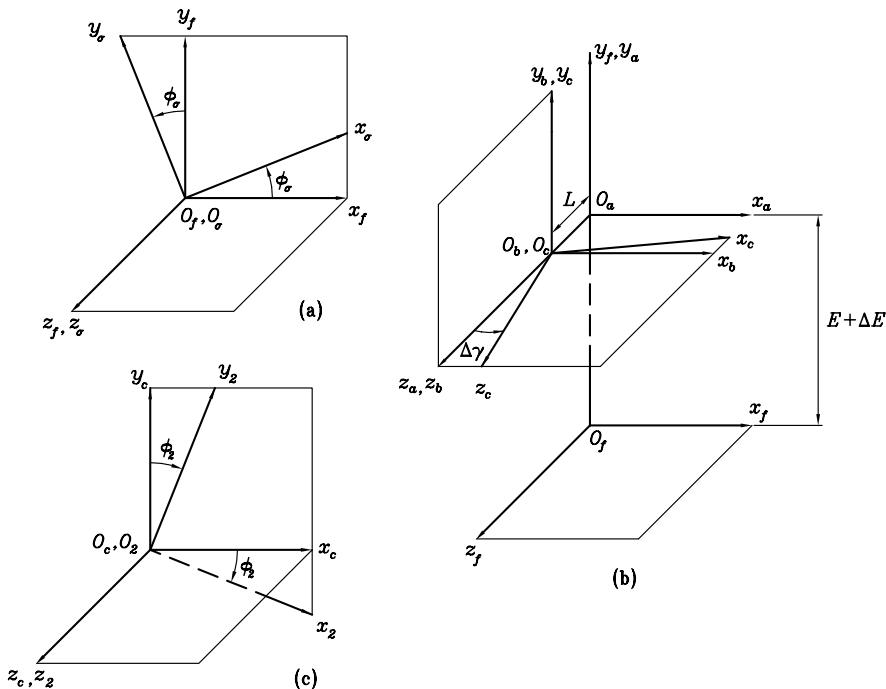
Figure 15.4.3: Operating circles in an aligned gear drive: (a) change of center distance $\Delta E = 0$ when no errors are applied; (b) $\Delta E \neq 0$.

system is again a straight line but now passes through point M^* instead of M. The line of action is the set of points of tangency of meshing surfaces in a fixed coordinate system.

(9) Considering the contact of helicoid surfaces in the 3D space, we find out that the surfaces have a common normal and common position vectors at any point of surface tangency. The normal does not change its orientation during the process of meshing in a fixed coordinate system.

(10) Although profile-crowned helicoids are not sensitive to the change of center distance and have localized surface contact, this type of gearing should not be applied because the change of the shaft angle and the difference of lead angles will cause a discontinuous linear function of transmission errors (see below). Then, vibration and noise become inevitable. This is the reason why a double-crowned pinion has to be applied instead of a profile-crowned one. Application of a double-crowned pinion provides a predesigned parabolic function of transmission errors, and the linear function of transmission errors caused by errors of assembly and manufacture is absorbed (see Section 15.7).

(11) The conceptual considerations for meshing for profile-crowned helicoids are true for all types of Novikov–Wildhaber gears, including the meshing of profile-crowned involute helical gears.

(12) The analytical investigation of profile-crowned modified helical gears is accomplished by application of TCA (Tooth Contact Analysis) (see below).

Algorithm of Analytical Simulation

Simulation of meshing and contact have been performed for two cases of design wherein: (i) the pinion of the gear drive is profile-crowned, and (ii) the pinion is double-crowned (see Sections 15.5, 15.6, and 15.7). Comparison of the output for both cases

Figure 15.4.4: Illustration of installment of coordinate systems for simulation of misalignment.

(Sections 15.4 and 15.7) shows that double-crowning of the pinion reduces transmission errors and noise and vibration of the gear drive.

The algorithm of simulation of meshing and contact is based on conditions of continuous tangency of contacting tooth surfaces of the pinion and the gear (see Section 9.4). The algorithm for profile-crowned involute gears is applied as follows. Knowing the representation of tooth surfaces Σ_σ and Σ_2 in coordinate systems S_σ and S_2 that are rigidly connected to the pinion and the gear, we may represent surfaces Σ_σ and Σ_2 in fixed coordinate system S_f taking into account the errors of alignment (see Fig. 15.4.4). We use for this purpose the coordinate transformation from S_σ and S_2 to S_f (Fig. 15.4.4).

We recall that tooth surfaces Σ_σ and Σ_2 are profile-crowned and therefore they are in point tangency. Tangency of Σ_σ and Σ_2 at common point M means that they have at M the same position vector and the surface normals are collinear. Then we obtain the following system of vector equations:

$$\mathbf{r}_f^{(\sigma)}(u_c, \theta_c, \psi_\sigma, \phi_\sigma) - \mathbf{r}_f^{(2)}(u_t, \theta_t, \psi_2, \phi_2) = 0 \tag{15.4.2}$$

$$\mathbf{N}_f^{(\sigma)}(u_c, \psi_\sigma, \phi_\sigma) - v\mathbf{N}_f^{(2)}(u_t, \psi_2, \phi_2) = 0 \tag{15.4.3}$$

$$f_{c\sigma}(u_c, \theta_c, \psi_\sigma) = 0 \tag{15.4.4}$$

$$f_{t2}(u_t, \theta_t, \psi_2) = 0. \tag{15.4.5}$$

Here, $f_{c\sigma} = 0$ and $f_{t2} = 0$ are the equations of meshing of the pinion and gear with the respective generating rack-cutters Σ_c and Σ_t; ϕ_σ and ϕ_2 are the angles of rotation of the

profile-crowned pinion and gear; $\nu \neq 0$ is a scalar factor in the equation of collinearity of surface normals.

One of the parameters, say ϕ_σ, is chosen as the input one. The Jacobian D of the system of scalar equations obtained from Eqs. (15.4.2)–(15.4.5) has to differ from zero as the precondition of point tangency of surfaces Σ_σ and Σ_2. In accordance with the theorem of implicit function system existence [Korn & Korn, 1968], observation of inequality $D \neq 0$ enables us to solve the system of equations (15.4.2)–(15.4.5) by functions

$$\{u_c(\phi_\sigma), \theta_c(\phi_\sigma), \psi_\sigma(\phi_\sigma), u_t(\phi_\sigma), \theta_t(\phi_\sigma), \psi_2(\phi_\sigma), \phi_2(\phi_\sigma)\} \in C^1. \qquad (15.4.6)$$

Solution of system of nonlinear equations (15.4.2)–(15.4.5) is an iterative computerized process based on application of the Newton–Raphson method [Visual Numerics, Inc., 1998].

The computational procedure provides the paths of contact on pinion and gear tooth surfaces and the function of transmission errors. We have applied for the simulation of meshing the following coordinate systems (Fig. 15.4.4):
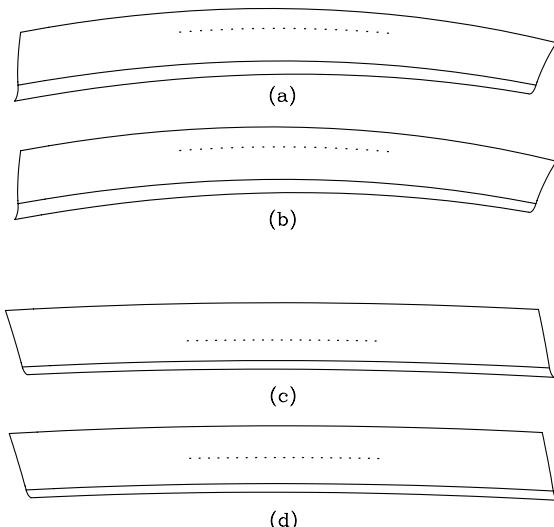
(i) Movable coordinate systems S_σ and S_2 that are rigidly connected to the pinion and the gear, respectively [Figs. 15.4.4(a) and 15.4.4(c)].
(ii) The fixed coordinate system S_f where the meshing of tooth surfaces Σ_σ and Σ_2 of the pinion and gear is considered.
(iii) All errors of assembly are referred to the gear. An additional fixed coordinate system S_c [Figs. 15.4.4(c) and 15.4.4(b)] is applied to simulate the errors of installment ΔE and $\Delta \gamma$ as parameters of installment of coordinate system S_c with respect to S_f. Rotation of the gear is considered as rotation of coordinate system S_2 with respect to S_c.
(iv) Errors of ΔE and $\Delta \gamma$ are illustrated in Fig. 15.4.4(b). Parameter L shown in Fig. 15.4.4(b) is applied to simulate an error $\Delta \gamma$ of the shaft angle such that the shortest distance between the crossed axes z_σ and z_2 does not coincide with y_f.

An example of meshing of profile-crowned pinion and gear tooth surfaces has been investigated for the following data: $N_1 = 21, N_2 = 77, m = 5.08$ mm, $s_{12} = 1, \beta = 30°$, $\alpha_d = \alpha_c = 25°$, and the parabola coefficient $a_c = 0.002$ mm^{-1}. The following errors of alignment have been simulated: (i) change of center distance $\Delta E = 1$ mm, (ii) error $\Delta \lambda = 3$ arcmin of the lead angle, (iii) change of shaft angle $\Delta \gamma = 3$ arcmin and $L = 0$, and (iv) change of $\Delta \gamma = 15$ arcmin and $L = 15$ mm.

The results of computation are as follows:

(1) Figure 15.4.5 illustrates the shift of bearing contact caused by error ΔE.
(2) The path of contact is indeed oriented longitudinally (Figs. 15.4.5, 15.4.6(b), and 15.4.6(c)).
(3) Error ΔE of shortest center distance does not cause transmission errors. The gear ratio m_{12} remains constant and of the same magnitude:

$$m_{12} = \frac{\omega^{(1)}}{\omega^{(2)}} = \frac{N_2}{N_1}. \qquad (15.4.7)$$

Figure 15.4.5: Shift of bearing contact caused by ΔE for the following cases: (a) path of contact on pinion surface when no error of center distance is applied and (b) when an error $\Delta E = 1$ mm is applied; (c) path of contact on gear surface when no error is applied and (d) when an error $\Delta E = 1$ mm is applied.

However, change of ΔE is accompanied with change in the radii of operating pitch cylinders and in the operating pressure angle of cross-profiles (Fig. 15.4.3).

(4) The main disadvantage of meshing of profile-crowned tooth surfaces is that $\Delta \gamma$ and $\Delta \lambda$ cause a discontinuous linear function of transmission errors as shown in Fig. 15.4.6(a). Such functions cause vibration and noise and this is the reason why a double-crowned pinion instead of a profile-crowned one is applied. Errors $\Delta \gamma$ and $\Delta \lambda$ also cause the shift of the bearing contact on the pinion and gear tooth surfaces. Our investigation shows that the main defects of the gear drive for the case in which $L \neq 0$ [see parameter L in Fig. 15.4.4(b)] and $\Delta \gamma \neq 0$ are the unfavorable functions of transmission errors, similar to the one shown in Fig. 15.4.6.
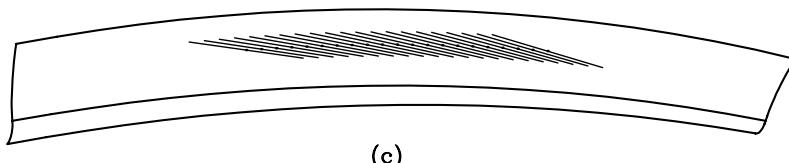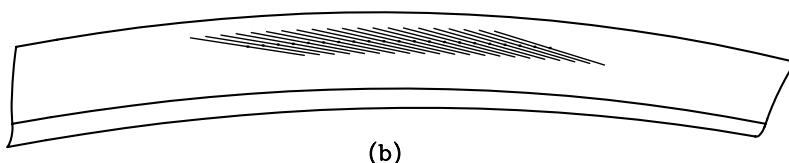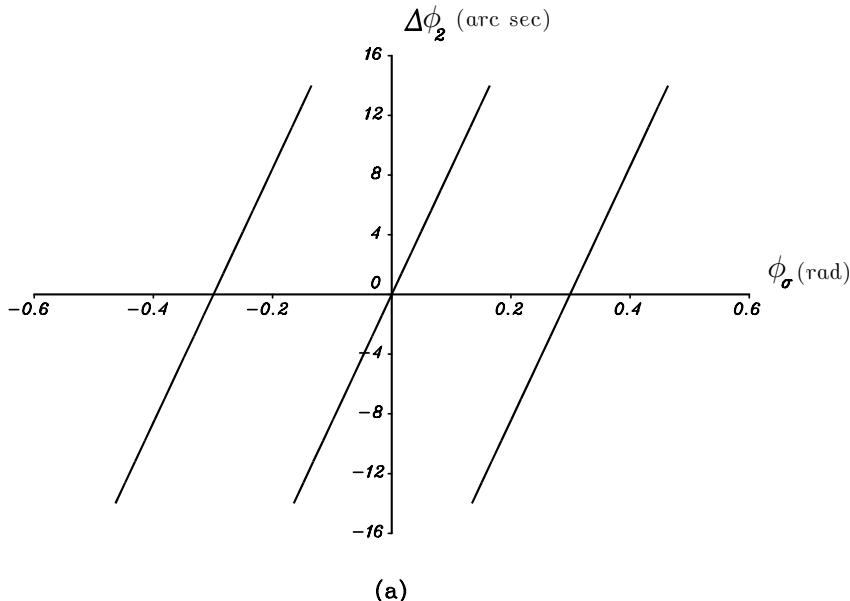
15.5 LONGITUDINAL CROWNING OF PINION BY A PLUNGING DISK

We remind the reader that errors of shaft angle and lead angle cause a discontinuous linear function of transmission errors (see Section 15.4), and high acceleration and vibration of the gear drive become inevitable. Longitudinal crowning of the pinion tooth surface, in addition to profile-crowning, is provided for transformation of the shape of the function of transmission errors and reduction of noise and vibration. This section covers longitudinal crowning of the pinion by application of a plunging generating disk. The same goal (double-crowning) may be achieved by application of a generating worm (see Section 15.6).

Application of a Plunging Disk
The approach is based on the following ideas:

(i) The profile-crowned surface Σ_σ of the pinion is considered as given.

(a)

(b)

(c)

Figure 15.4.6: Illustration of transmission errors and shift of bearing contact on the pinion tooth surface of a profile-crowned gear drive caused by $\Delta\gamma$: (a) function of transmission errors with error $\Delta\gamma = 3$ arcmin; (b) path of contact when no errors are applied; (c) path of contact with error $\Delta\gamma = 3$ arcmin.

(ii) A disk-shaped tool Σ_D that is conjugated to Σ_σ is determined (Fig. 15.5.1). The axes of the disk and pinion tooth surface Σ_σ are crossed and the crossing angle γ_{Dp} is equal to the lead angle on the pinion pitch cylinder [Fig. 15.5.2(b)]. The center distance E_{Dp} [Fig. 15.5.2(a)] is defined as

$$E_{Dp} = r_{d1} + \rho_D \tag{15.5.1}$$

where r_{d1} is the dedendum radius of the pinion and ρ_D is the grinding disk radius.
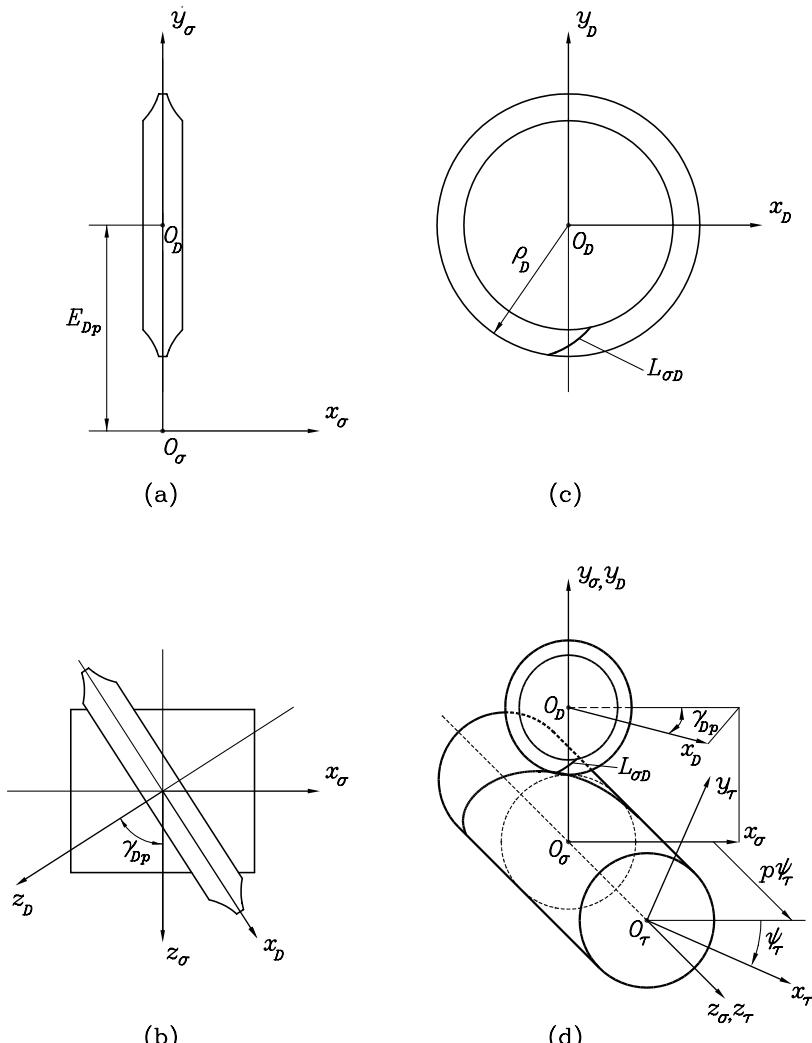
Figure 15.5.1: Generation of pinion by grinding disk.

(iii) Determination of disk surface Σ_D is based on the following procedure [Litvin, 1989, 1994]:
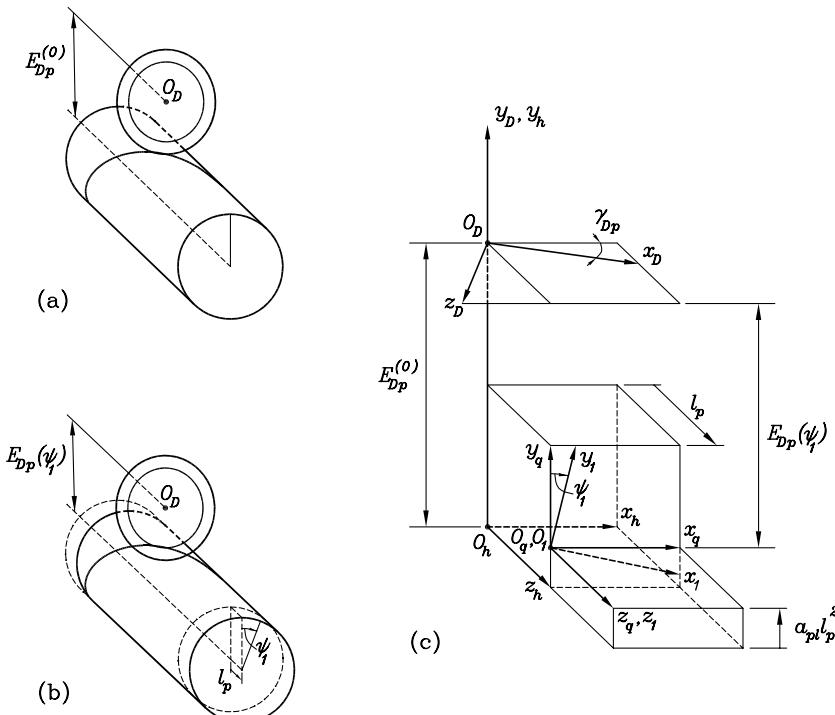
Step 1: Disk surface Σ_D is a surface of revolution. Therefore, there is such a line $L_{\sigma D}$ [Fig. 15.5.2(c)] of tangency of Σ_σ and Σ_D that the common normal to Σ_σ and Σ_D at each point of $L_{\sigma D}$ passes through the axis of rotation of the disk [Litvin, 1989, 1994]. Figure 15.5.2(c) shows line $L_{\sigma D}$ obtained on surface Σ_D. Rotation of $L_{\sigma D}$ about the axis of Σ_D enables representation of surface Σ_D as the family of lines $L_{\sigma D}$.

Step 2: It is obvious that screw motion of disk Σ_D about the axis of pinion tooth surface Σ_σ provides surface Σ_τ that coincides with Σ_σ [Fig. 15.5.2(d)].

**Figure 15.5.2:** Determination of disk surface Σ_D: (a) and (b) installment of grinding disk; (c) line $L_{\sigma D}$ of tangency of surfaces Σ_σ and Σ_D; (d) illustration of generation of surface Σ_τ by disk surface Σ_D.

(iv) The goal of obtaining a double-crowned surface Σ_1 of the pinion is accomplished by providing a combination of screw and plunging motions of the disk and the pinion. The generation of a double-crowned pinion tooth surface is illustrated in Fig. 15.5.3 and is accomplished as follows:

   (1) Figures 15.5.3(a) and 15.5.3(b) show two positions of the generated double-crowned pinion with respect to the disk. One of the two positions with center distance $E_{Dp}^{(0)}$ is the initial one; the other with $E_{Dp}(\psi_1)$ is the current position. The shortest distance $E_{Dp}^{(0)}$ is defined by Eq. (15.5.1).

   (2) Coordinate system S_D is rigidly connected to the generating disk [Fig. 15.5.3(c)] and is considered fixed.

Figure 15.5.3: Generation of double-crowned pinion surface Σ_1 by a plunging disk: (a) initial positions of pinion and disk; (b) schematic of generation; (c) applied coordinate systems.

(3) Coordinate system S_1 of the pinion performs a screw motion and is plunged with respect to the disk. Auxiliary systems S_h and S_q are used for a better illustration of these motions in Fig. 15.5.3(c). Such motions are described as follows:

Screw motion is accomplished by two components: (a) translational displacement l_p that is collinear to the axis of the pinion, and (b) rotational motion ψ_1 about the axis of the pinion [Figs. 15.5.3(b) and (c)]. The magnitudes l_p and ψ_1 are related through the screw parameter p of the pinion as

$$l_p = p\psi_1. \tag{15.5.2}$$

Plunging motion is accomplished by a translational displacement $a_{pl}l_p^2$ along the shortest distance direction [Fig. 15.5.3(c)]. Such motion allows definition of the shortest distance $E_{Dp}(\psi_1)$ [Fig. 15.5.3(b) and (c)] as a parabolic function

$$E_{Dp}(\psi_1) = E_{Dp}^{(0)} - a_{pl}l_p^2. \tag{15.5.3}$$

The translational motions l_p and $a_{pl}l_p^2$ are represented as displacement of system S_q with respect to system S_h. The same translational motions are

performed by system S_1 which performs rotational motion of angle ψ_1 with respect to system S_q.

(4)   The pinion tooth surface Σ_1 is determined as the envelope to the family of disk surface Σ_D generated in the relative motion between the disk and the pinion.

15.6 GRINDING OF DOUBLE-CROWNED PINION BY A WORM

Worm Installment
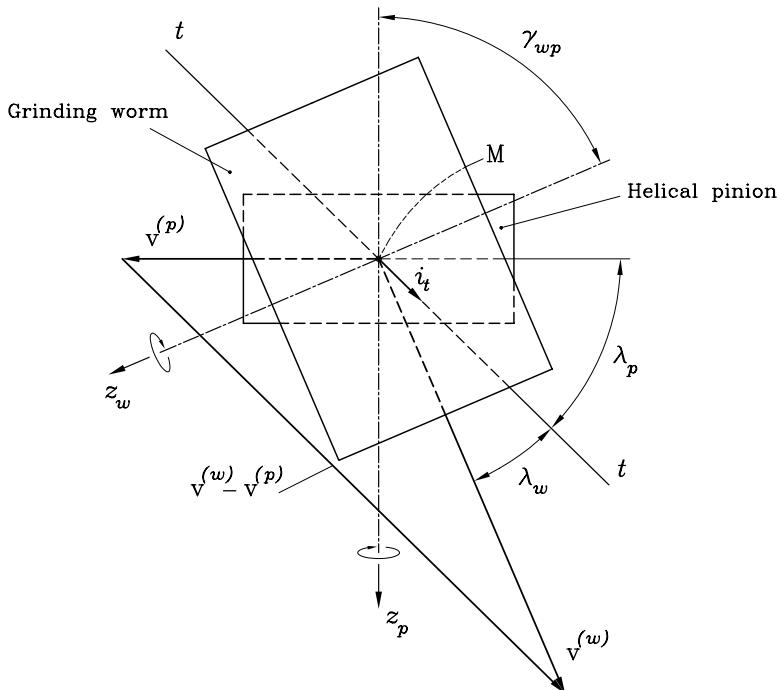
The installment of the grinding worm with respect to the pinion may be represented on the basis of the meshing of the two helicoids. Figure 15.6.1 illustrates the meshing of two left-hand helicoids, which represent the grinding worm and the pinion generated by the worm. Figure 15.6.2 yields that the crossing angle is

$$\gamma_{wp} = \lambda_p + \lambda_w \qquad (15.6.1)$$

where λ_p and λ_w are the lead angles on the pitch cylinders of the pinion and the worm.

**Figure 15.6.1:** Generation of pinion by grinding worm.

Figure 15.6.2: Installment of grinding (cutting) worm.

Figure 15.6.2 shows that the pitch cylinders of the worm and the pinion are in tangency at point M that belongs to the shortest distance between the crossed axes. The velocity polygon at M satisfies the relation

$$\mathbf{v}^{(w)} - \mathbf{v}^{(p)} = \mu \mathbf{i}_t. \tag{15.6.2}$$
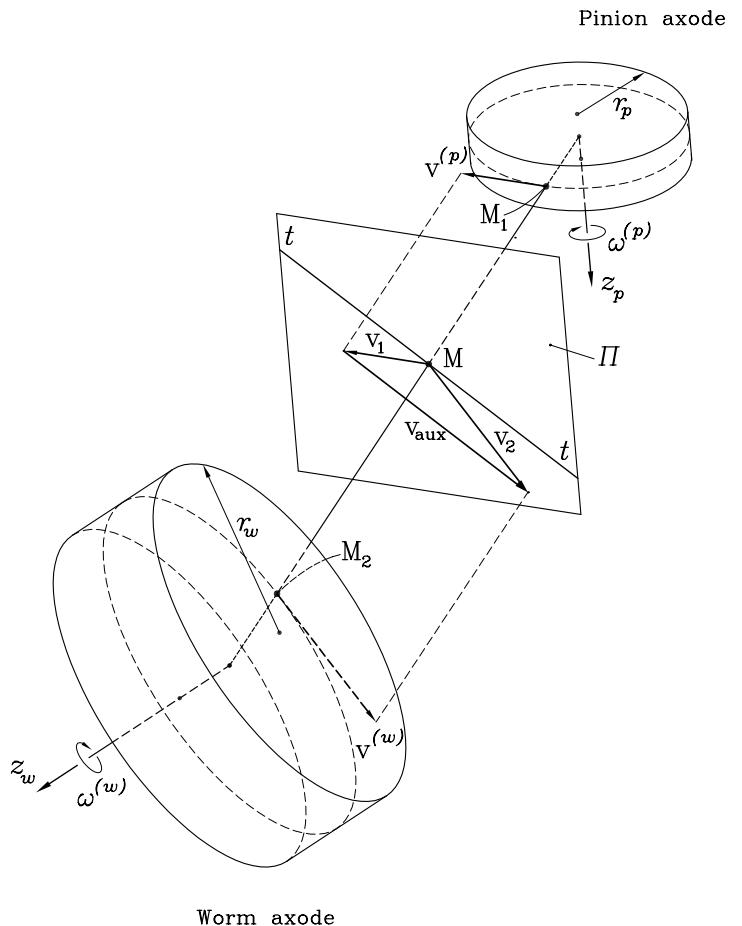
Here, $\mathbf{v}^{(w)}$ and $\mathbf{v}^{(p)}$ are the velocities of the worm and the pinion at M; $\mathbf{i}_t$ is the unit vector directed along the common tangent to the helices; μ is the scalar factor. Equation (15.6.2) indicates that the relative velocity at point M is collinear to the unit vector $\mathbf{i}_t$.

Determination of Worm Thread Surface Σ_w

In order to get the same pinion tooth surface Σ_σ that is generated by rack-cutter surface Σ_c (Section 15.3), the generation of Σ_w can be accomplished considering that the three surfaces Σ_c, Σ_σ, and Σ_w are simultaneously meshing. Figure 15.6.3 shows the axodes of these three surfaces wherein the shortest distance between pinion and worm axodes is extended. Plane Π represents the axode of the rack-cutter. Surface Σ_w is obtained using the following steps:

Step 1: The parabolic tooth surface Σ_c of the rack-cutter is considered as given.

Step 2: A translational motion of rack-cutter surface Σ_c, which is perpendicular to the axis of the pinion, and rotational motion of the pinion provide surface Σ_σ as an envelope to the family of surfaces of Σ_c (see Section 15.3). Velocity $\mathbf{v}_1$ (Fig. 15.6.3) is applied to the rack-cutter while the pinion is rotated with angular velocity $\boldsymbol{\omega}^{(p)}$. The

Pinion axode

Worm axode

Figure 15.6.3: For illustration of axodes of worm, pinion, and rack-cutter.

relation between v_1 and $\omega^{(p)}$ is defined as
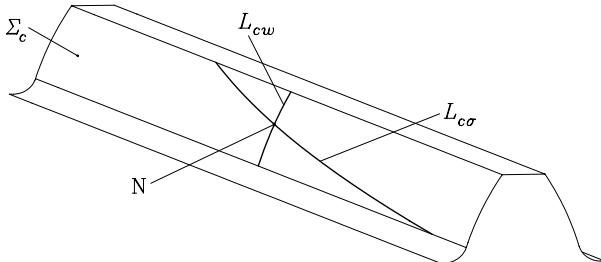
$$v_1 = \omega^{(p)} r_p \tag{15.6.3}$$

where r_p is the radius of the pinion pitch cylinder.

Step 3: An additional motion of surface Σ_c with velocity $\mathbf{v}_{\text{aux}}$ along direction $t-t$ of skew rack-cutter teeth (Fig. 15.6.3) is performed, and this motion does not affect surface Σ_σ. Vector equation $\mathbf{v}_2 = \mathbf{v}_1 + \mathbf{v}_{\text{aux}}$ allows us to obtain velocity $\mathbf{v}_2$ of rack-cutter Σ_c in a direction that is perpendicular to the axis of the worm. Then, we may represent the generation of worm surface Σ_w by rack-cutter Σ_c considering that the rack-cutter performs translational motion $\mathbf{v}_2$ while the worm is rotated with angular velocity $\boldsymbol{\omega}^{(w)}$. The relation between v_2 and $\omega^{(w)}$ is defined as

$$v_2 = \omega^{(w)} r_w \tag{15.6.4}$$

where r_w is the radius of the worm pitch cylinder. Worm surface Σ_w is generated as the envelope to the family of rack-cutter surfaces Σ_c.

Figure 15.6.4: Contact lines $L_{c\sigma}$ and L_{cw} corresponding to meshing of rack-cutter Σ_c with pinion and worm surfaces Σ_σ and Σ_w, respectively.

Step 4: The discussion above enables us to verify the simultaneous generation of profile-crowned pinion tooth surface Σ_σ and worm thread surface Σ_w by rack-cutter surface Σ_c. Each of the two generated surfaces Σ_σ and Σ_w are in line contact with rack-cutter surface Σ_c. However, the contact lines $L_{c\sigma}$ and L_{cw} do not coincide but intersect each other as shown in Fig. 15.6.4. Here, $L_{c\sigma}$ and L_{cw} represent the lines of contact between Σ_c and Σ_σ, and Σ_c and Σ_w, respectively. Lines $L_{c\sigma}$ and L_{cw} are obtained for any chosen value of related parameters of motion between Σ_c, Σ_σ, and Σ_w. Point N of intersection of lines L_{cw} and $L_{c\sigma}$ (Fig. 15.6.4) is the common point of tangency of surfaces Σ_c, Σ_σ, and Σ_w.

Profile Crowning of Pinion
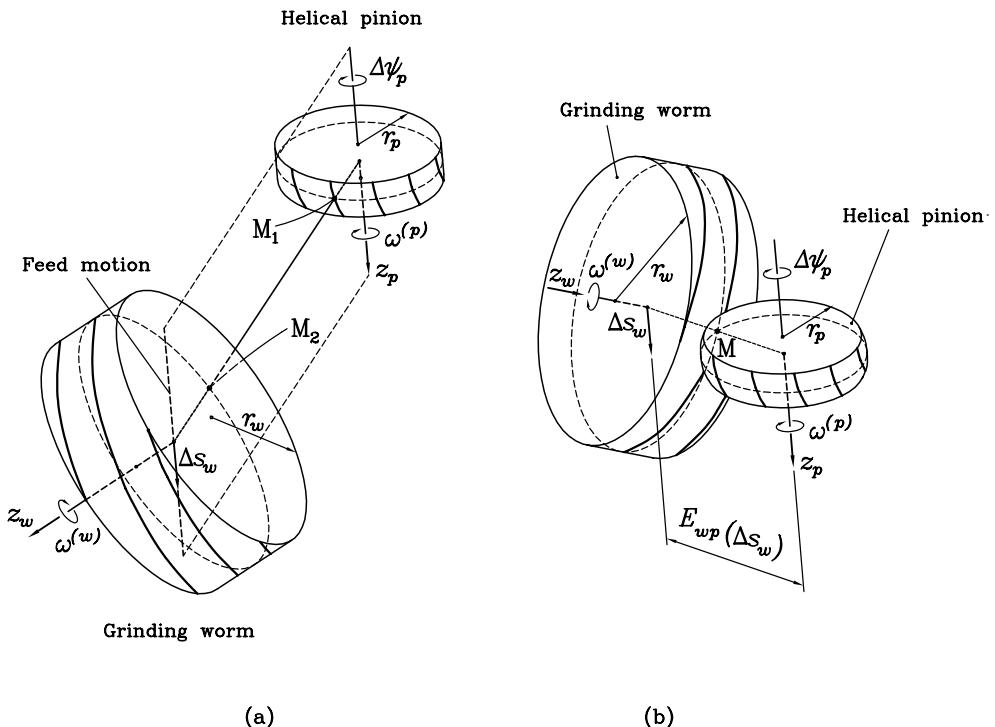
Profile-crowned pinion tooth surface Σ_σ was obtained above by using rack-cutter surface Σ_c. Direct derivation of generation of Σ_σ by the grinding worm Σ_w may be accomplished as follows:

(a) Consider that worm surface Σ_w and pinion tooth surface Σ_σ perform rotation between their crossed axes with angular velocities $\omega^{(w)}$ and $\omega^{(p)}$. It follows from the discussion above that Σ_w and Σ_σ are in point contact and N is one of the instantaneous points of contact of Σ_w and Σ_σ (Fig. 15.6.4).

(b) The concept of direct derivation of Σ_σ by Σ_w is based on the two-parameter enveloping process. The process of such enveloping is based on application of two independent sets of parameters of motion [Litvin, 1994; Litvin & Seol, 1996]:

(i) One set of parameters relates the angles of rotation of the worm and the pinion as

$$m_{wp} = \frac{\omega^{(w)}}{\omega^{(p)}} = \frac{N_p}{N_w} = N_p \qquad (15.6.5)$$

where the number N_w of worm threads is considered as $N_w = 1$, and N_p is the teeth number of the pinion.

(ii) The second set of parameters of motion is provided as a combination of two components: (1) translational motion Δs_w of the worm that is collinear to the

Figure 15.6.5: Schematic of generation: (a) without worm plunging; (b) with worm plunging.

axis of the pinion [Fig. 15.6.5(a)]; (2) small rotational motion of the pinion about the pinion axis that is determined as

$$\Delta \psi_p = \frac{\Delta s_w}{p} \tag{15.6.6}$$

where p is the screw parameter of the pinion.

Analytical determination of a surface generated as the envelope to a two-parameter enveloping process is presented in Section 6.10. The schematic of generation of Σ_σ by Σ_w is shown in Fig. 15.6.5(a) in which the shortest center distance is shown as an extended one for the purpose of better illustration. In the process of meshing of Σ_w and Σ_σ, the worm surface Σ_w and the profile-crowned pinion surface perform rotation about crossed axes. The shortest distance is executed as

$$E_{wp} = r_p + r_w. \tag{15.6.7}$$

Surfaces Σ_w and Σ_σ are in point tangency. Feed motion of the worm is provided as a screw motion with the screw parameter of the pinion. Designations in Fig. 15.6.5(a) indicate (1) M_1 and M_2 points on pitch cylinders (these points do not coincide with each other because the shortest distance is illustrated as extended), (2) $\omega^{(w)}$ and $\omega^{(p)}$ are the angular velocities of the worm and profile-crowned pinion in their rotation about crossed axes, (3) Δs_w and $\Delta \psi_p$ are the components of the screw motion of the feed motion; and (4) r_w and r_p are the radii of pitch cylinders.

Double Crowning of Pinion

We have presented above the generation by a worm of a profile-crowned surface Σ_σ of a pinion. However, our final goal is the generation by a worm of a *double-crowned* surface Σ_1 of a pinion. Two approaches are proposed for this purpose:

WORM PLUNGING. Additional pinion crowning (longitudinal crowning) is provided by plunging of the worm with respect to the pinion, shown schematically in Fig. 15.6.5(b). Plunging of the worm in the process of pinion grinding is performed as a variation of the shortest distance between the axes of the grinding worm and the pinion. The instantaneous shortest center distance $E_{wp}(\Delta s_w)$ between the grinding worm and the pinion is executed as [Fig. 15.6.5(b)]

$$E_{wp}(\Delta s_w) = E_{wp}^{(0)} - a_{pl}(\Delta s_w)^2. \tag{15.6.8}$$

Here, Δs_w is measured along the pinion axis from the middle of the pinion; a_{pl} is the parabola coefficient of the function $a_{pl}(\Delta s_w)^2$; $E_{wp}^{(0)}$ is the nominal value of the shortest distance defined by Eq. (15.6.7). Plunging of the worm with observation of Eq. (15.6.8) provides a parabolic function of transmission errors in the process of meshing of the pinion and the gear of the proposed version of the modified involute helical gear drive.

MODIFIED ROLL OF FEED MOTION. Conventionally, the feed motion of the worm is provided by observation of linear relation (15.6.6) between components Δs_w and $\Delta \psi_p$. For the purpose of pinion longitudinal crowning, the following function $\Delta \psi_p(\Delta s_w)$ is observed:

$$\Delta \psi_p(\Delta s_w) = \frac{\Delta s_w}{p} + a_{mr}(\Delta s_w)^2 \tag{15.6.9}$$

where a_{mr} is the parabola coefficient of the parabolic function (15.6.9).

Worm modified roll is provided instead of worm plunging. Application of function (15.6.9) allows modification of the pinion tooth surface and provides a parabolic function of transmission errors of the proposed gear drive.

The derivation of double-crowned surface Σ_1 of the pinion by application of both approaches mentioned above is based on determination of Σ_1 as a two-parameter enveloping process:

Step 1: We consider that surface Σ_w is determined as the envelope to the rack-cutter surface Σ_c. The determination of Σ_w is a one-parameter enveloping process.

Step 2: Double-crowned surface Σ_1 of the pinion is determined as an envelope of a two-parameter process by application of the following equations:

$$\mathbf{r}_1(u_w, \theta_w, \psi_w, \Delta s_w) = \mathbf{M}_{1w}(\psi_w, \Delta s_w)\mathbf{r}_w(u_w, \theta_w) \tag{15.6.10}$$

$$\mathbf{N}_w \cdot \mathbf{v}_w^{(w1, \psi_w)} = 0 \tag{15.6.11}$$

$$\mathbf{N}_w \cdot \mathbf{v}_w^{(w1, \Delta s_w)} = 0 \tag{15.6.12}$$

Here, (u_w, θ_w) are the worm surface parameters; $(\psi_w, \Delta s_w)$ are the generalized parameters of motion of the two-parameter enveloping process. Vector equation (15.6.10) represents the family of surfaces Σ_w of the worm in coordinate system S_1 of the pinion.

Equations (15.6.11) and (15.6.12) represent two equations of meshing. Vector $\mathbf{N}_w$ is the normal to the worm tooth surface Σ_w and is represented in system S_w. Vector $\mathbf{v}_w^{(w1,\psi_w)}$ represents the relative velocity between the worm and pinion determined under the conditions that parameter ψ_w of motion is varied and the other parameter Δs_w is held at rest. Vector $\mathbf{v}_w^{(w1,\Delta s_w)}$ is determined under the conditions that parameter Δs_w is varied and the other parameter of motion, ψ_w, is held at rest. Both vectors of relative velocity are represented in coordinate system S_w.

Vector equations (15.6.10), (15.6.11), and (15.6.12) considered simultaneously determine the double-crowned pinion tooth surface as the envelope to the two-parameter enveloping process (Section 6.10).

15.7 TCA OF GEAR DRIVE WITH DOUBLE-CROWNED PINION

Simulation of meshing of a gear drive with a double-crowned pinion is investigated by application of the same algorithm discussed in Section 15.4 for a gear drive with a profile-crowned pinion. The applied design parameters are shown in Table 15.7.1.
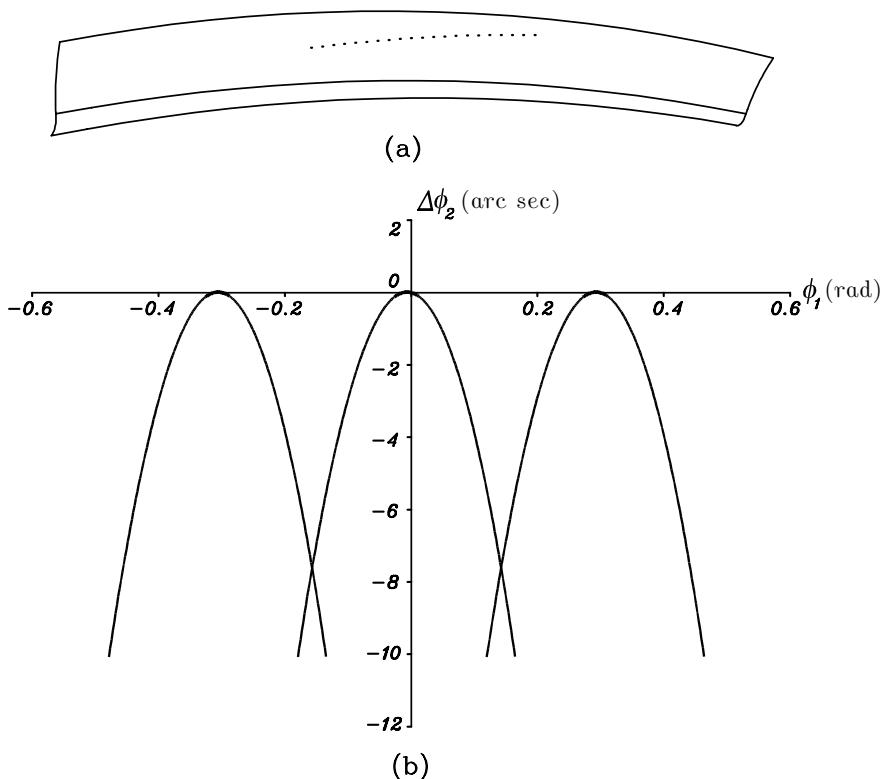
The parabolic coefficient of longitudinal crowning a_{pl} is of a magnitude that provides a maximal error of 8 arcsec of the predesigned function of transmission errors for a gear drive without errors of alignment. Figures 15.7.1(a) and 15.7.1(b) show the path of contact and the function of transmission errors, respectively. The TCA output shows that a parabolic function of transmission errors in meshing of the pinion and the gear is indeed obtained due to application of a double-crowned pinion.

The chosen approaches for TCA cover application of (i) a disk-shaped tool (Section 15.5), (ii) a plunging worm (Section 15.6), and (iii) a modified roll of feed motion (Section 15.6). These approaches yield almost the same TCA output.

The simulation of meshing is performed for the following errors of alignment: (i) change of center distance $\Delta E = 140\ \mu$m; (ii) change of shaft angle $\Delta\gamma = 3$ arcmin; (iii) error $\Delta\lambda = 3$ arcmin; and (iv) combination of errors $\Delta\gamma$ and $\Delta\lambda$ as $\Delta\gamma - \Delta\lambda = 0$ arcmin.

Table 15.7.1: Design parameters

|	
Number of teeth of the pinion, N_1	21
Number of teeth of the gear, N_2	77
Module, m	5.08 mm
Driving-side pressure angle, α_d	25°
Coast-side pressure angle, α_c	25°
Helix angle, β	30°
Parameter of rack-cutter, b	1
Face width	70 mm
Radius of the worm pitch cylinder, r_w	98 mm
Parabolic coefficient of pinion rack-cutter, a_c	0.002 mm^{-1}
Parabolic coefficient of longitudinal crowning, a_{pl}	0.000085 mm^{-1}
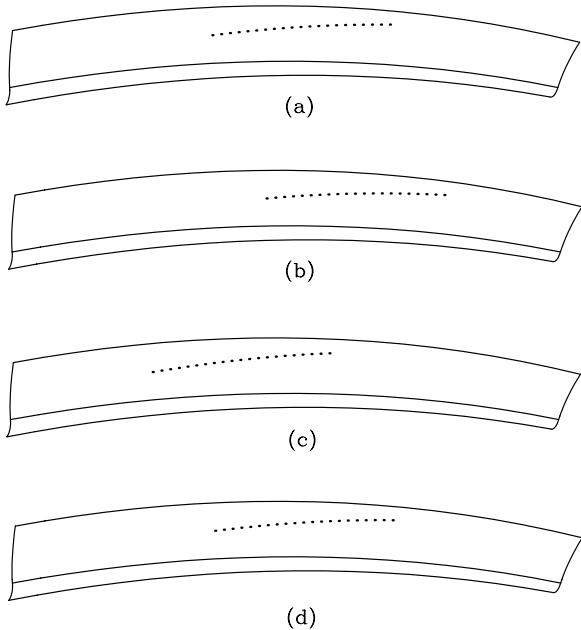
Figure 15.7.1: Output of TCA for a gear drive wherein the pinion is generated by plunging of the grinding worm; no errors are applied: (a) path of contact and (b) function of transmission errors.

The results of TCA are as follows:

(1) Figure 15.7.1(a) shows the orientation of the path of contact of the aligned gear drive.

(2) Figures 15.7.2(a), 15.7.2(b), and 15.7.2(c) show the shift of the paths of contact caused by errors of alignment ΔE, $\Delta \gamma$, and $\Delta \lambda$, respectively. Misalignment ΔE does not cause the shift of the bearing contact on the pinion surface. The shift of paths of contact caused by $\Delta \gamma$ may be compensated by correction $\Delta \lambda_1$ of the pinion (or $\Delta \lambda_2$ of the gear). Figure 15.7.2(d) shows that the location of the path of contact can be restored by correction of $\Delta \lambda_1$ of the pinion, taking $\Delta \gamma - \Delta \lambda_1 = 0$. This means that correction of $\Delta \lambda_1$ can be used for the restoration of the location of the path of contact. Correction of $\Delta \lambda_1$ or $\Delta \lambda_2$ may be applied for grinding of the pinion or the gear, respectively.

It was mentioned above (see Section 15.4) that double crowning of the pinion provides a predesigned parabolic function. Therefore, linear functions of transmission errors caused by $\Delta \gamma$, $\Delta \lambda$, and other errors are indeed absorbed by the predesigned parabolic function of transmission errors $\Delta \phi_2(\phi_1)$. The final function of transmission errors $\Delta \phi_2(\phi_1)$ remains a parabolic one. However, an increase in the magnitude of errors

(a)

(b)

(c)

(d)

Figure 15.7.2: Influence of errors of alignment on the shift of the path of contact for a modified involute helical gear drive wherein the pinion is generated by plunging of the grinding worm with the following errors: (a) $\Delta E = 140\ \mu$m; (b) $\Delta\gamma = 3$ arcmin; (c) $\Delta\lambda = 3$ arcmin; (d) $\Delta\gamma - \Delta\lambda_1 = 0$ arcmin.

$\Delta\gamma$ and $\Delta\lambda$ may result in the final function of transmission errors $\Delta\phi_2(\phi_1)$ becoming discontinued. In such a case, the predesigned parabolic function $\Delta\phi_2(\phi_1)$ has to be of a larger magnitude, or it becomes necessary to limit the range of $\Delta\gamma$, $\Delta\lambda$, and other errors.

15.8 UNDERCUTTING AND POINTING

Undercutting

Avoidance of undercutting is applied to pinion tooth surface Σ_σ and is based on the following ideas:

(i) Appearance of singular points on generated surface Σ_σ is the warning that the surface may be undercut in the process of generation [Litvin, 1989, 1994].

(ii) Singular points on surface Σ_σ are generated by regular points on the generating surface Σ_c when the velocity of a contact point in its motion over Σ_σ becomes equal to zero [Litvin, 1989, 1994]:

$$\mathbf{v}_r^{(\sigma)} = \mathbf{v}_r^{(c)} + \mathbf{v}^{(c\sigma)} = 0. \tag{15.8.1}$$

(iii) Equation (15.8.1) and differentiated equation of meshing

$$\frac{d}{dt}[f(u_c, \theta_c, \psi_\sigma)] = 0 \tag{15.8.2}$$

allow us to determine a line L on surface Σ_c that generates singular points on Σ_σ. By limiting Σ_c with line L, we may avoid the appearance of singular points on Σ_σ.

The derivation of line L is based on the following considerations:

(i) Equation (15.8.1) yields

$$\frac{\partial \mathbf{r}_c}{\partial u_c}\frac{du_c}{dt} + \frac{\partial \mathbf{r}_c}{\partial \theta_c}\frac{d\theta_c}{dt} = -\mathbf{v}_c^{(c\sigma)}. \tag{15.8.3}$$

Here, $\partial \mathbf{r}_c/\partial u_c$, $\partial \mathbf{r}_c/\partial \theta_c$, and $\mathbf{v}_c^{(c\sigma)}$ are three-dimensional vectors represented in system S_c of the pinion rack-cutter.

(ii) Equation (15.8.2) yields

$$\frac{\partial f}{\partial u_c}\frac{du_c}{dt} + \frac{\partial f}{\partial \theta_c}\frac{d\theta_c}{dt} = -\frac{\partial f}{\partial \psi_\sigma}\frac{d\psi_\sigma}{dt}. \tag{15.8.4}$$

(iii) Equations (15.8.3) and (15.8.4) represent a system of four linear equations in two unknowns: du_c/dt and $d\theta_c/dt$. This system has a certain solution for the unknowns if matrix

$$\mathbf{A} = \begin{bmatrix} \dfrac{\partial \mathbf{r}_c}{\partial u_c} & \dfrac{\partial \mathbf{r}_c}{\partial \theta_c} & -\mathbf{v}_c^{(c\sigma)} \\[2ex] \dfrac{\partial f}{\partial u_c} & \dfrac{\partial f}{\partial \theta_c} & -\dfrac{\partial f}{\partial \psi_\sigma}\dfrac{d\psi_\sigma}{dt} \end{bmatrix} \tag{15.8.5}$$

has the rank $r = 2$. This yields

$$\Delta_1 = \begin{vmatrix} \dfrac{\partial x_c}{\partial u_c} & \dfrac{\partial x_c}{\partial \theta_c} & -v_{xc}^{(c\sigma)} \\[2ex] \dfrac{\partial y_c}{\partial u_c} & \dfrac{\partial y_c}{\partial \theta_c} & -v_{yc}^{(c\sigma)} \\[2ex] \dfrac{\partial f}{\partial u_c} & \dfrac{\partial f}{\partial \theta_c} & -\dfrac{\partial f}{\partial \psi_\sigma}\dfrac{d\psi_\sigma}{dt} \end{vmatrix} = 0 \tag{15.8.6}$$

$$\Delta_2 = \begin{vmatrix} \dfrac{\partial x_c}{\partial u_c} & \dfrac{\partial x_c}{\partial \theta_c} & -v_{xc}^{(c\sigma)} \\[2ex] \dfrac{\partial z_c}{\partial u_c} & \dfrac{\partial z_c}{\partial \theta_c} & -v_{zc}^{(c\sigma)} \\[2ex] \dfrac{\partial f}{\partial u_c} & \dfrac{\partial f}{\partial \theta_c} & -\dfrac{\partial f}{\partial \psi_\sigma}\dfrac{d\psi_\sigma}{dt} \end{vmatrix} = 0 \tag{15.8.7}$$

$$\Delta_3 = \begin{vmatrix} \dfrac{\partial y_c}{\partial u_c} & \dfrac{\partial y_c}{\partial \theta_c} & -v_{yc}^{(c\sigma)} \\[2ex] \dfrac{\partial z_c}{\partial u_c} & \dfrac{\partial z_c}{\partial \theta_c} & -v_{zc}^{(c\sigma)} \\[2ex] \dfrac{\partial f}{\partial u_c} & \dfrac{\partial f}{\partial \theta_c} & -\dfrac{\partial f}{\partial \psi_\sigma}\dfrac{d\psi_\sigma}{dt} \end{vmatrix} = 0 \tag{15.8.8}$$

$$\Delta_4 = \begin{vmatrix} \dfrac{\partial x_c}{\partial u_c} & \dfrac{\partial x_c}{\partial \theta_c} & -v_{xc}^{(c\sigma)} \\[2ex] \dfrac{\partial y_c}{\partial u_c} & \dfrac{\partial y_c}{\partial \theta_c} & -v_{yc}^{(c\sigma)} \\[2ex] \dfrac{\partial z_c}{\partial u_c} & \dfrac{\partial z_c}{\partial \theta_c} & -v_{zc}^{(c\sigma)} \end{vmatrix} = 0. \tag{15.8.9}$$

Equation (15.8.9) yields the equation of meshing $f(u_c, \theta_c, \psi_\sigma) = 0$ and is not applied for investigation of singularities. The requirement that determinants Δ_1, Δ_2, and Δ_3 must be equal to zero simultaneously may be represented as

$$\Delta_1^2 + \Delta_2^2 + \Delta_3^2 = 0. \tag{15.8.10}$$

Equation (15.8.10) enables us to obtain for determination of singularities the following function:

$$F(u_c, \theta_c, \psi_\sigma) = 0 \tag{15.8.11}$$

NOTE. In most cases, it is sufficient for derivation of function $F = 0$ to use instead of (15.8.10) only one of the three following equations:

$$\Delta_1 = 0, \quad \Delta_2 = 0, \quad \Delta_3 = 0. \tag{15.8.12}$$

An exceptional case, when application of (15.8.10) is required, is discussed in Section 6.3.
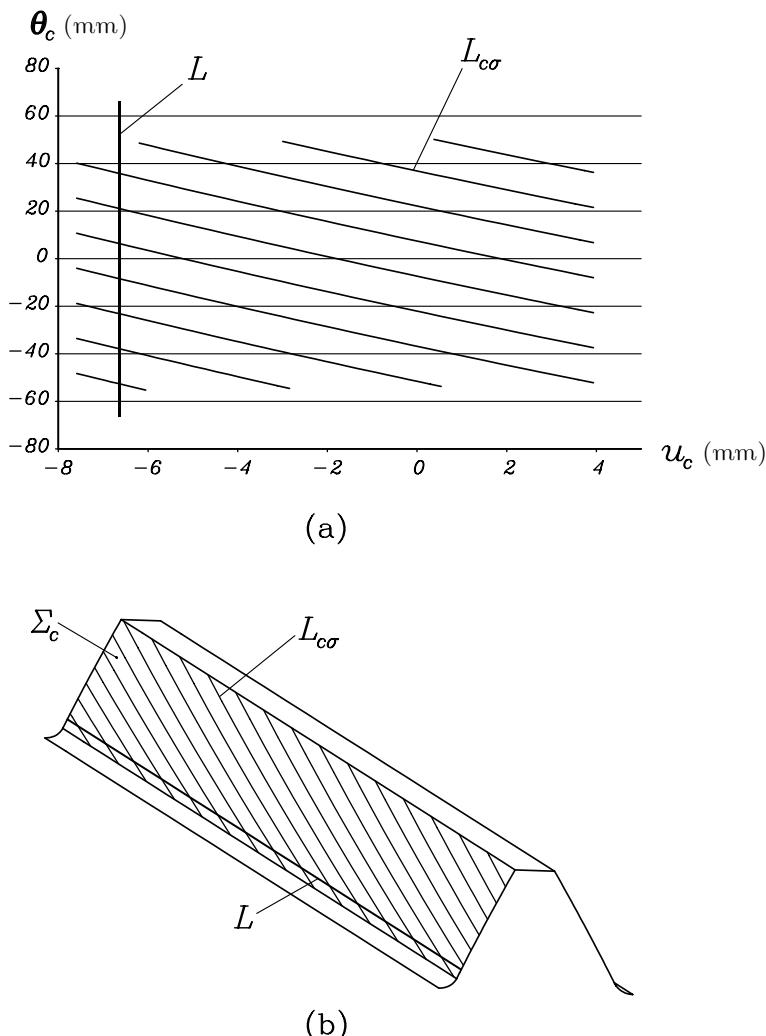
Singularities of the pinion may be avoided by limitation by line L of the rack-cutter surface Σ_c that generates the pinion. The determination of L [Fig. 15.8.1(a)] is based on the following procedure:

(1) Using equation of meshing $f(u_c, \theta_c, \psi_\sigma) = 0$, we may obtain in the plane of parameters (u_c, θ_c) the family of contact lines of the rack-cutter and the pinion. Each contact line is determined for a fixed parameter of motion ψ_σ.

(2) The sought-for limiting line L is determined in the space of parameters (u_c, θ_c) by simultaneous consideration of equations $f = 0$ and $F = 0$ [Fig. 15.8.1(a)]. Then, we can obtain the limiting line L on the surface of the rack-cutter [Fig. 15.8.1(b)]. The limiting line L on the rack-cutter surface is formed by *regular* points of the rack-cutter, but these points will generate *singular* points on the pinion tooth surface.

Limitations of the rack-cutter surface by L enable us to avoid singular points on the pinion tooth surface. Singular points on the pinion tooth surface can be obtained by coordinate transformation of line L on rack-cutter surface Σ_c to surface Σ_σ.

Pointing

Pointing of the pinion means that the width of the topland becomes equal to zero. Figure 15.8.2(a) shows the cross sections of the pinion and the pinion rack-cutter. Point A_c of the rack-cutter generates the limiting point A_σ of the pinion when singularity of the pinion is still avoided. Point B_c of the rack-cutter generates point B_σ of the pinion profile. Parameter s_a indicates the chosen width of the pinion topland. Parameter α_t indicates the pressure angle at point Q. Parameters h_1 and h_2 indicate the limitation of

θ_c (mm)

L

$L_{c\sigma}$

u_c (mm)

(a)

Σ_c

$L_{c\sigma}$

L

(b)
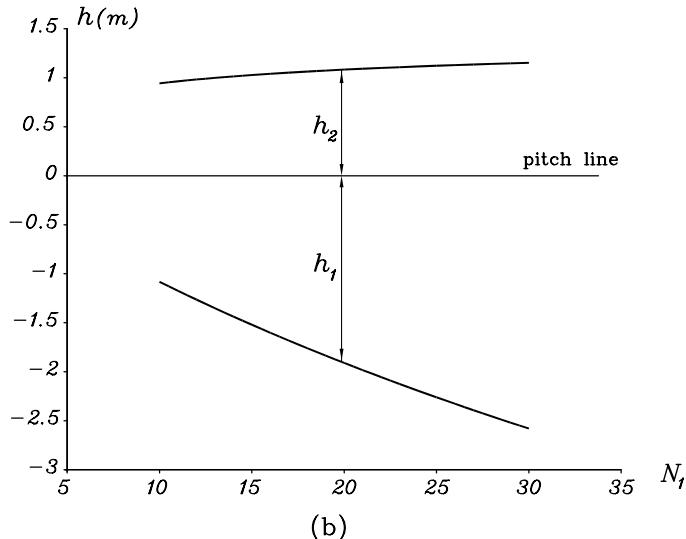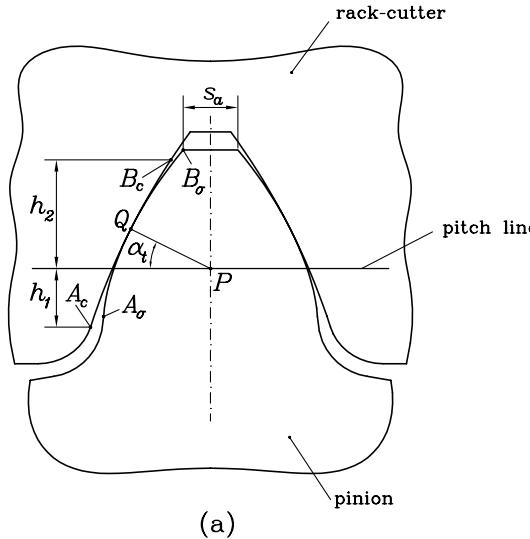
Figure 15.8.1: Contact lines $L_{c\sigma}$ and limiting line L: (a) in plane (u_c, θ_c); (b) on surface Σ_c.

location of limiting points A_c and B_c of the rack-cutter profiles. Figure 15.8.2(b) shows functions $h_1(N_1)$ and $h_2(N_1)$ (N_1 is the pinion tooth number) obtained for the following data: $\alpha_d = 25°$, $\beta = 30°$, parabola coefficient of pinion rack-cutter $a_c = 0.002$ mm^{-1}, $s_a = 0.3\ m$, parameter $s_{12} = 1.0$ [see Eq. (15.2.3)], and module $m = 1$ mm.

15.9 STRESS ANALYSIS
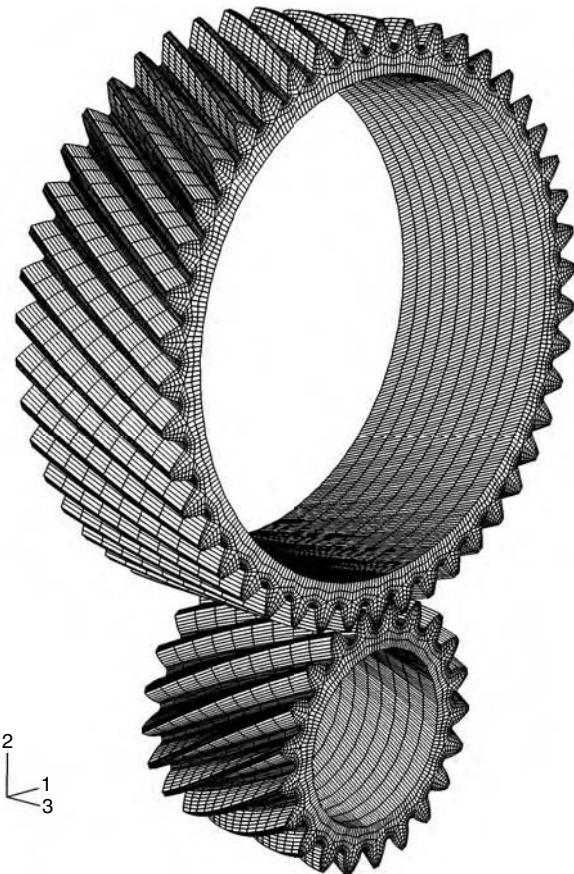
This section covers stress analysis and investigation of formation of bearing contact of contacting surfaces. The performed stress analysis is based on the finite element method [Zienkiewicz & Taylor, 2000] and application of a general computer program [Hibbit, Karlsson & Sirensen, Inc., 1998]. An enhanced approach for application of finite element analysis is presented in Section 9.5.
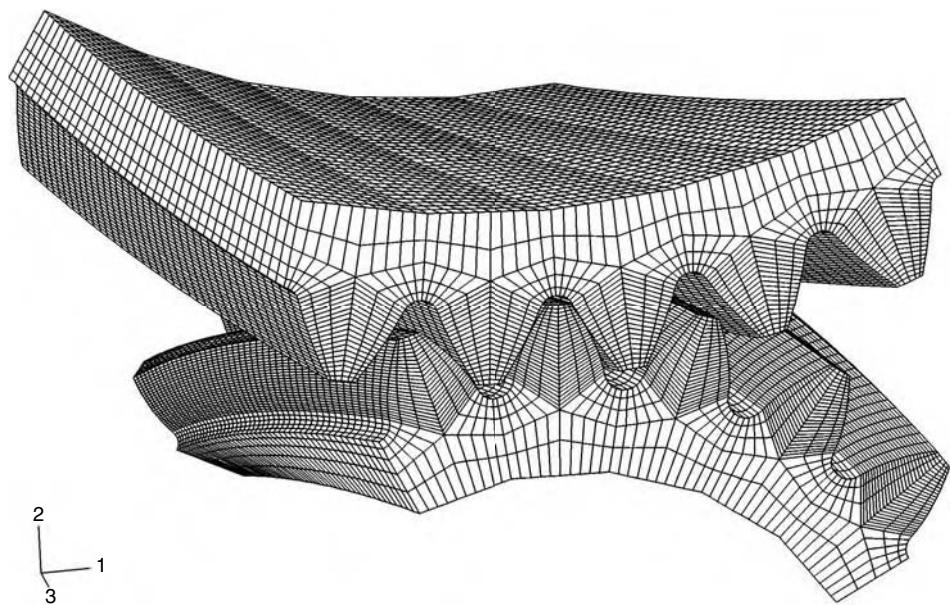
Figure 15.8.2: Permissible dimensions h_1 and h_2 of rack-cutter: (a) cross sections of pinion and rack-cutter; (b) functions $h_1(N_1)$ and $h_2(N_1)$.

Using the developed approach for stress analysis, the following advantages can be obtained:
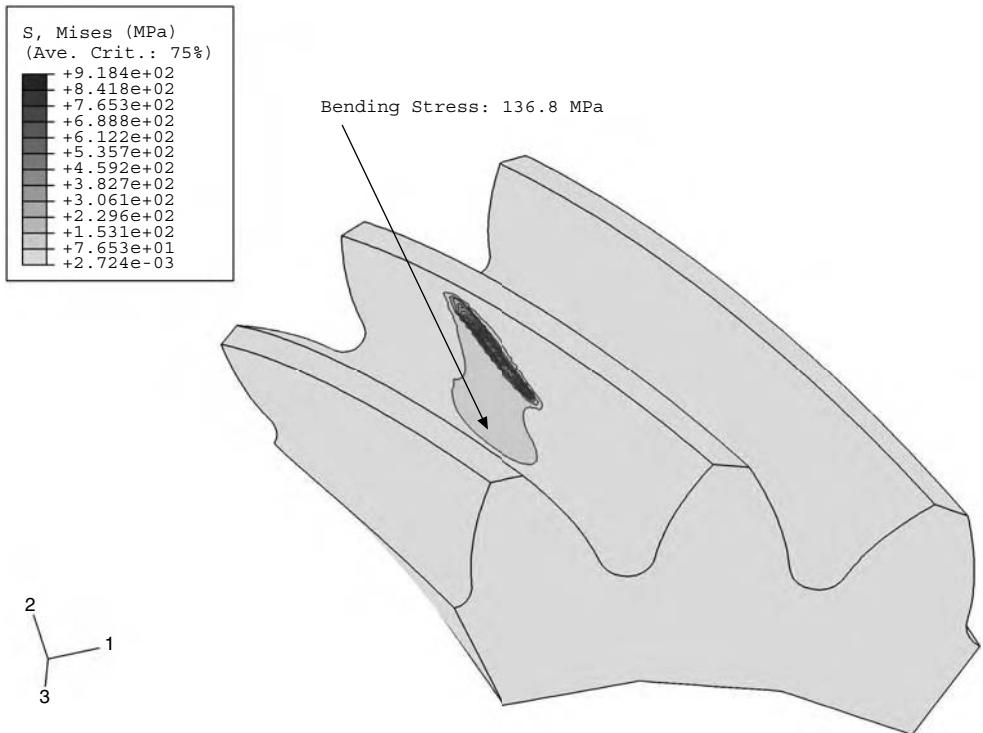
- Finite element models of the gear drive can be automatically obtained for any position of pinion and gear obtained from TCA. Stress convergence is assured because there is at least one point of contact between the contacting surfaces.
- Assumption of load distribution in the contact area is not required because the contact algorithm of the general computer program [Hibbit, Karlsson & Sirensen, Inc., 1998] is used to get the contact area and stresses by application of torque to the pinion while the gear is considered at rest.
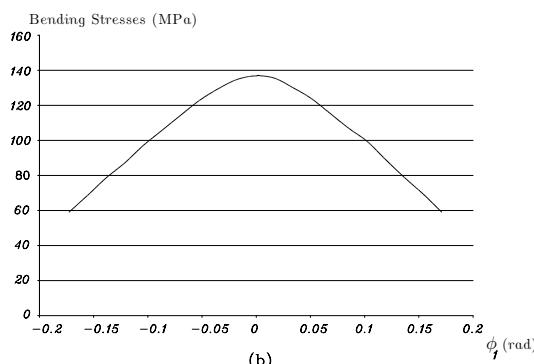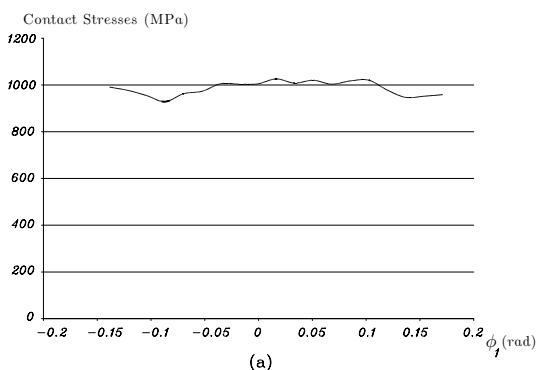
Figure 15.9.1: Whole gear drive finite element model.
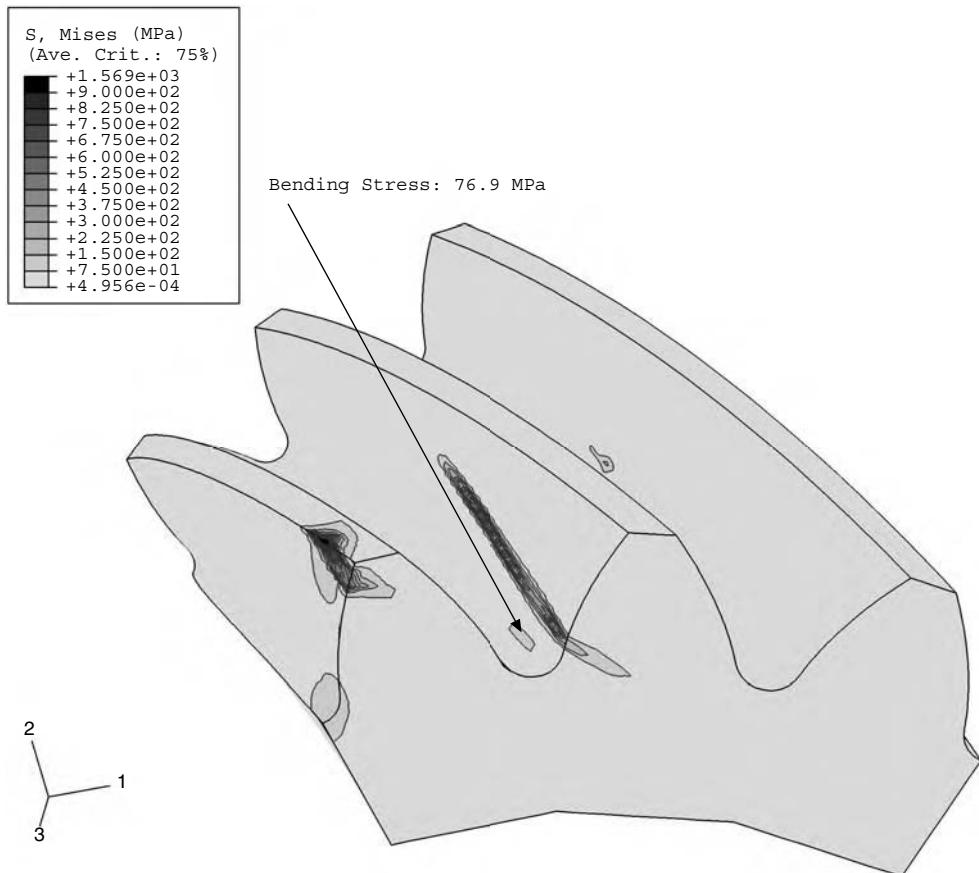
Figure 15.9.2: Contacting model of five pairs of teeth derived for stress analysis.

Figure 15.9.3: Contact and bending stresses in the middle point of the path of contact on the pinion tooth surface for a modified involute helical gear drive wherein the generation is performed by plunging of the grinding worm.

Figure 15.9.4: Contact and bending stresses during the cycle of meshing of the pinion.

```
S, Mises (MPa)
(Ave. Crit.: 75%)
   +1.569e+03
   +9.000e+02
   +8.250e+02
   +7.500e+02
   +6.750e+02
   +6.000e+02
   +5.250e+02
   +4.500e+02
   +3.750e+02
   +3.000e+02
   +2.250e+02
   +1.500e+02
   +7.500e+01
   +4.956e-04
```

Bending Stress: 76.9 MPa

Figure 15.9.5: Contact and bending stresses in the middle point of the path of contact on a conventional involute helical pinion with error $\Delta\gamma = 3$ arcmin: edge contact with high stresses occurs.
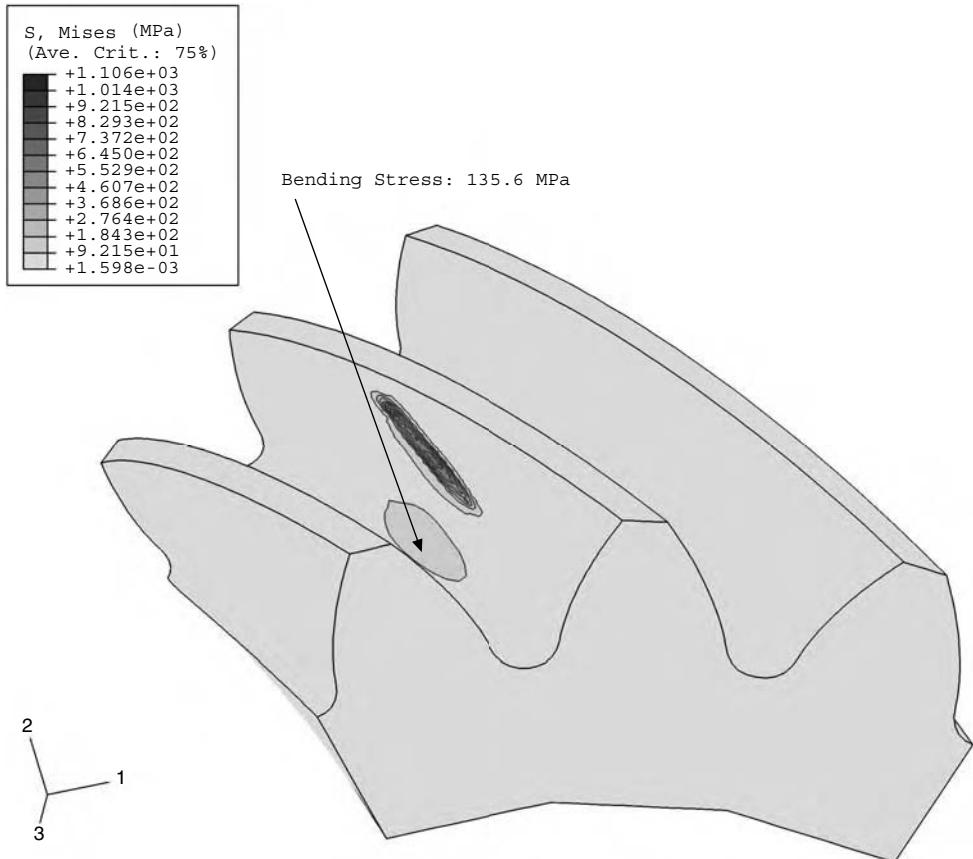
- Finite element models of any number of teeth can be obtained. As an example, Fig. 15.9.1 shows a whole gear drive finite element model. However, such a model is not recommended if an exact definition of the contact ellipse is required. Three- or five-tooth models are more adequate in such a case. Figure 15.9.2 shows a contacting model of five pairs of teeth derived for stress analysis.

The use of several teeth in the models has the following advantages:

 (i) Boundary conditions are far enough from the loaded areas of the teeth.
(ii) Simultaneous meshing of two pairs of teeth can occur due to the elasticity of surfaces. Therefore, the load transition at the beginning and at the end of the path of contact can be studied.

Numerical Example
Stress analysis has been performed for the gear drive with the design parameters shown in Table 15.7.1. A finite element model of three pairs of contacting teeth has been applied for each chosen point of the path of contact. Elements C3D8I [Hibbit, Karlsson & Sirensen, Inc., 1998] of first order (enhanced by incompatible modes to improve their

Figure 15.9.6: Contact and bending stresses in the middle point of the path of contact on the pinion tooth surface for a modified involute helical gear drive wherein an error $\Delta\gamma = 3$ arcmin is considered: edge contact is avoided.

bending behavior) have been used to form the finite element mesh. The total number of elements is 45,600 with 55,818 nodes. The material is steel with the properties of Young's Modulus $E = 2.068 \times 10^5$ MPa and Poisson's ratio of 0.29. A torque of 500 Nm has been applied to the pinion. Figure 15.9.3 shows the contact and bending stresses obtained at the mean contact point for the pinion.

The variation of contact and bending stresses along the path of contact has been also studied. Figure 15.9.4 illustrates the variation of contact and bending stresses for the pinion. Stress analysis has also been performed for a conventional helical involute drive with an error of the shaft angle of $\Delta\gamma = 3$ arcmin (Fig. 15.9.5). Recall that the tooth surfaces of an aligned conventional helical gear drive are in line contact, but they are in point contact with error $\Delta\gamma$. The results of computation show that error $\Delta\gamma$ causes an edge contact and an area of severe contact stresses.

Figure 15.9.6 shows the results of finite element analysis for the pinion of a modified involute helical gear drive wherein an error $\Delta\gamma = 3$ arcmin occurs. As shown in Fig. 15.9.6, a helical gear drive with modified geometry is indeed free of edge contact and areas of severe contact stresses.

16 Involute Helical Gears with Crossed Axes

16.1 INTRODUCTION

Involute helical gears are widely applied in the industry for transformation of rotation between parallel and crossed axes. Figure 16.1.1 shows an involute helical gear drive with crossed axes in 3D-space. A gear drive formed by a helical gear and a worm gear is a particular case of a gear drive with crossed axes (Figure 16.1.2). Gear tooth surfaces are in line contact for involute helical gear drives with parallel axes and in point contact for involute helical gear drives with crossed axes.

The theory of involute gears and research in this area have been presented by Litvin [1968], Colbourne [1987], Townsend [1991], and Litvin *et al.* [1999, 2001a, 2001c, 2001d] and the theory of shaving and honing technological processes are discussed in the works of Townsend [1991] and Litvin *et al.* [2001a]. Despite the broad investigation that has been accomplished in this area, the quality of misaligned involute helical gear drives is still a concern of manufacturers and designers. The main defects of such misaligned gear drives are (i) appearance of edge contact, (ii) high levels of vibration, and (iii) the shift of the bearing contact far from the central location.

To overcome the defects mentioned above, some corrections of gear geometry have been applied in the past: (i) correction of the lead angle of the pinion (requires regrinding), and (ii) crowning in the areas of the tip of the profile and the edge of the teeth (based on the experience of manufacturers). A more general approach for localization of bearing contact has been proposed in Litvin *et al.* [2001c].

The conditions of meshing of crossed involute gears are represented in this chapter as follows:
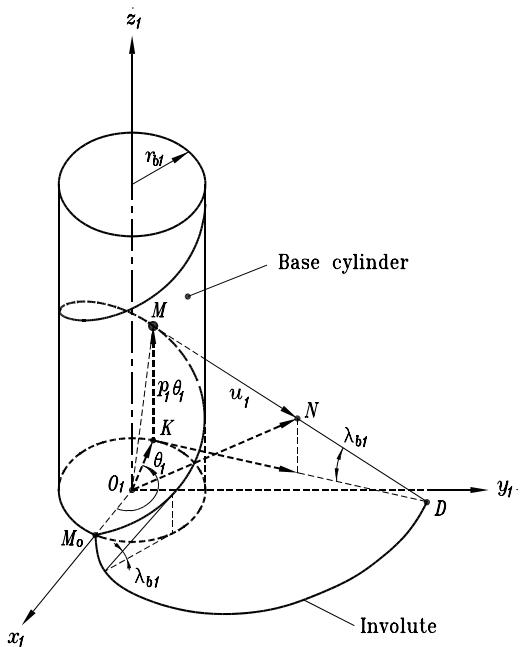
(1) It is shown that a special design (called the canonical one) provides a central location of bearing contact.
(2) Modification of the representation of lines of action (as the sets of contact points) allows the following:
  (i) representation of an edge contact as the result of the shift of lines of action in a misaligned gear drive
 (ii) relation of the sensitivity to an edge contact with the nominal value of the crossing angle.

Figure 16.1.1: Involute helical gears with crossed axes in 3D-space.

Figure 16.1.2: Gear drive formed by a worm and a helical gear.

Figure 16.2.1: Illustration of generation of a screw involute surface.

Algorithms for simulation of meshing (including simulation of edge contact) are represented. The theory is supported by numerical examples.
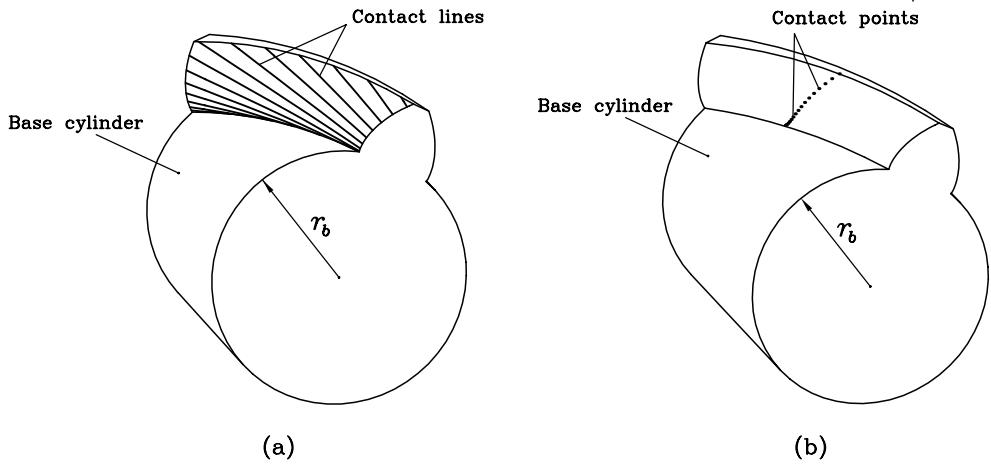
16.2 ANALYSIS AND SIMULATION OF MESHING OF HELICAL GEARS

Conceptual Considerations

It is well known [Litvin, 1968, 1989] that a screw involute surface can be generated by a screw motion of a straight line $\overline{MD}$ (Fig. 16.2.1), while in the process of motion the generating line keeps its orientation as the tangent to the helix on the base cylinder. The generated surface is a *developed* one [Litvin, 1968, 1989; Zalgaller, 1975], and the normals to the surface along $\overline{MD}$ are collinear. Figure 16.2.2(a) shows that the generated surface is formed as a family of straight lines that are tangent to the helix on the base cylinder. Tooth surfaces of mating helical gears (in an aligned gear drive with parallel axes) contact each other along the straight lines $\overline{MD}$ mentioned above.

Assume now that, using coordinate transformation, the lines of contact are represented in plane Π that is tangent to both base cylinders of the helical gears with parallel axes. Figure 16.2.3 shows plane Π that is tangent to the base cylinder of the pinion. Angle α_{ot1} is the pressure angle in the transverse section. Points O_1 and O_2 represent the centers of base circles of mating helical gears.
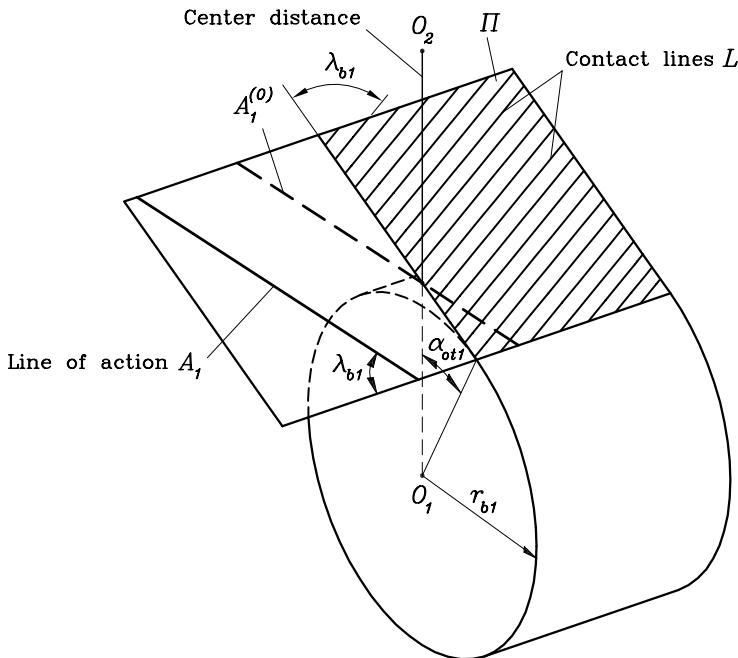
Using coordinate transformation, we represent in plane Π lines of contact of helical gears with parallel axes. The lines of contact L represented in plane Π (Fig. 16.2.3) are *parallel* straight lines. Plane Π of a gear drive with parallel axes is the *plane of action* in the fixed coordinate system rigidly connected to the housing of the gear drive.
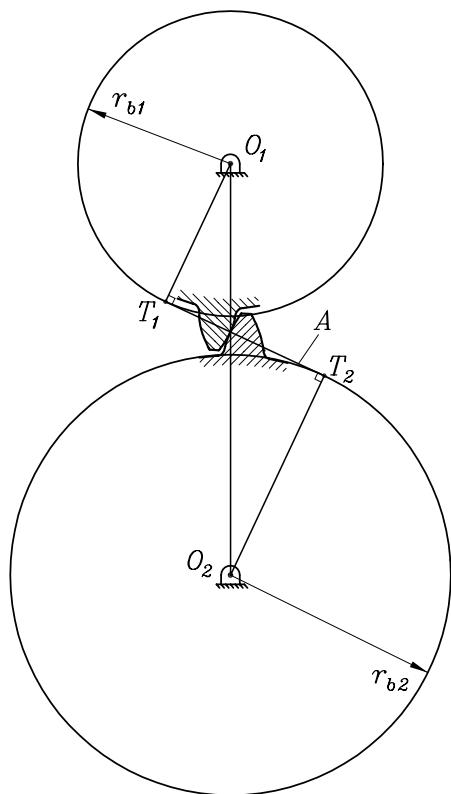
Figure 16.2.2: Types of contact of helical gears: (a) line contact in a gear drive with parallel axes, (b) point contact of crossed helical gears.

We emphasize the special features of the contact lines L:

(1)   We recall that Fig. 16.2.1 shows that the screw involute surface is generated by the screw motion of line $\overline{MD}$. The normals to the screw involute surface (at the instant position of $\overline{MD}$) are collinear and their orientation does not depend on the parameter of location of the point on $\overline{MD}$. We may consider that locally $\overline{MD}$ is a small strip of the screw involute surface with collinear normals.

Figure 16.2.3: Illustration of contact lines on plane of action Π.
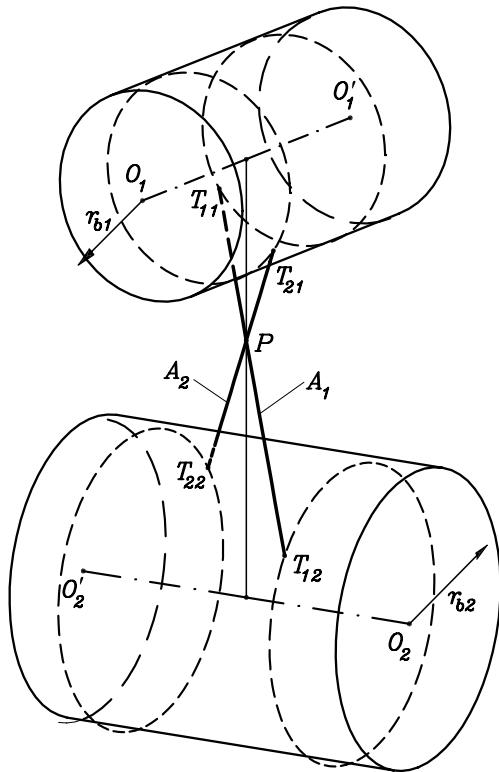
Figure 16.2.4: Line *A* of action of involute planar gearing.

(2) The normal to the screw involute surface at any contact point is *orthogonal* to the contact line. Therefore, the normals to the tooth surface are also orthogonal to contact lines represented on plane Π.

(3) The normals to the screw involute surface have the same constant orientation in the plane of action Π.

Figure 16.2.4 illustrates a planar involute gearing. Line T_1–T_2 is tangent to the base circles with radii r_{b1} and r_{b2}. Simultaneously, line T_1–T_2 is the common normal to the meshing involute profiles.

We may extend the conceptual considerations of meshing of a planar involute gearing to the case of crossed involute helical gears. The gear tooth surfaces of crossed helical gears contact each other at a point [Fig. 16.2.2(b)], but not at a line as in the case of helical gears with parallel axes [Fig. 16.2.2(a)]. Figure 16.2.5 shows the base cylinders of crossed helical gears. It is obvious that the crossed base cylinders of the gears may have a common tangent line but not a common tangent plane. There are two lines A_1 and A_2 that are tangent to the base cylinders and to the base helices at the same time. We may call A_1 and A_2 the *lines of action* of crossed helical gears. Lines A_1 and A_2 correspond to the meshing of the respective sides of the tooth surface.

It is shown below (see Appendices 16.A and 16.B) that the design of crossed helical gears may be accomplished by observation of a special relation between the shortest
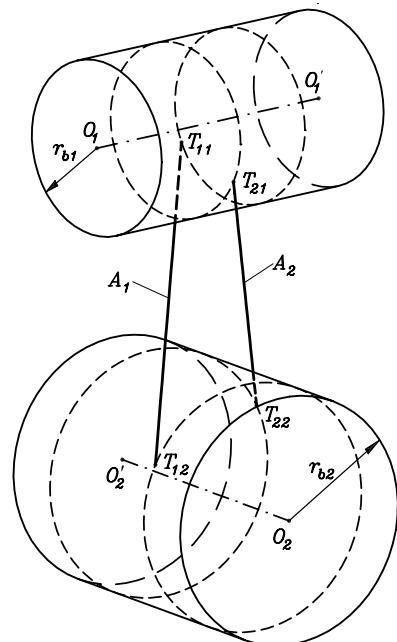
Figure 16.2.5: Lines of action of aligned crossed helical gears.

center distance of the gears and the crossing angle. Such a design provides that the lines of action intersect each other at a point that belongs to the shortest center distance. This design is called *canonical*.
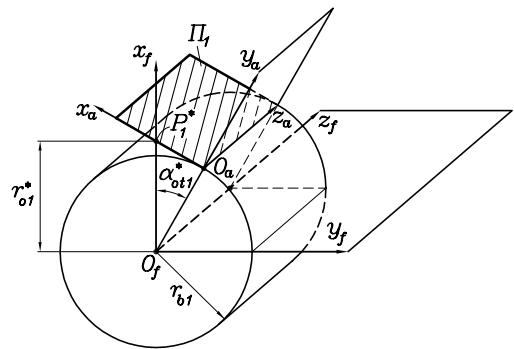
Figure 16.2.6 shows the lines of action for which the rules of canonical design are not observed, and the lines of action A_1 and A_2 are crossed but do not intersect each other. Each line A_i is still a tangent to both base cylinders and base helices of the crossed helical gears. The crossing of lines of action A_1 and A_2 is the result of an error $\Delta\gamma$ of the *nominal* value of the shaft angle γ_o of the gears or the result of an error ΔE of center distance (see below).

Analytical Determination of Line of Action
of Crossed Helical Gears
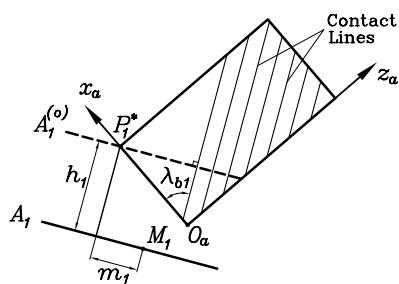
Analytical determination of the line of action of misaligned crossed helical gears is important for detection of edge contact. Edge contact occurs when the line of action is shifted from the theoretical position and is located outside of the face width (Figs. 16.2.7 and 16.2.8). The derivations that are represented as follows open the way for analytical determination of the appearance of edge contact. We have represented intersected and crossed lines of action of crossed helical gears in Figs. 16.2.5 and 16.2.6, respectively. In addition to this presentation, it is important to represent the lines of action in the *plane* that is tangent to the base cylinder of one of the crossed helical gears, say the
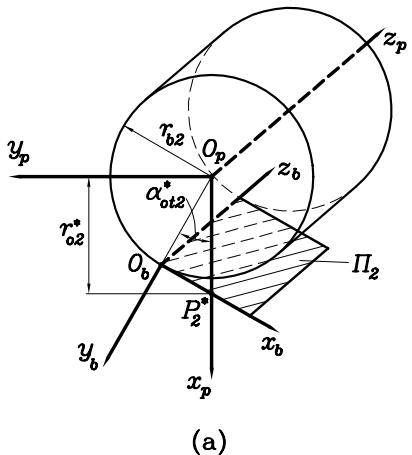
Figure 16.2.6: Lines of action in gear drive with error $\Delta\gamma$ of shaft angle.


Figure 16.2.7: Illustration of (a) plane Π_1 and contact lines on Π_1, and (b) line of action A_1 and parameters h_1 and m_1.

(a)
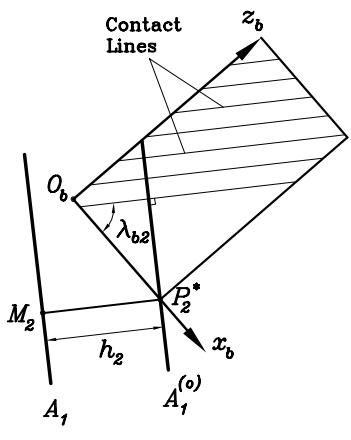
(b)

(a)

Figure 16.2.8: Illustration of (a) plane Π_2 and contact lines on Π_2, and (b) line of action A_1 and parameter h_2.

(b)

pinion. Determination of a line of action, say A_1, in plane Π (Fig. 16.2.3), requires the orientation and location.

The orientation of A_1 is determined easily as the one orthogonal to the lines of contact L. The orientation of lines of action is determined by the lead angle λ_{b1} of the pinion (Fig. 16.2.3). The *location* of A_1 in plane Π is determined below. Errors of alignment (change of shaft angle and shortest center distance) cause the shift of lines of action that might be accompanied by edge contact. The procedure for computation of the location of the lines of action is as follows.

Case 1: Error $\Delta\gamma$ of the Crossing Angle (Shaft Angle)

The input parameters of the computations are the radii of base cylinders r_{b1} and r_{b2}, the lead angles λ_{b1} and λ_{b2} on the base cylinders, the nominal value γ_o of the crossing angle, and the error $\Delta\gamma$ of the crossing angle.

Step 1: The pressure angle α_{on}^* in the normal section of rack-cutters (see Appendix 16.B) is determined as

$$\cos^2 \alpha_{on}^* = \frac{\cos^2 \lambda_{b1} \pm 2 \cos \lambda_{b1} \cos \lambda_{b2} \cos \gamma_o^* + \cos^2 \lambda_{b2}}{\sin^2 \gamma_o^*}. \tag{16.2.1}$$

Here and below, the superscript "*" indicates that a parameter of a misaligned gear drive is considered. The upper and lower signs in Eq. (16.2.1) correspond to helical gears with the *same* and *opposite* directions of helices.

Step 2: The pressure angle α_{oti}^* $(i = 1, 2)$ in the cross section of the pinion or the gear is determined as

$$\sin \alpha_{oti}^* = \frac{\sin \alpha_{on}^*}{\sin \lambda_{bi}} \quad (i = 1, 2). \tag{16.2.2}$$

Step 3: Radii r_{oi}^* indicate the operating pitch cylinders of helical gears used for generation of helical gears by rack-cutters and are determined as follows:

(i) The operating pitch cylinder of a helical gear is the axode in meshing with the generating rack-cutter (see Section 16.4). Figure 16.4.2 shows pitch cylinders of standard helical gears generated by rack-cutters.

(ii) The sum of radii r_{oi}^* $(i = 1, 2)$ of a misaligned gear drive with crossing angle γ_o^* differs from the nominal value of center distance $E_o = r_{o1} + r_{o2}$.

(iii) Radii r_{oi}^* are determined as

$$r_{oi}^* = \frac{r_{bi}}{\cos \alpha_{oti}^*} \quad (i = 1, 2). \tag{16.2.3}$$

Step 4: Determination of parameters h_1 and h_2 of the shift of the line of action. Parameter h_i $(i = 1, 2)$ is drawn perpendicular to the shifted line of action from point P_i^* $(i = 1, 2)$. Point P_i^* is the point of intersection of a cylinder of radius r_{oti}^* with the line of center distance.

Parameters h_1 and h_2 are determined from the equations (see below)

$$h_1 = \frac{r_{b2} + r_{b1} \dfrac{\cos \alpha_{ot2}^*}{\cos \alpha_{ot1}^*} - E_o \cos \alpha_{ot2}^*}{\sin \alpha_{ot2}^* \sin \gamma_o^*} \sin \lambda_{b1} \tag{16.2.4}$$

$$h_2 = \frac{A}{B} \tag{16.2.5}$$
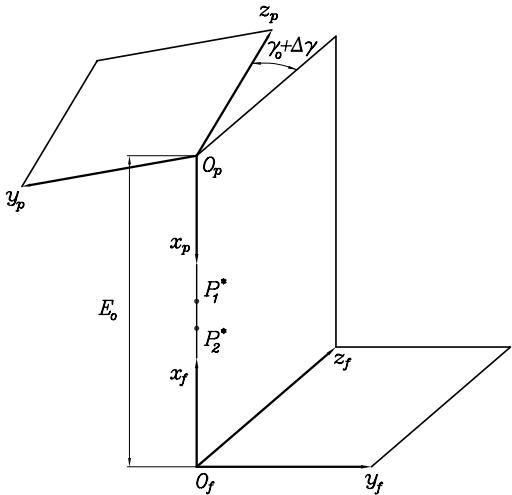
where

$$A = r_{b1} + r_{b2} \frac{\cos \alpha_{ot1}^*}{\cos \alpha_{ot2}^*} - E_o \cos \alpha_{ot1}^* \tag{16.2.6}$$

$$B = \sin \lambda_{b2} \sin \alpha_{ot1} \sin \gamma_o^* + \cos \lambda_{b2}(\cos \alpha_{ot1}^* \sin \alpha_{ot2}^* - \cos \alpha_{ot2}^* \sin \alpha_{ot1}^* \cos \gamma_o^*). \tag{16.2.7}$$

The derivation of equations above is based on the following considerations:

(1) Figure 16.2.7 shows coordinate systems S_f and S_a that are rigidly connected to the pinion. Plane Π_1 [Fig. 16.2.7(a)] is tangent to the base cylinder of radius r_{b1}.

Figure 16.2.9: Fixed coordinate systems S_f and S_p.

Contact lines between pinion tooth surface Σ_1 and generating rack-cutter surface Σ_{r1} are represented in plane Π_1 as parallel straight lines. The orientation of contact lines is determined by angle λ_{b1} [Fig. 16.2.7(b)].

(2) The line of action A_1 of a misaligned gear drive is shifted with respect to the line of action $A_1^{(o)}$ of an aligned gear drive. The shift is designated by h_1. The location of point M_1 on line A_1 is denoted by parameter m_1 [Fig. 16.2.7(b)].

(3) Figure 16.2.8 shows coordinate systems S_b and S_p that are rigidly connected to gear 2. Plane Π_2 is tangent to the base cylinder of radius r_{b2}. Lines of contact between the gear tooth surface Σ_2 and the generating rack-cutter surface Σ_{r2} are represented in plane Π_2. The orientation of such lines of contact is determined by angle λ_{b2}.

   Line of action A_1 is represented as a shifted one. The orientation of A_1 in plane Π_2 [Fig. 16.2.8(b)] is determined to be orthogonal to the lines of contact, and its location in plane Π_2 is represented by parameter h_2. Parameter h_2 has to be determined by a computational procedure (see below).

(4) Figure 16.2.9 shows the location and orientation of coordinate systems S_p and S_f. The computational procedure for determination of parameters h_1 and h_2 of the shift of lines of action in planes Π_1 and Π_2 is based on the following considerations:

   (i) Figure 16.2.7 represents point M_1 of the line of action (located in plane Π) by position vector

$$\mathbf{r}_f^{(1)}(h_1, m_1, r_{b1}, \lambda_{b1}, \alpha_{ot1}^*) \tag{16.2.8}$$

   where h_1 and m_1 are the parameters to be determined.

   (ii) Using coordinate transformation from S_b via S_p to S_f we may represent the position vector of point M_2 of the line of action (located in plane Π_2) as

$$\mathbf{r}_f^{(2)}(h_2, r_{b2}, \lambda_{b2}, \alpha_{ot2}^*, \gamma_o^*, E_o). \tag{16.2.9}$$

(iii) Taking into account that points M_1 and M_2 belong to the same line of action, vector equation $\mathbf{r}_f^{(1)}(M_1) = \mathbf{r}_f^{(2)}(M_2)$ yields a system of three linear equations for determination of h_1 and h_2 and the auxiliary parameter m_1.

Parameters h_1 and h_2 determine the shifts of the line of action in planes Π_1 and Π_2 by Eqs. (16.2.4) and (16.2.5), respectively.

The axial displacements of the line of action with respect to the pinion and the gear are determined as follows:

$$\Delta Z_1 = \frac{h_1}{\sin \lambda_{b1}} \tag{16.2.10}$$

$$\Delta Z_2 = \frac{h_2}{\sin \lambda_{b2}}. \tag{16.2.11}$$

Case 2: Error ΔE of the Center Distance
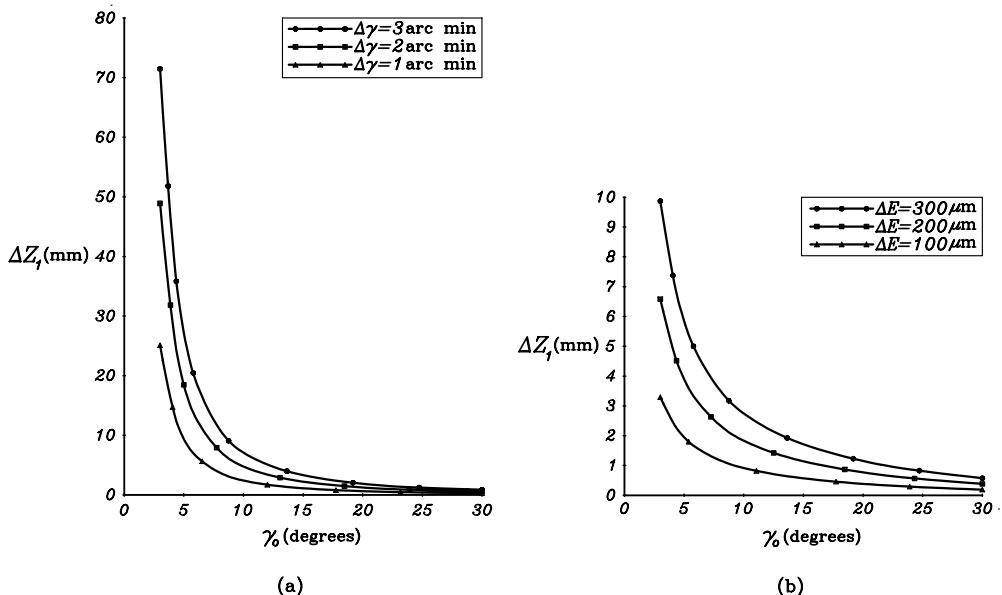
The determination of the shift of the line of action caused by error ΔE is based on a similar procedure discussed above, taking into account the following considerations:

(i) $\Delta \gamma = 0$ and therefore $\alpha_{on}^* = \alpha_{on}$, $\alpha_{oti}^* = \alpha_{oti}$ $(i = 1, 2)$.

(ii) However, the center distance due to error ΔE is represented as

$$E^* = E_o + \Delta E. \tag{16.2.12}$$

(iii) Then, the computational procedure enables us to obtain the shifts $h_1(\Delta E)$ and $h_2(\Delta E)$ caused by ΔE, and the corresponding axial displacements ΔZ_1 and ΔZ_2.

The shifts of the line of action in plane Π_1 caused by errors $\Delta \gamma$ and ΔE are represented in Figs. 16.2.10(a) and 16.2.10(b) by functions $\Delta Z_1(\Delta \gamma, \gamma_o)$ and $\Delta Z_1(\Delta E, \gamma_o)$,


(a)   (b)

Figure 16.2.10: Illustration of variation of the shift ΔZ_1 of the line of action due to errors (a) $\Delta \gamma$ and (b) ΔE.

respectively. Here, γ_o is the nominal crossing angle. In both cases, the sensitivity of the shift becomes very high for a nominal crossing angle γ_o of small value. In this case, edge contact is inevitable due to the large shift ΔZ_1 that requires unreasonable axial dimensions of the gears. The reduction of shift ΔZ_1 may be obtained (i) by changing the lead angle λ_{bi} and regrinding one of the gears, and (ii) by modification of the tooth surface geometry [Litvin *et al.*, 2001c].

16.3 SIMULATION OF MESHING OF CROSSED HELICAL GEARS

The algorithm for simulation of meshing and contact of cross helical gears is based on simulation of continuous tangency of gear tooth surfaces (see Section 9.4). The equations of tooth surfaces Σ_1 and Σ_2 of the gears and the unit normals are considered in a fixed coordinate system S_f rigidly connected to the housing. The conditions of continuous tangency are represented as follows:

$$\mathbf{r}_f^{(1)}(u_1, \psi_1, \phi_1) - \mathbf{r}_f^{(2)}(u_2, \psi_2, \phi_2) = 0 \qquad (16.3.1)$$

$$\mathbf{n}_f^{(1)}(\psi_1, \phi_1) - \mathbf{n}_f^{(2)}(\psi_2, \phi_2) = 0. \qquad (16.3.2)$$

Here, (u_i, ψ_i) $(i = 1, 2)$ are the surface parameters, ϕ_i are the angles of gear rotation, and $\mathbf{r}_f^{(i)}$ is the position vector of surface Σ_i. Vector equations (16.3.1) and (16.3.2) yield a system of five independent nonlinear equations in six unknowns taking into account that $|\mathbf{n}_f^{(1)}| = |\mathbf{n}_f^{(2)}| = 0$. One of the parameters, say ϕ_1, is chosen as the input one, and the solution of the five nonlinear equations is an iterative process.

The solution of five nonlinear equations discussed above is based on application of the theorem of implicit function system existence [Korn & Korn, 1968] and is represented by functions

$$\{u_1(\phi_1), \psi_1(\phi_1), u_2(\phi_1), \psi_2(\phi_1), \phi_2(\phi_1)\} \in C^1 \qquad (16.3.3)$$

that allow us to obtain the path of contact on the gear tooth surface and the transmission function $\phi_2(\phi_1)$. The deviations of $\phi_2(\phi_1)$ from the theoretical value represent the transmission errors

$$\Delta\phi_2(\phi_1) = \phi_2(\phi_1) - \frac{N_1}{N_2}\phi_1. \qquad (16.3.4)$$

The Jacobian of the system of equations provided by vector equations (16.3.1) and (16.3.2) has to differ from zero, and this is the sign that surfaces Σ_1 and Σ_2 are in point contact but not in line contact.

It was mentioned above that the existence of an edge contact of tooth surfaces Σ_1 and Σ_2 (instead of surface-to-surface contact) in misaligned gear drives is not excluded. In the case of edge contact, we have surface-to-curve meshing, and the algorithm for

simulation of meshing is determined as follows:
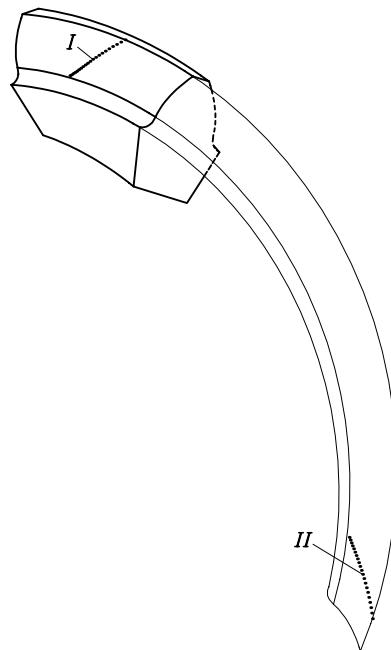
$$\mathbf{r}_f^{(1)}(u_1(\psi_1), \psi_1, \phi_1) - \mathbf{r}_f^{(2)}(u_2, \psi_2, \phi_2) = 0 \qquad (16.3.5)$$
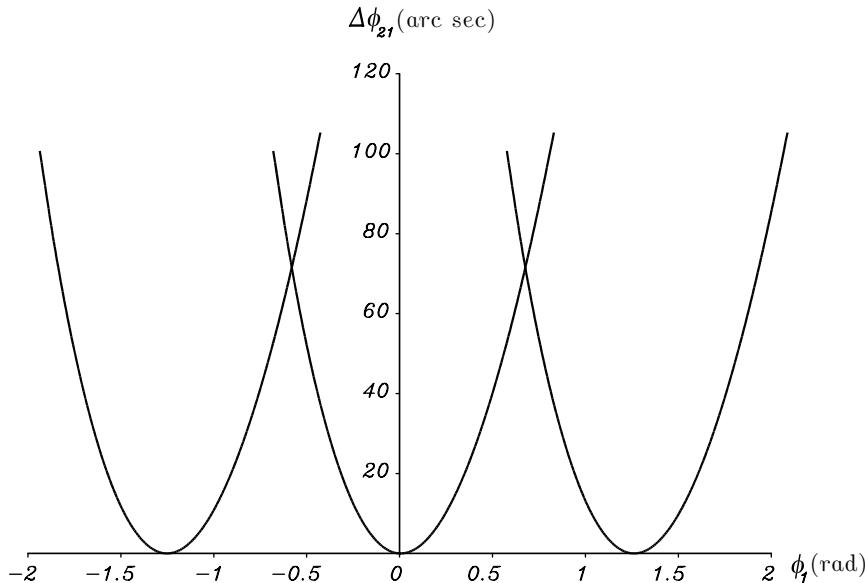
$$\frac{\partial \mathbf{r}_f^{(1)}}{\partial \psi_1} \cdot \mathbf{n}_f^{(2)} = 0. \qquad (16.3.6)$$

Here, $\mathbf{r}_f^{(1)}(u_1(\psi_1), \psi_1, \phi_1)$ represents at $\phi_1 = const$ the instantaneous position of the edge of the pinion tooth surface that is in mesh with the surface of gear 2; $\mathbf{r}_f^{(2)}(u_2, \psi_2, \phi_2)$ represents at $\phi_2 = const$ the instantaneous position of the gear tooth surface. Vector $\partial \mathbf{r}_f^{(1)} / \partial \psi_1$ represents the tangent to the edge of the pinion. Observation of Eqs. (16.3.5) and (16.3.6) means that the normal to surface Σ_2 is perpendicular to the edge of the pinion tooth surface and the pinion edge and surface Σ_2 are indeed in mesh. Similar equations can be applied wherein the surface of the pinion is in mesh with the edge of the gear tooth surface. Application of the developed computer program for TCA (Tooth Contact Analysis) shows (i) the change of shortest center distance and crossing angle do not cause transmission errors; and (ii) however, errors $\Delta \gamma$ and ΔE cause the shift of bearing contact from the working area.

Figure 16.3.1 illustrates the shift of bearing contact on the pinion tooth surfaces from position I to position II due to error $\Delta \gamma$ obtained for a crossed helical gear drive. The results obtained by numerical simulation are in agreement with the results obtained by application of the equations of the line of action.


Figure 16.3.1: Illustration of zones of contact on tooth surface of aligned and misaligned gear drives: *I* and *II* are zones of contact that correspond to $\Delta \gamma = 0$ and $\Delta \gamma \neq 0$, respectively.

Figure 16.3.2: Function of transmission errors in a gear drive formed by an Archimedes worm and an involute helical gear.

Numerical Example: Worm-Gear Drive

Conjugation of tooth surfaces and zero transmission error are provided in a gear drive formed by an involute worm and an involute helical gear. Application of a worm whose thread surface differs from an involute screw one is accompanied with transmission errors as shown in Fig. 16.3.2. The design parameters of the gear drive are represented in Table 16.3.1. The output of the developed TCA computer program (Fig. 16.3.2) shows that meshing of an Archimedes worm with a helical involute gear is accompanied with large transmission errors, and the function of transmission errors is *positive* instead of negative. Only a negative function of transmission errors wherein the driven gear is lagging with respect to the worm gear should be applied in a misaligned gear drive. Then the contact ratio of the gear drive might be increased due to the elastic deformations of the driven gear of the drive. The obtained results of simulation of meshing show that meshing of an involute helical gear with a worm that differs from an involute one should not be applied in the design.

Table 16.3.1: Design parameters of a worm and an involute helical gear
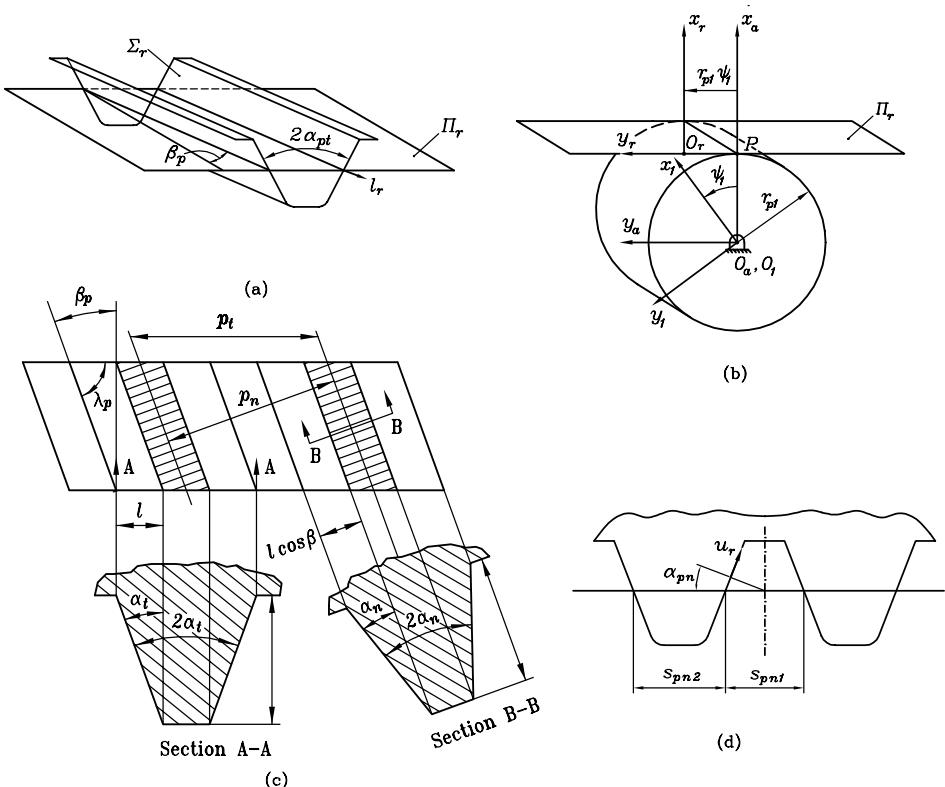
Number of threads of the worm, N_1	5
Number of teeth of the gear, N_2	48
Normal module, m_{pn}	4.0 mm
Normal pressure angle, α_{pn}	25°
Helix angle of the worm, β_{p1}	70°
Helix angle of the gear, β_{p2}	20°
Worm face width, F_1	70 mm
Gear face width, F_2	30 mm

16.4 GENERATION OF CONJUGATED TOOTH SURFACES OF CROSSED HELICAL GEARS

Generation of a Helical Gear

A helical gear can be generated by a hob or by a shaper. Consideration of generation of a helical gear by a rack-cutter is useful for considering conceptual aspects of gear generation. Figure 16.4.1 shows a skew rack-cutter. The generating surface Σ_r is a plane [Fig. 16.4.1(a)]. The normal and transverse sections of the rack-cutter are shown in Fig. 16.4.1(c). Angles $2\alpha_{pt}$ and $2\alpha_{pn}$ are the profile angles in the transverse and normal sections, respectively. The relations between parameters $2\alpha_{pt}$ and $2\alpha_{pn}$ are presented in Appendix 16.C and 16.E. The surface parameters of the rack-cutter are denoted as u_r [Fig. 16.4.1(d)] and l_r [Fig. 16.4.1(a)]. Figure 16.4.1(d) shows the normal section where α_{pn} is the normal pressure angle, and s_{pn1} and s_{pn2} represent the tooth thickness and the space width on the normal section, respectively.

Coordinate systems S_r and S_1 are rigidly connected to the rack-cutter and the pinion 1 [Fig. 16.4.1(b)]. In the process for generation, the pinion and the rack-cutter perform

Figure 16.4.1: Schematic illustration of (a) skew rack-cutter, (b) generation by rack-cutter of a helical gear, (c) transverse and normal sections of rack-cutter, and (d) relation of s_{pn1} and s_{pn2} in normal section.

related rotation and translation [Fig. 16.4.1(b)]. Plane Π_r of the rack-cutter and the pinion cylinder of radius r_{p1} are *axodes* that roll over each other in relative motion.

Consider that generating plane Σ_r is given and determination of the surface Σ_1 of the pinion as the envelope to Σ_r is required. The determination of Σ_1 is based on the equations

$$\mathbf{r}_1(u_r, l_r, \psi_1) = \mathbf{M}_{1r}(\psi_1)\mathbf{r}_r(u_r, l_r) \tag{16.4.1}$$

$$f_1(u_r, l_r, \psi_1) = 0 \tag{16.4.2}$$

where ψ_1 is the generalized parameter of motion in meshing of the rack-cutter with the helical gear. Vector function $\mathbf{r}_1(u_r, l_r, \psi_1)$ represents the family of rack-cutter surfaces in coordinate system S_1. Equation of meshing (16.4.2) may be determined by one of the following alternative approaches (see Chapter 6):

$$\left(\frac{\partial \mathbf{r}_1}{\partial u_r} \times \frac{\partial \mathbf{r}_1}{\partial l_r}\right) \cdot \frac{\partial \mathbf{r}_1}{\partial \psi_1} = 0 \tag{16.4.3}$$

or

$$\mathbf{N}_r \cdot \mathbf{v}_r^{(r\,1)} = 0 \tag{16.4.4}$$

where $\mathbf{N}_r$ is the normal to the rack-cutter generating plane and $\mathbf{v}_r^{(r\,1)}$ is the relative (sliding) velocity of the rack-cutter with respect to the pinion. Vectors $\mathbf{N}_r$ and $\mathbf{v}_r^{(r\,1)}$ are represented in coordinate system Σ_r (for the purpose of simplification of derivations).

Equations (16.4.1) and (16.4.2) considered simultaneously represent the pinion tooth surface by three related parameters. Taking into account that u_r and l_r are linear parameters, it is easy to eliminate one of them and represent surface Σ_i in two-parameter form, for instance, as $\mathbf{r}_1(\psi_1, u_r)$. The generated pinion tooth surface Σ_1 is a screw involute one. Such a surface may be represented as the one generated by a straight line $\overline{MD}$ performing a screw motion; line $\overline{MD}$ is shown in Fig. 16.2.1 (see Section 16.2).

The lines of contact of rack-cutter surfaces Σ_r and Σ_1 may be represented in various coordinate systems, for instance in coordinate system S_r. Such lines of contact (considering simultaneously vector function $\mathbf{r}_r(u_r, l_r)$ and equation of meshing (16.4.2)) are represented in S_r by the vector function

$$\mathbf{r}_r(u_r(\psi_1), l_r(\psi_1)). \tag{16.4.5}$$
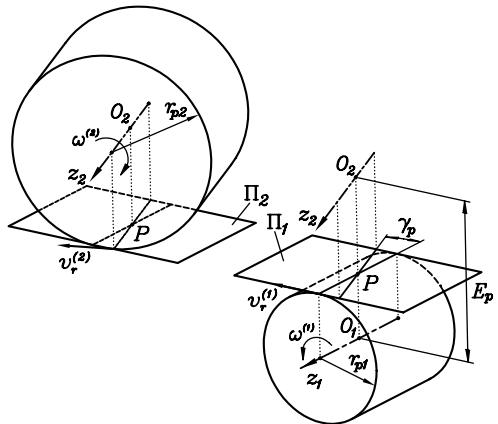
It is useful for conceptual purposes to represent the lines of contact L_{r1} in coordinate system S_q that is rigidly connected to a plane that is tangent to the base cylinder of pinion 1. Then we obtain the family of contact lines as

$$\mathbf{r}_q(\psi_1) = \mathbf{M}_{qa}\mathbf{M}_{ar}\mathbf{r}_r(u_r(\psi_1), l_r(\psi_1)). \tag{16.4.6}$$

The lines of contact L_{r1} of Σ_r and Σ_1 are represented in S_q as a family of parallel straight lines. Such a family is similar to the family of lines of contact shown in Fig. 16.2.3.

Generation of Conjugated Crossed Helical Gears

Crossed helical gears perform rotation between crossed axes with a constant gear ratio. The idea of generation of conjugated surfaces of pinion 1 and gear 2 is based on

Figure 16.4.2: Schematic of generation of crossed helical gears.

application of *two* generating rack-cutters that are provided with two coinciding generating planes $\Sigma_r^{(1)}$ and $\Sigma_r^{(2)}$. However, planes $\Sigma_r^{(1)}$ and $\Sigma_r^{(2)}$ may slide over each other. Magnitudes s_{pn1} and s_{pn2} [Fig. 16.4.1(d)] represent in the normal section the tooth thicknesses of the rack-cutters applied for generation of the pinion and the gear. Parameters s_{pn1} and s_{pn2} are related as

$$s_{pn1} + s_{pn2} = \pi m_{pn} \tag{16.4.7}$$

where m_{pn} is the normal module.

The schematic of the generation of conjugated crossed helical gears is shown in Fig. 16.4.2. Axes z_1 and z_2 of pinion 1 and gear 2 are crossed and form angle γ_p. The shortest distance between the axes in the case of generation of standard gears is

$$E_p = r_{p1} + r_{p2} \tag{16.4.8}$$

where r_{pi} $(i = 1, 2)$ is the radius of the pitch cylinder.

During the process of generation of pinion 1, the pinion is rotated with angular velocity $\omega^{(1)}$ about z_1, and the rack-cutter $\Sigma_r^{(1)}$ is translated with velocity

$$\mathbf{v}_r^{(1)} = \boldsymbol{\omega}_1^{(1)} \times \overline{O_1 P}. \tag{16.4.9}$$

Similarly, gear 2 is rotated with angular velocity ω_2 and the rack-cutter $\Sigma_r^{(2)}$ is translated with velocity

$$\mathbf{v}_r^{(2)} = \boldsymbol{\omega}_1^{(2)} \times \overline{O_2 P}. \tag{16.4.10}$$

Here, $\overline{O_1 P}$ and $\overline{O_2 P}$ are the radii of the pitch cylinders of the pinion and the gear. Planes Π_1 and Π_2 are perpendicular to the center distance and pass through point P of the center distance. Skew rack-cutters $\Sigma_r^{(1)}$ and $\Sigma_r^{(2)}$ have coinciding generating planes that may *slide* over each other during the process of generation. Angular velocities $\omega^{(1)}$ and $\omega^{(2)}$ are related as $m_{12} = \omega^{(1)}/\omega^{(2)}$ where m_{12} is the gear ratio.

The represented process of generation enables us to obtain tooth surfaces Σ_1 and Σ_2 of the pinion and the gear that are in point contact at any instant but not in line contact.

Rack-cutter $\Sigma_r^{(1)}$ and pinion 1 tooth surface Σ_1 are in line tangency L_{1r}. Similarly, $\Sigma_r^{(2)}$ and Σ_2 are also in line contact L_{2r}. However, lines of contact L_{1r} and L_{2r} do not coincide and therefore the generated crossed helical gears are in point contact at every instant [Fig. 16.2.2(b)].
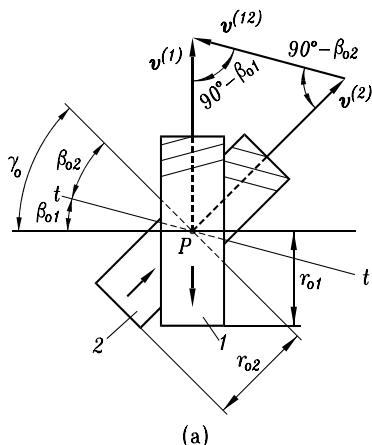
16.5 DESIGN OF CROSSED HELICAL GEARS

Direction of Helices
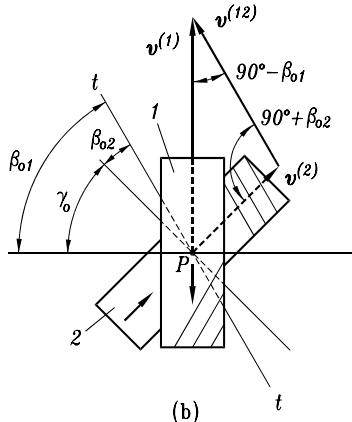
The mating helical gears may have helices either with the same or the opposite direction [Figs. 16.5.1(a) and 16.5.1(b)]. The helix angles β_{o1} and β_{o2}, if of opposite directions [Fig. 16.5.1(b)], are not equal as in the case of helical gears with parallel axes. The helix angles β_{o1} and β_{o2} and the crossing angle γ_o are related as

$$\gamma_o = |\beta_{o1} \pm \beta_{o2}| \tag{16.5.1}$$

where the upper and lower signs correspond to gears with the same [Fig. 16.5.1(a)] and opposite [Fig. 16.5.1(b)] direction of the helices.

Figure 16.5.1: Velocity polygons of crossed helical gears of (a) the same and (b) the opposite direction of the helices.

Gear Ratio

The derivation of gear ratio m_{12} is based on the velocity polygons of Fig. 16.5.1. The main idea of derivation is that the sliding velocity $\mathbf{v}^{(12)}$ at point P is directed along the common tangent t–t to the helices at point P of tangency of the pitch cylinders. Then we obtain that

$$m_{12} = \frac{\omega^{(1)}}{\omega^{(2)}} = \frac{r_{o2} \cos \beta_{o2}}{r_{o1} \cos \beta_{o1}} = \frac{r_{o2} \sin \lambda_{o2}}{r_{o1} \sin \lambda_{o1}}. \tag{16.5.2}$$

We emphasize that the change of the crossing angle and shortest center distance of crossed helical gears does not cause transmission errors. Therefore the gear ratio m_{12} may be expressed as

$$m_{12} = \frac{\omega^{(1)}}{\omega^{(2)}} = \frac{N_2}{N_1}. \tag{16.5.3}$$

However, errors of alignment mentioned above cause the shift of the bearing contact that may result in edge contact (see Section 16.2).

Standard and Nonstandard Gears

The generation of conjugated crossed helical gears is based on application of two skew rack-cutters with the same normal section (Fig. 16.4.1). In the case of standard gears, planes Π_1 and Π_2 are tangent to the respective pitch cylinders of the gears. The respective rack-cutters perform translation in planes Π_1 and Π_2. Planes Π_1 and Π_2 are tangent to *both* pitch cylinders. The shortest center distance E_p is equal to the sum of radii of pitch cylinders. The profile angle α_{pn} of each skew rack-cutter in normal section is the same as that of a rack-cutter applied for generation of spur gears. The operating pitch cylinders coincide with the pitch cylinders, and the nominal crossing angle γ_p is determined as

$$\gamma_p = |\beta_{p1} \pm \beta_{p2}| \tag{16.5.4}$$

where β_{p1} and β_{p2} are the helix angles of the pitch cylinders.
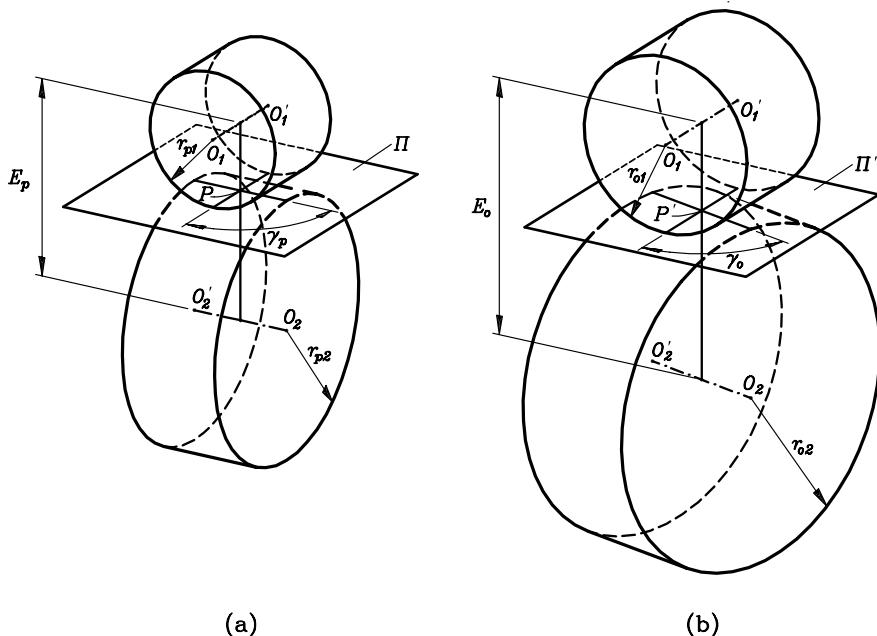
In the case of nonstandard gears, generation is also based on application of two skew rack-cutters. The rack-cutters also have a common normal section. The *operating* pitch cylinders of nonstandard gears do not coincide with the pitch cylinders of standard gears (Fig. 16.5.2). The shortest center distance of nonstandard gears is equal to the sum of radii of operating pitch cylinders but not to the sum of radii of pitch cylinders.

The nominal crossing angle is determined by Eq. (16.5.1) wherein angles β_{o1} and β_{o2} are the helix angles of the *operating* pitch cylinders.

The procedure of design of standard and nonstandard crossed helical gears is illustrated with numerical example 1 for standard gears and numerical examples 2 and 3 for nonstandard gears (see below).

Canonical Design

Canonical design provides related parameters of nominal values of crossing angle γ_o, normal profile α_{pn}, and center distance E_o that enable obtaining a favorable location of lines of action A_1 and A_2. The lines of action intersect each other at a point P that belongs to the line of shortest distance and is the point of tangency of the operating

(a)   (b)

Figure 16.5.2: Pitch cylinders (a) in a standard gear drive and (b) in a nonstandard gear drive.

pitch cylinders. Observation of γ_o and E_o obtained in canonical design as mentioned above avoids edge contact. Conditions of canonical design discussed for nonstandard gears can be applied as well for the design of standard crossed helical gears.

Due to errors of crossing angle γ_o and shortest center distance E_o or in the case of a special design, the relation between γ_o and E_o (determined for canonical design) might not be observed. Then the lines of action A_1 and A_2 are shifted from the theoretical positions, $A_1^{(o)}$ and $A_2^{(o)}$, and become crossed but not intersected (see Section 16.2). If sufficient axial dimensions of gears are not provided, edge contact is inevitable.

The authors have developed equations for determination of related parameters of γ_o, α_{on}, and E_o for canonical design, considering as given the radii of base cylinders and lead angles on these cylinders and the normal pressure angle α_{on} (see Appendices 16.A and 16.B). In numerical examples 1, 2, and 3 discussed below, the conditions of canonical design presented in Appendices 16.A and 16.B are observed.

Numerical Example 1: Design of Standard Gears

The input parameters are: $N_1 = 12$; $N_2 = 29$; $\beta_{p1} = 47.5°$; $\beta_{p2} = 42.5°$; $\gamma_p = 90°$; $m_{pn} = 4.0$ mm; and $\alpha_{pn} = 25°$.
Transverse pressure angles:

$$\alpha_{pt1} = \arctan\left(\frac{\tan\alpha_{pn}}{\cos\beta_{p1}}\right) = 34.6143°$$

$$\alpha_{pt2} = \arctan\left(\frac{\tan\alpha_{pn}}{\cos\beta_{p2}}\right) = 32.3122°.$$

Transverse modules:

$$m_{pt1} = \frac{m_{pn}}{\cos \beta_{p1}} = 5.9207 \text{ mm}$$

$$m_{pt2} = \frac{m_{pn}}{\cos \beta_{p2}} = 5.4254 \text{ mm.}$$

Radii of standard pitch cylinders:

$$r_{p1} = \frac{m_{pt1} N_1}{2} = 35.5245 \text{ mm}$$

$$r_{p2} = \frac{m_{pt2} N_2}{2} = 78.6678 \text{ mm.}$$

Radii of base cylinders:

$$r_{b1} = r_{p1} \cos \alpha_{pt1} = 29.2365 \text{ mm}$$

$$r_{b2} = r_{p2} \cos \alpha_{pt2} = 66.4859 \text{ mm.}$$

Lead angles of base cylinders:

$$\lambda_{b1} = \arctan \left(\frac{1}{\cos \alpha_{pt1} \tan \beta_{p1}} \right) = 48.0717°$$

$$\lambda_{b2} = \arctan \left(\frac{1}{\cos \alpha_{pt2} \tan \beta_{p2}} \right) = 52.2445°.$$

Shortest center distance:

$$E_p = r_{p1} + r_{p2} = 114.1923 \text{ mm.}$$

Tooth thicknesses on pitch cylinders:

$$s_{pt1} = r_{p1} \frac{\pi}{N_1} = 9.3003 \text{ mm}$$

$$s_{pt2} = r_{p2} \frac{\pi}{N_2} = 8.5221 \text{ mm.}$$

Radii of addendum and dedendum cylinders:

$$r_{pa1} = r_{p1} + m_{pn} = 39.5245 \text{ mm}$$

$$r_{pa2} = r_{p2} + m_{pn} = 82.6678 \text{ mm}$$

$$r_{pd1} = r_{p1} - 1.25 m_{pn} = 30.5245 \text{ mm}$$

$$r_{pd2} = r_{p2} - 1.25 m_{pn} = 73.6678 \text{ mm.}$$

It is easy to verify that Eq. (16.B.10) (see Appendix 16.B) that relates the crossing angle and the normal pressure angle for canonical design is satisfied for the standard gear drive.

Numerical Example 2: Approach 1 for Design of Nonstandard
Crossed Helical Gears

The discussed approach to design of nonstandard crossed helical gears is based on
the following considerations: (i) the tooth thicknesses s_{pt1} and s_{pt2} of the gears to
be designed are considered as given (s_{pt1} and s_{pt2} differ from similar parameters of
standard gears); and (ii) the design parameters $\lambda_{b1}, \lambda_{b2}, r_{b1}, r_{b2}$ are considered to be the
same as for standard gears. It is shown below that the discussed approach to design is
accompanied with a small change of the crossing angle determined for a similar design
of standard gears. The following is the explanation of the computation procedure.

Assume that the tooth thicknesses are $s_{pt1} = 10.9568$ mm and $s_{pt2} = 9.5341$ mm
which correspond to the corrections of rack-cutter settings $\chi_1 = 0.3m_{pn}$ and $\chi_2 =
0.2m_{pn}$. Transverse pressure angles of nonstandard crossing gears are related by the
following system of equations (see Appendix 16.D):

$$N_1 \, \mathrm{inv}\alpha_{ot1} + N_2 \, \mathrm{inv}\alpha_{ot2} = b \tag{16.5.5}$$

where

$$b = N_1 \left(\frac{s_{pt1}}{2r_{p1}} + \mathrm{inv}\alpha_{pt1} \right) + N_2 \left(\frac{s_{pt2}}{2r_{p2}} + \mathrm{inv}\alpha_{pt2} \right) - \pi$$

and (see Appendix 16.E)

$$\frac{\sin \alpha_{ot1}}{\sin \alpha_{ot2}} = \frac{\sin \lambda_{b2}}{\sin \lambda_{b1}}. \tag{16.5.6}$$

Using the system of two equations above, we obtain

$$\alpha_{ot1} = 36.1615°, \qquad \alpha_{ot2} = 33.7277°.$$

Radii of the operating pitch cylinders:

$$r_{o1} = \frac{r_{b1}}{\cos \alpha_{ot1}} = 36.2125 \text{ mm}$$

$$r_{o2} = \frac{r_{b2}}{\cos \alpha_{ot2}} = 79.9412 \text{ mm}.$$

Helix angles on the operating pitch cylinders:

$$\beta_{o1} = \arctan \left(\frac{r_{o1}}{r_{b1} \tan \lambda_{b1}} \right) = 48.0470°$$

$$\beta_{o2} = \arctan \left(\frac{r_{o2}}{r_{bi} \tan \lambda_{b2}} \right) = 42.9586°.$$

The nonstandard crossed helical gears are generated by two rack-cutters that have
the same normal pressure angle α_{on} determined by

$$\alpha_{on} = \arctan(\tan \alpha_{oti} \cos \beta_{oi}) = 26.0398° \quad (i = 1, 2).$$

The new normal module m_{on} is

$$m_{on} = \frac{2r_{oi} \cos \beta_{oi}}{N_i} = 4.0348 \text{ mm} \quad (i = 1, 2).$$

The new shortest center distance is

$$E_o = r_{o1} + r_{o2} = 116.1537 \text{ mm}.$$

The new crossing angle is

$$\gamma_o = \beta_{o1} + \beta_{o2} = 91.0055°.$$

The new radii of addendum and dedendum cylinders:

$$r_{oa1} = r_{o1} + m_{on} = 40.2473 \text{ mm}$$

$$r_{oa2} = r_{o2} + m_{on} = 83.9760 \text{ mm}$$

$$r_{od1} = r_{o1} - 1.25m_{on} = 31.1690 \text{ mm}$$

$$r_{od2} = r_{o2} - 1.25m_{on} = 74.8977 \text{ mm}.$$

It is easy to verify that Eq. (16.B.10) is satisfied for the obtained parameters of non-standard crossed helical gears.

Numerical Example 3: Approach 2 for Design of Nonstandard Crossed Helical Gears

Numerical example 2 (Approach 1) of design of nonstandard gears has shown that the crossing angle of the drive is slightly changed in comparison with the crossing angle of a similar design of standard gears. The main goal of Approach 2 of design is to keep the same crossing angle that is applied in a similar design of standard gears. The approach is based on the following considerations:

(i) The assigned crossing angle $\gamma_o = \gamma_p$ and the gear ratio m_{12} have to be observed.
(ii) Module m_{pn} and normal pressure angle α_{pn} of the common rack-cutter are given.
(iii) Settings of rack-cutter χ_1 and χ_2 for the pinion and the gear are applied respectively, and the tooth thicknesses of the pinion and gear must fit each other.

The observation of the assigned crossing angle of the gear drive is satisfied by modification of the skew angles of the rack-cutters. The computational procedure is an iterative process accomplished as follows.

Step 1: Determination of parameters on the pitch cylinders as a function of β_{p1} and β_{p2}:

$$r_{pi} = \frac{m_{pn}N_i}{2\cos\beta_{pi}} \quad (i = 1, 2)$$

$$\alpha_{pti} = \arctan\frac{\tan\alpha_{pn}}{\cos\beta_{pi}} \quad (i = 1, 2)$$

$$s_{pti} = \frac{\pi m_{pn}}{2\cos\beta_{pi}} + 2\chi_i m_{pn}\tan\alpha_{pti} \quad (i = 1, 2).$$

Step 2: Determination of parameters on the base cylinders:

$$r_{bi} = r_{pi} \cos \alpha_{pti} \quad (i = 1, 2)$$

$$\lambda_{bi} = \arctan \frac{1}{\tan \beta_{pi} \cos \alpha_{pti}} \quad (i = 1, 2)$$

$$s_{bti} = r_{bi} \left(\frac{s_{pti}}{r_{pi}} + 2 \mathrm{inv} \alpha_{pti} \right) \quad (i = 1, 2).$$

Step 3: Determination of parameters on the operating pitch cylinders:

$$\cos \alpha_{on} = \frac{(\cos^2 \lambda_{b1} \pm 2 \cos \lambda_{b1} \cos \lambda_{b2} \cos \gamma_o + \cos^2 \lambda_{b2})^{0.5}}{\sin \gamma_o}$$

$$r_{oi} = \frac{r_{bi} \sin \lambda_{bi}}{\sqrt{\cos^2 \alpha_{on} - \cos^2 \lambda_{bi}}} \quad (i = 1, 2)$$

$$\lambda_{oi} = \arctan \frac{r_{bi} \tan \lambda_{bi}}{r_{oi}} \quad (i = 1, 2)$$

$$\alpha_{oti} = \arccos \frac{r_{bi}}{r_{oi}} \quad (i = 1, 2)$$

$$s_{oti} = r_{oi} \left(\frac{s_{bi}}{r_{bi}} - 2 \mathrm{inv} \alpha_{oti} \right) \quad (i = 1, 2)$$

$$m_{on} = \frac{2 r_{o1} \sin \lambda_{o1}}{N_1}.$$

Step 4: Determination of the following functions:

$$f_1 = \frac{r_{b2} \sin \lambda_{b2}}{r_{b1} \sin \lambda_{b1}} - m_{12}$$

$$f_2 = s_{ot1} \sin \lambda_{o1} + s_{ot2} \sin \lambda_{o2} - \pi m_{on}.$$

The iterative process for determination of β_{p1} and β_{p2} is applied as follows:

(i)   Initially, in the first iteration, the applied magnitudes β_{p1} and β_{p2} are the same as in standard design. Generally, the equations of Step 4 are not satisfied simultaneously.

(ii) In the process of iterations, β_{p1} and β_{p2} are changed and steps 1, 2, and 3 are repeated until observation of Eqs. $f_1 = 0$ and $f_2 = 0$.

The computations have been applied for the following example. The settings of the rack-cutters are $\chi_1 = 0.3 m_{pn}$, $\chi_2 = 0.2 m_{pn}$. The crossing angle $\gamma_o = \gamma_p = 90°$. The iterative process yields:

$$\beta_{p1} = 46.9860°, \quad \beta_{p2} = 42.0010°.$$

Using the equations from Step 1 to Step 3 all the parameters of the gear drive can be determined. The new center distance is

$$E_o = r_{o1} + r_{o2} = 115.1898 \text{ mm}.$$

The assigned crossing angle $\gamma_o = 90°$ is observed because

$$\gamma_o = 180° - \lambda_{o1} - \lambda_{o2} = 180° - 42.4631° - 47.5369° = 90.0000°.$$
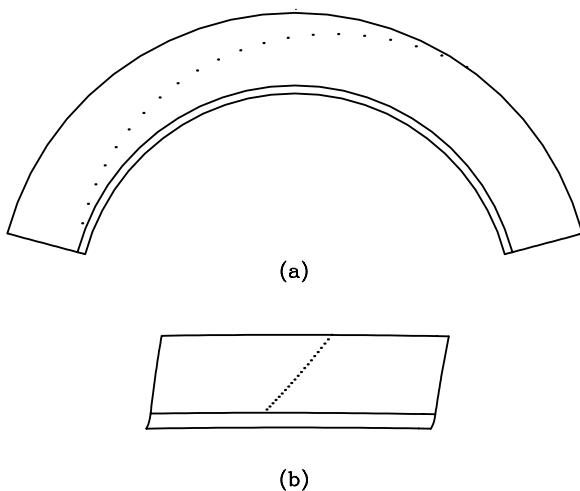
16.6 STRESS ANALYSIS

The goal of stress analysis presented in this section is determination of contact and bending stresses and the investigation of formation of the bearing contact in a crossed helical gear drive formed by an involute helical worm that is in mesh with an involute helical gear. A similar approach may be applied for stress analysis in a gear drive formed by mating helical gears. The performed stress analysis is based on the finite element method [Zienkiewicz & Taylor, 2000] and application of a general purpose computer program [Hibbit, Karlsson & Sirensen, Inc., 1998]. The developed approach for the finite element models is described in Section 9.5.
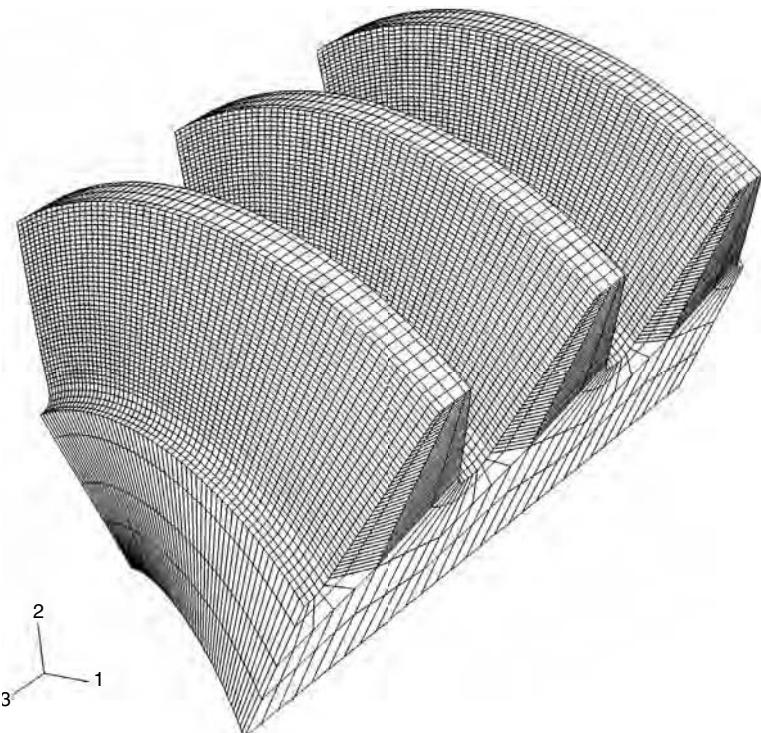
Numerical Example

Finite element analysis has been performed for a gear drive formed by an involute worm and an involute helical gear. The applied design parameters are the same as those shown in Table 16.3.1, but an involute worm and not an Archimedes' worm is considered in this case. Therefore, transmission errors do not occur. The output from TCA [see Figs. 16.6.1(a) and 16.6.1(b)] and the developed approach for the finite element models automatically builds one model for every point of contact.
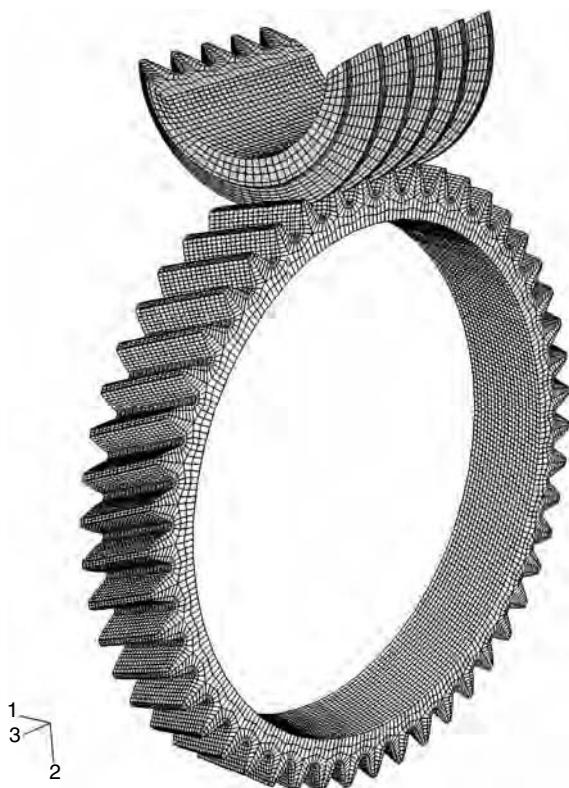
Figure 16.6.2 shows a three-tooth model of an involute worm. Figure 16.6.3 shows the finite element model of the whole worm gear drive. A three-tooth model has been applied for finite element analysis at each chosen point of the path of contact (Fig. 16.6.4). An angle of $60°$ has been applied to delimit the worm gear body. Elements C3D8I of first order (enhanced by incompatible modes to improve their bending behavior) [Hibbit, Karlsson & Sirensen, Inc., 1998] have been used to form the finite element mesh. The total number of elements is 59,866 with 74,561 nodes. The material is steel with the properties of Young's Modulus $E = 2.068 \times 10^5$ MPa and Poisson's ratio of 0.29. A torque of 40 Nm has been applied to the worm.

(a)

(b)
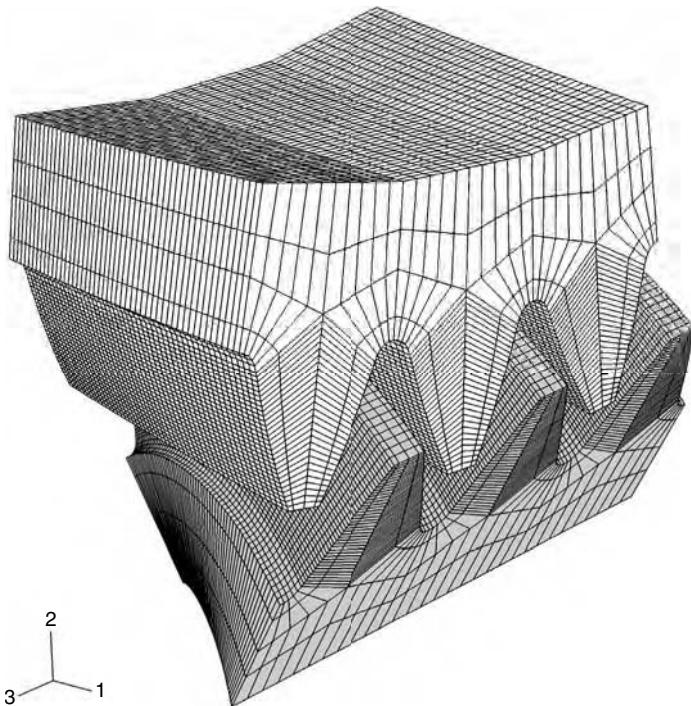
Figure 16.6.1: Paths of contact on (a) the worm and (b) the gear.

Figure 16.6.2: Three-tooth model of an involute worm.

**Figure 16.6.3:** Whole worm gear drive finite element model.

Figure 16.6.4: Finite element model with three pairs of teeth.

Figures 16.6.5 and 16.6.6 show the distribution of pressure on the worm and gear surfaces, respectively, in a chosen point of contact. The variation of contact and bending stresses along the path of contact has been also studied. Figures 16.6.7(a) and 16.6.7(b) illustrate the variation of contact stresses of the pinion and the gear, respectively, using the Von Mises criteria. Figures 16.6.8(a) and 16.6.8(b) show the evolution of bending stresses in the pinion and the gear, respectively. Areas of severe contact stresses are inevitable as a consequence of a crossed path of contact. The obtained results of stress analysis show that a gear drive formed by crossed helical gears should be applied as a light loaded gear drive only.

APPENDIX 16.A: DERIVATION OF SHORTEST CENTER DISTANCE FOR CANONICAL DESIGN

The goal is to derive the shortest center distance considering as given parameters r_{b1}, λ_{b1}, r_{b2}, λ_{b2}, and α_{on}.

Step 1: Derivation of the equation:

$$\cos \lambda_{oi} = \frac{\cos \lambda_{bi}}{\cos \alpha_{on}} \qquad (i = 1, 2). \qquad (16.A.1)$$
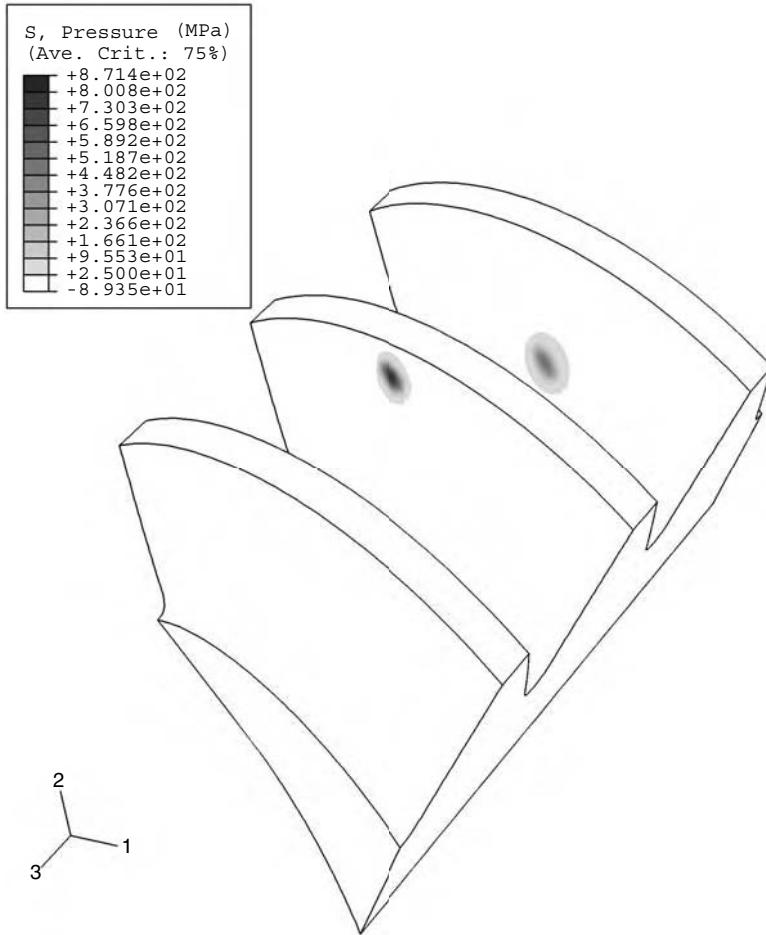
Figure 16.6.5: Distribution of pressure on the worm model.

The derivation is based on two relations between the transverse profiles and normal profiles of a rack-cutter that yield (see Chapter 14)

$$\tan \alpha_{oti} = \frac{\tan \alpha_{on}}{\sin \lambda_{oi}} \qquad (i = 1, 2) \tag{16.A.2}$$

$$\cos \alpha_{oti} = \frac{\tan \lambda_{oi}}{\tan \lambda_{bi}} \qquad (i = 1, 2). \tag{16.A.3}$$
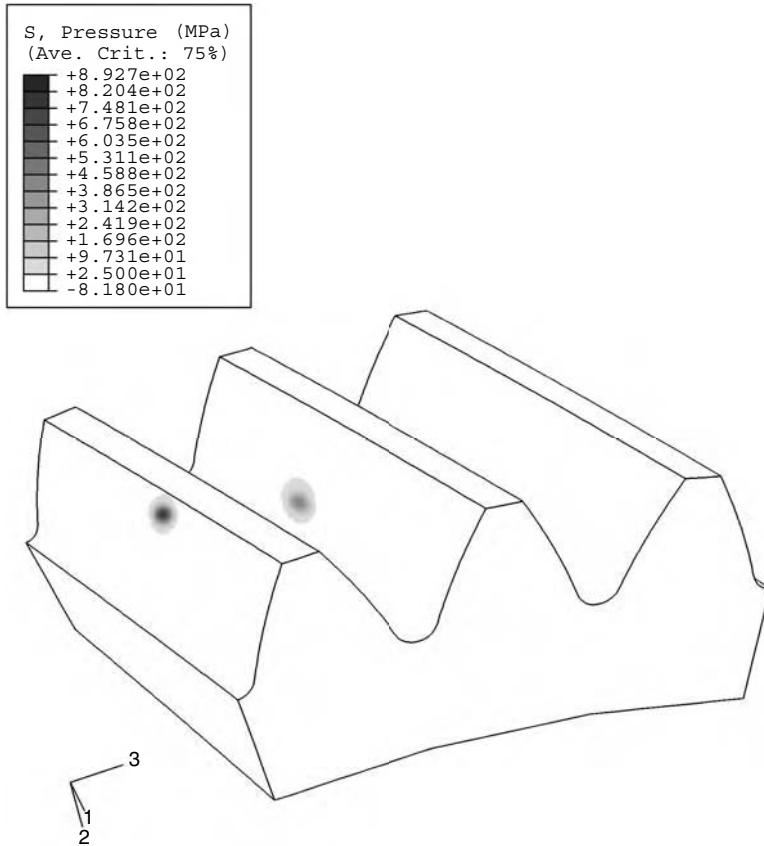
Equations (16.A.2) and (16.A.3) yield the following transformations:

(a)

$$1 + \frac{\tan^2 \alpha_{on}}{\sin^2 \lambda_{oi}} = 1 + \tan^2 \alpha_{oti} = \frac{1}{\cos^2 \alpha_{oti}} = \frac{\tan^2 \lambda_{bi}}{\tan^2 \lambda_{oi}}. \tag{16.A.4}$$

Then we obtain

$$1 + \frac{\tan^2 \alpha_{on}}{\sin^2 \lambda_{oi}} = \frac{\tan^2 \lambda_{bi}}{\tan^2 \lambda_{oi}}. \tag{16.A.5}$$

Figure 16.6.6: Distribution of pressure on the gear model.

(b) Equation (16.A.5) yields the following transformations:

$$\sin^2 \lambda_{oi} + \tan^2 \alpha_{on} = \cos^2 \lambda_{oi} \tan^2 \lambda_{bi} \qquad (16.A.6)$$

$$1 - \cos^2 \lambda_{oi} + \tan^2 \alpha_{on} = \cos^2 \lambda_{oi} \tan^2 \lambda_{bi} \qquad (16.A.7)$$

$$1 + \tan^2 \alpha_{on} = \cos^2 \lambda_{oi} (1 + \tan^2 \lambda_{bi}) \qquad (16.A.8)$$

$$\frac{1}{\cos^2 \alpha_{on}} = \frac{\cos^2 \lambda_{oi}}{\cos^2 \lambda_{bi}}. \qquad (16.A.9)$$
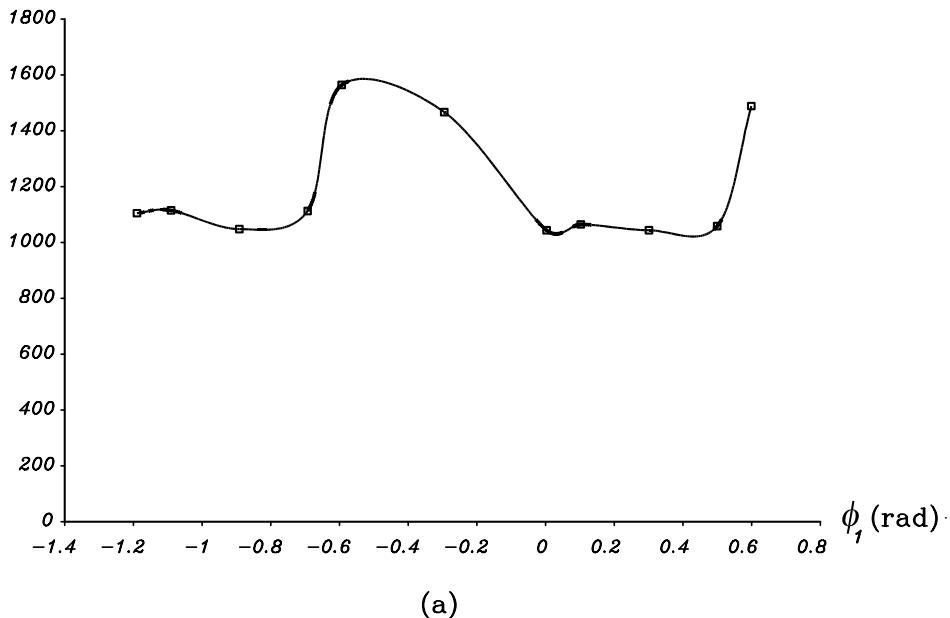
Finally, we obtain relation (16.A.1).

Step 2: Consider as given Eq. (16.A.1) and derive the relation between r_{oi} and r_{bi} taking into account that

$$r_{oi} \tan \lambda_{oi} = r_{bi} \tan \lambda_{bi} = p_i \qquad (16.A.10)$$
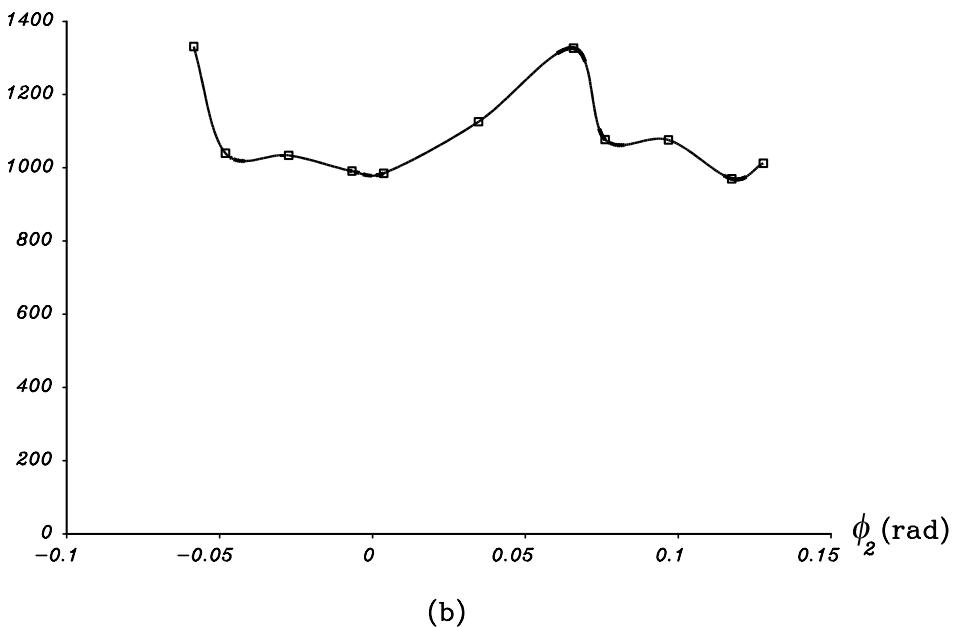
where p_i is the screw parameter.

Contact Stresses (MPa)

(a)
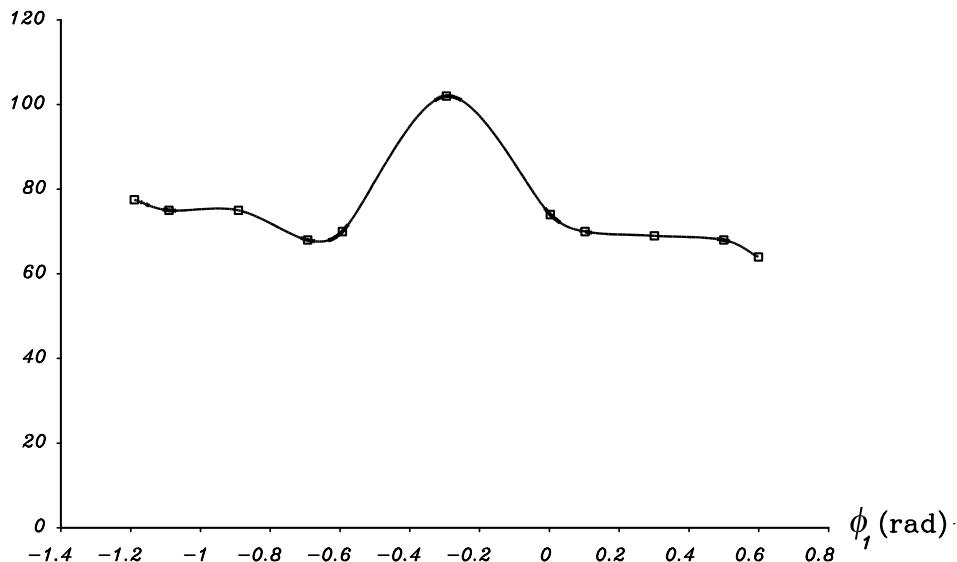
Contact Stresses (MPa)

(b)
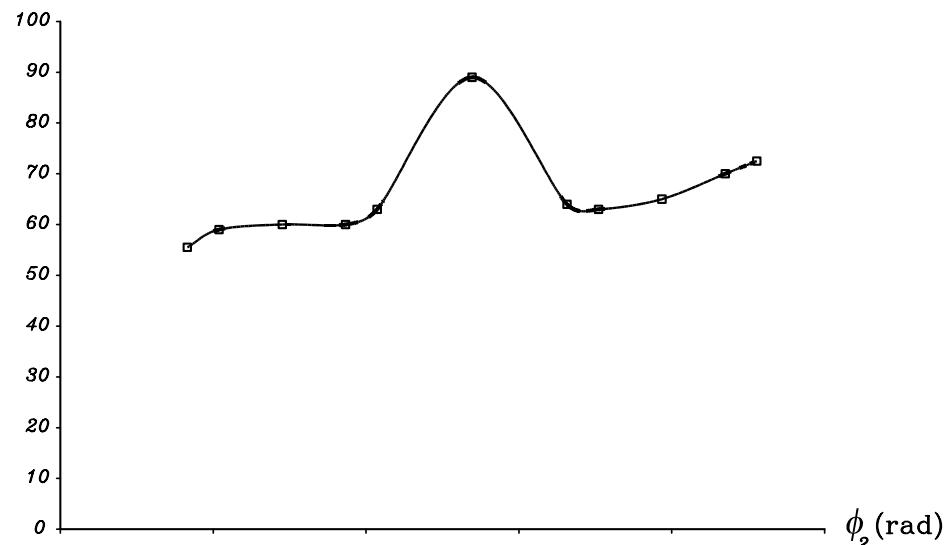
Figure 16.6.7: Variation of contact stresses on (a) the worm surface and (b) the gear surface.

Bending Stresses (MPa)

(a)

Bending Stresses (MPa)

(b)

Figure 16.6.8: Variation of bending stresses on (a) the worm surface and (b) the gear surface.

Then we obtain

$$r_{oi} = \frac{r_{bi} \tan \lambda_{bi}}{\tan \lambda_{oi}} \qquad (16.A.11)$$

and

$$E_o = r_{o1} + r_{o2} = \frac{r_{b1} \tan \lambda_{b1}}{\tan \lambda_{o1}} + \frac{r_{b2} \tan \lambda_{b2}}{\tan \lambda_{o2}}. \qquad (16.A.12)$$

Taking into account Eq. (16.A.1), we obtain the following final equation for E_o:

$$E_o = \frac{r_{b1} \sin \lambda_{b1}}{(\cos^2 \alpha_{on} - \cos^2 \lambda_{b1})^{0.5}} + \frac{r_{b2} \sin \lambda_{b2}}{(\cos^2 \alpha_{on} - \cos^2 \lambda_{b2})^{0.5}}. \qquad (16.A.13)$$

APPENDIX 16.B: DERIVATION OF EQUATION OF CANONICAL DESIGN $f(\gamma_o, \alpha_{on}, \lambda_{b1}, \lambda_{b2}) = 0$

Consider as given the equation

$$\cos \alpha_{on} = \frac{\cos \lambda_{bi}}{\cos \lambda_{oi}} \qquad (i = 1, 2) \qquad \text{[see Eq. (16.A.1)]}, \qquad (16.B.1)$$

which yields

$$\frac{\cos \lambda_{o1}}{\cos \lambda_{o2}} = \frac{\cos \lambda_{b1}}{\cos \lambda_{b2}} \qquad (16.B.2)$$

and the equation

$$\gamma_o = |\beta_{o1} \pm \beta_{o2}|. \qquad (16.B.3)$$

Step 1: Equations of $\cos \gamma_o$ and $\sin \gamma_o$ using Eq. (16.B.3) are represented as

$$\cos \gamma_o = \cos \beta_{o1} \cos \beta_{o2} \mp \sin \beta_{o1} \sin \beta_{o2} \qquad (16.B.4)$$

$$\sin \gamma_o = \sin \beta_{o1} \cos \beta_{o2} \pm \cos \beta_{o1} \sin \beta_{o2}. \qquad (16.B.5)$$

Step 2: The transformation of Eqs. (16.B.4) and (16.B.5) taking into account that $\beta_{oi} = 90° - \lambda_{oi}$ yields

$$\cos \gamma_o = \sin \lambda_{o1} \sin \lambda_{o2} \mp \cos \lambda_{o1} \cos \lambda_{o2} \qquad (16.B.6)$$

$$\sin \gamma_o = \cos \lambda_{o1} \sin \lambda_{o2} \pm \sin \lambda_{o1} \cos \lambda_{o2}. \qquad (16.B.7)$$

Step 3: The further transformation is based on Eq. (16.B.6) which yields

$$\sin \lambda_{o1} \sin \lambda_{o2} = \cos \gamma_o \pm \cos \lambda_{o1} \cos \lambda_{o2} \qquad (16.B.8)$$

$\sin^2 \gamma_o \cos^2 \alpha_{on}$

$$= \cos^2 \lambda_{b1} \sin^2 \lambda_{o2} \pm 2 \cos \lambda_{b1} \cos \lambda_{b2} \sin \lambda_{o1} \sin \lambda_{o2} + \cos^2 \lambda_{b2} \sin^2 \lambda_{o1}$$

$$= \cos^2 \lambda_{b1} \pm 2 \cos \lambda_{b1} \cos \lambda_{b2} \sin \lambda_{o1} \sin \lambda_{o2} + \cos^2 \lambda_{b2} - \frac{2 \cos^2 \lambda_{b1} \cos^2 \lambda_{b2}}{\cos^2 \alpha_{on}}.$$

$$(16.B.9)$$

Step 4: Equations (16.B.8) and (16.B.9) yield the following final expression:

$$\cos^2 \alpha_{on} \sin^2 \gamma_o = \cos^2 \lambda_{b1} \pm 2 \cos \lambda_{b1} \cos \lambda_{b2} \cos \gamma_o + \cos^2 \lambda_{b2}. \quad (16.B.10)$$

The advantage of Eq. (16.B.10) is that it allows us to obtain the relation between α_{on} and γ_o considering as input parameters λ_{b1} and λ_{b2}. One parameter from the pair of parameters α_{on} and γ_o has to be chosen. Equation (16.B.10) may be applied for canonical design of standard and nonstandard crossed involute helical gears.

APPENDIX 16.C: RELATIONS BETWEEN PARAMETERS α_{pt} AND α_{pn}

The transverse and normal sections of a skew rack-cutter are shown in Fig. 17.7.4(b). The derivation between parameters α_{pt} and α_{pn} is based on the following considerations: (i) the height of profiles in the transverse and normal sections is the same; and (ii) the distance p_n and p_t [Fig. 17.7.4(b)] are related by parameter β_p (λ_p). Thus we obtain

$$\tan \alpha_{pt} = \frac{\tan \alpha_{pn}}{\sin \lambda_p} = \frac{\tan \alpha_{pn}}{\cos \beta_p}. \quad (16.C.1)$$

APPENDIX 16.D: DERIVATION OF EQUATION (16.5.5)

The derivation of Eq. (16.5.5) is based on the following considerations (Chapter 10):

(1) The tooth thickness (space width) of the rack-cutter measured in the cross section along the tangent to the gear pitch circle is equal to the gear space width (tooth thickness) on the pitch circle because the gear and rack-cutter axodes roll without sliding. Thus we have

$$s_{ot1} \sin \lambda_{o1} + s_{ot2} \sin \lambda_{o2} = p_{on} = \frac{\pi}{P_{on}} = \pi m_{on}. \quad (16.D.1)$$

(2) Relations between the tooth thicknesses of involute gears measured on various circles yield (Section 10.6)

$$s_{ot1} = \left[\frac{s_{pt1}}{r_{p1}} + 2(\text{inv} \alpha_{pt1} - \text{inv} \alpha_{ot1}) \right] r_{o1} \quad (16.D.2)$$

$$s_{ot2} = \left[\frac{s_{pt2}}{r_{p2}} + 2(\text{inv} \alpha_{pt2} - \text{inv} \alpha_{ot2}) \right] r_{o2} \quad (16.D.3)$$

where

$$r_{oi} = \frac{N_i m_{oti}}{2} \quad (i = 1, 2) \quad (16.D.4)$$

$$m_{oti} = \frac{m_{on}}{\sin \lambda_{oi}} \quad (i = 1, 2). \quad (16.D.5)$$

Equations (16.D.1) to (16.D.5) yield Eq. (16.5.5).

APPENDIX 16.E: DERIVATION OF ADDITIONAL RELATIONS
BETWEEN α_{ot1} AND α_{ot2}

The goal is to prove Eq. (16.5.6) and the following one:

$$\frac{\sin \alpha_{pt1}}{\sin \alpha_{pt2}} = \frac{\sin \alpha_{ot1}}{\sin \alpha_{ot2}}. \tag{16.E.1}$$

The proof is based on the following considerations:

(i) Equation (16.A.2) yields

$$\frac{\tan \alpha_{ot1}}{\tan \alpha_{ot2}} = \frac{\sin \lambda_{o2}}{\sin \lambda_{o1}}. \tag{16.E.2}$$

(ii) Equations

$$\cos \alpha_{oti} = \frac{r_{bi}}{r_{oi}}$$

$$r_{bi} \tan \lambda_{bi} = r_{oi} \tan \lambda_{oi}$$

yield

$$\frac{\cos \alpha_{ot1}}{\cos \alpha_{ot2}} = \frac{r_{b1} r_{o2}}{r_{b2} r_{o1}} = \frac{\tan \lambda_{o1} \tan \lambda_{b2}}{\tan \lambda_{o2} \tan \lambda_{b1}}. \tag{16.E.3}$$

(iii) Equations (16.E.2) and (16.E.3) yield

$$\frac{\sin \alpha_{ot1}}{\sin \alpha_{ot2}} = \frac{\cos \lambda_{o2} \tan \lambda_{b2}}{\cos \lambda_{o1} \tan \lambda_{b1}}. \tag{16.E.4}$$

(iv) Equations (16.E.4) and (16.A.1) yield the relation

$$\frac{\sin \alpha_{ot1}}{\sin \alpha_{ot2}} = \frac{\sin \lambda_{b2}}{\sin \lambda_{b1}}. \tag{16.E.5}$$

(v) A similar approach yields

$$\frac{\sin \alpha_{pt1}}{\sin \alpha_{pt2}} = \frac{\sin \lambda_{b2}}{\sin \lambda_{b1}}. \tag{16.E.6}$$

(vi) Equation (16.E.1) follows from Eqs. (16.E.5) and (16.E.6).

17 New Version of Novikov–Wildhaber Helical Gears

17.1 INTRODUCTION

Wildhaber [1926] and Novikov [1956] have proposed helical gears based on generation by circular arc rack-cutters. The difference between the two inventions is that the gear tooth surfaces of Wildhaber gears are in line contact and the gear tooth surfaces of Novikov gears are in point contact. Figures 17.1.1 and 17.1.2 show the first and second versions of Novikov gears with one and two zones of meshing, respectively.
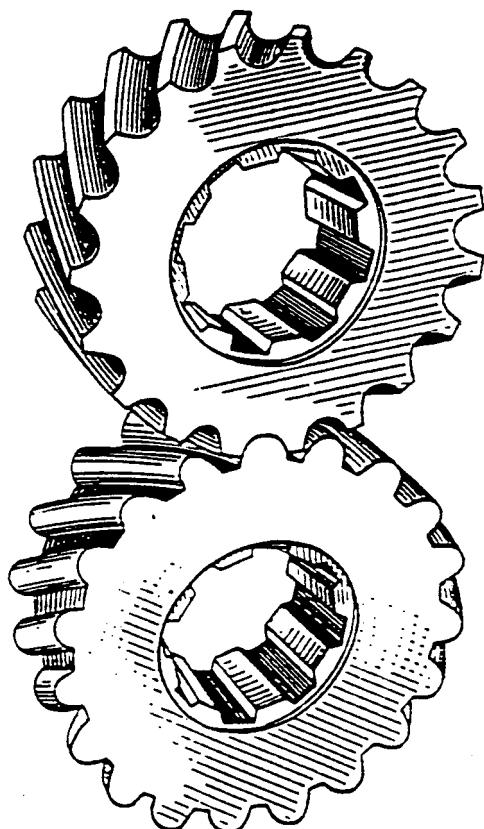
Point contact in Novikov gears has been achieved by application of two mismatched rack-cutters for generation of the pinion and the gear, respectively. The principle of mismatching of generating surfaces had already been applied for generation of spiral bevel gears and hypoid gears for localization of bearing contact before Novikov's invention was proposed. However, Novikov was the first who (i) applied mismatched tool surfaces for generation of helical gears, and (ii) achieved reduction of contact stresses due to small difference of curvatures of generating and generated tooth surfaces.

There are two weak points in Novikov design:
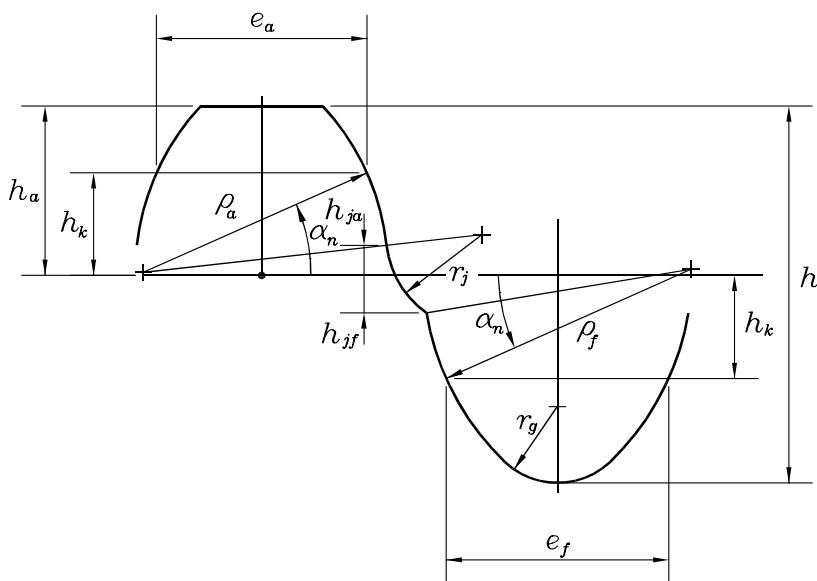
(i) The function of transmission errors of a misaligned gear drive is a discontinuous linear one, and the transfer of meshing between neighboring teeth is accompanied by high acceleration that causes a high level of vibration and noise [Litvin & Lu, 1995].
(ii) Bending stresses of Novikov gears, especially of the first design, are of large magnitude.

The manufacturing of Wildhaber–Novikov gears is based on application of two mating hobs that are conjugated to the respective mismatched rack-cutters. Improvement of bearing contact of misaligned Novikov gears is achieved by running the gears in their own housing and lapping. This is why Novikov gears of the existing design have been applied for low-speed transmissions only, and hardened materials and grinding of tooth surfaces have not been applied.

Novikov–Wildhaber gears have been the subject of intensive research [Wildhaber, 1926; Novikov, 1956; Niemann, 1961; Winter & Jooman, 1961; Litvin, 1962; Wells & Shotter, 1962; Davidov, 1963; Chironis, 1967; Litvin & Tsay, 1985; Litvin, 1989; Litvin & Lu, 1995; Litvin *et al.,* 2000c]. New designs of helical gear drives

**Figure 17.1.1:** Previous design of Novikov gears with one zone of meshing.

Figure 17.1.2: Profiles of rack-cutter for Novikov gears with two zones of meshing.

Figure 17.1.3: 3D model of new version of Novikov–Wildhaber gears.

are now based on application of a double-crowned pinion tooth surface. Crowning in the profile direction enables localization of the bearing contact. Crowning in the longitudinal direction provides a predesigned parabolic function with a limited value of maximal transmission errors [Litvin *et al.,* 2001c]. Profile crowning but not double-crowning was applied in the initially proposed Novikov gears (Figs. 17.1.1 and 17.1.2). Therefore, the noise of such gears was inevitable.

A new version of Novikov–Wildhaber gears (Fig. 17.1.3) that is free of the disadvantages of the existing design is presented in this chapter. The chapter covers (i) various methods for generation of pinion and gear tooth surfaces of the new design, (ii) avoidance of undercutting, and (iii) stress analysis. The proposed new version of helical gears is based partially on the ideas that have been presented in the patent [Litvin *et al.,* 2001c] and in the literature [Litvin *et al.,* 2000c, 2002d] as follows:
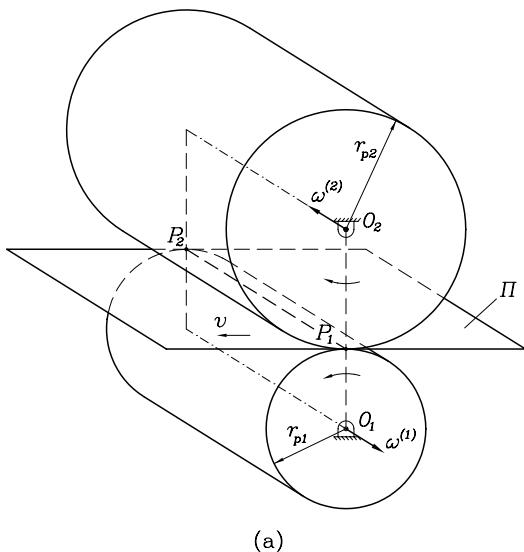
(1) Two mismatched parabolic rack-cutters are applied instead of rack-cutters with the circular arc profiles proposed for Novikov–Wildhaber gears. This increases tooth rigidity and decreases bending stresses. A reduction of contact stresses is obtained due to the small magnitude of relative curvatures.

(2) The tooth surface of the pinion is double-crowned (in the profile and longitudinal directions) whereas in conventional Novikov–Wildhaber gears only profile crowning is provided. Crowning in the longitudinal direction is obtained by plunging of the tool that generates the pinion. Plunging of the pinion tool is executed by a

parabolic function and enables us to obtain a predesigned parabolic function of transmission errors.
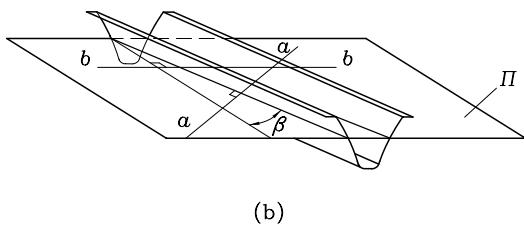
(3) An alternative method of obtaining of a parabolic function of transmission errors is based on application of modified roll (see Section 17.7).

(4) The generation of pinion and gear tooth surfaces may be accomplished by a grinding disk or a grinding worm in addition to generation by a hob. The possibility of grinding has opened up the possibility for application of hardened tooth surfaces with potential "distortion free" surfaces. Absorption of transmission errors caused by misalignment (due to the existence of a proposed predesigned parabolic function of transmission errors) reduces noise.

17.2 AXODES OF HELICAL GEARS AND RACK-CUTTER

The concept of axodes is applied when meshing and generation of helical gears are considered. Figure 17.2.1(a) shows that gears 1 and 2 perform rotation about parallel axes with angular velocities $\omega^{(1)}$ and $\omega^{(2)}$ with the ratio $\omega^{(1)}/\omega^{(2)} = m_{12}$ where m_{12} is the gear ratio. The axodes of the gears are two cylinders of radii r_{p1} and r_{p2} [Fig. 17.2.1(a)]

Figure 17.2.1: Axodes of pinion, gear, and rack-cutter: (a) axodes; (b) tooth surface of a skew rack-cutter.

and the line of tangency of the cylinders designated as P_1–P_2 is the instantaneous axis of rotation. The axodes roll over each other without sliding. Plane Π is tangent to the gear axodes; it is the axode of the rack-cutter and performs translational motion with velocity $\mathbf{v}$ [Fig. 17.2.1(a)] defined as

$$\mathbf{v} = \boldsymbol{\omega}^{(1)} \times \overline{O_1 P} = \boldsymbol{\omega}^{(2)} \times \overline{O_2 P} \tag{17.2.1}$$

where P belongs to P_1–P_2.

Figure 17.2.1(b) shows the tooth surface of a rack-cutter applied for generation of helical gears. The rack-cutter is installed in plane Π and is provided with skew teeth (the tooth surface is a cylindrical one). It is obvious from the drawings that a left-hand rack-cutter generates a left-hand pinion and a right-hand gear. The rack-cutter shown in Fig. 17.2.1(b) will generate a pinion and a gear whose surfaces are in *line* contact at every instant. Generation of pinion and gear tooth surfaces that are in point contact requires application of two rack-cutters with mismatched surfaces that separately generate the pinion and the gear.

17.3 PARABOLIC RACK-CUTTERS

The geometry of rack-cutters presented in this section is the basis for the design of tools (grinding disks, hobs, and worms) for the generation of the helical gears discussed above.

Normal and Transverse Sections

Henceforth, we consider the normal and transverse sections of the rack-cutter tooth surface. The normal section a–a of the rack-cutter is obtained by a plane that is perpendicular to plane Π and whose orientation is determined by angle β [Fig. 17.2.1(b)]. The transverse section of the rack-cutter is determined as a section by a plane that has the orientation of b–b [Fig. 17.2.1(b)].
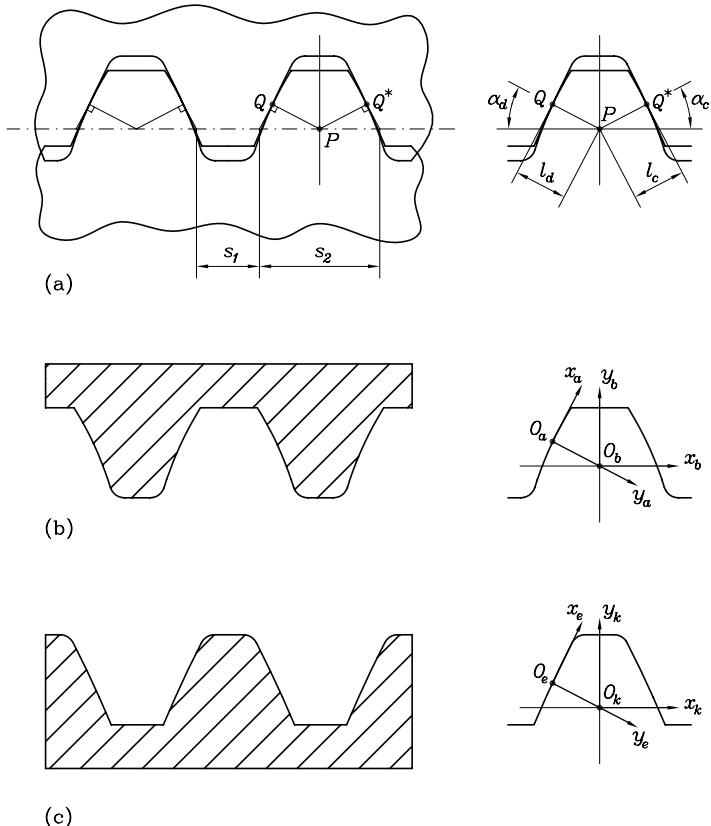
Mismatched Parabolic Rack-Cutters

It was mentioned above that two mismatched rack-cutters are applied for separate generation of the pinion and the gear of the new version of helical gears. Figure 17.3.1(a) shows the profiles of the normal sections of the rack-cutters. Figures 17.3.1(b) and 17.3.1(c) show the profiles of the pinion and gear rack-cutters, respectively. Dimensions s_1 and s_2 are related by module m and parameter s_{12} as follows:

$$s_1 + s_2 = \pi m \tag{17.3.1}$$
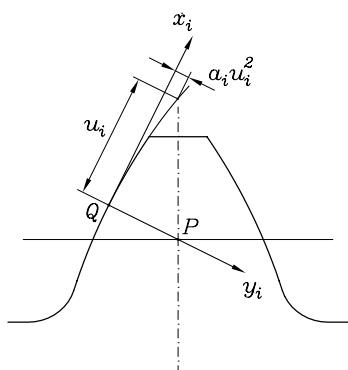
$$s_{12} = \frac{s_1}{s_2}. \tag{17.3.2}$$

Here, s_{12} is chosen in the process of optimization, relates pinion and gear tooth thicknesses, and can be varied in the design to modify the relative rigidity. In a conventional case of design, we have $s_{12} = 1$.

Figure 17.3.1: Normal sections of pinion and gear rack-cutters: (a) mismatched profiles; (b) profiles of pinion rack-cutter in coordinate systems S_a and S_b; (c) profiles of gear rack-cutter in coordinate systems S_e and S_k.

The profiles of the rack-cutters are parabolic curves that are in internal tangency. Points Q and Q^* [Fig. 17.3.1(a)] are the points of tangency of the normal profiles of the driving and coast sides of the teeth, respectively. The common normal to the profiles passes through point P that belongs to the instantaneous axis of rotation P_1-P_2

Figure 17.3.2: Parabolic profiles of rack-cutter in normal section.

[Fig. 17.2.1(a)]. A parabolic profile of a rack-cutter is represented in parametric form in an auxiliary coordinate system $S_i(x_i, y_i)$ as follows (Fig. 17.3.2):

$$x_i = u_i, \quad y_i = a_i u_i^2 \tag{17.3.3}$$

where a_i is the parabola coefficient. The origin of S_i coincides with Q.

Pinion Parabolic Rack-Cutter

The surface of the rack-cutter is designated by Σ_c and is derived as follows:

(i) The mismatched profiles of pinion and gear rack-cutters are represented in Figure 17.3.1(a). The pressure angles are α_d for the driving profile and α_c for the coast profile. The locations of points Q and Q^* are designated by $|\overline{QP}| = l_d$ and $|\overline{Q^*P}| = l_c$ where l_d and l_c are defined as

$$l_d = \frac{\pi m}{1 + s_{12}} \cdot \frac{\sin \alpha_d \cos \alpha_d \cos \alpha_c}{\sin(\alpha_d + \alpha_c)} \tag{17.3.4}$$
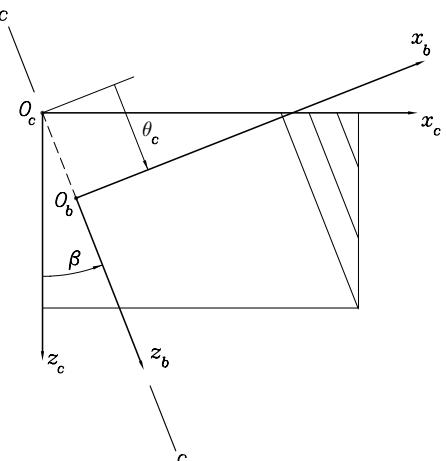
$$l_c = \frac{\pi m}{1 + s_{12}} \cdot \frac{\sin \alpha_c \cos \alpha_c \cos \alpha_d}{\sin(\alpha_d + \alpha_c)}. \tag{17.3.5}$$

(ii) Coordinate systems S_a and S_b are located in the plane of the normal section of the rack-cutter [Fig. 17.3.1(b)]. The normal profile is represented in S_b by the matrix equation

$$\mathbf{r}_b(u_c) = \mathbf{M}_{ba}\mathbf{r}_a(u_c) = \mathbf{M}_{ba}[u_c \quad a_c u_c^2 \quad 0 \quad 1]^{\mathrm{T}}. \tag{17.3.6}$$

(iii) The rack-cutter surface Σ_c is represented in coordinate system S_c (Fig. 17.3.3) wherein the normal profile performs translational motion along c–c. Then we obtain that surface Σ_c is determined by vector function

$$\mathbf{r}_c(u_c, \theta_c) = \mathbf{M}_{cb}(\theta_c)\mathbf{r}_b(u_c) = \mathbf{M}_{cb}(\theta_c)\mathbf{M}_{ba}\mathbf{r}_a(u_c). \tag{17.3.7}$$


Figure 17.3.3: For derivation of pinion rack-cutter.

Gear Parabolic Rack-Cutter

We apply coordinate systems S_e and S_k [Fig. 17.3.1(c)] and coordinate system S_t which is similar to system S_c (Fig. 17.3.3). The coordinate transformation from S_k to S_t is similar to the transformation from S_b to S_c. The gear rack-cutter surface is represented by the following matrix equation:

$$\mathbf{r}_t(u_t, \theta_t) = \mathbf{M}_{tk}(\theta_t)\mathbf{M}_{ke}\mathbf{r}_e(u_t). \qquad (17.3.8)$$

Rack-Cutters for Modified Involute Helical Gears

The idea of mismatched rack-cutters may be extended to the design of modified involute helical gears as follows:

(i) The rack-cutter for the pinion is applied as a parabolic one, but the rack-cutter for the gear is a conventional one and has straight-line profiles in the normal section.

(ii) In addition to profile crowning, the pinion is crowned in the longitudinal direction to provide a parabolic function of transmission errors (see Sections 17.6, 17.7, and 17.8).

(iii) The principle of the new design of modified involute helical gears localizes the bearing contact, avoids edge contact, and reduces transmission errors (see Chapter 15). However, the contact stresses of modified involute helical gears are larger than those in the new version of Novikov gears.

An example of involute helical gears is presented in Section 17.10 for comparison of stresses in the new version of Novikov–Wildhaber helical gears and modified involute helical gears.

17.4 PROFILE-CROWNED PINION AND GEAR TOOTH SURFACES
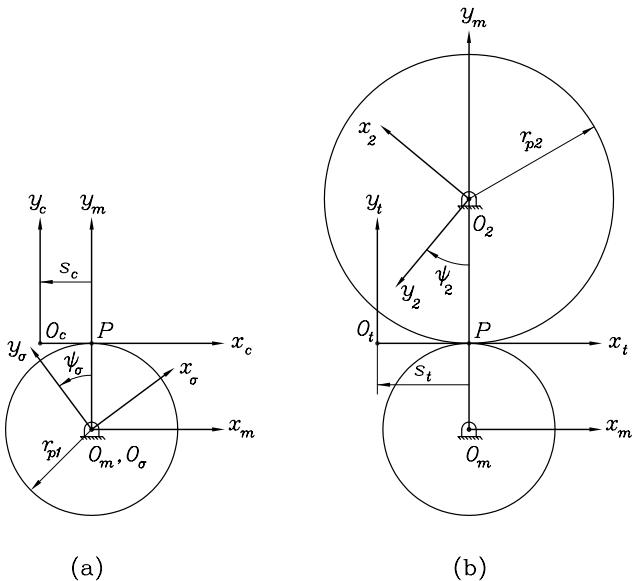
The profile-crowned pinion and gear tooth surfaces are designated as Σ_σ and Σ_2, respectively, whereas Σ_1 indicates the double-crowned pinion tooth surfaces.

Generation of Σ_σ

Profile-crowned pinion tooth surface Σ_σ is generated as the envelope to the pinion rack-cutter surface Σ_c. The derivation of Σ_σ is based on the following considerations:

(i) Movable coordinate systems $S_c(x_c, y_c)$ and $S_\sigma(x_\sigma, y_\sigma)$ are rigidly connected to the pinion rack-cutter and the pinion, respectively [Fig. 17.4.1(a)]. The fixed coordinate system S_m is rigidly connected to the cutting machine.

(ii) The rack-cutter and the pinion perform related motions, as shown in Fig. 17.4.1(a), where $s_c = r_{p1}\psi_\sigma$ is the displacement of the rack-cutter in its translational motion, and ψ_σ is the angle of rotation of the pinion.

(iii) A family of rack-cutter surfaces is generated in coordinate system S_σ and is determined by the matrix equation

$$\mathbf{r}_\sigma(u_c, \theta_c, \psi_\sigma) = \mathbf{M}_{\sigma c}(\psi_\sigma)\mathbf{r}_c(u_c, \theta_c). \qquad (17.4.1)$$

Figure 17.4.1: Generation of profile-crowned tooth surfaces by application of rack-cutters: (a) for pinion generation by rack-cutter Σ_c; (b) for gear generation by rack-cutter Σ_t.

(iv) The pinion tooth surface Σ_σ is determined as the envelope to the family of surfaces $\mathbf{r}_\sigma(u_c, \theta_c, \psi_\sigma)$ and is represented by simultaneous consideration of vector function $\mathbf{r}_\sigma(u_c, \theta_c, \psi_\sigma)$ and the equation of meshing

$$f_{c\sigma}(u_c, \theta_c, \psi_\sigma) = 0. \tag{17.4.2}$$

Equation $f_{c\sigma} = 0$ may be determined applying one of two approaches (see Section 6.1):

(a) The common normal to surfaces Σ_c and Σ_σ at their line of tangency must pass through the instantaneous axis of rotation P_1–P_2 [Fig. 17.2.1(a)].
(b) The second approach is based on the following equation of meshing:

$$\mathbf{N}_c^{(c)} \cdot \mathbf{v}_c^{(c\sigma)} = 0. \tag{17.4.3}$$

Here, $\mathbf{N}_c^{(c)}$ is the normal to Σ_c represented in S_c, and $\mathbf{v}_c^{(c\sigma)}$ is the relative velocity represented in S_c.

Generation of Gear Tooth Surface Σ_2
The schematic of generation of Σ_2 is represented in Fig. 17.4.1(b). Surface Σ_2 is represented by the following two equations considered simultaneously:

$$\mathbf{r}_2(u_t, \theta_t, \psi_2) = \mathbf{M}_{2t}(\psi_2)\mathbf{r}_t(u_t, \theta_t) \tag{17.4.4}$$

$$f_{t2}(u_t, \theta_t, \psi_2) = 0. \tag{17.4.5}$$

Here, vector equation $\mathbf{r}_t(u_t, \theta_t)$ represents the gear rack-cutter surface Σ_t; (u_t, θ_t) are the surface parameters of Σ_t; matrix $\mathbf{M}_{2t}(\psi_2)$ represents the coordinate transformation

from S_t to S_2; and ψ_2 is the generalized parameter of motion. Equations (17.4.4) and (17.4.5) represent surface Σ_2 by three related parameters.

Necessary and Sufficient Conditions of Existence of an Envelope to a Parametric Family of Surfaces

Such conditions are formulated in the case of profile-crowned pinion tooth surface Σ_σ, as follows (see Section 6.4):

(i) Vector function $\mathbf{r}_\sigma(u_c, \theta_c, \psi_\sigma)$ of class C^2 is considered.

(ii) We designate by point $M(u_c^{(0)}, \theta_c^{(0)}, \psi_\sigma^{(0)})$ the set of parameters that satisfies the equation of meshing (17.4.2) at M as well as the following conditions [see items (iii) to (v)].

(iii) Generating surface Σ_c of the rack-cutter is a *regular* one, and we have at M that

$$\frac{\partial \mathbf{r}_c}{\partial u_c} \times \frac{\partial \mathbf{r}_c}{\partial \theta_c} \neq 0. \tag{17.4.6}$$

Vectors $\partial \mathbf{r}_c / \partial u_c$ and $\partial \mathbf{r}_c / \partial \theta_c$ represent in coordinate systems S_σ tangents to coordinate lines of rack-cutter surface Σ_c. Inequality (17.4.6) means that normal $\mathbf{N}_c^{(c)}$ to surface Σ_c differs from zero. The designations of $\mathbf{N}_c^{(c)}$ indicate that the normal to Σ_c is represented in coordinate system S_c.

(iv) Partial derivatives of the equation of meshing (17.4.2) satisfy at M the inequality

$$\left| \frac{\partial f_{c\sigma}}{\partial u_c} \right| + \left| \frac{\partial f_{c\sigma}}{\partial \theta_c} \right| \neq 0. \tag{17.4.7}$$

(v) Singularities of surface Σ_σ are avoided by using the procedure described in Section 17.9.

By observation of conditions (i) to (v), the envelope Σ_σ is a *regular* surface; it contacts the generating surface Σ_c along a line and the normal to Σ_σ is collinear to the normal of Σ_c. Vector function $\mathbf{r}_\sigma(u_c, \theta_c, \psi_\sigma)$ and Eq. (17.4.2) considered simultaneously represent surface Σ_σ in three-parameter form by three related parameters $(u_c, \theta_c, \psi_\sigma)$.

Representation of Envelope Σ_σ in Two-Parameter Form

The representation of Σ_σ in two-parameter form is based on the following considerations:

(i) Assume that inequality (17.4.7) is observed because

$$\frac{\partial f_{c\sigma}}{\partial \theta_c} \neq 0. \tag{17.4.8}$$

(ii) The theorem of implicit function system existence [Korn & Korn, 1968] yields that due to observation of inequality (17.4.8) equation of meshing (17.4.2) may be solved in the neighborhood of point M by function

$$\theta_c = \theta_c(u_c, \psi_\sigma). \tag{17.4.9}$$

(iii) Then, surface Σ_σ can be represented as

$$\mathbf{R}_\sigma(u_c, \psi_\sigma) = \mathbf{r}_\sigma(u_c, \theta_c(u_c, \psi_\sigma), \psi_\sigma). \tag{17.4.10}$$

Similar representations of pinion tooth surfaces may be obtained for the case in which inequality (17.4.7) is observed, because $\partial f_{c\sigma}/\partial u_c \neq 0$, instead of inequality (17.4.8). The pinion profile-crowned tooth surface in this case may be represented as

$$\mathbf{R}_\sigma(\theta_c, \psi_\sigma) = \mathbf{r}_\sigma(u_c(\theta_c, \psi_\sigma), \theta_c, \psi_\sigma). \tag{17.4.11}$$
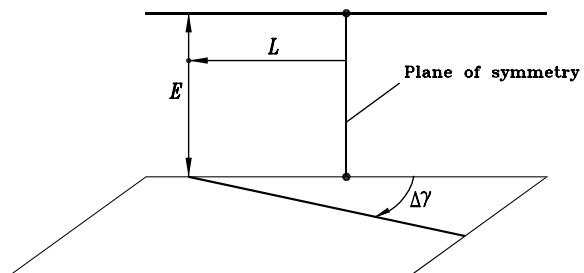
Representation of a Gear Profile-Crowned Tooth Surface in Two-Parameter Form

We recall that the profile-crowned gear tooth surface is represented in three-parameter form by vector function $\mathbf{r}_2(u_t, \theta_t, \psi_2)$ [see Eq. (17.4.4) and equation of meshing (17.4.5)]. A similar approach allows us to represent the gear tooth surface in two-parameter form as $\mathbf{R}_2(u_t, \psi_2)$ or as $\mathbf{R}_2(\theta_t, \psi_2)$.
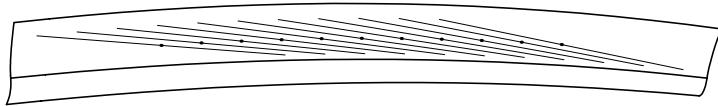
17.5 TOOTH CONTACT ANALYSIS (TCA) OF GEAR DRIVE WITH PROFILE-CROWNED PINION

The algorithm of tooth contact analysis (TCA) for simulation of meshing provides conditions of continuous tangency of contacting tooth surfaces of the pinion and the gear (see Section 9.4). Two cases have been considered for simulation of meshing and contact: (i) the pinion of the gear drive is profile-crowned, and (ii) the pinion is double-crowned (see Sections 17.6, 17.7, and 17.8). Comparison of the output for the two cases shows that double-crowning of the pinion reduces transmission errors as well as noise and vibration of the gear drive. A double-crowned pinion is also favorable for avoiding edge contact.
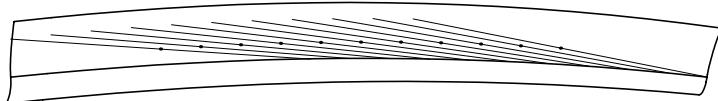
An example of meshing of profile-crowned pinion and gear tooth surfaces has been investigated with the following data: $N_1 = 17$, $N_2 = 77$, $m = 5.08$ mm, $s_{12} = 0.7$, $\beta = 20°$, $\alpha_d = \alpha_c = 25°$, $a_c = 0.016739$ mm^{-1}, and $a_t = 0.0155$ mm^{-1}. The following errors of alignment have been simulated: (i) change of center distance $\Delta E = 70$ μm, (ii) error $\Delta\lambda = 2$ arcmin of the lead angle, and (iii) change of shaft angle $\Delta\gamma = 2$ arcmin. The change of shaft angle $\Delta\gamma$ means that the axes of the pinion and the gear are crossed and the shortest distance E between the axes is displaced on a magnitude L (Fig. 17.5.1) from the plane of symmetry of the gear drive.
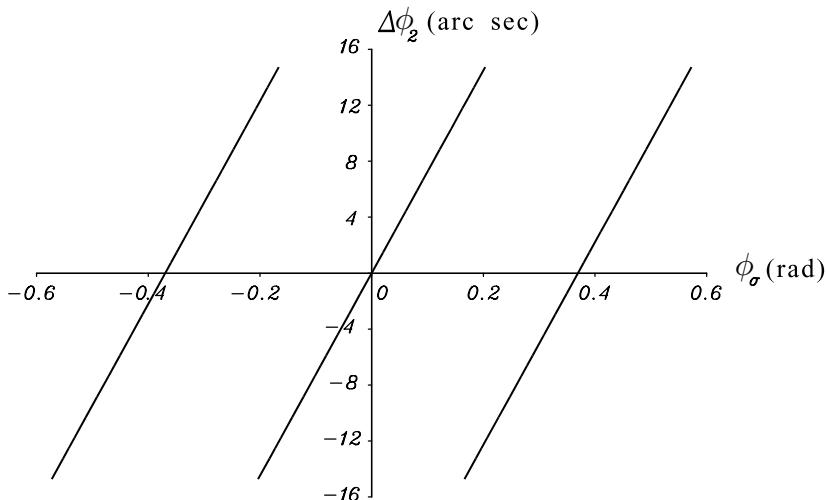

Figure 17.5.1: Effect of the change of the shaft angle on the shortest distance between axes.

(a)

(b)

(c)

Figure 17.5.2: Output of TCA of a profile-crowned gear drive: (a) path of contact with error ΔE [70 μm]; (b) path of contact with error $\Delta\gamma$ [2 arcmin]; (c) functions of transmission errors with error $\Delta\gamma$ [2 arcmin].

Combinations of L and $\Delta\gamma$ may cause the following cases of meshing and contact inside the cycle of meshing:

  (i) The bearing contact is formed by points of tangency of tooth surfaces of the pinion and gear.
 (ii) Edge contact occurs in the process of meshing wherein a *curve* (it is an edge of one of the mating surfaces) is in mesh with a *surface* (the other mating surface).
(iii) The bearing contact is formed as the result of a combination of the meshing in cases (i) and (ii).

Investigation of meshing in the case of edge contact is discussed in Section 9.6.

The output of TCA has been obtained for the previous example wherein edge contact has not occurred. The results obtained by computation are as follows:

(1) The path of contact is indeed oriented longitudinally [Figs. 17.5.2(a) and 17.5.2(b)].
(2) Error ΔE of the center distance does not cause transmission errors, but causes the shift of the bearing contact.
(3) However, errors of alignment $\Delta\gamma$ and $\Delta\lambda$ cause a discontinuous linear function of transmission errors $\Delta\phi_2(\phi_\sigma)$ [Fig. 17.5.2(c)]. Therefore, the transfer of meshing from one pair of teeth to the neighboring one is accompanied with high acceleration, and vibration and noise become inevitable.

Noise and vibration of all types of Novikov–Wildhaber gear drives are inevitable if only profile crowning of pinion-gear tooth surfaces is provided. This statement is true as well for Novikov–Wildhaber gears of the existing design. Substantial reduction of acceleration is obtained by double-crowning of the pinion that provides a parabolic function of transmission errors as discussed in Section 9.2. Such a function is able to absorb linear functions of transmission errors caused by misalignment. It follows from the discussion above that design of a gear drive formed by a double-crowned pinion and a profile-crowned gear is the precondition for reduction of noise and vibration and localization of bearing contact.

17.6 LONGITUDINAL CROWNING OF PINION BY A PLUNGING DISK

Longitudinal crowning of the pinion tooth surface, in addition to profile crowning, is applied for transformation of the shape of the function of transmission errors and reduction of noise and vibration. We recall that errors of shaft angle and lead angle cause a discontinuous linear function of transmission errors [see Section 17.5 and Fig. 17.6.2(c)], and high acceleration and vibration of the gear drive become inevitable. Generation of the pinion by a plunging disk enables avoidance of this defect.

Application of a Disk-Shaped Tool
Figure 17.6.1 shows the generating disk and the pinion in the 3D-space. The surface of the disk is a surface of revolution and is conjugated to the profile-crowned surface of the pinion. The profile-crowned surface Σ_σ of the pinion is a helicoid and is determined as the envelope to the parabolic rack-cutter (see Section 17.4).

It is assumed that during the process of generation of the pinion, the pinion performs a screw motion about its axis and is plunged with respect to the generating disk that is held at rest. The plunging motion of the pinion is performed along the shortest center distance between the axes of the disk and the pinion. The plunging motion is executed by a parabolic function (see below). The generating disk performs rotation about its axis, but the angular velocity of rotation is not related to the process of generation. It is assumed that the two components of pinion screw motion and the plunging motion are provided to the pinion. However, one or two of these three components of motions may be provided to the generating disk but not to the pinion.

Figure 17.6.1: Generation of pinion by disk.

Details of the developed approach are as follows:

(i) The profile-crowned surface Σ_σ of the pinion is considered as given.
(ii) A disk-shaped tool Σ_D that is conjugated to Σ_σ is determined [Fig. 17.6.2(a)] (see in addition Chapter 24). The axes of the disk and pinion tooth surface Σ_σ are crossed and the crossing angle γ_{Dp} is equal to the lead angle on the pinion pitch cylinder [Fig. 17.6.2(b)]. The nominal center distance E_{Dp} [Fig. 17.6.2(a)] is defined as
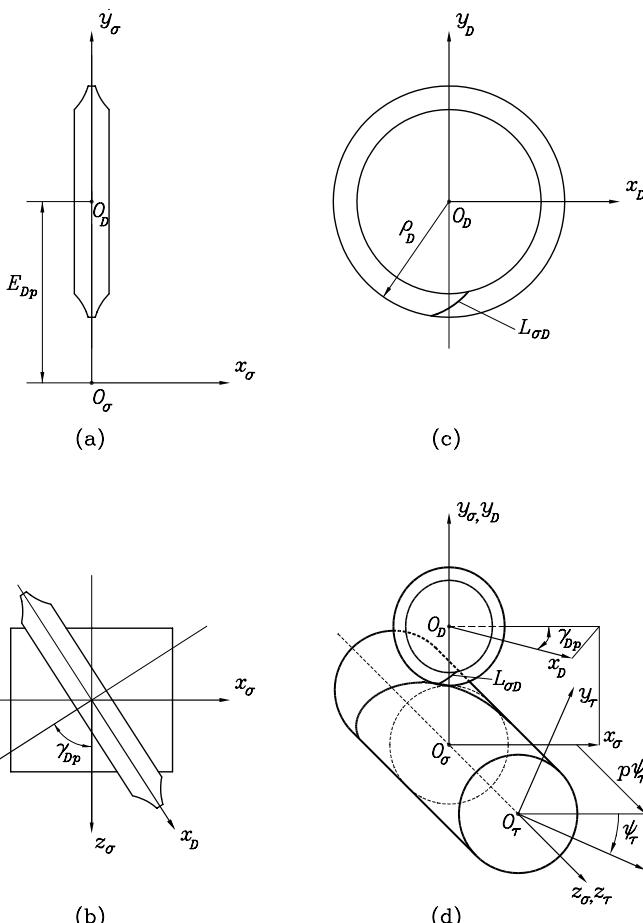
$$E_{Dp} = r_{d1} + \rho_D \tag{17.6.1}$$

where r_{d1} is the dedendum radius of the pinion and ρ_D is the generating disk radius.
(iii) Determination of disk surface Σ_D is based on the following procedure (see Chapter 24):
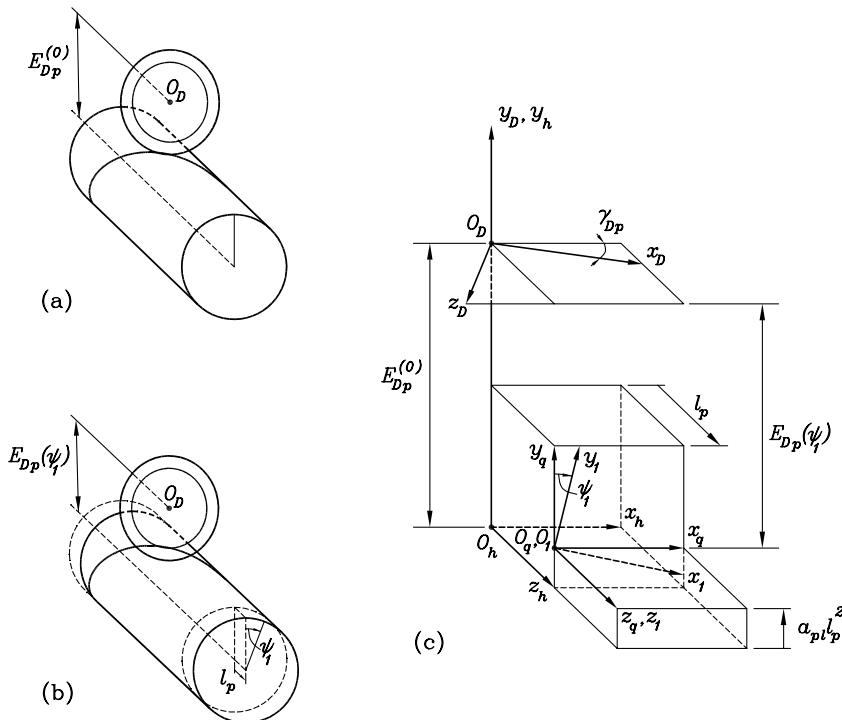
Step 1: Disk surface Σ_D is a surface of revolution. Therefore, there is such a line $L_{\sigma D}$ [Fig. 17.6.2(c)] of tangency of Σ_σ and Σ_D that the common normal to Σ_σ and Σ_D at each point of $L_{\sigma D}$ passes through the axis of rotation of the disk (see Chapter 24). Figure 17.6.2(c) shows line $L_{\sigma D}$ obtained on surface Σ_D. Rotation of $L_{\sigma D}$ about the axis of Σ_D enables representation of surface Σ_D as the family of lines $L_{\sigma D}$.

Step 2: It is obvious that screw motion of disk Σ_D about the axis of pinion tooth surface Σ_σ provides a surface that coincides with Σ_σ [Fig. 17.6.2(d)].

Figure 17.6.2: Determination of disk surface Σ_D: (a) and (b) installment of generating disk; (c) line $L_{\sigma D}$ of tangency of surfaces Σ_σ and Σ_D; (d) illustration of generation of surface Σ_τ by disk surface Σ_D.

(iv) Our goal is to obtain a double-crowned surface Σ_1 of the pinion, and this is accomplished by providing a combination of screw and plunging motions of the disk and the pinion. The generation of a double-crowned pinion tooth surface is illustrated in Fig. 17.6.3 and is accomplished as follows:

(1) Figures 17.6.3(a) and 17.6.3(b) show two positions of the generated double-crowned pinion with respect to the disk. One of the two positions with center distance $E_{Dp}^{(0)}$ is the initial one; the other with $E_{Dp}(\psi_1)$ is the current position. The shortest distance $E_{Dp}^{(0)}$ is defined by Eq. (17.6.1).

(2) Coordinate system S_D is rigidly connected to the generating disk [Fig. 17.6.3(c)] and is considered fixed.

(3) Coordinate system S_1 of the pinion performs a screw motion and is plunged with respect to the disk. Auxiliary systems S_b and S_q are used for better illustration of these motions in Fig. 17.6.3(c). Such motions are described as

Figure 17.6.3: Generation of double-crowned pinion surface Σ_1 by a plunging disk: (a) initial positions of pinion and disk; (b) schematic of generation; (c) applied coordinate systems.

follows. Screw motion is accomplished by two components: (a) translational displacement l_p that is collinear to the axis of the pinion, and (b) rotational motion ψ_1 about the axis of the pinion [Figs. 17.6.3(b) and 17.6.3(c)]. The magnitudes l_p and ψ_1 are related through the screw parameter p of the pinion as

$$l_p = p\psi_1. \tag{17.6.2}$$

Plunging motion is accomplished by a translational displacement $a_{pl}l_p^2$ along the shortest distance direction [Fig. 17.6.3(c)]. Such motion allows us to define the shortest distance $E_{Dp}(\psi_1)$ [Figs. 17.6.3(b) and 17.6.3(c)] as a parabolic function

$$E_{Dp}(\psi_1) = E_{Dp}^{(0)} - a_{pl}l_p^2. \tag{17.6.3}$$

The translational displacements l_p and $a_{pl}l_p^2$ are represented as displacement of system S_q with respect to system S_h. The same translational displacements are performed by system S_1 which performs rotation of angle ψ_1 with respect to system S_q.

(4) The pinion tooth surface Σ_1 is determined as the envelope to the family of disk surfaces Σ_D generated in the relative motion between the disk and the pinion.

Figure 17.7.1: Generation of pinion by worm.

17.7 GENERATION OF DOUBLE-CROWNED PINION BY A WORM

Figure 17.7.1 shows a single-thread generating worm and the pinion in 3D-space. The worm surface shown in Fig. 17.7.1 belongs to the same thread of the worm. Details of the developed approach are given below.
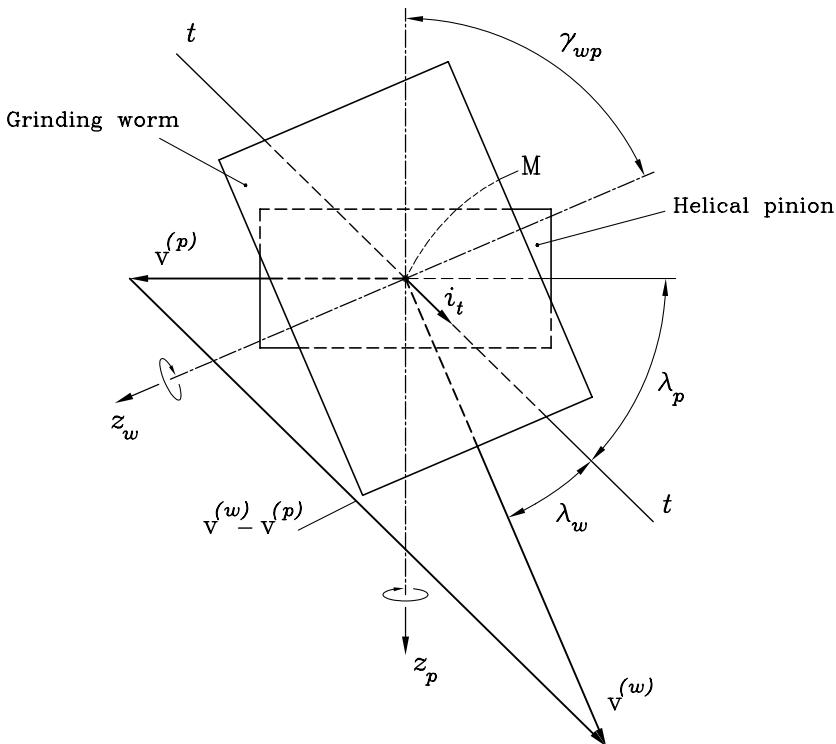
Worm Installment

The installment of the generating worm with respect to the pinion may be represented on the basis of meshing of two helicoids. Figure 17.7.2 illustrates the meshing of two left-hand helicoids, which represent the generating worm and the pinion generated by the worm, respectively. Figure 17.7.2 yields that the crossing angle is

$$\gamma_{wp} = \lambda_p + \lambda_w \tag{17.7.1}$$

where λ_p and λ_w are the lead angles on the pitch cylinders of the worm and the pinion.

Figure 17.7.2 shows that the pitch cylinders of the worm and the pinion are in tangency at point M which belongs to the shortest distance between the crossed axes. The

Figure 17.7.2: Installment of generating worm.

velocity polygon at M satisfies the relation

$$\mathbf{v}^{(w)} - \mathbf{v}^{(p)} = \mu \mathbf{i}_t. \tag{17.7.2}$$
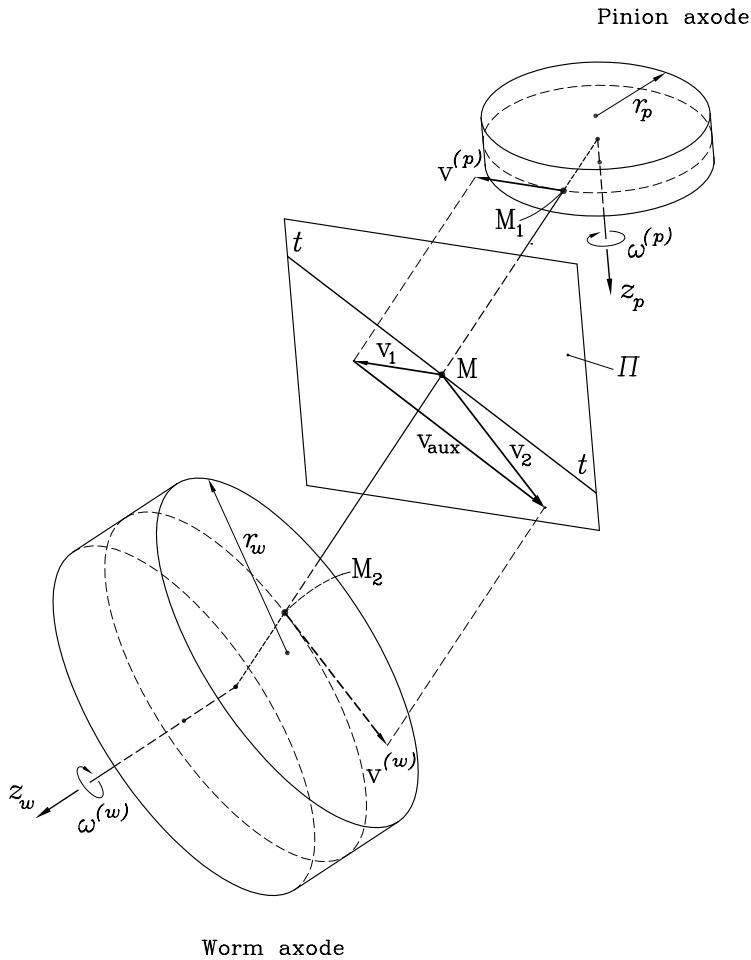
Here, $\mathbf{v}^{(w)}$ and $\mathbf{v}^{(p)}$ are the velocities of the worm and the pinion at M; $\mathbf{i}_t$ is the unit vector directed along the common tangent to the helices; and μ is the scalar factor. Equation (17.7.2) indicates that the relative velocity at point M is collinear to the unit vector $\mathbf{i}_t$.

Determination of Worm Thread Surface Σ_w

In order to get the same pinion tooth surface Σ_σ that is generated by rack-cutter surface Σ_c, the generation of Σ_w can be accomplished by considering that three surfaces Σ_c, Σ_σ, and Σ_w are simultaneously in meshing. Figure 17.7.3 shows the axodes of these three surfaces, and for the purpose of better illustration the shortest distance between the pinion and worm axodes is extended. Plane Π represents the axode of the rack-cutter. Surface Σ_w is obtained using the following steps:

    Step 1: Parabolic tooth surface Σ_c of the rack-cutter is considered as given.

    Step 2: A translational motion of rack-cutter surface Σ_c, which is perpendicular to the axis of the pinion, and rotational motion of the pinion provide surface Σ_σ as an envelope to the family of surfaces of Σ_c (see Section 17.4). Velocity $\mathbf{v}_1$ (Fig. 17.7.3) of

Figure 17.7.3: For illustration of axodes of worm, pinion, and rack-cutter.

the rack-cutter corresponds to rotation of the pinion with angular velocity $\boldsymbol{\omega}^{(p)}$. The relation between v_1 and $\omega^{(p)}$ is defined as
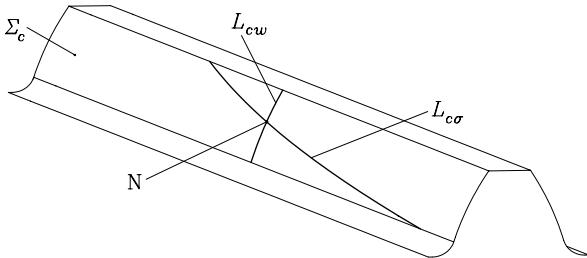
$$v_1 = \omega^{(p)} r_p \tag{17.7.3}$$

where r_p is the radius of the pinion pitch cylinder.

Step 3: An additional motion of surface Σ_c with velocity $\mathbf{v}_{\text{aux}}$ along direction $t-t$ of skew rack-cutter teeth (Fig. 17.7.3) is performed and this motion does not affect the generation of surface Σ_σ. Vector equation $\mathbf{v}_2 = \mathbf{v}_1 + \mathbf{v}_{\text{aux}}$ allows us to obtain velocity $\mathbf{v}_2$ of rack-cutter Σ_c in a direction that is perpendicular to the axis of the worm. Then, we may represent the generation of worm surface Σ_w by rack-cutter Σ_c considering that the rack-cutter performs translational motion $\mathbf{v}_2$ while the worm is rotated with angular velocity $\boldsymbol{\omega}^{(w)}$. The relation between v_2 and $\omega^{(w)}$ is defined as

$$v_2 = \omega^{(w)} r_w \tag{17.7.4}$$

where r_w is the radius of the worm pitch cylinder.

Figure 17.7.4: Contact lines $L_{c\sigma}$ and L_{cw} corresponding to meshing of rack-cutter Σ_c with pinion and worm surfaces Σ_σ and Σ_w, respectively.

Worm surface Σ_w is generated as the envelope to the family of rack-cutter surfaces Σ_c.

Step 4: The discussion above enables us to verify simultaneous generation of profile-crowned pinion tooth surface Σ_σ and worm thread surface Σ_w by rack-cutter surface Σ_c. Each of the two generated surfaces Σ_σ and Σ_w are in line contact with rack-cutter surface Σ_c. However, the contact lines $L_{c\sigma}$ and L_{cw} do not coincide but rather intersect each other as shown in Fig. 17.7.4. Here, $L_{c\sigma}$ and L_{cw} represent the lines of contact between Σ_c and Σ_σ, and between Σ_c and Σ_w, respectively. Lines $L_{c\sigma}$ and L_{cw} are obtained for a chosen value of related parameters of motion between Σ_c, Σ_σ, and Σ_w. Point N of intersection of lines L_{cw} and $L_{c\sigma}$ (Fig. 17.7.4) is the common point of tangency of surfaces Σ_c, Σ_σ, and Σ_w.

Profile Crowning of Pinion

Profile-crowned pinion tooth surface Σ_σ has been previously obtained by using rack-cutter surface Σ_c. Direct derivation of generation of Σ_σ by the worm Σ_w may be accomplished as follows:
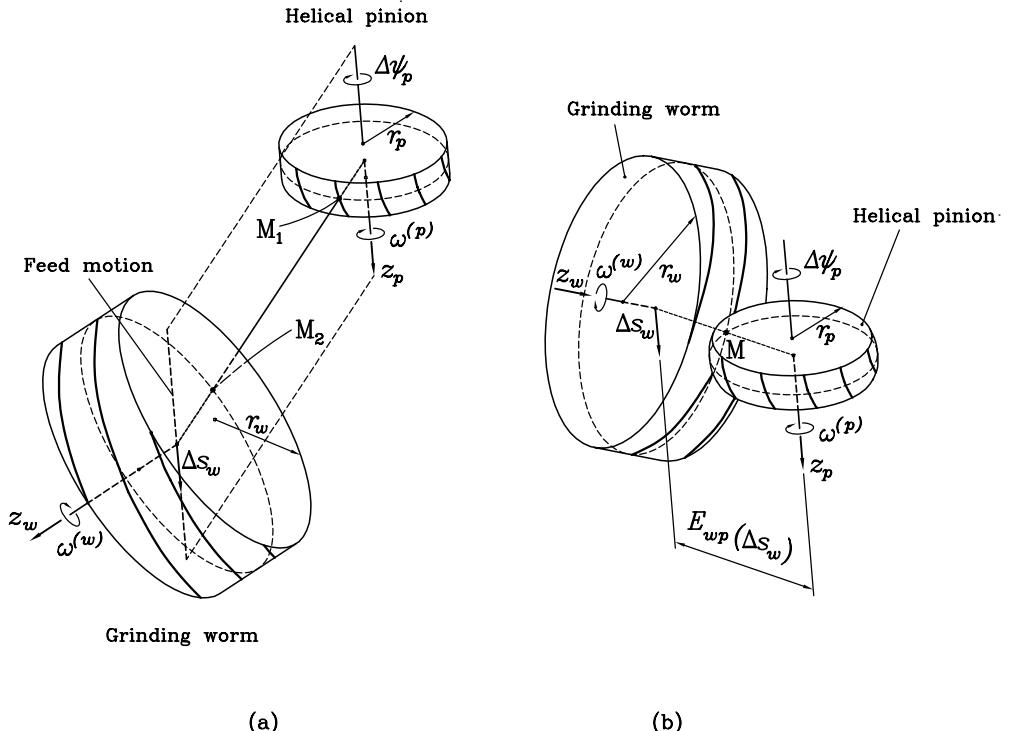
(a) Consider that worm surface Σ_w and pinion tooth surface Σ_σ perform rotation between their crossed axes with angular velocities $\boldsymbol{\omega}^{(w)}$ and $\boldsymbol{\omega}^{(p)}$. It follows from previous discussions that Σ_w and Σ_σ are in point contact and N is one of the instantaneous points of contact of Σ_w and Σ_σ (Fig. 17.7.4).

(b) The concept of direct derivation of Σ_σ by Σ_w is based on the two-parameter enveloping process (see Section 6.10). The process of such enveloping is based on application of two independent sets of parameters of motion [Litvin & Seol, 1996]:

   (i) One set of parameters relates the angles of rotation of the worm and the pinion as

$$m_{wp} = \frac{\omega^{(w)}}{\omega^{(p)}} = N_p \qquad (17.7.5)$$

   where the number N_w of worm threads is considered as $N_w = 1$, and N_p is the number of teeth of the pinion.

   (ii) The second set of parameters of motion is provided as a combination of two components: (1) translational motion $\Delta\mathbf{s}_w$ of the worm that is performed

Figure 17.7.5: Schematic of generation: (a) without worm plunging; (b) with worm plunging.

collinear to the axis of the pinion [Fig. 17.7.5(a)], and (2) small rotational motion of the pinion about the pinion axis determined as

$$\Delta \psi_p = \frac{\Delta s_w}{p} \tag{17.7.6}$$

where p is the screw parameter of the pinion.

Analytical determination of a surface generated as the envelope to a two-parameter enveloping process is presented in Section 6.10.

The schematic generation of Σ_σ by Σ_w is shown in Fig. 17.7.5(a) wherein the shortest center distance is shown as an extended one for the purpose of better illustration. In the process of meshing of Σ_w and Σ_σ, the worm surface Σ_w and the profile-crowned pinion surface perform rotation about crossed axes. The shortest distance is executed as

$$E_{wp} = r_p + r_w. \tag{17.7.7}$$

Surfaces Σ_w and Σ_σ are in point tangency. Feed motion of the worm is provided as a screw motion with the screw parameter of the pinion. Designations in Fig. 17.7.5(a) indicate (1) M_1 and M_2 are points on pitch cylinders (these points do not coincide with each other because the shortest distance is illustrated as extended); (2) $\omega^{(w)}$ and $\omega^{(p)}$ are the angular velocities of the worm and profile-crowned pinion in their rotation about

crossed axes; (3) $\Delta \mathbf{s}_w$ and $\Delta \psi_p$ are the components of the screw motion of the feed motion; and (4) r_w and r_p are the radii of pitch cylinders.

Double Crowning of Pinion

We have presented above the generation by a worm of a profile-crowned surface Σ_σ of the pinion. However, our final goal is the generation by a worm of a double-crowned surface Σ_1 of the pinion. Two approaches are proposed for this purpose:

WORM PLUNGING. Additional pinion crowning (longitudinal crowning) is provided by plunging of the worm with respect to the pinion which is shown schematically in Fig. 17.7.5(b). Plunging of the worm in the process of pinion generation is performed as variation of the shortest distance between the axes of the grinding worm and the pinion. The instantaneous shortest center distance $E_{wp}(\Delta s_w)$ between the grinding worm and the pinion is executed as [Fig. 17.7.5(b)]:

$$E_{wp}(\Delta s_w) = E_{wp}^{(0)} - a_{pl}(\Delta s_w)^2. \tag{17.7.8}$$

Here, Δs_w is measured along the pinion axis from the middle of the pinion; a_{pl} is the parabola coefficient of the function $a_{pl}(\Delta s_w)^2$; and $E_{wp}^{(0)}$ is the nominal value of the shortest distance defined by Eq. (17.7.7). Plunging of the worm with observation of Eq. (17.7.8) provides a parabolic function of transmission errors in the process of meshing of the pinion and the gear of the proposed new version of the Novikov–Wildhaber helical gear drive.

MODIFIED ROLL OF FEED MOTION. Conventionally, the feed motion of the worm is provided by observation of relation (17.7.6) between components Δs_w and $\Delta \psi_p$. For the purpose of pinion longitudinal crowning, the following function $\Delta \psi_p(\Delta s_w)$ is observed:

$$\Delta \psi_p(\Delta s_w) = \frac{\Delta s_w}{p} + a_{mr}(\Delta s_w)^2 \tag{17.7.9}$$

where a_{mr} is the parabola coefficient of the parabolic function in Eq. (17.7.9). Modified roll motion is provided to the worm instead of worm plunging. Application of function $\Delta \psi_p(\Delta s_w)$ enables us to modify the pinion tooth surface and provide a parabolic function of transmission errors of the proposed gear drive.

The derivation of double-crowned surface Σ_1 of the pinion by application of both previously mentioned approaches is based on determination of Σ_1 as a two-parameter enveloping process:

Step 1: We consider that surface Σ_w is determined as the envelope to the rack-cutter surface Σ_c. The determination of Σ_w is a one-parameter enveloping process.

Step 2: Double-crowned surface Σ_1 of the pinion is determined as an envelope of a two-parameter enveloping process by application of the following equations:

$$\mathbf{r}_1(u_w, \theta_w, \psi_w, s_w) = \mathbf{M}_{1w}(\psi_w, s_w)\mathbf{r}_w(u_w, \theta_w) \tag{17.7.10}$$

$$\mathbf{N}_w \cdot \mathbf{v}_w^{(w1,\psi_w)} = 0 \tag{17.7.11}$$

$$\mathbf{N}_w \cdot \mathbf{v}_w^{(w1,s_w)} = 0. \tag{17.7.12}$$

Here, (u_w, θ_w) are the worm surface parameters, and (ψ_w, s_w) are the generalized parameters of motion of the two-parameter enveloping process. Vector equation (17.7.10) represents the family of surfaces Σ_w of the worm in coordinate system S_1 of the pinion. Equations (17.7.11) and (17.7.12) represent two equations of meshing. Vector $\mathbf{N}_w$ is the normal to the worm tooth surface Σ_w and is represented in system S_w. Vector $\mathbf{v}_w^{(w1,\psi_w)}$ represents the relative velocity between the worm and pinion determined under the condition that parameter ψ_w of motion is varied and the other parameter s_w is held at rest. Vector $\mathbf{v}_w^{(w1,s_w)}$ is determined under the condition that parameter s_w is varied and the other parameter of motion ψ_w is held at rest. Both vectors of relative velocity are represented in coordinate system S_w. Vector equations (17.7.10), (17.7.11), and (17.7.12) (considered simultaneously) determine a double-crowned pinion tooth surface obtained by a two-parameter enveloping process (see Section 6.10).

17.8 TCA OF A GEAR DRIVE WITH A DOUBLE-CROWNED PINION

Simulation of meshing of a gear drive with a double-crowned pinion is investigated by application of the same algorithm discussed in Section 17.5 for a gear drive with a profile-crowned pinion and gear tooth surfaces. The TCA has been performed for the following cases:

(1) The new version of the Novikov–Wildhaber helical gear drive.
(2) The modified involute helical gear drive, whose design is based on the following ideas: (i) a pinion rack-cutter with a parabolic profile and a conventional gear rack-cutter with a straight profile are applied for the generation of the pinion and the gear, respectively; and (ii) the pinion of the gear drive is double-crowned.
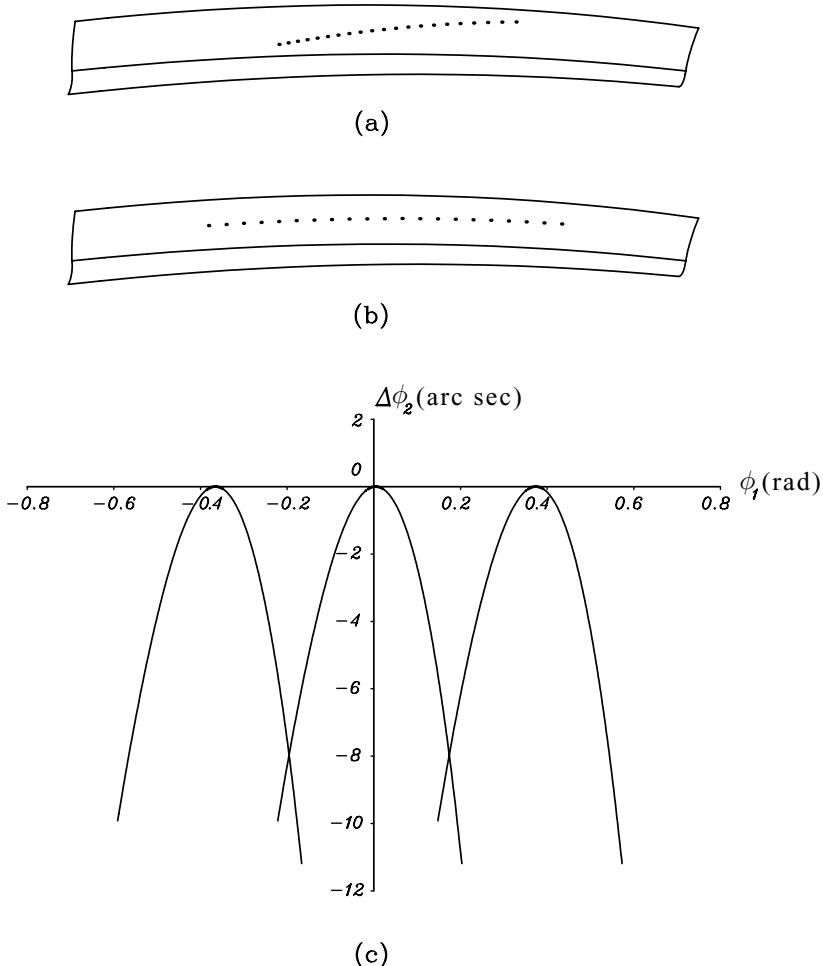
The applied design parameters are shown in Table 17.8.1 for both the new version of the Novikov–Wildhaber gear drive (case 1) and the modified involute helical gear

Table 17.8.1: Design parameters

Number of teeth of the pinion, N_1	17
Number of teeth of the gear, N_2	77
Module, m	5.08 mm
Driving-side pressure angle, α_d	25°
Coast-side pressure angle, α_c	25°
Helix angle, β	20°
Parameter of rack-cutter, b	0.7
Face width	90 mm
Radius of the worm pitch cylinder, r_w	98 mm
Parabolic coefficient of pinion rack-cutter[a], a_c	0.016739 mm^{-1}
Parabolic coefficient of gear rack-cutter[a], a_t	0.0155 mm^{-1}
Parabolic coefficient of plunging[a], a_{pl}	0.00005 mm^{-1}
Parabolic coefficient of pinion rack-cutter[b], a_c	0.016739 mm^{-1}
Parabolic coefficient of gear rack-cutter[b], a_t	0.0 mm^{-1}
Parabolic coefficient of plunging[b], a_{pl}	0.0000315 mm^{-1}
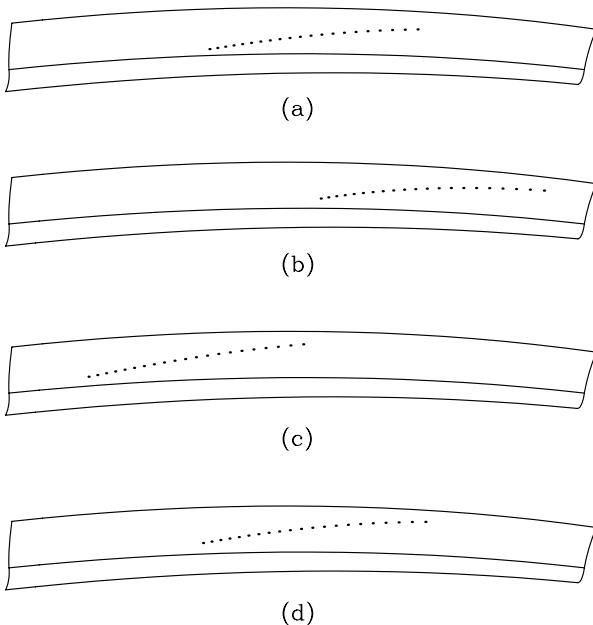
[a] Novikov–Wildhaber helical gear drive.
[b] Modified involute helical gear drive.

Figure 17.8.1: Output of TCA for a gear drive wherein the pinion is generated by plunging of the grinding worm: (a) path of contact and (c) function of transmission errors for the new version of the Novikov–Wildhaber helical gear drive; (b) path of contact for the modified involute helical gear drive.

drive (case 2). The same parabolic coefficient of profile crowning for the pinion rack-cutter a_c has been used for both the new version of the Novikov–Wildhaber gear drive and the modified involute helical gear drive. The parabolic coefficient of longitudinal crowning a_{pl} used in each case provides a limited error of 8 arcsec of the predesigned function of transmission errors for a gear drive without errors of alignment. Figures 17.8.1(a) and 17.8.1(b) show the path of contact for cases (1) and (2), respectively. Figure 17.8.1(c) shows the function of transmission errors for case (1). The function of transmission errors for case (2) is similar and also provides a maximum transmission error of 8 arcsec. The TCA output shows that a parabolic function of transmission errors is indeed obtained in the meshing of the pinion and the gear due to application of a double-crowned pinion.

The approaches chosen for TCA cover application of (i) a disk-shaped tool (Section 17.6), (ii) a plunging worm (Section 17.7), and (iii) modified roll of feed motion

(a)

(b)

(c)

(d)

Figure 17.8.2: Influence of errors of alignment in the shift of the path of contact for a Novikov–Wildhaber helical gear drive wherein the pinion is generated by plunging of the generating worm: (a) with error ΔE [70 μm]; (b) with error $\Delta \gamma$ [3 arcmin]; (c) with error $\Delta \lambda$ [3 arcmin]; (d) with $\Delta \gamma + \Delta \lambda_1 = 0$ arcmin.

(Section 17.7). These approaches yield almost the same output of TCA. The simulation of meshing is performed for the following errors of alignment: (i) change of center distance $\Delta E = 70$ μm, (ii) change of shaft angle $\Delta \gamma = 3$ arcmin, (iii) error $\Delta \lambda = 3$ arcmin, and (iv) combination of errors $\Delta \gamma$ and $\Delta \lambda$ as $\Delta \gamma + \Delta \lambda = 0$.

The results of TCA accomplished for the design parameters represented in Table 17.8.1 are as follows:

(1) Figures 17.8.1(a) and 17.8.1(b) show that the paths of contact of aligned gear drives are oriented longitudinally in both cases of design Novikov–Wildhaber gears and modified helical gears. Deviation from the longitudinal direction is less for modified involute helical gear drives in comparison with the new version of the Novikov–Wildhaber helical gear drive. However, the advantage of the new Novikov–Wildhaber gear drive is the reduction of stresses (see Section 17.10).

(2) Figures 17.8.2(a), 17.8.2(b), and 17.8.2(c) show the shift of the paths of contact caused by errors of alignment ΔE, $\Delta \gamma$, and $\Delta \lambda$, respectively. The shift of paths of contact caused by $\Delta \gamma$ may be compensated by correction $\Delta \lambda_1$ of the pinion (or $\Delta \lambda_2$ of the gear). Figure 17.8.2(d) shows that the location of the path of contact can be restored by correction of $\Delta \lambda_1$ of the pinion by taking $\Delta \gamma + \Delta \lambda_1 = 0$. This means that correction of $\Delta \lambda_1$ can be used for the restoration of the location of the path of contact. Correction of $\Delta \lambda_1$ or $\Delta \lambda_2$ may be applied in the process of generation of the pinion or the gear, respectively.

It was previously mentioned (see Section 17.5) that double crowning of the pinion provides a predesigned parabolic function of transmission errors. Therefore, linear functions of transmission errors caused by $\Delta\gamma$, $\Delta\lambda$, and other errors are absorbed by the predesigned parabolic function of transmission errors $\Delta\phi_2(\phi_1)$. The final function of transmission errors $\Delta\phi_2(\phi_1)$ remains a parabolic one. However, increase of the magnitude of errors $\Delta\gamma$ and $\Delta\lambda$ may result in the final function of transmission errors $\Delta\phi_2(\phi_1)$ becoming a *discontinued* one. In such a case, the predesigned parabolic function $\Delta\phi_2(\phi_1)$ has to be of larger magnitude or it becomes necessary to limit the range of $\Delta\gamma$, $\Delta\lambda$, and other errors.

17.9 UNDERCUTTING AND POINTING

The pinion of the drive is more sensitive to undercutting than the gear because the pinion has a smaller number of teeth.

Undercutting
Avoidance of undercutting is applied to pinion tooth surface Σ_σ and is based on the following ideas:

 (i) The appearance of singular points on generated surface Σ_σ is the warning that the surface may be undercut in the process of generation [Litvin, 1989].
 (ii) Singular points on surface Σ_σ are generated by regular points on the generating surface Σ_c when the velocity of a contact point in its motion over Σ_σ becomes equal to zero [Litvin, 1989; Litvin, 1994]:

$$\mathbf{v}_r^{(\sigma)} = \mathbf{v}_r^{(c)} + \mathbf{v}^{(c\sigma)} = 0. \qquad (17.9.1)$$

(iii) Equation (17.9.1) and differented equation of meshing

$$\frac{d}{dt}[f(u_c, \theta_c, \psi_\sigma)] = 0 \qquad (17.9.2)$$
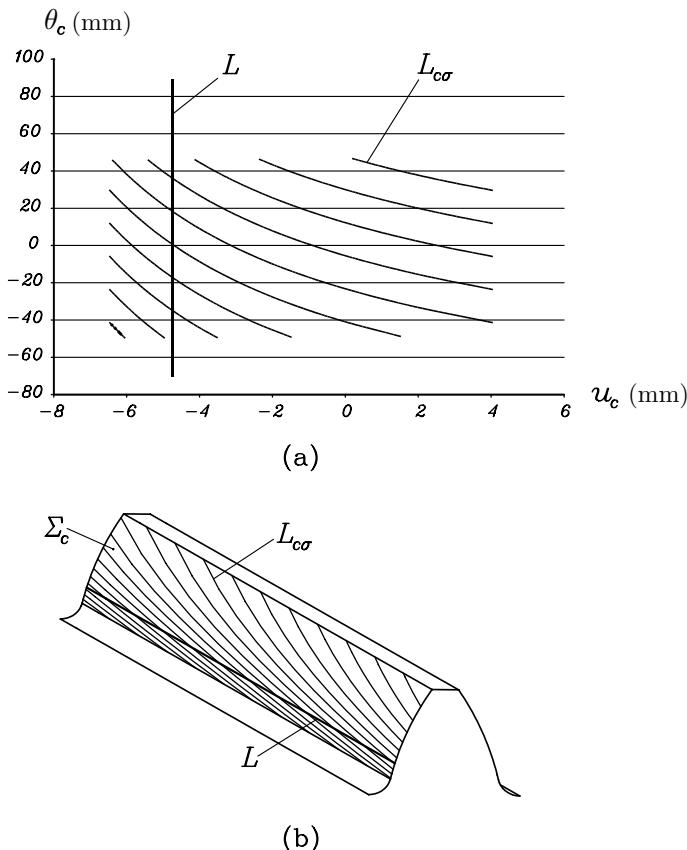
allow us to determine a function

$$F(u_c, \theta_c, \psi_\sigma) = 0 \qquad (17.9.3)$$

that relates parameters u_c, θ_c, and ψ_σ at a point of singularity of surface Σ_σ.

The limitation of generating surface Σ_c for avoidance of singularities of generated surface Σ_σ is based on the following procedure:

(1) Using equation of meshing $f_{\sigma c}(u_c, \theta_c, \psi_\sigma) = 0$ between the rack-cutter and the pinion, we may obtain in plane of parameters (u_c, θ_c) the family of contact lines of the rack-cutter and the pinion. Each contact line is determined for a fixed parameter of motion ψ_σ.
(2) The sought-for limiting line L [Fig. 17.9.1(a)] that limits the rack-cutter surface is determined in the space of parameters (u_c, θ_c) by simultaneous consideration of equations $f_{\sigma c} = 0$ and $F = 0$ [Fig. 17.9.1(a)]. Then we can obtain the limiting
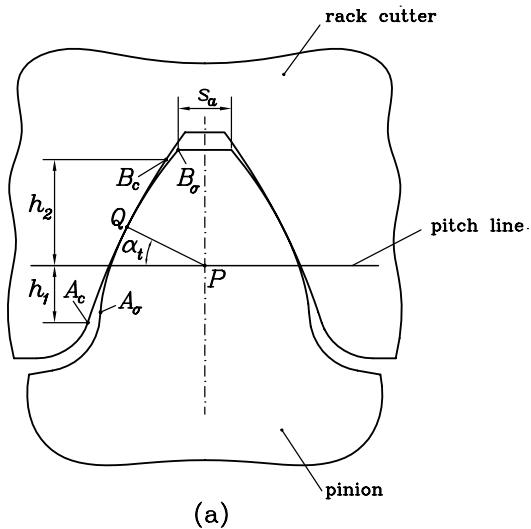
Figure 17.9.1: Contact lines $L_{\sigma c}$ and limiting line L: (a) in plane (u_c, θ_c), and (b) on surface Σ_c.

line L on the surface of the rack-cutter [Fig. 17.9.1(b)]. The limiting line L on the rack-cutter surface is formed by *regular* points of the rack-cutter, but these points will generate *singular* points on the pinion tooth surface.

Limitations of the rack-cutter surface by L enables us to avoid singular points on the pinion tooth surface. Singular points on the pinion tooth surface can be obtained by coordinate transformation of line L on rack-cutter surface Σ_c to surface Σ_σ.
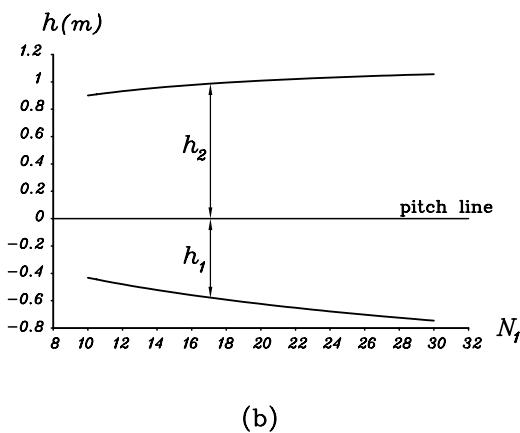
Pointing
Pointing of the pinion means that the width of the topland becomes equal to zero. Figure 17.9.2(a) shows cross sections of the pinion and the pinion rack-cutter. Point A_c of the rack-cutter generates the point A_σ that is the limiting point of the cross section of the pinion tooth surface which is still free of singularities. Point B_c of the rack-cutter generates point B_σ of the pinion profile. Parameter s_a indicates the chosen width of the pinion topland. Parameter α_t indicates the pressure angle at point Q. Parameters h_1 and h_2 indicate the limitation of location of limiting points A_c and B_c of the rack-cutter profiles. Figure 17.9.2(b) shows functions $h_1(N_1)$ and $h_2(N_1)$ (N_1 is the pinion tooth number) obtained for the following data: $\alpha_d = 25°$, $\beta = 20°$, parabola

Figure 17.9.2: Permissible dimensions h_1 and h_2 of rack-cutter: (a) cross sections of pinion and rack-cutter; (b) functions $h_1(N_1)$ and $h_2(N_1)$.

coefficient of pinion rack-cutter $a_c = 0.016739$ mm^{-1}, $s_a = 0.3m$, parameter $s_{12} = 1.0$ [see Eq. (17.3.2)], and module $m = 1$ mm. Functions $h_1(N_1)$ and $h_2(N_2)$ are obtained as discussed in Section 15.8.

17.10 STRESS ANALYSIS

Stress analysis and investigation of formation of bearing contact have been performed: (i) for the proposed new version of Novikov–Wildhaber, and (ii) for a gear drive with modified involute helical gears. The second type of gearing has been proposed by patent [Litvin *et al.*, 2001c] and is formed by a double-crowned helical pinion and a conventional involute helical gear. The second type of gear drive has been predesigned with a parabolic function of transmission errors, similar to the function of transmission errors of the proposed version of Novikov–Wildhaber gear drives (see Section 17.8).
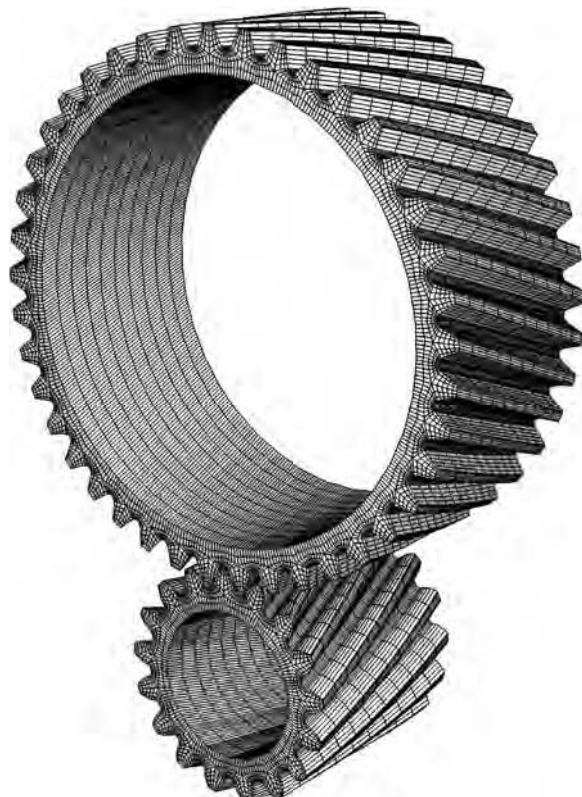
The difference between the two types of gear drives that have been investigated is that the Novikov–Wildhaber gear drives are generated by two parabolic rack-cutters that

are in internal tangency, whereas the modified involute helical gears are generated by application of two rack-cutters that are in external tangency. The pinion rack-cutter has a parabolic profile and the gear rack-cutter is a conventional one and has a conventional straight-line profile. Comparison of obtained bending and contact stresses confirms several advantages of the new version of Novikov–Wildhaber gear drives. The performed stress analysis is based on the finite element method [Zienkiewicz & Taylor, 2000] and application of a general computer program [Hibbit, Karlsson & Sirensen, Inc., 1998].
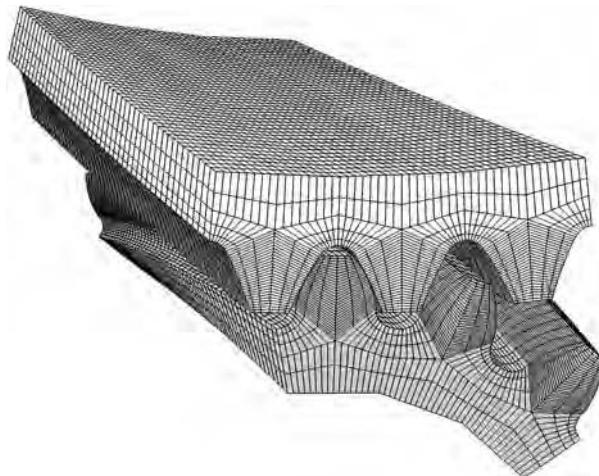
Development of Finite Element Models

The approach followed for finite element models is summarized in Section 9.5 and has the following characteristics:
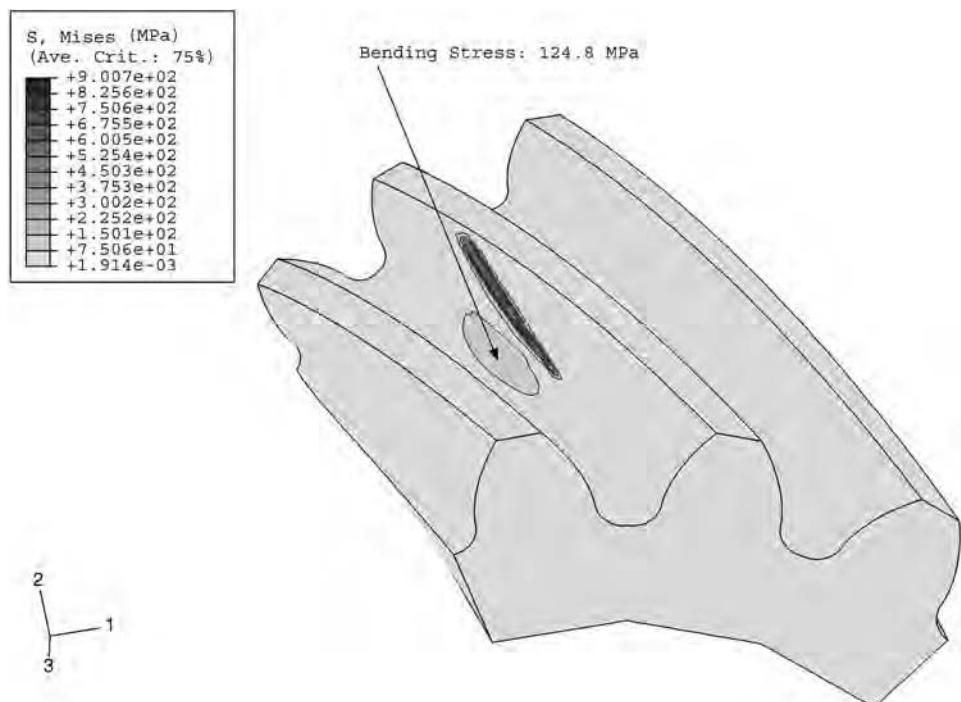
(i) Finite element models of the gear drive are automatically obtained for any position of pinion and gear obtained from tooth contact analysis (TCA). Stress convergence is assured because there is at least one point of contact between contacting surfaces.

(ii) Assumption of load distribution in the contact area is not required because the algorithm of contact of the general computer program [Hibbit, Karlsson & Sirensen, Inc., 1998] will determine it by application of torque to the pinion, whereas the gear is considered at rest.

(iii) Finite element models of any number of teeth can be obtained. As an example, Figure 17.10.1 shows a whole gear drive finite element model. However, three- or
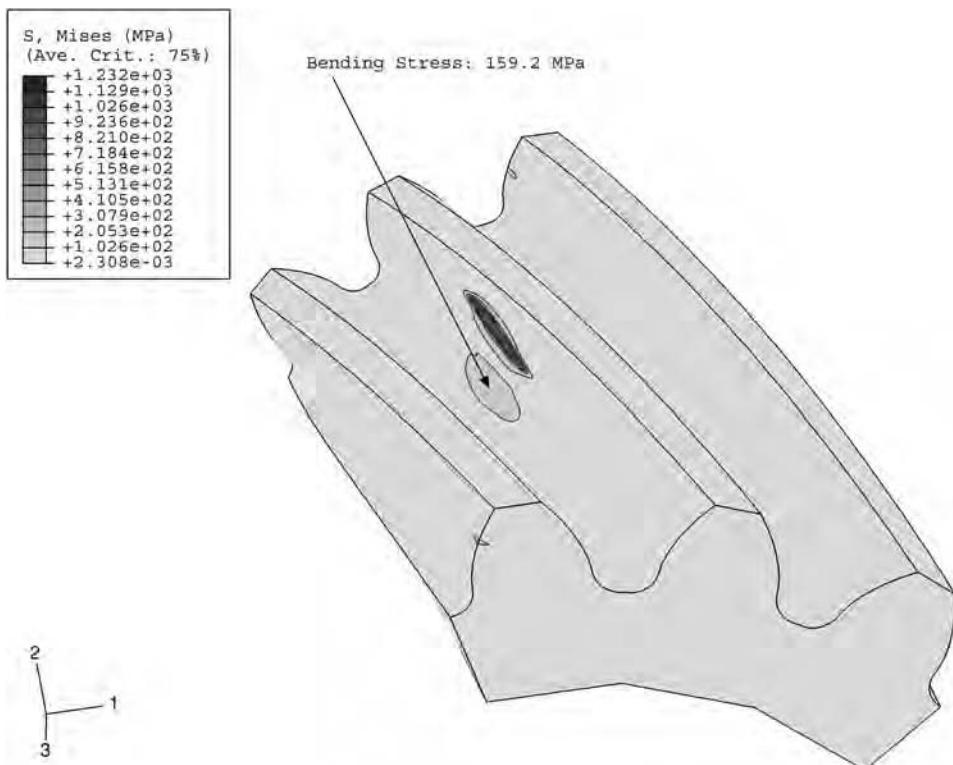
Figure 17.10.1: Whole gear drive finite element model.

Figure 17.10.2: Finite element model with three pairs of teeth.

Figure 17.10.3: Contact and bending stresses at the middle point of the path of contact on the pinion tooth surface for a Novikov–Wildhaber gear drive wherein the generation is performed by plunging of the grinding worm.

Figure 17.10.4: Contact and bending stresses at the middle point of the path of contact on the pinion tooth surface for a modified involute helical gear drive wherein the generation is performed by plunging of the grinding worm.

five-tooth models are more adequate for consideration of a more refined mesh that will allow the contact ellipses to be determined accurately. The use of several pairs of contacting teeth in the finite element models has the following advantages:
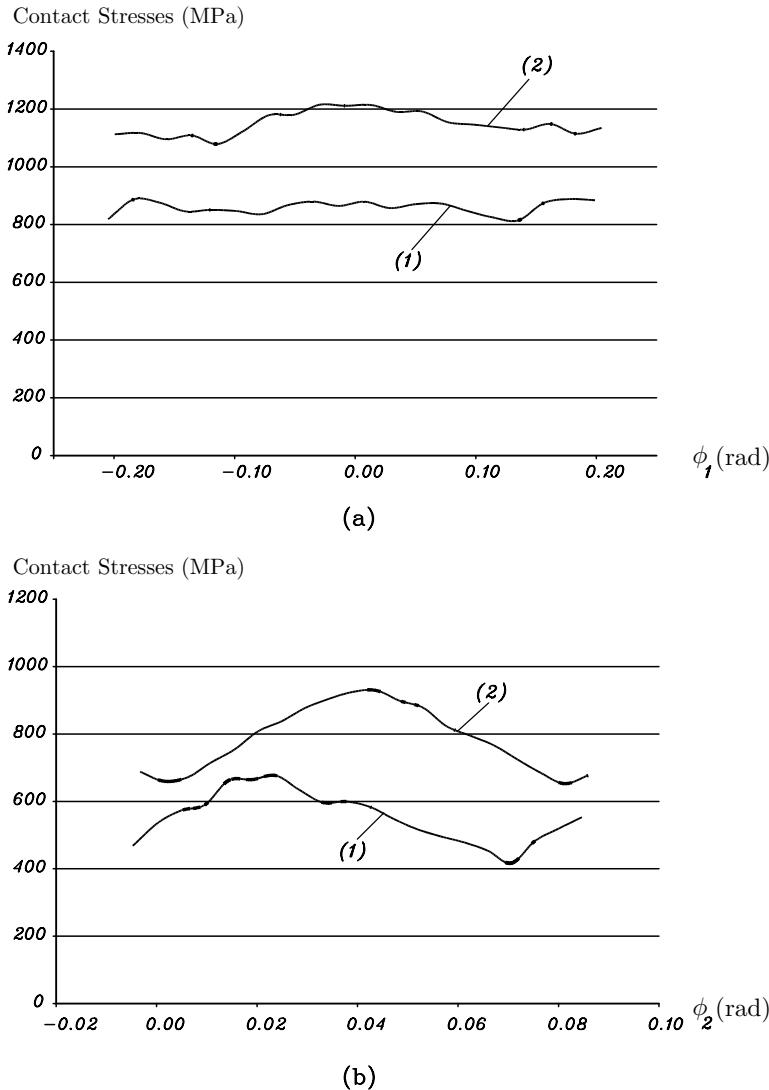
(a) Boundary conditions are far enough from the loaded areas of the teeth.
(b) Simultaneous meshing of two pairs of teeth can occur due to the elasticity of surfaces. Therefore, the load transition at the beginning and at the end of the path of contact can be studied.

Numerical Example

Finite element analyses have been performed for the following cases:
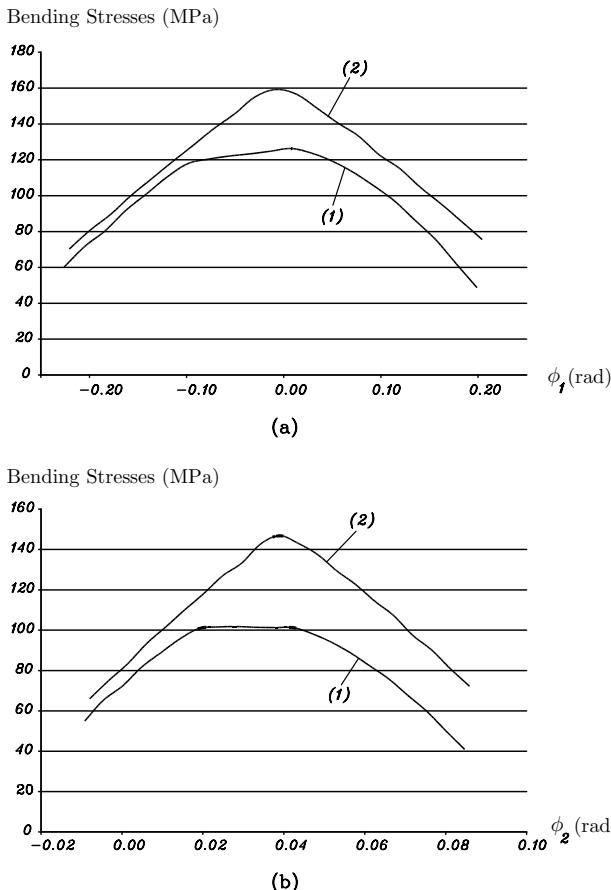
(1) the new version of the Novikov–Wildhaber helical gear drive
(2) a modified involute helical gear drive.

The applied design parameters are shown in Table 17.8.1 (see Section 17.8). The output of TCA [see Figs. 17.8.1(a) and 17.8.1(b)] allows the designer to design the finite element model at any point of contact.

Contact Stresses (MPa)

(a)

Contact Stresses (MPa)

(b)

Figure 17.10.5: Variation of functions of contact stresses during the cycle of meshing for the two gear drives of design (1) and (2) for (a) the pinion and (b) the gear.

A three-tooth model is applied for each chosen point of the path of contact. Elements C3D8I [Hibbit, Karlsson & Sirensen, Inc., 1998] of first order (enhanced by incompatible modes to improve their bending behavior) are used to form the finite element mesh. The total number of elements is 71,460 with 87,360 nodes. The material is steel with the properties of Young's Modulus $E = 2.068 \times 10^5$ MPa and Poisson's ratio of 0.29. A torque of 500 Nm is applied to the pinion in both cases. Figure 17.10.2 shows the finite element mesh for case (1) at the mean contact point. Figures 17.10.3 and 17.10.4 show the maximum contact and bending stresses obtained at the mean contact point for cases (1) and (2), respectively.

Bending Stresses (MPa)

(a)

Bending Stresses (MPa)

(b)

Figure 17.10.6: Variation of functions of bending stresses during the cycle of meshing for the two gear drives of design (1) and (2) for (a) the pinion and (b) the gear.

Figures 17.10.5 and 17.10.6 illustrate the variation of contact and bending stresses, respectively, for both cases. A substantial reduction of contact stresses has been achieved by using the new version of Novikov–Wildhaber helical gear drive in comparison with the gear drive of modified helical gears. Bending stresses are reduced as well. The results obtained confirm reduction of stresses with the proposed Novikov–Wildhaber gear drive in comparison with the modified involute helical gear drive.

18 Face-Gear Drives

18.1 INTRODUCTION

A conventional face-gear drive is formed by an involute spur pinion and a conjugated face-gear (Fig. 18.1.1). Such a gear drive may be applied for transformation of rotation between intersected and crossed axes. An important example of application of a face-gear drive with intersected axes is in the helicopter transmission (Fig. 18.1.2).
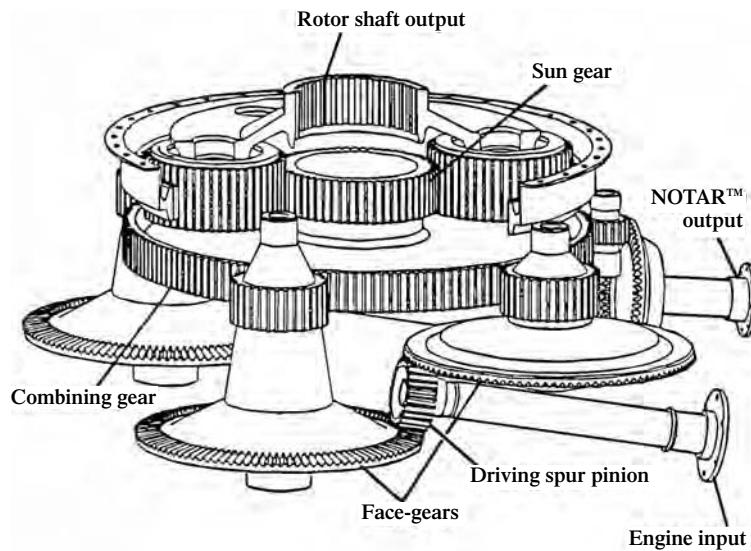
The manufacturing of face-gears by a shaper was invented by the Fellow Corporation. The basic idea of generation is based on simulation of meshing of the generating shaper with the face-gear being generated as the meshing of the pinion of the drive with the face-gear. In the process of generation, the surfaces of the teeth of the shaper and the face-gear are in *line contact* at every instant. However, when the shaper is exactly identical to the pinion of the face-gear drive, the generated face-gear drive becomes sensitive to misalignment. This causes an undesirable shift of the bearing contact and even separation of the surfaces. Therefore, it is necessary to provide an instantaneous *point contact* between the tooth surfaces of the pinion and the face-gear instead of a line contact. Then, the bearing contact will be localized and the face-gear drive will be less sensitive to misalignment. Point contact between the pinion and face-gear tooth surfaces is provided by application of a shaper of number of teeth $N_s > N_p$ where N_p is the number of teeth of the pinion of the drive (see Section 18.4).

The geometry, design, manufacturing, and recently stress analysis of face-gear drives were subjects of research of many researchers (Davidov [1950], Litvin *et al.* [1992, 2000a, 2002b], Handschuh *et al.* [1996]). A method of grinding of face-gears by a worm of a special shape [Litvin *et al.*, 2000a] has been recently invented (Fig. 18.1.3). Grinding of the spur pinion of the drive does not cause difficulties. The possibility of grinding of the face-gear and the pinion of the drive enables us to harden the tooth surfaces and to increase the permissible contact stresses. The worm shown in Fig. 18.1.3 may be also applied as the basis of design of a hob for generation of face-gears (instead of their generation by a shaper). The number of turns of the thread of the worm has to be limited to avoid appearance of singularities on the worm surface (see Section 18.14). Threads with singularities are indicated in Fig. 18.1.3 by "A."
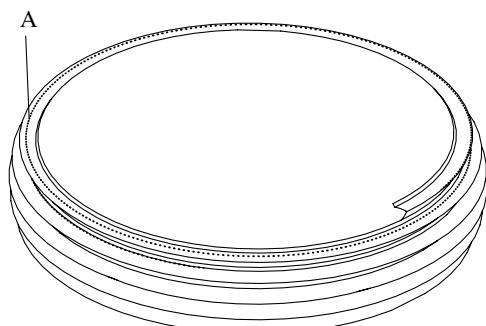
The structure of a face-gear tooth is shown in Fig. 18.1.4(a). The surface of the tooth consists of two parts: (i) the working part formed by lines L_{2s} of tangency of the shaper and the face-gear, and (ii) the fillet surface generated by the edge of the top of the
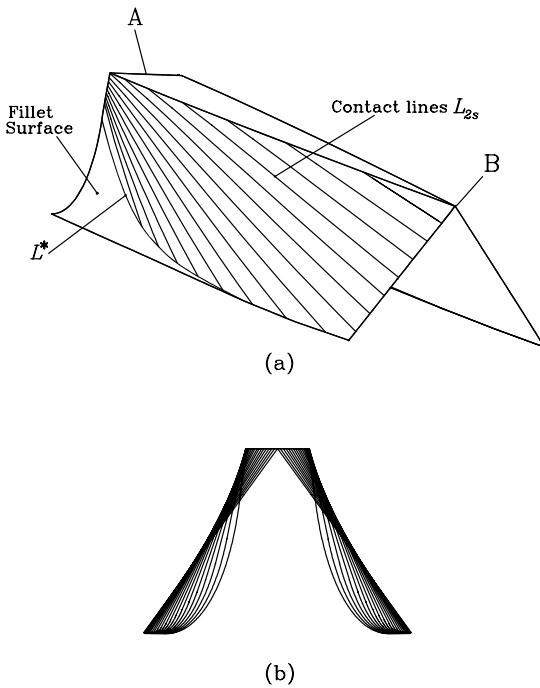
**Figure 18.1.1:** Face-gear drive in 3D-space.

**Figure 18.1.2:** Application of face-gear drive in helicopter transmission.

Figure 18.1.3: Illustration of worm applied for grinding of face-gears. Designation "A" indicates thread surfaces with singularities.

(a)

(b)

Figure 18.1.4: Structure of face-gear tooth: (a) contact lines L_{2s} and fillet; (b) cross sections of face-gear tooth.

shaper. Line L^* is the common line of the fillet and the working part of the surface. Figure 18.1.4(b) shows the cross sections of the tooth surface.

While designing a face-gear drive, it is necessary to avoid possible undercutting in area "A" and tooth pointing in area "B" [Fig. 18.1.4(a) and Sections 18.6 and 18.7].

18.2 AXODES, PITCH SURFACES, AND PITCH POINT

The concepts of *axodes*, *pitch surfaces*, and *pitch point* are important for the visualization of meshing of face-gear drives.

Axodes
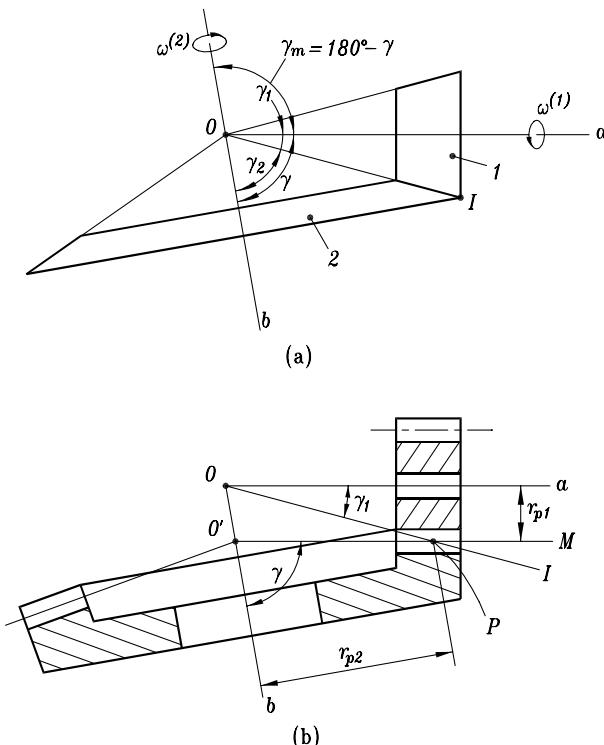
Consider that rotation is performed between the intersected axes Oa–Ob that form angle γ [Fig. 18.2.1(a)]. The gear ratio is

$$m_{12} = \frac{\omega^{(1)}}{\omega^{(2)}} = \frac{N_2}{N_1} \tag{18.2.1}$$

where $\omega^{(i)}$ and N_i are the angular velocity and the number of teeth, respectively, for the pinion ($i = 1$) and the face-gear ($i = 2$).

The axodes are two cones of semiangles γ_1 and γ_2 that are determined with the equations (see Section 3.4)

$$\cot \gamma_1 = \frac{m_{12} + \cos \gamma}{\sin \gamma}, \quad \cot \gamma_2 = \frac{m_{21} + \cos \gamma}{\sin \gamma} = \frac{1 + m_{12} \cos \gamma}{m_{12} \sin \gamma} \tag{18.2.2}$$

Figure 18.2.1: Axodes and pitch cones.
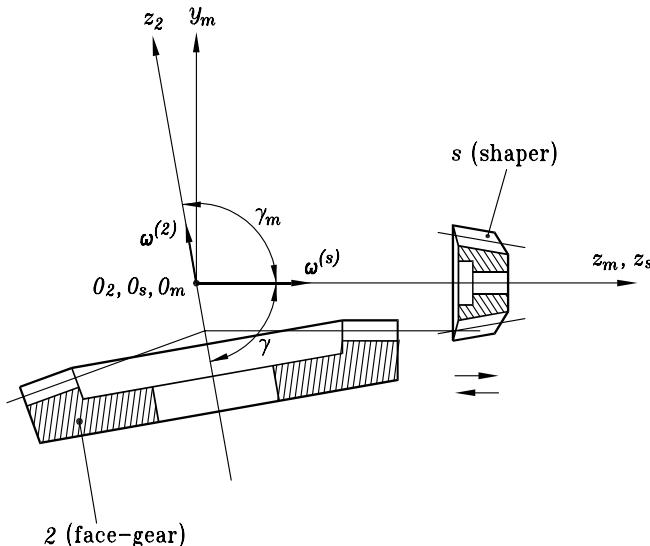
where

$$m_{21} = \frac{1}{m_{12}}.$$

The line of tangency of the cones, OI, is the *instantaneous axis of rotation* in relative motion. An axode is the family of instantaneous axes of rotation that is generated in coordinate systems S_i ($i = 1, 2$) rigidly connected to pinion 1 and gear 2, respectively. The axodes are the *pitch cones* of the bevel gear drive. These cones are used as the basis for the design of a bevel gear drive.

Pitch Surfaces
A face-gear drive is formed by a pinion and a face-gear that is conjugated to the pinion. The reference surfaces (pitch surfaces) of a face-gear drive are (i) the cylinder of radius r_{p1} as the pitch surface of the pinion, and (ii) the cone of semiangle γ as the pitch surface of the face-gear [Fig. 18.2.1(b)]. In the case of crossing angle $\gamma = 90°$, the pitch surface of the face-gear is a plane. The *pitch line* is $O'M$, the line of tangency of the pitch surfaces. We call point P, the point of intersection of the pitch line ($O'M$) with the instantaneous axis of rotation (OI), the *pitch point*. The variation of location of the pitch point on the instantaneous axis of rotation affects the conditions of pointing of the face-gear teeth and the dimensions of the area of meshing (see Section 18.3). The

Figure 18.3.1: Face-gear generation.

relative motion at point P is pure rolling, and sliding and rolling at other points of the pitch line $O'M$.

18.3 FACE-GEAR GENERATION
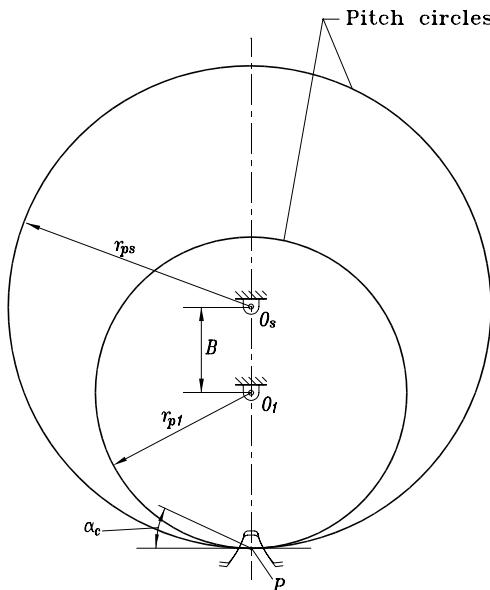
The generation of a face-gear by a shaper is shown in Fig. 18.3.1. The shaper and the gear perform rotation between intersected axes with angular velocities $\omega^{(s)}$ and $\omega^{(2)}$ that are related as

$$\frac{\omega^{(s)}}{\omega^{(2)}} = \frac{N_2}{N_s} \tag{18.3.1}$$

where N_s and N_2 are the tooth numbers of the shaper and the face-gear, respectively. The shaper also performs a reciprocating motion (the feed motion) in the direction of the generatrix of the face-gear cone that is parallel to the shaper axis. It is obvious that the axes of the shaper and the face-gear form angle γ which is equal to the angle formed by the axes of the pinion and the face-gear [Fig. 18.2.1(b)]. Angle γ_m is defined as $\gamma_m = 180° - \gamma$.

18.4 LOCALIZATION OF BEARING CONTACT

The process for generation of the face-gear is an exact simulation of meshing of the pinion with the face-gear if the shaper is an identical copy of the pinion, with the same number of teeth. However, such a process for generation cannot be applied in practice, as the face-gear drive is likely to be misaligned. This is why the bearing contact between the pinion and the face-gear must be localized, and this can be
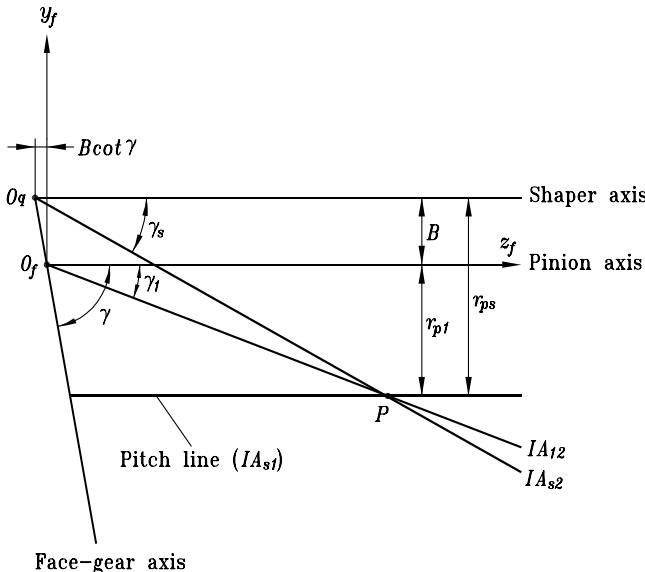
Figure 18.4.1: Tangency of pinion and shaper tooth profiles.

achieved if the process for generation provides an instantaneous *point* contact between the tooth surfaces of the pinion and the face-gear, instead of instantaneous *line* contact.

The localization of the bearing contact is based on the following ideas:

(i) The tooth number N_s of the shaper is chosen to be larger than the tooth number N_1 of the pinion. Usually, $N_s - N_1$ is chosen to be 2 or 3.

(ii) The installation of the shaper for generation simulates an imaginary internal meshing of shaper "s" with pinion "1, " as shown exaggeratedly in Fig. 18.4.1.

(iii) The axodes in meshing of the shaper and the pinion are the pitch cylinders of radii r_{ps} and r_{p1} (Fig. 18.4.1). The tangent to the pitch cylinders is parallel to the axes of rotation of the shaper and the pinion, passes through the pitch point P, and is the instantaneous axis of rotation IA_{s1} in the relative motion of the shaper with respect to the pinion (Fig. 18.4.2).

(iv) We may consider now that three surfaces, Σ_s, Σ_2, and Σ_1 are in mesh simultaneously. Surfaces Σ_s and Σ_2 are in *line* contact at every instant in the process of generation of the face-gear by the shaper. Surfaces Σ_s and Σ_1 are in *line* contact at every instant in the process of imaginary meshing of the shaper and the pinion. The generated face-gear tooth surface Σ_2 and the pinion tooth surface Σ_1 are in *point* contact at every instant.

(v) Figure 18.4.2 illustrates the location and orientation of the instantaneous axes of rotation in the meshing of Σ_s, Σ_2, and Σ_1. The instantaneous axes of rotation are designated as IA_{s2}, IA_{s1}, and IA_{12}. The subscripts "$s2$," "$s1$," and "12" indicate that the respective meshings between "s" and "2, " "s" and "1, " and "1" and "2" are considered. Angle γ_s that is formed between the shaper axis and IA_{s2} is

Figure 18.4.2: Instantaneous axes of rotation.

determined with the equation
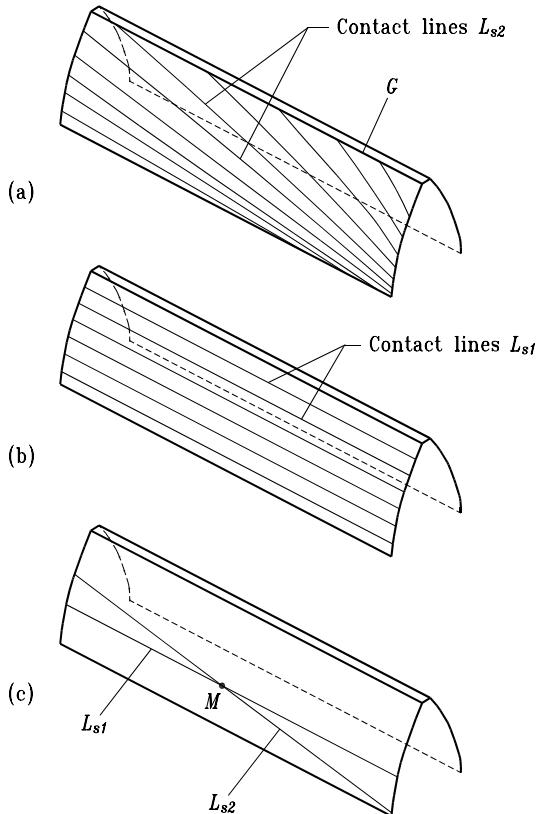
$$\cot \gamma_s = \frac{m_{s2} + \cos \gamma}{\sin \gamma} = \frac{\dfrac{N_2}{N_s} + \cos \gamma}{\sin \gamma} \qquad (18.4.1)$$

which is similar to Eq. (18.2.2) for determination of γ_1. The instantaneous axis of rotation IA_{s1} coincides with the pitch line. All three instantaneous axes of rotation intersect each other at point P which may be called the *pitch point*. The shortest distance B between the axes of the pinion and the shaper is determined as

$$B = r_{ps} - r_{p1} = \frac{N_s - N_1}{2 P_d}. \qquad (18.4.2)$$

(vi) We have to distinguish between the contact lines L_{s2} and L_{s1} that are represented on the shaper tooth surface Σ_s [Figs. 18.4.3(a) and 18.4.3(b)]. The contact lines correspond to the meshing of the shaper with face-gear 2 and pinion 1, respectively. The current instantaneous point of tangency of surfaces Σ_2 and Σ_1 is represented on surface Σ_s as point M that is the point of intersection of respective current contact lines L_{s1} and L_{s2} [Fig. 18.4.3(c)].

We may determine the *path of contact* of surfaces Σ_1 and Σ_2 (the set of instantaneous points of contact between Σ_1 and Σ_2) using the following consideration: the normal to the generating surface Σ_s at the instantaneous contact point M [Fig. 18.4.3(c)] must pass through the pitch point P [Figs. 18.4.2 and 18.2.1(b)]. Detailed derivations of the path of contact are discussed in Section 18.13.

Figure 18.4.3: Contact lines on shaper tooth surface: (a) lines L_{s2} in meshing of shaper "s" with face-gear "2"; (b) lines L_{s1} in meshing of shaper "s" with pinion "1" of a face-gear drive wherein $N_s > N_1$; (c) determination of point M of intersection of lines L_{s2} and L_{s1}.

18.5 EQUATIONS OF FACE-GEAR TOOTH SURFACE

Generation by Involute Shaper
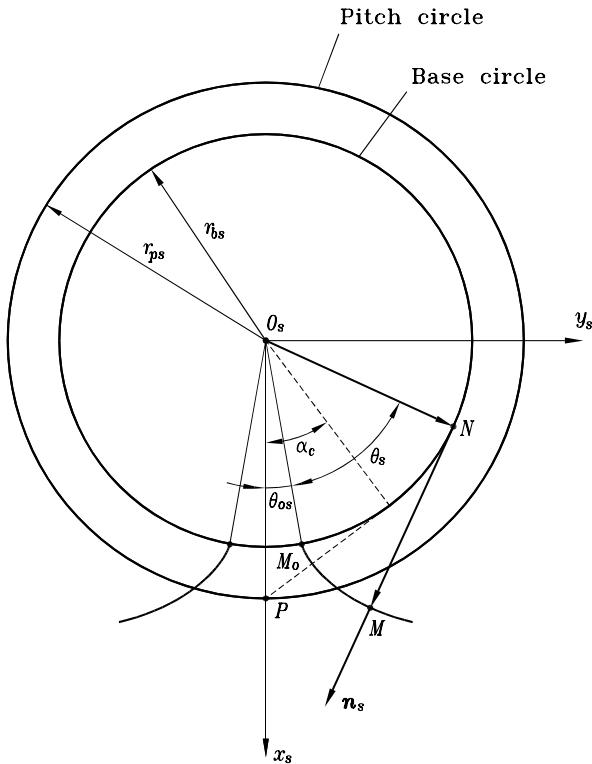
We consider two types of geometry of face-gear drives wherein (i) the face-gear is generated by an involute shaper (presented in this section), and (ii) the face-gear is generated by a shaper conjugated to a parabolic rack-cutter (Section 18.9).

Shaper Tooth Surfaces

Plane $y_s = 0$ is the plane of symmetry of the space of the shaper (Fig. 18.5.1). Limiting the discussion to the right-side of the space with the involute profile $M_0 M$ in the cross section, we represent the position vector $\overline{O_s M}$ of current point M by the vector equation

$$\overline{O_s M} = \overline{O_s N} + \overline{NM} \quad \left(|\overline{NM}| = \overset{\frown}{M_o N} = r_{bs} \theta_s \right). \tag{18.5.1}$$

Here, θ_s is the parameter of the involute profile. Using Eq. (18.5.1) and designating by u_s the surface parameter of shaper tooth surface Σ_s in the direction of z_s, we represent

Figure 18.5.1: For derivation of equations of the involute profile of the shaper.

surface Σ_s by the vector function
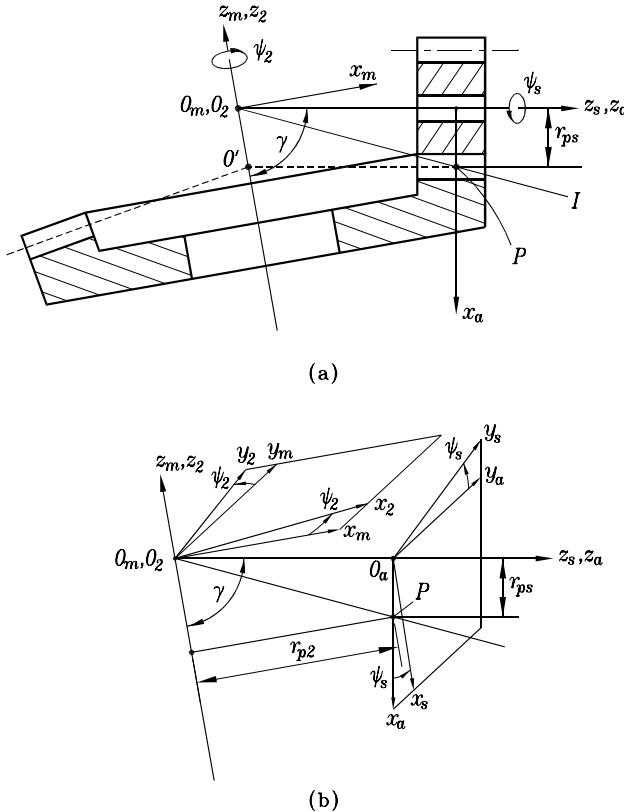
$$
\mathbf{r}_s(u_s, \theta_s) = \begin{bmatrix} r_{bs}[\cos(\theta_{0s} + \theta_s) + \theta_s \sin(\theta_{0s} + \theta_s)] \\ r_{bs}[\sin(\theta_{0s} + \theta_s) - \theta_s \cos(\theta_{0s} + \theta_s)] \\ u_s \\ 1 \end{bmatrix}. \tag{18.5.2}
$$

Here, r_{bs} is the radius of the shaper base circle, and θ_{0s} determines half of the width of the space of the shaper on the base circle (Fig. 18.5.1). Parameter θ_{0s} for a standard shaper is represented by the equation

$$
\theta_{0s} = \frac{\pi}{2N_s} - \operatorname{inv}\alpha_c \tag{18.5.3}
$$

where α_c is the pressure angle, and N_s is the tooth number of the shaper.
The unit normal to the shaper tooth surface is represented as (Fig. 18.5.1)

$$
\mathbf{n}_s = \frac{\mathbf{N}_s}{|\mathbf{N}_s|} = \begin{bmatrix} \sin(\theta_{0s} + \theta_s) \\ -\cos(\theta_{0s} + \theta_s) \\ 0 \end{bmatrix}. \tag{18.5.4}
$$

(a)

(b)

Figure 18.5.2: Coordinate systems applied for generation of face-gear surface Σ_2: (a) illustration of installation; (b) for derivation of coordinate transformation.

Face-Gear Tooth Surface Σ_2

Surface Σ_2 is determined as the envelope to the family of shaper tooth surfaces Σ_s. We apply for derivations the following coordinate systems: (i) movable coordinate systems S_s and S_2 rigidly connected to the shaper and the face-gear (Fig. 18.5.2), and (ii) fixed coordinate systems S_a and S_m. Coordinate axis $O_a x_a$ passes through pitch point P (Fig. 18.5.2).

During the generation, the shaper and the face-gear perform rotations about axes z_a and z_m related as follows:

$$\frac{\psi_s}{\psi_2} = \frac{N_2}{N_s}. \tag{18.5.5}$$

The family of shaper surfaces Σ_s is represented in coordinate system S_2 by the matrix equation [Fig. 18.5.2(b)]

$$\mathbf{r}_2(u_s, \theta_s, \psi_s) = \mathbf{M}_{2m}\mathbf{M}_{ma}\mathbf{M}_{as}(\psi_s)\mathbf{r}_s(u_s, \theta_s). \tag{18.5.6}$$

Here,

$$\mathbf{M}_{as}(\psi_s) = \begin{bmatrix} \cos \psi_s & -\sin \psi_s & 0 & 0 \\ \sin \psi_s & \cos \psi_s & 0 & 0 \\ 0 & 0 & 1 & 0 \\ 0 & 0 & 0 & 1 \end{bmatrix} \tag{18.5.7}$$

$$\mathbf{M}_{ma} = \begin{bmatrix} -\cos \gamma & 0 & \sin \gamma & r_{p2} \\ 0 & 1 & 0 & 0 \\ -\sin \gamma & 0 & -\cos \gamma & -r_{p2} \cot \gamma \\ 0 & 0 & 0 & 1 \end{bmatrix} \tag{18.5.8}$$

where γ is formed by the axes of the shaper and the face-gear as shown in Fig. 18.5.2, and

$$\mathbf{M}_{2m} = \begin{bmatrix} \cos \psi_2 & \sin \psi_2 & 0 & 0 \\ -\sin \psi_2 & \cos \psi_2 & 0 & 0 \\ 0 & 0 & 1 & 0 \\ 0 & 0 & 0 & 1 \end{bmatrix}. \tag{18.5.9}$$

The equation of meshing is determined as (see Section 6.1)

$$\mathbf{n}_s \cdot \mathbf{v}_s^{(s2)} = f_{s2}(u_s, \theta_s, \psi_s) = 0. \tag{18.5.10}$$

Computerized determination of relative velocity $\mathbf{v}_s^{(s2)}$ is based on the procedure presented in Section 2.2. Designations in Figs. 18.5.2(a) and 18.5.2(b) indicate the angle γ formed by negative axis z_m and z_a, the radii r_{ps} and r_{p2} of pitch circles of the shaper and the face-gear, and the pitch point P [see Fig. 18.2.1(b)].

Surface Σ_2 of the face-gear is determined in three-parameter form by vector equation $\mathbf{r}_2(u_s, \theta_s, \psi_s)$ and equation of meshing $f_{s2} = 0$. Surface Σ_s may be represented in two-parameter form using the theorem of implicit function system existence. The procedure is as follows [Zalgaller & Litvin, 1977]:

(i) Consider that equation $f_{s2} = 0$ is satisfied at a point $(u_s^{(0)}, \theta_s^{(0)}, \psi_s^{(0)})$, and at this point

$$\frac{\partial f_{s2}}{\partial u_s} \neq 0. \tag{18.5.11}$$

(ii) Then, equation $f_{s2} = 0$ may be solved by function

$$u_s = u_s(\theta_s, \psi_s) \in C^1, \tag{18.5.12}$$

and surface Σ_2 may be represented as

$$\mathbf{r}_2(u_s(\theta_s, \psi_s), \theta_s, \psi_s) = \mathbf{R}_2(\theta_s, \psi_s). \tag{18.5.13}$$

Contact lines L_{2s} on the face-gear tooth surface are determined by vector function $\mathbf{R}_2(\theta_s, \psi_s)$ taking $\psi_s = \text{const.}$ (Fig. 18.1.4).

18.6 CONDITIONS OF NONUNDERCUTTING OF FACE-GEAR TOOTH SURFACE (GENERATED BY INVOLUTE SHAPER)

Appearance of singularities on surface Σ_2 is the herald of oncoming undercutting. Therefore, to avoid undercutting of Σ_2, it is necessary to avoid singularities on Σ_2. Singularities on Σ_2 occur at the point where normal $\mathbf{N}_2$ to Σ_2 becomes equal to zero. Normal $\mathbf{N}_2$ is given by

$$\mathbf{N}_2 = \frac{\partial \mathbf{R}_2}{\partial \theta_s} \times \frac{\partial \mathbf{R}_2}{\partial \psi_s}. \tag{18.6.1}$$

Another approach for determination of singularities of Σ_2 is based on the following considerations:

(i) It is proven that at a singular point of Σ_2, the following equation holds [Litvin, 1989]:

$$\mathbf{v}_r^{(s)} + \mathbf{v}_s^{(s2)} = 0 \tag{18.6.2}$$

where $\mathbf{v}_r^{(s)}$ is the velocity of a point of contact in its motion over surface Σ_s of the shaper.

(ii) In addition to Eq. (18.6.2), we apply the differentiated equation of meshing $f_{s2} = 0$ that yields

$$\frac{\partial f_{s2}}{\partial u_s} \frac{du_s}{dt} + \frac{\partial f_{s2}}{\partial \theta_s} \frac{d\theta_s}{dt} + \frac{\partial f_{s2}}{\partial \psi_s} \frac{d\psi_s}{dt} = 0. \tag{18.6.3}$$

(iii) Application of Eqs. (18.6.2) and (18.6.3) yields a system of four linear equations in two unknowns $(du_s/dt, d\theta_s/dt)$; $d\psi_s/dt$ is considered as given.

(iv) The system of linear equations has a certain solution for the unknowns if the matrix

$$\mathbf{A} = \begin{bmatrix} \dfrac{\partial \mathbf{r}_s}{\partial u_s} & \dfrac{\partial \mathbf{r}_s}{\partial \theta_s} & -\mathbf{v}_s^{(2s)} \\[3mm] \dfrac{\partial f_{s2}}{\partial u_s} & \dfrac{\partial f_{s2}}{\partial \theta_s} & -\dfrac{\partial f_{s2}}{\partial \psi_s} \dfrac{d\psi_s}{dt} \end{bmatrix} \tag{18.6.4}$$

has the rank $r = 2$. Then, we obtain that

$$\Delta_1^2 + \Delta_2^2 + \Delta_3^2 = 0 \tag{18.6.5}$$

where Δ_i ($i = 1, 2, 3$) are three determinants obtained from matrix $\mathbf{A}$. The equality of $\Delta_4 = 0$ (Δ_4 is the fourth determinant) yields the equation of meshing and therefore is not considered.

Determinants Δ_i ($i = 1, 2, 3, 4$) are given by

$$\Delta_1 = \begin{vmatrix} \dfrac{\partial x_s}{\partial u_s} & \dfrac{\partial x_s}{\partial \theta_s} & -v_{xs}^{(s2)} \\[2mm] \dfrac{\partial y_s}{\partial u_s} & \dfrac{\partial y_s}{\partial \theta_s} & -v_{ys}^{(s2)} \\[2mm] \dfrac{\partial f_{s2}}{\partial u_s} & \dfrac{\partial f_{s2}}{\partial \theta_s} & -\dfrac{\partial f_{s2}}{\partial \psi_s}\dfrac{d\psi_s}{dt} \end{vmatrix} = 0 \tag{18.6.6}$$

$$\Delta_2 = \begin{vmatrix} \dfrac{\partial x_s}{\partial u_s} & \dfrac{\partial x_s}{\partial \theta_s} & -v_{xs}^{(s2)} \\[2mm] \dfrac{\partial z_s}{\partial u_s} & \dfrac{\partial z_s}{\partial \theta_s} & -v_{zs}^{(s2)} \\[2mm] \dfrac{\partial f_{s2}}{\partial u_s} & \dfrac{\partial f_{s2}}{\partial \theta_s} & -\dfrac{\partial f_{s2}}{\partial \psi_s}\dfrac{d\psi_s}{dt} \end{vmatrix} = 0 \tag{18.6.7}$$

$$\Delta_3 = \begin{vmatrix} \dfrac{\partial y_s}{\partial u_s} & \dfrac{\partial y_s}{\partial \theta_s} & -v_{ys}^{(s2)} \\[2mm] \dfrac{\partial z_s}{\partial u_s} & \dfrac{\partial z_s}{\partial \theta_s} & -v_{zs}^{(s2)} \\[2mm] \dfrac{\partial f_{s2}}{\partial u_s} & \dfrac{\partial f_{s2}}{\partial \theta_s} & -\dfrac{\partial f_{s2}}{\partial \psi_s}\dfrac{d\psi_s}{dt} \end{vmatrix} = 0 \tag{18.6.8}$$

$$\Delta_4 = \begin{vmatrix} \dfrac{\partial x_s}{\partial u_s} & \dfrac{\partial x_s}{\partial \theta_s} & -v_{xs}^{(s2)} \\[2mm] \dfrac{\partial y_s}{\partial u_s} & \dfrac{\partial y_s}{\partial \theta_s} & -v_{ys}^{(s2)} \\[2mm] \dfrac{\partial z_s}{\partial u_s} & \dfrac{\partial z_s}{\partial \theta_s} & -v_{zs}^{(s2)} \end{vmatrix} = 0. \tag{18.6.9}$$
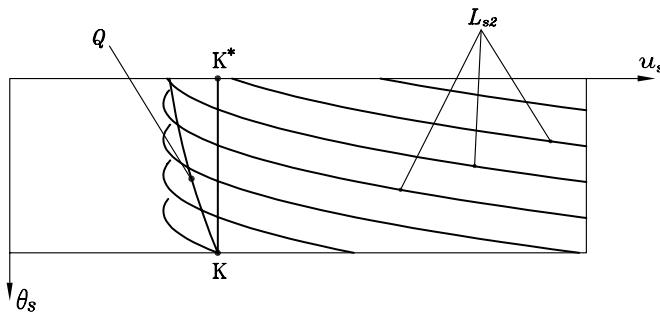
(v) Equation (18.6.5) yields a relation

$$F_{s2}(u_s, \theta_s, \psi_s) = 0. \tag{18.6.10}$$

(vi) Equations $F_{s2} = 0$ and $f_{s2} = 0$ enable us to obtain a line on the shaper tooth surface that generates singular points on surface Σ_2. Limitations of parameters (u_s, θ_s, ψ_s) observed by design enable us to avoid singularities of face-gear tooth surface Σ_2.

The procedure of limitation of parameters (u_s, θ_s, ψ_s) for avoidance of singularities of Σ_2 is as follows:

Step 1: We consider the plane of surface parameters (u_s, θ_s) of the shaper and represent in this space: (i) lines of tangency L_{s2} of shaper Σ_s and surface Σ_2, and (ii) line Q

Figure 18.6.1: Limitation of space of parameters (u_s, θ_s) for avoidance of singularities.

of points (u_s, θ_s, ψ_s) that correspond to singular points of Σ_2. We apply for this purpose equations $f_{s2}(u_s, \theta_s, \psi_s) = 0$ and $F_{s2}(u_s, \theta_s, \psi_s) = 0$.
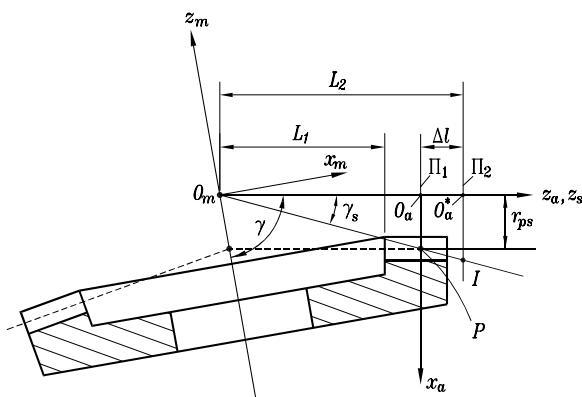
Step 2: Figure 18.6.1 shows lines L_{s2} and line Q which is the image of singularities of Σ_2 on plane (u_s, θ_s). Points of line Q are obtained as points that satisfy simultaneously equations $f_{s2} = 0$ and $F_{s2} = 0$.

Step 3: Avoidance of singularities of Σ_2 is achieved by elimination of line Q of the space of parameters (u_s, θ_s). Taking into account that Q designates the parameter of the shaper measured along its axis, it is sufficient to eliminate line $K–K^*$ of the shaper, where K corresponds to the addendum of the shaper.

Directions for Computations

Our goal is determination of the magnitude of L_1 that will avoid singularities of the face-gear tooth surface Σ_2 (Fig. 18.6.2). Parameter L_2 (Fig. 18.6.2) determines the zone free of pointing of Σ_2 (see Section 18.7). The computation of L_1 is based on the following procedure:

(a) Limiting point K of the line of singularities of the face-gear belongs to the addendum of the shaper. Parameter θ_s of limiting point K is determined from the

Figure 18.6.2: Illustration of limiting tooth dimensions L_1 and L_2 of face-gear.

equation

$$\theta_s = \frac{\left(r_{as}^2 - r_{bs}^2\right)^{0.5}}{r_{bs}} \tag{18.6.11}$$

where r_{as} and r_{bs} are the radii of the addendum circle and base circle of the shaper.
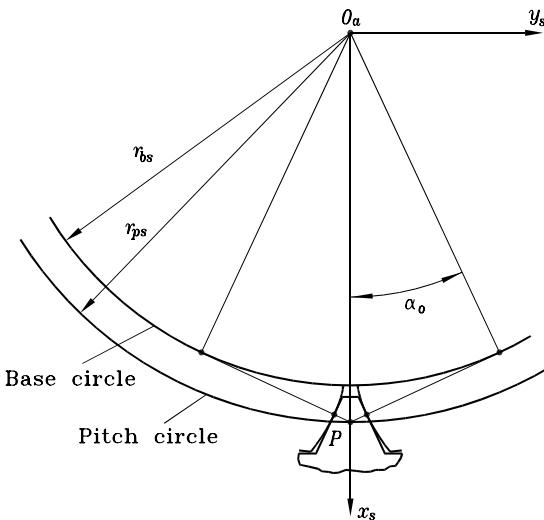
(b) Investigation shows that for determination of singularities of Σ_2 it is sufficient to take $\Delta_2 = 0$ or $\Delta_3 = 0$ instead of Eq. (18.6.4). Determinants $\Delta_2 = 0$ or $\Delta_3 = 0$ include elements $\partial z_s / \partial u_s$ and $\partial z_s / \partial \theta_s$, whereas determinant Δ_1 does not include such elements. Using, let us say, Δ_2 and equation of meshing $f_{s2} = 0$, we obtain two equations in two unknowns ϕ_s and u_s.

(c) Parameter u_s determines the sought-for magnitude of L_1 (Fig. 18.6.2).

18.7 POINTING OF FACE-GEAR TEETH GENERATED BY INVOLUTE SHAPER
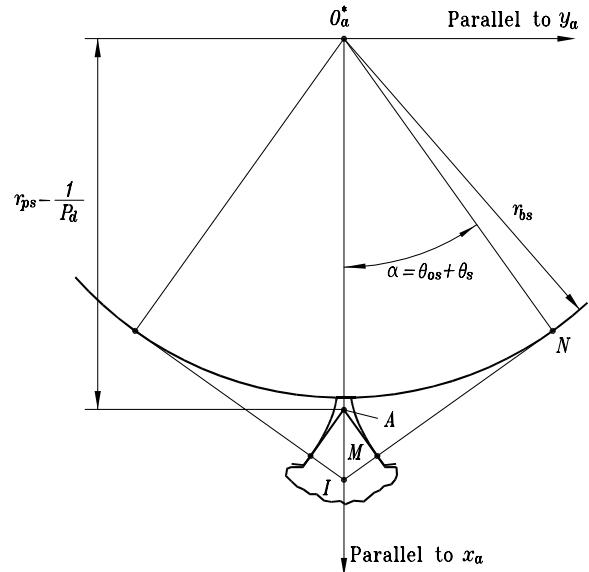
Pointing of teeth means that the tooth thickness on the top of the tooth becomes equal to zero. The location of a tooth pointing area may be determined by considering the intersection of the two opposite tooth surfaces at the topland of the tooth. A computer program to solve this problem has been developed by the authors of this book. An alternative but approximate solution to this problem is discussed in this chapter.

Consider that the face-gear is generated by a shaper. The axes of rotation of the shaper and the face-gear are designated by z_s and z_2, respectively [Figs. 18.5.2(a) and 18.6.2]. The instantaneous axis of rotation in the process of generation is $O_m I$. Consider cross sections of the shaper that are determined by planes Π_1 and Π_2 that are perpendicular to axis z_s and pass through pitch point P and a point I chosen on instantaneous axis of rotation $O_m P$ (Fig. 18.6.2). The goal is to determine the location on plane Π_2 where the profiles of the tooth sides of the face-gear intersect.

Profiles of the shaper and the face-gear in planes Π_1 and Π_2 are shown in Figs. 18.7.1 and 18.7.2, respectively. The point of intersection of profiles of the face-gear in plane

Figure 18.7.1: Cross section profiles of face-gear and shaper in plane Π_1.

Figure 18.7.2: Cross section profiles of face-gear and shaper in plane Π_2.

Π_2 is designated by "A" (Fig. 18.7.2). Point A has to be located on the addendum line of the face-gear, and therefore its location with respect to axis y_a is determined by $r_{ps} - 1/P_d$ (Fig. 18.7.2). The goal is determination of magnitude L_2 defined by distance Δl between planes Π_1 and Π_2 (Fig. 18.6.2). Figures 18.6.2 and 18.7.2 illustrate the procedure of derivation of magnitude Δ_l and L_2. The computation of L_2 is based on the following procedure:

Step 1: Determination of pressure angle α of pointed teeth (Fig. 18.7.2).

We use vector equation (Fig. 18.7.2)

$$\overline{O_a^* N} + \overline{NM} + \overline{MA} = \overline{O_a^* A}. \tag{18.7.1}$$

(See the location of point O_a^* in Fig. 18.6.2.) Here,

$$\overline{O_a^* A} = r_{ps} - \frac{1}{P_d} = \frac{N_s - 2}{2P_d} \tag{18.7.2}$$

where P_d is the diametral pitch; point M is the point of tangency of profiles of the shaper and the face-gear in plane Π_2 (Fig. 18.7.2); $|\overline{MA}| = \lambda_s$; $|\overline{NM}| = r_{bs}\theta_s$.

Vector equation (18.7.1) yields two scalar equations in two unknowns α and λ_s:

$$r_{bs}(\cos\alpha + \theta_s \sin\alpha) - \lambda_s \cos\alpha = \frac{N_s - 2}{2P_d} \tag{18.7.3}$$

$$r_{bs}(\sin\alpha - \theta_s \cos\alpha) - \lambda_s \sin\alpha = 0. \tag{18.7.4}$$

Here, $r_{bs} = (N_s/(2P_d))\cos\alpha_0$; $\theta_s = \alpha - \theta_{0s}$; $\theta_{0s} = \pi/(2N_s) -$ inv α_0. Eliminating λ_s, we obtain the following equation for determination of α:

$$\alpha - \sin\alpha \frac{N_s - 2}{N_s \cos\alpha_0} = \frac{\pi}{2N_s} - \text{inv}\,\alpha_0. \tag{18.7.5}$$

The sought-for angle α is obtained by solving the nonlinear equation (18.7.5).

Step 2: Determination of magnitude L_2 (Fig. 18.6.2).
Figure 18.7.2 yields

$$\overline{O_a^* I} = \frac{r_{bs}}{\cos \alpha} = \frac{N_s \cos \alpha_0}{2 P_d \cos \alpha}. \tag{18.7.6}$$

Then, we obtain (Fig. 18.6.2)

$$L_2 = \frac{\overline{O_a^* I}}{\tan \gamma_s} = \frac{N_s \cos \alpha_0}{2 P_d \cos \alpha \tan \gamma_s}. \tag{18.7.7}$$

Knowing the magnitudes of L_1 and L_2 (Fig. 18.6.2), it becomes possible to design a face-gear of the gear drive that is free of undercutting and pointing.

18.8 FILLET SURFACE

Two types of fillet surfaces might be provided: (i) those generated by the generatrix G of the addendum cylinder [Fig. 18.4.3(a)], and (ii) those generated by the rounded top of the shaper (Fig. 18.8.1).

Case 1: Generation of the fillet by edge G [Fig. 18.4.3(a)].

Using Fig. 18.5.1, we represent edge G [Fig. 18.4.3(a)] in coordinate system S_s by vector function $\mathbf{r}_s(u_s, \theta_s^*)$ where
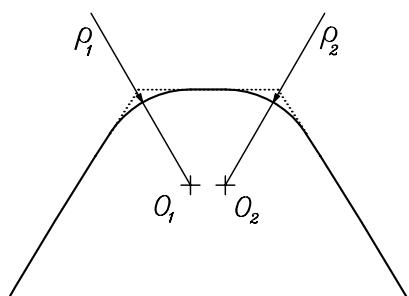
$$\theta_s^* = \frac{\left(r_{as}^2 - r_{bs}^2\right)^{0.5}}{r_{bs}}, \quad r_{as} = r_{ps} + \frac{1.25}{P_d} = \frac{N_s + 2.5}{2 P_d}. \tag{18.8.1}$$

The fillet surface is represented in S_2 by the equation
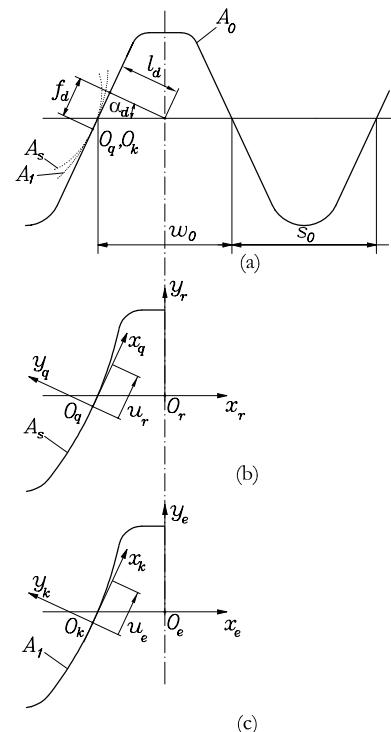
$$\mathbf{r}_2(u_s, \psi_s) = \mathbf{M}_{2s}(\psi_s)\mathbf{r}_s(u_s, \theta_s^*). \tag{18.8.2}$$

Case 2: Generation of the fillet by the rounded top of the shaper.

The fillet is generated as the envelope to the family of circles of radius ρ (Fig. 18.8.1). The investigation of bending stresses shows that application of a shaper with a rounded top reduces bending stresses on approximately 10% with respect to those obtained by application of an edged top shaper.

Figure 18.8.1: Rounded top of the shaper tooth.

Figure 18.9.1: Illustration of rack-cutter profiles; (b) and (c) parabolic profiles of the shaper and pinion rack-cutters, respectively.

18.9 GEOMETRY OF PARABOLIC RACK-CUTTERS

Basic Concept
The second version of the geometry of face-gear drives is based on the following ideas Litvin *et al.* [2002b]:

(i) Two imaginary rigidly connected rack-cutters designated as A_1 and A_s are applied for generation of the pinion and the shaper, respectively. Designation A_0 indicates a reference rack-cutter with straight-line profiles (Fig. 18.9.1).

(ii) Rack-cutters A_1 and A_s are provided with mismatched parabolic profiles that deviate from the straight-line profiles of reference rack-cutter A_0. Figure 18.9.1(a) shows schematically an exaggerated deviation of A_1 and A_s from A_0. The parabolic profiles of rack-cutters A_1 and A_s for one tooth side are shown schematically in Figs. 18.9.1(b) and 18.9.1(c).

(iii) The tooth surfaces Σ_1 and Σ_s of the pinion and the shaper are determined as envelopes to the tooth surfaces of rack-cutters A_1 and A_s, respectively.

(iv) The tooth surfaces of the face-gear Σ_2 are generated by the shaper and are determined by a sequence of two enveloping processes wherein (a) the parabolic rack-cutter A_s generates the shaper, and (b) the shaper generates the face-gear. The face-gear tooth surface Σ_2 may also be ground (or cut) by a worm (hob) of a special shape (see Section 18.14).

(v) The pinion and face-gear tooth surfaces are in point contact at every instant because: (i) rack-cutters A_1 and A_s are mismatched [Fig. 18.9.1(a)] due to application of two

different parabola coefficients, and (ii) the pinion and the shaper are provided with a different number of teeth. Figures 18.9.1(b) and 18.9.1(c) show schematically the profiles of the rack-cutters of the pinion and the shaper, respectively. Application of both items, (i) and (ii), provides more freedom for observation of the desired dimensions of the instantaneous contact ellipse and for the predesign of a parabolic function of transmission errors.

(vi) An alternative method of generation of face-gears is based on application of a worm of a special shape, which might be applied for grinding or cutting (Fig. 18.1.3). Grinding enables us to harden the tooth surfaces and to increase the permissible contact stresses. It is shown below that the derivation of the worm thread surface is based on simultaneous meshing of the shaper with the face-gear and the worm (see Section 18.14).

Reference and Parabolic Rack-Cutters

Reference rack-cutter A_0 has straight-line profiles [Fig. 18.9.1(a)]. Parabolic rack-cutters designated as A_s and A_1 are in mesh with the shaper and the pinion. Parabolic profiles of A_s and A_1 deviate from straight-line profiles of A_0.

Coordinate systems S_q and S_r are applied for derivation of equations of shaper rack-cutter A_s. Parameters u_r and parabola coefficient a_r determine the parabolic profile of rack-cutter A_s [Fig. 18.9.1(b)]. Respectively, coordinate systems S_k and S_e are applied for derivation of equations of rack-cutter A_1. Parameters u_e and parabola coefficient a_e determine the parabolic profile of rack-cutter A_1 [Fig. 18.9.1(c)]. Origins O_q and O_k of coordinate systems S_q and S_k, respectively [Figs. 18.9.1(b) and 18.9.1(c)], coincide, and their location is determined by parameter f_d. The profiles of the rack-cutter are considered for the side with profile angle α_d [Fig. 18.9.1(a)].

The design parameters of reference rack-cutter A_0 [Fig. 18.9.1(a)] are w_0, s_0, and α_d. Taking into account that

$$w_0 + s_0 = p = \frac{\pi}{P} \tag{18.9.1}$$

we obtain

$$s_0 = \frac{p}{1 + \lambda} = \frac{\pi}{(1 + \lambda)P}; \qquad w_0 = \frac{\lambda p}{1 + \lambda} = \frac{\lambda \pi}{(1 + \lambda)P}. \tag{18.9.2}$$

Here, $\lambda = w_0/s_0$, and p and P are the circular and diametral pitches, respectively.

The tooth surface of rack-cutter A_s is represented in coordinate system S_r [Fig. 18.9.1(a)] as

$$\mathbf{r}_r(u_r, \theta_r) = \begin{bmatrix} (u_r - f_d) \sin \alpha_d - l_d \cos \alpha_d - a_r u_r^2 \cos \alpha_d \\ (u_r - f_d) \cos \alpha_d + l_d \sin \alpha_d + a_r u_r^2 \sin \alpha_d \\ \theta_r \\ 1 \end{bmatrix}. \tag{18.9.3}$$

Parameter θ_r is measured along the z_r axis. Parameter l_d is shown in Fig. 18.9.1(a). Normal $\mathbf{N}_r$ to the shaper rack-cutter is represented as
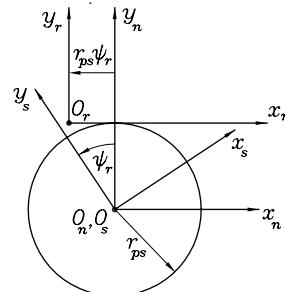
$$\mathbf{N}_r(u_r) = \begin{bmatrix} \cos\alpha_d + 2a_r u_r \sin\alpha_d \\ -\sin\alpha_d + 2a_r u_r \cos\alpha_d \\ 0 \end{bmatrix}. \tag{18.9.4}$$

Similarly, we may represent vector function $\mathbf{r}_e(u_e, \theta_e)$ of pinion rack-cutter A_1 and normal $\mathbf{N}_e(u_e)$.
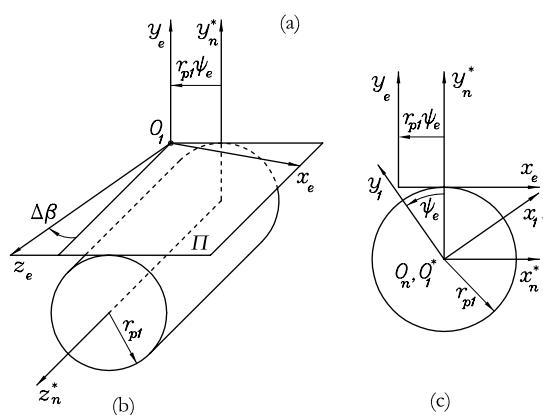
18.10 SECOND VERSION OF GEOMETRY: DERIVATION OF TOOTH SURFACES OF SHAPER AND PINION

Shaper Tooth Surface

We apply for derivation of shaper tooth surface Σ_s: (i) movable coordinate systems S_r and S_s that are rigidly connected to the shaper rack-cutter and the shaper, and (ii) fixed coordinate system S_n [Fig. 18.10.1(a)]. Rack-cutter A_s and the shaper perform related motions of translation and rotation determined by $(r_{ps}\psi_r)$ and ψ_r [Fig. 18.10.1 (a)].

Figure 18.10.1: For generation of shaper of pinion by rack-cutters: (a) generation of the shaper, (b) installation of pinion rack-cutter, and (c) generation of the pinion.

The shaper tooth surface Σ_s is determined as the envelope to the family of rack-cutter surfaces A_s considering simultaneously the following equations:

$$\mathbf{r}_s(u_r, \theta_r, \psi_r) = \mathbf{M}_{sr}(\psi_r)\mathbf{r}_r(u_r, \theta_r) \tag{18.10.1}$$

$$\mathbf{N}_r(u_r) \cdot \mathbf{v}_r^{(sb)} = f_{sr}(u_r, \psi_r) = 0. \tag{18.10.2}$$

Here, vector function $\mathbf{r}_s(u_r, \theta_r, \psi_r)$ represents in S_s the family of rack-cutter A_s tooth surfaces; matrix $\mathbf{M}_{sr}(\psi_r)$ describes coordinate transformation from S_r to S_s; vector function $\mathbf{N}_r(u_r)$ represents the normal to the rack-cutter A_s [see Eq. (18.9.4)]; $\mathbf{v}_r^{(sb)}$ is the relative (sliding) velocity.

Equation (18.10.2) (the equation of meshing) yields

$$f_{sr}(u_r, \psi_r) = \frac{x_r N_{yr} - y_r N_{xr}}{r_{ps} N_{yr}} - \psi_r = 0. \tag{18.10.3}$$

Finally, we represent the surface of the shaper by vector function

$$\mathbf{r}_s(u_r(\psi_r), \psi_r, \theta_r) = \mathbf{R}_s(\psi_r, \theta_r). \tag{18.10.4}$$

The normal to the shaper is represented in coordinate system S_s as

$$\mathbf{N}_s = \frac{\partial \mathbf{R}_s}{\partial \psi_r} \times \frac{\partial \mathbf{R}_s}{\partial \theta_r}. \tag{18.10.5}$$

Pinion Tooth Surface

Movable coordinate systems S_e and S_1 are rigidly connected to the pinion rack-cutter and the pinion, respectively [Figs. 18.10.1(b) and 18.10.1(c)]; S_n^* is the fixed coordinate system. The installation angle $\Delta\beta$ [Fig. 18.10.1(b)] is provided for the improvement of the bearing contact between the pinion and the face-gear (see Section 18.13). Derivations of pinion tooth surfaces are similar to those applied for derivation of shaper tooth surfaces and are based on the following procedure:

Step 1: We obtain the family of pinion rack-cutters represented in coordinate system S_1 as

$$\mathbf{r}_1(u_e, \theta_e, \psi_e) = \mathbf{M}_{1e}(\psi_e)\mathbf{r}_e(u_e, \theta_e) \tag{18.10.6}$$

where matrix $\mathbf{M}_{1e}$ describes coordinate transformation from S_e via S_n^* to S_1 [Figs. 18.10.1(b) and 18.10.1(c)].

Step 2: Using the equation of meshing between the rack-cutter and the shaper, we obtain

$$u_e(\psi_e) = \frac{x_e N_{ye} - y_e N_{xe}}{r_{p1} N_{ye}} - \psi_e. \tag{18.10.7}$$

Step 3: We represent the pinion tooth surfaces by vector function

$$\mathbf{r}_1(u_e(\psi_e), \psi_e, \theta_e) = \mathbf{R}_1(\psi_e, \theta_e). \tag{18.10.8}$$

18.11 SECOND VERSION OF GEOMETRY: DERIVATION OF FACE-GEAR TOOTH SURFACE

Preliminary Considerations

The face-gear tooth surface is determined as the result of two enveloping processes wherein (i) a parabolic rack-cutter generates the shaper tooth surface (see Section 18.10), and (ii) the shaper generates the face-gear tooth surface. The second enveloping process is based on the algorithm presented in Section 18.5 wherein an involute shaper generates the face-gear tooth surface of the first version of geometry. Recall that the shaper tooth surface of the second version of geometry is represented in two-parameter form by vector function $\mathbf{R}_s(\psi_r, \theta_r)$ [see Eq. (18.10.4)]. The normal to the surface mentioned above is represented by vector function (18.10.5). Investigation of undercutting of surface Σ_2 (of the second version of geometry) is based on the algorithm discussed in Section 18.6.

Structure of Face-Gear Tooth Surface Σ_2

The type of a surface may be defined by the Gaussian curvature that represents the product of principal surface curvatures at the chosen surface point. Thus, the Gaussian curvature K at a surface point M is defined as

$$K = K_I K_{II} \tag{18.11.1}$$

where K_I and K_{II} are the principal surface curvatures at M. The type of surface point (elliptical, parabolic, or hyperbolic) depends on the sign of Gaussian curvature K.

Direct determination of Gaussian curvature for a surface represented by three, sometimes four, related parameters requires complex derivations and computations. The derivations and computations previously mentioned may be simplified using proposed relations between the curvatures of the generating and generated surfaces (see Chapter 8).
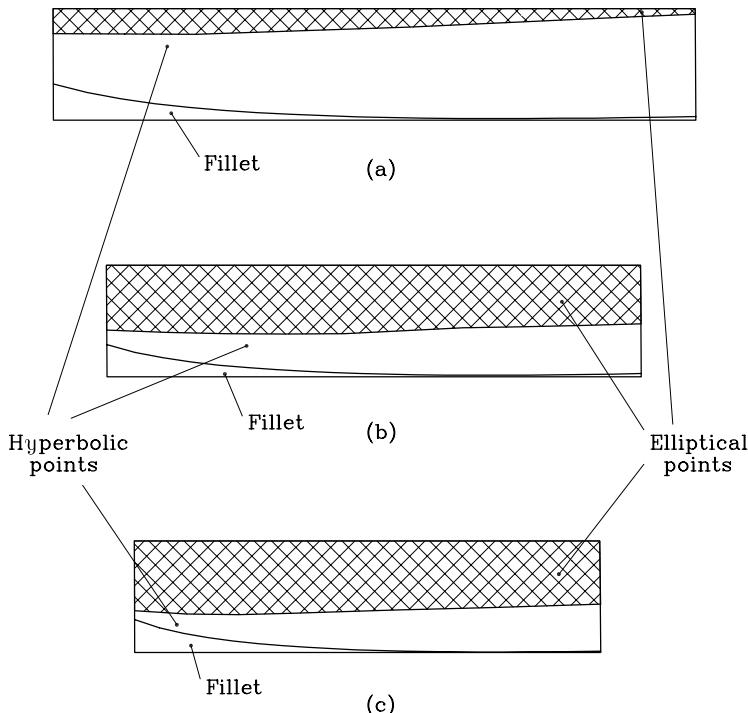
Investigation shows that surface Σ_2 has elliptical ($K > 0$) and hyperbolic ($K < 0$) points (Fig. 18.11.1). The common line of both sub-areas is the line of parabolic points. The dimensions of the area of surface elliptical points depend on the magnitude of the parabola coefficient a_r of the shaper rack-cutter. Surface Σ_2 of the first version of geometry contains only hyperbolic points.

18.12 DESIGN RECOMMENDATIONS

The bending stresses in a face-gear drive depend on the unitless coefficient
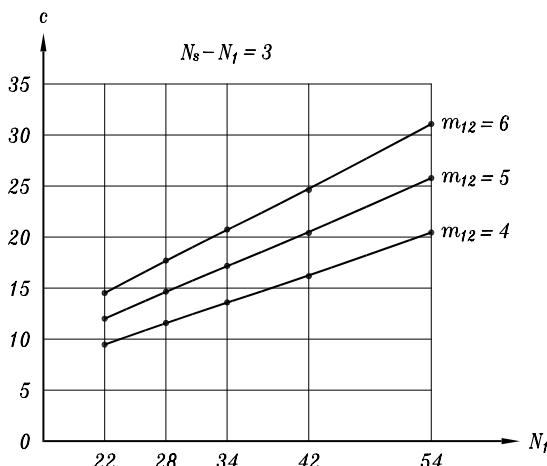
$$c = P_d \, \Delta l = P_d (L_2 - L_1). \tag{18.12.1}$$

(See the designations of L_2 and L_1 in Fig. 18.6.2.) Usually, the coefficient c is chosen as $c = 10$ for high-power transmissions. The coefficient c can be increased for face-gear drives by choosing a higher gear ratio and increasing the tooth number. This statement can be confirmed by the graphs shown in Fig. 18.12.1 for face-gear drives of the first type of geometry.
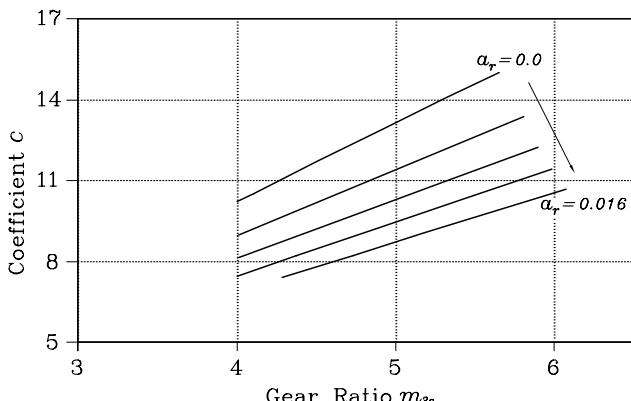
Figure 18.11.1: Areas of elliptical and hyperbolic points of face-gear tooth surface Σ_2 for rack-cutter parabola coefficients (a) $a_r = 0.01$ 1/mm, (b) $a_r = 0.02$ 1/mm, and (c) $a_r = 0.03$ 1/mm.

The investigation of the influence of coefficient c on the structure of the face-gear teeth is based on the following considerations: Assume that the outer radius L_2 is known (it has been determined from the conditions of avoidance of pointing). We are able to eliminate the portion of the tooth where the fillet exists (Figs. 18.6.2 and 18.11.1) by increasing the inner radius L_1. This means that the coefficient c will be decreased [see

Figure 18.12.1: Graphs of coefficient c for face-gears of the first type of geometry.

Figure 18.12.2: Illustration of influence of parabola coefficient a_r and gear ratio m_{2s} on coefficient c.

Eq. (18.12.1)]. However, observing a sufficient value of c enables us to obtain a more uniform structure, eliminating the weaker part of the face-gear tooth.

Figure 18.12.2 shows the influence of the parabola coefficient a_r of the parabolic profile of the rack-cutter and the gear ratio on the possible tooth length of the face-gear of the second type of geometry. Results of the investigation of undercutting and pointing are shown in Fig. 18.12.2, which represents the influence of gear ratio m_{2s} and parabola coefficient a_r on the coefficient c represented in Eq. (18.12.1).
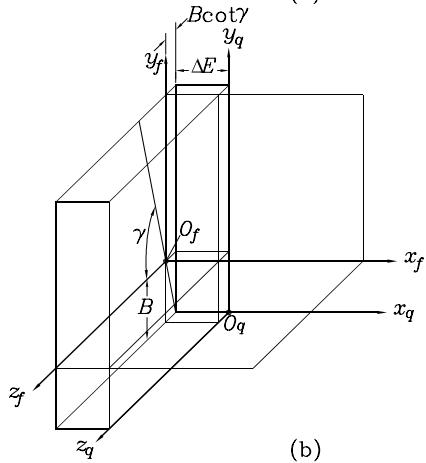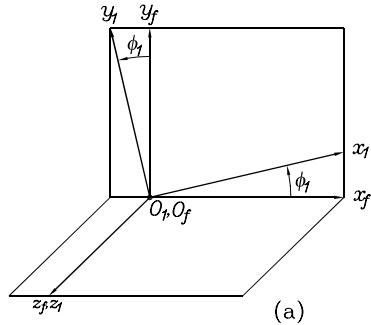
18.13 TOOTH CONTACT ANALYSIS (TCA)

Tooth contact analysis is directed at simulation of meshing and contact of surfaces Σ_1 and Σ_2 and enables investigation of the influence of errors of alignment on transmission errors and the shift of bearing contact. The algorithm for simulation of meshing is based on equations that describe the continuous tangency of surfaces Σ_1 and Σ_2 and is presented in Section 9.4.
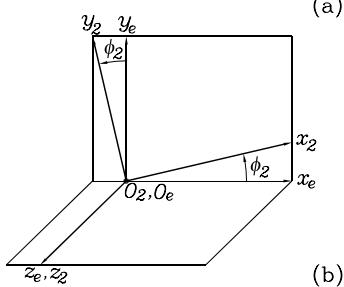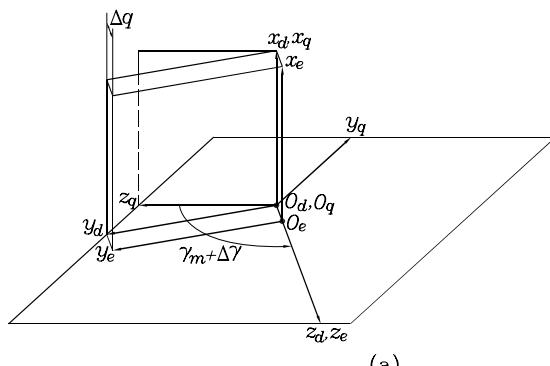
Applied Coordinate Systems
The following coordinate systems are applied for TCA: (a) coordinate system S_f, rigidly connected to the frame of the face-gear drive [Fig. 18.13.1(a)]; (b) coordinate systems S_1 [Fig. 18.13.1(a)] and S_2 [Fig. 18.13.2(b)], rigidly connected to the pinion and the face-gear respectively; and (c) auxiliary coordinate systems S_d, S_e, and S_q, applied for simulation of errors of alignment of the face-gear drive [Figs. 18.13.2(a) and 18.13.2(b)].

All misalignments are referred to the gear. Parameters ΔE, B, and $B \cot \gamma$ determine the location of origin O_q with respect to O_f [Fig. 18.13.1(b)]. Here, ΔE is the shortest distance between the pinion and the face-gear axes when the axes are crossed but not intersected. The location and orientation of coordinate systems S_d and S_e with respect to S_q are shown in Fig. 18.13.2(a). The misaligned face-gear performs rotation about the z_e axis [Fig. 18.13.2(b)].

(a)

(b)

Figure 18.13.1: Coordinate systems applied for simulation of meshing, I.

(a)

Figure 18.13.2: Coordinate systems applied for simulation of meshing, II.

(b)

Computational Procedure

The algorithm of TCA is based on simulation of continuous tangency of surfaces Σ_1 and Σ_2 accomplished as follows (see Section 9.4):

(1) Surfaces Σ_1 and Σ_2 and their unit normals are represented in the fixed coordinate system S_f by vector functions

$$\mathbf{r}_f^{(i)}(u_i, \theta_i, \phi_i) \quad (i = 1, 2) \tag{18.13.1}$$

$$\mathbf{n}_f^{(i)}(u_i, \theta_i, \phi_i) \quad (i = 1, 2). \tag{18.13.2}$$

(2) Continuous tangency of Σ_1 and Σ_2 is represented by vector equations

$$\mathbf{r}_f^{(1)}(u_1, \theta_1, \phi_1) - \mathbf{r}_f^{(2)}(u_2, \theta_2, \phi_2) = 0 \tag{18.13.3}$$

$$\mathbf{n}_f^{(1)}(u_1, \theta_1, \phi_1) - \mathbf{n}_f^{(2)}(u_2, \theta_2, \phi_2) = 0. \tag{18.13.4}$$

Here, (u_i, θ_i) $(i = 1, 2)$ are the surface parameters of Σ_1 and Σ_2, ϕ_1 and ϕ_2 are the angles of rotation of the pinion and the face-gear in the process of meshing. Vector equations (18.13.3) and (18.13.4) yield a system of five independent scalar equations (because $\left|\mathbf{n}_f^{(1)}\right| = \left|\mathbf{n}_f^{(2)}\right| = 1$) represented in terms of six unknowns as

$$f_i(u_1, \theta_1, \phi_1, u_2, \theta_2, \phi_2) = 0, \qquad f_i \in C^1 \qquad (i = 1, \dots, 5). \tag{18.13.5}$$

(3) Surfaces Σ_1 and Σ_2 are in point contact at every instant and one of the parameters, say ϕ_1, may be chosen as the input one. The requirement of point contact yields the inequality

$$\frac{\partial(f_1, f_2, f_3, f_4, f_5)}{\partial(u_1, \theta_1, u_2, \theta_2, \phi_2)} \neq 0. \tag{18.13.6}$$

Then the solution of system of equations (18.13.5) may be represented by functions

$$\{u_1(\phi_1), \theta_1(\phi_1), u_2(\phi_1), \theta_2(\phi_1), \phi_2(\phi_1)\} \in C^1. \tag{18.13.7}$$

The solution of system of equations (18.13.3) and (18.13.4) by functions (18.13.7) is an iterative process and requires as a first guess the set of parameters

$$\mathbf{P}^{(0)}\left(u_1^{(0)}, \theta_1^{(0)}, \phi_1^{(0)}, u_2^{(0)}, \theta_2^{(0)}, \phi_2^{(0)}\right) \tag{18.13.8}$$

that satisfies system of equations (18.13.3) and (18.13.4).

(4) The solution by functions (18.13.7) enables us to obtain:
(a) transmission function $\phi_2(\phi_1)$ and function of transmission errors

$$\Delta\phi_2(\phi_1) = \phi_2(\phi_1) - \frac{N_1}{N_2}\phi_1; \tag{18.13.9}$$

(b) the paths of contact on surfaces Σ_1 and Σ_2 that are represented, respectively, as

$$\mathbf{r}_1(u_1(\phi_1), \theta_1(\phi_1)) \tag{18.13.10}$$

$$\mathbf{r}_2(u_2(\phi_1), \theta_2(\phi_1)). \tag{18.13.11}$$

Results of Investigation

The results of investigation of the first version of geometry are represented in Fig. 18.13.3 which shows the shift of the bearing contact due to errors of alignment. It has been found that the bearing contact of the face-gear drive is oriented across the tooth surface and is sensitive to the change $\Delta\gamma$ of the shaft angle. Such an orientation of the bearing contact may cause an edge contact wherein the formation of the bearing contact is considered (in addition to stress analysis).
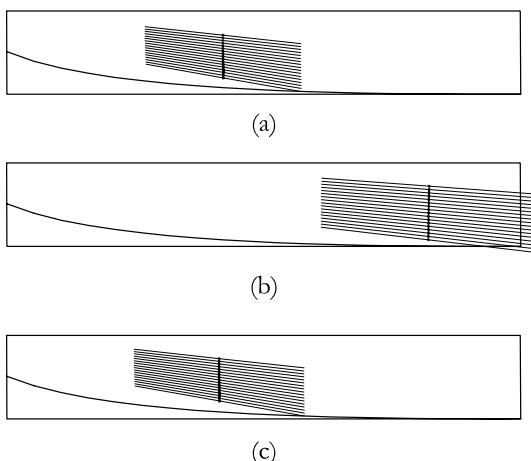
The sensitivity of face-gear drives of the first version of geometry to the change $\Delta\gamma$ of the shaft angle may be compensated by the axial correction Δq of the face-gear in the process of assembly [Fig. 18.13.3(c)]. The advantage of the first version of geometry is that the transmission errors of the gear drive are equal to zero. This is the result of application of an involute shaper for generation that has equidistant profiles.

The results of TCA of the second version of geometry are represented in Figs. 18.13.4 and 18.13.5. The main advantages of the mentioned type of geometry are as follows:
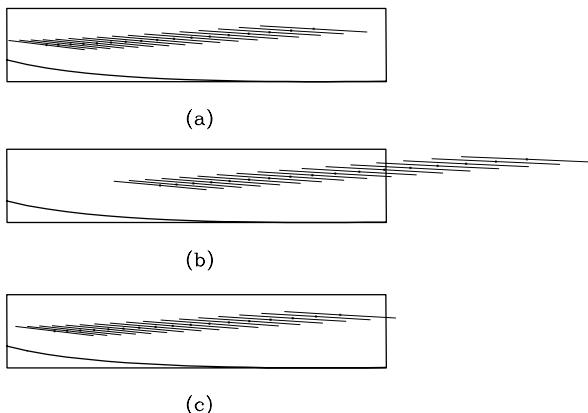
(i) Longitudinal orientation of bearing contact that enables us to avoid the edge contact.
(ii) Reduction of stresses (see Section 18.15).

The sensitivity of the gear drive of the second type of geometry to error $\Delta\gamma$ may be compensated as well by correction Δq.

For face-gear drives of the second type of geometry, the misalignment of the gear drive is accompanied with transmission errors. However, application of a predesigned parabolic function of transmission errors provides a favorable shape of the function of errors of the drive and reduces the magnitude of maximal transmission errors (see

(a)

(b)

(c)

Figure 18.13.3: Path of contact, bearing contact, and major axis of contact ellipses for the following examples: (a) no errors of alignment, (b) $|\Delta\gamma| = 3$ arcmin, and (c) adjustment of path of contact by applying the axial displacement Δq of the face-gear with respect to the pinion ($|\Delta\gamma| = 3$ arcmin, $|\Delta q| = 550 \ \mu$m).

(a)

(b)

(c)
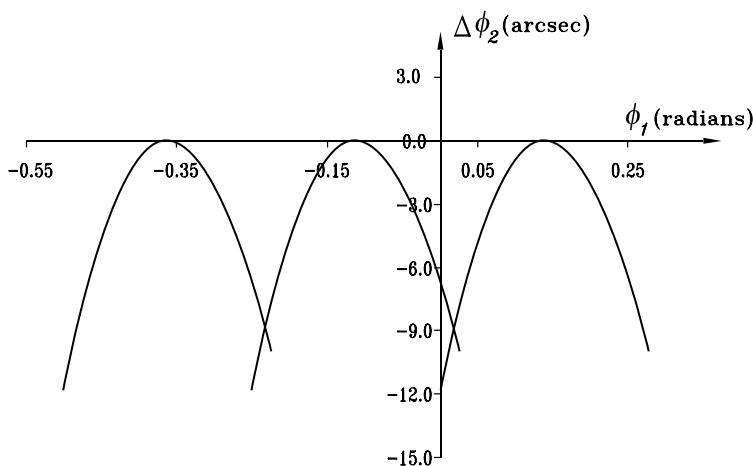
Figure 18.13.4: Path of contact, bearing contact, and major axis of contact ellipses for the following examples: (a) no errors of alignment, (b) $|\Delta\gamma| = 2$ arcmin, and (c) adjustment of path of contact by application of correction Δq: $|\Delta\gamma| = 2$ arcmin, $|\Delta q| = 350 \ \mu m$.

Section 9.2). The predesigned parabolic function of transmission errors is obtained by (i) mismatch of parabolic rack-cutters for the shaper and the pinion of the gear drive, and (ii) application of a shaper with tooth number $N_s > N_p$, where N_p is the tooth number of the pinion of the gear drive.
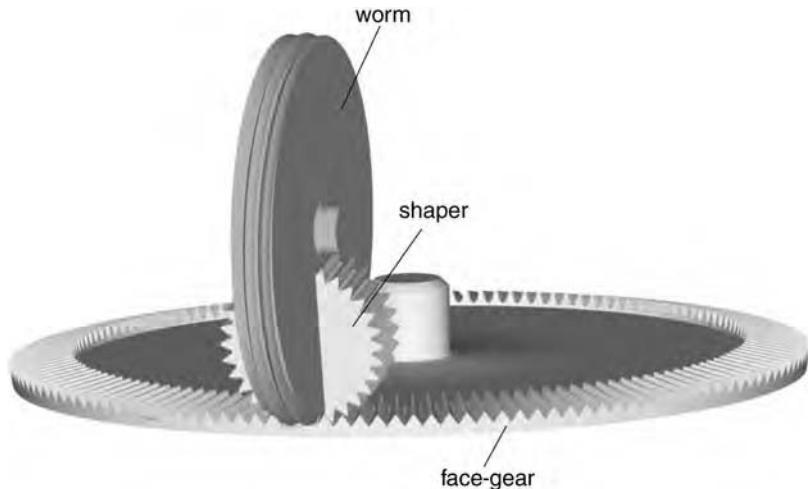
18.14 APPLICATION OF GENERATING WORM

Concept of Generating Worm

The conventional method for generation of a face-gear is based on (i) application of an involute shaper, and (ii) manufacturing of the face-gear performed as the simulation of meshing of the shaper and the face-gear being generated.

Figure 18.13.5: Parabolic function of transmission errors for proposed geometry.

Figure 18.14.1: Illustration of simultaneous meshing of shaper, worm, and face-gear.

Edward W. Miller proposed in 1942 the generation of the face-gear by a hob [Miller, 1942]. The next step was done by the patent proposed by Litvin et al. [Litvin *et al.,* 2000a] that has formulated the exact determination of the thread surface of a generating worm that provides the necessary conditions of conjugation of the tooth surfaces of the hob, the shaper, and the face-gear; the concept of worm design; and avoidance of worm singularities. The worm design as proposed above may be applied for grinding and cutting of face-gears [Litvin *et al.,* 2002a].

Designations Σ_s, Σ_w, and Σ_2 indicate surfaces of the shaper, worm, and face-gear, respectively. Simultaneous meshing of Σ_s, Σ_w, and Σ_2 is illustrated by Fig. 18.14.1. Shaper surface Σ_s is considered as the envelope to the family of rack-cutter A_s surfaces and is represented by vector function $\mathbf{R}_s(\psi_r, \theta_r)$ [see Eq. (18.10.4)]. Surfaces Σ_w and Σ_2 are generated as the envelopes to the family of shaper surfaces Σ_s.
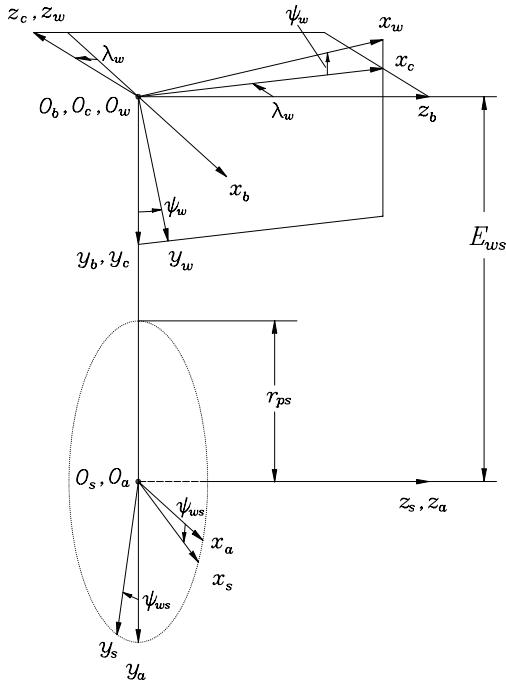
Recall that with the second type of geometry, the shaper is provided with non-involute profiles (see Section 18.10). We discuss in this section application of the worm for generation of a face-gear of the second type of geometry. However, the discussed idea may be applied as well for the generation of face-gears of the first type of geometry.

Crossing Angle Between Axes of Shaper and Worm

Figure 18.14.2 shows fixed coordinate systems S_a, S_b, and S_c applied for illustration of installation of the worm with respect to the shaper. Movable coordinate systems S_s and S_w are rigidly connected to the shaper and the worm. Axis z_s (it coincides with z_a) is the axis of rotation of the shaper. Axis z_w (it coincides with z_c) is the axis of rotation of the worm. Axes z_s and z_w are crossed and form a crossing angle of $90^\circ \pm \lambda_w$. The upper (and lower) sign corresponds to application of a right-hand (left-hand) worm. The shortest distance between axes z_s and z_w is designated as E_{ws}.

The crossing angle λ_w is

$$\lambda_w = \arcsin \frac{r_{ps}}{N_s(E_{ws} + r_{ps})}. \qquad (18.14.1)$$

Figure 18.14.2: Coordinate systems S_s, S_w, and worm installation.

Here, r_{ps} is the pitch radius of the shaper, and E_{ws} (Fig. 18.14.2) is the shortest distance between the axes of the shaper and the worm. The magnitude of E_{ws} affects the dimensions of the grinding worm and the conditions of avoidance of surface singularities of the worm (see below).

Determination of Worm Surface Σ_w

The worm surface Σ_w is determined in coordinate system S_w (Fig. 18.14.2) by the following equations:

$$\mathbf{r}_w(\psi_r, \theta_r, \psi_w) = \mathbf{M}_{ws}(\psi_w)\mathbf{R}_s(\psi_r, \theta_r) \tag{18.14.2}$$

$$\left(\frac{\partial \mathbf{R}_s}{\partial \psi_r} \times \frac{\partial \mathbf{R}_s}{\partial \theta_r}\right) \cdot \mathbf{v}_s^{(sw)} = f_{ws}(\psi_r, \theta_r, \psi_w) = 0. \tag{18.14.3}$$

Here, relative velocity $\mathbf{v}_s^{(sw)}$ is determined by differentiation and transformation of matrix $\mathbf{M}_{ws}$ that are similar to derivations in Section 2.2; vector function $\mathbf{r}_w(\psi_r, \theta_r, \psi_w)$ is the family of shaper surfaces Σ_s represented in S_w; matrix $\mathbf{M}_{ws}(\psi_w)$ describes coordinate transformation from S_s to S_w; Eq. (18.14.3) is the equation of meshing between Σ_s and Σ_w. Parameters (ψ_r, θ_r) in vector function $\mathbf{R}_s(\psi_r, \theta_r)$ represent the surface parameters of the shaper; parameter ψ_w is the generalized parameter of motion in the process of generation of the worm by the shaper. Recall that during generation of the worm, the shaper and the worm perform rotations about crossed axes z_a and z_w (Fig. 18.14.2).

Angles of rotation ψ_{ws} and ψ_w (Fig. 18.14.2) are related by the equation

$$\frac{\psi_{ws}}{\psi_w} = \frac{1}{N_s} \qquad (18.14.4)$$

where N_s is the number of teeth of the shaper. It is assumed that a single-thread worm is applied.

Equations (18.14.2) and (18.14.3) represent the worm surface Σ_w by three related parameters. We may represent Σ_w in two-parameter form using the following procedure:

(i) We apply the theorem of implicit function system existence and consider that one of the derivatives of f_{ws}, say $\partial f_{ws}/\partial \theta_r$, is not equal to zero.

(ii) Then, we can solve equation $f_{ws} = 0$ by function $\theta_r(\psi_r, \psi_w) \in C^1$ and represent the worm surface Σ_w by

$$\mathbf{r}_w(\psi_r, \theta_r(\psi_r, \psi_w), \psi_w) = \mathbf{R}_w(\psi_r, \psi_w). \qquad (18.14.5)$$

Conceptual Consideration of Simultaneous Meshing of Surfaces Σ_S, Σ_w, and Σ_2
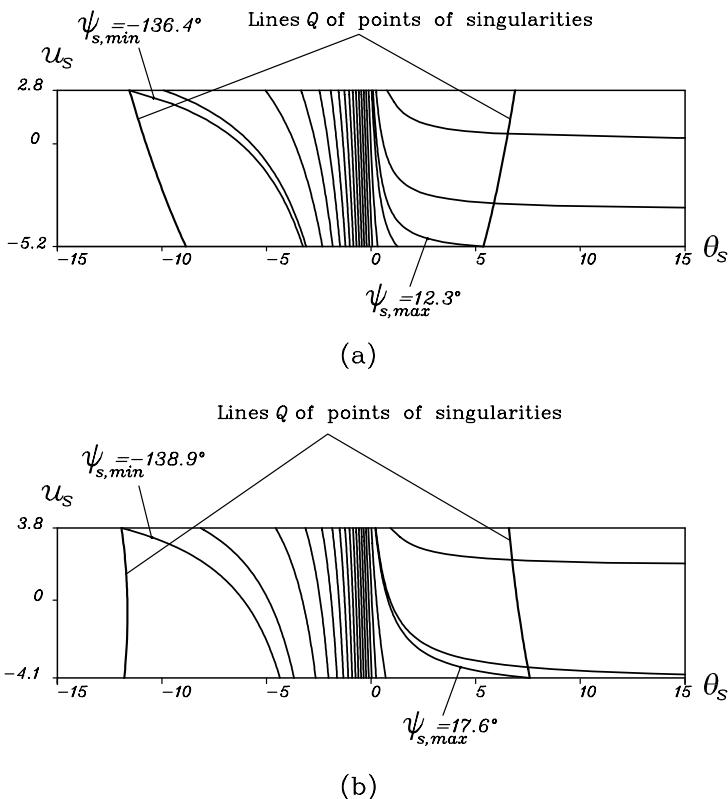
The shaper surface Σ_s is in line contact with the worm surface Σ_w and the face-gear tooth surface Σ_2. This type of surface contact is obtained because Σ_w and Σ_2 are generated as envelopes to shaper surface Σ_s. We designate by L_{ws} the lines of tangency between Σ_s and Σ_w and by L_{2s} the lines of tangency between Σ_s and Σ_2. Investigation of lines L_{ws} and L_{2s} shows that they do not coincide with each other but are intersected at any position of meshing.

Generation of Surface Σ_2 by Worm Surface Σ_w

We recall that the shaper surface Σ_s is in line contact with worm surface Σ_w and with face-gear tooth surface Σ_2. However, surfaces Σ_w and Σ_2 are in point contact with each other at any instant. This means that finishing grinding of Σ_2 by worm surface Σ_w cannot be accomplished as a one-parameter enveloping process. A grinding process based on one-parameter enveloping of the worm and the face-gear will provide only a strip on required surface Σ_2. Therefore, generation of Σ_2 by the worm has to be based on a two-parameter enveloping process wherein two independent sets of parameters are provided as: (i) a set of angles of rotation (ψ_w, ψ_2) of the worm and the face-gear, and (ii) a translational motion l_w of the worm. Parameters ψ_w and ψ_2 are the angles of rotation of the worm and the face-gear related by the equation

$$\frac{\psi_w}{\psi_2} = \frac{N_2}{N_w} \qquad (18.14.6)$$

where N_2 and N_w are the number of teeth of the face-gear and the number of threads of the worm. Usually, a single-thread worm is applied and $N_w = 1$. Parameter l_w of translational motion is provided as collinear to the axis of the shaper (see below). Surface Σ_2 generated by the grinding worm as a two-parameter enveloping process coincides with surface Σ_2 generated by the shaper.
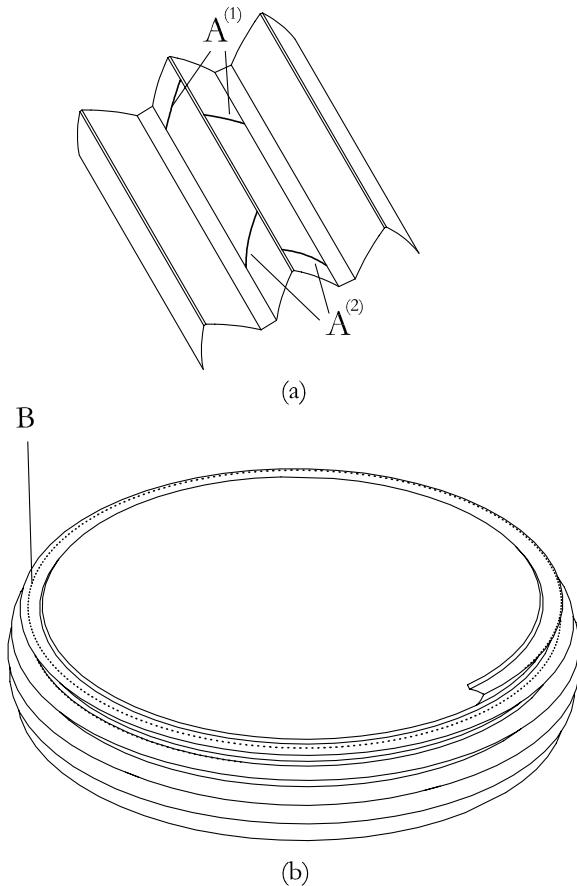
Figure 18.14.3: Contact lines between the shaper and the worm in the plane of surface parameters (u_s, θ_s) for (a) the first type of geometry, and (b) the second type of geometry.

The approach for determination of worm singularities is the same as that applied for determination of singularities of face-gear tooth surface Σ_2 (Section 18.6). Figures 18.14.3(a) and 18.14.3(b) show, in the space of surface parameters, lines of tangency of the shaper with the worm that are determined for the existing and proposed design, respectively. Lines Q are the image of singular points on the plane of surface parameters of the shaper. Figure 18.14.3 enables us to determine the maximal angle of rotation of the shaper permissible for avoidance of worm singularities. Then it becomes possible to determine the maximal number of turns of the thread of the worm.

Figure 18.14.4(a) shows lines $A^{(1)}$ and $A^{(2)}$ on the shaper tooth surface formed by regular points of the shaper. Points of lines $A^{(1)}$ and $A^{(2)}$ generate singular points on the worm surface. The worm surface Σ_w must be limited with two lines B to avoid undercutting of the worm.

Dressing of the Worm

The worm dressing is based on generation of its surface Σ_w point by point by a plane or by a conical disk that has the same profile as the rack-cutter that generated the shaper. The execution of motions of the disk or the plane with respect to the worm is accomplished by application of a CNC machine. The determination of instantaneous

(a)

(b)

Figure 18.14.4: Illustration of worm singularities: (a) regular points A of shaper that generate worm singularities; (b) singularities B on worm thread surface.

installments of the grinding disk with respect to the worm requires application of a computer program.

The computational procedure is as follows:

Step 1: Consider vector function $\mathbf{r}_w(\psi_r, \psi_r(\theta_r, \psi_w), \psi_w)$ [see Eq. (18.14.4)] and take $\psi_r = \text{const}$.

Step 2: Assign θ_r and obtain ψ_w from $\psi_w = \psi_w(\psi_r, \theta_r)$.

Step 3: Compute x_w, y_w, z_w from $\mathbf{r}_w(\psi_r, \theta_r, \psi_w(\psi_r, \theta_r)) = \mathbf{R}_w(\psi_r, \theta_r)$.

Step 4: Knowing ψ_r, it is easy to get the unit normal to the shaper determined as $\mathbf{n}_s(\psi_r)$ and then determine the unit normal to the worm surface determined as

$$\mathbf{n}_w(\psi_r, \psi_w) = \mathbf{L}_{ws}(\psi_w)\mathbf{n}_s(\psi_r). \tag{18.14.7}$$

Step 5: The data $(x_w, y_w, z_w, \mathbf{n}_w)$ are sufficient for the installation of the tool (a plane or a disk) using a CNC machine.

The second type of geometry allows application of a worm with a larger number of turns of the thread.

18.15 STRESS ANALYSIS

The goals of stress analysis presented in this section are:

(i) Comparison of contact and bending stresses of two types of geometry of face-gear drives
(ii) Comparison of bending stresses of two versions of face-gears generated with edged and rounded top shapers, respectively (Fig. 18.8.1)
(iii) Determination of contact and bending stresses and investigation of formation of the bearing contact during the cycle of meshing.

The performed stress analysis is based on the finite element method [Zienkiewicz & Taylor, 2000] and application of a general purpose computer program [Hibbit, Karlsson & Siresen, Inc., 1998]. The authors' approach to application of finite element analysis is based on the following ideas:

(a) The generation of finite element models is performed *automatically* by using the equations of the tooth surfaces and taking into account the corresponding fillets and portion of the rim. Loss of accuracy due to the development of solid models by using CAD computer programs is avoided.
(b) The proposed approach does not require an assumption of load distribution in the contact area. The contact algorithm of the general purpose computer program [Hibbit, Karlsson & Siresen, Inc., 1998] is used to get the contact area and stresses by application of torque to the pinion. The face-gear is considered at rest.
(c) Finite element models are developed numerically at the chosen contact point of the path of contact. Stress convergence is assured because there is at least one point of contact between the contacting surfaces.
(d) Finite element models of three pairs of teeth are applied and therefore the boundary conditions are far enough from the loaded areas of the teeth.

Numerical Example

Finite element analysis has been performed for two types of geometry of face-gear drives represented in Tables 18.15.1 and 18.15.2. For the second type of geometry of face-gear

Table 18.15.1: Design parameters of face-gear of first type of geometry
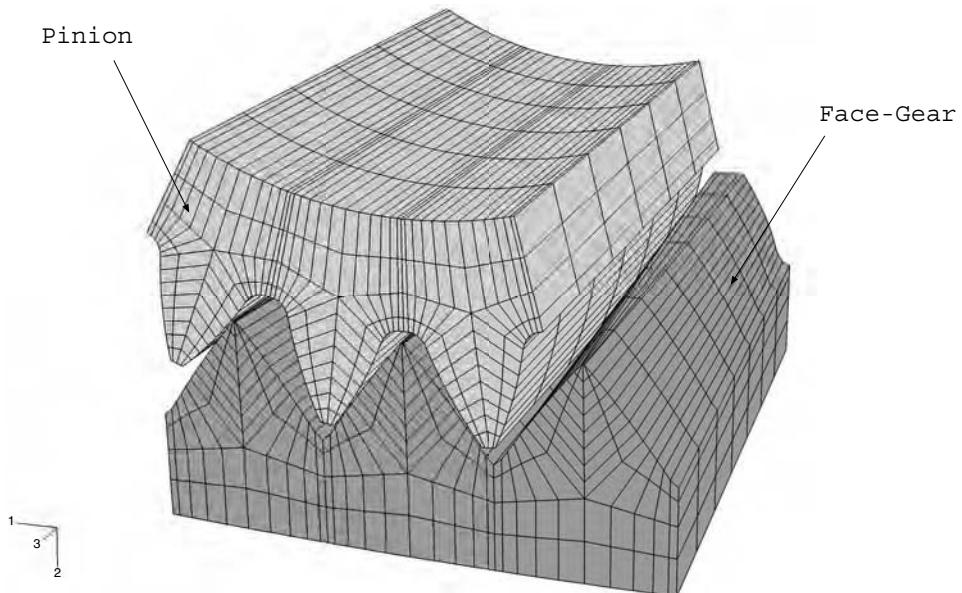
Number of teeth of the pinion	$N_1 = 25$
Number of teeth of the shaper	$N_s = 28$
Number of teeth of the face-gear	$N_2 = 160$
Module	$m = 6.35$ mm
Driving-side pressure angle	$\alpha_d = 25.0^\circ$
Coast-side pressure angle	$\alpha_c = 25.0^\circ$
Shaft angle	$\gamma_m = 90.0^\circ$
Inner radius of the face-gear	471.0 mm
Outer radius of the face-gear	559.0 mm

Table 18.15.2: Design parameters of face-gear of second type of geometry

Number of teeth of the pinion	$N_1 = 25$
Number of teeth of the shaper	$N_s = 28$
Number of teeth of the face-gear	$N_2 = 160$
Module	$m = 6.35$ mm
Driving-side pressure angle	$\alpha_d = 25.0^o$
Coast-side pressure angle	$\alpha_c = 25.0^o$
Shaft angle	$\gamma_m = 90.0^o$
Inner radius of the face-gear	493.0 mm
Outer radius of the face-gear	567.0 mm
Rack-cutter dimensional coefficient	$\lambda_t = 0.90$
Parabola coefficient of rack-cutter A_s	$a_s = 7.50 \cdot 10^{-3}$ 1/mm
Parabola coefficient of rack-cutter A_1	$a_1 = 3.00 \cdot 10^{-3}$ 1/mm
Driving-side offset parabola	$f_d = 2.00$ mm
Coast-side offset parabola	$f_c = 0.00$ mm
Pinion helix angle	$\Delta\beta = 0.05^o$

drives, the application of a rounded top shaper (Fig. 18.8.1) has also been considered in order to compare the bending stresses at the fillet of the generated face-gear.
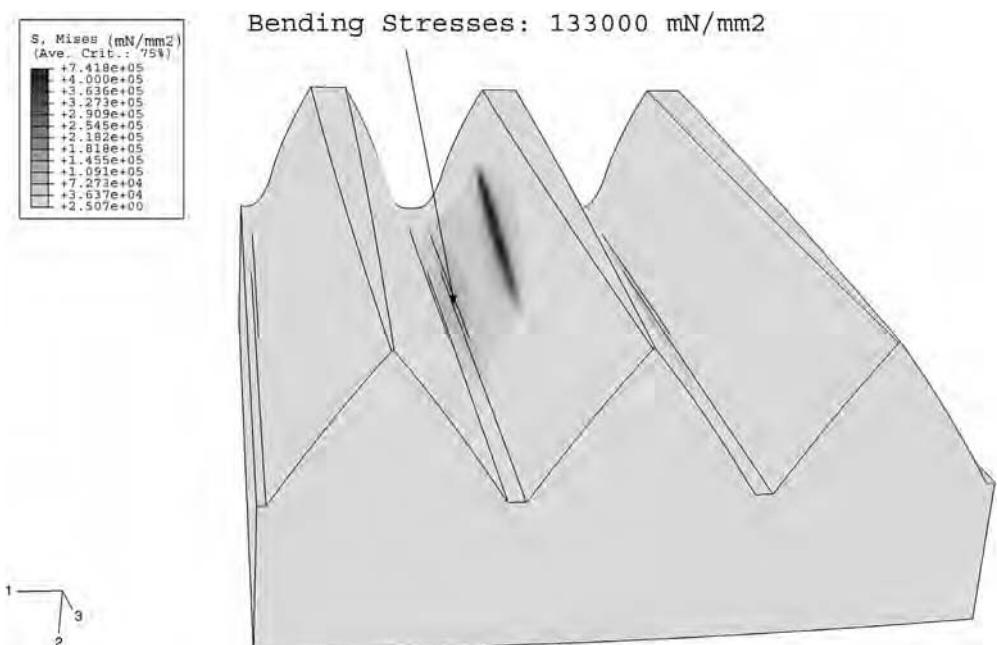
The finite element mesh of three pairs of teeth of the second type of geometry is represented in Fig. 18.15.1. Continuum solid elements of first order, enhanced by in-compatible nodes to improve their bending behavior, have been used to form the finite element mesh. The total number of elements is 44,820 with 58,327 nodes. The material is steel with the properties of Young's Modulus $E = 2.068 \times 10^8$ mN/mm² and Poisson's
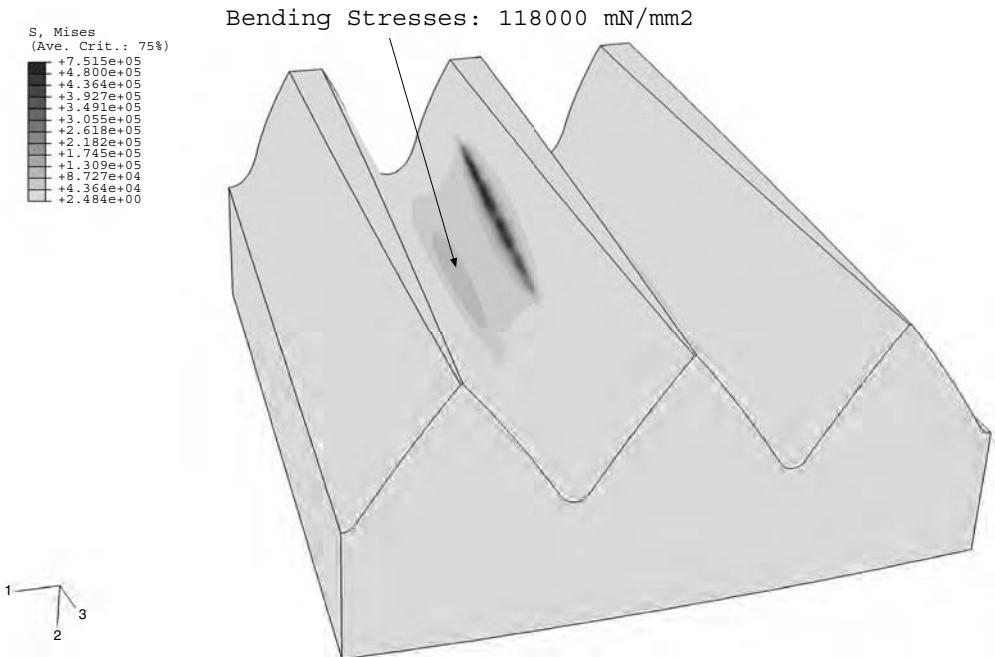
Figure 18.15.1: Three-pairs-of-teeth face-gear drive finite element model.

Figure 18.15.2: Contact and bending stresses for the first type of geometry of face-gear drive.

Figure 18.15.3: Contact and bending stresses for the second type of geometry of face-gear drive generated with an edged-top shaper.

Bending Stresses: 118000 mN/mm2

S, Mises
(Ave. Crit.: 75%)
  +7.515e+05
  +4.800e+05
  +4.364e+05
  +3.927e+05
  +3.491e+05
  +3.055e+05
  +2.618e+05
  +2.182e+05
  +1.745e+05
  +1.309e+05
  +8.727e+04
  +4.364e+04
  +2.484e+00

Figure 18.15.4: Contact and bending stresses for the second type of geometry of face-gear generated with a rounded-top shaper.
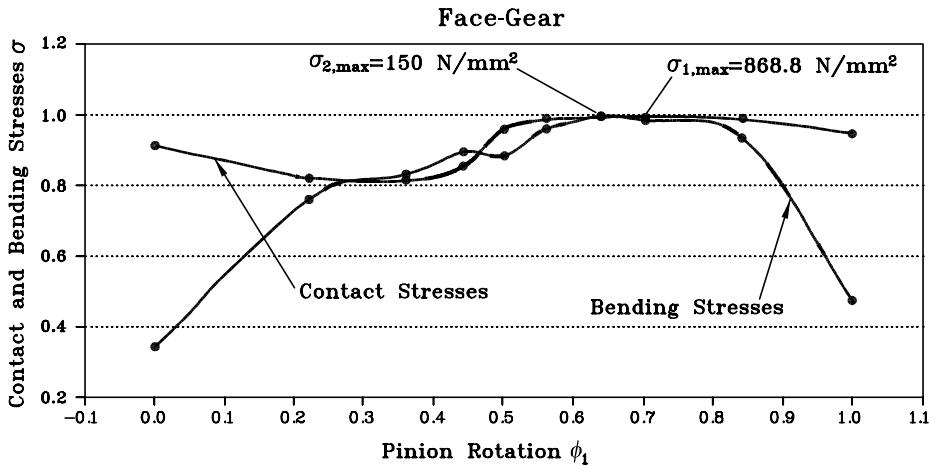
ratio of 0.29. A torque of 1600 Nm has been applied to the pinion for both versions of face-gear drive.

Figures 18.15.2 and 18.15.3 show the maximum contact and bending stresses obtained at the mean contact point for the first and second type of geometry, respectively. For such examples, a traditional edged-top shaper has been applied. Comparison between Figs. 18.15.1 and 18.15.2 shows that:
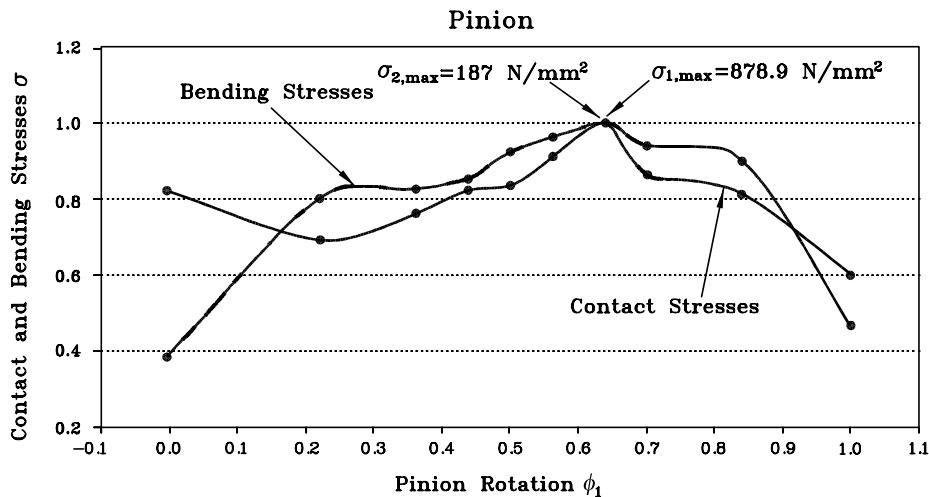
 (i) Edge contact can be avoided, reducing the magnitude of the maximum contact stress up to 40%.
(ii) For a considerable part of the cycle of meshing only one pair of teeth is in contact. The maximum bending stress at the fillet of the first type of geometry of face-gear is 43% lower.

Figure 18.15.4 confirms that application of a rounded-top shaper (Fig. 18.8.1) reduces the bending stresses of the face-gear from 6 to 12% during the cycle of meshing. This enables us to keep the increment of the bending stresses for the second type of geometry to less than 40%.

The performed stress analysis has been complemented with investigation of formation of the bearing contact (Figs. 18.15.2 to 18.15.5). Figures 18.15.5 and 18.15.6 illustrate the variation of bending and contact stresses of the gear and the pinion during the cycle of meshing for the second type of geometry, an application of an edged-top shaper and

Face-Gear

(a)
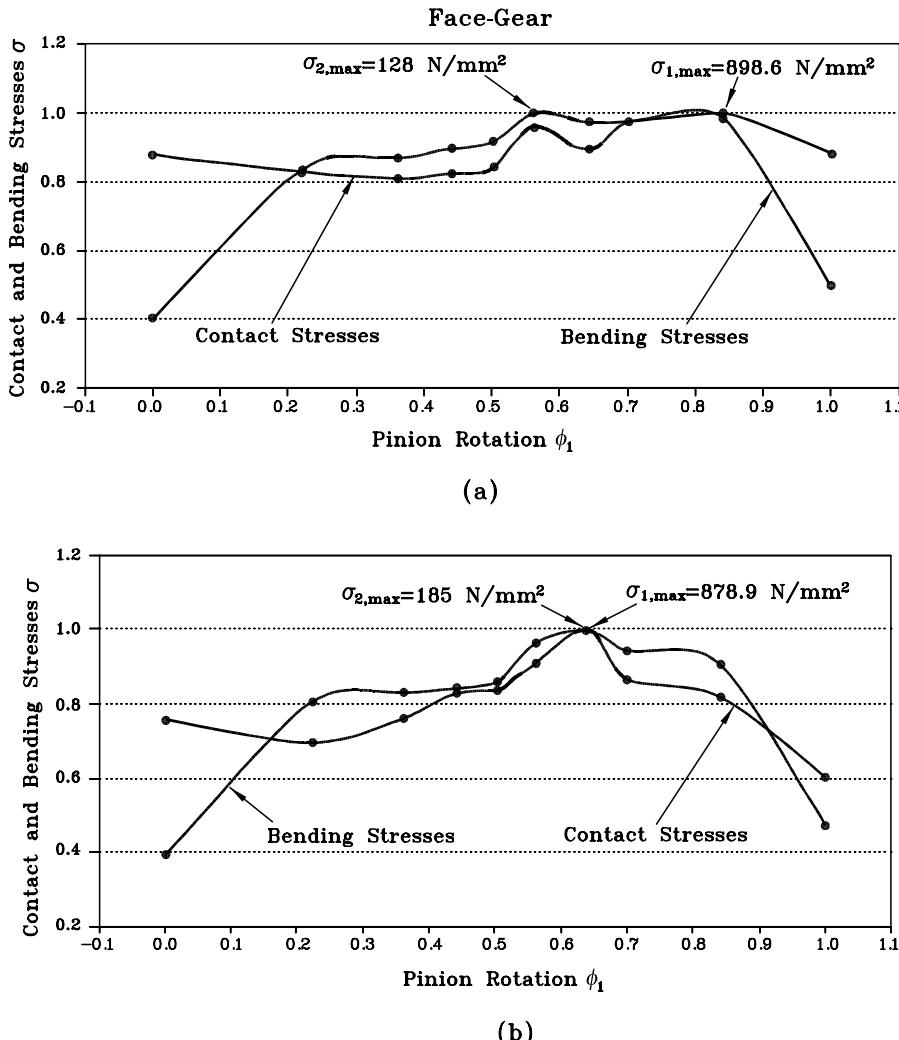
Pinion

(b)

Figure 18.15.5: Variation of functions of contact and bending stresses during the cycle of meshing for (a) the face-gear, and (b) the pinion of the second type of geometry and an edged-top shaper.

a rounded-top shaper, respectively. The stresses are represented as functions of unitless parameter ϕ represented as

$$\phi = \frac{\phi_P - \phi_{in}}{\phi_{fin} - \phi_{in}}, \quad 0 \leq \phi \leq 1. \tag{18.15.1}$$

Here, ϕ_P is the pinion rotation angle; ϕ_{in} and ϕ_{fin} are the magnitudes of the pinion angular positions in the beginning and at the end of the cycle of meshing.

Figure 18.15.6: Variation of functions of contact and bending stresses during the cycle of meshing for (a) the face-gear, and (b) the pinion of the second type of geometry and a rounded-top shaper.

The unitless stress coefficient σ (Figs. 18.15.5 and 18.15.6) is defined as

$$\sigma = \frac{\sigma_P}{\sigma_{P_{max}}}, \quad |\sigma| \leq 1. \tag{18.15.2}$$

Here, σ_P is the variable of function of stresses, and $\sigma_{P_{max}}$ is the magnitude of maximal stress.
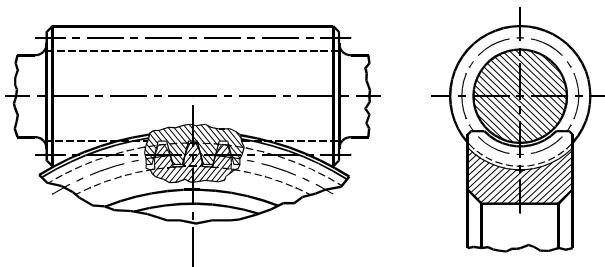
19 **Worm-Gear Drives with Cylindrical Worms**

19.1 INTRODUCTION

There are two types of worm-gear drives: (i) those with cylindrical worms (Fig. 19.1.1) (single-enveloping worm-gear drives), and (ii) those with hourglass worms (see Chapter 20) (double-enveloping worm-gear drives). The terms "single-enveloping" and "double-enveloping" are confusing because in both cases the surface of the worm-gear tooth is the envelope to the one-parameter family of worm thread surfaces that are generated in the coordinate system rigidly connected to the worm-gear. The thread surface of a cylindrical worm is a helicoid. (We recall that a helicoid is the surface that is generated by a given curve while it performs a screw motion.)

This chapter covers (i) the generation and geometry of cylindrical worms, and (ii) the basic design problems (relations between design parameters). Depending on the method for generation, we differentiate henceforth the following types of cylindrical worms (see German Standards DIN 3975):

(i) **ZA worms, with surface A**. The worm surface is a *ruled* surface that is generated by a straight line while it performs a screw motion with respect to the worm axis. The generating line intersects the worm axis and therefore the axial section of the worm surface is a straight line that is just the generating line. The cross section of the ZA worm is an Archimedes spiral (see Section 19.4).

(ii) **ZN worms, with surface N**. The worm surface is also a ruled surface. However, the generating line lies in a plane that passes through the perpendicular to the worm axis and forms angle λ_p with the worm axis (see Section 19.5). Here, λ_p is the lead angle on the pitch cylinder on the worm. The cross section of the worm is an extended involute (see Section 19.5).

(iii) **ZI worms, with surface I**. The worm surface is a screw involute surface that may be considered a particular case of a ruled surface. Such a surface can be generated by a straight line that performs a screw motion about the worm axis and is tangent to the helix on the base cylinder of the worm. The cross section of the worm surface is an involute curve. The ZI worm is identical to an involute helical gear whose tooth number is the number of worm threads.

(iv) **ZK worms, with surface K**. The worm surface is not a ruled surface but an envelope to the family of cone surfaces. Such a family of surfaces is generated by the surface

Figure 19.1.1: Worm-gear with cylindrical worm.

of a cone (the tool surface) that performs a screw motion about the axis of the worm (see Section 19.7).
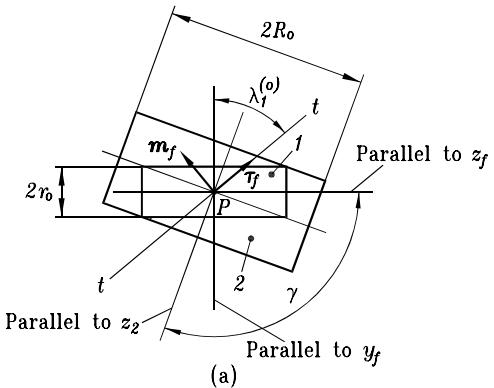
(v) **Flender worms, with convex–concave (CC) surface.** Again, the worm surface is not a ruled surface but an envelope to the family of generating surfaces. The generating surface is a surface of revolution and its axial section is an arc of a circle. The family of generating surfaces is formed by the screw motion of the tool about the worm axis.

Worm-gear drives are sensitive to errors of assembly (the change of center distance, shaft angle, and axial displacement of the worm-gear) that result in the shift of the bearing contact to the edge and cause a piecewise almost-linear function of transmission errors. The frequency of transmission errors is the same as the cycle of meshing of a pair of teeth. A more stable bearing contact of worm-gear drives and a more favorable function of transmission errors can be obtained by a proper mismatch between the surfaces of the worm and the hob.
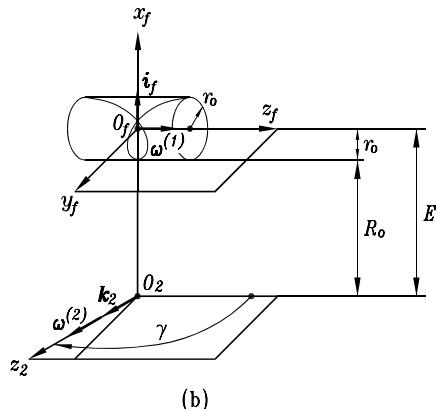
19.2 PITCH SURFACES AND GEAR RATIO

We recall that in the case of transformation of motions between crossed axes the relative motion is the screw one and the axodes are hyperboloids of revolution. There is nothing common to the pitch surfaces of a worm-gear drive and the axodes. The pitch surfaces are two cylinders with the same twist angle as that of the worm-gear drive. The purpose of application of such pitch surfaces is to provide by synthesis a main point of contact of the worm and the worm-gear surfaces, the same as the point of tangency of the crossed cylinders – the pitch surfaces. Henceforth, we differentiate between *ordinary* pitch surfaces and *operating* pitch surfaces. In the case of ordinary pitch surfaces, the cross cylinders are the pitch cylinders of the worm and the worm-gear.

Figure 19.2.1(a) shows the operating pitch cylinders of the worm and the worm-gear. Axes z_f and z_2 of these cylinders form the crossing angle γ, and their shortest distance is E [Figs. 19.2.1(a) and 19.2.1(b)]. Angle γ is measured clockwise from z_f to z_2. The operating pitch cylinders are in tangency at point P. We assume that the worm is located above the worm-gear. The intersection of the respective cylinder with the surface of the worm thread and the worm-gear tooth surface represents a helix on the cylinder; the common tangent to both helices is $t–t$; the unit tangent is $\boldsymbol{\tau}_f$; and $\lambda_1^{(o)}$

Figure 19.2.1: Illustration of (a) operating pitch cylinders of the worm and the gear, and (b) the worm helix.

is the lead angle on the worm operating pitch cylinder. Figure 19.2.1(a) corresponds to the case when the worm and the worm-gear are right-handed. The direction of the worm helix is shown in Fig. 19.2.1(b); tangent t–t is drawn to the helix at point P, located on the bottom of the worm cylinder.

Our goal is to represent the worm-gear ratio considering that the operating pitch cylinders are in tangency at point P and the input data are r_o, R_o, $\lambda_1^{(o)}$, and γ. We may consider that the direction and magnitude of $\boldsymbol{\omega}^{(1)}$ are chosen and we have to determine the magnitude and the direction of $\boldsymbol{\omega}^{(2)}$ considering that the line of action of $\boldsymbol{\omega}^{(2)}$ is the z_2 axis of gear rotation.

We consider a fixed coordinate system $S_f(x_f, y_f, z_f)$ where z_f is the axis of worm rotation. Points P_1 and P_2 of the respective operating pitch cylinders coincide with each other at point P. The velocities of points P_1 and P_2 are represented by the equations

$$\mathbf{v}^{(1)} = \boldsymbol{\omega}^{(1)} \times \mathbf{r}_f, \qquad \mathbf{v}^{(2)} = (\boldsymbol{\omega}^{(2)} \times \mathbf{r}_f) + (\mathbf{E} \times \boldsymbol{\omega}^{(2)}) \qquad (19.2.1)$$

where $\mathbf{r}_f = \overline{O_f P}$ and $\mathbf{E} = \overline{O_f O_2}$. Velocities $\mathbf{v}^{(1)}$ and $\mathbf{v}^{(2)}$ lie in plane Π that is perpendicular to the x_f axis; this plane is tangent to the operating pitch cylinders at point P. Thus,

$$\mathbf{v}^{(1)} \cdot \mathbf{i}_f = \mathbf{v}^{(2)} \cdot \mathbf{i}_f = 0 \qquad (19.2.2)$$

where $\mathbf{i}_f$ is the unit vector of axis x_f.

To determine the gear ratio, we can use one of the two following equations:

$$\left(\mathbf{v}_f^{(1)} - \mathbf{v}_f^{(2)}\right) \times \boldsymbol{\tau}_f = \mathbf{v}_f^{(12)} \times \boldsymbol{\tau}_f = 0 \tag{19.2.3}$$

or

$$\mathbf{v}_f^{(1)} \cdot \mathbf{m}_f = \mathbf{v}_f^{(2)} \cdot \mathbf{m}_f. \tag{19.2.4}$$

Here,

$$\mathbf{m}_f = \mathbf{i}_f \times \boldsymbol{\tau}_f. \tag{19.2.5}$$

Vector $\mathbf{m}_f$ lies in plane Π and is perpendicular to $\boldsymbol{\tau}_f$ [Fig. 19.2.1(a)]. The subscript f indicates that the introduced vectors are represented in S_f. Equation (19.2.3) follows from the fact that the relative (sliding) velocity at point P is collinear to $\boldsymbol{\tau}_f$. Equation (19.2.4) indicates that

$$\left(\mathbf{v}_f^{(1)} - \mathbf{v}_f^{(2)}\right) \cdot \mathbf{m}_f = \mathbf{v}_f^{(12)} \cdot \mathbf{m}_f = 0 \tag{19.2.6}$$

because $\mathbf{m}_f$ is perpendicular to $\boldsymbol{\tau}_f$.

For further derivations we use Eqs. (19.2.1), (19.2.4), and (19.2.5), which yield

$$\omega^{(1)} r_o \sin \lambda_1^{(o)} = \omega^{(2)} R_o \sin \left(\gamma - \lambda_1^{(o)}\right). \tag{19.2.7}$$

For the case where $\gamma > \lambda_1^{(o)}$, $\omega^{(2)}$ is positive and $\boldsymbol{\omega}^{(2)}$ has the same direction as $\mathbf{k}_2$ [Fig. 19.2.1(b)]. The negative sign for $\omega^{(2)}$ when $\gamma < \lambda_1^{(o)}$ indicates that in this case $\boldsymbol{\omega}^{(2)}$ is opposite to $\mathbf{k}_2$. Equation (19.2.7) cannot be satisfied for the case when $\gamma = \lambda_1^{(o)}$ because the helix on the gear operating pitch cylinder turns into a circle and $\mathbf{v}^{(1)} \cdot \mathbf{m} \neq \mathbf{v}^{(2)} \cdot \mathbf{m}$.

Equation (19.2.7) enables representation of the gear ratio as follows:

$$m_{21} = \frac{|\omega^{(2)}|}{\omega^{(1)}} = \pm \frac{r_o \sin \lambda_1^{(o)}}{R_o \sin \left(\gamma - \lambda_1^{(o)}\right)} \qquad \left(\text{provided} \quad \gamma \neq \lambda_1^{(o)}\right). \tag{19.2.8}$$

Here, the upper sign corresponds to the case when $\gamma > \lambda_1^{(o)}$, and the lower sign corresponds to the case when $\gamma < \lambda_1^{(o)}$.

Equations (19.2.3) and (19.2.4) may be interpreted geometrically with the velocity polygon that is shown in Fig. 19.2.2. The drawings confirm that the sliding velocity $\mathbf{v}^{(12)}$ is collinear to $\boldsymbol{\tau}$, and the projections of $\mathbf{v}^{(1)}$ and $\mathbf{v}^{(2)}$ on $\mathbf{m}$ have the same magnitude and direction.
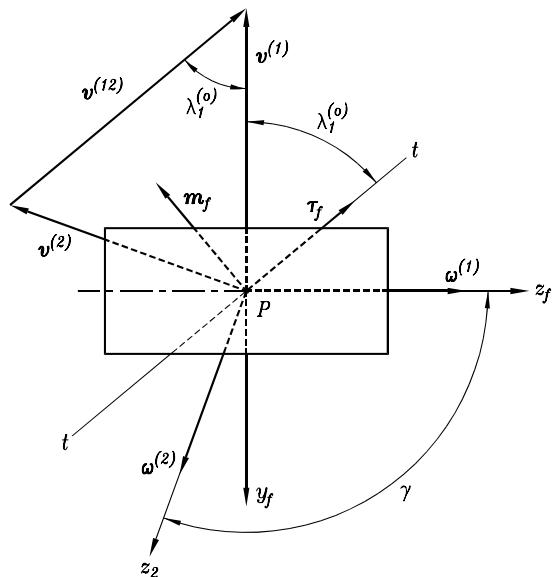
Figure 19.2.3 shows the operating pitch cylinders for a left-hand worm and worm-gear. Derivations similar to those discussed above yield the following gear ratio:

$$m_{21} = \frac{r_o \sin \lambda_1^{(o)}}{R_o \sin \left(\gamma + \lambda_1^{(o)}\right)}. \tag{19.2.9}$$
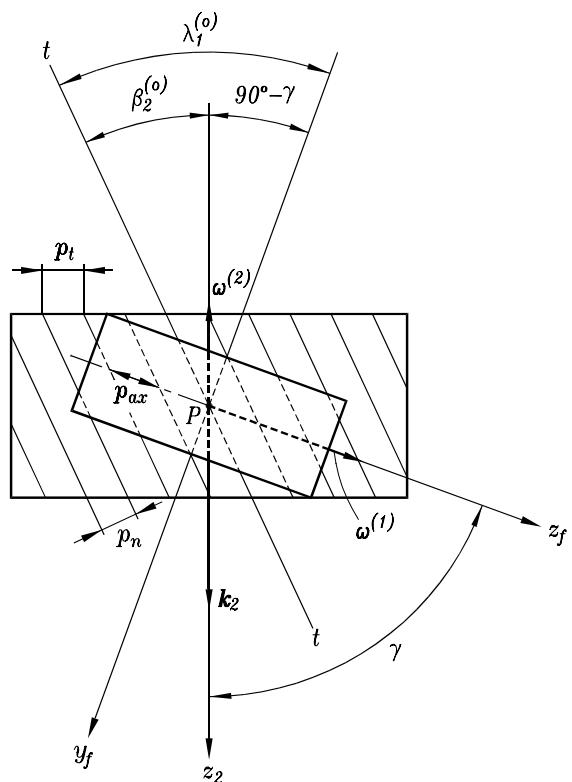
The magnitude of $\lambda_1^{(o)}$ is considered as a positive value. The derivations yield that for the chosen direction of $\boldsymbol{\omega}^{(1)}$ (Fig. 19.2.3), vector $\boldsymbol{\omega}^{(2)}$ is opposite to $\mathbf{k}_2$.

The velocity polygon is shown in Fig. 19.2.4. In the most common case, the crossing angle γ is 90° and
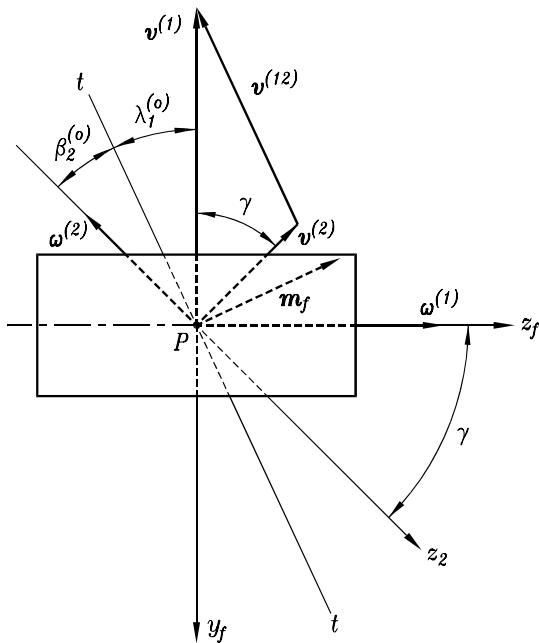
$$m_{21} = \frac{r_o}{R_o} \tan \lambda_1^{(o)}. \tag{19.2.10}$$

**Figure 19.2.2:** Velocity polygon for right-hand worm-gear drive.

Figure 19.2.3: Operating pitch cylinders for left-hand worm-gear drive.
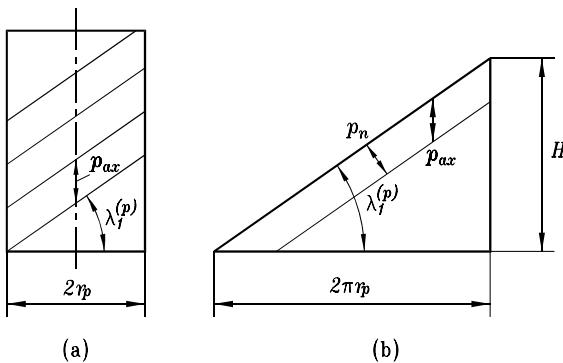
Figure 19.2.4: Velocity polygon for left-hand worm-gear drive.

It is also possible to express the gear ratio that is represented by Eqs. (19.2.8), (19.2.9), and (19.2.10) in terms of the number of worm threads N_1 and the number of gear teeth N_2 [see Eq. (19.3.11)].

19.3 DESIGN PARAMETERS AND THEIR RELATIONS

Worm Pitch Diameter, Lead Angle, and Axial Pitch

Figure 19.3.1(a) shows the pitch diameter d_p of the worm ordinary pitch cylinder; p_{ax} is the axial distance between the neighboring threads of the worm, which is measured along the generatrix of the pitch cylinder. We designate with P_{ax} the ratio $P_{ax} = \pi/p_{ax}$. The

Figure 19.3.1: Worm pitch cylinder (a) in 3D-space, and (b) developed on a plane.

worm pitch diameter may be chosen as

$$d_p = 2r_p = \frac{q}{P_{ax}}. \tag{19.3.1}$$

The value of q depends on the number N_1 of threads of the worm and the number N_2 of gear teeth and may be picked up from a recommended set $(7 \le q \le 25)$.

Let us develop the pitch cylinder on a plane [Fig. 19.3.1(b)]. The helix for each worm thread is represented by a straight line. The distance p_{ax} between the neighboring straight lines is

$$p_{ax} = \frac{H}{N_1} \tag{19.3.2}$$

where N_1 is the number of worm threads, and H is the lead. Considering as known r_p and P_{ax}, we can determine the lead angle on the pitch cylinder from the following equation [Fig. 19.3.1(b)]:

$$\tan \lambda_1^{(p)} = \frac{H}{\pi d_p} = \frac{p_{ax} N_1}{2\pi r_p} = \frac{N_1}{2 P_{ax} r_p}. \tag{19.3.3}$$

Lead Angle on Worm Operating Pitch Cylinder

The lead angles on the worm operating pitch cylinder and ordinary pitch cylinder are related as

$$\tan \lambda_1^{(o)} r_o = \tan \lambda_1^{(p)} r_p = p \tag{19.3.4}$$

where $p = H/(2\pi)$ is the screw parameter. Equations (19.3.3) and (19.3.4) yield

$$\tan \lambda_1^{(o)} = \frac{N_1}{2 P_{ax} r_o} \tag{19.3.5}$$

where r_o is the chosen radius of the operating pitch cylinder. The difference between r_o and r_p affects the shape of contact lines between the surfaces of the worm and the worm-gear.

Relation Between Worm and Worm-Gear Pitches
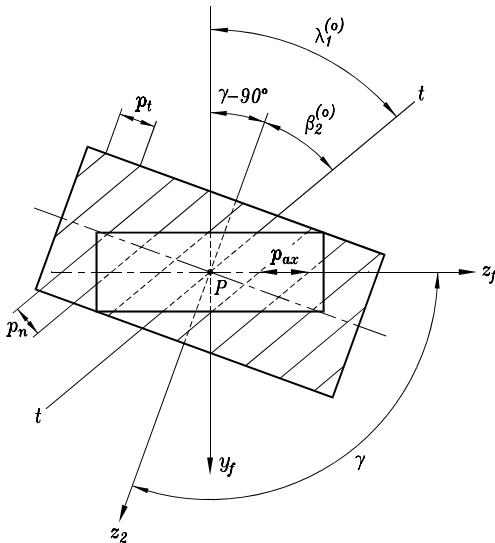
We emphasize that we now consider the worm and worm-gear pitches on the operating pitch cylinder (Fig. 19.3.2). The axial section of two neighboring teeth represents two parallel curves. Therefore, the worm axial pitch p_{ax} is the same for the worm pitch cylinder and the operating pitch cylinder. The normal pitch p_n is the same for the worm and the worm-gear and is represented by the equation

$$p_n = p_{ax} \cos \lambda_1^{(o)}.$$

The worm-gear transverse pitch, p_t, is represented by the equation (Fig. 19.3.2)

$$p_t = \frac{p_n}{\cos \beta_2^{(o)}} = \frac{p_{ax} \cos \lambda_1^{(o)}}{\cos \left[90° \pm \left(\lambda_1^{(o)} - \gamma \right) \right]} = \pm \frac{p_{ax} \cos \lambda_1^{(o)}}{\sin \left(\gamma - \lambda_1^{(o)} \right)} \tag{19.3.6}$$

$$\left(\text{provided } \gamma - \lambda_1^{(o)} \neq 0 \right).$$

Figure 19.3.2: Worm and worm-gear operating pitch cylinders.

Here, $\beta_2^{(o)}$ is the gear helix angle on the worm-gear operating pitch cylinder. The upper sign corresponds to the case where $\gamma > \lambda_1^{(o)}$, and the lower sign corresponds to $\gamma < \lambda_1^{(o)}$. Equation (19.3.6) provides the positive sign for p_t. Similar derivations for the left-hand worm and worm-gear (Fig. 19.2.3) yield

$$p_t = \frac{p_{ax} \cos \lambda_1^{(o)}}{\sin \left(\gamma + \lambda_1^{(o)}\right)}. \tag{19.3.7}$$

It is obvious that for the case of an orthogonal worm-gear drive (with $\gamma = 90°$) we obtain that $p_t = p_{ax}$.

Radius of Worm-Gear Operating Pitch Cylinder

We take into account that

$$p_t N_2 = 2\pi R_o. \tag{19.3.8}$$

Equations (19.3.6), (19.3.7), and (19.3.8) yield the following:

(i) R_o is represented for the right-hand worm and worm-gear as

$$R_o = \pm \frac{p_{ax} N_2 \cos \lambda_1^{(o)}}{2\pi \sin \left(\gamma - \lambda_o^{(1)}\right)} \quad \left(\text{provided} \quad \gamma - \lambda_1^{(o)} \neq 0\right). \tag{19.3.9}$$

The upper sign corresponds to the case when $\gamma > \lambda_1^{(o)}$, and the lower sign corresponds to the case when $\gamma < \lambda_1^{(o)}$.

(ii) For the left-hand worm and worm-gear, we have

$$R_o = \frac{p_{ax} N_2 \cos \lambda_1^{(o)}}{2\pi \sin \left(\gamma + \lambda_1^{(o)}\right)}. \tag{19.3.10}$$

Representation of m_{21} in Terms of N_1 and N_2

The gear ratio m_{21} was represented for the right-hand and left-hand worms and worm-gears by Eqs. (19.2.8) and (19.2.9), respectively. Equations (19.2.8), (19.2.9), (19.3.9), and (19.3.10) yield

$$m_{21} = \frac{N_1}{N_2}. \tag{19.3.11}$$

Shortest Distance E

The shortest distance E between the axes of the worm and the worm-gear is

$$E = r_o + R_o \tag{19.3.12}$$

where

$$r_o = \frac{N_1 p_{ax}}{2\pi \tan \lambda_1^{(o)}}, \tag{19.3.13}$$

and R_o is represented by Eq. (19.3.9) or Eq. (19.3.10). For the case when $\gamma = 90°$ and the operating pitch cylinders coincide with the ordinary pitch cylinders, we obtain

$$E = \frac{p_{ax}}{2\pi} \left(\frac{N_1}{\tan \lambda_1^{(o)}} + N_2 \right). \tag{19.3.14}$$

Relations Between Profile Angles in Axial, Normal, and Transverse Sections

Consider the transverse, normal, and axial sections of the worm surface. The transverse section is obtained by cutting of the surface by plane $z = 0$ [Fig. 19.3.3(a)]. The axial section is obtained by cutting of the surface by plane $y = 0$ [Fig. 19.3.3(d)]. Figure 19.3.3(b) shows the unit tangent $\mathbf{a}$ to the helix on the pitch cylinder at point P of the helix. The normal section [Fig. 19.3.3(c)] is obtained by cutting of the surface by plane Π that passes through the x axis and is perpendicular to vector $\mathbf{a}$ [Fig. 19.3.3(b)]. The normal section is shown in Fig. 19.3.3(c), and the unit tangent to the profile at point P is $\mathbf{b}$.

The unit normal $\mathbf{n}$ to the worm surface at P is represented as

$$\mathbf{n} = \mathbf{a} \times \mathbf{b} \tag{19.3.15}$$
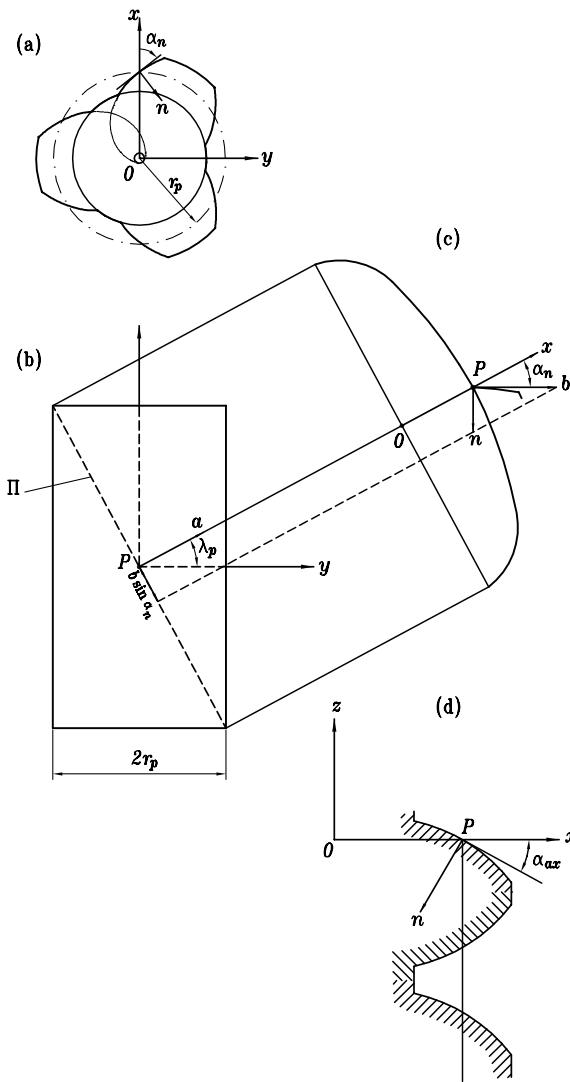
where

$$\begin{aligned}
\mathbf{a} &= [0 \quad \cos \lambda_p \quad \sin \lambda_p]^{\mathrm{T}} \\
\mathbf{b} &= [\cos \alpha_n \quad \sin \alpha_n \sin \lambda_p \quad -\sin \alpha_n \cos \lambda_p]^{\mathrm{T}},
\end{aligned} \tag{19.3.16}$$

and λ_p is the lead angle of the helix at the pitch cylinder. Equations (19.3.15) and (19.3.16) yield

$$\mathbf{n} = [-\sin \alpha_n \quad \cos \alpha_n \sin \lambda_p \quad -\cos \alpha_n \cos \lambda_p]^{\mathrm{T}}. \tag{19.3.17}$$

Projections of the unit normal are shown in Fig. 19.3.3. The orientations of the tangents to the profiles in the transverse, normal, and axial sections are represented by

Figure 19.3.3: Sections of worm surface: (a) tooth cross section; (b) worm pitch cylinder in 3D-space; (c) section of pitch cylinder by plane Π; (d) axial section of worm tooth.

angles α_t, α_n, and α_{ax}, respectively. It is evident from Fig. 19.3.3 that

$$\tan \alpha_t = -\frac{n_x}{n_y} = \frac{\tan \alpha_n}{\sin \lambda_p}, \qquad \tan \alpha_{ax} = \frac{n_x}{n_z} = \frac{\tan \alpha_n}{\cos \lambda_p}.$$

Thus,

$$\tan \alpha_n = \tan \alpha_t \sin \lambda_p = \tan \alpha_{ax} \cos \lambda_p. \tag{19.3.18}$$

Equation (19.3.18) relates the profile angles in normal, transverse, and axial sections.

Let us now consider a particular case, an involute worm. We may express the radius r_b of the base cylinder of an involute worm in terms of the screw parameter p, the lead angle on the pitch cylinder λ_p, and the axial profile angle α_{ax}. The derivations are based

on the following considerations:

$$\cos \alpha_t = \frac{r_b}{r_p} = \frac{\tan \lambda_p}{\tan \lambda_b}. \tag{19.3.19}$$

Equation (19.3.18) yields

$$\tan \alpha_t = \frac{\tan \alpha_{ax}}{\tan \lambda_p}. \tag{19.3.20}$$

The radius of the base cylinder is represented as

$$r_b = \frac{p}{\tan \lambda_b} = \frac{p}{\tan \lambda_p} \cos \alpha_t = \frac{p}{\tan \lambda_p (1 + \tan^2 \alpha_t)^{1/2}}. \tag{19.3.21}$$

Equations (19.3.20) and (19.3.21) yield the following final expression for r_b:

$$r_b = \frac{p}{(\tan^2 \alpha_{ax} + \tan^2 \lambda_p)^{1/2}}. \tag{19.3.22}$$
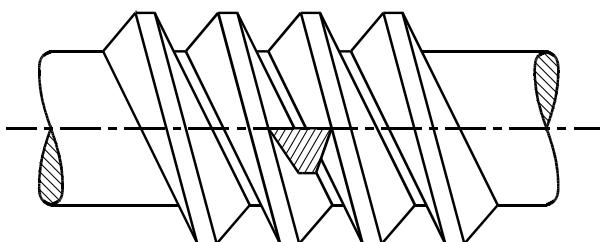
19.4 GENERATION AND GEOMETRY OF ZA WORMS

The worm is generated by a straight-lined blade (Fig. 19.4.1). The cutting edges of the blade are installed in the axial section of the worm.

Henceforth we consider two generating lines, *I* and *II*, that generate the surface sides *I* and *II* of the worm space, respectively (Fig. 19.4.2). The generating lines are represented in coordinate system S_b that is rigidly connected to the blade. The respective surfaces of both sides of the worm thread are generated while coordinate system S_b performs the screw motion about the worm axis (Fig. 19.4.3). The generated surface is represented in coordinate system S_1 by the matrix equation

$$\mathbf{r}_1(u, \theta) = \mathbf{M}_{1b}(\theta) \, \mathbf{r}_b(u). \tag{19.4.1}$$

Here, the coordinate system S_1 is rigidly connected to the worm; θ is the angle of rotation in the screw motion; parameter u determines the location of a current point on the generating line and is measured from the point of intersection of the generating line with the z_b axis. Thus $u = |\overline{BB'}|$ for the current point B' of the left generating line *II*. Similarly, $u = |\overline{AA'}|$ for the current point A' of the right generating line *I*.

Figure 19.4.1: Installation of blade for generation of an Archimedes worm.
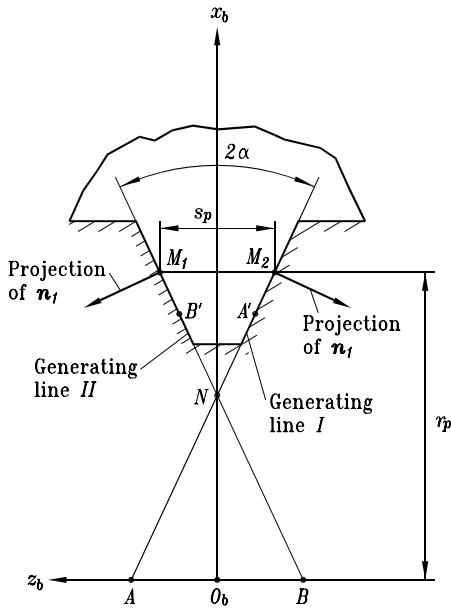
Figure 19.4.2: Geometry of straight-lined blade.

The unit surface normal is represented in coordinate system S_1 by the equations

$$\mathbf{n}_1(u, \theta) = \pm k \, \mathbf{N}_1 = \pm k \left(\frac{\partial \mathbf{r}_1}{\partial u} \times \frac{\partial \mathbf{r}_1}{\partial \theta} \right) \tag{19.4.2}$$

where $k = 1/|\mathbf{N}_1|$. The upper or lower sign must be chosen with the condition that the surface unit normal will be directed *toward* the worm thread.

Matrix $\mathbf{M}_{1b}$ is represented by the equation (Fig. 19.4.3)

$$\mathbf{M}_{1b} = \begin{bmatrix} \cos\theta & -\sin\theta & 0 & 0 \\ \sin\theta & \cos\theta & 0 & 0 \\ 0 & 0 & 1 & \pm p\theta \\ 0 & 0 & 0 & 1 \end{bmatrix}. \tag{19.4.3}$$
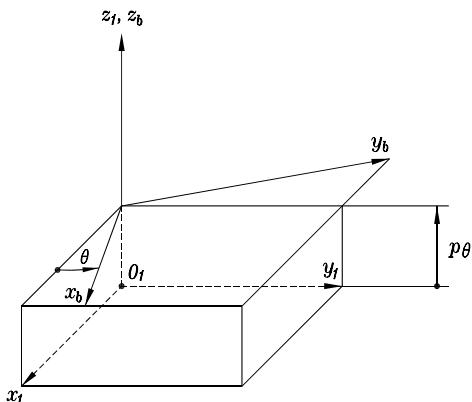
Figure 19.4.3: Coordinate transformation in the case of screw motion.

Here, p is the screw parameter that is considered as an arithmetic value ($p > 0$). The upper and lower signs for $p\theta$ correspond to the cases when a right-hand worm and a left-hand worm are generated, respectively. Figure 19.4.3 shows the generation of a right-hand worm. The surface sides I and II for right-hand and left-hand worms are generated by generating line I and generating line II, respectively.

Using Eqs. (19.4.1) and (19.4.2) we may represent the surface equations and the surface unit normals for both sides of the worm thread in S_1 as follows:

(i) **Surface side I, right-hand worm:**

$$
\begin{aligned}
x_1 &= u\cos\alpha\cos\theta \\
y_1 &= u\cos\alpha\sin\theta \\
z_1 &= -u\sin\alpha + \left(r_p\tan\alpha - \frac{s_p}{2}\right) + p\theta.
\end{aligned}
\tag{19.4.4}
$$

The surface unit normal is

$$
\mathbf{n}_1 = -k[(p\sin\theta + u\sin\alpha\cos\theta)\,\mathbf{i}_1 - (p\cos\theta - u\sin\alpha\sin\theta)\,\mathbf{j}_1 + u\cos\alpha\,\mathbf{k}_1]
$$

$$
\text{(provided } \cos\alpha \neq 0)
\tag{19.4.5}
$$

where $k = 1/(p^2 + u^2)^{0.5}$. We recall that parameter u is measured along the generating line I from point A of intersection of this line with axis z_b (Fig. 19.4.2). Design parameter s_p is equal to the axial width w_{ax} of the worm space in the axial section. For standard worm gear drives we have

$$
w_{ax} = \frac{\pi}{2P_{ax}}
\tag{19.4.6}
$$

where P_{ax} is the axial diametral pitch.

(ii) **Surface side II, right-hand worm:**

$$
\begin{aligned}
x_1 &= u\cos\alpha\cos\theta \\
y_1 &= u\cos\alpha\sin\theta \\
z_1 &= u\sin\alpha - \left(r_p\tan\alpha - \frac{s_p}{2}\right) + p\theta.
\end{aligned}
\tag{19.4.7}
$$

The surface unit normal is

$$
\mathbf{n}_1 = k[(p\sin\theta - u\sin\alpha\cos\theta)\,\mathbf{i}_1 - (p\cos\theta + u\sin\alpha\sin\theta)\,\mathbf{j}_1 + u\cos\alpha\,\mathbf{k}_1]
$$

$$
\text{(provided } \cos\alpha \neq 0)
\tag{19.4.8}
$$

where $k = 1/(p^2 + u^2)^{0.5}$.

(iii) **Surface side I, left-hand worm:**

$$
\begin{aligned}
x_1 &= u\cos\alpha\cos\theta \\
y_1 &= u\cos\alpha\sin\theta \\
z_1 &= -u\sin\alpha + \left(r_p\tan\alpha - \frac{s_p}{2}\right) - p\theta.
\end{aligned}
\tag{19.4.9}
$$

The surface unit normal is

$$
\mathbf{n}_1 = -k[(-p\sin\theta + u\sin\alpha\cos\theta)\,\mathbf{i}_1 + (p\cos\theta + u\sin\alpha\sin\theta)\,\mathbf{j}_1 + u\cos\alpha\,\mathbf{k}_1]
$$

$$
\text{(provided } \cos\alpha \neq 0)
\tag{19.4.10}
$$

where $k = 1/(p^2 + u^2)^{0.5}$.

(iv) **Surface side *II*, left-hand worm:**

$$x_1 = u \cos \alpha \cos \theta$$
$$y_1 = u \cos \alpha \sin \theta \qquad\qquad (19.4.11)$$
$$z_1 = u \sin \alpha - \left(r_p \tan \alpha - \frac{s_p}{2}\right) - p\theta.$$

The surface unit normal is

$$\mathbf{n}_1 = k[-(p \sin \theta + u \sin \alpha \cos \theta)\, \mathbf{i}_1 + (p \cos \theta - u \sin \alpha \sin \theta)\, \mathbf{j}_1 + u \cos \alpha\, \mathbf{k}_1]$$

$$(\text{provided} \ \ \cos \alpha \neq 0) \qquad\qquad (19.4.12)$$

where $k = 1/(p^2 + u^2)^{0.5}$.

Problem 19.4.1

The worm surface Σ_1 is represented by Eqs. (19.4.7). Consider the axial section of Σ_1 as the intersection of Σ_1 by plane $y_1 = 0$. Equations (19.4.7) with $y_1 = 0$ provide two solutions:

(i) Derive the equations of two axial sections as $x_1 = x_1(u)$, and $z_1 = z_1(u)$.
(ii) Determine coordinates x_1 and z_1 for the point of intersection of the respective axial section with the pitch cylinder of radius r_p.

Solution

(i) *Solution 1*

$$x_1 = u \cos \alpha, \quad y_1 = 0, \quad z_1 = u \sin \alpha - \left(r_p \tan \alpha - \frac{s_p}{2}\right).$$

Solution 2

$$x_1 = -u \cos \alpha, \quad y_1 = 0, \quad z_1 = u \sin \alpha - \left(r_p \tan \alpha - \frac{s_p}{2}\right) + p\pi.$$

(ii) *Solution 1*

$$\theta = 0, \quad x_1 = r_p, \quad z_1 = \frac{s_p}{2}.$$

Solution 2

$$\theta = \pi, \quad x_1 = -r_p, \quad z_1 = \frac{s_p}{2} + p\pi.$$
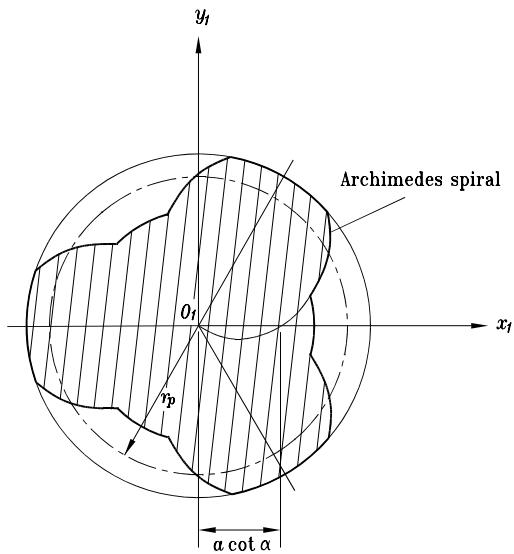
Problem 19.4.2

The worm surface Σ_1 is represented by Eqs. (19.4.7). Consider the cross section of Σ_1 by plane $z_1 = 0$. Investigate the equation $r_1 = r_1(\theta)$, where $r_1 = (x_1^2 + y_1^2)^{0.5}$, and verify that it represents the Archimedes spiral.

Solution

(i) Equation $z_1 = 0$ yields

$$u = \frac{r_p \tan \alpha - \dfrac{s_p}{2} - p\theta}{\sin \alpha} = \frac{a - p\theta}{\sin \alpha}.$$

Figure 19.4.4: Cross section of an Archimedes worm.

(ii) The cross section is represented by equations

$$x_1 = (a - p\theta)\cot\alpha\cos\theta, \quad y_1 = (a - p\theta)\cot\alpha\sin\theta.$$

(iii) Equation

$$r_1 = \left(x_1^2 + y_1^2\right)^{0.5}$$

yields

$$r_1 = (a - p\theta)\cot\alpha.$$
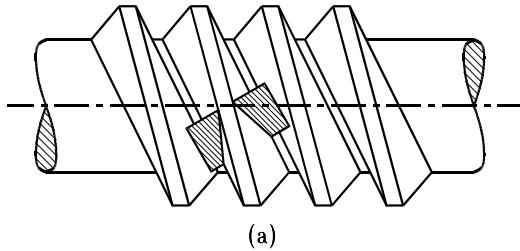
The magnitude of the initial position vector for $\theta = 0$ is $r_1 = a\cot\alpha$. The increment and decrement of the magnitude of the position vector is proportional to θ, and this is the proof that the cross section is an Archimedes spiral. Figure 19.4.4 shows the cross section of the ZA worm with three threads.

19.5 GENERATION AND GEOMETRY OF ZN WORMS
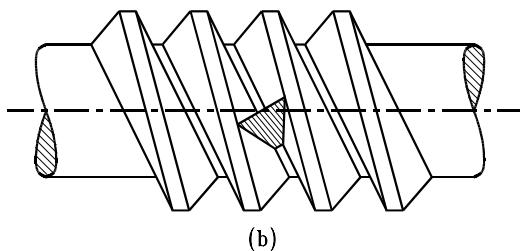
Generation

ZA worms are used if the lead angle of the worm is small enough ($\lambda_p \leq 10°$). In the case of generation of worms with large lead angles, the blade is installed as shown in Figs. 19.5.1(a) or (b) to provide better conditions of cutting. The first version of installation [Fig. 19.5.1(a)] provides straight-lined shapes in the normal section of the *thread*. Straight-lined shapes are provided in the normal section of the *space* with the second version of installation [Fig. 19.5.1(b)]. The surfaces of the worm will be generated by the blade performing a screw motion with respect to the worm.

To describe the installation of the blade with respect to the worm, we use coordinate systems S_a and S_b that are rigidly connected to the blade and the worm. We start the discussion with the generation of the worm space (Fig. 19.5.2). Axis z_b coincides with

(a)
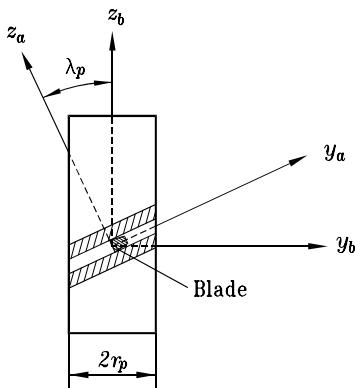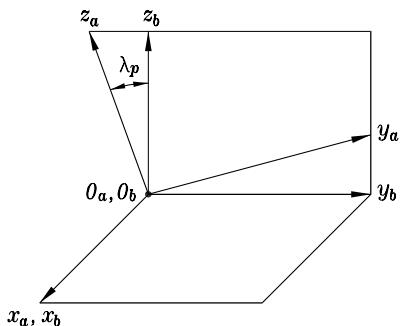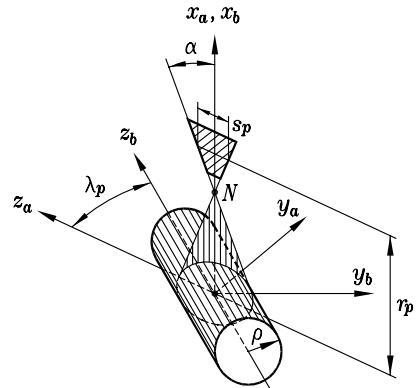
Figure 19.5.1: Blade installation for genera-
tion of ZN worm: (a) for thread generation;
(b) for space generation.

(b)

Blade

$2r_p$
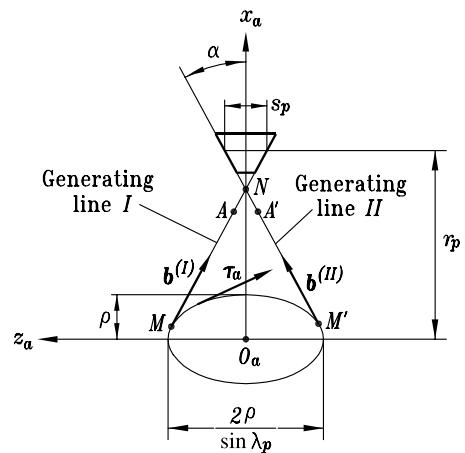
Figure 19.5.2: Coordinate systems applied for blade in-
stallation.

Figure 19.5.3: Representation of generating lines in coordinate system S_a.

the worm axis; axes z_a and z_b form angle λ_p that is the lead angle on the worm pitch cylinder; the origins O_a and O_b lie on the worm axis.

The straight-lined shapes of the blades are shown in Fig. 19.5.3. The extended straight lines are in tangency with the cylinder of the to-be-determined radius ρ. The intersection of plane $y_a = 0$ of coordinate system S_a with the cylinder represents an ellipse with axes 2ρ and $2\rho/\sin\lambda_p$. The coordinate transformation from S_a to S_b is represented by the matrix $\mathbf{M}_{ba}$:

$$\mathbf{M}_{ba} = \begin{bmatrix} 1 & 0 & 0 & 0 \\ 0 & \cos\lambda_p & \mp\sin\lambda_p & 0 \\ 0 & \pm\sin\lambda_p & \cos\lambda_p & 0 \\ 0 & 0 & 0 & 1 \end{bmatrix}. \tag{19.5.1}$$

The upper and lower signs correspond to the generation of a right-hand worm and left-hand worm, respectively.
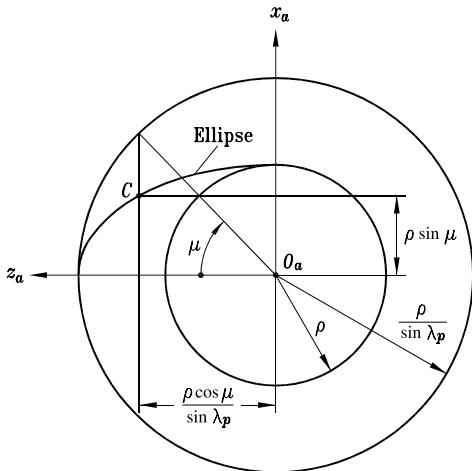
Figure 19.5.4: Interpretation of ellipse equations.

Representation of Generating Lines in Coordinate Systems S_a

Henceforth we consider the generating lines *I* and *II* (Fig. 19.5.3). Each generating line is tangent to the ellipse whose equations are represented in S_a in parametric form as

$$\mathbf{R}_a = \begin{bmatrix} \rho \sin \mu & 0 & \dfrac{\rho}{\sin \lambda_p} \cos \mu \end{bmatrix}^{\mathrm{T}}. \tag{19.5.2}$$

Figure 19.5.4 illustrates the determination of coordinates of current point C of the ellipse; μ is the variable parameter.

The unit tangent $\boldsymbol{\tau}_a$ to the ellipse is represented by the equation

$$\boldsymbol{\tau}_a = \frac{\mathbf{T}_a}{|\mathbf{T}_a|} = \frac{\rho}{|\mathbf{T}_a|} \begin{bmatrix} \cos \mu & 0 & -\dfrac{\sin \mu}{\sin \lambda_p} \end{bmatrix}^{\mathrm{T}} \qquad \left(\mathbf{T}_a = \frac{d\mathbf{R}_a}{d\mu} \right). \tag{19.5.3}$$

The direction of $\boldsymbol{\tau}_a$ that is shown in Fig. 19.5.3 coincides with the direction of increment of parameter μ (Fig. 19.5.4).

The unit vectors $\mathbf{b}_a^{(i)}$ ($i = I, II$) of the generating lines *I* and *II* are represented in S_a as follows:

$$\mathbf{b}_a^{(I)} = [\cos \alpha \quad 0 \quad -\sin \alpha]^{\mathrm{T}} \tag{19.5.4}$$

$$\mathbf{b}_a^{(II)} = [\cos \alpha \quad 0 \quad \sin \alpha]^{\mathrm{T}}. \tag{19.5.5}$$

It is evident that at the point of tangency of the generating line with the ellipse (point M and respectively M'), we have $\mathbf{b}_a^{(I)} = \boldsymbol{\tau}_a^{(I)}$ and $\mathbf{b}_a^{(II)} = -\boldsymbol{\tau}_a^{(II)}$. Equations (19.5.3), (19.5.4), and (19.5.5) yield (see additional explanations in Notes 1 and 2, which

follow this section)

$$\frac{\rho}{|\mathbf{T}_a|} = \cos \delta, \quad \cos \mu^{(I)} = \frac{\cos \alpha}{\cos \delta}$$

$$\sin \mu^{(I)} = \frac{\sin \alpha \sin \lambda_p}{\cos \delta} = \tan \delta \tan \lambda_p \tag{19.5.6}$$

$$\cos \mu^{(II)} = -\frac{\cos \alpha}{\cos \delta}, \quad \sin \mu^{(II)} = \frac{\sin \alpha \sin \lambda_p}{\cos \delta} = \tan \delta \tan \lambda_p.$$

Here,

$$\cos \delta = (\cos^2 \alpha + \sin^2 \alpha \sin^2 \lambda_p)^{0.5}, \quad \sin \delta = \sin \alpha \cos \lambda_p. \tag{19.5.7}$$

The designations "*I*" and "*II*" indicate the generating lines *I* and *II*.

The generating lines are represented in S_a by the equations

$$x_a = \rho \sin \mu \pm u \cos \delta \cos \mu$$
$$y_a = 0 \tag{19.5.8}$$
$$z_a = \frac{\rho \cos \mu}{\sin \lambda_p} \mp u \frac{\cos \delta \sin \mu}{\sin \lambda_p}.$$

The upper and lower signs in Eqs. (19.5.8) correspond to the generating lines *I* and *II*, respectively. The designations "*I*" and "*II*" have been dropped but the magnitudes of μ are different for generating lines *I* and *II* [see Eqs. (19.5.6)]. Parameter u determines the location of current point A (or A') on the generating line; $u = |\overline{MA}|$ and $u = |\overline{M'A'}|$ as shown in Fig. 19.5.3.

Note 1: Determination of Expressions for cos δ and sin δ

Using the equality $\mathbf{b}_a^{(I)} = \tau_a^{(I)}$, and Eqs. (19.5.3) and (19.5.4), we obtain

$$\frac{\rho}{|\mathbf{T}_a|} \cos \mu^{(I)} = \cos \alpha, \quad \frac{\rho}{|\mathbf{T}_a|} \frac{\sin \mu^{(I)}}{\sin \lambda_p} = \sin \alpha. \tag{19.5.9}$$

Equations (19.5.9) yield

$$\cos \mu^{(I)} = \left(\frac{\rho}{|\mathbf{T}_a|}\right)^{-1} \cos \alpha, \quad \sin \mu^{(I)} = \left(\frac{\rho}{|\mathbf{T}_a|}\right)^{-1} \sin \alpha \sin \lambda_p. \tag{19.5.10}$$

Using Eqs. (19.5.10), we obtain that

$$\frac{\rho}{|\mathbf{T}_a|} = (\cos^2 \alpha + \sin^2 \alpha \sin^2 \lambda_p)^{0.5}. \tag{19.5.11}$$

Using for the purpose of simplification the designation

$$\frac{\rho}{|\mathbf{T}_a|} = \cos \delta, \tag{19.5.12}$$

we obtain the following expressions for cos δ and sin δ:

$$\cos \delta = (\cos^2 \alpha + \sin^2 \alpha \sin^2 \lambda_p)^{0.5}, \quad \sin \delta = (1 - \cos^2 \delta)^{0.5} = \sin \alpha \cos \lambda_p.$$

Equations (19.5.7) are confirmed.

Note 2: Derivation of Expressions for $\cos \mu$ and $\sin \mu$

Equations (19.5.9) yield

$$\cos \mu^{(I)} = \frac{\cos \alpha}{\cos \delta}, \quad \sin \mu^{(I)} = \frac{\sin \alpha \sin \lambda_p}{\cos \delta} \tag{19.5.13}$$

because $|\rho/\mathbf{T}_a| = \cos \delta$.

Taking into account that $\sin \delta = \sin \alpha \cos \lambda_p$ [see Eqs. (19.5.7)], we obtain

$$\cos \mu^{(I)} = \frac{\cos \alpha}{\cos \delta}, \quad \sin \mu^{(I)} = \tan \delta \tan \lambda_p. \tag{19.5.14}$$

Similarly, we can derive the expressions for $\cos \mu^{(II)}$ and $\sin \mu^{(II)}$. The expressions for $\cos \mu^{(i)}$, $\sin \mu^{(i)}$ ($i = I, II$) have been represented in Eqs. (19.5.6).

Determination of ρ

Equations (19.5.8) represent generating lines that are tangents to the ellipse shown in Fig. 19.5.3. The points of tangency are M and M', respectively. Equations (19.5.8) for point N of the generating lines (Fig. 19.5.3) are represented as

$$\rho \sin \mu \pm u^* \cos \delta \cos \mu = d, \quad \frac{\rho \cos \mu}{\sin \lambda_p} \mp \frac{u^* \cos \delta \sin \mu}{\sin \lambda_p} = 0 \tag{19.5.15}$$

where $u^* = |\overline{MN}| = |\overline{M'N}|$, $d = O_a N = r_p - (s_p/2) \cot \alpha$.

We consider Eqs. (19.5.15) as a system of two linear equations in the unknowns u^* and ρ and represent them as

$$a_{11}\rho + a_{12}u^* = d, \quad a_{21}\rho + a_{22}u^* = 0. \tag{19.5.16}$$

The solution for the unknown ρ is

$$\rho = \frac{\Delta_1}{\Delta} \tag{19.5.17}$$

where

$$\Delta_1 = \begin{vmatrix} d & a_{12} \\ 0 & a_{22} \end{vmatrix} = \mp \left(\frac{d \cos \delta \sin \mu}{\sin \lambda_p} \right) \tag{19.5.18}$$
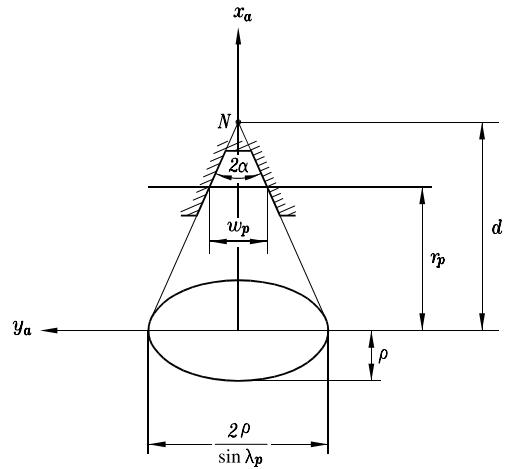
$$\Delta = \begin{vmatrix} a_{11} & a_{12} \\ a_{21} & a_{22} \end{vmatrix} = \mp \left(\frac{\cos \delta}{\sin \lambda_p} \right). \tag{19.5.19}$$

Equations (19.5.16) to (19.5.19) yield

$$\rho = d \frac{\sin \alpha \sin \lambda_p}{(\cos^2 \alpha + \sin^2 \alpha \sin^2 \lambda_p)^{0.5}} \tag{19.5.20}$$

where

$$d = r_p - \frac{s_p}{2} \cot \alpha.$$

Figure 19.5.5: Worm thread generation [Fig. 19.5.1(a)]: representation of generating lines in S_a.

For the case where the blades are installed as shown in Fig. 19.5.1(a), we obtain that (Fig. 19.5.5)

$$d = r_p + \frac{w_p}{2} \cot \alpha. \qquad (19.5.21)$$

Here, w_p is the distance between the blades measured as shown in Fig. 19.5.5.

Equations of Surfaces of Worm Thread

The surface of the worm thread is generated by the edge of the blade (the generating line) that performs a screw motion about the worm axis. The vector equation of the surface is represented in S_1 by the following matrix equation:

$$\mathbf{r}_1(\theta, u) = \mathbf{M}_{1b}(\theta)\mathbf{M}_{ba}\mathbf{r}_a(u). \qquad (19.5.22)$$

Here, $\mathbf{r}_a(u)$ is the vector equation of the generating line that is represented in coordinate system S_a; matrix $\mathbf{M}_{ba}$ is represented by (19.5.1); matrix $\mathbf{M}_{1b}$ is represented by (19.4.3).

The surface unit normal is represented as follows:

$$\mathbf{n}_1(u, \theta) = \pm\frac{\mathbf{N}_1}{|\mathbf{N}_1|}, \quad \mathbf{N}_1 = \frac{\partial \mathbf{r}_1}{\partial u} \times \frac{\partial \mathbf{r}_1}{\partial \theta}. \qquad (19.5.23)$$

Choosing the proper sign in Eqs. (19.5.23), we may obtain that the surface normal will be directed *toward* the worm thread.

Surfaces and surface unit normals of ZN worms are represented as follows:

(i) **Surface side *I*, right-hand worm:**

$$\begin{aligned}
x_1 &= \rho \sin(\theta + \mu) + u \cos \delta \cos(\theta + \mu) \\
y_1 &= -\rho \cos(\theta + \mu) + u \cos \delta \sin(\theta + \mu) \\
z_1 &= \rho \frac{\cos \alpha \cot \lambda_p}{\cos \delta} - u \sin \delta + p\theta.
\end{aligned} \qquad (19.5.24)$$

Here,

$$\cos\mu = \frac{\cos\alpha}{\cos\delta}, \quad \sin\mu = \frac{\sin\alpha\,\sin\lambda_p}{\cos\delta},$$

$$\cos\delta = (\cos^2\alpha + \sin^2\alpha\,\sin^2\lambda_p)^{1/2}, \quad \sin\delta = \sin\alpha\,\cos\lambda_p. \tag{19.5.25}$$

Surface unit normal components:

$$n_{x1} = -\frac{1}{k}[(p + \rho\tan\delta)\sin(\theta + \mu) + u\sin\delta\,\cos(\theta + \mu)]$$

$$n_{y1} = -\frac{1}{k}[-(p + \rho\tan\delta)\cos(\theta + \mu) + u\sin\delta\,\sin(\theta + \mu)] \tag{19.5.26}$$

$$n_{z1} = -\frac{u\cos\delta}{k}.$$

Here,

$$k = [(p + \rho\tan\delta)^2 + u^2]^{0.5}.$$

(ii) **Surface side *II*, right-hand worm:**

$$\begin{aligned} x_1 &= \rho\sin(\theta + \mu) - u\cos\delta\,\cos(\theta + \mu) \\ y_1 &= -\rho\cos(\theta + \mu) - u\cos\delta\,\sin(\theta + \mu) \\ z_1 &= -\rho\frac{\cos\alpha\,\cot\lambda_p}{\cos\delta} + u\sin\delta + p\theta. \end{aligned} \tag{19.5.27}$$

Here, $\cos\mu = -\cos\alpha/\cos\delta$, $\sin\mu = \sin\alpha\,\sin\lambda_p/\cos\delta$; the expressions for $\cos\delta$ and $\sin\delta$ are the same as those in Eqs. (19.5.25).

Surface unit normal components:

$$n_{x1} = \frac{1}{k}[-(p + \rho\tan\delta)\sin(\theta + \mu) + u\sin\delta\,\cos(\theta + \mu)]$$

$$n_{y1} = \frac{1}{k}[(p + \rho\tan\delta)\cos(\theta + \mu) + u\sin\delta\,\sin(\theta + \mu)] \tag{19.5.28}$$

$$n_{z1} = \frac{u\cos\delta}{k}.$$

(iii) **Surface side *I*, left-hand worm:**

$$\begin{aligned} x_1 &= -\rho\sin(\theta - \mu) + u\cos\delta\,\cos(\theta - \mu) \\ y_1 &= \rho\cos(\theta - \mu) + u\cos\delta\,\sin(\theta - \mu) \\ z_1 &= \rho\frac{\cos\alpha\,\cot\lambda_p}{\cos\delta} - u\sin\delta - p\theta. \end{aligned} \tag{19.5.29}$$

Here,

$$\cos\mu = \frac{\cos\alpha}{\cos\delta}, \quad \sin\mu = \frac{\sin\alpha\,\sin\lambda_p}{\cos\delta} = \tan\delta\,\tan\lambda_p. \tag{19.5.30}$$

Surface unit normal components:

$$n_{x1} = \frac{1}{k}[(p + \rho \tan \delta) \sin(\theta - \mu) - u \sin \delta \cos(\theta - \mu)]$$

$$n_{y1} = \frac{1}{k}[-(p + \rho \tan \delta) \cos(\theta - \mu) - u \sin \delta \sin(\theta - \mu)] \qquad (19.5.31)$$

$$n_{z1} = -\frac{u \cos \delta}{k}.$$

(iv) **Surface side *II*, left-hand worm:**

$$x_1 = -\rho \sin(\theta - \mu) - u \cos \delta \cos(\theta - \mu)$$
$$y_1 = \rho \cos(\theta - \mu) - u \cos \delta \sin(\theta - \mu) \qquad (19.5.32)$$
$$z_1 = -\rho \frac{\cos \alpha \cot \lambda_p}{\cos \delta} + u \sin \delta - p\theta.$$

Here,

$$\cos \mu = -\frac{\cos \alpha}{\cos \delta}, \qquad \sin \mu = \frac{\sin \alpha \sin \lambda_p}{\cos \delta} = \tan \delta \tan \lambda_p. \qquad (19.5.33)$$

Surface unit normal components:

$$n_{x1} = \frac{1}{k}[(p + \rho \tan \delta) \sin(\theta - \mu) + u \sin \delta \cos(\theta - \mu)]$$

$$n_{y1} = \frac{1}{k}[-(p + \rho \tan \delta) \cos(\theta - \mu) + u \sin \delta \sin(\theta - \mu)] \qquad (19.5.34)$$

$$n_{z1} = \frac{u \cos \delta}{k}.$$

Kinematic Interpretation of Surface Generation

The visualization of generation of the worm surface is based on the following considerations:

(i) The generating line $L^{(j)}$ ($j = I, II$) may be represented in plane $\Pi^{(j)}$ that is tangent to the cylinder of radius ρ (superscripts I and II indicate the generating lines I and II, respectively).

(ii) $L^{(j)}$ and the worm axis represent two crossed straight lines. Thus, $L^{(j)}$ may be represented in a coordinate system $S_\tau^{(j)}$ whose unit vectors we designate as $\mathbf{e}_1^{(j)}$, $\mathbf{e}_2^{(j)}$, and $\mathbf{e}_3^{(j)}$. The unit vector $\mathbf{e}_3^{(j)}$ is directed along the worm axis and $\mathbf{e}_3^{(j)} = \mathbf{k}_b$. Unit vector $\mathbf{e}_1^{(j)}$ is directed along the shortest distance between the unit vectors of the generating line and the worm axis. Unit vector $\mathbf{e}_2^{(j)}$ is determined as the cross product of $\mathbf{e}_1^{(j)}$ and $\mathbf{e}_3^{(j)}$ (see below).

(iii) Coordinate systems $S_\tau^{(j)}$ ($j = I, II$) and S_b (Figs. 19.5.6 and 19.5.7) are rigidly connected to each other and perform a screw motion with the screw parameter p about the worm axis. Point $M^{(j)}$ of the intersection of $L^{(j)}$ with $\mathbf{e}_1^{(j)}$ generates in screw motion a helix on the cylinder of radius ρ. The unit tangent to the helix at point $M^{(j)}$ and the unit vector $\mathbf{b}^{(j)}$ of $L^{(j)}$ do not coincide in the case of ZN worms and form a certain angle.

Figure 19.5.6: Representation of generating line *I* in S_τ.
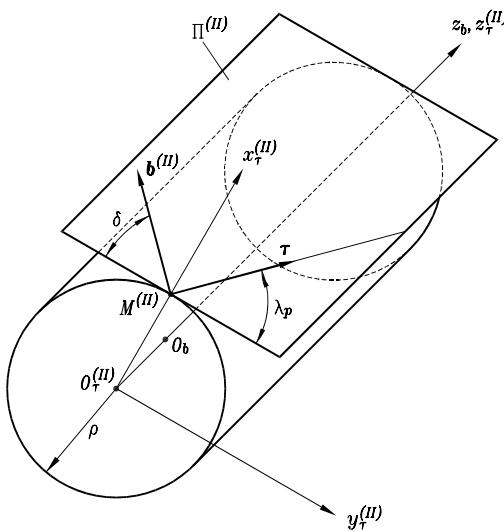
(iv) We may consider now two rigidly connected straight lines with unit vectors $\mathbf{b}^{(j)}$ and $\boldsymbol{\tau}$ that lie in tangent plane $\Pi^{(j)}$ and have a common point $M^{(j)}$ as the point of their intersection. Both of these straight lines perform the same screw motion, and straight line $L^{(j)}$ generates the worm surface that is a convolute surface. Line $L^{(j)}$ would generate a screw involute surface if $L^{(j)}$ were to coincide with $\boldsymbol{\tau}^{(j)}$.

For further derivations, we consider the following equation:

$$\overline{O_b N} = \overline{O_b O_\tau^{(j)}} + \overline{O_\tau^{(j)} M^{(j)}} + \overline{M^{(j)} N}. \qquad (19.5.35)$$

Here, N is the point of intersection of both generating lines (Fig. 19.5.3), and

$$\overline{O_b N} = d\,\mathbf{i}_b. \qquad (19.5.36)$$

Figure 19.5.7: Representation of generating line *II* in S_τ.

Vectors $\overline{O_b O_\tau^{(j)}}$, $\overline{O_\tau^{(j)} M^{(j)}}$, and $\overline{M^{(j)} N}$ may be represented in S_b as

$$\overline{O_b O_\tau^{(j)}} = \lambda^{(j)} \mathbf{k}_b \qquad (j = I, II) \tag{19.5.37}$$

$$\overline{O_\tau^{(j)} M^{(j)}} = \rho\, \mathbf{e}_{1b}^{(j)} \tag{19.5.38}$$

where

$$\mathbf{e}_{1b}^{(j)} = \pm \frac{\mathbf{b}_b^{(j)} \times \mathbf{k}_b}{\left| \mathbf{b}_b^{(j)} \times \mathbf{k}_b \right|} \tag{19.5.39}$$

$$\overline{M^{(j)} N} = m\, \mathbf{b}_b^{(j)} \tag{19.5.40}$$

$$\mathbf{e}_{2b}^{(j)} = \mathbf{e}_{3b}^{(j)} \times \mathbf{e}_{1b}^{(j)}. \tag{19.5.41}$$

The subscript "b" in $\mathbf{e}_{1b}^{(j)}$ and $\mathbf{e}_{2b}^{(j)}$ indicates that these vectors are represented in S_b.

The determination of the proper sign in Eq. (19.5.39) is based on the following considerations:

(i) Equations (19.5.35) to (19.5.39) yield

$$d\left(\mathbf{i}_b \cdot \mathbf{e}_{1b}^{(j)}\right) = \rho. \tag{19.5.42}$$

(ii) Taking into account that d and ρ are positive, we get

$$\mathbf{i}_b \cdot \mathbf{e}_{1b}^{(j)} > 0. \tag{19.5.43}$$

(iii) Equations (19.5.42) and (19.5.43) yield that the upper (lower) sign in Eq. (19.5.39) corresponds to the case where $j = I$ ($j = II$).

Using expressions (19.5.39) and (19.5.40), we can determine the direction cosines for vectors $\mathbf{e}_{1b}^{(j)}$ and $\mathbf{e}_{2b}^{(j)}$ ($j = I, II$) in coordinate system S_b. We can determine as well the location of origin $O_\tau^{(j)}$ ($j = I, II$) in S_b using vector equation (19.5.35). Then we obtain the following matrices for coordinate transformation,

$$\mathbf{M}_{\tau b}^{(I)} = \begin{bmatrix} \tan \lambda_p \tan \delta & -\dfrac{\cos \alpha}{\cos \delta} & 0 & 0 \\[2ex] \dfrac{\cos \alpha}{\cos \delta} & \tan \lambda_p \tan \delta & 0 & 0 \\[2ex] 0 & 0 & 1 & -\dfrac{d \cos \alpha \tan \delta}{\cos \delta} \\[2ex] 0 & 0 & 0 & 1 \end{bmatrix} \tag{19.5.44}$$

$$\mathbf{M}_{\tau b}^{(II)} = \begin{bmatrix} \dfrac{\sin \alpha \sin \lambda_p}{\cos \delta} & \dfrac{\cos \alpha}{\cos \delta} & 0 & 0 \\[2ex] -\dfrac{\cos \alpha}{\cos \delta} & \dfrac{\sin \alpha \sin \lambda_p}{\cos \delta} & 0 & 0 \\[2ex] 0 & 0 & 1 & \dfrac{d \cos \alpha \tan \delta}{\cos \delta} \\[2ex] 0 & 0 & 0 & 1 \end{bmatrix}. \tag{19.5.45}$$

The generating lines are represented in $S_\tau^{(j)}$ by the following equations (Figs. 19.5.6 and 19.5.7):

$$\mathbf{b}_\tau^{(I)} = [\, 0 \quad \cos\delta \quad -\sin\delta \,]^{\mathrm{T}} \tag{19.5.46}$$

$$\mathbf{b}_\tau^{(II)} = [\, 0 \quad -\cos\delta \quad \sin\delta \,]^{\mathrm{T}}. \tag{19.5.47}$$

The tangent to the helix at point $M^{(j)}$ is represented in $S_\tau^{(j)}$ by

$$\boldsymbol{\tau}_\tau^{(j)} = [\, 0 \quad \cos\lambda_\rho \quad \sin\lambda_\rho \,]^{\mathrm{T}} \tag{19.5.48}$$

where

$$\lambda_\rho = \arctan\left(\frac{p}{\rho}\right). \tag{19.5.49}$$
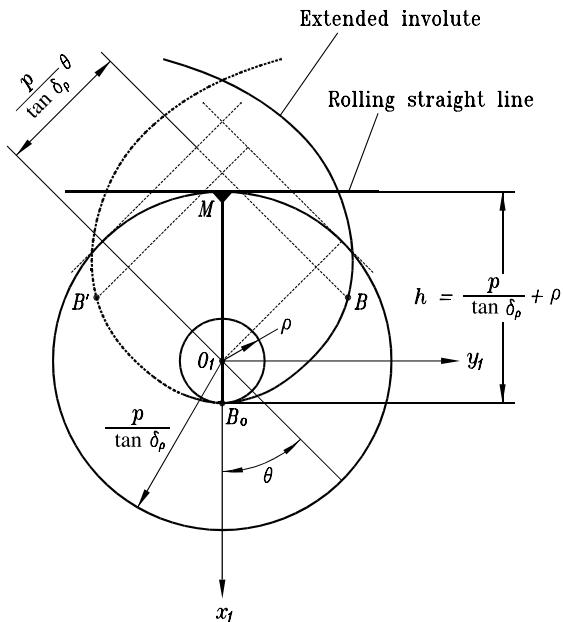
Using similar derivations for a right-hand worm, we obtain the equations of generating lines for the left-hand worm. The generating lines are represented in coordinate systems $S_\tau^{(j)}$ ($j = I, II$) that enable us to determine the orientation of the generating line in plane $\Pi^{(j)}$ that is tangent to the cylinder of radius ρ (Figs. 19.5.6 and 19.5.7).

The unit vectors of the right and left generating lines are represented in $S_\tau^{(I)}$ and $S_\tau^{(II)}$ as follows:
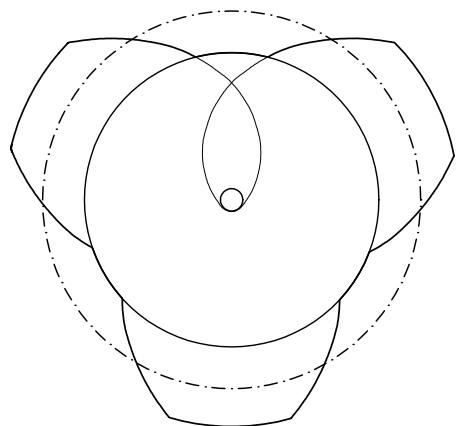
$$\mathbf{b}_\tau^{(I)} = [\, 0 \quad -\cos\delta \quad -\sin\delta \,]^{\mathrm{T}} \tag{19.5.50}$$

$$\mathbf{b}_\tau^{(II)} = [\, 0 \quad \cos\delta \quad \sin\delta \,]^{\mathrm{T}}. \tag{19.5.51}$$

The cross section of the worm surface is an *extended* involute (Fig. 19.5.8) that is traced out by point B_o of the segment B_oM; this segment is rigidly connected to the

Figure 19.5.8: Extended involute as the profile of ZN worm cross section.

Figure 19.5.9: Cross section of ZN worm.

straight line that rolls over the circle of radius $p/\tan\delta_\rho$. The cross section of a ZN worm with three threads is represented in Fig. 19.5.9.

Particular Cases

The surface of Archimedes worm (ZA) is a particular case of the screw convolute surface (ZN). Equations of surface ZA can be derived from the equations of surface ZN taking $\rho = 0$ and $\delta = \alpha$, $\mu = 0$ and $\mu = \pi$ for the surface sides *I* and *II*, respectively. The screw involute surface can be derived from the equations of convolute screw surface (ZN) by considering that the generating line is the tangent to the helix on the cylinder of radius ρ (see below).

Problem 19.5.1

Consider that the worm surface represented by Eqs. (19.5.24) is cut by the plane $y_1 = 0$. Axis x_1 is the axis of symmetry of the space in axial section. The point of intersection of the axial profile with the pitch cylinder is determined with the coordinates

$$x_1 = r_p, \quad z_1 = -\frac{w_{ax}}{2} = -\frac{p_{ax}}{4} = -\frac{\pi}{4P_{ax}}.$$

Here, w_{ax} is the nominal value of the space width in axial section that is measured along the generatrix of the pitch cylinder; p_{ax} is the distance between two neighboring threads along the generatrix of the pitch cylinder; $P_{ax} = \pi/p_{ax}$ is the worm axial diametral pitch.

Derive the system of equations to be applied to determine s_p (Fig. 19.5.3) considering r_p, p, w_{ax}, and α as given.

Solution

Angle θ can be obtained from the following equation:

$$r_p\left(\frac{\sin\theta}{\tan\lambda_p} + \tan\lambda_p\,\theta\right) + \frac{w_{ax}}{2} = 0. \tag{19.5.52}$$

Then, s_p can be expressed as

$$s_p = 2r_p \left[(1 - \cos\theta) \tan\alpha - \frac{\sin\theta}{\sin\lambda_p} \right]. \qquad (19.5.53)$$

While solving the nonlinear equation, we take for the first guess $\sin\theta \approx \theta$.

Directions

(1) Equation (19.5.52) can be derived considering the following system of equations:

$$x_1 = \rho\sin(\theta + \mu) + u\cos\delta\cos(\theta + \mu) = r_p \qquad (19.5.54)$$

$$y_1 = -\rho\cos(\theta + \mu) + u\cos\delta\sin(\theta + \mu) = 0 \qquad (19.5.55)$$

$$z_1 = \rho\frac{\cos\alpha\cot\lambda_p}{\cos\delta} - u\sin\delta + p\theta = -\frac{w_{ax}}{2}. \qquad (19.5.56)$$

Equation (19.5.55) yields

$$u\cos\delta = \frac{\rho}{\tan(\theta + \mu)}. \qquad (19.5.57)$$

Equations (19.5.54) and (19.5.55) considered simultaneously yield

$$\rho = r_p\sin(\theta + \mu). \qquad (19.5.58)$$

We may consider Eqs. (19.5.54), (19.5.55), and (19.5.56) as a system of three linear equations in the unknowns u and ρ. If such a system indeed exists, the rank of the augmented matrix must be equal to 2. This requirement yields an equation that coincides with Eq. (19.5.52) represented above.

(2) The derivation of Eq. (19.5.53) is based on the following considerations:

(a) According to Eq. (19.5.20), we have

$$\rho = \left(r_p - \frac{s_p}{2}\cot\alpha \right) \frac{\sin\alpha\sin\lambda_p}{(\cos^2\alpha + \sin^2\alpha\sin^2\lambda_p)^{0.5}}.$$

(b) We transform this equation using the substitutions [see Eqs. (19.5.58) and (19.5.25)]

$$\rho = r_p\sin(\theta + \mu), \quad \cos\mu\cos\delta = \cos\alpha, \quad \sin\mu\cos\delta = \sin\alpha\sin\lambda_p$$

$$\cos\delta = (\cos^2\alpha + \sin^2\alpha\sin^2\lambda_p)^{0.5}.$$
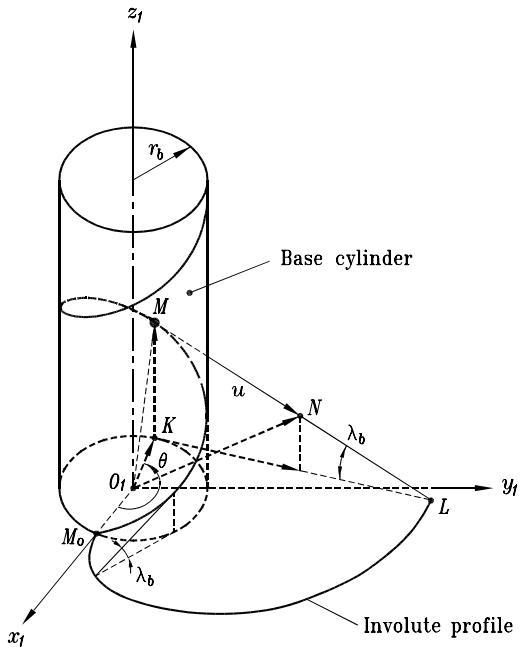
After transformations, we obtain Eq. (19.5.53) represented above.

19.6 GENERATION AND GEOMETRY OF ZI (INVOLUTE) WORMS

Surface Equations

The worm surface is generated by a straight line that performs a screw motion and is tangent to the helix $M_o M$ on the *base* cylinder (Fig. 19.6.1). The position vector $\overline{O_1 N}$ of a current point of the surface side I for a right-hand worm is represented as

$$\overline{O_1 N} = \overline{O_1 K} + \overline{KM} + \overline{MN}. \qquad (19.6.1)$$

Figure 19.6.1: Generation of screw involute surface for the surface side I of a right-hand worm.

Here,

$$\overline{O_1K} = r_b(\cos\theta\ \mathbf{i}_1 + \sin\theta\ \mathbf{j}_1), \quad \overline{KM} = p\theta\ \mathbf{k}_1,$$

$$\overline{MN} = u\cos\lambda_b(\sin\theta\ \mathbf{i}_1 - \cos\theta\ \mathbf{j}_1) - u\sin\lambda_b\ \mathbf{k}_1 \tag{19.6.2}$$

where r_b is the radius of the base cylinder, λ_b is the helix lead angle, $p = r_b\tan\lambda_b$ is the screw parameter, and variables u and θ are the surface parameters.

Equations (19.6.1) and (19.6.2) yield

$$\begin{aligned}
x_1 &= r_b\cos\theta + u\cos\lambda_b\sin\theta \\
y_1 &= r_b\sin\theta - u\cos\lambda_b\cos\theta \\
z_1 &= -u\sin\lambda_b + p\theta.
\end{aligned} \tag{19.6.3}$$
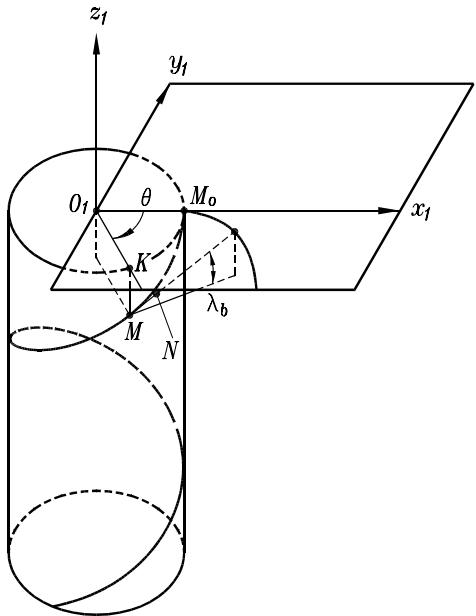
The surface unit normal directed toward the worm thread is represented by

$$\mathbf{n}_1 = \frac{\mathbf{N}_1}{|\mathbf{N}_1|}, \quad \mathbf{N}_1 = \frac{\partial\mathbf{r}_1}{\partial\theta} \times \frac{\partial\mathbf{r}_1}{\partial u}. \tag{19.6.4}$$

Then we derive that

$$\mathbf{n}_1 = [-\sin\lambda_b\sin\theta \quad \sin\lambda_b\cos\theta \quad -\cos\lambda_b]^{\mathrm{T}} \tag{19.6.5}$$

$$(\text{provided } u\cos\lambda_b \neq 0).$$

The orientation of surface unit normal $\mathbf{n}_1$ does not depend on u. This means that the unit normals along the generating line have the same orientation, and the worm surface is a ruled developed one. (We recall that the surfaces of ZA worms and ZN worms are ruled but undeveloped surfaces.)

Figure 19.6.2: Derivation of screw involute surface for the surface side *II* of a right-hand worm.

It is easy to verify that $N_1 = 0$ when $u = 0$. Thus, the surface point is singular at the point of tangency of the generating line with the helix. At such a point, vectors $\partial r_1 / \partial u$ and $\partial r_1 / \partial \theta$ are collinear.

The cross section of the worm surface by $z_1 = c$ is an *involute* curve with the radius of base circle r_b.

The derivation of surface side *II* of the right-hand worm is based on drawings represented in Fig. 19.6.2. Using considerations similar to those discussed above, we obtain the following equations for the surface and its unit normal:

$$
\begin{aligned}
x_1 &= r_b \cos\theta + u \cos\lambda_b \sin\theta \\
y_1 &= -r_b \sin\theta + u \cos\lambda_b \cos\theta \\
z_1 &= u \sin\lambda_b - p\theta
\end{aligned}
\tag{19.6.6}
$$
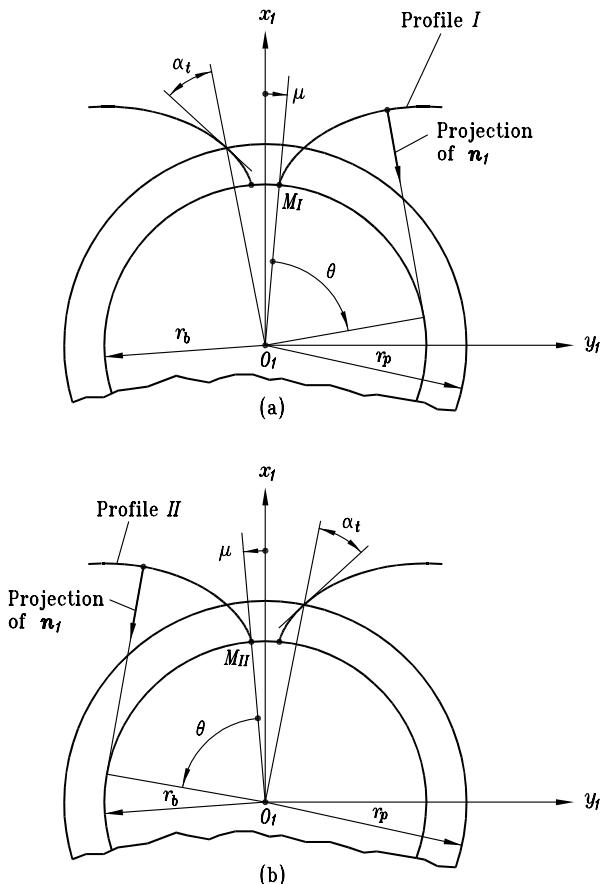
$$
\mathbf{n}_1 = \left[-\sin\lambda_b \sin\theta \quad -\sin\lambda_b \cos\theta \quad \cos\lambda_b\right]^{\mathrm{T}}
\tag{19.6.7}
$$
$$
(\text{provided } u \cos\lambda_b \neq 0).
$$

Our next goal is to represent the surface equations for both sides with the x_1 axis as the axis of symmetry for the cross section $z_1 = 0$. Figure 19.6.3 yields that

$$
\mu = \frac{w_t}{2r_p} - \mathrm{inv}\,\alpha_t.
\tag{19.6.8}
$$

Here, w_t is the cross section space width on the pitch cylinder and α_t is the profile angle in transverse section (formed between the position vector $O_1 P$ and the tangent to the profile at point P). It is known from the involute trigonometry that

$$
\mathrm{inv}\,\alpha_t = \tan\alpha_t - \alpha_t, \quad \alpha_t = \arccos\left(\frac{r_b}{r_p}\right).
\tag{19.6.9}
$$

Figure 19.6.3: Involute worm cross sections: (a) with profile I; (b) with profile II.

We recall that the transverse and axial shape angles, α_t and α_{ax}, are related by Eq. (19.3.20), and the radius of the base cylinder is represented by Eq. (19.3.21). The final expressions for both sides of the worm surface, for right-hand and left-hand worms, are as follows:

(i) **Surface side I, right-hand worm:**

$$x_1 = r_b \cos(\theta + \mu) + u \cos \lambda_b \sin(\theta + \mu)$$
$$y_1 = r_b \sin(\theta + \mu) - u \cos \lambda_b \cos(\theta + \mu) \qquad (19.6.10)$$
$$z_1 = -u \sin \lambda_b + p\theta$$

$$\mathbf{n}_1 = [-\sin \lambda_b \sin(\theta + \mu) \quad \sin \lambda_b \cos(\theta + \mu) \quad -\cos \lambda_b]^{\mathrm{T}}. \qquad (19.6.11)$$

Angles θ and μ are measured clockwise from $\overline{O_1 M_I}$ to the direction of the y_1 axis for an observer located on the negative axis z_1.

(ii) **Surface side *II*, right-hand worm:**

$$x_1 = r_b \cos(\theta + \mu) + u \cos \lambda_b \sin(\theta + \mu)$$
$$y_1 = -r_b \sin(\theta + \mu) + u \cos \lambda_b \cos(\theta + \mu) \qquad (19.6.12)$$
$$z_1 = u \sin \lambda_b - p\theta$$

$$\mathbf{n}_1 = [- \sin \lambda_b \sin(\theta + \mu) \quad - \sin \lambda_b \cos(\theta + \mu) \quad \cos \lambda_b]^T. \qquad (19.6.13)$$

Angles θ and μ are measured counterclockwise from $\overline{O_1 M_{II}}$ to the direction of negative axis y_1 for an observer located on the negative axis z_1.

(iii) **Surface side *I*, left-hand worm:**

$$x_1 = r_b \cos(\theta + \mu) + u \cos \lambda_b \sin(\theta + \mu)$$
$$y_1 = r_b \sin(\theta + \mu) - u \cos \lambda_b \cos(\theta + \mu) \qquad (19.6.14)$$
$$z_1 = u \sin \lambda_b - p\theta$$

$$\mathbf{n}_1 = [- \sin \lambda_b \sin(\theta + \mu) \quad \sin \lambda_b \cos(\theta + \mu) \quad \cos \lambda_b]^T. \qquad (19.6.15)$$

Angles θ and μ are measured clockwise from $\overline{O_1 M_I}$ to the direction of the y_1 axis for an observer located on the negative axis z_1.

(iv) **Surface side *II*, left-hand worm:**
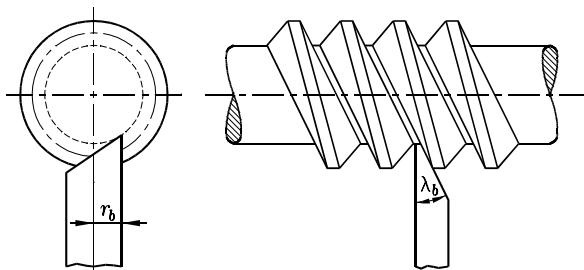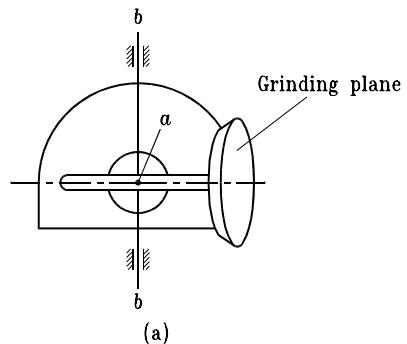
$$x_1 = r_b \cos(\theta + \mu) + u \cos \lambda_b \sin(\theta + \mu)$$
$$y_1 = -r_b \sin(\theta + \mu) + u \cos \lambda_b \cos(\theta + \mu) \qquad (19.6.16)$$
$$z_1 = -u \sin \lambda_b + p\theta$$

$$\mathbf{n}_1 = [- \sin \lambda_b \sin(\theta + \mu) \quad - \sin \lambda_b \cos(\theta + \mu) \quad - \cos \lambda_b]^T. \qquad (19.6.17)$$

Angles θ and μ are measured counterclockwise from $\overline{O_1 M_{II}}$ to the direction of negative axis y_1 for an observer located on the negative axis z_1.

Methods for Generation
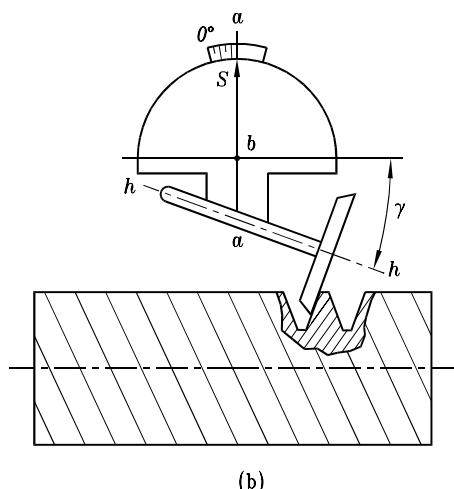
The worm surface can be generated (i) by a blade, (ii) by a milling cutter, and (iii) by a grinding plane. Generation by a blade is based on simulation of the screw motion of the generating straight line that is the tangent to the helix on the base cylinder (Fig. 19.6.4). The coincidence of the blade edge with the generating line is provided if the face plane of the blade is tangent to the worm base cylinder, and the profile angle of the edge is equal to the lead angle λ_b (Fig. 19.6.4). Each side surface of the worm must be generated separately.

Figure 19.6.4: Generation of involute worm by a blade.
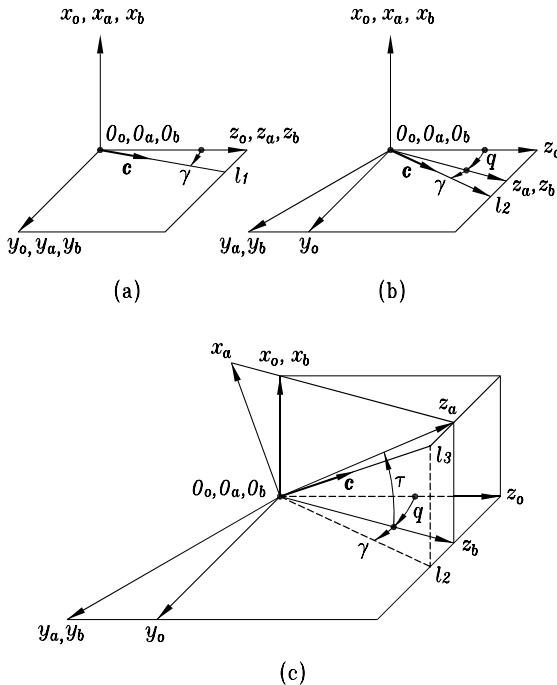
Figure 19.6.5: Generation of involute worm by plane: installment of grinding plane with respect to (a) b–b, and (b) h–h.

Generation by a plane becomes possible because the worm surface is a developed ruled surface. Such a method is used for grinding, for instance, by D. Brown Co. (Fig. 19.6.5). The grinding is performed by a plane. The head with the grinding wheel has two degrees of freedom and can be installed with respect to the worm axis by turning about the mutually perpendicular axes a–a and b–b. The third degree of freedom – rotation of the grinding wheel about the h–h axis – is not related with the process of generation and provides the desired velocity of grinding. The turn of the grinding wheel about the a–a and b–b axes provides that the grinding plane Σ_t becomes tangent to the worm surface Σ_1. Plane Σ_t and surface Σ_1 contact each other at every instant along a straight line that is the generating line L. The normals to Σ_1 along L and axis h–h of the grinding wheel have the same orientation. The relative motion of the worm with respect to the grinding wheel is the screw motion about the worm axis with the screw parameter p of the screw involute surface. The worm surface is originated as the family of straight lines L that are generated in the screw motion described above.

The installation of the grinding wheel with respect to the worm is based on the following considerations:

(i) We set up three coordinate systems (Fig. 19.6.6): (a) movable system S_a that is rigidly connected to the grinding wheel, (b) movable coordinate system S_b that

Figure 19.6.6: Installation of grinding wheel and applied coordinate systems: initial installation of grinding wheel with (a) position l_1 of vector $\mathbf{c}$, (b) position l_2 of $\mathbf{c}$, and (c) position l_3 of $\mathbf{c}$.

is rigidly connected to the grinding head, and (c) fixed coordinated system S_o that is rigidly connected to the frame where the head with the grinding wheel is mounted. Coordinate system S_b may be rotated about the b–b axis of the frame, and coordinate system S_a may be rotated about the a–a axis that is mounted in S_b.

(ii) Consider that initially axis h–h of the grinding wheel and the axis of the worm lie in parallel planes and form angle γ [Fig. 19.6.6(a)]. The unit vector $\mathbf{c}$ of the axis of the grinding wheel will be in position l_1.

(iii) Then, consider that coordinate systems S_a and S_b are turned about the x_b axis (about the b–b axis) under the angle q [Fig. 19.6.6(b)]. Unit vector $\mathbf{c}$ will be in position l_2.

(iv) Figure 19.6.6(c) shows that coordinate system S_a is turned about the y_b axis (axis a–a) under angle τ. Unit vector $\mathbf{c}$ will take position l_3.

We may represent unit vector $\mathbf{c}$ in coordinate system S_o using the following matrix equation:

$$\mathbf{c}_o = \mathbf{M}_{ob}\mathbf{M}_{ba}\mathbf{c}_a. \tag{19.6.18}$$

Equation (19.6.18) yields

$$\mathbf{c}_o = \sin\tau\cos\gamma\,\mathbf{i}_o + (\sin\gamma\cos q + \cos\gamma\sin q\cos\tau)\,\mathbf{j}_o$$
$$+ (-\sin\gamma\sin q + \cos\gamma\cos q\cos\tau)\,\mathbf{k}_o. \tag{19.6.19}$$

(v) The unit normal $\mathbf{n}_1$ to the worm surface was represented in S_1 by Eq. (19.6.5). Changing the direction of $\mathbf{n}_1$ for the opposite one, after derivations, we represent in

coordinate system S_o the unit normal $\mathbf{n}_o$ of the worm surface as

$$\mathbf{n}_o = [\sin \lambda_b \sin(\phi_1 + \theta) \quad -\sin \lambda_b \cos(\phi_1 + \theta) \quad \cos \lambda_b]^{\mathrm{T}} \qquad (19.6.20)$$

where ϕ_1 is the angle of worm rotation in the screw motion.

Taking into account that $\mathbf{n}_o = \mathbf{c}_o$, we may obtain two independent equations that relate four parameters: $(\phi_1 + \theta)$, γ, q, and τ. Two of these parameters must be chosen, and then the remaining two can be derived. Considering, for instance, that $(\phi_1 + \theta) = \pi/2 + \alpha_t$, we may use the following computation procedure for determination of τ and q considering that γ is chosen.

Step 1: Determination of τ.

$$\sin \tau = \frac{\sin \lambda_b \cos \alpha_t}{\cos \gamma} = \frac{\sin \lambda_p \cos \alpha_n}{\cos \gamma}. \qquad (19.6.21)$$

Equation (19.6.21) provides two solutions for τ, but it is assumed that the solution with the smaller value of τ is to be chosen.

Step 2: Determination of q.

The unique solution for q is determined with the following equations:

$$\begin{aligned} \sin q &= \frac{\sin \lambda_b \sin \alpha_t \cos \gamma \cos \tau - \sin \gamma \cos \lambda_b}{1 - \cos^2 \gamma \sin^2 \tau} \\ &= \frac{\sin \alpha_n \cos \gamma \cos \tau - \sin \gamma \cos \lambda_b}{1 - \sin^2 \lambda_p \cos^2 \alpha_n} \end{aligned} \qquad (19.6.22)$$
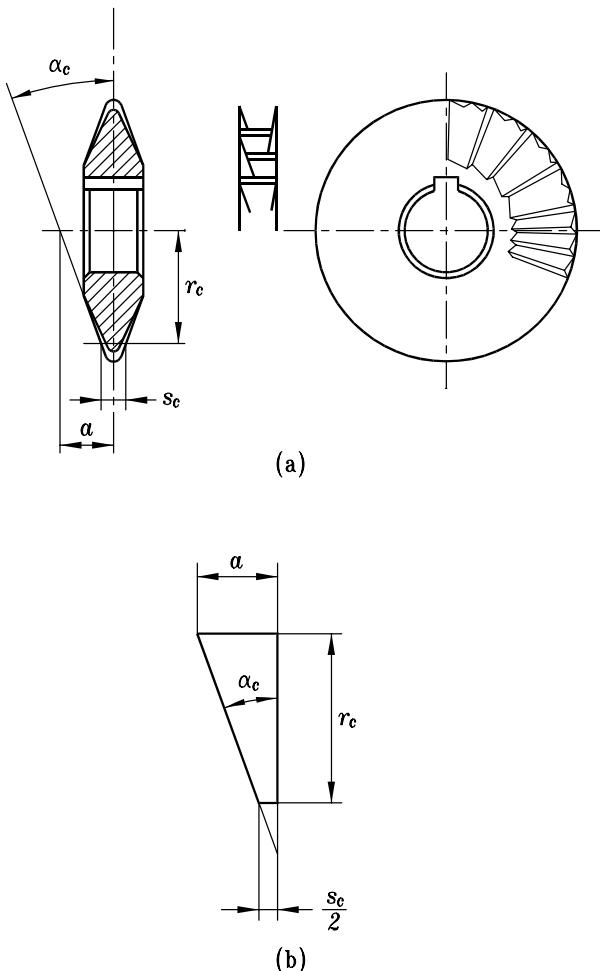
$$\begin{aligned} \cos q &= \frac{\cos \gamma \cos \tau \cos \lambda_b + \sin \gamma \sin \lambda_b \sin \alpha_t}{1 - \cos^2 \gamma \sin^2 \tau} \\ &= \frac{\cos \gamma \cos \tau \cos \lambda_b + \sin \gamma \sin \alpha_n}{1 - \sin^2 \lambda_p \cos^2 \alpha_n}. \end{aligned} \qquad (19.6.23)$$

The profile angles α_t and α_n, in the transverse and normal sections, respectively, are related by Eq. (19.3.18).

19.7 GEOMETRY AND GENERATION OF K WORMS

Generation

The most important advantage of involute worm-gear drives is the possibility of grinding the worm surface by a plane. An alternative method for grinding, developed for K worms, is based on application of a grinding cone. The axes of the grinding wheel and the worm being generated are crossed. The same method for generation can be used for milling by a cutter that is shown in Fig. 19.7.1. The axial section of the tool (grinding wheel or milling cutter) has the shape of the blade that is used for the generation of N worms (Fig. 19.5.3), but the K worm surface differs from the N worm surface because the K worms are generated by the tool surface, not by a blade.
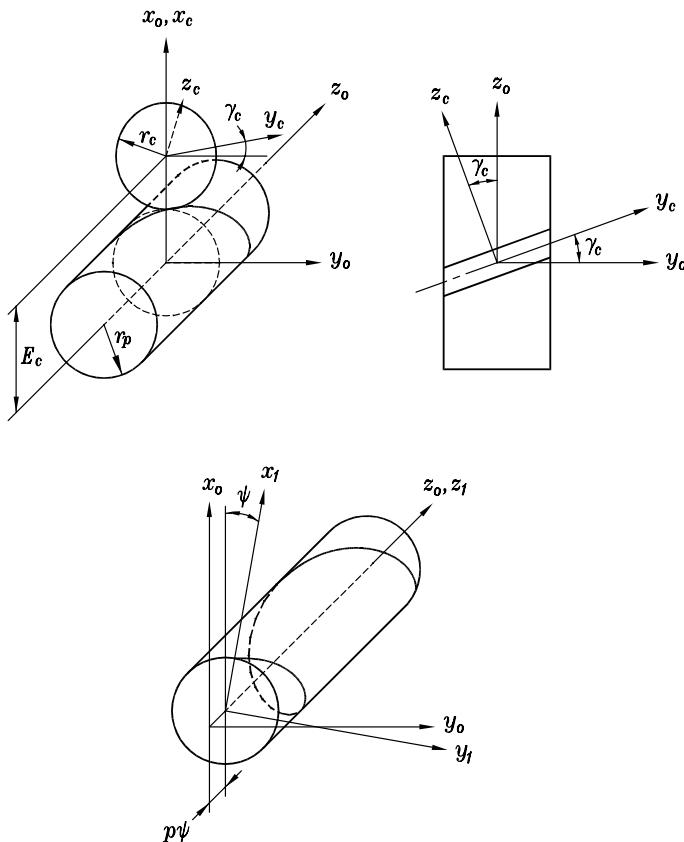
Figure 19.7.1: Cutter for milling of K worms: (a) illustration of the cutter; (b) illustration of parameters a, $s_c/2$, and r_c of the cutter.

Applied Coordinate Systems

We use coordinate systems S_c and S_1 rigidly connected to the cutter (tool) and the worm. S_o is a fixed coordinate system used for description of applied tool settings and worm motion. We consider that the tool in the process of generation is at rest, and the worm being generated performs the screw motion about its axis with the screw parameter p (Fig. 19.7.2); the axes of the tool and the worm are crossed forming the angle γ_c; usually, $\gamma_c = \lambda_p$, where λ_p is the lead angle on the worm pitch cylinder. In the process of grinding, the tool performs rotation about its axis as well, but this is related to the desired velocity of cutting (grinding) only and may be ignored when the mathematical aspects of worm generation are considered.

Worm Surface Equations

There is a family of tool surfaces Σ_c that is generated in coordinate system S_1. The worm surface Σ_1 is determined as the *envelope* to the family of tool surfaces. Surface

Figure 19.7.2: Coordinate systems applied for generation of K worms.

Σ_1 is represented as the family of lines of contact of surfaces Σ_c and Σ_1 by the following equations:
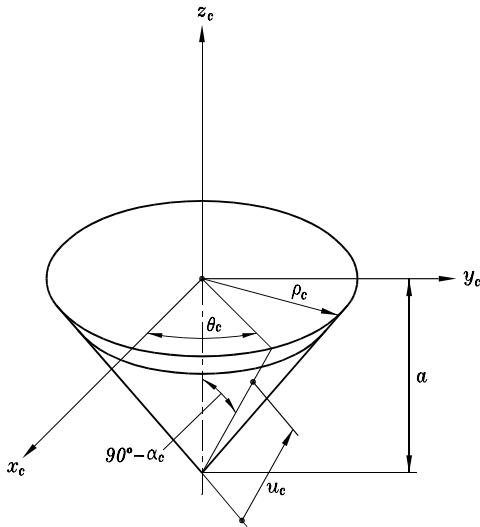
$$\mathbf{r}_1(u_c, \theta_c, \psi) = \mathbf{M}_{10}\mathbf{M}_{oc}\mathbf{r}_c(u_c, \theta_c) \tag{19.7.1}$$

$$\mathbf{N}_c(\theta_c) \cdot \mathbf{v}_c^{(c1)}(u_c, \theta_c) = f(u_c, \theta_c) = 0. \tag{19.7.2}$$

Equation (19.7.1) represents the family of tool surfaces; (u_c, θ_c) are the Gaussian coordinates of the tool surface, and ψ is the angle of rotation in the screw motion. Equation (19.7.2) is the equation of meshing. Vectors $\mathbf{N}_c$ and $\mathbf{v}_c^{(c1)}$ are represented in S_c and indicate the normal to Σ_c and the relative (sliding) velocity, respectively. It is proven below [see Eq. (19.7.8)] that Eq. (19.7.2) does not contain parameter ψ. Equations (19.7.1) and (19.7.2) considered simultaneously represent the surface of the worm in terms of three related parameters (u_c, θ_c, ψ).

For further derivations we will consider that the surface side I of a right-hand worm is generated. The cone surface is represented by the equations (Fig. 19.7.3)

$$\mathbf{r}_c = u_c \cos \alpha_c (\cos \theta_c \, \mathbf{i}_c + \sin \theta_c \, \mathbf{j}_c) + (u_c \sin \alpha_c - a) \, \mathbf{k}_c. \tag{19.7.3}$$

Figure 19.7.3: Generating cone surface.

Here, u_c determines the location of a current point on the cone generatrix; "a" determines the location of the cone apex.

The unit normal to the cone surface is determined as

$$\mathbf{n}_c = \frac{\mathbf{N}_c}{|\mathbf{N}_c|}, \quad \mathbf{N}_c = \frac{\partial \mathbf{r}_c}{\partial u_c} \times \frac{\partial \mathbf{r}_c}{\partial \theta_c}, \tag{19.7.4}$$

which yields

$$\mathbf{n}_c = [- \sin \alpha_c \cos \theta_c \quad - \sin \alpha_c \sin \theta_c \quad \cos \alpha_c]^{\mathrm{T}}. \tag{19.7.5}$$

The relative velocity is represented as the velocity in screw motion (Fig. 19.7.4)

$$\mathbf{v}_c^{(c1)} = -\boldsymbol{\omega}_c \times \mathbf{r}_c - \mathbf{R}_c \times \boldsymbol{\omega}_c - p\,\boldsymbol{\omega}_c \tag{19.7.6}$$
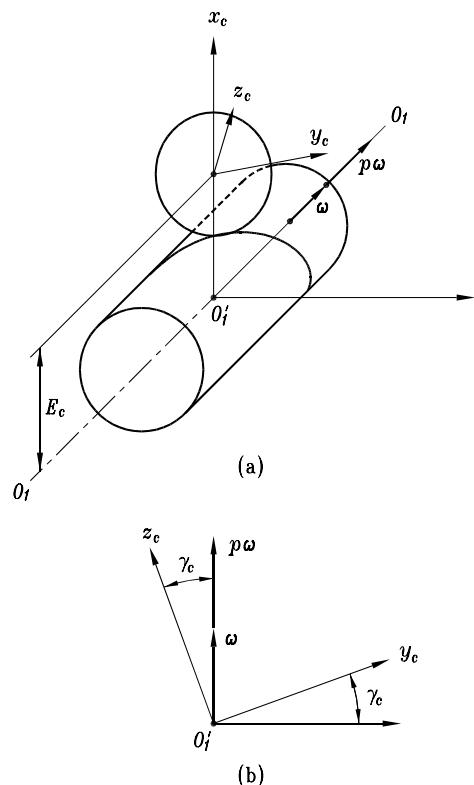
where $\mathbf{R}_c = -E_c\,\mathbf{i}_c$ is the position vector of point O_1' of the line of action of $\boldsymbol{\omega}$. Equation (19.7.6) yields

$$\mathbf{v}_c^{(c1)} = \omega \begin{bmatrix} - \sin \gamma_c\, z_c + \cos \gamma_c\, y_c \\ - \cos \gamma_c\, (x_c + E_c) - p \sin \gamma_c \\ \sin \gamma_c\, (x_c + E_c) - p \cos \gamma_c \end{bmatrix}. \tag{19.7.7}$$
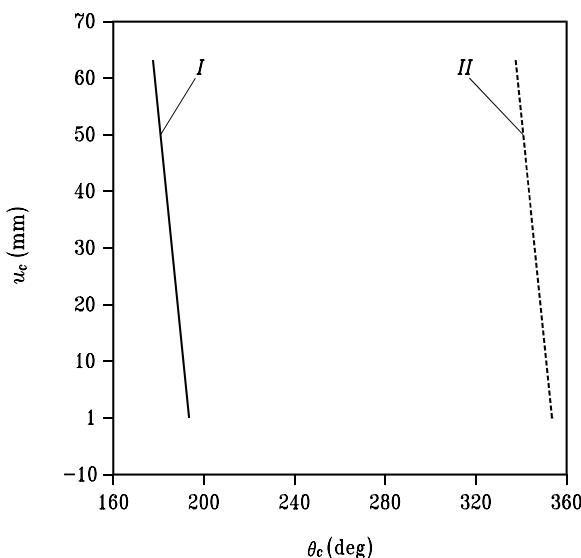
The equation of meshing of the grinding surface with the worm surface after elimination of $(-\omega \sin \gamma_c \cos \theta_c)$ is represented as

$$\mathbf{n}_c \cdot \mathbf{v}_c^{(c1)} = f(u_c, \theta_c) = a \sin \alpha_c - (E_c \sin \alpha_c \cot \gamma_c + p \sin \alpha_c) \tan \theta_c$$
$$- \frac{(E_c - p \cot \gamma_c) \cos \alpha_c}{\cos \theta_c} - u_c = 0 \tag{19.7.8}$$
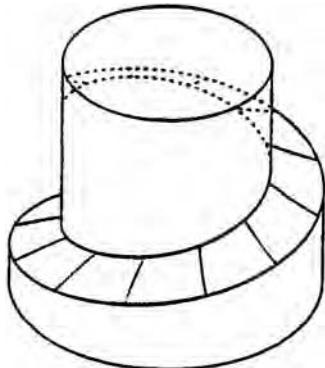
where $u_c > 0$. Equation (19.7.8) with the given value of u_c provides two solutions for θ_c and determines two curves, I and II in the plane (u_c, θ_c) (Fig. 19.7.5). Only curve I is the real contact line in the space of parameters (u_c, θ_c).

Figure 19.7.4: Installment of grinding cone: (a) illustration of installment parameter E_c; (b) illustration of installment parameter γ_c.

Figure 19.7.5: Line of contact between generating cone and K worm surface: representation in plane of parameters.

Figure 19.7.6: Contact lines between generating cone and worm on worm surface.

Equations (19.7.3) and (19.7.8) considered simultaneously represent in S_c the line of contact between Σ_c and Σ_1. The line of contact is not changed in the screw motion of the worm because equation of meshing (19.7.8) does not contain parameter of motion ψ. The worm surface Σ_1 is represented by Eqs. (19.7.1) and (19.7.8) considered simultaneously.

Figure 19.7.6 shows the contact lines on Σ_1 between Σ_1 and Σ_c. The design parameters of the worm surface are related with the equations

$$\tan \alpha_c = \tan \alpha_{ax} \cos \lambda_p \qquad (19.7.9)$$

where α_{ax} is the profile angle of the worm in its axial section, and λ_p is the lead angle on the worm pitch cylinder, and

$$s_c \approx w_{ax} \cos \lambda_p \qquad (19.7.10)$$

where w_{ax} is the width of worm space in the axial section, and w_{ax} is measured on the pitch cylinder. The exact value of required s_c can be determined using the equations of the axial section of the generated worm.

The design parameters r_c and a are represented as

$$r_c = E_c - r_p \qquad (19.7.11)$$

$$a = r_c \tan \alpha_c + \frac{s_c}{2}. \qquad (19.7.12)$$

The derivation of Eqs. (19.7.11) and (19.7.12) is based on Figs. (19.7.1) and (19.7.2).

The final expressions for both sides of the right-hand and left-hand worms and the surface unit normals are represented by the following equations:

(i) **Surface side *I*, right-hand worm:**

$$x_1 = u_c(\cos\alpha_c \cos\theta_c \cos\psi + \cos\alpha_c \cos\gamma_c \sin\theta_c \sin\psi$$
$$- \sin\alpha_c \sin\gamma_c \sin\psi) + a \sin\gamma_c \sin\psi + E_c \cos\psi$$
$$y_1 = u_c(-\cos\alpha_c \cos\theta_c \sin\psi + \cos\alpha_c \cos\gamma_c \sin\theta_c \cos\psi \qquad (19.7.13)$$
$$- \sin\alpha_c \sin\gamma_c \cos\psi) + a \sin\gamma_c \cos\psi - E_c \sin\psi$$
$$z_1 = u_c(\sin\alpha_c \cos\gamma_c + \cos\alpha_c \sin\gamma_c \sin\theta_c) - p\psi - a\cos\gamma_c$$

$$n_{x_1} = \cos\psi \sin\alpha_c \cos\theta_c + \sin\psi(\cos\gamma_c \sin\alpha_c \sin\theta_c + \sin\gamma_c \cos\alpha_c)$$
$$n_{y_1} = -\sin\psi \sin\alpha_c \cos\theta_c + \cos\psi(\cos\gamma_c \sin\alpha_c \sin\theta_c + \sin\gamma_c \cos\alpha_c) \quad (19.7.14)$$
$$n_{z_1} = \sin\gamma_c \sin\alpha_c \sin\theta_c - \cos\gamma_c \cos\alpha_c$$

where

$$u_c = a\sin\alpha_c - (E_c\sin\alpha_c \cot\gamma_c + p\sin\alpha_c)\tan\theta_c - \frac{(E_c - p\cot\gamma_c)\cos\alpha_c}{\cos\theta_c}.$$
$$(19.7.15)$$

(ii) **Surface side *II*, right-hand worm:**

$$x_1 = u_c(\cos\alpha_c \cos\theta_c \cos\psi + \cos\alpha_c \cos\gamma_c \sin\theta_c \sin\psi$$
$$+ \sin\alpha_c \sin\gamma_c \sin\psi) - a \sin\gamma_c \sin\psi + E_c \cos\psi$$
$$y_1 = u_c(-\cos\alpha_c \cos\theta_c \sin\psi + \cos\alpha_c \cos\gamma_c \sin\theta_c \cos\psi \qquad (19.7.16)$$
$$+ \sin\alpha_c \sin\gamma_c \cos\psi) - a \sin\gamma_c \cos\psi - E_c \sin\psi$$
$$z_1 = u_c(-\sin\alpha_c \cos\gamma_c + \cos\alpha_c \sin\gamma_c \sin\theta_c) - p\psi + a\cos\gamma_c$$

$$n_{x_1} = \cos\psi \sin\alpha_c \cos\theta_c + \sin\psi(\cos\gamma_c \sin\alpha_c \sin\theta_c - \sin\gamma_c \cos\alpha_c)$$
$$n_{y_1} = -\sin\psi \sin\alpha_c \cos\theta_c + \cos\psi(\cos\gamma_c \sin\alpha_c \sin\theta_c - \sin\gamma_c \cos\alpha_c) \quad (19.7.17)$$
$$n_{z_1} = \sin\gamma_c \sin\alpha_c \sin\theta_c + \cos\gamma_c \cos\alpha_c$$

where

$$u_c = a\sin\alpha_c + (E_c\sin\alpha_c \cot\gamma_c + p\sin\alpha_c)\tan\theta_c - \frac{(E_c - p\cot\gamma_c)\cos\alpha_c}{\cos\theta_c}.$$
$$(19.7.18)$$

(iii) **Surface side *I*, left-hand worm:**

$$
\begin{aligned}
x_1 &= u_c(\cos\alpha_c \cos\theta_c \cos\psi + \cos\alpha_c \cos\gamma_c \sin\theta_c \sin\psi \\
&\quad + \sin\alpha_c \sin\gamma_c \sin\psi) - a\sin\gamma_c \sin\psi + E_c \cos\psi \\
y_1 &= u_c(-\cos\alpha_c \cos\theta_c \sin\psi + \cos\alpha_c \cos\gamma_c \sin\theta_c \cos\psi \qquad\qquad (19.7.19)\\
&\quad + \sin\alpha_c \sin\gamma_c \cos\psi) - a\sin\gamma_c \cos\psi - E_c \sin\psi \\
z_1 &= u_c(\sin\alpha_c \cos\gamma_c - \cos\alpha_c \sin\gamma_c \sin\theta_c) + p\psi - a\cos\gamma_c
\end{aligned}
$$

$$
\begin{aligned}
n_{x_1} &= \cos\psi \sin\alpha_c \cos\theta_c + \sin\psi(\cos\gamma_c \sin\alpha_c \sin\theta_c - \sin\gamma_c \cos\alpha_c) \\
n_{y_1} &= -\sin\psi \sin\alpha_c \cos\theta_c + \cos\psi(\cos\gamma_c \sin\alpha_c \sin\theta_c - \sin\gamma_c \cos\alpha_c) \quad (19.7.20)\\
n_{z_1} &= -\sin\gamma_c \sin\alpha_c \sin\theta_c - \cos\gamma_c \cos\alpha_c
\end{aligned}
$$

where

$$
u_c = a\sin\alpha_c + (E_c \sin\alpha_c \cot\gamma_c + p\sin\alpha_c)\tan\theta_c - \frac{(E_c - p\cot\gamma_c)\cos\alpha_c}{\cos\theta_c}.
$$

$$(19.7.21)$$

(iv) **Surface side *II*, left-hand worm:**

$$
\begin{aligned}
x_1 &= u_c(\cos\alpha_c \cos\theta_c \cos\psi + \cos\alpha_c \cos\gamma_c \sin\theta_c \sin\psi \\
&\quad - \sin\alpha_c \sin\gamma_c \sin\psi) + a\sin\gamma_c \sin\psi + E_c \cos\psi \\
y_1 &= u_c(-\cos\alpha_c \cos\theta_c \sin\psi + \cos\alpha_c \cos\gamma_c \sin\theta_c \cos\psi \qquad\qquad (19.7.22)\\
&\quad - \sin\alpha_c \sin\gamma_c \cos\psi) + a\sin\gamma_c \cos\psi - E_c \sin\psi \\
z_1 &= u_c(-\sin\alpha_c \cos\gamma_c - \cos\alpha_c \sin\gamma_c \sin\theta_c) + p\psi + a\cos\gamma_c
\end{aligned}
$$

$$
\begin{aligned}
n_{x_1} &= \cos\psi \sin\alpha_c \cos\theta_c + \sin\psi(\cos\gamma_c \sin\alpha_c \sin\theta_c + \sin\gamma_c \cos\alpha_c) \\
n_{y_1} &= -\sin\psi \sin\alpha_c \cos\theta_c + \cos\psi(\cos\gamma_c \sin\alpha_c \sin\theta_c + \sin\gamma_c \cos\alpha_c) \quad (19.7.23)\\
n_{z_1} &= -\sin\gamma_c \sin\alpha_c \sin\theta_c + \cos\gamma_c \cos\alpha_c
\end{aligned}
$$

where

$$
u_c = a\sin\alpha_c - (E_c \sin\alpha_c \cot\gamma_c + p\sin\alpha_c)\tan\theta_c - \frac{(E_c - p\cot\gamma_c)\cos\alpha_c}{\cos\theta_c}.
$$

$$(19.7.24)$$

Particular Case

It can be proven that for the case when $\gamma_c = 0$ the generated worm surface is a screw involute surface. This statement is correct for all four types of worm surfaces represented by Eqs. (19.7.13), (19.7.16), (19.7.19), and (19.7.22), respectively.

The proof is based on the following considerations:

(i) The equation of meshing (19.7.15) provides that

$$
\sin\theta_c = \frac{p\cot\alpha_c}{E_c}.
$$

$$(19.7.25)$$

This means that θ_c is constant and Σ_c contacts Σ_1 along a straight line, the generatrix of the cone.

(ii) The worm surface is generated by a straight line, that is, it is a ruled surface. It is a developed surface as well because the surface normal does not depend on surface coordinate u_c. Recall that u_c determines the location of a current point on the generating line.

(iii) Considering the equations of the worm surface and the unit normal to the surface, we may represent a current point of the surface normal by the equation

$$\mathbf{R}_1(u_c, \psi, m) = \mathbf{r}_1(u_c, \psi) + m\mathbf{n}_1(\psi) \tag{19.7.26}$$

where the variable parameter m determines the location of the current point on the surface normal. Function $\mathbf{R}_1(u_c, \psi, m)$ represents the one-parameter family of curves that are traced out in S_1 by a current point of the surface normal.

(iv) The envelope to the family of curves is determined with Eq. (19.7.26) and the equation (see Section 6.1)

$$\left(\frac{\partial \mathbf{R}_1}{\partial u_c} \times \frac{\partial \mathbf{R}_1}{\partial \psi} \right) \cdot \frac{\partial \mathbf{R}_1}{\partial m} = 0. \tag{19.7.27}$$

(v) Equations (19.7.26) and (19.7.27) yield that the normals to the worm surface are tangents to the cylinder of radius r_b and form the angle of $(90° - \lambda_b)$ with the worm axis.

Here,

$$r_b = E_c \sin \theta_c = p \cot \alpha_c, \qquad \lambda_b = \alpha_c. \tag{19.7.28}$$

Problem 19.7.1

Consider that the worm surface represented by Eqs. (19.7.13) is cut by the plane $y_1 = 0$. Axis x_1 is the axis of symmetry of the space in axial section. The point of intersection of the axial profile with the pitch cylinder is determined with the coordinates

$$x_1 = r_p, \quad y_1 = 0, \quad z_1 = -\frac{w_{ax}}{2} = -\frac{p_{ax}}{4} = -\frac{\pi}{4 P_{ax}}.$$

Here, w_{ax} is the nominal value of the space width in axial section that is measured along the generatrix of the pitch cylinder; p_{ax} is the distance between two neighboring threads along the generatrix of the pitch cylinder, and $P_{ax} = \pi / p_{ax}$ is the worm diametral pitch in axial section. Derive the system of equations to be applied to determine s_c (Fig. 19.7.1) considering r_p, r_c, E_c, α_c, p, and w_{ax} as given.

Solution

$$u_c = a \sin \alpha_c - (E_c \sin \alpha_c \cot \gamma_c + p \sin \alpha_c) \tan \theta_c - \frac{(E_c - p \cot \gamma_c) \cos \alpha_c}{\cos \theta_c}$$

$$\tan \psi = \frac{u_c(\cos \alpha_c \sin \theta_c \cos \gamma_c - \sin \alpha_c \sin \gamma_c) + a \sin \gamma_c}{u_c \cos \alpha_c \cos \theta_c + E_c}$$

$$\frac{u_c \cos \alpha_c \cos \theta_c + E_c}{\cos \psi} - r_p = 0$$

$$u_c(\sin \alpha_c \cos \gamma_c + \cos \alpha_c \sin \gamma_c \sin \theta_c) - p\psi - a \cos \gamma_c + \frac{w_{ax}}{2} = 0$$

where

$$a = r_c \tan \alpha_c + \frac{s_c}{2}.$$

The derived equation system contains four equations in four unknowns: θ_c, ψ, u_c, and a. The solution of the system for the unknowns provides the sought-for value of s_c.

Problem 19.7.2

Consider the particular case of the installment of the tool when $\gamma_c = 0$. Derive (i) the equation of meshing (19.7.27), and (ii) the equations of the envelope to the family of normals to the worm surface (19.7.13). Recall that the envelope is represented by Eqs. (19.7.26) and (19.7.27) which have to be considered simultaneously.

Solution
(i)

$$u_c \cos \alpha_c + m \sin \alpha_c + E_c \cos \theta_c = 0.$$

(ii)
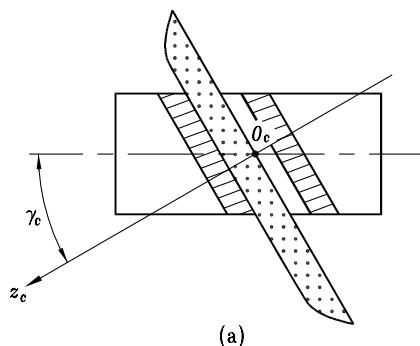
$$X_1 = E_c \sin \theta_c \sin(\theta_c - \psi)$$

$$Y_1 = -E_c \sin \theta_c \cos(\theta_c - \psi)$$

$$Z_1 = \frac{u_c}{\sin \alpha_c} + E_c \cot \alpha_c \cos \theta_c - p\psi - a.$$
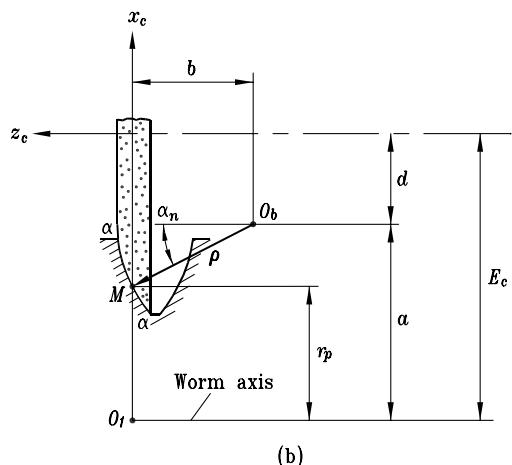
19.8 GEOMETRY AND GENERATION OF F-I WORMS (VERSION I)

F worms with concave–convex surfaces have been proposed by Niemann and Heyer (1953) and applied in practice by the Flender Co., Germany. The great advantage of the F worm-gear drives is the improvement of conditions of lubrication that is achieved due to the favorable shape of contact lines between the worm and the worm-gear surfaces. We consider two versions of F worms: (i) the original one, F-I, and (ii) the modified one, F-II, proposed by Litvin (1968). Both versions of worm-gear drives are designed as nonstandard ones: the radius $r_p^{(o)}$ of the worm operating pitch cylinder differs from the radius r_p of the worm pitch cylinder, and $r_p^{(o)} - r_p \approx 1.3/P_{ax}$. To avoid pointing of

Figure 19.8.1: Installation of grinding wheel generating worm F-I: (a) illustration of installation parameter γ_c; (b) illustration of installation parameter E_c.

teeth of worm-gears, the tooth thickness of the worm on the pitch cylinder is designed as $t_p = 0.4 p_{ax} = 0.4\pi/P_{ax}$.

Installment of the Grinding Wheel for F-I
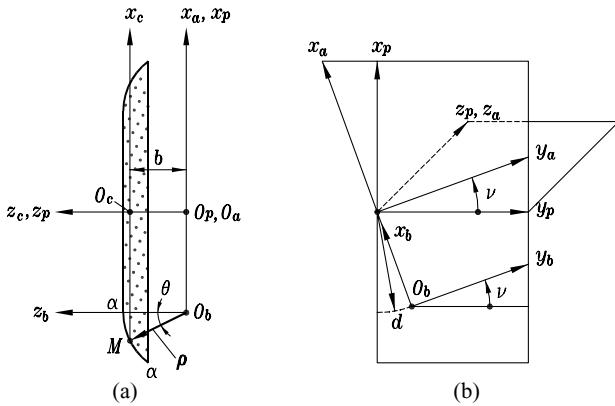
The surface of the grinding wheel is a torus. The axial section of the grinding wheel is the arc α–α of radius ρ [Fig. 19.8.1(b)]. In the following discussion we consider the generation of the surface side *II* of the right-hand worm.

The radius ρ is chosen as approximately equal to the radius r_p of the worm pitch cylinder. The installation of the grinding wheel with respect to the worm is shown in Fig. 19.8.1(a). The axes of the grinding wheel and the worm form the angle $\gamma_c = \lambda_p$, where λ_p is the lead angle on the worm pitch cylinder, and the shortest distance between these axes is E_c. Figure 19.8.2(a) shows the section of the grinding wheel and the worm by a plane that is drawn through the z_c axis, which is the axis of rotation of the grinding wheel, and the shortest distance $O_c O_1$ [Fig. 19.8.1(b)]. It is assumed that the line of shortest distance passes through the mean point M of the worm profile; a and b determine the location of center O_b of the circular arc α–α with respect to O_c.

Here,

$$b = \rho \cos \alpha_n \qquad (19.8.1)$$

where ρ is the radius of arc α–α.

Figure 19.8.2: Generation of grinding wheel with torus surface: (a) section of the grinding wheel and (b) applied coordinate systems.

Equations of Generating Surface Σ_c

We set up coordinate systems S_c and S_p that are rigidly connected to the grinding wheel; coordinate systems S_b and S_a are rigidly connected to the circular arc of radius ρ (Fig. 19.8.2). The circular arc α–α is represented in S_b by the equation

$$\mathbf{r}_b = \rho[-\sin\theta \quad 0 \quad \cos\theta \quad 1]^{\mathrm{T}}. \tag{19.8.2}$$

Figure 19.8.2(a) shows coordinate systems S_a and S_b in the initial position. The surface of the grinding wheel is generated in S_c while the circular arc with coordinate systems S_a and S_b is rotated about the z_p axis [Fig. 19.8.2(b)].

The coordinate transformation is based on the following matrix equation:

$$\mathbf{r}_c(\theta, \nu) = \mathbf{M}_{cp}\mathbf{M}_{pa}\mathbf{M}_{ab}\mathbf{r}_b = \mathbf{M}_{cb}\mathbf{r}_b. \tag{19.8.3}$$

Here,

$$\mathbf{M}_{cp} = \begin{bmatrix} 1 & 0 & 0 & 0 \\ 0 & 1 & 0 & 0 \\ 0 & 0 & 1 & -b \\ 0 & 0 & 0 & 1 \end{bmatrix}, \quad \mathbf{M}_{pa} = \begin{bmatrix} \cos\nu & \sin\nu & 0 & 0 \\ -\sin\nu & \cos\nu & 0 & 0 \\ 0 & 0 & 1 & 0 \\ 0 & 0 & 0 & 1 \end{bmatrix}$$

$$\mathbf{M}_{ab} = \begin{bmatrix} 1 & 0 & 0 & -d \\ 0 & 1 & 0 & 0 \\ 0 & 0 & 1 & 0 \\ 0 & 0 & 0 & 1 \end{bmatrix}, \quad \mathbf{M}_{cb} = \begin{bmatrix} \cos\nu & \sin\nu & 0 & -d\cos\nu \\ -\sin\nu & \cos\nu & 0 & d\sin\nu \\ 0 & 0 & 1 & -b \\ 0 & 0 & 0 & 1 \end{bmatrix}. \tag{19.8.4}$$

We use the following designations [Fig. 19.8.1(b)]:

$$a = r_p + \rho\sin\alpha_n \tag{19.8.5}$$

$$d = E_c - a = E_c - (r_p + \rho\sin\alpha_n) \tag{19.8.6}$$

and

$$b = \rho \cos \alpha_n.$$

Equations (19.8.2) to (19.8.4) yield

$$\begin{aligned}
x_c &= -(\rho \sin \theta + d) \cos \nu \\
y_c &= (\rho \sin \theta + d) \sin \nu \\
z_c &= \rho \cos \theta - b.
\end{aligned} \tag{19.8.7}$$

The unit normal to Σ_c is represented as

$$\mathbf{n}_c = \frac{\mathbf{N}_c}{|\mathbf{N}_c|}, \quad \mathbf{N}_c = \frac{\partial \mathbf{r}_c}{\partial \theta} \times \frac{\partial \mathbf{r}_c}{\partial \nu}.$$

Then we obtain

$$\mathbf{n}_c = [\sin \theta \cos \nu \quad -\sin \theta \sin \nu \quad -\cos \theta]^{\mathrm{T}}. \tag{19.8.8}$$

Equations of Meshing of Grinding Wheel and Worm

The unit normal $\mathbf{n}_c$ is directed *toward* the generating surface and *outward* to the worm surface. The worm surface is generated as the envelope to the family of surfaces that is generated in S_1 by Σ_c in its relative motion with respect to the worm surface Σ_1. Coordinate system S_1 is rigidly connected to the worm.

The equation of meshing is

$$\mathbf{n}_c \cdot \mathbf{v}_c^{(c1)} = 0 \tag{19.8.9}$$

where $\mathbf{v}_c^{(c1)}$ is the velocity in relative motion of the grinding wheel with respect to the worm. Vectors in Eq. (19.8.9) are represented in S_c.

We consider that the worm performs the screw motion with the screw parameter p (Fig. 19.7.4) with respect to the grinding wheel, and $\mathbf{v}_c^{(c1)}$ is represented by Eqs. (19.7.7). After transformations, the equation of meshing of the grinding wheel surface with the worm surface is represented by

$$f(\theta, \nu) = \tan \theta - \frac{E_c - p \cot \gamma_c - d \cos \nu}{b \cos \nu + (E_c \cot \gamma_c + p) \sin \nu} = 0. \tag{19.8.10}$$

The equation of meshing does not contain parameter ψ in screw motion because the relative motion is the screw one. Equation (19.8.10) with the given value of θ provides two solutions for ν, but only the solution for $0 < \nu < 90°$ should be used for further derivations. Recall that Eq. (19.8.10) is derived for the case when the surface side *II* of a right-hand worm is generated.

Lines of Contact on Worm Surface

The line of contact between Σ_c and Σ_1 is a single line on Σ_c and is represented in S_c by Eqs. (19.8.7) and (19.8.10) considered simultaneously. Figure 19.8.3 shows the line of contact in the space of parameters θ, ν; the dashed line represents the line of contact that is out of the working part of the grinding wheel.

The worm surface is represented in S_1 as the set of contact lines between surfaces Σ_c and Σ_1. Using this approach, we have derived the equations of the worm surfaces
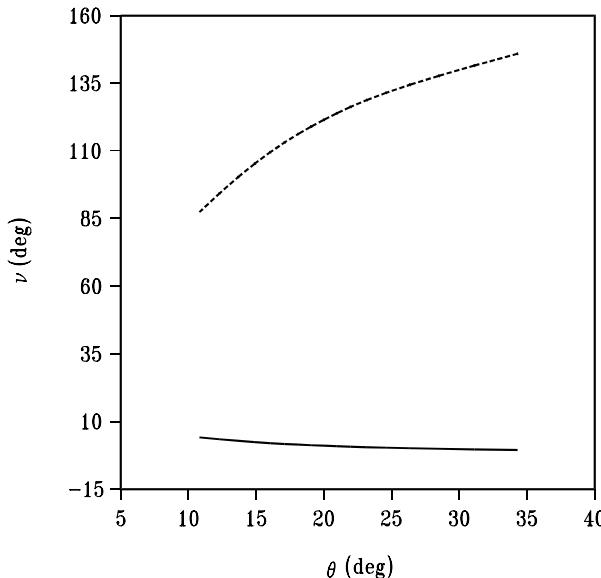
Figure 19.8.3: Line of contact between grinding wheel and worm F-I surfaces.

for both sides, considering the right-hand and left-hand worms. Axis x_1 in the derived equations is the axis of *symmetry* for any section of the worm space by a plane that is drawn through the x_1 axis. An axial section of the worm space is obtained by intersecting the space by the plane $y_1 = 0$. To provide the above-mentioned location of the x_1 axis, as the axis of symmetry of the axial section of the space, we have to consider the following:

(i) The initially applied coordinate system S_1^* is substituted by a parallel coordinate system S_1 whose origin is displaced along the z_1^* axis at the distance a_o (Fig. 19.8.4).

(ii) The coordinates of the point of intersection of the axial section of the worm space with the pitch cylinder must be

$$x_1 = r_p, \quad y_1 = 0, \quad z_1 = \frac{w_{ax}}{2} \qquad (19.8.11)$$

where w_{ax} is the space width on the pitch cylinder.
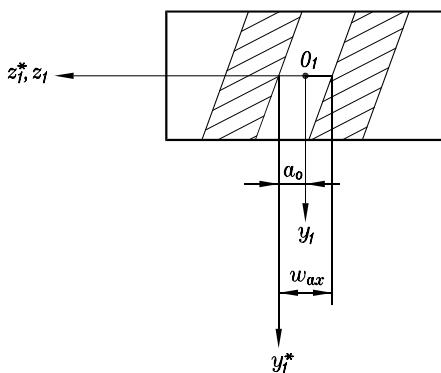
Figure 19.8.4: Derivation of axial section of worm F-I.

The results of derivations of the worm surface and the surface unit normal are as follows:

(i) **Surface side I, right-hand worm:**

$$x_1 = (\rho \sin \theta_c + d)(-\cos \nu \cos \psi + \sin \nu \sin \psi \cos \gamma_c)$$
$$+ (\rho \cos \theta_c - b) \sin \psi \sin \gamma_c + E_c \cos \psi$$
$$y_1 = (\rho \sin \theta_c + d)(\cos \nu \sin \psi + \sin \nu \cos \psi \cos \gamma_c) \qquad (19.8.12)$$
$$+ (\rho \cos \theta_c - b) \cos \psi \sin \gamma_c - E_c \sin \psi$$
$$z_1 = (\rho \sin \theta_c + d) \sin \nu \sin \gamma_c + (b - \rho \cos \theta_c) \cos \gamma_c - p\psi + a_o$$

where

$$a_o = -\frac{w_{ax}}{2} - (\rho \sin \theta_c + d) \sin \nu \sin \gamma_c - (b - \rho \cos \theta_c) \cos \gamma_c + p\psi. \qquad (19.8.13)$$

$$n_{x1} = \sin \theta_c (-\cos \nu \cos \psi + \sin \nu \sin \psi \cos \gamma_c) + \cos \theta_c \sin \psi \sin \gamma_c$$
$$n_{y1} = \sin \theta_c (\cos \nu \sin \psi + \sin \nu \cos \psi \cos \gamma_c) + \cos \theta_c \cos \psi \sin \gamma_c \qquad (19.8.14)$$
$$n_{z1} = \sin \theta_c \sin \nu \sin \gamma_c - \cos \theta_c \cos \gamma_c.$$

Parameters θ_c and ν in Eqs. (19.8.12) and (19.8.14) are related to the equation of meshing,

$$\tan \theta_c = \frac{E_c - p \cot \gamma_c - d \cos \nu}{b \cos \nu - (E_c \cot \gamma_c + p) \sin \nu}. \qquad (19.8.15)$$

(ii) **Surface side II, right-hand worm:**

$$x_1 = (\rho \sin \theta_c + d)(-\cos \nu \cos \psi + \sin \nu \sin \psi \cos \gamma_c)$$
$$- (\rho \cos \theta_c - b) \sin \psi \sin \gamma_c + E_c \cos \psi$$
$$y_1 = (\rho \sin \theta_c + d)(\cos \nu \sin \psi + \sin \nu \cos \psi \cos \gamma_c) \qquad (19.8.16)$$
$$- (\rho \cos \theta_c - b) \cos \psi \sin \gamma_c - E_c \sin \psi$$
$$z_1 = (\rho \sin \theta_c + d) \sin \nu \sin \gamma_c - (b - \rho \cos \theta_c) \cos \gamma_c - p\psi + a_o$$

where

$$a_o = \frac{w_{ax}}{2} - (\rho \sin \theta_c + d) \sin \nu \sin \gamma_c + (b - \rho \cos \theta_c) \cos \gamma_c + p\psi. \qquad (19.8.17)$$

$$n_{x1} = \sin \theta_c (-\cos \nu \cos \psi + \sin \nu \sin \psi \cos \gamma_c) - \cos \theta_c \sin \psi \sin \gamma_c$$
$$n_{y1} = \sin \theta_c (\cos \nu \sin \psi + \sin \nu \cos \psi \cos \gamma_c) - \cos \theta_c \cos \psi \sin \gamma_c \qquad (19.8.18)$$
$$n_{z1} = \sin \theta_c \sin \nu \sin \gamma_c + \cos \theta_c \cos \gamma_c.$$

Parameters θ_c and ν in Eqs. (19.8.16) and (19.8.18) are related with the equation of meshing,

$$\tan \theta_c = \frac{E_c - p \cot \gamma_c - d \cos \nu}{b \cos \nu + (E_c \cot \gamma_c + p) \sin \nu}. \qquad (19.8.19)$$

(iii) **Surface side *I*, left-hand worm:**

$$x_1 = (\rho \sin \theta_c + d)(-\cos v \cos \psi + \sin v \sin \psi \cos \gamma_c)$$
$$\quad - (\rho \cos \theta_c - b) \sin \psi \sin \gamma_c + E_c \cos \psi$$
$$y_1 = (\rho \sin \theta_c + d)(\cos v \sin \psi + \sin v \cos \psi \cos \gamma_c) \qquad (19.8.20)$$
$$\quad - (\rho \cos \theta_c - b) \cos \psi \sin \gamma_c - E_c \sin \psi$$
$$z_1 = -(\rho \sin \theta_c + d) \sin v \sin \gamma_c + (b - \rho \cos \theta_c) \cos \gamma_c + p\psi + a_o$$

where

$$a_o = -\frac{w_{ax}}{2} + (\rho \sin \theta_c + d) \sin v \sin \gamma_c - (b - \rho \cos \theta_c) \cos \gamma_c - p\psi. \quad (19.8.21)$$

$$n_{x1} = \sin \theta_c(-\cos v \cos \psi + \sin v \sin \psi \cos \gamma_c) - \cos \theta_c \sin \psi \sin \gamma_c$$
$$n_{y1} = \sin \theta_c(\cos v \sin \psi + \sin v \cos \psi \cos \gamma_c) - \cos \theta_c \cos \psi \sin \gamma_c \qquad (19.8.22)$$
$$n_{z1} = -\sin \theta_c \sin v \sin \gamma_c - \cos \theta_c \cos \gamma_c.$$

Parameters θ_c and v in Eqs. (19.8.20) and (19.8.22) are related to the equation of meshing,

$$\tan \theta_c = \frac{E_c - p \cot \gamma_c - d \cos v}{b \cos v + (E_c \cot \gamma_c + p) \sin v}. \qquad (19.8.23)$$

(iv) **Surface side *II*, left-hand worm:**

$$x_1 = (\rho \sin \theta_c + d)(-\cos v \cos \psi + \sin v \sin \psi \cos \gamma_c)$$
$$\quad + (\rho \cos \theta_c - b) \sin \psi \sin \gamma_c + E_c \cos \psi$$
$$y_1 = (\rho \sin \theta_c + d)(\cos v \sin \psi + \sin v \cos \psi \cos \gamma_c) \qquad (19.8.24)$$
$$\quad + (\rho \cos \theta_c - b) \cos \psi \sin \gamma_c - E_c \sin \psi$$
$$z_1 = -(\rho \sin \theta_c + d) \sin v \sin \gamma_c - (b - \rho \cos \theta_c) \cos \gamma_c + p\psi + a_o$$

where
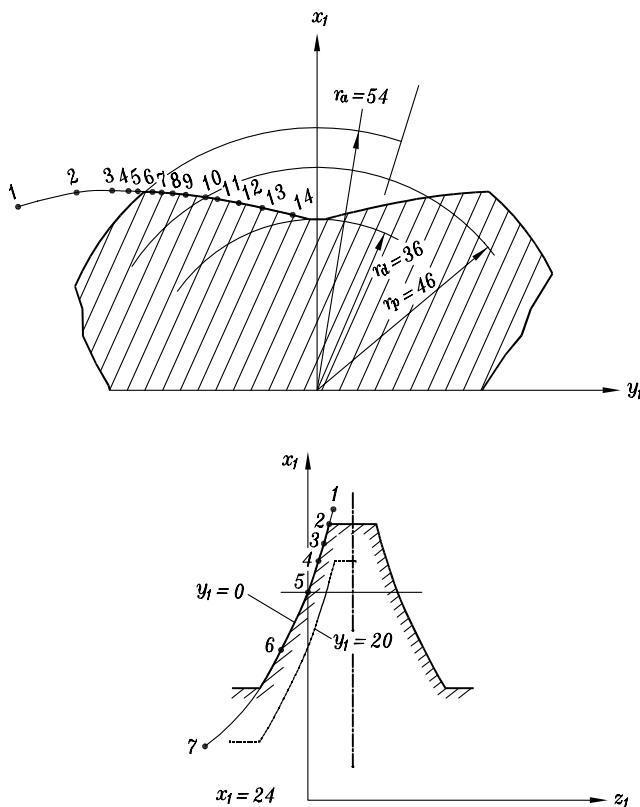
$$a_o = \frac{w_{ax}}{2} + (\rho \sin \theta_c + d) \sin v \sin \gamma_c + (b - \rho \cos \theta_c) \cos \gamma_c - p\psi. \quad (19.8.25)$$

$$n_{x1} = \sin \theta_c(-\cos v \cos \psi + \sin v \sin \psi \cos \gamma_c) + \cos \theta_c \sin \psi \sin \gamma_c$$
$$n_{y1} = \sin \theta_c(\cos v \sin \psi + \sin v \cos \psi \cos \gamma_c) + \cos \theta_c \cos \psi \sin \gamma_c \qquad (19.8.26)$$
$$n_{z1} = -\sin \theta_c \sin v \sin \gamma_c + \cos \theta_c \cos \gamma_c.$$

Parameters θ_c and v in Eqs. (19.8.24) and (19.8.26) are related with the equation of meshing,

$$\tan \theta_c = \frac{E_c - p \cot \gamma_c - d \cos v}{b \cos v - (E_c \cot \gamma_c + p) \sin v}. \qquad (19.8.27)$$

Figure 19.8.5 shows the cross section and axial section of the F-I worm that have been obtained for the following input parameters: $N_1 = 3$; $N_2 = 31$; $r_p = 46$ mm; axial

Figure 19.8.5: Cross section and axial section of worm F-I.
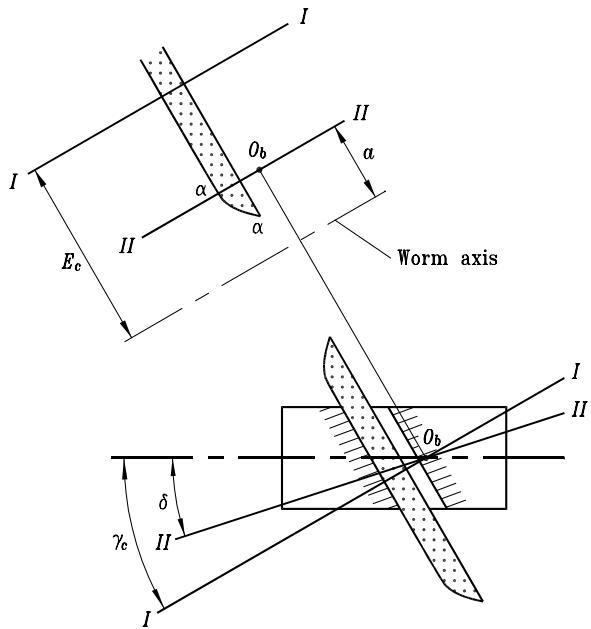
module $m_{ax} = 8$ mm. The radius of the operating pitch cylinder is $r_{po} = r_p + 1.25m_{ax} = 56$ mm; $\rho = 46$ mm; $\gamma_c = \lambda_p = 14°37'15''$; $\alpha_n = 20°$; $a = r_p + \rho \sin \alpha_n = 61.733$ mm; $b = \rho \cos \alpha_n = 43.226$ mm.

19.9 GEOMETRY AND GENERATION OF F-II WORMS (VERSION II)

Method for Grinding

The grinding of F worms of version II can be performed by the same tool that is used for generation of worms of version I. The difference is in the application of special setting parameters. The geometry of F worms of version II has certain advantages in comparison with the worms of version I: (i) the line of contact between the grinding surface Σ_c and the worm surface is a planar curve, the circular arc of the axial section of the torus; and (ii) the shape of the line of contact does not depend on the diameter of the grinding wheel and the shortest center distance E_c.

The main idea of the proposed method for grinding is based on application of *axes of meshing*. There are two axes of meshing when a helicoid is generated by a peripheral tool with a surface of revolution. One of the axes of meshing, $I-I$, coincides with the axis of rotation of the tool (Fig. 19.9.1); the location and orientation of the other axis of

Figure 19.9.1: Axes of meshing in the case of grinding of worm F-II.

meshing, II–II, parameters a and δ, respectively, are determined with the equations

$$a = p \cot \gamma_c \tag{19.9.1}$$

where p is the screw parameter and γ_c is the angle formed by the axes of the grinding wheel and the worm, and

$$\delta = \arctan\left(\frac{p}{E_c}\right) \tag{19.9.2}$$

where E_c is the shortest distance between the previously mentioned axes.
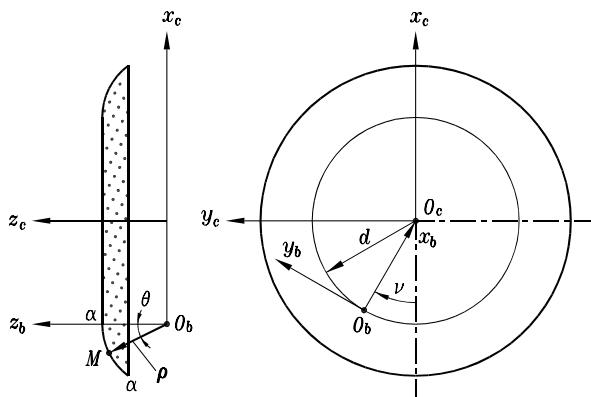
The installation of the grinding wheel is based on observation of the following requirements:

(a) Center O_b of the circular arc α–α (Fig. 19.9.2) is located on the x_c axis which is the line of shortest distance between the axes of the grinding wheel and the worm.

(b) The distance a from the worm axis (Fig. 19.9.1) and the crossing angle γ_c must be related by the equation

$$\gamma_c = \arctan\left(\frac{p}{a}\right) \tag{19.9.3}$$

where p is the screw parameter of the screw motion of the worm in the process of grinding.

The normal to Σ_c already intersects the axis of the grinding wheel, that is the axis of meshing, I–I, as well. The normal to Σ_c also intersects the other axis of meshing, II–II, because the O_b center of the circular arc α–α is located on II–II.

Figure 19.9.2: Grinding wheel for worm F-II.

Equation (19.9.3) requires only the relation between a and γ_c, but a can be chosen arbitrarily. However, the shape of lines of contact between the worm and the worm-gear surfaces, Σ_1 and Σ_2, depends on a. Based on preliminary investigation, the recommended choice is

$$a = r_p + p \sin \alpha_n. \tag{19.9.4}$$

Summarizing, we may formulate the difference in the installations of the grinding wheel for generation of worms F-I and F-II as follows:

Version 1: $b \neq 0$; the line of shortest distance passes through the middle point M of circular arc α–α; $\gamma_c = \lambda_p$; $a = r_p + \rho \sin \alpha_n$ (Figs. 19.8.1 and 19.8.2).

Version 2: $b = 0$; the line of shortest distance passes through O_b; $\gamma_c \neq \lambda_p$, but γ_c and a are related with Eq. (19.9.1) (Fig. 19.9.1).

Equation of Meshing
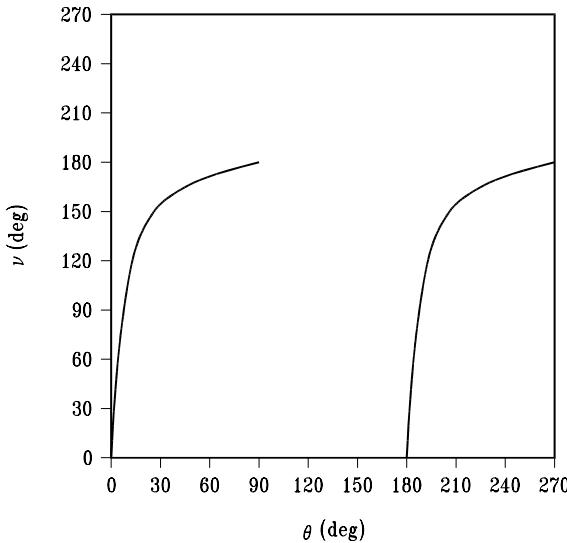
We may derive for the F-II worm the equation of meshing between surfaces Σ_c and Σ_1 considering the previously derived Eq. (19.8.10) but taking $b = 0$, $d = E_c - a$, and $a \tan \gamma_c = p$. After the derivations, we obtain the following equation of meshing for the F-II worm:

$$\sin \theta (E_c \cot \gamma_c + p) \sin \nu - (E_c - a)(1 - \cos \nu) \cos \theta = 0. \tag{19.9.5}$$

There are two solutions to Eq. (19.9.5): (i) with $\nu = 0$ and any value of θ, and (ii) with the relation between θ and ν determined as

$$\tan \frac{\nu}{2} - \frac{(E_c \cot \gamma_c + p) \tan \theta}{E_c - a} = 0. \tag{19.9.6}$$

The meaning of the first solution is that the line of contact between Σ_c and Σ_1 is the circular arc α–α, the axial section of the grinding wheel. The second solution provides a contact line on Σ_c that is out of the working part of the grinding wheel. Both contact lines in the space of parameters θ and ν are shown in Fig. 19.9.3.

Figure 19.9.3: Line of contact between grinding wheel and worm F-II surfaces.

Following an approach similar to that applied for F-I worms, we have derived the following equations for the surface of F-II worms and the surface unit normal:

(i) **Surface side I, right-hand worm:**

$$x_1 = -\rho(\sin\theta_c \cos\psi - \cos\theta_c \sin\psi \sin\gamma_c) + a\cos\psi$$
$$y_1 = \rho(\sin\theta_c \sin\psi + \cos\theta_c \cos\psi \sin\gamma_c) - a\sin\psi \qquad (19.9.7)$$
$$z_1 = -\rho\cos\theta_c \cos\gamma_c - p\psi + a_o$$

where

$$a_o = -\frac{w_{ax}}{2} + \rho\cos\theta_c \cos\gamma_c + p\psi. \qquad (19.9.8)$$

$$n_{x1} = -\sin\theta_c \cos\psi + \sin\gamma_c \cos\theta_c \sin\psi$$
$$n_{y1} = \sin\theta_c \sin\psi + \sin\gamma_c \cos\theta_c \cos\psi \qquad (19.9.9)$$
$$n_{z1} = -\cos\gamma_c \cos\theta_c.$$

(ii) **Surface side II, right-hand worm:**

$$x_1 = -\rho(\sin\theta_c \cos\psi + \cos\theta_c \sin\psi \sin\gamma_c) + a\cos\psi$$
$$y_1 = \rho(\sin\theta_c \sin\psi - \cos\theta_c \cos\psi \sin\gamma_c) - a\sin\psi \qquad (19.9.10)$$
$$z_1 = \rho\cos\theta_c \cos\gamma_c - p\psi + a_o$$

where

$$a_o = \frac{w_{ax}}{2} - \rho\cos\theta_c \cos\gamma_c + p\psi. \qquad (19.9.11)$$

$$n_{x1} = -\sin\theta_c \cos\psi - \sin\gamma_c \cos\theta_c \sin\psi$$
$$n_{y1} = \sin\theta_c \sin\psi - \sin\gamma_c \cos\theta_c \cos\psi \qquad (19.9.12)$$
$$n_{z1} = \cos\gamma_c \cos\theta_c.$$

(iii) **Surface side I, left-hand worm:**

$$x_1 = -\rho(\sin\theta_c \cos\psi + \cos\theta_c \sin\psi \sin\gamma_c) + a\cos\psi$$
$$y_1 = \rho(\sin\theta_c \sin\psi - \cos\theta_c \cos\psi \sin\gamma_c) - a\sin\psi \qquad (19.9.13)$$
$$z_1 = -\rho\cos\theta_c \cos\gamma_c + p\psi + a_o$$

where

$$a_o = -\frac{w_{ax}}{2} + \rho\cos\theta_c \cos\gamma_c - p\psi. \qquad (19.9.14)$$

$$n_{x1} = -\sin\theta_c \cos\psi - \sin\gamma_c \cos\theta_c \sin\psi$$
$$n_{y1} = \sin\theta_c \sin\psi - \sin\gamma_c \cos\theta_c \cos\psi \qquad (19.9.15)$$
$$n_{z1} = -\cos\gamma_c \cos\theta_c.$$

(iv) **Surface side II, left-hand worm:**

$$x_1 = -\rho(\sin\theta_c \cos\psi - \cos\theta_c \sin\psi \sin\gamma_c) + a\cos\psi$$
$$y_1 = \rho(\sin\theta_c \sin\psi + \cos\theta_c \cos\psi \sin\gamma_c) - a\sin\psi \qquad (19.9.16)$$
$$z_1 = \rho\cos\theta_c \cos\gamma_c + p\psi + a_o$$

where

$$a_o = \frac{w_{ax}}{2} - \rho\cos\theta_c \cos\gamma_c - p\psi. \qquad (19.9.17)$$

$$n_{x1} = -\sin\theta_c \cos\psi + \sin\gamma_c \cos\theta_c \sin\psi$$
$$n_{y1} = \sin\theta_c \sin\psi + \sin\gamma_c \cos\theta_c \cos\psi \qquad (19.9.18)$$
$$n_{z1} = \cos\gamma_c \cos\theta_c.$$

Axis x_1 in all four cases is the axis of symmetry of the axial section of the worm space (see Fig. 19.8.4).
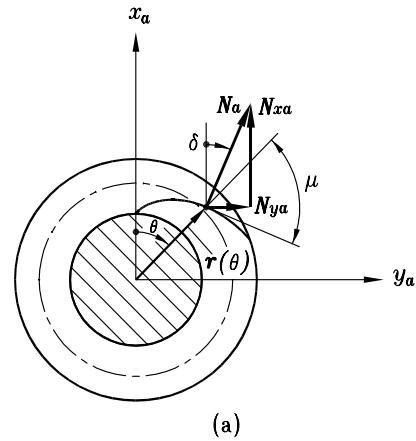
19.10 GENERALIZED HELICOID EQUATIONS

Consider that the cross section of the worm is represented in parametric form in the auxiliary coordinate system S_a as [Fig. 19.10.1(a)]
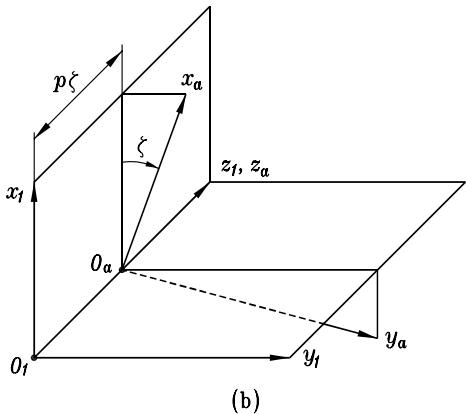
$$\mathbf{r}_a(\theta) = r(\theta)\cos\theta \, \mathbf{i}_a + r(\theta)\sin\theta \, \mathbf{j}_a \qquad (19.10.1)$$

where $r(\theta)$ is the polar equation of the cross section. The worm surface now can be represented as the surface that is generated by the curve $\mathbf{r}_a(\theta)$ that is performing the screw motion about the worm z_1 axis [Fig. 19.10.1(b)]. The worm surface can be determined by the matrix equation

$$\mathbf{r}_1(\theta, \zeta) = \mathbf{M}_{1a}(\zeta)\mathbf{r}_a(\theta) \qquad (19.10.2)$$

(a)

Figure 19.10.1: For derivation of generalized helicoid.

(b)

where [Fig. 19.10.1(b)]

$$
\mathbf{M}_{1a} =
\begin{bmatrix}
\cos\zeta & -\sin\zeta & 0 & 0 \\
\sin\zeta & \cos\zeta & 0 & 0 \\
0 & 0 & 0 & p\zeta \\
0 & 0 & 0 & 1
\end{bmatrix}.
\tag{19.10.3}
$$

Using Eqs. (19.10.1) to (19.10.3), we represent the worm surface as follows:

$$
\mathbf{r}_1(\theta, \zeta) = r\cos(\theta + \zeta)\,\mathbf{i}_1 + r\sin(\theta + \zeta)\,\mathbf{j}_1 + p\zeta\,\mathbf{k}_1.
\tag{19.10.4}
$$

For the following derivations we need angle μ that is formed between the position vector $\mathbf{r}_a(\theta)$ and the tangent to this curve [Fig. 19.10.1(a)]. It is known that

$$
\mu = \arctan\left(\frac{r(\theta)}{r_\theta}\right) \qquad \left(r_\theta = \frac{dr}{d\theta}\right).
\tag{19.10.5}
$$

An alternative equation for determination of μ is based on the expression [Fig. 19.10.1(a)]

$$\mu = 90° - \theta + \delta = 90° - \theta + \arctan\left(\frac{N_{ya}}{N_{xa}}\right) \qquad (19.10.6)$$

where $\mathbf{N}_a$ is the normal to the planar curve $\mathbf{r}_a(\theta)$.

The unit normal to surface (19.10.4) is determined with the equations

$$\mathbf{n}_1 = \frac{\mathbf{N}_1}{|\mathbf{N}_1|}, \qquad \mathbf{N}_1 = \frac{\partial \mathbf{r}_1}{\partial \theta} \times \frac{\partial \mathbf{r}_1}{\partial \zeta}, \qquad (19.10.7)$$

which yield

$$\mathbf{n}_1 = \frac{1}{(p^2 + r^2 \cos^2 \mu)^{0.5}}[p\sin(\theta + \zeta + \mu)\,\mathbf{i}_1 - p\cos(\theta + \zeta + \mu)\,\mathbf{j}_1 + r\cos\mu\,\mathbf{k}_1].$$

$$(19.10.8)$$

We recall that because the worm surface is a helicoid, the coordinates of the worm surface and the surface unit normal are related by the following equation (see Section 5.5):

$$y_1 n_{x1} - x_1 n_{y1} - p n_{z1} = 0. \qquad (19.10.9)$$

The screw parameter p is positive for a right-hand worm.

The advantage of Eqs. (19.10.4) and (19.10.8) is that the worm surface and its normal are represented in two-parameter form. However, this approach requires the analytical or numerical determination of the worm cross section. The discussed approach is especially effective in the case when the worm is generated by the surface of a grinding wheel and the worm surface is represented by three parameters.

19.11 EQUATION OF MESHING OF WORM AND WORM-GEAR SURFACES

The equation of meshing determines the relation between the worm surface Σ_1 parameters and the angle of rotation ϕ_1 of the worm that is in mesh with the worm-gear surface Σ_2. Surfaces Σ_1 and Σ_2 are in contact along a line (L) at every instant. The determination of L is based on the requirement that at any point of L the following equations must hold:

$$\mathbf{N}_i \cdot \mathbf{v}_i^{(12)} = 0 \qquad (i = 1, 2, f). \qquad (19.11.1)$$

Here, the subscripts $(1, 2, f)$ designate coordinate systems S_1, S_2, and S_f that are rigidly connected to the worm, the gear, and the frame (housing); $\mathbf{N}_i$ is the normal to the worm surface; $\mathbf{v}_i^{(12)}$ is the relative velocity of Σ_1 with respect to Σ_2 (see Chapter 2).

We can simplify the equation of meshing, taking into account that the worm is a helicoid. For simplification of the equation of meshing, we can use Eq. (19.10.9) or the equation

$$y_f n_{xf} - x_f n_{yf} - p n_{zf} = 0. \qquad (19.11.2)$$

Using Eq. (19.11.1) with $i = 1$, and Eq. (19.10.9), we represent the equation of meshing in S_1 as follows:

$$(z_1 \cos \phi_1 + E \cot \gamma \sin \phi_1)N_{x1} + (-z_1 \sin \phi_1 + E \cot \gamma \cos \phi_1)N_{y1}$$

$$- \left[(x_1 \cos \phi_1 - y_1 \sin \phi_1 + E) - p \frac{1 - m_{21} \cos \gamma}{m_{21} \sin \gamma} \right] N_{z1} = 0. \qquad (19.11.3)$$

Here, $m_{21} = N_1/N_2$ is the gear ratio; (x_1, y_1, z_1) are the coordinates of the worm surface; (N_{x1}, N_{y1}, N_{z1}) are the projections of the normal $\mathbf{N}_1$ to the worm surface; γ is the twist angle. The equation of meshing can be represented in the coordinate system S_f as

$$z_f N_{xf} + E \cot \gamma N_{yf} - \left(x_f + E - p \frac{1 - m_{21} \cos \gamma}{m_{21} \sin \gamma} \right) N_{zf} = 0. \qquad (19.11.4)$$

Consider now the case when the worm surface is represented as a generalized helicoid (see Section 19.10). The equation of meshing is represented in this case as

$$r \left[r \cos(\theta + \zeta + \phi_1) + E - p \frac{1 - m_{21} \cos \gamma}{m_{21} \sin \gamma} \right] \cos \mu + E p \cot \gamma \cos \tau$$

$$= p z_f \sin \tau = p^2 \zeta \sin \tau. \qquad (19.11.5)$$

Here, $r = r(\theta)$ is the magnitude of the position vector of the current point of the worm cross section [Fig. 19.10.1(a)]; $\tau = \theta + \zeta + \phi_1 + \mu$. The coordinates of a current contact point can be expressed in S_f by the equations

$$x_f = r \cos(\theta + \zeta + \phi_1), \qquad y_f = r \sin(\theta + \zeta + \phi_1), \qquad z_f = p\zeta. \qquad (19.11.6)$$

Any of equations (19.11.3), (19.11.4), and (19.11.5) yields the relation between the worm surface parameters (u, θ) and the angle of worm rotation, that is,

$$f(u, \theta, \phi_1) = 0. \qquad (19.11.7)$$

Equations

$$\mathbf{r}_1 = \mathbf{r}_1(u, \theta), \qquad f(u, \theta, \phi_1) = 0 \qquad (19.11.8)$$

where $\mathbf{r}_1 = \mathbf{r}_1(u, \theta)$ is the worm surface Σ_1, represent in S_1 the family of contact lines on surface Σ_1; ϕ_1 is a fixed-in parameter of motion, the parameter of the family of contact lines.
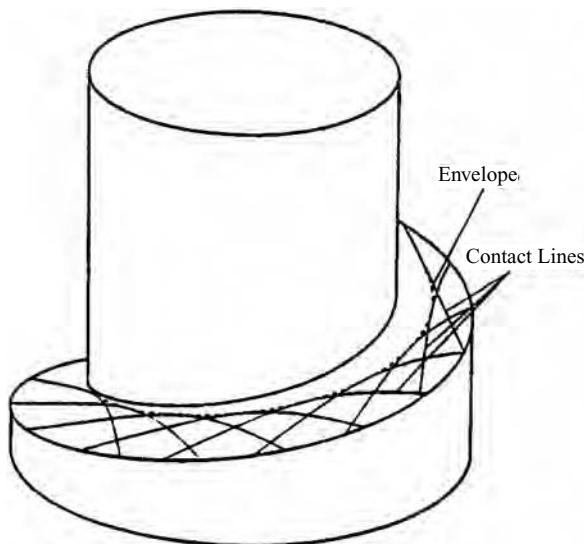
Contact lines on the worm-gear surface are represented by equations

$$\mathbf{r}_2(u, \theta, \phi_1) = \mathbf{M}_{21}\mathbf{r}_1(u, \theta), \qquad f(u, \theta, \phi_1) = 0 \qquad (19.11.9)$$

where $\mathbf{M}_{21}$ is the matrix that describes the coordinate transformation from coordinate system S_1 to coordinate system S_2. Here, S_1 and S_2 are rigidly connected to the worm and the worm-gear, respectively.
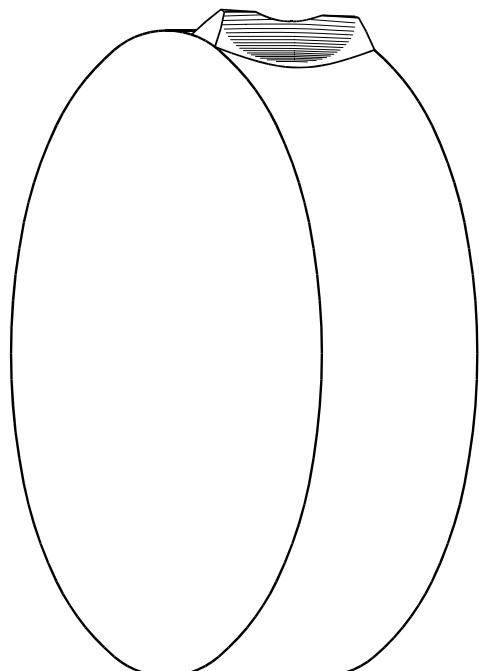
Figure 19.11.1 shows the contact lines on the surface of an Archimedes worm. Figure 19.11.2 shows the contact lines on the worm-gear surface.

It was mentioned in Section 6.6 that the contact lines on the generating surface may have an envelope. In the case of a worm-gear drive, the generating surface is the worm

Figure 19.11.1: Contact lines on worm surface.

surface. The envelope to contact lines on an Archimedes worm surface is shown in Fig. 19.11.1. Figures 19.11.1 and 19.11.2 correspond to a worm-gear drive with the following parameters: the number of worm threads and gear teeth are $N_1 = 2$ and $N_2 = 30$, respectively; the axial worm module is $m_{ax} = 8$ mm; the twist angle is $\gamma = 90°$; the shortest distance between the axes of the worm and the worm-gear is $E = 176$ mm.


Figure 19.11.2: Contact lines on worm-gear surface.
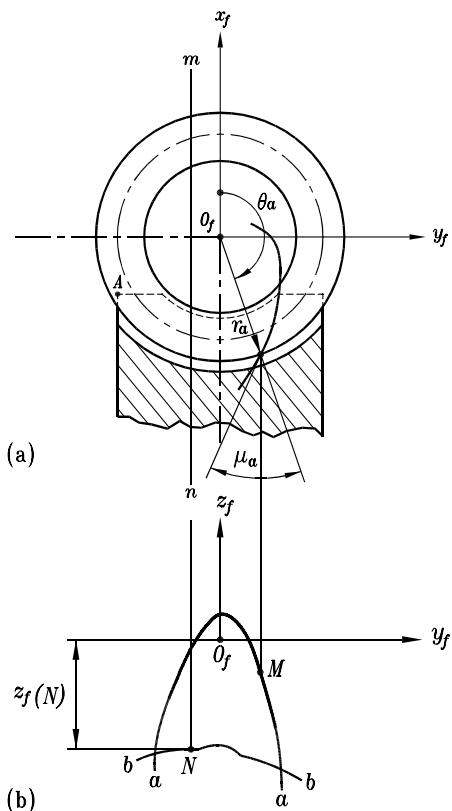
The instantaneous line contact exists only for an ideal worm-gear drive, without misalignment and errors of manufacturing. In reality, the contact of surfaces Σ_1 and Σ_2 is an instantaneous point contact, which might be accompanied with the shift of the bearing contact to the edge and an undesirable shape of the function of transmission errors. Such transmission errors cause vibration during the meshing.

To minimize the influence of misalignment and errors of manufacturing, it is necessary to localize the bearing contact between Σ_1 and Σ_2 using the proper mismatch between the theoretical and real worm surfaces.

19.12 AREA OF MESHING

The area of meshing is the active part of the *surface of action*. The surface of action is the set of lines of contact between the worm and worm-gear surfaces that are represented in the fixed coordinate system S_f. Knowing the area of meshing, we are able to determine the working axial length of the worm and the working axial width of the worm-gear (see below). The following derivations are based on representation of the worm surface as a generalized helicoid (see Section 19.11).

Figure 19.12.1(b) shows the area of meshing of an orthogonal worm-gear drive that is limited in plane (z_f, y_f) with curves a–a and b–b. The area of meshing is represented

Figure 19.12.1: For derivation of area of meshing.
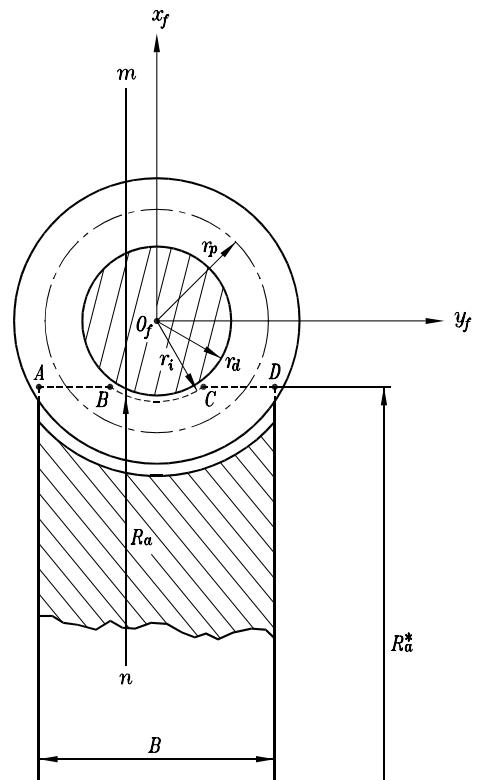
in the fixed coordinate system S_f. Curve a–a corresponds to the entry into meshing of those points of the worm surface that belong to the worm addendum cylinder of radius r_a [Fig. 19.12.1(a)]. Curve b–b corresponds to the entry into meshing of those points of the worm-gear surface that belong to the gear addendum cylinder. Current point M of curve a–a is determined by the following equations:

$$\sin(\theta_a + \zeta + \phi_1) = \frac{y_f}{r_a} \tag{19.12.1}$$
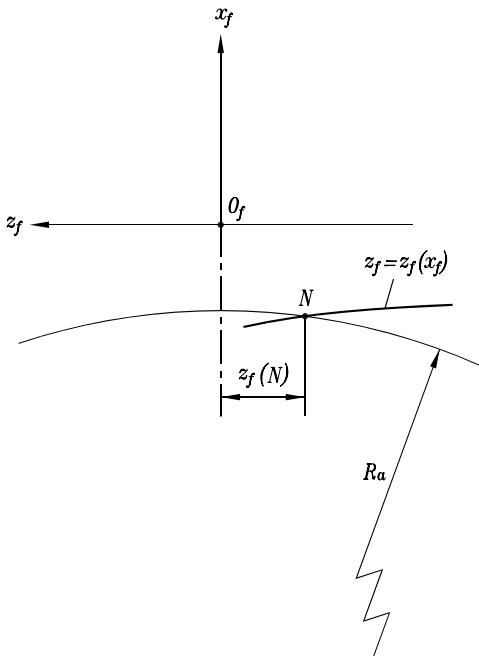
$$z_f = \frac{r_a \left[r_a \cos(\theta_a + \zeta + \phi_1) + E - \dfrac{p}{m_{21}} \right] \cos \mu_a}{p \sin[\mu_a + (\theta_a + \zeta + \phi_1)]} \tag{19.12.2}$$

$$x_f = r_a \cos(\theta_a + \zeta + \phi_1). \tag{19.12.3}$$

The input for the solution of the system of Eqs. (19.12.1) to (19.12.3) is the current value of y_f; r_a, θ_a, and μ_a are considered as known. Equations of the system above are represented in echelon form. Varying y_f, we can determine the corresponding values of z_f and x_f of curve a–a. Equation (19.12.1) provides two solutions for the angle $(\theta_a + \zeta + \phi_1)$, but only the solution that corresponds to $x_f < 0$ must be used. This consideration is based on the specific location of the area of meshing (Figs. 19.12.1 and 19.12.2).

Figure 19.12.2: Intersection of worm and worm-gear surfaces by plane m–n.

Figure 19.12.3: For derivation of curve b–b shown in Fig. 19.12.1.

Let us now consider the determination of current point N of curve b–b [Fig. 19.12.1(b)]. We limit the discussion to the shape of the addendum surface of the worm-gear that is shown in Fig. 19.2.2. Surface AB (or CD) of the worm-gear addendum surface is a cylinder of radius R_a^*; the axis of the cylinder coincides with the worm-gear axis. Surface BC of the worm-gear addendum surface is a cylinder of radius r_i; the axis of this cylinder coincides with the axis of the worm. The intersection of surface BC by plane mn is the arc of the circle of radius R_a (Figs. 19.12.2 and 19.12.3). Point N of curve b–b can be determined as the point of intersection of curve $z_f(x_f)$ and the circle of radius R_a (Fig. 19.12.3). Curve $z_f(x_f)$ is obtained as the result of intersection of the surface of action by plane $y_f = \text{const}$.

The determination of current point N of curve b–b for the BC gear addendum surface is based on the following equations:

$$y_f - r(\theta)\sin(\theta + \zeta + \phi_1) = f_1(\theta, (\zeta + \phi_1)) = 0 \qquad (19.12.4)$$

$$z_f - \frac{r(\theta)\left[r(\theta)\cos(\theta + (\zeta + \phi_1)) + E - \dfrac{p}{m_{21}}\right]\cos\mu(\theta)}{p\sin[\mu(\theta) + (\theta + (\zeta + \phi_1))]} = f_2(\theta, (\zeta + \phi_1)) = 0$$
$$(19.12.5)$$

$$x_f - r(\theta)\cos(\theta + (\zeta + \phi_1)) = f_3(\theta, (\zeta + \phi_1)) = 0 \qquad (19.12.6)$$

$$\left\{[E + x_f(\theta, (\zeta + \phi_1))]^2 + z_f^2(\theta, (\zeta + \phi_1))\right\}^{0.5} - E + \left[r_i^2 - y_f^2(\theta, (\zeta + \phi_1))\right]^{0.5}$$
$$= f_4(\theta, (\zeta + \phi_1)) = 0. \qquad (19.12.7)$$

Here, $r_i = r_d + c$, where r_d is the radius of the worm dedendum cylinder and c is the clearance; usually, $c = 0.25/P$. Equations (19.12.5) and (19.12.6) are designated for determination of $x_f(\theta, (\zeta + \phi_1))$ and $z_f(\theta, (\zeta + \phi_1))$ used in Eq. (19.12.7); coordinate y_f is considered as the input data; $\tan \mu = r(\theta)/r_\theta$, where $r_\theta = dr/d\theta$.

Equation system (19.12.4) to (19.12.7) may be considered as a system of two nonlinear equations in two unknowns, θ and $(\zeta + \phi_1)$. The two-equation system is formed by Eqs. (19.12.4) and (19.12.7) and can be solved by using a numerical subroutine [More *et al.*, 1980; Visual Numerics, Inc., 1998]. An iterative process for the solution based on the following procedure can be applied as well:

Step 1: We use Eq. (19.12.4) considering y_f as given and choosing a value of θ. Then, we can determine $\sin(\theta + \zeta + \phi_1)$ from Eq. (19.12.4). This equation provides two solutions for $(\theta + \zeta + \phi_1)$, but only the solution with $x_f(\theta + \zeta + \phi_1) < 0$ should be selected (see the location of the area of meshing in Figs. 19.12.1 and 19.12.2).

Step 2: We determine the values of $z_f(\theta + \zeta + \phi_1)$ and $x_f(\theta + \zeta + \phi_1)$ using Eqs. (19.12.5) and (19.12.6), respectively.

Step 3: We check if Eq. (19.12.7) is satisfied with the chosen value of θ and the respective value of $(\zeta + \phi_1)$ determined from Eq. (19.12.4). If not, it is necessary to start a new iteration with the new value of θ.

The determination of current point N of curve b–b (Fig. 19.12.1) for the AB (and CD) gear addendum surface (Fig. 19.12.2) is based on the equation system that contains Eqs. (19.12.4), (19.12.5), (19.12.6), and the equation

$$R_a^* - \left[(E + x_f)^2 + z_f^2 \right]^{0.5} = f_5(\theta, (\zeta + \phi_1)) = 0. \qquad (19.12.8)$$

Equation (19.12.8) is used instead of Eq. (19.12.7). Parameter R_a^* is shown in Fig. 19.12.2.
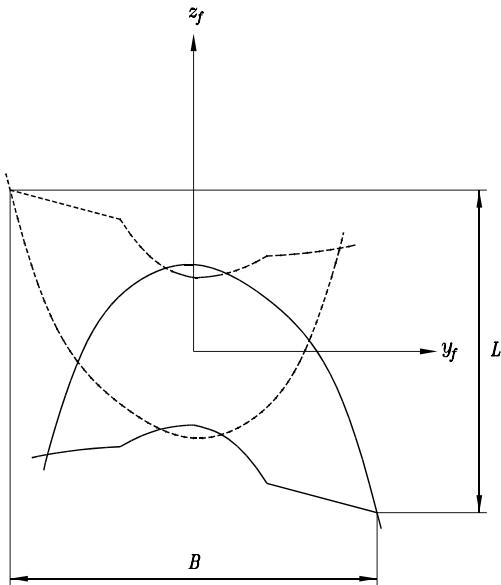
Equations (19.12.4) and (19.12.8) considered simultaneously represent a system of two nonlinear equations in the unknowns θ and $(\zeta + \phi_1)$. Equations (19.12.5) and (19.12.6) are used in this case for determination of coordinates x_f and z_f for current point N of curve b–b.

The determination of the area of meshing enables us to determine the length L of the working part of the worm and the width B of the working part of the gear. The area of meshing for a worm-gear drive with the ZA worm (Archimedes worm) is represented in Figs. 19.12.4 and 19.12.5. The input data for computation is as follows: $N_1 = 2$, $N_2 = 30$, $r_p = 46$ mm, $m_{ax} = 8$ mm. The operating pitch radius is $r_p^{(o)} = r_p + \zeta m_{ax}$, where $\zeta = 0$ (Fig. 19.12.4) and $\zeta = 1$ (Fig. 19.12.5). The center distance is $E = r_p + N_2 m_{ax}/2 + \zeta m_{ax}$.

19.13 PROSPECTS OF NEW DEVELOPMENTS
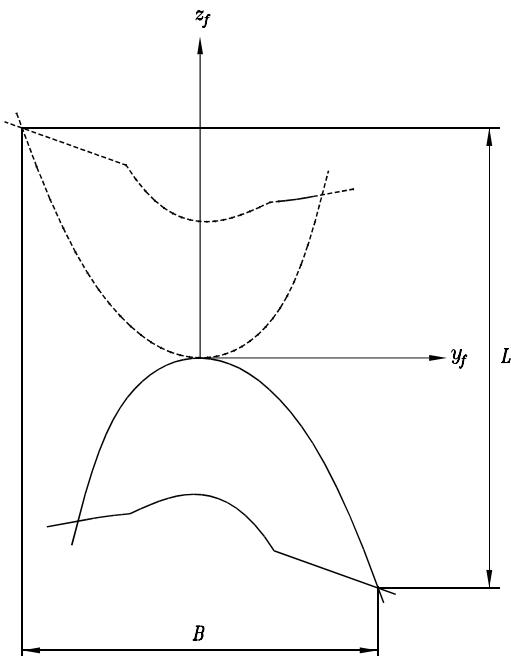
Introductory Remarks

Worm-gear drives with cylindrical worms are still an example of gear drives for which a satisfactory bearing contact is obtained by lapping under a load in the gear drive house. However, such lapping is expensive in terms of time and is not sufficiently effective.

Figure 19.12.4: Area of meshing for a standard worm-gear drive with the ZA (Archimedes) worm ($\zeta = 0$).

The quality of gear drives of existing design depends substantially on the matching of the hob to the worm of the drive. The instantaneous contact of the worm and the worm-gear is a line contact. New trends toward localization of bearing contact have still neglected the area of worm-gear drives. Modification of the geometry of worm-gear drives is inevitable. The previous sections of this chapter cover the geometry of

Figure 19.12.5: Area of meshing for a non-standard worm-gear drive with the ZA (Archimedes) worm ($\zeta = 1$).

cylindrical worm-gear drives with instantaneous line contact of worms and worm-gears. The purpose of this section is to briefly describe perspectives on a new geometry.

Double Crowning of the Worm

The approach toward modification of the geometry of worm-gear drives with brighter prospects should be based on double crowning of the worm with respect to the hob. This means that the surfaces of the worm will be properly deviated from the surfaces of the hob. The basic principle of existing design is based on application of worms and hobs that are identical to each other.

The proposed modification of geometry achieved by double crowning of the worm is an extension of the approach that has been already developed for spiral bevel gears, hypoid gears, helical gears, and spur gears. Double crowning of the worm means that its surfaces are deviated in the *profile* and *longitudinal* directions, respectively, from the hob surface.

Profile crowning of the worm with respect to the hob is equivalent to application of two mismatched helicoids where one helicoid represents the worm of the drive and the other one is the hob that generates the gear. The surfaces of mismatched helicoids are in tangency along a common helix. The mismatch of helicoids is the precondition of localization of contact between the surfaces of the worm of the drive and the worm-gear.

It was mentioned above that longitudinal crowning of the worm has to be applied in addition to profile crowning. The purpose of longitudinal crowning is to reduce the shift of the bearing contact, avoid edge contact, and reduce transmission errors. All of these defects are caused by misalignments. Longitudinal crowning of the worm provides a parabolic function of transmission errors of the worm-gear drive in the process of meshing. Such a function is able to absorb discontinuous linear functions of transmission errors caused by misalignments.
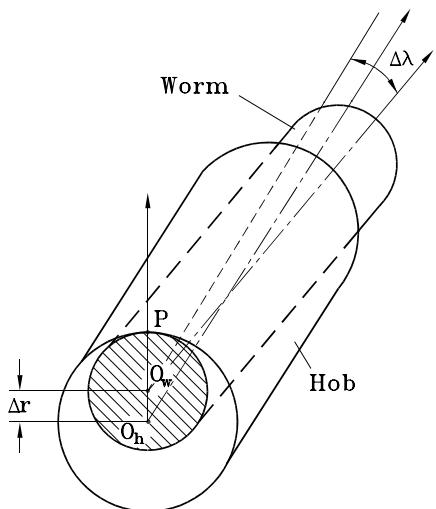
Double crowning of the worm as a combination of profile and longitudinal crowning is especially effective for worm-gear drives with multi-thread worms. Gear drives with multi-thread worms are more sensitive to misalignment that cause larger transmission errors and vibrations. These defects are reduced due to the effect of application of a parabolic function of transmission errors (see Sections 17.4, 17.6, and 17.7).

Application of Oversized Hob

Modification of the geometry of worm-gear drives has been based in the past on application of oversized hobs [Colbourne, 1989; Seol & Litvin, 1996]. The main idea of design of an oversized hob is based on the increase of the number of threads of the hob with respect to the worm of the worm-gear drive. This approach requires an increase in the pitch diameter of the hob.

We may illustrate the idea of application of an oversized hob considering the hob and the worm of the drive to be in internal meshing and their axes crossed (Fig. 19.13.1). The main features of meshing of the oversized hob with the worm are as follows:
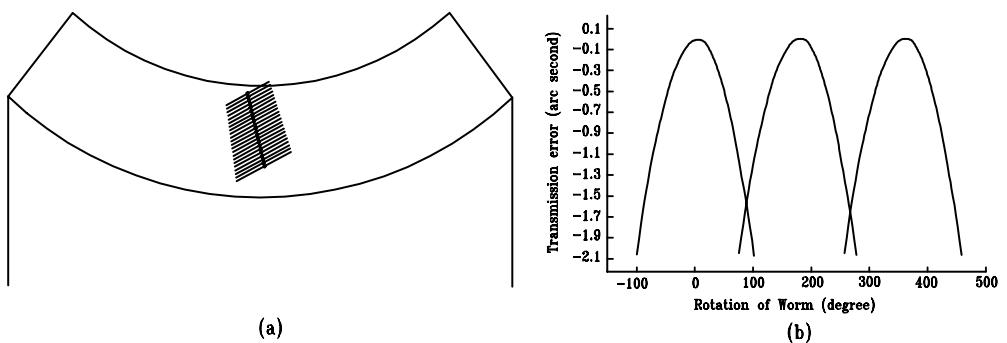
(i) The pitch cylinder of the hob is larger than the one of the worm, and $\Delta\lambda$ and Δr are the crossing angle and the shortest center distance between the axes (Fig. 19.13.1).

Figure 19.13.1: Tangency of pitch cylinders of worm and hob. $\Delta\lambda$ is the crossing angle of axes; Δr is the shortest center distance.

(ii) Point P of tangency of the hob and the worm pitch cylinders belongs to the shortest distance between the hob and the worm-gear, and to axes II–II of meshing (see Section 6.11). It is easy to verify that the normals to the surfaces of the hob, worm, and worm-gear pass through point "P" and that these surfaces are in simultaneous tangency in the beginning of meshing.

(iii) The hob is provided with the same type of thread surface as that of the worm.

(iv) It is obvious that the surfaces of the hob and the worm-gear being generated are in line contact at every instant, but surfaces of the worm and the worm-gear are in point contact at every instant.

(v) The chosen oversized Δr affects the magnitude of the major axis of the instantaneous contact ellipses and the level of transmission errors.

(vi) The generation of the worm-gear by an oversized hob must be accomplished with the following installation parameters

$$E_{hg} = E_{wg} + \Delta r, \qquad \gamma_{hg} = 90° - \Delta\gamma$$

Figure 19.13.2: Example of TCA for localization of contact obtained by an oversized hob: (a) path of contact; (b) function of transmission errors of parabolic type.

where E_{hg} and E_{wg} are the center distances between the hob and the worm-gear and between the worm and the worm-gear, respectively; $\Delta r = r_{ph} - r_{pw}$; r_{ph} and r_{pw} are the radii of pitch cylinders of the hob and the worm, respectively; $\Delta \gamma = \lambda_w - \lambda_h$; λ_w and λ_h are the lead angles of the worm and the hob, respectively.

For instance, in the case of an involute worm-gear drive the hob and the worm are two involute helicoids. In the case of K worm-gear drives (see Section 19.7), the hob and the worm are generated by a cone with the same profile angle.

Figure 19.13.2 shows the output of TCA for a K worm-gear drive wherein the worm-gear has been generated by an oversized hob [Seol & Litvin, 1996]. The path of contact is oriented across the worm-gear surface and is located around the center of the worm-gear surface [Fig. 19.13.2(a)]. The function of transmission errors is of a parabolic type [Fig. 19.13.2(b)].

For some cases of misalignment, an oversized hob that is too small fails to provide a continuous function of transmission errors. In the opinion of the authors of this book, localization of the bearing contact by double crowning of the worm is the approach with much greater potential.

20 Double-Enveloping Worm-Gear Drives

20.1 INTRODUCTION

The invention of the double-enveloping worm-gear drive is a breathtaking story with two dramatic characters, Friedrich Wilhelm Lorenz and Samuel I. Cone, each acting in distant parts of the world – one in Germany and the other in the United States [Litvin, 1998]. The double-enveloping worm-gear drive was invented by both Cone and Lorenz independently, and we have to credit them both for it [Litvin, 1998]. The invention of Samuel I. Cone in the United States has been applied by a company that bears the name of the inventor, known by the name Cone Drive.
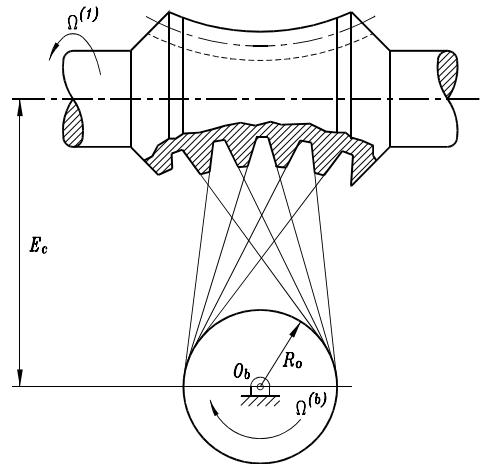
The invented gear drive is a significant achievement. The special shape of the worm increases the number of teeth that are simultaneously in mesh and improves the conditions of force transmission. The conditions of lubrication and the efficiency of the invented drive (in comparison with a worm-gear drive with a cylindrical worm) are substantially better due to the special shape of lines of contact between the worm and gear surfaces (see below).

The theory of double-enveloping worm-gear drives has been the subject of intensive research by many scientists. This chapter is based on the work by Litvin [1994]. We consider in this chapter the Cone double-enveloping worm-gear drive.

20.2 GENERATION OF WORM AND WORM-GEAR SURFACES

Worm Generation

The worm surface is generated by a straight-lined blade (Fig. 20.2.1). The blade performs rotational motion about axis O_b with the angular velocity $\Omega^{(b)} = d\Psi_b/dt$, while the worm rotates about its axis with the angular velocity $\Omega^{(1)} = d\Psi_1/dt$; ψ_b and ψ_1 are the angles of rotation of the blade and the worm in the process for generation (Fig. 20.2.2). The shortest distance between the axes of rotation of the blade and the worm is E_c. The generating lines of the blade in the process of generation keep the direction of tangents to the circle of radius R_o. The directions of rotation shown in Figs. 20.2.1 and 20.2.2 correspond to the case of generation of a right-hand worm.
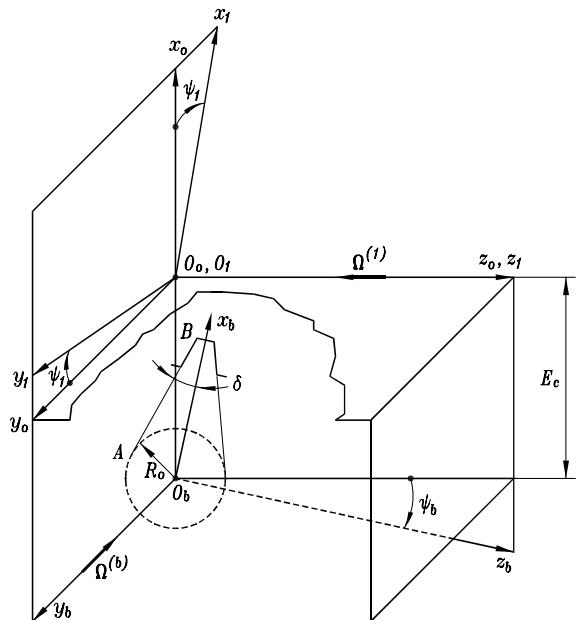
Figure 20.2.1: Worm generation.

Worm-Gear Generation
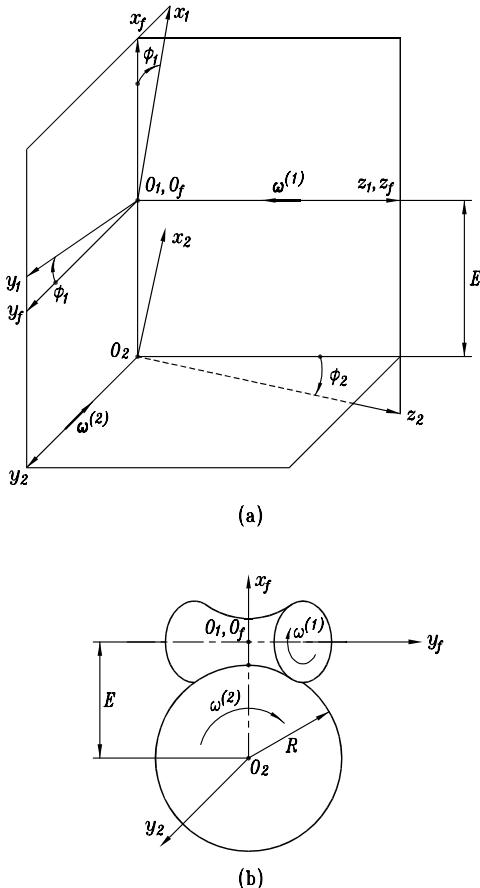
The generation of the worm-gear is based on simulation of meshing of the worm and the worm-gear in the process of worm-gear generation. A hob *identical* to the generated worm is in mesh with the worm-gear being generated on the cutting machine. The axes of rotation of the hob and the worm-gear are crossed; the shortest distance E between the axes is the same as in the designed worm-gear drive; the ratio m_{21} between the angular velocities of the hob (worm) and the worm-gear is also the same. Here,

$$m_{21} = \frac{\omega^{(2)}}{\omega^{(1)}} = \frac{N_1}{N_2} \tag{20.2.1}$$

where N_1 and N_2 are the numbers of worm threads and gear teeth.

Figure 20.2.2: Coordinate systems applied for worm generation.

Figure 20.2.3: Illustration of (a) applied coordinate systems S_1, S_2, and S_f; and (b) schematic of double-enveloping worm-gear drive.
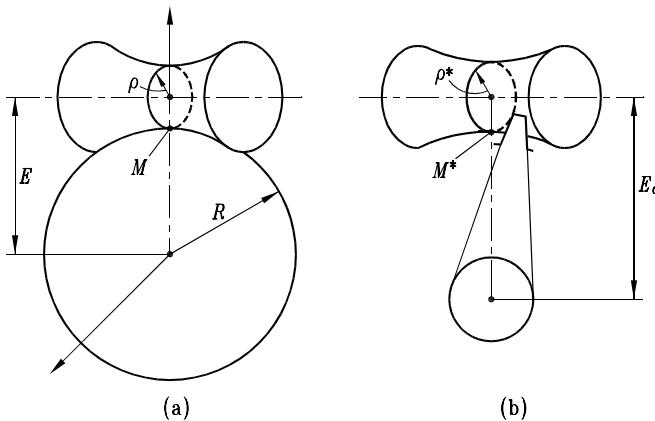
Applied Coordinate Systems

We limit the discussion to the case of an orthogonal worm-gear drive, with a crossing angle of $90°$. Moveable coordinate systems S_1 and S_2 are rigidly connected to the worm and the worm-gear, respectively (Fig. 20.2.3); S_f is a fixed coordinate system that is rigidly connected to the housing of the worm-gear drive. In the process of meshing the worm rotates about the z_1 axis, while the gear rotates about the y_2 axis.

Worm-Gear Surface

The analytical determination of the worm-gear surface Σ_2 is based on the following ideas:

(i) Consider that the worm (hob) surface Σ_1 is known.

(ii) Using the method of coordinate transformation, we can derive a family of surfaces Σ_1 that is represented in coordinate system S_2.

(iii) Surface Σ_2 is the envelope to the family of surfaces Σ_1. Obviously, Σ_1 and Σ_2 are in line contact at every instant.

Figure 20.2.4: Schematic of (a) unmodified and (b) modified gear drives.

Unmodified and Modified Gearing

The conjugation of surfaces Σ_1 and Σ_2 requires that the hob surface be the same as the worm surface. The principle of conjugation will not be infringed if the same values of m_{b1} and E_c are used for generation of the worm and the hob. Here,

$$m_{b1} = \frac{d\psi_b}{dt} \div \frac{d\psi_1}{dt} \tag{20.2.2}$$

is the cutting ratio. However, m_{b1} and E_c may differ from m_{21} and E given for the designed worm-gear drive.

Henceforth, we differentiate two types of gearing for double-enveloping worm-gear drives: (i) unmodified gearing when $m_{b1} = m_{21}$, and $E_c = E$; and (ii) modified gearing when $E_c \neq E$ ($E_c > E$). The cutting ratio m_{b1} for the modified gearing may be chosen to be equal to m_{21} or to differ from it. Surfaces Σ_1 and Σ_2 are conjugated in both cases, for unmodified and modified gearings, but there are some advantages when the modified gearing is used.

Consider that $E_c \neq E$ is chosen. The decision regarding how to choose m_{b1} will affect the radius ρ of the throat of the worm (hob) and other worm dimensions. The following discussion provides an explanation of this statement.

The unmodified and modified gearings are shown in Figs. 20.2.4(a) and 20.2.4(b), respectively. The gear ratio for an orthogonal drive satisfies the equation

$$m_{21} = \frac{\rho \tan \lambda}{E - \rho} = \frac{N_1}{N_2}. \tag{20.2.3}$$

The cutting ratio m_{b1} may be determined considering an imaginary worm-gear drive that is represented in Fig. 20.2.4(b); the blade for worm cutting is considered as the worm-gear tooth. Then, we obtain

$$m_{b1} = \frac{\rho^* \tan \lambda^*}{E_c - \rho^*}. \tag{20.2.4}$$

Here, λ and λ^* are the worm lead angles at M and M^*.

According to the existing practice of design, the lead angle at M is chosen to be the same for both designs. We consider as given N_1, N_2, E, ρ, and E_c. Our goal is to determine ρ^* and m_{b1}. Equations (20.2.3) and (20.2.4) with $\lambda^* = \lambda$ yield

$$\frac{m_{b1}(E_c - \rho^*)}{\rho^*} = \frac{N_1(E - \rho)}{\rho N_2}. \tag{20.2.5}$$

Equation (20.2.5) just relates parameters m_{b1} and ρ^*, and the solution for m_{b1} and ρ^* is not unique. We may consider the two following cases:

(i) The cutting ratio m_{b1} is chosen to be equal to m_{21}. Then, we obtain the following solution for ρ^*:

$$\rho^* = \frac{E_c}{E}\rho. \tag{20.2.6}$$

This means that the worm of the modified worm-gear drive will have an increased throat radius ρ^* and other dimensions in comparison with the worm of the un-modified drive. The axial diametral pitch of the modified worm is

$$P^* = \frac{\rho}{\rho^*}P. \tag{20.2.7}$$

(ii) The radius of the throat is chosen to be the same for both designs. Thus, $\rho^* = \rho$ and we obtain that

$$m_{b1} = \frac{N_1(E - \rho)}{N_2(E_c - \rho)} \tag{20.2.8}$$

$$P^* = P. \tag{20.2.9}$$

The dimensions of the worm are the same for both designs, but $m_{b1} \neq m_{21}$. There are other possible options for m_{b1} and ρ^* in addition to those discussed.

20.3 WORM SURFACE EQUATIONS
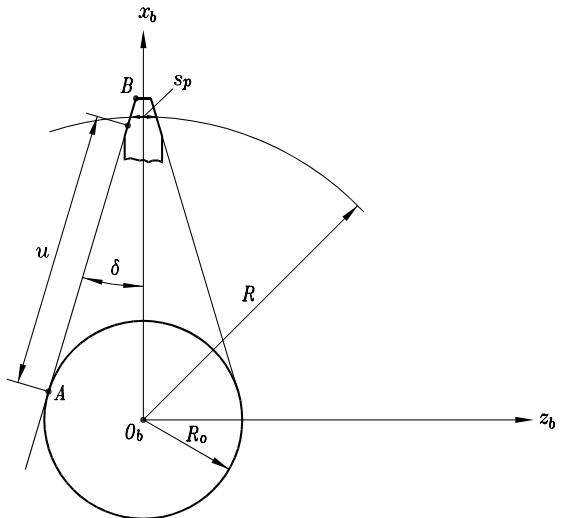
We set up three coordinate systems for derivation of the worm surface (Fig. 20.2.2); S_1 and S_b rigidly connected to the worm and the blade, respectively, and the fixed coordinate system S_0 rigidly connected to the machine for worm generation. The generating straight line AB is represented in S_b by the equations (Fig. 20.3.1)

$$x_b = u \cos \delta + R_o \sin \delta, \quad y_b = 0, \quad z_b = u \sin \delta - R_o \cos \delta \tag{20.3.1}$$

where the variable parameter u determines the location of a current point on the blade, and

$$\delta = \arcsin\left(\frac{R_o}{R}\right) - \frac{s_p}{2R}. \tag{20.3.2}$$

Here, R is the radius of the reference circle where the thickness of the blade is given.

Figure 20.3.1: Blade representation.

The worm surface Σ_1 is generated as the family of straight lines and is a *ruled* surface. We may derive the equations of the worm surface using Eqs. (20.3.1) and the coordinate transformation from S_b to S_1. Then we obtain

$$x_1 = \cos\psi_1[u\cos(\delta + \psi_b) + R_o\sin(\delta + \psi_b) - E_c]$$

$$y_1 = \sin\psi_1[u\cos(\delta + \psi_b) + R_o\sin(\delta + \psi_b) - E_c] \qquad (20.3.3)$$

$$z_1 = u\sin(\delta + \psi_b) - R_o\cos(\delta + \psi_b)$$

where $\psi_b = \psi_1 m_{b1}$.

The generalized parameter $\psi \equiv \psi_1$ and parameter u represent the surface coordinates (Gaussian coordinates). Equations (20.3.3) with the fixed value of ψ represent on Σ_1 the *u-coordinate line*, the generating straight line. Equations (20.3.3) with the fixed parameter u represent in Σ_1 the ψ-coordinate line, that is, a spatial curve. This curve can be obtained by intersection of Σ_1 by a torus. The axial section of the torus is the circle of radius $(u^2 + R_o^2)^{1/2}$. Equations (20.3.3) work for the modified and unmodified worms. For the case of the unmodified worm-gear drive, we have to take in these equations $E_c = E$, and $m_{b1} = m_{21}$.

The surface normal is represented by vector equation $\mathbf{N}_1 = \partial\mathbf{r}_1/\partial u \times \partial\mathbf{r}_1/\partial\psi$, which yields

$$N_{x1} = um_{b1}\sin\psi_1 - \sin(\delta + \psi_b)\cos\psi_1[u\cos(\delta + \psi_b) + R_o\sin(\delta + \psi_b) - E_c]$$

$$= um_{b1}\sin\psi_1 - x_1\sin(\delta + \psi_b)$$

$$N_{y1} = -um_{b1}\cos\psi_1 - \sin(\delta + \psi_b)\sin\psi_1[u\cos(\delta + \psi_b) + R_o\sin(\delta + \psi_b) - E_c]$$

$$= -um_{b1}\cos\psi_1 - y_1\sin(\delta + \psi_b)$$

$$N_{z1} = \cos(\delta + \psi_b)[u\cos(\delta + \psi_b) + R_o\sin(\delta + \psi_b) - E_c].$$

$$(20.3.4)$$

Surface (20.3.3) is an *undeveloped* one, because the surface normals along the generating line are not collinear (the orientation of the surface normal depends on u).

20.4 EQUATION OF MESHING

We consider the meshing of surfaces Σ_1 and Σ_2. Worm surface Σ_1 may be generated as unmodified or modified. The worm and the gear perform rotational motions about crossed axes as shown in Fig. 20.2.3. Surface Σ_2 is the envelope to the family of Σ_1 that is represented in S_2. The necessary condition of existence of an envelope (see Section 6.1) is represented by the equation of meshing,

$$\mathbf{N}_1 \cdot \mathbf{v}_1^{(12)} = f(u, \psi_1, \phi) = 0. \tag{20.4.1}$$

The subscript "1" shows that vectors $\mathbf{N}_1$ and $\mathbf{v}_1^{(12)}$ are represented in S_1. Vector $\mathbf{N}_1$ is the normal to Σ_1, and $\mathbf{v}_1^{(12)}$ is the sliding velocity that is determined in terms of constant parameters $\omega^{(1)}$, $\omega^{(2)}$, E, and m_{21}, and varied parameter $\phi \equiv \phi_1$, because $\mathbf{v}_1^{(12)}$ is represented in S_1 (see Section 2.1). Parameter ϕ is the generalized parameter of motion. We recall that angle ϕ_2 of rotation of worm-gear 2 is represented as

$$\phi_2 = m_{21}\phi_1. \tag{20.4.2}$$

Vector $\mathbf{N}_1$ is represented by Eqs. (20.3.4) in terms of varied surface parameters u and ψ_1 and constant parameters E_c and m_{b1}. The designation $f(u, \psi_1, \phi) = 0$ indicates the relation between the varied parameters. Using this relation, we are able to determine the lines of contact between Σ_1 and Σ_2 and represent the lines of contact in S_1, S_2, and S_f. The equation of meshing is derived for two cases: unmodified and modified gearing.

Unmodified Gearing

We take in Eqs. (20.3.4) for the worm surface normal that $m_{b1} = m_{21}$, and $E_c = E$. Using Eq. (20.4.1), after transformations, we obtain

$$\begin{aligned}
u^2 &[(1 - \cos\theta)\cos(\delta + \psi_b) + m_{21}\sin\theta\sin(\delta + \psi_b)] \\
&+ u\{R_o[(1 - \cos\theta)\sin(\delta + \psi_b) - m_{21}\sin\theta\cos(\delta + \psi_b)] \\
&- E(1 - \cos\theta)[1 + \cos^2(\delta + \psi_b)]\} \\
&+ E\cos(\delta + \psi_b)(1 - \cos\theta)[E - R_o\sin(\delta + \psi_b)] = 0
\end{aligned} \tag{20.4.3}$$

where $\theta = \psi_1 - \phi_1$. Equation (20.4.3) may be represented as

$$2\sin\frac{\theta}{2}(u^2 P + u Q + M) = 0 \tag{20.4.4}$$

where

$$P = \sin\frac{\theta}{2}\cos(\delta + \psi_b) + m_{21}\cos\frac{\theta}{2}\sin(\delta + \psi_b) \qquad (20.4.5)$$

$$Q = R_o\left[\sin\frac{\theta}{2}\sin(\delta + \psi_b) - m_{21}\cos\frac{\theta}{2}\cos(\delta + \psi_b)\right]$$
$$- E\sin\frac{\theta}{2}\left[1 + \cos^2(\delta + \psi_b)\right] \qquad (20.4.6)$$

$$M = E\sin\frac{\theta}{2}\cos(\delta + \psi_b)[E - R_o\sin(\delta + \psi_b)]. \qquad (20.4.7)$$

Equation (20.4.4) is satisfied if at least one of the two following conditions is observed:

(i)

$$\sin\frac{\theta}{2} = 0. \qquad (20.4.8)$$

(ii)

$$u^2 P + uQ + M = 0. \qquad (20.4.9)$$

This means that two types of contact lines may exist simultaneously on Σ_1: (i) a straight line (the generating line), and (ii) a spatial curve determined with Eq. (20.4.9). The existence on Σ_1 of a contact line that coincides with the generating line AB (Fig. 20.3.1) does not depend on the *shape* of the generating line. The contact line of type "i" will coincide with the generating line as well if the worm is generated by a *curved* blade. The existence of contact lines of type "ii" means that a part of surface Σ_2 is generated as the envelope to the family of surfaces Σ_1.

Modified Gearing

The derivation of the equation of meshing in this case is also based on Eq. (20.4.1), but it is assumed that the worm surface is generated with $E_c \neq E$. However, the cutting ratio m_{b1} may be equal to m_{21} or may differ from it. The performed derivations yield the following equation of meshing when $m_{b1} = m_{21}$:

$$u^2[(1 - \cos\theta)\cos(\delta + \psi_b) + m_{21}\sin\theta\sin(\delta + \psi_b)]$$
$$+ u\{R_o[(1 - \cos\theta)\sin(\delta + \psi_b) - m_{21}\sin\theta\cos(\delta + \psi_b)]$$
$$- E_c(1 - \cos\theta)[1 + \cos^2(\delta + \psi_b) - (E - E_c)\cos^2(\delta + \psi_b)]\}$$
$$+ \cos(\delta + \psi_b)(E - E_c\cos\theta)[E_c - R_o\sin(\delta + \psi_b)] = 0 \qquad (20.4.10)$$

where $\psi_b = m_{b1}\psi_1$. Taking in Eq. (20.4.10) $E = E_c$, we obtain equation of meshing (20.4.3) for the unmodified gearing.

20.5 CONTACT LINES

We consider the contact lines on worm surface Σ_1, on worm-gear surface Σ_2, and in the fixed coordinate system S_f, respectively.

Contact Lines on Σ_1

The contact lines on the worm surface Σ_1 are represented by the equations

$$\mathbf{r}_1 = \mathbf{r}_1(u, \psi_1), \quad f\left(u, \psi_1, \phi^{(i)}\right) = 0 \quad (i = 1, 2, \ldots, n). \tag{20.5.1}$$

Equations (20.5.1) represent the worm surface and the equation of meshing, and these equations are considered simultaneously. The designation $\phi^{(i)}$ $(i = 1, 2, \ldots, n)$ indicates that the generalized parameter ϕ is fixed-in when the instantaneous contact line is considered. Surface Σ_1 is in tangency with Σ_2 at every instant at two lines: one is the generating straight line, the other is the line of contact between surface Σ_1 and those parts of surface Σ_2 that are the envelope to the family of Σ_1.

Contact Lines on Σ_2

The contact lines on Σ_2 are represented by the equations

$$\mathbf{r}_2\left(u, \psi_1, \phi^{(i)}\right) = \mathbf{M}_{21}\mathbf{r}_1\left(u, \psi_1\right), \quad f\left(u, \psi_1, \phi^{(i)}\right) = 0 \quad (i = 1, 2, \ldots, n). \tag{20.5.2}$$

Matrix $\mathbf{M}_{21}$ describes the coordinate transformation from S_1 to S_2. Surface Σ_2 is represented by Eqs. (20.5.2) as the family of instantaneous contact lines. We may expect that Σ_2 is represented by two parts because two contact lines exist simultaneously at every instant. In reality, Σ_2 consists of three parts due to undercutting (see below).

Contact Lines on the Surface of Action
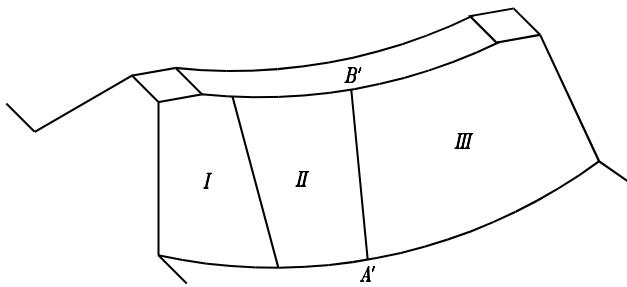
The totality of contact lines in coordinate system S_f represents the *surface of action*, which we designate by Σ_f. The surface of action is represented by the equations

$$\mathbf{r}_f(u, \psi_1, \phi) = \mathbf{M}_{f1}(\phi)\mathbf{r}_1(u, \psi_1), \quad f(u, \psi_1, \phi) = 0. \tag{20.5.3}$$

Matrix $\mathbf{M}_{f1}$ describes the coordinate transformation from S_1 to S_f.

20.6 WORM-GEAR SURFACE EQUATIONS

Using Eqs. (20.5.2), we may represent Σ_2 in terms of three varied but related parameters (u, ψ_1, ϕ). We consider the cases of unmodified and modified gearings separately.

Figure 20.6.1: Three parts of worm-gear surface.

Unmodified Gearing

Surface Σ_2 is represented by the equations
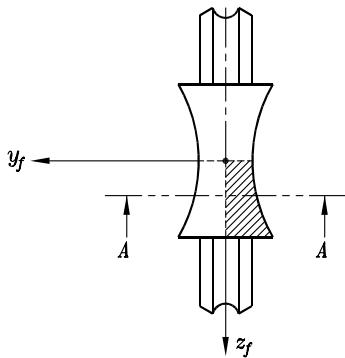
$$
\begin{aligned}
x_2 &= u[\cos\theta\cos(\delta+\psi_b)\cos\phi_2 + \sin(\delta+\psi_b)\sin\phi_2] \\
&\quad + R_o[\cos\theta\sin(\delta+\psi_b)\cos\phi_2 - \cos(\delta+\psi_b)\sin\phi_2] \\
&\quad - E(\cos\theta\cos\phi_2 - \cos\phi_2) \\
y_2 &= [u\cos(\delta+\psi_b) + R_o\sin(\delta+\psi_b) - E]\sin\theta \\
z_2 &= u[-\cos\theta\cos(\delta+\psi_b)\sin\phi_2 + \sin(\delta+\psi_b)\cos\phi_2] \\
&\quad - R_o[\cos\theta\sin(\delta+\psi_b)\sin\phi_2 + \cos(\delta+\psi_b)\cos\phi_2] \\
&\quad + E(\cos\theta\cos\phi_2 - \sin\phi_2) \\
\sin&\frac{\theta}{2}(u^2 P + uQ + M) = 0
\end{aligned}
\tag{20.6.1}
$$

where $\theta = \psi_1 - \phi_1$, and P, Q, and M are represented by Eqs. (20.4.5), (20.4.6), and (20.4.7), respectively.
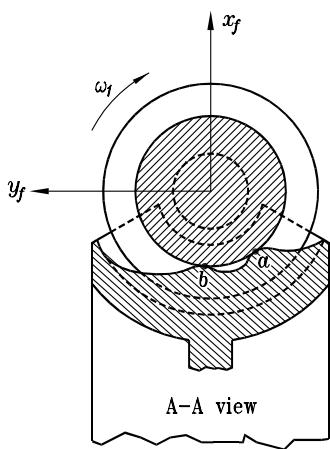
It was previously mentioned that there are two lines of contact between Σ_1 and Σ_2 at every instant. Taking in Eq. (20.6.1) $\sin(\theta/2) = 0$, we obtain that these equations represent in S_2 a straight line $\overline{A'B'}$ (Fig. 20.6.1) that lies in the middle plane of the worm-gear. This plane is determined with $y_2 = 0$. All of the straight lines that form Σ_1 coincide in turn with the *single straight line* $\overline{A'B'}$ on the worm-gear surface while the worm is in mesh with the worm-gear.

Taking in (20.6.1) $\sin(\theta/2) \neq 0$ and $u^2 P + uQ + M = 0$, we obtain the equations of that part of Σ_2 that is the envelope to the family of Σ_1. Unfortunately, this part of surface Σ_2 is partially undercut in the process for generation of Σ_2. The undercutting is performed by the edge of the hob. Considering the first three equations in equation system (20.6.1) and taking $\psi_b = -\delta$, $\psi_1 = m_{1b}\psi_b$, $\phi_1 = m_{12}\phi_2$, and $m_{1b} = m_{12}$, we represent the undercut part of the worm-gear tooth surface by the equations

$$
\begin{aligned}
x_2 &= (q\cos\tau + E)\cos\phi_2 - R_o\sin\phi_2 \\
y_2 &= q\sin\tau \\
z_2 &= -(q\cos\tau + E)\sin\phi_2 - R_o\cos\phi_2
\end{aligned}
\tag{20.6.2}
$$

Figure 20.6.2: For explanation of existence of two contact lines.
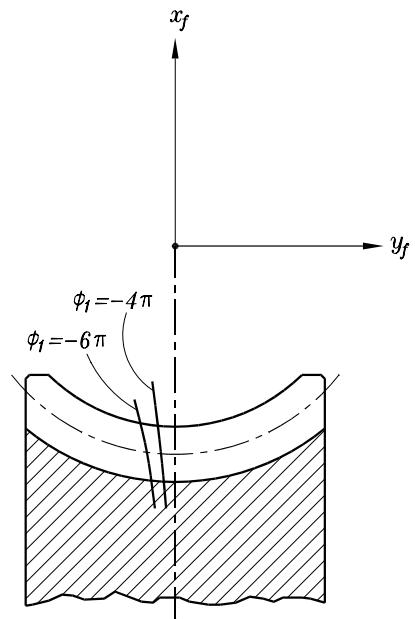
where

$$q = u - E, \qquad \tau = -m_{12}(\delta + \phi_2).$$

Equations (20.6.2) represent a ruled surface that is generated by the edge of the hob.

Figure 20.6.1 shows three parts of surface Σ_2. Part II is the envelope to the family of Σ_1. Parts I and III represent the ruled surface that is generated by the edge of the hob. Parts II and III of Σ_2 intersect each other along the straight line $A'B'$ that lies in plane $y_2 = 0$.

The disadvantage of unmodified gearing of the double-enveloping worm-gear drive is that surface Σ_2 is partially undercut. However, the presence of two contact lines that exist simultaneously is the advantage of this type of gearing. This statement is based on the following considerations: Let b be the point of contact line $A'B'$ (Fig. 20.6.2), and a the point of the other contact line. There is a closed space in coordinate system S_f whose section in Fig. 20.6.2 is a–b. While the worm is rotated in the direction shown in Fig. 20.6.2, the oil is pumped into space a–b, and the hydrodynamic pressure in the oil film is increased. We may expect that the best conditions of lubrication exist in the dashed quadrant. The other advantage of the unmodified gearing is the shape of instantaneous lines of contact (Fig. 20.6.3). Favorable conditions of lubrication with such a shape are
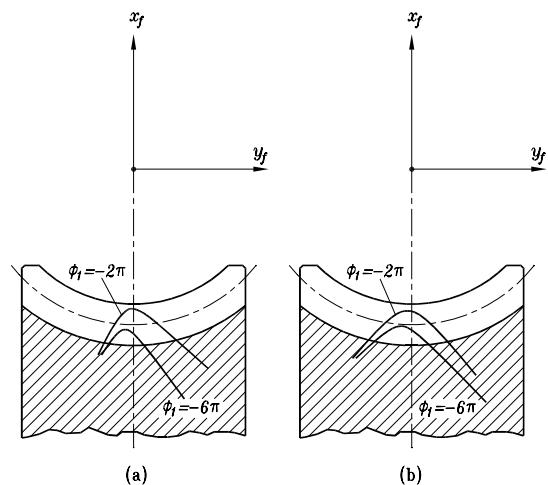
Figure 20.6.3: Contact lines of unmodified worm-gear drive.

provided because the linear velocity of the worm forms a small angle with the normal to the contact line.

Modified Gearing

The lines of contact shown in Fig. 20.6.3 have been determined for a worm-gear drive with the following parameters: module $m = 2.5$ mm $(m = 1/P)$; $N_1 = 1$; $N_2 = 47$; $\delta = 20°$; $E = 80$ mm. We may determine surface Σ_2 of the modified worm-gear with Eqs. (20.6.1), representing the equation of meshing by (20.4.10). The application of modified gearing enables us to avoid undercutting of Σ_2, but the shape of contact lines is less favorable (Fig. 20.6.4), at least when the worm is generated by a straight blade.

Figure 20.6.4: Contact lines of modified worm-gear drive with parameters: (a) $E_c = 85$ mm, $m_{b1} = 0.0196$; (b) $E_c = 90$ mm, $m_{b1} = 0.0182$.

We expect that new methods for generation of modified worm-gear drives will remove this obstacle.

The contact lines that are shown in Fig. 20.6.4 have been determined for worm-gear drives with the following parameters:

(a) module $m = 2.5$ mm ($m = 1/P$); $N_1 = 1$; $N_2 = 47$; $\delta = 20°$; $E = 80$ mm; $E_c = 85$ mm; $m_{b1} = 0.0196$.

(b) $E_c = 90$ mm; $m_{b1} = 0.0182$; other parameters are the same as in case (a).

21 Spiral Bevel Gears

21.1 INTRODUCTION

Spiral bevel gears have found broad application in helicopter and truck transmissions and reducers for transformation of rotation and torque between intersected axes. Design and stress analysis of such gear drives has been a topic of research by many scientists including the authors of this book [Krenzer, 1981; Handschuh & Litvin, 1991; Stadtfeld, 1993, 1995; Zhang *et al.*, 1995; Gosselin *et al.*, 1996; Litvin *et al.*, 1998a, 2002a; Argyris *et al.*, 2002; Fuentes *et al.*, 2002]. Reduction of noise and stabilization of bearing contact of misaligned spiral bevel gear drives are still very challenging topics of research although manufacturing companies [Gleason Works (USA), Klingelnberg–Oerlikon (Germany–Switzerland)] have developed skilled methods and outstanding equipment for manufacture of such gear drives.

The conditions of meshing and contact of spiral bevel gears depend substantially on the machine-tool settings applied. Such settings are not standardized but have to be determined for each case of design, depending on the parameters of the gears and generating tools, to guarantee the required quality of the gear drives. This chapter covers an integrated approach for the design and stress analysis of spiral bevel gears that has been developed by the authors of the book and their associates. The approach provides the solution to the following problems:

(1) Determination of machine-tool settings for generation of low-noise stable bearing contact spiral bevel gear drives.
(2) Computerized analysis of meshing and contact of gear tooth surfaces.
(3) Investigation of formation of bearing contact and determination of contact and bending stresses by application of the finite element method.

The procedures developed for items (2) and (3) above enable us to evaluate the quality of the design and to correct, if necessary, the applied machine-tool settings. These computerized procedures have to be performed before the expensive process of manufacturing. The solution to the problems previously enumerated is provided for two types of spiral bevel gear drives: (i) face-milled generated gear drives and (ii) formate-cut spiral bevel gear drives. Formate is a trademark of the Gleason Works, Rochester, N.Y.
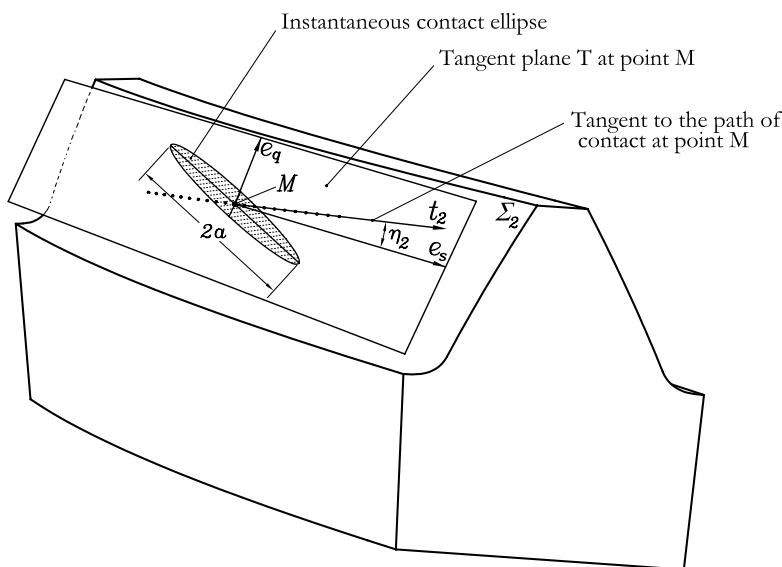
21.2 BASIC IDEAS OF THE DEVELOPED APPROACH

The basic ideas of the approach presented in this chapter are as follows:

(1) The gear machine-tool settings are considered as given (adapted, for instance, from the data of manufacturing). The to-be-determined pinion machine-tool settings have to meet the assigned conditions of meshing and contact of the gear drive. This is achieved by application of the procedure of local synthesis as follows:

   (a) Mean point M of tangency of pinion and gear tooth surfaces Σ_1 and Σ_2 is chosen on Σ_2. Then, respective pinion machine-tool settings are determined to provide that Σ_1 will be in tangency with Σ_2 at M.

   (b) The input parameters of local synthesis are a, η_2, and m'_{21} that are taken at the mean point M of tangency (Fig. 21.2.1). Here, $2a$ is the major axis of the instantaneous contact ellipse; η_2 determines the orientation of the tangent to the contact path at M; and $m'_{21} = d^2(\phi_2(\phi_1))/d\phi_1^2$ is the second derivative of the transmission function $\phi_2(\phi_1)$.

   The developed procedure of local synthesis provides a system of ten equations for determination of ten parameters of pinion machine-tool settings [Litvin, 1994; Litvin *et al.*, 1998a]. Observation of assigned parameter a is based on application of relations between the curvatures of contacting surfaces (see Chapter 8). Considering as known the gear and pinion machine-tool settings and the parameters of generating tools, it becomes possible to derive the equations of the pinion and gear tooth surfaces applying the theory of enveloping [Favard, 1957; Litvin, 1968; Zalgaller, 1975; Zalgaller & Litvin, 1977; Litvin, 1994].

(2) Low noise of the gear drive is achieved by application of a predesigned parabolic function of transmission errors of a limited value of maximal transmission errors,

Figure 21.2.1: Illustration of parameters η_2 and a applied for local synthesis.

of 6–8 arcsec (see Section 9.2). A predesigned parabolic function of transmission errors is able to absorb almost-linear discontinuous functions of transmission errors caused by errors of alignment. Such transmission errors are the source of high noise and vibration.

(3)   A longitudinal direction of the path of contact is considered in order to reduce contact and bending stresses and avoid edge contact.

(4)   Development and application of the tooth contact analysis (TCA) computer program enables us to simulate the meshing and contact of pinion–gear tooth surfaces Σ_1 and Σ_2. The algorithm of TCA is based on continuous tangency of Σ_1 and Σ_2 wherein Σ_1 and Σ_2 are in point contact (see Section 9.4). The algorithm of TCA requires solution of five nonlinear equations in six unknowns. One of the unknowns, say angle ϕ_1 of pinion rotation, is chosen as the input parameter, and the solution is obtained by five functions of ϕ_1. The procedure of computation for TCA is an iterative process based on application of the Newton–Raphson method [Visual Numerics, Inc., 1998].

The procedure of computations is based on simultaneous application of local synthesis, TCA, and finite element analysis (FEA) and is performed by application of the following four stages:

STAGE 1   Obtainment of a path of contact of the desired shape and direction. This stage is based on the following three steps:

   Step 1: The input parameter m'_{21} for local synthesis is applied as a variable parameter, whereas parameters a and η_2 are considered the assigned ones. Angle η_2 is the one that provides a longitudinally oriented path of contact. Then, we may obtain the pinion machine-tool settings by using the developed equations.
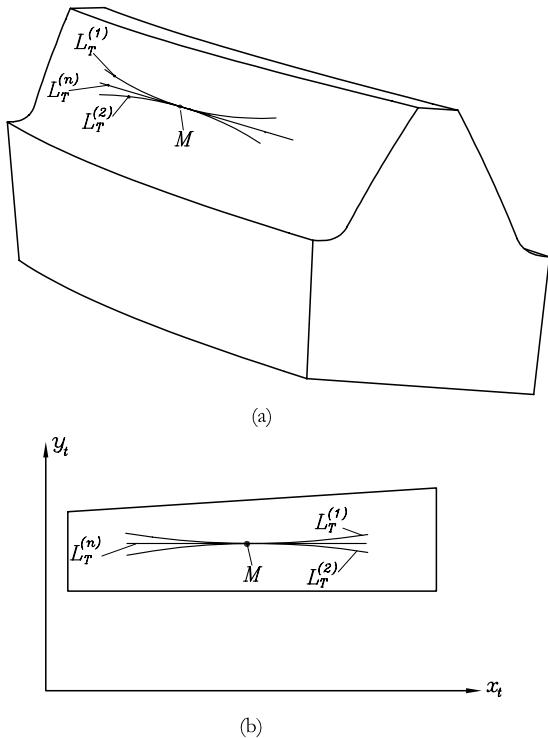
   Step 2: Using the pinion and gear machine-tool settings, the equations of the pinion and gear tooth surfaces are derived and the procedure of TCA is applied. The outputs of TCA are the bearing contact and the function of transmission errors.

   Step 3: By varying parameter m'_{21}, the shape of the path of contact is modified at each iteration until the desired shape of the path of contact is obtained.

Figure 21.2.2(a) shows paths of contact $L_T^{(1)}$, $L_T^{(2)}$, and $L_T^{(n)}$ that might be obtained as results of some iterations. We represent at this step the radial projection of the paths of contact on a coordinate system S_t wherein the axial coordinate and the radius of the points along the path of contact will be represented in axes x_t and y_t, respectively, as shown in Fig. 21.2.2(b). The goal of the iterative process is to obtain a radial projection of a straight-line shape as given by $L_T^{(n)}$ in Figure 21.2.2 for a longitudinally oriented path of contact. Using a subroutine of regression [Visual Numerics, Inc., 1998], we may represent $L_T^{(i)}$ in coordinate system S_t [Fig. 21.2.2(b)] as the following parabolic curve:

$$y_t(x_t, m'_{21}) = \beta_0(m'_{21}) + \beta_1(m'_{21})x_t + \beta_2(m'_{21})x_t^2. \tag{21.2.1}$$

The goal is accomplished by variation of m'_{21} in the process of iteration until β_2 becomes equal to zero. The solution of Eq. (21.2.1) for $\beta_2 = 0$ is obtained by application of the secant method [Press *et al.*, 1992] that is illustrated by Fig. 21.2.3. Designations $\beta_2^{(i)}$ ($i = 1, 2, 3, \ldots$) (Fig. 21.2.3) indicate the magnitude of β_2 obtained in the process of

Figure 21.2.2: (a) Representation of various paths of contact on gear tooth surface; (b) radial projection of paths of contact on coordinate system S_t.

(a)

(b)

iteration. The drawings show the change of function $\beta_2(m'_{21})^{(i)}$ by variation of $(m'_{21})^{(i)}$ ($i = 1, 2, 3, \ldots, n$), when parameter β_2 will become equal to zero.
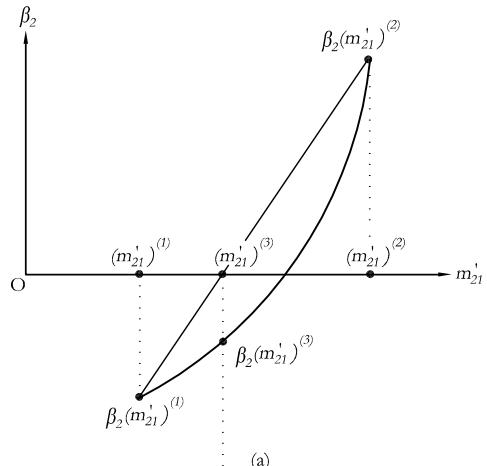
STAGE 2 Whereas Stage 1 enables us to obtain the desired shape L_T of the path of contact, the shape of the function of transmission errors $\Delta\phi_2^{(1)}(\phi_1)$ and the magnitude $\Delta\Phi$ of maximal transmission errors do not satisfy the requirements of design for a low-noise gear drive.

The goal of Stage 2 is to obtain a parabolic function of *negative* transmission errors and of a limited value $\Delta\Phi$ of maximal transmission errors. This goal is obtained by application of modified roll for pinion generation and application of the TCA computer program. We emphasize that the pinion machine-tool settings have already been obtained as a result of Stage 1. The application of modified roll does not imply either a change of machine-tool settings or a change in the shape of the path of contact. The algorithm of Stage 2 is as follows.
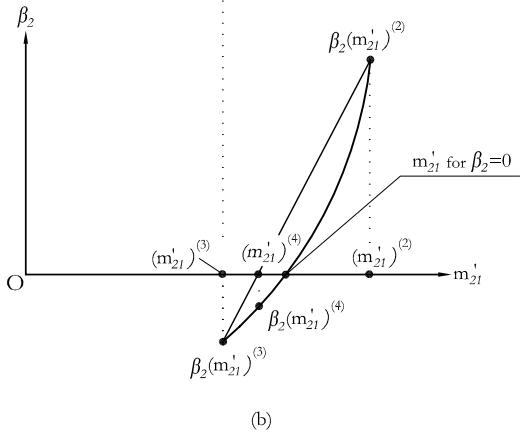
Step 1: Stage 1 enables us to obtain function $\Delta\phi_2^{(1)}(\phi_1)$ numerically. We represent $\Delta\phi_2^{(1)}(\phi_1)$ as a polynomial function up to the third member to be included [Visual Numerics, Inc., 1998]:

$$\Delta\phi_2^{(1)}(\phi_1) = a_0 + a_1\phi_1 + a_2\phi_1^2 + a_3\phi_1^3, \quad -\frac{\pi}{N_1} \leq \phi_1 \leq \frac{\pi}{N_1}. \quad (21.2.2)$$

Function (21.2.2) has to be transformed into a predesigned parabolic function of transmission errors with limited magnitude of maximal errors. The advantage of a parabolic

Figure 21.2.3: Schematic representation of computational procedure for determination of $\beta_2(m'_{21})$.

function of transmission errors is that such a function is able to absorb linear functions of transmission errors caused by errors of alignment and substantially reduce the level of noise [Litvin, 1989, 1994, 1998].

Step 2: Transformation of function $\Delta\phi_2^{(1)}(\phi_1)$ is accomplished by application of modified roll for pinion generation. Modified roll means that the following function is executed for pinion generation:

$$\psi_1(\psi_{c1}) = m_{1c}\psi_{c1} - b_2\psi_{c1}^2 - b_3\psi_{c1}^3. \tag{21.2.3}$$
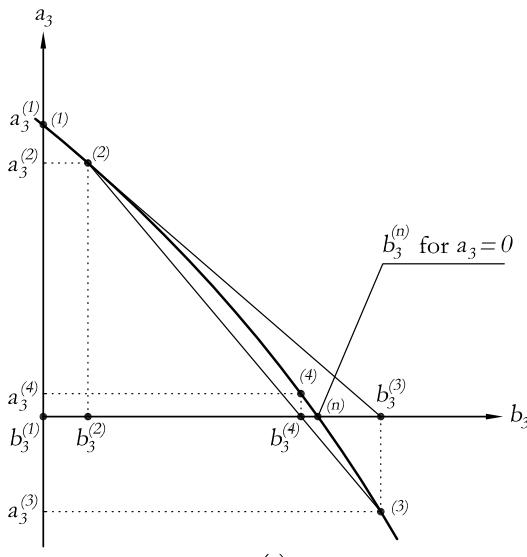
Here, ψ_1 is the angle of pinion rotation during its generation; ψ_{c1} is the angle of rotation of the so-called cradle of the cutting machine (see Section 21.3 and Fig. 21.4.1); and m_{1c} is the first derivative of function $\psi_1(\psi_{c1})$ taken at $\psi_{c1} = 0$ (for mean contact point M) and is obtained by the procedure of local synthesis [Litvin *et al.*, 1998a]. The head-cutter for pinion generation is mounted on the cradle and performs rotation with the cradle (see Section 21.3).

Transformation of function $\Delta\phi_2^{(1)}(\phi_1)$ into $\Delta\phi_2(\phi_1)$ is obtained by variation of coefficients b_2 and b_3 of function (21.2.3). Here,
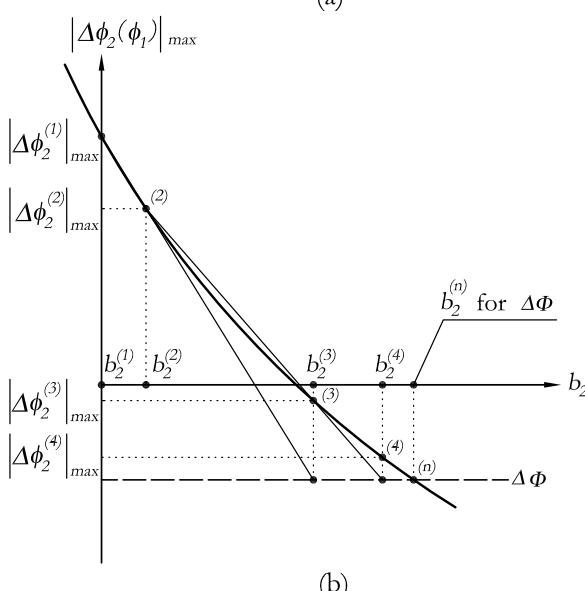
$$\Delta\phi_2(\phi_1) = -a_2\phi_1^2, \quad -\frac{\pi}{N_1} \le \phi_1 \le \frac{\pi}{N_1} \tag{21.2.4}$$

$$|\Delta\phi_2(\phi_1)|_{\max} = a_2\left(\frac{\pi}{N_1}\right)^2 = \Delta\Phi. \tag{21.2.5}$$

The variation of b_2 and b_3 is performed independently and is illustrated by Fig. 21.2.4. Figure 21.2.4(a) illustrates variation of coefficient b_3 of modified roll, used to obtain

(a)

(b)

Figure 21.2.4: Schematic representation of computational procedure for determination of coefficients b_2 and b_3 of modified roll.

coefficient $a_3 = 0$ in function (21.2.2). Function $a_3(b_3)$ is determined from the output of TCA by variation of modified roll. Figure 21.2.4(b) illustrates variation of coefficient b_2 of modified roll, used to obtain a parabolic function of transmission errors of an assigned value of $\Delta\Phi$ determined by Eq. (21.2.5).

STAGE 3. The purpose of Stage 3 is the selection of an optimal parabola coefficient for the parabolic profile of the blades that will generate the gear tooth surfaces to avoid the appearance of hidden areas of severe contact for high loaded spiral bevel gear drives. In the first iteration, a straight-line profile for the blades will be considered (parabola coefficient equal to zero). For further iterations, and based on the results obtained from the investigation of formation of bearing contact (Stage 4), a larger parabola coefficient is chosen until those areas of severe contact stresses are avoided and contact stresses are reduced all over the path of contact (see Section 21.9).

We recall that Stages 1 and 2 are performed by simultaneous application of computerized algorithms of local synthesis and tooth contact analysis (TCA). The bearing contact on the gear tooth surface is designed to be directed longitudinally by the proper selection of η_2 (Fig. 21.2.1) which determines the orientation of the tangent to the path of contact at M, controlling the shape of the radial projection of L_T (Fig. 21.2.2).

STAGE 4. The purposes of Stage 4 are investigation of formation of bearing contact and determination of contact and bending stresses for more than one cycle of meshing. The goals are obtained by application of the finite element method by a commercial finite element analysis computer program [Hibbit, Karlsson & Sirensen, Inc., 1998].
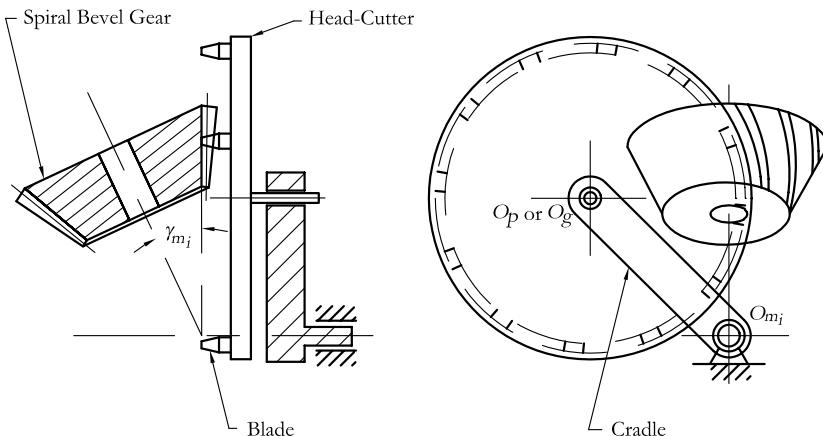
Investigation of formation of bearing contact enables us to discover hidden areas of severe contact due to the elastic deformation of the gear teeth. Such a contact may be discovered if finite element models of several pairs of teeth are developed and analyzed in contact positions corresponding to more than one cycle of meshing. Such contact positions are obtained by application of a TCA computer program.

Hidden areas of severe contact are accompanied with a substantial increase of contact stresses (see Section 21.9). Those areas of severe contact might be avoided by increasing the mismatch of generating surfaces. We could achieve this goal by application of a combination of straight-line profile blades and parabolic profile blades of the pair of head-cutters that generate the pinion and the gear, respectively (see Section 21.9). However, in some cases (for instance, of gear drives of a gear ratio close to 1), parabolic blades have to be applied either for the pinion or the gear. Parabolic blades are also applied for the generation of the formate-cut gear for better conditions of conjugation of gear tooth surfaces (see Section 21.3).

21.3 DERIVATION OF GEAR TOOTH SURFACES

Introduction

We recall that two approaches to the design of spiral bevel gears are considered wherein generated and formate-cut gear tooth surfaces are applied. Figure 21.3.1 shows schematically the generation of a spiral bevel gear as the envelope to the family of head-cutter
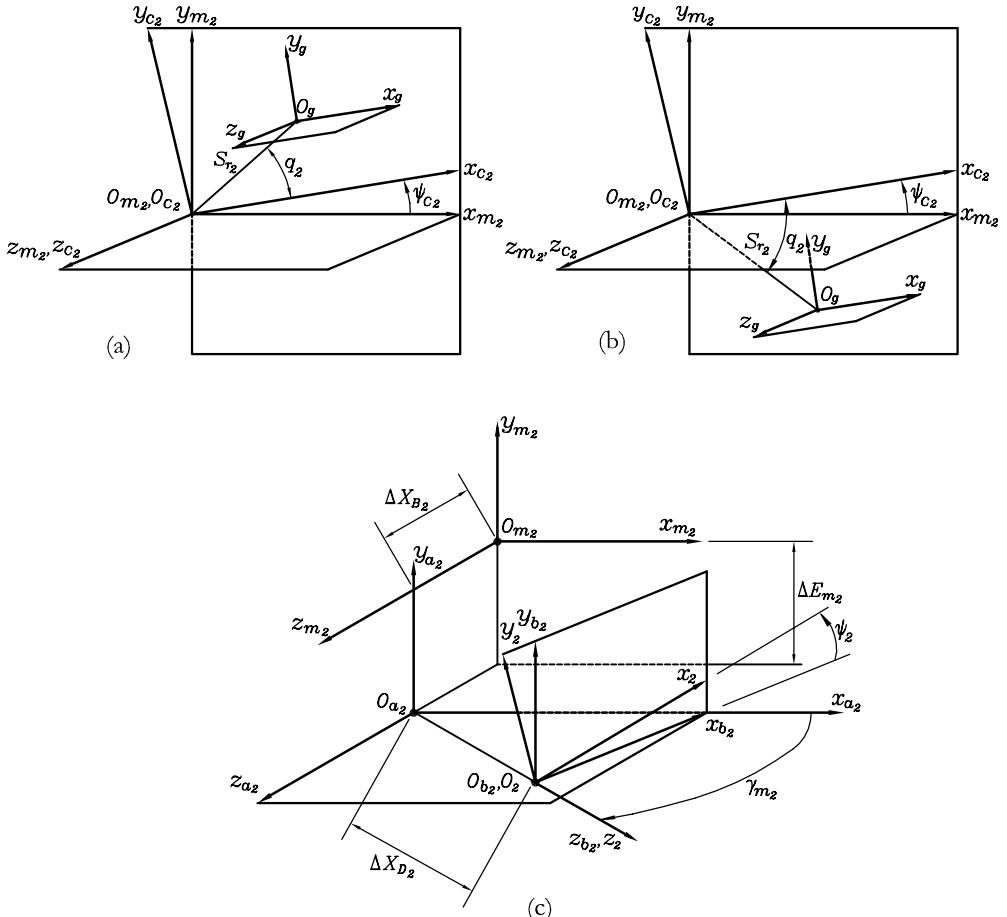
Figure 21.3.1: Schematic representation of generation of a spiral bevel gear.

surfaces. The head-cutter is mounted on the cradle and performs a planetary motion: (i) rotation in transfer motion (with the cradle) about the cradle axis, and (ii) rotation in relative motion (relative to the cradle) about the head-cutter axis. The spiral bevel gear (pinion) to be generated is installed with angle γ_{m_i} with respect to the head-cutter and rotates about the gear (pinion) axis. Angle γ_{m_i} is called the machine root angle and represents a setting for the gear to be generated. Rotation of the cradle and the gear are related. The angular velocity of rotation of the head-cutter about its axis is not related to the process of generation and is chosen to provide the desired velocity of cutting. Henceforth, we consider that the head-cutter is provided with generating surfaces formed by the blades when they are rotated about the head-cutter axis. Each space of the gear or pinion is generated separately. The process of generation is interrupted after generation of the current space is finished; then the workspace is indexed to the next space, and the process of generation is repeated.

In the case of generation of a formate-cut gear, the cradle is held at rest. The head-cutter that is installed on the cradle is rotated about its axis with the desired velocity of cutting and generates the gear tooth surface as the copy of the surface of the head-cutter. During generation of the formate-cut gear, the gear does not perform any rotation either about its own axis or related to the cradle.

Applied Coordinate Systems

Coordinate systems S_{m_2}, S_{a_2}, and S_{b_2} are the fixed ones and they are rigidly connected to the cutting machine (Fig. 21.3.2). The movable coordinate systems are S_2 and S_{c_2} that are rigidly connected to the gear and the cradle, respectively. Coordinate system S_g is rigidly connected to the gear head-cutter. It is considered that the head-cutter is a cone or a surface of revolution, and the rotation of the head-cutter about the z_g axis does not affect the process of generation. The head-cutter is mounted on the cradle, and coordinate system S_g is rigidly connected to the cradle coordinate system S_{c_2}. The cradle and the gear perform related rotations about the z_{m_2} axis and the z_{b_2} axis, respectively, for the case of a generated spiral bevel gear. Angles ψ_{c_2} and ψ_2 are related
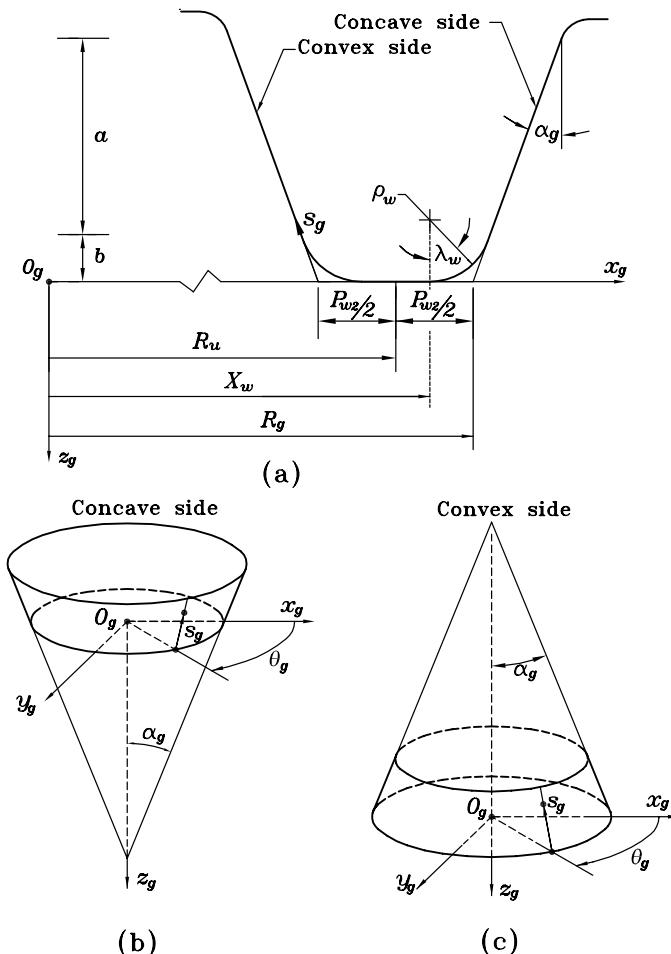
Figure 21.3.2: Coordinate systems applied for gear generation: (a) and (b) illustration of tool installment for generation of right- and left-hand gears; (c) illustration of installment of machine-tool settings.

and represent the current angles of rotation of the cradle and the gear. The ratio of gear roll is designated as m_{2c_2} and is determined as

$$m_{2c_2} = \frac{\omega^{(2)}}{\omega^{(c_2)}} = \frac{d\psi_2}{dt} \div \frac{d\psi_{c_2}}{dt}. \tag{21.3.1}$$

Equation (21.3.1) is not applied for the case of a formate-cut spiral bevel gear because there is no rotation of the gear or the cradle during generation.

The installment of the tool on the cradle is determined by parameters S_{r_2} and q_2, which are called the radial distance and the basic cradle angle. The installments of the head-cutter on the cradle for generation of right-hand and left-hand gears are shown in Figs. 21.3.2(a) and 21.3.2(b), respectively. Parameters ΔX_{B_2}, ΔE_{m_2}, ΔX_{D_2}, and γ_{m_2} represent the settings of a generated spiral bevel gear [Fig. 21.3.2(c)].

Figure 21.3.3: Blade and generating cones for gear straight-line head-cutter: (a) illustration of straight-line profile of the blade; (b) and (c) generating tool cones for concave and convex sides.

Head-Cutter Surfaces

The blades of a head-cutter with straight-line profiles are shown in Fig. 21.3.3(a). Each side of the blade generates two sub-surfaces. The segment of the straight line with the profile angle α_g generates the working part of the gear tooth surface. The circular arc of radius ρ_w generates the fillet of the gear tooth surface. The generating surfaces of the head-cutter are formed by rotation of the blade about the z_g axis of the head-cutter; the rotation angle is θ_g. Therefore, the generating surfaces are the conical surface and the surface of the torus formed by the arc. A point on the generating surface is determined by parameters s_g and θ_g for the conical surface, and by λ_w and θ_g for the surface of the torus. Parameter s_g is considered as a positive value and angles α_g and λ_w as the acute ones. In the case of grinding, the profiles shown in Fig. 21.3.3(a) are the axial profiles of the grinder that is applied instead of a head-cutter.

The conical surface and the torus surface of the head-cutter are designed as parts (a) and (b) of the head-cutter generating surfaces. Surface $\Sigma_g^{(a)}$ of the head-cutter is

represented by vector function $r_g^{(a)}(s_g, \theta_g)$ as

$$r_g^{(a)}(s_g, \theta_g) = \begin{bmatrix} (R_g \pm s_g \sin \alpha_g) \cos \theta_g \\ (R_g \pm s_g \sin \alpha_g) \sin \theta_g \\ -s_g \cos \alpha_g \end{bmatrix} \qquad (21.3.2)$$

where s_g and θ_g are the surface coordinates, α_g is the blade angle, and R_g is the cutter point radius. The upper and lower signs in Eqs. (21.3.2) correspond to generation of the concave and convex sides of the gear tooth surface, respectively.

The unit normal to the gear generating surface $\Sigma_g^{(a)}$ is represented by the equations

$$n_g^{(a)}(\theta_g) = \frac{N_g}{|N_g|}, \quad N_g = \frac{\partial r_g^{(a)}}{\partial s_g} \times \frac{\partial r_g^{(a)}}{\partial \theta_g}. \qquad (21.3.3)$$

Equations (21.3.2) and (21.3.3) yield

$$n_g^{(a)}(\theta_g) = \begin{bmatrix} \cos \alpha_g \cos \theta_g \\ \cos \alpha_g \sin \theta_g \\ \pm \sin \alpha_g \end{bmatrix}. \qquad (21.3.4)$$

Surface $\Sigma_g^{(b)}$ is represented in S_g as

$$r_g^{(b)}(\lambda_w, \theta_g) = \begin{bmatrix} (X_w \pm \rho_w \sin \lambda_w) \cos \theta_g \\ (X_w \pm \rho_w \sin \lambda_w) \sin \theta_g \\ -\rho_w(1 - \cos \lambda_w) \end{bmatrix}, \quad 0 \le \lambda_w \le \frac{\pi}{2} - \alpha_g \qquad (21.3.5)$$

where

$$X_w = R_g \mp \rho_w(1 - \sin \alpha_g)/\cos \alpha_g.$$
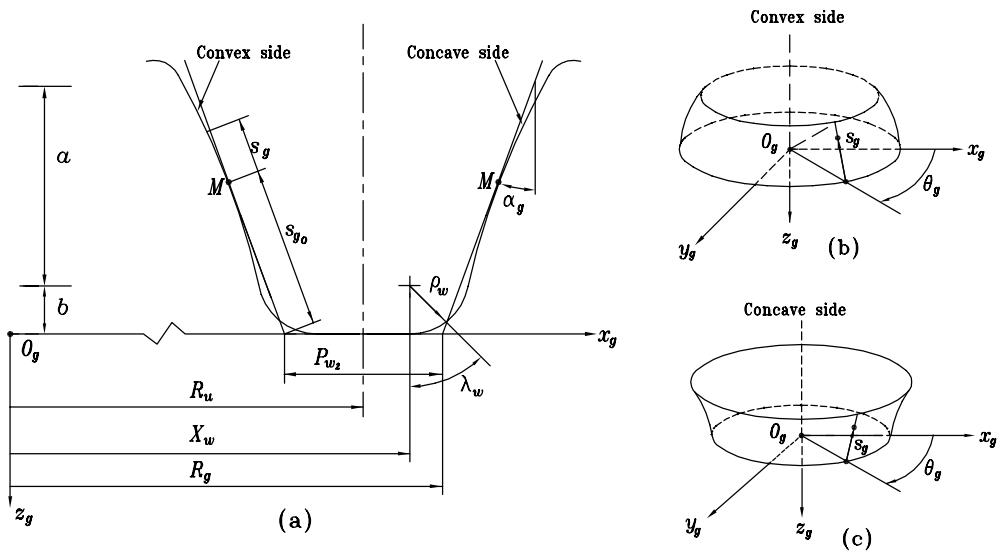
Here, ρ_w is the edge radius of the head-cutter for the gear. The cutter point radius R_g (Fig. 21.3.3) is determined for the generating tool cones for the concave and convex sides of the gear tooth surfaces, respectively, as

$$R_g = R_u \pm \frac{P_{w2}}{2}$$

where R_u is the cutter mean radius and P_{w2} is the cutter point width.

The unit normal to the gear generating surface $\Sigma_g^{(b)}$ is represented by the equations

$$n_g^{(b)}(\theta_g) = \frac{N_g^{(b)}}{|N_g^{(b)}|}, \quad N_g = \frac{\partial r_g^{(b)}}{\partial \lambda_w} \times \frac{\partial r_g^{(b)}}{\partial \theta_g}. \qquad (21.3.6)$$

Figure 21.3.4: Blade and generating revolution surfaces for the gear parabolic-profile head-cutter: (a) illustration of parabolic profile of the blade; (b) and (c) generating tool surfaces for concave and convex sides.

Equations (21.3.6) yield

$$n_g^{(b)}(\theta_g) = \begin{bmatrix} \sin \lambda_w \cos \theta_g \\ \sin \lambda_w \sin \theta_g \\ \pm \cos \lambda_w \end{bmatrix}. \tag{21.3.7}$$

We recall that hidden areas of severe contact between contacting surfaces of the pinion and the gear can be avoided by using blades of parabolic profile. Figure 21.3.4(a) shows the blades of a head-cutter with parabolic profile. The segment (a) of the parabolic profile generates the working part of the gear tooth surface. The circular arc of radius ρ_w generates the fillet of the gear tooth surface. The generating surfaces of the parabolic-profile head-cutter are formed by rotation of the blade about the z_g axis of the head-cutter [Figs. 21.3.4(b) and 21.3.4(c)]; the rotation angle is θ_g. Therefore, the generating surfaces are (i) the surface of revolution formed by rotation of the blade of parabolic profile (part a), and (ii) the surface of the torus formed by rotation of the circular arc profiles (part b). A point on the generating surface is determined by parameters s_g and θ_g for the working surface and by λ_w and θ_g for the fillet surface. Angle α_g is formed between the tangent line of the blade at point M and the vertical center line of the blade. Parameter s_g measured from point M in the chosen direction is considered as a positive one and angles α_g and λ_w as the acute ones. The apex of the parabola is located at point M determined by parameter s_{g_o}, called the parabola vertex location parameter. We recall that in the case of grinding, the profiles shown in Fig. 21.3.4(a) represent the axial profiles of the grinder.

The surface of revolution and the torus surface of the head-cutter are designated as parts (a) and (b) of the head-cutter generating surface. Surface $\Sigma_g^{(a)}$ of the head-cutter is represented by vector function $\mathbf{r}_g^{(a)}(s_g, \theta_g)$ as

$$\mathbf{r}_g^{(a)}(s_g, \theta_g) = \begin{bmatrix} \left(R_g \pm (s_g + s_{g_o}) \sin \alpha_g \pm a_c s_g^2 \cos \alpha_g\right) \cos \theta_g \\ \left(R_g \pm (s_g + s_{g_o}) \sin \alpha_g \pm a_c s_g^2 \cos \alpha_g\right) \sin \theta_g \\ -(s_g + s_{g_o}) \cos \alpha_g + a_c s_g^2 \sin \alpha_g \end{bmatrix} \qquad (21.3.8)$$

where s_g and θ_g are the surface coordinates, α_g is the blade angle at point M, a_c is the parabola coefficient, and R_g is the cutter point radius (Fig. 21.3.4) that is given by

$$R_g = R_u \pm \frac{P_{w_2}}{2}. \qquad (21.3.9)$$

The upper and lower signs in Eqs. (21.3.8) and (21.3.9) correspond to the concave and convex sides of the gear tooth surfaces, respectively.

The unit normal to the gear generating surface $\Sigma_g^{(a)}$ is represented by the equations

$$\mathbf{n}_g^{(a)}(s_g, \theta_g) = \frac{\mathbf{N}_g^{(a)}}{|\mathbf{N}_g^{(a)}|}, \quad \mathbf{N}_g^{(a)} = \frac{\partial \mathbf{r}_g^{(a)}}{\partial s_g} \times \frac{\partial \mathbf{r}_g^{(a)}}{\partial \theta_g}. \qquad (21.3.10)$$

Equations (21.3.8) and (21.3.10) yield

$$\mathbf{n}_g^{(a)}(s_g, \theta_g) = \begin{bmatrix} (\cos \alpha_g - 2a_c s_g \sin \alpha_g) \cos \theta_g \\ (\cos \alpha_g - 2a_c s_g \sin \alpha_g) \sin \theta_g \\ \pm \sin \alpha_g \pm 2a_c s_g \cos \alpha_g \end{bmatrix} \div \sqrt{1 + 4a_c^2 s_g^2}. \qquad (21.3.11)$$
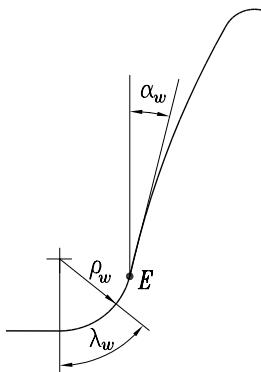
Surface $\Sigma_g^{(b)}$ is represented in S_g as

$$\mathbf{r}_g^{(b)}(\lambda_w, \theta_g) = \begin{bmatrix} (X_w \pm \rho_w \sin \lambda_w) \cos \theta_g \\ (X_w \pm \rho_w \sin \lambda_w) \sin \theta_g \\ -\rho_w(1 - \cos \lambda_w) \end{bmatrix}, \quad 0 \leq \lambda_w \leq \frac{\pi}{2} - \alpha_w \qquad (21.3.12)$$

where angle α_w is the pressure angle of the blade parabolic profile at the point E of connection with the circular arc profile of the fillet of radius ρ_w (see Fig. 21.3.5). Parameters X_w and α_w (Figs. 21.3.4 and 21.3.5) depend on the parabola coefficient and have to be determined numerically to guarantee the tangency of the circular arc of radius ρ_w with a parabola of coefficient a_c. The unit normal to the gear generating surface $\Sigma_g^{(b)}$ is determined by Eq. (21.3.6) and represented by Eq. (21.3.7).

Equations of the Generated Gear Tooth Surface

The derivation of the equations of the generated gear tooth surface is based on application of two equations that have to be considered simultaneously: (i) the equation of the family of head-cutter surfaces represented in coordinate system S_2, and (ii) the equation of meshing. Such equations have to be derived for surfaces $\Sigma_2^{(a)}$ and $\Sigma_2^{(b)}$ that represent the working part of the tooth surface and the fillet.

Figure 21.3.5: Illustration of pressure angle α_w of parabolic profile at point E of connection with the circular arc profile of the fillet.

Then, the surface $\Sigma_2^{(a)}$ will be represented as follows:

$$\mathbf{r}_2^{(a)}(s_g, \theta_g, \psi_2) = \mathbf{M}_{2g}(\psi_2)\mathbf{r}_g^{(a)}(s_g, \theta_g) \tag{21.3.13}$$

$$\left(\frac{\partial \mathbf{r}_2^{(a)}}{\partial s_g} \times \frac{\partial \mathbf{r}_2^{(a)}}{\partial \theta_g}\right) \cdot \frac{\partial \mathbf{r}_2^{(a)}}{\partial \psi_2} = f_{2g}^{(a)}(s_g, \theta_g, \psi_2) = 0. \tag{21.3.14}$$

Here, ψ_2 is the generalized parameter of motion; matrix $\mathbf{M}_{2g}$ represents the coordinate transformation from S_g to S_2 (Fig. 21.3.2) and is given by

$$\mathbf{M}_{2g}(\psi_2) = \mathbf{M}_{2b_2}\mathbf{M}_{b_2a_2}\mathbf{M}_{a_2m_2}\mathbf{M}_{m_2c_2}\mathbf{M}_{c_2g} \tag{21.3.15}$$

where

$$\mathbf{M}_{c_2g} = \begin{bmatrix} 1 & 0 & 0 & S_{r_2}\cos q_2 \\ 0 & 1 & 0 & S_{r_2}\sin q_2 \\ 0 & 0 & 1 & 0 \\ 0 & 0 & 0 & 1 \end{bmatrix}$$

$$\mathbf{M}_{m_2c_2} = \begin{bmatrix} \cos\psi_{c_2} & -\sin\psi_{c_2} & 0 & 0 \\ \sin\psi_{c_2} & \cos\psi_{c_2} & 0 & 0 \\ 0 & 0 & 1 & 0 \\ 0 & 0 & 0 & 1 \end{bmatrix}$$

$$\mathbf{M}_{a_2m_2} = \begin{bmatrix} 1 & 0 & 0 & 0 \\ 0 & 1 & 0 & \Delta E_{m_2} \\ 0 & 0 & 1 & -\Delta X_{B_2} \\ 0 & 0 & 0 & 1 \end{bmatrix}$$

$$\mathbf{M}_{b_2 a_2} = \begin{bmatrix} \sin \gamma_{m_2} & 0 & -\cos \gamma_{m_2} & 0 \\ 0 & 1 & 0 & 0 \\ \cos \gamma_{m_2} & 0 & \sin \gamma_{m_2} & -\Delta X_{D_2} \\ 0 & 0 & 0 & 1 \end{bmatrix}$$

$$\mathbf{M}_{2b_2} = \begin{bmatrix} \cos \psi_2 & \sin \psi_2 & 0 & 0 \\ -\sin \psi_2 & \cos \psi_2 & 0 & 0 \\ 0 & 0 & 1 & 0 \\ 0 & 0 & 0 & 1 \end{bmatrix}.$$

An alternative approach for the derivation of the equation of meshing (21.3.14) is given in Section 6.1 as

$$\mathbf{n}_g^{(a)} \cdot \mathbf{v}^{(g2)} = f_g^{(a)}(s_g, \theta_g, \psi_2) = 0. \tag{21.3.16}$$

Surface $\Sigma_2^{(a)}$ is represented in three-parameter form. Simultaneous consideration of equations (21.3.13) and (21.3.14) or (21.3.13) and (21.3.16) enables us to represent $\Sigma_2^{(a)}$ in two-parameter form as

$$\mathbf{R}_2^{(a)}(\theta_g, \psi_2) = \mathbf{r}_2^{(a)}(s_g(\theta_g, \psi_2), \theta_g, \psi_2). \tag{21.3.17}$$

Similar considerations for $\Sigma_2^{(b)}$ enable us to obtain

$$\mathbf{r}_2^{(b)}(\lambda_w, \theta_g, \psi_2) = \mathbf{M}_{2g}(\psi_2)\, \mathbf{r}_g^{(b)}(\lambda_w, \theta_g) \tag{21.3.18}$$

$$\left(\frac{\partial \mathbf{r}_2^{(b)}}{\partial \lambda_w} \times \frac{\partial \mathbf{r}_2^{(b)}}{\partial \theta_g} \right) \cdot \frac{\partial \mathbf{r}_2^{(b)}}{\partial \psi_2} = f_{2g}^{(b)}(\lambda_w, \theta_g, \psi_2) = 0. \tag{21.3.19}$$

Equation of meshing (21.3.19) may also be represented as

$$\mathbf{n}_g^{(b)} \cdot \mathbf{v}^{(g2)} = f_g^{(b)}(\lambda_w, \theta_g, \psi_2) = 0. \tag{21.3.20}$$

Surface $\Sigma_2^{(b)}$ may be represented in two-parameter form as

$$\mathbf{R}_2^{(b)}(\theta_g, \psi_2) = \mathbf{r}_2^{(b)}(\lambda_w(\theta_g, \psi_2), \theta_g, \psi_2). \tag{21.3.21}$$

The derivation of gear tooth surfaces requires knowledge of gear machine-tool settings. Such settings of a head-cutter or a grinding wheel are presented in Table 21.3.1. We consider the gear machine-tool settings as known (adapted, for instance, from the data of manufacturing), but the pinion machine-tool settings are determined in the process of local synthesis (see Section 21.4).

Equations of the Formate-Cut Gear Tooth Surface

We recall that the formate-cut gear tooth surface is a copy of the surface of the head-cutter, which is a surface of revolution. The cradle wherein the gear head-cutter is mounted (Fig. 21.3.1) is held at rest during the process of cutting or grinding. The

Table 21.3.1: Machine-tool settings of a generated gear

Name	Notation	Reference
Blade angle	α_g	(Fig. 21.3.3)
Cutter (grinding wheel) radius	R_u	(Fig. 21.3.3)
Point width	P_{w_2}	(Fig. 21.3.3)
Cutter point radius ($R_g = R_u \pm P_{w_2}/2$)	R_g	(Fig. 21.3.3)
Radial setting	S_{r_2}	(Fig. 21.3.2)
Basic cradle angle	q_2	(Fig. 21.3.2)
Machine center to back	ΔX_{D_2}	(Fig. 21.3.2)
Sliding base	ΔX_{B_2}	(Fig. 21.3.2)
Blank offset	ΔE_{m_2}	(Fig. 21.3.2)
Machine root angle	γ_{m_2}	(Fig. 21.3.2)
Ratio of gear roll	m_{2c_2}	[Eq. (21.3.1)]
Edge radius of head-cutter	ρ_w	(Fig. 21.3.3)

rotation of the head-cutter about the z_g axis is necessary for the cutting or grinding process but does not affect the shape of gear tooth surfaces.

The surfaces $\Sigma_2^{(a)}$ and $\Sigma_2^{(b)}$ that represent the working part of the gear tooth surface and the fillet of a formate-cut gear are represented as follows, respectively,

$$\mathbf{r}_2^{(a)}(s_g, \theta_g) = \mathbf{M}_{2g}\mathbf{r}_g^{(a)}(s_g, \theta_g) \tag{21.3.22}$$

$$\mathbf{r}_2^{(b)}(\lambda_w, \theta_g) = \mathbf{M}_{2g}\mathbf{r}_g^{(b)}(\lambda_w, \theta_g). \tag{21.3.23}$$

Here,

$$\mathbf{M}_{2g} = \mathbf{M}_{2a_2}\mathbf{M}_{a_2m_2}\mathbf{M}_{m_2g} \tag{21.3.24}$$
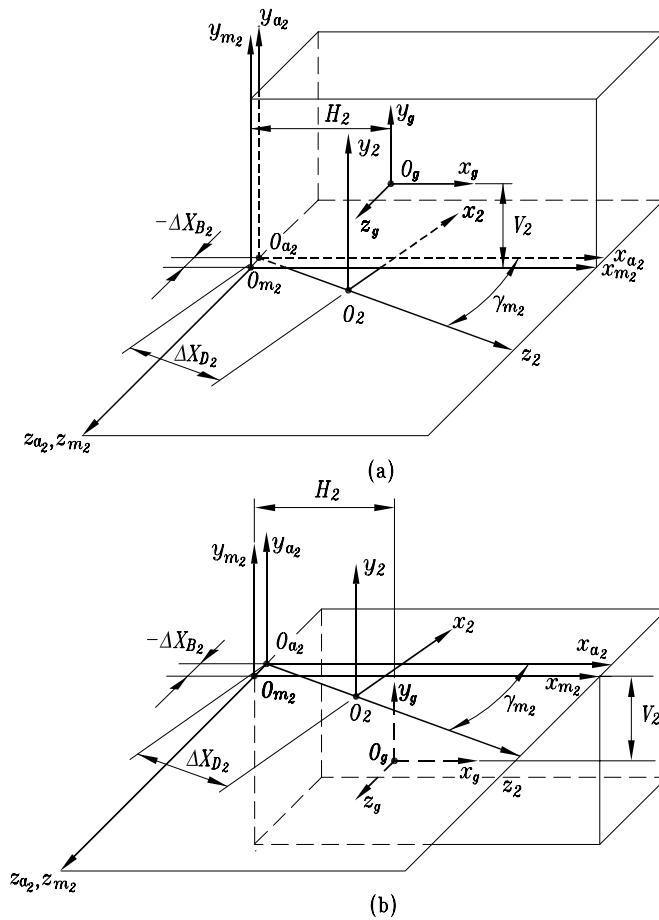
where

$$\mathbf{M}_{m_2g} = \begin{bmatrix} 1 & 0 & 0 & H_2 \\ 0 & 1 & 0 & \pm V_2 \\ 0 & 0 & 1 & 0 \\ 0 & 0 & 0 & 1 \end{bmatrix}$$

$$\mathbf{M}_{a_2m_2} = \begin{bmatrix} 1 & 0 & 0 & 0 \\ 0 & 1 & 0 & 0 \\ 0 & 0 & 1 & -\Delta X_{B_2} \\ 0 & 0 & 0 & 1 \end{bmatrix}$$

$$
\mathbf{M}_{2a_2} = \begin{bmatrix} \sin\gamma_{m_2} & 0 & -\cos\gamma_{m_2} & 0 \\ 0 & 1 & 0 & 0 \\ \cos\gamma_{m_2} & 0 & \sin\gamma_{m_2} & -\Delta X_{D_2} \\ 0 & 0 & 0 & 1 \end{bmatrix}.
$$

Parameters V_2, H_2, ΔX_{B_2}, ΔX_{D_2}, and γ_{m_2} (Fig. 21.3.6) are the gear machine-tool settings. The upper and lower signs in front of V_2 correspond to right-hand and left-hand gears, respectively. The whole set of machine-tool settings for a formate-cut gear is presented in Table 21.3.2.

Figure 21.3.6: Coordinate systems applied for cutting or grinding of a formate-cut gear: (a) for right-hand gear; (b) for left-hand gear.

Table 21.3.2: Machine-tool settings of a formate-cut gear

Name	Notation	Reference
Blade angle	α_g	(Fig. 21.3.4)
Blade parabolic coefficient	a_c	[Eq. (21.3.8)]
Parabola apex location	s_{g_o}	(Fig. 21.3.4)
Cutter (grinding wheel) radius	R_u	(Fig. 21.3.4)
Point width	P_{w_2}	(Fig. 21.3.4)
Cutter point radius	$R_g = R_u \pm P_{w_2}/2$	(Fig. 21.3.4)
Horizontal setting	H_2	(Fig. 21.3.6)
Vertical setting	V_2	(Fig. 21.3.6)
Sliding base	ΔX_{B_2}	(Fig. 21.3.6)
Machine center to back	ΔX_{D_2}	(Fig. 21.3.6)
Machine root angle	γ_{m2}	(Fig. 21.3.6)
Edge radius of head-cutter	ρ_w	(Fig. 21.3.4)

21.4 DERIVATION OF PINION TOOTH SURFACE

We limit the discussion to the generation of the pinion by straight-line blades of the head-cutter. However, application of blades of parabolic profile for pinion generation is beneficial in some cases, for instance for design of a gear ratio close to 1.

Applied Coordinate Systems
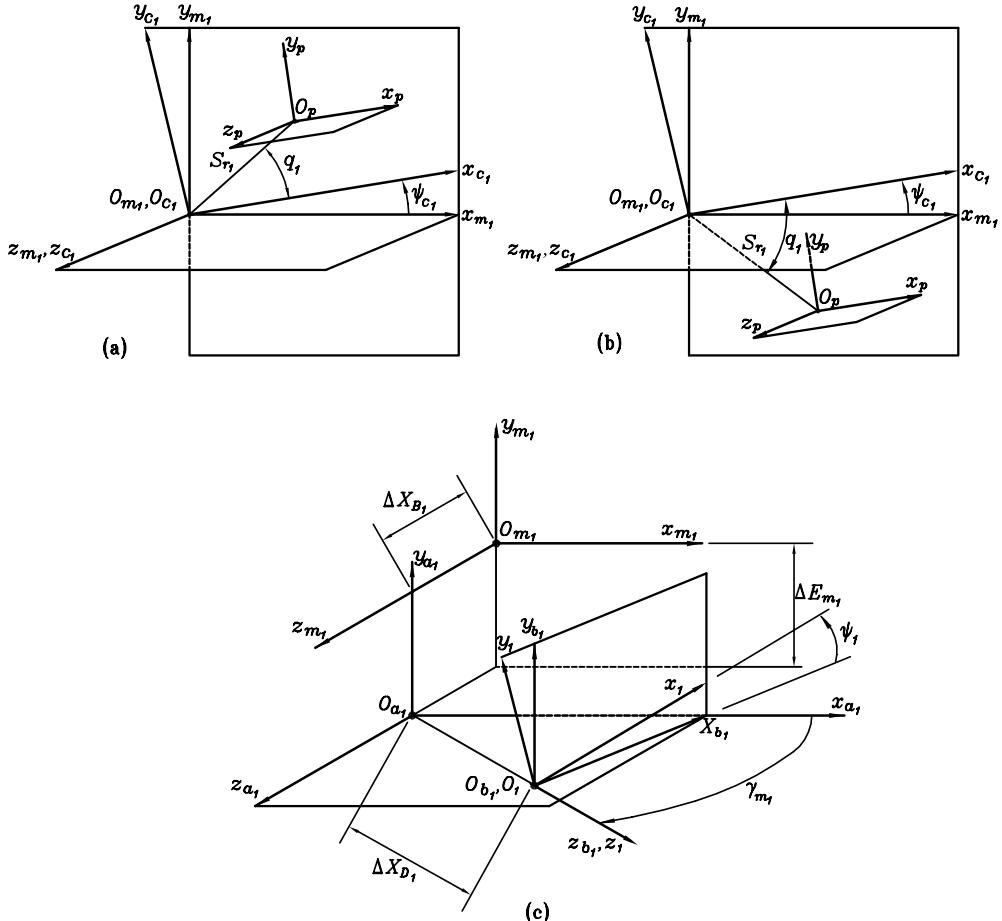
Coordinate systems applied for generation of the pinion are shown in Fig. 21.4.1. Coordinate systems S_{m1}, S_{a1}, S_{b1} are the fixed ones and they are rigidly connected to the cutting machine. The movable coordinate systems S_1 and S_{c1} are rigidly connected to the pinion and the cradle, respectively. They are rotated about the z_{b1} axis and the z_{m1} axis, respectively, and their rotations are related with a polynomial function $\psi_1(\psi_{c1})$ wherein modified roll is applied (see below). The ratio of instantaneous angular velocities of the pinion and the cradle is defined as $m_{1c}(\psi_1(\psi_{c1})) = \omega^{(1)}(\psi_{c1})/\omega^{(c)}$. The magnitude $m_{1c}(\psi_1)$ at $\psi_{c1} = 0$ is called ratio of roll or velocity ratio. Parameters ΔX_{D_1}, ΔX_{B_1}, ΔE_{m_1}, and γ_{m1} are the basic machine-tool settings for pinion generation.

Coordinate system S_p [Figs. 21.4.1(a) and 21.4.1(b)] is applied for illustration of installment of the head-cutter on the cradle and corresponds to generation of the right-hand and left-hand pinion, respectively.

Head-Cutter Surfaces

The pinion generating surfaces are formed by surface $\Sigma_p^{(a)}$ and $\Sigma_p^{(b)}$ generated by straight-line and circular arc parts of the blades. Surface $\Sigma_p^{(a)}$ is represented as

$$r_p^{(a)}(s_p, \theta_p) = \begin{bmatrix} (R_p \mp s_p \sin \alpha_p) \cos \theta_p \\ (R_p \mp s_p \sin \alpha_p) \sin \theta_p \\ -s_p \cos \alpha_p \end{bmatrix} \qquad (21.4.1)$$

Figure 21.4.1: Coordinate systems applied for pinion generation: (a) and (b) illustration of tool installment for generation of right- and left-hand pinions; (c) illustration of installment of machine-tool settings.
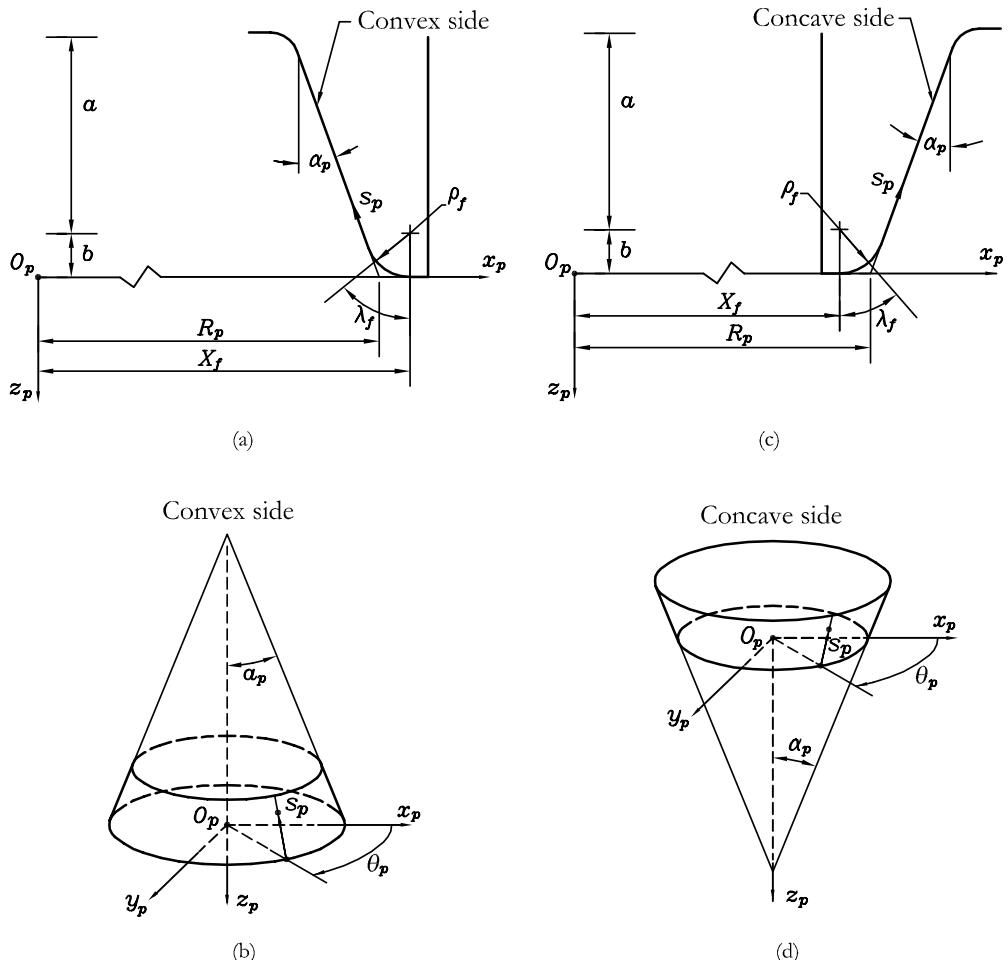
where s_p and θ_p are the surface coordinates, α_p is the blade angle, and R_p is the cutter point radius (Fig. 21.4.2). The upper and lower signs in Eq. (21.4.1) correspond to the convex and concave sides of the pinion tooth, which are in mesh with the concave and convex sides of the gear, respectively.

The unit normal to the pinion generating surface $\Sigma_p^{(a)}$ is represented by the equations

$$n_p^{(a)}(\theta_p) = \frac{N_p}{|N_p|}, \quad N_p = \frac{\partial r_p^{(a)}}{\partial s_p} \times \frac{\partial r_p^{(a)}}{\partial \theta_p}. \tag{21.4.2}$$

Equations (21.4.1) and (21.4.2) yield

$$n_p^{(a)}(\theta_p) = \begin{bmatrix} \cos\alpha_p \cos\theta_p \\ \cos\alpha_p \sin\theta_p \\ \mp\sin\alpha_p \end{bmatrix}. \tag{21.4.3}$$

Figure 21.4.2: Blades and generating cones for pinion generating tool with straight blades: (a) convex side blade; (b) convex side generating cone; (c) concave side blade; (d) concave side generating cone.

For surface $\Sigma_p^{(b)}$, we obtain

$$r_p^{(b)}(\lambda_f, \theta_p) = \begin{bmatrix} (X_f \mp \rho_f \sin\lambda_f)\cos\theta_p \\ (X_f \mp \rho_f \sin\lambda_f)\sin\theta_p \\ -\rho_f(1 - \cos\lambda_f) \end{bmatrix}, \quad 0 \le \lambda_f \le \frac{\pi}{2} - \alpha_p \quad (21.4.4)$$

where

$$X_f = R_p \pm \rho_f(1 - \sin\alpha_p)/\cos\alpha_p$$

and ρ_f is the edge radius of the head-cutter for the pinion (Fig. 21.4.2).

The unit normal to the pinion generating surface of part (b) is represented by the equations

$$\boldsymbol{n}_p^{(b)}(\theta_p) = \frac{\boldsymbol{N}_p^{(b)}}{|\boldsymbol{N}_p^{(b)}|}, \quad \boldsymbol{N}_p = \frac{\partial \boldsymbol{r}_p^{(b)}}{\partial \lambda_f} \times \frac{\partial \boldsymbol{r}_p^{(b)}}{\partial \theta_p}. \tag{21.4.5}$$

Equations (21.4.4) and (21.4.5) yield

$$\boldsymbol{n}_p^{(b)}(\theta_p) = \begin{bmatrix} \sin \lambda_f \cos \theta_p \\ \sin \lambda_f \sin \theta_p \\ \mp \cos \lambda_p \end{bmatrix}. \tag{21.4.6}$$

Families of Pinion Tooth Surfaces

Such families are represented as

$$\boldsymbol{r}_1^{(a)}(s_p, \theta_p, \psi_{c1}) = \mathbf{M}_{1p}(\psi_{c1}) \, \boldsymbol{r}_p^{(a)}(s_p, \theta_p) \tag{21.4.7}$$

$$\boldsymbol{r}_1^{(b)}(\lambda_f, \theta_p, \psi_{c1}) = \mathbf{M}_{1p}(\psi_{c1}) \, \boldsymbol{r}_p^{(b)}(\lambda_f, \theta_p) \tag{21.4.8}$$

where

$$\mathbf{M}_{1p} = \mathbf{M}_{1b_1} \mathbf{M}_{b_1 a_1} \mathbf{M}_{a_1 m_1} \mathbf{M}_{m_1 c_1} \mathbf{M}_{c_1 p}$$

$$\mathbf{M}_{c_1 p} = \begin{bmatrix} 1 & 0 & 0 & S_{r_1} \cos q_1 \\ 0 & 1 & 0 & S_{r_1} \sin q_1 \\ 0 & 0 & 1 & 0 \\ 0 & 0 & 0 & 1 \end{bmatrix}$$

$$\mathbf{M}_{m_1 c_1} = \begin{bmatrix} \cos \psi_{c_1} & -\sin \psi_{c_1} & 0 & 0 \\ \sin \psi_{c_1} & \cos \psi_{c_1} & 0 & 0 \\ 0 & 0 & 1 & 0 \\ 0 & 0 & 0 & 1 \end{bmatrix}$$

$$\mathbf{M}_{a_1 m_1} = \begin{bmatrix} 1 & 0 & 0 & 0 \\ 0 & 1 & 0 & \Delta E_{m_1} \\ 0 & 0 & 1 & -\Delta X_{B_1} \\ 0 & 0 & 0 & 1 \end{bmatrix}$$

$$\mathbf{M}_{b_1 a_1} = \begin{bmatrix} \sin \gamma_{m_1} & 0 & -\cos \gamma_{m_1} & 0 \\ 0 & 1 & 0 & 0 \\ \cos \gamma_{m_1} & 0 & \sin \gamma_{m_1} & -\Delta X_{D_2} \\ 0 & 0 & 0 & 1 \end{bmatrix}$$

$$\mathbf{M}_{1b_1} = \begin{bmatrix} \cos \psi_1 & \sin \psi_1 & 0 & 0 \\ -\sin \psi_1 & \cos \psi_1 & 0 & 0 \\ 0 & 0 & 1 & 0 \\ 0 & 0 & 0 & 1 \end{bmatrix}.$$

When modified roll is applied in the process of generation, the rotation angles ψ_1 of the pinion and ψ_{c_1} of the cradle are related as

$$\psi_1 = b_1 \psi_{c_1} - b_2 \psi_{c_1}^2 - b_3 \psi_{c_1}^3 \tag{21.4.9}$$

$$= b_1 \left(\psi_{c_1} - \frac{b_2}{b_1} \psi_{c_1}^2 - \frac{b_3}{b_1} \psi_{c_1}^3 \right)$$

$$= m_{1c} \left(\psi_{c_1} - C \psi_{c_1}^2 - D \psi_{c_1}^3 \right)$$

where b_1, b_2, and b_3 are the modified roll parameters and C and D are the modified roll coefficients. The derivative of function $\psi_1 (\psi_{c1})$ taken at $\psi_{c1} = 0$ determines the so-called ratio of roll or velocity ratio, determined in Eq. (21.4.9) by b_1 or m_{1c}.

Equation of Meshing

The pinion tooth surface Σ_1 is the envelope to the family of cutter surfaces. The modified roll is applied in the process of generation. The equation of meshing is represented as

$$\mathbf{n}_{m_1}^{(a)} \cdot \mathbf{v}_{m_1}^{(p1)} = f_{1p}^{(a)}(s_p, \theta_p, \psi_{c1}) = 0 \tag{21.4.10}$$

where $\mathbf{n}_{m_1}^{(a)}$ is the unit normal to the surface, and $\mathbf{v}_{m_1}^{(p1)}$ is the velocity in relative motion. The vectors are represented in the fixed coordinate system S_{m_1} as follows:

$$\mathbf{n}_{m_1}^{(a)} = \mathbf{L}_{m_1 c_1} \mathbf{L}_{c_1 p} \mathbf{n}_p^{(a)}(\theta_p) \tag{21.4.11}$$

$$\mathbf{v}_{m_1}^{(p1)} = \left[\left(\boldsymbol{\omega}_{m_1}^{(p)} - \boldsymbol{\omega}_{m_1}^{(1)} \right) \times \mathbf{r}_{m1} \right] - \left(\overline{O_{m_1} O_{a_2}} \times \boldsymbol{\omega}_{m_1}^{(1)} \right). \tag{21.4.12}$$

The 3×3 matrices $\mathbf{L}_{m_1 c_1}$ and $\mathbf{L}_{c_1 p}$ in Eq. (21.4.11) and in similar derivations are the sub-matrices of the 4×4 matrices $\mathbf{M}_{m_1 c_1}$ and $\mathbf{M}_{c_1 p}$, respectively. They are obtained by elimination of the last row and column of $\mathbf{M}_{m_1 c_1}$ and $\mathbf{M}_{c_1 p}$, respectively. Elements of matrices $\mathbf{L}_{m_1 c_1}$ and $\mathbf{L}_{c_1 p}$ represent the direction cosines formed by the respective axes of coordinate systems S_{m_1} and S_{c_1} for $\mathbf{L}_{m_1 c_1}$ and coordinate systems S_{c_1} and S_p for $\mathbf{L}_{c_1 p}$ (see Chapter 1).

Position vector $\boldsymbol{r}_{m_1}$ in Eq. (21.4.12) is determined as

$$\boldsymbol{r}_{m1} = \mathbf{M}_{m_1 c_1} \mathbf{M}_{c_1 p}\, \boldsymbol{r}_p^{(a)}(s_p, \theta_p)$$

$$\overline{O_{m_1} O_{a_2}} = [0 \quad -\Delta E_{m_1} \quad \Delta X_{B_1}]^{\mathrm{T}}$$

$$\boldsymbol{\omega}_{m_1}^{(1)} = [\cos \gamma_{m_1} \quad 0 \quad \sin \gamma_{m_1}]^{\mathrm{T}}$$

$$\boldsymbol{\omega}_{m_1}^{(p)} = [0 \quad 0 \quad m_{1c}(\psi_{c_1})]^{\mathrm{T}}.$$

The ratio $m_{1c}(\psi_{c_1})$ is not constant because modified roll is applied and it can be represented as

$$m_{1c}(\psi_{c_1}) = \frac{\omega_{c_1}}{\omega_1} = \frac{d\psi_{c_1}/dt}{d\psi_1/dt} = \frac{1}{d\psi_1/d\psi_{c_1}} = \frac{1}{m_{1c}\left(1 - 2C\psi_{c_1} - 3D\psi_{c_1}^2\right)}$$

$$= \frac{1}{m_{1c} - 2b_2\psi_{c_1} - 3b_3\psi_{c_1}^2} \tag{21.4.13}$$

where C and D are the modified roll coefficients.

Finally, we obtain the equations for pinion tooth surface part (a) as

$$\boldsymbol{r}_1^{(a)}(s_p, \theta_p, \psi_{c_1}) = \mathbf{M}_{1p}(\psi_{c_1})\, \boldsymbol{r}_p^{(a)}(s_p, \theta_p) \tag{21.4.14}$$

$$f_{1p}(s_p, \theta_p, \psi_{c_1}) = 0. \tag{21.4.15}$$

Using similar derivations, the fillet surface may be represented as

$$\boldsymbol{r}_1^{(b)}(\lambda_f, \theta_p, \psi_{c_1}) = \mathbf{M}_{1p}(\psi_{c_1})\, \boldsymbol{r}_p^{(b)}(\lambda_f, \theta_p) \tag{21.4.16}$$

$$f_{1p}(\lambda_f, \theta_p, \psi_{c_1}) = 0. \tag{21.4.17}$$

21.5 LOCAL SYNTHESIS AND DETERMINATION OF PINION MACHINE-TOOL SETTINGS

The purpose of local synthesis is to obtain favorable conditions of meshing and contact at the chosen mean contact point M. Such conditions at M are defined by η_2, a, and m'_{21} (Fig. 21.2.1). The gear machine-tool settings are considered as known and they may be adapted, for instance, from the manufacturing summary.

The procedure of local synthesis is a part of the proposed integrated approach for the design of spiral bevel gears with localized bearing contact and reduced levels of vibration and noise based on application of a longitudinally directed path of contact and application of parabolic blades for generation of the gear to avoid hidden areas of severe contact.

The procedure of local synthesis is represented as a sequence of three stages that provide: (i) the tangency at M of gear tooth surface Σ_2 and gear head-cutter surface Σ_g, (ii) the tangency at M of gear and pinion tooth surfaces Σ_2 and Σ_1, and (iii) the tangency at M of pinion tooth surface Σ_1 and pinion head-cutter surface Σ_p. Finally, we obtain that all four surfaces Σ_2, Σ_g, Σ_1, and Σ_p are in tangency at M. At all stages,

the relationships between the principal curvatures and directions of meshing surfaces are applied (provided in Section 21.6). Then, it becomes possible to obtain the sought-for pinion machine-tool settings.

The procedure of local synthesis is applied for both cases of design of spiral bevel gear drives: (i) face-milled generated gears, and (ii) formate-cut spiral bevel gears. The procedure for the case of face-milled generated spiral bevel gear drives is represented below. The procedure of local synthesis for formate-cut spiral bevel gear drives can be considered as a particular case of the one applied for face-milled generated spiral bevel gear drives and is discussed below.

Local Synthesis of Face-Milled Generated Spiral Bevel Gear Drives
The procedure of local synthesis of face-milled generated spiral bevel gear drives is illustrated by the following three stages:

STAGE 1: TANGENCY OF SURFACES Σ_2 AND Σ_g AT CHOSEN POINT A. Point A on surface Σ_2 is chosen as a candidate for the mean contact point M of pinion–gear tooth surfaces.

Step 1: The meshing of surfaces Σ_2 and Σ_g is represented in coordinate system S_{m_2} (Fig. 21.3.2) by the following equations:

$$\boldsymbol{r}_{m_2}(s_g, \theta_g, \psi_2) = \mathbf{M}_{m_2 g}(\psi_2)\, \boldsymbol{r}_g(s_g, \theta_g) \tag{21.5.1}$$
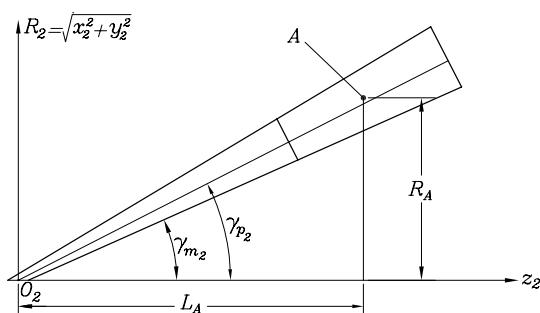
$$f_{2g}(s_g, \theta_g, \psi_2) = 0. \tag{21.5.2}$$

Equation (21.5.1) represents in S_{m_2} the family of surfaces Σ_g, and Eq. (21.5.2) is the equation of meshing. The generated surface Σ_2 is represented in S_2 by the matrix equation

$$\boldsymbol{r}_2(s_g, \theta_g, \psi_2) = \mathbf{M}_{2g}(\psi_2)\, \boldsymbol{r}_g(s_g, \theta_g) \tag{21.5.3}$$

and the equation of meshing (21.5.2).

Step 2: Mean point A on surface Σ_2 is chosen by designation of parameters L_A and R_A (Fig. 21.5.1), where A is the candidate for the mean contact point M of surfaces Σ_2

Figure 21.5.1: Representation of point A in coordinate system S_2.

and Σ_1. Then we obtain the following system of two equations in three unknowns:

$$\begin{cases} Z_2(s_g^*, \theta_g^*, \psi_2^*) = L_A \\ X_2^2(s_g^*, \theta_g^*, \psi_2^*) + Y_2^2(s_g^*, \theta_g^*, \psi_2^*) = R_A^2 \end{cases} \qquad (21.5.4)$$

where X_2, Y_2, Z_2 are the projections of position vector $r_2(s_g^*, \theta_g^*, \psi_2^*)$ (see Eq. (21.5.3)). The third equation for determination of these three unknowns is the equation of meshing (21.5.2).

Step 3: Equations (21.5.2), (21.5.3), and (21.5.4) considered simultaneously allow the determination of parameters $(s_g^*, \theta_g^*, \psi_2^*)$ for point A. Vector functions $r_g(s_g, \theta_g)$ and $n_g(\theta_g)$ determine the position vector and surface unit normal for a current point of surface Σ_g. Taking in these vector functions $s_g = s_g^*$ and $\theta_g = \theta_g^*$, we can determine the position vector $r_g^{(A)}$ of point A and the surface unit normal at A.

Step 4: Parameters s_g^* and θ_g^* and the unit vectors e_g and e_u of principal directions on surface Σ_g are considered as known. For a head-cutter with blades of straight-line profiles:

$$e_g = \frac{\partial r_g^{(a)}}{\partial s_g} \div \left| \frac{\partial r_g^{(a)}}{\partial s_g} \right| = \begin{bmatrix} \pm \sin \alpha_g \cos \theta_g \\ \pm \sin \alpha_g \sin \theta_g \\ -\cos \alpha_g \end{bmatrix} \qquad (21.5.5)$$

$$e_u = \frac{\partial r_g^{(a)}}{\partial \theta_g} \div \left| \frac{\partial r_g^{(a)}}{\partial \theta_g} \right| = \begin{bmatrix} -\sin \theta_g \\ \cos \theta_g \\ 0 \end{bmatrix}. \qquad (21.5.6)$$

In this case, the generating surface is a conical surface, and the principal curvatures k_g and k_u of Σ_g can be determined by the following equations:
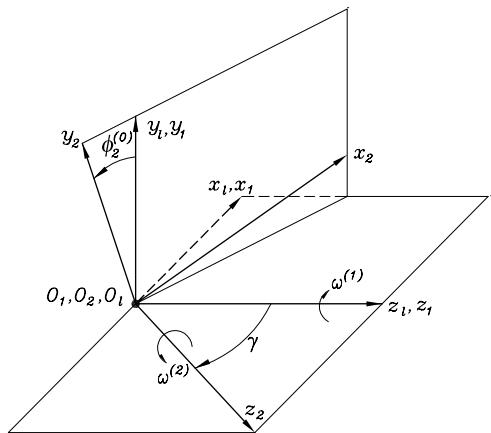
$$\begin{cases} k_g = 0 \\ k_u = \dfrac{\cos \alpha_g}{R_{cg} \pm s_g \sin \alpha_g}. \end{cases} \qquad (21.5.7)$$

The upper and lower signs correspond to the concave and convex sides of the gear tooth, respectively.

The approach discussed in Section 21.6 enables the determination at point A of (i) the principal curvatures k_s and k_q of Σ_2, and (ii) the unit vectors e_s and e_q of principal directions on surface Σ_2. The unit vectors e_s and e_q are represented in S_{m_2}. The general procedure presented in Section 8.4 can be applied for determination of principal curvatures k_g and k_u of the surfaces of the blades of parabolic profile.

STAGE 2: TANGENCY OF SURFACES Σ_2, Σ_g, AND Σ_1 AT MEAN CONTACT POINT M

Step 1: The derivations accomplished at Stage 1 enable the determination of the position vector $r_2^{(A)}$ and the surface unit normal $n_2^{(A)}$ of point A of tangency of surfaces Σ_2 and Σ_g. The goal now is to determine such a point M in the fixed coordinate system

Figure 21.5.2: Coordinate systems S_2, S_ℓ, and S_1 applied for local synthesis.

S_ℓ (Fig. 21.5.2) where three surfaces, Σ_2, Σ_g, and Σ_1, will be in tangency with each other.

It can be imagined that surface Σ_g is rigidly attached to Σ_2 at point A and that both surfaces, Σ_g and Σ_2, perform motion as a rigid body turning about the gear axis on a certain angle $\phi_2^{(0)}$. Using the coordinate transformation from S_2 to S_ℓ (Fig. 21.5.2), we may obtain $r_\ell^{(A)}$ and $n_\ell^{(A)}$. The new position of point A in S_ℓ will be the point of tangency of Σ_2 and Σ_1 (designated as M), if the following equation of meshing between Σ_2 and Σ_1 is observed:

$$n_\ell^{(A)}(\phi_2^{(0)}) \cdot v_\ell^{(21,A)}(\phi_2^{(0)}) = 0 \tag{21.5.8}$$

Here, $n_\ell^{(A)} \equiv n_\ell^{(M)}$ and $v_\ell^{(21,A)} \equiv v_\ell^{(21,M)}$; $v_\ell^{(21,A)}$ is the relative velocity at point A determined with the ideal gear ratio

$$m_{21}^{(0)} = \frac{\omega^{(2)}}{\omega^{(1)}}. \tag{21.5.9}$$

The solution of Eq. (21.5.8) for $\phi_2^{(0)}$ provides the value of the turning angle $\phi_2^{(0)}$. It is evident that three surfaces, Σ_2, Σ_g, and Σ_1, are now in tangency with each other at point M. We emphasize that the procedure in Step 1 enables us to avoid the tilt of the head-cutter for generation of the pinion.

Step 2: We consider as known at point M the principal curvatures k_s and k_q of surface Σ_2, and the unit vectors e_s and e_q of principal directions on Σ_2. The unit vectors e_s and e_q are represented in S_ℓ. The goal is to determine at point M the principal curvatures k_f and k_h of surface Σ_1, and the unit vectors e_f and e_h of principal directions on Σ_1. This goal can be achieved by application of the procedure described in Section 21.6. It is shown in Section 21.6 that the determination of k_f, k_h, e_f, and e_h becomes possible if parameters m'_{21}, η_2 (or η_1), and a/δ are assumed to be known or are used as input data.

STAGE 3: TANGENCY OF SURFACES Σ_2, Σ_g, Σ_1, AND Σ_p AT MEAN CONTACT POINT M. We consider in this stage two sub-stages: (a) derivation of basic equations of surface tangency, and (b) determination of pinion machine-tool settings that satisfy the equations

of surface tangency. Tangency of Σ_2, Σ_g, and Σ_1 at mean contact point M has already been provided in the previous stages. The position vector $r_\ell^{(M)}$ of point M and the surface unit normal $n_\ell^{(M)}$ at point M were determined in coordinate system S_ℓ. Let us imagine now that coordinate system S_1 that coincides with S_ℓ (Fig. 21.5.2) and surface Σ_1 are installed in coordinate system S_{m_1} (Fig. 21.4.1). Angle $\psi_1^{(0)}$ shown in Fig. 21.4.1 is the installment angle of the pinion. Using coordinate transformation from S_1 to S_{m_1}, we may determine in S_{m_1} position vector $r_{m_1}^{(M)}$ of point M and the surface unit normal $n_{m_1}^{(M)}$. In Section 21.6 the conditions of improved meshing and contact of pinion and gear tooth surfaces Σ_1 and Σ_2 are considered, and the relationships between the principal curvatures and directions of surfaces for such conditions of meshing and contact are determined [see Eqs. (21.6.27)]. The point of tangency of surfaces Σ_1 and Σ_p is designated in Section 21.6 as point B. The pinion generating surface Σ_p is installed in S_{m_1}, taking that the cradle angle ψ_{c_1} is equal to zero. The position vector of point B of surface Σ_p and the surface unit normal at B are represented in S_{m_1} as $r_{m_1}^{(B)}$ and $n_{m_1}^{(B)}$. The tangency of Σ_1 and Σ_p at the mean contact point M is satisfied, if the following vector equations are observed:

$$n_{m_1}^{(M)} = n_{m_1}^{(B)} \tag{21.5.10}$$

$$r_{m_1}^{(M)} = r_{m_1}^{(B)} \tag{21.5.11}$$
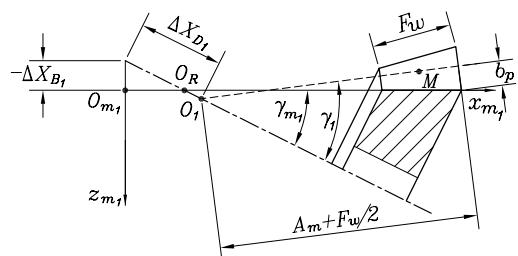
$$n_{m_1}^{(M)} \cdot v_{m_1}^{(1p)} = 0 \tag{21.5.12}$$

where Eq. (21.5.12) is the equation of meshing. Observation of Eqs. (21.5.10) to (21.5.12) means that all four surfaces (Σ_2, Σ_g, Σ_1, and Σ_p) are in contact at point M.

Using Eqs. (21.5.10) to (21.5.12) and Eq. (21.6.27), it becomes possible to obtain the settings of the pinion and the head-cutter that guarantee the improved conditions of meshing and contact at point M. The machine-tool settings to be determined are as follows:

(i) ΔX_{B_1}, ΔE_{m_1}, ΔX_{D_1} (Figs. 21.4.1 and 21.5.3) and $m_{1p} = \omega^{(1)}/\omega^{(p)}$. Setting ΔX_{B_1} and ΔX_{D_1} are related by the equation (Fig. 21.5.3)

$$\Delta X_{B_1} = -\left(\Delta X_{D_1} - \left|\overline{O_R O_1}\right|\right) \sin \gamma_{m_1} \tag{21.5.13}$$

Figure 21.5.3: For derivation of pinion machine-tool settings.

where

$$|\overline{O_R O_1}| = \frac{[(A_m + F_w/2)\sin \gamma_1 - b_p \cos \gamma_1]}{\tan \gamma_{m1}}$$
$$- [(A_m + F_w/2)\cos \gamma_1 + b_p \sin \gamma_1].$$

Here, A_m is the mean cone distance, F_w is the face width, b_p is the pinion dedendum, and γ_1 is the pitch cone angle of the pinion. Equation (21.5.13) is determined for the case of design of a spiral bevel gear with different apexes of the pitch and root cones.

(ii) Design parameter R_p of the head-cutter (Fig. 21.4.2).

(iii) Parameters S_{r_1} and q_1 that determine the installment of the head-cutter on the cradle (Fig. 21.4.1).

(iv) Parameter $\psi_1^{(0)}$ that determines the initial installment of coordinate system S_1 with respect to S_{b_1} (Fig. 21.4.1), and surface parameter θ_p of the head-cutter surface Σ_p.

After completion of the first sub-stage (the derivation of equations of tangency of surfaces Σ_2, Σ_g, Σ_1, and Σ_p, we may start the next sub-stage, the derivation of pinion machine-tool settings that provide the tangency of surfaces mentioned above. The procedure for computation is as follows:

Step 1: Calculate the values of θ_p and $\psi_1^{(0)}$ (two unknowns). Equation (21.5.10) is used for determination of θ_p and $\psi_1^{(0)}$, taking into account that

$$n_{m_1}^{(B)}(\theta_p) = \begin{bmatrix} \cos \alpha_p \cos \theta_p \\ \cos \alpha_p \sin \theta_p \\ \mp \sin \alpha_p \end{bmatrix} \tag{21.5.14}$$

and (Fig. 21.4.1)

$$n_{m_1}^{(M)} = L_{m_1 b_1} L_{b_1 1} n_1^{(M)} \tag{21.5.15}$$

where $n_1^{(M)} \equiv n_\ell^{(M)}$ because S_1 coincides with S_ℓ (Fig. 21.5.2). Here (Fig. 21.4.1),

$$L_{m_1 b_1} = \begin{bmatrix} \sin \gamma_{m_1} & 0 & \cos \gamma_{m_1} \\ 0 & 1 & 0 \\ -\cos \gamma_{m_1} & 0 & \sin \gamma_{m_1} \end{bmatrix} \tag{21.5.16}$$

$$L_{b_1 1} = \begin{bmatrix} \cos \psi_1^{(0)} & -\sin \psi_1^{(0)} & 0 \\ \sin \psi_1^{(0)} & \cos \psi_1^{(0)} & 0 \\ 0 & 0 & 1 \end{bmatrix}. \tag{21.5.17}$$

Equations (21.5.10) and (21.5.14)–(21.5.17) yield the following expressions for θ_p and $\psi_1^{(0)}$:

$$\cos\theta_p = \frac{n_{\ell z} \pm \sin\gamma_{m_1} \sin\alpha_p}{\cos\gamma_{m_1} \cos\alpha_p} \tag{21.5.18}$$

$$\sin\psi_1^{(0)} = \frac{-n_{\ell y}\cos\theta_p\cos\alpha_p + n_{\ell x}\sin\gamma_{m_1}\sin\theta_p\cos\alpha_p + n_{\ell y}n_{\ell z}\cos\gamma_{m_1}}{\sin\gamma_{m_1}\left(n_{\ell x}^2 + n_{\ell y}^2\right)} \tag{21.5.19}$$

$$\cos\psi_1^{(0)} = \frac{\sin\theta_p\cos\alpha_p - n_{\ell x}\sin\psi_1^{(0)}}{n_{\ell y}} \tag{21.5.20}$$

where α_p is the given value of the profile angle of the head-cutter and $n_{\ell x}, n_{\ell y}, n_{\ell z}$ are the three components of vector $\boldsymbol{n}_\ell^{(M)}$. The great advantage of the approach developed is that the requirement of the coincidence of the normals does not require a nonstandard profile angle α_p or the tilt of the head-cutter with respect to the cradle. Using θ_p, it becomes possible to determine the unit vectors $\boldsymbol{e}_p$ and $\boldsymbol{e}_t$ of principal directions on surface Σ_p at point M.

Step 2: Determination of machine-tool settings $\Delta X_{B_1}(\Delta X_{D_1})$, ΔE_{m_1}, m_{1p}, and the design parameter R_p of the head-cutter (five unknowns).

As a reminder, ΔX_{B_1} and ΔX_{D_1} are related by Eq. (21.5.13). The determination of the machine-tool settings mentioned above is based on application of the system of equations (21.6.27) and Eq. (21.5.12) that represent a system of four nonlinear equations with four unknowns: ΔX_{D_1}, ΔE_{m_1}, m_{1p}, and R_p. Also, the design parameters mentioned above provide improved conditions of meshing and contact at the mean contact point M.

Step 3: Determination of machine-tool settings S_{r_1} and q_1 (Fig. 21.4.1) and the pinion surface parameter s_p (three unknowns).

Determination of the three parameters is based on application of Eq. (21.5.11), considering that generating surface Σ_p is a cone. The final equations are as follows:

$$S_{r_1}\cos q_1 + (R_p \mp s_p\sin\alpha_p)\cos\theta_p = X_{m_1}^{(M)} \tag{21.5.21}$$

$$S_{r_1}\sin q_1 + (R_p \mp s_p\sin\alpha_p)\sin\theta_p = Y_{m_1}^{(M)} \tag{21.5.22}$$

$$-s_p\cos\alpha_p = Z_{m_1}^{(M)}. \tag{21.5.23}$$

We can summarize all the stages as follows:

(i) It is necessary to determine ten unknowns: six machine-tool settings (ΔX_{B_1}, ΔE_{m_1}, ΔX_{D_1}, q_1, S_r, m_{1p}), two surface parameters (θ_p, s_p), one cutter parameter R_p, and one position parameter $\psi_1^{(0)}$ which defines the pinion turn (Fig. 21.4.1).

(ii) The equation system for determination of the unknowns is formed as follows:

$$\boldsymbol{n}_{m_1}^{(M)} = \boldsymbol{n}_{m_1}^{(B)} \tag{21.5.24}$$

$$\boldsymbol{r}_{m_1}^{(M)} = \boldsymbol{r}_{m_1}^{(B)} \tag{21.5.25}$$

$$\boldsymbol{n}_{m_1}^{(M)} \cdot \boldsymbol{v}_{m_1}^{(1p)} = 0 \tag{21.5.26}$$

$$\Delta X_{B_1} = -\left(\Delta X_{D_1} - \left|\overline{O_R O_1}\right|\right)\sin\gamma_{m_1}. \tag{21.5.27}$$

In addition, the three following curvature equations are applied:

$$\tan 2\sigma^{(1p)} = \frac{-2d_{13}d_{23}}{d_{23}^2 - d_{13}^2 - (k_f - k_b)d_{33}}$$

$$k_t - k_p = \frac{-2d_{13}d_{23}}{d_{33}\sin 2\sigma^{(1p)}} \qquad (21.5.28)$$

$$k_t + k_p = k_f + k_b + \frac{d_{13}^2 + d_{23}^2}{d_{33}}.$$

Equation (21.5.24) is equivalent to two independent scalar equations; Eq. (21.5.25) is equivalent to three scalar equations; and Eqs. (21.5.26), (21.5.27), and (21.5.28) represent five scalar equations. Thus, the system of equations provides ten scalar equations for determination of ten unknowns. The solution for the unknowns requires: (1) a solution of a subsystem of four nonlinear equations (see Step 2), and solution of six remaining equations represented in echelon form (each of the six equations contains one unknown to be determined).

Local Synthesis of Formate-Cut Spiral Bevel Gear Drives

The local synthesis procedure for formate-cut spiral bevel gear drives is based on the same four stages previously represented for generated spiral bevel gear drives. The only modification of the procedure of local synthesis for generated spiral bevel gears affects Stage 1. Stages 2, 3, and 4 are applied without modification for the case of formate-cut spiral bevel gears.

The formate-cut gear tooth surface is the copy of the surface of the generating tool. The cradle and the gear being cut or ground are held at rest. Only the head-cutter is rotating around its own axis of rotation with the desired velocity of cutting or grinding. Therefore, principal curvatures k_s and k_q of Σ_2 and the unit vectors $\mathbf{e}_s$ and $\mathbf{e}_q$ of principal directions on surface Σ_2 coincide with the principal curvatures k_g and k_u and the unit vectors $\mathbf{e}_g$ and $\mathbf{e}_u$, respectively, of principal directions on surface Σ_g of the surface of revolution of the generating tool. The procedure represented in Section 21.6 for determination of (i) the principal curvatures k_s and k_q of Σ_2, and (ii) the unit vectors $\mathbf{e}_s$ and $\mathbf{e}_q$ of principal directions on surface Σ_2 at point A is not applied for the case of formate-cut spiral bevel gear drives.

21.6 RELATIONSHIPS BETWEEN PRINCIPAL CURVATURES AND DIRECTIONS OF MATING SURFACES

The relationships represented below are used for the procedure of local synthesis for the determination of the pinion machine-tool settings. Henceforth, two types of instantaneous contact of meshing surfaces are considered: (i) those along a line, and (ii) those at a point. Line contact is provided in meshing of the surface being generated with the tool surface. Point contact is provided for the generated pinion and gear tooth surfaces. The determination of the required relationships is based on the approach proposed in

Chapter 8. The basic equations in the approach developed are as follows:

$$v_r^{(2)} = v_r^{(1)} + v^{(12)} \tag{21.6.1}$$

$$\dot{n}_r^{(2)} = \dot{n}_r^{(1)} + \omega^{(12)} \times n \tag{21.6.2}$$

$$\frac{d}{dt}[n \cdot v^{(12)}] = 0. \tag{21.6.3}$$

Equations (21.6.1) and (21.6.2) relate the velocities of the contact point and the tip of the unit normal in their motions over the contacting surfaces. Equation (21.6.3) represents the differentiated equation of meshing. Equations (21.6.1) and (21.6.2) yield a skew-symmetric system of three linear equations in two unknowns x_1 and x_2 of the following structure:

$$a_{i_1} x_1 + a_{i_2} x_2 = a_{i_3} \qquad (i = 1, 2, 3). \tag{21.6.4}$$

Here, x_1 and x_2 are the projections of the velocity of the contact point in the motion over one of the surfaces on the principal directions of the mating surface. In the case of surfaces in line contact, the solution for the unknowns is indefinite and the rank of the system matrix of the linear equations is 1. In the case of surfaces in point contact, the solution for the unknowns is definite, and the rank of the system matrix is 2. The properties mentioned above are used for the derivation of the sought-for relationships between the principal curvatures and directions of the surfaces in mesh.

Meshing of Surfaces Σ_g and Σ_2

The tool surface Σ_g generates the gear tooth surface Σ_2. Surfaces Σ_g and Σ_2 are in line contact and their meshing is considered in coordinate system S_{m_2} (Fig. 21.3.2). Equations (21.6.1) to (21.6.3) yield a system of three linear equations,

$$c_{i_1} v_g^{(2)} + c_{i_2} v_u^{(2)} = c_{i_3} \qquad (i = 1, 2, 3) \tag{21.6.5}$$

where

$$v_g^{(2)} = v_r^{(2)} \cdot e_g, \qquad v_u^{(2)} = v_r^{(2)} \cdot e_u, \tag{21.6.6}$$

and e_g and e_u are the unit vectors of principal directions on Σ_g.

The following are considered known: point A of tangency of Σ_g and Σ_2, the common surface unit normal and the relative velocity $v^{(g2)}$, and the principal directions and curvatures k_g and k_u of surface Σ_g at A. The goal is to determine (i) the principal curvatures k_s and k_q of surface Σ_2, and (ii) angle $\sigma^{(g2)}$ that is formed between the unit vectors e_g and e_s that represent the first principal directions on Σ_g and Σ_2. The solution is based on the property that the rank of the system matrix (21.6.5) is 1 and is

represented as follows:

$$\tan 2\sigma^{(g2)} = \frac{-2c_{13}c_{23}}{c_{23}^2 - c_{13}^2 - (k_g - k_u)c_{33}}$$

$$k_q - k_s = \frac{-2c_{13}c_{23}}{c_{33}\sin 2\sigma^{(g2)}} \tag{21.6.7}$$

$$k_q + k_s = k_g + k_u + \frac{c_{13}^2 + c_{23}^2}{c_{33}}.$$

Here,

$$c_{13} = -k_g v_g^{(g2)} + \left[(n \times \omega^{(g2)}) \cdot e_g\right]$$

$$c_{23} = -k_u v_u^{(g2)} + \left[(n \times \omega^{(g2)}) \cdot e_u\right]$$

$$c_{33} = -k_g \left(v_g^{(g2)}\right)^2 - k_u \left(v_u^{(g2)}\right)^2 + \left[(n \times \omega^{(g2)}) \cdot v^{(g2)}\right] \tag{21.6.8}$$

$$\quad - n \cdot \left[(\omega^{(g)} \times v_{tr}^{(2)}) - (\omega^{(2)} \times v_{tr}^{(g)})\right]$$

where

$$v_g^{(g2)} = v^{(g2)} \cdot e_g, \quad v_u^{(g2)} = v^{(g2)} \cdot e_u. \tag{21.6.9}$$

Meshing of Surfaces Σ_2 and Σ_1

Surfaces Σ_1 and Σ_2 are in point contact and their meshing is considered in fixed co-ordinate system S_ℓ (Fig. 21.5.2). Equations (21.6.1) to (21.6.3) yield a system of three linear equations [Litvin, 1989, 1994],

$$a_{i_1} v_s^{(1)} + a_{i_2} v_q^{(1)} = a_{i_3} \qquad (i = 1, 2, 3) \tag{21.6.10}$$

where

$$v_s^{(1)} = v_r^{(1)} \cdot e_s, \quad v_q^{(1)} = v_r^{(1)} \cdot e_q \tag{21.6.11}$$

$$a_{11} = k_s - k_f \cos^2\sigma^{(12)} - k_h \sin^2\sigma^{(12)}$$

$$a_{12} = a_{21} = 0.5(k_f - k_h)\sin 2\sigma^{(12)}$$

$$a_{13} = a_{31} = -k_s v_s^{(12)} + \left[(n \times \omega^{(12)}) \cdot e_s\right]$$

$$a_{22} = k_q - k_f \sin^2\sigma^{(12)} - k_h \cos^2\sigma^{(12)} \tag{21.6.12}$$

$$a_{23} = a_{32} = -k_q v_q^{(12)} + \left[(n \times \omega^{(12)}) \cdot e_q\right]$$

$$a_{33} = k_s \left(v_s^{(12)}\right)^2 + k_q \left(v_q^{(12)}\right)^2 - \left[(n \times \omega^{(12)}) \cdot v^{(12)}\right]$$

$$\quad - n \cdot \left[(\omega^{(1)} \times v_{tr}^{(2)}) - (\omega^{(2)} \times v_{tr}^{(1)})\right] + m_{21}'(n \times k_2) \cdot r.$$

The following are considered known: point M of tangency of surfaces Σ_1 and Σ_2, the common surface unit normal, the relative velocity $v^{(12)}$, the principal curvatures k_s and k_q and directions on Σ_2 at M, and the elastic deformation δ of surfaces at M. The goal

is to determine the principal curvatures k_f and k_h and the angle $\sigma^{(12)}$ formed by the unit vectors e_f and e_s.

The velocity $v_r^{(i)}$ $(i = 1, 2)$ of the contact point on surface Σ_i has a definite direction and therefore the rank of the system matrix (21.6.10) is 1. This property yields the following relation:

$$\begin{vmatrix} a_{11} & a_{12} & a_{13} \\ a_{21} & a_{22} & a_{23} \\ a_{31} & a_{32} & a_{33} \end{vmatrix} = F\left(k_f,\ k_h,\ k_s,\ k_q,\ \sigma^{(12)},\ m'_{21}\right) = 0. \qquad (21.6.13)$$

The sought-for solution for k_f, k_h, and $\sigma^{(12)}$ can be obtained if the following parameters are chosen: the derivative m'_{21}; the ratio a/δ, where a is the major axis of the contact ellipse; the direction at M of the tangent to the contact path on one of the contacting surfaces Σ_1 or Σ_2. The relation between the directions at M of the tangents to the contact paths on both surfaces is represented by the equation

$$\tan \eta_1 = \frac{-a_{13}v_q^{(12)} + \left(a_{33} + a_{13}v_s^{(12)}\right)\tan\eta_2}{a_{33} + a_{23}\left(v_q^{(12)} - v_s^{(12)}\tan\eta_2\right)}. \qquad (21.6.14)$$

Choosing η_2 at point M, we can determine η_1.

Procedure of Determination of k_f, k_h, and $\sigma^{(12)}$

Step 1: Determine η_1 choosing η_2.
Step 2:

$$v_s^{(1)} = \frac{a_{33}}{a_{13} + a_{23}\tan\eta_1} \qquad (21.6.15)$$

$$v_q^{(1)} = \frac{a_{33}\tan\eta_1}{a_{13} + a_{23}\tan\eta_1}. \qquad (21.6.16)$$

Step 3:

$$A = \frac{\delta}{a^2}. \qquad (21.6.17)$$

Step 4:

$$K_\Sigma = \frac{\dfrac{a_{13}^2 + a_{23}^2}{\left(v_s^{(1)}\right)^2 + \left(v_q^{(1)}\right)^2} - 4A^2}{\dfrac{a_{13}v_s^{(1)} + a_{23}v_q^{(1)}}{\left(v_s^{(1)}\right)^2 + \left(v_q^{(1)}\right)^2} + 2A}. \qquad (21.6.18)$$

Step 5:

$$\begin{bmatrix} a_{11} \\ a_{12} \\ a_{22} \end{bmatrix} = \frac{1}{\left(v_s^{(1)}\right)^2 + \left(v_q^{(1)}\right)^2} \begin{bmatrix} a_{13}v_s^{(1)} - a_{23}v_q^{(1)} + \left(v_q^{(1)}\right)^2 K_\Sigma \\ a_{13}v_q^{(1)} + a_{23}v_s^{(1)} - v_s^{(1)}v_q^{(1)} K_\Sigma \\ -a_{13}v_s^{(1)} + a_{23}v_q^{(1)} + \left(v_s^{(1)}\right)^2 K_\Sigma \end{bmatrix}. \qquad (21.6.19)$$

Step 6:

$$\tan 2\sigma^{(12)} = \frac{2a_{12}}{g_2 - (a_{11} - a_{22})} \tag{21.6.20}$$

where $g_2 = k_s - k_q$.

Step 7:

$$g_1 = \frac{2a_{12}}{\sin 2\sigma^{(12)}}. \tag{21.6.21}$$

Step 8:

$$K_\Sigma^{(1)} = K_\Sigma^{(2)} - K_\Sigma \tag{21.6.22}$$

where $K_\Sigma^{(2)} = k_s + k_q$.

Step 9:

$$k_f = \left(K_\Sigma^{(1)} + g_1\right)/2. \tag{21.6.23}$$

Step 10:

$$k_h = \left(K_\Sigma^{(1)} - g_1\right)/2. \tag{21.6.24}$$

The procedure provided above can be used to obtain the sought-for curvatures k_f and k_h at point M of tangency of surfaces Σ_2 and Σ_1 and the principal directions on Σ_1 at M.

Meshing of Surfaces Σ_1 and Σ_p

The tool surface Σ_p generates the pinion tooth surface Σ_1. Surfaces Σ_p and Σ_1 are in line contact and point B is the given point of the instantaneous line of contact. The meshing of surfaces is considered in S_{m_1} (Fig. 21.4.1). At point B the following data are assumed as given: the curvatures k_f and k_h of surface Σ_1; the unit vectors e_f and e_h of principal directions on Σ_1; the surfaces' unit normals; the relative velocity $v^{(12)}$. The goal is to determine the principal curvatures k_p and k_t of surface Σ_p, and the angle $\sigma^{(1p)}$ that is formed by the unit vectors e_f and e_p.

Equations (21.6.1) to (21.6.3) yield a system of three linear equations,

$$d_{i_1}v_f^{(p)} + d_{i_2}v_h^{(p)} = d_{i_3} \qquad (i = 1, 2, 3) \tag{21.6.25}$$

where

$$v_f^{(p)} = v_r^{(p)} \cdot e_f, \qquad v_h^{(p)} = v_r^{(p)} \cdot e_h. \tag{21.6.26}$$

The direction of $v_r^{(p)}$ is indefinite because surfaces Σ_p and Σ_1 are in line contact. Therefore, the rank of the system matrix of equations is equal to 1. Using this property, the

following equations are obtained:

$$\tan 2\sigma^{(1p)} = \frac{-2d_{13}d_{23}}{d_{23}^2 - d_{13}^2 - (k_f - k_h)d_{33}}$$

$$k_t - k_p = \frac{-2d_{13}d_{23}}{d_{33}\sin 2\sigma^{(1p)}} \qquad (21.6.27)$$

$$k_t + k_p = k_f + k_h + \frac{d_{13}^2 + d_{23}^2}{d_{33}}.$$

Here,

$$d_{13} = -k_f v_f^{(1p)} + \left[\left(\mathbf{n} \times \boldsymbol{\omega}^{(1p)}\right) \cdot \mathbf{e}_f\right]$$

$$d_{23} = -k_h v_h^{(1p)} + \left[\left(\mathbf{n} \times \boldsymbol{\omega}^{(1p)}\right) \cdot \mathbf{e}_h\right]$$

$$d_{33} = -k_f \left(v_f^{(1p)}\right)^2 - k_h \left(v_h^{(1p)}\right)^2 + \left[\left(\mathbf{n} \times \boldsymbol{\omega}^{(1p)}\right) \cdot \mathbf{v}^{(1p)}\right] \qquad (21.6.28)$$

$$- \mathbf{n} \cdot \left[\left(\boldsymbol{\omega}^{(1)} \times \mathbf{v}_{tr}^{(p)}\right) - \left(\boldsymbol{\omega}^{(p)} \times \mathbf{v}_{tr}^{(1)}\right)\right]$$

where

$$v_f^{(1p)} = \mathbf{v}^{(1p)} \cdot \mathbf{e}_f, \quad v_h^{(1p)} = \mathbf{v}^{(1p)} \cdot \mathbf{e}_h. \qquad (21.6.29)$$

21.7 SIMULATION OF MESHING AND CONTACT
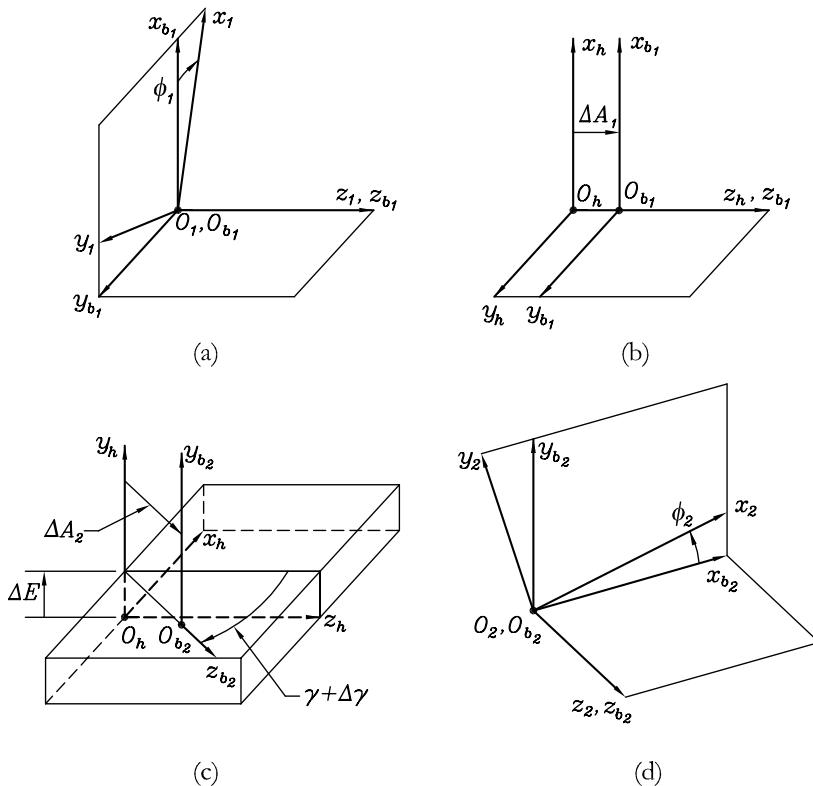
The main goal of simulation of meshing and contact is the determination of the bearing contact that corresponds to the pinion machine-tool settings obtained in Section 21.5. We recall that the gear machine-tool settings are adapted from the data of manufacturing of the gear. The combination of adapted gear machine-tool settings and determined pinion machine-tool settings has to provide favorable conditions of meshing and contact.

The expected shape of the function of transmission errors and formation of the bearing contact are tested by computerized simulation of meshing and contact and application of stress analysis based on the finite element method (see Section 21.8). The TCA computer program developed for simulation of meshing and contact allows us to obtain the path of contact and the function of transmission errors at each stage of iteration (see Section 9.4). The following is a description of the approach applied for tooth contact analysis (TCA).

Applied Coordinate Systems
The meshing of gear tooth surfaces is considered in the fixed coordinate system S_h that is rigidly connected to the housing (Fig. 21.7.1). Movable coordinate systems S_1 and S_2 are rigidly connected to the pinion and the gear, respectively. Auxiliary coordinate systems S_{b_1} and S_{b_2} are used to represent the rotation of the pinion (with respect to S_{b_1}) and the gear (with respect to S_{b_2}). The errors of alignment are simulated by respective installation of S_{b_1} and S_{b_2} with respect to S_h (Fig. 21.7.1).

The errors of assembly are ΔA_1 – the axial displacement of the pinion, $\Delta \gamma$ – the change of the shaft angle γ, ΔE – the shortest distance between the axes of the pinion

Figure 21.7.1: Coordinate systems applied for simulation of meshing: (a) illustration of pinion rotation; (b) illustration of misalignment ΔA_1; (c) illustration of misalignment ΔA_2, ΔE, and $\Delta \gamma$; (d) illustration of gear rotation.

and the gear when the pinion–gear axes are not intersected but crossed, ΔA_2 – the axial displacement of the gear. In the case of an aligned gear drive we consider that ΔA_1, $\Delta \gamma$, ΔE, and ΔA_2 are all equal to zero.

Simulation Algorithm

During the process of meshing, the pinion and gear tooth surfaces must be in continuous tangency, and this condition is provided if their position vectors and normals coincide at any instant. Pinion and gear tooth surfaces are represented in coordinate system S_h as follows:

$$r_h^{(1)}\left(s_p, \theta_p, \psi_1, \phi_1\right) = \mathbf{M}_{h b_1} \mathbf{M}_{b_1 1}\left(\phi_1\right) r_1\left(s_p, \theta_p, \psi_1\right) \tag{21.7.1}$$

$$f_{1p}(s_p, \theta_p, \psi_1) = 0 \tag{21.7.2}$$

$$r_h^{(2)}\left(s_g, \theta_g, \psi_2, \phi_2\right) = \mathbf{M}_{h b_2} \mathbf{M}_{b_2 2}\left(\phi_2\right) r_2\left(s_g, \theta_g, \psi_2\right) \tag{21.7.3}$$

$$f_{2g}(s_g, \theta_g, \psi_2) = 0. \tag{21.7.4}$$

Here,

$$
\mathbf{M}_{b_1 1} = \begin{bmatrix} \cos\phi_1 & \sin\phi_1 & 0 & 0 \\ -\sin\phi_1 & \cos\phi_1 & 0 & 0 \\ 0 & 0 & 1 & 0 \\ 0 & 0 & 0 & 1 \end{bmatrix}
$$

$$
\mathbf{M}_{bb_1} = \begin{bmatrix} 1 & 0 & 0 & 0 \\ 0 & 1 & 0 & 0 \\ 0 & 0 & 1 & \Delta A_1 \\ 0 & 0 & 0 & 1 \end{bmatrix}
$$

$$
\mathbf{M}_{b_2 2} = \begin{bmatrix} \cos\phi_2 & -\sin\phi_2 & 0 & 0 \\ \sin\phi_2 & \cos\phi_2 & 0 & 0 \\ 0 & 0 & 1 & 0 \\ 0 & 0 & 0 & 1 \end{bmatrix}
$$

$$
\mathbf{M}_{bb_2} = \begin{bmatrix} \cos(\gamma + \Delta\gamma) & 0 & -\sin(\gamma + \Delta\gamma) & -\Delta A_2 \sin(\gamma + \Delta\gamma) \\ 0 & 1 & 0 & \Delta E \\ \sin(\gamma + \Delta\gamma) & 0 & \cos(\gamma + \Delta\gamma) & \Delta A_2 \cos(\gamma + \Delta\gamma) \\ 0 & 0 & 0 & 1 \end{bmatrix}.
$$

Vector equation $r_1\,(s_p, \theta_p, \psi_1)$ and equation $f_{1p}(s_p, \theta_p, \psi_1) = 0$ represent the pinion tooth surface in coordinate system S_1 by three related parameters. Similarly, vector equation $r_2\,(s_g, \theta_g, \psi_2)$ and equation $f_{2g}(s_g, \theta_g, \psi_2) = 0$ represent the gear tooth surface in coordinate system S_2 by three related parameters.

Unit normals to tooth surfaces of the pinion and the gear are represented in S_b by the following equations:

$$
n_b^{(1)}\,(s_p, \theta_p, \psi_1, \phi_1) = \mathbf{L}_{b1}\,(\phi_1)\,n_1\,(s_p, \theta_p, \psi_1) \tag{21.7.5}
$$

$$
f_{1p}(s_p, \theta_p, \psi_1) = 0 \tag{21.7.6}
$$

$$
n_b^{(2)}\,(s_g, \theta_g, \psi_2, \phi_2) = \mathbf{L}_{bb_2}\mathbf{L}_{b_2 2}\,(\phi_2)\,n_2\,(s_g, \theta_g, \psi_2) \tag{21.7.7}
$$

$$
f_{2g}(s_g, \theta_g, \psi_2) = 0. \tag{21.7.8}
$$

Here,

$$\mathbf{L}_{b1} = \begin{bmatrix} \cos\phi_1 & \sin\phi_1 & 0 \\ -\sin\phi_1 & \cos\phi_1 & 0 \\ 0 & 0 & 1 \end{bmatrix}$$

$$\mathbf{L}_{b_2 2} = \begin{bmatrix} \cos\phi_2 & -\sin\phi_2 & 0 \\ \sin\phi_2 & \cos\phi_2 & 0 \\ 0 & 0 & 1 \end{bmatrix}$$

$$\mathbf{L}_{bb_2} = \begin{bmatrix} \cos(\gamma + \Delta\gamma) & 0 & -\sin(\gamma + \Delta\gamma) \\ 0 & 1 & 0 \\ \sin(\gamma + \Delta\gamma) & 0 & \cos(\gamma + \Delta\gamma) \end{bmatrix}.$$

Conditions of continuous tangency of pinion and gear tooth surfaces are represented by the following equations:

$$\mathbf{r}_b^{(1)}(s_p, \theta_p, \psi_1, \phi_1) - \mathbf{r}_b^{(2)}(s_g, \theta_g, \psi_2, \phi_2) = \mathbf{0} \tag{21.7.9}$$

$$\mathbf{n}_b^{(1)}(s_p, \theta_p, \psi_1, \phi_1) - \mathbf{n}_b^{(2)}(\theta_g, \psi_2, \phi_2) = \mathbf{0} \tag{21.7.10}$$

$$f_{1p}(s_p, \theta_p, \psi_1) = 0 \tag{21.7.11}$$

$$f_{2g}(s_g, \theta_g, \psi_2) = 0. \tag{21.7.12}$$

Surfaces Σ_1 and Σ_2 are represented in S_b by three related parameters. Equations (21.7.11) and (21.7.12) are the equations of meshing of surfaces Σ_1 and Σ_p, and Σ_2 and Σ_g, respectively. Equations (21.7.9), (21.7.10), (21.7.11), and (21.7.12) describe that surfaces Σ_1 and Σ_2 have coinciding position vectors and surface unit normals at their point of tangency. Vector equations (21.7.9) and (21.7.10) yield three and two scalar equations, respectively. The system of equations from (21.7.9) to (21.7.12) provides seven equations for determination of seven unknowns. The angle of rotation of the pinion, ϕ_1, is considered as the input parameter in the range $-\pi/N_1 < \phi_1 < \pi/N_1$. Parameters $s_p, \theta_p, \psi_1, s_g, \theta_g, \psi_2$, and ϕ_2 are the sought-for unknowns that are determined by solving the seven equations mentioned above [Visual Numerics, Inc., 1998]. It is assumed that the Jacobian of the system (21.7.9), (21.7.10), (21.7.11), and (21.7.12) differs from zero at each iteration.

The paths of contact on the pinion and gear tooth surfaces are represented by the following functions:

$$\mathbf{r}_1(s_p(\phi_1), \theta_p(\phi_1), \psi_1(\phi_1)) \tag{21.7.13}$$

$$\mathbf{r}_2(s_g(\phi_1), \theta_g(\phi_1), \psi_2(\phi_1)). \tag{21.7.14}$$

The function of transmission errors is defined as

$$\Delta\phi_2(\phi_1) = \phi_2(\phi_1) - \frac{N_1}{N_2}\phi_1. \tag{21.7.15}$$

The bearing contact is formed as a set of instantaneous contact ellipses. The lengths of the major and minor axes of the instantaneous contact ellipse and their orientation are determined using the approach proposed in Section 9.3. The computation procedure is based on relations between the principal curvatures and directions between the contacting surfaces. The elastic approach of surfaces is considered to be known. The avoidance of interference in the neighborhood of the contact point M may be tested following the approach represented in Litvin *et al.* [1998a]. An example of design and optimization of a spiral bevel gear drive is represented in Section 21.9.

21.8 APPLICATION OF FINITE ELEMENT ANALYSIS FOR THE DESIGN OF SPIRAL BEVEL GEAR DRIVES
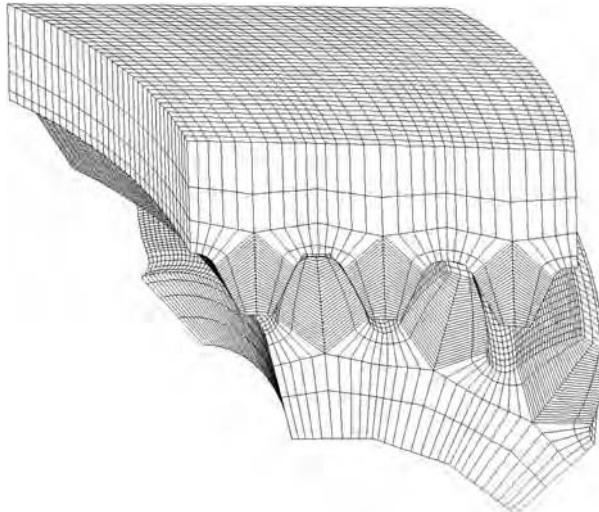
Application of finite element analysis (FEA) enables:

(1) Determination of contact and bending stresses for pinion and gear
(2) Investigation of formation of bearing contact and transfer of load to the next contacting pair of teeth
(3) Detection and avoidance of areas of severe contact stresses for high-loaded gear drives.

Application of the finite element method requires the development of the finite element model formed by the finite element mesh, the definition of contacting surfaces, and the establishment of boundary conditions to load the gear drive with the desired torque. The authors apply a general purpose computer program [Hibbit, Karlsson & Sirensen, Inc., 1998] to perform the finite element analysis.

A modified approach for the performance of finite element analysis has been applied for the design of spiral bevel gear drives (see Section 9.5). One of the main ideas of the applied FEA approach is the automatization of the contacting model of gear teeth by direct application of tooth surfaces (see Section 9.5). This approach enables us to determine contact and bending stresses for the whole cycle of meshing, investigate the formation of the bearing contact and determine, if they exist, hidden areas of severe contact wherein the contact stresses are substantially increased (see Section 21.9).
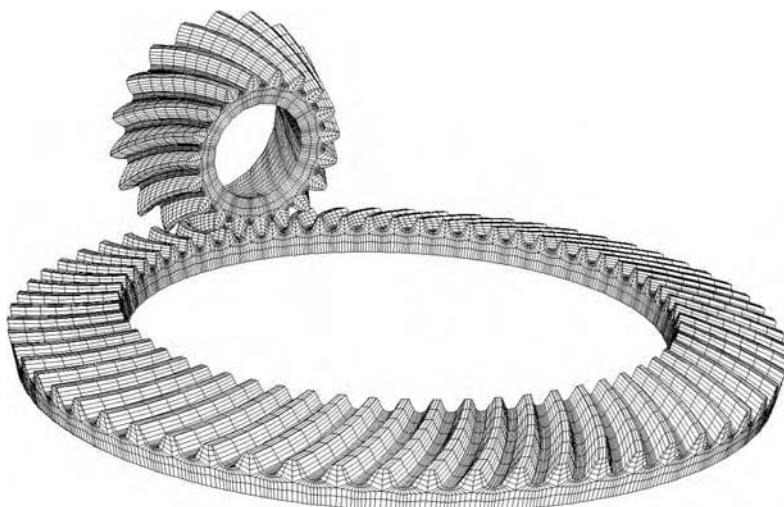
Figures 21.8.1 and 21.8.2 illustrate a finite element mesh with three pairs of teeth and a whole gear drive finite element mesh, respectively. Finite elements of first order enhanced by incompatible modes of deformation to improve their bending behavior [Hibbit, Karlsson & Sirensen, Inc., 1998] are used to build the finite element mesh. The material is steel with the properties of Young's modulus $E = 2.068 \cdot 10^8$ mN/mm^2 and a Poisson's ratio of $\nu = 0.29$.

Figure 21.8.1: Finite element model of three pairs of contacting teeth.

21.9 EXAMPLE OF DESIGN AND OPTIMIZATION OF A SPIRAL BEVEL GEAR DRIVE

An example of design and optimization of a face-milled generated spiral bevel gear drive of gear ratio 9×33 is considered. Table 21.9.1 shows the blank data of the gear drive. Three different cases of design have been considered and they are summarized as follows:

Figure 21.8.2: Finite element model of a whole gear mesh.

Table 21.9.1: Blank data

Design features	Pinion	Gear
Number of teeth of pinion and gear	9	33
Module (mm)	4.8338	4.8338
Shaft angle (deg.)	90.0000	90.0000
Mean spiral angle (deg.)	32.0000	32.0000
Hand of spiral	RH	LH
Face width (mm)	27.5000	27.5000
Mean cone distance (mm)	68.9200	68.9200
Whole depth (mm)	9.4300	9.4300
Pitch angles (deg.)	15.2551	74.7449
Root angles (deg.)	13.8833	69.5833
Face angles (deg.)	20.4167	76.1167
Clearance (mm)	1.0300	1.0300
Addendum (mm)	6.6400	1.7600
Dedendum (mm)	2.7900	7.6700

- **Case 1a:** The existing design is obtained directly from the data of manufacturing of the gear and the pinion of the gear drive. Application of TCA and FEA allows simulation of the performance of the existing design and establishes the baseline level of transmission errors and stresses before optimization.
- **Case 1b:** This is the result of application of the first iteration of stages 1 to 4 as described in Section 21.2 wherein a longitudinal path of contact is provided and straight-line blade profiles have been used for generation of the pinion and gear.
- **Case 1c:** This is the result of application of stages 1 to 4 wherein a longitudinal path of contact is provided and blades of *parabolic* profile have been used for gear generation. The pinion is generated by blades of straight-line profiles. The parabola coefficient has been obtained to avoid hidden areas of severe contact.

For all cases of design, both sides of the gear space are generated simultaneously by the head-cutter. The data of the gear head-cutter that generates the gear tooth surfaces for the three cases of design are represented in Table 21.9.2. Table 21.9.3 shows the pinion machine-tool settings considered for the existing design (Case 1a) and the pinion machine-tool settings obtained from computations that provide improved conditions of meshing and contact of the gear drive (Cases 1b and 1c of design).

We consider the convex side of the pinion tooth surface as the driving side and the concave side of the gear tooth surface as the driven side. Figure 21.9.1 shows the results of TCA for the case of design 1a corresponding to the existing design of the spiral bevel gear drive. The path of contact for the existing design is directed across the surface. The obtained shape of the function of transmission errors is a parabolic one with a maximum level of about 8 arcsec.

Table 21.9.2: Parameters and installment settings of the gear head-cutter for design cases 1a, 1b, and 1c

Applied settings	Cases 1a and 1b	Case 1c
Average cutter diameter (mm)	127.0000	127.0000
Point width (mm)	2.5400	2.5400
Pressure angle, concave (outside blade) (deg.)	22.0000	22.0000
Pressure angle, convex (inside blade) (deg.)	22.0000	22.0000
Blade profile parabola coefficient, concave (1/mm)	0.0000	0.0020
Blade profile parabola coefficient, convex (1/mm)	0.0000	0.0000
Parabola vertex location, concave (mm)	0.0000	4.7279
Parabola vertex location, convex (mm)	0.0000	4.7069
Root fillet radius, concave and convex (mm)	1.5240	1.5240
Machine center to back (mm)	0.0000	0.0000
Sliding base (mm)	−0.2071	−0.2071
Blank offset (mm)	0.0000	0.0000
Radial distance (mm)	64.3718	64.3718
Machine root angle (deg.)	69.5900	69.5900
Cradle angle (deg.)	−56.7800	−56.7800
Velocity ratio	1.032331	1.032331

Application of finite element analysis allows us to investigate the formation of the bearing contact for the whole cycle of meshing and investigate the transfer of load between neighboring pairs of teeth.
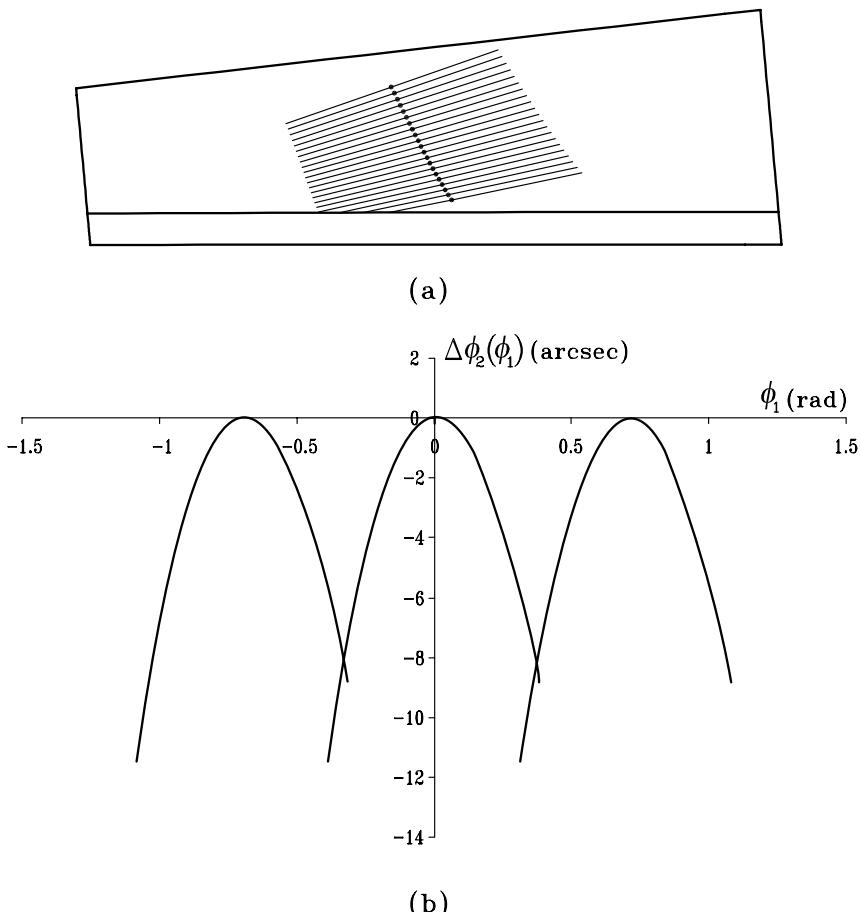
Figures 21.9.2 and 21.9.3 show the bending and contact stresses obtained for the pinion and gear, respectively, of design case 1a at the most unfavorable position of meshing. A torque of 419.16 Nm has been applied to the pinion of the gear drive. Severe areas of contact have been found for the pinion and the gear at the contact point shown in Figs. 21.9.2 and 21.9.3 wherein high contact stresses occur.

In the first iteration of computation, after completion of stages 1 and 4, the pinion machine-tool settings of case 1b are obtained. Application of finite element analysis allows us to investigate the formation of the bearing contact for this new design of the gear drive and detect a small area of severe contact for both the pinion and the gear inside the cycle of meshing. Figure 21.9.4 shows the contact and bending stresses for the pinion for design case 1b at the most unfavorable point of meshing inside the cycle of meshing wherein such small areas of severe contact occur. Figure 21.9.5 shows similar results for the gear for design case 1b. However, contact stresses for this case of design have already been drastically reduced.

The appearance of those areas of severe contact wherein a longitudinal path of contact is provided can be avoided if mismatch is provided between the profiles of the head-cutters that generate the gear and the pinion. The author's approach is based on application of parabolic blades for generation of the gear whereas the pinion is still generated by blades of straight-line profile. However, if more mismatch is necessary, parabolic blades can also be applied for pinion generation.

Table 21.9.3: Parameters and installment settings of the pinion head-cutter for design cases 1a, 1b, and 1c

Applied settings	Case 1a		Case 1b		Case 1c	
	Concave	Convex	Concave	Convex	Concave	Convex
Cutter point diameter (mm)	116.8400	138.6840	114.3483	136.1114	114.3483	138.9061
Pressure angle (deg.)	22.0000	22.0000	22.0000	22.0000	22.0000	22.0000
Root fillet radius (mm)	0.6350	0.6350	0.6350	0.6350	0.6350	0.6350
Machine center to back (mm)	-0.7749	1.2739	-1.9793	5.4860	-1.9793	6.3096
Sliding base (mm)	-6.0857	-6.2067	-0.3352	-2.1264	-0.3352	-2.3241
Blank offset (mm)	-0.6288	1.6201	-2.9984	-10.9672	-2.9984	-9.4557
Radial distance (mm)	62.7493	66.3276	62.2550	79.4459	62.2550	79.3430
Machine root angle (deg.)	13.8833	13.8833	13.8833	13.8833	13.8833	13.8833
Cradle angle (deg.)	53.0400	59.4500	59.3751	55.5190	59.3751	55.3037
Swivel angle (deg.)	-20.8800	28.6300	0.0000	0.0000	0.00000	0.0000
Tilt Angle (deg.)	-5.4400	4.1200	0.0000	0.0000	0.00000	0.0000
Velocity ratio	3.837460	3.779475	3.667770	4.543130	3.667770	4.546945
Modified Roll Coefficient C	0.00000	0.0000	-0.001180	0.00704	-0.001180	0.00653
Modified Roll Coefficient D	0.00000	0.0000	0.006460	-0.14949	0.006460	-0.15951

(a)

(b)
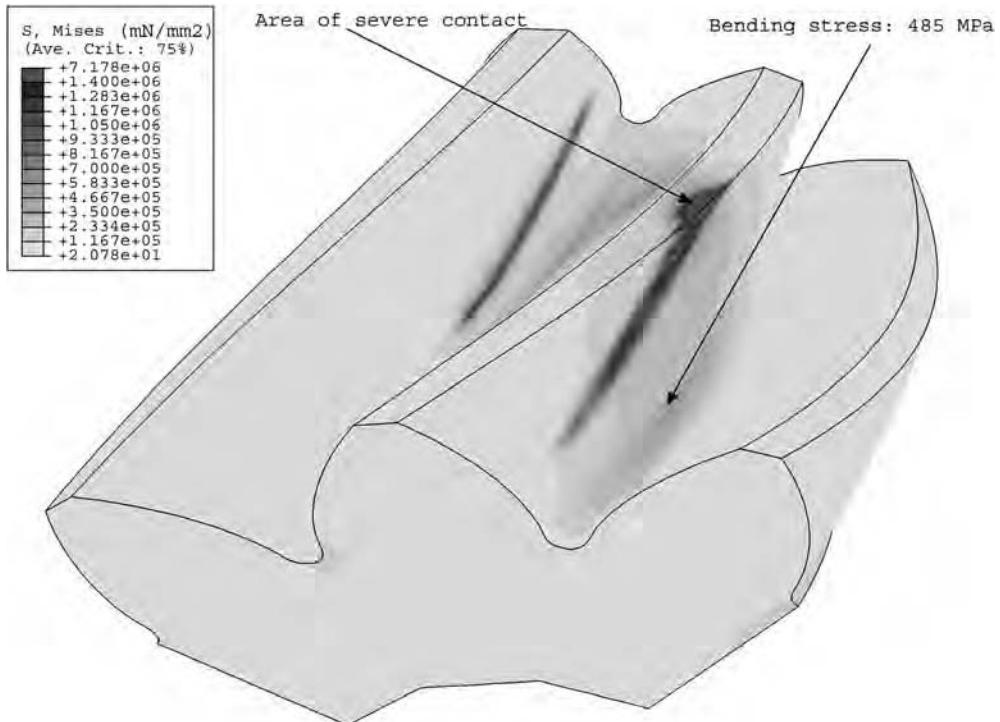
Figure 21.9.1: (a) Bearing contact, and (b) function of transmission errors of existing design (case 1a).
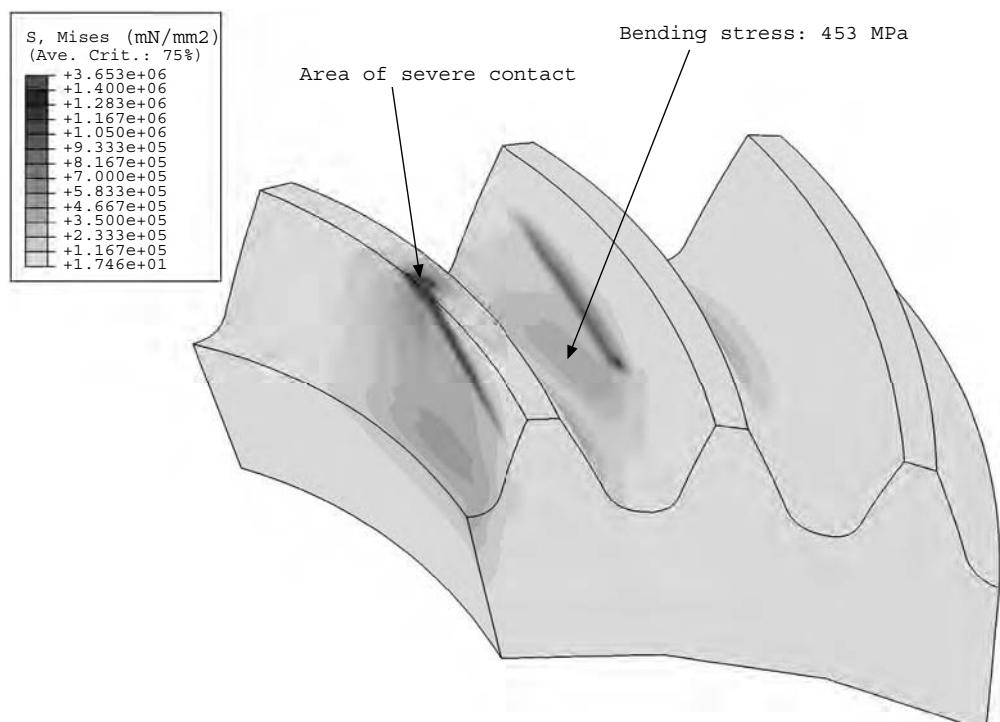
Figures 21.9.6(a) and 21.9.6(b) show the bearing contact obtained for design cases 1b and 1c, respectively. Figure 21.9.6(c) shows the predesigned parabolic function of transmission errors for both cases of design. Figure 21.9.7 shows the contact and bending stresses for the pinion for design case 1c at the same contact position as the one represented in Fig. 21.9.4. It is shown in Fig. 21.9.7 that areas of severe contact have been avoided for the pinion for design case 1c wherein parabolic blades have been applied for generation of the gear.

Figure 21.9.8 shows the contact and bending stresses for the gear for design case 1c at the same contact position as that in Fig. 21.9.5. It is shown in Fig. 21.9.8 that areas of severe contact have been avoided for the gear for design case 1c as well. Figures 21.9.9 and 21.9.10 show the evolution of contact and bending stresses for the pinion and the gear, respectively, for design cases 1a, 1b, and 1c.
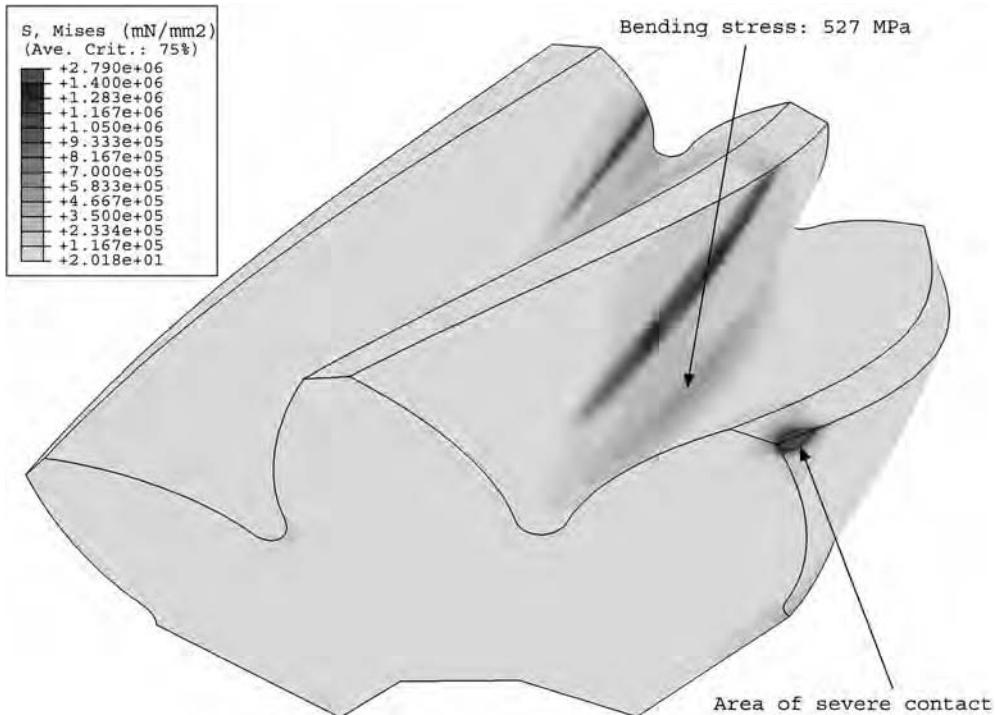
A substantial reduction of contact stresses could be achieved for the pinion in design cases 1b and 1c with respect to the existing design of the pinion of the gear drive. Design
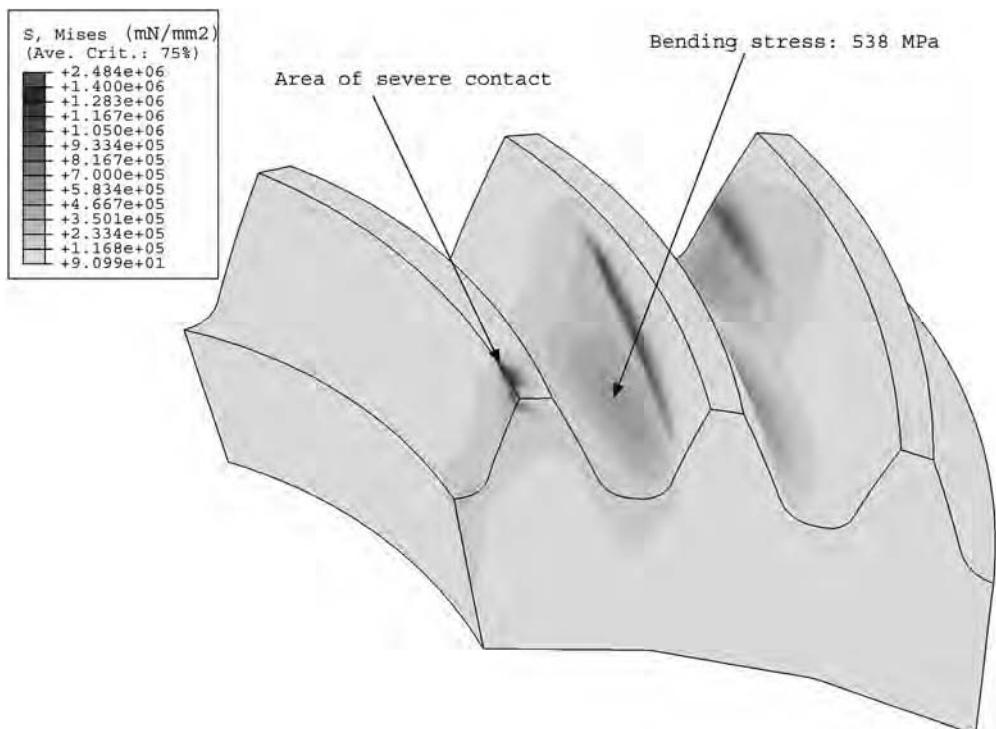
Figure 21.9.2: Contact and bending stresses for the pinion for design case 1a.
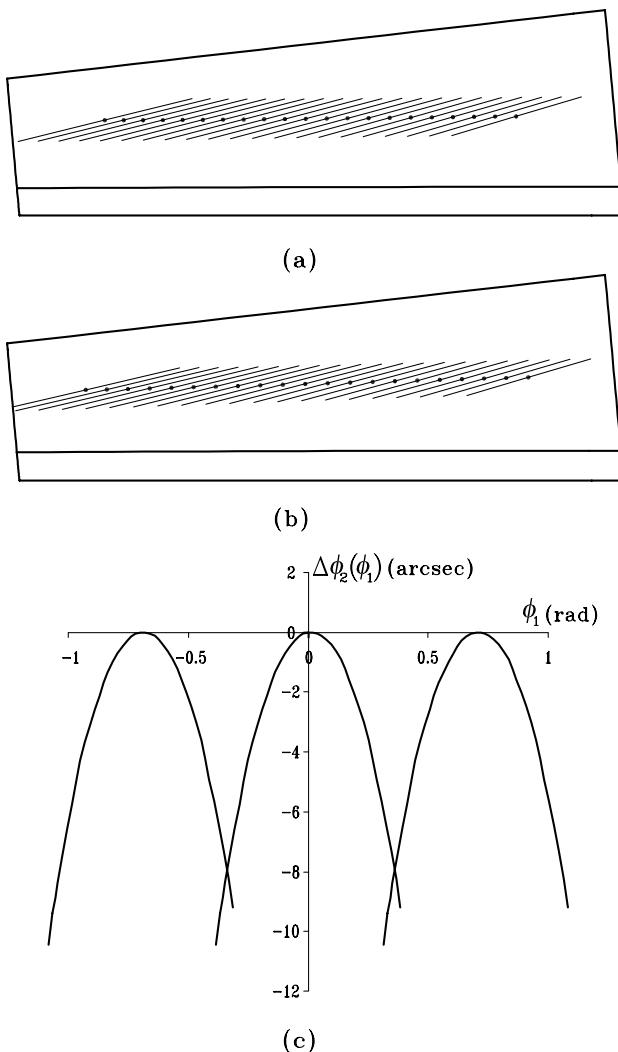
Figure 21.9.3: Contact and bending stresses for the gear for design case 1a.
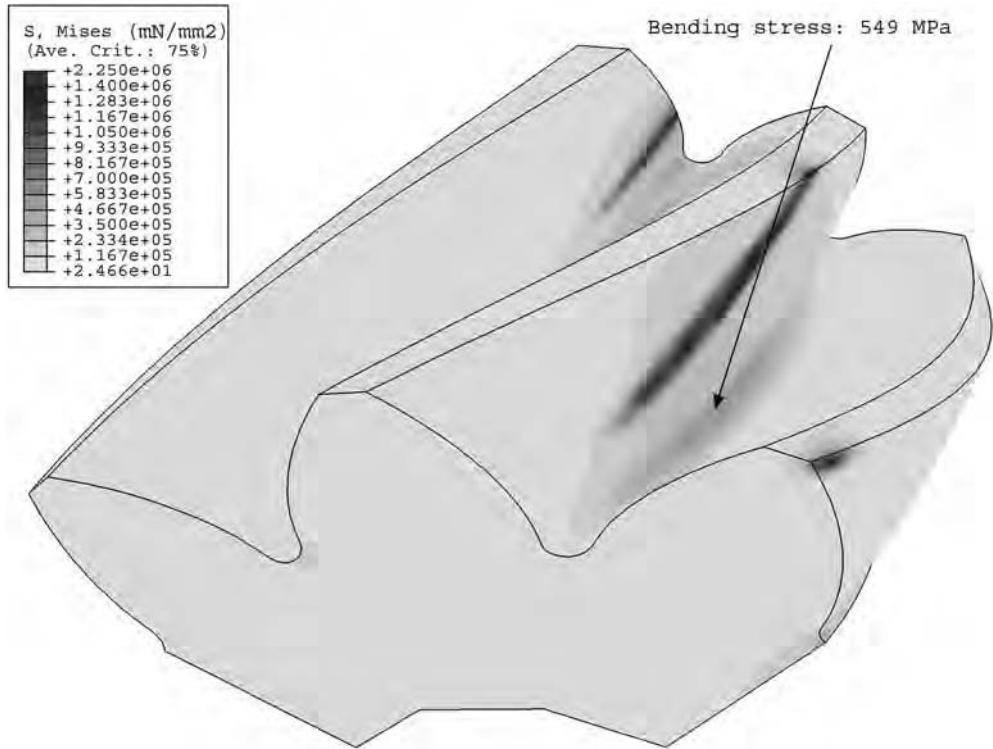
Figure 21.9.4: Contact and bending stresses for the pinion for design case 1b.
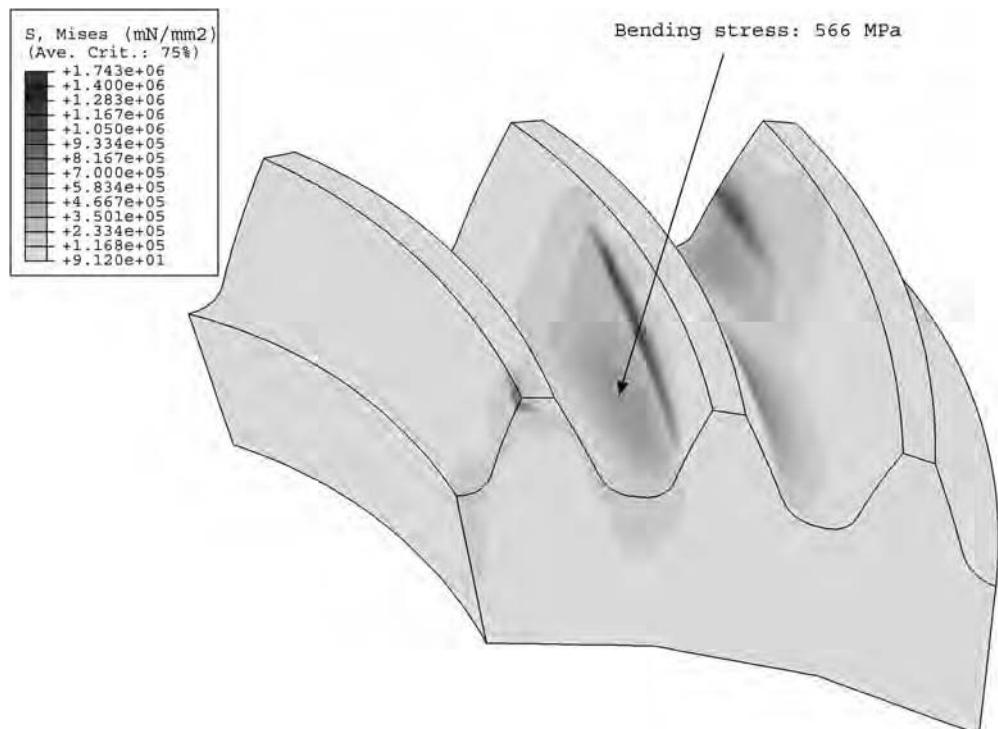
Figure 21.9.5: Contact and bending stresses for the gear for design case 1b.

(a)

(b)

(c)
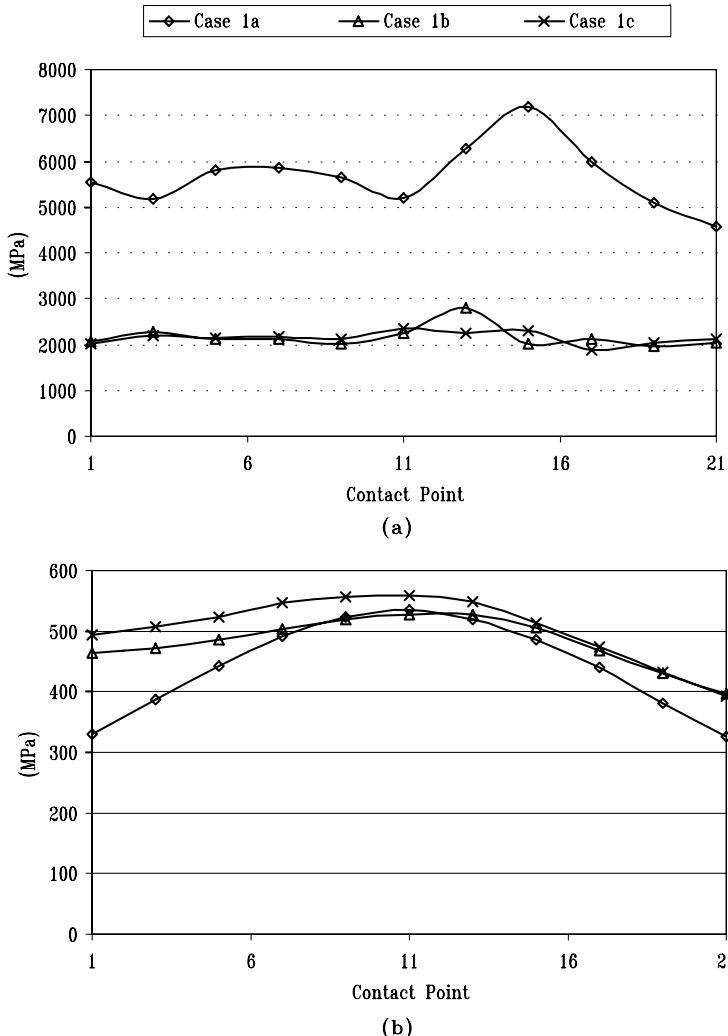
Figure 21.9.6: (a) and (b) bearing contact for design cases 1b and 1c, respectively, and (c) function of transmission errors for both cases of design.

Figure 21.9.7: Contact and bending stresses for the pinion for design case 1c.
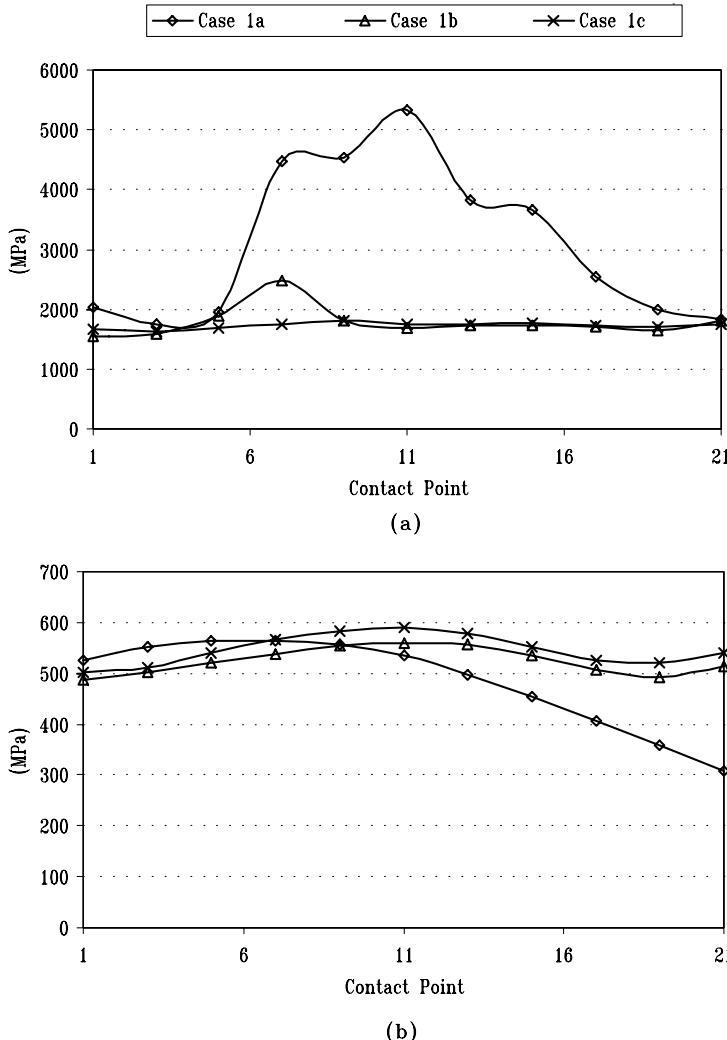
Figure 21.9.8: Contact and bending stresses for the gear for design case 1c.

Figure 21.9.9: Evolution of contact and bending stresses for the pinion for design cases 1a, 1b, and 1c.

case 1c enables us to avoid the appearance of a small area of severe contact at the top edge of the pinion with a higher level of contact stresses as shown in Figure 21.9.9(a). On the contrary, bending stresses for design cases 1b and 1c are higher than they are for the existing case of design as shown in Fig. 21.9.9(b).

A substantial reduction of contact stresses could be achieved as well for the gear for design cases 1b and 1c with respect to the existing design of the gear of the gear drive. The same results as previously discussed for the pinion have been obtained for the gear for design cases 1b and 1c as shown in Fig. 21.9.10.
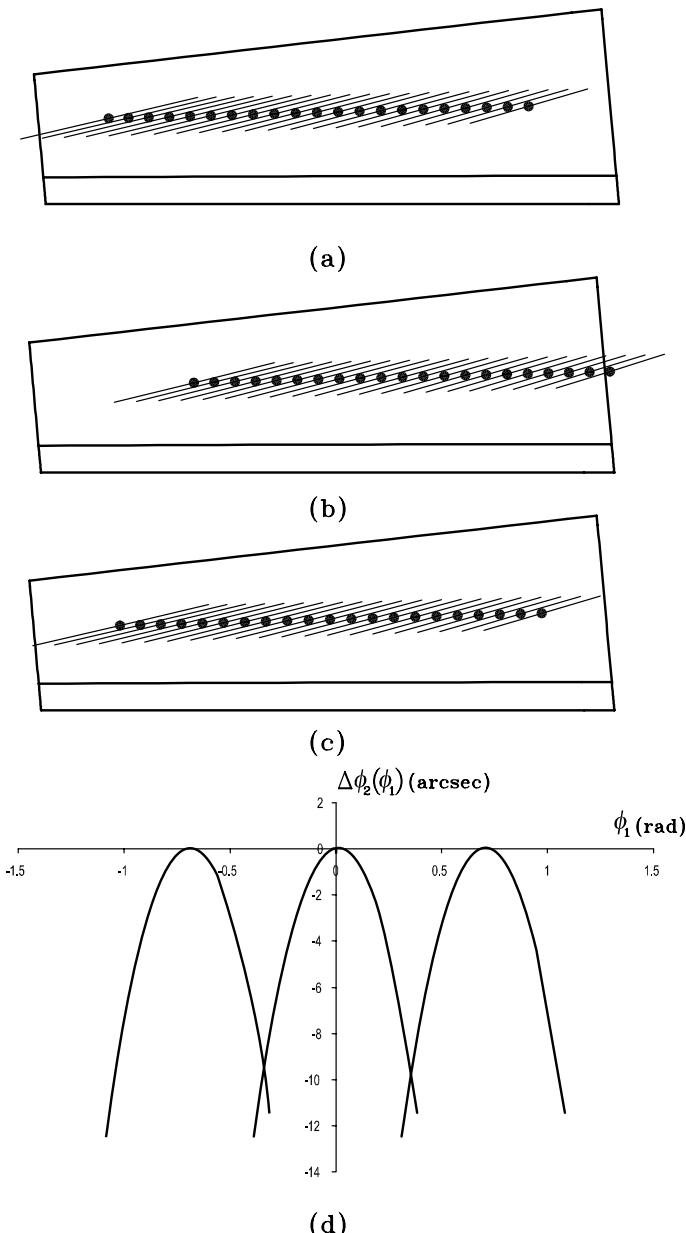
Figure 21.9.10: Evolution of contact and bending stresses for the gear for design cases 1a, 1b, and 1c.

21.10 COMPENSATION OF THE SHIFT OF THE BEARING CONTACT

Spiral bevel gear drives are very sensitive to the shortest distance between the axes of the pinion and the gear, ΔE, when the pinion–gear axes are not intersected but crossed. However, the shift of the bearing contact due to error of alignment ΔE can be compensated by the axial displacement ΔA_1 of the pinion. Figure 21.10.1 shows an example of compensation of an error of alignment $\Delta E = 0.02$ mm for design case 1c.

Figure 21.10.1(a) shows the path of contact for design case 1c when no errors of alignment occur. Figure 21.10.1(b) shows the path of contact for an error of alignment

(a)

(b)

(c)

(d)

Figure 21.10.1: Design case 1c: (a) path of contact when no errors of alignment occur, (b) path of contact for error of alignment $\Delta E = 0.02$ mm, (c) path of contact when error of alignment $\Delta E = 0.02$ mm is compensated by $\Delta A_1 = -0.05$ mm, (d) function of transmission errors for conditions of item (c).

$\Delta E = 0.02$ mm. Figure 21.10.1(c) shows the path of contact for an error of alignment $\Delta E = 0.02$ mm and an axial displacement of the pinion $\Delta A_1 = -0.05$ mm. As shown in Fig. 21.10.1(c), an axial displacement of the pinion may compensate the shift of the path of contact caused by an error ΔE of the shortest distance between axes. Figure 21.10.1(d) shows the function of transmission errors when an error of alignment $\Delta E = 0.02$ mm is compensated by an axial displacement of the pinion $\Delta A_1 = -0.05$ mm. The function of transmission errors is still of parabolic shape.

22 **Hypoid Gear Drives**

22.1 INTRODUCTION

Hypoid gear drives have found a broad application in the automotive industry for transformation of rotation between crossed axes. Enhanced design and generation of hypoid gear drives requires an approach based on the ideas discussed for spiral bevel gears (see Chapter 21).

The contents of this chapter are limited to (i) design of pitch cones, (ii) pinion and gear machine-tool settings, and (iii) equations of pinion–gear tooth surfaces. Design of pitch cones for hypoid gears was the subject of research performed by Baxter [1961], Litvin *et al.* [1974, 1990] and Litvin [1994]. Details of determination of machine-tool settings for manufacture of hypoid gears are given in Litvin & Gutman [1981].

22.2 AXODES AND OPERATING PITCH CONES
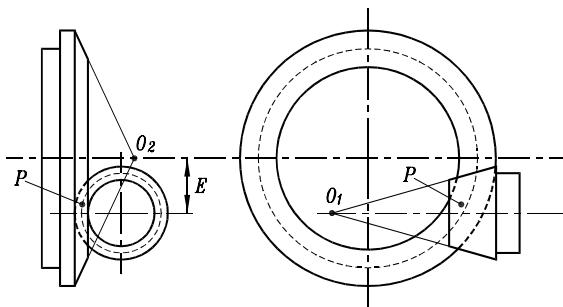
Spiral bevel gears perform rotation about intersected axes, and their axodes are two cones (Section 3.4). The line of tangency of these cones is the instantaneous axis of rotation in relative motion. In the case of standard spiral bevel gears, the gear axodes coincide with the pitch cones.

Hypoid gears perform rotation about crossed axes, the relative motion is a screw motion, and instead of the instantaneous axis of rotation we have to consider the instantaneous screw axis s–s (Section 3.5). The gear axodes are two hyperboloids of revolution that are in tangency along the axis of screw motion s–s (Fig. 3.5.1). The hypoid pinion–gear axodes (the hyperboloids of revolution) perform in relative motion rotation about and translation along s–s.

The concept of axodes of hypoid gears has found a limited application in design and is used merely for visualization of relative velocity. The main reason for this is that the location of axodes is out of the zone of meshing of hypoid gears.

The design of blanks of hypoid gears is meant to determine operating pitch cones instead of hyperboloids of revolution, the hypoid gear axodes. The operating pitch cones (Fig. 22.2.1) must satisfy the following requirements:

(a) The axes of the pitch cones form the prescribed crossing angle γ between the axes of rotation (usually, $\gamma = 90°$).
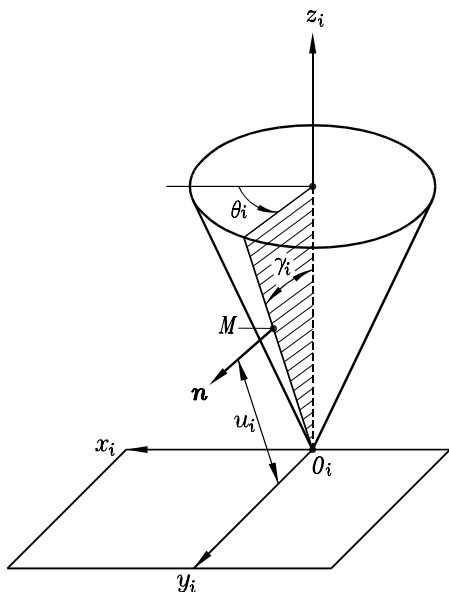
Figure 22.2.1: Operating pitch cones of hypoid gears.

(b)   The shortest distance E between the axes of the pitch cones is equal to the prescribed value of the hypoid gear drive.

(c)   The pitch cones are in tangency at the prescribed point P that is located in the zone of meshing of the pinion–gear tooth surfaces.

(d)   The relative (sliding) velocity at point P is directed along the common tangent to the "helices" of contacting pitch cones. The term "helix" is used to denote a curve obtained by intersection of the tooth surface by the pitch cone.

22.3 TANGENCY OF HYPOID PITCH CONES

A cone is represented in coordinate system S_i by the equations (Fig. 22.3.1)

$$
\begin{aligned}
x_i &= u_i \sin \gamma_i \cos \theta_i \\
y_i &= u_i \sin \gamma_i \sin \theta_i \quad (i = 1, 2) \\
z_i &= u_i \cos \gamma_i
\end{aligned}
\tag{22.3.1}
$$

Figure 22.3.1: Operating pitch cone and its parameters.

where (u_i, θ_i) are the surface coordinates (the Gaussian coordinates). The surface unit normal is represented by the equations

$$\mathbf{n}_i = \frac{\mathbf{N}_i}{|\mathbf{N}_i|}, \quad \mathbf{N}_i = \frac{\partial \mathbf{r}_i}{\partial u_i} \times \frac{\partial \mathbf{r}_i}{\partial \theta_i}. \tag{22.3.2}$$

Equations (22.3.1) and (22.3.2) yield (providing $u_i \sin \gamma_i \neq 0$)

$$\mathbf{n}_i = [\cos \theta_i \cos \gamma_i \quad \sin \theta_i \cos \gamma_i \quad - \sin \gamma_i]^\mathrm{T}. \tag{22.3.3}$$

To derive the equations of tangency of the pitch cones at the pitch point P, we represent the pitch cones in the fixed coordinate system S_f.

The location and orientation of coordinate systems S_1 and S_2 with respect to S_f are shown in Fig. 22.4.1. Coordinate transformation from S_1 and S_2 to S_f allows us to represent in coordinate system S_f the pitch cones of the pinion and the gear and their unit normals by the following vector functions:

$$\mathbf{r}_f^{(1)}(u_1, \theta_1) = \begin{bmatrix} r_1 \cos \theta_1 \\ r_1 \sin \theta_1 \\ r_1 \cot \gamma_1 - d_1 \end{bmatrix} \tag{22.3.4}$$

$$\mathbf{n}_f^{(1)}(\theta_1) = \begin{bmatrix} \cos \gamma_1 \cos \theta_1 \\ \cos \gamma_1 \sin \theta_1 \\ - \sin \gamma_1 \end{bmatrix} \tag{22.3.5}$$

$$\mathbf{r}_f^{(2)}(u_2, \theta_2) = \begin{bmatrix} r_2 \cos \theta_2 + E \\ -r_2 \cot \gamma_2 + d_2 \\ r_2 \sin \theta_2 \end{bmatrix} \tag{22.3.6}$$

$$\mathbf{n}_f^{(2)}(\theta_2) = \begin{bmatrix} - \cos \gamma_2 \cos \theta_2 \\ - \sin \gamma_2 \\ - \cos \gamma_2 \sin \theta_2 \end{bmatrix}. \tag{22.3.7}$$

Here, d_i $(i = 1, 2)$ determines the location of the apex of the pitch cone.

The pitch cones are in tangency at the pitch point P, and the equations of tangency are

$$\mathbf{r}_f^{(1)}(u_1, \theta_1) = \mathbf{r}_f^{(2)}(u_2, \theta_2) = \mathbf{r}_f^{(P)} \tag{22.3.8}$$

$$\mathbf{n}_f^{(1)}(\theta_1) = \mathbf{n}_f^{(2)}(\theta_2) = \mathbf{n}_f^{(P)} \tag{22.3.9}$$

where $\mathbf{r}_f^{(P)}$ and $\mathbf{n}_f^{(P)}$ are the position vector and the common normal to the pitch cones at pitch point P. The mating pitch cones are located above and below the pitch plane. Therefore, their surface unit normals have opposite directions at P and the coincidence of the surface unit normals is provided with the negative sign in Eq. (22.3.9).

Vector equations (22.3.8) and (22.3.9) provide the six scalar equations

$$r_1 \cos \theta_1 = r_2 \cos \theta_2 + E = x_f^{(P)} \tag{22.3.10}$$

$$r_1 \sin \theta_1 = -r_2 \cos \theta_2 + d_2 = y_f^{(P)} \tag{22.3.11}$$

$$r_1 \cot \gamma_1 - d_1 = r_2 \sin \theta_2 = z_f^{(P)}, \tag{22.3.12}$$

where $r_i = u_i \sin \gamma_i$ is the radius of the pitch cone at P, and

$$\cos \gamma_i \cos \theta_i = -\cos \gamma_2 \cos \theta_2 = n_{xf}^{(P)} \tag{22.3.13}$$

$$\cos \gamma_i \sin \theta_i = -\sin \gamma_2 = n_{yf}^{(P)} \tag{22.3.14}$$

$$-\sin \gamma_1 = -\cos \gamma_2 \sin \theta_2 = n_{zf}^{(P)}. \tag{22.3.15}$$

Only two equations of the equation system (22.3.13) to (22.3.15) are independent because $|\mathbf{n}_f^{(1)}| = |\mathbf{n}_f^{(2)}| = 1$.

Eliminating $\cos \theta_i$ and $\sin \theta_i$, we obtain after some transformation the following equations:

$$\frac{r_1}{r_2} = \frac{(E/r_2) \cos \gamma_1}{\sqrt{\cos^2 \gamma_1 - \sin^2 \gamma_2}} - \frac{\cos \gamma_1}{\cos \gamma_2} \tag{22.3.16}$$

$$d_1 = -\frac{r_2}{\cos \gamma_2 \sin \gamma_1} + \frac{E \cos \gamma_1 \cot \gamma_1}{\sqrt{\cos^2 \gamma_1 - \sin^2 \gamma_2}} \tag{22.3.17}$$

$$d_2 = \frac{r_2}{\cos \gamma_2 \sin \gamma_2} - \frac{E \sin \gamma_2}{\sqrt{\cos^2 \gamma_1 - \sin^2 \gamma_2}} \tag{22.3.18}$$

$$x_f^{(P)} = E - \frac{r_2 \sqrt{\cos^2 \gamma_1 - \sin^2 \gamma_2}}{\cos \gamma_2} \tag{22.3.19}$$

$$y_f^{(P)} = r_2 \tan \gamma_2 - \frac{E \sin \gamma_2}{\sqrt{\cos^2 \gamma_1 - \sin^2 \gamma_2}} \tag{22.3.20}$$

$$z_f^{(P)} = \frac{r_2 \sin \gamma_1}{\cos \gamma_2} \tag{22.3.21}$$

$$n_{xf}^{(P)} = \sqrt{\cos^2 \gamma_2 - \sin^2 \gamma_1} \tag{22.3.22}$$
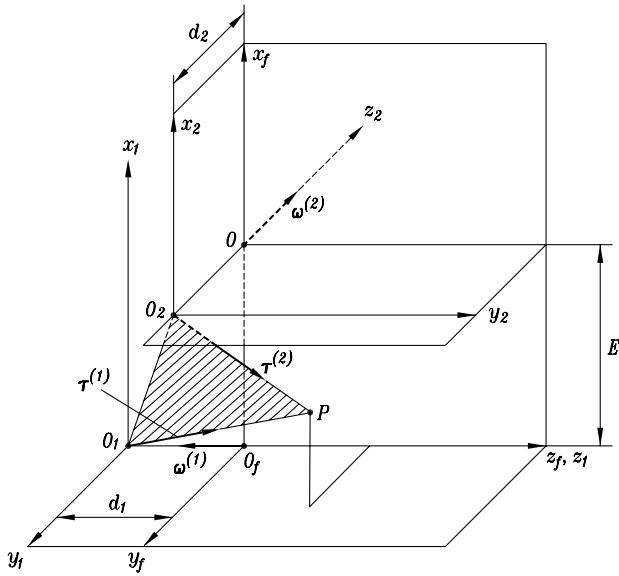
$$n_{yf}^{(P)} = -\sin \gamma_2 \tag{22.3.23}$$

$$n_{zf}^{(P)} = -\sin \gamma_1. \tag{22.3.24}$$

The derived equations are the basis for the design of hypoid pitch cones (see Section 22.5).

22.4 AUXILIARY EQUATIONS

The plane of tangency of the pitch cones is determined as the plane that passes through the cone apexes O_1 and O_2 and the pitch point P (Fig. 22.4.1). Unit vectors $\boldsymbol{\tau}^{(1)}$ and $\boldsymbol{\tau}^{(2)}$ represent the generatrices of the pitch cones that lie in the pitch plane and intersect each other at pitch point P. For further derivations we use the concept of the tooth longitudinal shape and the sliding velocity at the pitch point.
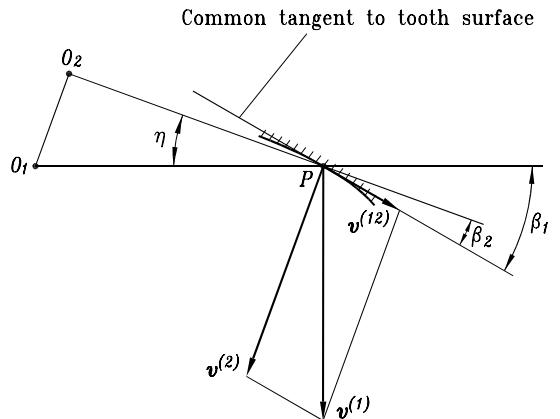
Figure 22.4.1: Pitch plane.

Tooth Longitudinal Shapes

The longitudinal shape of the tooth in the pitch plane is the curve of intersection of the tooth surface with the pitch plane. It would be incorrect to call the longitudinal shape a helix or a spiral. Figure 22.4.2 shows that the longitudinal shapes are in tangency at P. The so-called "spiral" angle β_i in the pitch plane is formed by the common tangent to the longitudinal shape and the generatrix to the respective pitch cone that passes through P.

The generatrices of the pitch cones form angle η that is represented by the equation

$$\cos \eta = \boldsymbol{\tau}^{(1)} \cdot \boldsymbol{\tau}^{(2)}. \tag{22.4.1}$$

Figure 22.4.2: Orientation of relative velocity at the pitch point.

The unit vectors $\boldsymbol{\tau}^{(i)}$ ($i = 1, 2$) of generatrices $\overline{O_i P}$ are represented by the equations

$$\boldsymbol{\tau}^{(1)} = \frac{\overline{O_1 P}}{|\overline{O_1 P}|} = \frac{\dfrac{\partial \mathbf{r}_f^{(1)}}{\partial u_1}}{\left| \dfrac{\partial \mathbf{r}_f^{(1)}}{\partial u_1} \right|} = [\sin \gamma_1 \cos \theta_1 \quad \sin \gamma_1 \sin \theta_1 \quad \cos \gamma_1]^{\mathrm{T}} \quad (22.4.2)$$

$$\boldsymbol{\tau}^{(2)} = \frac{\overline{O_2 P}}{|\overline{O_2 P}|} = \frac{\dfrac{\partial \mathbf{r}_f^{(2)}}{\partial u_2}}{\left| \dfrac{\partial \mathbf{r}_f^{(2)}}{\partial u_2} \right|} = [\sin \gamma_2 \cos \theta_2 \quad -\cos \gamma_2 \quad \sin \gamma_2 \sin \theta_2]^{\mathrm{T}}. \quad (22.4.3)$$

Using Eqs. (22.4.1), (22.4.2), and (22.4.3), we obtain

$$\cos \eta = \tan \gamma_1 \tan \gamma_2. \quad (22.4.4)$$

Taking into account that $\eta = \beta_1 - \beta_2$, we derive

$$\cos(\beta_1 - \beta_2) = \tan \gamma_1 \tan \gamma_2. \quad (22.4.5)$$

Sliding Velocity at the Pitch Point

The sliding velocity of the pinion with respect to the gear is represented at the pitch point P by the equations

$$\mathbf{v}^{(12)} = \mathbf{v}^{(1)} - \mathbf{v}^{(2)} = \left[(\boldsymbol{\omega}^{(1)} - \boldsymbol{\omega}^{(2)}) \times \mathbf{r}^{(P)} \right] - (\mathbf{E} \times \boldsymbol{\omega}^{(2)}). \quad (22.4.6)$$

Here, $\mathbf{r}^{(P)} = \overline{O_f P}$ is the position vector of P in coordinate system S_f; angular velocity vector $\boldsymbol{\omega}^{(1)}$ passes through the origin O_f of S_f (Fig. 22.4.1); $\mathbf{E}$ is the position vector that is drawn from O_f to an arbitrary point of the line of action of $\boldsymbol{\omega}^{(2)}$.

Because vectors $\mathbf{v}^{(1)}$ and $\mathbf{v}^{(2)}$ are determined for point P, they lie in the pitch plane and are perpendicular to the generatrices $\overline{O_1 P}$ and $\overline{O_2 P}$ of the pitch cones, respectively (Fig. 22.4.2). Using Eq. (22.4.6), we obtain after some transformations the equations

$$\mathbf{v}^{(12)} = -\omega_1 r_1 (\tan \beta_1 - \tan \beta_2) \cos \beta_1 \begin{bmatrix} 0 \\ \sin \beta_1 \\ \cos \beta_1 \end{bmatrix} \quad (22.4.7)$$

$$m_{12} = \frac{\omega_1}{\omega_2} = \frac{r_2 \cos \beta_2}{r_1 \cos \beta_1} = \frac{N_2}{N_1} \quad (22.4.8)$$

where N_1 and N_2 are the numbers of teeth.

Vector $\mathbf{v}^{(12)}$ is represented in coordinate system S_e ($\mathbf{e}_1, \mathbf{e}_2, \mathbf{e}_3$) [see Litvin *et al.*, 1989 and Litvin, 1994]. Here, $\mathbf{e}_1$ is the unit normal to the pitch plane, $\mathbf{e}_3 = \boldsymbol{\tau}^{(1)}$ is the unit vector to the generatrix of the pinion pitch cone (Fig. 22.4.1), and $\mathbf{e}_2 = \mathbf{e}_3 \times \mathbf{e}_1$.

$$\tan \beta_1 = \frac{m_{12} r_1 - r_2 \cos \eta}{r_2 \sin \eta}. \quad (22.4.9)$$

$$\tan \beta_2 = \frac{r_1 \cos \eta - m_{21} r_2}{r_1 \sin \eta}. \quad (22.4.10)$$

22.5 DESIGN OF HYPOID PITCH CONES

The basic design parameters of pitch cones are β_i, γ_i, and d_i ($i = 1, 2$). Here, γ_i is the pitch cone angle (Fig. 22.3.1); β_i is the "spiral" angle (Fig. 22.4.2); and d_i determines the location of the pitch cone apex (Fig. 22.4.1).

Relations Between β_i and γ_i ($i = 1, 2$)
Four parameters β_i, γ_i are related with three equations of the following structure:

$$f_1(\gamma_1, \gamma_2, \beta_1) = 0 \tag{22.5.1}$$

$$f_2(\gamma_1, \gamma_2, \beta_1, \beta_2) = 0 \tag{22.5.2}$$

$$f_3(\gamma_1, \gamma_2, \beta_1, \beta_2) = 0. \tag{22.5.3}$$

Parameter β_1 is considered as given (usually, $\beta_1 = 45°$). Our goal is to derive equation system (22.5.1) to (22.5.3). Equations (22.5.1) and (22.5.2) are the same for both types of hypoid gear drives, with face-milled tapered teeth and face-hobbed teeth of uniform depth. The third equation must be derived for each type of hypoid gear drive separately. Face-milled teeth are generated by a surface, the cone surface of the head-cutter. Face-hobbed teeth are generated by a line, the blade edge.

Derivation of Equations (22.5.1) and (22.5.2)
The derivation is based on the following procedure:
  Step 1: Equations (22.3.16) and (22.4.8) yield

$$\frac{\dfrac{E}{r_2}\cos\gamma_1}{(\cos^2\gamma_1 - \sin^2\gamma_2)^{0.5}} - \frac{\cos\gamma_1}{\cos\gamma_2} = \frac{N_1\cos\beta_2}{N_2\cos\beta_1}. \tag{22.5.4}$$

Thus,

$$\cos\beta_2 = \frac{\cos\beta_1}{b} \tag{22.5.5}$$

where

$$b = \frac{N_1\cos\gamma_2(\cos^2\gamma_1 - \sin^2\gamma_2)^{0.5}}{N_2\cos\gamma_1\left[\dfrac{E}{r_2}\cos\gamma_2 - (\cos^2\gamma_1 - \sin^2\gamma_2)^{0.5}\right]}. \tag{22.5.6}$$

  Step 2: We represent Eq. (22.4.5) as

$$\cos(\beta_1 - \beta_2) = \cos\beta_1\cos\beta_2 + \sin\beta_1\sin\beta_2 = a \tag{22.5.7}$$

where

$$a = \tan\gamma_1\tan\gamma_2. \tag{22.5.8}$$

Equations (22.5.5) and (22.5.7) yield

$$\left(\frac{\cos^2 \beta_1}{b} - a\right)^2 = (-\sin \beta_1 \sin \beta_2)^2 = (1 - \cos^2 \beta_1)(1 - \cos^2 \beta_2)$$

$$= (1 - \cos^2 \beta_1)\left(1 - \frac{\cos^2 \beta_1}{b^2}\right). \tag{22.5.9}$$

Using Eq. (22.5.9), we obtain after simple transformations that

$$\cos^2 \beta_1 - \frac{(1 - a^2)b^2}{1 + b^2 - 2ab} = 0. \tag{22.5.10}$$

We recall that b and a are expressed in terms of γ_1 and γ_2 considering N_1, N_2, E, and r_2 as known [see Eqs. (22.5.6) and (22.5.8)]. This means that Eqs. (22.5.10) can be represented as

$$f_1(\gamma_1, \gamma_2, \beta_1) = \cos^2 \beta_1 - \frac{(1 - a^2)b^2}{1 + b^2 - 2ab} = 0, \tag{22.5.11}$$

and the derivation of Eq. (22.5.1) is completed.

   Step 3: Equation (22.5.2) has been already obtained: it was represented by Eqs. (22.5.7) and (22.5.8) that provide

$$\cos(\beta_1 - \beta_2) - \tan \gamma_1 \tan \gamma_2 = 0.$$

Thus,

$$f_2(\beta_1, \beta_2, \gamma_1, \gamma_2) = \cos(\beta_1 - \beta_2) - \tan \gamma_1 \tan \gamma_2 = 0, \tag{22.5.12}$$

and the derivation of Eq. (22.5.2) has been completed as well.

Derivation of Equation (22.5.3)
Case 1: Hypoid gear drive with face-milled teeth is considered
The derivation of the required equation is based on the concept of the limit normal proposed by Wildhaber (Section 6.8) and applied by the Gleason Works for the design of face-milled hypoid gear drives. In accordance with this approach, the limit normal to the gear tooth surface at P forms with the pitch plane the angle α_n that is represented by the equation
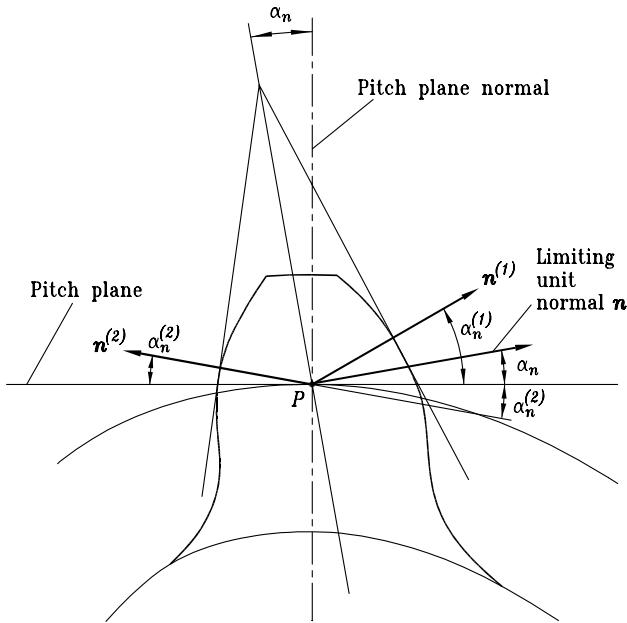
$$\tan \alpha_n = \frac{\dfrac{r_2}{\sin \gamma_2} \sin \beta_2 - \dfrac{r_1}{\sin \gamma_1} \sin \beta_1}{\dfrac{r_2}{\cos \gamma_2} + \dfrac{r_1}{\cos \gamma_1}}. \tag{22.5.13}$$

Equation (22.5.13) may require that $\alpha_n < 0$. We have represented Eq. (22.5.13) in its final form, dropping the details of its derivations. These derivations can be accomplished by using the basic equation (6.7.3) (see Section 6.7).

   Figure 22.5.1 shows the profiles of both gear tooth sides in the normal section that passes through the pitch point P. The surface unit normals to the concave and convex tooth sides are designated by $\mathbf{n}^{(1)}$ and $\mathbf{n}^{(2)}$; the unit vector of the limit normal is designated by $\mathbf{n}$. The unit normals $\mathbf{n}^{(1)}$ and $\mathbf{n}^{(2)}$ form the same angle with the line of action of $\mathbf{n}$.

Figure 22.5.1: Hypoid gear tooth profiles in normal section.

This results in the pressure angles $\alpha_n^{(1)}$ and $\alpha_n^{(2)}$ for both profiles being related as follows:

$$\alpha_n^{(1)} - |\alpha_n| = \alpha_n^{(2)} + |\alpha_n|. \tag{22.5.14}$$

This means that in accordance with the Gleason approach, different pressure angles for the gear concave and convex sides are provided: the pressure angle $\alpha_n^{(1)}$ on the concave side is larger than the pressure angle $\alpha_n^{(2)}$ for the concave side.
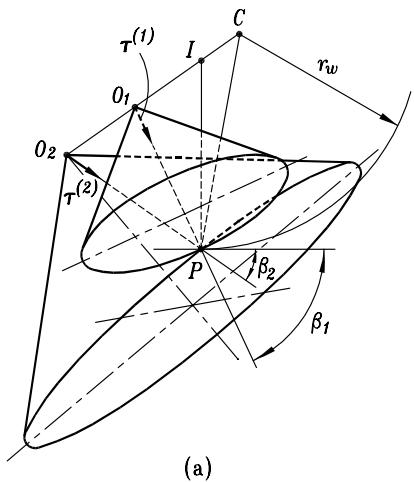
An additional equation that relates the limiting profile angle α_n with the design parameters of the pitch cones is based on the following consideration. A formate cut hypoid gear is provided with a non-generated gear tooth surface that coincides with the head-cutter surface. The intersection of the gear tooth surface with the pitch plane represents a circle of radius r_c where r_c is the mean radius of the head-cutter. The radius r_c is represented by the equation

$$r_c = \cfrac{\tan \beta_1 - \tan \beta_2}{\cfrac{\sin \gamma_1}{r_1 \cos \beta_1} - \cfrac{\sin \gamma_2}{r_2 \cos \beta_2} - \left(\cfrac{\tan \beta_1 \cos \gamma_1}{r_1} + \cfrac{\tan \beta_2 \cos \gamma_2}{r_2} \right) \tan \alpha_n}. \tag{22.5.15}$$

Details of the derivations have been omitted. Equations (22.5.13) and (22.5.15) considered together provide the required equation (22.5.3).
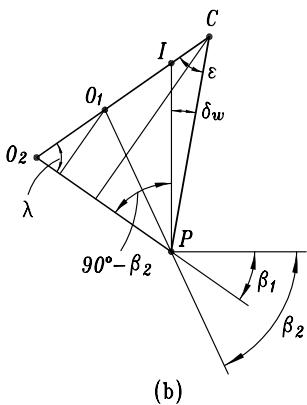
Case 2: Hypoid gear drive with face-hobbed teeth

The derivation of Eq. (22.5.3) is based on the specific location of the head-cutter for the generation of hypoid gears with face-hobbed teeth of uniform depth. Figure 22.5.2 shows the pitch cones being in tangency at point P. The generatrices of the pitch cones $\overline{O_1 P}$ and $\overline{O_2 P}$ lie in the pitch plane that is tangent to both pitch cones and passes

Figure 22.5.2: For orientation of the head-cutter axis in the pitch plane: (a) determination of location of instantaneous center I of rotation; (b) for derivation of Eq. (22.5.26).

through points O_1, O_2, and P (Figs. 22.5.2 and 22.4.1). Vectors τ_1 and τ_2 are the unit vectors of pitch cone generatrices $\overline{O_1P}$ and $\overline{O_2P}$.

Consider now that point C is the point of intersection of the axis of the head-cutter with the pitch plane. We assume the installment of the head-cutter satisfies the requirement that point C belongs to the extended line O_1–O_2. The head-cutter is provided with N_w number of finishing blades. We may also consider that there is an imaginary crown gear that is simultaneously in mesh with the pinion and the gear of the hypoid gear drive. (The crown gear plays the same role as the rack that is in mesh with two spur or helical gears.) The axode of the crown gear being in mesh with the hypoid pinion and gear is the pitch plane or a circular cone. We assume as well that while the head-cutter rotates about C with the angular velocity ω_t, the imaginary crown gear rotates about O_2 with the angular velocity ω_c. (The axes of rotation of the head-cutter and the crown gear are perpendicular to the pitch plane.) The instantaneous center of rotation of the head-cutter with respect to the crown gear is I [Fig. 22.5.2(a)] and its location is determined with the equation

$$\frac{O_2 I}{I C} = \frac{\omega_t}{\omega_c} = \frac{N_c}{N_w} = \frac{N_2}{N_w \sin \gamma_2}. \tag{22.5.16}$$

Here,

$$N_c = \frac{N_2}{\sin \gamma_2} \qquad (22.5.17)$$

where N_c and N_2, are the numbers of teeth of the crown gear and the hypoid gear, respectively; γ_2 is the gear pitch cone angle; N_c must be an integer number.

The finishing blade is located in the plane that is perpendicular to the pitch plane and passes through line PI. Point P of the finishing blade generates in the pitch plane an extended epicycloid whose normal at P coincides with PI. It is evident [Fig. 22.5.2(b)] that

$$\frac{O_1 A}{O_2 A} = \frac{CB}{O_2 B}. \qquad (22.5.18)$$

Further derivations are based on the expressions

$$O_2 P = \frac{r_2}{\sin \gamma_2} = \frac{N_2 m_n}{2 \sin \gamma_2 \cos \beta_2} \qquad (22.5.19)$$

$$O_1 P = \frac{r_1}{\sin \gamma_1} = \frac{N_1 m_n}{2 \sin \gamma_1 \cos \beta_1} \qquad (22.5.20)$$

$$CP = r_w \qquad (22.5.21)$$

where m_n is the normal module of teeth.

$$O_1 A = O_1 P \sin(\beta_1 - \beta_2). \qquad (22.5.22)$$

$$O_2 A = O_2 P - O_1 P \cos(\beta_1 - \beta_2). \qquad (22.5.23)$$

$$CB = r_w \cos(\beta_2 - \delta_w). \qquad (22.5.24)$$

$$O_2 B = O_2 P - r_w \sin(\beta_2 - \delta_w). \qquad (22.5.25)$$

Equation (22.5.18) and expressions (22.5.19) to (22.5.25) yield the sought-for equation (22.5.3) that is represented by

$$f_3(\gamma_1, \gamma_2, \beta_1, \beta_2) = \frac{r_w \cos(\beta_2 - \delta_w)}{r_2 - r_w \sin \gamma_2 \sin(\beta_2 - \delta_w)}$$

$$- \frac{N_1 \cos \beta_2 \sin(\beta_1 - \beta_2)}{N_2 \cos \beta_1 \sin \gamma_1 - N_1 \cos \beta_2 \sin \gamma_2 \cos(\beta_1 - \beta_2)} = 0 \qquad (22.5.26)$$

where

$$\sin \delta_w = \frac{N_w r_2 \cos \beta_2}{N_2 r_w}. \qquad (22.5.27)$$

The derivation of Eq. (22.5.27) is based on relations that follow from Fig. 22.5.2(b):

$$\frac{\sin \delta_w}{\sin \varepsilon} = \frac{CI}{PI}, \qquad \frac{O_2 I}{PI} = \frac{\cos \beta_2}{\sin \lambda}, \qquad \frac{O_2 P}{CP} = \frac{\sin \varepsilon}{\sin \lambda}. \qquad (22.5.28)$$

Computational Procedure for Determination of γ_1, γ_2, and β_2

The equation system (22.5.1) to (22.5.3) consists of three nonlinear equations. The input data for the solutions are $\beta_1, r_2, E, N_1, N_2$ (and N_w for the case of face-hobbed

gears). In the case where pitch cone outer radius r_2^* and face width F are given instead of pitch cone mean radius r_2, the following relation between r_2^*, F, and r_2 must be used at each iteration:

$$r_2 = r_2^* - \frac{F \sin \gamma_2}{2}.$$

The solution of nonlinear equations for the unknowns is an iterative process. We may consider that at each iteration the equations are represented in echelon form and can be solved separately if one of the unknowns (for instance, γ_2) is considered as given. Then the third nonlinear equation will be used in the iterative process for checking.

A computer-aided solution for the unknowns γ_1, γ_2, and β_2 is based on application of a numerical subroutine for solution of nonlinear equations. However, while using such a subroutine, it must be complemented with the following requirements:

$$\tan \gamma_1 \tan \gamma_2 < 1, \quad \cos^2 \gamma_1 - \sin^2 \gamma_2 > 0.$$

For the first guess, choosing the initial value of γ_2 so that $\gamma_2 < \tan^{-1}(N_1/N_2)$ is recommended.

22.6 GENERATION OF FACE-MILLED HYPOID GEAR DRIVES
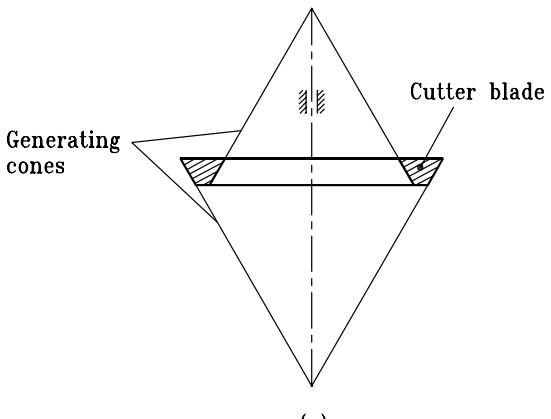
The discussions are limited to the presentation of basic machine-tool settings applied for the generation of the gear and the pinion.
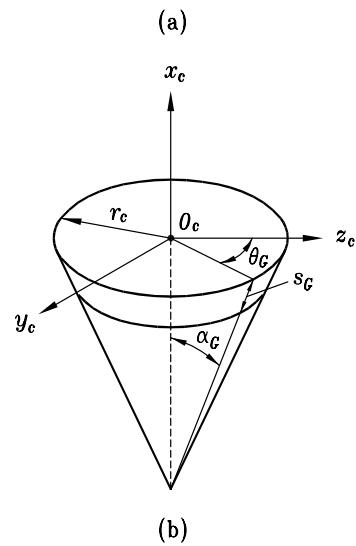
Gear Generation
The face-milled gear is generated as formate-cut, which means that each side of the tooth surface is generated as a copy of the surface of the tool (of the head-cutter). The tool surface is a cone. In the process of manufacturing, the gear is held at rest so that no generating motions are provided. The advantage of using formate-cut gear generation is the higher productivity of manufacturing. Two cones that are shown in Fig. 22.6.1(a) represent both sides of the gear space. Henceforth, we consider the following coordinate systems: S_{t_2} that is rigidly connected to the head-cutter, S_{m_2} that is rigidly connected to the cutting machine, and S_2 that is rigidly connected to the gear. In the case of formate generation we may consider that all three coordinate systems, S_{t_2}, S_{m_2}, and S_2 are rigidly connected to each other. The following equations represent in coordinate system S_{t_2} tool surfaces for both sides and the unit normals to such surfaces [Fig. 22.6.2(b)]:

$$\mathbf{r}_{t_2} = \begin{bmatrix} -s_G \cos \alpha_G \\ (r_c - s_G \sin \alpha_G) \sin \theta_G \\ (r_c - s_G \sin \alpha_G) \cos \theta_G \\ 1 \end{bmatrix} \tag{22.6.1}$$

$$\mathbf{n}_{t_2} = \begin{bmatrix} \sin \alpha_G \\ -\cos \alpha_G \sin \theta_G \\ -\cos \alpha_G \cos \theta_G \end{bmatrix}. \tag{22.6.2}$$

Figure 22.6.1: Illustration of generating cones for formate face-milled hypoid gear: (a) generating cones; (b) for derivation of equations of the generating cone.

Here, $\mathbf{r}_{t_2}$ is the position vector and $\mathbf{n}_{t_2}$ is the cone surface unit normal; r_c is the cutter tip radius; α_G is the cutter blade angle ($\alpha_G > 0$ for the convex side and $\alpha_G < 0$ for the concave side).
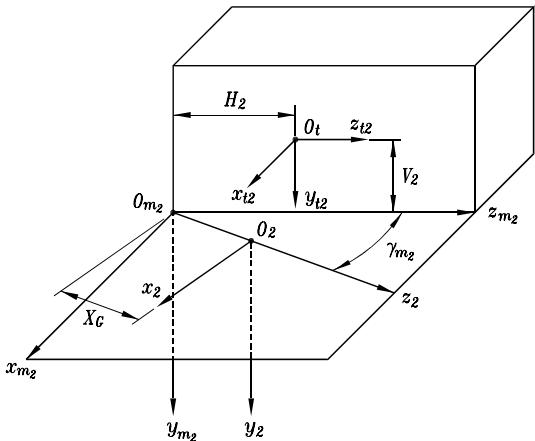
Figure 22.6.2 shows the installment of the generating cone on the cutting machine. To represent in S_2 the theoretical gear tooth surface Σ_2 and the unit normal to Σ_2, we use the matrix equations

$$\mathbf{r}_2(s_G, \theta_G, d_j) = \mathbf{M}_{2t_2}\, \mathbf{r}_{t_2}(s_G, \theta_G) \tag{22.6.3}$$

$$\mathbf{n}_2(s_G, \theta_G, d_j) = \mathbf{L}_{2t_2}\, \mathbf{n}_{t_2}(s_G, \theta_G) \tag{22.6.4}$$

where

$$\mathbf{M}_{2t_2} = \mathbf{M}_{2m_2}\, \mathbf{M}_{m_2 t_2} = \begin{bmatrix} \cos\gamma_{m_2} & 0 & -\sin\gamma_{m_2} & 0 \\ 0 & 1 & 0 & 0 \\ \sin\gamma_{m_2} & 0 & \cos\gamma_{m_2} & X_G \\ 0 & 0 & 0 & 1 \end{bmatrix} \begin{bmatrix} 1 & 0 & 0 & 0 \\ 0 & 1 & 0 & -V_2 \\ 0 & 0 & 1 & H_2 \\ 0 & 0 & 0 & 1 \end{bmatrix}. \tag{22.6.5}$$

Figure 22.6.2: Machine-tool settings for formate face-milled hypoid gear.
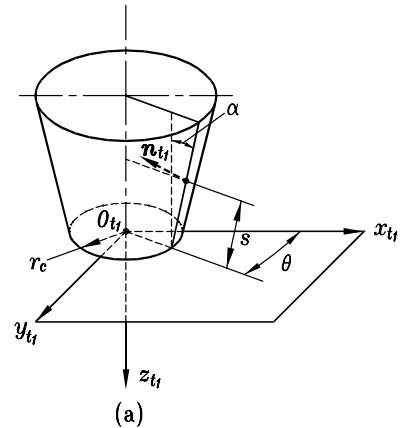
The surface Gaussian coordinates are s_G and θ_G and d_j (γ_m, V_2, H_2, and X_G) are the machine-tool settings.

Pinion Generation

Unlike the gear, the generation of the pinion is not formate-cut. The pinion tooth surface is generated as the envelope to the family of tool surfaces that are cone surfaces (Fig. 22.6.3). Henceforth, we consider the following coordinate systems: (i) the fixed ones, S_{m_1} and S_q that are rigidly connected to the cutting machine (Figs. 22.6.4 and 22.6.5); (ii) the movable coordinate systems S_c and S_1 that are rigidly connected to the cradle of the cutting machine and the pinion, respectively; and (iii) coordinate system S_{t_1} that is rigidly connected to the head-cutter. In the process of generation the cradle with S_c performs rotational motion about the z_{m_1} axis with angular velocity $\omega^{(c)}$, and the pinion with S_1 performs rotational motion about the x_q axis with angular velocity $\omega^{(1)}$ (Fig. 22.6.5).
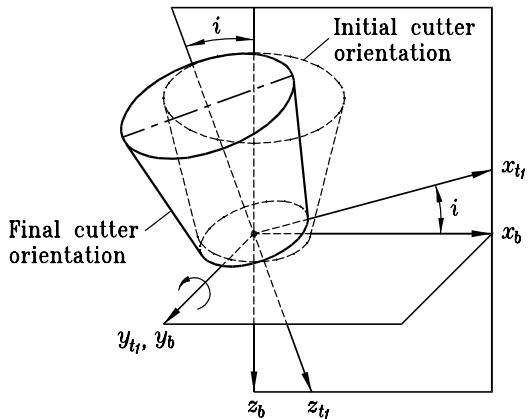
The tool (head-cutter) is mounted on the cradle and performs rotational motion *with* the cradle. Coordinate system S_{t_1} is rigidly connected to the cradle. To describe the installment of the tool with respect to the cradle we use coordinate system S_b (Figs. 22.6.3 and 22.6.4). The required orientation of the head-cutter with respect to the cradle is accomplished as follows: (i) coordinate systems S_b and S_{t_1} are rigidly connected and then they are turned as one rigid body about the z_c axis through the swivel angle $j = 2\pi - \delta$ (Fig. 22.6.4); and (ii) then the head-cutter with coordinate system S_{t_1} is tilted about the y_b axis under the angle i [Fig. 22.6.3(b)]. (More details about the settings of a tilted head-cutter are given in Litvin *et al.* [1988]. The head-cutter is rotated about its axis z_{t_1}, but the angular velocity in this motion is not related to the generating process and depends only on the desired velocity of cutting.

The pinion setting parameters are E_{m_1} – the machine offset, γ_{m_1} – the machine-root angle, ΔB – the sliding base, and ΔA – the machine center to back (Fig. 22.6.5). The head-cutter setting parameters are S_R – radial setting, θ_c – initial value of cradle angle, j – the swivel angle (Fig. 22.6.4), and i – the tilt angle [Fig. 22.6.3(b)].

Figure 22.6.3: Pinion head-cutter: (a) initial representation in coordinate system S_{t1}; (b) representation in S_{t1} after the tilt under the angle i.

Pinion Tool Surface Equations
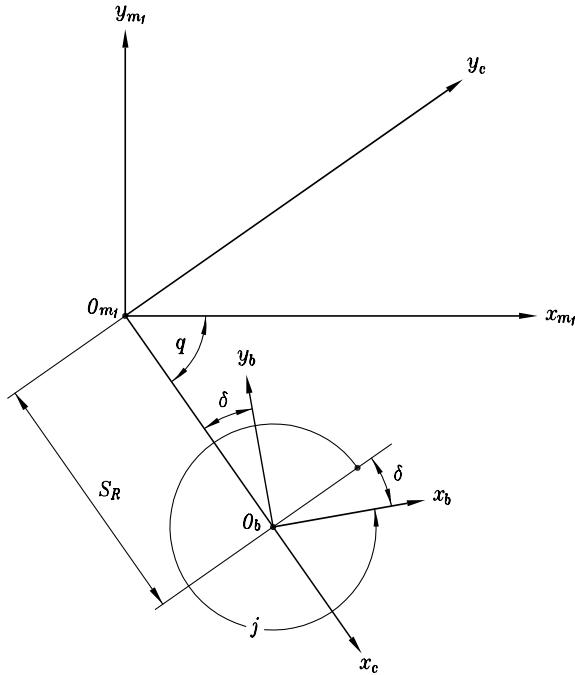
The head-cutter surface is a cone and is represented in S_{t_1} [Fig. 22.6.3(a)] as

$$
\mathbf{r}_{t_1}(s, \theta) = \begin{bmatrix} (r_c + s \sin \alpha) \cos \theta \\ (r_c + s \sin \alpha) \sin \theta \\ -s \cos \alpha \\ 1 \end{bmatrix}. \tag{22.6.6}
$$
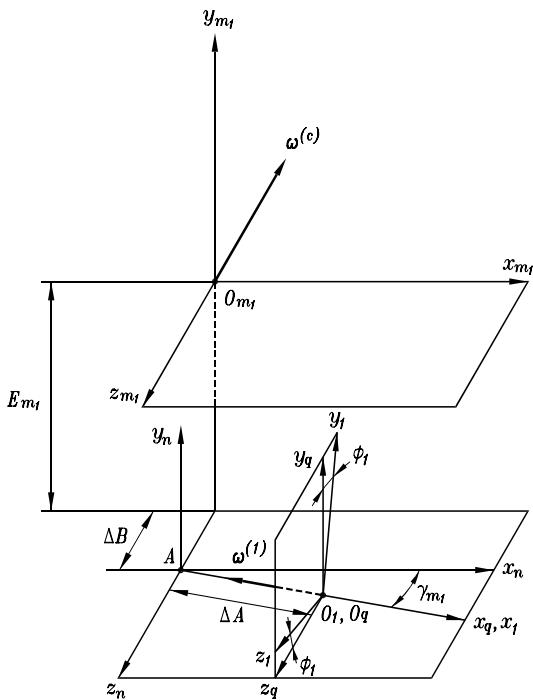
Here, (s, θ) are the Gaussian coordinates, α is the blade angle, and r_c is the cutter point radius. Vector function (22.6.6) with positive α and negative α represents surfaces of two head-cutters that are used to cut the pinion concave side and convex side, respectively.

The unit normal to the head-cutter surface is represented in S_{t_1} by the equations

$$
\mathbf{n}_{t_1} = [-\cos \alpha \cos \theta \quad -\cos \alpha \sin \theta \quad -\sin \alpha]^{\mathrm{T}}. \tag{22.6.7}
$$

Figure 22.6.4: Coordinate systems S_{m_1}, S_c, and S_b.

Figure 22.6.5: Pinion generation.

The family of tool surfaces is represented in S_1 by the matrix equation

$$\mathbf{r}_1(s, \theta, \phi_p) = \mathbf{M}_{1q}\mathbf{M}_{qn}\mathbf{M}_{nm_1}\mathbf{M}_{m_1c}\mathbf{M}_{cb}\mathbf{M}_{bt_1}\mathbf{r}_{t_1}(s, \theta). \tag{22.6.8}$$

Here, S_n is an auxiliary fixed coordinate system whose axes are parallel to the S_{m_1} axes and

$$\mathbf{M}_{bt_1} = \begin{bmatrix} \cos i & 0 & \sin i & 0 \\ 0 & 1 & 0 & 0 \\ -\sin i & 0 & \cos i & 0 \\ 0 & 0 & 0 & 1 \end{bmatrix}$$

$$\mathbf{M}_{cb} = \begin{bmatrix} -\sin j & -\cos j & 0 & S_R \\ \cos j & -\sin j & 0 & 0 \\ 0 & 0 & 1 & 0 \\ 0 & 0 & 0 & 1 \end{bmatrix}$$

$$\mathbf{M}_{m_1c} = \begin{bmatrix} \cos q & \sin q & 0 & 0 \\ -\sin q & \cos q & 0 & 0 \\ 0 & 0 & 1 & 0 \\ 0 & 0 & 0 & 1 \end{bmatrix}$$

$$\mathbf{M}_{nm_1} = \begin{bmatrix} 1 & 0 & 0 & 0 \\ 0 & 1 & 0 & E_m \\ 0 & 0 & 1 & -\Delta B \\ 0 & 0 & 0 & 1 \end{bmatrix}$$

$$\mathbf{M}_{qn} = \begin{bmatrix} \cos\gamma_m & 0 & \sin\gamma_m & -\Delta A \\ 0 & 1 & 0 & 0 \\ -\sin\gamma_m & 0 & \cos\gamma_m & 0 \\ 0 & 0 & 0 & 1 \end{bmatrix}$$

$$\mathbf{M}_{1q} = \begin{bmatrix} 1 & 0 & 0 & 0 \\ 0 & \cos\phi_1 & -\sin\phi_1 & 0 \\ 0 & \sin\phi_1 & \cos\phi_1 & 0 \\ 0 & 0 & 0 & 1 \end{bmatrix}$$

with $q = \theta_c + m_{c1}\phi_1$ where θ_c is the initial cradle angle and $m_{c1} = \omega^{(c)}/\omega^{(1)}$.

Equation of Meshing

This equation is represented as (see Section 6.1)

$$\mathbf{n}^{(1)} \cdot \mathbf{v}^{(c1)} = \mathbf{N}^{(1)} \cdot \mathbf{v}^{(c1)} = f(s, \theta, \phi_1) = 0 \tag{22.6.9}$$

where $\mathbf{n}^{(1)}$ and $\mathbf{N}^{(1)}$ are the unit normal and the normal to the tool surface, and $\mathbf{v}^{(c1)}$ is the velocity in relative motion. Equation (22.6.9) is invariant with respect to the coordinate system where the vectors of the scalar product are represented. These vectors in our derivations have been represented in S_{m_1} as follows:

$$\mathbf{n}_{m_1} = \mathbf{L}_{m_1 c} \mathbf{L}_{cb} \mathbf{L}_{bt_1} \mathbf{n}_{t_1}$$

$$\mathbf{v}_{m_1}^{(c1)} = \left[\left(\boldsymbol{\omega}_{m_1}^{(c)} - \boldsymbol{\omega}_{m_1}^{(1)} \right) \times \mathbf{r}_{m_1} \right] + \left(\overline{O_{m_1} A} \times \boldsymbol{\omega}_{m_1}^{(1)} \right).$$

Here,

$$\mathbf{r}_{m_1} = \mathbf{M}_{m_1 c} \mathbf{M}_{cb} \mathbf{M}_{bt_1} \mathbf{r}_{t_1}$$

$$\overline{O_{m_1} A} = [0 \quad -E_{m1} \quad \Delta B]^{\mathrm{T}}$$

$$\boldsymbol{\omega}_{m_1}^{(1)} = -[\cos \gamma_{m1} \quad 0 \quad \sin \gamma_{m1}]^{\mathrm{T}} \quad \left(\left| \boldsymbol{\omega}_{m_1}^{(1)} \right| = 1 \right)$$

$$\boldsymbol{\omega}_{m_1}^{(c)} = -[0 \quad 0 \quad m_{c1}]^{\mathrm{T}}.$$

Pinion Tooth Surface

Equations (22.6.8) and (22.6.9) represent the pinion tooth surface in three-parameter form with parameters s, θ, and ϕ_1. However, because Eq. (22.6.9) is linear with respect to s, we can eliminate s and represent the pinion tooth surface in two-parameter form as

$$\mathbf{r}_1(\theta, \phi_1, d_j). \tag{22.6.10}$$

Here, d_j ($j = 1, \ldots, 8$) designate the installment parameters: E_{m1}, γ_{m1}, ΔB, ΔA, S_R, θ_c, j, and i. The unit normal to the pinion tooth surface is represented as

$$\mathbf{n}_1(\theta, \phi_1, d_k) \tag{22.6.11}$$

where d_k ($k = 1, 2, 3, 4$) designate the installment parameters γ_{m1}, θ_c, j, and i.

23 **Planetary Gear Trains**

23.1 INTRODUCTION

Planetary gear trains were the subject of intensive research directed at determination of dynamic response of the trains, vibration, load distribution, efficiency, enhanced design, and other important topics [Lynwander, 1983; Ishida & Hidaka, 1992; Kudrjavtzev *et al.*, 1993; Kahraman, 1994; Saada & Velex, 1995; Chatterjee & Tsai, 1996; Hori & Hayashi, 1996a, 1996b; Velex & Flamand, 1996; Lin & Parker, 1999; Chen & Tseng, 2000; Kahraman & Vijajakar, 2001; Litvin *et al.*, 2002e].

This chapter covers gear ratio, conditions of assembly, relations of tooth numbers, efficiency of a planetary train, proposed modification of geometry of tooth surfaces, determination of transmission errors, etc. Special attention is given to the regulation of backlash for improvement of load distribution.
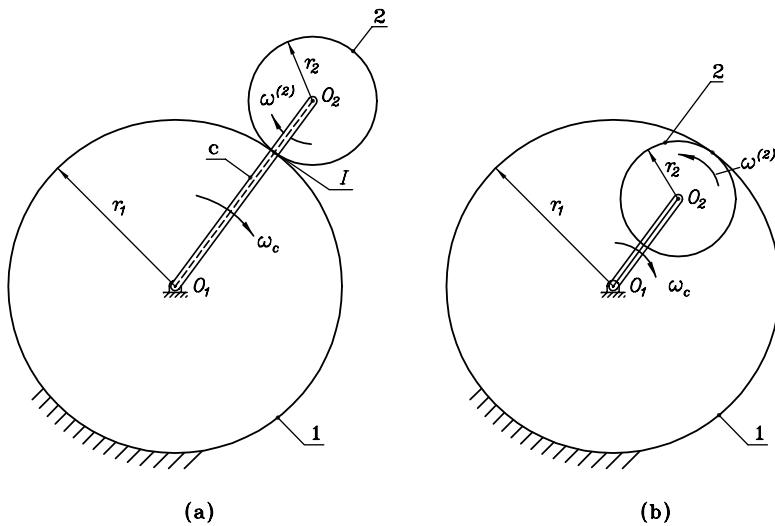
23.2 GEAR RATIO

A planetary gear mechanism has at least one gear whose axis is movable in the process of meshing.

Planetary Mechanisms of Figs. 23.2.1 (a) and (b)

Figures 23.2.1(a) and (b) represent two simple planetary gear mechanisms formed by two gears 1 and 2 that are in external or internal meshing, respectively, and a carrier c on which the gear with the movable axis is mounted. Gear 1 is fixed and planet gear 2 performs a planar motion of two components: (i) transfer rotation with the carrier, and (ii) relative rotation about the carrier. The resulting motion of planet gear 2 with respect to fixed gear 1 is rotation about the instantaneous center I of motion that is the point of tangency of centrodes r_1 and r_2 (the pitch circles) of gears 1 and 2.

In addition to a planetary mechanism, we consider a respective inverted mechanism formed by gears of the planetary mechanism. The carrier of the inverted mechanism is fixed. The inversion is based on the idea that the gears of both mechanisms, the planetary and the inverted one, perform rotation about the carrier with the *same* angular velocity.

Figure 23.2.1: Three-link planetary mechanisms with (a) external and (b) internal meshing of the gears.

The angular velocities of the links of the planetary mechanism are related by the following equation [Willis, 1841]:

$$\frac{\omega_2 - \omega_c}{\omega_1 - \omega_c} = m_{21}^{(c)}. \tag{23.2.1}$$

Here, ω_k $(k = 1, 2)$ is the angular velocity of gear k in absolute motion with respect to the frame of the planetary mechanism; $(\omega_k - \omega_c)$ is the angular velocity of gear ω_k in its relative motion with respect to the carrier; ω_c is the angular velocity of the carrier; $m_{21}^{(c)}$ is the gear ratio of the inverted mechanism wherein the transformation of motion is performed from gear 2 to gear 1 while the carrier is held at rest. The gear ratio $m_{21}^{(c)}$ is considered as an algebraic quantity: $m_{21}^{(c)}$ is negative $(m_{21}^{(c)} < 0)$ if the direction of rotation from gear 2 to gear 1 of the inverted mechanism is opposite. Similarly, $m_{21}^{(c)}$ is positive wherein directions of rotations of gears 2 and 1 of the inverted mechanism coincide.

Then, we obtain
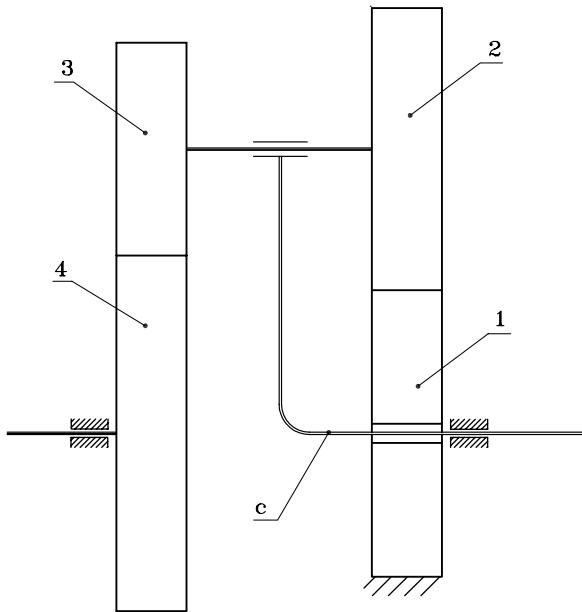
(i) $m_{21}^{(c)} = (-1)N_1/N_2$ for the inverted planetary gear train of Fig. 23.2.1(a).
(ii) Similarly, $m_{21}^{(c)} = (+1)N_1/N_2$ for the inverted planetary gear train of Fig. 23.2.1(b).

Taking into account that $\omega_1 = 0$ (gear 1 is fixed), we obtain from Eq. (23.2.1) the following results:

$$\omega_2 - \omega_c = (\pm)\left(\frac{N_1}{N_2}\right)\omega_c \tag{23.2.2}$$

$$\omega_2 = \left(1 \pm \frac{N_1}{N_2}\right)\omega_c. \tag{23.2.3}$$

Here, $(\omega_2 - \omega_c)$ is the angular velocity of rotation of gear 2 in its relative motion, in rotation about the carrier c; ω_2 is the angular velocity of gear 2 in its absolute motion,

Figure 23.2.2: Planetary gear train with external meshing of gears.

that is rotation about the instantaneous center I (Figs. 23.2.1(a) and (b)); the angular velocity of rotation of gear 1 about the carrier is $(-1)\omega_c$. The lower and upper signs in Eqs. (23.2.2) and (23.2.3) correspond to planetary gear trains shown in Figs. 23.2.1(a) and (b), respectively.

Planetary Mechanism of Fig. 23.2.2

The planetary mechanism shown in Fig. 23.2.2 is formed by two pairs of gears that are in external meshing. Gear 1 is the fixed one. The relation between the angular velocities of gears 4 and 1 is

$$\frac{\omega_4 - \omega_c}{-\omega_c} = m_{41}^{(c)} \tag{23.2.4}$$

where

$$m_{41}^{(c)} = m_{43}^{(c)} \cdot m_{21}^{(c)} = (-1)\left(\frac{N_3}{N_4}\right) \cdot (-1)\frac{N_1}{N_2} = \frac{(N_3)(N_1)}{(N_4)(N_2)}. \tag{23.2.5}$$

Equations (23.2.4) and (23.2.5) yield

$$\frac{\omega_4}{\omega_c} = 1 - m_{41}^{(c)}. \tag{23.2.6}$$

The ratio (ω_4/ω_c) represents the ratio between the angular velocities of link 4 (gear 4) and link c (carrier c) of the planetary gear train. The negative or positive signs of the ratio (ω_4/ω_c) indicate that the rotation of gear 4 and the carrier c are performed in either the opposite or the same direction.

Numerical Example 23.2.1

Consider that $N_3 = 101$, $N_1 = 99$, $N_4 = N_2 = 100$. Application of nonstandard tooth element proportions for the gears is required. Then we obtain that

$$\frac{\omega_4}{\omega_c} = 1 - m_{41}^{(c)} = 1 - 0.9999 = 0.0001.$$
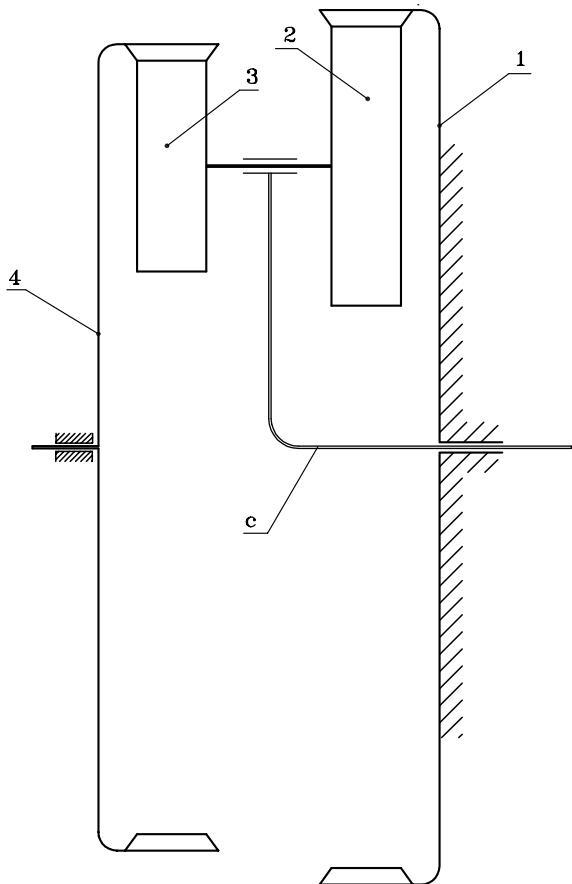
In the case that $N_3 = N_1 = 100$, $N_4 = 101$, $N_2 = 99$, we obtain that

$$\frac{\omega_4}{\omega_c} = -\frac{1}{9999} = -0.0001.$$

The negative sign of (ω_4/ω_c) indicates that gear 4 and carrier c perform rotation in opposite directions. The gear train previously discussed (Fig. 23.2.2) provides a high reduction of the angular velocity of the driving link c (by 1000 times). However, gear trains with such a large reduction of the speed of carrier c are not applied in the practice due to the low efficiency of the train (see Section 23.5).

Planetary Mechanism of Fig. 23.2.3

The planetary mechanism shown in Fig. 23.2.3 is designed with two pairs of gears, 1–2 and 3–4, being in internal meshing. Gear 1 is fixed, planet gears 2 and 3 have a joint

Figure 23.2.3: Planetary gear train with internal meshing of gears.

shaft and are mounted on carrier c. Due to internal meshing of gears 1–2 and 3–4, the efficiency of the planetary gear train is higher in comparison with the planetary gear train shown in Fig. 23.2.2 (see Section 23.5). This advantage is the result of lower relative velocity of sliding in internal meshing, especially if a small difference in the number of teeth of contacting pairs of gears is used.

The relation ω_4/ω_c between the angular velocities of the driven and driving links is determined from the equation

$$\frac{\omega_4 - \omega_c}{-\omega_c} = m_{41}^{(c)}. \tag{23.2.7}$$

The gear ratio $m_{41}^{(c)}$ of the inverted mechanism is determined as follows:

$$m_{41}^{(c)} = m_{43}^{(c)} \cdot m_{21}^{(c)} = (+1)\left(\frac{N_3}{N_4}\right) \cdot (+1)\frac{N_1}{N_2} = \frac{(N_3)(N_1)}{(N_4)(N_2)}. \tag{23.2.8}$$

Then we obtain

$$\frac{\omega_4}{\omega_c} = 1 - \frac{(N_3)(N_1)}{(N_4)(N_2)}. \tag{23.2.9}$$

Large reduction of angular velocity of driven gear 4 with respect to angular velocity of carrier c in the examples previously discussed is obtained because $m_{41}^{(c)}$ is positive. This statement is correct for both planetary gear mechanisms of Figs. 23.2.2 and 23.2.3. The gear ratio $m_{14}^{(c)}$ is negative for a planetary gear mechanism with mixed-type meshing of gears 1–2 and 3–4, as the combination of internal and external meshing of contacting gears. In this case, a large reduction of angular velocity ω_4 cannot be obtained.

Planetary Gear Train of Fig. 23.2.4

The gear train is applied in helicopter transmissions and other cases of design. Gear 3 (called the ring gear) is fixed and the carrier c carries n planet gears ($n = 5$ is shown in Fig. 23.2.4). The relation between angular velocities ω_1 of the sun gear and the carrier c is based on the following equation:

$$\frac{\omega_1 - \omega_c}{-\omega_c} = m_{13}^{(c)}. \tag{23.2.10}$$

Here, $m_{13}^{(c)}$ is the gear ratio of the inverted mechanism

$$m_{13}^{(c)} = m_{12}^{(c)} \cdot m_{23}^{(c)} = (-1)\left(\frac{N_2}{N_1}\right) \cdot (+1)\left(\frac{N_3}{N_2}\right) = (-1)\left(\frac{N_3}{N_1}\right). \tag{23.2.11}$$
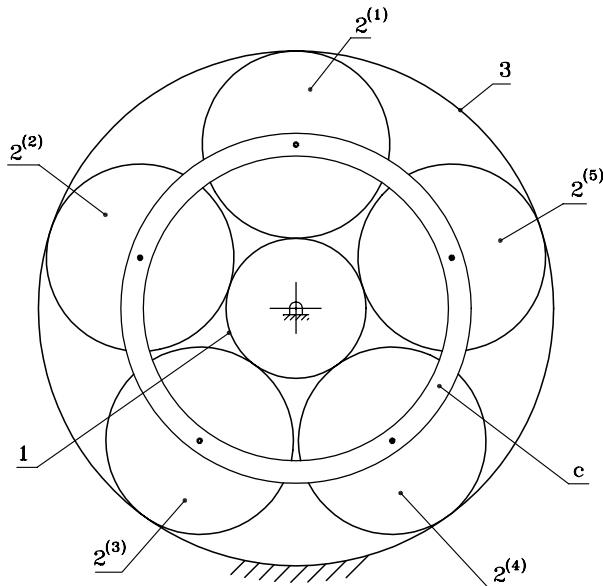
Equations (23.2.10) and (23.2.11) yield

$$\frac{\omega_c}{\omega_1} = \frac{N_1}{N_1 + N_3}. \tag{23.2.12}$$

The reduction of angular velocity ω_c is obtained wherein gear 1 and carrier c are the driving and driven links, respectively.

Bevel Gear Differential of Fig. 23.2.5

The bevel gear differential shown in Fig. 23.2.5 is applied for addition or subtraction of angular velocities of two input links. The mechanism contains four movable
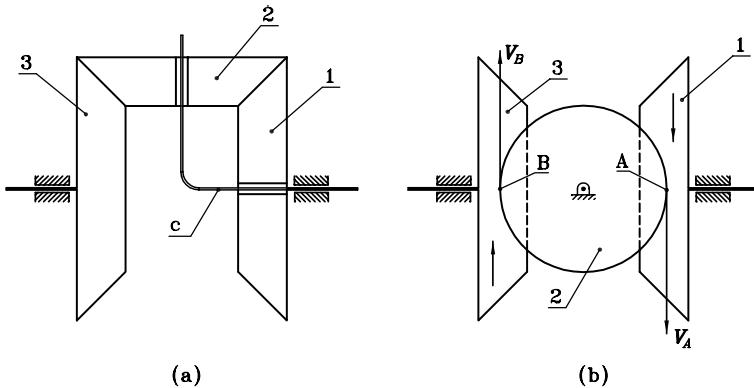
Figure 23.2.4: Schematic representation of planetary gear train applied in helicopter transmissions.

links: (a) the carrier c, (b) two sun gears 1 and 3, and (c) the planet gear 2 which is mounted on carrier c. Usually, the discussed differential contains two planet gears mounted on the carrier, but the application of the second planet gear is not necessary in a kinematic sense. The discussed mechanism is a coaxial differential – the axes of rotation of gears 1, 3, and the carrier coincide, but they may rotate with different angular velocities ω_1, ω_3, and ω_c. It is obvious that gears 1 and 3 have equal numbers of teeth N_1 and N_3.

Angular velocities of the links of the differential are related as

$$m_{31}^{(c)} = \frac{\omega_3 - \omega_c}{\omega_1 - \omega_c} \tag{23.2.13}$$

where $m_{31}^{(c)}$ is the angular velocity ratio of the inverted mechanism.

(a)   (b)

Figure 23.2.5: Bevel gear differential: (a) schematic representation of the gear train; (b) for derivation of gear ratio $m_{31}^{(c)}$.

It is easy to prove that $m_{31}^{(c)} = -1$. This result is obtained from the following considerations [Fig. 23.2.5(b)]. Suppose that the carrier is fixed and gears 1 and 2, and 3 and 2 are in contact at points A and B, respectively. Vectors $\mathbf{V}_A$ and $\mathbf{V}_B$ represent linear velocities of corresponding gears at points A and B. Taking into account that $N_1 = N_3$ and $\mathbf{V}_A = -\mathbf{V}_B$, we get that $m_{31}^{(c)} = -1$. The negative sign of $m_{31}^{(c)}$ means that gears 1 and 3 of the inverted mechanism are rotated in opposite directions. Equation (23.2.13) with $m_{31}^{(c)} = -1$ yields that

$$\omega_c = \frac{\omega_1 + \omega_3}{2}. \qquad (23.2.14)$$

Let us consider the following cases of transformation of motion:

(1) Assume that one of the sun gears (of gears 1 and 3), for instance gear 1, is fixed. Equation (23.2.14) with $\omega_1 = 0$ yields

$$\omega_c = \frac{\omega_3}{2}. \qquad (23.2.15)$$

The discussed mechanism works as a planetary gear train.

(2) Consider now that gears 1 and 3 are rotated with equal angular velocities in the same direction. Equation (23.2.14) with $\omega_1 = \omega_3$ yields that

$$\omega_c = \omega_1 = \omega_3. \qquad (23.2.16)$$

Consequently, gear 1, 3, and the carrier c are rotated with the same angular velocity. The gear train is like a clutch: all movable links are rotated as one rigid body.

(3) Considering that gears 1 and 3 are rotated with equal angular velocities in opposite directions ($\omega_1 = -\omega_3$), we get that $\omega_c = 0$ [see Eq. (23.2.14)]. The discussed mechanism operates as a gear train with fixed axes of rotation.

23.3 CONDITIONS OF ASSEMBLY

Observation of Assigned Backlash Between Planet Gears
[Litvin et al., 2002e]
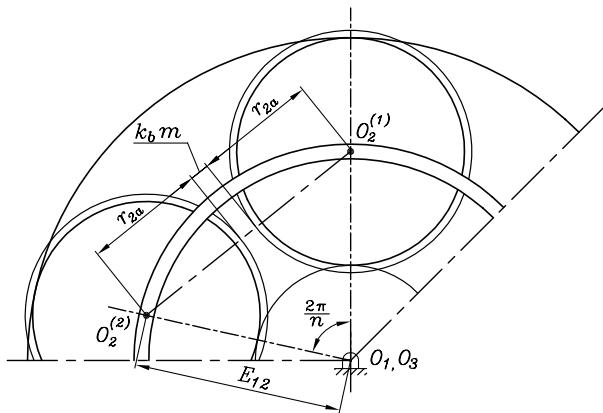
We consider the condition of assembly for the planetary mechanism shown in Fig. 23.2.4. The obtained results may be extended for other planetary gear trains. Figure 23.3.1 shows two neighboring planet gears with the backlash $k_b m$, where m is the module of the gears and k_b is the unitless coefficient. Our goal is to derive an equation that relates N_1, k_b, and the gear ratio $m_{c1}^{(3)} = \omega_c/\omega_1$ of a planetary gear train wherein gear 3 is fixed. The derivation is based on application of the following equation:

$$r_{2a} = E_{12} \sin\left(\frac{\pi}{n}\right) - \frac{k_b m}{2}. \qquad (23.3.1)$$

Here, r_{2a} is the radius of the addendum circle of gear 2; E_{12} is the shortest distance; n is the number of planet gears. It is easy to verify that

$$E_{12} = \frac{N_1 + N_2}{2} m \qquad (23.3.2)$$

$$r_{2a} = \left(\frac{N_2}{2} + 1\right) m. \qquad (23.3.3)$$

Figure 23.3.1: For derivation of distance between two neighboring planet gears.

In addition to Eqs. (23.3.1) to (23.3.3), we use equation

$$N_2 = \frac{N_3 - N_1}{2} \tag{23.3.4}$$

obtained from Fig. 23.2.4, and the equation [see Eq. (23.2.12)]

$$\frac{\omega_c}{\omega_1} = \frac{N_1}{N_1 + N_3} = m_{c1}^{(3)}. \tag{23.3.5}$$

Using the system of equations (23.3.1) to (23.3.5), we obtain the following relations between N_1, $m_{c1}^{(3)}$, and k_b:

$$N_1 = \frac{2m_{c1}^{(3)}(2 + k_b)}{2m_{c1}^{(3)} + \sin\left(\dfrac{\pi}{n}\right) - 1}. \tag{23.3.6}$$

Because $N_1 > 0$, we obtain that
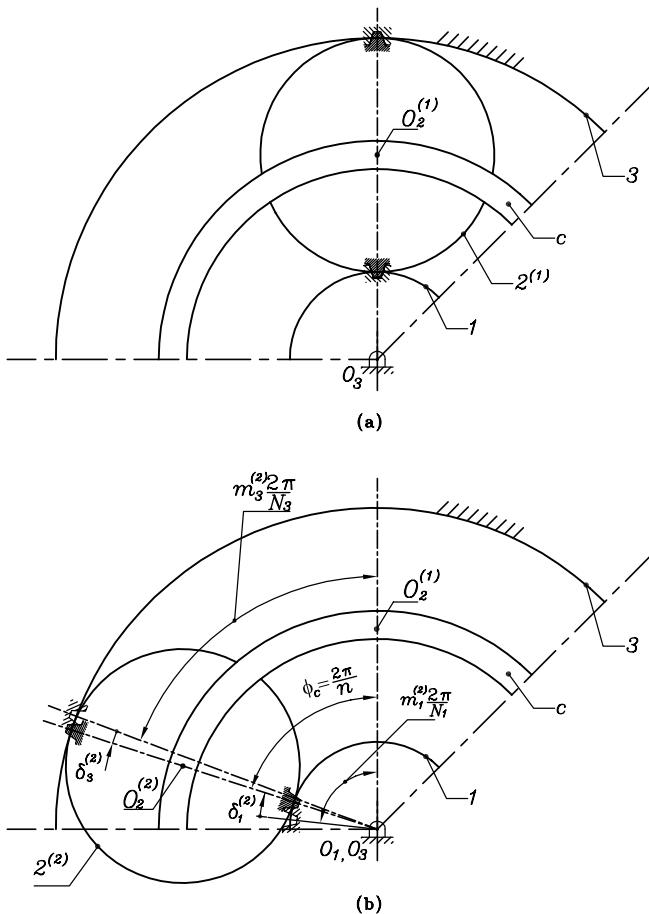
$$m_{c1}^{(3)} > \frac{1 - \sin\left(\dfrac{\pi}{n}\right)}{2}. \tag{23.3.7}$$

Inequality (23.3.7) represents the restriction for the minimum value of $m_{c1}^{(3)}$ considering as given the number n of planet gears.

Relation Between Tooth Numbers of Planetary Train of Fig. 23.2.4

The conditions of assembly of the planetary gear train shown in Fig. 23.2.4 yield, as shown below, a relation between tooth numbers N_1 and N_3 and the number n of planet gears. The number of teeth N_2 of planet gears does not affect the conditions of assembly. The derivations are based on the following considerations [Litvin *et al.*, 2002e]:

Step 1: Consider initially the assembly of a train that is formed by gears 1, 3, and planet gear $2^{(1)}$ [Fig. 23.3.2(a)]. Carrier c is in the position shown in the figure and the axes of tooth symmetry of gear $2^{(1)}$ coincide with reference line $\overline{O_3 O_2^{(1)}}$ and the axes of spaces of gears 1 and 3.

Figure 23.3.2: Installment of planet gears $2^{(1)}$ and $2^{(2)}$.

NOTE: The drawings correspond to the case wherein the tooth number of $2^{(1)}$ ($i = 1, \ldots, n$) is even, but the following derivations are true for gear $2^{(i)}$ with an odd number of teeth.

Step 2: Consider now that the neighboring planet gear $2^{(2)}$ has to be installed in the gear train wherein gears 1, 3, and $2^{(1)}$ have the positions shown in Fig. 23.3.2(a). Gear $2^{(2)}$ is mounted on carrier c; the axis of symmetry of gear $2^{(2)}$ teeth coincides with $\overline{O_3 O_2^{(2)}}$ that forms with $\overline{O_3 O_2^{(1)}}$ angle $\phi_c = 2\pi/N$. The axis of space symmetry of gear 3 forms (i) angle $m_3^{(2)}(2\pi/N_3)$ with line $\overline{O_3 O_2^{(1)}}$ ($m_3^{(2)}$ is an integer number), and (ii) angle $\delta_3^{(2)}$ with the line $\overline{O_3 O_2^{(2)}}$. Similarly, the axis of space symmetry of gear 1 forms (i) angle $m_1^{(2)}(2\pi/N_1)$ with line $\overline{O_3 O_2^{(1)}}$ ($m_1^{(2)}$ is an integer number), and (ii) angle $\delta_1^{(2)}$ with the line $\overline{O_3 O_2^{(2)}}$. The superscript "(2)" in the designations $m_3^{(2)}$ and $m_1^{(2)}$, $\delta_3^{(2)}$ and $\delta_1^{(2)}$ indicates that planet gear $2^{(2)}$ is considered. Angles $m_k^{(2)}(2\pi/N_j)$, $\delta_k^{(2)}$ ($k = 1, 3$) and ϕ_c are measured counterclockwise from line $\overline{O_3 O_2^{(1)}}$ of center distance. It is evident that

the planet gear $2^{(2)}$ cannot be put into mesh with gears 1 and 3 [Fig. 23.3.2(b)] because $\delta_3^{(2)}$ and $\delta_1^{(2)}$ differ from zero.

Step 3: To put gear $2^{(2)}$ into mesh with gears 1 and 3, it is necessary to turn gears 1, 3, and $2^{(1)}$ holding at rest carrier c. Gears 1 and 3 are turned in opposite directions and therefore angles $\delta_1^{(2)}$, $\delta_3^{(3)}$ indicate deviations from $\overline{O_3 O_2^{(2)}}$ of axes of symmetry of spaces of gears 1 and 3 in opposite directions. The ratio $\delta_3^{(2)}/\delta_1^{(2)}$ is determined as N_1/N_3 that is the gear ratio of the inverted gear drive formed by movable gears 1, $2^{(1)}$, 3, and the fixed carrier c. The magnitude $\delta_k^{(2)}$ ($k = 1, 3$) must be less than the angular distance between neighboring teeth. The magnitude $m_k^{(2)}$ ($k = 1, 3$) represents the integer number of spaces of gear 1 and 3 located in the area formed by lines $\overline{O_3 O_2^{(1)}}$ and $\overline{O_3 O_2^{(2)}}$ [Fig. 23.3.2(b)].

Step 4: Figure 23.3.2(b) enables us to determine the magnitude of related turns $\delta_3^{(2)}$ and $\delta_1^{(2)}$ required for the assembly of planet gear $2^{(2)}$ with gears 1 and 3. The generalized conditions of assembly of a planet gear $2^{(k)}$ ($k = 2, \dots, n$) in a gear drive with n planet gears are represented by the following equations:

(i) Figure 23.3.2(b) extended for an assembly of planet gear $2^{(k)}$ yields

$$m_1^{(k)} \frac{2\pi}{N_1} - \delta_1^{(k)} = \frac{(k-1)2\pi}{n} \qquad \left(\delta_1^{(k)} < \frac{2\pi}{N_1} \right) \tag{23.3.8}$$

$$m_3^{(k)} \frac{2\pi}{N_3} - \delta_3^{(k)} = \frac{(k-1)2\pi}{n} \qquad \left(\delta_3^{(k)} < \frac{2\pi}{N_3} \right) \tag{23.3.9}$$

$$\frac{\delta_3^{(k)}}{\delta_1^{(k)}} = \frac{N_1}{N_3}. \tag{23.3.10}$$

(ii) Equations (23.3.8) to (23.3.10) yield the following relation:

$$\frac{(k-1)(N_1 + N_3)}{n} = m_1^{(k)} + m_3^{(k)} \qquad (k = 2, \dots, n) \tag{23.3.11}$$

(iii) Taking into account that $(m_1^{(k)} + m_3^{(k)})$ is an integer number, we obtain that $(N_1 + N_3)/n$ has to be an integer number as well. This condition is observed, for instance, in the case where $N_1 = 62$, $N_3 = 228$, and $n = 5$.

Determination of $m_1^{(k)}$, $m_3^{(k)}$, $\delta_1^{(k)}$, and $\delta_3^{(k)}$ ($k = 1, \dots, n$)

Equations (23.3.8) and (23.3.9) and inequalities for $\delta_1^{(i)}$ and $\delta_3^{(i)}$ yield the following inequalities for determination of $m_1^{(k)}$ and $m_3^{(k)}$:

$$m_1^{(k)} - \frac{(k-1)N_1}{n} < 1 \qquad (k = 2, \dots, n) \tag{23.3.12}$$

$$\frac{(k-1)N_3}{n} - m_3^{(k)} < 1 \qquad (k = 2, \dots, n) \tag{23.3.13}$$

where $m_1^{(k)}$ and $m_3^{(k)}$ are integer numbers. We recall that $m_1^{(i)}$ and $m_3^{(i)}$ are the integer number of spaces of gears 1 and 3 that neighbor to the line of center distance $\overline{O_3 O_2^{(i)}}$. Figure 23.3.2(b) shows $m_3^{(2)}$ and $m_1^{(2)}$ of such spaces that neighbor to the line $\overline{O_3 O_2^{(2)}}$.

Table 23.3.1: Parameters $m_1^{(k)}$, $m_3^{(k)}$, $\delta_1^{(k)}$, and $\delta_3^{(k)}$

i	$m_1^{(k)}$	$m_3^{(k)}$	$\delta_1^{(k)}$	$\delta_3^{(k)}$
1	0	0	0	0
2	13	45	$\frac{3}{5\cdot62}2\pi$	$\frac{3}{5\cdot228}2\pi$
3	25	91	$\frac{1}{5\cdot62}2\pi$	$\frac{1}{5\cdot228}2\pi$
4	38	136	$\frac{4}{5\cdot62}2\pi$	$\frac{4}{5\cdot228}2\pi$
5	50	182	$\frac{2}{5\cdot62}2\pi$	$\frac{2}{5\cdot228}2\pi$

Determination of $\delta_1^{(k)}$ and $\delta_3^{(k)}$ that represent the turning angles of gears 1 and 3 for the assembly of planet gear $2^{(i)}$ with gears 1 and 3 is based on the following equations:

$$\delta_1^{(k)} = m_1^{(k)} \frac{2\pi}{N_1} - \frac{(k-1)2\pi}{n} \qquad (k = 2, \ldots, n) \qquad (23.3.14)$$

$$\delta_3^{(k)} = \frac{(k-1)2\pi}{n} - m_3^{(k)} \frac{2\pi}{N_3} \qquad (k = 2, \ldots, n). \qquad (23.3.15)$$
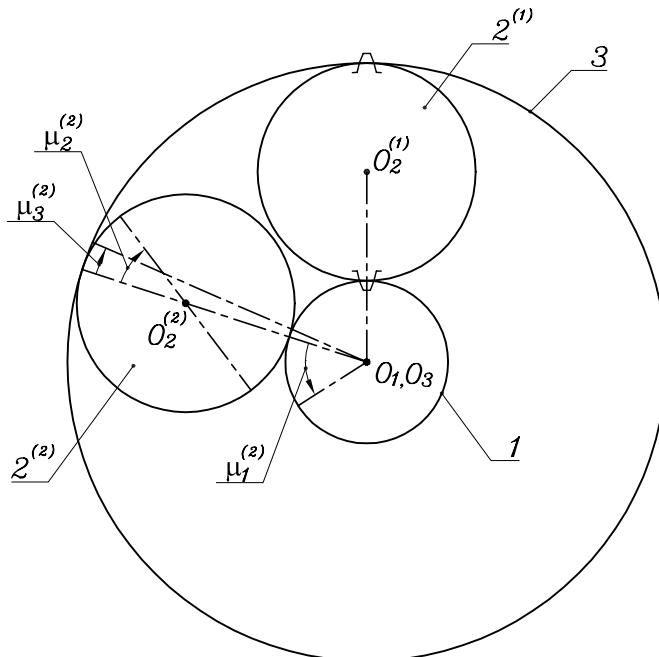
Numerical Example 23.3.1

A planetary gear drive with $N_1 = 62$, $N_3 = 228$, and $n = 5$ is considered. It is easy to verify that $(N_1 + N_3)/n$ is an integer number and the requirement (23.3.11) is observed indeed. The results of computations of $m_1^{(k)}$, $m_3^{(k)}$, $\delta_1^{(k)}$, and $\delta_3^{(k)}$ are presented in Table 23.3.1.

23.4 PHASE ANGLE OF PLANET GEARS

The concept of the phase angle is used in this chapter for computation of transmission errors (see Sections 23.7 and 23.8). A phase angle determines the angle that is formed by the axis of symmetry of the tooth (space) with the respective line of the center distance. The phase angle is zero wherein the axis of tooth (space) symmetry coincides with the respective line of center distance as shown in Fig. 23.3.2(a).

Figure 23.3.2(b) shows that axes of tooth (space) symmetry of gears 1, 2, and 3 will coincide with $\overline{O_3 O_2^{(2)}}$ after the related turns through angles $\delta_1^{(2)}$ and $\delta_3^{(2)}$ of gear 1 and 3 are accomplished (the gear drive formed by gears 1, $2^{(1)}$, and 3 is considered). However, such a turn will cause the respective axes of tooth (space) symmetry of gears 1, $2^{(1)}$, and 3 to be deviated from the line of center distance $\overline{O_3 O_2^{(2)}}$. To restore the orientation of tooth (space) axis of symmetry of gears 1, $2^{(1)}$, and 3 as shown in Fig. 23.3.2(a), we provide turns of gear 1 and 3 of the gear drive formed by 1, $2^{(1)}$, $2^{(2)}$, and 3 whereas carrier c is held at rest. The turn of gears 1 and 3 of the gear drive $(1, 2^{(1)}, 2^{(2)}, 3)$ is performed in the direction that is opposite to the direction of the turns $\delta_1^{(2)}$ and $\delta_2^{(2)}$. The

Figure 23.4.1: Illustration of orientation of tooth (spaces) axes of symmetry of gears 1, $2^{(2)}$, and 3 with respect to center distance $\overline{O_3 O_2^{(2)}}$.

turn mentioned above is accomplished for gears 1 and 3 of the gear drive formed by $(1, 2^{(1)}, 3)$.

Figure 23.4.1 shows the obtained orientation of respective axes of tooth (space) symmetry after the two sets of related turns are accomplished. Axes of tooth (space) symmetry of gears 1, $2^{(1)}$, and 3 are located on line $\overline{O_3 O_2^{(1)}}$. Angles $\mu_1^{(2)}$, $\mu_2^{(2)}$, and $\mu_3^{(2)}$ indicate the deviation of the respective axes of tooth (space) symmetry of gears 1, $2^{(2)}$, and 3 from $\overline{O_3 O_2^{(2)}}$.
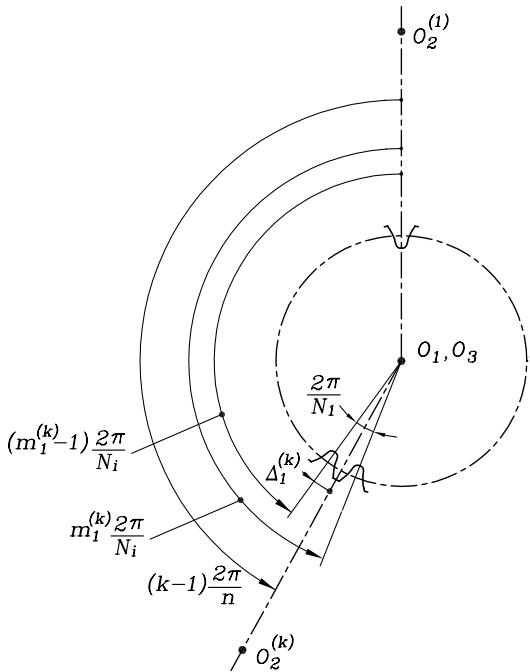
Figure 23.4.2 represents in enlarged scale the orientation of spaces of gear 1 in the area determined by spaces of numbers 1 and $m_1^{(k)}$ ($k = 2, 3, 4, 5$). The phase angle $\Delta_1^{(k)}$ is formed by line $\overline{O_3 O_2^{(k)}}$ and the space number ($m_1^{(k)} - 1$) that neighbors to $\overline{O_3 O_2^{(k)}}$ and is measured clockwise, in the direction of rotation of gear 1 in the gear drive with the carrier held at rest (Fig. 23.2.4).

Figure 23.4.2 yields the following equation for determination of the phase angle:

$$\Delta_1^{(k)} = \frac{(k-1)2\pi}{n} - (m_1^{(k)} - 1)\frac{2\pi}{N_1} \qquad (k = 2, \dots, 5) \qquad (23.4.1)$$

Using the input data for numerical example 23.3.1, we obtain the following results:

$$\Delta_1^{(2)} = \frac{2}{5 \cdot 62}2\pi; \quad \Delta_1^{(3)} = \frac{4}{5 \cdot 62}2\pi; \quad \Delta_1^{(4)} = \frac{1}{5 \cdot 62}2\pi; \quad \Delta_1^{(2)} = \frac{3}{5 \cdot 62}2\pi.$$

Figure 23.4.2: For derivation of phase angle $\Delta_1^{(k)}$.

23.5 EFFICIENCY OF A PLANETARY GEAR TRAIN

Let us compare a planetary gear train with a conventional one, with fixed gear axes, designed for the same gear ratio of angular velocities of the input and output mechanism links. The comparison shows the following:

(i) The planetary gear train has smaller dimensions than the conventional one. A conventional design requires application of a *set* of conventional gear drives but not a single train is applied for the assigned reduction of speed.

(ii) However, a planetary gear train usually has a much lower efficiency in comparison with a conventional gear train. An exception is the planetary gear train shown in Fig. 23.2.4 (see Example 23.5.2 below).

The determination of the efficiency of a planetary gear train is a complex problem. A simple solution to this problem is proposed by Kudrjavtzev *et al.* [1993] and is based on the following considerations:

(i) The efficiency of a planetary gear train is related to the efficiency of an inverted train when the relative velocities of the planetary train and the inverted one are observed to be the same. The inverted train is obtained from the planetary train wherein the carrier is held at rest and gear j, which has been fixed in the planetary train, is released.

(ii) Two cases of efficiency of a planetary train designated by $\eta_{ic}^{(j)}$ and $\eta_{ci}^{(j)}$ may be considered. Here, designations in $\eta_{ic}^{(j)}$ indicate that gear i and carrier c are the driving and driven links of the planetary train. Respectively, designations in $\eta_{ci}^{(j)}$

indicate that carrier c and gear i are the driving and driven links of the planetary train. In both cases, the superscript (j) indicates that gear j is the fixed one.

(iii) We consider gear i or carrier c as the driving link of the planetary gear train if

$$M_k \omega_k > 0, \quad (k = 1, c) \tag{23.5.1}$$

where M_k is the torque applied to link k; ω_k is the angular velocity of link i in absolute motion, in rotation about the frame of the planetary gear train.

(iv) It is assumed that a torque M_i of the same magnitude is applied to link i of the planetary and inverted gear trains. Torque M_i is considered as positive if i (but not c) is the driving link. In the case in which the driving link is the carrier, torque M_i is the resisting moment and $M_i < 0$. The ratio (ω_c/ω_i) may be obtained from the kinematics of the planetary gear train using the following equation for the train with fixed gear j:

$$\frac{\omega_1 - \omega_c}{-\omega_c} = m_{ij}^{(c)}. \tag{23.5.2}$$

The determination of the efficiency of planetary gear trains is considered for two typical examples. The discussed approach may be extended and applied to various examples of planetary gear trains.

Example 23.5.1
The planetary gear train shown in Fig. 23.2.4 is considered for the following conditions: (i) gear 3 is fixed ($j = 3$); and (ii) gear 1 and carrier c are the driving and driven links, respectively. Equation (23.5.2) yields

$$\frac{\omega_c}{\omega_1} = \frac{N_1}{N_3 + N_1}. \tag{23.5.3}$$

Consider now the inverted gear train where rotation is provided from gear 1 to gear 3 wherein the carrier is fixed. Torque M_1 is applied to gear 1 and M_1 is positive because gear 1 is the driving gear in the planetary gear train. The angular velocity ω_1 of gear 1 of the planetary gear train is of the same direction as M_1, and $M_1 \omega_1 > 0$.

The efficiency $\eta_{1c}^{(3)}$ of the planetary train is determined as

$$\eta_{1c}^{(3)} = \frac{M_1 \omega_1 - P_l}{M_1 \omega_1}. \tag{23.5.4}$$

Here, $(M_1 \omega_1 - P_l)$ is the output power, and $M_1 \omega_1$ is the input power ($M_1 \omega_1 > 0$). The key for determination of $\eta_{1c}^{(3)}$ is that the power P_l lost in the *planetary* gear train is determined as the power lost in the *inverted* train. The input power of the inverted train is $M_1(\omega_1 - \omega_c) > 0$, because $M_1 > 0$ and $(\omega_1 - \omega_c) > 0$. We consider as known the coefficient $\Psi^{(c)} = 1 - \eta^{(c)}$ of the inverted train. Then, we may determine the power lost in the inverted gear train as

$$P_l = \Psi^{(c)} M_1 (\omega_1 - \omega_c). \tag{23.5.5}$$

Equations (23.5.3), (23.5.4), and (23.5.5) yield

$$\eta_{1c}^{(3)} = 1 - \psi^{(c)} \left(\frac{N_3}{N_1 + N_3} \right). \tag{23.5.6}$$

Example 23.5.2

The same planetary gear train is considered given the conditions that the driving and driven links of the planetary gear train are the carrier and link 1, respectively. Gear 1 is now the driven link of the planetary gear train; $M_1 < 0$ because M_1 is the resisting moment. We consider now the inverted train taking into account that $M_1(\omega_1 - \omega_c) < 0$, because $M_1 < 0$ and $(\omega_1 - \omega_c) > 0$.

The power P_l lost in the inverted train is determined as follows:

$$P_l = \frac{1}{\eta^{(c)}}(-M_1)(\omega_1 - \omega_c) - (-M_1)(\omega_1 - \omega_c) = \frac{1 - \eta^{(c)}}{\eta^{(c)}}(-M_1)(\omega_1 - \omega_c). \quad (23.5.7)$$

Equation (23.5.7) provides that the lost power P_l is positive. (Recall that $M_1 < 0$ and $(\omega_1 - \omega_c) > 0$.)

Then we obtain

$$\eta_{c1}^{(3)} = \frac{P_{\text{driven}}}{P_{\text{driven}} + P_l} = \frac{-M_1\omega_1}{-M_1\omega_1 + \dfrac{1 - \eta^{(c)}}{\eta^{(c)}}(-M_1)(\omega_1 - \omega_c)}$$

$$= \frac{1}{1 + \dfrac{1 - \eta^{(c)}}{\eta^{(c)}}\left(1 - \dfrac{\omega_c}{\omega_1}\right)} = \frac{1}{1 + \dfrac{1 - \eta^{(c)}}{\eta^{(c)}}\left(\dfrac{N_3}{N_1 + N_3}\right)}. \quad (23.5.8)$$

It follows from Eq. (23.5.8) that the efficiency $\eta_{c1}^{(3)} > \eta^{(c)}$. This means that the planetary gear train shown in Fig. 23.2.4 has higher efficiency than the inverted gear train if the rotation in the planetary gear train is transformed from the carrier c to the sun gear 1.

23.6 MODIFICATIONS OF GEAR TOOTH GEOMETRY

We limit the discussion to the modification of gear tooth geometry for the planetary gear train shown in Fig. 23.2.4. Spur gears of involute profile are applied in the existing design. The purposes of modification of tooth geometry are as follows:

(i) Improvement of bearing contact and reduction of transmission errors. This goal is achieved by application of double-crowned planet gears.
(ii) Reduction of backlash between the planet gears and sun gear 1 and ring gear 3. The reduction of backlash enables us to obtain a more uniform distribution of load between the planet gears (see below).

Modification of Geometry of Planet Gears

The developed modification is based on double crowning of planet gears accomplished as a combination of profile crowning and longitudinal crowning (see Litvin *et al.* [2001c] and Chapter 15). Longitudinal crowning enables us to substitute instantaneous line contact of tooth surfaces by point contact and avoid an edge contact. Longitudinal crowning is achieved by tool plunging. Profile crowning of a planet gear enables us to substitute the involute profile by a profile that is conjugated to a parabolic profile of a rack-cutter (see Chapter 15). Then, a parabolic function of transmission errors can

be predesigned. Such a function of transmission errors is able to absorb almost linear functions of transmission errors caused by errors of alignment (see Section 9.2).

Modification of Tooth Geometry of Gears 1 and 3

The purpose of modification is to regulate backlash caused by angular errors of installment of the planet gears on the carrier [Litvin et al., 2002e]. The goal mentioned above is achieved as follows:

(i) The tooth surface of Σ_1 is designed as an external screw involute one of a small helix angle. Respectively, the tooth surface of Σ_3 is designed as an internal screw involute one of the same helix angle and direction as Σ_1.
(ii) The regulation of backlash between a planet gear $2^{(i)}$ and gears 1 and 3 is achieved by axial translation of gear $2^{(i)}$ that is accomplished during the assembly. The regulation has to be performed for the whole set of planet gears.

Figure 23.6.1 illustrates schematically how the backlash between planet gear $2^{(i)}$ and gears 1 and 3 is regulated. Figure 23.6.1(a) shows the backlash $\Delta x^{(i)}$ existing before regulation. Figure 23.6.1(b) shows that the backlash is eliminated by axial displacement $\Delta z^{(i)}$ of planet gear $2^{(i)}$. The regulation described above has to be accomplished for all planet gears of the set $2^{(i)}$ $(i = 1, \ldots, n)$.

23.7 TOOTH CONTACT ANALYSIS (TCA)

The TCA computer program enables simulation of misaligned gear drives for determination of transmission errors and conditions of contact.

Conventional Gear Drive

In the case of a conventional gear drive formed by two gears, there are two contacting gear tooth surfaces and the simulation of meshing is based on the following procedure (see Section 9.4).
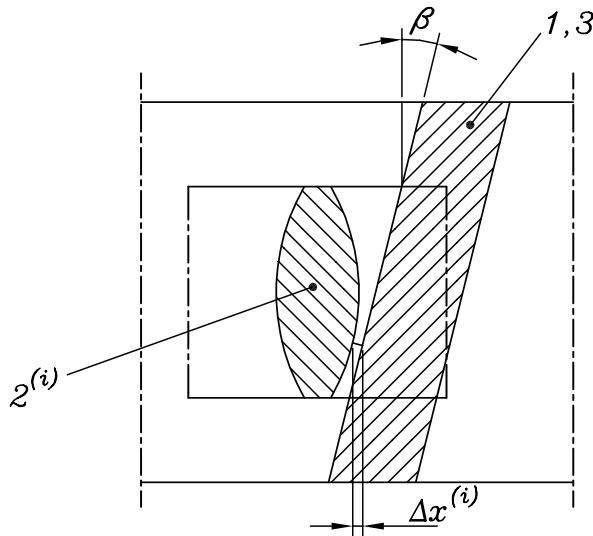
(i) The gear tooth surfaces are represented in a mutual coordinate system S_f rigidly connected to the housing of the gear drive.
(ii) The instantaneous tangency of gear tooth surfaces Σ_1 and Σ_2 is represented by the following vector equations:

$$\mathbf{r}_f^{(1)}(u_1, \theta_1, \phi_1) - \mathbf{r}_f^{(2)}(u_2, \theta_2, \phi_2) = \mathbf{0} \qquad (23.7.1)$$
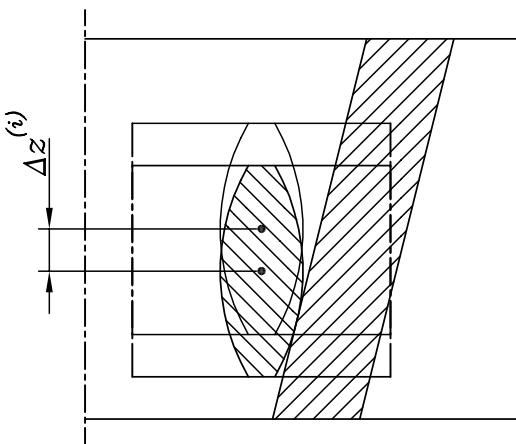
$$\mathbf{n}_f^{(1)}(u_1, \theta_1, \phi_1) - \mathbf{n}_f^{(2)}(u_2, \theta_2, \phi_2) = \mathbf{0}. \qquad (23.7.2)$$

Here, designations (u_i, θ_i) $(i = 1, 2)$ indicate surface parameters; ϕ_i $(i = 1, 2)$ are generalized parameters of motion of gears.

Vector equation (23.7.1) means that at a point M of tangency, surfaces Σ_1 and Σ_2 have a common position vector. Vector equation (23.7.2) confirms that the surfaces have a common unit vector of the normals to the surfaces.

(a)

(b)

Figure 23.6.1: Schematic illustration of regulation of backlash: (a) backlash between gears 1, 3, and $3^{(i)}$ before regulation; (b) elimination of backlash by axial displacement of $\Delta z^{(i)}$ of planet gear $2^{(i)}$.

Vector equations (23.7.1) and (23.7.2) yield a system of only five independent scalar equations because $|\mathbf{n}_f^{(1)}| = |\mathbf{n}_f^{(2)}| = 1$. One of the parameters, let us say ϕ_1, may be chosen as the input one. Surfaces Σ_1 and Σ_2 are in point contact if the respective Jacobian for the system of Eqs. (23.7.1) and (23.7.2) differs from zero (see Section 9.4). Then, at the point of tangency of Σ_1 and Σ_2, the system of equations (23.7.1) and (23.7.2) can be solved by functions (see Section 9.4)

$$\{u_1(\phi_1), \theta_1(\phi_1), u_2(\phi_1), \theta_2(\phi_1), \phi_2(\phi_1)\} \in C^1. \tag{23.7.3}$$

Using functions (23.7.3) and surface equations, we can determine the path of contact on surfaces Σ_1 and Σ_2, and the function of transmission errors (see Section 9.4).

Application of TCA for a Planetary Gear Drive (Fig. 23.2.4)
A planetary gear drive with several planet gears is a multi-body system. Considering the misaligned gear drive as a system of rigid bodies, we may find out that only one planet gear is in mesh at every instant. Conditions of tangency are determined as follows:

Step 1: The tooth surfaces of gears 1, $2^{(i)}$, and 3 are represented in fixed coordinate system S_3.

Step 2: The rotation of gears 1 and $2^{(i)}$ is determined by three parameters ϕ_1, $\phi_{2c}^{(i)}$, and ϕ_c. Here, ϕ_1 is the angle of rotation of gear 1, $\phi_{2c}^{(i)}$ is the angle of rotation of planetary gear $2^{(i)}$ with respect to the carrier c, and ϕ_c is the angle of rotation of the carrier.

Step 3: The conditions of tangency of gears 1 and $2^{(i)}$, and gears $2^{(i)}$ and 3 provide ten independent scalar equations. These equations contain eight surface parameters of gears 1, $2^{(i)}$, and 3 and three motion parameters ϕ_1, $\phi_{2c}^{(i)}$, and ϕ_c. Considering ϕ_1 as the input parameter, we may obtain from the TCA computer program the transmission function $\phi_c(\phi_1)$ and then determine the function of transmission errors of the misaligned planetary gear train.

The solution of ten non-linear equations can be simplified by representing them as two subsystems of five equations each and then applying an iterative process of solution. Applying tooth contact analysis (TCA) for various planet gears $2^{(i)}$, we may determine which of the planet gears is in mesh at the considered position ϕ_1.

Function of Transmission Errors of Sub-Gear Drives
For the purpose of regulation of backlash, we may determine the backlash considering sub-gear drives but not the planetary gear drive. The sub-gear drives used for such an approach are formed by gears $(1, 2^{(i)})$, $(2^{(i)}, 3)$, and $(1, 2^{(i)}, 3)$ $(i = 1, n)$.

Transformation of rotation of the sub-gear drives is performed whereas the carrier is held at rest. Applying TCA for the sub-gear drives, it becomes possible to determine the functions of transmission errors and the backlash as well. Then, it becomes possible to minimize and equalize the backlash of five planetary gears by regulation.
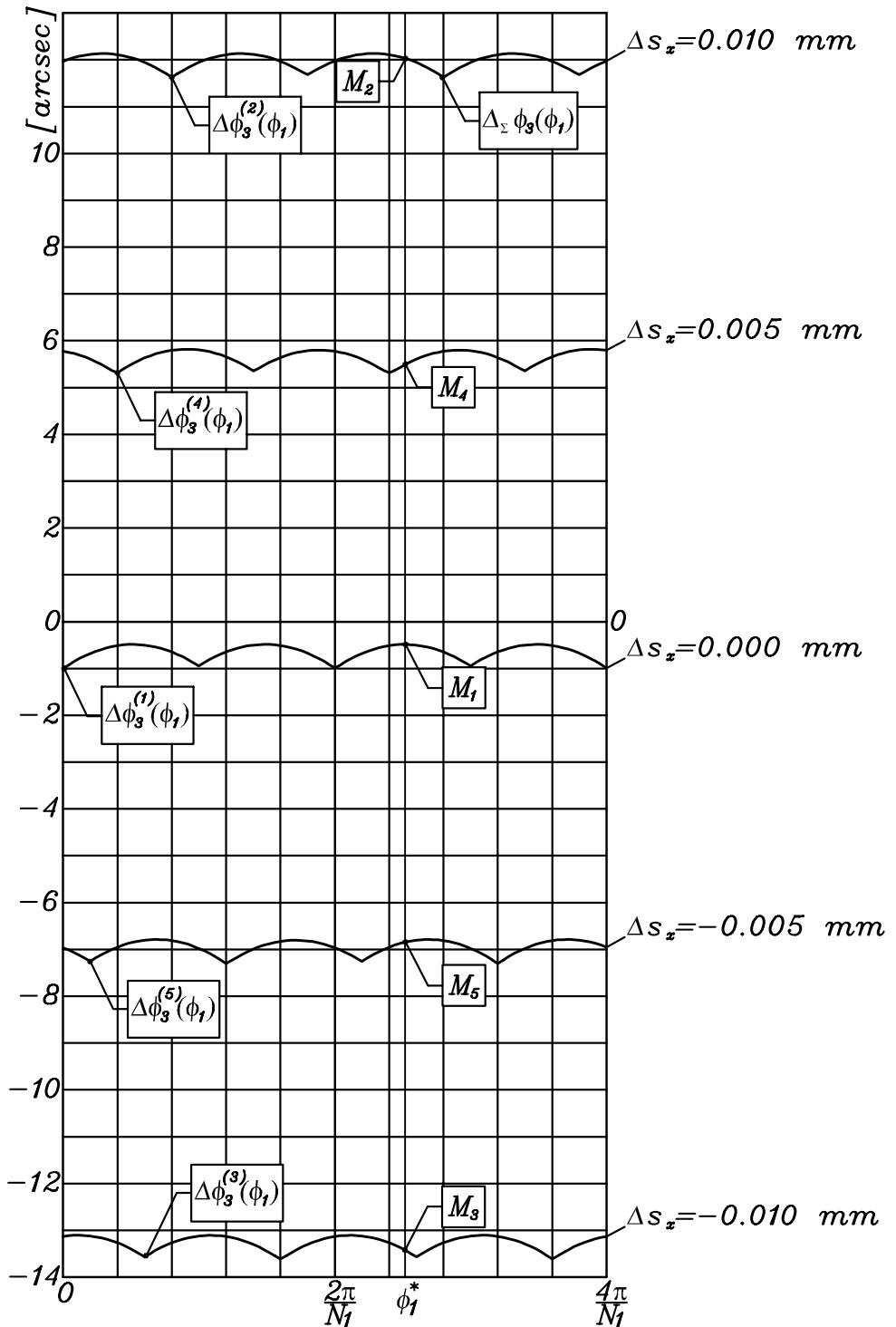
The resulting function of transmission errors of the sub-gear drive $(1, 2^{(i)}, 3)$ is determined as

$$\Delta\phi_3(\phi_1) = \phi_3(\phi_2(\phi_1)) - \frac{N_1}{N_3}\phi_1 \tag{23.7.4}$$

where $\phi_3(\phi_2(\phi_1))$ is obtained from the TCA computer program. An approximate solution for $\Delta\phi_3(\phi_1)$ is represented as

$$\Delta\phi_3(\phi_1) \approx \frac{N_2}{N_3}\Delta\phi_2(\phi_1) + \Delta\phi_3\left(\frac{N_1}{N_2}\phi_1\right). \tag{23.7.5}$$

An additional goal of application of developed TCA is the analysis of reduction of transmission errors obtained by regulation of installment of planet gears (see below).
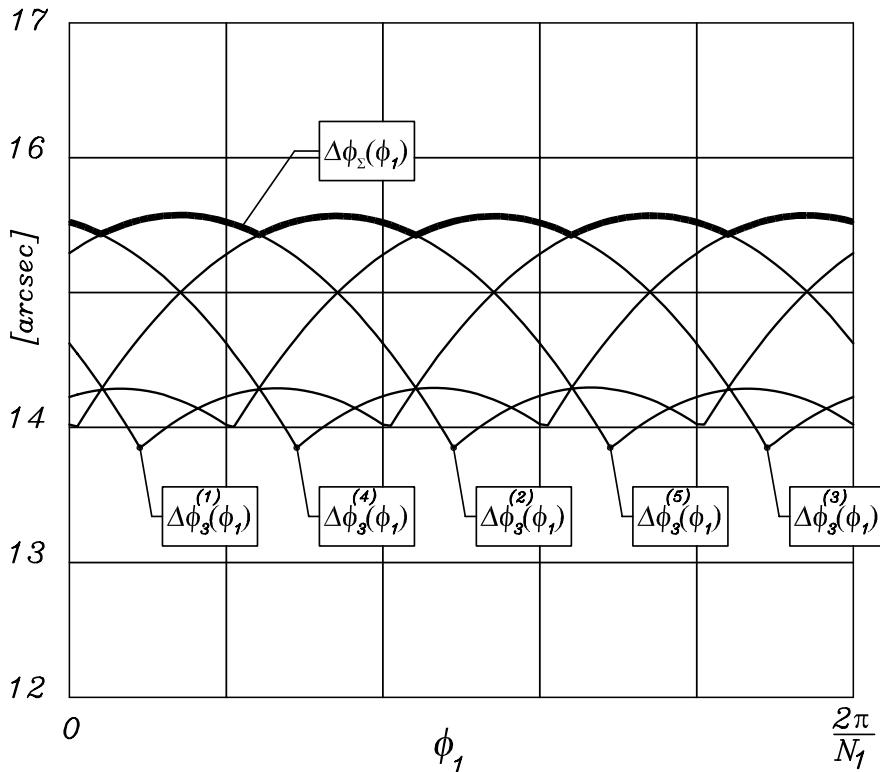
Figure 23.8.1: Functions of transmission errors $\Delta\phi_3^{(i)}(\phi_1)$ caused by double crowning and errors of location of planetary gears.

23.8 ILLUSTRATION OF THE EFFECT OF REGULATION OF BACKLASH

A planetary gear drive with $n = 5$ planet gears is considered (Fig. 23.2.4). Considering $n = 5$ sets of sub-gear drives, we may obtain functions of transmission errors for all sub-gear drives of the set of five planet gears as shown in Fig. 23.8.1. The transmission errors are caused as the result of double crowning of planet gears and errors of location of planet gears on the carrier. The designation Δs_x indicates an error of location of the planet gear measured in a direction that is perpendicular to the shortest distance between the planet gear and gear 1 (Fig. 23.2.4). Functions of transmission errors are represented in Fig. 23.8.1 taking into account the phase angles of planet gears (see Section 23.4). It is important to recognize that errors of functions $\Delta\phi_3^{(i)}(\phi_1)$ might be positive or negative (Fig. 23.8.1).

Analysis of the shape of the functions of transmission errors represented in Fig. 23.8.1 shows the following:

(a) Only one planetary gear of the set of five planets is in tangency with gear 3.
(b) It can happen, as shown in Fig. 23.8.1, that the *same* planet gear of the set of five is in mesh with gear 3, whereas the remaining planet gears are not in mesh with gear 3. The graphs of Fig. 23.8.1 show that the planet gear that is in mesh is

Figure 23.8.2: Illustration of functions of transmission errors for sub-drives and integrated function of transmission error.

gear $2^{(2)}$. The backlash at the position $\phi_1 = \phi_1^*$ between gears $2^{(k)}$ ($k = 1, 3, 4, 5$) is determined by $\Delta\phi_3 = M_2 M_k$ ($k = 1, 3, 4, 5$).

The backlash in sub-gear drives can be reduced by regulation of installment of planet gears on the carrier (see Fig. 23.6.1). Figure 23.8.2 shows the integrated function $\Delta\phi_\Sigma(\phi_1)$ of transmission errors obtained after the regulation mentioned above. Although a backlash does not remain constant, its variation in the process of meshing is reduced substantially. Taking into account the elastic deformation under the load, we may expect that the load will be distributed between the planet gears almost uniformly.

24 Generation of Helicoids

24.1 INTRODUCTION

Generation of worms, screws, and helical gears by milling cutters or grinding wheels is considered. Two types of tools for this process are applied: (i) the finger-shaped tool, and (ii) the disk-shaped one. Figures 24.1.1(a) and 24.1.2 show the finger-shaped and disk-shaped milling cutters, respectively. There are two main problems of design when generation of helicoids is considered: (i) the tool surface Σ_c is given and surface Σ_p of the workpiece must be determined, and (ii) the inverse problem, when surface Σ_p is given and Σ_c is to be determined.

Henceforth, we use coordinate systems S_c, S_p, and S_f, which are rigidly connected to the tool, the workpiece, and the frame of the cutting machine, respectively. Figure 24.1.3 shows the installation of the disk-shaped tool. Here, r_p is the pitch radius of the workpiece; r_c is the cutter mean radius; E_c and γ_c are the shortest distance and the crossing angle between the axes of rotation of the tool and the workpiece. In the case of application of the finger-shaped cutter, coordinate systems S_c and S_f coincide, and the tool axis is x_c [Fig. 24.1.1(b)].

The relative motion of the workpiece with respect to the tool is the screw one in both cases and is shown in Fig. 24.1.1(c); ψ and p are the angle of rotation and the screw parameter in the screw motion, respectively. Methods used for generation of helicoids, discussed in this chapter, have been developed by Litvin [1968].

24.2 GENERATION BY FINGER-SHAPED TOOL: TOOL SURFACE IS GIVEN

Surface Σ_c is a surface of revolution represented in S_c by the vector function
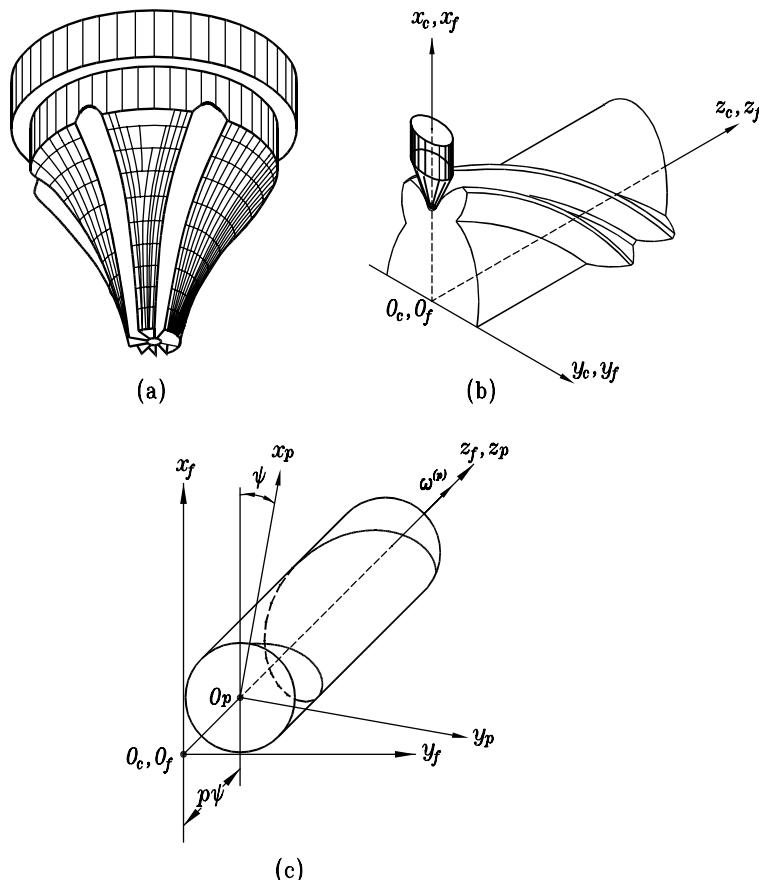
$$\mathbf{r}_c(u_c, \theta_c) = m(u_c)\, \mathbf{i}_c + g(u_c) \sin \theta_c\, \mathbf{j}_c + g(u_c) \cos \theta_c\, \mathbf{k}_c. \qquad (24.2.1)$$

Here, u_c, θ_c are the surface coordinates. Functions $m(u_c)$, $g(u_c)$ represent in plane $y_c = 0$ a planar curve that generates Σ_c by rotation about the x_c axis (see Section 5.5).
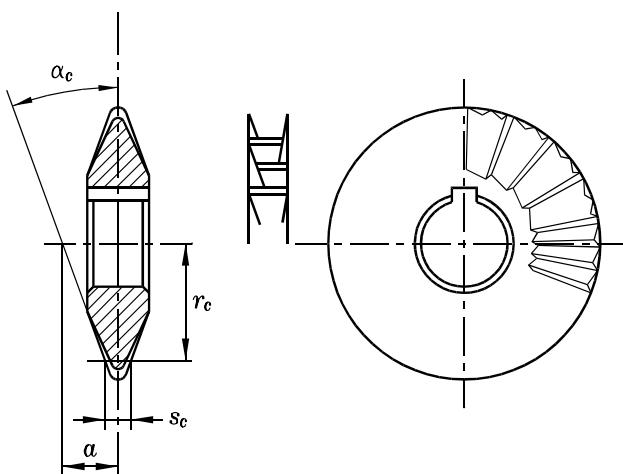
The normal to Σ_c is represented in S_c as

$$\mathbf{N}_c = \frac{\partial \mathbf{r}_c}{\partial u_c} \times \frac{\partial \mathbf{r}_c}{\partial \theta_c} = -g_u g\, \mathbf{i}_c + m_u g \sin \theta_c\, \mathbf{j}_c + m_u g \cos \theta_c\, \mathbf{k}_c \qquad (24.2.2)$$
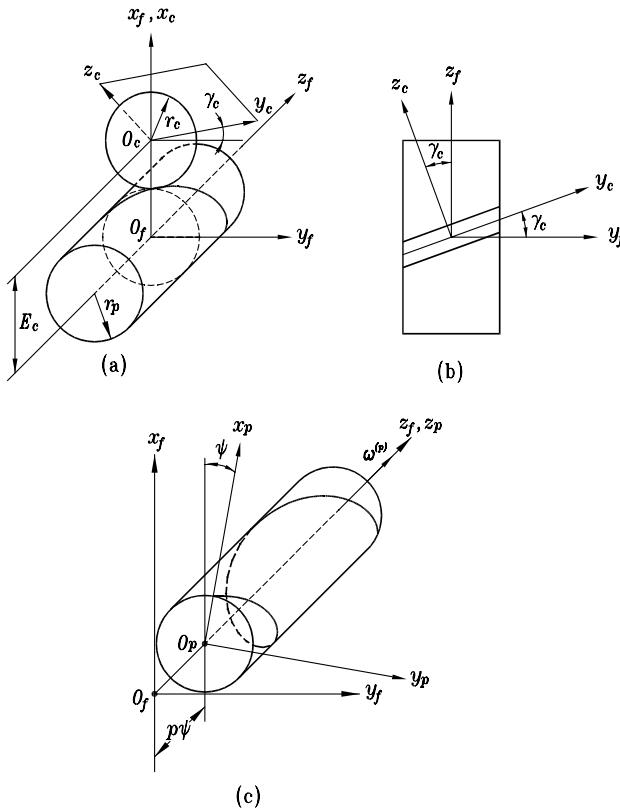
where $m_u = \partial m(u_c)/\partial u_c$, $g_u = \partial g(u_c)/\partial u_c$, and $g = g(u_c)$.

(a)   (b)

(c)

Figure 24.1.1: Generation by finger-shaped milling cutter: (a) illustration of cutter; (b) illustration of tool installment; (c) illustration of screw motion of coordinate system S_p.

Figure 24.1.2: Disk-shaped milling cutter.

Figure 24.1.3: Coordinate system applied for generation of workpiece by disk-shaped cutter: (a) installment of cutter; (b) illustration of crossing angle γ_c; (c) illustration of screw motion of the workpiece.

It is useful to verify for further derivations that for a surface of revolution, we have

$$y_c\, N_{zc} - z_c\, N_{yc} = 0. \tag{24.2.3}$$

The goals of the following development are (i) to derive the equation of meshing between Σ_c and Σ_p, and (ii) to determine Σ_p as the envelope to the family of Σ_c. It is important to recognize that the finger-shaped tool generates two surfaces for both sides of the tooth space of the workpiece [Fig. 24.1.1(b)].

Equation of Meshing

This equation is represented as

$$\mathbf{N}_c \cdot \mathbf{v}_c^{(cp)} = 0 \tag{24.2.4}$$

where $\mathbf{v}_c^{(cp)}$ is the relative velocity. The workpiece performs the screw motion [Fig. 24.1.1(c)] and

$$\mathbf{v}_c^{(cp)} = \mathbf{v}_c^{(c)} - \mathbf{v}_c^{(p)} = -\mathbf{v}_c^{(p)} = -\left(\boldsymbol{\omega}_c^{(p)} \times \mathbf{r}_c\right) - p\, \boldsymbol{\omega}_c^{(p)}. \tag{24.2.5}$$

Here, p is the screw parameter, and $\boldsymbol{\omega}_c^{(p)}$ is the angular velocity in the screw motion.

Equations (24.2.1) to (24.2.5) yield

$$f(u_c, \theta_c) = (gg_u + mm_u)\sin\theta_c + pm_u\cos\theta_c = 0. \tag{24.2.6}$$

Equations (24.2.1) and (24.2.6) determine on surface Σ_c two lines L_c of tangency between Σ_c and Σ_p (recall that Σ_c is in tangency with both sides of the tooth surfaces of the workpiece). Lines L_c do not depend on the parameter ψ of screw motion, because a helicoid is generated and p is constant.

Equation

$$f(u_c, \theta_c) = 0 \tag{24.2.7}$$

represents two planar curves in the plane of surface parameters (u_c, θ_c). Each of the curves is the image of contact lines L_c for the respective tooth side of the workpiece. In a more general case, when p is a function of ψ, there is a family of contact lines L_c on Σ_c.

Derivation of Generated Surface Σ_p

Surface Σ_p is defined in S_p as the family of contact lines L_c; Σ_p is represented by the equations

$$\mathbf{r}_p(u_c, \theta_c, \psi) = \mathbf{M}_{pc}(\psi)\mathbf{r}_c(u_c, \theta_c), \quad f(u_c, \theta_c) = 0. \tag{24.2.8}$$

Matrix $\mathbf{M}_{pc}$ describes the coordinate transformation in transition from S_c to S_p [Figs. 24.1.1(b) and 24.1.1(c)]. Equations (24.2.8) determine two surfaces, for both sides of the tooth, because there are two contact lines L_c defined by Eq. (24.2.7).

Problem 24.2.1

Surface Σ_c is a cone. The axial section of Σ_c intersected by plane $y_c = 0$ is shown in Fig. 24.2.1. Surface Σ_c is generated by straight line $\overline{NM}$ being rotated about the x_c axis. The location of current point M on the generating line is determined by the parameter $u_c = |\overline{NM}|$ (Fig. 24.2.1).

(1) Derive functions $m(u_c)$ and $g(u_c)$ using equations of $\overline{NM}$ in plane $y_c = 0$.
(2) Derive Eq. (24.2.2) of normal $\mathbf{N}_c$ to Σ_c.
(3) Derive Eq. (24.2.6) of meshing.
(4) The equation of meshing determines in the plane of surface parameters (u_c, θ_c) two lines L_c of tangency of Σ_c and Σ_p. Represent the graphs of L_c in the area

$$\frac{s_c}{2\sin\alpha_c} + \frac{p_{ax}}{\pi\cos\alpha_c} > u_c > 0, \quad 180° > \theta_c > -180°.$$
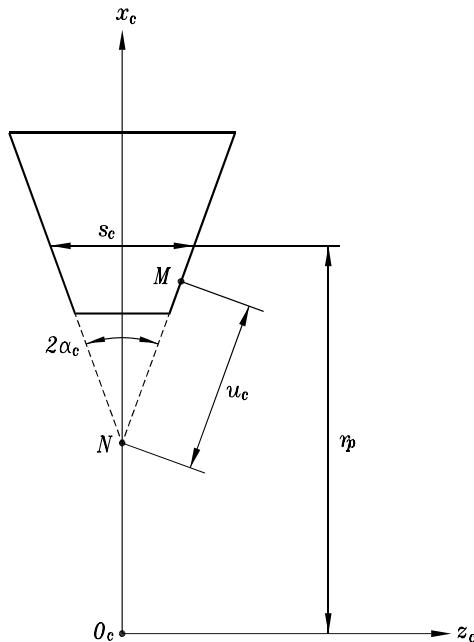
Here, p_{ax} is the axial distance between the neighboring worm threads determined as

$$p_{ax} = \frac{H}{N_1} = \pi m$$

where m is the axial module of the worm. Use the following worm data:

$$N_1 = 3; \quad r_p = 46 \text{ mm}; \quad m = 8 \text{ mm}.$$
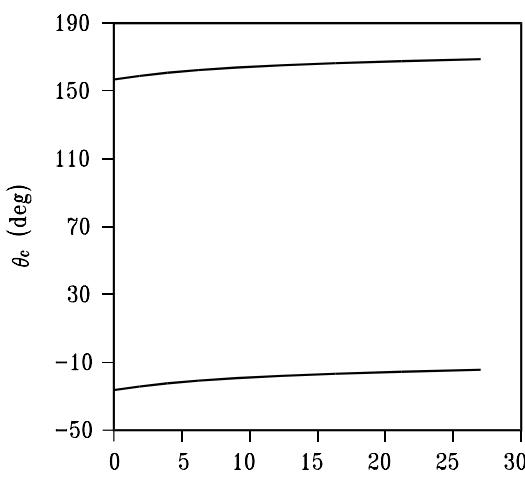
The cone data are $\alpha_c = 20°$; $s_c = 12.1594$ mm.
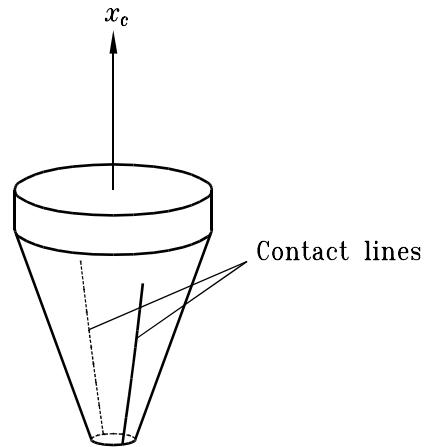
Figure 24.2.1: Cone axial section.

Solution

(1) $m(u_c) = (r_p - \frac{s_c}{2} \cot \alpha_c) + u_c \cos \alpha_c; \quad g(u_c) = u_c \sin \alpha_c.$

(2) $\mathbf{N}_c = u_c \sin \alpha_c (- \sin \alpha_c \, \mathbf{i}_c + \cos \alpha_c \sin \theta_c \, \mathbf{j}_c + \cos \alpha_c \cos \theta_c \, \mathbf{k}_c).$

(3) $f(u_c, \theta_c) = [u_c + (r_p - \frac{s_c}{2} \cot \alpha_c) \cos \alpha_c] \sin \theta_c + p \cos \alpha_c \cos \theta_c = 0.$

(4)   Two lines L_c in the plane of parameters (u_c, θ_c) are shown in Fig. 24.2.2. Lines L_c on the tool surface are shown in Fig. 24.2.3.

Figure 24.2.2: Finger-shaped tool: contact lines in space of surface parameters (u_c, θ_c).

Figure 24.2.3: Contact lines on cutter conical surface.

24.3 GENERATION BY FINGER-SHAPED TOOL: WORKPIECE SURFACE IS GIVEN

Our goal is to determine the tool surface Σ_c that generates the *given* surface Σ_p of the workpiece. The keystone in our approach is the following theorem (proposed by Litvin [1968]):

The line of tangency between Σ_p and Σ_c is one at which the normals to Σ_p intersect the axis of rotation of the finger-shaped tool.

The theorem follows from the facts that the tool surface Σ_c is a surface of revolution and the normal to Σ_c intersects the axis of rotation of the tool, and therefore the normal to Σ_p at the point of tangency with Σ_c must intersect the axis of the finger-shaped tool as well.

The procedure of derivation of equations of Σ_c is as follows:

Step 1: Consider that Σ_p and its normal are represented in S_p by the vector equations

$$\mathbf{r}_p(u_p, \theta_p) = f_1(u_p, \theta_p)\, \mathbf{i}_p + f_2(u_p, \theta_p)\, \mathbf{j}_p + f_3(u_p, \theta_p)\, \mathbf{k}_p \qquad (24.3.1)$$

$$\mathbf{N}_p = \frac{\partial \mathbf{r}_p}{\partial u_p} \times \frac{\partial \mathbf{r}_p}{\partial \theta_p} \qquad (\text{provided } \mathbf{N}_p \neq 0). \qquad (24.3.2)$$

Step 2: The coordinates of current point M of intersection of a normal to Σ_c with the x_c axis are represented in S_c as

$$\mathbf{r}_c^{(M)} = [X_c \quad 0 \quad 0 \quad 1]^{\mathrm{T}}. \qquad (24.3.3)$$

Point M is represented in S_p by using the equation

$$\mathbf{r}_p^{(M)} = \mathbf{M}_{pc}\mathbf{r}_c^{(M)} = [X_c \cos \psi \quad -X_c \sin \psi \quad -p\psi \quad 1]^{\mathrm{T}}. \qquad (24.3.4)$$

Matrix $\mathbf{M}_{pc}$ describes the coordinate transformation from S_c (S_c is identical to S_f) to S_p [Fig. 24.1.1(c)].

Step 3: The equations of the common normal to Σ_p and Σ_c are

$$\frac{X_c \cos \psi - x_p(u_p, \theta_p)}{N_{xp}(u_p, \theta_p)} = \frac{-X_c \sin \psi - y_p(u_p, \theta_p)}{N_{yp}(u_p, \theta_p)} = \frac{-p\psi - z_p(u_p, \theta_p)}{N_{zp}(u_p, \theta_p)}. \qquad (24.3.5)$$

Equation system (24.3.5) after elimination of X_c provides the relation

$$F(u_p, \theta_p, \psi) = 0. \qquad (24.3.6)$$

Equations (24.3.1) and (24.3.6) with fixed-in parameter ψ determine the family of lines of tangency L_p on Σ_p between surfaces Σ_p and Σ_c.

Step 4: There is a single line L_c on surface Σ_c that is the line of tangency of Σ_c with surface Σ_p where Σ_p is the surface of the respective side of the tooth (thread) of the workpiece. Lines L_p that cover surface Σ_p coincide in turn with line L_c in the process of generation. We may determine L_c taking $\psi = 0$ in Eqs. (24.3.5) and considering that coordinate systems S_c and S_p coincide at such an instant.

Equations (24.3.5) with $\psi = 0$ yield

$$f(u_p, \theta_p) = y_p N_{zp} - z_p N_{yp} = 0. \qquad (24.3.7)$$

The instantaneous line of tangency L_p (determined with $\psi = 0$) is represented as

$$\mathbf{r}_p = \mathbf{r}_p(u_p, \theta_p), \qquad f(u_p, \theta_p) = 0. \qquad (24.3.8)$$

Step 5: The shape of the finger-shaped tool may be represented by the function $\rho(x_c)$ (Fig. 24.3.1). Taking into account that $\psi = 0$, we have

$$x_c = x_p(u_p, \theta_p)$$

$$\rho_c = (y_p^2 + z_p^2)^{0.5} = |y_p| \left[1 + \left(\frac{N_{zp}}{N_{yp}} \right)^2 \right]^{0.5} = |z_p| \left[1 + \left(\frac{N_{yp}}{N_{zp}} \right)^2 \right]^{0.5}. \qquad (24.3.9)$$

We obtain the following system for computation of $\rho(x_c)$:

$$f(u_p, \theta_p) = 0, \quad x_c = x_p(u_p, \theta_p), \quad \rho_c = |z_p| \left[1 + \left(\frac{N_{yp}}{N_{zp}} \right)^2 \right]^{0.5}. \qquad (24.3.10)$$

Problem 24.3.1.
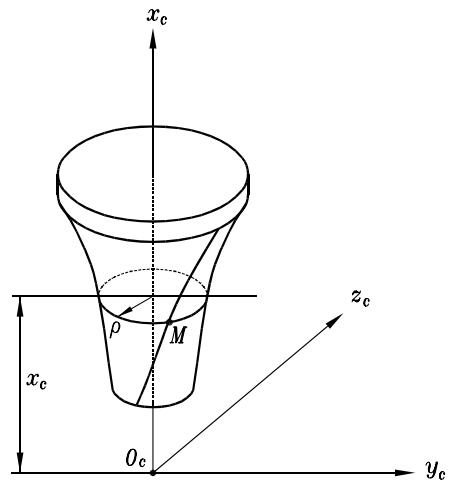
An involute worm is generated by the finger-shaped milling cutter. The screw involute surface side I of the tooth of a right-hand worm is represented by the equations (see Section 19.6),

$$x_p = r_b \cos(\theta_p + \mu) + u_p \cos \lambda_b \sin(\theta_p + \mu)$$
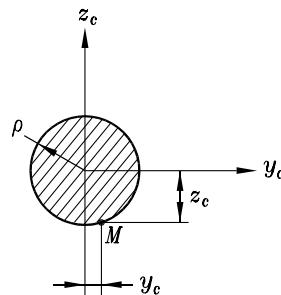
$$y_p = r_b \sin(\theta_p + \mu) - u_p \cos \lambda_b \cos(\theta_p + \mu) \qquad (24.3.11)$$

$$z_p = -u_p \sin \lambda_b + p\theta_p.$$

Here, r_b is the radius of the base cylinder; λ_b is the lead angle on the base cylinder, and

Figure 24.3.1: For determination of finger-shaped tool profile.

μ can be determined as

$$\mu = \frac{w_t}{2r_p} - \operatorname{inv}\alpha_t \tag{24.3.12}$$

where α_t is the pressure angle in cross section; w_t is the space width in the cross section measured on the pitch cylinder. For the case when the width of the space on the pitch cylinder is equal to the tooth thickness, we have

$$\frac{w_t}{2r_p} = \frac{\pi}{2N_1}.$$

We recall as well other relations between the worm design parameters (see Section 19.3),

$$\tan\alpha_t = \frac{\tan\alpha_n}{\sin\lambda_p}$$

$$\tan\lambda_b = \frac{r_p \tan\lambda_p}{r_b} = \frac{\tan\lambda_p}{\cos\alpha_t}$$

$$P_t = P_n \sin\lambda_p$$

$$r_p = \frac{N_1}{2P_t} = \frac{N_1}{2P_n \sin\lambda_p}$$

$$r_b = r_p \cos\alpha_t.$$

The surface unit normal is $\mathbf{n}_p = \mathbf{N}_p/|\mathbf{N}_p|$, where $\mathbf{N}_p = \partial\mathbf{r}_p/\partial\theta_p \times \partial\mathbf{r}_p/\partial u_p$ (provided $\mathbf{N}_p \neq 0$). Thus,

$$\mathbf{n}_p = [-\sin\lambda_b \sin(\theta_p + \mu) \quad \sin\lambda_b \cos(\theta_p + \mu) \quad -\cos\lambda_b]^{\mathrm{T}}. \qquad (24.3.13)$$

DERIVE:

(1) Equation of meshing (24.3.7)
(2) The system of equations for determination of the profile of the tool.

Solution

(1) $f(u_p, \theta_p) = u_p \cos(\theta_p + \mu) - r_b \cos\lambda_b \sin(\theta_p + \mu) - p\theta_p \sin\lambda_b \cos(\theta_p + \mu) = 0.$
(2) The tool profile is determined with the system of equations

$$f(u_p, \theta_p) = u_p \cos(\theta_p + \mu) - r_b \cos\lambda_b \sin(\theta_p + \mu) - p\theta_p \sin\lambda_b \cos(\theta_p + \mu) = 0$$

$$x_c = r_b \cos(\theta_p + \mu) + u_p \cos\lambda_b \sin(\theta_p + \mu)$$

$$z_p = -u_p \sin\lambda_b + p\theta_p$$

$$\rho = |z_p|\big[1 + \tan^2\lambda_b \cos^2(\theta_p + \mu)\big]^{0.5}.$$

The input for computation is θ_p, and the output data is $\rho(x_c)$.

24.4 GENERATION BY DISK-SHAPED TOOL: TOOL SURFACE IS GIVEN

The tool surface Σ_c is a surface of revolution. The axial section of the tool is a planar curve α–α that is represented in an auxiliary coordinate system S_a as [Fig. 24.4.1(a)]

$$x_a = m(u_c), \quad y_a = 0, \quad z_a = g(u_c) \qquad (24.4.1)$$

where u_c is the variable parameter that determines the location of a current point on α–α. The tool surface Σ_c is generated while coordinate system S_a with curve α–α is rotated about the z_c axis [Fig. 24.4.1(b)]. Surface Σ_c is represented in S_c by the matrix equation

$$\mathbf{r}_c(u_c, \theta_c) = \mathbf{M}_{ca}\mathbf{r}_a, \qquad (24.4.2)$$

which yields

$$\mathbf{r}_c(u_c, \theta_c) = m(u_c)\cos\theta_c \, \mathbf{i}_c - m(u_c)\sin\theta_c \, \mathbf{j}_c + g(u_c) \, \mathbf{k}_c. \qquad (24.4.3)$$
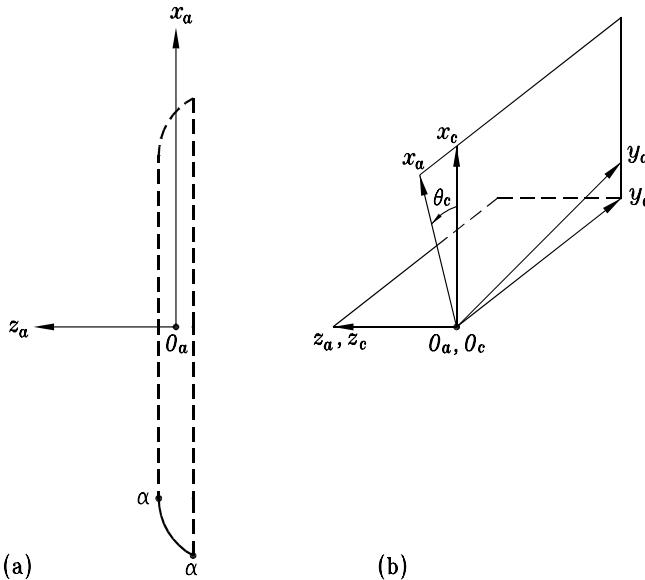
The surface normal is represented in S_c by the following equation:

$$\mathbf{N}_c = \frac{\partial\mathbf{r}_c}{\partial u_c} \times \frac{\partial\mathbf{r}_c}{\partial\theta_c} = g_u m \cos\theta_c \, \mathbf{i}_c - g_u m \sin\theta_c \, \mathbf{j}_c - m m_u \, \mathbf{k}_c. \qquad (24.4.4)$$

Equation of Meshing

The equation of meshing is represented as

$$\mathbf{N}_c \cdot \mathbf{v}_c^{(cp)} = 0. \qquad (24.4.5)$$

Figure 24.4.1: Disk-shaped tool surface generated by planar curve: (a) illustration of tool surface; (b) illustration of coordinate systems S_a and S_c.

The workpiece performs a screw motion with the angular velocity $\omega^{(p)}$ and the translational velocity $p\omega^{(p)}$ [Fig. 24.1.3(c)]. The velocity $\mathbf{v}_c^{(cp)}$ is determined by the equation

$$\mathbf{v}_c^{(cp)} = \mathbf{v}_c^{(c)} - \mathbf{v}_c^{(p)} = -\mathbf{v}_c^{(p)}. \tag{24.4.6}$$

Because the milling cutter is held at rest, vector $\mathbf{v}_c^{(p)}$ can be represented by the following equation:

$$\mathbf{v}_c^{(p)} = \left(\boldsymbol{\omega}_c^{(p)} \times \mathbf{r}_c\right) + \left(\mathbf{R}_c \times \boldsymbol{\omega}_c^{(p)}\right) + p\,\boldsymbol{\omega}_c^{(p)}. \tag{24.4.7}$$

Here [Fig. 24.1.3(a)],

$$\mathbf{R}_c = \overline{O_c O_f} = -E_c\,\mathbf{i}_c. \tag{24.4.8}$$

Taking into account that $\psi = 0$, we have

$$\boldsymbol{\omega}_c^{(p)} = \mathbf{L}_{cp}\boldsymbol{\omega}_p^{(p)} = \mathbf{L}_{cf}\mathbf{L}_{fp}\boldsymbol{\omega}_p^{(p)} = \omega^{(p)}[0 \quad \sin\gamma_c \quad \cos\gamma_c]^{\mathrm{T}}. \tag{24.4.9}$$

After transformations, we obtain

$$\mathbf{v}_c^{(cp)} = -\omega^{(p)} \begin{bmatrix} \sin\gamma_c\,z_c - \cos\gamma_c\,y_c \\ \cos\gamma_c\,(x_c + E_c) + p\sin\gamma_c \\ -\sin\gamma_c\,(x_c + E_c) + p\cos\gamma_c \end{bmatrix} \tag{24.4.10}$$

$$\mathbf{N}_c \cdot \mathbf{v}_c^{(cp)} = -\omega^{(p)}\{(\sin\gamma_c\,z_c - \cos\gamma_c\,y_c)\,N_{xc} + [\cos\gamma_c\,(x_c + E_c)$$
$$+ p\sin\gamma_c]N_{yc} + [-\sin\gamma_c\,(x_c + E_c) + p\cos\gamma_c]N_{zc}\} = 0. \tag{24.4.11}$$

There is a relation for a surface of revolution whose axis of rotation is the z_c axis:

$$x_c N_{yc} - y_c N_{xc} = 0. \tag{24.4.12}$$

The final expression for the equation of meshing is

$$f(u_c, \theta_c) = \sin \gamma_c \; z_c N_{xc} + (E_c \cos \gamma_c + p \sin \gamma_c) N_{yc}$$
$$+ [- \sin \gamma_c \, (x_c + E_c) + p \cos \gamma_c] N_{zc} = 0. \tag{24.4.13}$$

Equation (24.4.13) may determine more than one planar curve in the plane of parameters $E \in (u_c, \theta_c)$. Only the curve in the working area of E should be considered. This curve is the image of L_c in E, where L_c is the line of tangency of Σ_c and Σ_p.

Generated Surface

Surface Σ_p is represented in S_p by the following equations:

$$\mathbf{r}_p(u_c, \theta_c, \psi) = \mathbf{M}_{pf} \mathbf{M}_{fc} \mathbf{r}_c(u_c, \theta_c), \quad f(u_c, \theta_c) = 0. \tag{24.4.14}$$

Matrix $\mathbf{M}_{fc}$ describes the coordinate transformation from S_c to S_f, and matrix $\mathbf{M}_{pf}$ describes the coordinate transformation from S_f to S_p (Fig. 24.1.3). Equations (24.4.14) represent the generated surface in terms of three parameters, (u_c, θ_c, ψ), but (u_c, θ_c) are related with the equation of meshing.

Problem 24.4.1

Curve α–α is an arc of a circle of radius ρ (Fig. 24.4.2). The current point of α–α is represented by angle u_c. The location of center C of the circular arc is represented by coordinates

$$x_a^{(c)} = -d, \quad y_a^{(c)} = 0, \quad z_a^{(c)} = -b.$$

(i) Represent the cutter surface in coordinate system S_c by vector equation $\mathbf{r}_c = \mathbf{r}_c(u_c, \theta_c)$.
(ii) Derive the equation of meshing.
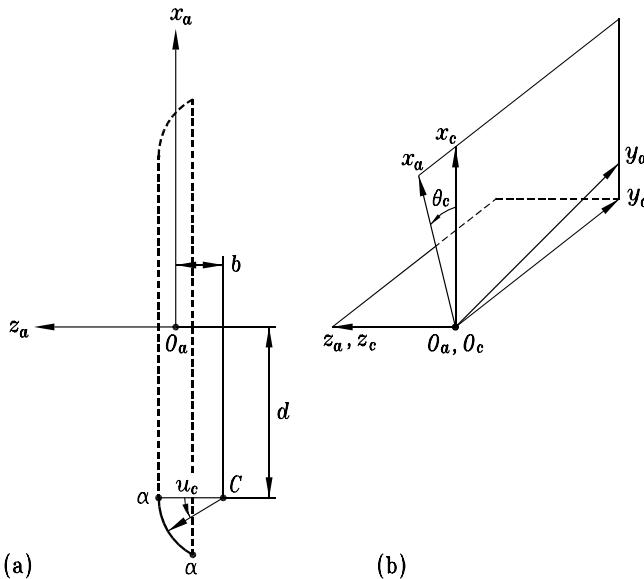
Solution
(i)

$$x_c = -(d + \rho \sin u_c) \cos \theta_c, \quad y_c = (d + \rho \sin u_c) \sin \theta_c, \quad z_c = -b + \rho \cos u_c.$$

(ii)

$$f(u_c, \theta_c) = b \sin \gamma_c \sin u_c \cos \theta_c + d \sin \gamma_c \cos \theta_c \cos u_c$$
$$+ E_c(\sin \theta_c \cos \gamma_c \sin u_c - \sin \gamma_c \cos u_c)$$
$$+ p(\sin \gamma_c \sin \theta_c \sin u_c + \cos \gamma_c \cos u_c) = 0.$$
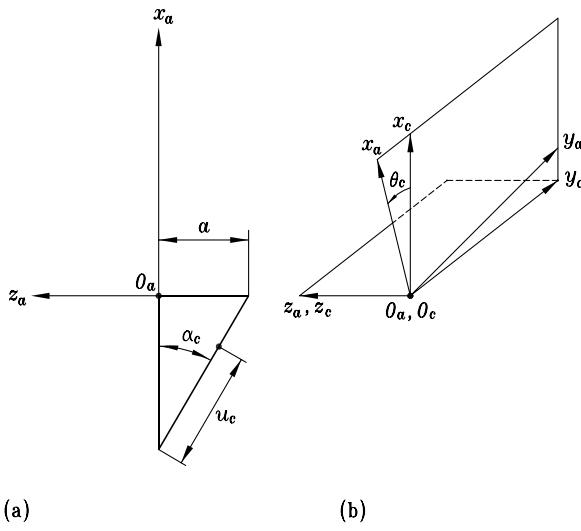
Figure 24.4.2: Disk-shaped tool surface generated by circular arc curve: (a) illustration of circular arc profile; (b) illustration of coordinate systems S_a and S_c.

Problem 24.4.2

The grinding wheel is generated by straight line α–α (Fig. 24.4.3).

(i) Represent the cutter surface by vector equation $\mathbf{r}_c = \mathbf{r}_c(u_c, \theta_c)$.
(ii) Derive the equation of meshing.

Figure 24.4.3: Cone tool surface generated by a straight line: (a) illustration of straight-line profile; (b) illustration of coordinate systems S_a and S_c.

Solution

(i)

$$x_c = (-a/\tan\alpha_c + u_c\cos\alpha_c)\cos\theta_c$$

$$y_c = (a/\tan\alpha_c - u_c\cos\alpha_c)\sin\theta_c$$

$$z_c = -u_c\sin\alpha_c.$$

(ii)

$$u_c = -E_c\left(\cot\gamma_c\tan\theta_c\sin\alpha_c + \frac{\cos\alpha_c}{\cos\theta_c}\right)$$

$$+ p\left(\frac{\cot\gamma_c\cos\alpha_c}{\cos\theta_c} - \tan\theta_c\sin\alpha_c\right)$$

$$+ a\cot\alpha_c\cos\alpha_c.$$

24.5 GENERATION BY DISK-SHAPED TOOL: WORKPIECE SURFACE IS GIVEN

The surface of a workpiece is given by the vector function

$$\mathbf{r}_p = \mathbf{r}_p(u_p, \theta_p). \tag{24.5.1}$$

The normal to the workpiece surface is determined with the following equation:

$$\mathbf{N}_p = \frac{\partial\mathbf{r}_p}{\partial u_p} \times \frac{\partial\mathbf{r}_p}{\partial\theta_p} = \mathbf{N}_p(u_p, \theta_p). \tag{24.5.2}$$

Equation of Meshing

The derivation of the equation of meshing is based on the same theorem that was applied in Section 24.3:

The line of tangency between Σ_p and tool surface Σ_c is one at which the normals to Σ_p intersect the rotation axis of the disk-shaped tool.

The common normal to surfaces Σ_p and Σ_c is represented by the following equation:

$$\frac{X_p - x_p(u_p, \theta_p)}{N_{xp}(u_p, \theta_p)} = \frac{Y_p - y_p(u_p, \theta_p)}{N_{yp}(u_p, \theta_p)} = \frac{Z_p - z_p(u_p, \theta_p)}{N_{zp}(u_p, \theta_p)}. \tag{24.5.3}$$

Here, (X_p, Y_p, Z_p) are the coordinates of the point of intersection of the normal with the z_c axis of the tool in S_p. We consider the position when S_p coincides with S_f ($\psi = 0$). The point of intersection of the normal with the z_c axis can be represented by the equation

$$\begin{bmatrix} X_p \\ Y_p \\ Z_p \\ 1 \end{bmatrix} = \mathbf{M}_{pc}\begin{bmatrix} 0 \\ 0 \\ Z_c \\ 1 \end{bmatrix} = \begin{bmatrix} 1 & 0 & 0 & E_c \\ 0 & \cos\gamma_c & -\sin\gamma_c & 0 \\ 0 & \sin\gamma_c & \cos\gamma_c & 0 \\ 0 & 0 & 0 & 1 \end{bmatrix}\begin{bmatrix} 0 \\ 0 \\ Z_c \\ 1 \end{bmatrix}. \tag{24.5.4}$$

Equations (24.5.3) and (24.5.4) yield

$$\frac{E_c - x_p}{N_{xp}} = \frac{-Z_c \sin \gamma_c - y_p}{N_{yp}} = \frac{Z_c \cos \gamma_c - z_p}{N_{zp}}. \tag{24.5.5}$$

Using Eq. (24.5.5), we can eliminate Z_c. Then, we can simplify the obtained equation of meshing using the relation obtained for a helicoid (see Section 5.5):

$$y_p N_{xp} - x_p N_{yp} - p N_{zp} = 0. \tag{24.5.6}$$

The final expression of the equation of meshing is

$$f(u_p, \theta_p) = (E_c - x_p + p \cot \gamma_c) N_{zp} + E_c \cot \gamma_c N_{yp} + z_p N_{xp} = 0. \tag{24.5.7}$$

Determination of Contact Line on the Tool Surface

There is a family of contact lines on the workpiece surface. We consider a *single* contact line on the workpiece surface determined with $\psi = 0$. This line is determined on Σ_p by the equations

$$\mathbf{r}_p = \mathbf{r}_p(u_p, \theta_p), \qquad f(u_p, \theta_p) = 0. \tag{24.5.8}$$

The contact line on the cutter surface is determined with the equations

$$\mathbf{r}_c(u_p, \theta_p) = \mathbf{M}_{cf} \mathbf{M}_{fp} \mathbf{r}_p(u_p, \theta_p), \qquad f(u_p, \theta_p) = 0. \tag{24.5.9}$$

Matrix $\mathbf{M}_{fp}$ is a unitary matrix because coordinate systems S_f and S_p coincide when ψ is equal to zero (Fig. 24.1.3).

Determination of the Tool Profile

Figure 24.5.1 shows the line of tangency of surfaces Σ_c and Σ_p on the cutter surface Σ_c; M is the current point of this line with coordinates (x_c, y_c, z_c). The profile of the tool obtained by intersection of the tool surface by plane $y_c = 0$ (axial section) can be represented by coordinates (x_c, z_c). The computational procedure is as follows:

Step 1: Use equation of meshing (24.5.7) and consider θ_p as the input data, and then determine the respective value u_p. Be advised that equation $f(u_p, \theta_p) = 0$ determines more than one curve in the plane of parameters (u_p, θ_p). Eliminate the curve that does not belong to the working part of the workpiece.
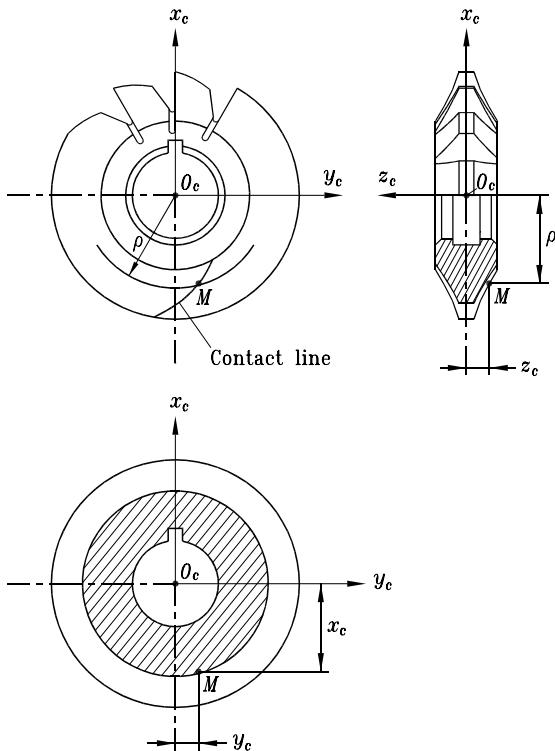
Step 2: Knowing the couple (u_p, θ_p), determine the coordinates (x_c, y_c, z_c) of the contact line from the matrix equation

$$\mathbf{r}_c(u_p, \theta_p) = \mathbf{M}_{cf} \mathbf{M}_{fp} \mathbf{r}_p(u_p, \theta_p).$$

(Use for derivations of matrices $\mathbf{M}_{cf}$ and $\mathbf{M}_{fp}$ the drawings of Fig. 24.1.3)

Step 3: Determine ρ using the equation

$$\rho = \left(x_c^2 + y_c^2\right)^{0.5} = \rho(u_p, \theta_p). \tag{24.5.10}$$

Figure 24.5.1: For derivation of disk-shaped tool profile.

Step 4: Considering θ_p as the input parameter and using Eqs. (24.5.9) and (24.5.10), we determine the coordinates

$$x_c(\theta_p) = -\rho(\theta_p), \quad z_c(\theta_p)$$

of the tool axial profile.

Problem 24.5.1

Given: the surface side I of an involute helical gear that is represented by the equations [see Eqs. (14.3.5)]

$$
\begin{aligned}
x_p &= r_b \cos(\theta_p + \mu) + u_p \cos \lambda_b \sin(\theta_p + \mu) \\
y_p &= r_b \sin(\theta_p + \mu) - u_p \cos \lambda_b \cos(\theta_p + \mu) \\
z_p &= -u_p \sin \lambda_b + p\theta_p.
\end{aligned}
\tag{24.5.11}
$$

Here, r_b is the radius of the base cylinder; λ_b is the lead angle on the base cylinder; μ is determined as

$$\mu = \frac{w_t}{2r_p} - \tan \alpha_t + \alpha_t.$$

DERIVE:

(i) The equation of meshing (24.5.7)
(ii) The system of equations for determination of the profile of the tool.

Solution

(i)

$$f(u_p, \theta_p) = (u_p - p\theta_p \sin \lambda_b) \sin(\theta_p + \mu) - (E_c + p \cot \gamma_c) \cos \lambda_b$$
$$+ (E_c \cot \gamma_c \sin \lambda_b + r_b \cos \lambda_b) \cos(\theta_p + \mu) = 0.$$

(ii)

$$x_c = r_b \cos(\theta_p + \mu) + u_p \cos \lambda_b \sin(\theta_p + \mu) - E_c$$
$$y_c = [r_b \sin(\theta_p + \mu) - u_p \cos \lambda_b \cos(\theta_p + \mu)] \cos \gamma_c + [-u_p \sin \lambda_b + p\theta_p] \sin \gamma_c$$
$$z_c = [-r_b \sin(\theta_p + \mu) + u_p \cos \lambda_b \cos(\theta_p + \mu)] \sin \gamma_c + [-u_p \sin \lambda_b + p\theta_p] \cos \gamma_c$$
$$f(u_p, \theta_p) = 0.$$

Considering the previously represented system of equations and choosing θ_p as the input parameter, we determine the coordinates of the tool axial profiles as

$$x_c(\theta_p) = -(x_c^2 + y_c^2)^{0.5}, \quad z_c(\theta_p).$$

25 Design of Flyblades

25.1 INTRODUCTION

Flyblades are used for generation of worm-gears in small-scale production to avoid the manufacture of expensive hobs. However, the production of worm-gears by flyblades is less effective in comparison with production by hobs. The profiles of the flyblades are determined as profiles of the worm thread in the normal tooth section obtained by intersection of the thread by plane Π (Fig. 25.1.1). The orientation of the plane Π is determined with the lead angle λ_p on the worm pitch cylinder.
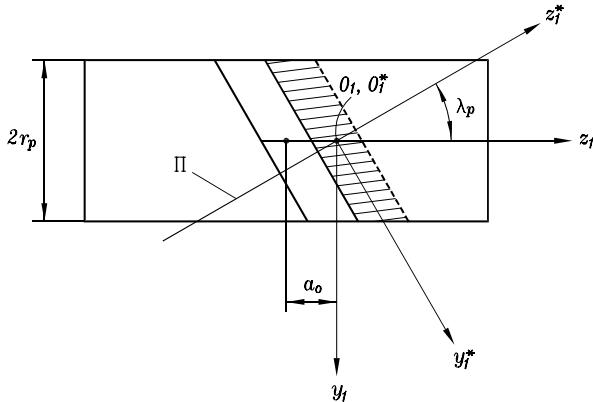
A symmetrical location of the profiles of the flyblade in coordinate system $S_1^\star$ can be obtained if the $x_1^\star$ axis is the axis of symmetry of the worm *thread*. In Chapter 19, we have derived equations of worm surfaces for the case when the x_1 axis of coordinate system S_1 is the axis of symmetry of the worm *space*. To obtain the desired location of axis x_1 (as the axis of tooth symmetry), it is necessary to displace the origin O_1 of coordinate system S_1 in the axial direction at the magnitude $a_o = p_{ax}/2$, where p_{ax} is the axial distance between two neighboring threads of the worm.

The process of generation of the worm-gear by a flyblade simulates the meshing of the worm with the worm-gear in such a specific case when the worm performs translational motion in an axial direction in addition to the worm rotational motion. The angle of rotation ϕ_2 of the worm-gear in the process for generation is a sum of the two following components:

$$\phi_2 = \frac{\phi_1 N_1}{N_2} + \frac{s_{tr}}{p}. \tag{25.1.1}$$

Here, ϕ_1 is the angle of rotation of the worm, N_1 is the number of worm threads, N_2 is the number of worm-gear teeth, $p = r_p \tan \lambda_p$ is the screw parameter, and s_{tr} is the worm (flyblade) axial translation that is an imput parameter chosen from technological considerations.

In the case of a drive with a multi-thread worm, the flyblade generates only those teeth of the worm-gear that are in mesh with the respective threads of the worm. Therefore, indexing of the worm-gear is required to generate the entire number of worm-gear teeth. Indexing can be avoided if N_1 and N_2 are prime numbers (they do not have a common multiplier), for instance, when we have $N_1 = 3$, $N_2 = 32$. In such a case the flyblade

Figure 25.1.1: For determination of profiles of flyblade.

after each revolution of the worm-gear will start to generate the worm-gear teeth that are in mesh with the next thread of the multi-thread worm.

The following part of this chapter covers the determination of profiles of the flyblade for various types of worm geometry of worm-gear drives. The computational procedure represented below covers two cases of representation of worm geometry: (i) the two-parameter form, and (ii) the three-parameter form (but with related parameters) of worm surface representation.

25.2 TWO-PARAMETER FORM REPRESENTATION OF WORM SURFACES

Step 1: Consider that the worm thread surface (say, the surface side I) is represented by the vector equation (see Chapter 19)

$$\mathbf{r}_1(u, \theta) = x_1(u, \theta)\,\mathbf{i}_1 + y_1(u, \theta)\,\mathbf{j}_1 + z_1(u, \theta)\,\mathbf{k}_1, \tag{25.2.1}$$

and the x_1 axis is the axis of symmetry of the worm *space*. To provide that the x_1 axis will be the axis of symmetry of the worm thread, it is necessary to displace the origin O_1 of coordinate system S_1 along the z_1 axis on $a_o = p_{ax}/2$. Thus, we obtain that

$$z_1 = z_1(u, \theta) + a_o. \tag{25.2.2}$$
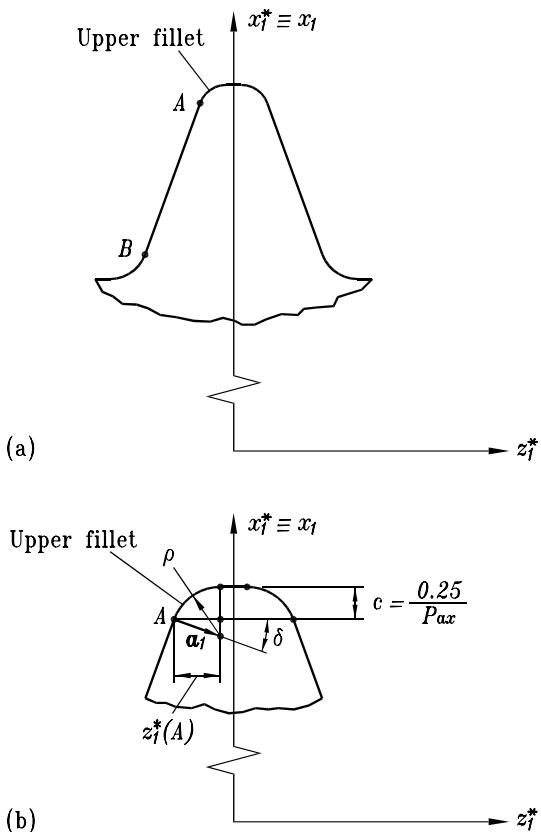
Step 2: The profiles of the worm thread are considered in plane Π of the normal section. Thus, we have

$$y_1 + z_1 \tan \lambda_p = 0. \tag{25.2.3}$$

Equations (25.2.2) and (25.2.3) yield

$$F(u, \theta) = y_1(u, \theta) + \tan \lambda_p [z_1(u, \theta) + a_o] = 0. \tag{25.2.4}$$

Step 3: Consider that θ is the input parameter. Solving Eq. (25.2.4), we will obtain function $u(\theta)$ (provided $\partial F/\partial \theta \neq 0$). The requirement $\partial F/\partial \theta \neq 0$ follows from the theorem of implicit function system existence (see Korn & Korn [1968] and Litvin [1989]).

Figure 25.2.1: (a) Illustration of flyblade profile; (b) for derivation of upper fillet.

Step 4: We can determine now the profile of one side of the flying blade using the equations

$$x_1(u, \theta) = x_1(u(\theta), \theta) = x_1(\theta), \quad z_1^{\star}(\theta) = -\frac{y_1(u(\theta), \theta)}{\sin \lambda_p}. \tag{25.2.5}$$

Step 5: Functions $x_1(\theta)$, $z_1^{\star}(\theta)$ determine the profile of the flyblade (Fig. 25.2.1). The range of θ is determined with the following conditions:

(i) Point A of the normal section of the worm thread must belong to the worm cylinder of radius r_a. Here,

$$\left\{ [x_1(\theta)]^2 + [y_1(\theta)]^2 \right\}^{0.5} = r_a \tag{25.2.6}$$

is the radius of the worm addendum cylinder.

(ii) Point B of the normal section of the worm thread belongs to the worm cylinder of radius $(r_d + c)$ and is determined with the equation

$$\left\{ [x_1(\theta)]^2 + [y_1(\theta)]^2 \right\}^{0.5} = r_d + c. \tag{25.2.7}$$

Here, r_d is the radius of the worm dedendum cylinder; c is the clearance between the worm and the worm-gear.

Step 6: The upper path of the profile of the flyblade must be complemented with the upper *fillet* [Fig. 25.2.1(a)]. To provide the tangency of the fillet with the segment AB, we will have to determine the normal $\mathbf{a}_1$ to the planar curve AB at point A. Consider that normal $\mathbf{N}_1$ to the worm thread surface is represented in coordinate system $S_1(x_1, y_1, z_1)$. Then, using the coordinate transformation from S_1 to $S_1^\star(x_1, y_1^\star, z_1^\star)$, we will determine the normal $\mathbf{N}_1^\star$ and then obtain

$$\mathbf{a}_1 = N_{x1}^\star \mathbf{i}_1^\star + N_{z1}^\star \mathbf{k}_1^\star. \tag{25.2.8}$$

Step 7: Using Fig. 25.2.1(b), we can derive the following equation for the fillet radius ρ:

$$\rho = \frac{c}{1 - \sin \delta} \quad (\text{provided } \rho \cos \delta \leq |z_1^\star(A)|) \tag{25.2.9}$$

where

$$\tan \delta = \left| \frac{n_{x1}^\star}{n_{z1}^\star} \right| \quad \left(0 < \delta < \frac{\pi}{2} \right). \tag{25.2.10}$$

The upper fillet generates the bottom of the space of the worm-gear. The bottom fillet of the flyblade is to be obtained similarly. The described procedure can be applied for the ZA, ZN, and ZI worms (see Chapter 19).

25.3 THREE-PARAMETER FORM REPRESENTATION OF WORM SURFACES

The worm thread surface is the envelope to the family of tool surfaces and is represented by the equations

$$\mathbf{r}_1(u_c, \theta_c, \psi) = x_1(u_c, \theta_c, \psi) \, \mathbf{i}_1 + y_1(u_c, \theta_c, \psi) \, \mathbf{j}_1 + z_1(u_c, \theta_c, \psi, a_o) \, \mathbf{k}_1 \tag{25.3.1}$$

$$f(u_c, \theta_c) = 0. \tag{25.3.2}$$

Here, u_c, θ_c are the surface parameters of the tool; ψ is the parameter of motion in the process for generation of the worm by the tool surface; Eq. (25.3.2) is the equation of meshing.

Equations (25.3.1) and (25.3.2) represent the thread surfaces of the ZK and ZF worms (see Chapter 19). The thread profile is located in plane Π (Fig. 25.1.1), and

$$y_1(u_c, \theta_c, \psi) + z_1(u_c, \theta_c, \psi) \tan \lambda_p = 0. \tag{25.3.3}$$

Equations (25.3.1) and (25.3.3) yield

$$F(u_c, \theta_c, \psi) = 0. \tag{25.3.4}$$

The system of Eqs. (25.3.2) and (25.3.4) represents two relations for the set of three parameters (u_c, θ_c, ψ). Choosing one of the three parameters as the input one, say θ_c, we can determine the coordinates $x_1(\theta_c), z_1^\star(\theta_c)$ of the flyblade profile. The following is the application of the computational procedures described above for the determination of flyblade profiles.

25.4 WORKING EQUATIONS

ZA (Archimedes) Worm
The surface side I of the worm thread (dashed line in Fig. 25.1.1) for the right-hand worm is represented by the equations (see Section 19.4)

$$x_1 = u \cos \alpha \cos \theta$$

$$y_1 = u \cos \alpha \sin \theta \tag{25.4.1}$$

$$z_1 = -u \sin \alpha + \left(r_p \tan \alpha - \frac{s_p}{2} \right) + p\theta + \frac{p_{ax}}{2}$$

where the nominal value of $s_p = p_{ax}/2$. The normal to the worm thread is determined with the equations

$$N_{x1} = -(p \sin \theta + u \sin \alpha \cos \theta)$$

$$N_{y1} = (p \cos \theta - u \sin \alpha \sin \theta) \tag{25.4.2}$$

$$N_{z1} = -u \cos \alpha.$$

Following the previously described procedure of derivations, we obtain

$$u(\theta) = \frac{-\left(r_p \tan \alpha + \frac{s_p}{2} + p\theta \right)}{(\sin \theta \cot \lambda_p - \tan \alpha) \cos \alpha} \tag{25.4.3}$$

$$x_1(\theta) = u(\theta) \cos \alpha \cos \theta, \quad z_1^\star = -\frac{u(\theta) \cos \alpha \sin \theta}{\sin \lambda_p}. \tag{25.4.4}$$

Equations (25.4.3) and (25.4.4) enable us to determine the profile of the flyblade. The range of θ for computations is determined with Eqs. (25.2.6) and (25.2.7). The starting value of θ for computations by application of Eq. (25.4.3) is $\theta = 0$. The upper fillet is determined as described in Section 25.2.

ZN (Convolute) Worm
The surface side I of the thread for the right-hand worms is represented as (see Section 19.5)

$$x_1 = \rho \sin(\theta + \mu) + u \cos \delta \cos(\theta + \mu)$$

$$y_1 = -\rho \cos(\theta + \mu) + u \cos \delta \sin(\theta + \mu) \tag{25.4.5}$$

$$z_1 = \rho \frac{\cos \alpha \cot \lambda_p}{\cos \delta} - u \sin \delta + p\theta + \frac{p_{ax}}{2}$$

where the x_1 axis is the axis of symmetry of the thread. We recall that the worm surface is generated by a straight line that performs the screw motion about the worm axis. The straight line is tangent to the worm cylinder of radius ρ and the orientation of the

generating straight line is determined with parameter α. Here,

$$\cos\mu = \frac{\cos\alpha}{\cos\delta}, \qquad \cos\delta = (\cos^2\alpha + \sin^2\alpha\sin^2\lambda_p)^{\frac{1}{2}}$$

$$\rho = \left(r_p - \frac{s_p}{2}\cot\alpha\right)\frac{\sin\alpha\sin\lambda_p}{(\cos^2\alpha + \sin^2\alpha\sin^2\lambda_p)^{\frac{1}{2}}}$$

(see the designations of s_p and α in Fig. 19.5.3).

The normal to the worm thread is represented by the equations

$$N_{x1} = -[(p + \rho\tan\delta)\sin(\theta + \mu) + u\sin\delta\cos(\theta + \mu)]$$

$$N_{y1} = (p + \rho\tan\delta)\cos(\theta + \mu) - u\sin\delta\sin(\theta + \mu) \qquad (25.4.6)$$

$$N_{z1} = -u\cos\delta.$$

The profile of the flyblade is determined with the following systems of equations:

$$u = \frac{\rho\left[\cos(\theta + \mu) - \dfrac{\cos\alpha}{\cos\delta}\right]\cot\lambda_p - p\theta - \dfrac{p_{ax}}{2}}{[\sin(\theta + \mu)\cot\lambda_p - \tan\delta]\cos\delta}$$

$$x_1 = \rho\sin(\theta + \mu) + u\cos\delta\cos(\theta + \mu) \qquad (25.4.7)$$

$$z_1^\star = \frac{\rho\cos(\theta + \mu) - u\cos\delta\sin(\theta + \mu)}{\sin\lambda_p}.$$

The starting value of θ for computations is $\theta = 0$. The range of θ is determined with Eqs. (25.2.6) and (25.2.7). The upper fillet is determined as described in Section 25.2.

ZI (Involute) Worm

The surface side I of the thread for the right-hand worm is represented as (see Section 19.6)

$$x_1 = r_b\cos(\theta + \mu) + u\cos\lambda_b\sin(\theta + \mu)$$

$$y_1 = r_b\sin(\theta + \mu) - u\cos\lambda_b\cos(\theta + \mu) \qquad (25.4.8)$$

$$z_1 = -u\sin\lambda_b + p\theta + \frac{p_{ax}}{2}.$$

The surface normal is represented with equations,

$$N_{x1} = -\sin\lambda_b\sin(\theta + \mu)$$

$$N_{y1} = \sin\lambda_b\cos(\theta + \mu) \qquad (25.4.9)$$

$$N_{z1} = -\cos\lambda_b.$$

Here, axis x_1 is the axis of symmetry of thread in the $y_1 = 0$ plane, r_b is the radius of the base cylinder, and λ_b is the radius of the lead angle on the base cylinder. Angle μ is

determined as

$$\mu = \frac{w_t}{2r_p} - \text{inv}\,\alpha_t$$

where w_t is the space width (see Fig. 19.6.3).

The flyblade profile is determined with the following equations:

$$u(\theta) = \frac{r_b \sin(\theta + \mu) \cot \lambda_p + p\theta + \dfrac{p_{ax}}{2}}{[\tan \lambda_b + \cos(\theta + \mu) \cot \lambda_p] \cos \lambda_b}$$

$$x_1 = r_b \cos(\theta + \mu) + u \cos \lambda_b \sin(\theta + \mu) \tag{25.4.10}$$

$$z_1^{\star} = -\frac{r_b \sin(\theta + \mu) - u \cos \lambda_b \cos(\theta + \mu)}{\sin \lambda_p}.$$

The initial value θ for computations is $\theta = 0$. The range of θ is determined with Eqs. (25.2.6) and (25.2.7). The upper fillet is determined as described in Section 25.2.

ZK (Klingelnberg) Worm

We remind the reader that the thread surface is generated by a cone surface (see Section 19.7).

The surface side I of the thread of the right-hand worm is represented by the equations

$$x_1 = u_c(\cos \alpha_c \cos \theta_c \cos \psi + \cos \alpha_c \cos \gamma_c \sin \theta_c \sin \psi$$
$$- \sin \alpha_c \sin \gamma_c \sin \psi) + a \sin \gamma_c \sin \psi + E_c \cos \psi$$

$$y_1 = u_c(-\cos \alpha_c \cos \theta_c \sin \psi + \cos \alpha_c \cos \gamma_c \sin \theta_c \cos \psi \tag{25.4.11}$$
$$- \sin \alpha_c \sin \gamma_c \cos \psi) + a \sin \gamma_c \cos \psi - E_c \sin \psi$$

$$z_1 = u_c(\sin \alpha_c \cos \gamma_c + \cos \alpha_c \sin \gamma_c \sin \theta_c) - p\psi - a \cos \gamma_c + \frac{p_{ax}}{2}.$$

Here,

$$u_c = a \sin \alpha_c - (E_c \sin \alpha_c \cot \gamma_c + p \sin \alpha_c) \tan \theta_c - \frac{(E_c - p \cot \gamma_c) \cos \alpha_c}{\cos \theta_c} \tag{25.4.12}$$

where (25.4.12) is the equation of meshing of the tool and the thread surfaces. The normal to the thread surface is represented by the equations

$$N_{x1} = \cos \psi \sin \alpha_c \cos \theta_c + \sin \psi(\cos \gamma_c \sin \alpha_c \sin \theta_c + \sin \gamma_c \cos \alpha_c)$$

$$N_{y1} = -\sin \psi \sin \alpha_c \cos \theta_c + \cos \psi(\cos \gamma_c \sin \alpha_c \sin \theta_c + \sin \gamma_c \cos \alpha_c) \tag{25.4.13}$$

$$N_{z1} = \sin \gamma_c \sin \alpha_c \sin \theta_c - \cos \gamma_c \cos \alpha_c.$$

Usually, $\gamma_c = \lambda_p$. Equation

$$y_1 + z_1 \tan \lambda_p = 0$$

yields

$$F(\psi, u_c, \theta_c) = \cos \psi \, [u_c(\cos \alpha_c \cos \gamma_c \sin \theta_c - \sin \alpha_c \sin \gamma_c) + a \sin \gamma_c]$$
$$- \sin \psi \, (u_c \cos \alpha_c \cos \theta_c + E_c) - p \tan \lambda_p \psi$$
$$+ \tan \lambda_p \Big[u_c(\sin \alpha_c \cos \gamma_c + \cos \alpha_c \sin \gamma_c \sin \theta_c)$$
$$- a \cos \gamma_c + \frac{p_{ax}}{2} \Big] = 0. \tag{25.4.14}$$

The procedure of computations is as follows:

Step 1: Consider simultaneously the system of nonlinear equations (25.4.12) and (25.4.14) in the unknowns (ψ, u_c, θ_c). Solve numerically the above system by functions $u_c(\theta_c)$, $\psi(\theta_c)$, where θ_c is the input variable. The first guess for the solution of Eqs. (25.4.12) and (25.4.14) is based on the following assumptions: $\theta_c = \pi$, $\sin \psi \approx \psi$, $\cos \psi \approx 1$. Then, using Eqs. (25.4.12) and (25.4.14), we obtain

$$\psi = \frac{\dfrac{p_{ax}}{2} \tan \lambda_p}{E_c + p \tan \lambda_p - u_c \cos \alpha_c} \tag{25.4.15}$$

where

$$u_c = a \sin \alpha_c + (E_c - p \cot \gamma_c) \cos \alpha_c. \tag{25.4.16}$$

Step 2: Determine the coordinates $x_1^\star \equiv x_1$ and $z_1^\star$ of the blade profile using Eqs. (25.4.17). Here, $x_1^\star = x_1(\psi, u_c, \theta_c)$ is the first equation of equation system (25.4.11), and

$$z_1^\star = -[u_c(- \cos \alpha_c \cos \theta_c \sin \psi + \cos \alpha_c \cos \gamma_c \sin \theta_c \cos \psi$$
$$- \sin \alpha_c \sin \gamma_c \cos \psi) + a \sin \gamma_c \cos \psi - E_c \sin \psi] / \sin \lambda_p. \tag{25.4.17}$$

The range of θ_c for computations is determined with Eqs. (25.2.6) and (25.2.7). The upper fillet is determined as described in Section 25.2.

F-I (Flender Version I) Worm

Recall that the worm thread surface is the envelope to the family of tool surfaces (see Section 19.8). The surface side I of the thread for right-hand worms is represented by the equations (see Section 19.8)

$$x_1 = (\rho \sin \theta_c + d)(- \cos v \cos \psi + \sin v \sin \psi \cos \gamma_c)$$
$$+ (\rho \cos \theta_c - b) \sin \psi \sin \gamma_c + E_c \cos \psi$$
$$y_1 = (\rho \sin \theta_c + d)(\cos v \sin \psi + \sin v \cos \psi \cos \gamma_c) \tag{25.4.18}$$
$$+ (\rho \cos \theta_c - b) \cos \psi \sin \gamma_c - E_c \sin \psi$$
$$z_1 = (\rho \sin \theta_c + d) \sin v \sin \gamma_c + (b - \rho \cos \theta_c) \cos \gamma_c - p\psi + a_o + \frac{p_{ax}}{2}$$

where

$$\tan \theta_c = \frac{E_c - p \cot \gamma_c - d \cos v}{b \cos v - (E_c \cot \gamma_c + p) \sin v}. \qquad (25.4.19)$$

Equation (25.4.19) is the equation of meshing of the worm thread surface with the tool surface. Parameter a_o enables us to obtain that the axis of symmetry of the axial section of the worm space will coincide with the x_1 axis. Taking in Eqs. (25.4.18) $y_1 = 0$, $x_1 = r_p$, and $z_1 = p_{ax}/4$, we obtain

$$a_o = -(\rho \sin \theta_c + d) \sin v \sin \gamma_c - (b - \rho \cos \theta_c) \cos \gamma_c + p\psi - \frac{p_{ax}}{4}. \qquad (25.4.20)$$

The normal to the worm thread surface is represented by the equations

$$N_{x1} = \sin \theta_c(-\cos v \cos \psi + \sin v \sin \psi \cos \gamma_c) + \cos \theta_c \sin \psi \sin \gamma_c$$

$$N_{y1} = \sin \theta_c(\cos v \sin \psi + \sin v \cos \psi \cos \gamma_c) + \cos \theta_c \cos \psi \sin \gamma_c \qquad (25.4.21)$$

$$N_{z1} = \sin \theta_c \sin v \sin \gamma_c - \cos \theta_c \cos \gamma_c.$$

Equation

$$y_1 + z_1 \tan \lambda_p = 0$$

yields

$$\begin{aligned}
F(\psi, \theta_c, v) = {} & \cos \psi [(\rho \sin \theta_c + d) \sin v \cos \gamma_c + (\rho \cos \theta_c - b) \sin \gamma_c] \\
& + \sin \psi [(\rho \sin \theta_c + d) \cos v - E_c] - p \tan \lambda_p \psi \\
& + \left[(\rho \sin \theta_c + d) \sin v \sin \gamma_c + (b - \rho \cos \theta_c) \cos \gamma_c \right. \\
& \left. + a_o + \frac{p_{ax}}{2} \right] \tan \lambda_p = 0.
\end{aligned} \qquad (25.4.22)$$

Nonlinear equations (25.4.19) and (25.4.22) relate three unknowns: v, θ_c, and ψ.

The procedure for computations of the blade profile is as follows:

Step 1: Using Eq. (25.4.19), we obtain numerically function $\theta_c(v)$. Equation (25.4.19) with the input value of v provides two solutions for θ_c, but only the solution $0 < \theta_c < 180°$ must be used (see Section 19.8).

Step 2: Knowing the related parameters v and θ_c, we can solve Eq. (25.4.22) for ψ. The first guess for the solution is based on the following considerations:

(i) Taking $v = 0$, $\rho = r_p$, and $\gamma_c = \lambda_p$, we obtain from Eq. (25.4.19)

$$\tan \theta_c = \frac{E_c - p \cot \lambda_p - d}{b} = \tan \alpha_n.$$

Thus, $\theta_c = \alpha_n$.

(ii) Taking $\sin \psi \approx \psi$, $\cos \psi \approx 1$, $\theta_c = \alpha_n$, we obtain from Eq. (25.4.22) that the initial value of ψ is

$$\psi = \frac{\left[(b - \rho \cos \alpha_n) \cos \gamma_c + a_o + \dfrac{p_{ax}}{2}\right] \tan \lambda_p + (\rho \cos \alpha_n - b) \sin \gamma_c}{p \tan \lambda_p - (\rho \sin \alpha_n + d - E_c)} \quad (25.4.23)$$

$$\psi = \frac{\left(a_0 + \dfrac{p_{ax}}{2} \sin 2\lambda_p\right)}{2r_p}.$$

Usually, $\gamma_c = \lambda_p$ and ρ is chosen equal to r_p.

Step 3: Knowing the related parameters v, θ_c, and ψ and using the first equation of equation system (25.4.18), we obtain the coordinate $x_1^\star = x_1(v, \theta_c, \psi)$ of the blade profile. The coordinate $z_1^\star(v, \theta_c, \psi)$ of the blade profile is represented by the equation

$$z_1^\star = -[(\rho \sin \theta_c + d)(\cos v \sin \psi + \sin v \cos \psi \cos \gamma_c)$$
$$+ (\rho \cos \theta_c - b) \cos \psi \sin \gamma_c - E_c \sin \psi]/ \sin \lambda_p. \quad (25.4.24)$$
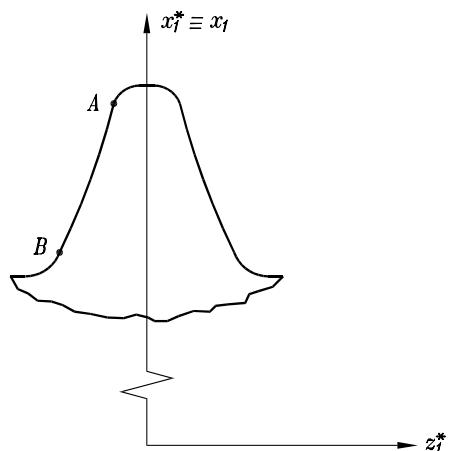
The range of v, θ_c, and ψ for determination of the coordinates $x_1^\star$ and $z_1^\star$ is determined with Eqs. (25.2.6) and (25.2.7). The upper fillet is determined as described in Section 25.2.

Problem 25.4.1

The surface side I of the thread for the right-hand worm F-I is represented by Eqs. (25.4.18); x_1 is the axis of symmetry of the thread. To avoid pointing of the teeth of worm-gears, the tooth thickness of the worm on the pitch cylinder is designed as $t_p = 0.4 p_{ax} = 0.4\pi/P_{ax}$.

Figure 25.4.1 shows the profiles of the flyblade for generation of the F-I worm-gear. The design data of the worm are $N_1 = 3$, $r_p = 46$ mm, axial module $m_{ax} = 8$ mm,

Figure 25.4.1: Flyblade for F-I worm-gear.

$\rho = 46$ mm, $\gamma_c = \lambda_p = 14°37'15''$, $\alpha_n = 20°$, $a = r_p + \rho \sin \alpha_n = 61.733$ mm, and $b = \rho \cos \alpha_n = 43.226$ mm.

F-II (Flender Version II) Worm

Unlike the F-I worm thread surface, the F-II thread surface is represented in two-parameter form (but not in three-parameter form). The surface equations are (see Section 19.9)

$$x_1 = -\rho(\sin\theta_c \cos\psi - \cos\theta_c \sin\psi \sin\gamma_c) + a\cos\psi$$

$$y_1 = \rho(\sin\theta_c \sin\psi + \cos\theta_c \cos\psi \sin\gamma_c) - a\sin\psi \qquad (25.4.25)$$

$$z_1 = -\rho\cos\theta_c \cos\gamma_c - p\psi + a_o + \frac{p_{ax}}{2}.$$

To derive the expression for a_o, we consider in the axial worm section by plane $y_1 = 0$ the point with coordinates $x_1 = r_p$, $y_1 = 0$, $z_1 = p_{ax}/4$. Then we obtain

$$a_o = -\frac{p_{ax}}{4} + \rho\cos\theta_c \cos\gamma_c + p\psi. \qquad (25.4.26)$$

The normal to the thread surface is represented by

$$N_{x1} = -\sin\theta_c \cos\psi + \sin\gamma_c \cos\theta_c \sin\psi$$

$$N_{y1} = \sin\theta_c \sin\psi + \sin\gamma_c \cos\theta_c \cos\psi \qquad (25.4.27)$$

$$N_{z1} = -\cos\gamma_c \cos\theta_c.$$

Equation

$$y_1 + z_1 \tan\lambda_p = 0$$

yields

$$F(\psi, \theta_c) = \rho\cos\theta_c \sin\gamma_c \cos\psi + (\rho\sin\theta_c - a)\sin\psi - p\tan\lambda_p\psi$$
$$+ \left(a_o - \rho\cos\theta_c \cos\gamma_c + \frac{p_{ax}}{2}\right)\tan\lambda_p = 0. \qquad (25.4.28)$$

Usually, $\tan\gamma_c = p/a$.

The procedure of computations of the blade profile is as follows:

Step 1: Considering θ_c as the input parameter and solving Eq. (25.4.28) for ψ, we obtain numerically function $\psi(\theta_c)$. The first guess for the solution of Eq. (25.4.28) is based on the following considerations:

(i) We take in Eq. (25.4.28) $\sin\psi \approx \psi$, $\cos\psi \approx 1$, and $\theta_c \approx \alpha_n$.

(ii) Then, we obtain the following expression for the first guess of ψ:

$$\psi = \frac{\left[\left(a_o - \rho\cos\alpha_n\cos\gamma_c + \frac{p_{ax}}{2}\right)\tan\lambda_p + \rho\cos\alpha_n\sin\gamma_c\right]\cos^2\lambda_p}{r_p}. \qquad (25.4.29)$$

Step 2: The coordinates $x_1^\star$ and $z_1^\star$ of the blade profile are determined with the equations

$$x_1^\star = x_1 = -\rho(\sin\theta_c \cos\psi - \cos\theta_c \sin\psi \sin\gamma_c) + a\cos\psi$$

$$z_1^\star = -\frac{\rho(\sin\theta_c \sin\psi + \cos\theta_c \cos\psi \sin\gamma_c) - a\sin\psi}{\sin\lambda_p}. \tag{25.4.30}$$

The range of ψ and θ_c for determination of $x_1^\star$ and $z_1^\star$ is determined with Eqs. (25.2.6) and (25.2.7).

The upper fillet is determined as described in Section 25.2.

26 Generation of Surfaces by CNC Machines

26.1 INTRODUCTION
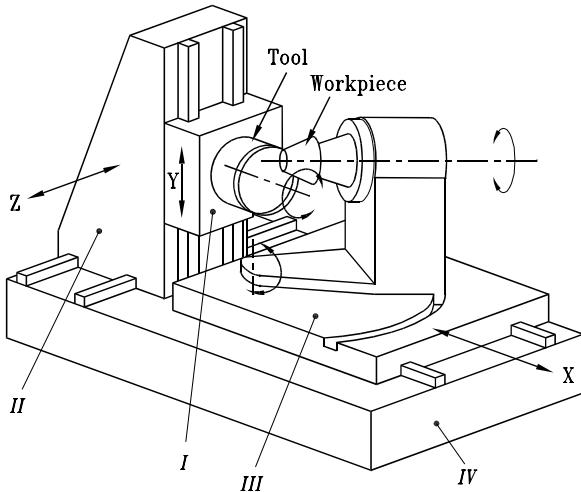
The design of computer controlled machines extended the opportunity for the development of gears with a new topology of tooth surfaces. The new topology must provide the localization of the bearing contact, its stability even for misaligned gear drives, and the reduction of vibrations caused by transmission errors. The new topology of gear tooth surfaces can provide a predesigned function of transmission errors of a parabolic type that will be able to absorb piecewise linear functions of transmission errors caused by gear misalignment (see Section 9.2). The advantages of new surface topology can be achieved by application of generating tools of a simple enough shape just because the computer controlled machine is able to provide properly varied relations between the motions of the tool and the workpiece.

An additional advantage of application of a computer controlled machine is the possibility of increasing the precision of the installation of the machine-tool settings. In the most general case, a computer controlled machine for generation of gear tooth surfaces must have six degrees-of-freedom. Five of these degrees-of-freedom are necessary for the control of related motions of the tool and the workpiece. The sixth degree-of-freedom is required to provide the desired velocity of cutting (grinding) and is not related to the process of surface generation.

In the following sections of this chapter we consider three cases of generation of the workpiece surface Σ_p by the given tool surface Σ_t:

(i) Surfaces Σ_t and Σ_p are in continuous tangency and they contact each other at every instant at a *point* but not at a line.

(ii) Surfaces Σ_t and Σ_p are in continuous tangency and they contact each other at every instant at a *line*. Surface Σ_p is generated in this case as the *envelope* to the *family* of surfaces Σ_t. The family of surfaces is generated in *relative* motion of Σ_t to Σ_p.

(iii) An approximate method is developed for generation of a surface Σ_g (ground or cut) with an optimal approximation to the ideal surface Σ_p.

An example of case 1 is the generation, for instance, of a die designated for forging of a gear. Generation of conventional spiral bevel gears and hypoid gears by the CNC

Figure 26.2.1: Schematic of "Phoenix" machine.

machine is the example of case 2 of generation. Case 3 is the basic idea for a new method for surface generation discussed in Section 26.4.
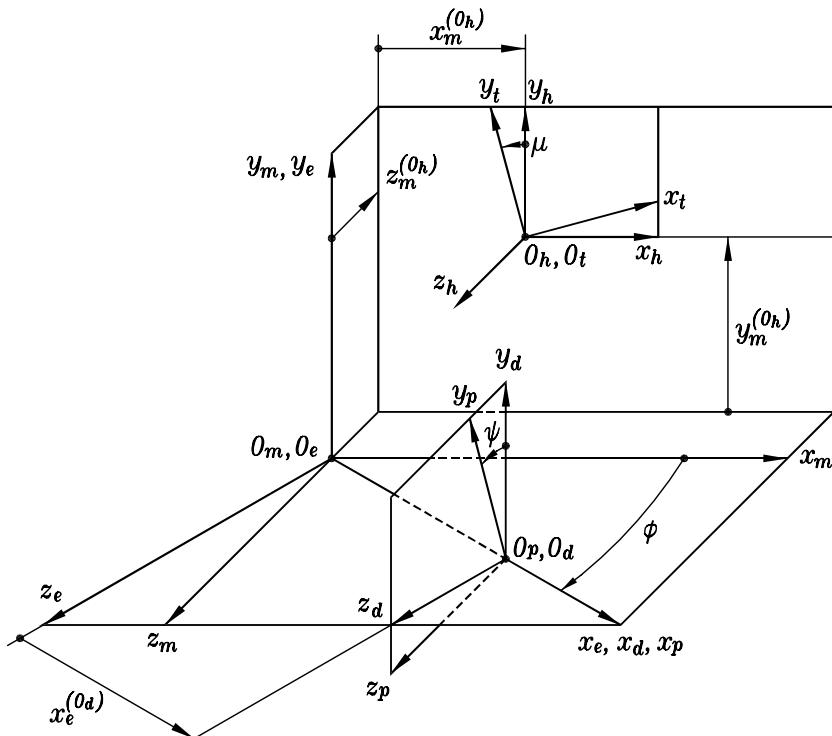
26.2 EXECUTION OF MOTIONS OF CNC MACHINES

Schematic of "Phoenix" CNC Machine

The "Phoenix" CNC machine (Fig. 26.2.1) was designed by the Gleason Works for generation of spiral bevel gears and hypoid gears. The machine is provided with six degrees-of-freedom for three rotational motions, and three translational motions. The translational motions are performed in three mutually perpendicular directions. Two rotational motions are provided as rotation of the workpiece and the rotation that enables the machine to change the angle between the axes of the workpiece and the tool. The third rotational motion is provided as rotation of the tool about its axis and generally is not related to the process of generation. The motions of the other five degrees-of-freedom are provided as related motions in the process of surface generation.

Coordinate Systems Applied for "Phoenix" CNC machine

Coordinate systems S_t (x_t, y_t, z_t) and S_p (x_p, y_p, z_p) are rigidly connected to the tool and the workpiece, respectively (Fig. 26.2.2). For further discussion, we distinguish four reference frames designated in Fig. 26.2.1 as I, II, III, and IV. The reference frame IV is the fixed one (it is the housing of the machine). Reference frames I, II, and III perform translations in three mutually perpendicular directions, respectively. We designate coordinate systems S_h and S_m that represent reference frames I and III, respectively (Figs. 26.2.1 and 26.2.2). Coordinate axes of S_h and S_m are parallel to each other and the location of S_h with respect to S_m is represented by $(x_m^{(O_h)}, y_m^{(O_h)},$ and $z_m^{(O_h)})$. Coordinate system S_t performs rotational motion with respect to S_h about the z_h axis. To describe the coordinate transformation from S_m to S_p, we use coordinate systems S_e and S_d (Fig. 26.2.2).

Figure 26.2.2: Coordinate systems applied to the "Phoenix" machine.
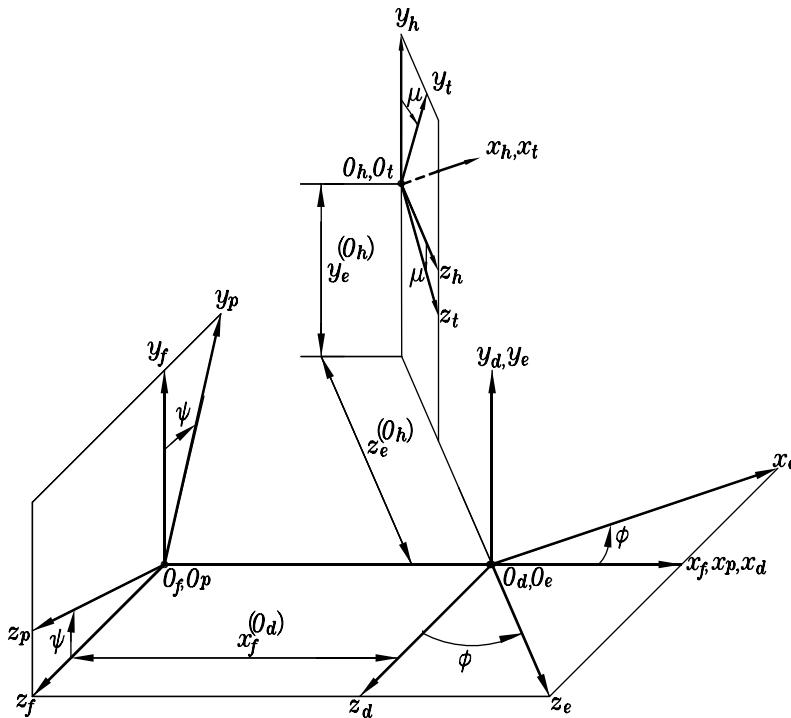
Coordinate system S_e performs rotational motion with respect to S_m about the y_m axis. Coordinate axes of system S_d are parallel to the respective axes of S_e; the location of origin O_d with respect to O_e is determined with the parameter $x_e^{(O_d)} = $ const. Coordinate system S_p performs rotational motion with respect to S_d about the x_d axis.

Schematic of "Star" CNC Machine

We consider the version of a "Star" CNC machine that is provided with six degrees-of-freedom (Fig. 26.2.3). Coordinate systems S_t (x_t, y_t, z_t), S_p (x_p, y_p, z_p), and S_f (x_f, y_f, z_f) are rigidly connected to the tool, workpiece, and frame, respectively. Coordinate system S_d is parallel to system S_f and the location of S_d with respect to S_f is represented in S_f by $(x_f^{(O_d)}, 0, 0)$. Coordinate system S_e performs rotational motion with respect to S_d about the y_d axis. Coordinate system S_h is parallel to S_e and the location of S_h with respect to S_e is represented in S_e by $(0, y_e^{(O_h)}, z_e^{(O_h)})$. Coordinate system S_t performs rotational motion with respect to the fixed coordinate system S_f about the x_f axis. Altogether there are three translational motions along axes x_f, y_e, and z_e and three rotational motions about axes x_f, y_d, and x_h.

Basic Principle of Execution of Motions

Consider that the location and orientation of the tool with respect to the workpiece are given in coordinate systems that are represented for a conventional generator (see below) or for an abstract process for generation. Our goal is to develop the algorithm for

Figure 26.2.3: Schematic of "Star" CNC machine.

the execution of motions of the CNC machine using the initial information mentioned above. Goldrich [1989] has used for this purpose the existence of a common trihedron for the two pairs of coordinate systems $(S_t^{(C)}, S_p^{(C)})$ and $(S_t^{(G)}, S_p^{(G)})$ that are applied for the CNC machine and for the generating process, respectively. The approach used in this chapter is as follows:

(i) Consider that 4×4 matrices $\mathbf{M}_{pt}^{(k)}$ and 3×3 matrices $\mathbf{L}_{pt}^{(k)}$ $(k = C, G)$ have been derived. The superscripts "C" and "G" indicate the CNC machine and the abstract generating process, respectively.

(ii) The matrix equality

$$\mathbf{L}_{pt}^{(C)} = \mathbf{L}_{pt}^{(G)} \tag{26.2.1}$$

provides the same orientation of $S_t^{(k)}$ with respect to $S_p^{(k)}$ $(k = C, G)$ in both reference frames.

(iii) The matrix equality

$$\mathbf{M}_{pt}^{(C)}[0 \quad 0 \quad 0 \quad 1]^{\mathrm{T}} = \mathbf{M}_{pt}^{(G)}[0 \quad 0 \quad 0 \quad 1]^{\mathrm{T}} \tag{26.2.2}$$

provides the same position vector $(\overline{O_p O_t})$ for both reference frames.

The application of Eqs. (26.2.1) and (26.2.2) for the execution of motions of the Phoenix machine is considered for the two following cases: (i) a hypoid pinion is generated by application of a conventional generator, and (ii) a surface Σ_g with optimal approximation to the ideal surface Σ_p is generated.

Derivation of Matrix $L_{pt}^{(C)}$ and Position Vector $(\overline{O_tO_p})_p^{(C)}$

Using a routine procedure for coordinate transformations, we obtain

$$L_{pt}^{(C)}(\mu, \phi, \psi) = L_{pd}(\psi)L_{de}L_{em}(\phi)L_{mb}L_{bt}(\mu)$$

$$= \begin{bmatrix} \cos\mu\cos\phi & -\sin\mu\cos\phi & \sin\phi \\ \begin{array}{c} -\cos\mu\sin\phi\sin\psi \\ +\sin\mu\cos\psi \end{array} & \begin{array}{c} \sin\mu\sin\phi\sin\psi \\ +\cos\mu\cos\psi \end{array} & \cos\phi\sin\psi \\ \begin{array}{c} -\cos\mu\sin\phi\cos\psi \\ -\sin\mu\sin\psi \end{array} & \begin{array}{c} \sin\mu\sin\phi\cos\psi \\ -\cos\mu\sin\psi \end{array} & \cos\phi\cos\psi \end{bmatrix}. \quad (26.2.3)$$

We note that L_{de} and L_{mb} are unitary matrices.

The derivation of the position vector $(\overline{O_tO_p})^{(C)}$ in S_p is based on the following considerations:

(i)

$$(\overline{O_mO_t})_p^{(C)} + (\overline{O_tO_p})_p^{(C)} = (\overline{O_mO_p})_p^{(C)}.$$

Thus,

$$(\overline{O_tO_p})_p^{(C)} = (\overline{O_mO_p})_p^{(C)} - (\overline{O_mO_t})_p^{(C)} = (\overline{O_eO_d})_p^{(C)} - (\overline{O_mO_b})_p^{(C)}$$

$$= x_e^{(O_d)}(\mathbf{i}_e)_p - x_m^{(O_b)}(\mathbf{i}_m)_p - y_m^{(O_b)}(\mathbf{j}_m)_p - z_m^{(O_b)}(\mathbf{k}_m)_p. \quad (26.2.4)$$

Here, $x_e^{(O_d)} = $ const; $x_m^{(O_b)}$, $y_m^{(O_b)}$, and $z_m^{(O_b)}$ are considered as algebraic values.

(ii)   Vector $(\overline{O_tO_p})^{(C)}$ can be represented in coordinate system $S_p^{(C)}$ with the matrix equation

$$(\overline{O_tO_p})_p^{(C)} = x_e^{(O_d)}\mathbf{i}_p - x_m^{(O_b)}L_{pm}[1 \quad 0 \quad 0]^T$$

$$- y_m^{(O_b)}L_{pm}[0 \quad 1 \quad 0]^T - z_m^{(O_b)}L_{pm}[0 \quad 0 \quad 1]^T \quad (26.2.5)$$

where $L_{pm} = L_{pd}L_{de}L_{em}$ (L_{de} is a unitary matrix).

Equation (26.2.5) yields

$$(\overline{O_tO_p})_p^{(C)} = \begin{bmatrix} x_e^{(O_d)} - x_m^{(O_b)}\cos\phi - z_m^{(O_b)}\sin\phi \\ x_m^{(O_b)}\sin\phi\sin\psi - y_m^{(O_b)}\cos\psi - z_m^{(O_b)}\cos\phi\sin\psi \\ x_m^{(O_b)}\sin\phi\cos\psi + y_m^{(O_b)}\sin\psi - z_m^{(O_b)}\cos\phi\cos\psi \end{bmatrix}. \quad (26.2.6)$$

26.3 GENERATION OF HYPOID PINION

Derivation of $L_{pt}^{(G)}$ and $(\overline{O_tO_p})^{(G)}$

The generation of a hypoid pinion by a conventional generator was described in Chapter 22. The coordinate systems applied for the CNC machine are represented in Fig. 26.2.2.

The performed coordinate transformation yields

$$(\mathbf{L}_{pt})^{(G)} = [a_{kl}(q)] \qquad (k = 1, 2, 3; l = 1, 2, 3). \tag{26.3.1}$$

Here,

$$a_{11} = \cos i \, \cos \gamma_m \sin(q - j) - \sin i \, \sin \gamma_m$$

$$a_{12} = - \cos(q - j) \cos \gamma_m$$

$$a_{13} = \sin i \, \cos \gamma_m \sin(q - j) + \cos i \, \sin \gamma_m$$

$$a_{21} = \cos i \, \sin \gamma_m \sin \phi_p \sin(q - j) + \cos i \, \cos(q - j) \cos \phi_p$$
$$\quad + \sin i \, \cos \gamma_m \sin \phi_p$$

$$a_{22} = - \cos(q - j) \sin \gamma_m \sin \phi_p + \sin(q - j) \cos \phi_p$$

$$a_{23} = \sin i \, \sin \gamma_m \sin \phi_p \sin(q - j) + \sin i \, \cos(q - j) \cos \phi_p \tag{26.3.2}$$
$$\quad - \cos i \, \sin \gamma_m \sin \phi_p$$

$$a_{31} = - \cos i \, \sin \gamma_m \cos \phi_p \sin(q - j) + \cos i \, \cos(q - j) \sin \phi_p$$
$$\quad - \sin i \, \cos \gamma_m \cos \phi_p$$

$$a_{32} = \sin \gamma_m \cos \phi_p \cos(q - j) + \sin(q - j) \sin \phi_p$$

$$a_{33} = - \sin i \, \sin \gamma_m \sin(q - j) \cos \phi_p + \sin i \, \cos(q - j) \sin \phi_p$$
$$\quad + \cos i \, \cos \gamma_m \cos \phi_p.$$

The variable parameters q and ϕ_p are related and therefore the coefficients a_{kl} ($k = 1, 2, 3; l = 1, 2, 3$) are functions of q.

The position vector $(\overline{O_t O_p})_p^{(G)}$ is represented as follows:

$$(\overline{O_t O_p})_p^{(G)} = -(\mathbf{M}_{pt})^{(G)}[0 \ 0 \ 0 \ 1]^{\mathrm{T}}$$

$$= - \begin{bmatrix} S_R \cos q \cos \gamma_m - \Delta B \sin \gamma_m - \Delta A \\ -S_R(\sin q \cos \phi_p - \cos q \sin \gamma_m \sin \phi_p) \\ \quad + E_m \cos \phi_p + \Delta B \cos \gamma_m \sin \phi_p \\ -S_R(\sin q \sin \phi_p + \cos q \sin \gamma_m \cos \phi_p) \\ \quad + E_m \sin \phi_p - \Delta B \cos \gamma_m \cos \phi_p \\ 1 \end{bmatrix} = - \begin{bmatrix} a_{14}(q) \\ a_{24}(q) \\ a_{34}(q) \\ 1 \end{bmatrix}. \tag{26.3.3}$$

Execution of Motions of CNC Machine

Matrix equality (26.2.1) provides nine dependent equations for determination of functions $\phi(q)$, $\psi(q)$, and $\mu(q)$. We can determine these functions using the following procedure:

Step 1: Determination of ϕ.

$$\sin \phi = a_{13}(q). \tag{26.3.4}$$

This equation provides two solutions for ϕ; the smaller value of ϕ can be chosen.

Step 2: Determination of ψ.

$$\cos \phi \sin \psi = a_{23}(q), \qquad \cos \phi \cos \psi = a_{33}(q). \qquad (26.3.5)$$

These equations provide a unique solution for ψ, considering ϕ as given.

Step 3: Determination of μ.

$$\cos \mu \cos \phi = a_{11}(q), \qquad -\sin \mu \cos \phi = a_{12}(q). \qquad (26.3.6)$$

These equations provide a unique solution for μ, considering ϕ as given.

In the case of generation of a face-milled hypoid pinion, a tool with a conical surface is applied. The tool surface is a surface of revolution; the rotation of the tool about its axis is not related to μ. Functions (26.3.6) must be applied and executed only in the case of generation of a face-hobbed hypoid pinion, which is cut by a blade.

Vector equality

$$(\overline{O_t O_p})_p^{(G)} = (O_t O_p)_p^{(C)} \qquad (26.3.7)$$

enables us to determine functions $x_m^{(O_b)}(q)$, $y_m^{(O_b)}(q)$, and $z_m^{(O_b)}(q)$. Equations (26.2.6), (26.3.3), and (26.3.7) considered simultaneously represent a system of three linear equations in the unknowns $x_m^{(O_b)}$, $y_m^{(O_b)}$, and $z_m^{(O_b)}$. The solution to these equations enables us to determine the translational motions on the CNC machine.
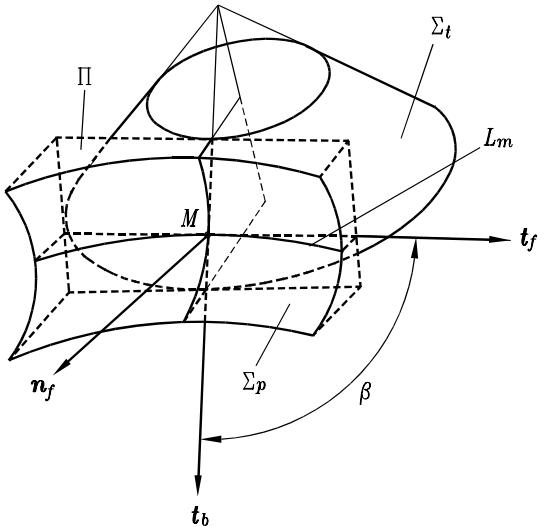
26.4 GENERATION OF A SURFACE WITH OPTIMAL APPROXIMATION

Introduction

This section is based on the research accomplished by Litvin, Chen, Zhang, Krenzer, and Handschuh [1993a], and is directed at generation of a surface (Σ_g) that must be in optimal approximation to the theoretical (ideal) surface Σ_p.

The method for generation of Σ_g is based on the following ideas:

(1) A mean line L_m on the ideal surface Σ_p is chosen as shown in Fig. 26.4.1.
(2) The tool surface Σ_t is a properly designed surface of revolution (in particular cases Σ_t is a circular cone as shown in Fig. 26.4.1) that moves along L_m. Surfaces Σ_t and Σ_p are in continuous tangency along L_m; M is the current point of tangency (Fig. 26.4.1). The orientation of Σ_t with respect to Σ_p (determined with angle β) is continuously varying. Angle β at current point M of tangency is formed by the tangents $\mathbf{t}_f$ and $\mathbf{t}_b$ to L_m and the tool generatrix, respectively (Fig. 26.4.1). Tangents $\mathbf{t}_f$ and $\mathbf{t}_b$ form plane Π that is tangent to Σ_t and Σ_p at point M.
(3) The tool surface Σ_t in its motion with respect to Σ_p swept out a region of space as a family of surfaces Σ_t. The envelope to the family of Σ_t is surface Σ_g (the ground, cut surface) that is in tangency with the theoretical surface Σ_p at any point M of L_m and must be in optimal approximation to Σ_p in any direction that differs from L_m.
(4) The optimal approximation of Σ_g to Σ_p is obtained by variation of angle β (Fig. 26.4.1).

Figure 26.4.1: Installment and orientation of tool surface Σ_t with respect to ideal surface Σ_p.

(5) The continuous tangency of tool surface Σ_t with Σ_p and properly varied orientation of Σ_t can be obtained by the execution of required motions of the tool by a computer controlled multidegree-of-freedom machine. One of these degrees of freedom, rotation of the tool about its axis, provides the desired velocity of grinding (cutting) and is not related to the process for generation of Σ_g.

This section covers the following topics:

(i) Determination of the equation of meshing between the tool surface Σ_t and the generated surface Σ_g. The equation of meshing provides the necessary condition of existence of the envelope to the family of surfaces.
(ii) Determination of generated surface Σ_g as the envelope to the family of surfaces Σ_t swept out by the tool. Surface Σ_g coincides with the theoretical (ideal) surface Σ_p along the mean line L_m and deviates from Σ_p out of L_m.
(iii) Determination of deviations of Σ_g from Σ_p (in regions that differ from L_m) and minimizations of deviations for optimal approximation of Σ_g to Σ_p.
(iv) Determination of curvatures of Σ_g that are required when the simulation of meshing and contact of two mating surfaces are considered.
(v) Execution of required motions of Σ_t with respect to Σ_p by application of a multidegree-of-freedom, computer numerically controlled machine.

An effective approach for the derivation of the necessary condition of the envelope Σ_g existence is discussed. This method is based on the idea of motion of the Darboux–Frenet trihedron along L_m, the chosen mean line of Σ_p. An additional effective approach for determination of curvatures of generated surface Σ_g is discussed as well. This approach is based on the fact that the normal curvatures and surface torsions (geodesic torsions) of Σ_g are (i) equal to the normal curvatures and surface torsions of Σ_p along L_m, and (ii) equal to the normal curvatures and surface torsions of tool surface Σ_t along the characteristic L_g (the instantaneous line of tangency of Σ_t and Σ_g).

Mean Line on Ideal Surface Σ_p

The ideal surface Σ_p is considered as a regular one and is represented as

$$\mathbf{r}_p(u_p, \theta_p) \in C^2, \quad \frac{\partial \mathbf{r}_p}{\partial u_p} \times \frac{\partial \mathbf{r}_p}{\partial \theta_p} \neq 0, \quad (u_p, \theta_p) \in E \tag{26.4.1}$$

where (u_p, θ_p) are the Gaussian coordinates of Σ_p. The unit normal to Σ_p is represented as

$$\mathbf{n}_p = \frac{\mathbf{N}_p}{|\mathbf{N}_p|}, \quad \mathbf{N}_p = \frac{\partial \mathbf{r}_p}{\partial u_p} \times \frac{\partial \mathbf{r}_p}{\partial \theta_p}. \tag{26.4.2}$$

The determination of the mean line on L_m is based on the following procedure:

(i) Initially, we determine numerically n points on surface Σ_p that will belong approximately to the desired mean line L_m.

(ii) Then, we can derive a polynomial function

$$u_{pi}(\theta_{pi}) = \sum_{j=1}^{n} a_j \theta_{pi}^{(n-j)} \quad (i = 1, \ldots, n) \tag{26.4.3}$$

that will relate surface parameters (u_p, θ_p) for the n points of the mean line on Σ_p.

The mean line L_m, tangent $\mathbf{T}_p$, and unit tangent $\mathbf{t}_p$ to the mean line are represented as follows:

$$\mathbf{r}_p(u_p(\theta_p), \theta_p), \quad \mathbf{T}_p = \frac{\partial \mathbf{r}_p}{\partial \theta_p} + \frac{\partial \mathbf{r}_p}{\partial u_p} \frac{du_p}{d\theta_p}, \quad \mathbf{t}_p = \frac{\mathbf{T}_p}{|\mathbf{T}_p|}. \tag{26.4.4}$$

The constraint for $\mathbf{t}_p$ is that it must be of the same sign and differ from zero at the same intervals of interpolation.

Tool Surface

The tool surface Σ_t is represented in coordinate system S_t rigidly connected to the tool by the following equations:

$$x_t = x_t(u_t) \cos \theta_t, \quad y_t = x_t(u_t) \sin \theta_t, \quad z_t = z_t(u_t). \tag{26.4.5}$$
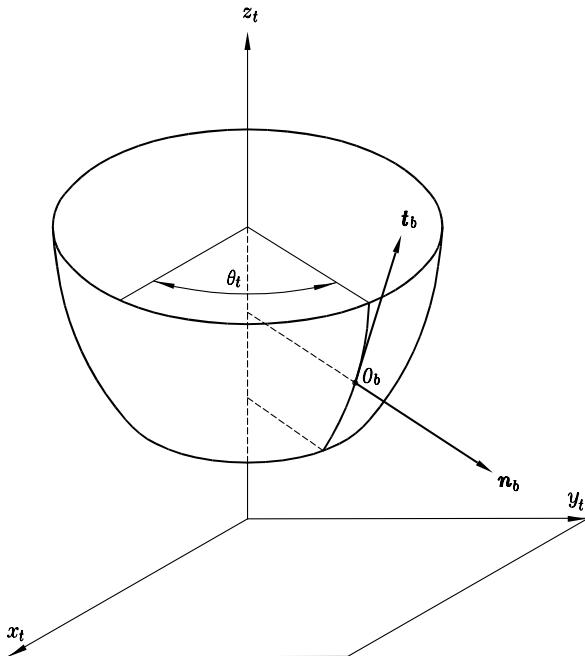
The axial section of Σ_t obtained by taking $\theta_t = 0$ represents a circular arc, or a straight line in the case when Σ_t is a circular cone. The surface of the tool is formed by rotation of the axial section of Σ_t about the z_t axis. The surface unit normal is determined as

$$\mathbf{n}_t = \frac{\mathbf{N}_t}{|\mathbf{N}_t|}, \quad \mathbf{N}_t = \frac{\partial \mathbf{r}_t}{\partial \theta_t} \times \frac{\partial \mathbf{r}_t}{\partial u_t}. \tag{26.4.6}$$

Equation of Meshing Between Σ_t and Σ_g

The equation of meshing represents the necessary condition of existence of envelope Σ_g to the family of surfaces Σ_t that is swept out by the tool surface Σ_t. Recall that the equation of meshing can be derived by using the equation (see Chapter 6)
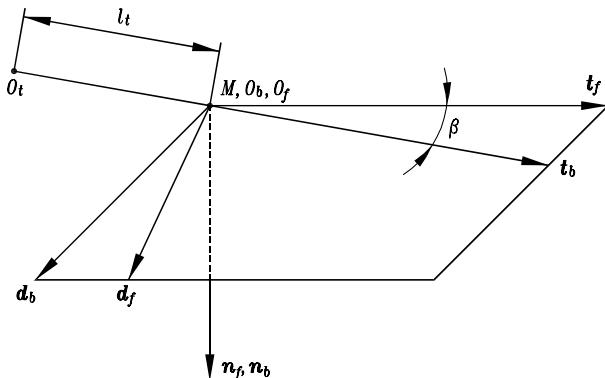
$$\mathbf{N}_i^{(t)} \cdot \mathbf{v}_i^{(tg)} = 0. \tag{26.4.7}$$
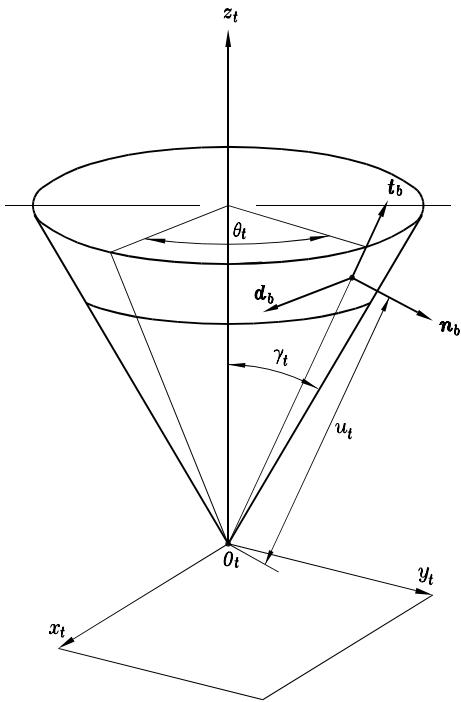
Figure 26.4.2: Tool surface Σ_t.

Here, i indicates the coordinate system S_i where the vectors of the scalar product are represented; $\mathbf{N}^{(t)}$ is the normal to surface Σ_t; $\mathbf{v}^{(tg)}$ is the relative velocity in the motion of Σ_t with respect to Σ_g.

Henceforth, we consider two basic coordinate systems, S_t and S_p, that are rigidly connected to the tool surface Σ_t and the ideal surface Σ_p. In addition, we consider two trihedrons: $S_b(\mathbf{t}_b, \mathbf{d}_b, \mathbf{n}_b)$ and $S_f(\mathbf{t}_f, \mathbf{d}_f, \mathbf{n}_f)$. Trihedron S_b is rigidly connected to Σ_t and coordinate system S_t (Fig. 26.4.2). Here, O_b is the point of the chosen generatrix of Σ_t where the trihedron is located; $\mathbf{t}_b$ is the unit tangent to the generatrix at O_b; $\mathbf{n}_b$ is the surface unit normal of Σ_t at O_b; $\mathbf{d}_b = \mathbf{n}_b \times \mathbf{t}_b$; vectors $\mathbf{t}_b$ and $\mathbf{d}_b$ form the tangent plane to Σ_t at O_b. Trihedron S_f moves along the mean line L_m (Fig. 26.4.3); $\mathbf{t}_f$ is the tangent

Figure 26.4.3: Orientation of trihedron S_b with respect to S_f.

Figure 26.4.4: Surface of grinding tool cone.

to the mean line L_m at current point M (Fig. 26.4.3); $\mathbf{n}_f$ is the surface unit normal to Σ_p at point M; $\mathbf{d}_f = \mathbf{n}_f \times \mathbf{t}_f$; vectors $\mathbf{t}_f$ and $\mathbf{d}_f$ form the tangent plane to Σ_p at point M.

The tool with surface Σ_t and trihedron S_t moves along mean line L_m of Σ_p, and O_b coincides with current point M of mean line L_m. Surfaces Σ_t and Σ_p are in tangency at any current point M of mean line L_m. The orientation of S_b with respect to S_f is determined with angle β that is varied in the process for generation (Fig. 26.4.3).

We start the derivations with the case when Σ_t is a circular cone (Fig. 26.4.4). The angular velocity $\boldsymbol{\omega}_f$ of rotation of S_f with respect to S_p is represented as (see Chapter 7)

$$\boldsymbol{\omega}_f = \left(t\mathbf{t}_f - k_n\mathbf{d}_f + k_g\mathbf{n}_f \right)\frac{ds}{dt}. \tag{26.4.8}$$

Here, t is the surface torsion (geodesic torsion), k_n and k_g are the normal and geodesic curvatures of surface Σ_p at current point M of mean line L_m, and ds is the infinitesimal displacement along L_m.

The angular velocity $\boldsymbol{\Omega}_f$ of trihedron S_b is represented in S_f as

$$\boldsymbol{\Omega}_f = \boldsymbol{\omega}_f + \frac{d\beta}{dt}\mathbf{n}_f = \begin{bmatrix} t & -k_n & k_g + \dfrac{d\beta}{ds} \end{bmatrix}^{\mathrm{T}}\frac{ds}{dt}. \tag{26.4.9}$$

The orientation of cone Σ_t is determined by function $\beta(\theta_p)$ and

$$\frac{d\beta}{ds} = \frac{d\beta}{d\theta_p}\frac{d\theta_p}{ds} = \left(\frac{d\beta}{d\theta_p}\right)\frac{1}{|\mathbf{T}_p|} \tag{26.4.10}$$

where $\mathbf{T}_p$ is the tangent to the mean line L_m at current point M.

The transformations of vector components in transition from S_t to S_b and S_b to S_f are represented by 3×3 matrix operators $\mathbf{L}_{bt}$ and $\mathbf{L}_{fb}$. Here,

$$
\mathbf{L}_{fb} = \begin{bmatrix} \cos \beta & -\sin \beta & 0 \\ \sin \beta & \cos \beta & 0 \\ 0 & 0 & 1 \end{bmatrix} \tag{26.4.11}
$$

$$
\mathbf{L}_{bt} = \begin{bmatrix} \sin \gamma_t \cos \theta_t & \sin \gamma_t \sin \theta_t & \cos \gamma_t \\ \sin \theta_t & -\cos \theta_t & 0 \\ \cos \gamma_t \cos \theta_t & \cos \gamma_t \sin \theta_t & -\sin \gamma_t \end{bmatrix}. \tag{26.4.12}
$$

The conical surface Σ_t is represented in S_t as (Fig. 26.4.4)

$$
\mathbf{r}_t = u_t [\sin \gamma_t \cos \theta_t \quad \sin \gamma_t \sin \theta_t \quad \cos \gamma_t]^{\mathrm{T}} \tag{26.4.13}
$$

where (u_t, θ_t) are the surface parameters and γ_t is the cone apex angle. The unit normal to the conical surface is

$$
\mathbf{n}_t = u_t [\cos \gamma_t \cos \theta_t \quad \cos \gamma_t \sin \theta_t \quad -\sin \gamma_t]^{\mathrm{T}}. \tag{26.4.14}
$$

The sought-for equation of meshing (necessary condition of existence of envelope Σ_g) is represented in the form

$$
\mathbf{n}_f^{(t)} \cdot \mathbf{v}_f^{(tg)} = 0 \tag{26.4.15}
$$

where

$$
\mathbf{n}_f^{(t)} = \mathbf{L}_{ft} \mathbf{n}_t. \tag{26.4.16}
$$

The derivation of expression $\mathbf{v}_f^{(tg)}$ is simplified while taking into account the following considerations:

(a) The relative velocity vector $\mathbf{v}_f^{(tg)}$ can be represented as

$$
\mathbf{v}_f^{(tg)} = \boldsymbol{\Omega}_f^{(s)} \mathbf{r}_f^{(t)} + \frac{ds}{dt} \mathbf{t}_f. \tag{26.4.17}
$$

Here, $\boldsymbol{\Omega}_f^{(s)}$ is the skew-symmetric matrix represented as

$$
\boldsymbol{\Omega}_f^{(s)} = \begin{bmatrix} 0 & -\omega_3 & \omega_2 \\ \omega_3 & 0 & -\omega_1 \\ -\omega_2 & \omega_1 & 0 \end{bmatrix}. \tag{26.4.18}
$$

Vector $\boldsymbol{\Omega}_f$ is represented by

$$
\boldsymbol{\Omega}_f = \omega_1 \mathbf{t}_f + \omega_2 \mathbf{d}_f + \omega_3 \mathbf{n}_f = \begin{bmatrix} t & -k_n & k_g + \dfrac{d\beta}{ds} \end{bmatrix}^{\mathrm{T}} \frac{ds}{dt}. \tag{26.4.19}
$$

(b) Consider that point N on surface Σ_t is the point of the characteristic (the line of tangency of Σ_t and the generated surface Σ_g). Certainly, the equation of meshing must be satisfied for point N. The position vector $\overline{O_f N}$ can be represented as

$$\overline{O_f N} = \overline{O_t N} - \overline{O_t O_f}. \tag{26.4.20}$$

Here, $\overline{O_t N}$ is the position vector of point N that is drawn from the origin O_t of S_t to N; vector $\overline{O_t N}$ is represented in S_t as

$$\overline{O_t N} = u_t \mathbf{e}_t = u_t (\sin \gamma_t \cos \theta_t \; \mathbf{i}_t + \sin \gamma_t \sin \theta_t \; \mathbf{j}_t + \cos \gamma_t \; \mathbf{k}_t) \tag{26.4.21}$$

where

$$\mathbf{e}_t = \frac{\dfrac{\partial}{\partial u_t}(\mathbf{r}_t)}{\left| \dfrac{\partial}{\partial u_t}(\mathbf{r}_t) \right|} \tag{26.4.22}$$

is the unit vector of cone generatrix $\overline{O_f N}$. Vector $\overline{O_t O_f}$ (Fig. 26.4.3) is represented in S_b as

$$\overline{O_t O_f} = l_t \; \mathbf{i}_b \tag{26.4.23}$$

where $l_t = \left| \overline{O_t O_f} \right|$. Vector $\overline{O_f N}$ is represented in S_f using the matrix equation

$$\mathbf{r}_f^{(t)} = u_t \mathbf{L}_{ft} \mathbf{e}_t - l_t \mathbf{L}_{fb} \mathbf{i}_b. \tag{26.4.24}$$

(c) We represent now the equation of meshing as

$$\mathbf{n}_f^{(t)} \cdot \mathbf{v}_f^{(tg)} = \mathbf{n}_f^{(t)} \cdot \left[\mathbf{\Omega}_f^{(s)} (u_t \mathbf{L}_{ft} \mathbf{e}_t - l_t \mathbf{L}_{fb} \mathbf{i}_b) \right] + \left(\mathbf{n}_f^{(t)} \cdot \mathbf{t}_f \right) \frac{ds}{dt}. \tag{26.4.25}$$

(d) The further simplification of the equation of meshing is based on the following rule for operations with skew-symmetric matrices [Goldstein, 1950]:

$$\mathbf{A}^\mathrm{T} \mathbf{B}^{(s)} \mathbf{A} = \mathbf{C}^{(s)}. \tag{26.4.26}$$

Here, $\mathbf{B}^{(s)}$ and $\mathbf{C}^{(s)}$ designate skew-symmetric matrices, and $\mathbf{A}^\mathrm{T}$ is the transpose matrix for $\mathbf{A}$.

Considering that elements of $\mathbf{B}^{(s)}$ are represented in terms of components of vector

$$\mathbf{b} = [b_1 \quad b_2 \quad b_3]^\mathrm{T}, \tag{26.4.27}$$

we obtain that the elements of skew-symmetric matrix $\mathbf{C}^{(s)}$ are represented in terms of components of vector $\mathbf{c}$, where

$$[c_1 \quad c_2 \quad c_3]^\mathrm{T} = \mathbf{A}^\mathrm{T} [b_1 \quad b_2 \quad b_3]^\mathrm{T}. \tag{26.4.28}$$

Using the above considerations and eliminating ds/dt, the final expression of the equation of meshing can be represented as

$$\mathbf{n}_f^{(t)} \cdot \mathbf{v}_f^{(tg)} = f(u_t, \theta_t, \theta_p) = u_t \mathbf{n}_t^\mathrm{T} \mathbf{A}^{(s)} \mathbf{e}_t - l_t \mathbf{n}_b^\mathrm{T} \mathbf{B}^{(s)} \mathbf{i}_b + \mathbf{n}_t^\mathrm{T} \mathbf{L}_{ft}^\mathrm{T} \mathbf{t}_f = 0. \tag{26.4.29}$$

Here,

$$\mathbf{A}^{(s)}\frac{ds}{dt} = \mathbf{L}_{ft}^{\mathrm{T}}\mathbf{\Omega}_{f}^{(s)}\mathbf{L}_{ft}, \quad \mathbf{B}^{(s)}\frac{ds}{dt} = \mathbf{L}_{fb}^{\mathrm{T}}\mathbf{\Omega}_{f}^{(s)}\mathbf{L}_{fb} \tag{26.4.30}$$

$$\mathbf{A}^{(s)} = \begin{bmatrix} 0 & -a_3 & a_2 \\ a_3 & 0 & -a_1 \\ -a_2 & a_1 & 0 \end{bmatrix} \tag{26.4.31}$$

$$\begin{bmatrix} a_1 \\ a_2 \\ a_3 \end{bmatrix} = -\begin{bmatrix} t\cos\beta\sin\gamma_t - k_n\sin\beta\sin\gamma_t + \left(k_g + \dfrac{d\beta}{ds}\right)\cos\gamma_t \\ t\sin\beta + k_n\cos\beta \\ t\cos\beta\cos\gamma_t - k_n\sin\beta\cos\gamma_t - \left(k_g + \dfrac{d\beta}{ds}\right)\sin\gamma_t \end{bmatrix} \tag{26.4.32}$$

$$\mathbf{B}^{(s)} = \begin{bmatrix} 0 & -b_3 & b_2 \\ b_3 & 0 & -b_1 \\ -b_2 & b_1 & 0 \end{bmatrix}, \quad \begin{bmatrix} b_1 \\ b_2 \\ b_3 \end{bmatrix} = \begin{bmatrix} t\cos\beta - k_n\sin\beta \\ -t\sin\beta - k_n\cos\beta \\ \left(k_g + \dfrac{d\beta}{ds}\right) \end{bmatrix}. \tag{26.4.33}$$

The family of characteristics L_g, the instantaneous lines of tangency of Σ_t and Σ_g, is represented in S_t by the equations

$$\mathbf{r}_t = \mathbf{r}_t(u_t, \theta_t), \quad f(u_t, \theta_t, \theta_p) = 0 \tag{26.4.34}$$

where θ_p is the parameter of the family of L_g. Taking $\theta_p = \theta_p^{(i)}$ $(i = 1, 2, \ldots, n)$, we obtain the current characteristics on surface Σ_t.

It is easy to verify that the equation of meshing between Σ_t and Σ_g is satisfied for the current point M of mean line L_m on the ideal surface Σ_p. This means that the characteristic L_g intersects L_m at point M, for which we can take $\theta_t = 0$ because Σ_t is a surface of revolution. In the case when Σ_t is a circular cone (Fig. 26.4.4), we can take for point M that $u_t = |\overline{O_t O_b}| = l_t$. This approach for the derivation of the equation of meshing can be easily extended for application in the more general case when the tool surface is a general surface of revolution.

Determination of Generated Surface Σ_g

The ground surface Σ_g is generated as the envelope to the family of tool surface Σ_t; surface Σ_g is represented in S_p by the following equations:

$$\mathbf{r}_g^{(p)}(u_p(\theta_p), \theta_p, u_t, \theta_t) = \mathbf{L}_{pf}\mathbf{r}_f^{(t)} + \mathbf{r}_p^{(M)}(u_p(\theta_p), \theta_p), \quad f(u_t, \theta_t, \theta_p) = 0. \tag{26.4.35}$$

Here, $f(u_t, \theta_t, \theta_p) = 0$ is the equation of meshing; $\mathbf{r}_f^{(t)}(u_t, \theta_t)$ is the equation of tool surface Σ_t represented in S_f; $\mathbf{r}_p^{(M)}(u_p(\theta_p), \theta_p)$ is the vector function that represents in S_p the mean line L_m; the 3×3 matrix operator $\mathbf{L}_{pf}$ which transforms vectors in transition

from S_f to S_p is represented as

$$\mathbf{L}_{pf} = \begin{bmatrix} t_{px} & d_{px} & n_{px} \\ t_{py} & d_{py} & n_{py} \\ t_{pz} & d_{pz} & n_{pz} \end{bmatrix} \tag{26.4.36}$$

where

$$\mathbf{t}_p = \frac{\dfrac{\partial}{\partial \theta_p}\left(\mathbf{r}_p^{(M)}\right)}{\left|\dfrac{\partial}{\partial \theta_p}\left(\mathbf{r}_p^{(M)}\right)\right|} \tag{26.4.37}$$

is the unit tangent to the mean line L_m,

$$\mathbf{n}_p = \pm \frac{\dfrac{\partial \mathbf{r}_p}{\partial u_p} \times \dfrac{\partial \mathbf{r}_p}{\partial \theta_p}}{\left|\dfrac{\partial \mathbf{r}_p}{\partial u_p} \times \dfrac{\partial \mathbf{r}_p}{\partial \theta_p}\right|} \tag{26.4.38}$$

$$\mathbf{d}_p = \mathbf{n}_p \times \mathbf{t}_p. \tag{26.4.39}$$

The sign chosen in Eq. (26.4.38) must provide the direction of $\mathbf{n}_p$ *toward* the surface "body."

Equations (26.4.35) represent in S_p the generated surface Σ_g in three-parameter form but with related parameters. Parameter u_t is linear in the equation of meshing when Σ_t is a cone, therefore this parameter can be eliminated and the generated surface Σ_g can be represented in S_p as
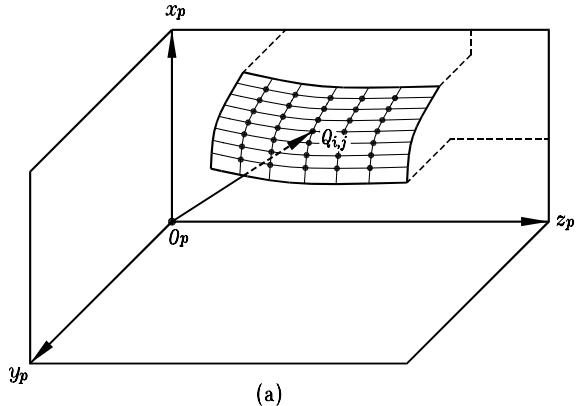
$$\mathbf{r}_p^{(g)} = \mathbf{r}_g = \mathbf{r}_g(\theta_p, \theta_t). \tag{26.4.40}$$

Recall that surfaces Σ_g and Σ_p have a common line L_m where they are in tangency. Surface Σ_g is in tangency with Σ_t along the instantaneous contact line L_g that passes through current point M of line L_m. The tangents to L_g and L_m lie in the plane that passes through M and is tangent to three surfaces (Σ_p, Σ_g, and Σ_t) simultaneously.
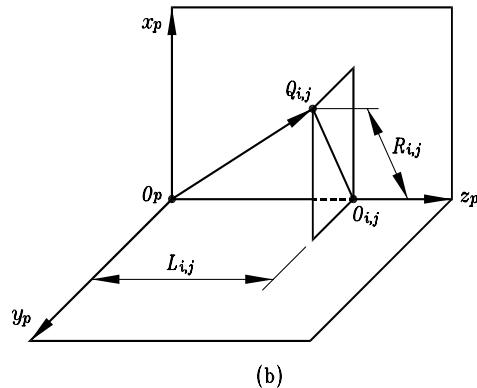
Optimal Approximation of Generated Surface Σ_g to Ideal Surface Σ_p
The procedure of optimal approximation of Σ_g to Σ_p is divided into the following stages: (i) design of the grid on Σ_p, the net of points, where the deviation of Σ_g from Σ_p will be determined; (ii) determination of initial function $\beta^{(1)}(\theta_p)$ for the first iteration; angle β determines the orientation of the tool surface Σ_t with respect to Σ_p (Figs. 26.4.1 and 26.4.3); (iii) determination of deviations of Σ_g from Σ_p with the initial function $\beta^{(1)}(\theta_p)$; and (iv) optimal minimization of deviations.

GRID ON SURFACE Σ_p. Figure 26.4.5(a) shows the grid on surface Σ_p, the net of (n, m) points, where the deviations of Σ_g from Σ_p are considered. The position vector

(a)

Figure 26.4.5: Grid on surface Σ_p.

(b)

is $\overline{O_p Q_{ij}} = \mathbf{r}_p^{(i,j)}$ [Fig. 26.4.5(b)]. The computation is based on the following proce-
dure:

(i) The desired components $L_{i,j}$ and $R_{i,j}$ of the position vector $\mathbf{r}_p^{(i,j)}$ are considered as
known.

(ii) Taking into account that

$$L_{i,j} = z_p^{(i,j)}, \quad R_{i,j}^2 = \left[x_p^{(i,j)}(u_p, \theta_p)\right]^2 + \left[y_p^{(i,j)}(u_p, \theta_p)\right]^2, \tag{26.4.41}$$

we will obtain the surface Σ_p parameters $(u_p^{(i,j)}, \theta_p^{(i,j)})$ for each grid point.

DETERMINATION OF INITIAL FUNCTION $\beta^{(1)}(\theta_p)$. The determination of $\beta^{(1)}(\theta_p)$ is based
on the following idea: the instantaneous direction of $\mathbf{t}_b$ (the tool generatrix) with respect
to tangent $\mathbf{t}_f$ to the mean line L_m (Fig. 26.4.1) must provide the minimal value $|k_n^{(r)}|$.
Here, $k_n^{(r)}$ is the relative normal curvature determined as

$$k_n^{(r)} = k_n^{(t)} - k_n^{(p)} \tag{26.4.42}$$

where $k_n^{(t)}$ and $k_n^{(p)}$ are the normal curvatures of surfaces Σ_t and Σ_p along $\mathbf{t}_b$. In the case of nondevelopable ruled surface Σ_p, vector $\mathbf{t}_b$ can be directed along the asymptote of Σ_p.

The requirement that $|k_n^{(r)}|$ be minimal enables us to determine function $\beta^{(1)}(\theta_p)$ numerically. Because we need for further computations the derivative $d\beta/d\theta_p$, function $\beta^{(1)}(\theta_p)$ is represented as a polynomial function that must satisfy the numerical data obtained for the chosen points of mean line L_m.

DETERMINATION OF DEVIATIONS OF Σ_g FROM Σ_p. We are able at this stage of our investigation to determine the equation of meshing between surfaces Σ_t and Σ_g, and surface Σ_g as previously discussed. The computation of deviations of Σ_g from Σ_p at the grid points is based on the following considerations:

(i) Surfaces Σ_p and Σ_g are represented in the same coordinate system (S_p) by the vector functions

$$\mathbf{r}_p(u_p, \theta_p), \quad \mathbf{r}_g(\theta_g, \theta_t). \tag{26.4.43}$$

Parameter θ_g of surface Σ_g determines the location of the current point on the mean line of surface Σ_g.

(ii) The position vector $\mathbf{r}_p^{(i,j)}$ and surface coordinates $(u_p^{(i,j)}, \theta_p^{(i,j)})$ are known for each point $Q_p^{(i,j)}$ of the grid on surface Σ_p.

(iii) Point $Q_g^{(i,j)}$ on surface Σ_g corresponds to point $Q_p^{(i,j)}$ on surface Σ_p. The surface Σ_g parameters $(\theta_g^{(i,j)}, \theta_t^{(i,j)})$ can be determined by using the following two equations:

$$\begin{aligned} y_g^{(i,j)}(\theta_g^{(i,j)}, \theta_t^{(i,j)}) &= y_p^{(i,j)}(u_p^{(i,j)}, \theta_p^{(i,j)}) \\ z_g^{(i,j)}(\theta_g^{(i,j)}, \theta_t^{(i,j)}) &= z_p^{(i,j)}(u_p^{(i,j)}, \theta_p^{(i,j)}). \end{aligned} \tag{26.4.44}$$

(iv) Due to deviations of Σ_g from Σ_p, we have that $x_g^{(i,j)} \neq x_p^{(i,j)}$. The deviation of Σ_g from Σ_p at the grid point $Q_p^{(i,j)}$ is determined by the equation
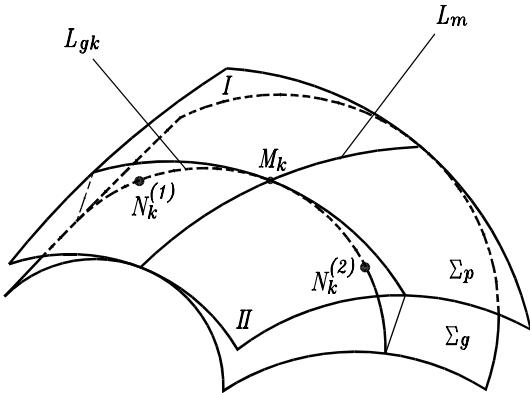
$$\delta_{i,j} = \mathbf{n}_p^{(i,j)} \cdot \left(\mathbf{r}_g^{(i,j)} - \mathbf{r}_p^{(i,j)} \right) \tag{26.4.45}$$

where $\mathbf{n}_p^{(i,j)}$ is the unit normal to surface Σ_p at the grid point $Q_p^{(i,j)}$.

The deviation $\delta_{i,j}$ can be positive or negative. We designate as positive such a deviation when $\delta_{i,j} > 0$ considering that $\mathbf{n}_p^{(i,j)}$ is directed into the "body" of surface Σ_p. Positive deviations of Σ_g with respect to Σ_p provide that Σ_g is inside of Σ_p and surface Σ_g is "crowned."

It is not excluded that initially the inequality $\delta_{i,j} > 0$ is not yet observed for all points of the grid. Positive deviations $\delta_{i,j}$ can be provided choosing the following options:

(1) Choosing a surface of revolution with a circular arc in the axial section instead of a circular cone; a proper radius of the circular arc must be determined.
(2) Changing parameter $l_t = |\overline{O_t O_b}|$ (Fig. 26.4.3); this means that the grinding cone will be displaced along $\mathbf{t}_b$ with respect to the mean line L_m.
(3) Varying the initially chosen function $\beta^{(1)}(\theta_p)$.

Figure 26.4.6: Determination of maximal deviations along line L_{gk}.

MINIMIZATION OF DEVIATIONS $\delta_{i,j}$. Consider that deviations $\delta_{i,j}$ ($i = 1, \ldots, n; j = 1, \ldots, m$) of Σ_g with respect to Σ_p have been determined at the (n, m) grid points. The minimization of deviations can be obtained by corrections of previously obtained function $\beta^{(1)}(\theta_p)$. The correction of angle β is equivalent to the correction of the angle that is formed by the principal directions on surfaces Σ_t and Σ_g. The correction of angle β can be achieved by turning of the tool about the common normal to surfaces Σ_t and Σ_p at their instantaneous point of tangency M_k.

The minimization of deviations $\delta_{i,j}$ is based on the following procedure:

Step 1: Consider the characteristic L_{gk}, the line of contact between surfaces Σ_t and Σ_g, that passes through current point M_k of mean line L_m on surface Σ_p (Fig. 26.4.6). Determine the deviations δ_k between Σ_t and Σ_p along line L_{gk} and find out the maximal deviations designated as $\delta_{k\max}^{(1)}$ and $\delta_{k\max}^{(2)}$. Points of L_{gk} where the deviations are maximal are designated as $N_k^{(1)}$ and $N_k^{(2)}$. These points are determined in regions I and II of surface Σ_g with line L_m as the border. The simultaneous consideration of maximal deviations in both regions enables us to minimize the deviations for the whole surface Σ_g.

Note. The deviations of Σ_t from Σ_p along L_{gk} are simultaneously the deviations of Σ_g from Σ_p along L_{gk} because L_{gk} is the line of tangency of Σ_t and Σ_g.

Step 2: The minimization of deviations is accomplished by correction of angle β_k that is determined at point M_k (Fig. 26.4.6). The minimization of deviations is performed locally, for a piece k of surface Σ_g with the characteristic L_{gk}. The process of minimization is a computerized iterative process based on the following considerations:

(i) The objective function is represented as

$$F_k = \min\left(\delta_{k\max}^{(1)} + \delta_{k\max}^{(2)}\right) \tag{26.4.46}$$

with the constraint $\delta_{i,j} \geq 0$.

(ii) The variable of the objective function is $\Delta\beta_k$. Then, considering the angle

$$\beta_k^{(2)} = \beta_k^{(1)} + \Delta\beta_k \tag{26.4.47}$$

and using the equation of meshing with β_k, we can determine the new characteristic, the piece of envelope $\Sigma_g^{(k)}$, and the new deviations. The applied iterations provide

the sought-for objective function. The final correction of angle β_k we designate as $\beta_k^{(opt)}$.

Note 1. The new contact line $L_{gk}^{(2)}$ (determined with $\beta_k^{(2)}$) slightly differs from the real contact line because the derivative $d\beta_k^{(1)}/ds$ but not $d\beta_k^{(2)}/ds$ is used for determination $L_{gk}^{(2)}$. However, $L_{gk}^{(2)}$ is very close to the real contact line.

Step 3: The discussed procedure must be performed for the set of pieces of surfaces Σ_g with the characteristic L_{gk} for each surface piece.

Recall that the deviations for the whole surface must satisfy the inequality $\delta_{i,j} \geq 0$. The procedure of optimization is illustrated with the flowchart in Fig. 26.4.7.

Curvatures of Ground Surface Σ_g

The direct determination of curvatures of Σ_g by using surface Σ_g equations is a complicated problem. The solution to this problem can be substantially simplified using the following conditions proposed by the authors: (i) the normal curvatures and surface torsions (geodesic torsions) of surfaces Σ_p and Σ_g are equal along line L_m, respectively; and (ii) the normal curvatures and surface torsions of surfaces Σ_t and Σ_g are equal along line L_g. This enables us to derive four equations that represent the principal curvatures of surface Σ_g in terms of normal curvatures and surface torsions of Σ_p and Σ_t. However, only three of these equations are independent (see below).

Further derivations are based on the following equations:

$$k_n = k_I \cos^2 q + k_{II} \sin^2 q = \frac{1}{2}(k_I + k_{II}) + \frac{1}{2}(k_I - k_{II})\cos 2q \quad (26.4.48)$$

$$t = 0.5(k_{II} - k_I)\sin 2q. \quad (26.4.49)$$
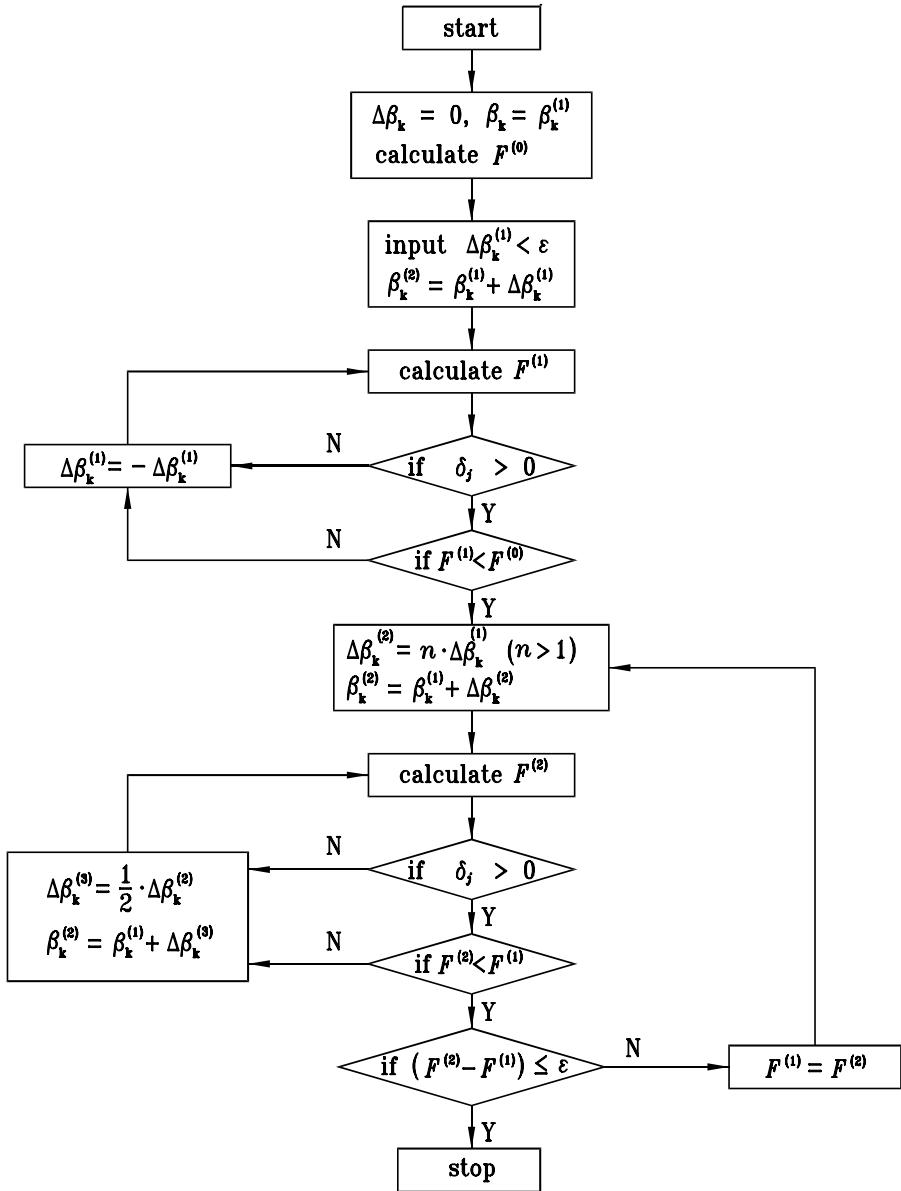
Here, k_I and k_{II} are the surface principal curvatures and angle q is formed by unit vectors $\mathbf{e}_I$ and $\mathbf{e}$ and is measured counterclockwise from $\mathbf{e}_I$ and $\mathbf{e}$; $\mathbf{e}_I$ is the principal direction with principal curvature k_I; $\mathbf{e}$ is the unit vector for the direction where the normal curvature is considered; t is the surface torsion for the direction represented by $\mathbf{e}$. Equation (26.4.48) is known as the Euler equation. Equation (26.4.49) is known in differential geometry as the Bonnet–Germain equation (see Chapter 7).

The determination of the principal curvatures and principal directions for Σ_g is based on the following computational procedure (see Section 7.9):

Step 1: Determination of $k_n^{(1)}$ and $t^{(1)}$ for surface Σ_g at the direction determined by the tangent to L_m. The determination is based on Eqs. (26.4.48) and (26.4.49) applied to surface Σ_p. Recall that Σ_p and Σ_g have the same values of $k_n^{(1)}$ and $t^{(1)}$ along the previously mentioned direction.
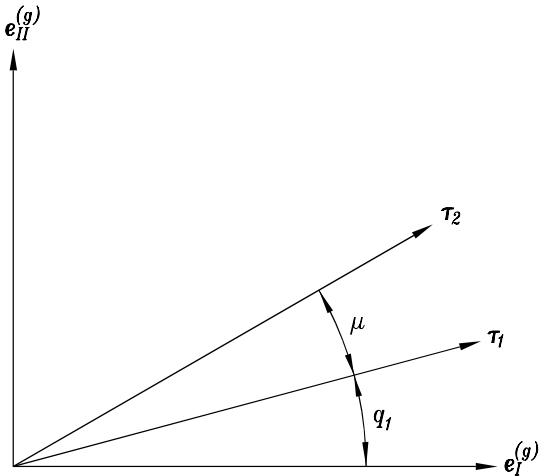
Step 2: Determination of $k_n^{(2)}$ and $t^{(2)}$. The designations $k_n^{(2)}$ and $t^{(2)}$ indicate the normal curvatures of Σ_g and the surface torsion along the tangent to L_g. Recall that $k_n^{(2)}$ and $t^{(2)}$ are the same for Σ_t and Σ_g along L_g. We determine $k_n^{(2)}$ and $t^{(2)}$ for surface Σ_t using Eqs. (26.4.48) and (26.4.49), respectively.

Step 3: We consider at this stage of computation that for surface Σ_g the following are known: $k_n^{(1)}$ and $t^{(1)}$, and $k_n^{(2)}$ and $t^{(2)}$ for two directions with tangents τ_1 and τ_2 that form the known angle μ (Fig. 26.4.8). Our goal is to determine angle q_1 (or q_2)

Figure 26.4.7: Flowchart for optimization.

for the principal direction $e_I^{(g)}$ and the principal curvatures $k_I^{(g)}$ and $k_{II}^{(g)}$ (Fig. 26.4.8). Using Eqs. (26.4.48) and (26.4.49), we can prove that $k_n^{(i)}$ and $t^{(i)}$ $(i = 1, 2)$ given for two directions represented by τ_1 and τ_2 are related with the following equation:

$$\frac{t^{(1)} + t^{(2)}}{k_n^{(2)} - k_n^{(1)}} = \cot \mu \qquad (26.4.50)$$

Figure 26.4.8: For determination of principal directions of generated surface Σ_g.

Step 4: Using Eqs. (26.4.48) and (26.4.49), we can derive the following three equations for determination of q_1, $k_I^{(g)}$, and $k_{II}^{(g)}$:

$$\tan 2q_1 = \frac{t^{(1)} \sin 2\mu}{t^{(2)} - t^{(1)} \cos 2\mu} \tag{26.4.51}$$

$$k_I^{(g)} = k_n^{(1)} - t^{(1)} \tan q_1 \tag{26.4.52}$$

$$k_{II}^{(g)} = k_n^{(1)} + t^{(1)} \cot q_1. \tag{26.4.53}$$

Equation (26.4.51) provides two solutions for q_1 ($q_1^{(2)} = q_1^{(1)} + 90°$) and both are correct. We choose the solution with the smaller value of q_1.

Numerical Example: Grinding of an Archimedes Worm Surface

The worm surface shown in Fig. 26.4.9 is a ruled undeveloped surface formed by the screw motion of straight line $\overline{KN}$ ($|\overline{KN}| = u_p$). The screw motion is performed in coordinate system S_p [Fig. 26.4.9(b)]. The to-be-ground surface Σ_p is represented in S_p as

$$r_p = u_p \cos\alpha \cos\theta_p \, \mathbf{i}_p + u_p \cos\alpha \sin\theta_p \, \mathbf{j}_p + (p\theta_p - u_p \sin\alpha) \, \mathbf{k}_p \tag{26.4.54}$$
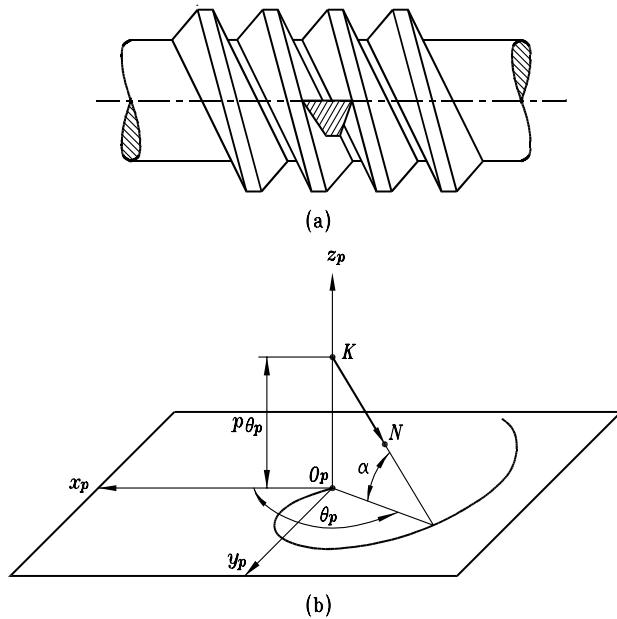
where u_p and θ_p are the surface parameters.

The surface unit normal is

$$\mathbf{n}_p = \frac{\mathbf{N}_p}{|\mathbf{N}_p|}, \quad \mathbf{N}_p = \frac{\partial r_p}{\partial u_p} \times \frac{\partial r_p}{\partial \theta_p}. \tag{26.4.55}$$

Thus

$$\mathbf{n}_p = \frac{1}{(u_p^2 + p^2)^{0.5}} \begin{bmatrix} p \sin\theta_p + u_p \sin\alpha \cos\theta_p \\ -p \cos\theta_p + u_p \sin\alpha \sin\theta_p \\ u_p \cos\alpha \end{bmatrix} \quad \text{(provided } \cos\alpha \neq 0\text{).} \tag{26.4.56}$$

(a)

(b)
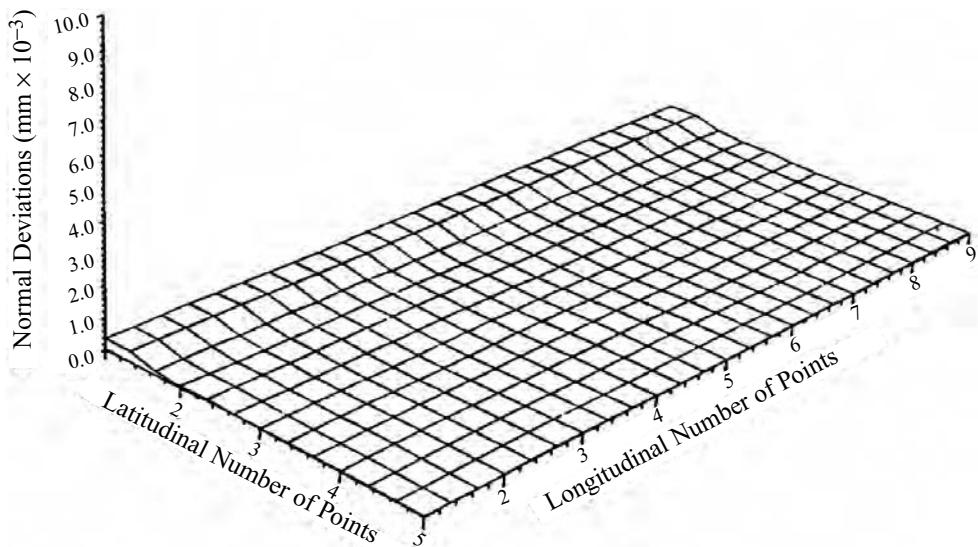
Figure 26.4.9: Surface of an Archimedes worm.

The design data are: number of threads $N_1 = 2$; axial diametral pitch $P_{ax} = 8/\text{in}$; $\alpha = 20°$; the radius of the pitch cylinder is 1.25 in. The remaining design parameters are determined from the following equations:

(i) The screw parameter is

$$p = \frac{N_1}{2P_{ax}} = 0.125 \text{ in.}$$

Figure 26.4.10: Deviations of the ground surface Σ_g from ideal surface Σ_p of an Archimedes worm.

(ii) The lead angle is

$$\tan \lambda_p = \frac{p}{r_p} = \frac{0.125}{1.25}, \quad \lambda_p = 5.7106°.$$

The mean line is determined as

$$\mathbf{r}_p(u_m, \theta_p), \quad u_m = \frac{\left(r_p + \dfrac{1}{P_{ax}}\right) + \left(r_p - \dfrac{1.25}{P_{ax}}\right)}{2 \cos \alpha} = \frac{r_p - \dfrac{0.125}{P_{ax}}}{\cos \alpha} = 1.3136 \text{ in.}$$

where $1/P_{ax}$ and $1.25/P_{ax}$ determine the addendum and dedendum of the worm.

The worm is ground by a cone with the apex angle $\gamma_t = 30°$, and outside diameter 8 in. The inside angle $\beta^{(1)} = -88.0121°$ provides the coincidence of both generatrices of the cone and the Archimedes worm. The maximal deviation of the ground surface Σ_g from the ideal surface Σ_p with the above value of $\beta^{(1)}$ is 3 μm.

The optimal angle $\beta^{(opt)} = -94.6788°$ has been determined by the developed optimization method. The deviations of the ground surface Σ_g from Σ_p with the optimal $\beta^{(opt)}$ are positive and the maximal deviation has been reduced to 0.35 μm (Fig. 26.4.10).

27 **Overwire (Ball) Measurement**

27.1 INTRODUCTION

Indirect determination of gear tooth thickness by overwire (ball) measurement has found broad application. This topic has been the subject of research by many scientists. The earliest publications dealing with such measurement of worms and spatial gears are Litvin's papers and books. Detailed references regarding the history of the performed research are given in Litvin [1968].

The application of computers and subroutines for the solution of systems of non-linear equations is a significant step forward in this area that was accomplished by Litvin *et al.* [1998b]. This chapter covers the following topics:

 (i) Algorithms for determination of location of a wire or a ball placed into the space of a workpiece with symmetric and nonsymmetric location of tooth surfaces
(ii) Relation between the tooth thickness and overwire measurement – this relation enables us to use the developed algorithms for a workpiece with various tolerances.

The developed theory was applied for measurement of tooth thickness of worms, screws, and involute helical gears. Computer programs for this purpose have been developed.

27.2 PROBLEM DESCRIPTION

Consider that a ball (a wire) is placed into the space of a workpiece (a worm, screw, or gear). The surfaces of the ball and the workpiece are in tangency at two points whose location depends on the geometry of the surfaces of the workpiece, the width of the space, and the diameter of the ball. The surface geometry of the workpiece is represented analytically and the width of the space and the ball (wire) diameter are given. Then, we can determine analytically (i) the distance of the center of the ball from the axis of the workpiece, or (ii) the shortest distance between the axes of the wire and the workpiece. The measurement over the ball (the wire) and the comparison of the obtained data with the analytically determined data enable us to find out if the space width satisfies the requirements.

The following is a description of the analytical approach that has been developed for the determination of points of tangency of a ball (wire) with the surfaces of the space of a workpiece. In the most general case there is no symmetry in the location and orientation of the two surfaces that form the space of the workpiece. This is typical, for instance, wherein the workpiece is a spiral bevel pinion or a hypoid pinion. Thus, we have to consider in such a case the simultaneous tangency of the ball or the wire with both surfaces of the space.

Consider that the two surfaces of the space and the unit normals to the surfaces are represented by vector equations,

$$\mathbf{r}^{(i)} = \mathbf{r}^{(i)}\left(u^{(i)}, \theta^{(i)}\right) \qquad (i = 1, 2) \tag{27.2.1}$$

$$\mathbf{n}^{(i)} = \frac{\mathbf{N}^{(i)}}{|\mathbf{N}^{(i)}|}, \qquad \mathbf{N}^{(i)} = \mathbf{r}_u^{(i)} \times \mathbf{r}_\theta^{(i)} \qquad (i = 1, 2) \tag{27.2.2}$$

where $\mathbf{r}_u^{(i)} = \partial\mathbf{r}^{(i)}/\partial u^{(i)}$, $\mathbf{r}_\theta^{(i)} = \partial\mathbf{r}^{(i)}/\partial\theta^{(i)}$, and $(u^{(i)}, \theta^{(i)})$ are the Gaussian coordinates of the surface.

The designation $(i = 1, 2)$ indicates the surfaces for both sides of the space. It is assumed that the surface normal is directed *outward* from the space, *toward* the tooth, and such a direction can be provided by the proper order of cofactors in the cross-products for $\mathbf{N}^{(i)}$.

Consider that

$$\mathbf{U} = [X \quad Y \quad Z]^{\mathrm{T}} \tag{27.2.3}$$

is the position vector of center C of the ball, or the point of intersection of both normals with the wire axis. It is evident from the conditions of force transmissions by the measurement, that both normals to the wire intersect the wire axis at the *same* point. We consider that z is the axis of the workpiece, and Z is chosen to determine the location of point C in a plane that is perpendicular to the axis of the workpiece.
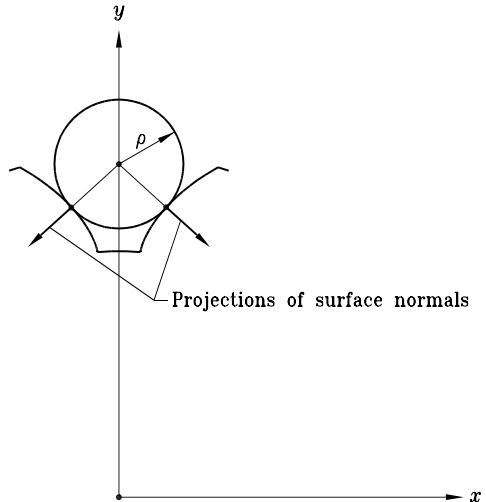
The tangency of the wire (ball) with the surfaces of the space is represented by the equation (Fig. 27.2.1)

$$\mathbf{U} + \rho\mathbf{n}^{(i)} = \mathbf{r}^{(i)}\left(u^{(i)}, \theta^{(i)}\right) \tag{27.2.4}$$

where $\mathbf{U} = [X \quad Y \quad Z]^{\mathrm{T}}$. This equation yields

$$\frac{X - x^{(i)}\left(u^{(i)}, \theta^{(i)}\right)}{n_x^{(i)}\left(u^{(i)}, \theta^{(i)}\right)} = \frac{Y - y^{(i)}\left(u^{(i)}, \theta^{(i)}\right)}{n_y^{(i)}\left(u^{(i)}, \theta^{(i)}\right)}$$

$$= \frac{Z - z^{(i)}\left(u^{(i)}, \theta^{(i)}\right)}{n_z^{(i)}\left(u^{(i)}, \theta^{(i)}\right)} = -\rho \quad (i = 1, 2) \tag{27.2.5}$$

where ρ is the radius of the wire (ball).

Figure 27.2.1: Measurement by a single ball.

Our goal is to determine the distance

$$R = (X^2 + Y^2)^{1/2} \qquad (27.2.6)$$

of point C from the axis of the workpiece. Then, knowing R, we may determine the overwire (ball) measurement M. Three wires are used for the measurement of worms and screws, and in this case

$$M = 2(R + \rho). \qquad (27.2.7)$$

Equation (27.2.7) works for the measurement of a gear with an *even* number of teeth. The equation for M, when a gear with an *odd* number of teeth is measured by *two balls*, is represented as (Fig. 27.2.2)
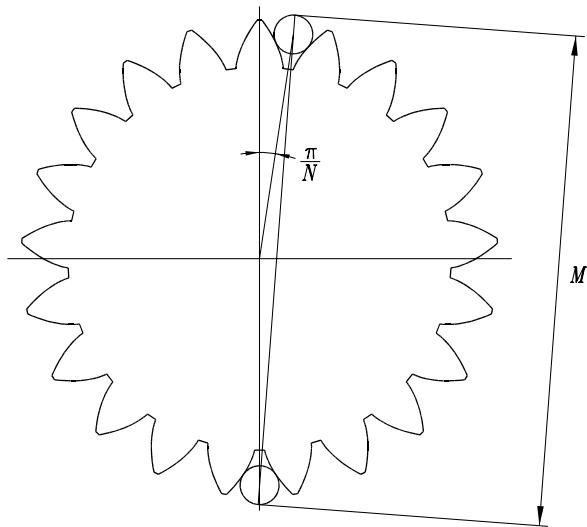
$$M = 2R\left(\cos\frac{90°}{N}\right) + 2\rho \qquad (27.2.8)$$

where N is the number of gear teeth. There is a special approach for determination of M when a gear with an odd number of teeth is measured by *two wires* (see Section 27.3).

Procedure of Computation

The procedure of computation for overwire (ball) measurement may be represented as follows:

Step 1: Equations (27.2.5) represent a system of six equations in six unknowns: X, Y, $u^{(i)}$, $\theta^{(i)}$ ($i = 1, 2$). We may represent this system of equations by a subsystem of four non-linear equations, and a system of two linear equations. The subsystem of four

Figure 27.2.2: Measurement by two balls.

nonlinear equations is

$$\frac{Z - z^{(1)}\left(u^{(1)}, \theta^{(1)}\right)}{n_z^{(1)}\left(u^{(1)}, \theta^{(1)}\right)} = -\rho \tag{27.2.9}$$

$$\frac{Z - z^{(2)}\left(u^{(2)}, \theta^{(2)}\right)}{n_z^{(2)}\left(u^{(2)}, \theta^{(2)}\right)} = -\rho \tag{27.2.10}$$

$$x^{(1)}\left(u^{(1)}, \theta^{(1)}\right) - \rho n_x^{(1)}\left(u^{(1)}, \theta^{(1)}\right) = x^{(2)}\left(u^{(2)}, \theta^{(2)}\right) - \rho n_x^{(2)}\left(u^{(2)}, \theta^{(2)}\right) \tag{27.2.11}$$

$$y^{(1)}\left(u^{(1)}, \theta^{(1)}\right) - \rho n_y^{(1)}\left(u^{(1)}, \theta^{(1)}\right) = y^{(2)}\left(u^{(2)}, \theta^{(2)}\right) - \rho n_y^{(2)}\left(u^{(2)}, \theta^{(2)}\right). \tag{27.2.12}$$

Equations (27.2.9) to (27.2.12) considered simultaneously provide the solution for four unknowns: $u^{(1)}, \theta^{(1)}, u^{(2)},$ and $\theta^{(2)}$. A subroutine for the solution of the above system of four nonlinear equations is required [for instance, we can use the one contained in the IMSL library [Visual Numerics, Inc., 1998]].

The unknowns X and Y may be determined from the following two linear equations:

$$X = x^{(i)}\left(u^{(i)}, \theta^{(i)}\right) - \rho n_x^{(i)}\left(u^{(i)}, \theta^{(i)}\right) \quad (i = 1 \text{ or } 2) \tag{27.2.13}$$

$$Y = y^{(i)}\left(u^{(i)}, \theta^{(i)}\right) - \rho n_y^{(i)}\left(u^{(i)}, \theta^{(i)}\right) \quad (i = 1 \text{ or } 2). \tag{27.2.14}$$

Step 2: We have considered the radius ρ of the ball (the wire) as known. In reality, we have to determine a value of ρ that satisfies the equation

$$(R + \rho) - r_a = \delta. \tag{27.2.15}$$

Here, r_a is the radius of the addendum circle in the plane $Z = d$, and δ is the desired difference between $(R + \rho)$ and r_a. The proper value of ρ can be determined by variation

of ρ in Eqs. (27.2.9) to (27.2.15) until the desired value of δ is obtained. Then, an even value of ρ may finally be chosen, and we can start the computations using Eqs. (27.2.9) to (27.2.14).

Step 3: The width w_t of the space on the reference (pitch circle) r_p may vary in accordance to the prescribed tolerance dw_t. The nominal value of M is obtained for the nominal value of w_t. The determination of the ratio dM/dw_t in addition to the nominal value of M enables us to determine the real value of the space width.

Particular Case 1

The surfaces of the space have a plane of symmetry, say $Y = 0$. Then, we may consider conditions of tangency of the wire (ball) with *one* side surface only. Equations (27.2.5) applied for this case yield

$$\frac{R - x(u, \theta)}{n_x(u, \theta)} = \frac{-y(u, \theta)}{n_y(u, \theta)} = \frac{Z - z(u, \theta)}{n_z(u, \theta)} = -\rho \qquad (27.2.16)$$

where Z is considered as chosen.

Equations (27.2.16) represent a system of three equations in three unknowns. The solution of a subsystem of two nonlinear equations enables us to determine the unknowns (u, θ). Then, we may determine R from the remaining equation that is the linear one with respect to the unknown R.

Particular Case 2

A screw with asymmetric space surfaces is considered. Both surfaces of the space are helicoids. A cross section of the screw will coincide with another one after rotating through a certain angle about the axis of the screw. For this reason, any value of Z can be chosen in Eqs. (27.2.9) and (27.2.10), for instance, $Z = 0$.

Particular Case 3

The surfaces of the space are symmetric and they are helicoids. In this case, we can use Eqs. (27.2.16) and take $Z = 0$.

27.3 MEASUREMENT OF INVOLUTE WORMS, INVOLUTE HELICAL GEARS, AND SPUR GEARS

Basic Equations

Equations of involute worms are represented in Section 19.6. Equation (27.2.16) with $Z = 0$ yields the following computational procedure:

$$\text{inv}\,(\theta + \mu) = \text{inv}\,\alpha_t + \frac{\rho}{r_b \sin \lambda_b} - \frac{w_t}{2r_p} \qquad (27.3.1)$$

$$R = \frac{r_b}{\cos(\theta + \mu)} \qquad (27.3.2)$$

$$dR = -\frac{dw_t \cos \alpha_t}{2 \sin(\theta + \mu)}. \qquad (27.3.3)$$

These equations work for the right-hand and left-hand involute worms and helical gears. In case of spur gears, we have to take $\lambda_b = 90°$.

Determination of M

In the case of three-wire measurement, M is determined from Eq. (27.2.7). The same equation is applied for measurement by two balls (wires) of gears with an even number of teeth. Equation (27.2.8) is applied for the measurement by two balls of helical and spur gears with an odd number of teeth and for the measurement of spur gears with an odd number of teeth by two wires. Measurement of helical gears with an odd number of teeth by two wires is based on the approach developed by Litvin [1968].

Representation of the Unit Vectors of Wire Axes and the Shortest Distance Between the Axes of Two Wires

Consider that wire 1 is installed into gear space $\Sigma_2^{(1)}$. Vectors $\mathbf{a}^{(1)}$ and $\mathbf{r}^{(1)}$ (Fig. 27.3.1) represent the unit vector of the wire axis in S_2, and the shortest distance between $\mathbf{a}^{(1)}$ and the gear axis, respectively. Here,

$$\mathbf{r}_2^{(1)} = R\, \mathbf{i}_2 \tag{27.3.4}$$

$$\mathbf{a}_2^{(1)} = \sin \beta_R\, \mathbf{j}_2 + \cos \beta_R\, \mathbf{k}_2 \tag{27.3.5}$$
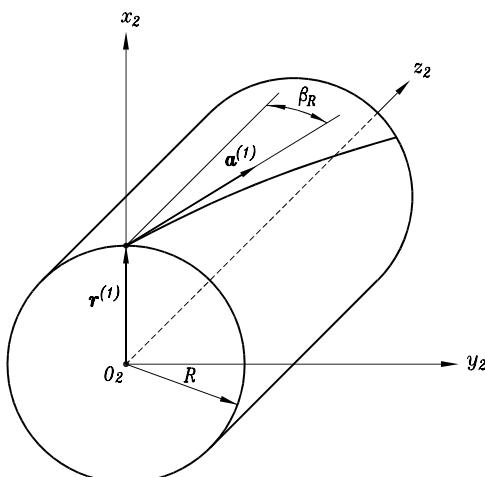
$$\cot \beta_R = \frac{p}{R} \tag{27.3.6}$$

where p is the screw parameter of the helicoid.

Consider now that wire 2 is installed into the space $\Sigma_2^{(2)}$ that forms angle γ with the first space. Angle γ is measured in the plane that is perpendicular to the gear axis. Here,

$$\gamma = \pi \left(1 \pm \frac{1}{N} \right)$$

where N is the teeth number.

Figure 27.3.1: Location and orientation of wire 1 in S_2.

We set up two coordinate systems S_a and S_b that are rigidly connected to wire 2. Coordinate system S_a initially coincides with S_2. The installment of wire 2 in S_b is represented in S_b by equations similar to (27.3.4) and (27.3.5):
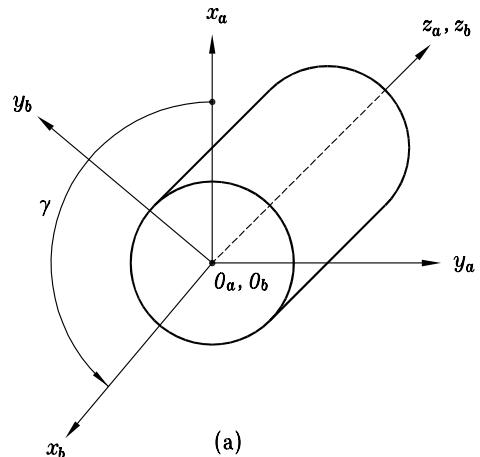
$$\mathbf{r}_b^{(2)} = R \, \mathbf{i}_b \tag{27.3.7}$$

$$\mathbf{a}_b^{(2)} = \sin \beta_R \, \mathbf{j}_b + \cos \beta_R \, \mathbf{k}_b. \tag{27.3.8}$$
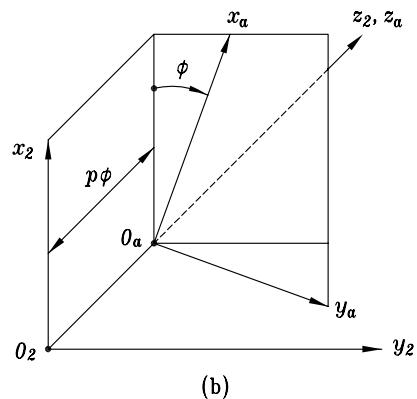
We may imagine that wire 2 with coordinate systems S_a and S_b performs a screw motion about the axis of the helical gear that is in tangency with the surfaces of space $\Sigma_2^{(2)}$. Vector of shortest distance $\mathbf{r}_2^{(2)}$ between $\mathbf{a}_2^{(2)}$ and the gear axis, and unit vector $\mathbf{a}_2^{(2)}$ are represented in S_2 by the equations
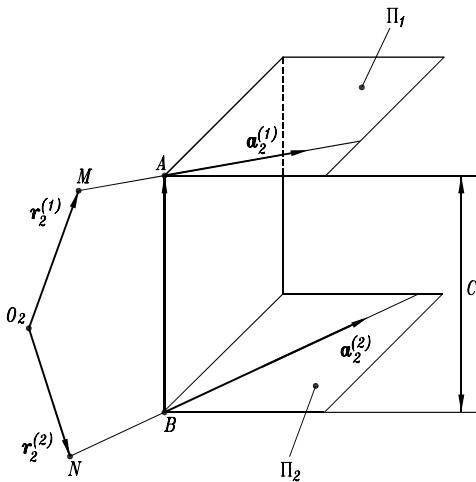
$$\mathbf{r}_2^{(2)} = \mathbf{M}_{2a} \mathbf{M}_{ab} \mathbf{r}_b^{(2)}, \quad \mathbf{a}_2^{(2)} = \mathbf{L}_{2a} \mathbf{L}_{ab} \mathbf{a}_b^{(2)}. \tag{27.3.9}$$

Matrices $\mathbf{M}_{2a}$ and $\mathbf{M}_{ab}$ may be derived using Fig. 27.3.2. Figure 27.3.2(a) shows the orientation of coordinate systems S_a and S_b, one with respect to the other. Coordinate systems S_a and S_b are rigidly connected, and initially S_a coincides with S_2. Figure 27.3.2(b) shows the orientation and location of S_a with respect to S_2 after the rotation through angle ϕ and the displacement of $p\phi$ in the screw motion.

Figure 27.3.2: For derivation of location and orientation of wire 2 in S_2.

Figure 27.3.3: For derivation of shortest distance between two wires.

Equations (27.3.9) yield

$$\mathbf{r}_2^{(2)} = R[\cos(\gamma - \phi)\,\mathbf{i}_2 - \sin(\gamma - \phi)\,\mathbf{j}_2 + \phi\,\cot\beta_R\mathbf{k}_2] \tag{27.3.10}$$

$$\mathbf{a}_2^{(2)} = \sin\beta_R\sin(\gamma - \phi)\,\mathbf{i}_2 + \sin\beta_R\cos(\gamma - \phi)\,\mathbf{j}_2 + \cos\beta_R\,\mathbf{k}_2. \tag{27.3.11}$$

The variable parameter ϕ represents the rotation of wire 2 in its screw motion about the gear axis.

Determination of the Overwire Measurement M

We may now derive the equation of the unit vector $\mathbf{c}_2$ of the shortest distance between vectors $\mathbf{a}_2^{(1)}$ and $\mathbf{a}_2^{(2)}$ as follows (Fig. 27.3.3):

$$\mathbf{c}_2 = \frac{\mathbf{a}_2^{(1)} \times \mathbf{a}_2^{(2)}}{\left|\mathbf{a}_2^{(1)} \times \mathbf{a}_2^{(2)}\right|}$$

$$= \frac{1}{\left[1 + \tan^2\beta_R\cos^2\left(\dfrac{\gamma - \phi}{2}\right)\right]^{1/2}} \begin{bmatrix} \sin\left(\dfrac{\gamma - \phi}{2}\right) \\[2mm] \cos\left(\dfrac{\gamma - \phi}{2}\right) \\[2mm] -\tan\beta_R\cos\left(\dfrac{\gamma - \phi}{2}\right) \end{bmatrix}$$

$$\left(\text{provided } \sin\left(\frac{\gamma - \phi}{2}\right) \neq 0\right). \tag{27.3.12}$$

The shortest distance C between the wires is represented as

$$C(\phi) = \left(\mathbf{r}_2^{(1)} - \mathbf{r}_2^{(2)}\right) \cdot \mathbf{c}_2 = \frac{2\sin\left(\dfrac{\gamma - \phi}{2}\right) + \phi\cos\left(\dfrac{\gamma - \phi}{2}\right)}{\left[1 + \tan^2\beta_R\cos^2\left(\dfrac{\gamma - \phi}{2}\right)\right]^{1/2}}\,R. \tag{27.3.13}$$

(See derivations below.) The overwire measurement is performed when function $C(\phi)$ reaches its extreme value, that is,

$$\frac{dC(\phi)}{d\phi} = 0. \tag{27.3.14}$$

Equation (27.3.14) yields

$$\phi = \tan^2 \beta_R \sin(\gamma - \phi). \tag{27.3.15}$$

Equations (27.3.13) and (27.3.15) yield that the extreme value of C is

$$C = 2R \sin\left(\frac{\gamma - \phi}{2}\right) \left[1 + \tan^2 \beta_R \cos^2\left(\frac{\gamma - \phi}{2}\right)\right]^{1/2} \tag{27.3.16}$$

and

$$M = C + 2\rho. \tag{27.3.17}$$

The derivation of equation

$$\left(\mathbf{r}_2^{(1)} - \mathbf{r}_2^{(2)}\right) \cdot \mathbf{c}_2 = C \tag{27.3.18}$$

is based on the following considerations:

(i) Unit vectors $\mathbf{a}_2^{(1)}$ and $\mathbf{a}_2^{(2)}$ of the axes of two wires are crossed and lie in parallel planes Π_1 and Π_2 (Fig. 27.3.3). The shortest distance between $\mathbf{a}_2^{(1)}$ and $\mathbf{a}_2^{(2)}$ is

$$C = \overline{BA} = C \frac{\mathbf{a}_2^{(1)} \times \mathbf{a}_2^{(2)}}{\left|\mathbf{a}_2^{(1)} \times \mathbf{a}_2^{(2)}\right|}.$$

(ii) Position vectors $\mathbf{r}_2^{(1)} = \overline{O_2 M}$, and $\mathbf{r}_2^{(2)} = \overline{O_2 N}$ are drawn from origin O_2 of coordinate system S_2 to current points M and N of the axes of the wires.

(iii) Figure 27.3.3 yields

$$\mathbf{r}_2^{(1)} + \lambda_1 \mathbf{a}_2^{(1)} = \mathbf{r}_2^{(2)} + \lambda_2 \mathbf{a}_2^{(2)} + \mathbf{C} \tag{27.3.19}$$

where

$$\lambda_1 \mathbf{a}_2^{(1)} = \overline{MA}, \qquad \lambda_2 \mathbf{a}_2^{(2)} = \overline{NB}.$$

Then, we obtain

$$\mathbf{r}_2^{(1)} - \mathbf{r}_2^{(2)} = \mathbf{C} + \lambda_2 \mathbf{a}_2^{(2)} - \lambda_1 \mathbf{a}_2^{(1)}. \tag{27.3.20}$$

We multiply both sides of Eq. (27.3.20) by the unit vector

$$\mathbf{c}_2 = \frac{\mathbf{a}_2^{(1)} \times \mathbf{a}_2^{(2)}}{\left|\mathbf{a}_2^{(1)} \times \mathbf{a}_2^{(2)}\right|}$$

and take into account that

$$\mathbf{C} \cdot \mathbf{c}_2 = C, \quad \mathbf{a}_2^{(1)} \cdot \left(\mathbf{a}_2^{(1)} \times \mathbf{a}_2^{(2)}\right) = \mathbf{a}_2^{(2)} \cdot \left(\mathbf{a}_2^{(1)} \times \mathbf{a}_2^{(2)}\right) = 0. \tag{27.3.21}$$

Then, we obtain Eq. (27.3.18).

Relation Between dM and dR

The relation between dM and dR may be obtained by differentiation of Eqs. (27.3.16) and (27.3.17) that yields

$$dM = \left[\frac{C}{R} - \frac{2R}{C}\tan^2\beta_R \sin^2(\gamma - \phi)\right]dR \qquad (27.3.22)$$

where dR is represented by (27.3.3). The derivation of (27.3.22) is based on the following auxiliary relations:

$$d\phi = \frac{2\tan\beta_R \sin(\gamma - \phi)}{\cos^2\beta_R[1 + \tan^2\beta_R \cos(\gamma - \phi)]}d\beta_R \qquad (27.3.23)$$

$$d\beta_R = \sin\beta_R \cos\beta_R \frac{dR}{R}. \qquad (27.3.24)$$

Numerical Example: Measurement of Involute Helical Gear

Input Data:

Profile angle of rack-cutter in normal section	$\alpha_n = 20°$
Diametral pitch in normal section	$P_n = 10.0$ (1/in.)
Helix angle on pitch cylinder	$\beta_p = 30°$
Number of teeth	$N_1 = 21$
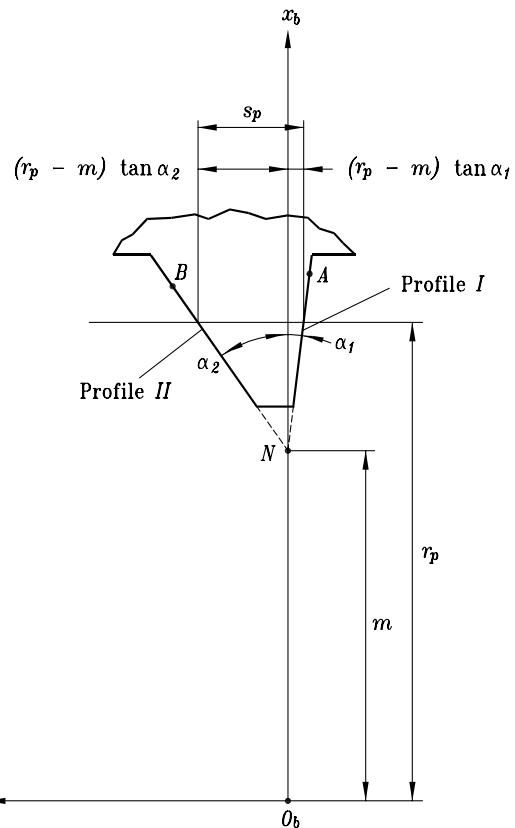
Auxiliary Data:

Diametral pitch in cross section	$P_t = 8.660254$ (1/in.)
Radius of pitch cylinder	$r_p = 1.212436$ in.
Screw parameter	$p = 2.100000$ in.
Circular pitch in cross section	$p_t = 0.362760$ in.
Distance between the tip points of the ball and involute helical gear [see Eq. (27.2.15)]	$\delta = 0.0100$ in.

Output Data:

Radius of ball	$\rho = 0.083000$ in.
Distance between the axes of the wire and involute helical gear	$R = 1.237895$ in.
Shortest distance between two wire axes	$C = 2.465225$ in.
Measurement over wires	$M = 2.631225$ in.
Relation between dM and dw_t	$\dfrac{dM}{dw_t} = -2.116686$

The nominal values of R and M in the preceding table are obtained for the nominal value of w_t, that is, the space width measured on the pitch circle. The ratio dM/dw_t enables us to determine the real space width.

Figure 27.4.1: Blade profiles.

27.4 MEASUREMENT OF ASYMMETRIC ARCHIMEDES SCREW

Figure 27.4.1 shows the blade that is used for generation of a screw with asymmetric tooth surfaces. Each side of the space surface of the screw may be considered as the surface of an Archimedes worm. The profile angles of the tooth side screw surfaces are different because the profile angles of the blade are different (Fig. 27.4.1).

The generating lines of the blade are represented in the auxiliary coordinate system S_b (Fig. 27.4.1). Point N is the point of intersection of the generating lines and axis x_b passes through point N. Axis z_b coincides with the axis of the screw to be generated.
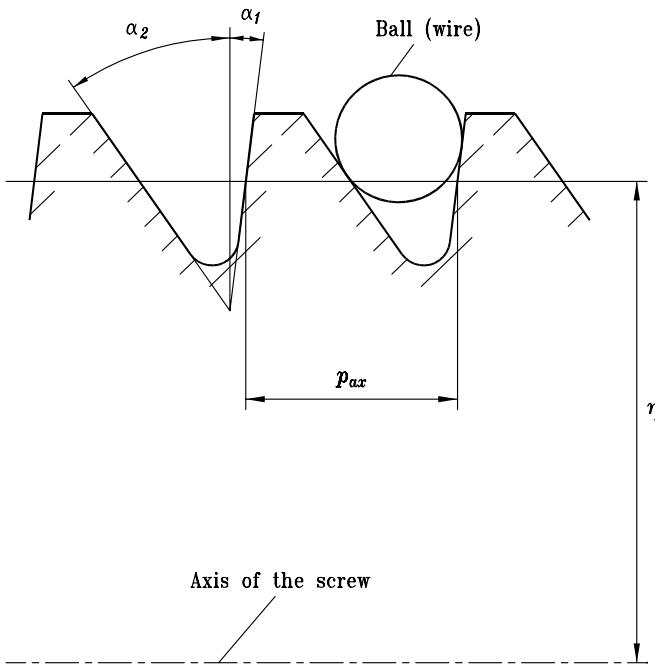
Figure 27.4.1 yields

$$s_p = (r_p - m)(\tan\alpha_1 + \tan\alpha_2). \tag{27.4.1}$$

The nominal value of s_p is determined as

$$s_p = \frac{p_{ax}}{2} = \frac{H}{2N_1} = \frac{\pi}{2P_{ax}}. \tag{27.4.2}$$

Here, p_{ax} is the axial distance between the neighboring worm threads (Fig. 27.4.2); $H = 2\pi r_p \tan\lambda_p$ is the lead; r_p is the radius of the worm pitch cylinder; P_{ax} is the diametral pitch that corresponds to p_{ax}.

Figure 27.4.2: Axial section of screw threads.

Using Eq. (27.4.1), we obtain

$$m = r_p - \frac{s_p}{\tan\alpha_1 + \tan\alpha_2}. \tag{27.4.3}$$

Current point A (or B) of the generating line is represented in S_b by the equations

$$\mathbf{r}_b^{(A)} = [m + u_1\cos\alpha_1 \quad 0 \quad -u_1\sin\alpha_1]^\mathrm{T} \tag{27.4.4}$$

$$\mathbf{r}_b^{(B)} = [m + u_2\cos\alpha_2 \quad 0 \quad u_2\sin\alpha_2]^\mathrm{T} \tag{27.4.5}$$

where $u_1 = |\overline{NA}|$, $u_2 = |\overline{NB}|$.

The screw surfaces are generated while the blade performs the screw motion about the screw axis with the screw parameter $p = H/(2\pi)$ (Fig. 19.4.3). Using the procedure of coordinate transformation, we obtain the following equations for the screw space surfaces and the surface unit normals.

(i) **Side I surface, right-hand worm:**

$$\begin{aligned} x_1 &= (m + u_1\cos\alpha_1)\cos\theta_1 \\ y_1 &= (m + u_1\cos\alpha_1)\sin\theta_1 \\ z_1 &= -u_1\sin\alpha_1 + p\theta_1. \end{aligned} \tag{27.4.6}$$

Surface unit normal:

$$\begin{aligned} n_{x1} &= -k_1(d_1\cos\alpha_1\sin\theta_1 + \sin\alpha_1\cos\theta_1) \\ n_{y1} &= -k_1(-d_1\cos\alpha_1\cos\theta_1 + \sin\alpha_1\sin\theta_1) \\ n_{z1} &= -k_1\cos\alpha_1 \end{aligned} \tag{27.4.7}$$

where

$$m = r_p - \frac{s_p}{\tan\alpha_1 + \tan\alpha_2}, \quad d_1 = \frac{p}{m + u_1\cos\alpha_1}, \quad k_1 = \frac{1}{\left(1 + d_1^2\cos^2\alpha_1\right)^{1/2}}.$$

(ii) **Side II surface, right-hand worm:**

$$x_2 = (m + u_2\cos\alpha_2)\cos\theta_2$$
$$y_2 = (m + u_2\cos\alpha_2)\sin\theta_2 \qquad\qquad (27.4.8)$$
$$z_2 = u_2\sin\alpha_2 + p\theta_2.$$

Surface unit normal:

$$n_{x2} = k_2(d_2\cos\alpha_2\sin\theta_2 - \sin\alpha_2\cos\theta_2)$$
$$n_{y2} = k_2(-d_2\cos\alpha_2\cos\theta_2 - \sin\alpha_2\sin\theta_2) \qquad\qquad (27.4.9)$$
$$n_{z2} = k_2\cos\alpha_2$$

where

$$d_2 = \frac{p}{m + u_2\cos\alpha_2}, \quad k_2 = \frac{1}{\left(1 + d_2^2\cos^2\alpha_2\right)^{1/2}}.$$

Numerical Example: Measurement of Asymmetric Screw

The procedure of computation is based on the algorithm discussed in Section 27.2 [see Eqs. (27.2.9) to (27.2.14)]. Because the space surfaces are helicoids, any value of Z can be chosen, for instance $Z = 0$.

Input Data:

Pitch diameter	d_p	= 1.125 in.
Diametral pitch	P_{ax}	= 10.0 (1/in.)
Side I axial pressure angle	α_1	= 7°
Side II axial pressure angle	α_2	= 45°
Number of threads	N_1	= 8

Auxiliary Data:

Lead angle	λ_p	= 35.417055°
Space width on pitch cylinder in axial section	s_p	= 0.157080 in.
Screw parameter	p	= 0.400000 in.
Lead	H	= 2.51327 in.

Output Data:

Radius of the ball (wire)	ρ	= 0.071000 in.
Distance between the axes of the wire and the worm	R	= 0.598838 in.
Relation between dR and ds_p	$\dfrac{dR}{ds_p}$	= -0.829939

28 Minimization of Deviations of Gear Real Tooth Surfaces
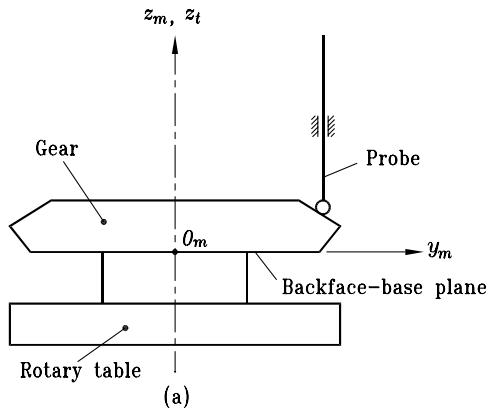
28.1 INTRODUCTION

Coordinate measurements of gear real tooth surfaces enable us to determine surface deviations from the ideal surface. The goal is to minimize the surface deviations by proper correction of the initial machine-tool settings.
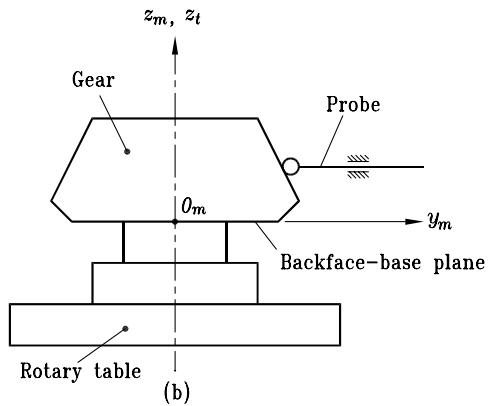
The technological aspects of the problem are as follows:

(i) The deviations of real tooth surfaces are inevitable due to surface distortion by heat-treatment, errors in initial machine-tool settings, deflection by manufacturing, and so on.

(ii) Application of an additional finishing operation for elimination of the deviations would be too expensive in comparison with the approach based on corrections of initially applied machine-tool settings. The advantage of this approach is the possibility of using the same equipment to correct the deviations. The disadvantage is that the approach will be successful only if the deviations are repeatable.

(iii) The coordinate measurements must be performed with high precision, which currently prohibits them from being performed simultaneously with the manufacturing. Therefore, the coordinate measurements are performed after manufacturing, but only the first gear of the whole gear set to be manufactured is tested.

(iv) In some cases master-gears are used and the coordinate measurements provide the information about the deviations from the master-surface for the surface being tested. The authors consider this approach less effective than computerized determination of surface deviations and corrections of machine-tool settings.

The described technique has been developed in response to the increasing requirements of high quality gear transmissions. Minimizing the deviations of real tooth surfaces results in a reduction in the level of transmission errors that cause gear noise and vibration. This chapter is based on research performed by Litvin, Kuan, Wang, Handschuh, Masseth, and Maruyama [1993b].
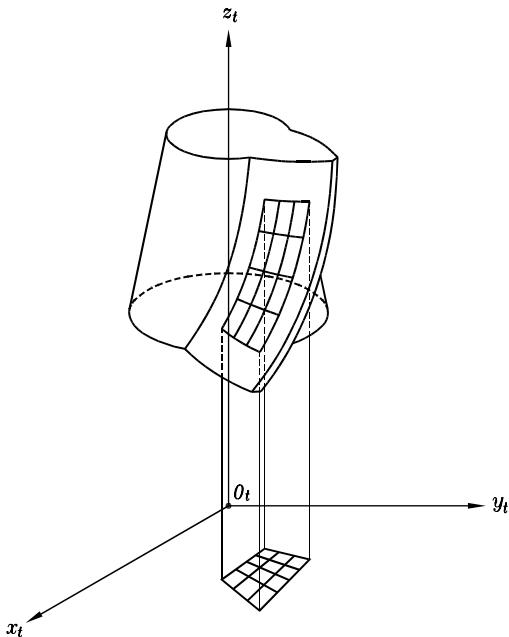
Figure 28.2.1: Surface measurement.

28.2 OVERVIEW OF MEASUREMENT AND MODELLING METHOD

The surface deviations obtained initially in Cartesian coordinates are transformed into deviations along the normal to the theoretical surface. The coordinate measurements are performed by a machine with four or five degrees-of-freedom. In the case of four degrees-of-freedom, the probe performs three translational motions (Fig. 28.2.1); the fourth motion, rotation, is performed by a rotary table. The axis of rotational motion coincides with the axis of the workpiece. In the case of a five-degree-of-freedom machine, the fifth degree of freedom is used to provide the deflections of the probe in the direction of the normal to the theoretical surface. The probe is provided with a changeable spherical surface whose diameter can be chosen from a wide range.

The motions of the probe and the workpiece by coordinate measurements are computer controlled, and therefore a grid comprised of the set of surface points to be measured must be chosen (Fig. 28.2.2). There is a *reference* point on the grid that is necessary for the initial installments of the probe. There are two orientations of the probe installment that are used to measure a gear [Fig. 28.2.1(a)] and a pinion [Fig. 28.2.1(b)], depending on the angle of the pitch cone.

Figure 28.2.2: Grid.
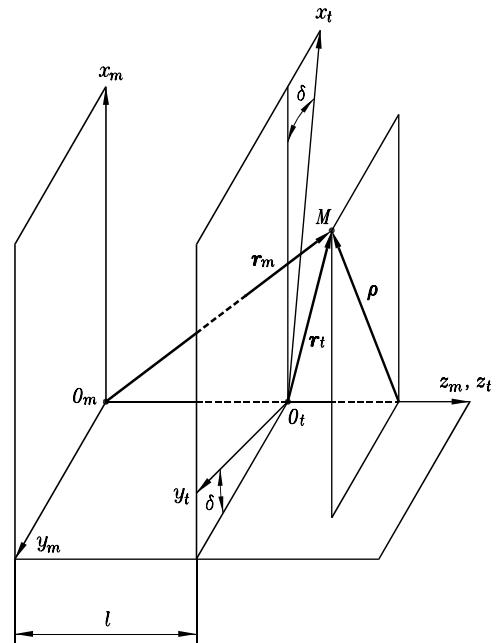
The mathematical aspects of coordinate measurements will now be described: First, it is necessary to derive the equations of the theoretical surface; in many cases this surface can be derived as the envelope to the family of generating surfaces, namely the tool surfaces. Next, the results of coordinate measurements must be transformed into deviations of the real surface represented in the direction of the surface normal. Then, the relations between the surface variations and the corrections to the machine-tool settings must be determined. The surface deviations obtained from coordinate measurements and the surface variations determined by the corrections of machine-tool settings can be represented by an overdetermined system of linear equations. The number of these equations, k, is equal to the number of points of the grid, and the number of unknowns, m, is equal to the number of corrections of machine-tool settings ($m \ll k$). The optimal solution to such a system of linear equations results in the determination of the machine-tool setting corrections.

28.3 EQUATIONS OF THEORETICAL TOOTH SURFACE Σ_t

Considering that the theoretical surface can be determined directly, we represent it in coordinate system S_t in two-parameter form as

$$\mathbf{r}_t(u, \theta), \quad \mathbf{n}_t(u, \theta). \tag{28.3.1}$$

Here, $\mathbf{r}_t$ and $\mathbf{n}_t$ are the position vector and the surface unit normal, respectively; (u, θ) are the Gaussian coordinates (surface coordinates).

Figure 28.4.1: Coordinate transformation.

For the case when surface Σ_t is the envelope to the family of generating surface Σ_c, we represent surface Σ_t and the unit normal $\mathbf{n}_t$ to Σ_t in S_t as

$$\mathbf{r}_t = \mathbf{M}_{tc}\mathbf{r}_c(u_c, \theta_c), \qquad f(u_c, \theta_c, \phi) = 0 \tag{28.3.2}$$

$$\mathbf{n}_t = \mathbf{L}_{tc}\mathbf{n}_c(u_c, \theta_c), \qquad f(u_c, \theta_c, \phi) = 0. \tag{28.3.3}$$

Here, (u_c, θ_c) are the Gaussian coordinates of the generating surface Σ_c; ϕ is the generalized parameter of motion in the process for generation. The equation of meshing is given by

$$f(u_c, \theta_c, \phi) = \mathbf{N}^{(c)} \cdot \mathbf{v}^{(ct)} = 0 \tag{28.3.4}$$

where $\mathbf{N}^{(c)}$ is the normal to Σ_c, and $\mathbf{v}^{(ct)}$ is the relative velocity for a point of contact of Σ_c and Σ_t. The 4×4 matrix $\mathbf{M}_{tc}$ and the 3×3 matrix $\mathbf{L}_{tc}$ describe the coordinate transformation from S_c to S_t of a position vector and a surface unit normal, respectively.

28.4 COORDINATE SYSTEMS USED FOR COORDINATE MEASUREMENTS

Coordinate systems S_m and S_t are rigidly connected to the coordinate measuring machine (CMM) and the workpiece being measured, respectively (Fig. 28.4.1). The back face of the gear is installed flush with the base plane of the CMM. The distance l between the origins O_m and O_t is known, but the parameter of orientation δ must be determined (see Section 28.5). The coordinate transformation from S_t to S_m is represented by the matrix equation

$$\mathbf{r}_m = \mathbf{M}_{mt}\mathbf{r}_t. \tag{28.4.1}$$

28.5 GRID AND REFERENCE POINT

The grid is a set of points on Σ_t chosen as points of contact between the probe and Σ_t (Fig. 28.4.1). Fixing the value of z_t for the point of the grid, and the value of, say y_t (or x_t), we can obtain the equations

$$y_t\left(u_{(i)}, \theta_{(i)}\right) = h_i, \quad z_t\left(u_{(i)}, \theta_{(i)}\right) = l_i \quad (i = 1, \ldots, k) \tag{28.5.1}$$

where k is the number of grid points.

We consider h_i and l_i as given and solve Eqs. (28.5.1) for $(u_{(i)}, \theta_{(i)})$. Then we can determine the position vectors and the unit normals for k points of the grid using the equations

$$\mathbf{r}_t^{(i)} = \left[x_t\left(u_{(i)}, \theta_{(i)}\right) \quad y_t\left(u_{(i)}, \theta_{(i)}\right) \quad z_t\left(u_{(i)}, \theta_{(i)}\right)\right]^{\mathrm{T}} \quad (i = 1, \ldots, k) \tag{28.5.2}$$

$$\mathbf{n}_t^{(i)} = \left[n_{xt}\left(u_{(i)}, \theta_{(i)}\right) \quad n_{yt}\left(u_{(i)}, \theta_{(i)}\right) \quad n_{zt}\left(u_{(i)}, \theta_{(i)}\right)\right]^{\mathrm{T}} \quad (i = 1, \ldots, k). \tag{28.5.3}$$

The position vector for the center of the probe, if the deviations are zero, is represented by the equation

$$\mathbf{R}_t^{(i)} = \mathbf{r}_t^{(i)} + \rho \mathbf{n}_t^{(i)} \tag{28.5.4}$$

where ρ is the radius of the probe tip and i is the grip point.

The reference point

$$\mathbf{r}_t^{(0)} = \left[x_t\left(u^{(0)}, \theta^{(0)}\right) \quad y_t\left(u^{(0)}, \theta^{(0)}\right) \quad z_t\left(u^{(0)}, \theta^{(0)}\right)\right]^{\mathrm{T}} \tag{28.5.5}$$

is usually chosen as the mean point of the grid. The center of the probe that corresponds to the reference point on Σ_t is determined from Eq. (28.5.4) as

$$\mathbf{R}_t^{(0)} = \left[X_t\left(u^{(0)}, \theta^{(0)}\right) \quad Y_t\left(u^{(0)}, \theta^{(0)}\right) \quad Z_t\left(u^{(0)}, \theta^{(0)}\right)\right]^{\mathrm{T}}. \tag{28.5.6}$$

Here, $(u^{(0)}, \theta^{(0)})$ are known values. The coordinates of the reference center of the probe are represented in coordinate system S_m of the measuring machine by the matrix equation

$$\mathbf{R}_m^{(0)} = \mathbf{M}_{mt}(\delta) \, \mathbf{R}_t^{(0)}. \tag{28.5.7}$$

Equation (28.5.7) yields

$$X_m^{(0)} = X_m^{(0)}\left(\delta, u^{(0)}, \theta^{(0)}\right)$$

$$Y_m^{(0)} = Y_m^{(0)}\left(\delta, u^{(0)}, \theta^{(0)}\right) \tag{28.5.8}$$

$$Z_m^{(0)} = Z_m^{(0)}\left(\delta, u^{(0)}, \theta^{(0)}\right).$$

The three equations of system (28.5.8) contain four unknowns: δ, $X_m^{(0)}$, $Y_m^{(0)}$, $Z_m^{(0)}$. To solve these equations we may consider that one of the coordinates of the reference point of the probe center, say $Y_m^{(0)}$, may be chosen equal to zero. Then the system of equations (28.5.8) allows the determination of δ, $X_m^{(0)}$, and $Z_m^{(0)}$. Coordinates $X_m^{(0)}$, $Y_m^{(0)} = 0$, $Z_m^{(0)}$ are necessary for the initial installment of the center of the probe.

28.6 DEVIATIONS OF THE REAL SURFACE

The deviations of the real surface are caused by errors of manufacturing, heat treatment, and so on. Vector positions of the center of the probe for the theoretical surface and the real surface can be represented as follows:

$$\mathbf{R}_m = \mathbf{r}_m(u, \theta) + \rho \mathbf{n}_m(u, \theta) \tag{28.6.1}$$

$$\mathbf{R}_m^* = \mathbf{r}_m(u, \theta) + \lambda \mathbf{n}_m(u, \theta). \tag{28.6.2}$$

Here, $\mathbf{r}_m$ and $\mathbf{n}_m$ are the position vector and the unit normal to the theoretical surface, respectively, that are represented in coordinate system S_m of the measuring machine; λ determines the real location of the probe center and it is considered along the normal to the theoretical surface; $\mathbf{R}_m$ and $\mathbf{R}_m^*$ represent in S_m the position vector of the probe center for the theoretical and real surfaces, respectively. Equations (28.6.1) and (28.6.2) yield

$$\mathbf{R}_m^* - \mathbf{R}_m = (\lambda - \rho)\mathbf{n}_m = \Delta n\, \mathbf{n}_m \tag{28.6.3}$$

and

$$\Delta n = (\mathbf{R}_m^* - \mathbf{R}_m) \cdot \mathbf{n}_m. \tag{28.6.4}$$

The position vector $\mathbf{R}_m^*$ is determined by coordinate measurements for points of the grid. Equation (28.6.4) determines numerically the function

$$\Delta n_i = \Delta n_i \left(u_{(i)}, \theta_{(i)} \right) \quad (i = 1, \ldots, k) \tag{28.6.5}$$

that represents the deviations of the real surface for each point of the grid.

28.7 MINIMIZATION OF DEVIATIONS

The procedure of minimization of deviations can be represented in two stages: (i) determination of variations of the theoretical surface caused by changes in applied machine-tool settings, and (ii) minimization of deviations of the real surface by appropriate correction of machine-tool settings.

We consider that the theoretical surface is represented in S_t as

$$\mathbf{r}_t = \mathbf{r}_t(u, \theta, d_j) \quad (j = 1, \ldots, m) \tag{28.7.1}$$

where parameters d_j are the machine-tool settings. The surface variations are represented by

$$\delta \mathbf{r}_t = \frac{\partial \mathbf{r}_t}{\partial u} \delta u + \frac{\partial \mathbf{r}_t}{\partial \theta} \delta \theta + \sum_{j=1}^{m} \frac{\partial \mathbf{r}_t}{\partial d_j} \delta d_j. \tag{28.7.2}$$

We multiply both sides of Eq. (28.7.2) by the surface unit normal $\mathbf{n}_t$ and take into

account that $\partial \mathbf{r}_t / \partial \theta \cdot \mathbf{n}_t = \partial \mathbf{r}_t / \partial u \cdot \mathbf{n}_t = 0$ because $\partial \mathbf{r}_t / \partial \theta$ and $\partial \mathbf{r}_t / \partial u$ lie in the plane that is tangent to the surface. Then we obtain

$$\delta \mathbf{r}_t \cdot \mathbf{n}_t = \left(\sum_{j=1}^{m} \frac{\partial \mathbf{r}_t}{\partial d_j} \cdot \mathbf{n}_t \right) \delta d_j = \sum_{j=1}^{m} a_j \, \delta d_j. \qquad (28.7.3)$$

We can now consider a system of k linear equations in m unknowns ($m \ll k$) of the following structure:

$$a_{11} \delta d_1 + a_{12} \delta d_2 + \cdots + a_{1m} \delta d_m = b_1$$
$$\vdots \qquad (28.7.4)$$
$$a_{k1} \delta d_1 + a_{k2} \delta d_2 + \cdots + a_{km} \delta d_m = b_k.$$

Here,

$$b_i = \Delta n_i = \left(\mathbf{R}_{mi}^* - \mathbf{R}_{mi} \right) \cdot \mathbf{n}_{mi}. \qquad (28.7.5)$$

where i designates the number of grid points; a_{ij} $(i = 1, \ldots, k; j = 1, \ldots, m)$ represent the dot product of partial derivatives $\partial \mathbf{r}_t / \partial d_j$ and unit normal $\mathbf{n}_t$.

The system of linear equations (28.7.4) is overdetermined because $m \ll k$. The essence of the procedure of minimization of deviations is the determination of such unknowns δd_j $(j = 1, \ldots, m)$ that will minimize the difference between the left and right sides of Eqs. (28.7.4). The solution can be accomplished by the method of least squares.

The success of minimization of deviations depends on the number of parameters that may be varied (the number of machine-tool settings that may be corrected). The number of pinion machine-tool settings is larger than that for the gear. The minimization of deviations can be performed for each pinion tooth side separately. However, it must be performed simultaneously for both sides of the gear tooth because the gear is usually cut by the duplex method. For these reasons the minimization of deviations is more effective for the pinion than it is for the gear.

References

Argyris, J., Litvin, F. L., Peng, A., & Stadtfeld, H. J. 1998. Axes of Meshing and Their Application in Theory of Gearing. *Computer Methods in Applied Mechanics and Engineering*, **163**(1–4), 293–310.

Argyris, J., Fuentes, A., & Litvin, F. L. 2002. Computerized Integrated Approach for Design and Stress Analysis of Spiral Bevel Gears. *Computer Methods in Applied Mechanics and Engineering*, **191**, 1057–1095.

Baxter, M. L. 1961. Basic Geometry and Tooth Contact of Hypoid Gears. *Industrial Mathematics*, 1–28.

Chatterjee, G., & Tsai, L.-W. 1996. Computer-Aided Sketching of Epicyclic-Type Automatic Transmission Gear Trains. *ASME Journal of Mechanical Design*, **118**(3), 405–411.

Chen, J.-L., & Tseng, C.-H. 2000. Design Considerations for Assembly in Planetary Gear Trains. *Proceedings of International Conference of Gearing, Transmissions, and Mechanical Systems*, pp. 157–166. Nothingham Trent University, UK.

Cheng, H. H. 1992. Derivation of Explicit Solution of the Inverse Involute Function and Its Application. *Advancing Power Transmission into the 21st Century, ASME DTC 1992*, **1**, 161–168.

Cheng, H. H., & Gupta, K. C. 1989. An Historical Note on Finite Rotations. *ASME Journal of Applied Mechanics*, **56**, 139–145.

Chironis, N. P. 1967. Design of Novikov Gears. In *Gear Design and Application*. New York: McGraw-Hill.

Colbourne, J. R. 1987. *The Geometry of Involute Gears*. Berlin: Springer-Verlag.

Colbourne, J. R. 1989. The Use of Oversize Hobs to Cut Worm Gears. *AGMA Paper 89FTM8*.

Davidov, J. S. 1950. *Noninvolute Gearing*. Mashgiz Moscow (in Russian).

Davidov, J. S. 1963. *The Generation of Conjugate Surfaces by Two Rigidly Connected Tool Surfaces*. Vestnik Mashinostroyenia (in Russian).

Demenego, A., Vecchiato, D., Litvin, F. L., Nervegna, N., & Manco, S. 2002. Design and Simulation of Meshing of a Cycloidal Pump. *Mechanism and Machine Theory*, **37**, 311–332.

Denavit, J., & Hartenberg, R. S. 1955. A Kinematic Notation for Lower Pair Mechanisms Based on Matrices. *ASME Journal of Applied Mechanics*, **22**, 215–221.

Dudley, D. W. 1962. *Gear Handbook. The Design, Manufacture, and Application of Gears*. New York: McGraw-Hill.

Favard, J. 1957. *Course of Local Differential Geometry*. Paris: Gauthier-Villars (in French translated into Russian).

Feng, P.-H., Litvin, F. L., Townsend, D. P., & Handschuh, R. F. 1999. Determination of Principal Curvatures and Contact Ellipses for Profile Crowned Helical Gears. *ASME Journal of Mechanical Design*, **121**(1), 107–111.

Finikov, S. P. 1961. *Differential Geometry*. Moscow University (in Russian).

Fuentes, A., Litvin, F. L., Mullins, B. R., Woods, R., & Handschuh, R. F. 2002. Design and Stress Analysis of Low-Noise Adjusted Bearing Contact Spiral Bevel Gears. *ASME Journal of Mechanical Design*, **124**(Sep.), 524–532.

Goldrich, R. N. 1989. Theory of 6-axis CNC Geneneration of Spiral Bevel and Hypoid Gears. *AGMA Paper 89FTM9*.

Goldstein, H. 1950. *Classical Mechanics,* 2nd ed. Reading, MA: Addison-Wesley.

Gosselin, C., Shiono, Y., Nonaka, T., & Kubo, A. 1996. A Computer Based Approach Aimed at Reproducing Master Spiral Bevel and Hypoid Pinions and Gears. *AGMA Paper 96FTM1*.

Hall, A. S. 1966. *Kinematics and Linkage Design.* West Lafayette, IN: Balt Publishers.

Handschuh, R. F., & Litvin, F. L. 1991. A Method for Determining Spiral-Bevel Gear Tooth Geometry for Finite Element Analysis. *NASA Technical Paper 3096, AVSCOM Technical Report 91-C-020*.

Handschuh, R. F., Lewicki, D. G., Heath, G. F., & Bossler Jr., R. B. 1996. Experimental Evaluation of Face Gears for Aerospace Drive System Applications. *ASME Power Transmission and Gearing Conference*, **88**, 581–588.

Hibbit, Karlsson & Sirensen, Inc. 1998. *ABAQUS/Standard User's Manual.* 1800 Main Street, Pawtucket, RI 20860–4847.

Hori, K., & Hayashi, I. 1996a. Improvement of Efficiency of 3K-Type Mechanical Paradox Planetary Gear Drive by Equalizing Approach and Recess-Contact Ratios. *Proceedings of ASME Power Transmission and Gearing Conference*, **88**.

Hori, K., & Hayashi, I. 1996b. Optimization of the Profile-Shift Coefficient of Conventional Mechanical Paradox Planetary Gear Drives to Obtain the Maximum Efficiency. *Proceedings of ASME Power Transmission and Gearing Conference*, **88**.

Ishida, T., & Hidaka, T. 1992. Effects of Assembly and Manufacturing Errors on Transmission Error of Planetary Gears. *Proceedings of ASME Power Transmission and Gearing Conference*, **43**.

Kahraman, A. 1994. Load Sharing Characteristics of Planetary Transmissions. *Mechanism and Machine Theory*, **129**(8), 1151–1165.

Kahraman, A., & Vijajakar, S. 2001. Effect of Internal Gear Flexibility on the Quasi-Static Behaviour of a Planetary Gear Set. *ASME Journal of Mechanical Design*, **123**(Sep.), 408–415.

Kislitsin, S. G. 1955. Aproximate Solution of Equation $\varphi(\varphi(x)) = f(x)$. *Proceedings of Leningrad Pedagogical Institute*, **90**.

Korn, G. A., & Korn, T. M. 1968. *Mathematics Handbook for Scientists and Engineers,* 2nd ed. New York: McGraw-Hill.

Krenzer, T. J. 1981. *Tooth Contact Analysis of Spiral Bevel and Hypoid Gears Under Load.* Rochester, New York: The Gleason Works.

Kudrjavtzev, V. N. *et al.* 1993. *Computation of Design of Gear Reducers.* Politechnika S. Peterburg (in Russian).

Lin, J., & Parker, R. G. 1999. Analytical Characterization of the Unique Properties of Planetary Gear Free Vibration. *Journal of Vibration and Acoustics*, **121**(July), 316–321.

Litvin, F. L. 1955. Application of Matrices and Dual Number Calculations to Analysis of Spatial Gearings. *Proceedings of Leningrad Polytechnic Institute*, **182** (in Russian).

Litvin, F. L. 1956. *Noncircular Gears: Design, Theory of Gearing, and Manufacture*, 2nd ed. Gos Tech Isdat, Leningrad, Moscow (in Russian).

Litvin, F. L. 1962. The Investigation of the Geometric Properties of a Variety of Novikov Gearing. *Proceedings of the Leningrad Mechanical Institute* (in Russian).

Litvin, F. L. 1968. *Theory of Gearing*, 2nd ed. Moscow: Nauka (in Russian).

Litvin, F. L. 1969. Die Beziehungen Zwischen den Krümmungen der Zahnoberflächen be Räumlichen Versahnungen (Relation Between Curvatures of Tooth Surfaces in Spatial Gearing). *Zeitschrift fur Angewandte Mathematik und Mechanik*, **49**, 685–690 (in German).

Litvin, F. L. 1975. Determination of Envelope of Characteristics of Mutually Enveloping Surfaces. *Mathematics*, **161**(10), 47–50 (in Russian).

Litvin, F. L. 1989. *Theory of Gearing.* Washington, D.C.: NASA RP-1212 (AVSCOM 88-C-C035).

Litvin, F. L. 1994. *Gear Geometry and Applied Theory.* Englewood Cliffs, New Jersey: Prentice Hall, Inc.

Litvin, F. L. 1998. Development of Gear Technology and Theory of Gearing. *NASA Reference Publication 1406, ARL-TR-1500.*

Litvin, F. L., & Pavlov, G. G., 1951. Machine for Hobbing of Noncircular Gears with Convex Centrodes. *Ministry of Machine Building of USSR, Invention No. 97454.*

Litvin, F. L., Petrov, K. M., & Ganshin, V. A. 1974. The Effect of Geometrical Parameters of Hypoid and Spiroid Gears on Their Quality Characteristics. *ASME Journal of Engineering for Industry*, **96**, 330–334.

Litvin, F. L., Krylov, N. N., & Erikhov, M. L. 1975. Generation of Tooth Surfaces by Two-Parameter Enveloping. *Mechanism and Machine Theory*, **10**(5), 365–373.

Litvin, F. L., & Gutman, Y. 1981. Methods of Synthesis and Analysis for Hypoid Gear Drives of Formate and Helixform. Parts 1, 2, and 3. *ASME Journal of Mechanical Design*, **103**(1), 83–113.

Litvin, F. L., & Tsay, C.-B. 1985. Helical Gears with Circular Arc Teeth: Simulation of Conditions of Meshing and Bearing Contact. *ASME Journal of Mechanisms, Transmissions, and Automation in Design*, **107**, 556–564.

Litvin, F. L., Zhang, Y., Lundy, M., & Heine, C. 1988. Determination of Settings of a Tilted Head Cutter for Generation of Hypoid and Spiral Bevel Gears. *ASME Journal of Mechanism, Transmissions, and Automation in Design*, **110**, 495–500.

Litvin, F. L., Zhang, Y., Krenzer, T. J., & Goldrich, R. N. 1989. Hypoid Gear Drive with Face-Milled Teeth: Condition of Pinion Non-Undercutting and Fillet Generation. *AGMA Paper 89FTM7.*

Litvin, F. L., Chaing, W.-S., Lundy, M., & Tsung, W.-J. 1990. Design of Pitch Cones for Face-hobbed Hypoid Gears. *ASME Journal of Mechanical Design*, **112**, 413–418.

Litvin, F. L., & Zhang, Y. 1991. Local Synthesis and Tooth Contact Analysis of Face-Milled Spiral Bevel Gears. *NASA Contractor Report 4342, AVSCOM Technical Report 90-C-028.*

Litvin, F. L., & Kin, V. 1992. Computerized Simulation of Meshing and Bearing Contact for Single-Enveloping Worm-Gear Drives. *ASME Journal of Mechanical Design*, **114**, 313–316.

Litvin, F. L., Zhang, Y., Wang, J.-C., Bossler, R. B., & Chen, Y.-J., D. 1992. Design and Geometry of Face-Gear Drives. *ASME Journal of Mechanical Design*, **114**, 642–647.

Litvin, F. L., & Hsiao, C.-L. 1993. Computerized Simulation of Meshing and Bearing Contact of Enveloping Gear Tooth Surfaces. *Computer Methods in Applied Mechanics and Engineering*, **102**(Feb.), 337–366.

Litvin, F. L., Chen, N. X. Zhang, Y., Krenzer, T. J., & Handschuh, R. F. 1993a. Computerized Generation of Surfaces with Optimal Approximation to Ideal Surfaces. *Computer Methods in Applied Mechanics and Engineering*, **110**, 39–55.

Litvin, F. L., Kuan, C., Wang, C. C., Handschuh, R. F., Masseth, J., & Maruyama, N. 1993b. Minimization of Deviations of Gear Real-Tooth Surfaces Determined by Coordinate Measurements. *ASME Journal of Mechanical Design*, **115**(4), 995–1001.

Litvin, F. L., Hsiao, C.-L., Wang, J.-C. & Zhou, X 1994. Computerized Simulation of Generation of Internal Involute Gears and Their Assembly. *ASME Journal of Mechanical Design*, **116**(3), 683–689.

Litvin, F. L., & Lu, J. 1995. Computerized Design and Generation of Double Circular-Arc Helical Gears With Low Transmission Errors. *ASME Journal of Mechanical Design*, **127**(1-4), 57–86.

Litvin, F. L., Chen, N. X., Lu, J., & Handschuh, R. F. 1995. Computerized Design and Generation of Low-Noise Helical Gears with Modified Surface Topology. *ASME Journal of Mechanical Design*, **117**(2), 254–261.

Litvin, F. L., & Seol, I. H. 1996. Computerized Determination of Gear Tooth Surface as Envelope to Two Parameter Family of Surfaces. *Computer Methods in Applied Mechanics and Engineering*, **138**(1-4), 213–225.

Litvin, F. L., Wang, A. G., & Handschuh, R. F. 1998a. Computerized Generation and Simulation of Meshing and Contact of Spiral Bevel Gears with Improved Geometry. *Journal of Computer Methods in Applied Mechanics and Engineering*, **158**(1–2), 35–64.

Litvin, F. L., Hsiao, C.-L., & Ziskind, M. D. 1998b. Computerized Overwire (Ball) Measurement of Tooth Thickness of Worms, Screws and Gears. *Mechanism and Machine Theory*, **33**(6), 851–877.

Litvin, F. L., Lu, J., Townsend, D. P., & Howkins, M. 1999. Computerized Simulation of Meshing of Conventional Helical Involute Gears and Modification of Geometry. *Mechanism and Machine Theory*, **34**(1), 123–147.

Litvin, F. L., Chen, Y.-J., Heath, G. F., Sheth, V. J., & Chen, N. 2000a. Apparatus and Method for Precision Grinding Face Gears. *USA Patent 6,146,253*.

Litvin, F. L., Lian, Q., & Kapelevich, A. L. 2000b. Asymmetric Modified Spur Gear Drives: Reduction of Noise, Localization of Contact, Simulation of Meshing and Stress Analysis. *Computer Methods in Applied Mechanics and Engineering*, **188**(1–3), 363–390.

Litvin, F. L., Feng, P.-H., & Lagutin, S. A. 2000c. Computerized Generation and Simulation of Meshing and Contact of New Type of Novikov–Wildhaber Helical Gear. *NASA/CR-2000-209415, ARL-CR-428*.

Litvin, F. L., Fan, Q., Vecchiato, D., Demenego, A., Handschuh, R. F., & Sep, T. M. 2001a. Computerized Generation and Simulation of Meshing of Modified Spur and Helical Gears Manufactured by Shaving. *Computer Methods in Applied Mechanics and Engineering*, **190**, 5037–5055.

Litvin, F. L., Demenego, A., & Vecchiato, D. 2001b. Formation by Branches of Envelope to Parametric Families of Surfaces and Curves. *Computer Methods in Applied Mechanics and Engineering*, **190**, 4587–4608.

Litvin, F. L., *et al.* 2001c. Helical and Spur Gear Drive with Double Crowned Pinion Tooth Surfaces and Conjugated Gear Tooth Surfaces. *US Patent Office, Patent No. 6,205,879*, March 27.

Litvin, F. L., Fuentes, A., Demenego, A., Vecchiato, D., & Fan, Q. 2001d. New Developments in the Design and Generation of Gear Drives. *Mechanical Engineering Science, Part C., Proceedings of the Institution of Mechanical Engineers*, **215**(C7), 747–758.

Litvin, F. L., Fuentes, A., Fan, Q., & Handschuh, R. F. 2002a. Computerized Design, Simulation of Meshing and Contact, and Stress Analysis of Face-Milled Formate Generated Spiral Bevel Gears. *Mechanism and Machine Theory*, **37**(5), 441–459.

Litvin, F. L., Fuentes, A., Zanzi, C., & Pontiggia, M. 2002b. Design, Generation, and Stress Analysis of Two Versions of Geometry of Face-Gear Drives. *Mechanism and Machine Theory*, **37**, 1179–1211.

Litvin, F. L., Fuentes, A., Zanzi, C., Pontiggia, M., & Handschuh, R. F. 2002c. Face Gear Drive with Spur Involute Pinion: Geometry, Generation by a Worm, Stress Analysis. *Computer Methods in Applied Mechanics and Engineering*, **191**, 2785–2813.

Litvin, F. L., Fuentes, A., Gonzalez-Perez, I., Carnevali, L., & Sep, T. M. 2002d. New Version of Novikov-Wildhaber Helical Gears: Computerized Design, Simulation of Meshing and Stress Analysis. *Computer Methods in Applied Mechanics and Engineering*, **191**, 5707–5740.

Litvin, F. L., Vecchiato, D., Demenego, A., Karedes, E., Hansen, B., & Handschuh, R. F. 2002e. One Stage Planetary Gear Train with Improved Conditions of Load Distribution and Reduced Transmission Errors. *ASME Journal of Mechanical Design*, **124**, 745–752.

Litvin, F. L., Fuentes, A., Gonzalez-Perez, I., Carnevali, L., Kawasaki, K., & Handschuh, R. F. 2003. Modified Involute Helical Gears: Computerized Design, Simulation of Meshing, and Stress Analysis. *Computer Methods in Applied Mechanics and Engineering,* **192**, 3619–3655.

Lynwander, P. 1983. Gear Drive System Design and Application. New York: Marcel Dekker Inc.

Miller, E. W. 1942. Hob for Generation of Crown Gears. *USA Patent 2,304,588*, December 8.

More, J. J., Garbow, B. S., & Hilstrom, K. E. 1980. User Guide for MINPACK-1. Argonne, IL: Argonne National Laboratory, Report ANL-80-74.

NIEMANN, G., & HEYER, E. 1953. Investigations of Worm Gears. *VDI 95*, 141–157.

NIEMANN, G. 1961. Novikov Gear System and Other Special Gear Systems for High Load Carrying Capacity. *VDI Berichte*, **47**.

NOVIKOV, M. L. 1956. USSR Patent No. 109,750.

NUTBOURNE, A. W., & MARTIN, R. R. 1988. *Differential Geometry Applied to Curve and Surface Design.* Vol. 1. Chichester, West Sussex, England: Ellis Horwood Limited.

POLDER, J. W. 1991. Interference of Internal Gears. In *Dudley's Gear Handbook,* P. Townsend, ed. New York: McGraw-Hill.

PRESS, W. H., TEUKOLSKY, S. A., VETTERLING, W. T., & FLANNERY, B. P. 1992. *Numerical Recipes in Fortran 77: The Art of Scientific Computing*, 2nd ed. New York: Cambridge University Press.

RASHEVSKI, P. K. 1956. *Course of Differential Geometry*, 4th ed. State Publishing House of Technical and Theoretical Literature, Moscow (in Russian).

SAADA, A., & VELEX, P. 1995. An Extended Model for the Analysis of the Dynamic Behavior of Planetary Trains. *ASME Journal of Mechanical Design*, **117**(June), 241–247.

SCHREIER, G. 1961. *Stirnrad-Verzahnung.* Berlin: *VEB Verlag "Technik."*

SEOL, I. H., & LITVIN, F. L. 1996. Computerized Design, Generation and Simulation of Meshing and Contact of Worm-Gear Drives with Improved Geometry. *Computer Methods in Applied Mechanics and Engineering*, **138**(1-4), 73–103.

SHABANA, A. A. 1989. *Dynamics of Multibody Systems.* New York: Wiley.

SHEVELEVA, G. I. 1999. *Theory of Formation and Contact of Moving Bodies.* Moscow State Technological University Stankin, Moscow (in Russian).

SMITH, W. C. 1995. The Math of Noncircular Gearing. *Gear Technology,* **1**(January/February).

STADTFELD, H. J. 1993. *Handbook of Bevel and Hypoid Gears: Calculation, Manufacturing, and Optimization.* Rochester, New York: Rochester Institute of Technology.

STADTFELD, H. J. 1995. *Gleason Bevel Gear Technology – Manufacturing, Inspection and Optimization, Collected Publications.* Rochester, New York: The Gleason Works.

STOSIC, N. 1998. On Gearing of Helical Screw Compressor Rotors. *Proceedings of IMechE, Journal of Mechanical Engineering Science*, **212**, 587–594.

STRANG, G. 1988. *Linear Algebra and Its Application* 3rd. ed. San Diego: Harcourt Brace Jovanovich.

SUH, C. H., & RADCLIFFE, E. 1978. Kinematics and Mechanism Design. New York: Wiley.

TOWNSEND, D. P. 1991. *Dudley's Gear Handbook,* 2nd ed. New York: McGraw-Hill.

VECCHIATO, D., DEMENEGO, A., ARGYRIS, J., & LITVIN, F. L. 2001. Geometry of a Cycloidal Pump. *Computer Methods in Applied Mechanics and Engineering*, **190**(18–19), 2309–2330.

VELEX, P., & FLAMAND, L. 1996. Dynamic Response of Planetary Trains to Mesh Parametric Excitations. *ASME Journal of Mechanical Design*, **118**(March), 7–14.

VIGODSKY, M. Y. 1949. *Differential Geometry.* Leningrad: Gos Tech Isdat.

VISUAL NUMERICS, INC. 1998. IMSL Fortran 90 MP Library, v. 3.0. info@boulder.vni.com.

WELLS, C. F., & SHOTTER, B. A. 1962. The Development of 'Circarc' Gearing. London: *AEI Engineering.*

WILDHABER, E. 1926. Helical Gearing. *United States Patent Office, Patent No. 1,601,750.*

WILDHABER, E. 1956. Surface Curvature. *Production Engineering*, **27**, 184–191.

WILLIS, R. I. 1841. *Principles of Mechanisms.* London: Longman, Green and Co.

WINTER, H., & JOOMAN, J. 1961. Tools for Making Helical Circular Arc Spur Gears. *VDI Berichte*, **47**.

ZALGALLER, V. A. 1975. *Theory of Envelopes.* Moscow: Publishing House Nauka (in Russian).

ZALGALLER, V. A., & LITVIN, F. L. 1977. Sufficient Condition of Existence of Envelope to Contact Lines and Edge of Regression on the Surface of the Envelope to the Parametric Family of Surfaces Represented in Parametric Form. *Proceedings of Universities: Mathematics* (in Russian), **178**(3), 20–23.

ZHANG, Y., LITVIN, F. L., & HANDSCHUH, R. F. 1995. Computerized Design of Low-Noise Face-Milled Spiral Bevel Gears. *Mechanism and Machine Theory*, **30**(8), 1171–1178.

ZIENKIEWICZ, O. C., & TAYLOR, R. L. 2000. *The Finite Element Method*, 5th ed. New York: Wiley.

Index